AD-A071 047 ROCKWELL INTERNATIONAL THOUSAND OAKS CALIF SCIENCE --ETC F/G 14/2
PROCEEDINGS OF THE ARPA/AFML REVIEW OF PROGRESS IN QUANTITATIVE--ETC(U)
JAN 79 D O THOMPSON F33615-74-C-5180
UNCLASSIFIED SC595.51AR AFML-TR-78-205 NL

1 OF 6
AD A071047

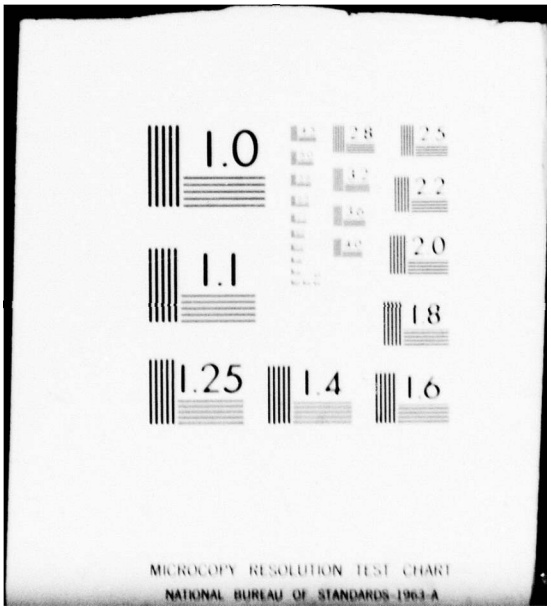
1.0
1.1
1.25
1.4
1.6
2.2
2.0
1.8
MICROCOPY RESOLUTION TEST CHART
NATIONAL BUREAU OF STANDARDS 1963-A

AFML-TR-78-205

PROCEEDINGS OF THE ARPA/AFML REVIEW OF PROGRESS IN QUANTITATIVE NDE

Science Center, Rockwell International
1049 Camino Dos Rios
Thousand Oaks, California 91360

JANUARY 1979

Fourth Annual Report 1 July 1977 - 30 June 1978

Submitted to: AIR FORCE PROJECT ENGINEER
AIR FORCE MATERIALS LABORATORY
AIR FORCE WRIGHT AERONAUTICAL LABORATORIES
AIR FORCE SYSTEMS COMMAND
WRIGHT-PATTERSON AIR FORCE BASE, OHIO 45433

Prepared for: ADVANCED RESEARCH PROJECTS AGENCY
1400 WILSON BOULEVARD
ARLINGTON, VIRGINIA 22209

AIR FORCE MATERIALS LABORATORY
AIR FORCE WRIGHT AERONAUTICAL LABORATORIES
AIR FORCE SYSTEMS COMMAND
WRIGHT-PATTERSON AIR FORCE BASE, OHIO 45433

NOTICE

When Government drawings, specifications, or other data are used for any purpose other than in connection with a definitely related Government procurement operation, the United States Government thereby incurs no responsibility nor any obligation whatsoever; and the fact that the government may have formulated, furnished, or in any way supplied the said drawings, specifications, or other data, is not to be regarded by implication or otherwise as in any manner licensing the holder or any other person or corporation, or conveying any rights or permission to manufacture, use, or sell any patented invention that may in any way be related thereto.

This report has been reviewed by the Information Office (OI) and is releasable to the National Technical Information Service (NTIS). At NTIS, it will be available to the general public, including foreign nations.

This technical report has been reviewed and is approved for publication.

Thomas J. Moran
THOMAS J. MORAN
Project Engineer

D. M. FORNEY, Jr., Chief
Nondestructive Evaluation Branch
Metals and Ceramics Division

FOR THE COMMANDER

Lawrence N. Hjelm
LAWRENCE N. HJELM
Acting Chief
Metals and Ceramics Division

"If your address has changed, if you wish to be removed from our mailing list, or if the addressee is no longer employed by your organization please notify AFML/LLP *,W-PAFB, OH 45433 to help us maintain a current mailing list".*

Copies of this report should not be returned unless return is required by security considerations, contractual obligations, or notice on a specific document.

AIR FORCE/56780/20 June 1979 — 575

AD-A060 763

held 17-21 July 1978, La Jolla, California.

UNCLASSIFIED
SECURITY CLASSIFICATION OF THIS PAGE (When Data Entered)

REPORT DOCUMENTATION PAGE	READ INSTRUCTIONS BEFORE COMPLETING FORM
1. REPORT NUMBER: AFML-TR-78-205	2. GOVT ACCESSION NO. / 3. RECIPIENT'S CATALOG NUMBER
4. TITLE (and Subtitle): PROCEEDINGS OF THE ARPA/AFML REVIEW OF PROGRESS IN QUANTITATIVE NONDESTRUCTIVE EVALUATION	5. TYPE OF REPORT & PERIOD COVERED: Fourth Annual Report 07/01/77 thru 06/30/78
	6. PERFORMING ORG. REPORT NUMBER: SC595.51AR
7. AUTHOR(s): Donald O. Thompson, Program Manager	8. CONTRACT OR GRANT NUMBER(s): F33615-74-C-5180
9. PERFORMING ORGANIZATION NAME AND ADDRESS: Science Center, Rockwell International, 1049 Camino Dos Rios, Thousand Oaks, California 91360	10. PROGRAM ELEMENT, PROJECT, TASK AREA & WORK UNIT NUMBERS: 7351
11. CONTROLLING OFFICE NAME AND ADDRESS: Advanced Research Projects Agency, 1400 Wilson Boulevard, Arlington, Virginia 22209	12. REPORT DATE: January 1979 13. NUMBER OF PAGES: 534
14. MONITORING AGENCY NAME & ADDRESS (if different from Controlling Office): Air Force Materials Laboratory, Air Force Systems Command, Wright-Patterson Air Force Base, Dayton, Ohio 45433	15. SECURITY CLASS. (of this report): UNCLASSIFIED 15a. DECLASSIFICATION/DOWNGRADING SCHEDULE

545p.

16. DISTRIBUTION STATEMENT (of this Report)

Approved for Public Release; Distribution Unlimited

Rept. no. 4 (Annual) 1 Jul 77-30 Jun 78

17. DISTRIBUTION STATEMENT (of the abstract entered in Block 20, if different from Report)

18. SUPPLEMENTARY NOTES

19. KEY WORDS (Continue on reverse side if necessary and identify by block number)

nondestructive evaluation; nondestructive testing; qualitative ultrasonics; signal processing; adhesive bonds; composites' residual stress; acoustic emission; reliability; quality

20. ABSTRACT (Continue on reverse side if necessary and identify by block number)

The edited transcripts of the ARPA/AFML Review of Quantitative Nondestructive Evaluation (NDE) held on July 17-21, 1978, at Scripps Institution of Oceanography, La Jolla, California, are presented in this document. Several key topics form the core of these presentations and discussions. They include quantitative ultrasonics, adhesives and composites, emissions related to failure prediction, residual stress, and reliability of ceramics. It is believed that this document provides a reasonable summary of NDE research and development currently underway.

DD FORM 1 JAN 73 1473 EDITION OF 1 NOV 65 IS OBSOLETE

UNCLASSIFIED
SECURITY CLASSIFICATION OF THIS PAGE (When Data Entered)

389 949

PREFACE

This report contains the edited transcripts of the Review of Progress in Quantitative NDE held at the Scripps Institution of Oceanography, July 17-21, 1978. The Review was sponsored by the Advanced Research Projects Agency and the Air Force Materials Laboratory as a part of the Interdisciplinary Program for Quantitative Flaw Definition, Contract No. F33615-74-C-5180. Arrangements for the Review were made by the Science Center, Rockwell International, host organization for the Interdisciplinary Program, and the Scripps Institution of Oceanography, Dr. William A. Nierenberg, Director.

The format selected for this review was the same as that adopted for the previous meeting at Cornell University. This format included a number of poster sessions in addition to the more traditional technical sessions. It has been found that the poster sessions provide a good way to accommodate the increased activity in this field while maintaining a forum that is highly conducive to technical interchange. As a further means of stimulating this exchange, a number of papers were included which are directly related to the principal technical interests of ARPA/AFML program even though they were not directly sponsored by ARPA/AFML.

The program emphasized several areas of progress in quantitative NDE. In addition to the work in quantitative ultrasonics, which has been a main program activity, new work in quantitative eddy current research and the methodology for the generation of rational accept/reject criteria were reported. In all these areas, strong emphasis is placed upon the physical interpretation of the quantitative measurements and their evaluation in terms of appropriate failure models. A session was also devoted to the presentation of work being pursued in reducing research results to practice, some of which is now beginning to flow from earlier work in the ARPA/AFML program as well as from other sources. This technology transition, as well as the research lead that is being developed, are both considered to be important products of this program.

Dr. James S. Kane, Associate Director for Basic Energy Sciences, Department of Energy, gave an excellent overview on the importance of NDE in energy systems. In his presentation, which is included in these Proceedings, he identified several areas of NDE activity which are of significance to the DoE in establishing safe and reliable energy systems at minimum cost. It is felt that this cross-stimulation with the ARPA/AFML work is highly beneficial for all, for there are many areas of commonality in which a problem solution generated in one program may benefit other programs of national interest. A series of short overviews of ongoing NDE research activities was given by a number of guests from overseas. These overviews also provided a beneficial cross-stimulation.

The organizers of the Review wish to acknowledge the financial support and encouragement provided by the Advanced Research Projects Agency and the Air Force Materials Laboratory and the technical participation of members of the Materials Research Council. Special thanks are due to Dr. Kane for his overview. The organizers also wish to thank speakers, session chairmen, authors of poster presentations, and participants who collaborated to provide a stimulating meeting. They wish to acknowledge with thanks the assistance of Mrs. Diane Harris who managed the organizational matters of the meeting, Mrs. Nadine Brinkman for her assistance at the meeting, and Mrs. Carmen Byrne and Mrs. Sarah Bergmann for the preparation of the Proceedings. They are also indebted to the management of the Scripps Institution of Oceanography, particularly Dr. William Nierenberg and Mr. Nelson Fuller, and to Mrs. Shirlee Long, UCSD, for their cooperative support in the conduct of the meeting.

Donald O. Thompson

Donald O. Thompson
Program Manager
Center for Advanced NDE

ADVANCED RESEARCH PROJECTS AGENCY/AIR FORCE MATERIALS LABORATORY

REVIEW OF PROGRESS IN QUANTITATIVE NDE

July 17 - 21, 1978
Scripps Institution of Oceanography
University of California
La Jolla, California

TABLE OF CONTENTS

SESSION VI - NDE FOR ADVANCED MATERIALS (POSTER) PAGE

SESSION X - FUNDAMENTALS AND NEW TECHNIQUES (POSTER) (CONTINUED) PAGE

THE DARPA INVESTMENT STRATEGY IN QUANTITATIVE NDE

Michael J. Buckley
Defense Advanced Research Projects Agency
Arlington, Virginia 22209

ABSTRACT

Some of the contributions that quantitative NDE may make in support of the mission of the Department of Defense are presented. In addition, the general DARPA investment criteria is reviewed along with the current and possible future directions of the DARPA NDE program.

INTRODUCTION

This morning I would like to attempt to provide you with some insight into the quantitative NDE program supported by the Defense Advanced Research Projects Agency. Specifically, I will address the following areas:

1. A personal view of the potential role of quantitative NDE on the mission of the Department of Defense or why invest in NDE?

2. A discussion of the criteria by which we make our research investments in this area.

3. A short overview of our present program, and

4. Some of the future directions and/or opportunities that this program must address in the not-too-distant future.

WHY INVEST IN NDE?

This subject could easily form the basis for an extensive monolog if not a large book; however, if you will permit me to present a rather simplistic, eclectic rationale, I believe I can relate progress in NDE to our overall military capability.

The initial budget request for the Department of Defense for FY79 may be displayed in a simplified manner as inputs consisting of allocations for RDT&E, Procurement, Operation and Maintenance and Military Pay and outputs consisting of Strategic, General Purpose and Airlift and Sealift forces.

However, the effectiveness of the outputs of the Department of Defense, i.e., the military forces) are significantly reduced due to scheduled and unscheduled maintenance. The availability of weapons systems certainly varies, but an overall estimate of 70% would not be unreasonable. Therefore, we are not obtaining perhaps 30% of the military capability achievable if all our systems were failure and maintenance free. Clearly, if we could predict the failure of systems and schedule the necessary maintenance, we should be able to increase the availability of weapons systems and achieve a significantly enhanced military capability for the same or possibly lower defense costs. In addition, the ability to predict failure has a major impact on all of us in its intrinsic ability to increase the safety of systems, such as aircraft, automobiles, nuclear reactors, etc.

We have also learned, in principal, how this technology may play a key role in minimizing life cycle costs by permitting us to make conscious trade-offs between acquisition and in-service related costs. Conceptually, there is an optimum inspection criteria that minimizes the total life cycle cost of a component by minimizing the sum of the manufacturing and failure related costs.

The major technical challenges limiting the application of this methodology include the problem of obtaining the necessary data, such as the initial flaw distribution, required for the calculation of the probability of failure, as well as the practical problem of assigning reasonable failure related costs.

In summary, we have two major reasons for investing in the development of a quantitative NDE capability: the potential of increasing the reliability and availability of weapons systems and as a necessary component in a life cycle costs minimization effort.

As pointed out in a recent NMAB report, the cost savings possible with advanced NDE will not be obtained by reducing the already small direct costs currently associated with inspection, but rather, by taking advantage of the leverage this technology provides in developing a holistic approach to life cycle management.

INVESTMENT CRITERIA

Now I would like to discuss briefly our research investment criteria at DARPA and the scope of our technical interests in this area.

We must ask ourselves four basic investment questions before initiating any new program at DARPA. They are:

1. What are your trying to do (objectives in terms of today's capabilities)?

2. What makes your approach unique (reasons for confidence in view of risks)?

3. Assuming success, what difference will it make (translation of technology impact - market question)?

4. When can we expect results and how much will it cost (milestone plans)?

In addition, it should be noted that DARPA is charged with fulfilling the corporate or central research function for DoD and does not generally support programs that may only impact one of the Services or is aimed at solving a specific Service problem.

In the area of NDE, we do not support programs that are aimed at increasing the sensitivity of non-quantitative NDE techniques or reducing the cost of using conventional NDE procedures. Rather, our efforts are focussed on developing and demonstrating a quantitative measurement capability so that we will have a rational basis for making accept/reject decisions.

There is one other major consideration that I personally look for, and that is a champion, a person who is committed to achieving the goals of the program and has committed his professional career to that end. The next most important attribute is good communication between the sponsor and the research performer. All too often, we do not achieve the desired objectives because they were never fully understood by both parties.

THE PRESENT DARPA PROGRAM IN NDE

The present DARPA supported program in NDE primarily utilizes ultrasonics or stress wave propagation to inspect a structure. The decision to emphasize one technical approach was a conscious one in that it was decided that ultrasonics has the greatest ultimate potential, and the area of greatest interest in research laboratories. It was also decided that we would not disperse our resources among too many approaches in order to minimize the possibility that not meeting the objectives was due to financial rather than technical limitations.

The program we are reviewing at this meeting has formed the core of our investment in the NDE science base. Perhaps the greatest achievement of this program is that NDE now is a reasonably acceptable area in which to perform research. The joint support of this research by DARPA and the Air Force is precedent-setting and I believe has significantly contributed to the overall success of this effort. Since this meeting is the technical forum in which this program is reviewed, I will not attempt to outline the objectives and scope of this program. We have enlarged the initial scope of the program somewhat in that we now have a growing effort utilizing electromagnetic inspection techniques for surface flaw characterization. Hopefully, in this program, we will develop methodologies that will permit us to use whatever combination of techniques is necessary in order to obtain the required data for the characterization of structural defects.

We have increased our investments in demonstration test beds significantly in the last year. We are now supporting an engine disk "retirement for cause" study with Failure Analysis Associates, as well as two ultrasonic test beds; one with the Rockwell Science Center and the other with Adaptronics and Battelle NW. There are more detailed presentations scheduled during this meeting on each of these programs. So once again, I will defer to other speakers for a detailed discussion of the objectives and approaches.

Another program that will be presented during this meeting is one with Battelle NW to develop an inflight Acoustic Emission System for use on an Australian Air Force jet trainer.

We are planning to initiate a program to develop a portable ultrasonic imaging system that will have the capability of replacing conventional "A" scan pulse echo systems for a wide variety of applications.

The DARPA investment in NDE has been growing rapidly. In FY 75, the NDE program was funded at slightly less than $500,000 while in FY 79, the program has grown to an expenditure rate of over $2,500,000 per year.

FUTURE DIRECTIONS/OPPORTUNITIES

In the following discussion of future directions, it must be understood that there are many technical, financial and institutional issues that could cause a radical change in our program. However, at this point in time, I can describe how I see this program evolving.

Our support for the NDE Science Base I see focusing to a large degree on coupling the NDE measurement tasks with the "effect of defects" area. The program that Tony Evans will present on the NDE of ceramic components is one example of the type of program I would like to see for all structural materials. I believe it is time we broke down the artificial barriers between the NDE and life prediction or fracture mechanics community and developed a new technology base that can actually be utilized for quantitative life prediction.

The insights necessary to develop and implement rational accept/reject criteria will only be developed by a collection of a few individuals willing and able to chart new areas in materials sciences. We are going to have to work closely with the Services to arrange for tri-Service support of this program, since DARPA, by its charter, cannot institutionalize research and that is just what is needed today.

I expect our investments to shift more towards the demonstration test bed area in such areas as engine disk retirement for cause, inflight monitoring, and in process inspection and control.

There is one additional horizon or goal that deserves special mention - and that is the coupling of a quantitative life prediction capability into the design phase. It is clear that we gain the greatest benefit at the least cost by making the "right" design initially. How do we incorporate advanced manufacturing methods, NDE capabilities and inspection intervals in the design process, so that we can be confident of obtaining a given level of reliability for a system in the design phase, rather than only after it is deployed. We are still seeking the ability to manufacture Oliver Wendell Holmes' "one-hoss shay."

BALANCING TECHNOLOGICAL OPPORTUNITIES VS. OPERATIONAL REQUIREMENTS: AN AFML CHALLENGE

T. J. Moran
Air Force Materials Laboratory, AFML/LLP
Wright-Patterson AFB, OH 45433

ABSTRACT

The mission of the NDE Branch of the Air Force Materials Laboratory is twofold: first, to support the overhaul and maintenance functions, and second, to provide new technology to allow the development of more durable and higher performance equipment. The lack of a mature NDE technology base, coupled with identifiable future needs, necessitates a long term commitment to providing generic capabilities. However, the severity of present day problems and the high payoff which would result from their solution, creates a strong demand for programs aimed at short term results. The attempt by the Materials Laboratory to balance these competing demands will be discussed. In addition, a potential application of quantitative NDE to an Air Force problem will be discussed in terms of the NDE requirements and possible benefits. This will illustrate the necessity of maintaining the effort to develop the technology base.

I would like to welcome you to this meeting on behalf of the Air Force Materials Laboratory. This is the fourth annual review of this program and I must say that the progress which has been made over the last four years has been dramatic. I attended the first meeting back in '74 as a member of the University research community who was just beginning work in the Nondestructive Evaluation (NDE) field. My major impression from that meeting was that NDE was a field with many horrendous practical problems and very little in the way of a scientific foundation for the techniques used.

During the four years of the ARPA/AFML program's existence, significant progress has been made in constructing a science base. Beyond the technical advances, the assembly of a multidisciplinary research group from the university and industrial communities devoted to the development of the NDE science base has been a major achievement. This is in contrast to the research along disciplinary lines which was the norm prior to the inception of this program.

As an example on the technical side, we have progressed from attempting to quantitatively predict scattering from individual model defects to the point where we are now addressing the inverse problem, i.e. the description of the source geometry from a limited knowledge of the scattered ultrasonic fields. The next step is to integrate these results into new component life management concepts in an effort to obtain greater reliability and longer service life for aircraft components.

In this talk, I would like to briefly touch on the changes which will have to be made for this program to remain as the core of the effort to develop the NDE science base. In addition, I will try to show how the program fits into the overall AFML NDE program and lastly, I will discuss in some detail a possible application for the quantitative NDE capability we are developing.

For this program to serve as a base for future advances in NDE, it is essential that the core be maintained and preferably expanded. The Air Force Materials Laboratory has committed itself to maintaining its support at least at the present level for the next several years. For an expansion to occur, other agencies, such as the Army and Navy, will have to be brought into a coordinated effort. At the present time, a subpanel of the Joint Directors of Laboratories Council has been chartered to look into the needs of the Department of Defense in the NDE field. It is possible that the recommendations of this subpanel may result in expanded programs in both the fundamental and application areas.

In terms of the overall Air Force Materials Laboratory NDE program, this program is a major part, but not the largest. The Laboratory is a mission oriented organization with the job of transitioning technology into field use as well as developing it. As such, a large number of our programs are applications oriented, designed to answer short term needs and transition technology into the field. The lack of a mature NDE technology base, however, required the commitment to a long term fundamental research effort, such as this one, which the Laboratory has made. The competition between long and short term needs and the ever present limits on available financial resources produced the overall program focus on the development of ultrasonic and electromagnetic techniques which may be applied to our most pressing problems. The largest portion of AFML NDE funds is concentrated in the Manufacturing Technology area which represents the final step in the process of transitioning the technology.

The technical goals of the applications efforts are primarily to improve the reliability of detection in present inspection procedures, among which are ultrasonics and eddy current. This improvement is needed to insure the present safety of our aircraft and to allow the implementation of the quantitative NDE techniques in conjunction with life extension programs in the future. Without the defined reliability that flaws larger than a given critical size can be found, it makes little sense to implement sophisticated quantitative techniques, since the present safety margin in the allowed service life is large enough to take into account the high probability of missing the small defects which must be detected and measured in most life management programs. A second requirement for improved reliability is the need to reduce the number of parts which are rejected when, in fact, they have no flaws present. While errors in this case do not affect safety, in many instances the economic cost becomes prohibitive.

I would like to take a more detailed look at a potential application area where a quantitative NDE capability is essential to the success of the proposed program. The effort is referred to as Retirement for Cause. It's primary goal is to extend the service life of engine components, such as disks, which are now retired after a fixed number of fatigue cycles, independent of any detection of a rejectable flaw, at a point where the probability of failure is 0.02%. This number of fatigue cycles is derived from design life calculations which assume the largest flaw likely to go undetected is actually present in the part. Figure 1 shows how the service life of the part can be extended if reliable, quantitative NDE is available. If all detectable cracks have length less than A_o at each inspection, and there is confidence that no cracks of length greater than A_o have not been detected, the part can be returned to service with confidence that the remaining life should be at least equal to the original design life. As techniques improve, it may even be possible at some point to put parts back into service with cracks just slightly smaller than A^* with the confidence that these cracks will not reach the critical size, A_c before the next inspection.

The simple relationship between the crack surface length and the component lifetime implied by Fig. 1 is valid only for those cases where the aspect ratio ($^a/_{2c}$ = crack depth/surface length) is a constant. In the real world of the alloys found in engines, the aspect ratio is a variable which must be taken into account. This is illustrated in Fig. 2 where the crack growth as a function of number of flights is plotted for bolt hole cracks in the third stage turbine disk in the TF-33 engine. From this figure one immediately comes to the conclusion that crack depth must be accurately measured as well as surface length.

At first glance it might appear that we have identified all the parameters which must be measured by our quantitative NDE techniques; however this is not the case. Figures 1 and 2 are idealizations in the sense that they are valid for elliptical cracks. While real cracks may be elliptical, in many cases they have rather ragged boundaries. This is especially true in coarse grained materials where relatively large cracks can form as a result of the link-up of many small ones. As our NDE techniques improve, it is anticipated that through an iterative procedure with developments in fracture mechanics the essential details of crack geometery needed for remaining life calculations may be identified and the needed techniques developed.

Now let us take a look at how NDE fits into the overall Retirement for Cause strategy. This is illustrated in Fig. 3 where the current and proposed maintenance flow charts are shown. As was mentioned before, the present system retires the disk after one design life even if no flaws are detected in the part. It has been estimated that at least 85% of the disks in one of our newest engines could go for more than 10 design lifetimes without failure. For the retirement for cause program to succeed, the required NDE and analytical techniques which are necessary to separate this long life 85% from the 15% which would fail earlier must be developed.

In the proposed program, NDE comes into the

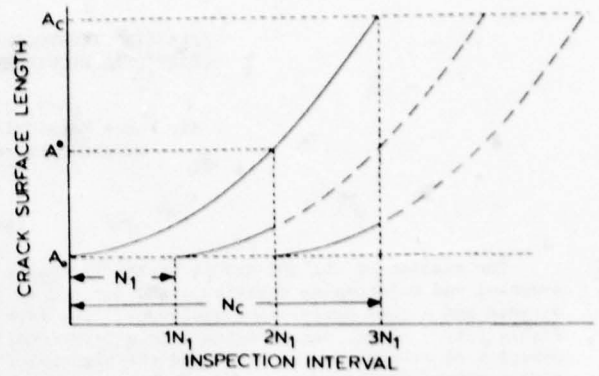

Fig. 1. Crack growth - NDE relationship for Retirement for Cause program.

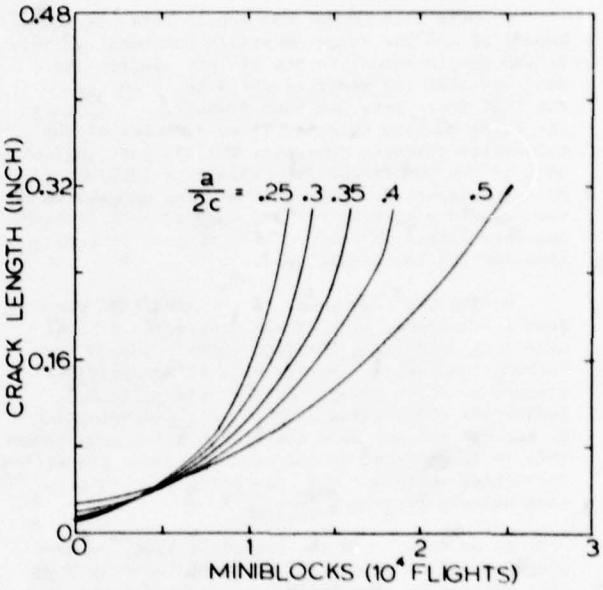

Fig. 2. Crack growth as a function of aspect ratio for 3rd stage turbine disk in the TF-33 engine.

disk evaluation process in two very important places. The first is the initial evaluation of the disk at one design lifetime. Here, the disk is examined for the presence of cracks. If no flaws (cracks, changes in microstructure, etc) are found, it may be put back into service for an additional lifetime. I should mention at this point that it may be necessary to also inspect for nondiscrete defects such as abnormal residual stresses in the part, which may also cause premature failure. Unfortunately, present residual stress measurement techniques are extremely poor except for near surface stress measurements. A great deal of progress would be necessary in this area before we could say we had an acceptable method for measuring bulk stresses.

In the case where a crack is found, accept/reject criteria for the part must be developed. For cracks above a certain size, the disk will have to be rejected, for very small cracks it could be

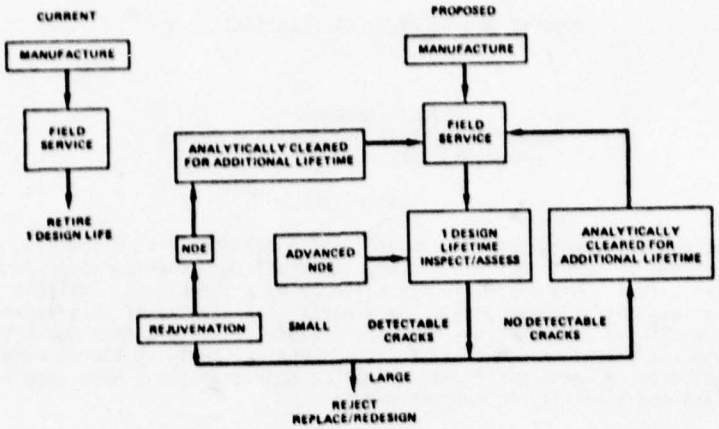

Fig. 3. Disk Retirement for Cause Strategy.

put back into service with no attempt at repair. In the intermediate range, if the techniques are sufficiently developed, the part could be repaired or rejuvenated. After this stage NDE must again be used to determine if the rejuvenation has been successful and no additional damage has been introduced.

In summary, the Retirement for Cause program depends in a critical way on the development of a reliable quantitative NDE capability. It will be a very expensive program due to the large amount of testing needed to provide the statistics, but the potential payoff is so great that it may make the difference between a sufficiently large and reliable Air Force and a severely limited one due to the high cost of maintenance. I have tried in this description of our Retirement for Cause program to give some feeling of the need for a quantitative NDE capability. The research papers to be presented in this conference will bring us up to date on our progress toward this goal. I hope you will find them interesting and leave with the feeling that a great deal of progress has been made and that our goal appears to be achievable.

PURPOSE AND PROGRESS OF QUANTITATIVE NDE

D. O. Thompson
Rockwell International Science Center
Thousand Oaks, California 91360

ABSTRACT

In this paper the purposes and benefits of quantitative NDE are first discussed, emphasizing the "bridging" that is required to couple the measurements to fracture mechanics to produce an integrated, failure predictive discipline. This discussion is followed by a summary of highlights of the ARPA/AFML program aimed at the attainment of these goals. As a particular example of this approach the building blocks that have been developed and which now form the skeletal structure of a quantitative ultrasonics technology are reviewed and placed in perspective. The technical building blocks composing this structure have not only contributed to the desired long-term project objectives, but have also led to spin-off solutions with immediate applicability to current problems.

INTRODUCTION

There are two purposes for this introductory overview. The first of these is to describe the general thrust and nature of work of the ARPA/AFML Program for Quantitative Flaw Definition so that a common framework may be set for the results that will be presented in these proceedings. Secondly, a review of some of the highlights of the work to date is given. In this review, emphasis is placed upon the work that has been done in the development of a quantitative ultrasonics capability and the "building blocks" that have systematically been put in place in order that a firm foundation for an operative ultrasonic technology might be established. It is considered important that the reader have an opportunity to view the "building blocks" in the context of the complete ultrasonics structure, for in the course of the meeting in which expert presentations of various elements of work are given, the overall structure may not be readily apparent. It is regrettable that time simply does not permit a detailed review of all the work that has been accomplished by the program participants and members of the ARPA Materials Research Council who have contributed significantly to program progress and whose contributions and interest are deeply appreciated. The reader is encouraged to seek further information from the author or the program investigators.

PROGRAM THRUST AND BENEFITS

Even though the research work that is embodied in the ARPA/AFML program is quite specific and aimed at the accomplishment of certain goals, it is also useful and important to place this work in the perspective of a longer range goal, i.e., the evolution of a new, non-destructive evaluation technology. The requirements for this new technology have, in fact, been set for some time. Simply and briefly, they specify that the new technology shall contribute to the improved safety and reliability of components and structures at reduced cost, requirements which are at first sight mutually inconsistent and unattainable under current capabilities. It is the purpose of this section to identify and discuss the nature of research work that is necessary to accomplish this evolutionary change in inspection and evaluation capabilities and thereby provide a framework into which the results to be presented in the next several days (these proceedings) can be placed.

Perhaps the most direct way to compare existing non-destructive testing technology with the desired non-destructive evaluation technology is to examine the appropriate definitions and to comment upon their scope and content. There are significant differences that are sometimes lost in the variously used acronyms. According to current practice,[1] definitions that are commonly (although not universally accepted) are given in Fig. 1.

ND?

NDT: "...the development and application of nondestructive test methods..."

NDI: "...the performance of inspections to established specifications or procedures using NDT methods to detect anomalies."

NDE: "...the capability to assess the state of a material, a component, or a structure from a set of quantitative NDT measurements and to predict the remaining serviceability of the item in question from these measurements when evaluated in the context of appropriate failure models."

Fig. 1 Variously used definitions.

According to these definitions, non-destructive testing (NDT) refers only to the development and application of various test methods. No emphasis is placed upon an interpretation of the results of the test and the nature of the interaction of the probing technique with the flaw or materials phenomenon in question. Without attention being given to this key area, it is impossible to make judgments as to the severity of the flaw in question

and to the assessment of the ability of the component or structure to perform an assigned mission in its presence. This key omission lends a feeling that the test method per se is the important objective and not the results to be obtained from it. The concept of non-destructive inspection (NDI) extends the definition of the NDT technology only in the sense that it prescribes that inspections be performed in accordance with a prescribed format. This format may take the form of specifications which relate to the method, frequency, or spatial coverage of an inspection. However, the definition contains no specification for additional information that will enable the requirements for improved reliability at reduced cost to be met any more so than does the previous definition for NDT. On the other hand, the definition given for non-destructive evaluation (NDE) represents an enormous extension in scope, scientific content, and ultimate payoff from either of those given for NDT or NDI. There are essentially three new and important concepts contained within this definition that are not specifically contained in the other two. They are the concepts of quantitative NDT measurements, the assessment of a flaw's criticality in a material or component, and the prediction of the remaining serviceability of the component because of the presence of the flaw. The introduction of quantitative test methods is an essential ingredient of the NDE test technology. Simply, the words mean that the test techniques are sufficiently advanced so that quantitative, rather than qualitative, information is available concerning the target of interest, or flaw. In a philosophical sense, the capability to perform quantitative measurements is a first principle of any scientific or engineering technology; without that capability, the history of science has shown many times over that it is impossible to advance further. In turn, this means that the nature of the interaction between the interrogating energy and the target (flaw) can be understood in terms of sound physical models, and further, that the target or flaw can be characterized and evaluated in terms of appropriate failure models. A quantitative requirement also means that essentially all current NDT techniques must be advanced significantly, for none of those in current operational practice can be classed as quantitative. The second and third concepts given are not completely independent of each other, and each in turn relies critically on the ability to perform a quantitative NDT measurement. More specifically, the assessment of a flaw's criticality is related to the concept of accept/reject criteria, i.e., the set of rules whereby an operator makes his decision as to whether to accept a component or to reject it. Although the need for rational accept/reject criteria has long been recognized as a necessary part of the inspector's arsenal, such criteria have not, in general, been recognized as adjuncts dependent upon the development of quantitative testing techniques. According to the definition of NDE given above and as pursued in this program, the generationof such criteria is just as essential to the performance of the NDE function as are the quantitative measurement techniques upon which they depend. The development of rational accept/reject criteria also forces a multidisciplinary marriage between the measurement procedure and materials scientists and engineers, for materials failure models (such as fracture mechanics) form the framework within which the quantitative NDT measurements can be interpreted and the flaw criticality evaluated. As will be noted later, it is in fact the combination of quantitative measurement and the capability of characterizing a flaw and its criticality under specified loading conditions that provide the "window" for maintaining the safety and reliability of a component or system under reduced cost conditions.

In Fig. 2 is given a schematic diagram in which the concepts of quantitative NDE discussed above are shown in relation to each other. The idealized operational NDE function is shown within the full circle; a part is received, it is inspected by a quantitative NDT technique, an appropriate physical property of a detected flaw is extracted, a judgment is made of its severity in terms of analytical models (perhaps presented in the form of look-up tables), and the part is then either returned to or retired from service. Current operational capabilities are indicated by the hashed section of the upper left quadrant only since no capabilities currently exist in the field for the exercise of the quantitative NDT measurement or application of a rational accept/reject cycle. (As will be noted later, this omission leads to the "zero defects" accept/reject rule in which all flawed parts are rejected resulting in excessive costs.) Functional research topics being pursued in the ARPA/AFML program aimed at developing this methodology are shown in labeled boxes both within and to the right of the circle. Elements of these multidisciplinary topics will be presented and discussed in detail during the course of this meeting. Two exceptions to the above comments may be noted in the figure. The first of these concerns the box labeled material processes improvement. Although not a direct line item in the NDE function, this is a most important result of its development and performance. Knowledge gained as a result of the measurement and analysis of material and component failure modes provides the basis for improvement so that the failure, hopefully, may be eliminated in the first place. Secondly, the box labeled economic choice on the right side of the figure is not a line item of the NDE function either; rather, it is a management function. Its inclusion on this figure is considered important, however, for it is through the quantitative NDE function and its utilization by the designer that management has a means to inject economic choices in the form of cost-risk tradeoffs into the operational cycle.

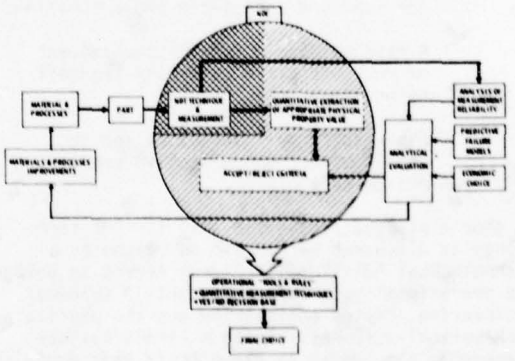

Fig. 2. Methodology required to reach operational requirement.

Without wishing to belabor the point regarding economic choice made above, it may be worthwhile to add a few comments in this regard since the relationship of quantitative NDE to reduced cost and predictable reliability may not be generally realized. One schematic representation of these relationships is given in Fig. 3. In this figure the probability that a measurement with an NDT technique yields the correct value of a physical property a is plotted against the actual value of the property. At this point, property a can be considered general in nature, and may, for example, be as diverse in nature as a crack length, the shape and size of an inclusion, or a material strength. As NDT techniques are made quantitative, the essentially flat response (shown as non-quantitative capability) is changed to a peaked response centered at the value of the property and with a "bandwidth" determined by the error and reliability of the measurement itself. The effects of this quantitative measurement upon the relative costs of ownership of the component or system, when evaluated in the framework of rational accept/reject criteria, are shown in the lower part of the figure. This cost curve considers two effects. The first is the unnecessary cost of rejecting materials and components when a detected flaw is in actuality smaller than a critical size (the costly "zero defects" philosophy). The second is that of costly component or system failure which may result if the detected flaw is greater than a critical size. Without going into details, it has been demonstrated (and it is also somewhat obvious) that a sharpening of the measurement capability will produce a minimum in the cost curve at some value of the physical property value of concern. This value, of course, will depend upon the materials used in the component and the design requirements placed upon the component. The essential point here, however, is simply to recognize that the development of the quantitative NDE function provides a basis for the development of rational cost-risk tradeoff strategies.

The benefits to be derived from evolution of a quantitative NDE discipline and its reduction to practice are both numerous and far-reaching. They may be summarized by recognizing that quantitative NDE, as defined above and as pursued in this program, provides:

- Non-arbitrary "tools and rules" for operational use with the potential for improved efficiency and automation.
- A rational basis for the development of more effective cost-risk tradeoff strategies.
- A necessary building block for the development of an effective predictive design technology.

It should also be recognized that the NDE technology as discussed herein can be viewed as a technological "missing link" that serves to bridge the operational gaps between materials science/engineering, device engineering and the physical/mathematical sciences. These multidisciplinary components are needed as elements of this evolving technology.

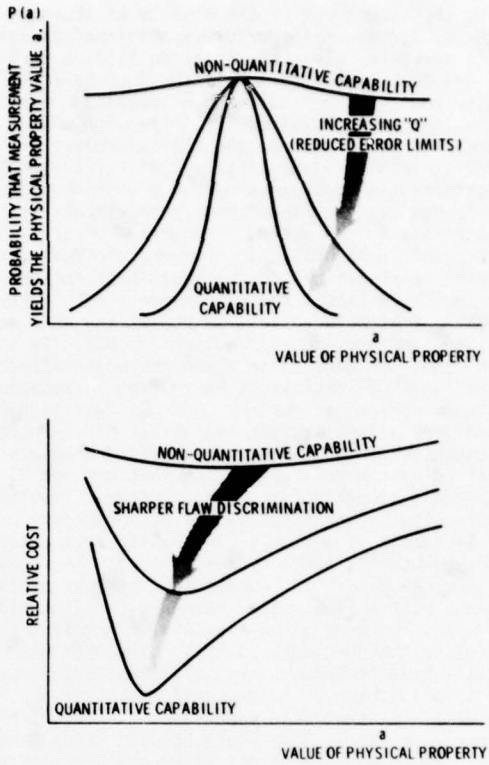

Fig. 3. Cost benefits of improved quantitative physical property measurement.

PROGRESS HIGHLIGHTS

In the first part of this paper, a generalized view of the thrust and goals of the ARPA/AFML program was given; it is the purpose of this portion of this overview to highlight more specific accomplishments that have been gained during the course of the program. As noted in the introduction, particular attention will be given to the work that has been done to produce the "building blocks" of a quantitative ultrasonic capability, its coupling to fracture mechanics, and their organization into an operative systems concept.

The research work in the ARPA/AFML program is separated into three projects. Because of space and time limitations, a detailed review of the many accomplishments in these three projects by the various program participants cannot be given here. Rather, a listing of the accomplishment and the principal investigator will be given. The reader is encouraged to seek details from this and other program reports and from the principal contributors and their publications. It is to be emphasized that key contributions have also been made to this work by members of the ARPA Materials Research Council who are not officially participants in the ARPA/AFML program. In particular, it is a pleasure to acknowledge the important contributions made by W. Kohn, B. Budianski, J. Rice and R. Thomson.

Project I. - Quantitative Acoustic Techniques for Measurement of Flaw Parameters.

- Quantitative Ultrasonics:

  ° Theory (J. Krumhansl, J. Gubernatis, E. Domany, J. Rose, J. Achenbach, V. Varadan)

  ° Sample development (N. Paton)

  ° Experimental procedures and data acquisition (B. Tittmann, R. Elsley, L. Adler)

  ° Inversion techniques (J. Richardson, J. Krumhansl, J. Rose, N. Bleistein, A. Mucciardi, G. Kino, K. Lakin)

  ° Extraction of flaw parameters that permit "bridging" to fracture mechanics (J. Richardson, J. Krumhansl, J. Rose, G. Kino, with key inputs from W. Kohn, B. Budianski, J. Rice, and R. Thomson)

- "Stand alone" items available for ultrasonic improvements:

  ° EMAT technology (R. B. Thompson, C. Fortunko, C. Vasile, B. Maxfield)

  ° Inverse filters (R. M. White)

  ° Integrated transducers (R. M. White)

  ° Procedures and apparatus for transducer characterization (K. Lakin, B. Tittmann, R. Elsley)

  ° New concepts for ultrasonic standards (D. O. Thompson, R. B. Thompson, B. Tittmann)

  ° Variety of computer-aided signal processing techniques (R. Elsley)

  ° Acoustic imaging techniques (G. Kino, K. Lakin)

Project II. - Quantitative Methods for Measurement of Surface Flaws.

  ° Ultrasonic techniques for sizing and determination of fracture mechanics parameters for surface flaws (B. Auld, G. Kino, B. Tittmann, O. Buck)

  ° Quantitative eddy current development (B. Auld, C. Fortunko, A. Bahr, T. Kincaid)

Project III. - Techniques for Measurement of Strength Related Properties in Advanced Materials

  ° Moisture diffusion analysis (including damage assessment) for composites (D. Kaelble)

  ° Acoustic emission of composites and a probable capability for remaining life predictability (L. Graham)

  ° Development of ultrasonic measurement techniques, including inversion procedures, for evaluation of finished adhesive bonds (G. Alers, F. Chang, K. Fertig)

  ° Generation of accept/reject criteria for ceramics (A. Evans, J. Richardson, K. Fertig, G. Kino, R. Addison, J. Schuldies).

  ° Acoustic residual stress determination in ferrous materials (R. B. Thompson)

  ° Non-linear ultrasonic detection of microcracks in Al alloys (O. Buck)

Quantitative Ultrasonics -A goal of project I of the ARPA/AFML program has been the development of a fundamentally correct structure for a quantitative ultrasonics technology that will help alleviate the various limitations of the current technology and which may be coupled directly to rational sets of accept/reject criteria as noted in the first part of this paper. In this section the technical approach that has been pursued will be outlined together with a limited description of the various "building blocks" that have gone into it.

The philosophy of the technical approach adopted for the construction of a quantitative ultrasonics capability is illustrated in Fig. 4. A set of procedures were established whereby the capability was built up from fundamental building blocks which began with the development of a theoretical understanding of the basic interaction of the ultrasound with the flaw. The development of approximate theories has been emphasized in this program because the number of flaw shapes which can be treated by exact techniques is extremely limited and because of the desire to extend the work to real flaws of complex shapes. A second major building block involved the performance of verifying and/or guiding experiments on a set of controlled samples in which flaws of carefully determined size and shape were placed. Close interaction between theoretical and experimental work was maintained to the advantage of both in this work. The third major building block in this construction involved the development of suitable and efficient inversion techniques, i.e., those procedures whereby flaw parameters are extracted from the data. An analogy to an integral equation has been used. The theory can be viewed as the kernel of the integral equation which relates ultrasonic measurements to physical parameters of the flaw. By solving the equation by whatever means is appropriate, a relationship that predicts the size, shape, and orientation of the defect in terms of certain measureables can be developed. The fourth major step then comes in verifying that these extracted values compare favorably with known values of the flaw parameters. The importance of the precisely controlled samples becomes apparent at this juncture. Finally, having determined the flaw parameters relative to size and orientation, flaw failure parameters which are of significance in fracture mechanics and failure prediction have been attained. Thus, a construction for a quantitative ultrasonics capability has been developed which extends from a knowledge of the fundamental ultrasound-flaw interaction to a determination of

the flaw's stress intensity factor, a key parameter for failure prediction. Selected highlights of these developments will be given in the following discussion.

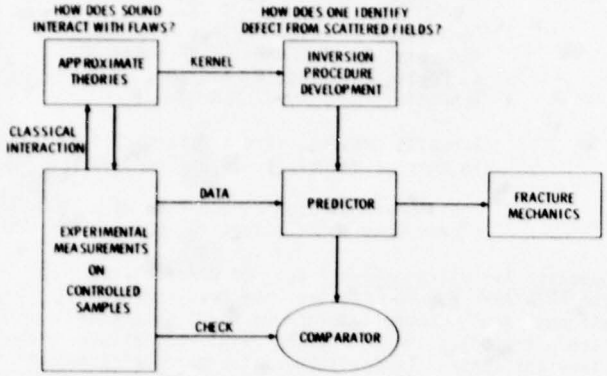

Fig. 4 Building blocks of quantitative ultrasonic technology.

Theory - The development of theoretical models has been governed by two considerations. First, it was necessary to base the models upon correct solutions to elastic wave scattering problems in solids as opposed to the use of analogies to scalar models developed for fluid media. An extensive literature exists in the latter case because of the practical importance in sonar. However, this information cannot be directly transferred to the solid case in which such effects as mode conversion play an important role. Second, approximate models have been emphasized. Exact solutions are available for a few simple geometries, but these theoretical models are not readily generalized to more complex shapes. Since it is the intent to provide the theoretical techniques necessary for the characterization of real flaws, the model development and approximations have been selected so that they may be extended as needed.

The major theoretical effort has been performed at Cornell University by Prof. J. A. Krumhansl and several students. They have used an integral equation formulation of the scattering problem[2] and developed a series of approximate techniques. The first, and simplest, is the Born approximation.[3] In this approach, the incident plane wave solution to the wave equation is used as the first approximation to the solution and the scattered fields are derived by substituting this for the actual solution within the integral. The results are rigorously correct only for weakly scattering defects, i.e., inclusions whose properties do not differ too greatly from those of the host medium. However, the results have been found to agree well with many experimental features over a much broader range of conditions.

In a series of papers,[4,5] Krumhansl, Gubernatis, Domany, Huberman, Teitel, and Rose have explored a series of other approximations for both three-dimensional volumetric and two-dimensional, crack-like flaws. Included have been the quasi-static approximation which gives the rigorous result in the limit or long wavelength, and an extended quasi-static approximation which is a combination of some of the features of both the Born approximation and the quasi-static approximation to extend the range of validity of each. Each of these approaches is primarily applicable when the wavelength is comparable to, or greater than, the dimensions of the flaw. On the other end of the spectrum, Prof. L. Adler at the University of Tennessee[6] and Prof. J. Achenbach at Northwestern University[7] have studied application of the geometrical diffraction theory of Keller to the elastic wave case.

The Born approximation has led to a number of important insights and results. Because of its simplicity, the results separate into a product of three factors -- one proportional to the square of the frequency, one determined by the elastic constants of the flaw, and one determined by the shape factor (a function which can be recognized as the spatial Fourier transform of a characteristic shape of the flaw). The approximation thus defines a clean path for reconstructing the flaw shape from experimental data. This is an important result. Secondly, use of the approximation has provided a way to visualize the scattering patterns rather easily. Examples are shown in Fig. 5. Here, isographic projections of equal scattered amplitudes are plotted for the scattering of a broadband longitudinal wave pulse from a sphere and an oblate spheroid at 45° incidence. The differences in the signatures of the direct, longitudinal-longitudinal scattering and the mode converted, longitudinal-shear wave scattering are striking. From this kind of information it has been possible not only to identify features of flaws, but also to estimate the transducer apertures required to differentiate between various flaw types and orientations.

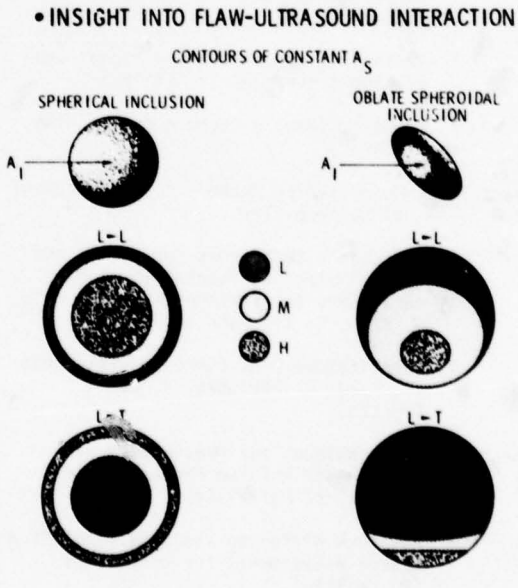

Fig. 5 Insight into flaw ultrasound interaction.

Experimental Technique - In order to carry through the approach outlined above, it was necessary to make measurements on samples in which flaws of known size, shape, and orientation have been placed. A procedure utilizing a diffusion bonding fabrication was selected to achieve this purpose. In this procedure, developed by N. Paton at the Science Center[8], two pieces of titanium alloy were carefully prepared with mating surfaces flat to within four optical bands. The desired defect was then machined accurately into the mating surfaces. Following this step, the two halves of the sample were carefully assembled in a mating jig and placed under pressure at approximately 1500°F. The bonding pressures were kept low in order to limit the specimen strain thereby preventing significant distortion of the machined defect geometry. Under these conditions, grain growth occurs across the bonding plane and produces a bond line which is indistinguishable from the parent metal both ultrasonically and metalallographically. Most of the samples prepared in this way have utilized the titanium alloy Ti-6Al-4V since it is an aerospace alloy of interest and because of the fact that at the bonding temperature it dissolves residual surface oxides (thus assuring a good bond). Special techniques have also been developed for producing such intentionally defected specimens from steel and aluminum alloys.

In Figs. 6 and 7 are shown a micrograph of a cut through a finished sample in which a hemisphere was embedded and a schematic showing the various kinds of void defect cavities that have been prepared. The micrograph demonstrates the metallurgical invisibility of the bond line nicely. Most of the defected samples, as shown in Fig. 7 have been prepared so that the defects retain one axis of symmetry. Thus, the set includes spherical cavities of different diameters and spheroids of revolution (both prolate and oblate). The size range varies from a 200 μm by 800 μm oblate spheroid to a 1600 μm by 400 μm prolate spheroid, thus producing a significant range in the aspect ratio of the spheroids. This range is sufficient to permit an examination of the limit as the spheroid of revolution approaches a crack-like flaw.

These defects have been placed in two sets of samples with different exterior shapes. One set is a right circular cylinder with a 2.5 cm height and a 10.2 cm diameter. The other set has a "doorknob" or "trailer hitch" shape as shown in Fig. 8. In these samples, the exterior surface is a sphere of 2.8 cm radius with the defect at its center. This feature makes it possible to perform fundamental measurements of the angular dependence (as well as the frequency dependence) of the ultrasonic scattering since transmitting and receiver transducers could be placed at nearly arbitrary angles without changing the ultrasonic path length. These measurements were further facilitated by a precision goniometer and the use of machined buffer caps which match the flat end of the transducers to the curved surface of the sphere. The data obtained in this idealized geometry were used both as a check on the theory and as a reference against which the data on the cylindrical samples could be tested to insure that correction for refraction and diffraction effects have been properly made. The development of such corrections is a crucial step in transferring the basic research results from the laboratory into field usable techniques for use on parts of complex shape.

Fig. 6. Single hemispherical defect magnified 100X

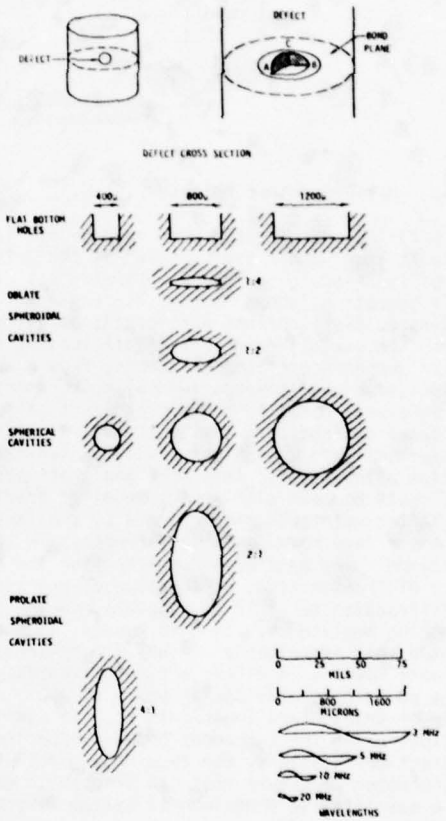

Fig. 7. Defect shapes in diffusion bonded samples.

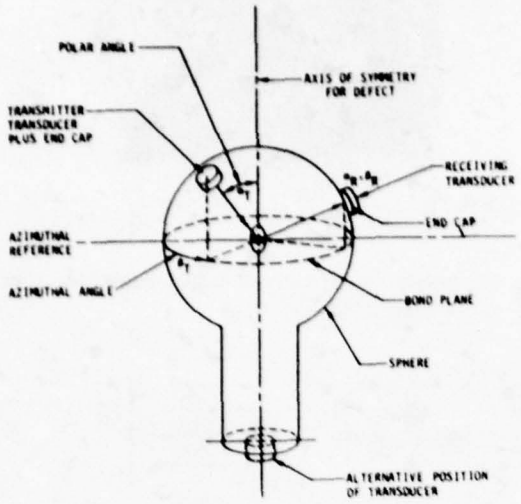

Fig. 8. Measurement coordinate system.

Detailed measurements were made by B. Tittmann at the Science Center and L. Adler at the University of Tennessee on samples containing all of the defect geometries shown in Fig. 7. Figure 9 illustrates the excellent agreement that exists between the exact theoretical predictions of the angular dependence of the scattering from a spherical inclusion and the experimental measurements.[9] This agreement established that an exact calculation based on isotropic elasticity models applies satisfactorily to the polycrystalline, two-phased titanium alloy used in this work and that measurements could be made with a high level of precision. This latter point was strengthened by the fact that there were no adjustable parameters in the comparison. The data were corrected for the efficiency of transduction, attenuation of ultrasound, and diffraction to yield an absolute measure of scattering amplitudes. In this regard, it should be noted that experimental points are presented that were taken with either a single transducer in the pulse-echo mode (solid point at 180°) or a pair of transducers (open points). In addition to illustrating the agreement between experiment and exact calculations, the results demonstrated a calibration procedure that can be used to ensure that a quantitative experimental system is properly functioning.

For more general defect types, exact calculations become increasingly difficult, and the approximate theories discussed above were used. The spherical geometry was used as a reference case in which these models could be compared against the well established exact result. As noted, the Born approximation is rigorously valid only for inclusions whose properties are similar to those of the host medium. However, it was found that it makes many useful predictions outside of this regime. For example, even for a cavity, it is found to make good predictions for the angular variations of scattering for angles near the back-scattered direction and for relatively low frequencies, i.e.

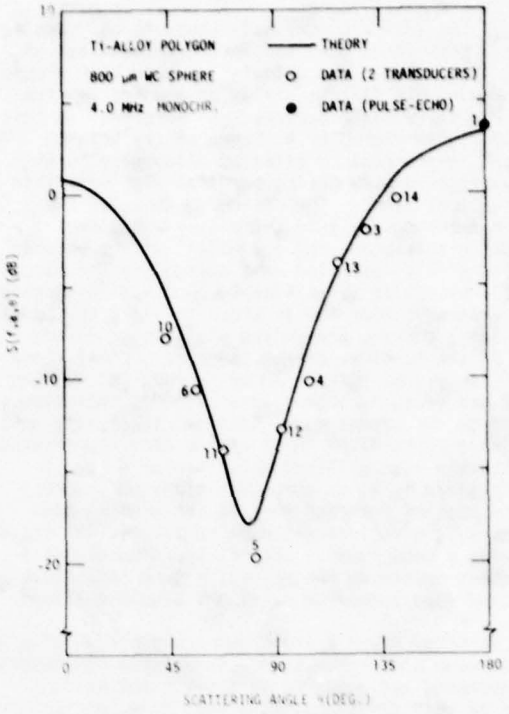

Fig. 9. Absolute comparison between system response and theoretical expectation curve for a spherical (inclusion) scatterer.

$ka \approx 1$ where a is the sphere radius. The detailed frequency dependence of the result was found to have systematic errors but, when averaged over a set of frequencies which comprised the broadband ultrasonic pulse, the results were again quite useful.[10]

These results, deduced for the case of the sphere by comparison with experiment for both exact and approximate models, have been further investigated in the spheroidal geometry by a direct comparison of experiment and the approximate theory.[11,12] In general, the same conclusions have been drawn. For example, Fig. 10 is a comparison of the back-scattered power from a pancake-like, 800 μm x 400 μm oblate spheroidal cavity. In this case the theoretical predictions were averaged over a range of frequencies corresponding to those produced by the transducer, and excellent agreement was obtained.

Other measurements at higher frequencies on crack like flaws have established bounds on the geometrical diffraction theories.[6] Both the theoretical and experimental work are continuing to increase the regime in which satisfactory agreement exists.

Inversion - The inversion techniques which have been investigated can be divided into three general classifications. One set of approaches, of which imaging is the most familiar example, is intended to reconstruct the detailed shape of the object. These approaches can, in general, be viewed as the reconstruction of the defect shape function from measured spatial Fourier components. Work devoted to the development of imaging systems

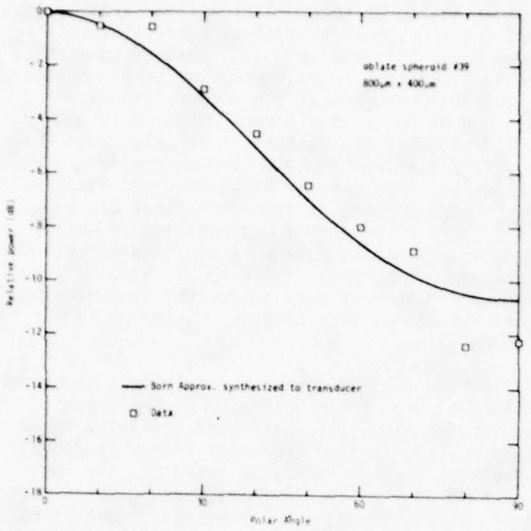

Fig. 10. Comparison of pulse-echo data as a function of polar angle α with predictions of Born approximation. (The calculations take into account the transducer characteristics)

in which the signal processing algorithms are based upon scalar models for the ultrasound-flaw interaction have been undertaken by Kino[13] and Lakin[14]. In addition, others have given greater attention to the development of data inversion techniques more closely related to rigorous solutions of the wave equation. Profs. N. Bleistein and J. Cohen of Denver University are considering the application of algorithms previously developed for the processing of seismic data to the ultrasound case.[15] Rose and Krumhansl have developed a conceptually similar approach based upon the Born approximation for the elastic wave case.[16] Measurements of the ultrasonic power scattered at various angles may be viewed as defining specific components of the Fourier transform of the defect shape function. This concept was tested by developing inversion formulae based upon the Born approximation and testing them using numerical results produced by exact theoretical calculations as input data. One of the results is shown in Fig. 11 for the case of a spherical cavity. Here the shape function is plotted as a function of radius. The reconstructed value is seen to approach very closely to the correct value, even though the input data was truncated for $\lambda < a$. Furthermore, addition of 50% random noise to the data produced very little degradation of the result. These results are quite promising, particularly in view of the relatively long wavelengths required for reconstruction.

The reconstruction techniques all rely upon some form of linearization of the scattering problem. However, in fact, the scattering process can be highly nonlinear, e.g., the scattering from adjacent facets of a flaw is not necessarily the superposition of the scattering from the facets considered individually. Analytical techniques

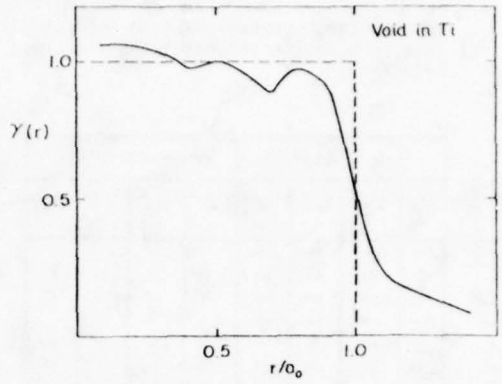

Fig. 11. The calculated characteristic function, $\gamma(r)$ for a spherical void in Ti is shown and compared with the exact result shown by dotted lines.

are not yet sufficiently developed to address the inversion of such a nonlinear problem. However, empirical, adaptive learning techniques have proven quite successful as demonstrated by A. N. Mucciardi of Adaptronics, Inc.[17] The basic problem is to define functional relationships between particular features of the scattered ultrasonic fields, e.g., the energy scattered at a given angle into a given frequency band, and particular parameters of the flaw. In order to accomplish this practically, it was necessary to represent the flaw by a small number of parameters. In this case, an oblate spheroid having major and minor semi axes of length B and A, respectively, and elevation and azimuthal angles α and β with respect to the measurement aperture, was assumed. In order to develop the prediction, it was necessary to have an extensive "training" base for the purpose of establishing correlations. This was done using the Born approximation to generate theoretical data corresponding to ellipsoids having a wide range of the parameters defined above. Once the functional form of the predictor had been established, it was tested using experimental measurements on the previously discussed samples as the input parameters. The data were restricted to 17 transducer locations in a circular aperture having a half-angle of 60° with respect to the flaw. No use of the detailed frequency dependence of the signals was made because of known systematic errors in the theoretical model.

A comparison of the predicted and known flaw parameters is given in Table I. It will be noted that the agreement is quite good, particularly in view of the approximate nature of the theory used in the training process. It can be anticipated that the use of more accurate approximations in the future will improve this performance further.

A third approach to the inversion problem has been made in the regime where the ultrasonic wavelength is large with respect to the flaw size, a regime of practical importance. Here the problem is again nonlinear, but analytic techniques can be used in the limit of long wavelength to solve the forward scattering problem in closed form. In particular, for a general flaw, it has

Table 1. Performance of spheroidal defect measurement system, synthesized from theoretical data on actual scattering data from real defects.

	SIZE (in Microns)				ORIENTATION (in Degrees)			
	ALA1*		ALA2		ALA3		ALA4	
DEFECT NO	TRUE	MEAS	TRUE	MEAS	TRUE	MEAS	TRUE	MEAS
	a	a	b	b	α	α	β	β
1	200	194	400	403	0	37	-	197
2	200	183	400	529	30	2	225	215
3	100	100	400	508	90	66	180	185
4	100	114	400	521	0	0	-	-
5	200	202	400	533	60	22	180	174
6	100	126	400	500	30	60	180	186
7	200	114	400	509	30	21	180	178
8	100	130	400	645	30	42	225	218
AVERAGE ABSOLUTE ERROR		20		119		23		9
PERCENT AVERAGE ABSOLUTE ERROR		15.0		27.3		25.6		2.2

been shown by Gubernatis[4] that there are 22 independent parameters which can in principle be deduced from scattering measurements.

Interest has been high in the long wavelength regime for several reasons. The fact that many flaw parameters are available in a regime where the theory is well developed and inversion problems can be attacked analytically is very attractive. The fact that the technique may give an average representation of the flaw as needed to use simple fracture prediction models rather than a detailed picture with more information than is desired, could be of great practical importance. This interest was sharpened by a recent paper by Budianski and Rice[18] which demonstrated that, for an elliptical crack, the maximum stress intensity factor could be directly deduced from long wave length scattering data, and to a large extent, independent of the eccentricity of the crack. Further analysis has been presented by Kino.[19] The most recent implementation of the techniques, as developed by Elsley and Richardson at the Science Center,[20] required that the frequency dependence of the ultrasonic scattering be deduced from measurements made at a number of transducer positions. From this data, the coefficient A_2 of the leading ω^2 term in a power series expansion of the scattered amplitude was determined. The parameters of the flaw are then deduced from the set of coefficients A_2 using an estimation theory approach. This methodology was applied to one of the 800 μm x 400 μm ellipsoidal cavities. Measurements were made of the backscattered signal at angles of 0°, 15°, 30°, 45°, 60°, 75°, and 90° with respect to the symmetry axis of the ellipsoid. The results of the prediction of the ellipsoid dimensions and orientations are amazingly accurate, clearly demonstrating that the potential of this new approach for defect characterization is high. Details of this work will be presented later in this meeting.

Fracture Mechanics - The last remaining "building block" shown in Fig. 4, Fracture Mechanics, has been a subject of major activity this past year. As noted earlier, the purpose of this effort is that of extracting numerical values of failure parameters from the ultrasonic data, thus providing non-destructive measurements of those parameters that have in the past been determined only through destructive tests. Success in this endeavor has to be regarded as a significant step. Since detailed reports of these activities will be presented at this meeting, only summary comments will be given here. Two approaches have been taken for the determination of the stress intensity factor. One of these is a direct approach in which the stress intensity factor can be calculated from the values measured for the flaw parameters. This approach has been used by Richardson and Tittmann (these proceedings). A second approach has been used by Kino et al (these proceedings) in which extensive use has been made of the theoretical calculations of Budianski and Rice.[18] Both of these approaches have been very successful in producing values for the stress intensity factor of the measured values.

Summary - The systematic and logical procedure outlined in Fig. 4 has been used to develop a quantitative ultrasonic structure utilizing three new approaches to flaw characterization involving generalized imaging, adaptive learning, and long wavelength scattering. Each of them is built upon results traceable to first principal interactions, and in each case, preliminary results which demonstrate the feasibility of the approach have been obtained. Further work must be designed to make specific improvements in each and to reduce them to practice. It is important to realize that an entire structure for quantitative ultrasonics has been demonstrated which can be direct-coupled to failure predictive techniques. This overall result must be considered an important accomplishment and a foundation for a new inspection technology.

REFERENCES

1. D. M. Forney, Jr., "USAF NDE Program - Requirements for Technology Transition" Proceedings of the ARPA/AFML Review of Progress in Quantitative NDE, August 31-September 3, 1976, AFML-TR-77-44 (1977)

2. J. E. Gubernatis, E. Domany, and J. A. Krumhansl, "Formal Aspects of the Theory of Scattering of Ultrasound by Flaws in Elastic Materials," J. Appl. Phys. 48, 2804 (1977)

3. J. E. Gubernatis, E. Domany, M. Huberman, J. A. Krumhansl, "The Born Approximation in the Theory of the Scattering of Elastic Waves by Flaws," J. Appl. Phys. 48,2812 (1977)

4. J. E. Gubernatis, "Long Wave Approximations for the Scattering of Elastic Waves from Flaws," Los Alamos Report LS-UR-77-2900 (1978)

5. E. Domany, J. A. Krumhansl, S. Teitel, J. Appl. Phys. (in press)

6. L. Adler and D. F. Lewis, "Scattering of Broadband Ultrasonic Pulse by Discontinuities," IEEE Trans. on Sonics and Ultrasonics, Vol. SU-23, 315 (1976)

7. J. D. Achenbach and A. K. Gautesen, "Geometrical Theory of Diffraction for 3-D Elastodynamics," J. Acoust. Soc. Amer. 61, 43 (1977)

8. N. E. Paton, "Sample Preparation," in Interdisciplinary Program for Quantitative Flaw Definition, Special Report Third-Year Effort, published by Science Center, Rockwell International, under Contract F33615-74-C-5180, 59, (1977)

9. B. R. Tittmann and D. O. Thompson, "Approach to Self-Consistent Calibration Procedure of an Ultrasonic System," Material Evaluation 35, 75 (1977)

10. B. R. Tittmann, "Mode Conversion and Angular Dependence for Scattering from Voids in Solids," 1975 Ultrasonics Symposium Proceedings (New York, IEEE, 1975, Catalog 75-CH0994-4SU), 111

11. B. R. Tittmann, "Ultrasonic Scattering Studies for Failure Prediction," 1976 Ultrasonics Symposium Proceedings (New York, IEEE, 1976, Catalog 76CH1120-5SU), 74.

12. L. Adler and Kent D. Lewis, "Ultrasonic Wave Scattering from Ellipsoidal Flaws in Metals," 1977 Ultrasonics Symposium Proceedings (New York, IEEE, 1977, Catalog 77CH1264-1SU), 44.

13. T. M. Waugh and G. S. Kino, "Real Time Ultrasonic Imaging with Shear Waves, Rayleigh Waves, and Lamb Waves," 1976 Ultrasonics Symposium Proceedings (New York, IEEE, 1976, Catalog 76CH1120-5SV), 125.

14. K. M. Lakin and A. Fedotowsky, "Characterization of NDE Transducers and Scattering Surfaces Using Phase and Amplitude Measurements of Ultrasonic Field Patterns," IEEE Trans.Sonics and Ultrasonics, Vol. SU-23.

15. N. Bleistein, "Physical Optics for Field Inverse Scattering in the Time Domain," J. Acoust. Soc. Amer., 60, 1249 (1977)

16. J. H. Rose and J. A. Krumhansl, "Inference of Flaw Characteristics from Ultrasonic Scattering Amplitudes," Interdisciplinary Program for Quantitative Flaw Definition, Semi-Annual Report, July 1977-January 1978, Contract F33615-74-C-5180, Science Center, Rockwell International.

17. A. N. Mucciardi, R. Shankar, M. F. Whalen, and M. J. Johnson, "Application of Adaptive Learning Techniques," Interdisciplinary Program for Quantitative Flaw Definition, Special Report Third Year Effort, published by Science Center, Rockwell International, under Contract F33615-74-C-5180, 176 (1977)

18. B. Budiansky and J. R. Rice, "On the Estimation of a Crack Fracture Parameter by Long-Wavelength Scattering," unpublished results.

19. G. S. Kino, "Measurement of a Crack Stress Intensity Factor," unpublished results.

20. R. K. Elsley, J. M. Richardson, R. B. Thompson, "Determination of Fracture Mechanics Parameters from Elastic Wave Scattering Measurements at Low Frequencies," Interdisciplinary Program for Quantitative Flaw Definition, Semi-Annual Report, July 1977-January 1978, Contract F33615-74-C-05180, Science Center, Rockwell International.

DISCUSSION

Neil Paton (Science Center): My name is Neil Paton, and I have a question for Tom Moran. He mentioned the rejuvenation of disks and specifically titanium disks. I would like to know, first of all, do you have any methods in mind for rejuvenation of those disks; and, secondly, is it just titanium in which you're interested, or are you also interested in nickle base super alloys? If so, what methods do you have in mind there?

Tom Moran (AFML): I can't answer.

Don Forney, Chairman (AFML): Harris, could you answer the question? Harris Burte is the AFML Chief Scientist. If he doesn't know the answer, we're all in trouble.

Harris M. Burte (AFML): The answer is quite a bit. There are a variety of things being explored at different levels. I am sure you're familiar with some of them, Neil. One approach assumes that a discrete flaw can be closed with isostatic pressure. If it happens to be a surface flaw a coating may be put on it so that we can bridge that flaw and still enable us to close it up. Another approach goes back 10 or 15 years based on a wide variety of investigations that say we need to understand some of the reasons that may lead to fatigue crack initiation. For example, by providing suitable heat treatment to the material at a particular stage of life we can rejuvenate the material and essentially extend its life if, in fact, we don't also give ourselves more problems in doing that by putting in residual stresses. I can't give you a simple answer to it because it is a very broad field. It doesn't have one specific approach. If anybody is interested in these particular items, I suggest they make appointments with some of the various people in the laboratory, either through Dr. Norman Tallon or myself.

Don Forney, Chairman: This rush of hands in the air, I can hardly hear. Yes?

Gerald C. Gardner (University of Houston): I would like any of the three to comment on the aspect of accept/reject criteria We have fallen into the pattern of considering that to be a dichotomic decision, either yes or no, but in point of fact if you had an adequate mechanical performance predictive technology, you ought to be able to classify a component, not simply in terms of whether it will or will not fail, but rather in terms of what service regimes it will perform adequately at acceptable levels of risk. This means that you're really making a multistaged decision rather than a simple dichotomic one, and I would just like to hear any one who wishes to comment on the relevance of the comment that I just made.

Don Forney, Chairman: Mike volunteered.

Mike Buckley (ARPA): I think we're saying the same thing. There is a probability of failure at all levels of different modes of operation. Different constraints, etc., have to be factored in, but eventually, it comes down to making a decision in a given anticipated environment or mission profile. So you do have to eventually make a decision. We're really talking about making a conscious one, knowing all the variables and their probabilities of failure, but eventually, it does have to become, "I will put it into service or I won't know what the risk is."

Don Forney, Chairman: I might add that as a matter of fact we do either knowingly or unknowingly utilize this idea, Gerald. There have been many occasions in the military aircract category, if you will, where we have flown aircraft in limited control flight conditions because of either a limitation in the strength of a component or the fact that we don't know the strength of a component pending tests. In actual fact we have frequently flown with restrictions.

Gerald Gardner: You constrain the envelope.

Don Forney, Chairman: That's right. We constrain the envelope. Military aircraft have red lines. We can fly them faster. We can drive the engines harder and make the aircraft fly faster, but it is unsafe. So every aircraft that I know of has a red line. That, in a sense, is a criterion.

TEST BED CONCEPT AS A MEANS OF INTRODUCING NEW TECHNOLOGY

A.L. Thompson, E.E. Weismantel and D.M. Comassar
The Aircraft Engine Group
General Electric Company
Evendale, Ohio 45215

ABSTRACT

The rapid evolution of ultrasonic testing technology over the last ten years has found industry unable to test or apply many of the new concepts resulting from this work due to limited facility resources to adopt these advanced methods. The testing of these methods is a desirable sequence in the evolution of new ideas to production usage and in many cases would require a test bed on which to try innovative ideas. This test bed concept would provide an avenue to resolve applications problems which might otherwise overshadow the significance of technology innovations. The availability of a test vehicle with which to prove or if necessary further modify these growth ideas further benefits these accomplishments by verifying their validity and performance. In recognition of this need, a program has been undertaken to establish an advanced ultrasonic work station with the ability to function as a test system for the application of these concepts to commonly encountered inspection tasks.

The present system contains all solid state instrumentation designed around the latest electronic concepts and features extensive computer interfacing with regard to both signal handling as well as command and feedback systems. The specially developed ultrasonic instrumentation contains programmable gates and interface synchronization and provides the capability to process the full R-F waveform during test. Output from the ultrasonic instrument is processed through a high speed digitizer between the instrument and the computer which is dedicated primarily to data acquisition, analysis and retention. Two-way communication linkages exist between the ultrasonic instrument and the computer as well as between the computer and the motion and position control to allow the incorporation of signal correction techniques to accomodate material attenuation, surface lens effects due to radii, etc., so that the computer can judge signal significance incorporating these corrections. Data output from the test is supplemented by graphic displays allowing the presentation of planar and rotated views with the expansion capability for the examination of selected volumes. This system is currently being applied to the evaluation of specially contoured shapes for advanced turbine engine programs in which signal characterization will play a significant part in the data analysis.

INTRODUCTION

The constant emphasis on improved production efficiency and productivity that has typified twentieth century industry has resulted in numerous changes in manufacturing methods and concepts. However, the changes that are incorporated are not as readily accomplished as one might imagine since minor changes in routine are often reflected in immediately increased costs even though, in the long run, the change might benefit overall cost and quality. The target of improved product cost resulting from increased efficiency in the use of materials, increased production capacity and increased productivity is a powerful driver that can make promising process innovations successful. Seasoned manufacturing management readily recognizes the importance of gaining the acceptance of new methods by the operating components before new ideas are fully committed to production. As a result, many manufacturers have adopted the concepts of prototype processes, pilot lines and the like to initially debug new methods, demonstrate capability and overcome those problems that might adversely influence the cost, productivity and permanence of these innovative methods.

This same approach influences the introduction of changes in the nondestructive test processes, such as ultrasonic inspection. In the case of the quality oriented processes, the gains obtained from technology advancements can be more difficult to introduce than are changes in the manufacturing processes where improvements are mostly related directly to the cost and thru put of the process. Improvements in flaw detection capability or significant changes in the the acceptance criteria applicable to hardware must first gain engineering acceptance before becoming a basis for product acceptance. Once engineering acceptance is achieved, the gaining of manufacturing acceptance further requires the proof that the change in method can be accomodated in the production area with minimal impact on production cost.

It has only been in the past ten to twenty years that a wide enough technical base has been established to regard nondestructive testing processes as technologies rather than skills. NDE as an art really came into being in the Second World War and the technology base currently is much more in its infancy than are most engineering and manufacturing oriented technologies. Until recently, even the advanced industries had not considered then NDE processes as much more than quality checks in the manufacturing cycle rather than information tools. Consequently there was little impedence for improving NDE processes to obtain more information from the inspection process itself.

In the electronically oriented processes, such as eddy current inspection and more notably in the ultrasonic area, the inspection processes have benefited markedly from very rapid advancements, resulting from the evaluation of solid state electronics. This situation has given impetus to the understanding of the "whys and

wherefores" of the inspection process rather than the "how-to-apply the process" emphasis that had existed previously. Heretofore, equipment noise, lack of stability or drift, lack of equipment standardization, etc., had precluded the ability to characterize waveforms of any significance. In addition, the response time of earlier forms of signal processing was not adequate to handle the very large quantities of data obtainable from the inspection process. The advent of solid state circuitry, high speed data gathering and computing capability vastly increased the potential of these processes.

Many new ideas in information gathering are evolving from these more recent advancements in equipment capability and a markedly modified approach to materials interrogation is forthcoming from this emerging technology. Typically, many of the accomplishments now resulting from the ARPA/AFML supported studies in Quantitative NDE require further demonstrations of validity and usefulness to gain generally broad acceptance and application to every day inspection tasks. The developement of new concepts for ultrasonically assessing, defining and quantifying flaw types, size and geometry resulting from these research programs must have a more direct avenue to the practical task of hardware inspection if the journey from the laboratory to industrial use is to be shortened. These advanced approaches to the inspection of materials face a potential barrier in the lack of suitable resources to test these innovations since normally available production oriented equipemnt is too limited in capability to serve these purposes.

A surprisingly large amount of inspection equipment existing in industry today is still of the older vintages, and, where many facilities may have solid state instrumentation, much of it is based upon 1950-1960 design concepts. Basically, many of the users of the inspection processes are still trying to accommodate the "how-to-apply" of the process since it is only the more technically advanced industries that have the incentive to strive for the benefits that might be attainable through the development of sophisticated techniques.

However, many of the suppliers of electronic inspection equipment are atuned to the demands of the market, the bulk of which is oriented to less ambitious commercial tasks. Because of the limited size and resources, these suppliers are not normally in the position to lead the industry by furthering the advancements in inspection technology. So it remains that, if improvements are to be gained in the amount of quantitative information attainable from these inspection processes, the advanced technology industries, namely aerospace and nuclear must fill this need. Without the testing and proving of the accomplishments forthcoming from the work aimed at upgrading the ultrasonic technology base, in fields ranging from the improvement of transducers to the definition of frequency response, scattering and imaging, their value could well go unnoticed and materials inspection practices would continue to follow the limited horizons of present production methods. Today's production methods rely primarily upon the measurement of response amplitude as a gage of acceptability or rejectability of the product, although it is broadly known that this amplitude information is perhaps only ten percent of the information available from the interaction of the response source and the sonic beam. The inability of commercially available equipment to work with much more than this is one of the inhibitors to the growth of application technology in the field of ultrasonics. The high level of sophistication coming from presently active development programs requires a degree of proof and demonstration beyond that which would normally be required for more straightforward process advancements. What is now needed is a test bed in which to test this evolving technology in order to sense out and prove the real potential of new innovations. This test bed would work under the conditions normally encountered in the production inspection of hardware while providing the inspection data accumulation and data processing capability needed to exercise the new ideas. It is most important that the presently subtle influences on the inspection process be eliminated or at least controlled to such a degree as to minimize their effects on the process so that the inspection innovations can truly be assessed. In a test bed arrangement, this can be done in a work environment that would simulate the conditions normally expected of a production system applied to production hardware.

Several years ago, the Aircraft Engine Group of the General Electric Compnay, began an effort to bring further sophistication to the ultrasonic inspection process. This effort has resulted in the establishment of a system which minimizes human involvement in the inspection, as well as providing a test bed for advanced inspection concepts.

Long range goals and targets for this inspection system were established. Commercially available instrumentation and facilities to act as base for development work were sought; neither electronic equipment nor the mechanical elements of the workstation were available to serve our purposes. Therefore, the program first started with the design and fabrication of the present workstation which is aimed at the testing of new inspection ideas prior to production applications. Basically, the test bed consists of four separate elements.

1. Electronic Instrumentation
2. Signal processing, analysis, computation and decision making components
3. System Motion Control
4. Mechanical System

ELECTRONIC INSTRUMENTATION

At the time this activity was started a survey of available ultrasonic instrumentation could not identify any available or near term instrumentation that would meet required system requirements which were:

1. Ability to process the total R-F waveform for subsequent signal analyses and interpretation
2. Capability of complete computer interfacing so that the resulting system could be truly computer controlled relative to establishing the various instrument settings, gates, etc.
3. Practically no instrument effects on the nature of the received signal
4. Very low instrument oriented background

At that time, a detailed specification was established for the electronics system and a con-

tract with our Corporate Research and Development Center at Schenectady was placed for its design and fabrication. The resulting prototype system was truly a first of its kind and met most of the original design specifications. This prototype was used for our early work and we subsequently procured a second iteration of the design (illustrated in Fig. 1) which now is in development use. This new electronics package has the following capabilities:

- Spike pulser
- Receiver bandwidth - .5 MHz to 18 MHz
- Programmable attenuator
- Waterpath delay/main data gate
- Pulse repetition rate - 10 Hz to 5 KHz
- Analog alarm outputs.
- Hewlett-Packard 182C scope
- Radio frequency and full wave rectified display
- Fully computer compatible
- Synchronizer - Keyboard readout
- Pulse trigger on/off
- Interface synchronizations of gate start
- Gated radio frequency and video output
- Digital readout of peak amplitude available

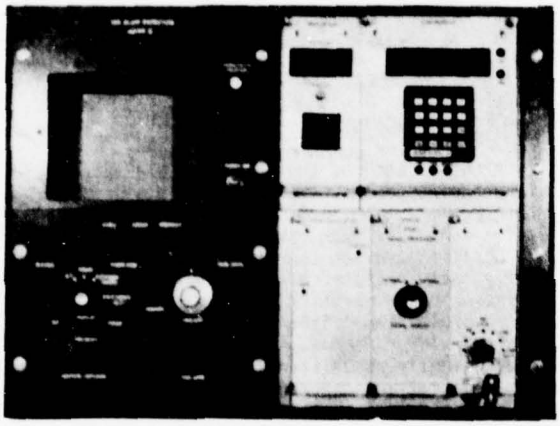

Fig. 1. Advanced computer interfaceable ultrasonic instrumentation

SIGNAL PROCESSING, ANALYSIS, COMPUTATION AND DECISION MAKING COMPONENTS

The components of the system that are involved with the signal processing, data analysis, computation and decision making include the Biomation 8100 Analog to Digital Converter, and the Digital Equipment Corporation PDP 11/55 computer illustrated in Fig. 2.

Biomation 8100 - The Biomation 8100 is a high speed analog to digital converter which is utilized for digitizing the radio frequency waveform as it comes from the ultrasonic instrumentation so that the system computer can further process and analyze the waveform information. The purpose of processing the total radio frequency waveform is to provide the capability to perform Fast Fourier Transforms (FFT) and spectral analysis of the inspection data as the need and technology develops.

PDP 11/55 Computer - The system computer performs a variety of tasks. These include setup and control of the Biomation 8100 and ultrasonic instrumentation with regard to data acquisition and inspection sensitivity. The computer's main task however, is to provide the signal analysis and decision making for the system. This includes performing a Distance Amplitude Correction for each pulse of data, correcting for signal degredation caused by lens effects of curved surfaces, as well as analyzing the amplitude of each pulse of information. Also, if during the course of an inspection a significant indication is detected, the computer must store all amplitude and positional information for further reference.

Fig. 2. PDP 11/55 computer and peripherals

SYSTEM MOTION CONTROL

The motion control of our ultrasonic inspection system is provided by a numerical control (GE 1050) which can be seen in Fig. 3. The choice of using an N/C for this task was made for two reasons. First, production ultrasonic inspection at GE has involved the use of N/C controls for several years. This experience was drawn upon in specifying the automated inspection system. Second, the GE inspection system has as one intent the complex analysis of the total Radio Frequecy Waveform. This involves significant computer processing power and prohibits the use of the system's computer for both data analysis and motion control.

The General Electric 1050 numerical control differs from conventional hard wired N/C equipment in that this control is a series of microprocessors, one for each axis of motion. These microprocessors control the motion of the system in both simultaneous linear and rotary motion. The fact that the control is microprocessor based provides the benefit that the major portion of the control logic is software based. This allows greater freedom in utilization as well as modification. The software based aspect is also a benefit in that it enhances communication between the N/C and the system computer.

The N/C is programmed using a unique program-

ming system developed by GE that allows for programming the N/C based totally on ultrasonic variables and not dependent on the conventional APT language most often used for N/C programming.

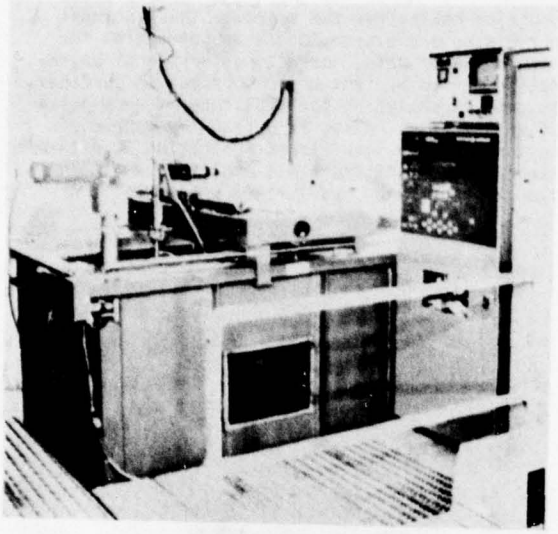

Fig. 3. Automated ultrasonic workstation including motion control - ultrasonic instrumentation and digitizer

MECHANICAL SYSTEM

The mechanical portion of the General Electric Inspection System was specified with rigidity and precision in mind. The mechanical system, shown in Fig. 3, consists of an immersion tank, rotating turntable with lift platform, three axis (X,Y,Z) bridge and double gimbal manipulator.

The immersion tank and turntable are fabricated of noncorrodible stainless steel. The turntable is completely enclosed to avoid any water turbulance at high rotational speeds. The lift platform provides the capability to load a part above water and then locate the part at a precise location below the water surface. The three axis (X,Y,Z) bridge is designed to machine tool accuracies for the rigidity and precision necessary to attain system reliability and repeatability requirements. The bridge provides the linear motion required to traverse a part during inspection. The double gimbal manipulator, also designed to machine tool tolerances, provides the rotary motions necessary to perform the inspection of complex contours.

These 5 axes of manipulator movement, 3 linear and 2 rotary, have been found to be necessary to perform the inspection of complex, contoured parts. The simultaneous movement of these 5 axes is accomplished through use of a mechanical system design requirements as shown in Fig. 4.

BRIDGE, X AND Y AXIS:

Positioning: ± 0.003 in./ft. (± 0.018 in. Total)
Resolution: 0.001 in.
Backlash: ± 0.001 in./ft.
Repeatability: ± 0.001in./ft.

SEARCH TUBE, Z AXIS:

Positioning: ± 0.003 in./ft. (± 0.012 in. Total)
Resolution: 0.001 in.
Backlash: ± 0.001 in./ft.
Repeatability: ± 0.001 in./ft.

SEARCH UNIT MANIPULATOR "a" AND "b" AXIS:

Positioning: ± 0.25°
Resolution: 0.1°
Backlash: ± 0.25°
Repeatability: ± 0.25°

ROTARY TURNTABLE, "c" AXIS:

Part Centering: 0.010in. TIR
Surface Runout (Full Load): 0.015 in. TIR
Elevating Positioning: ± 0.015 in.
RPM Constant Within 3% of Setting
Table to Bridge Parallelism (X Axis): ± 0.005 in./ft.
Table to Bridge Parallelism (Y Axis): ± 0.005 in./ft.
Table to Bridge Perpendicularity (Z Axis): ± 0.005 in./ft.
Table Lateral Movement: ± 0.010 in.

Fig. 4. General Electic near net shape ultrasonic inspection system - mechanical system accuracy requirements

THE SYSTEM IN TOTAL

Although each of the foregoing elements is unique and represents the latest of state-of-the-art technology, the real benefit from the system results when they each work in concert as part of an overall inspection operation. The following briefly describes the chain of communication and linkages already existing to provide a viable working production-oriented inspection system in which operator controls, influences and judgements are practically nonexistent. Figure 5 illustrates diagrammatically these relationships and communications linkages.

The inspection operation begins when the operator enters into the computer the part number of the component to be inspected. The inspection requirements for that component already exist in the computer memory from prior programming and/or communication with the CAD/CAM network. Information relative to the part configuration, required calibration level, the number and type of scans required, a definition of all manipulator movements, the scanning "evaluation" level, the evaluation accept/reject criteria are all in the computer file. The definition of the movements of the manipulator required to accomplish the inspection is transferred from the computer to the motion control. The inspection begins with the manipulator going from "home" position to that of locating the permanently fixed calibration block. The transducer is manipulated over the block in both longitudinal and shear positions to reach the prescribed calibration criteria, while the computer adjusts the instrument to provide the sensitivity level required for the inspection. Having established the inspection sensitivity, the transducer is moved to the inspection start position. Each step of the inspection operation is described

for the operator in alpha-numeric form on the control display device so the operator can follow the inspection sequence. The manipulator guides the transducer through each of the 20 or so positions required to obtain total part interrogation.

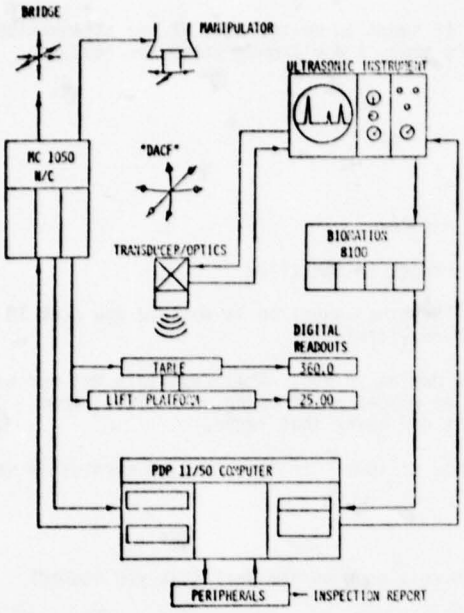

Fig. 5. Diagrammatic layout of near net shape system and communication linkages

During these movements, pulses from the instrument are interrogating the component relative to its internal quality. With the availability of the previously stored information relative to the part configurations, the computer continually adjusts the gating to exclude reflections associated with the front and rear surfaces. In addition, all returning signals are accessed relative to the part surfaces exposed to the beam, and returning signals, only slightly above the already low background noise level, are also considered relative to the depth below the surface where the signal is generated. The signal amplitude then is adjusted by the computer to accommodate the loss in signal strength due to attenuation. Adjustments in signal levels from reflectors on the near surface of the part also are adjusted automatically downward to accommodate the over inspections encountered in this area due to lens effects when inspecting cross section of any depth. As a result of these multiple corrections, each signal is considered at its "true" amplitude value.

With this information available, the computer considers the amplitude of the response in comparison with pre-established evaluation instructions. If the response amplitude is not considered significant, the data are discarded. However, if the responses exceeds the evaluation criteria, the response amplitude or the total R-F waveform of that indication can be digitized and entered into the computer memory along with the address location of all axes.

With the address of each suspect indication entered into the computer memory as it is encountered, the inspection continues uninterrupted until the total inspection sequence is completed. At this point, all suspect areas can be re-evaluated to better assess the character of the indication with already established evaluation routines. As an example, if a low level response was noted in a specific area, the computer would command the position control to return to that specific address. All axes would be located to satisfy the address requirement. At that point, an angulation maximizing routing would better assess the flaw to determine if, due to orientation, the signal could be increased above the level found during the scanning procedure. At this point, if an appropriate program were available, the R-F waveform response characteristics of the flaw could also be assessed from several positions. Once the evaluation data are obtained, then the computer can be programmed to treat the data in any prescribed way so as to make a decision relative to quality of the hardware or the nature of any suspect areas within it.

In this inspection system, we have available a total automated operating ultrasonic system which can be separately programmed to perform a specific or a sequence of pre-established inspection routines on live hardware configurations. The system can then subsequently process and manipulate the resulting resonse information in accordance with prescribed analysis routines, which include the processing of total R-F waveforms, or it can perform other manipulations required for enhanced flaw definitions. Thus, this powerful system becomes an available test bed which can further apply the theory and routines established in more limited laboratory evaluations. These approaches might enhance the assessing and quantifying of conditions associated with both the ultrasonic response character of different flaw types, as well as other effects. The successful testing of these technical developments under controlled conditions in real hardware with equipment adaptable to production use is one of the most pressing needs in bringing such advancements from the laboratory to production usage.

CONCLUSIONS

1. Advancements in ultrasonic technology offer the potential to gain a great deal more intelligence from the ultrasonic process than the type of inspecion data obtained heretofore.
2. A recently established test bed described in this paper can provide the facility capability to demonstrate the use of this advanced technology in hardware applications.
3. The demonstration of advanced technology applications on working production adaptable systems is a preferred direction to follow in gaining the acceptance of these advancements by the production oriented users.

DISCUSSION

Robert E. Green, Jr. (Johns Hopkins): Could I get the slide back that showed the performance characteristics themselves?

Dorothy Comassar (General Electric): Which performance characteristics?

Robert Green: What you talked about in the frequency range. It seems to me the bulk of the attenuation occurred using ten megahertz or five megahertz. If that's true, I don't understand the results.

Jerry Tiemann (General Electric): That's a typo.

Dorothy Comassar: That's a mistake.

Robert Green: What should it be?

Jerry Tiemann: Probably ten hertz to five kilohertz, but I'm not sure.

Dorothy Comassar: Let me check my write up. There were some errors in the slide.

Robert Green: It's very likely ten hertz to five kilohertz. The other question is why did you pick 18 megahertz as the limiting top frequency in the receiver band width?

Dorothy Comassar: I'm not really sure. Jerry, I'll pass that one on to you. That certainly met our needs and, I think, the system with the other constraints that we placed on it ended up in that range. I don't know that we designed it specifically for 18, but it did cover that range.

Jerry Tiemann: I think that arose from a tracing through of the minimum size flaw that we eventually wanted to detect which was of the order of a few mils.

Don Forney, Chairman (AFML): Another question over here?

George John (Aero Associates): How long does it take you to make a scan on the part that you showed?

Dorothy Comassar: We can achieve a 30 to 50 percent reduction in scan time merely by the automatic features of the system. A conventional system will not inspect that hardware. You have to have rectilinear shapes and a sufficient material envelope in order that the commercially available equipment will deal with it.

George John: So, what is the time?

Dorothy Comassar: An hour or so. I really would have to check if you want a precise answer.

George John: Well, it's not a minute.

Dorothy Comassar: No.

Don Forney, Chairman: Just one more question.

Harish Dalal (SKF Industries): You mentioned that to use the system all you have to do is to load the part and switch the system on and it goes. The sensitivity of the system also depends on the relationship between the transducer and the part.

Dorothy Comassar: One of the things I didn't mention because of the time is that the system automatically calibrates itself. There is a command, if you will, that starts the system. We can program in the sensitivity that we want to achieve and, resident in the tank, is the calibration block which sets the instrument setting.

Don Forney, Chairman: I'm afraid we've got to move on. Thank you very much, Dottie.

OVERVIEW OF PLANNED ULTRASONIC IMAGING SYSTEM WITH AUTOMATIC ALN DATA INTERPRETATION

A. N. Mucciardi and S. S. Lane
Adaptronics, Inc.
McLean, Virginia 22102

and

G. J. Posakony
Battelle-Northwest
Richland, Washington 99352

ABSTRACT

This presentation discusses a new program designed to investigate the effectiveness with which adaptive learning network (ALN) analysis can be combined with linear array, phase steered, ultrasonic imaging techniques to provide an enhanced means for automatic data interpretations. The DARPA-sponsored program is being performed as a team effort between Adaptronics, Inc. and Battelle-Northwest.[1] Battelle, under a subcontract from Adaptronics, is adapting the linear array imaging system being developed for the Electric Power Research Institute of Palo Alto, California, for use on this project. A special ultrasonic array will be developed to operate with the high-speed imaging system to acquire and record both specular and nonspecular signal information in both the time and frequency domains. Signal information from a multitude of simple and complex reflectors and defects will be recorded on the PDP 11 disk pack incorporated into the ultrasonic imaging system.

Adaptronics will utilize the time domain and frequency spectral data recorded from several thousand data points to develop algorithms and train networks which may describe uniquely the pattern of the reflections. The objective of the program is to provide a high-speed and automatic means for detecting, locating, sizing and displaying flaws in solid materials.

INTRODUCTION

It is generally recognized that the ultrasonic energy pattern or signature reflected from a given target contains substantially greater information than is being utilized by present ultrasonic nondestructive testing techniques. When an ultrasonic sound beam illuminates a given target, the pattern generated by the target contains reflected, diffracted and redirected energies which include time, amplitude and frequency spectral information that uniquely describes the reflector. Linear arrays afford the opportunity of capturing the pattern reflected from a flaw or target. The concept is shown in Fig. 1.

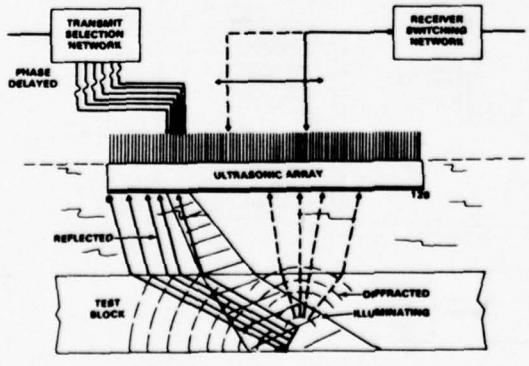

Fig. 1. Concept for acquiring ultrasonic data using phase-steered array

The figure describes an illuminating sound beam striking a target. In this instance, the target is not normal to the illuminating sound beam and little energy is reflected back to the elements which generated the sound beam. In a normal pulse-echo inspection, the target would not be seen as most of the energy reflected from the target falls outside the field of view. However, when an array is used, the length of the array extends the field of view to include capture of the reflected energy, the diffracted energy and any mode-converted redirected energy from the flaw. Reconstituting these energies into a pattern recognition "signature" which uniquely describes the defect as the source of the energy pattern requires computer interpretation of the acoustic "signature".

Battelle's effort on this research program is to develop the experimental procedure and acquire the ultrasonic "signatures". Adaptronics, using adaptive learning network analysis, is responsible for the characterization of the "signatures" for automatic interpretation and identification of the type, shape and nature of defect identified by the data.

The principal objective of the experimental effort is to develop new technology, demonstrating that ultrasonic arrays can provide the additional information available from the pattern of energy reflected from the flaw required to achieve automatic ALN interpretation.

[1] Contract DSA MDA 903-78-C-0223

LINEAR, PHASE-STEERED PROGRAM

The Electric Power Research Institute, under Contract RP 606-1, has funded Battelle-Northwest to develop an ultrasonic imaging system for the rapid and accurate characterization of flaws in heavy section steel structures. This ultrasonic system utilized two linear arrays: (1) a 120-element phase-steerable array for pulse-echo operation, and (2) a single illuminating transducer coupled to a 120-element linear array receiver for acquisition of the phase information. The computer-based ultrasonic system represents an advanced means for displaying subsurface defects in solid materials and can operate in either the pulse-echo or holographic modes. In its final form, the system will have the capability of providing B-scan, C-scan or isometric (combined B-C-scan) displays from the pulse-echo information and will be capable of high-speed computer reconstruction of the phase or holographic data. When complete, the system will provide an advanced means for visualization and interpretation of the size, shape and position of subsurface defects.

The major advantage of array technology, as used in the EPRI ultrasonic imaging system, is speed. The time required to perform an inspection in either the pulse-echo or the holographic mode is much less than that required to perform a similar inspection with conventional single transducer technology.

In the pulse-echo mode, the phase-steered ultrasonic sound field is nearly identical to the sound field that can be achieved with a monolithic single-element transducer. The electronic steering provides for high-speed zero and angle-beam inspections. Data from these inspections can be superpositioned on the display to provide a full perspective of the volume.

In the holographic mode of operation, the array network provides the means for high-speed acquisition of phase information from a large aperture (e.g., 6-inch x 6-inch - 150mm x 150mm). Operational details and performance results are given in other reports (1,2,3). The significance of this work is that the ultrasonic imaging system being developed is capable of providing "images" for enhancing the interpretation of the amplitude or phase information reflected from a given flaw. The theories involved in either the pulse-echo or holographic systems are within the state of known art.

The Electric Power Research Institute has agreed to make available the ultrasonic imaging system being developed on RP 606-1 for use on this program. The computer, display and mechanical scanning bridge components of the system will be utilized as the core for its technical effort. The imaging system, in its present configuration, is not directly adaptable to the investigations. Data acquisition rates for automatic interpretation research programs are much slower than those required for imaging. As an example, the illuminating sound field will remain in one position for the period of time required to switch through the various receiver locations and data from each appropriate position will be recorded. The imaging system samples each point once. To achieve the desired protocol, a separate electronic network will be fabricated. A block diagram of the functional requirements is shown in Fig. 2.

Eight elements of the 120-element array will be used to generate a sound field. The receiver switching netowrk will sample through 64 separate locations; amplitude, time, phase and RF waveform data will be recorded from specific locations. The RF waveforms will be recorded on a Biomation 8100 transient analyzer which interfaces with the EPRI computer system. This system is compatible with the Adaptronics computer networks.

The arrays used in the present EPRI imaging system are not directly adaptable. The EPRI pulse-echo array is a 120-element linear array which is 3.6 inches (91mm) long by 1-inch (25mm) wide and is designed to operate in a narrow-band mode at a center frequency of 2.3 MHz. The DARPA program requires a broad-band array that is somewhat longer and somewhat narrower. Consequently, a new array will be designed and fabricated that has the performance features desired to obtain both amplitude

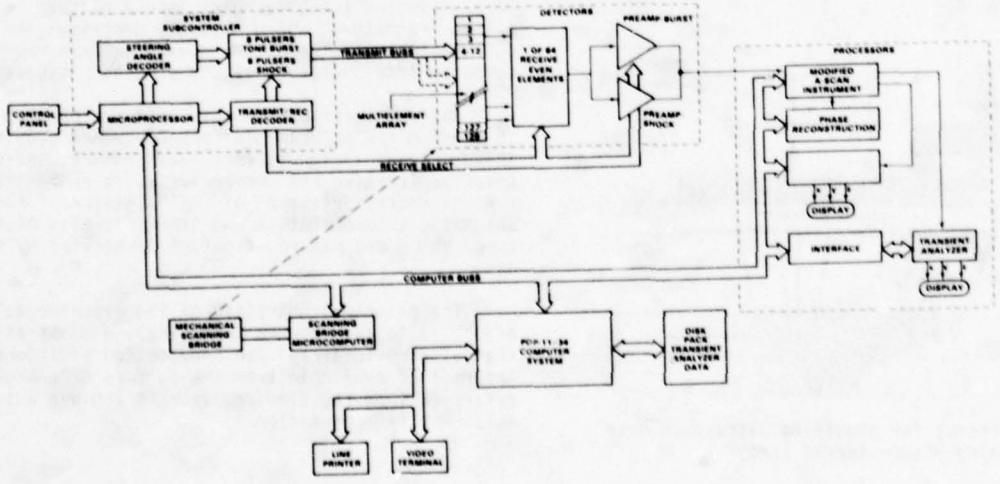

Fig. 2. Block diagram of electronic network

and spectral information.

TEST BLOCKS

For the initial demonstration of the concept, test blocks have been chosen which contain a series of machined defects, including flat-bottom holes, round-bottom holes and EDM notches. A total of 96 defects will be used in the initial part of the experiment. Table 1 shows the distribution of the machined defects. Defects will be placed in 2-inch (50mm) steel plates. The defect size range was chosen to cover both sub-wavelength and multiple wavelength reflectors. While machined defects are significantly easier to characterize than natural flaws, their characterization through ALN interpretation is an essential learning step.

Table 1. Machined defects in steel blocks

Flat Bottom Holes		Round Bottom Holes	
0^0	30^0	0^0	30^0
1/64	1/64	1/64	1/64
↓	↓	↓	↓
1/64	1/64	1/64	1/64
16	16	16	16

EDM Notches			
0^0	30^0	0^0	30^0
"3-1"	"5-1"	"3-1"	"5-1"
0.010	0.010	0.001	0.01
0.020	0.020	0.02	0.02
0.030	0.030	0.03	0.03
0.040	0.040	0.04	0.04
0.050	0.050	0.05	0.05
0.060	0.060	0.06	0.06
0.070	0.070	0.07	0.07
0.080	0.080	0.08	0.08
8	8	8	8

Total Number: 96

The shape of the machined defects (FBH, RBH, EDM) was chosen to represent laminations, spherical voids and crack-like defects. Theoretical work being performed under other DARPA/AFML programs may be directly correlatable to the experimental results achieved on this program. During the course of the program, other, more typical, "natural" defects will also be evaluated. The signature patterns reflected from the machined defects will establish the basis for future work.

DATA ACQUISITION AND IMAGE DISPLAY

Figure 1 shows the basic concept in which the flaw is illuminated by the transmitted beam and the reflected pattern is received at various locations along the length of the array. The engineering experiment is designed to acquire the data, identify its parameters and present these data so that the significant parameters can be selected for further analysis. Between 10 and 25 data points will be recorded for each of the 96 flaws in the test blocks. Figure 3 shows an RF waveform typical of the pattern recorded on the Biomation 8100 transient recorder. A printout of the 2048 sampling points from the Biomation, as well as a hard-copy RF waveform of the signals at each of the selected positions, will be recorded.

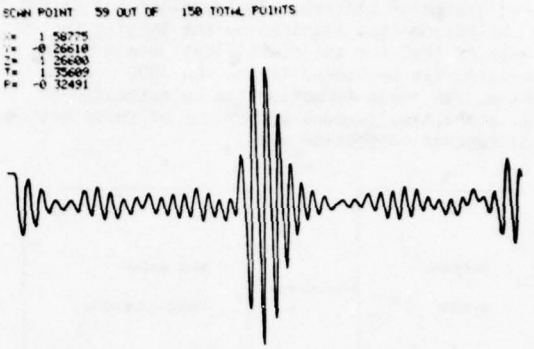

Fig. 3. Typical RF waveform digitized by Biomation transient recorder

To demonstrate the display capability of current technology, photographs and recordings of images of flaws within the test blocks will be taken. Commercially available pulse-echo C-scan techniques will be used as one of the display presentations. In addition, the ultrasonic array imaging system developed for EPRI to provide B-scan, C-scan and isometric (combined B-C-scan) images and to generate phase or holographic images of the various flaws will be employed.

AUTOMATIC ARRAY OPERATION

One of the most important features of the system described here is that it will demonstrate the feasibility of fully automatic collection and interpretation of the ultrasonic data. Ultimately, an ALN 4000 microcomputer, developed by Adaptronics, Inc., will, on initiation by an operator, scan the object under inspection with the ultrasonic array described above. Detection, classification and sizing will be carried out without operator intervention in the final configuration.

Array positioning and transmitting and receiving logic will be under the microcomputer's control, and will initially follow an optimum sequency for defect detection. Analysis of the returned signals in this mode will be made by the ALN 4000 and will result in a detection log, giving the locations of suspicious regions in the test specimen.

Once these regions of interest have been identified, the microcomputer will position the transducer array over each of them in turn. For each defect, a series of measurements will be made, again under computer control, which will result in a decision regarding the type of defect under examinatin and its orientation. After this classification step is completed, the system will proceed to defect sizing.

The sequence of operations involved in sizing defects will depend on the results of the classification step described above. The processor will position the array in the correct orientation (or orientations) and generate the required ultrasonic beams. Analysis of the returns at selected elements will yield an estimate of the defect size.

The EPRI imaging system will be compatible with the ALN 4000, so a visual image of the defect will be available at the same time. Figure 4 shows the shared system of control. Instructions for gathering the information required by the imaging system, as well as that for the classification and sizing procedure, can be stored in the ALN 4000. Consequently, the image formation can be automated as well, and a simultaneous comparison of these methods of ultrasonic inspection made.

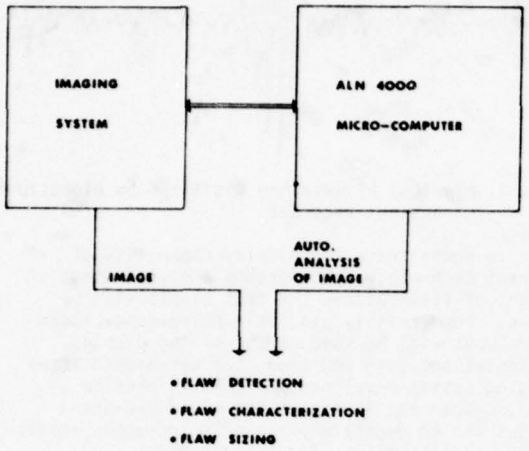

Fig. 4. Shared system of control between the EPRI imaging system and the ALN 4000 microcomputer interpretative system.

ALN CLASSIFICATION AND SIZING

An adaptive learning network will be developed to process the ultrasonic data in a mode parallel to that which provides the images of the previous section. Figure 5 shows the streams of data flow. Two sequential processes must be performed by the processing system: classification and sizing. They are sequential because the particular measurements and their interpretation for sizing depend, to some extent, on the nature of the target under examination.

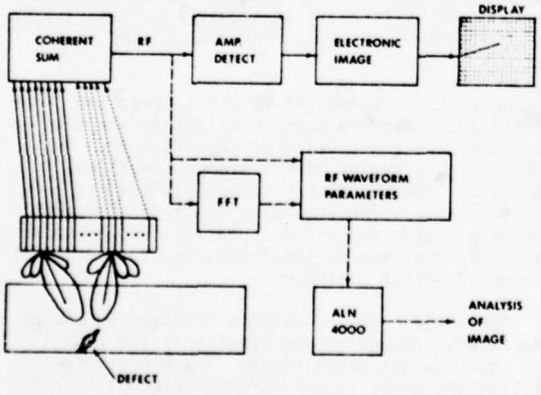

Fig. 5. Information flow for systems shown in Fig. 4.

Classification: It is anticipated that classification of the defects into planar or spherical voids or cracks can take place using time-domain parameters only. Advantage will be taken of the fact that the angular distribution of the reflected and diffracted power is determined by the shape and orientation, as well as the size of the defect. Thus, ratios of total power scattered in various directions, for a few directions of the incident energy, should be sufficient to distinguish between some of the types and orientations of defects to be encountered during this study. These ratios can be formed from powers measured from the time waveform, simplifying the data processing requirements.

Further information as to defect type will come from the location of the returned signal in the time-domain waveform. This information, combined with the velocity and path length of ultrasound in the test block, will give the defect's spatial location, assisting in discriminating between cracks growing from the back surface and voids within the metal.

Since, in general, mode conversion occurs when ultrasonic energy in solids strikes a defect, more than one type of returned wave may be detected by the receive array. Again, power ratios among these arrivals are expected to give information useful for classification.

Sizing: Once the nature and orientation of the defect have been determined, the appropriate RF waveforms will be acquired to proceed with sizing. Some of these waveforms may already have been taken during the classification process; if so, they will not be remeasured. Now, Fourier spectra of the data will be taken and additional parameters extracted. It is expected that the ratios of mode-converted energy determined in the classification step may also be used in the sizing step. These spectral and time-domain parameters will be input to an ALN trained to estimate the size of the particular defect type and orientation under inspection. Then the outputs of the classification ALN and the sizing ALN will be presented simultaneously to give the best available estimate of the defect type, orientation, and dimension.

REFERENCES

1. R. L. Becker, B. L. Crow, T. H. Davis, B. P. Hildebrand, G. J. Posakony and V. L. Crowe, "Development of an Ultrasonic Imaging System for the Inspection of Nuclear Reactor Pressure Vessels", Third Progress Report - September 1977, for the Electric Power Research Institute RP 606-1.

2. G. J. Posakony, F. L. Becker, B. L. Crow, J. C. Crowe, T. J. Davis and B. P. Hildebrand, "Development of an Ultrasonic Imaging System for Inspection of Nuclear Pressure Vessels", Proceedings of Sixth UIRAPT International High Pressure Conference, July 25-29, 1977, Boulder, Colorado.

3. G. J. Posakony, "Acoustic Imaging - A Review of Current Technologies for Utilizing Ultrasonic Linear Arrays for Producing Images of Flaws in Solids", Proceedings of Symposium on Electric Wave and Nondestructive Testing of Materials,

ASMA Annual Meeting, December 10-15, 1977, San Francisco, California.

DISCUSSION

Don Forney, Chairman (AFML): Thank you, Tony. The bell went off while the applause was going on, so the timing was perfect. We're running behind time, and as a result, I would like to press on without questions at this time. I know that the talks deserve an opportunity for questions and answers, but we're just running out of time and perhaps you can attack either Tony or Jerry during the poster session this afternoon and get some more details. Thank you.

Robert Green (Johns Hopkins): Don, could they just comment on when they'll get some results on this?

Don Forney, Chairman: Bob asked the question, "When do you expect some results from this that they can look at?"

Anthony N. Mucciardi (Adaptronics, Inc.): Preliminarily, within six months, and more specifically, by about this time next year.

Don Forney, Chairman: So you do have time to wait until this afternoon.

TEST BED FOR QUANTITATIVE NDE

R. C. Addison Jr. and R. B. Thompson
Rockwell International Science Center
Thousand Oaks, CA 91360

ABSTRACT

The ARPA/AFML Interdisciplinary Program for Quantitative Flaw Definition has demonstrated a number of new techniques for quantitatively sizing flaws, as are reported elsewhere in these proceedings. The next step required in the transfer of this technology to the production line is the assembly and demonstration of these techniques in a single, integrated measurement system. The technical plan of a recently initiated test bed program, which will serve this function, is described here.

The hardware system will consist of a California Data Corporation microcomputer based controller driving a six degree of freedom system composed of an Automation Industries manipulator and turntable plus an in-house bridge. Overall control of the system will be handled by a Data General, Eclipse S/200 minicomputer. This system will have a series of operational modes. Initial scanning of a part will be accomplished in a manner similar to that presently used in computer-controlled ultrasonic systems at several industrial facilities. In addition, the system will have an extended data gathering capability so that imaging, adaptive learning, and long wavelength flaw characterization techniques can be implemented under control of the minicomputer and with the aid of auxiliary hardware as appropriate. The computer will further be used in processing and displaying the derived, failure related information. System design will be sufficiently flexible that it can be used in the evaluation of other new research results as they are developed.

The ultrasonic test bed program has been initiated to complement the ARPA/AFML Interdisciplinary Program for Quantitative Flaw Definition. Specifically, we plan to implement the variety of new techniques that have arisen for obtaining quantitative data about flaws such as the size, shape, orientation and stress intensity factor.

The completed test bed will be self contained, will be based on the design used in commercially available contour following units and will use commercially available hardware and controllers coupled to a dedicated minicomputer.

All of the modes of flaw characterization that are being developed in the ARPA/AFML program will be incorporated in the test bed. These techniques will be applied to geometries that are found in real parts such as turbine disks. The test bed design will be sufficiently flexible to evaluate other new techniques as they become available.

An important feature of the test bed is that it is a fully dedicated facility that will be available for use by DoD contractors for a year after completion of the contract.

To facilitate the explanation of the test bed program, the feedback system shown in Fig. 1 will be used as a paradigm. The input to this system will be real parts containing flaws. A collection of data will be extracted from each part concerning the location and number of tentative flaws. Next, each flaw will be processed according to one or more of the established techniques for extracting quantitative values of the flaw parameters. These measured flaw parameters will then be compared to the actural flaw parameters and the results of this comparison will be fed back and used to improve the techniques for obtaining quantitative values of the flaw parameters.

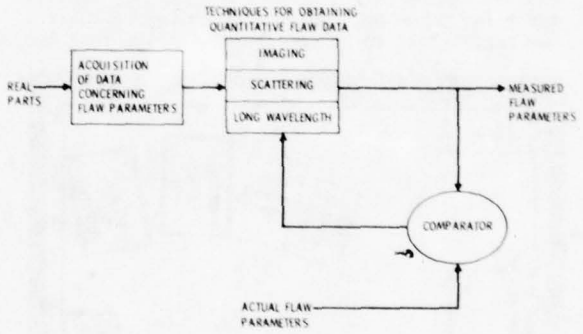

Fig. 1. Feedback system paradigm for test bed program.

The present ARPA/AFML program has fostered the development of the separate modules that make up the flaw processing block in the diagram. One of the functions of the test bed program will be to integrate these modules into a working system. It will be necessary to establish a suitable interconnection scheme for the modules and deal with any interfacing problems that occur. The test bed program will also address the problem of extracting data from flaws in real parts. The basis for doing this will be a conventional contour following system. The departure from a conventional system will occur when specific flaws are addressed in a detailed way, and in the use of an acoustic array to gather data. Finally, the test bed will provide a means for directly comparing the results of flaw evaluation techniques in real parts with the actual flaw parameters.

The benefits to be derived from the test bed program are closely related to the system shown in Fig. 1. The technology transfer items are:

1) The integration of the various research results or modules into a form suitable for transfer to DoD contractors.
2) The demonstration that the improved accept/reject criteria can be applied successfully to real parts.
3) A prototype for future, more specialized systems and stand alone spin-offs.

There are two interrelated items that are associated with the feedback loop to the research modules. First, there is the comparison of the measured flaw parameters with the actual flaw parameters and the refining of the measurement techniques. Second, if after suitable refinements have been made, one finds that practical constraints degrade the quality of some of the measured flow parameters, this information can also be fed back into the research program.

One of the laboratories within the Science Center will be dedicated for use by the test bed. The layout, shown in Fig. 2, includes the water tank, instrument racks and the minicomputer. Rockwell is providing the money for the capital equipment as well as the laboratory space. The benches on the left side of the room will provide space for other DoD contractors to set up their own experiments to be performed with the test bed.

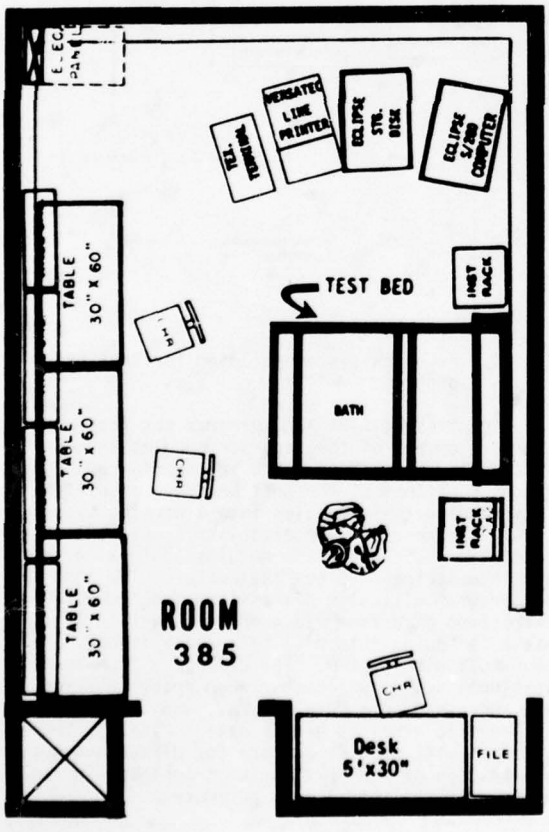

Fig. 2. Layout of test bed laboratory.

The test bed will operate in two distinct modes. First, there is the search mode during which the entire part is scanned. As the scan progresses, the echo waveforms are quickly compared in a fairly coarse way to some sort of reference. For those echoes that seem to come from flaws, the coordinates for the position of the flaw are stored in memory so that at a later time, the flaw can be fully evaluated. The test bed will then enter the evaluation mode and will take each of the tentatively identified flaws in turn and examine it in detail. The particular technique used for the examinations will depend on the size of the flaw relative to the wavelength of the ultrasonic beam. The appropriate parameter to use for categorizing flaws is ka, where $k = 2\pi/\lambda$, λ is the wavelength of the acoustic wave and a is the radius of the flaw. The four techniques of examination to be used are summarized in Fig. 3 according to the value of ka.

I. SEARCH MODE - RAPID SCAN TO LOCATE QUESTIONABLE AREAS.

II. EVALUATION MODE - MORE DETAILED EVALUATION OF IDENTIFIED AREAS.

TYPE	REGIME	ADVANTAGES
IMAGING	ka>6.3 (λ<a)	HIGH INFORMATION CONTENT EASILY INTERPRETED DISPLAY RESOLVES MULTIPLE FLAWS.
MODEL BASED RE-CONSTRUCTION	ka>3	PHYSICAL PRINCIPLES USED TO IMPROVE RESOLUTION AND TREAT MODE CONVERSION.
MODEL BASED ADAPTIVE LEARNING NETWORKS	0.4<ka<3	MULTIPLE SCATTERING TAKEN INTO ACCOUNT. GAIN MORE INFORMATION IN DIFFICULT REGIME.
LONG WAVELENGTH SCATTERING	ka<0.5	FRACTURE RELATED PARAMETERS DEDUCED FROM A FEW MEASUREMENTS MAY BE USEFUL IN AUTOMATION.

Fig. 3. Modes of operation.

For ka > 6.3, imaging is the preferred method of examination. It provides high information content and an easily interpreted display. An additional advantage of this technique is that it can provide a high resolution map of the flaw area and can separate multiple flaws, even when it cannot resolve details of the individual flaws. For ka $\geq$ 3, it is preferable to use a model based reconstruction technique, such as those being developed by Bleistein and Cohen[1], and also Rose[2]. Here, physical principles related to the wave propagation are used to improve the resolution and also treat mode conversion. For ka between 0.4 and 3, it is difficult to obtain information about the flaw unless one uses a model based on adaptive learning networks which takes account of multiple bounces within the scatterers. For ka < 0.5, we are in the long wavelength regime. Here, one can make a few measurements and by calculating the curvature of the spectrum of the defect signal, one can deduce the stress intensity factor. Thus, it is possible to obtain a single number that will characterize the flaw. This may prove advantageous for automating a system to categorize flaws.

In order to implement these techniques, we must establish a protocol for their use. In other words, we must determine how the various research modules are to be interconnected in the "quantitative flaw techniques" box shown in Fig. 1. The

system we intend to use is shown in Fig. 4.

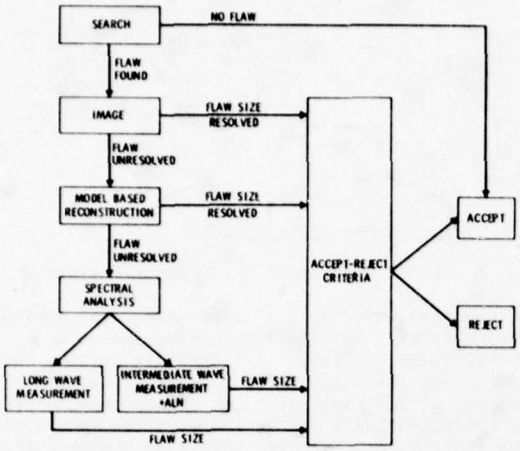

Fig. 4. System protocol.

The part is first searched and once a flaw is found, it is imaged. If the flaw size is resolved, the accept/reject criteria is used to decide if the part is acceptable. If it is unresolved, a map can be made to determine if there are multiple flaws within a small area. Next, appropriate data is taken so that a reconstruction technique can be used to form an image of the flaw. If the flaw is still unresolved, we will examine the Fourier transform of the defect signal with the transducer response properly deconvolved and determine the ka value of the flaw. Depending on the value of ka, we will then use either adaptive learning techniques or long wavelength techniques to characterize the flaw.

The road maps shown in Fig. 5 provide some additional insight concerning the way results obtained in the ARPA/AFML program will be factored into the test bed program. At the present time, we are in the detailed design phase of the program and are utilizing inputs from the four different data gathering regimes to help define the needs of the system. Later, when the techniques are being implemented, the feedback loop of Fig. 1 will be used to transfer information from the test bed to the ARPA/AFML program concerning the need for revision of some of the examination techniques. These revisions will subsequently be incorporated into the test bed program. This exchange will occur on a continuous basis for the entire period of overlap between these programs.

The block diagram for the physical test bed system is shown in Fig. 6. The transducer has five degrees of freedom. It can be moved rectilinearly along x, y and z, as well as having a double gimbal movement that will permit it to be rotated about two orthogonal axes. The two gimbal movements, as well as the z axis motion, are incorporated into a standard manipulator arm that is being provided by Automation Industries. The x and y motions are incorporated into an existing assembly. We expect to maintain a positioning accuracy for the overall system of about .040" over the entire range of motion. Stepping motors will be used to move the transducer in .001" increments. The control for the stepping motors will be handled by a microcomputer system that will be provided by California Data Corporation.

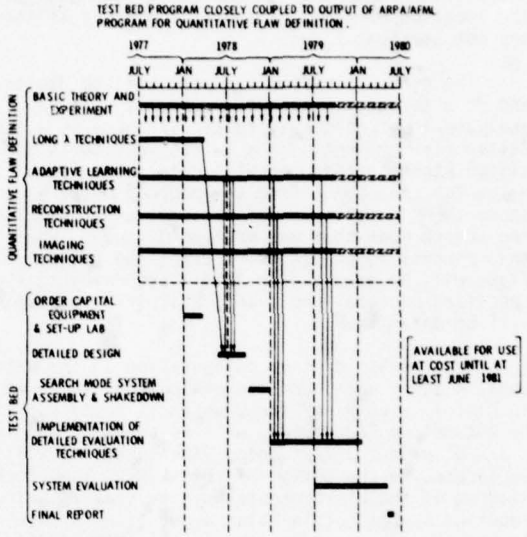

Fig. 5. Road maps.

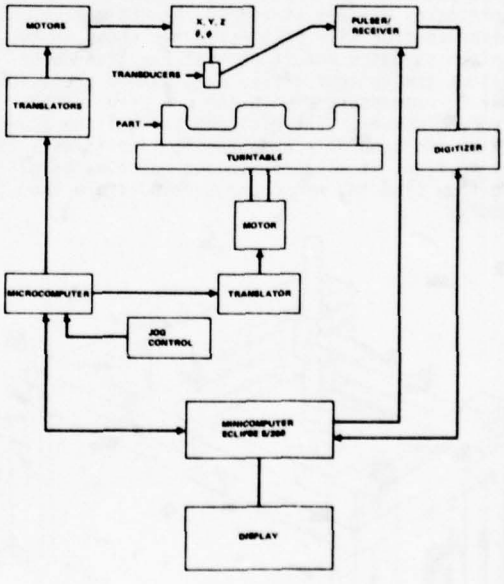

Fig. 6. Test bed block diagram.

In addition to the five degrees of freedom of the transducer, a sixth degree of freedom is provided by a turntable that provides a fast axis for rotationally symmetric parts such as turbine disks. In operation, the turbine disk will be rotated at

a speed that is selected on the basis of the desired resolution for the inspection as well as the maximum pulse repetition rate of the transducer. The transducer will be moved radially along the turbine disk and will be kept pointing along the normal to the surface of the disk. The microcomputer will control the movement along any one curve segment, and the minicomputer will specify the end points of the curve segments and the location of their center of curvature if they are not straight lines.

The echo train from the part will be digitized and sent to the minicomputer where it will be analyzed in a coarse way to see if there is a tentative flaw present. If a tentative flaw is identified, the minicomputer will obtain the coordinates for that point from the microcomputer and store them in memory. This process will comprise the search mode that was mentioned above. When this process is completed, each of the tentative flaws will be examined in detail according to the specified protocol and quantitative flaw parameters will be determined.

A schematic of the configuration of the water tank, x and y axes, and the manipulator is shown in Fig. 7. The water tank, which is being supplied by Automation Industries, will be about 5' long x 3 1/4' wide x 3 1/2' deep. The turntable will be located in the bottom of this tank. The block diagram of the microcomputer system that is being supplied by California Data Corporation is shown in Fig. 8. The minicomputer (an Eclipse S/200) will send over the starting and ending coordinates for the curve segments of a rotationally symmetric part. For an arc, the coordinates of the center of curvature will be sent over as well. These coordinates will be stored in the RAM memory. The master control will proportion the steps to the various stepping motors so that the transducer follows the contour of the part with a precision that is commensurate with the precision of the stepping motors. The minicomputer will be analyzing the echo data and when it identifies a tentative flaw, it will obtain the coordinates of the flaw from the microcomputer and store them in memory.

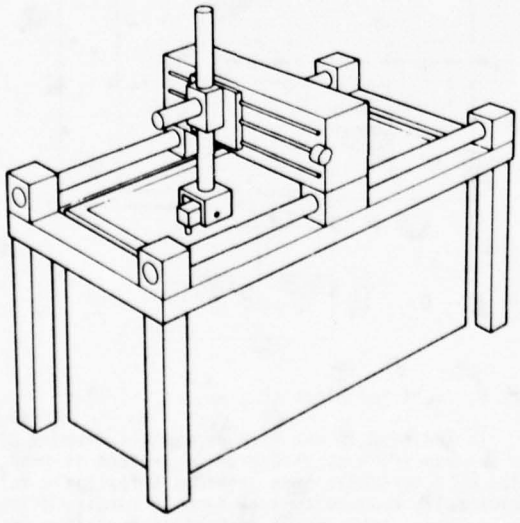

Fig. 7. Schematic of test bed.

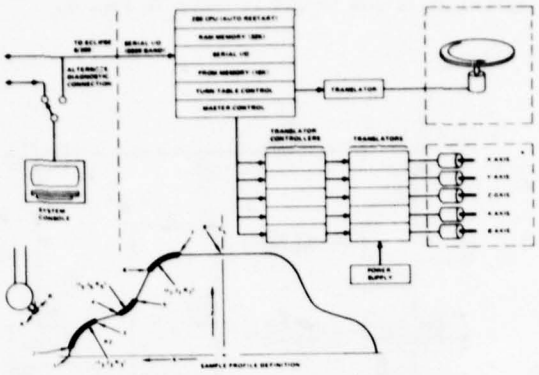

Fig. 8. Block diagram of microcomputer system.

We have been implicitly assuming that a single transducer will be utilized for the search mode described above. This will certainly be true during the initial phases of the program. We also plan to initially use only one or two transducers for collecting data during the detailed examination mode. Ultimately, we plan to use an acoustic array, both for forming images and also for obtaining scattering data. We are currently doing the design work for an array that will be suitable for these purposes. Figure 9 shows a linear array with time delay steering which would have a total of 240 elements. Only 16 contiguous receive and 16 contiguous transmit elements would be used at any one time. The delays for the elements would be programmable. This type of array would be advantageous for looking at real parts that have non-flat surfaces. The capability of tilting the beam and changing its focus would permit contour following at a much faster rate than is possible with stepping motors. Furthermore, one could adjust the focus to compensate for the deficiency caused by the curvature of the part. In the imaging mode, the second transverse dimension of the image could be generated by rotating the turntable. There are, of course, other possibilities as well. The array would utilize pulses of ultrasound and would work in the reflection or pitch catch mode. The contour of the part would be stored in the computer and would be used to steer and scan the beam formed by the array.

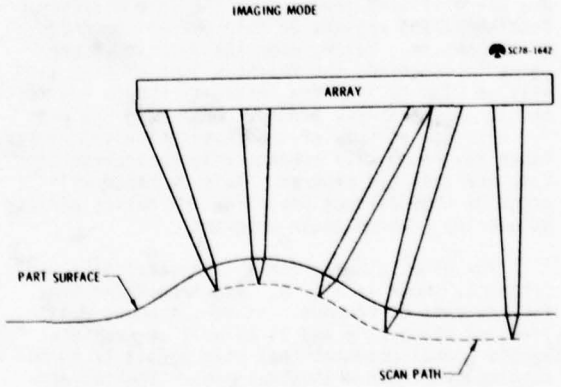

Fig. 9. Linear array used for reflection mode imaging.

For obtaining scattering data, the array could be used as shown in Fig. 10, i.e., in a pitch catch mode with the receive elements operating over a range of angles as the array is rotated about an axis passing through the flaw. Note that the array has the flexibility to operate in the pulse echo mode and also to use a group of elements displaced from the rotation axis as transmitters in a pitch catch configuration.

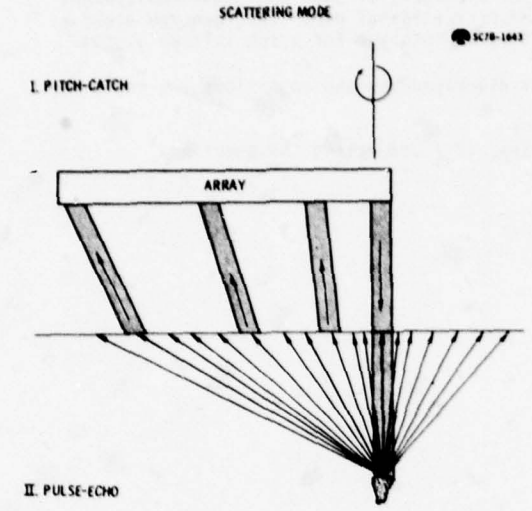

Fig. 10. Linear array used in a pitch catch mode for obtaining scattering data.

The electronics for driving this array (Fig. 11) will be comprised of 16 receive channels and 16 transmit channels. There will be a programmable digital delay line in each of the 16 transmit channels that will be switched to one of the 16 active transducer elements by a switching matrix. The delay lines and the switching matrix will be driven by a computer memory containing the part contour information. The active array elements will be shock excited. The receive channel will have a preamplifier, another programmable switching matrix and a programmable analog delay line. The outputs of the analog delay lines will be summed and digitized before sending them to the computer. We are currently working out the details of this design.

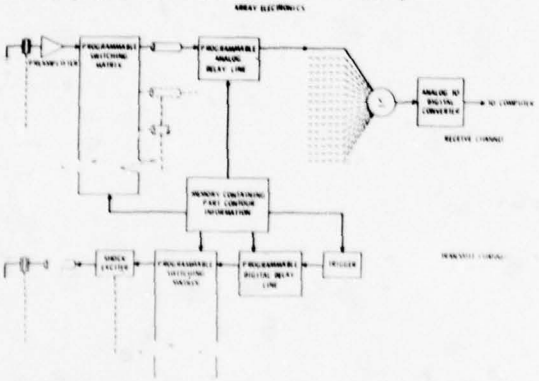

Fig. 11. Electronics for driving array.

We plan to look at a wide variety of different parts during the test bed program, including many of the samples that have been used during the ARPA/AFML program. In addition, we will specifically look at three categories of defects as a final exam. First, there will be a demonstration of the capability of the ultrasonic inspection system to predict the life of a cracked part subject to fatigue stresses. We will first measure the size and aspect ratio of a surface crack on a flat plate. Next, the sample will be fatigued and then ultrasonically measured. This cycle will be repeated several times in order to demonstrate that the crack growth can be tracked by ultrasonic measurements. A prediction of the life of the sample will be made and then it will be fatigued until failure. The actual lifetime will be compared with the predicted lifetime.

Next, there will be a demonstration of the capability of the test bed to detect and size internal inclusions in a real part. One of the parts that is of current interest is a turbine disk, and in particular, there is a need to be able to detect defects in the inner bore of a F-100 turbine disk. This inner bore is 7" in diameter and the test bed will be designed to access a bore of this size. Because of the difficulty of obtaining a turbine disk with a flaw in its inner bore, we will probably simulate this flaw by diffusion bonding two titanium disks together with an inclusion inside of them. The bonded disk will then be machined so that it is crescent shaped with the inner periphery of the crescent having a 7" diameter. The flaw will be just inside of this inner surface. Thus, we will have to access a flaw that is just below a concave cylindrical surface.

Finally, we will inspect a part with a complex geometry. We anticipate that this will be the third stage compressor disk that has been removed from a TF-33 engine. This disk will contain cracks emanating from bolt holes previously characterized by eddy current techniques. This will provide the most stringent test of the effects of complex geometry on the quantitative NDE procedures.

REFERENCES

1. Cohen, J. S., Bleistein, N. and Elsley, R. K. "An Inversion Technique for Reconstruction of Shape of Voids," Review of Progress in Quantitative NDE, La Jolla, 1978.

2. Rose, J., "Experimental and Theoretical Evaluation of Born Inversion Procedure," Ibid.

DISCUSSION

Paul Höller (Saarbrücken University): I'm accustomed to observe from this country that which is called "mock-ups" and you use the term "test bed." My question is: These test beds which were described which you're going to build, are they prototype equipment for automatic testing systems to relate to use in fabrication or are they just to demonstrate the capabilities of systems and methods you're developing under this program?

Robert C. Addison (Science Center): The test bed that I am working on I see, first of all, as a demonstration of some of the quantitative flaw techniques with real parts and second of all, as I mentioned in one of the slides, our test bed will probably will be more general than one might really want for a specific system. Thus, you would select a system or a class of parts and then you would specialize the system. This system could then be used as a prototype for a specialized system.

Paul Höller: We are not yet considering the environmental discrepancies and conditions you would have later on, so the mock up will be the next step?

Robert C. Addison: *Yes, I believe that will be the next step, if I understand the question.*

Paul Höller: Thank you very much.

ULTRASONIC IMAGING PROJECT AND TEST BED

B. J. McKinley
Lawrence Livermore Laboratory
Livermore, CA 94550

ABSTRACT

This paper describes the Lawrence Livermore Laboratory (LLL) Ultrasonic Imaging Project. The project's purpose is to increase resolution and produce accurate graphic ultrasonic images. Sub projects directed at achieving these goals are: (1) mathematic modeling of elastic wave scattering for realistic defects, (2) developing signal analysis techniques to allow thorough quantitative ultrasonic field measurements, (3) design and fabrication of a high precision, versatile, computer controlled two-transducer ultrasonic test bed with on-line computerized data acquisition, analysis, and image display.

Improved methods for quantitative evaluation of bond strength, cracks, and joining are required by current LLL programs. From these requirements the necessity for a two transducer test bed has become evident. The major emphasis of this paper is to describe the sophisticated new concept in ultrasonic test beds now under development.

INTRODUCTION

An Ultrasonic Imaging Project is in progress at Lawrence Livermore Laboratory (LLL). The purpose of the project is to increase resolution and produce accurate graphic ultrasonic images. The word "image" is used in a broad sense to include a variety of methods for displaying quantitative test results. A central feature of the project is the two-transducer ultrasonic test bed shown schematically in Fig. #1.

Our motivation comes from the need to satisfy an endless variety of LLL ultrasonic inspection requirements. The overall project goal is to make pertinent quantitative material evaluations with the highest attainable accuracy. Our requirements generally fall into four categories: First, bond strength evaluation; second, accurate surface crack depth measurement, third, definition of the size, shape and orientation of material defects, and fourth, the inspection of one of the above three categories in some complex configuration.

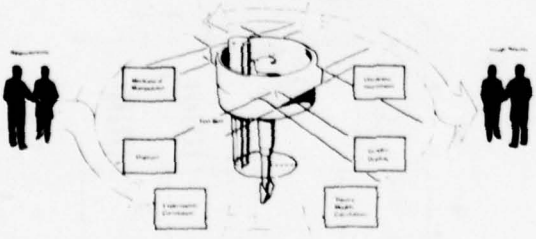

Fig. 1. Ultrasonic Imaging Project Schematic

The present state-of-the-art in ultrasonics is limited in its ability to produce quantitative measurements. To minimize these limitations, we have concentrated our efforts on improving our theoretical understanding and developing advanced test hardware. The theoretical research involves mathematical modeling of the scattered elastic fields from realistic defects and perfecting signal analysis techniques necessary for quantitative field measurements. The development effort involves upgrading existing ultrasonic test beds in terms of versatility, accuracy, online data analysis, and graphic display. The concepts for the new two-transducer ultrasonic test bed now under development have evolved out of practical experiences of the past 15 years. These experiences include ultra-precision machine tool design, ultrasonic instrument design, computer control of manipulators and data acquisition, and study of a wide range of theoretical approaches to the imaging problem. The versatility and precision of this test bed are absolutely necessary to realize the full potential of ultrasonics.

LLL PROGRAM REQUIREMENTS

There is a wide variety of ultrasonic tests which we are asked to do. They differ primarily in the geometry of the objects to be inspected. In our Lab, as in many others, the trend towards more efficient designs has made quantitative nondestructive testing extremely important. More complex designs, high strength requirements, composite materials, and a number of new joining techniques have made dramatic changes in ultrasonics, particularly with regard to the required resolution. In general, the test requirements can be divided into four categories which are discussed in the following section.

Bond Strength Evaluation Problems - In bond strength evaluation our task is to image the size and distribution of "island of unbond" and correlate the results with reduced bond strength. There

are three types of evaluations of immediate interest. The first and simplest geometry is the plain bonded surface. Examples are diffusion bonding and plating where the bond interface position is well defined. The second, and more complicated, is the multiple plain bond interface. An example is the bonding of two dissimilar materials with a thin plating of a third material between them. The third category, which includes a braze, is referred to as a "graded interface". These interfaces are more complicated because the lack of knowledge of exact depth of unbond defects within the bond zone, the variation of material constituents after solidification, and the uncertainty of the reflectivity of a normal braze.

Surface Crack Depth Measurements - Cracks which terminate at a free surface are of great concern. Our task is to describe the crack accurately. Fracture mechanics concepts can then be used to calculate the serviceability of a structure given the dimensions of the crack. An example is the "crack" that is the result of incomplete penetration of a butt weld. Since the position and orientation of such a crack is known, our objective is simply to measure its depth. The complications involve variations in material properties in the weld zone and adequate resolution when the crack critical dimension is on the order of a wavelength.

Material Defect Evaluation - Quantitative measurement of the size, shape, and orientation of material defects such as cracks, voids, and inclusions is an extremely broad category. It is an area where significant advancements have recently been made, particularly in mathematical modeling of the scattering of idealized defects such as ellipsoidal voids and penny shaped cracks. We intend to put a sizable effort into both the theory and experimental verification of the mathematical models predicted by the theory.

Inspection of Complex Configurations - LLL designers are extremely clever at producing objects that are almost impossible to inspect. A great deal of our effort involves fixturing to handle complex configurations or items which are one of a kind. The greatest difficulty occurs when it is necessary to manipulate two transducers independently to perform the inspection. A simple example is a small tube brazed into a cylinder with the tube axis not normal to the cylinder wall.

LIMITATIONS

The limitations of ultrasonics are easily stated. We need to increase resolution and produce intuitive images, or displays. The simplest way to increase resolution is to increase frequency as is done with an acoustic microscope. There are problems in inspecting industrial products which limit the frequency we can use, but in general our trend will be toward higher frequency. We need to improve the precision of our systems in an overall sense. We must design mechanical and electronic systems with a primary objective of accuracy and "built in" methods of maintaining and checking the accuracy over the life of the system. In other words, a fundamental limitation is the lack of imaging systems which can be calibrated.

There are two theoretical limitations which we are working on. First, we don't know what the fields "look like" that are being scattered by the various material anomalies we seek to evaluate. The mathematical models which presently exist describe only the simplest geometries, and these rarely appear in practice. Second, signal analysis techniques are inadequate. Improvements in range resolution and spectral analysis are necessary to perform the complex correlation between ultrasonic data and physical requirements of the test object.

SOLUTION ACTION

Looking at the requirements stated in a previous section we have recognized some fundamental limitations in our system. Our approach to correct these limitations is two phased. First, research aimed at mathematical modeling of the scattering process and development of improved signal analysis methods are in progress. Second, we have a continuous development project intended to upgrade existing test bed hardware, control technique, and data acquisition/analysis methods.

Research - We presently have a two man effort in the area of theoretical work. Specifically, we are interested in solutions or approaches which can be applied to practical problems. We have reviewed the literature on solutions to elastic wave equations. In general we are interested in the approximate theories. Two examples are the diffracted ray theory and the series of integral equation solutions which started with the Born approximation and have evolved to the extended quasistatic approximation.

We are perfecting the signal analysis techniques which we use for time and frequency domain analysis. Our major effort at this point is improvement in range resolution. Recent experiments have shown (Fig. 2) that we have the capability of resolving two pulses which are separated in time by 35 nanoseconds. Estimates of the relative amplitudes were also calculated.

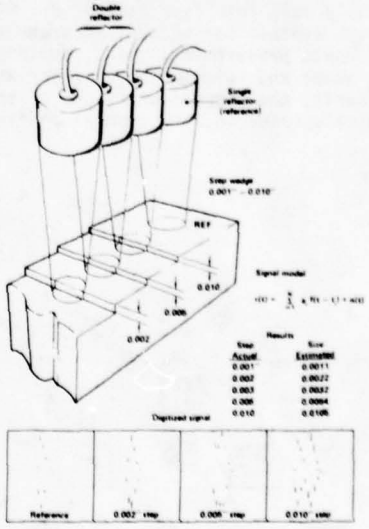

Fig. 2 Range Resolution Experiment

Development - A five man development effort is directed toward design and fabrication of the two transducer ultrasonic test bed. The features of this test bed represent the highest precision,

versatility, and reliability. The central features are shown in Fig. 3. The mechanical motions are completely computer controlled. Data acquisition, signal processing, graphic displays, and ultrasonic feedback control are also computerized. The base of the test bed is a five meter square granite block one meter thick. Both a horizontal and vertical spindle are included for rotating symmetric test objects. The sturdy overhead ways provide rectilinear motion of both transducers simultaneously in a controlled scan mode or for positioning the central cylindrical section relative to the test object. The central section provides two cylindrical motions (Figs. 4 and 6) which allows the two transducers to be independently positioned to any point within a 0.40 meter diameter cylinder 0.30 meter high. The accuracy goal is to position the transducer at a point in the space of the cylinder within a sphere of uncertainty 125 microns in diameter with reproducibility of position within 10 microns. There are two orthogonal angular motions which allow the transducer to "look at", or be directed at, any point in the cylinder completely independent of the position motions. This is a new concept for positioning the transducers relative to the test object. (See Fig. 5)

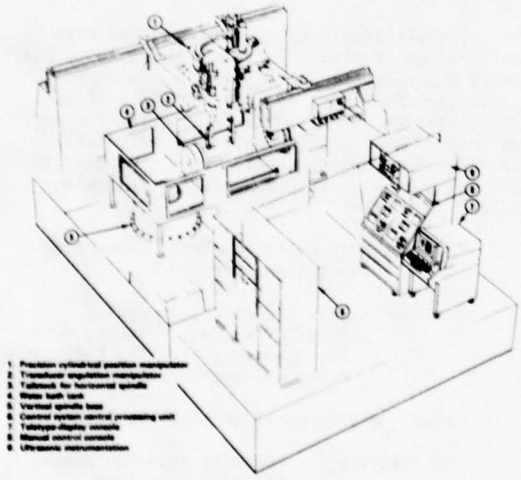

Fig. 3 Two Transducer Ultrasonic Test Bed

The principal of the concept is to maintain a fixed point in space at which the transducer is "looking" while changes in transducer angle relative to that point are made. The simplifying features which make this possible are: First the motions used to position the transducers in space are completely independent of the motions used to control the angular direction of the transducer and second the angular manipulators rotate about a fixed point in space. This greatly improves accuracy and simplifies the motions necessary to "map the field". I consider mapping the field at the water-to-part interface the most common mode of operation. For example, suppose we were to inspect a weld in a sphere. We would mount the sphere on the horizontal spindle with the weld in the vertical plane. The transmitting transducer would be positioned and the angle set for a refracted shear wave incident on the weld zone. The scattered field at the outside surface of the sphere would be recorded by manipulating the position of the receiving transducer over the necessary surface area while constantly changing its angular directions at each point to be normal to the wave fronts of the scattered field.

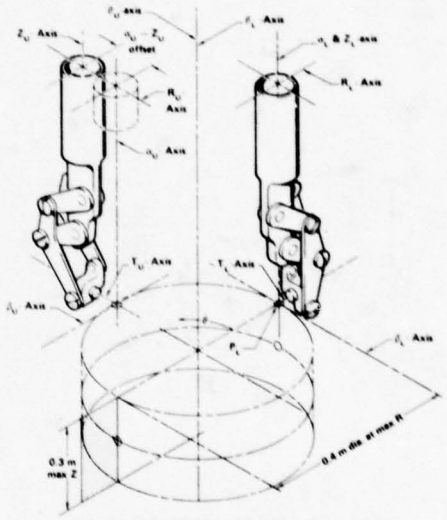

Fig. 4 Cylindrical Manipulation Schematic

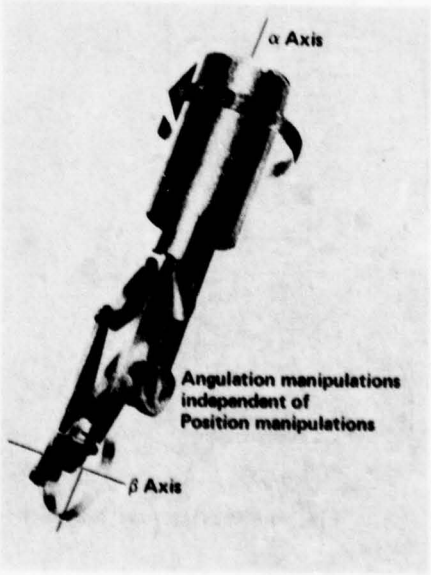

Fig. 5 Transducer Angulation Manipulator

There are fourteen precision axes of motion on this test bed. Figures 6a, and 6b, show the position accuracy and reproducibility for all axes, the straightness of the linear slideway axes and the axial and radial runout of the rotating axes. The computer control system, Fig. 7, will provide various control modes, including a "learning" mode which allows the operator to establish a routine for moving the transducer over an object. This is especially important when the test object is not a simple shape or accurate dimensions are not available.

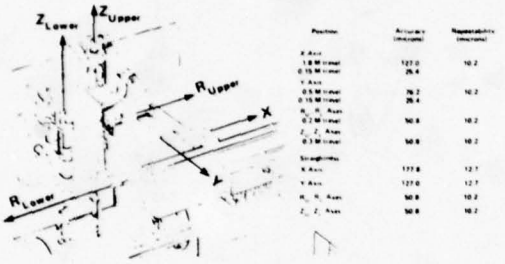

Fig. 6a Linear Axes Accuracy

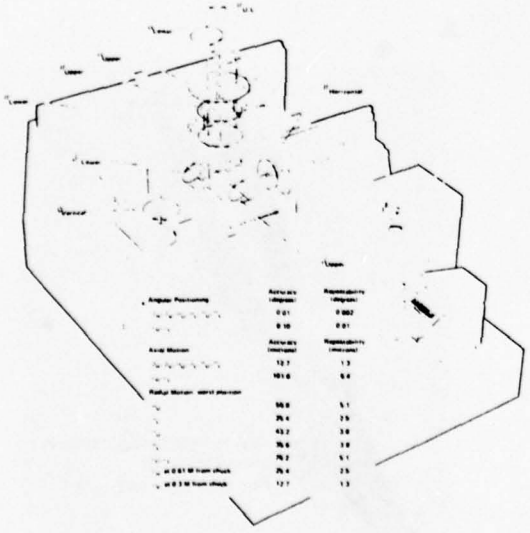

Fig. 6b Angular Axes Accuracy

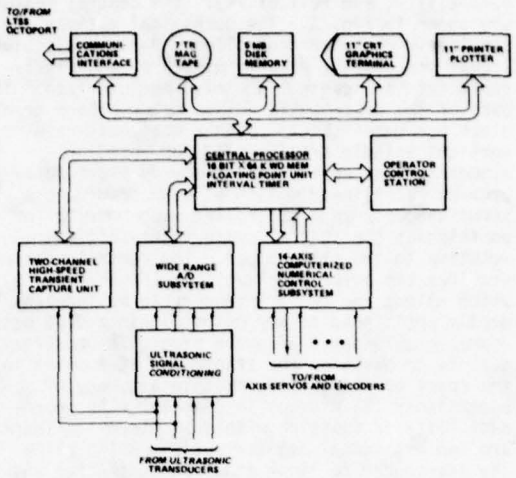

Fig. 7 Computer Control

Ultrasonic instrumentation is constantly being upgraded as new electronic innovations become available. The latest addition to our system is a high speed transient waveform digitizer. It has a 500 MHz sampling rate with six bit accuracy for a single recording cycle of 1024 data points. Improved resolution is easily attained by averaging.

The ultrasonic system was designed with calibration in mind. For example, it has a built in 25 MHz reference signal which is used to calibrate amplifiers and the peak RF amplitude to DC conversion section. We are looking for better methods of making this conversion which will increase the linear dynamic range. We periodically calibrate or at least tabulate the following system parameters:

Pulser - peak voltage, width, overshoot, repetition rate

Receiver - gain bandwidth, linearity, sensitivity/noise figure, overload recovery time for both large and small overloads

Gates - width, position accuracy (jitter)

Peak Sampling - linearity, dynamic range, effective bandwidth

UNIQUE TEST BED CAPABILITIES

The most fundamental motive for building the two transducer ultrasonic test bed is the growing necessity in routine inspection for two transducers, a transmitter and a receiver, which are accurately and independently manipulated.

The mathematical models now being generated are new approximate solutions for which no complete solutions exist. The mechanical versatility and accuracy of the two transducer ultrasonic test bed is absolutely necessary to verify the approximate solutions.

A very significant use of this test bed will be in feasibility studies where we identify, quantitatively, all the parameters necessary to design a production-line inspection fixture. The largest portion of our effort has been in the design of the fixturing. A problem we constantly face is the one of designing a test bed to do a feasibility study which later is used in the production test. There are several problems with that approach: More versatility must be designed into the system to do the feasibility study than is necessary to do the actual test. There is a problem with the time lapse necessary to build anything. The cost of adequate systems is prohibitive for a small program. When the job is complete the system goes to the production line and we are left with nothing but a technical report from which to start on the next task.

CONCLUSION

An ultrasonic imaging project is underway at Lawrence Livermore Laboratory. We are addressing the theoretical problems of scattering by realistic-defect geometries. We are perfecting the instrumentation and analytical techniques necessary for adequate ultrasonic signal analysis. We are building the sophisticated, high-precision, two-transducer ultrasonic test bed necessary to achieve the full potential of ultrasonics as a quantitative NDE tool.

ACKNOWLEDGMENTS

This report was prepared as an account of work sponsored by the United States Government. Neither the United States nor the Unites States Department of Energy, nor any of their employees, nor any of their contractors, subcontractors, or their employees, makes any warranty, express or implied, or assumes any legal liability or responsibility for the accuracy, completeness or usefulness of any information, apparatus, product or process disclosed or represents that its use would not infringe privately-owned rights.

Work performed under the auspices of the U.S. Department of Energy by the Lawrence Livermore Laboratory under contract number W-7405-ENG-48.

Reference to a company or product names does not imply approval or recommendation of the product by the University of California or the U.S. Department of Energy to the exclusion of others that may be suitable.

NEW EMAT APPLICATIONS: ULTRASONIC ELLIPSOMETER AND DETECTION OF CRACKS UNDER FASTENERS

R. B. Thompson and C. F. Vasile
Rockwell International Science Center
Thousand Oaks, California 91360

ABSTRACT

The ability to excite new wave types, such as the horizontally polarized shear (SH) waves, enables EMAT's to perform functions not easily realized with conventional piezoelectric transducers. This paper describes two examples. An ultrasonic ellipsometer is presented which can excite, and detect, shear waves of arbitrary elliptical polarization. It therefore becomes possible to make precision measurements of elastic properties by making direct comparison of the propagation properties of the SH and SV (vertically polarized) components of the wave. The principles of operation are demonstrated by measuring fluid level, a surface property which produces differential attenuation of the two components of the wave and thus a change in its elliptical polarization, and texture, a bulk property which produces differential velocity shifts. Preliminary data directed towards the measurement of adhesive bond strength is also included.

A second technique presented is a new approach to the problem of detecting cracks under fasteners in wing lap joints. It has been found that SH waves, excited on the outer surface of the wing, can be injected into the lower surface of the joint by a wave guiding effect. The reflections of these waves from fastener holes contains information indicating the presence, and size, of flaws. Preliminary experimental results demonstrating this new technique are included.

SUMMARY

Figure 1 illustrates the principles of the ultrasonic ellipsometer. In accordance with the objectives and approach delineated in part (a), it is desired to simultaneously excite SH and SV waves with controlled amplitude and phase so that the polarization of the elliptically polarized shear wave, formed by their superposition, is known. This is accomplished using the unique ability of EMAT's to excite both wave types as shown in part (b). Similarly, EMAT's are used to detect the two wave types, and the signals can again be recombined with selected amplitude and phase. By measuring changes in the output, a direct comparison of the propagation properties of the two wave components can be made. The functional block diagram of the device constructed is shown in part (c). Here separate EMAT's operating in the far field were used. In this first demonstration, full electronic control of phase and amplitude was not incorporated. However, provisions were made for looking at the individual SH or SV signals, and for combining the two with phase and amplitude adjusted for a null or sum output. Changes in material properties were detected by destruction of the null, with the output being proportioned to the imbalance of wave properties.

Such a device can be used on either thick specimen or thin plates. Figure 2 defines the operation point required in the latter case. Part (a) shows the dispersion curves for guided elastic waves on a flat plate. At the indicated point, the $n = 0$ symmetric Lamb mode and the $n = 1$ SH mode curves are tangent. Thus these waves have the same phase and group velocities. Further examination, as shown in part (b), reveals that each consists of plane shear waves bouncing at an angle of 45^0 between the plate surfaces. Thus, the resulting superposition is truly an elliptically polarized shear wave. If the plate is anisotropic, or has a layered structure, this degeneracy is split. Part (c) illustrates this splitting for the case of an adhesively bonded sandwich in which each of the metal sheets has a thickness equal to that of the single plate considered above. It can be seen that the initial pair of modes is split into two pairs, much as the modes of two identical harmonic oscillators are split by a weak coupling. It is believed that a precise measurement of these mode splittings will provide important information regarding the strength of the bond.

Figure 3 presents results of some simple initial experiments. In part (a), the variation in output at the null port has been plotted versus angular orientation on a 1/8 inch (0.318 cm) thick, rolled aluminum plate. The texturing of the plate is clearly detected. The results have been normalized to directly read the velocity difference between the two modes, and the high sensitivity of the device is illustrated by the small differences detected. These results illustrate the ability to detect small changes in bulk properties producing velocity shifts.

Part (b) shows the device output as a function of water level in a vessel with 1/8 inch (0.318 cm) thick plate walls. There the ratio of the SH amplitude to SV amplitude is plotted. As the portion of the propagation path in contact with the water increases, this ratio increases due to the absorption of the SV wave. The SH amplitude is unchanged since it does not couple to the fluid. This illustrates the detection of changes in surface properties producing attenuation shifts. In the ellipsometric mode, the null output can be adjusted to be zero for no water present with an increasing signal occurring as the fluid level increases (not shown). For the particular problem of fluid detection, this is less desirable because of decreased dynamic range (once the SV wave has been heavily attenuated, the null output is virtually a constant). However, for other measurements of surface conditions, such as detection of corrosion, for example, this might be the preferred mode.

Part (c) presents some preliminary data obtained on an adhesively bonded specimen. These two aluminum plates were joined with FM73 adhesive. One side of each plate was prepared for

bonding by anodizing, the other side was bonded in the received surface condition known to produce a considerably weaker bond. The oscilloscope photographs show the waveforms observed in the SH, SV, and null modes on the two sides of the plate. In each case the SH signal is a clean tone burst while the SV signal has a secondary peak. The origin of this peak is not fully understood at this time, but it is significant that it shifts abruptly in time as the transducers are moved from the "good" side of the plate to the "bad" side. This effect is accentuated in the null mode since the large peak is suppressed. This data is the result of the first measurements on an adhesively bonded sample. Further work is in progress to more completely define the origin of this potentially useful effect.

The remainder of the paper deals with a different problem: the detection of cracks under fasteners. A program has been recently initiated to attack this based on the EMAT technology used in a slightly different way. In progress results are presented here. Figure 4a presents the problem: the detection of cracks growing in the lower half of the lap joint where the presence of the upper plate and the fuel tank sealant make direct ultrasonic access quite difficult. The technical approach, as described in Fig. 4b, again makes use of the SH waves excited by EMAT's. Here, however, advantage is taken of the fact that these waves can propagate around corners, as in a waveguide, with fewer losses and spurious signals being generated by mode conversion, than is the case for SV waves. Figure 5 discusses some of those points in greater detail.

In Fig. 6, some of the technical data that led to this approach is presented. Part (a) gives measured values of the transmission and reflection coefficients for the n = 2 and n = 3 SH modes for both corners and S-Jogs in aluminum plate. The data demonstrates the ability to inject signals into the vicinity of the lower fastener hole from transducers mounted on the wing skin, away from the lap joint region. Part (b) shows the result of a second set of measurements, made on a flat plate with no geometrical complexities. Here the SH-wave back-scattering was measured as a functon of angle of illumination for a simple hole and a hole with a crack, growing in the upward direction as shown. The angular dependence in the scattering produced by the crack is striking, and contains information regarding the size and location of the crack.

It is the purpose of this program to combine these two results, the ability of SH waves to propagate around corners and the ability of SH waves to sense cracks growing from holes, into a technique for detecting cracks under fasteners. Figure 7 presents some preliminary results. These show that, for a partial simulation of the wing structure, the back reflected signal increases with slot depth. Fixtures are presently being made to enable this, and other measurement configurations, to be evaluated more completely. Emphasis will be on measurements made on the complete C5A wing lap joint structure.

In summary, the ability of EMAT's to excite SH modes has been used to advantage to make precise physical property measurements and to inspect complex structures. Their ability to operate without contact, such as on painted surfaces, suggests that many important applications will follow. Programs directed at the measurement of adhesive bond strength and at the detection of cracks under fasteners are already in progress as discussed in this paper.

ACKNOWLEDGEMENTS

This research was sponsored by the Center for Advanced NDE operated by the Science Center, Rockwell International, for the Advanced Research Projects Agency and the Air Force Materials Laboratory under Contract F33615-74-C-5180.

OBJECTIVES

- **HIGH PRECISION MEASUREMENTS OF CHANGES IN ELASTIC PROPERTIES AS NEEDED TO DETERMINE BOND STRENGTH, TEXTURE, OR OTHER PHYSICAL PROPERTIES**

APPROACH

- **HORIZONTALLY POLARIZED SHEAR (SH) WAVES AND VERTICALLY POLARIZED SHEAR (SV) WAVES ARE ARE EXCITED AND DETECTED IN A SINGLE EMAT DEVICE**
- **AMPLITUDE AND PHASE ADJUSTMENTS ARE MADE FOR NULL OUTPUT**
- **CHANGES IN ELASTIC PROPERTIES REMOVE NULL: OUTPUT IS PROPORTIONAL TO CHANGE**
- **COUPLING VARIATIONS AND DIFFRACTION LOSSES DO NOT AFFECT THIS NULL OUTPUT, SO TECHNIQUE IS MORE SENSITIVE THAN SIMPLE VELOCITY MEASUREMENT**

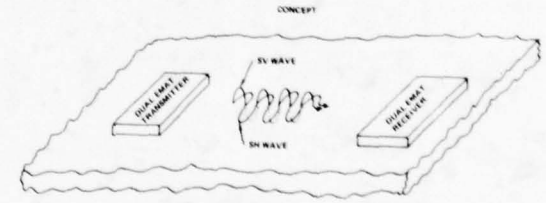

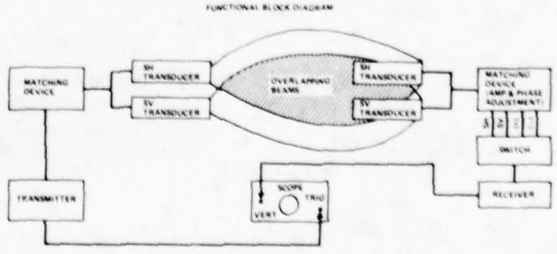

Fig. 1 Ellipsometer principles; (a) objectives, (b) concept, (c) functional block diagram.

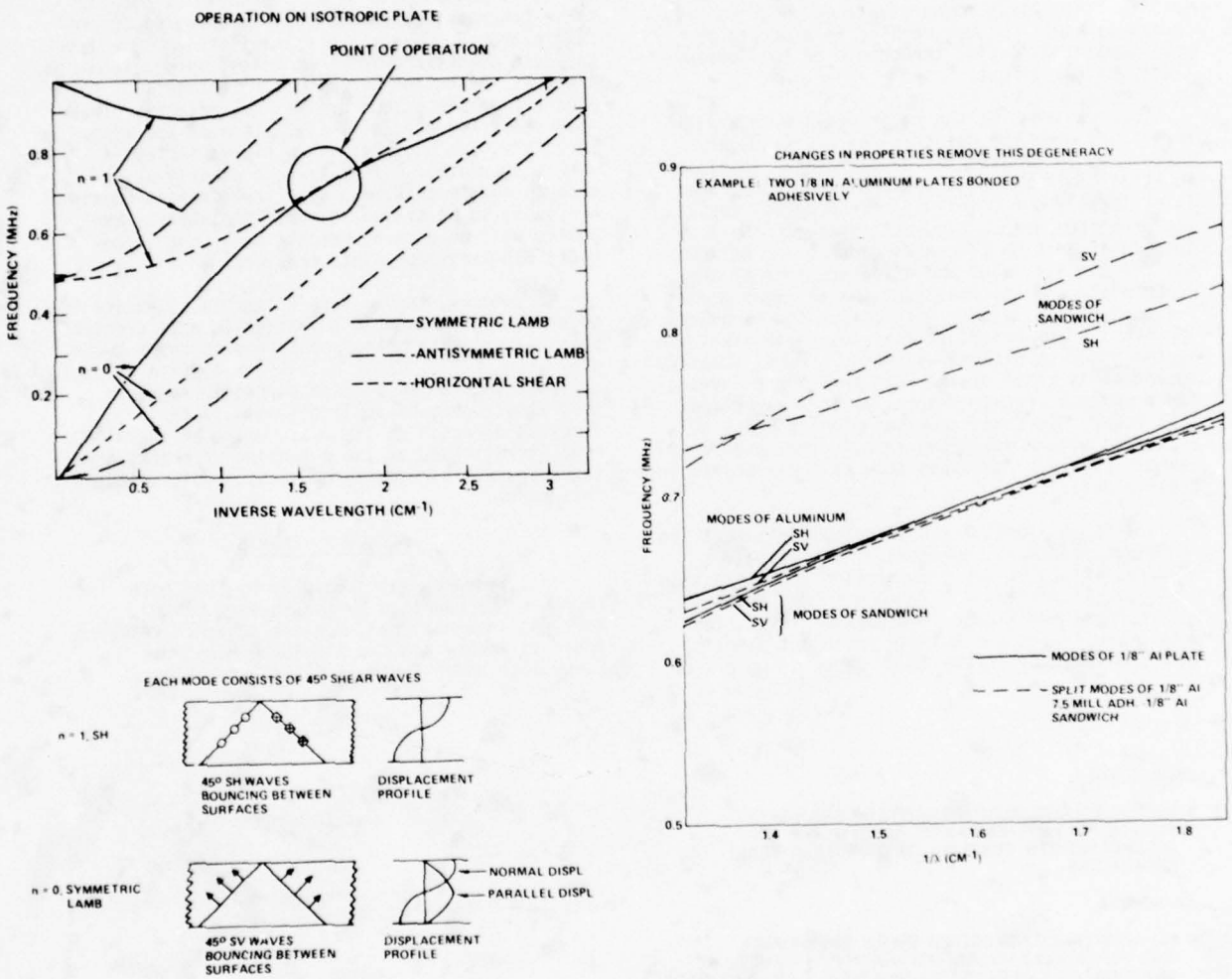

Fig. 2 Ellipsometric measurements on plates; (a) point of operations on isotropic plate, (b) details of mode profiles, (c) splitting occurring in an adhesive bond.

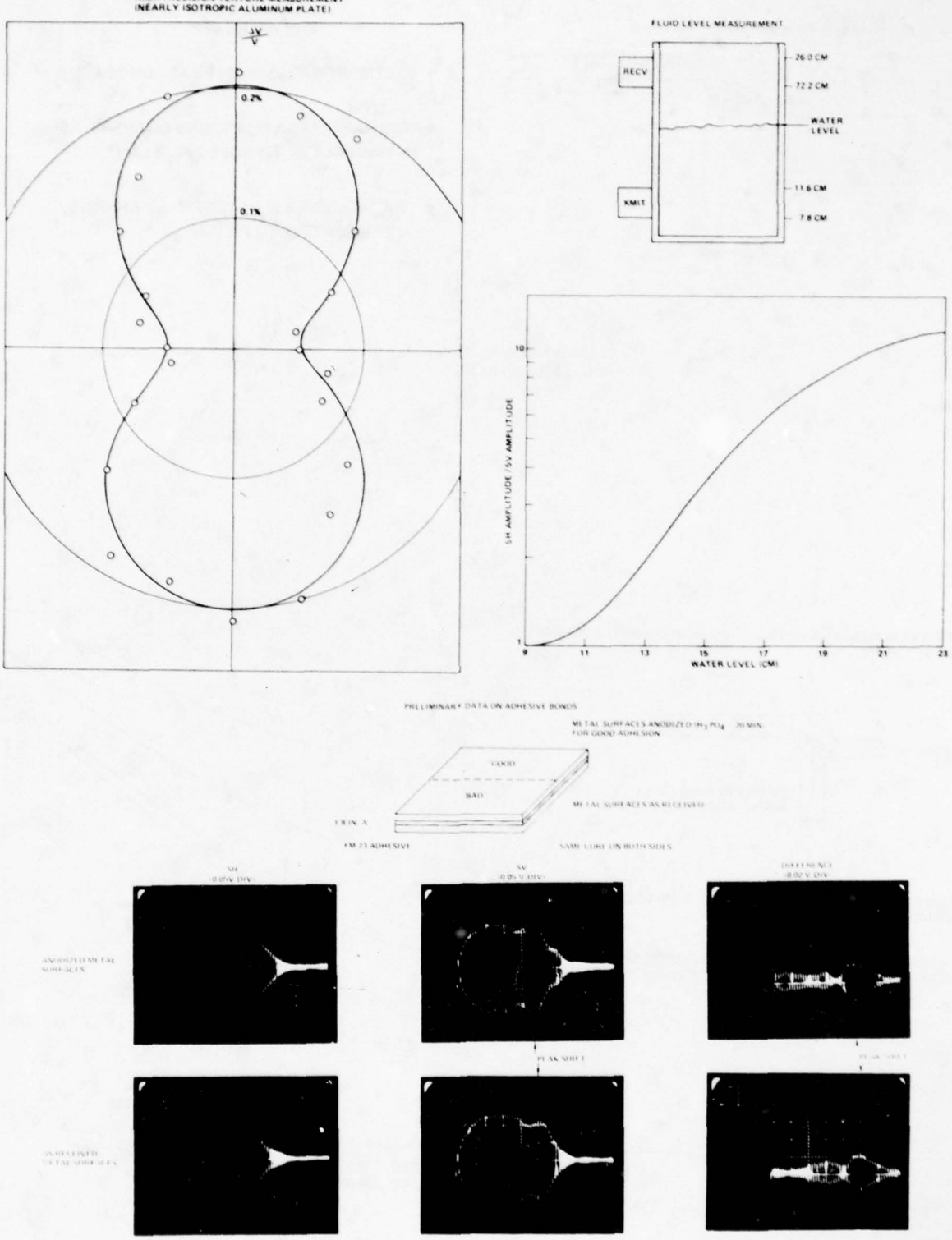

Fig. 3 Applications of ellipsometer; (a) measurement of texture, (b) measurement of fluid level, (c) measurement of bond strength adhesive.

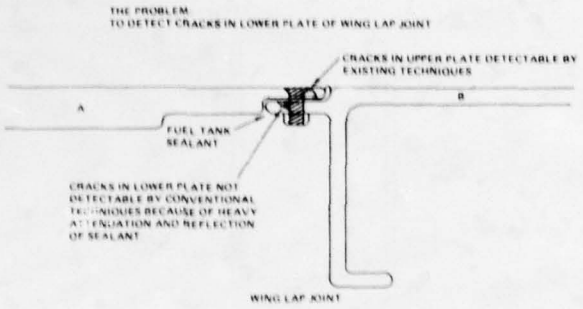

THE APPROACH

- **EXCITE SH WAVES WITH EMATS ON PLATE B.**
- **WAVES PROPAGATE AROUND CORNERS, AS IN WAVEGUIDE, TO HOLE AND FLAW.**
- **CRACKED HOLE IS DETECTED BY CHANGE IN THE SCATTERED FIELD.**

Fig. 4 Detection of cracks under fasteners; (a) problem, (b) approach.

- **THIN SKIN ACTS AS A WAVEGUIDE WHICH CHANNELS ENERGY TO *LOWER JOINT***

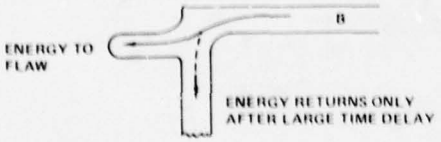

- **DISPERSION CURVE SHOULD BE USED TO SELECT FREQUENCY AND WAVELENGTH**
- **n = 2 AND n = 3 MODES APPEAR MOST USEFUL SINCE THEY ARE WELL SEPARATED FROM OTHER MODES FOR PRACTICAL TRANSDUCERS**

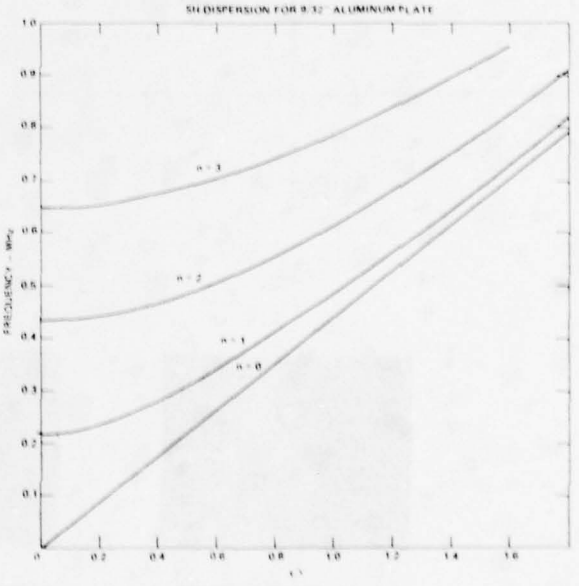

Fig. 5 Waveguiding effects on SM waves in lap joints; (a) energy guided to flaw, (b) modes must be selected using dispersion curve.

PARTICULAR SH WAVES WILL PROPAGATE AROUND CORNERS AND BENDS WITH LOW LOSS.

90° BEND (1/4 IN. ALUMINUM)

MODE	FREQUENCY	TRANSMISSION	REFLECTION
n = 2	0.693 MHz	0.88	–
n = 3	0.896 MHz	0.10	0.05

S JOG (1/4 IN. ALUMINUM)

MODE	FREQUENCY	TRANSMISSION	REFLECTION
n = 2	0.709 MHz	0.40	0.40
n = 3	0.919 MHz	0.24	0.20

NOTE: ENERGY IS NOT CONSERVED IN REFLECTION AND TRANSMISSION BECAUSE OF MODE CONVERSION.

CRACK IN HOLE SIGNIFICANTLY CHANGES SH WAVE SCATTERING

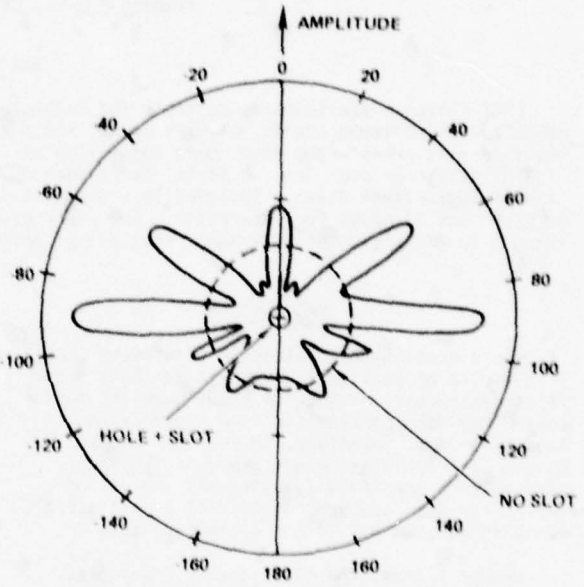

SH WAVE "BACK SCATTER" FROM HOLE AND SLOT AS MEASURED ON A 0.157 CM THICK PLATE AT 0.5 MHz.

(NOTE: TRANSMITTER AND RECEIVER WERE DISPLACED BY 5°)

Fig. 6 Experimental keys to detection of cracks; (a) SH energy propagates around bends and corners, (b) crack changes scattering from hole.

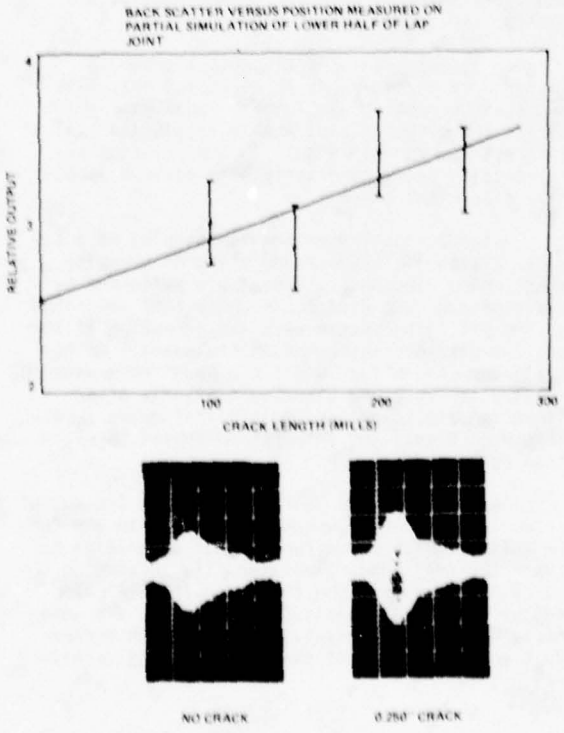

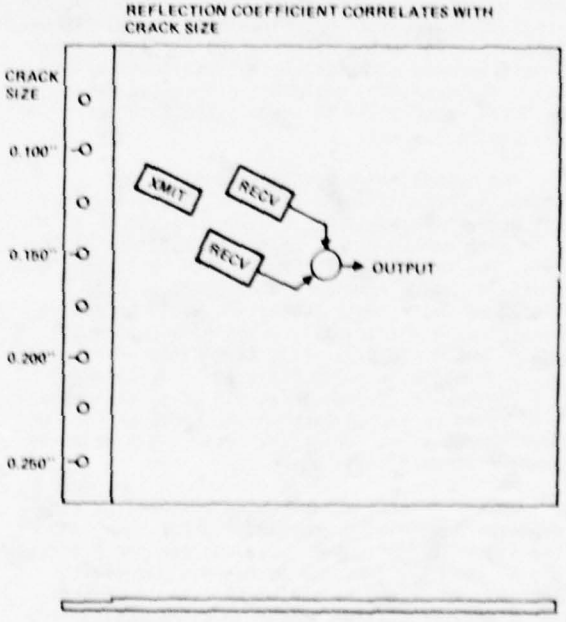

Fig. 7 Preliminary experimental results; (a) experimental configuration, (b) reflection versus crack size.

ADVANCED EMAT INSPECTION SYSTEMS: PROJECTILES AND WELDS

C. M. Fortunko and R. B. Thompson
Rockwell International Science Center
Thousand Oaks, California 91360

ABSTRACT

EMAT's appear particularly suitable for automated inspection systems because of their ability to operate at high temperatures, at high speed, and without couplant. This paper reviews the progress in two important areas: the high speed inspection of artillery projectiles and high temperature inspection of MIG welds. In each case, material is presented illustrating the system concept and the ease of detection of appropriate flaws. Included is a discussion of the operational characteristics of such systems using SH and SV waves for inspection. The paper also describes the advantages of employing SH waves for volumetric inspection of very thick sections of complex geometries.

PROJECTILES

The electromagnetic-acoustic transducer (EMAT) is a device of particular interest to those areas of nondestructive evaluation (NDE) when its application may lead to significantly higher rates of inspection and, therefore, to reduced inspection costs. The application described in the first five posters specifically addresses the use of EMAT's for near complete inspection of artillery projectiles (155 mm) in one inspection station.

Poster 2 shows the plane view of a proposed automated EMAT inspection station for nondestructive evaluation of artillery projectiles for crack-like flaws and other imperfections which could cause failure. The inspection is to be accomplished in one inspection station by using (1) eddy currents or acoustic surface waves to inspect the outer surface in the base, (2) angle shear waves launched from the circumference through the base to inspect the interior of the wall in the base region, (3) angle shear waves launched in the longitudinal direction to locate ID and OD circumferentially oriented defects, and (4) angle shear waves launched circumferentially to inspect the ogive and bourellet regions for longitudinally oriented defects and to inspect the interior of the projectile well.

The mechanical projectile handling device shown in Poster 2 would function as follows: (1) the projectile would be gripped from the ID at the nose with pressure applied to the shoulder of the base, (2) the projectile would then be lifted to a location ¼ inch from each electromagnet pole piece, (3) ultrasonic inspection would be accomplished by electronically scanning a raster of EMAT's while the projectile is rotated in the applied dc magnetic field bias, and (4) following the completion of the ultrasonic scan, the projectile would be placed back on the conveyor for further disposition. Defective projectiles would be shunted aside at this point.

Poster 3 shows the proposed system architecture for controlling the handling machinery and the electromagnet power supplies, and for processing of the data from the ultrasonic inspection channels to determine whether a flaw is present. The signal processing scheme involves a departure from conventional ultrasonic inspection techniques in that a correlation receiver is used to filter and demodulate the received ultrasonic signals. The main advantage of this scheme is that the signals from all the channels can be processed with uniform fidelity. Other new developments include the use of highly efficient power amplifiers for energizing the input EMAT's, and sensitive receiver preamplifiers which optimize the signal-to-noise performance. The design of new electronics was necessary because EMAT's are subject to different breakdown characteristics and present much lower input impedance levels than ordinary piezoelectric transducers. A typical ultrasonic inspection channel functions in a "pulse echo" mode, although provisions for using separate transducers for transmission and reception of the ultrasonic signals are included in the design. The received waveforms are demodulated by the correlation receiver and converted to digital format. They can then be processed by the central processor which also controls the functioning of the projectile handling machinery and determines the disposition of the projectile based on internally stored accept/reject criteria. Provisions are included for updating the stored set of accept/reject criteria as the experimental data base is expanded and verified by independent nondestructive and destructive testing.

The dynamic range of the system shown in Poster 3 is in excess of 70 dB at 1.8 MHz. The correlation receiver includes a range gate which blanks the output except when a resolution cell of interest comes into range. The correlation receiver also helps to discriminate against impulsive electrical noise.

Poster 4 illustrates the functioning of a typical ultrasonic channel operating in a "pulse echo" mode. The demonstration was performed by using most of the electronic subsystems described in the preceding poster with the exception of the digital data processor and multiplexers. An oscilloscope and a four digit LED panel were used to display the received ultrasonic signals after linear preamplification, multiplication by a reference rf signal and integration in the correlation receiver.

The bottom figure in Poster 4 shows the output of the A/D converter which is included in the correlation receiver as a function of separation between the EMAT and a simulated flaw located in the bourellet region at the 155 mm projectile. The output signal is maximized when the two are separated by approximately 1.25 inches which correspond to the setting of the center of the receiver range gate.

Poster 5 shows the detection of a simulated flaw (EDM notch) located in the OD in the bourellet region and also the detection of a material flaw located on the ID in the ogive region. Both signals are rf tone bursts centered at approximately 1.8 MHz.

The bottom table in this poster summarizes the peak amplitude of the received ultrasonic signals as a function of different simulated flaw sizes and locations on the projectile. The system's sensitivity is best illustrated by its ability to detect EDM notches as shallow as 0.009 inches.

In summary, it is believed that the presently available EMAT technology has sufficient sensitivity to locate flaw sizes which are currently of concern to projectile manufacturers.

WELDS

Bulk horizontally polarized shear waves (SH waves) can be excited in metal parts by means of periodic magnet electromatnetic transducers. The principle of transduction of such waves is illustrated in one of the figures in Poster 6. A periodic magnet is used to establish an alternating magnetic field at the surface of the metal part to be inspected. A coil carrying electrical rf currents, and placed between the magnet and the surface of the metal part, is used to induce eddy currents which penetrate into the metal within one skin depth at the frequency of operation. As a result of Lorentz forces on the lattice due to the interaction between the eddy current pattern and the periodic magnetic field, the ultrasonic beams are excited at the surface directly beneath the transducer. The notable feature of the above excitation process is that the excited shear waves are polarized in parallel in the plane of the surface of the metal part. Such waves exhibit many properties not exhibited by vertically polarized shear waves (SV waves) which are ordinarily generated by piezoelectric transducers. Because the direction of SH waves can be varied by changing, the rf frequency and the transducers are not sensitive to other wave types (surface, longitudinal and SV), they are of considerable interest. Because the SH waves are excited electromagnetically, the transducers are largely insensitive to surface conditions and can operate over rough unprepared metal surfaces and at elevated temperatures. New applications involving the use of SH waves in NDE are in prospect.

In certain ferromagnetic steels such as the Fe-2¼% Cr-1% Mo, the Lorentz excitation process is substantially enhanced by magnetostrictive processes. This leads to improved sensitivities and, therefore, to better defect detectabilities. In many applications, such as the inspection of welds at preheat temperatures, the above transducer and wave type properties are highly desirable because they cannot be matched with piezoelectric wedge transducers.

Poster 7 shows the results of some preliminary experiments with SH EMAT's on Fe-2¼% Cr-1% Mo steel plates, 4 inches in thickness which contained sections of MIG welds and simulated defects (3/32 inch side drilled holes). Of particular interest is the figure in the upper left hand corner of this poster. This figure shows that the SH wave signal transmitted through an Fe-2¼% Cr-1% Mo steel plate does not vary substantially over temperature ranging from ambient to 500°F. This is a significant result showing the independence of the transduction process to large thermal variations. Another interesting result is shown in the figure below. It shows the detection of a 3/32 inch side drilled hole in a MIG weld using 1.8 MHz SH waves excited at approximately 30° with respect to surface normal. A tone burst 10 cycles long was used in this test. The display is not an oscilloscope photo but an output of a Versatec copier. The signal was generated by using digital signal averaging techniques and represents the result of averaging together 250 frames of data. The echo at 10 microseconds represents a reflected signal generated by delamination in the Fe-2¼% Cr-1% Mo base metal, while the signal centered at approximately 25 microseconds represents the energy reflected from the side drilled hole used to simulate a lack of fusion defect. The sample used to generate the above data is shown in the photo on Poster 6.

It is hoped that the use of SH type shear waves will lead to better defect detectabilities because the transducers discriminate against spurious signals generated by mode conversion and because the ultrasonic beam can be electronically scanned, thereby allowing the concentration of the input acoustic power on the region of particular interest to the NDE inspector without physically moving the transducer element.

ACKNOWLEDGEMENT

This work was supported in part by ARRADCOM, U.S. Army under Contract DAAK10-77-2020.

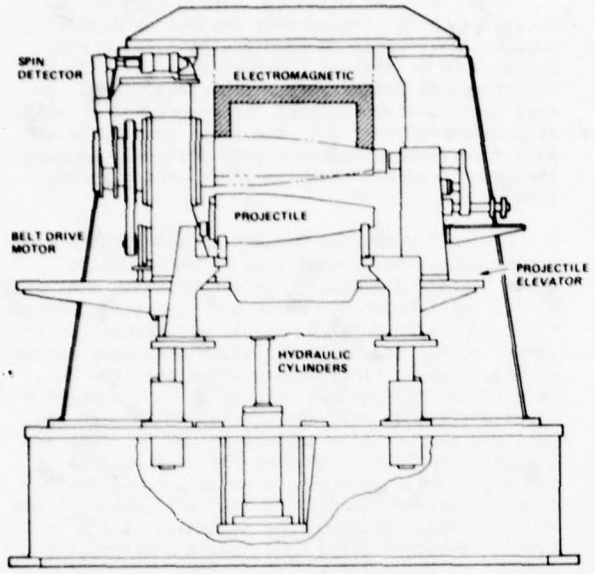

- LAUNCHING AND RECEIVING OF ULTRASONIC SIGNALS WITHOUT INTIMATE MECHANICAL CONTACT BETWEEN TRANSDUCER AND METAL PART.
- PROJECTILES AUTOMATICALLY INSERTED AND POSITIONED.
- EXPANDABLE ULTRASONIC DATA BASE BY ADDITION OF MORE ULTRASONIC CHANNELS.
- DECISIONS MADE AUTOMATICALLY BASED ON COMPARISON TO STORED ACCEPT/REJECT STANDARDS.
- INSPECTION RATE COMPATIBLE WITH ANTICIPATED PRODUCTION RATES.
- SINGLE ELECTROMAGNET PROVIDES MAGNETIC BIAS TO ENTIRE ARTILLERY PROJECTILE.

Poster 2.

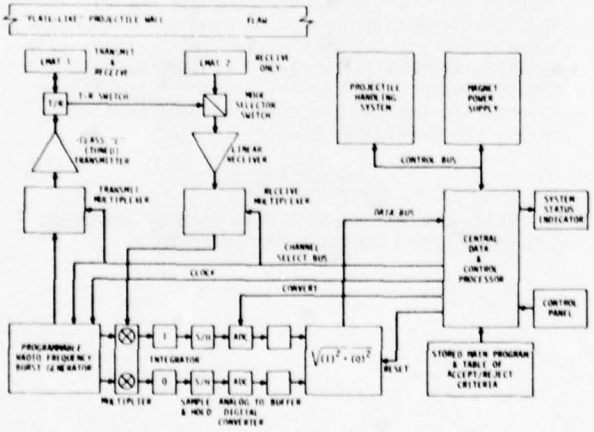

- CENTRAL DIGITAL PROCESSING UNIT CONTROLS ALL PHASES OF INSPECTION.
- EACH ULTRASONIC CHANNEL FUNCTION IN "PULSE- ECHO" OR "PITCH-CATCH" MODE.
- RECEIVED ULTRASONIC SIGNALS DETECTED BY MEANS OF A CORRELATION TECHNIQUE TO INSURE BETTER SENSITIVITY AND IMMUNITY TO IMPULSIVE AND CROSSTALK INTERFERENCE.
- ULTRASONIC CHANNELS SCANNED SEQUENTIALLY.
- ACCEPT-REJECT DECISIONS MADE BY CENTRAL CONTROL PROCESSOR ON A SCAN BY SCAN BASIS.
- SYSTEM CAN BE REPROGRAMMED FOR INSPECTION OF OTHER PROJECTILE TYPES.

Poster 3.

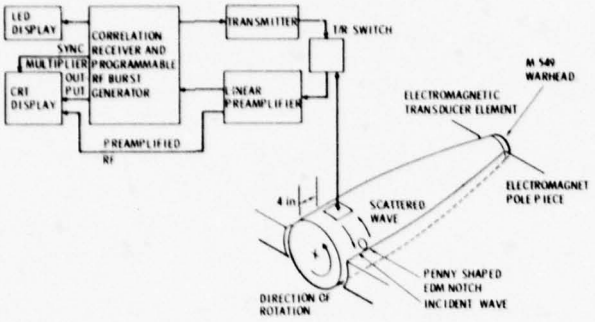

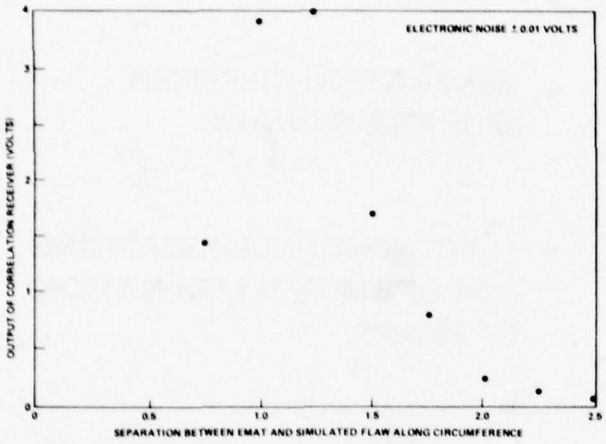

- **ADJUSTABLE RANGE GATE TO EXCLUDE UNWANTED SIGNALS.**
- **DETECTION OF SIMULATED FLAWS OF 0.009 INCH AVERAGE DEPTH.**
- **DISCRIMINATION AGAINST IMPULSIVE ELECTROMAGNETIC INTERFERENCE.**
- **TRANSDUCER POSITION FIXED WHILE PROJECTILE IS ROTATED TO PROVIDE OF ONE CIRCUMFERENTIAL SEGMENT.**
- **AVAILABLE DYNAMIC RANGE IN EXCESS OF 70 dB AT 1.8 MHz CENTER FREQUENCY.**

Poster 4.

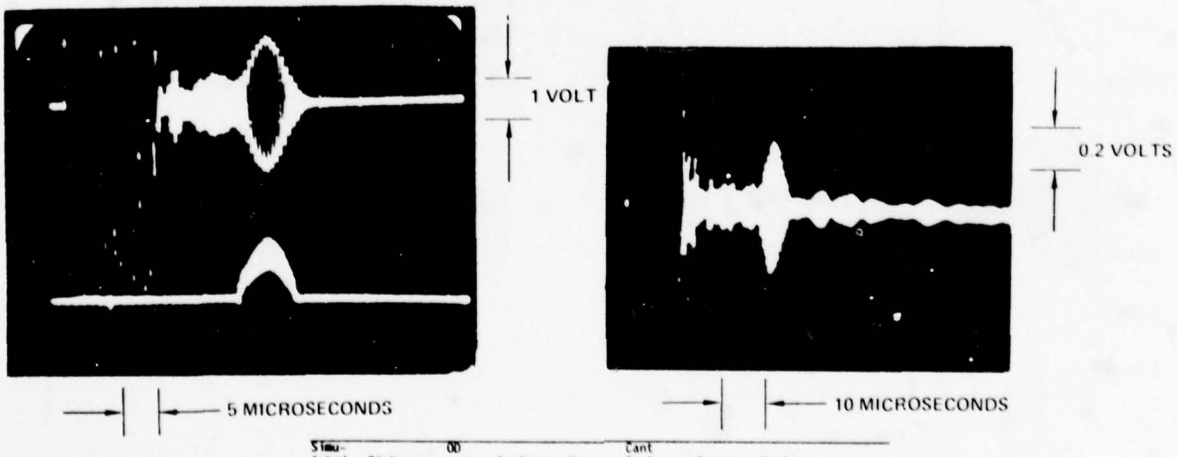

Simulated Defect No.	Distance From Base (inches)	OD / ID	Surface Length (inches)	Max. Depth (inches)	Cant Angle w/respect to axis	Output Level (V)	Field Configuration	Sample No.
1	6.5	O.D.	.146	.014	0	1.2	Parallel	88
2	8	O.D.	.158	.014	0	1.6	Parallel	88
3	9.5	O.D.	.186	.019	0	2	Parallel	88
4	9.5	O.D.	.256	.052	0	4	Parallel	88
5	11	O.D.	.116	.009	0	.8	Parallel	88
6	12.75	O.D.	.190	.022	0	2.8	Parallel	88
7	14.5	O.D.	.174	.015	0	1.2	Parallel	88
8	2	O.D.	.172	.020	10	.6	Parallel	85
9	2	O.D.	.177	.020	20	.2	Parallel	85
10	2	O.D.	.186	.018	30	.08	Parallel	85
11	2	O.D.	.374	.011	0	2.2	Parallel	09
12	3.5	O.D.	.222	.035	0	3.6	Parallel	09
13	5	O.D.	.105	.019	0	1.5	Parallel	09
14	3	O.D.	.179	.021	0	3	Parallel	51
15	5	O.D.	.157	.107	0	2	Parallel	51
16	2	I.D.	.030	?	90	.8	Normal	88
17	2	I.D.	.030	?	90	.6	Normal	88

Poster 5.

ULTRASONIC SIGNAL INDEPENDENT OF TEMPERATURE UP TO 500 F

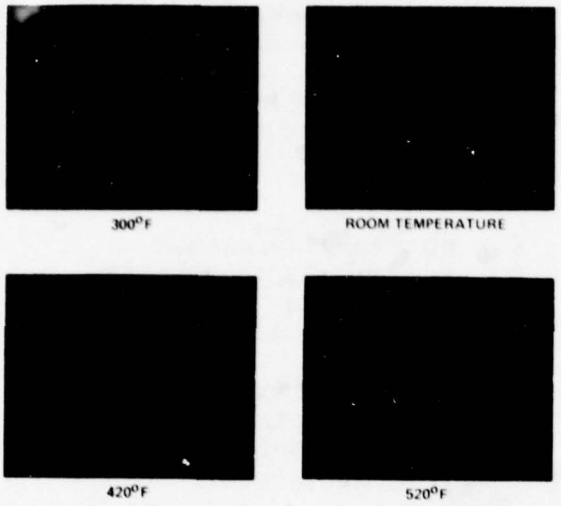

- GENERATION OF FEWER SPURIOUS SIGNALS.
- ELECTRONIC BEAM SCANNING FOR OPTIMUM ILLUMINATION OF FLAWS.

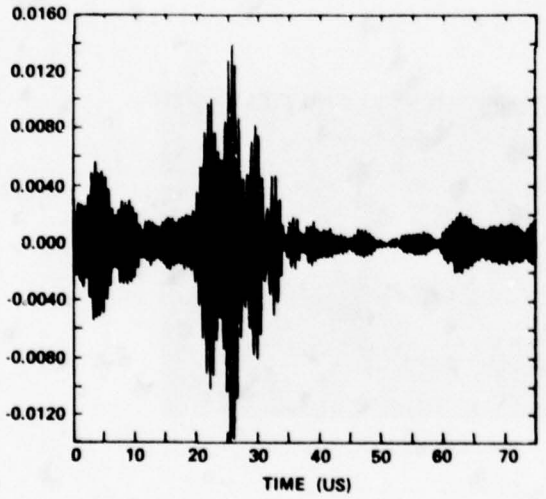

- ELECTRONIC PROCESSING OF RECEIVED SIGNALS FOR IMPROVED DYNAMIC RANGE (TIME AVERAGING).
- ABILITY TO INSPECT AT ELEVATED TEMPERATURES.

Poster 6.

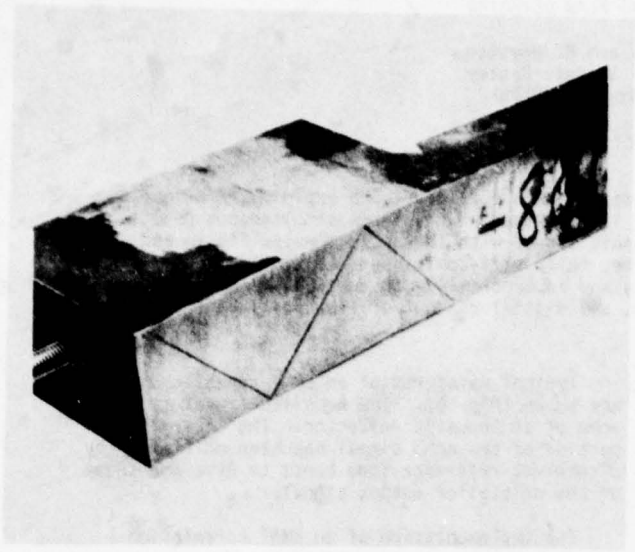

- SH WAVES CAN BE SCANNED BY CHANGING RF FREQUENCY.
- SH WAVE TRANSDUCERS DO NOT GENERATE OR RECEIVE BULK LONGITUDINAL AND SV WAVES, HEAD WAVES OR SURFACE WAVES.

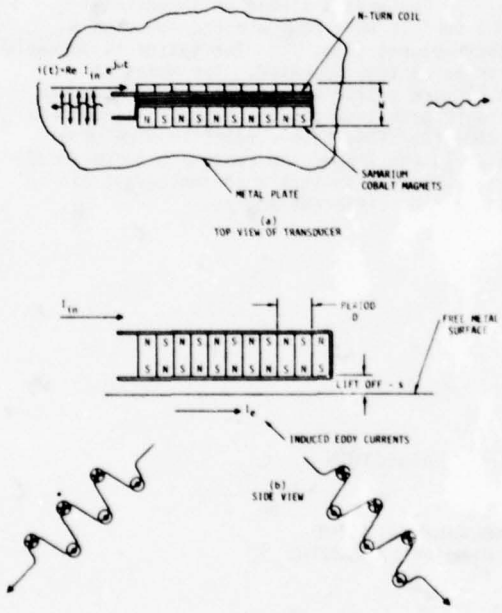

- TRANSDUCERS INSENSITIVE TO SURFACE CONDITIONS: ROUGHNESS AND TEMPERATURE.
- IN CERTAIN FERRO MAGNETS SIGNALS ENHANCED BY MAGNETOSTRICTIVE EFFECTS.

Poster 7.

CUSTOM EMAT INSTRUMENTATION: CORRELATION RECEIVER AND FLAW DETECTOR

C. F. Vasile, J. Liska and R. Houston
Rockwell International Science Center
Thousand Oaks, California 91360

ABSTRACT

New, custom instrumentation is presented which is designed to complement and exploit the unique properties of EMAT's. A two channel correlation receiver is described which allows simultaneous detection of the in-phase and quadrature components of an ultrasonic signal with the optimum noise figure and improved interference rejection. In addition, a prototype, fully self-contained EMAT flaw detector is presented. This is a surface wave device for handheld use and incorporates such features as battery operations, correlation detection, search and inspect modes, and digital readout of flaw position and reflected signal amplitude.

Figure 1 shows that custom instrumentation is being developed to detect flaws in certain materials. The technology involves the utilization of EMAT's, electromagnetic transducers, and correlation processing electronics. Flaw identification is accomplished by pattern recognition techniques on the processed waveforms.

Figure 2 shows that a basic flaw detection system can be formed using the realtime acoustic echo from both known and unknown reflectors. The echo signals are processed with known references to yield both in-phase and quadrature information. A realtime correlation technique is implemented to process the signals.

In Fig. 3, the relationships between the in-phase, V_I, and quadrature, V_Q signals are formulated. The conditions that determine the optimum signal to noise ratio, the phase of the detected acoustic signal, and the Fourier transform of the received signal are given.

*The development of the correlation receiver was supported by ARRADCOM, U.S. Army under Contract DAAK10-77-2020.

Typical waveforms of an EMAT acoustic signal are shown (Fig. 4). The received signal is the echo of an acoustic reflector. The central portion of the echo signal has been multiplied by a coherent reference tone burst to give the shape of the multiplier output signal.

The implementation of an EMAT correlation system has inherent advantages for NDE instrumentation. The system is capable of a high signal-to-noise ratio while minimizing the effects of clutter and electrical interference. Information on the relative phase and amplitude of the received acoustic signal is provided.

A prototype EMAT flaw detector has been built. It features a single unidirectional 1.0 MHz surface wave noncontact probe with a permanent magnet (Fig. 5). The system is portable and can be battery operated. Two modes of operation are possible. In the Search mode, an electronic gate inspects the acoustic echoes and indicates the distance and relative size of a target. In the Inspection mode, a predetermined range is selected so that a chosen target can be inspected from different angles.

- OPTIMUM SIGNAL TO NOISE RATIO
- ENHANCED ELECTRICAL INTERFERENCE REJECTION
- MINIMIZES EFFECTS OF CLUTTER
- PROVIDES SIMPLE MEANS FOR MEASURING RELATIVE PHASE AS WELL AS AMPLITUDE OF RECEIVED ACOUSTIC SIGNALS
- SIMPLIFIES SIGNAL AVERAGING
- REAL TIME FOURIER ANALYSIS
- ANALOG MULTIPLIER OUTPUTS WILL INDICATE FRESENCE OF DISPERSION

Fig. 1 Advantages of correlation receiver to NDE instrumentation.

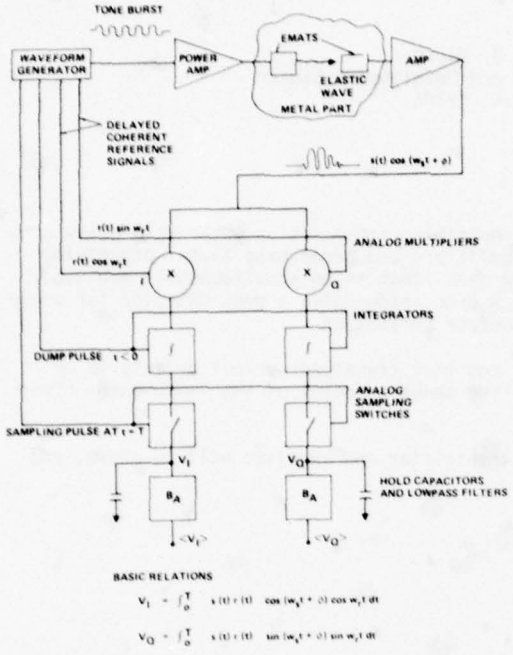

Fig. 2 Application of realtime correlation to NDE measurements.

GENERAL RESPONSE

$V_I = \int_0^T [n(t) + s(t) \cos(w_s t + \phi)]\, r(t) \cos w_r t\, dt$

$V_Q = \int_0^T [n(t) + s(t) \cos(w_s t + \phi)]\, r(t) \sin w_r t\, dt$

n(t) = NOISE IN SIGNAL CHANNEL

OPTIMUM RECEIVER

SELECT $\phi = 0$, $s(t) = r(t)$, $w_s = w_r$, $T = 2\pi M/w_r$

THEN IN PRESENCE OF THERMAL NOISE V_I WILL HAVE OPTIMUM SIGNAL TO NOISE RATIO

PHASE MEASUREMENT

FOR $n(t) = 0$ $\frac{V_Q}{V_I} = \tan\phi$; ϕ = PHASE OF DETECTED ACOUSTIC SIGNAL RELATIVE TO COHERENT REFERENCE

SIGNAL AVERAGING

$\langle V_I \rangle$ AND $\langle V_Q \rangle$ ARE TIME AVERAGES ACHIEVED BY USING MULTIPLE TONE BURSTS AND LOW PASS FILTERING (e.g. B_A < ¼ REPETITION RATE >)

FOURIER ANALYSIS

SELECT $w_r \neq w_s$, $r(t) = 1$, $n(t) = 0$, $s(t) = 0$ FOR $0 > t > T$

$V_I - jV_Q = \int_0^T s(t) \cos(w_s t + \phi)\, e^{-j w_r t}\, dt$

= FOURIER TRANSFORM OF RECEIVED SIGNAL EVALUATED AT $w = w_r$

Fig. 3 Measurement capabilities.

RECEIVED 0.5 MHz ACOUSTIC SIGNAL

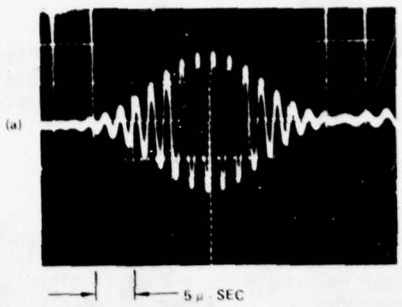

OUTPUT OF ANALOG MULTIPLIER WITH REFERENCE CONSISTING OF A 15 μs, 0.5 MHz TONE BURST IN PHASE WITH CENTRAL 15 μS, PORTION OF RECEIVED ACOUSTIC SIGNAL

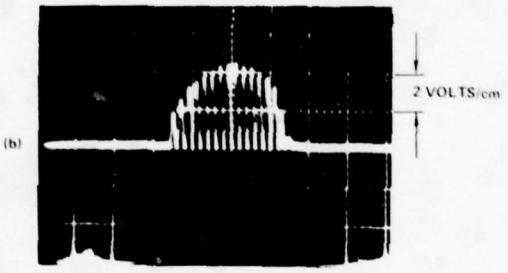

Fig. 4 Typical waveforms of an EMAT acoustic signal.

FEATURES

- 1 MHz NON-CONTACT SURFACE WAVE EMAT PROBE
- SINGLE UNIDIRECTIONAL TRANSMITTER/RECEIVER EMAT
- PERMANENT MAGNET TRANSDUCER
- PORTABLE – LOW POWER – BATTERY OPERATED
- INCORPORATES TWO CHANNEL CORRELATION RECEIVER
- SEARCH MODE
  - MANUAL IN X – ELECTRONIC IN Y
  - DIGITAL OUTPUT – ESTIMATE OF DEFECT SIZE AND DISTANCE FROM PROBE
- INSPECTION MODE
  - SELECTABLE RANGE GATES
  - SIGNAL AVERAGING

Fig. 5 Prototype EMAT flaw detector.

AN ULTRASONIC INSPECTION SYSTEM WITH HIGH NEAR-SURFACE DETECTABILITY

J. J. Tiemann and J. D. Young
General Electric Corporate Research and Development Center
Schenectady, New York 12301

ABSTRACT

An updated NDE instrument has been designed that is compatible with existing water path pulse echo instruments. The use of modern integrated circuit video amplifiers and broad band signal processing in the receiver permits improvements in signal-to-noise and band width to be simultaneously achieved. Additional circuits provide a variable depth--varialbe width processing gate, a peak detector for strip chart recording, and means for triggering from the front surface reflection.

These circuit improvements, together with a specially designed transducer permit defects to be sensed that lie within .050" of the surface--thus representing about a factor of two improvement compared to commercially available instruments.

Details of the electronics subsystems comprising the transmitter and receiver will be shown, and the structure of the transducer will be described.

ANNULAR ARRAY SEARCH UNITS AND THEIR POTENTIAL APPLICATION IN CONVENTIONAL ULTRASONIC TESTING SYSTEMS

Jerry T. McElroy and Kenneth F. Briers
Quality Assurance Systems and Engineering Division
Southwest Research Institute, San Antonio, TX

ABSTRACT

This paper is based on a program to investigate the potential of multi-element annular arrays for practical application in ultrasonic testing systems.

The annular array is comprised of coaxially-located, ring-shaped piezoelectric elements. By providing excitation pulses in a spherical time relationship, the transmitted beam may be focused at a specific range. By electronic switching, the focal point can be placed at various distances in the material under examination. Of particular interest is the length over which the beam can be held in collimation.

Fabrication methods, delayed excitation techniques, and beam patterns in water and steel are described.

INTRODUCTION

This paper is based upon an internal research program at Southwest Research Institute (SwRI). The purpose of the program was to investigate the potential use of multi-element, annular array search units for practical applications in ultrasonic nondestructive testing systems.

In all ultrasonic testing applications, control and directional manipulation of the ultrasonic beam are of utmost importance. Multi-element transducer arrays offer the potential of controlling the beam geometry and directionality by electronic switching and phased excitation.

An important advantage of annular arrays as compared to standard fixed focused search units is their ability to be dynamically focused. The focal spot is automatically scanned over a predetermined depth range of the material under examination. Beam focusing is accomplished by a piezoelectric element, which has been segmented into closely interspaced, coaxially-located annular rings. Each element of the array is individually driven in a phased, controlled manner. The transmitted and received signals are accomplished by using multichannel pulsers and receivers. The system operates in the pulse-echo or pulse-receiver mode. The position of the beam focal spot is determined by providing excitation pulses in a given spherical time relationship. The location of the focal point is determined by proper control of the spherical time relationship with respect to each annular ring-shaped element in the array. The array can be focused at different distances in the material under examination at electronic switching speeds.

PROGRAM

Through the course of this project, a variety of multi-element transducer arrays were designed, fabricated, and evaluated. A selection of prototype configurations is shown in Fig. 1. While some linear arrays were designed during this program, the major effort was directed toward a study of annular arrays. There is very limited information in the technical literature pertaining to annular arrays,[1-2] while there is substantial information and current ongoing effort in linear arrays.[3-11]

Each array is comprised of coaxially-located, ring-shaped piezoelectric elements. Early array designs used masked electrode patterns on the piezoelectric element to assign the closely interspaced active areas of the search unit. This technique proved to be unsatisfactory because of the inter-acoustic coupling (crosstalk) between the individual elements. A technique was developed using a circular cutting tool and abrasive powder to cut the piezoelectric element. The round piezoelectric element was cut through 3/4 of the thickness, thus dividing the element into the desired number of annular elements. This technique of cutting partially through the thickness proved effective in reducing the cross coupling to an acceptable degree.

Figure 2 shows an example of an annular array and the cutting tool used for this technique. By providing excitation pulses with a spherical time relationship with respect to each annular ring element, the transmitted beam may be focused at a specific range as shown in Fig. 3. Time delay schedules required for focusing are determined by the equation shown in Fig. 3. A computer program was developed to expedite the computations for various focal lengths. A number of annular array search units were designed and fabricated at 1.0, 2.25, 2.5, and 5 MHz with the number of elements ranging from 5 to 16. Table 1 gives the physical characteristics of the arrays produced during this program.

EXPERIMENTAL RESULTS, 0-DEGREE LONGITUDINAL

The geometry of the focused beams were investigated by measurement made in water. Figure 4 shows a family of distance versus (vs.) amplitude curves recorded for a 1.5-inch (38 mm) diameter, 2.5 MHz, 8-element, annular array. The theoretical distance at which the beam intensity should peak, based on the equation previously given, is

Table 1. Physical characterisitcs of annular arrays produced in the program.

Frequency	1.0 MHz	2.5 MHz	Segmented Array 2.5 MHz	Segmented Array 2.5 MHz	2.25 MHz	5 MHz
Number of Elements	5	8	10	16	9	9
Outside Diameter	38 mm (1.5)	38 mm (1.5)	38 mm (1.5)	38 mm (1.5)	19 mm (.75)	19 mm (.75)
Piezoelectric	----------Lead Metaniobate----------					
Element Width	3 mm (.125)	1.65 mm (.065)	3 mm (1.25)	1.65 mm (.065)	0.8 mm (.032)	0.8 mm (.032)
Element Center to Center Spacing	3.9 mm (.156)	2.4 mm (.097)	3.9 mm (.156)	2.4 mm (.097)	1 mm (.042)	1 mm (.042)
Space Between Elements	0.8 mm (.032)	0.8 mm (.032)	0.8 mm (0.32)	0.8 mm (.032)	0.25 mm (.010)	0.25 mm (.010)
Center Element Dia.	6.3 mm (.250)	3 mm (.125)	6.3 mm (.250)	3 mm (.125)	2 mm (.078)	2 mm (.078)

identified on the curves as FD (focal distance). The curve marked "Nonfocused Simultaneous Excitation" describes the axial pressure distribution of the beam when all elements are excitated simultaneously and is typical of a nonfocused search unit of this size and frequency.

To record a plan view of the beam intensity distribution, "C" scan recordings were made for various excitation delay schedules and focal distances. These recordings, shown in Fig. 5, reflect good agreement with the distance vs. amplitude curves shown in Fig. 4. The dark tone in the recordings represents the beam distribution with the recording gate threshold set at a signal amplitude of 6 dB below maximum; the lighter tone is gated at 18 dB down. Recording in this manner, it was possible to image the side lobes that can be expected from annular arrays. With an amplitude of 12 dB below the majority of the beam, side lobes should not adversely affect the use of the array in most applications. Of primary interest in these recordings is the length over which the beam is held in collimation. This capability would be advantageous in test applications where thicker material sections must be examined and good lateral resolution maintained.

Figure 6 shows distance vs. amplitude and beam width vs. distance plots made using 1/8-inch (3 mm), side-drilled hole reflectors in steel. The 6 dB beam width plots showed that considerable beam collimation can be maintained in steel and was in good agreement with the "C" scan recordings made in water. The excitation pulse delay schedule used during these plots was the same as that used for the 7.5-inch (190 mm) FD shown in Fig. 4. The operating water path was varied to study its effect on the beam geometry in steel.

The composite transverse and axial pressure distribution plot shown in Fig. 7 also displayed good correlation to the theoretical. A 1/8-inch (3 mm) diameter, receiver search unit was used in generating these x-y recordings. In this plot, the excitation pulse delay increment applied to each element was rounded off to the nearest 1/10 microsecond without serious deviations in the desired focal distance or overall beam geometry. This effect, however, could not be achieved with annular arrays of higher frequency and shorter focal distances. For higher frequencies and shorter focal distances, the time delay increment must be maintained accurately to within 15 nanoseconds.

EXPERIMENTAL RESULTS, 45-DEGREE SHEAR

To allow the use of annular arrays in shear wave applications, the beam must be presented to the material surface at an angular incidence. This results in a travel time difference to the material for the inclined portion of the beam vs. the declined portion of the beam. The programmed phased relationship required for focusing at the desired depth in the material would be destroyed unless this time of flight difference were corrected.

Figure 8 shows the distance vs. amplitude and beam width vs. distance performance of an uncorrected annular array operating at 45 degrees in steel. Beam distortion resulting from the loss of correct phase relationship was apparent in the beam width vs. distance diagrams as the operating water path was varied from 25.4 mm to 101. Beam distortion remained severe, but showed some slight improvement at the longer water path of 101 mm. At this longer water path, the beam approached an in-phase condition, and beam distortion was minimized. Longer operating water paths, however, were no solution because of the limited depth in steel at which the beam could be focused.

To compensate for the difference in travel time with respect to the inclined and declined portion of the array would require additional time delay corrections in the excitation of the array. A segmented annular array was designed that divided the ring-shaped elements into two sections. This allowed each semicircular element to be addressed separately and delayed in excitation to correct for the angular incidence desired. Figure 9 shows this segmented array configuration. The center disc element is used as a receiver.

Figure 10 shows the distance vs. amplitude and beam width vs. distance performance for the

segmented, time-corrected array at 45 degrees in steel. While total correction count not be achieved due to the semicircular geometry of the element, it was apparent that the severe distortion was eliminated and a uniform focal zone was achieved even at the shorter operating water path distances.

INSTRUMENTATION

The multi-channel pulsers used in these experiments were designed and built by the SwRI Instrumentation Research Division. The multi-channel pulser system is capable of pulse delay increments of 10 nanoseconds to 10 microseconds. Pulse width is adjustable, allowing optimized pulse duration for transducer frequencies of 1.0 to 5 MHz. This multi-channel pulser is synchronized by the trigger signal from a conventional ultrasonic flaw detector instrument. This allows the receiver, display, and gate sections of the conventional instrument to be used in a normal manner in recording array performance data.

It is forseeable that conventional ultrasonic flaw detectors could be used with multi-element arrays. With delayed pulser receivers addressed by computer, a 100 percent focused beam depth coverage of the material under examination could be obtained in one scan path.

CONCLUSION

The objective of this program was to investigate the potential use of the multi-element, annular array search units. Several designs have been developed and their capabilities defined. Annular arrays have demonstrated some very desirable capabilities. They have shown potential system performance improvements that are compatible with conventional instrumentation and would not require complex additions to the system. The annular array search unit did not display improved resolution as compared to a fixed focus search unit. However, the array provides the ability to focus the beam at various distances in the material under examination. With the extended collimation of the beam, it produces a longer working zone.

Segmented annular array configurations have demonstrated potential in applications where focused shear wave beams are desired.

REFERENCES

1. Burckhardt, C. B.; Franchamp, P. A.; and Hoffman, H. "Focusing Ultrasound over a Large Depth with an Annular Transducer - An Alternative Method," IEEE Transactions on Sonics and Ultrasonics SU-22, no. 1 (January 1975).
2. McElroy, J. T. "Transducer Design Study for Improved Defect Definition in Ultrasonic Examinations," Southwest Research Institute, Internal Research Report 17-9152.
3. Thurstone, F. L. and Von Ramm, O. T. "A New Ultrasound Imaging Technique Employing Two-Dimensional Electronic Beam Steering," Acoustical Holography and Imaging 5. New York: Plenum Press, 1973.
4. Somer, J. C. "Electronic Sector Scanning with Ultrasonic Beams," Proceedings of the First World Congress on Ultrasonic Diagnostics in Medicine, Vienna, Austria, 1969.
5. Bom, Nicoloas. "Multiscan Echocardiography," Medical Faculty and University Hospital, Erasmus University, Rotterdam.
6. Buschmann, W. "New Equipment and Transducers for Ophthalmic Diagnosis," Ultrasonics 18, 1965.
7. Uchida, R. "Electro-scanning Ultrasonic Diagnostic Equipment," Japan Med. El 58 1971/72.
8. "Ultrasonic Diagnosis Progress Report," Institute of Medical Physics TNO: 37 1968.
9. Thurston, F. L. and McKinney, F. M. "Focused Transducer Arrays in an Ultrasonic Scanning System for Biologic Tissue," Diagnostic Ultrasound. New York: Plenum Press, 1966.
10. Waugh, T. M.; Kino, G. S.; DeSilets, C. S.; and Fraser, J. D. "Acoustic Imaging Techniques for Nondestructive Testing," IEEE Transactions on Sonics and Ultrasonics SU23, no. 5 (September 1976).
11. Posakony, G. J.; Becher, F. L.; et. el. "Development of an Ultrasonic Imaging System for the Inspection of Nuclear Reactor Pressure Vessels," EPRI Contract No. RP606-1, Progress Reports 1, 2, and 3.

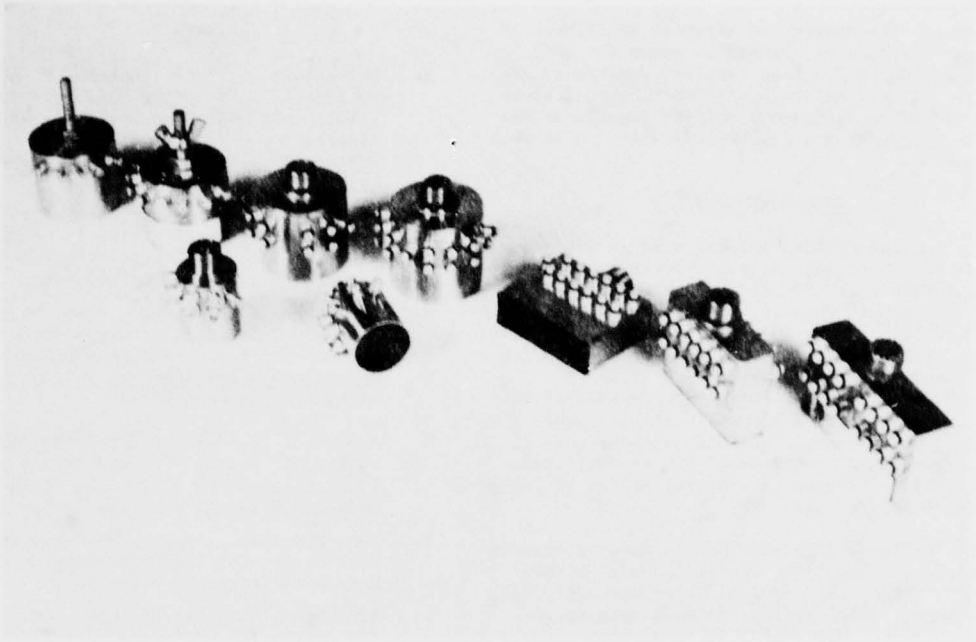

Fig. 1 Prototype multi-element array configurations.

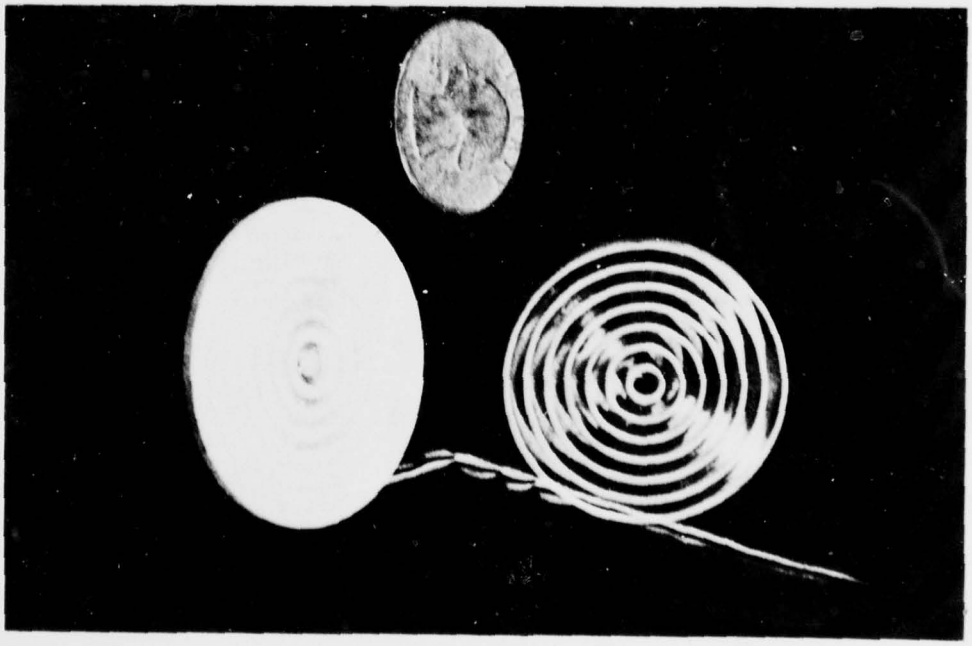

Fig. 2 Abrasive cutting tool and piezoelectric annular array.

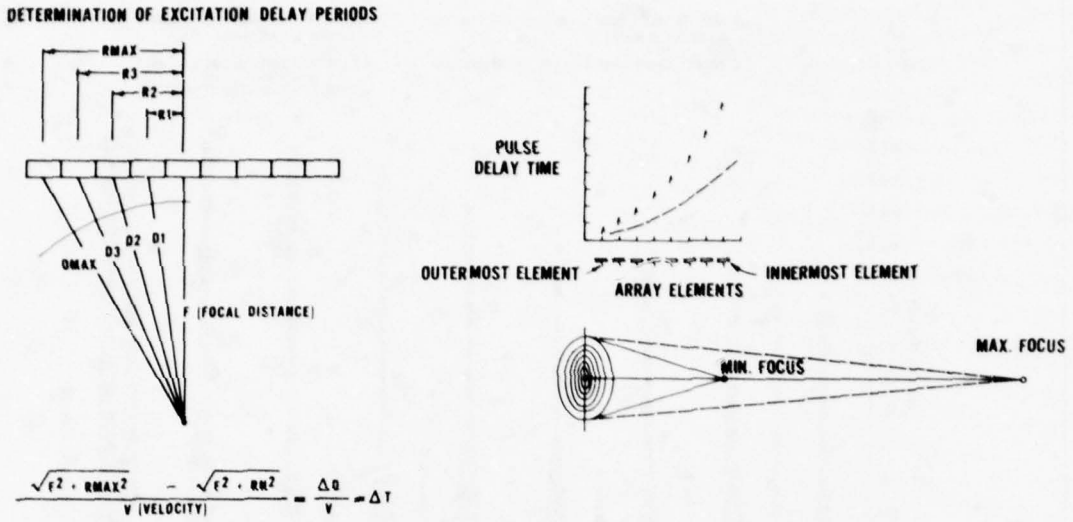

$$\frac{\sqrt{F^2 + RMAX^2} - \sqrt{F^2 + Rn^2}}{V\ (VELOCITY)} = \frac{\Delta Q}{V} = \Delta T$$

Fig. 3 Determination of excitation pulse delay schedule.

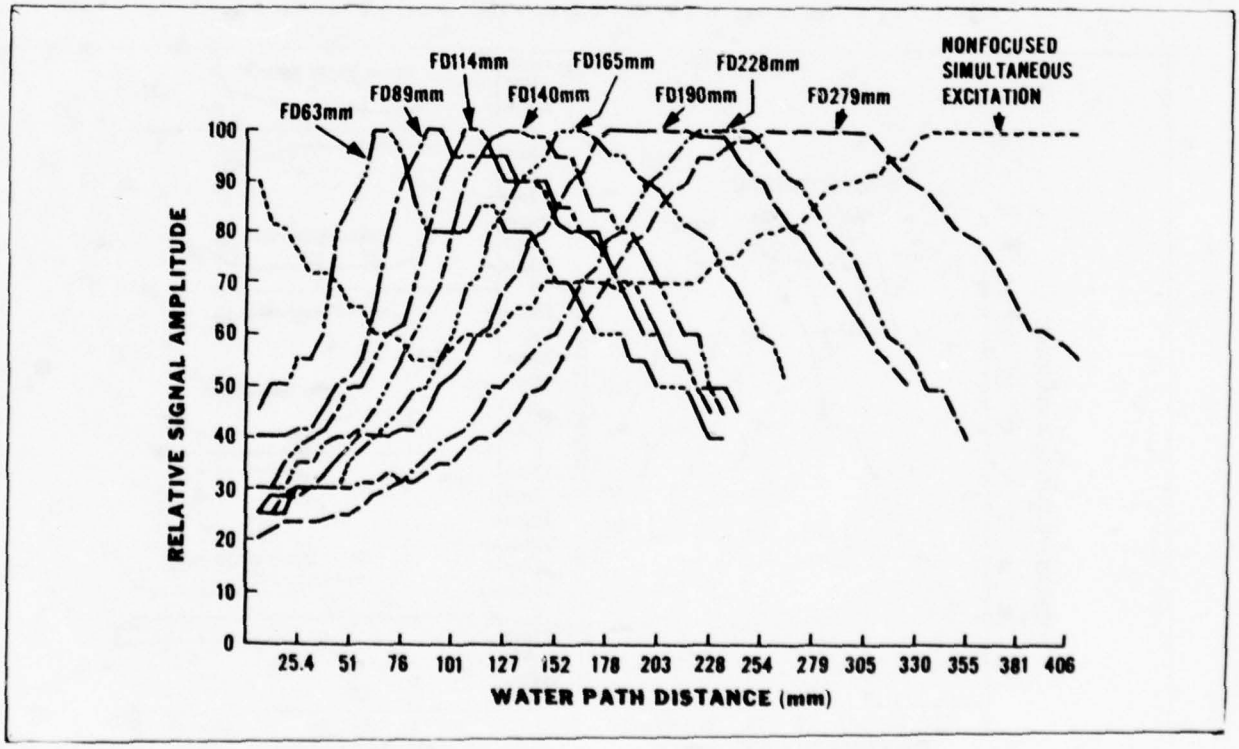

Fig. 4 Distance versus amplitude performance for a 2.5 MHz, 1.5-inch (38 mm), 8-element annular array.

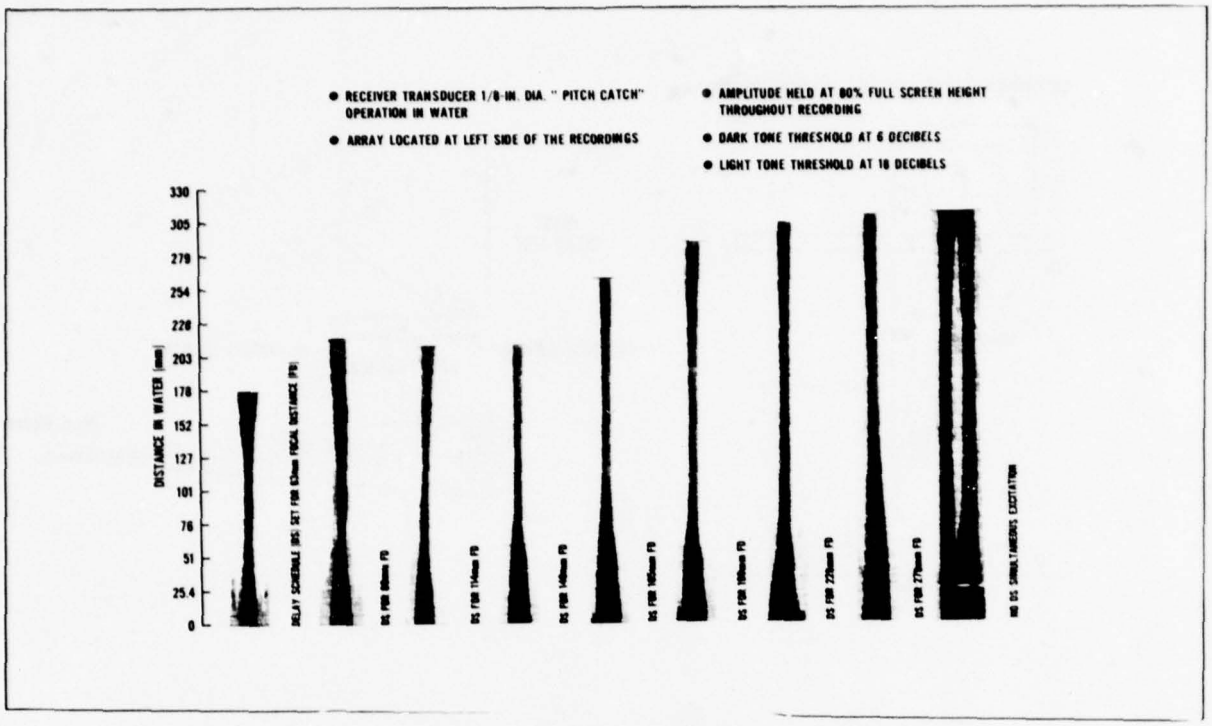

Fig. 5 "C" scan recordings of 2.5 MHz, 1.5-inch (38), 8-element annular array.

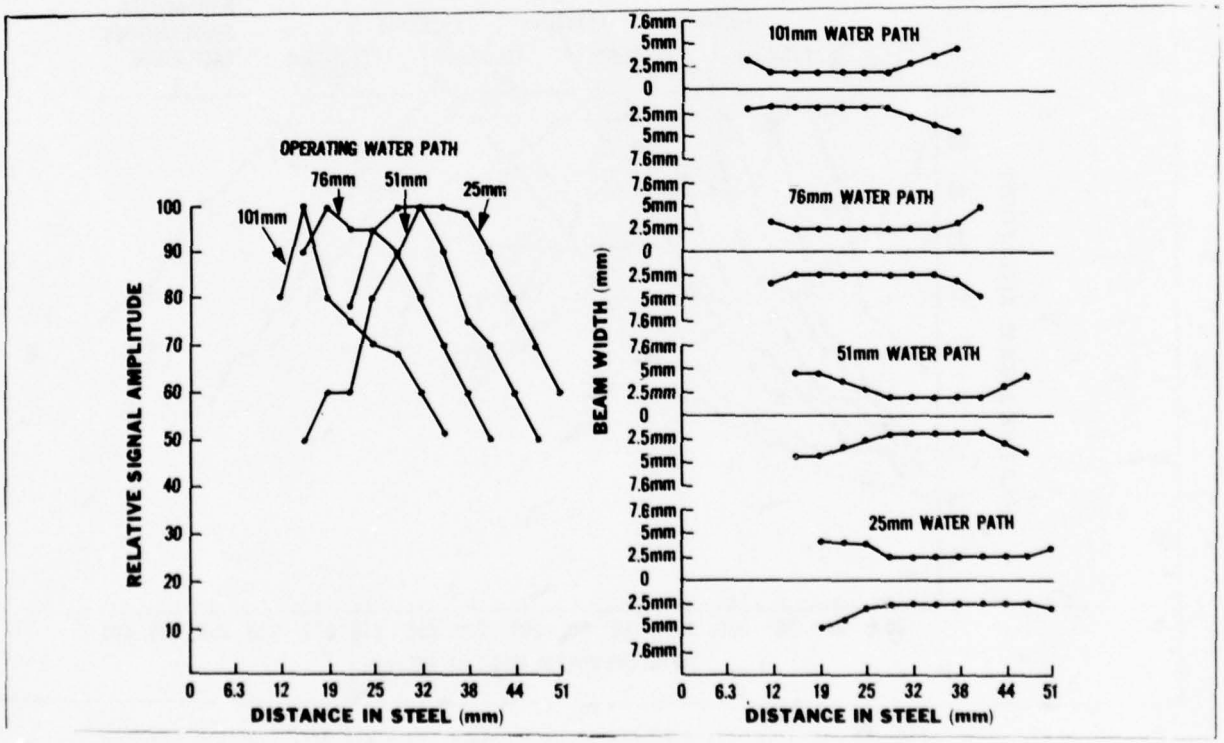

Fig. 6 Distance versus amplitude and beam width versus distance in steel, 0-degree longitudinal wave.

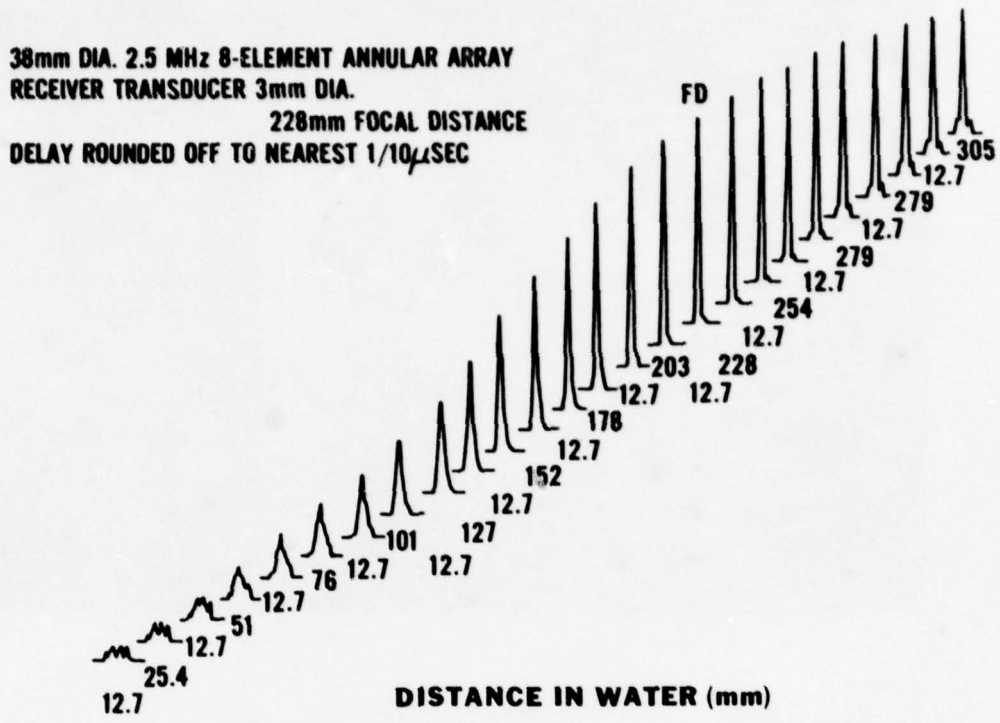

Fig. 7 Composite transverse and axial pressure distribution plots.

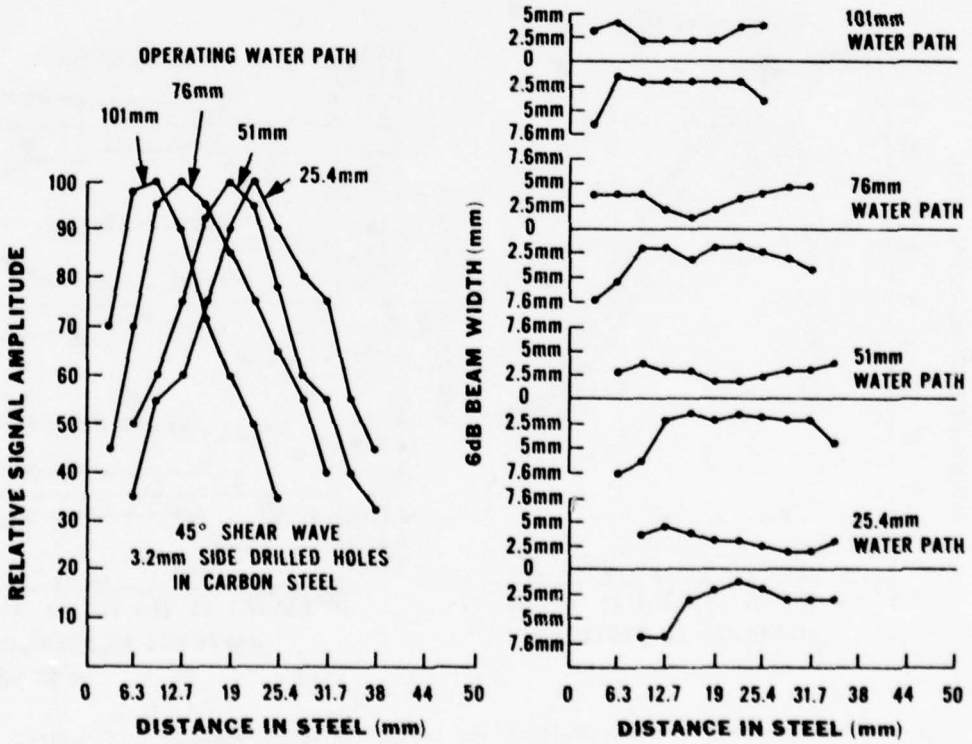

Fig. 8 Distance versus amplitude and beam width versus distance performance for uncorrected annular array at 45-degree shear in steel.

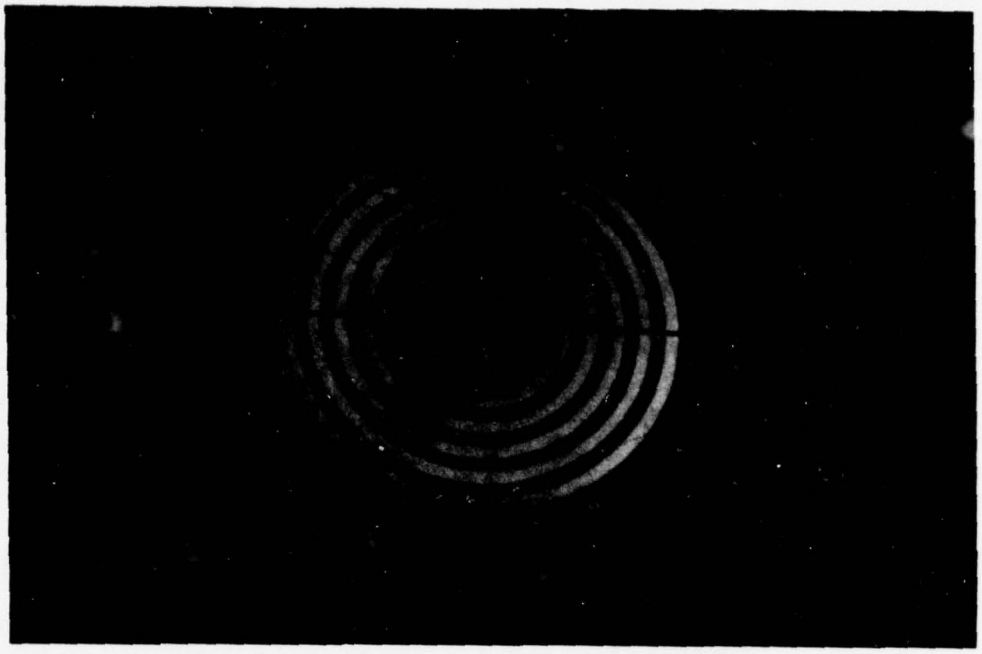

Fig. 9 Segmented annular array.

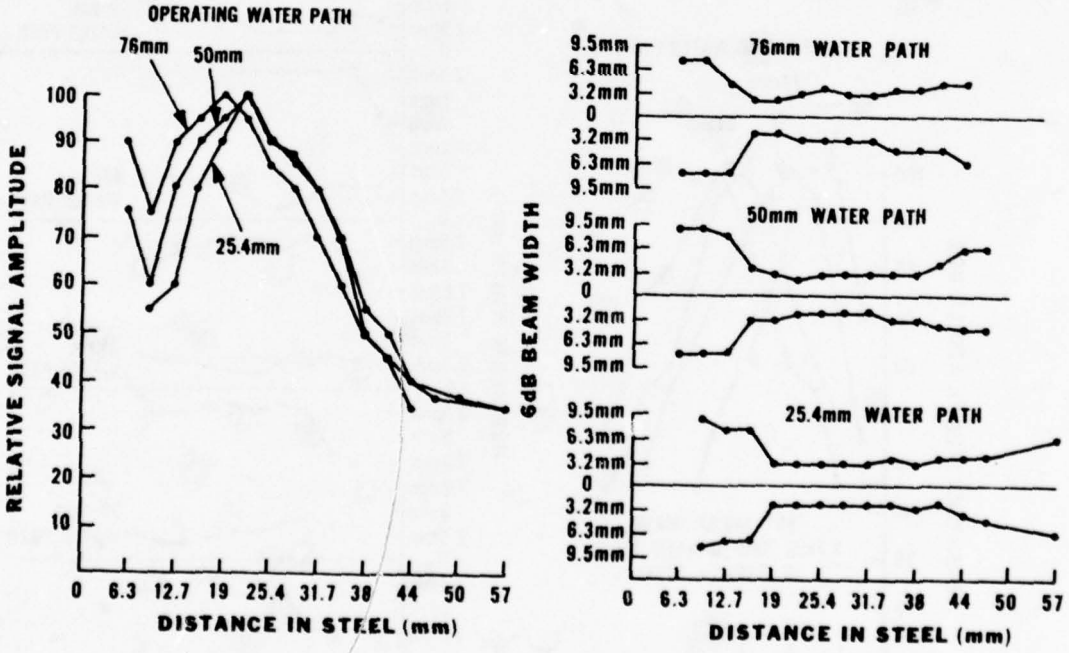

Fig. 10 Distance versus amplitude and beam width versus distance performance for corrected segmented annular array at 45-degree shear in steel.

QUANTITATIVE ULTRASONIC HOLOGRAPHIC DEFECT CHARACTERIZATION

J. W. Brophy, A. E. Holt, J. H. Flora
Nondestructive Methods and Instruments Section
Babcock & Wilcox Company
Lynchburg Research Center
P. O. Box 1260
Lynchburg, Virginia 24505

ABSTRACT

Ultrasonic holography has proven to be a useful and accurate tool for defect imaging and sizing in thick wall materials. The optical image formation gives a true two-dimensional cross-section of the flaw as a function of the angle at which the flaw is inspected. Recently Babcock & Wilcox participated in Oak Ridge Laboratories thermal shock program of HSST test vessels, under at EPRI contract, to attempt to define cracks induced into the vessels. The defects induced were "natural" cracks running the length of the vessel.

The purpose of the holographic inspection was to map the extent of the crack propagation extending from the inside diameter towards the outside diameter of the vessel. The crack propagation map provided by the holography inspection was compared to destructive analysis and found to be within 10 percent of the area of maximum crack propagation.

The potential of cultrasonic holography as a quantitative tool for characterizing defects has long been recognized. For large primary containment vessels used in nuclear power stations or other heavy section materials, time-gated pulse-echo holography has been demonstrated to be a fieldworthy technique. The basic technique of data acquisition and the production of a visual image whose dimensions are directly proportional to the defect dimensions are outlined.

For the specific data reported here, schematics of the Oak Ridge Laboratory test vessels are shown, as well as the basic geometry of the inspection procedure. The data being reported here is the holographic mapping of a thermal shock induced crack in a Heavy Section Steel Technology (HSST) test vessel. The B7W holography field units are shown in use at Oak Ridge as well as one of the two test vessels that was examined.

The reduced data and available destructive results are presented with the holographic and destructive analysis of prominent features tabulated. The holographic map of the through-wall dimension of the crack can be viewed directly in its through-wall extent on the reduced data plots.

All the defect images in this study were produced by optical reconstruction of the holograms. Future efforts by B&W are to implement direct computer data acquisition and image reconstruction into a field compatible unit. We show here some results of the computer technique of data acquisition and reconstruction and the corresponding optical hologram. The proposed computerized ultrasonic field unit would use a rugged minicomputer and would provide enhanced imaging techniques and displays with no loss in the time from data acquisition to image display.

REFERENCES

1. B. P. Hildebrand and B. B. Brenden, An Introduction to Acoustical Holography, Plenum Press, New York, New York, 1972.

2. A. E. Holt, Acoustical Holographic Development. Babcock & Wilcox Lynchburg Research Center, Lynchburg, Virginia, Report #9055, February 1977.

3. A. E. Holt, Evaluation of Welds by Acoustical Holography Imaging Techniques, Babcock & Wilcox Lynchburg Research Center, Lynchburg, Virginia, Report #LR:74:2197-01:01 and Report #LR:74:2089-01:02, September 1974.

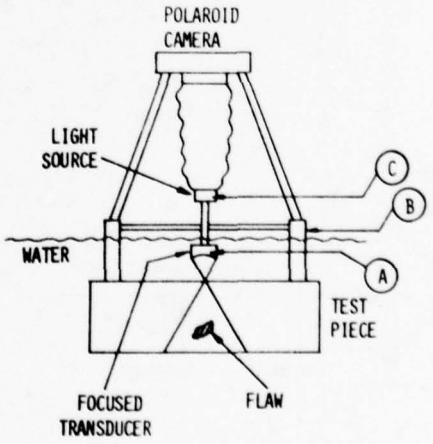

Fig. 1. Basic pulse-echo time-gated ultrasonic holography volume tested

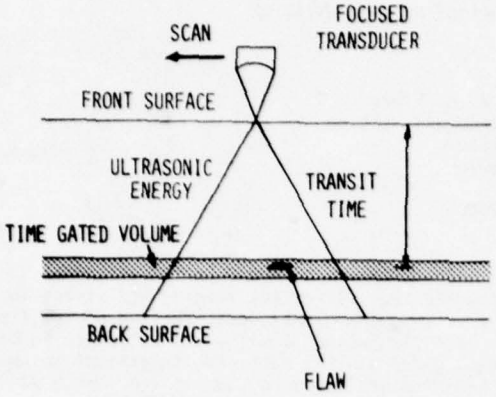

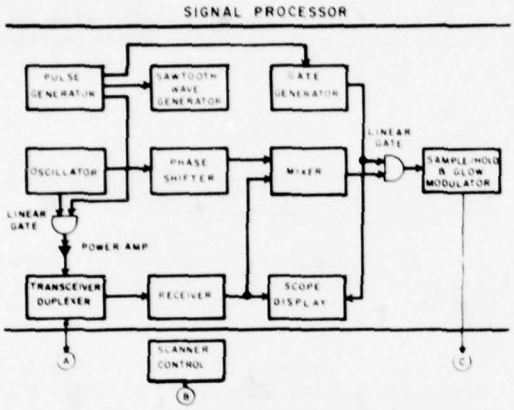

Fig. 2 Hardware Schematics

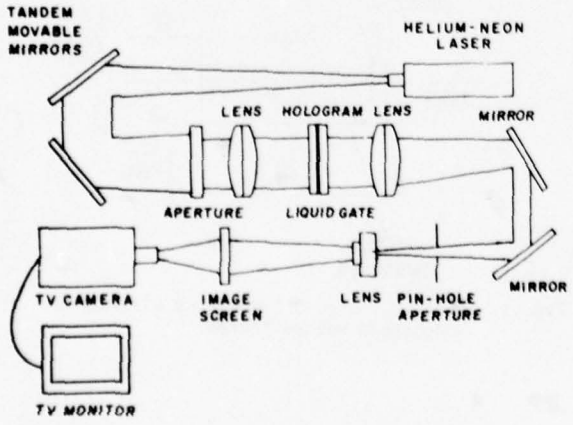

Fig. 3 Optical Processor Field Unit Configuration

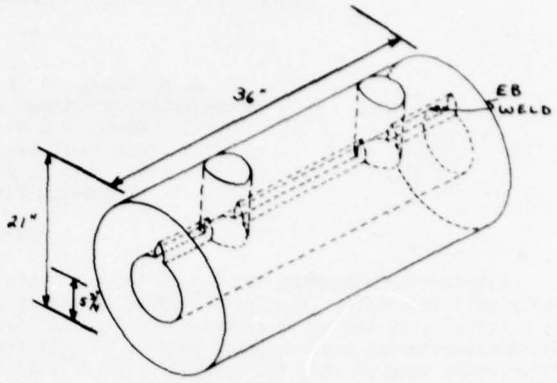

Fig. 4 Artist Illustration of HSST #1 Showing Machined Notch, EB Weld Zone and Trepans.

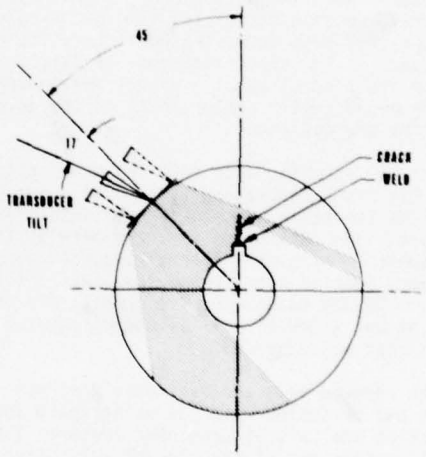

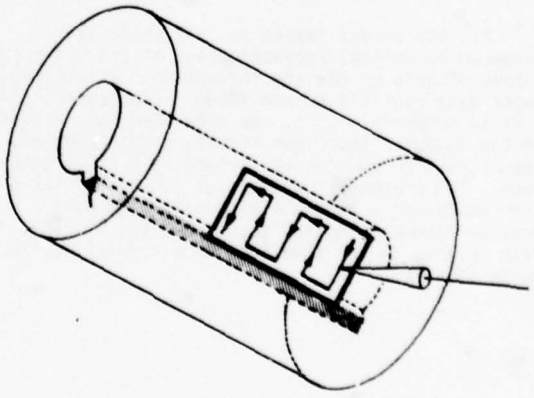

Fig. 5 End and Side Views Showing Scanned Region Geometry and Transducer Angle

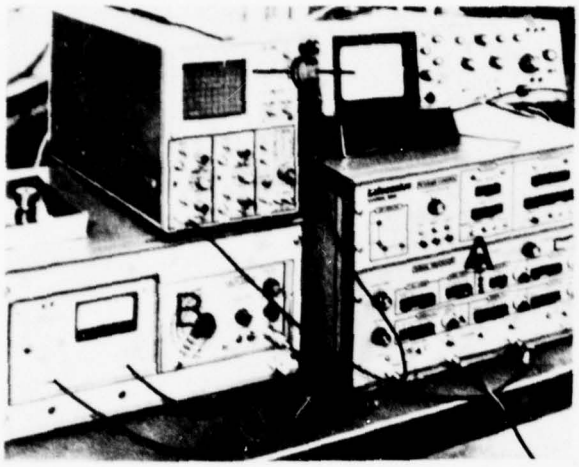

Fig. 6 Field Unit Electronic Hardware

a. Signal processor
b. Oscillator and power amplifier
c. Oscilloscope display units

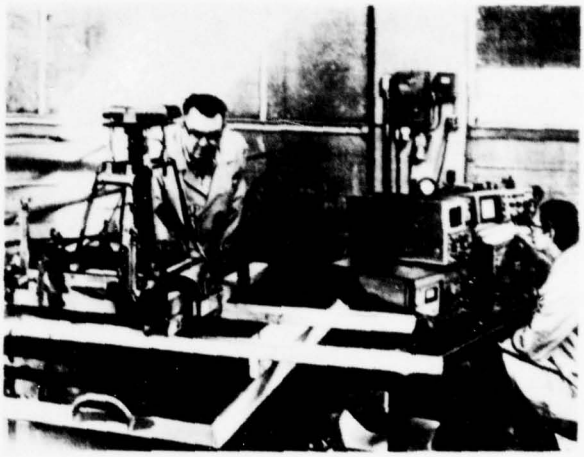

Fig. 7 Field Unit and Operators HSST Test Vessel Inspection at Oak Ridge Site

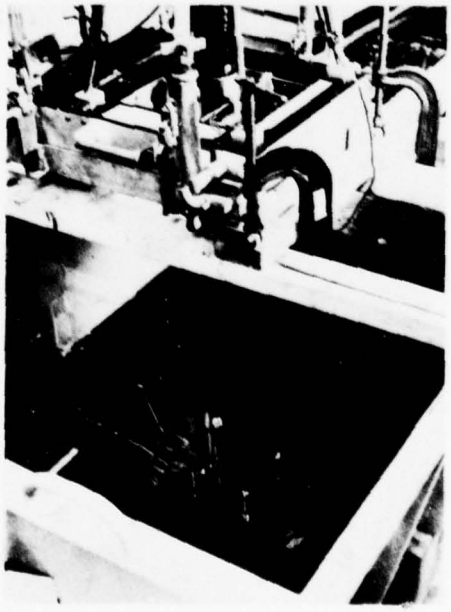

Fig. 8 HSST Vessel #2 Setup Scanner, Mounting Fixture and Camera Light Pipe. Scribe Marks on the Vessel Outline Relative Coordinate System Used

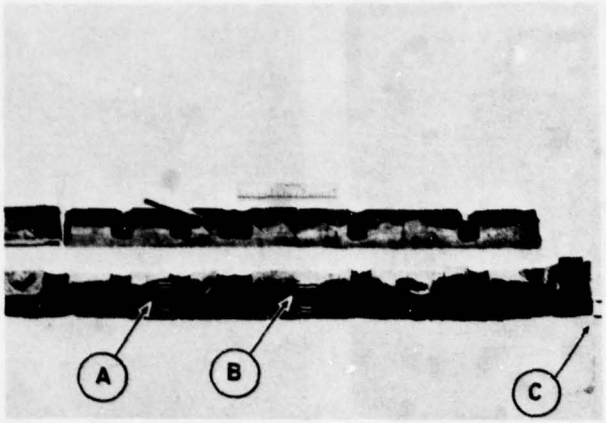

Fig. 9 Destructive Results for HSST #1

a. Maximum crack extent
b. Average crack extent
c. EB weld and machined notch

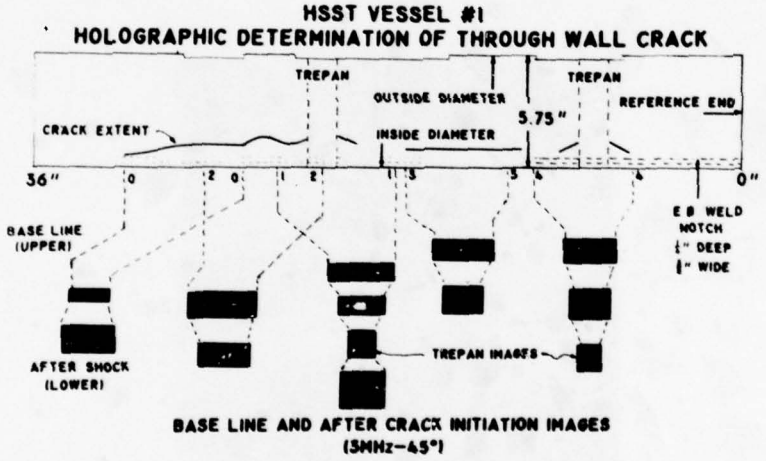

Fig. 10 Comparison of Destructive and Holographic Results

I) maximum crack extent

holographic	destructive
1.55"	1.7"

II) EB weld and notch extent

holographic	destructive
0.5"	0.5"

III) trepan diameters

holographic	destructive
0.95"	1.0"

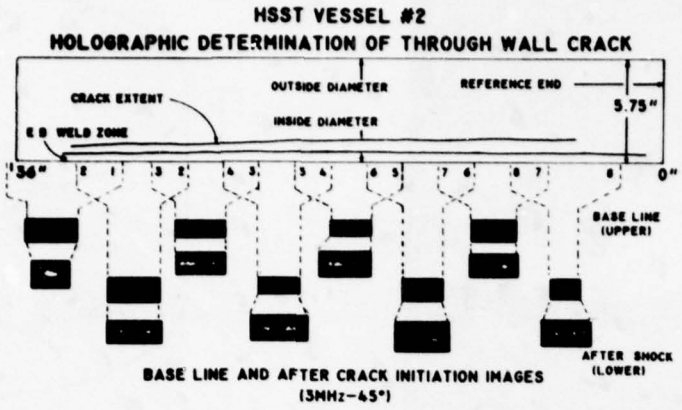

Fig. 11 Comparison of Destructive and Holographic Results

I) average crack extent

holographic	destructive
0.5"	0.5"

II) EB weld zone extent

holographic	destructive
0.5"	0.5"

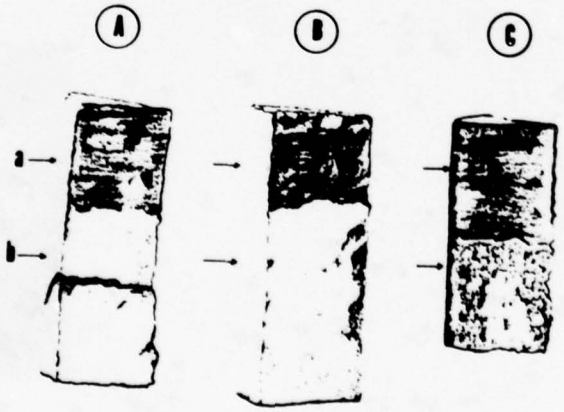

Fig. 12 Core Samples Removed from HSST #2 Arrows Point to Extent of EB Weld Area (a) and Extent of Crack Area (b)

Bottom view photo of "Y" test block.

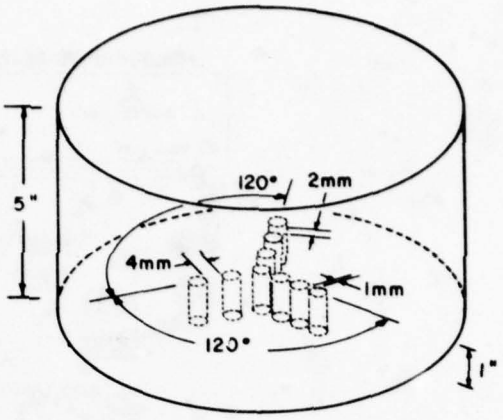

ALUMINUM TEST BLOCK

Schematic of "Y" block dimensions.

Fig. 13 Test Block Used to Evaluate Results Between Optical Image Reconstruction and Computer Image Reconstruction

Fig. 14 Optical media acoustic hologram of "Y" block.

Fig. 15 Optical reconstruction of "Y" block image

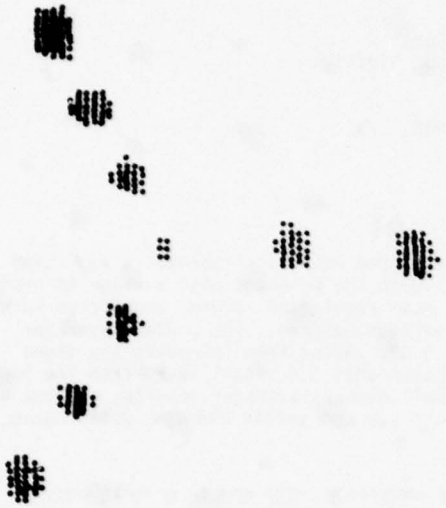

Grey scale plot.

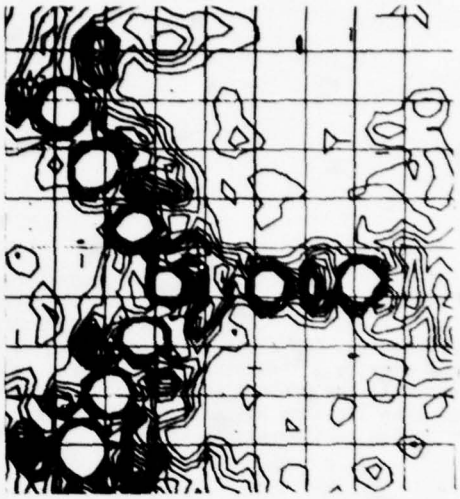

Contour plot with no noise suppression.

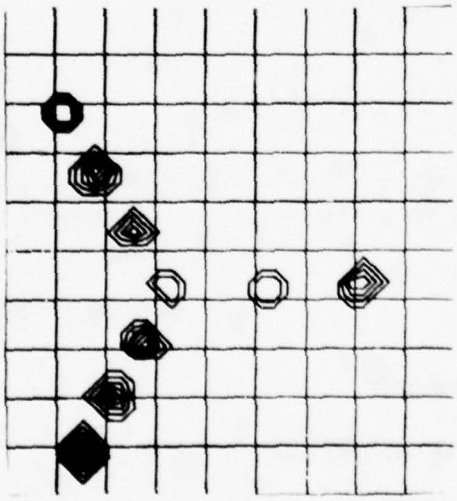

Contour plot with noise suppressed.

Fig. 16 Computer reconstructions of "Y" block image

REAL TIME CCD AVERAGER FOR ULTRASONIC APPLICATIONS

Earl DuBack, William McCabe
General Dynamics, Electric Boat Division
Department 443
Eastern Point Road
Groton, Connecticut 06340

ABSTRACT

An ultrasonic acquisition and processing system is being developed which incorporates a real time CCD averager. The averager sums the received ultrasonic signal with the weighted past average to produce the latest average. The averager performance is a function of scan resolution, signal repetition rate, scan velocity, CCD clock rate, weighting value and number of averages desired. The present averager should provide a theoretical improvement in signal to noise of 6 dB. Aside from improving the signal strength at the present scan position the averager is designed such that the signal level from the previous scan location has decayed by at least 10 dB. The paper will discuss averager results, and the various design considerations and simulation testing required to achieve and verify averager performance.

GENERAL DESCRIPTION - THE AVERAGER IS BEING CONSTRUCTED FOR USE IN ULTRASONIC PROCESSING SYSTEMS WHERE SIGNAL TO NOISE ENHANCEMENT IS REQUIRED. THE AVERAGER IS INSERTED BETWEEN THE TRANSDUCER AND DETECTOR TO SUPPLY CONTINUOUSLY WEIGHTED OF SIGNAL AVERAGES TO THE DETECTOR. THE AVERAGER REQUIRES A TRIGGER PULSE WHICH IS IN SYNCHRONISM WITH THE PULSED SIGNAL.

CHARACTERISTICS

- INPUT PROTECTED - -450 VOLTS PULSER
- SIGNAL BANDWIDTH - 5 MHZ
- FILTERING - MATCHED TO 3.5 MHZ TRANSDUCER
- MAXIMUM OF 36 μSEC STORAGE
- PULSE REPETITION RATE - 1 MHZ
- TTL TRIGGER INPUT
- LINEAR SIGNAL RANGE - ± 500 MV.
- EFFECTIVE INTERNAL CLOCKING RATE - 25 MHZ
- DIMENSIONS - 5" x 6" x 10"
- POWER - 115 VOLTS 60N
- INTERNAL POWER:
  - CCD - 20 VOLTS
  - DIGITAL CONTROL - 5 VOLTS
  - ANALOG - ± 15 VOLTS

Fig. 1. Real time CCD averager for ultrasonic application

- DECAY OF CCD SIGNAL/NOISE INCREASE
- TIME DELAY AND PHASE SHIFT OF AVERAGER LOOP
- FILTERING OF CCD CLOCK AND SIGNAL
- RECEIVED AMPLITUDE LEVELS

Fig. 2. Design considerations

- INPUT PROTECTION - CLIP MAIN PULSE TO ACCEPTABLE LEVEL.
- FILTERING - ENHANCE FREQUENCY REGION OF 3.5 MHZ SIGNAL AND REDUCE DIGITIZING FREQUENCY, 12.5 MHZ.
- CCD CLOCK CONTROL - ALLOW SYNCHRONOUS AND CONTROLLED TIMING OF CCD CLOCKING WITH PULSER.

Fig. 3. Key elements of averager

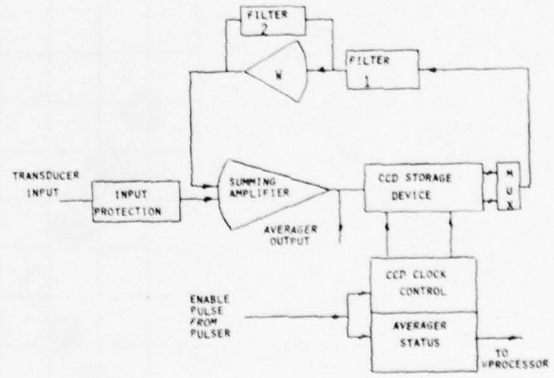

Fig. 4. Averager block diagram

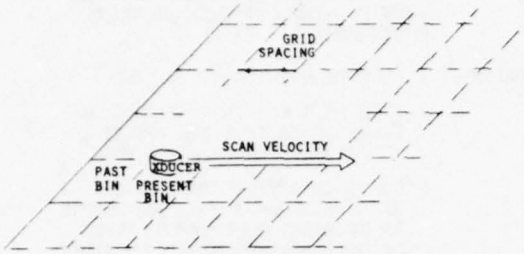

V IN/SEC = SCAN VELOCITY

L MIL/INCH = GRID SPACING

R PULSES/MILLISEC = PULSE REPETITION RATE

MAX NUMBER OF AVERAGES PER GRID = $\frac{R \times L}{V}$

Fig. 5. Scanner parameters

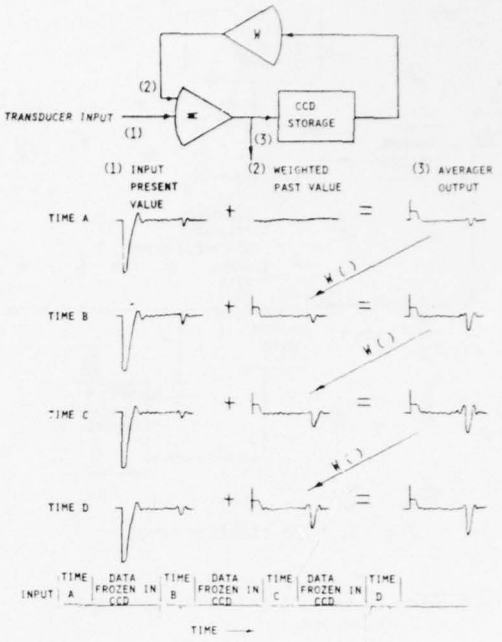

Fig. 7. Averager operation

GENERAL

$$E_O = E_{IN}\left[\underbrace{1 + W + W^2 + W^3}_{\text{PRESENT BIN}} + \underbrace{W^4 + W^5 + W^6 + W^7}_{\text{PREVIOUS BIN}} + W^8 + W^9 + \bullet\bullet\bullet e\right]$$

STEADY STATE

$$E_O = E_{IN} \cdot \left[\frac{1}{1 - W}\right] \qquad W < 1$$

E_O = OUTPUT VOLTAGE

E_{IN} = INPUT VOLTAGE

W = WEIGHING FACTOR

IN SELECTING W MUST CONSIDER TRADE OFF.

- MAXIMIZE SIGNAL/NOISE (W LARGE)
- HAVE AN ACCEPTABLE DECAY OF PREVIOUS BIN VALUE 10 - 20 DB. (W SMALL)

Fig. 6. Averager output

THE IMPROVEMENT IN S/N:

$$F_N = 10 \log_{10}\left[\left[\frac{1 + W}{1 - W}\right]\left[\frac{1 - W^N}{1 + W^N}\right]\right] \text{ DB}$$

THE AVERAGER OUTPUT WILL HAVE THE PREVIOUS BIN SIGNAL DOWN:

$$G_N = 20N \log_{10} W \text{ DB}$$

WHERE: W = WEIGHTING FUNCTION
N = NUMBER OF AVERAGES/GRID

Fig. 8. Averager performance

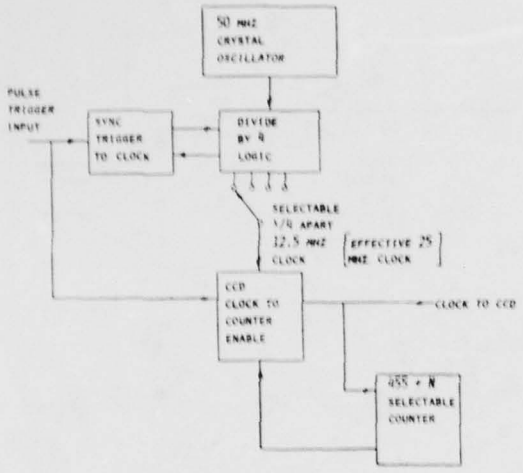

Fig. 9. CCD clock control

OBJECTIVE - TO VERIFY THE AVERAGER PROVIDES A SIGNAL TO NOISE GAIN.

PROCEDURE -
- o ADJUST THE OSCILLATOR INPUT AMPLITUDE TO 50 MV (NOISE FREE CONDITION)
- o ADJUST THE OSCILLATOR FREQUENCY TO THE TRANSDUCER CENTER FREQUENCY AND FINE TUNE UNTIL OUTPUT PEAKS. (CCD FREE RUNNING ∴ PHASE ALIGNING FEEDBACK WITH OUTPUT).
- o ADJUST THE FEEDBACK WEIGHTING FACTOR (W) UNTIL THE OUTPUT IS ≈ 6X INPUT.
- o ADD NOISE TO SIGNAL AND MEASURE SIGNAL TO NOISE AT INPUT AND OUTPUT.
- o SINCE THE CCD IS FREE RUNNING, THE AVERAGER FEEDBACK TIMING IS NOT BEING TESTED.

Fig. 10. Simulation test #1

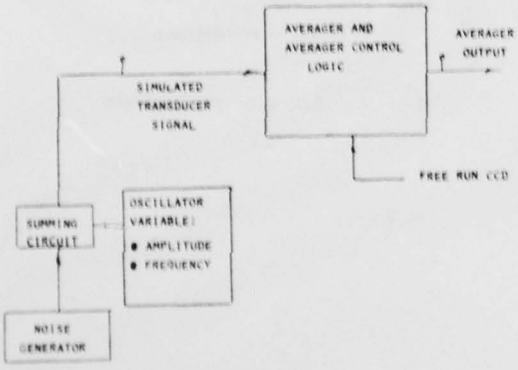

† - SCOPE AND SPECTRUM ANALYZER TEST POINTS.

Fig. 11. Simulation test #1

OBJECTIVE: TO VERIFY THE AVERAGER PROVIDES A SIGNAL TO NOISE GAIN FOR ULTRASONIC TYPE SIGNALS AND THAT THE CCD TIME CONTROL CAN CORRECT FOR SUMMING AMPLIFIER, FEEDBACK AMPLIFIER, AND PULSER TRIGGER DELAYS.

PROCEDURE:
- o ADJUST THE REPETITION RATE TO 1 KHZ.
- o CENTER THE 50 MV SIGNAL PULSE IN THE CCD STORAGE AND ADJUST THE PULSE WIDTH TO MATCH AN ACTUAL TRANSDUCER PULSE WIDTH.
- o INCREASE THE NUMBER OF COUNTS WHICH IN TURN ADVANCES DATA IN THE CCD AND CORRECTS FOR THE VARIOUS DELAYS MENTIONED ABOVE. INCREASE COUNTS UNTIL FEEDBACK TIME PHASED WITH INPUT.
- o FINE TUNE FEEDBACK ALIGNMENT BY SELECTING APPROPRIATE λ/4 CLOCK.
- o ADJUST THE FEEDBACK WEIGHTING FACTOR (W) UNTIL THE OUTPUT SIGNAL IS ≈ 6 X INPUT.
- o ADD NOISE TO SIGNAL AND MEASURE SIGNAL TO NOISE AT INPUT AND OUTPUT.

Fig. 12. Simulation test #2

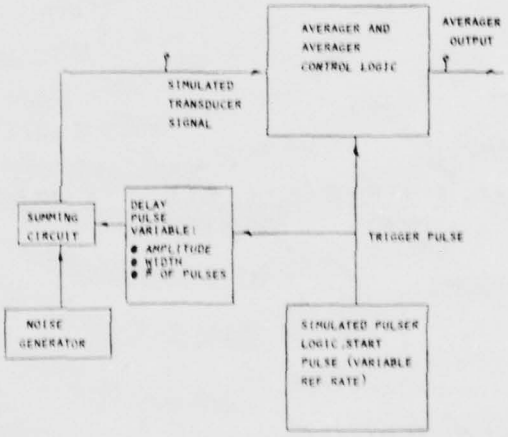

† - SCOPE AND SPECTRUM ANALYZER TEST POINTS

Fig. 13. Simulation test #2

- o IMPROVE SIGNAL DETECTION WHEN LOW LEVEL SIGNALS ARE ENCOUNTERED.
- o WHEN XDUCER DECOUPLING OCCURS IMPROVE POSSIBILITY OF SIGNAL RECEPTION IN A GRID BY TAKING MULTIPLE SAMPLES.
- o BY TAKING SPATIALLY MOVING AVERAGES IN A GRID DECORRELATE GRAIN NOISE.

Fig. 14. Possible benefits of averager

- ALL RESULTS ARE BASED ON AN EFFECTIVE CCD CLOCKING OF 33.2 MHZ. AT 25 MHZ THE 1/4 FINE TUNE COUNT CONTROL IS NECESSARY TO ALIGN FEEDBACK WITH INPUT SIGNAL FOR 5.5 MHZ TRANSDUCER. THIS FINE TUNE CONTROL IS BEING CONSTRUCTED.
- A SIGNAL INCREASE OF 6 TO 8 HAS BEEN ACHIEVED FOR A 1 MHZ TRANSDUCER.
- A SIGNAL INCREASE OF 4 TO 6 HAS BEEN ACHIEVED FOR A 5.5 MHZ TRANSDUCER.
- FILTER COMPENSATION IS NECESSARY FOR THE 5.5 MHZ TRANSDUCER.
- A NOTCH FILTER CENTERED AT CLOCK FREQUENCY HAS CAUSED CLOSED LOOP OSCILLATIONS AND HAS BEEN REMOVED.
- OLD CCD HAS 8 EQUALLY SPACED SPIKES ON OUTPUT WHICH INCREASE WITH AVERAGING. NEW, REDESIGNED, CCD HAS NOT BEEN TESTED IN AVERAGER, BUT SHOULD ELIMINATE THE PROBLEM SINCE SPIKES 20 DB LOWER.
- THE CCD COUNTER HAD A PROBLEM WHICH HAS BEEN CORRECTED. ALTHOUGH THE PULSER TRIGGER IS ASYNCHRONOUS TO THE CLOCK, CIRCUITRY MUST BE PROVIDED TO INSURE THE FIRST CLOCK PULSE TO THE COUNTER IS A FULL CLOCK PULSE OR ERRONEOUS COUNTS WILL OCCUR.
- CIRCUIT OSCILLATIONS OCCUR WHEN SIGNAL INCREASES GREATER THAN 6 TO 8 ARE ATTEMPTED. THIS INSTABILITY IS UNDER INVESTIGATION.
- DATA IS NOT CLOCKED THROUGH THE CCD UNTIL AFTER THE MAIN PULSE HAS OCCURRED 1μsec. DATA HAD BEEN CLOCKED THROUGH INCLUDING THE MAIN PULSE BUT THIS MAY IMPACT STABILITY.
- BECAUSE OF THE FAST RISE TIME OF THE MAIN PULSE, THERE IS SOME SPIKE LEAKAGE PAST THE DIODE PROTECTION.
- THE PULSER TRIGGER MUST OCCUR AT THE SAME INSTANT IN TIME WITH RESPECT TO THE MAIN PULSE. IN ONE ULTRASONIC UNIT THE TRIGGER PULSE MOVED IN TIME WHEN THE PULSER AMPLITUDE WAS INCREASED. THIS CAUSED MISALIGNMENT IN THE AVERAGER.
- USING A FET SWITCH, THE FEEDBACK RESISTOR ON THE SUMMING AMPLIFIER WAS SHORTED OUT DURING THE MAIN PULSE. ALTHOUGH ELIMINATING THE MAIN PULSE SPIKE TO THE CCD, THE SWITCH INTRODUCED IT'S OWN SPIKES AT THE SWITCH-IN AND SWITCH-OFF TIMES. FOR THIS REASON, THE SWITCH WAS REMOVED.

Fig. 15. Averager results as of 7/14/78

A PSEUDORANDOM BINARY NOISE ULTRASONIC SYSTEM

C. M. Elias
SRL, Inc.
Dayton, Ohio 45440

and

T. J. Moran
AFML/LLP
Wright-Patterson AFB, Ohio 45433

ABSTRACT

The random noise ultrasonic system represents the state-of-the-art in terms of sensitivity and resolution for ultrasonic NDE systems. The principle impediment to its use in the field is the lack of real-time inspection capability. If a pair of pseudorandom binary noise sources are substituted for the white noise source in the random noise system, a real-time capability is achieved. An instrument using such sources will be demonstrated and its capabilities will be discussed.

INTRODUCTION

The random signal ultrasonic system (1) represents the state-of-the-art for NDE ultrasonic systems. Correlation techniques are utilized to achieve very large signal to noise ratios and at the same time achieve range resolution limited only by the bandwidth of the ultrasonic transducers. A white noise source is used in either a cw or long burst mode to excite the transducer which insonifies the specimen, allowing high average power and deep penetration into highly attenuating materials to be obtained. Due to the uniqueness of a given noise burst, the reference signal for the correlation must be a suitably delayed version of the signal used to excite the transducer insonifying the specimen. This delayed reference signal is usually obtained by splitting the signal from the noise source into two channels and exciting a second transducer in an acoustic reference delay path. The path length is mechanically varied to obtain the required variable delay. Complete correlation occurs when the reference delay is equal to the signal delay. The entire specimen is scanned by sweeping the reference time delay. It is this mechanical scan which has been the principle impediment to use of this system outside of the laboratory. Data acquisition times are simply too long for field use.

This paper describes one possible method for speeding up data acquisition while retaining most of the signal to noise enhancement of the random signal system. A pseudorandom binary noise (PBN) source (2) is used in place of the white noise source. Since such a source is reproducible, a second identical source is used as the reference and the delay is obtained digitally. Elimination of the second acoustic path increases the effective bandwidth of the system as compared to the random signal system, improving range resolution. Resolution with the PBN system should be comparable to that obtained with the best conventional systems.

An instrument was designed and built incorporating a pair of identical PBN sources consisting of 16 stage shift registers with 4 taps and producing a 65,535 bit maximum length sequence (3). It is the purpose of this paper to present the results of an evaluation of the performance of this first generation instrument. A detailed discussion of the design will be given elsewhere (4).

SUMMARY

Present Instrument Capabilities:

- 65,535 bit pseudorandom maximum sequence.
- 25 MHz maximum master clock rate, 12.5 MHz PBN rate.
- 100 repetitions maximum per point.
- 999 clock period max. burst length.
- 9,999 clock period maximum acoustic cycle period.
- Operates easily with 2V peak to peak transducer drive.

Possible Applications:

- Greater penetration into highly attenuative materials.
- Measure attenuation at high frequencies in thin layers using phase modulated CW carrier.
- Apply quantitative NDE techniques which require good signal to noise for accuracy.

REFERENCES

1. Newhouse, V. L., Furgason, E. S., Bilgutay, N. M. and Cooper, G. R., "Random Signal Flaw Detection," Proc. of 1974 IEEE Ultrasonics Symp., IEEE Cat. No. 74-CHO-896-1-SU, p. 711-715 (1974).
2. Golomb, S. W., Shift Register Sequences, Holden-Day Inc. (1967) Chapter 3.
3. Motorola McMOS Handbook, Motorola Inc. (1974), Chapter 11, Section D.
4. Elias, C. M., "An Ultrasonic Pseudorandom Signal Correlation System." To be published.

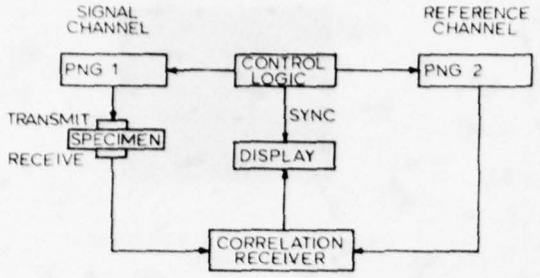

SYSTEM BLOCK DIAGRAM

Fig. 1 Pseudorandum binary noise generators (PNG) 1 and 2 produce identical 65,535 bit sequences. The control logic incorporates a stable oscillator to control both the bit length and the number of clock times PNG 2 is delayed relative to PNG 1.

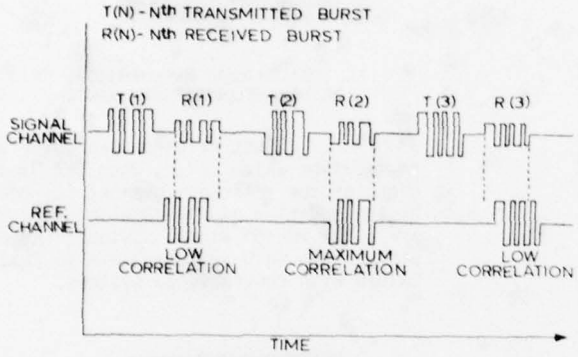

SIMPLIFIED SYSTEM OPERATION

Fig. 2 PNG 1 and PNG 2 are initially set to the same state. The first noise burst from each generator consists of a selected number of bits (P) of the sequence. Each succeeding burst consists of the next P bits of the sequence. The burst from PNG 2 is initially delayed a selected number of clock periods relative to PNG 1. This delay is held fixed for a set number of repetitions before being advanced one clock period to the next point where it is again repeated as before. This process is repeated until the maximum delay is reached, where the system either halts or repeats the scan as desired.

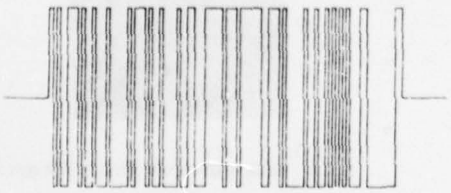

PSEUDORANDOM BINARY M-SEQUENCE: FIRST 100 BITS

Fig. 3

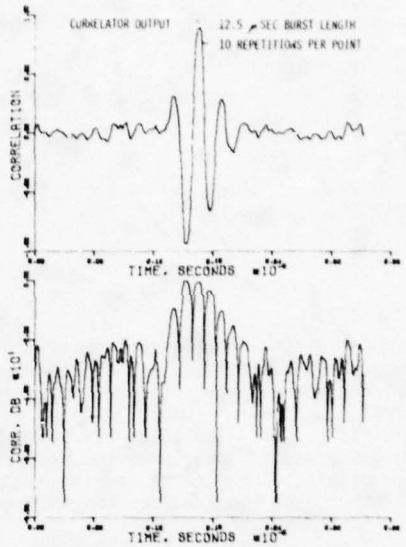

Fig. 4 Linear and log plots of the correlator output using a short drive burst and a small number of repetitions at each reference delay point. 5 MHz transducers and through transmission in water.

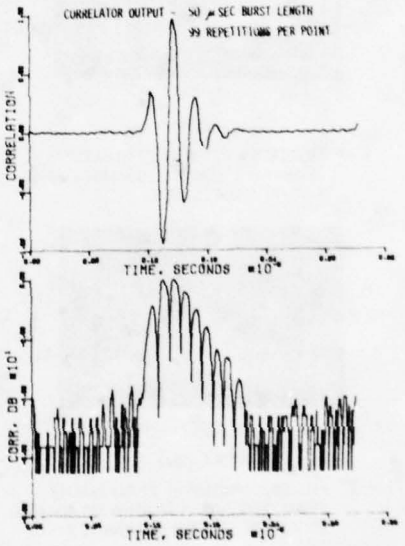

Fig. 5 Linear and log plots of the correlator output using the longest burst and largest number of repetitions the current instrument is capable of producing with a 20 MHz master oscillator. Note the improvement in signal to sidelobe ratio as compared to Figure 4.

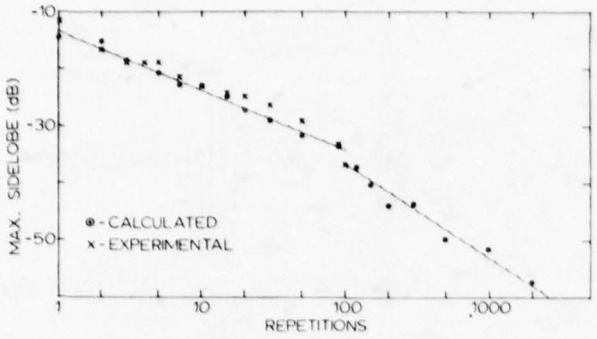

Fig. 6 Graph illustrating the effect of varying the number of repetitions on the sidelobe size. Calculated points were obtained from a computer simulation of the instrument. The solid line is a linear fit to the calculated data. The break in slope was found to occur when the product of the number of bits in the burst and the number of repetitions exceeds the sequence length. A 375 bit burst length was used.

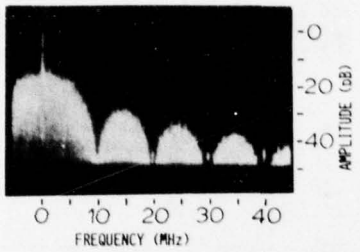

A. FREQUENCY SPECTRUM OF PSEUDORANDOM BINARY NOISE SEQUENCE OPERATING AT A 10 MHz CLOCK FREQUENCY.

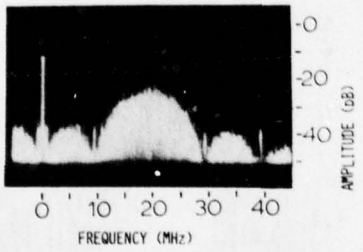

B. FREQUENCY SPECTRUM OF 20 MHz CARRIER SIGNAL PHASE MODULATED USING PBN SEQUENCE HAVING SAME SPECTRUM AS SHOWN IN A.

Fig. 7 Spectra of the PBN sequence used in this instrument and a CW carrier phase modulated by the same sequence. The signal shown in B should be useful for driving high frequency transducers since the center frequency may be matched to that of the transducer.

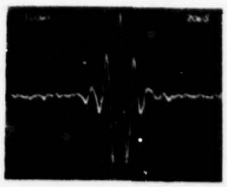

A. CORRELATOR OUTPUT WITH ACOUSTIC DELAY IN REFERENCE CHANNEL

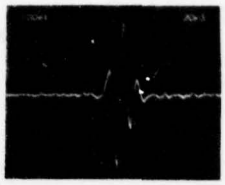

B. CORRELATOR OUTPUT WITH COMPLETELY DIGITALLY DELAYED REFERENCE CHANNEL

Fig. 8 Illustration of the pulse width degradation which occurs when the bandwidth of the reference channel is reduced by the addition of an acoustic delay path as in the random signal system. The pulse width shown in B is comparable to that obtained with conventional systems.

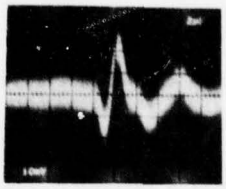

A. CONVENTIONAL PULSER-RECEIVER OUTPUT

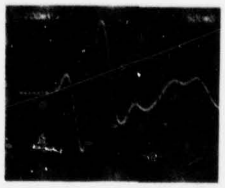

B. PSEUDORANDOM BINARY NOISE SYSTEM OUTPUT

Fig. 9 Illustration of the signal to noise enhancement which may be obtained with the present instrument.

AUTOMATIC DATA RECORDING FOR MANUAL ULTRASONIC EXAMINATIONS

A. R. Whiting
Southwest Research Institute
San Antonio, Texas 78284

ABSTRACT

There exists a need for improving the productivity and reliability of manual ultrasonic examination teams performing PSI or ISI work on nuclear power reactor systems. An analysis of current methods and procedures revealed that the greatest improvement in both areas can be obtained by streamlining data measurement, recording, and reporting. A research and development program for accomplishing this goal is currently near completion. The approach used in this program is to automate the tasks of position measurement and ultrasonic data recording and to use computers for data analysis and reporting.

This presentation discusses the automated Search Unit Tracking and Recording (SUTARS) data acquisition system that is being developed. When using the SUTAR system, the only function that the operator will need to perform during the examination is to guide the search unit so as to obtain complete coverage of the volume of interest. The system will automatically measure search unit position and yaw angle by a noncontacting method that eliminates the encumberances inherent in a mechanical position sensor. To measure the ultrasonic data, a commercial flaw detector was modified so that an auxiliary subsystem automatically digitized video information obtained from the volume of interest. The examination data will be recorded on a digital magnetic tape recorded situated at a convenient location remote from the operator. Also recorded will be ten different items of examination documentation data such as operator identification, refracted beam angle, data sheet number, instrument serial number, etc.

Southwest Research Institute's (SwRI) newly developed Search Unit Tracking and Recording System (SUTARS) represents a major advancement in manual ultrasonic inspection of welds. In conventional manual inspection, a large part of the inspection personnel's work effort is spent measuring position of the search unit and manually recording the data from indications that exceed the recording criteria of the code or standard. If an indication is detected which exceeds the acceptance criteria, additional inspection time is required to record data that is required to perform an evaluation. A need existed to reduce the time and cost associated with manual ultrasonic inspections and to improve the accuracy and credibility of these inspections. SUTARS was designed to accomplish these goals.

SUTARS automates the recording of all data pertaining to the ultrasonic impsection of welds, thereby relieving operating personnel of the time-comsuming task of data recording and allowing evaluation to be performed with the assistance of a computer.

The data acquisition portion of the SUTARS system is schematically shown in Fig. 1 and pictorially in Figs. 2 and 3. As can be seen, this subsystem includes an ultrasonic search unit, a linear array of sensors for detecting airborne acoustic signals, a SUTARS control and display console, and a magnetic tape recorder.

The acoustic sensors are a part of a system used to measure the position and angular orientation (skew angle) of the search unit (see Fig. 4). These sensors detect airborne acoustic pulses emitted by two beacons located at two corners on the search unit. The two beacons are activated alternately, and the locationof each beacon is calculated from the measured time of flight of acoustic signals from the beacons to the closest two sensors. The skew angle is then calculated from the relative position of the two beacons.

The tracking system provides accurate measurements over an area called a sector which is approximately 25 inches long in a direction parallel to the sensor array and approximately 8 inches wide. Areas larger than a sector are examined by repositioning the sensor array as many times as is necessary.

During an examination scan, the operator manually guides the search unit about the workpiece and, simultaneously, monitors the CRT display of a commercial flaw detector which is a part of the display console. It is important to note that, when using SUTARS, an operator uses exactly the same skills and procedures in manipulating the search unit that are used in conventional manual examinations. The location and angular orientation (skew angle) of the search unit are to be carefully adjusted to produce optimum signals for each reflector encountered throughout the examination.

Position data are acquired and recorded at the same time and rate as are ultrasonic data. During data processing, search unit position and skew angle data are used to calculate the true location of flaws relative to the weld. Since the operator is allowed to orient the search unit for optimum signal without introducing errors in calculated flaw location, SUTARS has a greater degree of freedom and repeatability than do most mechanical scanning systems in use today.

The SUTARS control unit, shown in Fig. 3, is the heart of the data acquisition subsystem and contains such features as:

(1) An electronic memory for storing examination parameters such as the gate starting and gate stopping points, operator identification, refracted beam angle used for a particular examinatio, the data sheet identification number pertaining to a particular examination, and so forth. The content of this memory is automatically recorded on the magnetic recorder along with search unit position and ultrasonic data.

(2) A time-corrected gain circuit that offers improved performance over conventional circuits.

(3) Numerical readouts which display search unit position.

(4) Several status indicators to notify the operator of important system conditions.

Of special important is the gate circuit developed for SUTARS. This gate detects and digitizes ultrasonic indications which occur between the gate starting and stopping points defined by the operator. The gate is equipped with a signal amplitude threshold detector that the operator can adjust to any desired level. When an ultrasonic signal large enough to exceed the threshold is detected, the gate is armed and goes into operation. The gate is capable of two different modes of operation, both of which are illustrated in Fig. 5. In mode 1, the gate examines the video signal and detects the peak value of every separate indication within the gated region. The peak values and the time location of the peaks are digitized and transmitted to the magnetic recorder. Since only the signal peaks are recorded, this mode is very economical in terms of magnetic tape consumed.

In mode 2 operation, as soon as any signal exceeds the threshold, the gate proceeds to sample and digitize the complete video trace at very fine intervals. This mode of operation records even the finest detail in the signals and is valuable for performing signal analysis with the highest possible accuracy.

Figs. 6 and 7 show SUTARS at the Edwin I. Hatch Nuclear Power Plant for a preservice examination of certain recirculation piping welds in austenitic material. If the data were being gathered during an inservice rather than preservice examination, data recording could be accomplished at a remote position of up to 200 meters from the point where the examination would be occurring.

After the examination data are recorded, the tape is converted and placed on a nine-track tape record. Thus, the original digital tape may be cycled back into service and be available for further data acquisition on a subsequent examination. Hardware typical of this process is shown in Fig. 8, and a schematic of the data flow through this system is shown in Fig. 9. The nine-track record, which represents the data base, can now be interrogated by utilizing the minicomputer; and many forms of data format and output are available. Currently the most useful forms for nuclear power plant component examination have been in the formats shown in Figs. 10, 11, 12, 13, 14, and 15. These data formats include parameter information as shown in Fig. 10, reflecting information regarding the component that was examined, the person that performed the examination, initial instrument settings for sensitivity, instrument settings reflecting parameters that were controlled and established regarding the gate position, all referenced information concerning procedures, and other required traceable items. Fig. 11 is a coverage plot showing positive confirmation that the examination was performed in the area of interest and that no interruptions occurred during that examination. The crosses indicate the physical location of the search unit in relation to the centerline of the weld and the receiving array units. This plot is extremely useful when meeting quality assurance requirements necessary to indicate that, in fact, the examination was performed in a satisfactory manner. Fig. 12 represents sequential sector locations on a given examination region should there be more than one involved. It allows presentation of the relationship of each sector with the other sectors to be established and recorded. Fig. 13 represents a tabular data sheet very similar in nature to those currently generated by manual ultrasonic examination. Parameter data are located at the top; tabulated below by sector is the identification number of each indication that exceeded the interrogation level (in this case 100 percent DAC). The transducer location on the surface of the component is recorded in both X and Y coordinates, along with the metal path dimension to the target reflector and the peak amplitude. Fig. 14 presents the same data as shown in Fig. 13, but in a different format. The difference is that reflector location is given in terms of the X, Y, and Z dimensions of the component where Z represents the throughwall dimension.

Fig. 15 is a summation of the tabular information just discussed, but presented in the form of a C-scan presentation (shown at the top of the figure and a B-scan presentation (shown at the bottom). The C-scan presentation given the relationship of the various reflectors to each other in the X and Y plane, whereas the B-scan presentation gives the relationship of the reflectors relative to the throughwall dimension.

The SUTARS data analysis method utilized a concept that divides each sector into a fixed number of cells and interrogates the data to determine whether or not reflectors exceeding the recording were received from each cell location. In normal operating modes, cell dimension is one-tenth of an inch. While this is sufficient in most instances, requests have been made for larger and smaller cells. This is easily accomplished by several means and is currently being addressed in modifications to this system.

Fig. 18 shown the correlation between data taken manually and data taken by utilizing SUTARS on a test block approximately 2 inches thick by 25 inches in length and 12 inches in width. The

reflectors, identified as A through H and depicted in the figure by the dashed lines, represent machined notches of varying depths placed in the surface opposite from the transducer. The manual data is plotted as a solid line, and the SUTARS data is plotted as a rectangular box. The dimensions of the box and the relationship of the fit to the actual reflector gives some evidence of the correlation that can be expected by utilizing this system. The dimensions of the SUTARS data box reflect the varying depths of the indicated targets.

One of the most exciting features of SUTARS is the capability of rapidly gathering ultrasonic information that can be converted to hard copy record. This allows data analysis to be done at a later time and at a remote location. In addition, a far more comprehensive amount of data is recorded than is normally taken when manual examination is performed. This is accomplished with fewer personnel in a radiation environment, thus minimizing exposure. These features, coupled with the ability to insure the credibility of the data by providing the sector coverage plot showing the examination as performed in all areas, make this system extremely desirable for a variety of applications. Many modifications are abailable as well as degrees of freedom which can be utilized for applications not yet envisioned.

SwRI feels that this system provides a major breakthrough in the ability to take sufficient ultrasonic information to allow data interpretation to be performed and data to be maintained in a manner long sought by ultrasonic examination personnel. The system also has much potential application as the technology of transducers evolves for it can be combined with any form of ultrasonic search unit that may be desired.

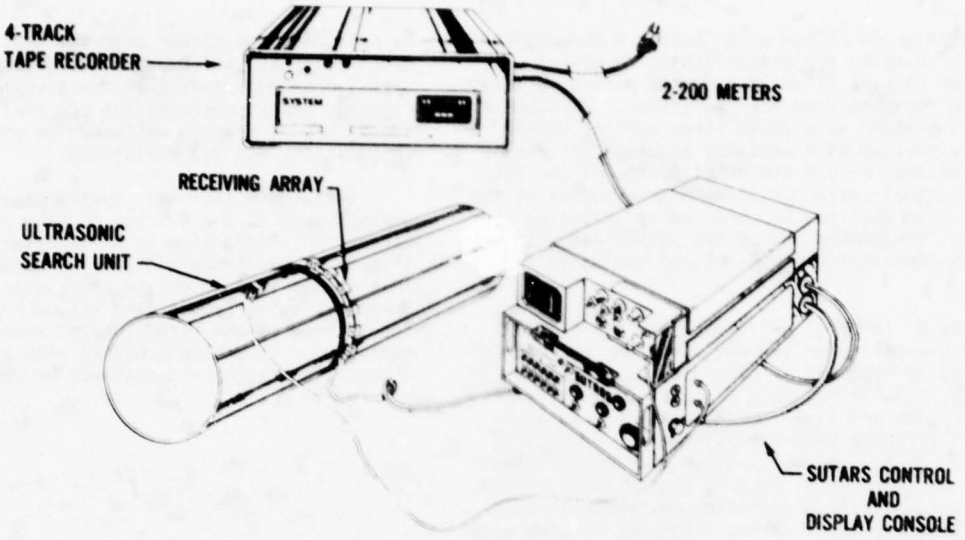

Fig. 1. SUTARS data acquisition subsystem

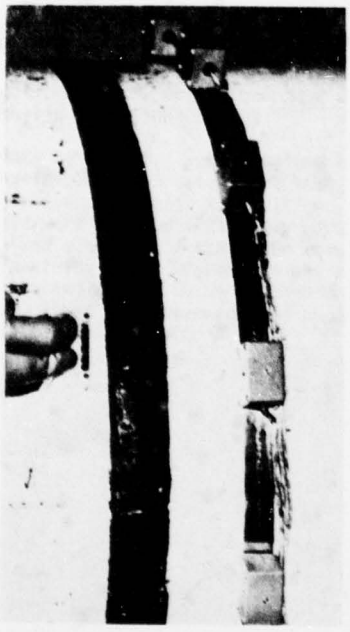

Fig. 2. Receiver array and search unit

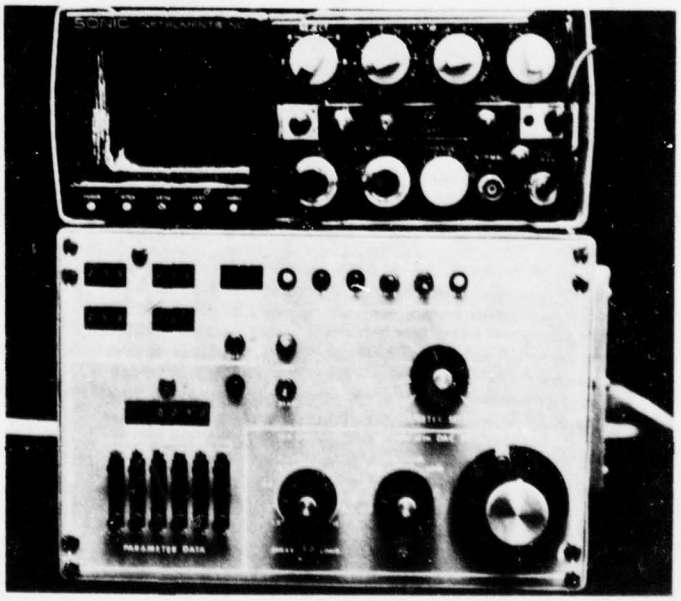

Fig. 3. SUTARS control and display console

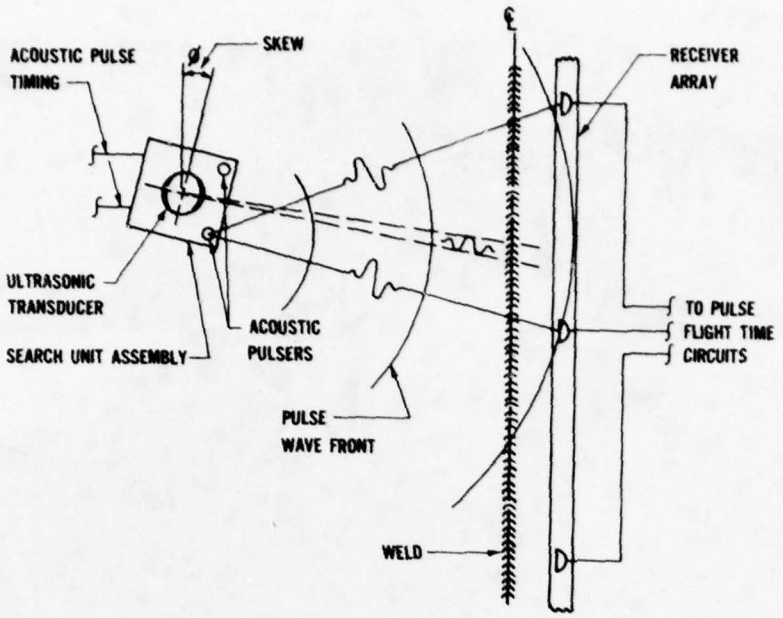

Fig. 4. Search unit tracking system

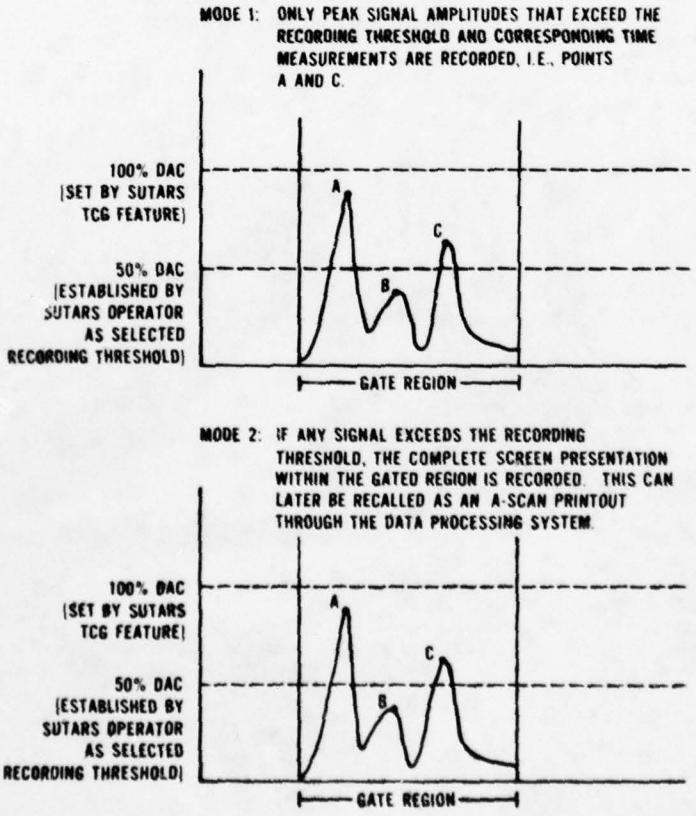

Fig. 5. Operating modes

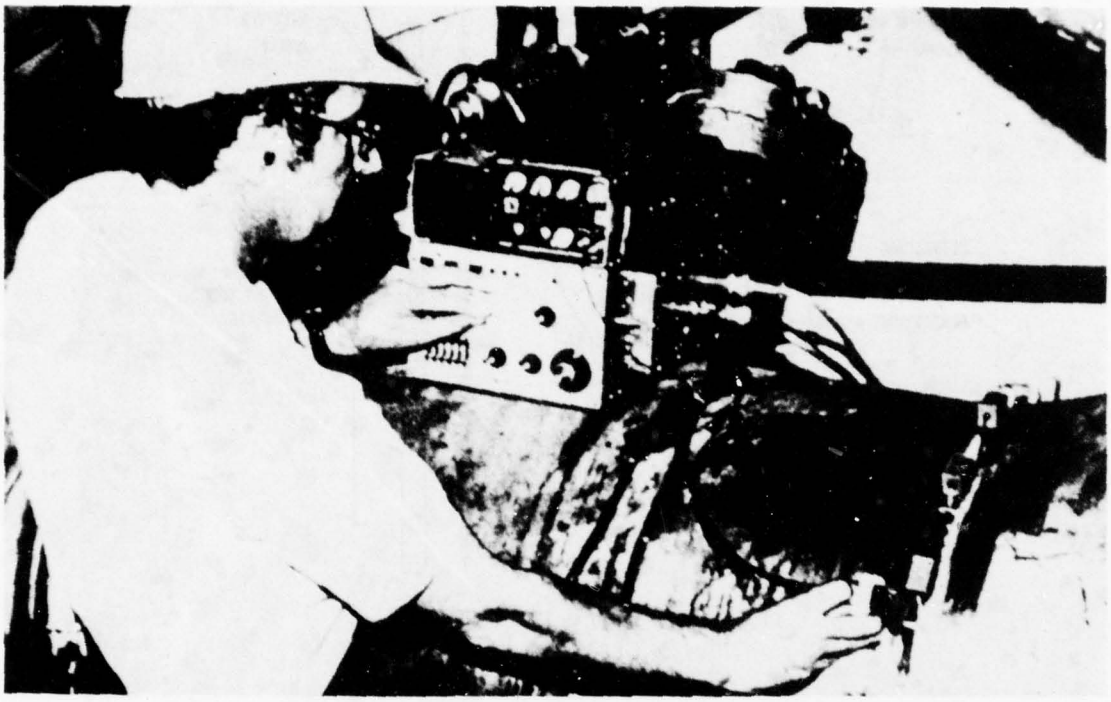

Fig. 6. SUTARS data acquisition at Edwin I. Hatch

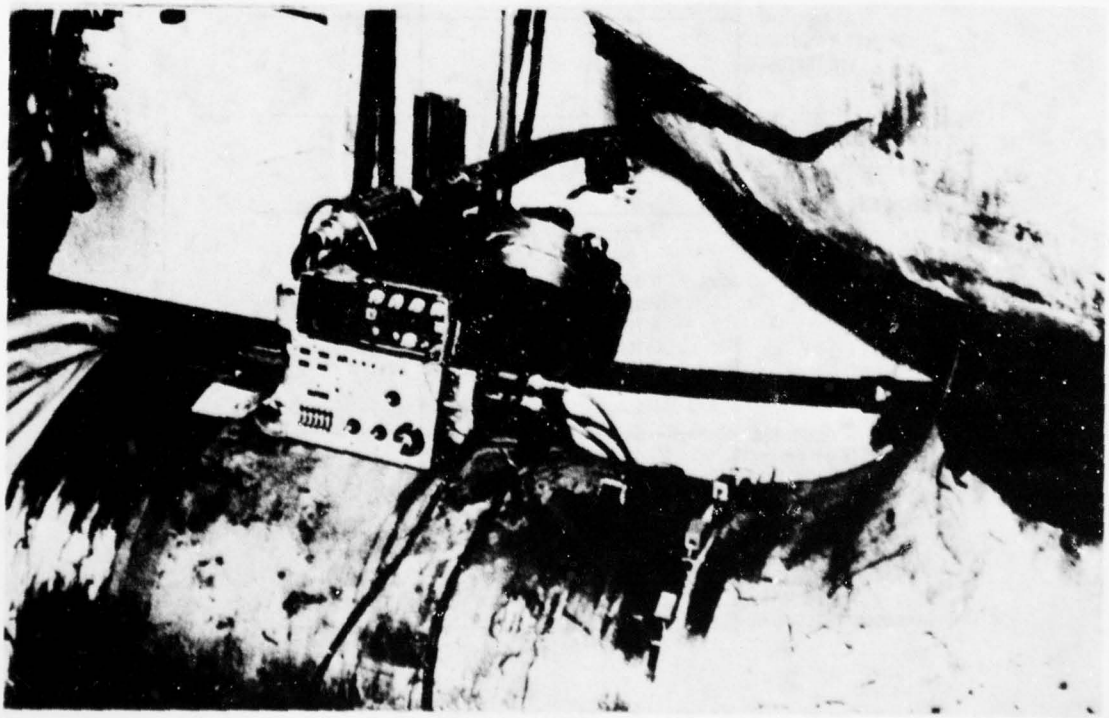

Fig. 7. SUTARS data acquisition at Edwin I. Hatch

Fig. 8. SUTARS data processing

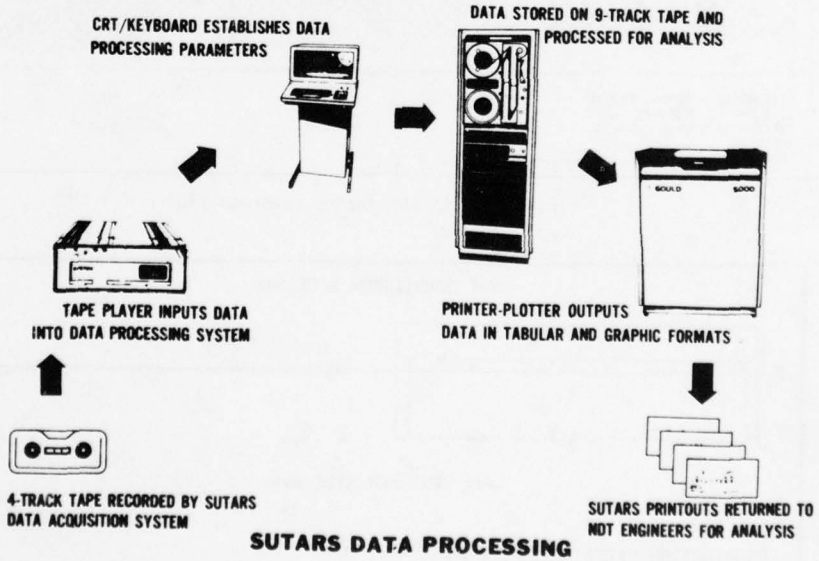

Fig. 9. SUTARS data processing configuration

```
*** SUTARS FIELD VERSION PARAMETER LISTING ***

SITE: FILE #25, TAPE #1: 20 DEC
PLANT: MATCH - SWRI
WELD I.D: S.B.12-H (J.GODWIN)
OPERATOR I.D: 2532
PROCEDURE NO: 800-50/0
CALIBRATION SHEET NO: N/A
DATA SHEET NO: 122001

INSTRUMENT I.D:     1
DELAY(1) =     5
DELAY(2) =    26
DELAY(3) =     8

INSPECTION ANGLE:  47 DEGREES.
THRESHOLD LEVEL: 50.% DAC
TRANSFER PATH THRESHOLD LEVEL:  0.% DAC
AMPLITUDE LEVEL (DAC):   8.00

OBSERVED METAL PATH:  0.50

WELD REF. POINTS:
     POS.      LENGTH(L)      WIDTH(W)
      1          0.00           0.00
      2          5.00           0.00

NO. OF SECTORS ON WELD:  1

SECTOR I.D. NO:  1
SECTOR LENGTH:  6.06 IN.,     WIDTH:  9.55 IN.
WALL THICKNESS:  1.60 IN.
NO. OF SENSORS ON BAND: 6
TOTAL WELD LENGTH:   26.37 IN.
VELOCITY OF SOUND IN AIR: 13646.7 IN/USEC
VELOCITY OF SOUND IN METAL: 62500.0 IN/USEC

COMPONENT GEOMETRY IS FLAT.

DATA CELL SIZE: 0.100 IN.
DISK STORAGE REQUIRED:   724 BLOCKS
PROCESSING MODE: PEAK AMPLITUDE
```

Fig. 10. SUTARS field version parameter listing

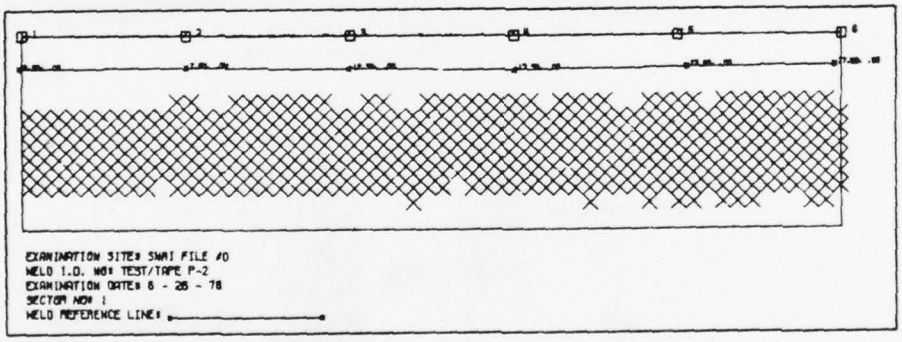

Fig. 11. SUTARS sector coverage plot

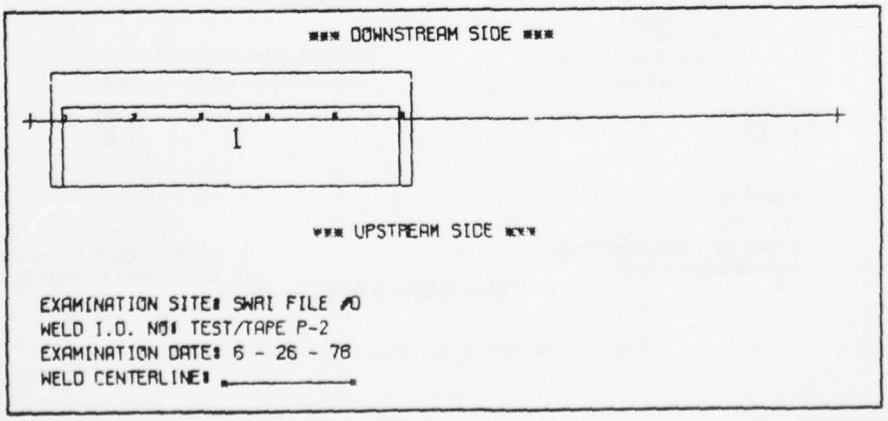

Fig. 12. SUTARS sector organization plot

SITE: SWRI FILE #8 — EXAMINATION DATE: 6-25-78

WELD: TEST/TAPE P-2 — EXAMINER I.D.: 4653

CALIB. SHEET NO: CP-6 — ANGLE: 46

DATA SHEET NO: 062382 — PROCEDURE NO: 800-58

WALL THICKNESS: 2.0000 — AMPLITUDE LEVEL: 100.0% DAC

SECTOR NO	INDIC. NO	XDUCER L1	XDUCER MAX AMP L	XDUCER L2	XDUCER W1	XDUCER MAX AMP W	XDUCER W2	METAL PATH @ W1	METAL PATH @ MAX AMP W.	METAL PATH @ W2	MAX AMP (% DAC)
1	1	1.7	1.7	3.3	1.6	2.4	2.4	2.70	3.30	3.30	144.0
1	2	4.8	4.9	6.6	2.1	2.4	2.9	2.80	3.00	3.30	144.0
1	3	8.1	8.2	9.8	1.6	2.0	2.5	2.80	3.00	3.30	144.3
1	4	11.7	11.7	13.5	2.3	2.3	2.3	3.00	3.00	3.00	144.0
1	5	15.3	15.3	17.0	2.1	2.1	2.1	3.10	3.10	3.10	144.0
1	6	18.6	18.8	20.6	2.5	2.5	2.5	3.10	3.10	3.00	144.0
1	7	22.4	22.9	24.1	1.8	2.2	2.3	2.90	3.10	3.20	144.0
1	8	26.2	27.1	27.3	2.6	2.6	2.6	3.10	3.10	3.10	135.0

Fig. 13. SUTARS data sheet

SITE: SWRI FILE #8 — EXAMINATION DATE: 6-25-78

WELD: TEST/TAPE P-2 — EXAMINER I.D.: 4653

CALIB. SHEET NO: CP-6 — ANGLE: 46

DATA SHEET NO: 062382 — PROCEDURE NO: 800-58

WALL THICKNESS: 2.0000 — AMPLITUDE LEVEL: 100.0% DAC

INDIC. NO	SECTOR NO	PEAK AMPL	PERCENT T.W.	X START	X LENGTH	X MAX	Y START	Y LENGTH	Y MAX	Z START	Z LENGTH	Z MAX
1	1	144.0	25.0	1.57	1.90	1.67	-0.44	0.00	-0.04	1.50	0.50	1.60
2	1	144.0	25.0	4.67	1.90	4.77	0.07	0.70	0.17	1.50	0.50	1.80
3	1	144.0	25.0	7.87	2.00	7.97	-0.42	0.70	-0.22	1.50	0.50	1.80
4	1	144.0	20.0	11.47	2.00	11.47	0.00	0.60	0.19	1.60	0.40	1.90
5	1	144.0	20.0	15.07	1.90	15.17	-0.30	0.50	-0.10	1.60	0.40	1.90
6	1	144.0	25.0	18.57	1.90	18.67	0.20	0.60	0.30	1.50	0.50	1.80
7	1	144.0	20.0	22.27	1.80	22.67	-0.39	0.60	0.01	1.60	0.40	1.70
8	1	135.0	15.0	26.27	1.30	27.26	0.12	0.30	0.33	1.70	0.30	1.80

Fig. 14. Advanced data sheet

AD-A071 047 ROCKWELL INTERNATIONAL THOUSAND OAKS CALIF SCIENCE --ETC F/G 14/2
PROCEEDINGS OF THE ARPA/AFML REVIEW OF PROGRESS IN QUANTITATIVE--ETC(U)
JAN 79 D O THOMPSON F33615-74-C-5180
UNCLASSIFIED SC595.51AR AFML-TR-78-205 NL

2 OF 6
AD A071047

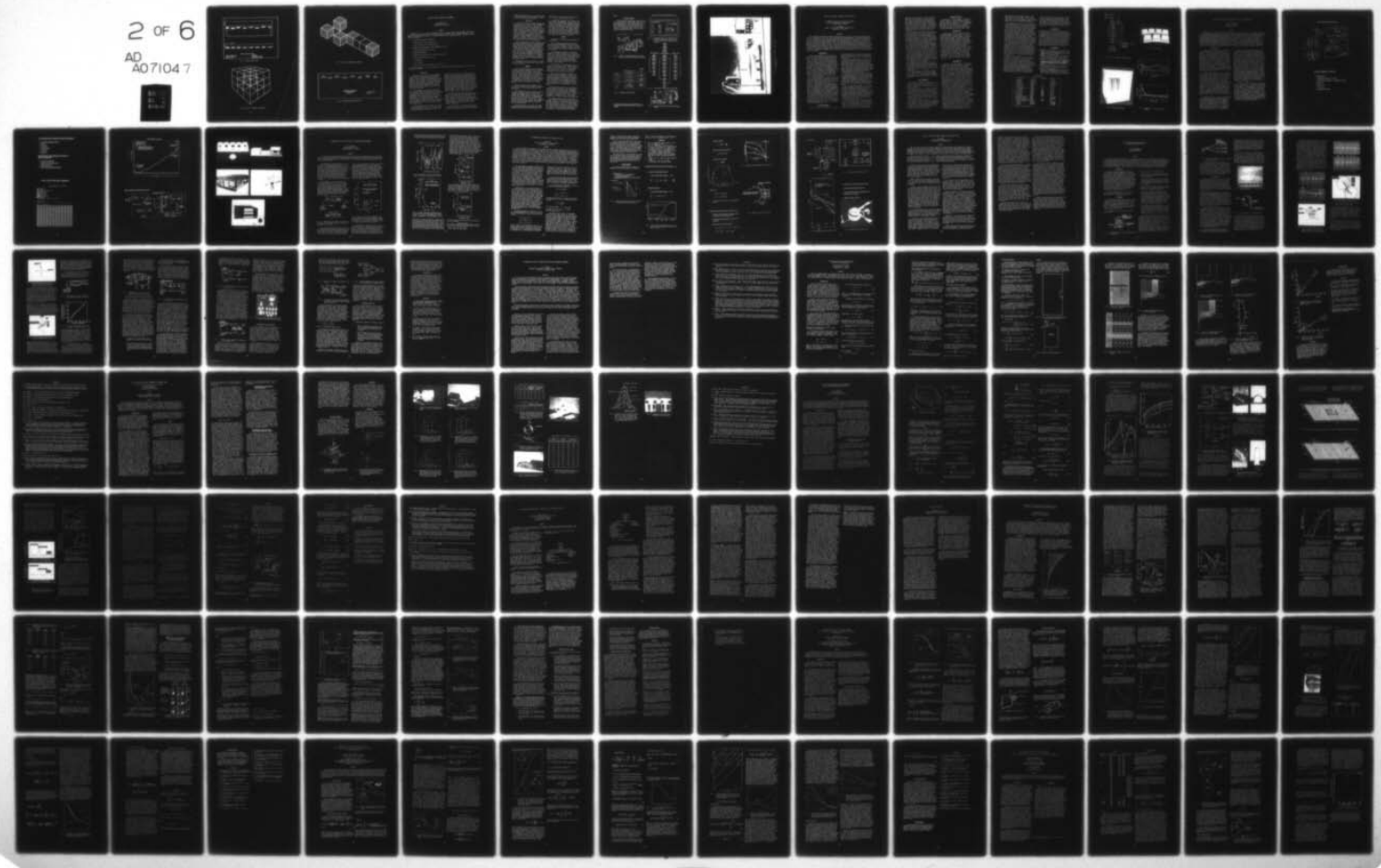

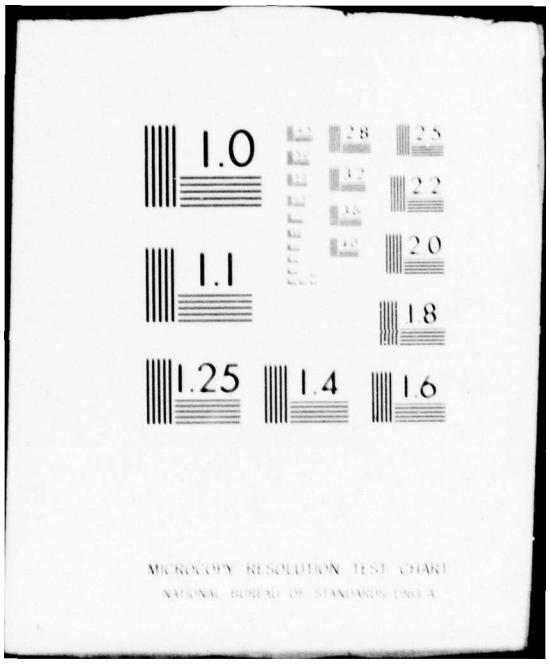
1.0
1.1
1.25
1.4
1.6
2.8
3.2
3.6
2.5
2.2
2.0
1.8
MICROCOPY RESOLUTION TEST CHART
NATIONAL BUREAU OF STANDARDS 1963-A

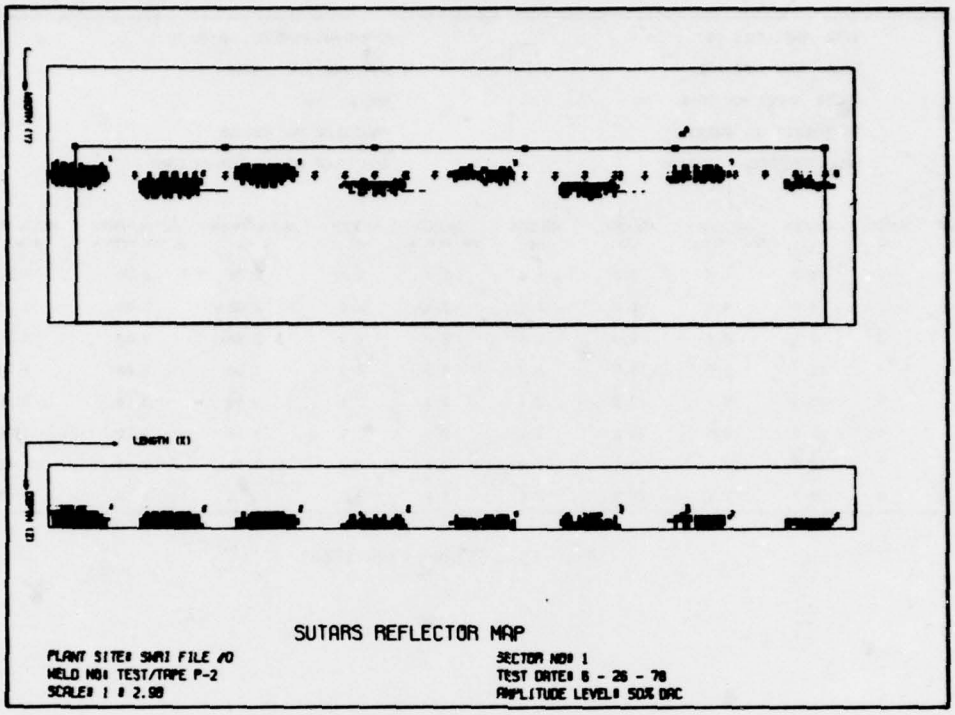

Fig. 15. SUTARS reflector map

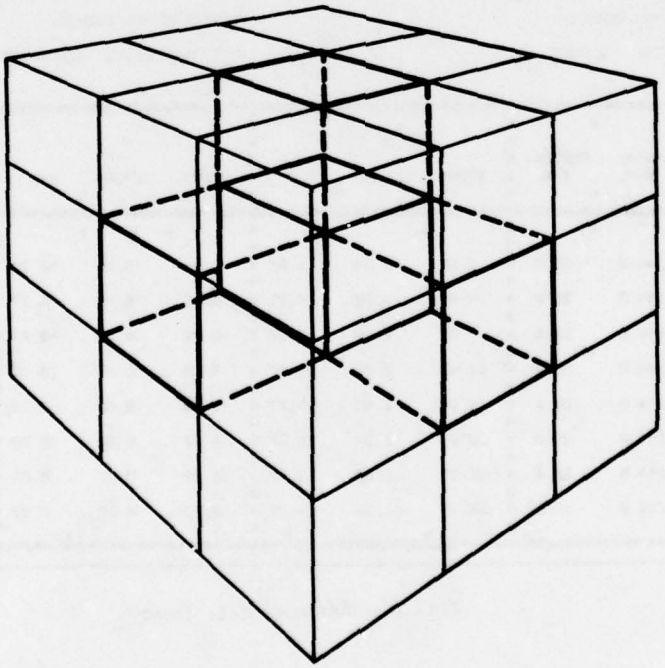

Fig. 16. Data cell adjacency requirements

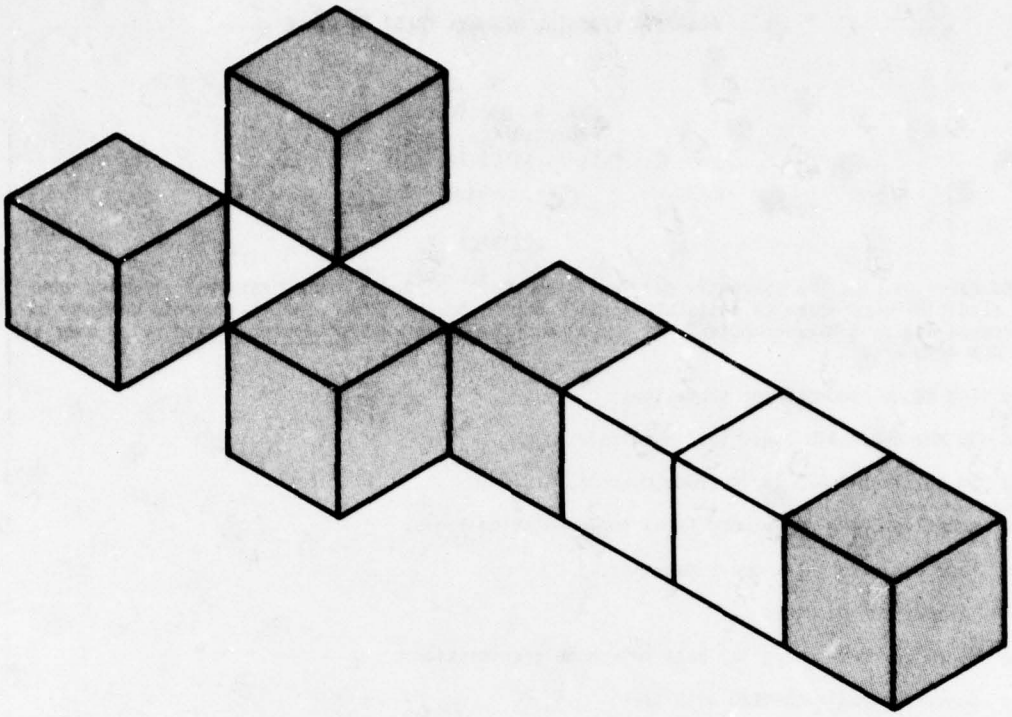

Fig. 17. Data cells grouped as indicated

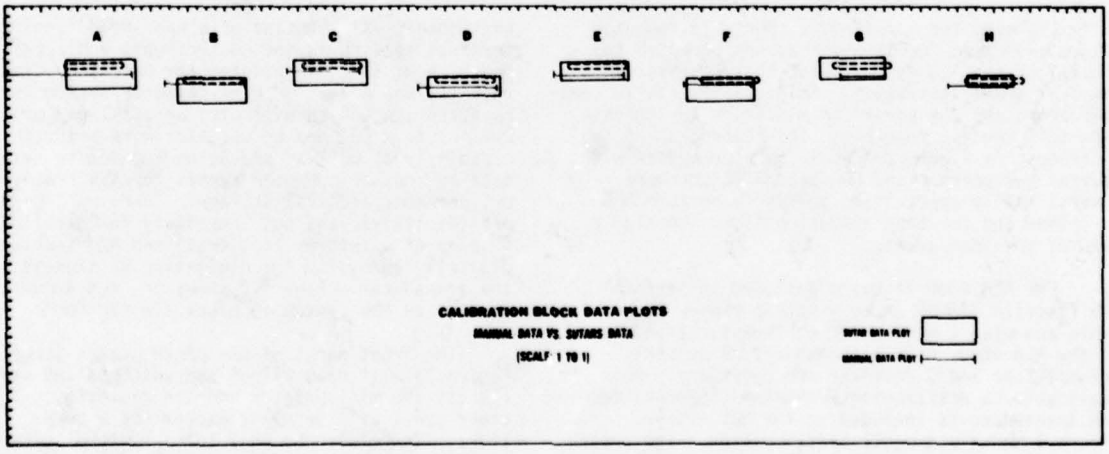

Fig. 18. Calibration block data plots

ADAPTIVE LEARNING NETWORK (ALN) HARDWARE

A. N. Mucciardi
Adaptronics, Inc.
McLean, Virginia 22102

ABSTRACT

Adaptronics, Inc. is currently developing a "smart" UT and EC interpretive instrument under funding by the Electric Power Research Institute (EPRI Contract No. RP1125). The instrument, denoted the "ALN 4000 Process Analysis Microcomputer", is a dual microprocessor microcomputer system. The over all features of the ALN 4000 are:

- o Two Z80 microprocessor subsystems;
- o 30 MHz 8-bit A/D logic (ultrasonics);
- o 50 KHz 12-bit A/D logic (eddy current);
- o Adaptive Learning Network (ALN) implementation logic;
- o Tape cassette bulk memory capacity;
- o Miniprinter display;
- o Modem for remote digital data telephone transmission;
- o Conversational mode I/O with user;
- o Programmable;
- o Fully portable;
- o Operable in hostile environments (dust, heat, etc.).

The ALN 4000 breadboard is currently operational. The first field-portable prototypes will be available in the Fall of 1978.

INTRODUCTION

The need for a real-time, portable computer system dedicated to NDE applications prompted the concept of the ALN 4000 Process Analysis Microcomputer smart instrument. New developments in semiconductors and the advent of miniature peripherals made this concept feasible. The foundation of the instrument is a powerful dual computer system with several peripherals and dedicated NDE software. Several highly specialized boards to perform NDE functions and decrease execution times are also a part of the instrument.

The ALN 4000 is being designed to perform the function of NDE in as simple a manner as possible and with a minimum of equipment. In addition to the ALN 4000, only a transducer, a pulser-preamplifier and a receiver are necessary. When applicable, a positioning mechanism (scanner) for the transducer is included in the NDE system. Figure 1 shows a typical configuration. The instrument will control signal conversion, data acquisition, ALN processing, data storage and the scanner, where appropriate.

The instrument will be packaged in two cases, each approximately 8-3/4" H x 20" D x 17" W with custom-designed front panels. The weight of each case will be held to a maximum of 35 lbs. The peripherals will consist of a hand-held Termiflex terminal serving as the control unit and keyboard, a Digitec miniprinter for hard-copy display results, and a dual 3M mini-cassette system for mass storage. Alternatively, an off-line Computer Devices terminal may be used for more printing capability as well as providing a modem to transfer data to another computer system for ALN training or, perhaps, archival storage. There will be D/A (digital-to-analog) capability for oscilloscope display of waveforms (optional) and A/D (analog-to-digital) capability for digitizing RF signals from the transducer. Figure 2 shows the ALN 4000 as part of an NDE system in block diagram form.

The front panel of one of the cases (see Figure 3) will have all of the switches and status lights, the mini-printer and the cassettes. The other panel will be blank except for a power light. There will be only three switches, POWER, RESET and PAUSE; all other functions are controlled via the terminal. There will be three status lights to indicate the current operation: RUN, STANDBY, DIAGNOSTICS.

The instrument will also contain, where the application requires it, the hardware and software to control the scanning device. This will permit

automatic inspection and will increase the speed of the inspection as well as reduce the number of operations performed by the operator.

OBJECTIVES

Flexibility of both the system hardware and software has been the major design consideration. The design reflects a desire to minimize the effort required to modify the instrument for different applications. The front end (data acquisition system) for ultrasonic applications, for example, can be programmed for different sampling rates (up to 20 MHz). To convert the instrument for use with eddy current applications, an A/D board and associated software will simply be replaced. Software changes are made as easily as changing a cassette. Data for specific applications can be entered via the keyboard, or prepared at an earlier date and stored on cassette.

Real-time operation is another important hardware and software design goal. The two hardware and software design efforts have proceeded simultaneously to achieve the maximum computational speeds. Multiplication, very slow in software, is performed much faster in hardware by means of a multiplier board using a high-speed multiplier chip. Similarly, an arithmetic processing unit (APU) chip has been interfaced to the ALN 4000 to provide a hardware implementation of functions such as the sin, cos, log, exp. etc. Assembly language is being used in the software to produce efficient programs, both in execution speeds and memory utilization.

Another objective is to provide an instrument that is reliable, requires minimum training, and is easy to operate.

HARDWARE

The instrument design uses two microcomputer systems, each one to perform a separate function, but in parallel with each other. One system, called the controller, performs the supervisory functions, and the other system, called the signal processor, acquires waveforms and performs all analyses. Both systems use the Zilog Z80 microprocessor with a clock speed of 4 MHz. Communication between the two systems is achieved by means of a DMA (direct memory access) in conjunction with each computer, to provide direct memory access.

The various boards in each computer system are linked by means of a bus system. An industrial-quality bus, the Intel (Multibus) SBC bus, has been chosen.

Each computing system will contain a total of 64K bytes of memory consisting of 48K of RAM (random access memory) capable of reading and writing and 16K of EPROM (read only memory) with non-volatile read-only capability. The EPROM memory will be used to store the software that is pertinent to all applications. The controller computing system will have the input-output (I/O) capability and the signal processing system will have the data acquisition module.

Two special boards will provide the software support mentioned earlier, namely the high-speed multiplier board and the APU function which is provided once in the controller system and four times in the signal processing system.

To summarize, there will be a total of thirteen boards in the ALN 4000. The controller will contain a CPU and DMA board, two memory boards of 32K each, one with a mix of 16K RAM and 16K EPROM, a board with one APU function and the D/A conversion logic, a multiplier board and an I/O board, for a total of six boards. The signal processor will contain an identical set of boards except that there will be four APU functions on a board and no D/A, there will be no I/O board, and will include two front-end boards for the data acquisition system for a total of seven boards.

SOFTWARE

Three modes of operation are anticipated for the ALN 4000.

One is a data collection and digitization mode to store sufficient data to provide a data base necessary for ALN network training, for example. If a scanner is present, it may be controlled by the ALN 4000 in this mode to automate the collection procedure.

A second mode of operation is the off-line analysis to provide an inspector with the capability of selecting waveforms from the mass storage device and to perform signal processing operations as desired. The use of the off-line terminal in this mode will provide printing capability. A modem will permit data transferral to another computer. Use of an oscilloscope will provide a display of the waveforms.

The third mode is on-line analysis to be performed at the inspection site. This includes control of the scanning device, signal conversion and ALN processing to provide crack detection and sizing on-line. Figure 4 is a flow chart demonstrating the three modes of operation.

There will be no operating system of the type found in general computers. Instead, there will be an interactive program that queries the operator regarding desired actions and prompts with possible replies. The operator usually will have to respond only with a numberical value or with a single key stroke representing "yes" or "no" and "continue". The philosophy is to minimize operator errors and references to a User's Guide.

Self-diagnostic routines will be provided to increase system reliability. Each component of the instrument will be informed of any problems that may exist and, where possible, suggestions will be made to solve the problem; i.e., "place cassette in a specified drive", "check to see if a component is plugged in", etc. User system diagnostics will also be provided when appropriate.

The software modules that are applicable in any NDE system will be permanently resident in the ALN 4000. These will include supervisory programs, self-test diagnostics, I/O drivers, DMA routines and signal processing routines. Those routines and data that are application-specific will be stored on cassettes and will include the transducer scanning protocols, ALN structure and coefficients, and routines to drive and control the scanning

device.

NDE APPLICATIONS

The ALN 4000 will be employed initially in UT and EC applications. The UT target areas are pipe crack detection and sizing, both in welds and heat-affected zones. The EC applications are currently detection and sizing of both hole cracks in the TF-33 engine disk (Figs. 5 and 6)[1], and detection, classification and sizing of defects in nuclear steam generator tubing.

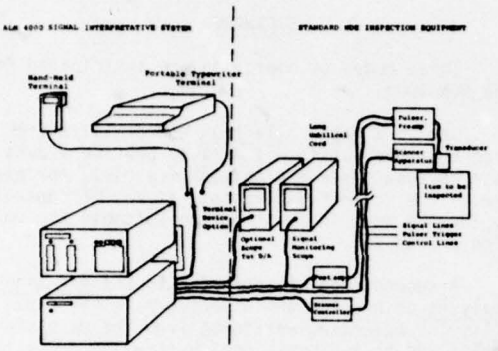

Fig. 1. Schematic of ALN 4000 NDE system interfaced to standard NDE inspection equipment

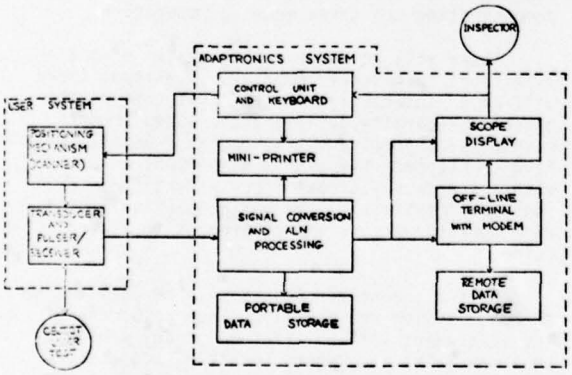

Fig. 2. Quantitative NDE system

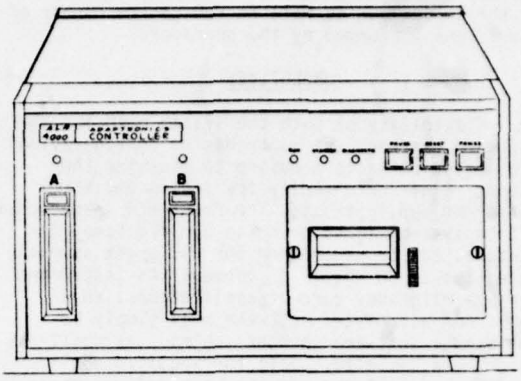

Fig. 3. Front panel layout of control unit of ALN 4000 showing tape cassettes, miniprinter, status lights and push button switches

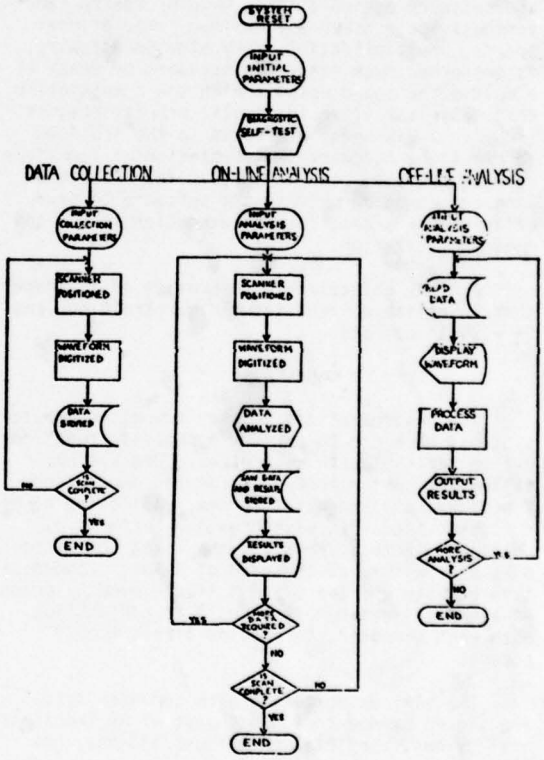

Fig. 4. Three modes of operation for ALN 4000

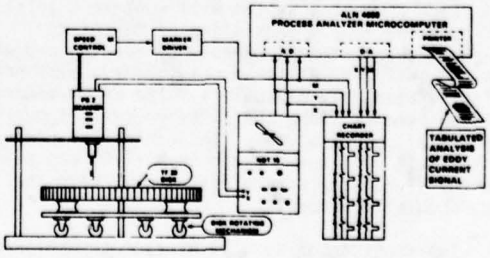

Fig. 5. Eddy current data collection and analysis system

[1] The engine disk eddy current application is sponsored by AFML under Contract No. F33615-77-C-5218.

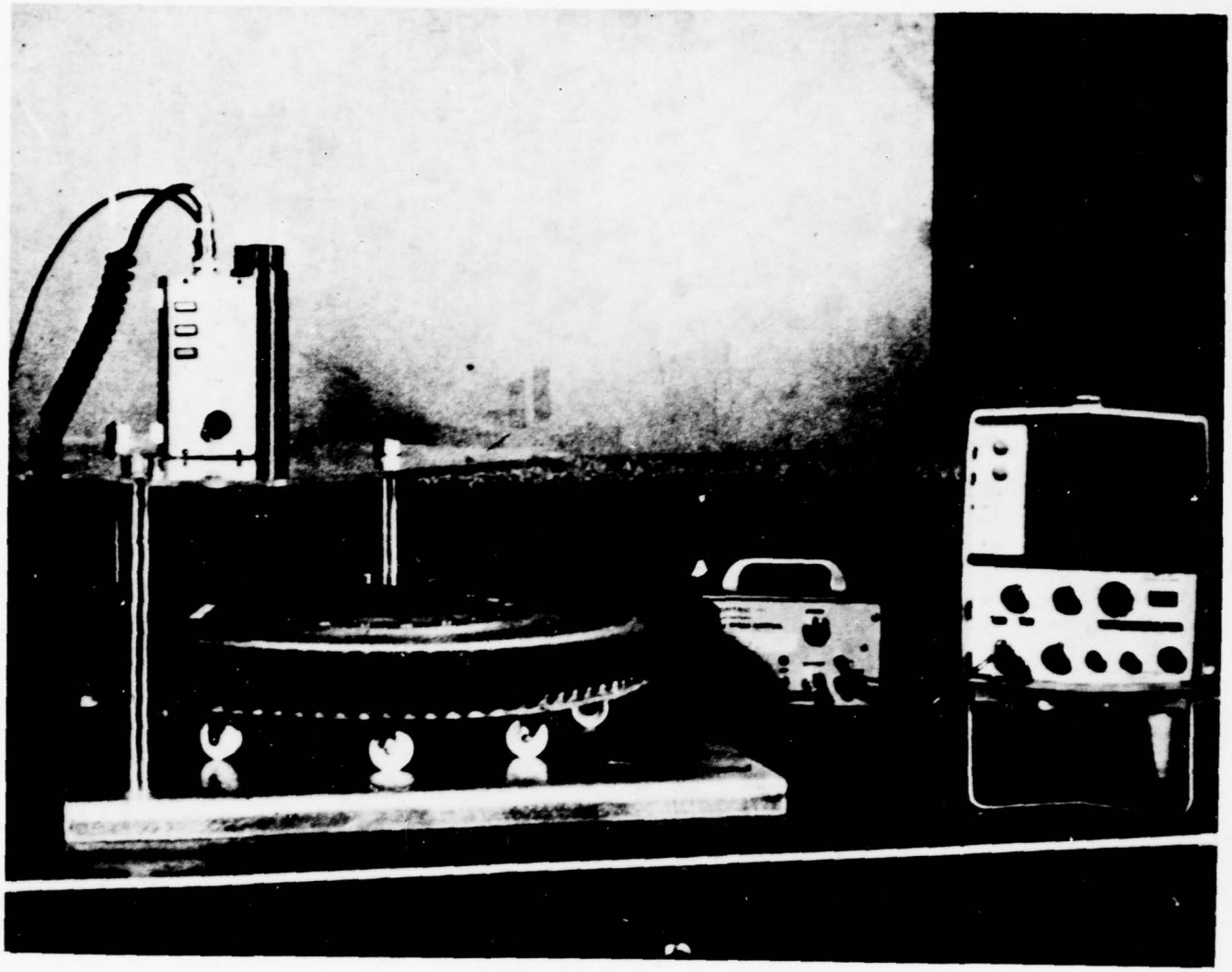

Fig. 6. TF-33 engine disk with eddy current scanner and eddy scope

ACOUSTIC EMISSION MULTI-PARAMETER ANALYZER--AEMPA

L.J. Graham, R. Govan, R.K. Elsley, G. Lindberg
Rockwell International Science Center
Thousand Oaks, CA 91360

R.L. Randall
Atomics International, Rockwell International
Canoga Park, CA 91304

ABSTRACT

A multi-parameter measurement system was designed and built to process signals from acoustic emission (AE) transducers in real time. The system makes selected measurements of each detected AE event as it occurs and stores 23 measured parameters which describe that event in digital form on a standard diskette with IBM format. Measurements recorded on the diskette include information on the shape, magnitude, and frequency content of each AE burst, its timing with respect to location on the specimen under test and its timing with respect to load conditions, pressure, test time, and event count. Over 8000 AE events can be stored on a single diskette at a maximum instantaneous rate of 6000 events/sec and a maximum average rate of 1000 events/sec. Two floppy disk units are included in the system so one can be operational while the diskette is being changed in the other. After a specimen test, the data are transmitted to a remote minicomputer with a standard RS232 interface. Rapid analysis and display of the data by the computer has been demonstrated using up to 8 of the AE parameters at one time in a pattern recognition routine.

INTRODUCTION

Techniques for detecting acoustic emission events vary from one application to another, but they all use some form of transducer to convert one or more modes of surface displacement to an electrical signal. These electrical signals may or may not be accurate analog representations of the surface displacement of the item under test. This depends on the coupling for the various modes and the sensitivity to surface movements versus frequency for the particular transducer system. Whatever the limitations of the transducer system, if it is sensitive enough to reliably detect acoustic emission events from the item under test, the variations of the electrical signals from event to event may contain useful information about the nature, status, and location of the flaws in the test specimen.

It has been shown that several features of the acoustic emission signal can be used, on occasion, to separate events from different causes such as flaws of different types, sizes, and orientations, electrical disturbances and mechanical noise.[1-4] These distinctive features may depend upon the material being tested and the test conditions, and usually a considerable amount of laborious detective work is required to identify them. An event-by-event analysis of several features of the emission signal simultaneously, if it could be accomplished, would be useful. It would greatly reduce the amount of specimen testing and data analysis required to identify the characteristic features of the various sources of emission, if they exist, for a particular material. It could also allow a similar characterization of the emission sources during a structural test, where repetitive testing is impossible. Instrumentation which was developed to achieve this is described in the following sections.

BASIC MEASUREMENTS

We start here with the premise that the electrical waveform from an AE event contains information about the source of the event that may be useful in evaluating the status of the material under test.

The most basic parameter we consider is the frequency content of the electrical signal from the transducer system. This may be strongly influenced by transducer related resonances and electrical filters in the signal amplifying and/or recording portions of the transducer system. However, if the transducer system is linear (no clipping of the signal waveform), variations of signal content from event to event may be measured. The range selected for the Rockwell AE characterization system was 20 kHz to 2 MHz.

Having established the frequency range, the next step was to select the various forms of amplitude measurements to be used. Digital means for recording many thousands of waveforms with 2 MHz bandwidth, 100 dB amplitude range, and event durations from microseconds to hundreds of milliseconds were apparently not economically feasible at this time. Therefore, analog techniques were selected for some basic amplitude measurements.

The first amplitude parameter to be selected was "peak value during event" on a log scale, in dB, from 0 to 100 dB, with 0 dB referring to a 1 microvolt signal level at the transducer.

Next, some form of envelope measurement was desired. The decision was made to utilize voltage to frequency converters and digital counters to measure the area under the envelope of each AE waveform. Sensitivity was set at 200 microvolt-microseconds per count with a capacity of 1,999,999 counts per event.

By this time we were getting down to the details of defining an "event." The decision was made to use a manually controlled discriminator with 79 discrete dB steps from 1.1 microvolt to 10 millivolts. A digital timer, monitoring the output of the discriminator, was specified to detect preset delays of 0.1 to 9.9 milliseconds

between threshold crossings. First the operator determined a discriminator threshold based on noise levels at the transducer. Next, the operator selected "rate delay," the minimum preset delay between threshold crossings in the same AE burst event. The start of an event is defined as the first threshold crossing after a quiet period exceeding the preset "rate delay." The end of an event is defined as the last threshold crossing preceeding a quiet period exceeding the preset "rate delay."

Next, digital circuits were specified to measure on a logarithmic scale: the total number of threshold crossings (ring down counts) per event; the duration of the event; and the rise time of the event. Rise time is defined as the period from the start of an event to the time when the "peak" is detected. The scale selected for these measurements was 0 to 118 dB with 0 dB equal to 1 count or 1 microsecond, respectively.

A bank of 8-quarter decade filters was specified to separate the various frequency components in each event. Each filter output is monitored with a peak detector with 80 dB range. A filter bank amplifier preset by the operator, expands the full scale sensitivity of the peak detectors from 100 millivolts to 11 microvolts in 79 dB steps.

Additional digital circuits were specified to record: the event number, the time of the event to the nearest millisecond; the load value (or any other dc voltage parameter) at the time of the event; the time delay in microseconds from a second transducer channel (if used); the time delay from a reference "start of load" pulse (if used); and a manually preset "run" number.

Circuits were also specified to discard events; when time delays between two transducers (if used) exceed a preset value (2nd Channel Time Out); or when events occur before a preset "load start delay" and when events occur after a preset "load delay limit" (if load gating is used as in a fatigue test).

The block diagram of the system is shown in Fig. 1. Photographs of the system are shown in Figs. 2 and 3. A list of recorded measurements for each event is presented in Table I, along with four parameters which are constant during a given "run".

DATA RECORDING

The specified measurements total up to 32 bytes of data per event. The problem is to store these at instantaneous rates up to 150 microseconds per event and at average rates up to 1000 events per second.

The solution was to use standard floppy discs with a hardware controller that loads an entire track or 3328 bytes with each revolution of the diskette. The system writes or reads an entire 77 track diskette in as little as 14 to 15 seconds.

An internal buffer stores up to 128 events at rates up to 150 microseconds per event, while reading from or writing to the diskette at about 1 millisecond per event.

The floppy disc units can be used to format new diskettes, record test data or play back test data. Diskette capacity with standard IBM format is 8008 events. Two disc drives are included in the system so one can be operational while the diskette is being changed in the other. This minimizes lost data during operation.

COMPUTER INTERFACE

Connection to a remote computer is made using a serial interface. This RS232C type interface transmits data to a computer in 10 bit segments (8 data bits plus start and stop). At a rate of 9600 BAUD, 960 eight-bits data bytes are transmitted per second. At this rate it takes about 4½ minutes to transmit one diskette. The interface has selectable BAUD rates from 19,200 to 1,200.

DATA DISPLAY

Outputs are provided for transmission of selected measurements to the display unit during either the record or playback modes. The display system (not operational at the time this paper is being written) includes a "KIM" microprocessor unit, with extra memory, digital to analog converters and an analog CRT display. The display unit will be used to provide real time CRT display of up to four selected parameter distribution functions as data accumulates during a test or during off-line playback of the diskettes.

A front panel LED display is also provided to display, during record or playback, any one of the 16, 16-bit words recorded for each event. This display is useful for monitoring selected test variables during an experiment such as event count, test time, load voltage, or particular measurements such as rise time, peak, ring down counts, etc. The LED display also has a manual override to show disc controller status at any time.

DATA ANALYSIS

Analysis of the data proceeds in two steps. During a test, the monitor (when it is made operational) will display the differential distributions of one, two or four of the acoustic emission signal parameters as they build up during a test. Provision will also be made for plotting these curves on an x-y recorder at selected times to record the trends in the distributions with time. These parameters may be any of the measured features of the emission signals such as amplitude, energy, time of occurrence within a fatigue load cycle, etc., or they may be ratios of the primary parameters such as pulse shape (pulse duration/peak amplitude) or frequency spectral type (peak amplitude at frequency 1 peak amplitude at frequency 2). Real time observation of trends in these distribution functions are expected to provide valuable guidance in the more extensive post-test analysis using the minicomputer.

The types of data processing that can be done on the minicomputer are essentially only limited by the imagination of the experimenter. At present, software has been developed to perform all of the conventional acoustic emission data analyses such as plotting one emission parameter against another or against time or load level, and forming distribution functions from the experimental data (e.g., amplitude distributions). These plots may also be obtained for a sub-set of the total number of AE events based on a selected range of one or more parameters such as amplitude, frequency spectral type, risetime or location of the source of the AE. In addition, a multi-parameter pattern recognition routine has been developed which analyzes the data in an n-dimensional vector space and looks for regions of

high event density. Clusters of events in the vector space indicate a common "type" of event which may be associated with a specific source by other means (from prior knowledge, comparison with loading history, metallography, fractography, etc.).

An example of the usefulness of the pattern recognition capability is in identifying different frequency spectral types.[5] Acoustic emissions from a graphite-epoxy bend specimen were analyzed in terms of an 8-dimensional vector space where spectral amplitude in each of seven frequency ranges and the time of occurrence of each event were the eight parameters used. During the early part of the test, most of the emission events had the frequency spectral type shown in Fig. 4a. As the specimen was loaded to near its ultimate strength level and about 90 seconds before a major load drop occurred, emissions having the spectral types shown in Fig. 4b first appeared. This type of emission then occurred throughout the remainder of the test and showed up as a separate cluster of points extending along the time axis in the 8-dimensional vector space. The cause of the load drop was a lengthwise delamination between the specimen plies. If it can be established that the mechanism which causes the low frequency type of acoustic emission is uniquely associated with the delamination process, as is suggested by these initial results, this would be a tremendous aid in interpreting results of proof tests of composite structures.

Another comparison made in Fig. 4 is in the appearance of the frequency spectral data when obtained by two methods. The acoustic emission signals from a graphite-epoxy specimen were recorded on a modified videotape recorder[3] and then, during post-test analysis, the two emission signals were analyzed by playing them back through a standard swept frequency spectrum analyzer (Hewlett Packard Model 141S/8553B/8552A) and an x-y recording of the spectrum obtained, and through the present AEMPA system. The same was done for a region of electronic background noise immediately preceding each of the two emission bursts in order to establish the relative amplitude levels obtained by the two methods. Comparison of the discrete and continuous spectral data shows that the two spectral types are easily recognizable by either method, and in fact a two-point spectral analysis would have been sufficient to separate the two types of emissions in this case.

CONCLUSIONS

An Acoustic Emission Multi-Parameter Analyzer System which includes the very important parameter of frequency spectral content has been constructed and demonstrated. With this system, previously observed correlations between the characteristics of emission signals and specific emission sources can be more rapidly and quantitatively explored, and it is expected that previously unobserved correlations will be discovered. The practical result of these studies will be guidance in the design of structural test equipment and a better understanding of the results of such tests.

REFERENCES

(1) Graham, L.J. and Alers, G.A., 1972, "Acoustic Emission from Polycrystalline Ceramics," Final Report, Naval Air Systems Command Contract No. N00019-72-C-0382, AD 754839.

(2) Graham, L.J. and Alers, G.A., 1974, "Spectrum Analysis of Acoustic Emission in A533-B Steel," Materials Evaluation, 32, (2) 31-37.

(3) Graham, L.J. and Alers, G.A., 1975, "Acoustic Emission in the Frequency Domain," Monitoring Structural Integrity by Acoustic Emission, ASTM STP 571, American Society for Testing and Materials, pp. 11-39.

(4) Woodward, B., 1977, "The Use of Signal Analysis to Identify Sources of Acoustic Emission," Acustica, 37, 190-197.

(5) Elsley, R.K. and Graham, L.J., 1976, "Pattern Recognition Techniques Applied to Sorting Acoustic Emission Signals," Proc. IEEE Ultrasonics Symposium, 1976, Annapolis, p.147-150.

TABLE I
DATA RECORD SUMMARY

Measurement	Scale	ODB REF	Range
1. Run Number	Hexadecimal		0 to 15
2. Event Number	BCD Counts		0 to 8007
3. Event Time	BCD Seconds		0 to 9999.999
4. Analog Volts	BCD Volts		0 to 19.99
5. Peak Amplitude	BCD DB	1 μV	0 to 99
6. Energy Counts	BCD 200μV-μs/count		0 to 1,999,999
7. Ring Down Count	BCD DB	1 count	0 to 118
8. Event Duration	BCD DB	1 μs	0 to 118
9. Event Rise Time	BCD DB	1 μs	0 to 118
10. Filter Amplifier Overflow	1 bit Flag		0 or 1
11. 31.6 kHz Peak	BCD DB	10μV*	0 to 79
12. 56.2 kHz Peak	BCD DB	10μV*	0 to 79
13. 100 kHz Peak	BCD DB	10μV*	0 to 79
14. 177.8 kHz Peak	BCD DB	10μV*	0 to 79
15. 316 kHz Peak	BCD DB	10μV*	0 to 79
16. 562 kHz Peak	BCD DB	10μV*	0 to 79
17. 1 MHz Peak	BCD DB	10μV*	0 to 79
18. 1.778 MHz Peak	BCD DB	10μV*	0 to 79
19. Triangulation Delay Time	BCD μs		0 to +99,999
20. Load Gate Delay Time	BCD ms		0 to 99,999
21. Filter Amplifier Gain	BCD DB	Unity	0 to 79
22. Channel 1 Discriminator Gain	BCD DB	10 mV	0 to 79
23. Channel 2 Discriminator Gain	BCD DB	10 mV	0 to 79
2nd Channel Time Out	Decimal μs		10 to 99,990
Load Start	Decimal ms		0 to 99,900
Load Limit	Decimal ms		0 to 99,900
Rate Delay	Decimal ms		0.1 to 9.9

*Varies with filter amplifier gain.

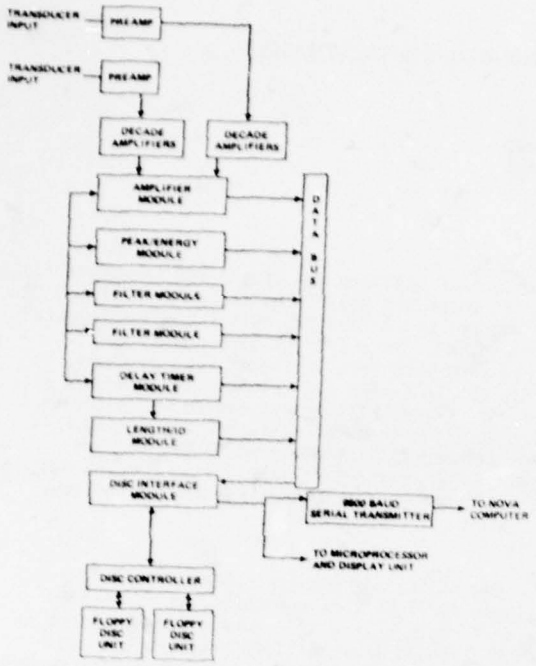

Fig. 1 Block diagram of AEMPA system.

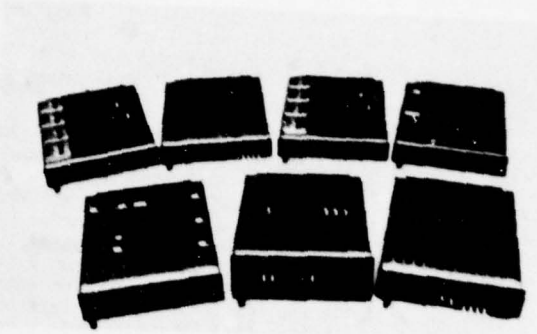

Fig. 3 Plug-in modules.

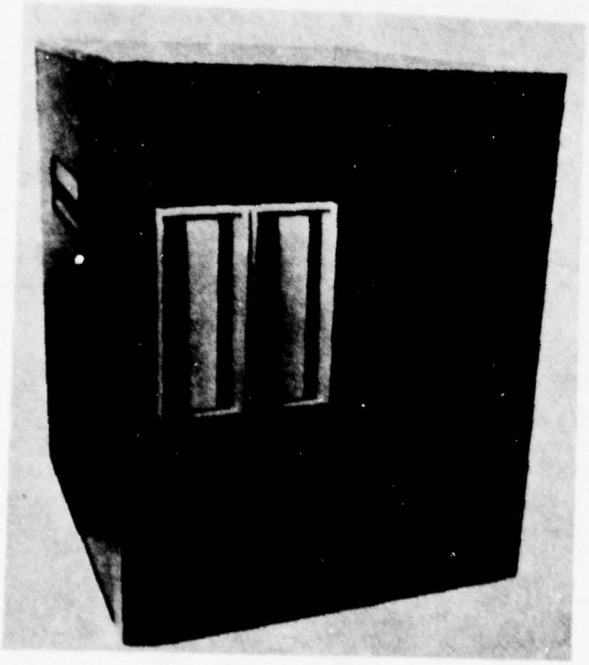

Fig. 2 Front panel layout.

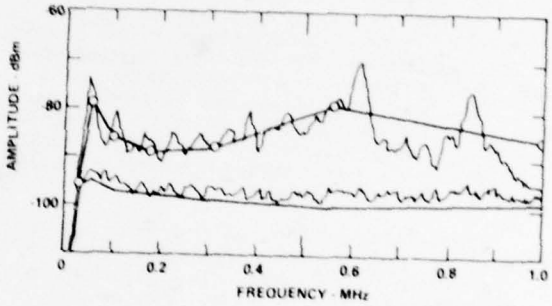

a

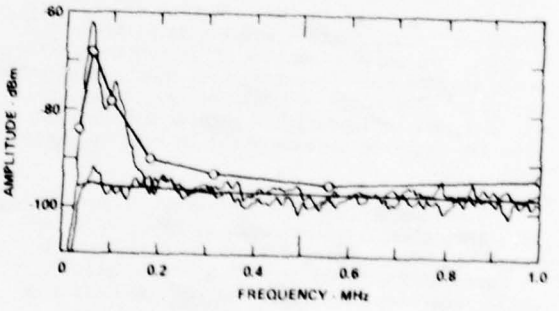

b

Fig. 4 Comparison of spectral analysis results.

ACOUSTIC EMISSION RECORDING USING NONVOLATILE DIGITAL MEMORIES

James R. Skorpik
Battelle-Northwest
Richland, WA 99352

ABSTRACT

The general trend in acoustic emission (AE) monitoring systems has been one of increasing complexity. This is particularly true in systems for continuous monitoring which are usually multichannel (perhaps 20 to 40) and incorporate a dedicated minicomputer. A unique concept which reverses this trend for selected applications has been developed at Battelle-Northwest, Richland, WA. This concept uses nonvolatile, postage stamp sized solid state digital memories to store acquired data in a permanent form which is easily retrieved. After data has been extracted the memories can be erased and reused. It also uses a fundamental method to accept AE data only from a selected area. The digital memory system which can be battery operated is designed for short term or long term (months) continuous, unattended monitoring. It has been successfully applied in laboratory testing such as fatigue crack growth studies, as well as field monitoring on bridges and piping to detect crack growth. The features of simplicity, compactness, versatility, and low cost contribute to expanded practical application of acoustic emission technology.

INTRODUCTION

The basic theory of acoustic emission monitoring is established and the technology is being applied in a wide range of material experiments and structural analysis programs. In the course of this work, the general trend in acoustic emission (AE) monitoring systems has been one of increasing complexity. This is particularly true of systems designed for continuous monitoring of a structure. These systems are usually multichannel (in the vicinity of 20 to 40 or more channels) and require a dedicated computer for data processing and storage. Such systems may cost from $100,000 to $500,000. Some applications require this degree of sophistication. An example is simultaneous monitoring of a large material volume such as a nuclear reactor pressure vessel during hydrostatic testing to detect and locate defects.

There are many structural monitoring applications of AE, however, where the system complexity just described is not needed. In a structure such as a pressure vessel or a bridge, once initial inspection has been accomplished, a large portion of the material volume is of no real concern to continued structural integrity. There remain selected areas of concern such as known high design stresses (e.g., nozzle penetrations of a pressure vessel) or portions of a structure which are especially critical to the integrity of the total structure (e.g., certain suspension members in a bridge). To apply a complex AE system to continuously monitor such selected areas over a long period of time would not only be very expensive but also may be impractical because an operator with the required skill may not be routinely available.

A unique concept for continuous AE monitoring in selected applications such as those described above has been developed at Battelle-Northwest. It reverses the trend to increasing complexity while retaining such important requirements as reliability, permanent data record, and easy retrieval of data for analysis. The original concept grew out of a special need in a program being performed for the U.S. Federal Highway Administration to apply AE to bridge monitoring.

BNW Digital AE Monitor (DAEM) System(s) are designed for long term monitoring of identified areas of concern in a structure. Their concept is centered around a solid state programmable read-only digital memory (EPROM) which is used to record acoustic emission information. Electronic time gated logic circuitry restricts the acceptance zone for acoustic signals thus providing a monitor which can selectively accept information only from a pre-determined material volume in a complex structure. The digital memory provides the basis for reducing system complexity and system cost without sacrifice of sensitivity or versatility. These memories are intended for use as a pre-programmed instructional device for use in computer systems. Through the use of specially designed programming circuitry, they were adapted to use as a dynamic recording device for BNW's DAEM system. One very important feature of the PROM's compared to other types of solid state digital memories is the fact that they are nonvolatile, i.e., recorded information is retained indefinitely without continued power supply. The memories can be erased by exposure to ultraviolet light and reused after the stored data is recovered.

The PROM's currently being used are 16K memories. This capability is utilized to provide 1024 address locations with a capacity of 65,535 counts in each address. The programming is controlled on a time basis normally. When the preset accumulation period is complete, the data is stored and a new counting period is started immediately. This process continues in sequential manner until the monitoring is completed or all the memory addresses are used. When a memory is full or at the end of a test, the used memory is removed and replaced with a fresh one. The used memory is then read out to a digital printer to provide a hard numerical copy. The memory is then erased and reused.

TYPICAL DIGITAL MEMORY APPLICATION

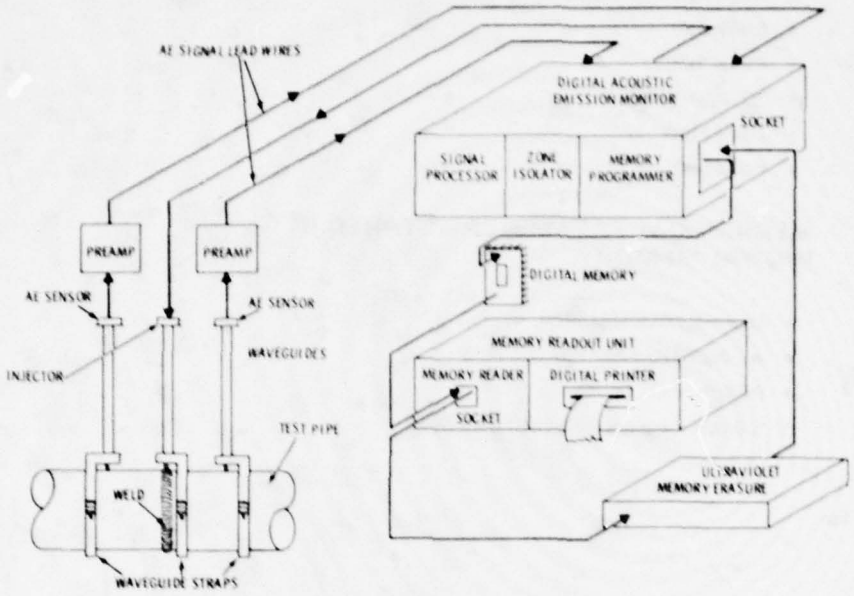

DIGITAL MEMORY FEATURES

- NONVOLATILE
- PERMANENT STORAGE >5 YEARS
- HIGH STORAGE CAPACITY >66 MILLION COUNTS
- COMPACT
- EASE OF USE
- LOW COST
- LOWER POWER DRAIN

AE PARAMETERS STORED IN DIGITAL MEMORY

- EVENT OR RINGDOWN COUNT
- ENERGY
- PEAK TIME
- PULSE HEIGHT
- LOCATION
- POLARITY

MECHANICAL PARAMETERS STORED IN DIGITAL MEMORY

- LOAD CYCLE NUMBER
- AE POSITION ON LOAD CYCLE
- RAMP LOAD LEVEL
- CRACK OPENING DETECTOR LEVEL

DATA LISTING FROM DIGITAL MEMORIES

BATTELLE NORTHWEST AE TEST PROFILE

AE TEST: 1-2A-6B
DATE: 5-8-78
TEMP. 550 F
INSTR. GE•DMD GEMINI NRC MTS
LOAD: 7.0/70.0 KIP
LOAD RATE: 2 HZ
TOT CYCLES: 70,000
DELTA CYCLES: 10,000
EPROM¤ 2716
PARAMETER: ZONE AE 2.2
UPDATE: 100 CYCS
ADDRESS: 100
PT\PH CORRELATOR: ¤1=A/B A/B ¤2=A/B B/C

EPROM¤ LISTING

H	F	6	D	J	G	8	Q	10	V	3	5

BLOCK ¤01 (0000-0024)

TOTAL	VALID	PT\PH	LD\VC	ENRGY	PT ¤1	PT ¤2	PT ¤3	PH ¤1	PH ¤2	PH ¤3	-POL.
00043	00011	00003	00004	00271	00011	00000	00000	00003	00002	00000	00004
00024	00004	00001	00002	00174	00003	00000	00000	00001	00000	00000	00003
00022	00000	00000	00000	00000	00000	00000	00000	00000	00000	00000	00000
00107	00000	00000	00000	00000	00000	00000	00000	00000	00000	00000	00000
00109	00000	00000	00000	00000	00000	00000	00000	00000	00000	00000	00000
00089	00000	00000	00000	00000	00000	00000	00000	00000	00000	00000	00000
00074	00001	00000	00001	00067	00001	00000	00000	00000	00000	00000	00000
00061	00002	00000	00002	00183	00001	00001	00000	00001	00000	00000	00000
00012	00001	00000	00001	00014	00000	00001	00000	00000	00000	00000	00000
00008	00000	00000	00000	00000	00000	00000	00000	00000	00000	00000	00000
00008	00000	00000	00000	00000	00000	00000	00000	00000	00000	00000	00000
00056	00004	00000	00003	00204	00002	00000	00001	00000	00000	00000	00002
00205	00009	00000	00008	01063	*00005*	*00000*	*00003*	*00000*	*00000*	00000	00007
00197	00011	00000	00011	01329	00011	00000	00000	00000	00000	00000	00006
00214	00006	00000	00006	00328	00005	00000	00001	00000	00000	00000	00005
00202	00007	00000	00007	00681	00007	00000	00000	00000	00000	00000	00005
00133	00005	00000	00005	00629	00005	00000	00000	00000	00000	00000	00003
00128	00005	00000	00005	00294	00005	00000	00000	00000	00000	00000	00003
00159	00009	00000	00008	00430	00008	00000	00000	00000	00000	00000	00006
00025	00002	00001	00002	00122	00002	00000	00000	00001	00000	00000	00002
00065	00002	00000	00001	00002	00001	00000	00000	00000	00000	00000	00002
00018	00000	00000	00000	00000	00000	00000	00000	00000	00000	00000	00000
00005	00000	00000	00000	00000	00000	00000	00000	00000	00000	00000	00000
00059	00001	00000	00001	00112	00001	00000	00000	00000	00000	00000	00000
00105	00002	00000	00002	00190	00002	00000	00000	00000	00000	00000	00000

DIGITAL MEMORY AE GRAPH

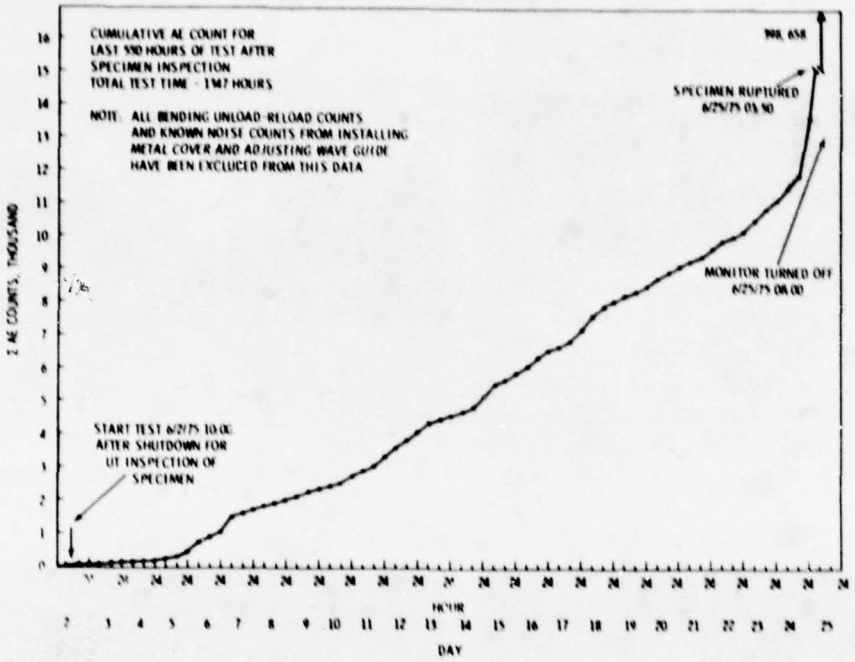

SINGLE CHANNEL TWO PARAMETER AE MONITOR

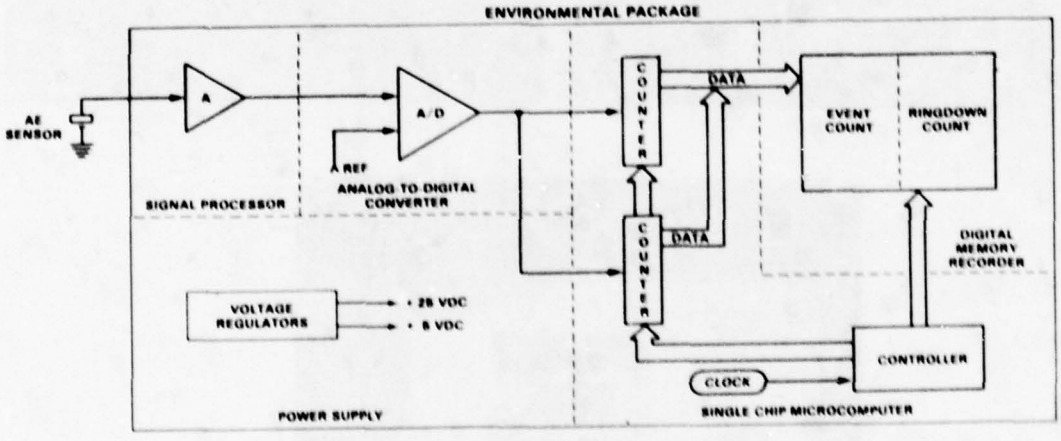

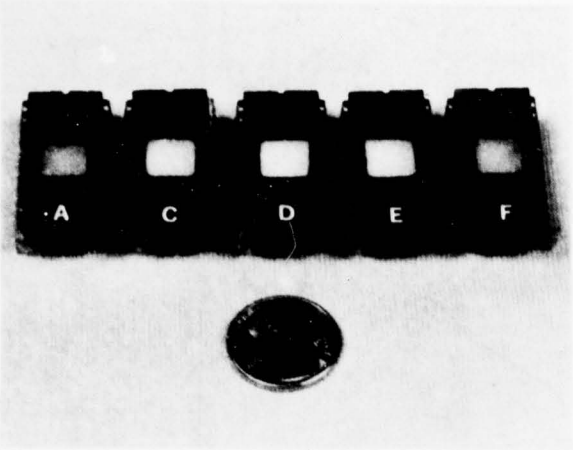

Digital Memories

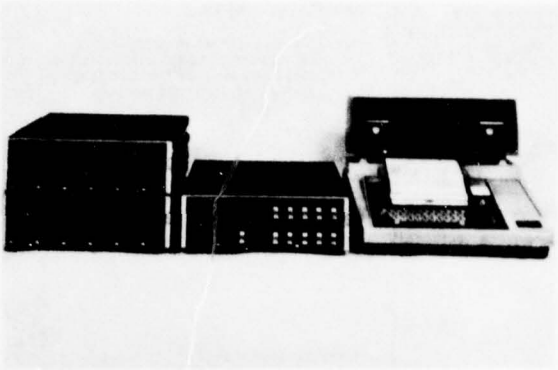

Multiparameter Digital Memory AE System

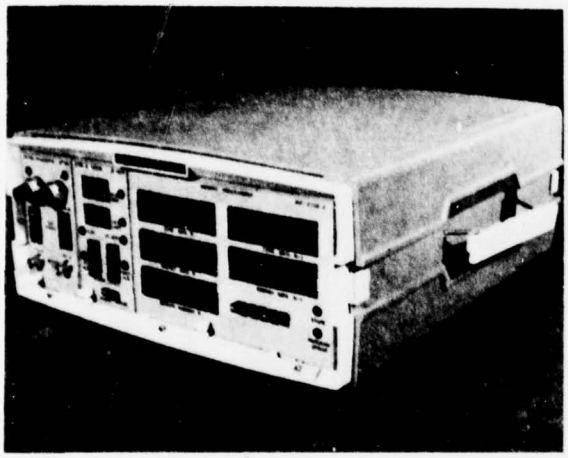

Stress Corrosion Cracking Digital Memory
AE Monitor

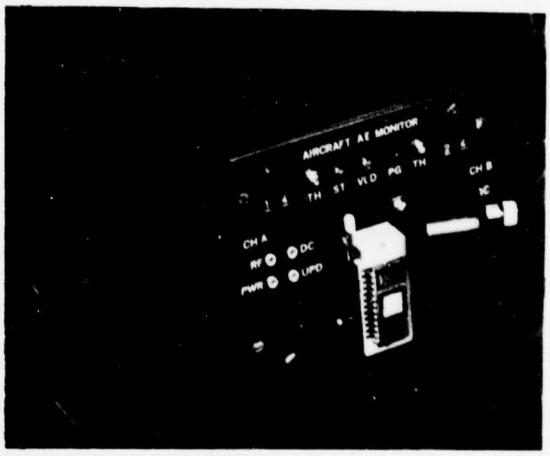

Aircraft Digital Memory AE Monitor

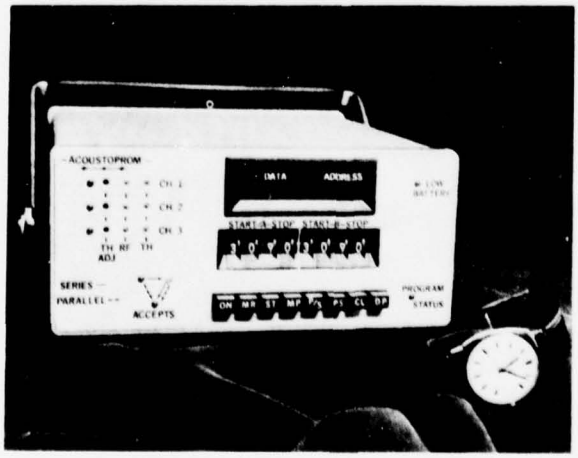

Battery Operated Digital Memory AE Monitor
for Highway Bridges

CANADIAN FORCES IN-FLIGHT ACOUSTIC EMISSION MONITORING PROGRAM

S.L. McBride
Royal Military College
Kingston, Ontario K7L 2W3

ABSTRACT

A crack growing in the forward wing trunnion of a CF100 aircraft was monitored for over 60 flying hours. Acoustic emission data was detected which indicated that during climb, following take-off, the 3mm crack made unstable advances on a few occasions. The detected crack advances produced about 1mm² of new fracture surface.

The programme involves monitoring a crack in the 7075-T6 Al forward wing trunnion of a CF100 aircraft. From NDT measurements the crack is known to be growing at an average rate of 5μ/flying hour and was about 3mm long at the beginning of the program which was undertaken in an attempt to evaluate the feasibility of using acoustic emission to detect crack growth in flight. The main effort has been directed toward highly stressed components which are reasonably well acoustically isolated from the rest of the airframe, viz. wing trunnions and wing attachment fittings.

The equipment was located in the CF100 aircraft as shown in Fig. 1. The stress wave picked up by the sensor was amplified, captured in a transient recorder and recorded on audio tape. Both the preamplifier and audio tape recorder were operated by the navigator. These tapes were then sent by base maintenance to the data analysis centre at the Royal Military College where both amplitude distribution and spectrum analysis of the recorded data was carried out signal by signal.

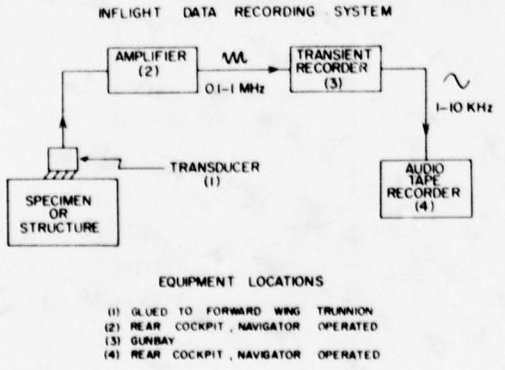

Fig. 1 A schematic diagram of the in-flight data recording system and the location of the various components in the CF100.

In a preliminary in-flight fleet survey it was found that the structural noise detected by the sensor could vary considerably between components of the same type (Fig. 2). Further, the number of recorded signals above the threshold trigger level varied considerably from flight to flight on a single component (Fig. 3). The amplitude distribution of the environmental noise signals picked up by the sensor was found to be similar from flight to flight with a well defined cutoff amplitude as seen in Fig. 4. Among several thousand recorded noise signals a few acoustic emission signals were detected and have been positively identified. The amplitude of the largest of these is indicated in Figure 4 where it is seen that this crack advance signal is well above the structural noise.

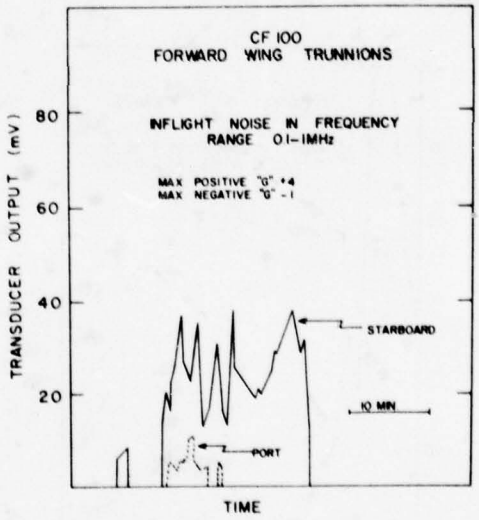

Fig. 2 Broad band noise data obtained with the sensor attached to the port and starboard forward wing trunnions. The in-flight manoeuvres covered the range -1>G>+4 in each case. The data of Figs 3 - 5 were obtained on the port trunnion.

Measurements of the amplitude of the signals was not sufficient to separate out acoustic emission due to crack extension from structural noises. Rather, this was done by acquiring experience of noise spectra measured in flight and of acoustic emission spectra measured in the laboratory. As is seen in Fig. 5 a typical noise spectrum decreased

monotonically with increasing frequency while the acoustic emission spectra have pronounced maxima in the vicinity of 200 and 500 kHz. Of course

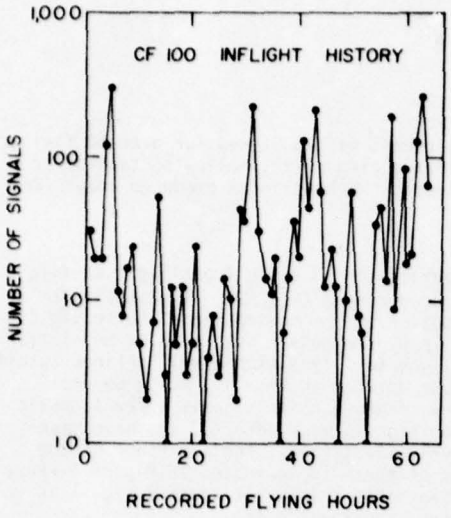

Fig. 3 The number of recorded signals above threshold obtained for each hour of flight.

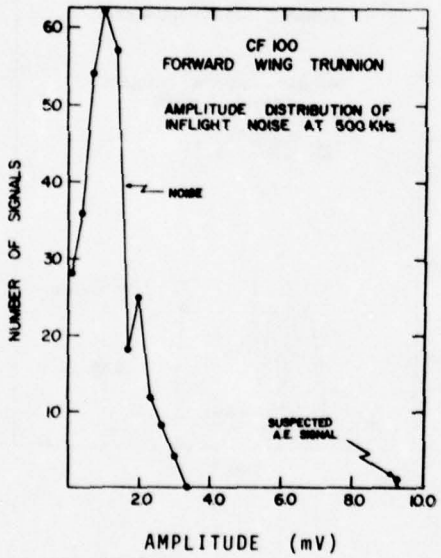

Fig. 4 A typical amplitude distribution of in-flight noise data (500 kHz, 24dB/octave bandpass filter). Also shown is the amplitude of the largest suspected A.E. signal observed in flight.

these maxima include the acoustical response of the wing trunnion and the response characteristics of the Dunegan/Endevco S9201 transducer used. Figure 6 shows the response of the trunnion-sensor system to the helium gas jet calibration source(1),(2) and the corresponding laboratory system calibration. This result shows that from the amplitude frequency point of view, the responses of the laboratory and field systems are spectrally similar but with the latter less sensitive by about 6dB. Hence the direct comparison of the laboratory and field spectra made in Figure 5 is meaningful and no correction has been made in this data for the difference between the systems. From the data of Figure 5 and our extensive laboratory testing of 7075-T6 Al we are able to state that the in-flight acoustic emission signal is due to a sudden crack advance which produced about 1mm^2 of new fracture surface in the forward wing trunnion. Further, correlation of the in-flight log with the data tapes showed clearly that the identified crack growth signals had all taken place during the climb following take-off.

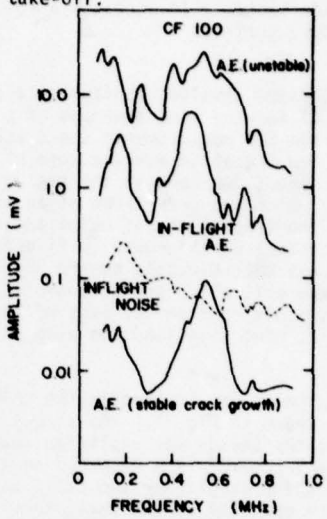

Fig. 5 Comparison of an in-flight recorded transient (A.E.) with representative A.E. spectra due to stable crack growth (≈ 0.1μ/cycle) and to an unstable crack advance (area = 5mm^2) in 7075-T6 Al. Also shown is a typical in-flight noise signal which does not have a similar spectrum.

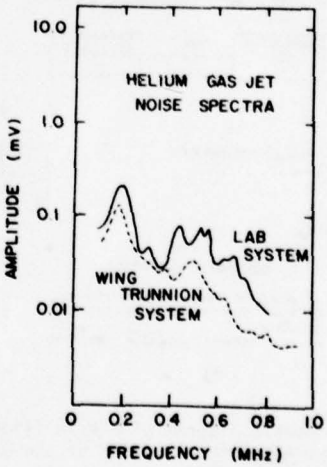

Fig. 6 The helium gas jet spectra of the laboratory and field systems.

Acknowledgements

This work was sponsored by the Directorate of Aerospace Projects and Resources, NDHQ, Ottawa, Ontario

1) Can. J. Phys. 54, 1824 (1976).
2) Can. J. Phys. 56, 504 (1978)

ELECTROCHEMICAL DETERMINATION OF HYDROGEN IN STEEL

F. Mansfeld
Rockwell International Science Center
Thousand Oaks, California

ABSTRACT

The electrochemical measurement of the permeation rate of hydrogen through metal foils consists of charging of the metal with hydrogen on one side of the foil and removal of hydrogen by electrochemical oxidation on the other side. The hydrogen diffusion coefficient can be determined by mathematical analysis of the time dependence of the oxidation current. This electrochemical technique can also be used to determine the hydrogen concentration in metals. For this purpose, an electrochemical cell is placed on the metal to be analyzed and a hydrogen concentration gradient is produced by oxidation of all hydrogen atoms which reach the surface. Under a contract with the Naval Air Development Center, a portable "barnacle cell" system - so-called because of its magnetic attachment to steel surfaces - is developed for field use such as determination of hydrogen concentration in aircraft landing gears. The system consists of two parts: the measuring cell in a cylindrical magnet (1.5 inch diameter) and the electronic system which allows recording of the permeation current-time trace and integration of this trace over pre-set time intervals.

The electrochemical permeation method, which was first described by Devanathan and Stachurski (1,2) has been used to determine the diffusion coefficient D and the concentration C_o of hydrogen in iron and steels and to a lesser extent also in other metals. In this method, hydrogen is produced on one side of a metal foil either as the result of the corrosion reaction in acids or by application of a cathodic current. On the other side of the foil, hydrogen which has diffused through the metal is removed by application of an anodic constant potential which leads to oxidation of hydrogen to water. The measurement is carried out in an alkaline solution in which iron is passive and the background current due to iron oxidation is very low.

A modification of the permeation method is the technique which is used in the "barnacle cell" (3,4), so-called because of its magnetic attachment to steel surfaces. With this technique use is made only of the oxidation process to determine the hydrogen concentration in steels. Under contract with the Naval Air Development Center (NADC) a portable barnacle cell system is developed for field use such as determination of the hydrogen concentration in plated steel parts, landing gears, etc. The cell system is developed at the Science Center, Rockwell International, while the electronic measurement system is being designed and fabricated at the Chemistry Department of Portland State University. Three prototypes of the combined system will be delivered to NADC in September 1978.

The permeation method is described in Fig. 1. The diffusion equations, Eqs. 1 and 2, are solved for the electrochemically controlled boundary conditions:

$$X = 0,\ t \geq 0,\ C = C_o$$

$$X = L,\ t \leq 0,\ C = 0$$

$$0 < X < L,\ t < 0,\ C = 0$$

In Eqs. 1 and 2, Z is the number of electrons involved in the oxidation reaction (Z = 1), F is the Faraday constant, D is the diffusion coefficient for hydrogen, C is the concentration of hydrogen in the metal and L is the thickness of the foil. Concentration contours for different times are also shown in Fig. 1 (5). Eqs. 1 and 2 can be solved by a Laplace transformation or a Fourier method. Figure 2 shows a comparison of experimental data obtained for Armco iron with the build-up transients predicted by the two methods (6).

The diffusion coefficient D and the hydrogen concentration C_o can be determined from the permeation transient (1) as shown in Fig. 3. The sensitivity of the electrochemical method exceeds that of conventional techniques significantly.

For the barnacle cell method Eqs. 1 and 2 are solved with the boundary conditions:

$$X = 0,\ t \geq 0,\ \frac{\partial C}{\partial x} = 0$$

$$X = L,\ t > 0,\ C = 0$$

$$0 < X < L,\ t \leq 0,\ C = C_o$$

Concentration profiles for different test periods are shown in Fig. 4 (3). For the conditions of Fig. 4:

$$J = F\, C_o \left(\frac{D}{\pi t}\right)^{\frac{1}{2}},$$

which holds for $\frac{L^2}{Dt} \geq 4$, i.e., $t_{max} = \frac{L^2}{4D}$.
For 4340 steel ($L = 1$ mm, $D = 2.5 \cdot 10^{-7}$ cm^2/sec) $t_{max} \approx 10^4$ sec.

The barnacle cell system to be developed under contract is shown in Fig. 5. The cell is attached to the sample and the hydrogen oxidation current is flowing between the steel and Ni/NiO driving electrode. Details of the cell and measuring system are shown in Fig. 6 and 7. The electrolyte (0.2 N NaOH) is contained in a sponge which provides electrical contact between the sample and the Ni/NiO counter electrode. The Ni electrode is used to check whether sufficient electrolyte is contained in the cell. The measurement system contains provisions to monitor the hydrogen oxidation current and to integrate the current-time trace. The current is displayed after a pre-set time interval, the start and the

interval of integration are preset, the total coulombs are used to calculate the hydrogen concentration for a given diffusion coefficient.

Figure 8 shows some experimental results obtained with the barnacle cell. In a log current-log time plot the points for charged specimens fall on a straight line with the theoretical slope of -0.5, while samples which had not been charged follow a line with a slope of -1 which presumably reflects the passivation characteristics of the steel surface. The average hydrogen concentration of the charged samples is about 0.32 ppm.

Some applications of the technique are listed in the last figure which also shows the barnacle cell attached to a steel tensile sample which had been charged and Cd plated at NADC to determine the relationship between hydrogen concentration and failure characteristic as a function of applied stress.

ACKNOWLEDGEMENT

This work was performed under contract N62269-77-C-0351 with the Naval Air Development Center. The hydrogen permeation experiments were carried out by S. L. Jeanjaquet and C. S. Tsai.

REFERENCES

1. M. A. V. Devanathan and Z. Stachurski, Proc. Roy. Soc. A270, 90 (1962).
2. M. A. V. Devanathan, Z. Stachurski and W. Beck, J. Electrochem. Soc. 110, 886 (1963).
3. D. A. Berman, W. Beck and J. J. DeLuccia in "Hydrogen in Metals," I. M. Bernstein and W. W. Thompson, editors, ASM (1974), p. 595.
4. D. A. Berman, "Indexing the Degree of Hydrogen Embrittlement of 4340 Steel Using the Barnacle Electrode," Naval Air Development Center, Report No. NADC-76359-30, Nov. 1976.
5. L. Nanis and J. J. DeLuccia, ASTM STP 445, 55 (1969).
6. J. McBreen, L. Nanis, and W. Beck, J.Electrochem. Soc. 113, 1218 (1966).

I. PERMEATION METHOD
- HYDROGEN GENERATED IN ELECTROCHEMICAL CELL
- DIFFUSION OF HYDROGEN THROUGH METAL FOIL
- OXIDATION OF DIFFUSED HYDROGEN
- MEASUREMENT AND ANALYSIS OF RESULTING PERMEATION CURRENT

PERMEATION RATE

(1) $P = \frac{J}{zF} = -D\left(\frac{\delta C}{\delta X}\right)_{X=L}$

FICK'S SECOND LAW

(2) $\frac{\delta^2 C}{\delta X^2} - \frac{1}{D}\frac{\delta C}{\delta t} = 0$

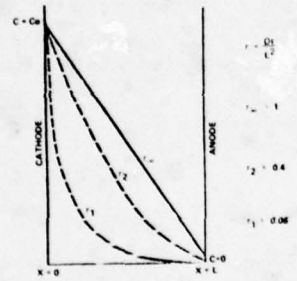

Fig. 1 Permeation method; concentration contours for progressive hydrogen diffusion.

- TWO METHODS OF SOLUTION OF EQUATIONS (1) - (2)

- LAPLACE TRANSFORM METHOD

VALID FOR SHORT TIMES ($0 < \tau < 0.5$)

$$\frac{J_\tau}{J_\infty} = \frac{2}{\sqrt{\pi\tau}} \exp\left[-\frac{1}{4\tau}\right], \quad \tau = \frac{Dt}{L^2}$$

- FOURIER METHOD

VALID FOR LONGER TIMES ($\tau > 0.15$)

$$\frac{J_\tau}{J_\infty} = 1 - 2\exp\left[-\pi^2\tau\right]$$

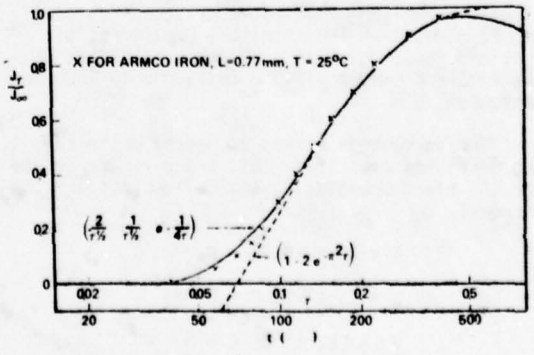

Fig. 2 Comparison of experimental data (x) with the theoretically predicted build up transients (-) and (---).

- **TIME LAG METHOD**

$$t_l = 0.63\, J_\infty = \frac{L^2}{6D}$$

- **BREAKTHROUGH TIME METHOD**

$$t_b = \frac{L^2}{D}\left(\frac{1}{6} - \frac{1}{\pi^2}\right)$$

- **STEADY STATE CURRENT**

$$J_\infty = \frac{ZDFCo}{L}$$

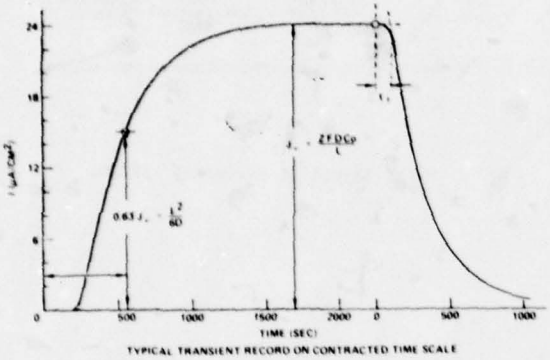

- **SENSITIVITY**

$1\mu A/cm^2 \cdot 0.203$ ppm H_2

for $D = 2.5 \times 10^{-7}\ cm^2/sec$

Fig. 3 Determination of D and Co from permeation current.

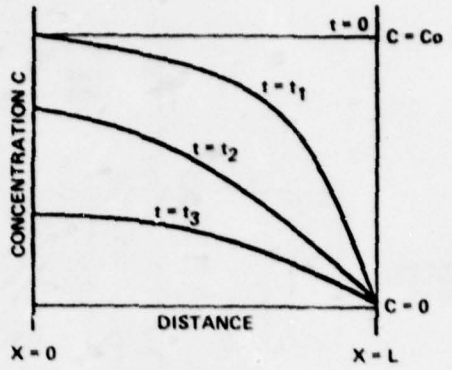

Fig. 4 Hydrogen extraction method "barnacle cell."

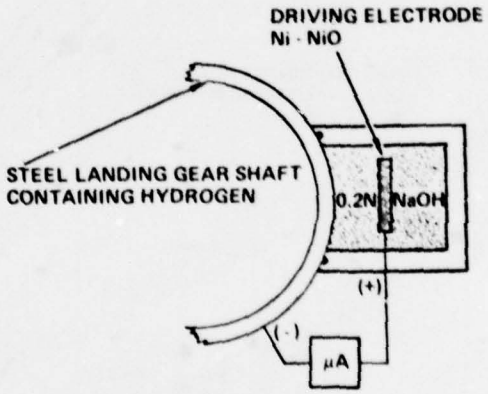

Fig. 5 Barnacle electrode principle.

II. HYDROGEN EXTRACTION METHOD ("BARNACLE CELL")

- *OUTDIFFUSION OF RESIDUAL HYDROGEN IN STEEL MEASURED IN ELECTROCHEMICAL CELL*
- **MEASUREMENT AND ANALYSIS OF EXTRACTION CURRENT**
- **SOLUTION OF EQUATIONS (1) AND (2)**

$$\frac{J}{ZF} = Co\left(\frac{D}{\pi t}\right)^{1/2}\left[1 - e^{-L^2/Dt} + e^{-4L^2/Dt} + \ldots\right]$$

FOR $e^{-L^2/Dt} \ll 1$, $\frac{J}{ZF} = Co\left(\frac{D}{\pi t}\right)^{1/2}$

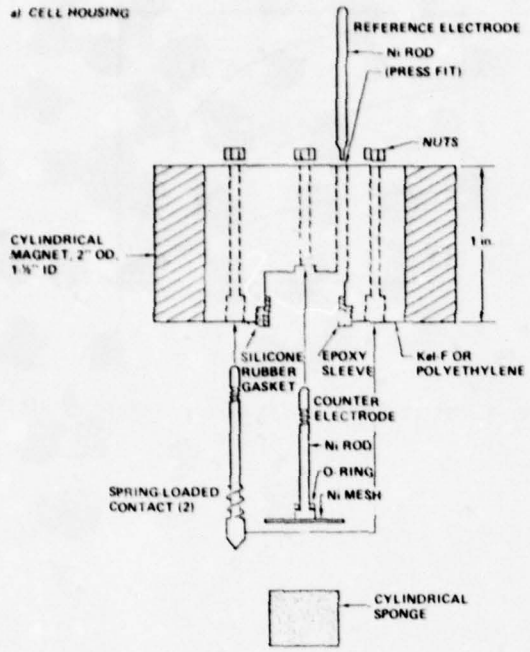

Fig. 6 Basic design for test cell.

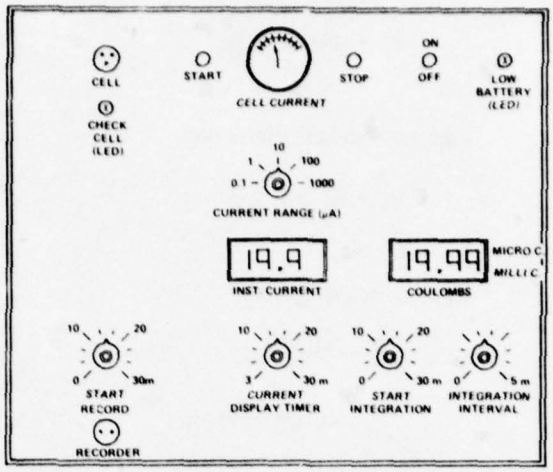

Fig. 7 Panel layout of measuring system.

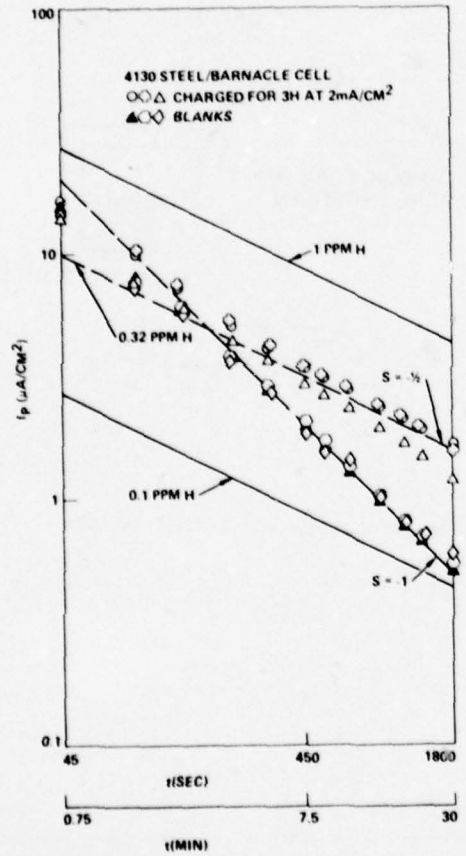

Fig. 8 Experimental results on 4130 steel.

- TESTING OF DIFFERENT HEATS OF STEEL
- FIELD USE (LANDING GEARS, ETC.)
- PLATING OPERATIONS (H_2 CODEPOSITION, BAKE-OUT EFFICIENCY)
- EMBRITTLEMENT STUDIES

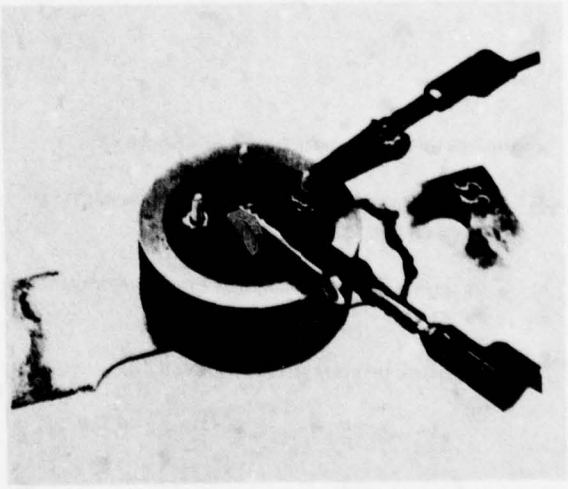

Fig. 9 Applications of barnacle cell.

STATE OF THE ART IN SINGLE FREQUENCY EDDY CURRENT TESTING

K.J. Law
K.J. Law Engineers, Inc.
Farmington Hills, Michigan 48024

ABSTRACT

NDE in the mass production automotive industry uses single frequency eddy current test systems for component parts integrity testing. Typical measures accomplished are: surface hardness (R_C), depth of hardened layer (case depth), core hardness, and soft spots on the surface caused by incorrect quench. Additionally, gross crack and seam defects are detected in production processes by this type equipment, on the order of .005" deep and .2" long. Some special results occur, such as: fillet combined hardness and case depth tests result in a direct correlation to fatigue life for the crankshafts of diesel engines.

Material sorting for alloy differences is another important inspection performed on incoming stock. Many low to high carbon steel alloys may be sorted; however, there are combinations which cannot be separated. However, multiple frequency testing is now improving this situation considerably. The equipment used must be highly reliable with MTBF's of 10,000 hrs. and long-term stability of months for successful high speed production testing at rates of 3600 to 72,000 parts per hour.

My business is primarily with the automotive industries. We're eddy current manufacturers who are staffed with highly technical people doing research and development in that area, but primarily on a commercial basis. In other words, we're not funded. That was a long way of saying it, but eddy current people don't get very many funds for this kind of thing because the techniques are not so applicable to many of the problems that go on in the military industry.

What I am going to tell you about is what we can do with so-called single frequency eddy current. I say "so-called" because we're finding out we can do an awful lot more if we use multiplexed frequency techniques.

We have a couple of speakers who will fill you in on multiple frequency testing as we proceed. We have two areas for eddy current testing. One is the non-ferrous materials. There, we don't do a lot of work, but we do have conductivity testers that can do many of the things with which you are familiar, such as materials sorting and the actual measurement of conductivity for its own purposes to monitor or check the quality of products that are supposed to have certain conductivity ranges. It can detect thickness of thin materials and we can do some heat treatment checking. For instance, many of the aluminum materials change conductivity when they are heat treated, as do some stainless materials that are non-magnetic. Thus we can do some heat treatment testing in this area with conductivity eddy current methods.

Most of our techniques are in the low frequency range. We operate from a hundred hertz to a hundred thousand hertz. Most of what I have seen in the aerospace industry is up in the higher frequency ranges, 500 kilohertz and megahertz ranges, but our primary business is in the ferrous industry.

To give you a little idea of what we can do there, I am just going to enumerate some of the tests that we perform. Most of what we do, of course, is in production. For instance, an automobile manufacturer makes piston pins and he has several things he wants to check that he cannot do destructively. Nondestructive evaluation is something, however, that he can do, and he can do it very rapidly - 3600 parts an hour. We can check such a part for surface hardness, decarburization on the surface or total lack of carburization. We can also check things like soft spots where parts will pass through the quench improperly, or what is called slack quench conditions. This occurs when the part does not quench rapidly enough. Things like this are giving automobile engines, as they become more highly sophisticated, a lot of problems. We can do cracks and seams, but not with the selectivity that you might be interested in in some of your work.

We can detect cracks five thousandths in depth and maybe a quarter inch in length. We can also detect soft spots. It means that if we have a very good material, say 52100 bearing steel, or we have a highly processed part like a piston pin or a part that is machined and ground, we can then check it for that kind of defect, but that is not a really large part of our applications.

There are two areas in which eddy currents are especially valuable. One is in the high frequency range (high for us). Ten thousand cycles per second is a frequency we typically would use to look at the surface hardness and look for shallow case depth in a part like the piston pin. The case depth is supposed to be 20 thousandths to 35 thousandths. At a high frequency, if it is a little shallower than twenty, we can usually detect it. Then we go to a lower frequency to look inside the part, because the eddy current penetrates into the surface of the part inversely as a function of the square of the frequency. Typically at 10 thousand hertz we're penetrating, maybe, 15 to 20 thousandths. At a hundred hertz we're penetrating on the order of one hundred fifty thousandths. That will vary from one hundred thousandths to two hundred thousandths, depending on the material.

Carbides in cast structures are of interest and are detectable. Cylinder sleeves for a diesel engine are spin cast. For some reason this process brings out carbide conditions on the surface of the part and this ruins the cutting tools. Also, it can create cracks, and we can detect both carbide and cracks.

Another thing with which we have had some correlation is microstructure. When you heat treat certain ferrous materials, the phase at which the

hardness just goes correctly into the value that you want is detectable as a function of the microstructure of the part. In many ferrous materials, this is determinable with eddy currents and causes a very easy way to sort correctly heat treated parts from incorrectly heat treated ones at a single frequency. We, of course, are depending somewhat on resonance characteristics or resonance effects of the materials as a function of the processing. The heat treating changes the structure, and then if you induce an eddy current frequency in it, the response of a particular alloy with a particular heat treat condition may occur at a different frequency than for another alloy of steel, heat treated in the same way to bring it up to the same kind of Rockwell C hardness. Primarily, we're attempting to determine that these parts have been processed properly and are correct for their use in terms of a Rockwell C scale hardness. It is almost exclusively used in the automotive industry as a measure of heat treat condition, right or wrong.

We're able to determine the Rockwell C hardness in most ferrous materials within a half a point on the RC scale of what you would normally do with a penetration test. In other words, we can almost match the average hardness of a series of parts with the average hardness as measured by the penetration test at the high hardness ranges up around 57 to 63 or 64 RC. When we get into lower hardness ranges with eddy currents, we become a little less discrete, and we cannot compare directly with the penetration test. For instance, at 40 to 45 RC hardness, we might be within two points of correlating with the average penetration tests. At lower hardnesses than that you can almost forget eddy currents as a method for measuring the hardness of the material.

Because there are these so-called resonance effects, one of our analysis techniques is to put parts within a coil, scan the frequencies, and plot the results from the eddy current instrument to separate parts that are properly heat treated and parts that have all of these other faults - decarburization, slack quench, etc., whatever the characteristics are that have created the reject part. If we do that, we then often find that there is a particular frequency, say, 750 hertz, at which we will be able to sort these reject parts. At other frequencies we may not be able to see any difference.

The same frequency sensitivity applies to attempting to sort steel alloys. You may find that certain alloys will sort well at five kilohertz and other alloys will not sort at all at that frequency, but you go to another frequency like four hundred hertz and you can sort those that did not respond at the five kilohertz.

Because of these considerations, we are now going into a series of tests at different frequencies. They are still single frequency tests in that we're not applying all the frequencies at one time, but we have developed multiplexing microprocessor systems where we can switch to four different frequencies and look at the results with two threshold levels at each of the four frequencies. The part tested sits inside or passes through a coil, the microprocessor system has let us do very rapid changes of frequency and very rapidly look at three or four frequencies while we're inspecting a single part and still be able to inspect at rates of two or three thousand parts and hour. This has created a big advantage in the ability to examine a part with more than a single frequency. In the past we have run tests in which we have had multiple coils in a row, each one operated at one or two frequencies. This is cumbersome, however, and leads us to the microprocessor approach.

The automotive industry has decided to lighten the weight of their cars to help meet the energy-mileage characteristics that are being promulgated by the department of transportation. In order to lighten the weight of an automobile, you have to go to higher strength steels. You have to go to lightweight metals, aluminum and plastics. The part we are involved in right now is in the high strength steel area which turns out to be a very difficult situation for the automobile manufacturer. In the new front-wheel-drive vehicles, they have gone away from the conventional, very heavy axle and very heavy differential gear assembly associated with the transmission, and gone to a much simpler, direct coupled front wheel drive that naturally removes a lot of weight in the car. In addition, they have gone to an integral spindle and hub assembly, in which the spindle and the hub have bearing races formed in the part instead of using the typical taper roller bearing assembly. This is a ball-bearing device. When they assemble the spindle and the hub together with the ball bearings, they have a very critical but light weight, small part that is high strength and carrying a much higher load than has ever been required of those kinds of parts in the past.

Using the microprocessor system, we are testing these parts using four different windings that inspect different bearing surfaces in different critical areas of the part simultaneously; in each of these windings we're cycling up to four different frequencies in order to completely insure that the induction hardened bearing races are correctly heat treated and that the rest of the part is not heat treated in a way that would make it fracture or fail in service.

MULTIFREQUENCY EDDY CURRENT INSPECTION WITH CONTINUOUS WAVE METHODS

T. J. Davis
Battelle-Northwest
Richland, WA 99352

ABSTRACT

This paper describes the application of continuous wave, multifrequency eddy current methods to nondestructive inspection of materials. A generalized description of the technology is included, followed by some results obtained in multifrequency examination of tubing. A major advantage of multifrequency inspection is the ability to discriminate against unwanted test parameters. The discrimination process is effected by combining the data from individual frequencies in a manner similar to simultaneous solution of multiple equations. Multifrequency tests are described showing how discrimination has been achieved against parameters such as probe motion, tube support plates and magnetic surface deposits.

INTRODUCTION

Continuous wave multifrequency eddy current inspection can provide substantially improved characterization of material parameters in a variety of applications. This is primarily due to its ability to eliminate unwanted parameters from test data. The basic approach relies on the skin effect phenomenon of current flowing in the specimen to provide independent information at different frequencies. The test results from individual frequencies can be combined in real time so as to obtain outputs which are free of certain parameters but which preserve other test data. The ability to select individual frequencies inherent in the continuous wave approach plays an important part in successful elimination of unwanted parameters.

This paper describes some field results of multifrequency testing and addresses some of the technology used in implementing the tests.

BACKGROUND

Continuous wave multifrequency testing is the direct equivalent of operating more than one single frequency unit with a common search coil. Two parameters are output from each frequency -- the in-phase and quadrature components of coil impedance. These components are directly relatable to Fourier amplitude coefficients of eddy currents flowing in the test specimen.

Implementation of a single-frequency test is shown in Fig. 1.

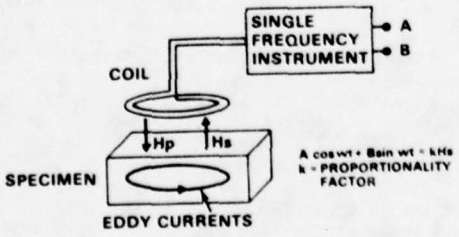

Fig. 1. Implementation of a single frequency eddy current test.

The test is based on the following events:

1. The search coil is excited with alternating current at the test frequency and positioned over the specimen.

2. The primary field (H_p) of the coil links with, and produces potential differences in, the conducting specimen. The potential differences cause circulating or eddy currents to flow in the specimen.

3. The eddy currents produce a secondary electromagnetic field (H_s) which links with the coil and induces a secondary voltage in it.

4. The secondary voltages are detected by most commercial instruments as a change in the equivalent impedance of the coil. The coil is connected as one leg of an impedance bridge in the instrument, and the secondary voltages alter the current delivered to the coil by the bridge, resulting in a change in equivalent impedance of the coil. Alternately, the secondary voltages may be detected directly by a second coil (send-receive method).

5. The Fourier amplitude coefficients A and B of the secondary voltage are detected and output by the instrument. These are used to interpret a variety of material properties, including conductivity, permeability, thickness, flaws (voids or inclusions), and probe-to-specimen spacing (liftoff).

In a continuous wave multiple-frequency test as shown in Fig. 2, the amplitude coefficients from each frequency are simultaneously output in real time. They can then be combined in real time by analog arithmetic circuitry to obtain the desired cancellation of unwanted parameters. The combination process may be likened to the simultaneous solution of multiple equations in which variables are eliminated by multiplying certain equations by an appropriate constant and adding the result to other equations. Hardware methods for implementing signal combination or mixing will be addressed in a following section of this paper.

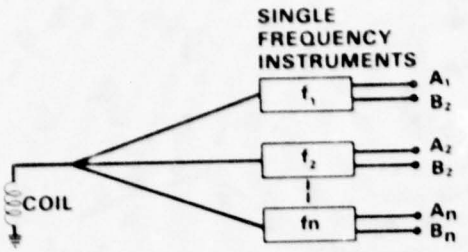

Fig. 2. Simple implementation of a multi-frequency eddy current system

Depending upon the test requirements, the optimal signal combination must be selected with a certain amount of caution. In general, there can be a wide variety of ways to combine outputs from various frequencies to cancel a given parameter, but not all of these combinations will provide meaningful or high sensitivity information on desired specimen parameters. Computer optimization techniques can be successfully used in many cases to determine the optimal combination.

APPLICATIONS

Results of three field applications of multi-frequency testing are described below. In two, steam generator tubing inspection and magnetic deposit thickness detection, output signals are directly mixed to eliminate unwanted parameters from the test data. A third application, dimensional gaging of tubing, uses two frequencies to obtain independent information on liftoff and wall thickness. Tubing ID is then obtained by combining these parameters.

Steam Generator Tubing Inspection -- Steam generator tubes in nuclear power plants are sometimes subject to corrosion mechanisms in which the amount of degradation is difficult to accurately quantify with conventional single-frequency inspection. Economic penalties to the utility are quite high if a tubing flaw inaccurately sized during routine inspection develops into a leaker during reactor operation. The plant must be shut down to plug the tube, during which the lost revenue for power sales can approach $400,000 per day.

Battelle-Northwest has developed a multifrequency eddy current system for inspecting steam generator tubing under a research contract with the Electric Power Research Institute (EPRI), Palo Alto, California. The system has been evaluated on a steam generator mockup using two-frequency inspection. The system is currently being prepared for evaluating three- and four-frequency inspection combined with advanced probe designs. Detailed information on the system is available in References 1 and 2, and results of the mockup evaluation are contained in Reference 3. A three-frequency system manufactured by Intercontrole, a French firm, has also undergone evaluation by EPRI on their steam generator mockup; these results are also included in Reference 3.

The Battelle system has demonstrated the ability of a two-frequency test to achieve total discrimination against probe wobble and partial discrimination against tube support indications. Alternately, if a tight-fitting or self-centering probe is used to eliminate probe wobble, total discrimination against the tube supports can be obtained. These results open substantial routes toward automated interpretation of test data, because the flaw information is no longer masked by the unwanted indications from wobble and supports.

The results described below were obtained using a two-coil differential probe of the type shown in Fig. 3. The probes are inserted through the tube past the U-bend region as shown in Fig. 4. Eddy current data are recorded as the probe is withdrawn, and then interpreted to determine the depth of flaws located in the tube. Typical support plates through which the tubes pass are made from mild steel with thicknesses up to 3/4 inch.

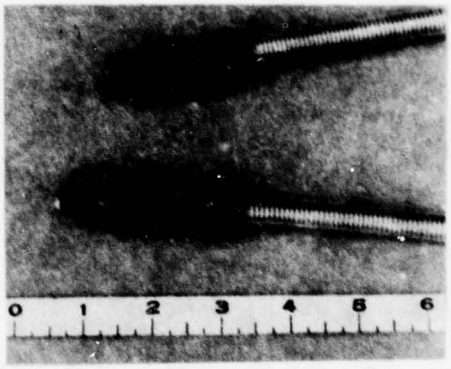

Fig. 3. Eddy current probes for steam generator tubing inspection

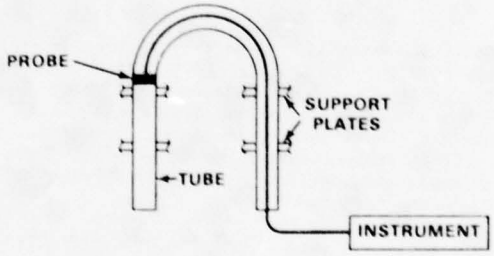

Fig. 4. Inspection of a steam generator tube

Flaw data are currently interpreted from a single-frequency test by observing the two tester outputs on an X-Y oscilloscope. A typical flaw will trace a figure-eight pattern on the oscilloscope due to the differential nature of the test. One lobe of the pattern corresponds to the first coil passing by the flaw; the other lobe is rotated 180^0 and is generated by the second coil. The phase angle of the flaw pattern on the display is used as a measure of flaw depth and corresponds to how far the eddy currents penetrated into the tubing wall before encountering the flaw.

Figures 5 and 6 compare the results of a two-frequency test with wobble eliminated to those of a conventional single-frequency test. In both cases, the probe was drawn through an ASME calibration tube containing a simulated support and flat bottom drill holes of the depths indicated in percent wall thickness. Figures 5a and 6a show the flaw outputs recorded on strip chart, and Figs. 5b and 6b show the same outputs plotted on an X-Y oscilloscope with support indications included. The probe wobble effect shows up on the horizontal axis of the single-frequency data in Fig. 5b as a random baseline variation which is larger than some of the flaw indications. In the two-frequency combined data of Fig. 6b, the wobble indications have been eliminated and all the flaw patterns originate from a common point. This permits electronic assessment of flaw depth by measuring and outputting the phase angle at the peak amplitude point of the flaw pattern. In contrast, the single frequency test requires visual interpretation of flaw pattern phase angle after the pattern has been stored on the screen of a memory X-Y oscilloscope.

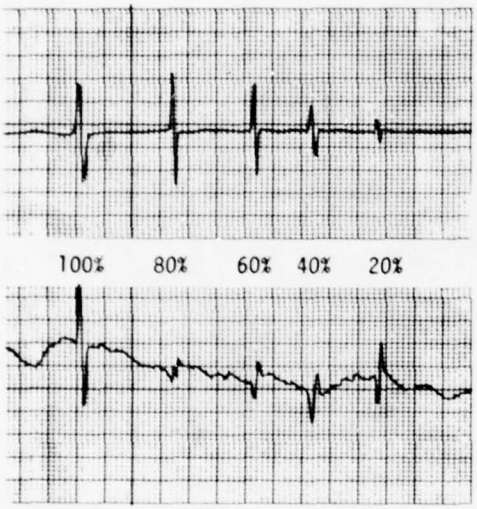

5a. Single Frequency Strip Chart Data

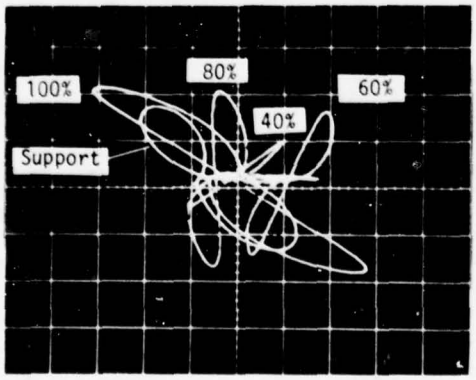

5b. X-Y Presentation of Above Data

Fig. 5. Single frequency inspection of steam generator calibration tube (400kHz). Defects are scaled in % wall thickness.

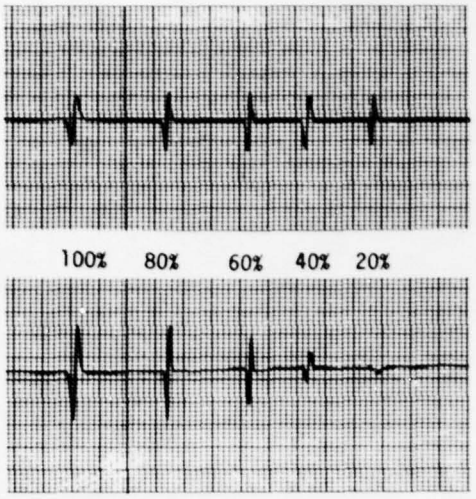

6a. Two Frequency Strip Chart Data

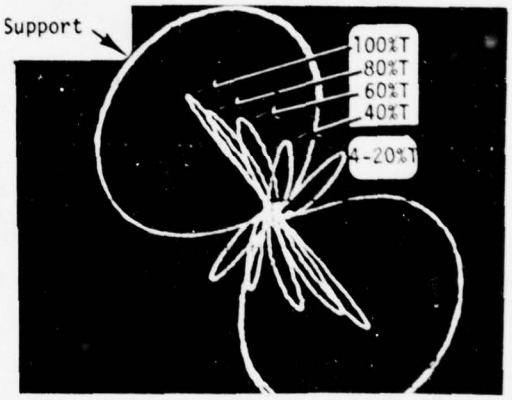

6b. X-Y Presentation of Above Data

Fig. 6 Two frequency (200 and 400 kHz) test results on calibration tube

The multifrequency data shown in Fig. 6 were obtained by combining the four outputs from a two-frequency test to obtain three outputs which are free of wobble information. A second iteration reduced these three outputs to the two outputs shown which contain maximum available sensitivity of phase angle of flaw depth. Note that this sensitivity is still substantially less than that available with single-frequency data, but it is wobble-free.

Another second iteration was performed in parallel on the three wobble-free outputs to obtain one final output which was free of support information. This result is shown in Fig. 7. The evaluation showed that a third frequency would be required to obtain two output channels which were both wobble- and support-free, but which still contained flaw depth information.

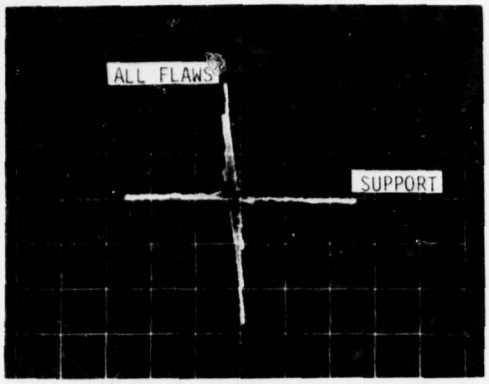

Fig. 7. Multifrequency output in which the vertical channel is free of tube support and wobble information.

In an alternate operating method, a tight-fitting or self-centering probe was used to eliminate probe wobble. This resulted in almost total elimination of the support signal while preserving flaw depth information. These results are shown in X-Y format in Fig. 8 . Use of the tight-fitting probe to eliminate wobble indications is not altogether practical for steam generator inspection because the tubing may undergo diameter variations which manifest themselves as wobble indications in the output and have the potential for masking flaw indications.

The data of Fig. 8 were obtained by directly adding in-phase and quadrature test outputs from each frequency. Prior to addition, the support signals were rotated until they were 180° out of phase and sized until they were equal in amplitude. The remaining flaw information has more sensitivity of phase angle to flaw depth than does the data of Fig. 6, but possesses reduced amplitude sensitivity to shallow defects.

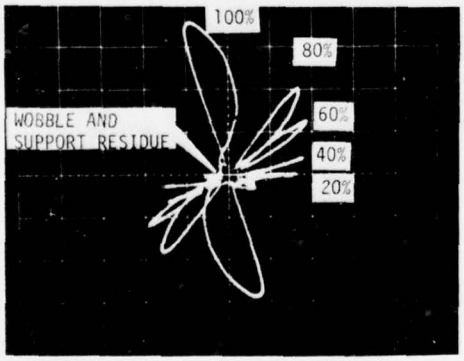

Fig. 8. Tube support discrimination with a two-frequency (200 and 400 kHz) test.

Magnetic Deposit Thickness Detection -- A two-frequency eddy current test was successfully used at Battelle to measure the thickness of an oxide containing a small percentage of magnetite which had been deposited on a base metal. A direct contact probe was used, and a frequency of 1 MHz was used to measure liftoff between probe and base metal. This relatively high frequency was chosen because its limited penetration into the base metal would eliminate metal thickness information from the output. A second test at a frequency of 2 kHz was used to detect permeability of the oxide while remaining insensitive to the presence of the base metal. This information was then used to correct the 1 MHz data against the influence of permeability, resulting in an output which contained pure liftoff or oxide thickness information.

A block diagram of this test is shown in Fig. 9 , and the results from inspecting a calibration sample are shown in Fig. 10 . An accuracy of ± 0.0006 in. was obtained over an oxide thickness range of 0.0 to 0.010 in.

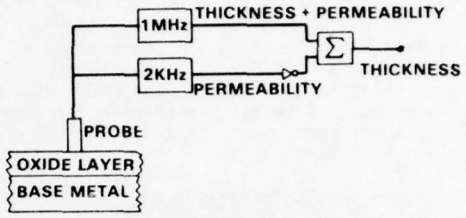

Fig. 9. A two-frequency test for thickness measurement of a magnetic oxide layer

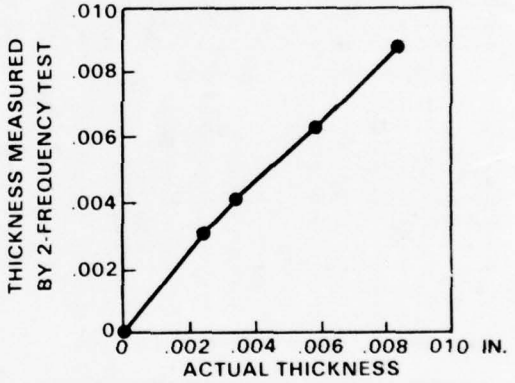

Fig. 10. Response of two-frequency test for thickness of magnetic oxide on metal

Dimensional Gaging of Tubing -- A two-frequency test has been demonstrated for measuring ID, OD and wall thickness in nonferrous tubing. The technique is easier to implement than its ultrasonic counterpart because there is no need for a water bath or other couplant to facilitate transferring energy into the part. It is, however, not quite as accurate as ultrasonic techniques, which can measure tubing dimensions with typical accuracy of 0.0001 in.

A block diagram of the test is shown in Fig. 11. A pair of diametrically opposed point probes was simultaneously excited with a high and a low frequency. The high frequency was chosen such that only shallow penetration of the tube wall occurred, while the low frequency was selected so that the nominal wall thickness was equal to one penetration depth. The high frequency tests were

used to measure liftoff. Both their outputs were subtracted from an adjustable offset constant to obtain a measure of the OD. The two low frequency outputs were processed to obtain liftoff-free measurements of wall thickness. These two values were summed together to obtain total wall thickness; this sum was then subtracted from the OD to obtain ID dimensions. The addition and subtraction was performed in real time with analog arithmetic circuitry.

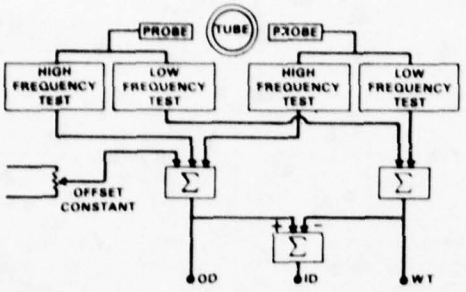

Fig. 11. Implementation of a two-frequency dimensional gaging test for tubing

MULTIFREQUENCY DATA ACQUISITION INSTRUMENTS

The basic approach in multifrequency data acquisition is to parallel an additional electronic channel onto the probe system for each additional frequency. The two main design differences between a single frequency system and a multifrequency system are: 1) the probe driver is usually a summing device which sums together sinusoids from all test frequencies, and 2) each output of the instrument must be generated in such a manner that it responds only to its particular test frequency while remaining insensitive to other frequencies.

This second requirement may be met in a variety of ways. One approach is to employ bandpass filtering for each frequency prior to detection of the amplitude coefficients. A second approach uses sequential commutation or multiplexing of individual test frequencies onto the probe system so that only one frequency at a time is present on the probes. A third method uses either analog or digital means to precisely multiply the composite probe signal by sine and cosine waves of each test frequency, followed by low pass filtering, to obtain individual amplitude coefficients. A fourth method, used in a Walsh function scheme by Battelle as described in References 1 and 2, employs simple synchronous detectors driven by square wave reference signals. Individual outputs are rendered free of amplitude coefficients from the other test frequencies by either:

a) requiring all test frequencies to be related to each other by an even integer, or

b) permitting test frequencies to be related by both even and odd integers and then combining the detector outputs in a predetermined manner to eliminate unwanted amplitude coefficients from other frequencies.

This fourth method enjoys a substantially reduced parts count and can be implemented in compact instrument packages. These four methods are described briefly below.

A multifrequency system employing one type of bandpass filtering is shown in Fig. 12. Each single-frequency channel taps the composite probe signal, buffers it with preamplification, and then eliminates the other frequencies with a bandpass filter. This method suffers from the fact that the filters must be retuned each time frequencies are changed. Additionally, a great deal of phase shift can occur in the filter outputs for slight drifts in oscillator frequency or filter center frequency.

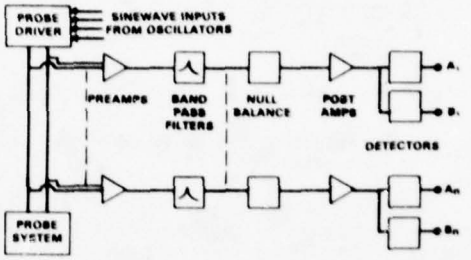

Fig. 12. A multifrequency system employing bandpass filtering

One type of multifrequency system which employs multiplexing of individual single-frequency instruments is described in Reference 4. The basic process involves using a dedicated single-frequency instrument for each test frequency; these can be off-the-shelf commercial instruments. The instruments are commutated onto the probe system one at a time in sequence. Their outputs are sampled while the probe data is being accessed and the sampled values are stored and used as system outputs. This approach is a highly expedient way to assemble an operational multifrequency system and it does not necessarily require a high degree of electronic expertise as compared to some of the other schemes. Caution must be used in multiplexing low test frequencies (1 kHz, for example) due to longer commutation times required to reach a steady state condition for sampling the data. This can force an undesirable upper limit on probe translation speed or on the rate at which probe data can change. Additionally, this approach can require substantial amounts of cabinet space to house the individual single frequency instruments.

The third method uses correlation-type phase sensitive amplitude detectors to extract amplitude coefficients of individual frequencies from a multiple-frequency waveform. This involves linear multiplication of the composite signal by sine and cosine waveforms of the test frequency to be extracted, as shown in Fig. 13. The reference sine and cosine signals must be synchronized with the test frequency and may be derived from the oscillator for that test frequency. The product of the multiplication will be a sine squared term plus a DC term. This DC term is one of the two desired amplitude coefficients and is extracted by a low pass filter. If the reference waveforms contain no harmonic distortion and the multipliers are perfectly linear, the outputs will contain no

contribution from other test frequencies in the composite waveform. In a typical analog implementation of this method, however, one can expect as much as 2% pollution of the outputs by other test frequencies. In most cases this is inconsequential.

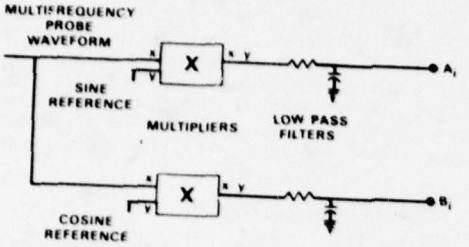

Fig. 13. Correlation type phase sensitive amplitude detection

The detection process of Fig. 13 may be implemented by either analog or digital techniques. Integrated circuit four quadrant multipliers followed by passive RC low pass filters form an analog technique suitable for some applications. This method has two main disadvantages: 1) analog multipliers are typically quite noisy devices, with some having an input noise level of 900 microvolts RMS, and 2) both a sine and a cosine reference wave must be generated for each frequency, requiring more sophisticated oscillators. In a digital implementation of the detection scheme of Fig. 13, small computers can be used to perform many of the functions in real time, including generating the probe drive and reference signals, multiplying, and averaging the product to extract amplitude coefficients. The digital probe drive signal from the computer is converted to an analog sinusoid by D/A conversion, and the probe output signal is digitized and input to the computer for processing. Computer speed determines the maximum test frequency, the maximum number of frequencies which can be used simultaneously, and the maximum translation speed of the probe.

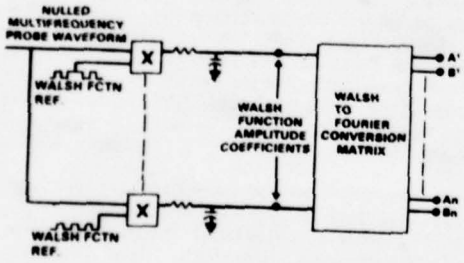

Fig. 14. A Walsh function method for implementing a multifrequency test.

Battelle has used the fourth detection method based on Walsh functions for implementing a multifrequency steam generator tubing inspection system (References 1 and 2). This method uses detectors similar to those shown in Fig. 13 except that the reference signals are binary (two state) waveforms. The gain of the multiplier is +1.0 during the reference high state, and -1.0 during the reference low state. The multiplier is a much simpler device than that required for true four-quadrant multiplication and does not inject noise into the signal. The reference signals are Walsh function waveforms synchronized to the test frequencies. Walsh functions (Reference 5) are a series of orthogonal binary waveforms. Some are 50% duty cycle square waves; the balance have additional state changes during a period.

A block diagram of the Walsh function scheme is shown in Fig. 14. The outputs of the detectors are amplitude coefficients of Walsh functions contained in the composite waveform. As the Walsh amplitude coefficients can be made up of Fourier amplitude coefficients from more than one frequency, they are input to an analog arithmetic matrix which converts from Walsh to Fourier amplitude coefficients. The main advantage of this approach is simplification of the circuitry. A four-frequency system (100, 200, 300 and 400 kHz) was fabricated onto two circuit boards in the prototype instrument shown in Fig. 15. This approach would work equally well for Rademacher functions, which are all 50% duty cycle square waves.

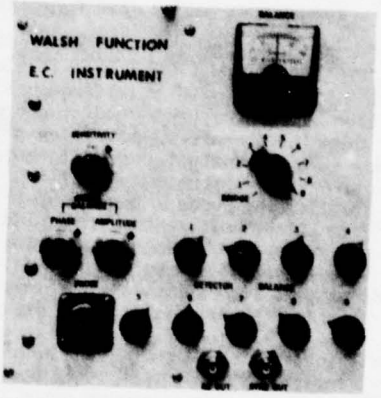

Fig. 15. A prototype four frequency eddy current instrument using Walsh function detectors

MULTIFREQUENCY DATA PROCESSING

In its simplest sense, the elimination of unwanted test parameters by processing of multifrequency data is equivalent to simultaneous solution of multiple equations. Linear combinations of output channels are performed in real time by analog arithmetic circuits. An example of this is shown in Fig. 16 where three signals containing information on three parameters are reduced to two signals which are both free of the parameter Z. This configuration could be used directly for eliminating probe wobble signals from a tubing test.

The probe wobble locus defined by any pair of outputs in a tubing test will usually plot as a straight line and can be eliminated by the simple technique shown in Fig. 16 . For more complex signals such as the figure-eight pattern from a support plate, a more sophisticated approach is required. One of these is shown in Fig. 17. The support indications from two different

frequencies are rotated and sized until they are 180° out of phase and equal in amplitude. The in-phase and quadrature components are then summed to produce two support-free output signals.

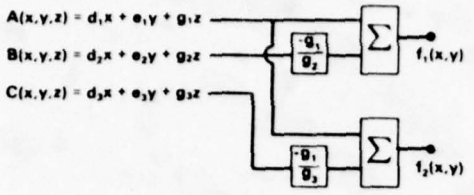

Fig. 16. Simplistic treatment of parameter elimination

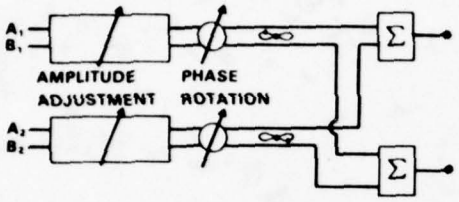

Fig. 17. Two-frequency data processing method for elimination of parameters having complex output indications

A third approach for eliminating unwanted parameters treats the signals from a perspective of N-dimensional vector space. A plane in the vector space is located which totally contains the unwanted indication. An output channel is then derived which is perpendicular to this plane and which thereby contains none of the unwanted information. This process can be implemented using a multiplicity of phase rotators of the type commonly used in commercial single-frequency instruments. A phase rotator is a four-terminal device with inputs X and Y and outputs X' and Y', and has a transfer characteristic of:

$$X' = X \cos \theta - Y \sin \theta$$

$$Y' = Y \cos \theta + X \sin \theta$$

where θ is the desired rotation angle.

A configuration of phase rotators used in the Battelle system for processing two-frequency data is shown in Fig. 18. Rotators 1, 2 and 3 are used to obtain three wobble-free indications from the four wobble-prone inputs. For tube support discrimination, rotators 4 and 5 are adjusted to obtain a two-dimensional X-Y presentation in which the plane of the figure-eight support indication is parallel to the discarded Z axis. The support indication thus appears as a straight line in an X-Y plot of these two outputs. Rotator 6 is then used to place the support line all into one of the final output channels, leaving the other one free of support information. A response of this type is shown in Fig. 7.

Some care is required in selecting the final combination of signals for a given test requirement.

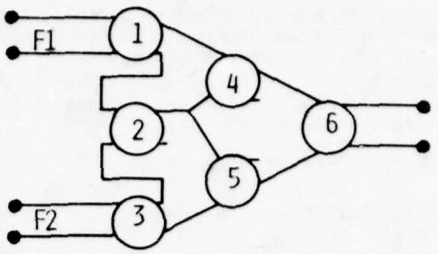

Fig. 18. A multifrequency data processing method using a multiplicity of phase rotators

There may be a variety of combinations which will eliminate an unwanted parameter, but only a few of these may provide meaningful or independent information. For example, in the arrangement of Fig. 16, outputs A and C could also be combined to achieve a third output, f_3, which is free of parameter Z. However, these three outputs will not necessarily all contain independent information on the desired specimen parameters. They must be examined in turn to determine which of them provide the desired information. Computer optimization techniques are somewhat useful in making these selections.

FREQUENCY SELECTION

The skin effect phenomenon, which predicts amplitude and phase distribution versus depth of eddy currents flowing in a conductor, is undoubtedly the most useful criterion in selecting test frequencies. The general objective in frequency selection is to obtain frequencies which have independent information on specimen parameters so that cancellation of one parameter does not result in cancellation of other desired parameters. The skin effect plays an important role in obtaining independent information from properly selected frequencies.

A generalized approach to frequency selection is:

1. Select a frequency range in which the skin effect provides independent information on wanted and unwanted specimen parameters.

2. Select frequencies in this range for which: A) the indications from unwanted parameters are similar enough for good cancellation, and B) the information remaining after cancellation contains meaningful information on other specimen parameters.

In many cases the separation between individual frequencies should be held to as small as 2:1. For example, in the previously described test for steam generator tubing, it was found that a frequency separation greater than 2:1 would not produce support plate indications that could be effectively cancelled. Frequencies of 200 kHz and 400 kHz were thus used for support cancellation. The support indication from the 100-kHz test

evidenced enough dissimilarities from that of the 400-kHz test to the point that these two frequencies did not produce effective cancellation of the support. This was attributed to the greater penetration depth of the 100-kHz eddy currents in the tube wall material, resulting in support indications being manifested at greater distances between the probe and the support region.

CONCLUSIONS

Continuous wave multifrequency eddy current inspection provides an extremely powerful assist in certain areas of material characterization. It provides the ability to eliminate or reduce unwanted parameters that may otherwise mask desired test information. Continuous wave testing offers an advantage over pulsed techniques in that individual frequencies may be matched to the particular test requirements. The responses from individual frequencies may be observed directly during the test development and frequency selection process. Continuous wave multifrequency testing may be implemented in a variety of ways, ranging from multiplexing of commercial single-frequency instruments to assembly of compact portable instruments or to fully computerized implementations.

REFERENCES

1. T.J. Davis, Multifrequency Eddy Current System for Steam Generator Tubing Inspection. Vol. I, Progress Summary. EPRI NP-758, Research Report Center, Electric Power Research Institute, P.O. Box 10090, Palo Alto, CA 94303.

2. T.J. Davis, "A Multifrequency Eddy Current System for Inspection of Steam Generator Tubing." BN-SA-842, presented for the Second International Conference on Nondestructive Evaluation in the Nuclear Industry, Salt Lake City, UT, February 13-15, 1978. (Co-sponsored by ASM).

3. S.D. Brown and E.R. Reinhart, "An Evaluation of PWR Steam Generator Tubing Inspection Methods." Presented at the Second International Conference on Nondestructive Evaluation in the Nuclear Industry, Salt Lake City, UT, February 13-15, 1978. (Co-sponsored by ASM).

4. W.R. Junker, "A Four Frequency Eddy Current Instrument." Presented at the Second International Conference on Nondestructive Evaluation in the Nuclear Industry, Salt Lake City, UT, February 13-15, 1978. (Co-sponsored by ASM).

5. N.M. Blachman, "Sinusoids Versus Walsh Functions." Proceedings of the IEEE. 62(3):346-354, March 1974.

A COMPARISON OF MULTIPLE FREQUENCY AND PULSED EDDY CURRENT TECHNIQUES

W. E. Deeds
Department of Physics, The University of Tennessee
Knoxville, Tennessee 37916

ABSTRACT

In principle, the same information should be obtainable from either pulsed or multiple frequency eddy current techniques, provided they utilize comparable frequency ranges. In practice, there are important differences and advantages for each method. Pulse instrmentation is generally cheaper, simpler, and less sophisticated. On the other hand, there has been greater development of theory and instrumentation using sinusoidal eddy currents, so that the quipment is generally more quantitative at present.

The basic problem of determining certain paramenters when others may also be varying can be solved by measuring enough quantities to eliminate the unwanted variables, for example, by measuring the pulse response at various time delays or the sinusoidal response at various frequencies. In practice, the number of useful frequencies is strictly limited. Little additional information is obtainable from frequencies for which the skin depth is much greater or much less than the thickness of the sample. Since the frequencies must be spaced to permit separation by filters, this puts a practical limit of about four on the number of frequencies useful for a given problem. This is not a serious limitation, since one can measure two quantities for each frequency and the total number of pertinent parameters rarely exceeds six. Pulse equipment can more readily handle a wide range of frequencies, but the instrmentation tends to become more elaborate, especially if high frequencies are needed for a particular application, and the repetition rate becomes low if low frequencies are necessary. The reproducibility of pulses is a problem which can be circumvented by the use of bridge techniques, differential coils and other standard techniques.

New computer programs and microprocessor equipment have been developed which now make it possible to set up tests and measure parameters directly and precisely without the lengthy optimization calculations once necessary, though the latter will continue to be useful for the design of optimized coils and experiments.

Actually, most of my experience has been with sinusoidal eddy currents, and until recently I have considered pulse methods to be relatively inaccurate. But recent advances in integrated circuits, microprocessors and memory chips have made it possible to acquire, store and process digital data in ways which may make pulsed eddy currents preferable for many applications.

Computers have revolutionized eddy current testing in two stages. First, large scale computers have made it possible to make accurate calculations of boundary value problems and optimize the testing conditions. New microcomputers have made feasible much more sophisticated equipment and data processing for either multifrequency or pulsed eddy currents.

According to the Fourier theorem, data taken in either the time or the frequency domain should be equivalent, though many bits of data might be needed to make a good transformation from one to the other. Sinusoidal eddy currents (a δ-function in the frequency domain) correspond to an infinitely broad "pulse" in the time domain, whereas a δ-function pulse in the time domain corresponds to a white spectrum in the frequency domain. Though theoretically equivalent, there are a number of practical differences between the two methods.

Sinusoidal excitation is easier to treat theoretically, whereas pulses generally lead to integral transforms. Therefore, the theory of sinusoidal eddy currents is more highly developed. However, the number of fixed frequencies that can provide useful information is limited to about four. The reasons for this are that little additional information can be obrained from frequencies for which the skin depth is much greater or much less than the thickness of the sample and the useful frequencies must be fairly widely spaced because sharp-cutting filters introduce problems of maintaining phase and amplitude information. The result is that multiple frequencies cannot usually provide more than about eight useful bits of information in a given test (for exampie, the magnitude and phase at each of the four frequencies). Fortunately there are seldom this many parameters to be determined or eliminated in a given test, so the limitation is not serious.

Pulse equipment can be simpler and, with a few exceptions, has been less highly developed than multifrequency equipment. However, a sharp pulse contains a wide range of frequencies and can easily provide multifrequency information. In the past, the reproducibility of pulses has been more of a problem than with steady-state devices, but it can be handled by the use of bridge techniques, differential coils and improved integrated circuits.

Inspection speed is somewhat more limited with pulses, since the pulse must be essentially complete before the probe moves to the next inspection region.

There are several ways to use pulsed eddy currents. The earliest was the pulse-echo technique. This does not work well because eddy currents obey essentially a diffusion equation, not a wave equiation. Hence, the wave form is not preserved, and one does not get sharp, distinct "echoes." Rather, there are simple variations in the build-up or decay of the signal. A good analogy would be to try to measure subterranean properties by measuring the surface temperature of the earth when it is struck with a pulse of solar radiation. The corresponding sinusoidal analogy would be to measure the phase and amplitude of the surface temperature relative to the (assumed sinusoidal) excitation. Mathematically, the solutions to a diffusion equation are real exponentials, not the oscillatory solutions of a wave equation.

Disregarding the pulse-echo technique then, should one work in the time or the frequency domain? Using frequency information from pulses generally involved analyzing the pulse into Fourier components, probably using Walsh filters, to obtain the same sort of data as in the multifrequency method, except that a very wide frequency range can be covered with one pulse without the necessity of special tuning for a particular application. Working in the time domain is womewhat simpler, since fast analog-to-digital converts and sophisticated pattern recognition techniques have been developed. Also, modern microcomputers have made polynomial curve fitting practical and extremely accurate.

At Oak Ridge National Laboratory C. V. Dodd and I have developed a number of new computer programs to optimize multifrequency eddy current tests, take data, perform least squares fitting of data to properties with a minicomputer and then calculate the properties of unknown samples on a real-time basis using an eddy current instrument with an on-board microcomputer. We are also developing pulsed instrumentation using similar techniques.

DISCUSSION

William Lord, Chairman (Colorado State University): At this time the floor is open for questions of any of the three speakers. I would like to remind you to give your name and affiliation if you have a question.

Wolfgang Sachse (Cornell University): The previous speaker mentioned that pulse eddy current measurements were not reproducible. I am not an expert--in fact, I don't know very much about eddy currents at all--but the question I have is, "Why is that so? What is the cause of this irreproducibility?"

W.E. Deeds (University of Tennessee): Well, as I said, I am not an expert on pulses or experimental things either, but it is my impression that you get heating of the sample and of the coil. If you look on an oscilloscope, you will see jitter. It is just electronic noise as far as I am concerned, but it is associated with heating effects and things like that.

Robert E. Green, Jr. (Johns Hopkins): I don't know much about eddy current either, but I have had trouble using eddy currents with heating effects. Could you, or anyone, comment on how you may eliminate heating effects?

W.E. Deeds: We have spent a lot of time on that. In the computer programs for designing coils it is possible to design the circuit components in such a way as to eliminate drift. You're quire right, differential coils, differential amplifiers, etc., mounted on the same heat sink can help. There are a lot of ways of doing it, but in general, you have to design the circuit to either compensate or eliminate drift.

Don Thompson (Science Center): Could any one of you give an overall assessment of what quantitative capability has been successfully demonstrated with eddy current techniques, whether they be pulsed or multifrequency?

W.E. Deeds: Well, let's see. I think just before I came here I was supposed to be getting a statistical sample of our three frequency measurements on tubing, but the only thing I recall were two frequency measurements on aluminum sheet and it seems to me that we separated the errors into three different categories. One was how reproducible the calculations were; another was how well they fit the actual data and what was the other one? There was a third one which I don't recall. I would say generally that thickness determination in the range of 70 or so mils would be better than a mil. I would say generally dimensional determinations would be of the order of a percent.

Don Thompson: I meant the question from a slightly different point of view. What is the capability of deducing, as we have been trying in the ultrasonic areas, to determine the quantitative characteristics of a flaw?

W.E. Deeds: The two-frequency apparatus is the only one that we have really made flaw measurements on so far, but as I recall, the flaw measurements were good to about 10 percent and the depths were good to roughly about 10 percent too. I hope we can do better than that, but at least we were happy to even do it.

THE APPLICATION OF FINITE ELEMENT METHOD ANALYSIS TO EDDY CURRENT NDE

T.G. Kincaid, M.V.K. Chari
General Electric Company
Schenectady, N.Y. 12345

ABSTRACT

The Finite Element Method for the computation of eddy current fields is presented. The method is described for geometries with a one component eddy current field. The use of the method for the calculation of the impedance of eddy current sensors in the vicinity of defects is shown. An example is given of the method applied to a C-magnet type sensor positioned over a crack in a plane conducting material.

INTRODUCTION

Eddy current NDE techniques detect defects in a conducting material by using a sensor which induces currents in the material, and then observing the changes in the impedance of the sensor in the vicinity of the defect. The theoretical analysis of the relation between the defect properties and the impedance change requires the solution of Maxwell's equations to determine the current fields in the material. For most practical problems, the geometry is too difficult for closed form analytic solutions, and numerical solutions are required.

The most promising numerical technique for computation of eddy current fields is the Finite Element Method. This method has long been used in stress analysis and heat flow problems (Ref. 1), and in recent years has been applied to the computation of eddy current fields in electrical machines (Ref. 2). The method has also been used to investigate a problem in magnetostatic NDE (Ref. 3), but has not been applied to eddy current NDE, which is a time varying field problem.

In this paper, the Finite Element Method for the computation of eddy current fields is presented. The method is described for geometries with one component eddy current field, for which the problem reduces to the solution of the two-dimensional diffusion equation. The use of the method for the calculation of the impedance of eddy current sensors is explained. An application of the technique to the case of a C-magnet type sensor over a crack in a plane conducting material is shown.

Derivation of the Diffusion Equation for One-Component Vector Potentials

In eddy current testing, the frequencies are usually low enough that the displacement current term in Maxwell's equations is negligible. Under this assumption, Maxwell's equations become

$$\nabla \times E = -\partial B/\partial t \tag{1}$$

$$\nabla \times H = J_e + J_s \tag{2}$$

where E is the electric field intensity, H is the magnetic field intensity, B is the magnetic flux density, J_e is the eddy current density, and J_s is the source current density.

The associated constituent relations are

$$B = \mu H \tag{3}$$

$$J_e = \sigma E \tag{4}$$

where μ is the permeability, and σ the conductivity of the medium. These parameters are assumed constant.

The magnetic vector potential A is defined by

$$B = \nabla \times A \tag{5}$$

Substituting Eqn. (5) into Eqn. (1) and using the fact that the electric scalar potential is zero in the one component vector potential case

$$E = -\partial A/\partial t \tag{6}$$

Combining Eqns. (4) and (6) gives

$$J_e = -\sigma \frac{\partial A}{\partial t} \tag{7}$$

which shows that the eddy current and magnetic potential vectors are in the same direction. Thus, the eddy current will also have only one component.

Then, substituting Eqns. (3),(5) and (7) into Eqn. (2) gives

$$(1/\mu)\ (\nabla \times \nabla \times A) = -\sigma\ (\partial A/\partial t) + J_s \tag{8}$$

For the sinusoidal steady state with angular frequency ω this becomes

$$(1/\mu)(\nabla \times \nabla \times A) = -j\omega\sigma A + J_s \tag{9}$$

Using the well-known vector identity

$$\nabla \times \nabla \times A = \nabla(\nabla \cdot A) - \nabla^2 A$$

and the fact that for one component vector potential fields

$$\nabla \cdot A = 0$$

Eqn. (9) becomes

$$(1/\mu)\ \nabla^2 A - j\omega\sigma A = -J_s \tag{10}$$

which is the linear diffusion equation for the sinusoidal steady state. The magnetic vector potential A can then be found by solving Eqn. (10) with the appropriate boundary conditions.

Finite Element Formulation for One Component Vector Potentials

For problems in which A has only a z component which varies only in x and y, an approximate solution to Eqn. (10) can be found by formulating the vector potential in variational terms by an energy functional, and minimizing the functional with respect to a convenient set of trial functions. The required energy functional is

$$\mathcal{F} = \int_S \{(1/2\mu)|\nabla A|^2 + j(\omega\sigma/2)A^2 - J_s \cdot A\} ds \qquad (11)$$

The minimization of the above functional yields the solution to Eqn. (10) with natural boundary conditions, provided that its Euler equation is identical to Eqn. (10). The Euler equation of a two-dimensional energy functional is given by (Ref. 5)

$$\frac{\partial}{\partial x}\left(\frac{\partial F}{\partial A_x}\right) + \frac{\partial}{\partial y}\left(\frac{\partial F}{\partial A_y}\right) - \frac{\partial F}{\partial A} = 0 \qquad (12)$$

where A_x and A_y are partial derivatives of A along the x and y axes, and F is the integrand of $\mathcal{F}$. Substituting the integrand of $\mathcal{F}$ in Eqn. (11) for F in Eqn. (12) gives

$$\frac{\partial}{\partial x}\left(\frac{1}{\mu}\frac{\partial A}{\partial x}\right) + \frac{\partial}{\partial y}\left(\frac{1}{\mu}\frac{\partial A}{\partial y}\right) - j\omega\sigma A + J_s = 0 \qquad (13)$$

Equation (13) is identical to Eqn. (10) since $1/\mu$ is constant. So minimization of the energy functional $\mathcal{F}$ of Eqn. (11) yields the solution to the problem.

In finite element analysis, the minimization of the functional $\mathcal{F}$ is carried out with respect to a set of functions defined as follows. The two-dimensional region of interest is divided into triangles, ensuring that the triangle edges coincide with the material interfaces and boundaries. The permeability and conductivity are assumed to be constant in each triangular region. The set of functions is constrained to be first order polynomials in each triangle, whose value at any point within the triangle is a linear interpolation of the vertex values. Thus,

$$A(x,y) = \frac{1}{2\Delta} \sum_{i=\ell,m,n} (a_i + b_i x + c_i) A_i \qquad (14)$$

where ℓ, m, n are the vertices of the triangle, Δ is the area of the triangle, and a, b, c are geometrical constants defined by the relations

$$\begin{aligned} a_\ell &= x_m y_n - y_m x_n \\ b_\ell &= y_m - y_n \\ c_\ell &= x_m - x_n \end{aligned} \qquad (15)$$

and similarly for m and n.

Substituting for A from Eqn. (14) into Eqn. (11) and setting the derivative with respect to each nodal potential A_ℓ, A_m, A_n to zero for a minimum gives a set of 3 equations in these variables for the triangle under consideration. Repeating the process for every triangle in the two-dimensional region, a set of simultaneous equations in the nodal potentials is obtained, which can be expressed in matrix notation as

$$[S][A] + j\omega[T][A] = [J] \qquad (16)$$

where [A] is the column vector of vertex values of A, and [S] and [J] are rectangular matrices whose entries are evaluated from the geometrical coordinates of the triangle vertices, and from the triangle permeabilities μ and conductivities σ respectively.

Calculation of Sensor Impedance

Since eddy current testing depends upon the change in impedance of a sensor in the vicinity of a defect, it is necessary to calculate the impedance of the sensor from the vector potential.

The resistance R of the coil is computed in terms of the average power dissipated P and the sensor driving current I from the equation

$$R = P/|I|^2 \qquad (17)$$

The average power dissipated is given by the equation

$$\begin{aligned} P &= (1/2)\int_V (1/\sigma)\, J \cdot J^* \, dv \\ &= (\omega^2/2)\int_V \sigma\, A \cdot A^* \, dv \end{aligned} \qquad (18)$$

The second equality is derived by substituting from Eqn. (4) for J, and then using Eqn. (7) to eliminate E. Substituting Eqn. (18) into Eqn. (17) gives

$$R = (\omega^2/2)\int_V \sigma\, A \cdot A^* \, dv/|I|^2 \qquad (19)$$

Similarly, the reactance X can be computed in terms of the average magnetic energy W_m stored in the volume as

$$X = 2\omega\, W_m/|I|^2 \qquad (20)$$

The average magnetic energy stored is

$$\begin{aligned} W_m &= (1/4)\int_V (1/\mu)\, B \cdot B^* \, dv \\ &= (1/4)\int_V A \cdot J^* \, dv \end{aligned} \qquad (21)$$

The second equality is derived by substituting from Eqn. (5) for B, and then using Eqn. (10) to derive the result. Substituting Eqn. (21) into Eqn. (20) gives for the reactance

$$X = (\omega/2)\int_V A \cdot J^* \, dv/|I|^2 = \omega L \qquad (22)$$

where L is the inductance of the coil.

Scaling of Solutions

A useful property of vector potential is that the field which solves Eqn. (10) is also the solution for all geometries which differ from the original only by a dimensional scale factor 1/k, provided the following scalings are made:

-All fields are dimensionally scaled by 1/k
-The frequency ω is scaled by k^2
-The source current density amplitude is scaled by k^2

These scalings will result in the following scalings to derived quantities:

-The magnetic flux density amplitude is scaled by k
-The sensor resistance is scaled by k and inductance by 1/k

This scaling property is useful because the calculations for one geometry apply to all dimensionally scaled geometries, so a "universal" solution is obtained for each geometry. Thus, the results of experiments performed in geometries of experimentally convenient size can be scaled to less convenient geometries.

The proof is outlines as follows: let A(x,y,z) be a solution to Eqn. (10). Introduce the dimensional scaling transformation

$$x = kx', \; y = ky', \; z = kz' \tag{23}$$

For $k < 1$, the geometry is enlarged by 1/k, and for $k > 1$, the geometry is shrunk by 1/k. Substituting the dimensional scaling transformation into Eqn. (8) multiplying both sides by k^2 and defining $A'(x',y',z')=A(kx',ky',kz')$ and $J_s'(x',y',z')=J_s(kx',ky',kz')$ gives

$$(1/\mu)\,(\nabla x \nabla x A') + jk^2\omega\sigma A' = k^2 J_s' \tag{24}$$

Thus, the first assertion is proved, since A' is just a dimensionally scaled version of A.

Now, note that

$$\begin{aligned} B'(x',y',z') &= \nabla x A'(x',y',z') \\ &= k[\nabla x A(kx',ky',kz')] \\ &= k\,B(x,y,z). \end{aligned} \tag{25}$$

The driving current density J_s is scaled in amplitude by k^2 and in area by $1/k^2$. so the driving current I will remain constant.

$$\begin{aligned} R' &= \omega^2 \int_{V'} A' \cdot A'^{*}\, dv'/|I|^2 \\ &= k^4\omega^2 \int_V A \cdot A^{*}\,(1/k^3)\, dv/|I|^2 = kR \end{aligned} \tag{26}$$

The new inductance is, from Eqn. (22)

$$\begin{aligned} L' &= \int_V A' \cdot J_s'^{*}\, dv'/|I|^2 \\ &= \int_V A \cdot k^2 J_s\,(1/k^3)\, dv/|I|^2 = (1/k)\,L. \end{aligned} \tag{27}$$

Example

As an example of the use of the FEM analysis applied to a specific problem, consider the test configuration shown in Figs. 1a and 1b. This is a cross section of a C-magnet position over a slot (i.e., simulated crack) in an aluminum block. The driving current conductors, magnet, slot, and block are infinite in extent both into and out of the page, so the theory described above applies to this example.

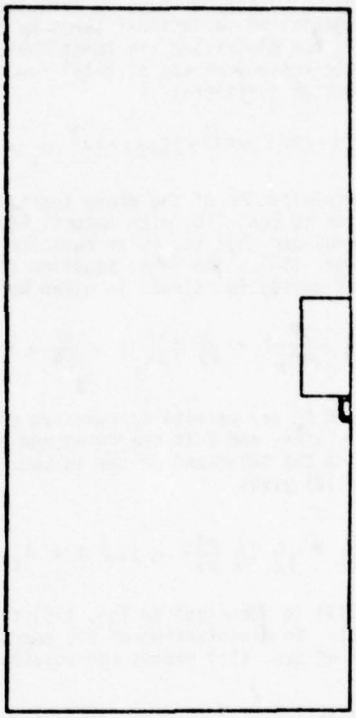

Fig. 1a. Test configuration showing boundary of Finite Element Analysis Region.

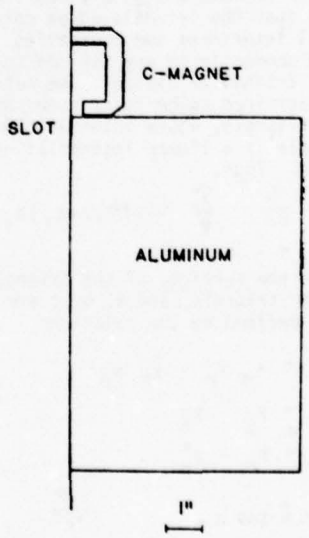

Fig. 1b. Detail of test configuration.

The division of the region shown in Fig. 1a into triangles, as required for FEM analysis, is shown in Fig. 2a. The blowup of Fig. 2b shows how much smaller triangles are used where the field variations are expected to be the greatest.

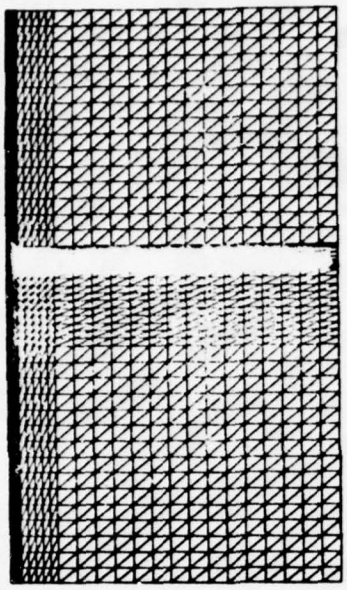

Fig. 2a. Division of Finite Element Analysis region into triangles.

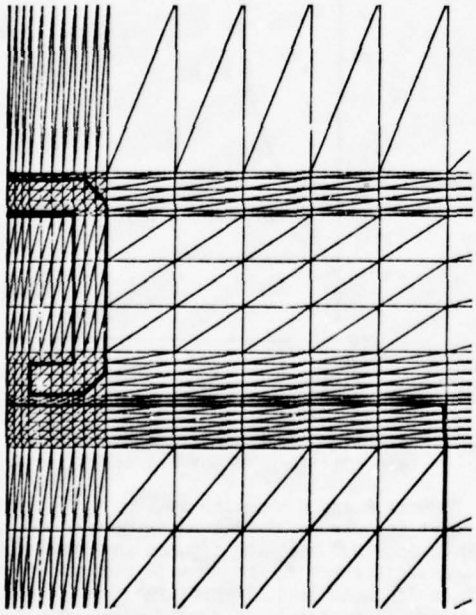

Fig. 2b. Detail of triangles in vicinity of C-magnet.

The contours of the magnitude of the magnetic vector potential A are shown in Fig. 3 for 1000 Hz. The direction of A is always perpendicular to the page. It can be shown that these contours are also the boundaries of tubes of magnetic flux Φ, where

$$\Phi = \int_S B \cdot da \qquad (28)$$

Each flux tube contains the same amount of flux.

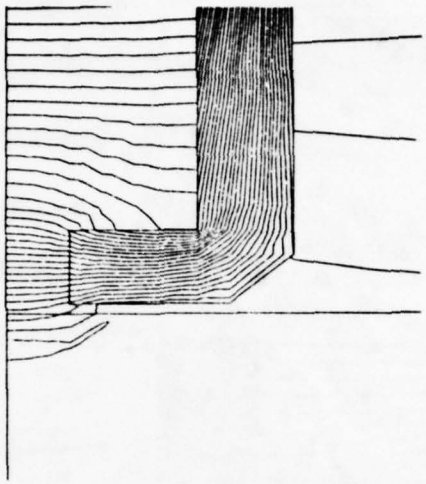

Fig. 3. Contours of the magnitude of A for no slot at 1000 Hz.

The contours of the real part of the eddy current density J_e are shown in Fig. 4 for 1000 Hz. The maximum of current is at the top surface, with the amplitude falling into the material, as expected. The closed contours below the surface indicate a local minima since the real part is an exponentially decaying cosine, emphasizing that eddy currents are a propagation wave phenomenon. Figures 5 and 6 are the same as 3 and 4 respectively, except the slot has been introduced. These figures show that the fields are changed little by the presence of the slot, as would be expected for currents parallel to the slot.

For purposes of eddy current testing, the most important feature of the FEM analysis is the ability to compute the impedance at the terminals of the sensor for various slot configurations and test frequencies. It is customary in the eddy current testing literature (Ref. 6) to plot a normalized impedance diagram for the particular test configuration, as shown in Fig. 7 for the example described here. The sensor resistance and reactance are normalized to ωL_o, the reactance of the sensor by itself. This graph has the familiar comma shape shown in the literature.

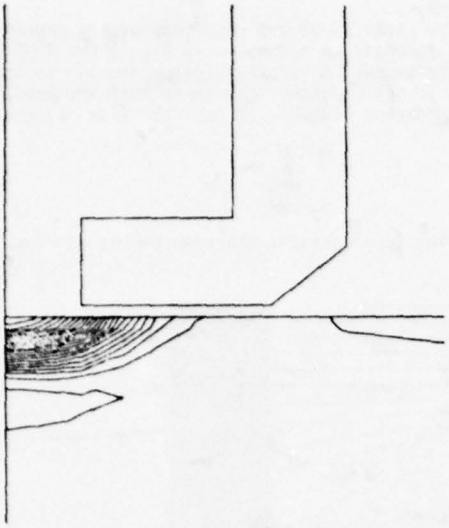

Fig. 4. Contours of the real part of J_e for no slot at 1000 Hz.

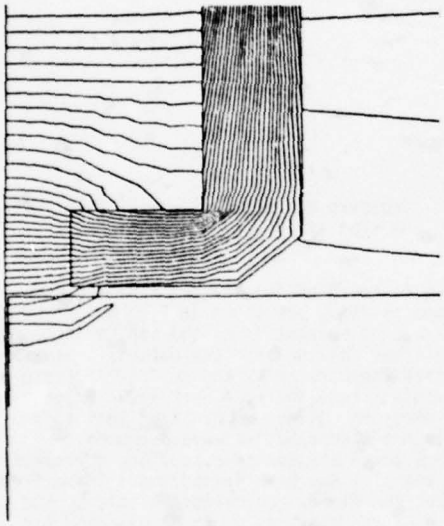

Fig. 5. Contours of the magnitude of A for a .01" x .55" slot at 1000 Hz.

In actual testing situations, the inspector uses an oscilloscope presentation of a small region of this diagram about the point on the curve corresponding to the operating frequency. He then notes the deflection of this point as the sensor is moved in the vicinity of a defect.

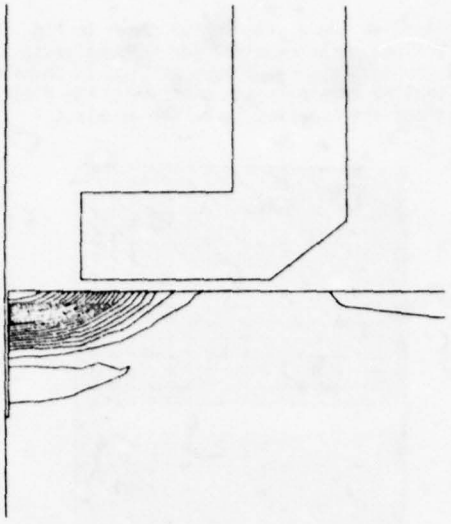

Fig. 6. Contours of the real part of J_e for a .01" x .55" slot at 1000 Hz.

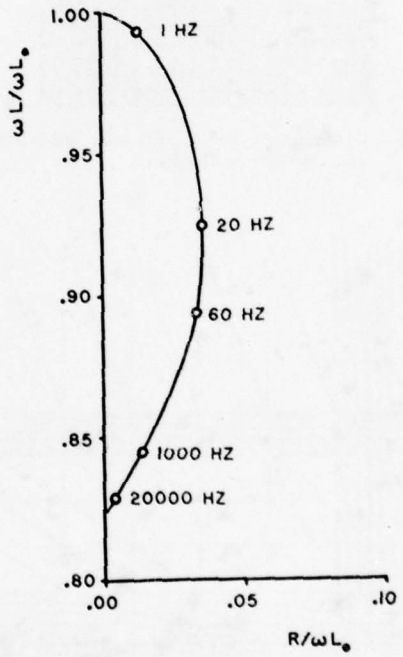

Fig. 7. Normalized Impedance Diagram for the test configuration of Fig. 1.

Figures 8 and 9 show the maximum deflection of the point for various depths and widths of the slot at 60 Hz and 1000 Hz. The figures show that the motion is different for changes in slot width and depth, which means that information about these parameters is contained in the impedance diagram, and could be extracted. By using the information at different frequencies, it may be possible to extract many slot parameters.

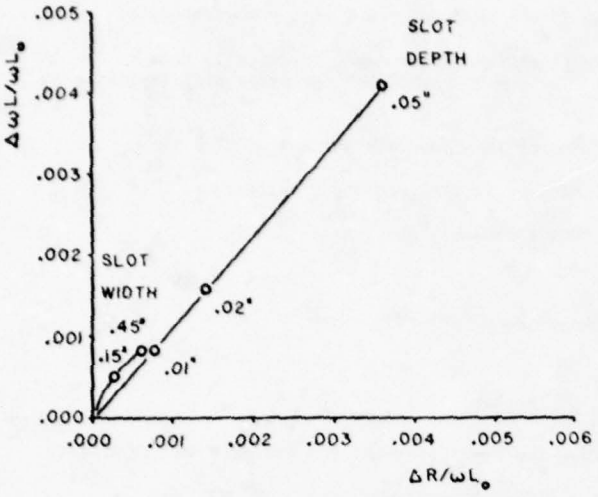

Fig. 8. Maximum deflection on the Impedance diagram for various slot depths and widths at 60 Hz.

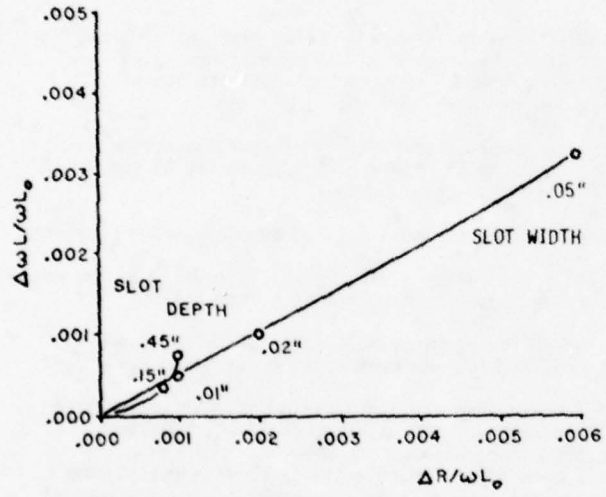

Fig. 9. Maximum deflection on the impedance diagram for various slot depths and widths at 1000 Hz.

CONCLUSIONS

The Finite Element Method for the calculation of the impedance of eddy current sensors in the vicinity of defects has been shown for one-component eddy current fields. The method can be used to calculate the impedance changes for changes in defect parameters without requiring special geometries for the solution of Maxwell's equations. Future work in this area will extend the Finite Element Method to three-dimensional geometries, removing the geometrical constraints on the impedance calculations.

ACKNOWLEDGMENT

This research was sponsored by the Center for Advanced NDE, operated by the Science Center, Rockwell International, for the Defense Advanced Research Projects and the Air Force Materials Laboratory under Contract F33615-74-C-5180.

REFERENCES

1. O.C. Zienkiewicz, The Finite Element Method in Engineering Science, McGraw-Hill, London, 1971.

2. M.V.K. Chari, "Finite-Element Solution of the Eddy-current Problem in Magnetic Structures", IEEE Trans. Vol. PAS-93, No. 1, 1973.

3. W. Lord and J.H. Hwang, "Numerical Techniques Applied to Magnetic Leakage Field Methods of Non-destructive Testing", Int. Conf. on Numerical Methods in Electrical and Magnetic Field Problems, Santa Margheritz, Italy, June, 1976.

4. P. Silvester, "High-order polynomial triangular finite elements for potential problems", Int. J. Engrg. Science, Vol. 7, pp. 849-861, 1969.

5. F.B. Hildebrand, Methods of Applied Mathematics, Englewood Cliffs, N.J.: Prentice Hall, 1965.

6. Metals Handbook, 8th Edition, Vol. 11, Nondestructive Inspection and Quality Control, American Society for Metals.

DISCUSSION

Bruce Thompson (Science Center): What is the restriction on the shape of flaws that you can handle?

T.G. Kincaid (General Electric): Providing I can make my triangle small enough, practically none. I'm free to make those flaws any size I want as long as they can be bounded by the sides of triangles.

Bruce Thompson: How small, practically speaking, in terms of the computational analysis?

T.G. Kincaid: Oh, you're asking me how many triangles I can put in that region, I think.

Bruce Thompson: I didn't phrase it quite that way, but that's probably about it.

T.G. Kincaid: Ask Chari to answer that one.

M.U.K. Chari (General Electric): Are you referring to the shape of a flaw?

Bruce Thompson: Yes.

M.U.K. Chari: There is absolutely no restriction in two dimensions.

Ellis L. Foster (Battelle- Columbus): I would like to know the application of the analysis to composites.

T. G. Kincaid: Please define composites. Everybody has a different word for that.

Ellis L. Foster: Fibrous composites, for example, with an organic matrix with a conducting fiber.

T.G. Kincaid: It is conducting?

Ellis L. Foster: Yes.

T.G. Kincaid: I can't tell you the answer to that unless we know the problem. If we have the problem, i.e., the geometry, we can say, "Yes, we can plug it into the computer," and perhaps by trying different frequencies or different sensor configurations, come to some sort of optimization of what would be appropriate for the particular problem you're interested in.

Gerald C. Gardner: Could you distinguish for us, in not too complicated terms, what the distinction is between the fine elements which you used to numerically calculate the apparent impedance of the test coil and the technique which Professor Deeds' computer program uses?

T.G. Kincaid: I think you're referring to Professor Deeds' statement about solving boundary value problems.

Gerald C. Gardner: Yes, I understand he has a program for numerically solving Maxwell's equations, the net effect of which is to produce a numerical answer for the apparent impedance of a test coil.

W.E. Deeds: This is also called the relaxation method, which is, perhaps, more familiar to some people. There is no real limitation except the size of the computer and how much computer time you can afford.

William Lord, Chairman (Colorado State University): If I could just add one other point. The relaxation technique merely models the finite difference representation of the possible different equations, whereas the finite element method is an energy functional approach to the problem. One can argue all day about the relative merits of the two approaches. The triangle is more useful in many respects in modeling the geometries and also there is some hope that one can apply finite development methods to nonlinear types of problems where the materials are ferromagnetic.

W.E. Deeds: If I may argue with you--

William Lord, Chairman: As I said, one could argue all day.

W.E. Deeds: There is a differential equation that you can approximate with a finite difference equation. It is entirely arbitrary whether you use triangles, squares, rectangles, hexagons, or whatever. It is just whatever you happen to prefer and any differential equation can be solved by this method. It is just a matter of how you set up your finite difference equation.

William Lord, Chairman: There is some excellent literature on this very topic in the electrical machines literature. The battle has raged for about a decade and I would refer you, if you are interested, to the I.E.E.E. transactions on par apparatus systems. It is some very good background material. Thank you.

SURFACE FLAW DETECTION WITH FERROMAGNETIC RESONANCE PROBES

B. A. Auld, G. Elston, and D. K. Winslow
Ginzton Laboratory
Stanford University
Stanford, California 94305

and

C. Fortunko
Rockwell International Science Center
Thousand Oaks, California 91360

ABSTRACT

Small ferromagnetic resonators have been shown to provide effective electromagnetic detectors for surface flaws in magnetic and nonmagnetic metals. As such a resonator is moved along the surface of a test piece it experiences a frequency shift when it passes over a flaw. Two detection mechanisms are present: (1) an eddy current effect (2) a perturbation of the dc magnetic bias field used to tune the resonator. Results are given for experiments performed on machined slots in aluminum, titanium and steel and on tightly closed fatigue cracks in titanium. Results are also presented for some measurements on titanium aircraft fasteners.

INTRODUCTION

This paper is concerned with reporting progress made during the past year on ferromagnetic resonance probes for NDE, first reported at the Cornell Meeting last year. The program during this period has been a joint effort involving Stanford, where the focus has been on developing two concepts and performing preliminary experiments on various probe geometrics, and the Rockwell Science Center, where attention has been directed to test sample preparation and the development of more sophisticated electronics.

The basic geometry is illustrated in Fig. 1 which shows a spherical sample of ferromagnetic crystal, yttrium iron garnet (YIG) or gallium-doped YIG, placed in a dc magnetic bias field and excited with a single-turn coupling loop containing H_{dc} in its plane. It is the extreme simplicity of the structure that makes it attractive compared to a conventional eddy current probe and the rigidness of construction that gives it an advantage over a Hall probe for dc NDE applications (flux leakage and magnetic particle techniques). Resonance of the YIG sphere takes the form of a procession of its magnetic dipole moment about the dc magnetic field as shown in the figure. The resonant frequency is controlled by the strength of the dc field and lies typically above 2 GHz. At these frequencies the skin depth in a good conductor is of the order of microns, much smaller than the flaw dimensions. This means that the eddy currents do not flow in depth around the surface flaw, as in conventional eddy currents, but enter its interior from the surface. An advantage of the feature is that it concentrates the current at the flaw. The probe is a detector of surface topography, the frequency of the resonator being perturbed by the changes in the surface current pattern as they flow into the flaw. One of the purposes of the present research is to develop a theory relating detection signal and flaw dimensions in this type of eddy current system. The presence of the magnetic bias field in Fig. 1, and its frequency-determining character, account for the dc mode of flaw detection with a ferromagnetic resonance probe. If the test piece shown is a magnetic material, the dc field at the resonator will change and this will cause a shift in resonant frequency. Our initial experiments were performed on long machined slots in aluminum, as shown, but more recently a series of measurements have been made on EDM notches in titanium and steel and on tightly closed fatigue cracks in titanium.

THEORY

It is clear from Fig. 1 that a number of different probe configurations are possible depending on the orientation of the dc field - tangential or normal to the surface, parallel or perpendicular to the slot. A general theory for all geometries has been developed under support of the NSF Thrust Program on Nondestructive Evaluation at Stanford.[1] The basis of this theory is the Lorentz reciprocity relation in its form applicable to gyromagnetic media.[2]

$$\nabla \cdot (\mathbf{H}_1 \times \hat{\mathbf{E}}_2 - \hat{\mathbf{H}}_2 \times \mathbf{E}_1) = 0 \qquad (1)$$

where subscripts 1 and 2 indicate two solutions to the field equations and the carat indicates that the magnetic bias field is reversed. This relation is integrated over the volume enclosed by a surface around the test piece, a surface enclosing the signal generator and a closure surface at infinity. In the vicinity of the resonator and the flaw the microwave magnetic field is represented by the quasistatic approximation, using a scalar potential ϕ. This differs from the theory of conventional eddy current testing, where a vector potential is used, but it is standard in ferromagnetic response theory and poses no problems at microwave frequencies, where the currents are confined to the surface of the test piece and flaw. After performing the manipulations described in Ref. 1, one arrives at the following relation for the changes in resonator frequency and Q due to the presence of a flaw

$$\frac{\delta\omega_o}{\omega_o} - \frac{i\delta Q_o}{2Q_o^2} = - \frac{\int_{S_F} \mu_o \phi_1 (\partial \hat{\phi}_2 / \partial n)\, ds}{2V} \,. \qquad (2)$$

where S_F is the surface opening of the flaw, the 1 and 2 potentials are in the absence and presence

of the flaw, respectively, the carat indicates reversed bias field, and V is the stored energy in the resonator.

Equation (2) is an exact expression but, because of the complication of the geometry, it is necessary to use approximations in evaluating the potentials ϕ_1 and ϕ_2. From an electromagnetic point of view a small slot of finite length is a waveguide below cutoff, and certain characteristics of the system can be deduced directly from this fact. That is to say, the depth of a flaw can be determined only if it is less than the decay distance of the least cut-off mode. On the basis of an approximate wave theory one finds that the detectors limit for a deep slot, with 10-to-1 length-to-width ration, is of the order of 0.002 inch, when using a 15 mil diameter YIG probe. For the long slot test geometry shown in Fig. 1, the length of the slot is not a relevant parameter, because the probe fields are concentrated only in its vicinity, Fig. 2b, and the slot can be considered to be of infinite length. In this case, it is appropriate to express the potentials ϕ_1 and ϕ_2 as Fourier integrals along the z direction. Since the potential $\hat{\phi}_2$ within the slot is a solution to Laplace's equation, each component of the spatial Fourier spectrum is of the form

$$\hat{\phi}_2(k) = A(k)\, e^{ky} e^{-ikz} \qquad (3)$$

This shows that the higher spatial frequency components decay more rapidly with flaw depth, indicating that the spatial frequency content of the probe field should be carefully chosen to optimize the sensitivity to depth - which is the critical parameter in a surface flaw. Because of the normal derivative of the second factor in Eq. (2), the k-dependence of the detection sensitivity goes as $kA^2(k)$. Figure 2(b) shows that the quantity passes through a maximum as a function of k. In order to measure the depth of a relatively deep flaw, it is necessary that most of the spectral energy be concentrated at low values of k and, as shown in Fig. 2, this feature is realized by using a spatially extended probe. From this general type of reasoning one may conclude that, in detecting a long slot with a spherical YIG probe, variations in depth do not become observable until it is less than the probe diameter. This effect will be noted in the experimental results of the next section. It should be noted in passing that the quasi-static potential approximation does not apply for all values of k down to zero in Fig. 2. However, the interesting structure of the curves occurs for k's of the order of (probe diameter)$^{-1}$, or 100 cm^{-1}, while the quasi-static approximation breaks down for k's of the order of (EM wavelength/10)$^{-1}$, or 1 cm^{-1}.

All of our experiments to date have been performed with the one-port resonator system shown in Fig. 1. However, the electronics being developed at Rockwell Science Center is aimed at a two-port resonator circuit because of its advantages for separating changes in resonator frequency and Q. The theory for this case has also been treated in Ref. 1. Within either context the probe may be operated either passively, as a resonator whose reflection or transmission characteristics may be observed by sweeping either frequency or field and observing the resonance line on a scope, or actively, as a YIG-tuned oscillator. In the latter case, the minimum detectable frequency shift, and, consequently, the minimum detectable flaw size is reduced by the narrower spectral width of the active system.

MEASUREMENTS ON LONG MACHINED SLOTS IN ALUMINUM

The first series of measurements were made in the geometry[3] using the passive probe illustrated in Fig. 3 where the YIG sphere is seen as the black dot at the center of the aperture in the base. The resonator is protected by a layer of plastic tape, which also serves to define the lift-off distance. Orientation of the dc magnetic field, produced by samarium cobalt bars (the dark strips on either side of the resonator), is tangential to the surface. The resonator is pure YIG and operates at 3.6 GHz. Figures 4 and 5 show measured frequency shifts as a function of slot width and depth. Note that the depth begins to affect the frequency shift only below 10-20 mils, that is, at depths comparable to the 15 mil diameter of the YIG sphere.

The same series of slots were measured with an active probe consisting of a standard negative resistance type of YIG oscillator (Fig. 6), again with tangential field. This is not the optimum circuit design for the application but has the advantage of being easily constructed as a direct copy of existing devices. The experimental results in Figs. 7 and 8 show the same general type of depth behavior as the passive probe. It is evident that the frequency shifts are large, even compared with the natural resonance width (≈3 MHz) of the passive system. Measurements on more realistic models are reported below.

MEASUREMENTS ON EDM SLOTS AND TIGHT FATIGUE CRACKS IN TITANIUM

These samples, which were fabricated by Murray Mahoney at the Science Center, were tested at Stanford - the EDM slots by Elston and the tight fatigue cracks by Elston and Fortunko. The notable features of these results (Fig. 9) are that shifts are very large for the slots and that the shift for the tight cracks is in the opposite sense (position) to that for the open slots. The latter effect is to be investigated by opening the crack under load. It is also noteworthy that the first and fifth entries in the upper table indicate a distinct depth sensitivity, which is more pronounced in the perpendicular field configuration. The tight cracks were also tested with the passive probe, giving comparable results.

MEASUREMENTS OF EDM SLOTS IN MAGNETIC STEEL

The previous tangentially-magnetized probes cannot be used on magnetic test pieces because the high permeability path across the magnet poles pulls the field away from the YIG resonator and destroys the resonance. In this case it is necessary to use the normal field geometry shown in Fig. 10. Figure 11 illustrates one of two similar probes of this type. The miniature co-axial feed line passes through a hole drilled in the samarium cobalt magnet and the YIG resonator, seen as a black dot in the photo, is mounted on a straight wire or half-loop coupler. Figure 12 shows a spring-loaded micrometer controlled scan mount for this type of probe. Using the arrangement, the measurements shown in Fig. 13 were taken. By

shielding the microwave currents from the steel sample by means of an aluminum film of thickness greater than a skin depth, it was determined that the observed frequency shift was almost entirely due to the shift in dc magnetic field due to the pressure of the flaw. This phenomenon appears to offer great promise as a method for performing magnetic particle detection in a quantitative manner. YIG probes do not suffer from the mechanical fragility of Hall field probes. Figure 14 shows a calibrated series of lift-off and displacement measurements on steel using the arrangement in Fig. 12, giving an indication of the stability of the device. Some preliminary tests have been made with this probe on tight cracks in steel, provided by Phil Hodgetts of Rockwell International, Los Angeles Division. These have not yet been detected and further work is needed to reduce the resonance line width of the normal field probe which is not yet as good as for the tangential field probe.

AIRPLANE FASTENERS

Some initial measurements have also been made on flaws in titanium airplane fasteners, provided by K. J. Law. The longitudinal seam type of flaw (Fig. 15) was easily detected. They were estimated to be 8-10 mils wide and 5 mils deep and gave frequency shifts in the range of 6 to 9 MHz. The shear head cracks were not detected because a pronounced step at the crack edge made it impossible to traverse the crack with the type of mounting arrangement used. It is not, apparently, a difficult problem to solve but further study of mounting and scanning techniques will be required.

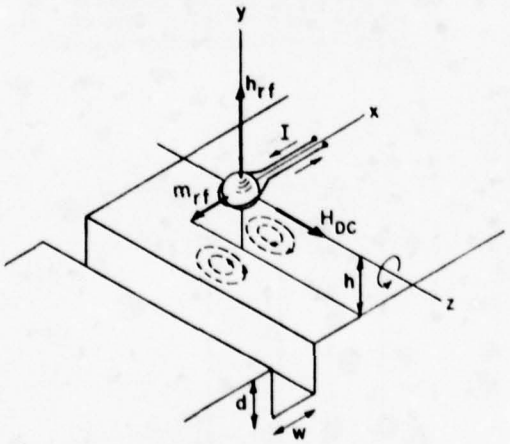

Fig. 1 Ferromagnetic resonator configuration featuring in-plan dc magnetic bias and rf coupling loop.

CONCLUSION

It has been demonstrated that the YIG ferromagnetic resonance probe is capable of easily detecting flaws of practical interest. Nevertheless, the work to date is still very exploratory in nature and more detailed calibration and comparison with theory will be required to accurately establish the limits. More complete measurements on loaded and unloaded fatigue cracks, as well as on fabricated slots of dimensions smaller than the probe will be required for this purpose. In addition, the theory needs to be extended to allow for the effects of material and contact losses in cracks and to explain the difference in behavior of open and closed cracks. Further parameters to be investigated are the influence of oscillator noise and lift-off fluctuations on the ultimate detection sensitivity and the effect of probe geometry on depth detection capability.

REFERENCES

1. B. A. Auld, "Theory of Ferromagnetic Resonance Probes for Surface Cracks in Metals", GL Report 2839, July 1978, Ginzton Laboratory, Stanford University, Stanford, Calif.
2. R. F. Harrington and A. T. Villeneuve, "Reciprocity Relationships for Gyrotropic Media," IRE Trans AATT-6, PP308-310 (1958).
3. B. A. Auld, G. Elston and D. K. Winslow, "A Novel Microwave Ferromagnetic Resonance Probe for Eddy Current Detection of Surface Flaws in Metals," to appear in the Proceedings of the 8th European Microwave Conference, Paris, September 1978.

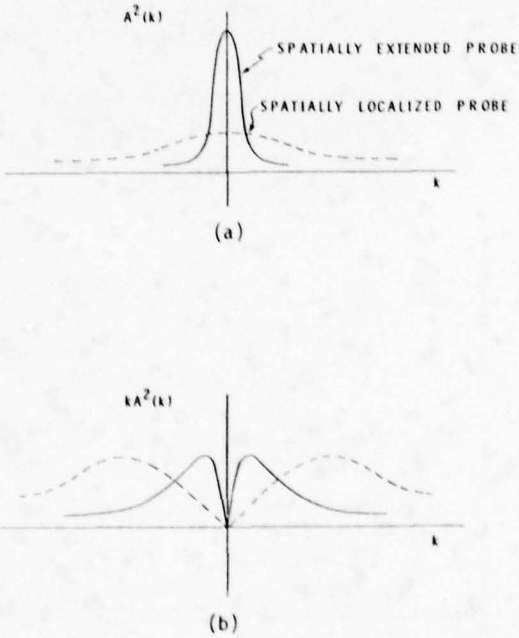

Fig. 2 (a) Spatial Fourier eddy current distribution spectra for an extended and localized ferromagnetic probe.
(b) Relative depth sensitivity functional for above.

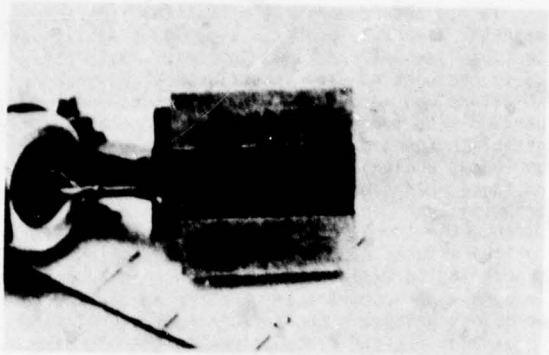

Fig. 3 Passive YIG probe with tangential dc magnetic field bias viewed from the bottom.

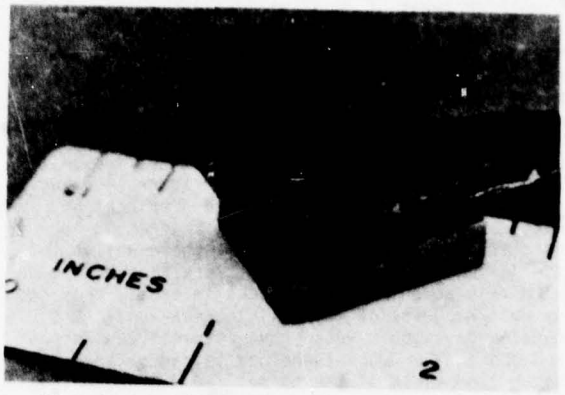

Fig. 6 Negative resistance active YIG probe viewed from the top.

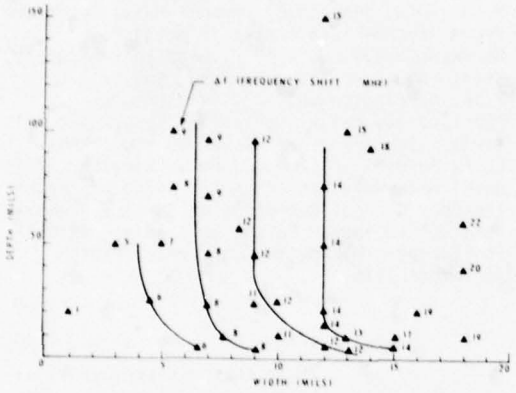

Fig. 4 Measurements of cracks in aluminum samples using passive probe with field tangential to surface and parallel to face of crack. Operating frequency was 3600 MHz.

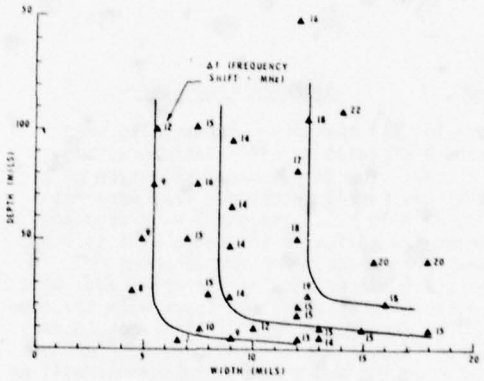

Fig. 7 Measurements of cracks in aluminum samples using active (YIG oscillator TOR) probe with field tangential to surface and parallel to face of crack operating frequency was 1900 MHz.

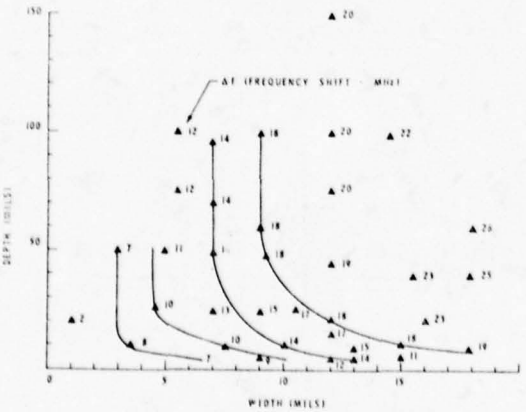

Fig. 5 Measurements of cracks in aluminum samples using passive probe with field tangential to surface and perpendicular to face of crack. Operating frequency was 3600 MHz.

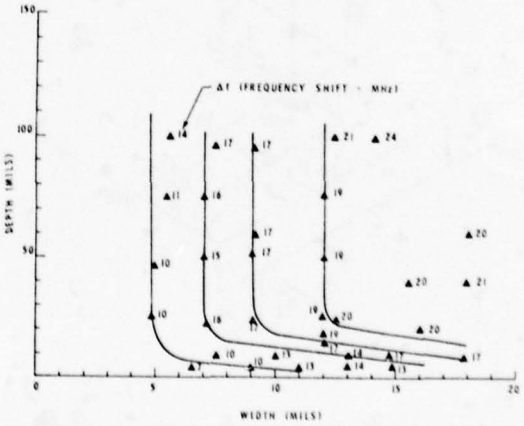

Fig. 8 Measurements of cracks in aluminum samples using active (YIG oscillator TOR) probe with field tangential to surface and perpendicular to face of crack. Operating frequency was 1900 MHz.

TITANIUM SAMPLES (CRACK WIDTH ~ 10 mils)			
CRACK LENGTH(mils)	CRACK DEPTH (mils)	FREQUENCY SHIFT WITH FIELD PERPENDICULAR TO FACE OF CRACK (MHz)	FREQUENCY SHIFT WITH FIELD PARALLEL TO FACE OF CRACK (MHz)
105	24	26	20
57	25	25	21
29	25	16	13
19	23	15	11
99	18	22	18

CLOSED CRACKS (WIDTH ~ 0 mils)

DEPTH (mils)	LENGTH (mils)	FREQUENCY SHIFT WITH FIELD PERPENDICULAR TO FACE OF CRACK (MHz)
55	169	3
46	133	2

Fig. 9 "Open" crack measurements taken using passive probe operating at 3600 MHz. "Closed" cracks measured using active (YIG oscillator) probe operating at 1900 MHz. Field is tangential to surface in both probes.

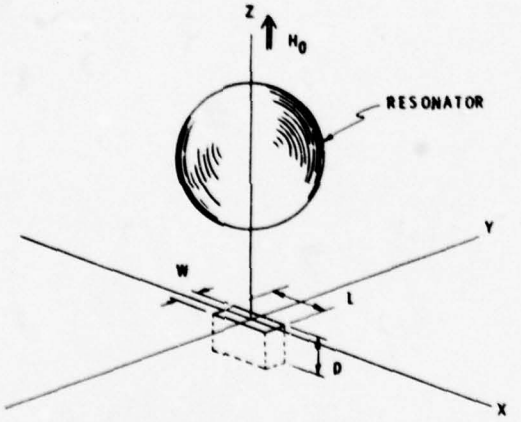

Fig. 10 Detection of an open crack using a spherical ferromagnetic resonator with normal DC magnetic field bias.

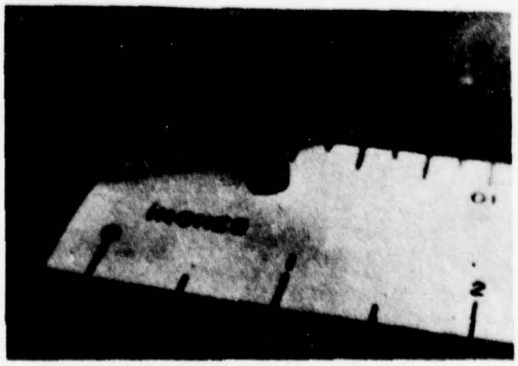

Fig. 11 Detail of the miniaturized probe with normal DC magnetic field bias.

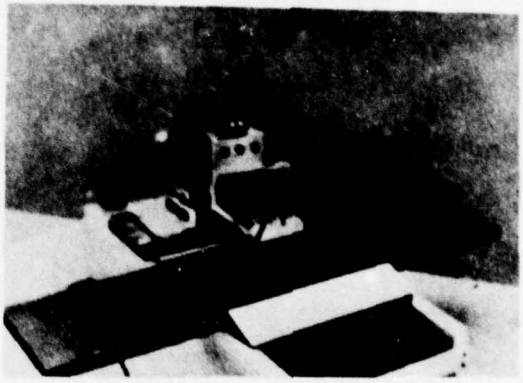

Fig. 12 Spring loaded scan mount for YIG probes.

STEEL SAMPLE (CRACK WIDTH ~ 5 mils)

CRACK DEPTH (MILS)	CRACK LENGTH(MILS)	FREQUENCY SHIFT (MHz)
8	25	27
10	25	28
13	26	27
18	26	27
23	26	27
8	307	27
10	152	27
9	92	28
10	41	28
9	15	15

Fig. 13 Data from steel sample using passive point probe with field normal to surface at a frequency of 1900 MHz.

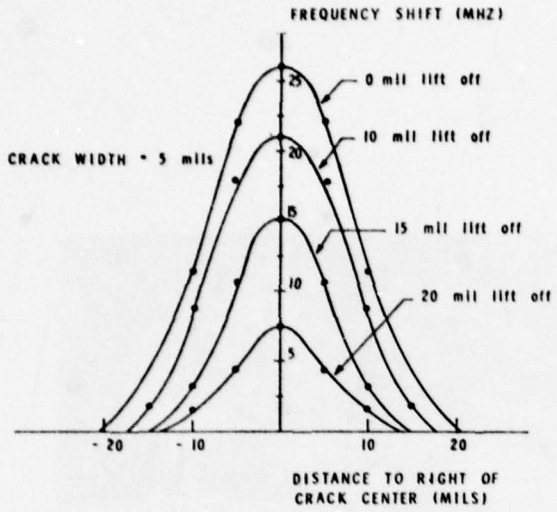

Fig. 14 Frequency shift over steel as a function of lift-off and distance from the crack. Field is normal to surface. Operating frequency was 2200 MHz. Data was taken using the miniaturized probe shown in Fig. 11 .

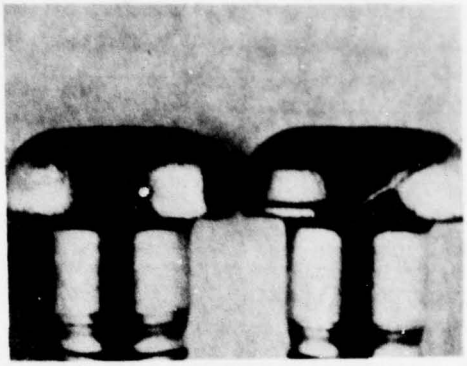

Fig. 15 Longitudinal seam type flaw in titanium airplane fasteners.

DISCUSSION

Tom Moran (AFML): What would be the natural line width of the apparatus?

B. A. Auld (Stanford University): If you use a good, uniform field, the line width is less than an oersted.

Tom Moran: What was the measured line width?

B. A. Auld: To give you an example, and I see Chris Fortunko has his hand up (he may give you a better answer than I), the last probe that we measured had a 12 megahertz line width. On the other hand the first probe I showed, the 3600 gigahertz probe with two magnets on the sides, had a width of three oersted, which is, maybe, not more than a factor of two above that of the material. You raise a good point. You must be careful of the magnetic field.

Don Forney (AFML): Bert, what would your YIG sphere see if you brought it next to the surface of a magnetized steel part where the strength of the field varied from point to point?

B. A. Auld: It would move it around a great deal. The frequency would shift. Roughly, it would shift about three megahertz for every oersted change in the field. So it would be very, very sensitive to these changes in the field.

Don Forney: Perhaps you might have a device that could measure variation in field strength from point to point that might do a better job than a Hall device. Is that a fair statement?

B. A. Auld: It certainly could be used for that purpose. On the other hand, these YIG spheres have been around for a while and people still use all probes. I think the accuracy of a Hall probe is better.

Chris Fortunko (Science Center): I would like to point out that when you pass the YIG sphere over a non-uniform magnetic field, then the shape of the line also changes because other modes may be excited and that may be an indication of a sudden change in the magnetic field. We did see that at the Science Center when the YIG sphere was mounted on a substrate with a cobalt lead-in wire.

B. A. Auld: The lines distort and you can also see, as Chris pointed out, that the height of the line changes. Seeing Chris standing up there talking reminds me of something I forgot to say. The tightly closed fatigue cracks that Chris brought up and measured with Ellston showed that with an open crack or slot the frequency shifted down, and with a tightly closed crack it moved up. We have no idea why that happens, but it seems to be something very significant.

Robert E. Green (Johns Hopkins): That would apply to a certain type of crack that won't be detected at all.

B. A. Auld: Nature being what she is, I would believe that.

William Lord, Chairman: At this point we'd better move on to the last paper today.

QUANTITATIVE MEASUREMENT OF CRACK PARAMETERS USING MICROWAVE EDDY-CURRENT TECHNIQUES

A. J. Bahr
SRI International
Menlo Park, California 94025

ABSTRACT

The objectives of this work were to develop an electromagnetic scattering model that can be used to predict the microwave scattering from a crack in a metallic surface, and to evaluate the potential of using microwave scattering measurements to determine the dimensions of the crack. The initial approach to this problem has been to model the surface crack as a section of rectangular waveguide shorted at one end. Theoretical and experimental results are presented for this case, and the potential for obtaining a quantitative evaluation of the crack dimensions is discussed.

INTRODUCTION

In the low-frequency eddy-current testing of metals, currents are caused to flow in the test specimen by placing it in the magnetic field of an induction coil. The flow of currents is affected by the electrical properties, the shape of the test specimen, and the presence of discontinuities and defects. In turn, these currents react back on the exciting coil and affect its impedance. Thus, the presence of a defect is determined by monitoring the test coil impedance.

Such eddy-current tests are typically conducted at frequencies of less than 1 MHz when induction fields predominate and the electromagnetic wavelength is greater than 300 m. Because the wavelength of the interrogating fields determines sensitivity and resolution, the need to find and characterize smaller and smaller flaws suggests that the use of higher (microwave) frequencies may prove advantageous in eddy-current inspection. In using microwave frequencies, the radiation fields associated with the sensors become an important consideration, and the physics involved is best described in terms of fields and waves. For example, the effect of a defect should be thought of as producing a change in the scattering of electromagnetic waves from the metal surface. It should also be noted that, since the use of microwave frequencies causes the currents induced in the test object to flow essentially on the surface (i.e., the skin depth is typically less than 1 μm at 100 GHz), microwave eddy-current techniques are limited to surface inspection in metals.

The use of microwave frequencies in the range 10 to 30 GHz for the detection and characterization of thin slits and cracks in metal surfaces has been studied previously by several workers.[1,2] Their results showed that good sensitivity to small cracks could be obtained. Cracks as small as 2 μm wide and 25 μm deep were detected.[2] There was also a clear correlation between crack depth and scattered energy. In view of these encouraging results, work was initiated in SRI's Remote Measurements Laboratory to study the use of microwave eddy-current techniques at frequencies around 100 GHz. In addition, development of an electromagnetic scattering model for predicting the microwave scattering from a crack in a metallic surface was undertaken so that the potential of such measurements for determining the dimensions (particularly the depth) of a crack could be evaluated.

As a first approximation, a crack was modeled as a slot with a rectangular cross section and straight sides. This simplification permitted the development of an analytic theory for the scattering from such a slot, which in turn allowed studies of the relation between scattered power, crack dimensions, and frequency. The derivation of this analytic theory is outlined in Section II. To provide a test comparison for the theory, measurements were made of the scattering from small slots machined in an aluminum plate. These experimental results are presented in Section III, and Section IV summarizes the conclusions derived from this work.

ELECTROMAGNETIC SCATTERING FROM A RECTANGULAR SLOT

Consider a rectangular slot having length a, width b, and depth d. The geometry and coordinate system for this slot are shown in Fig. 1. The transmitted and received waves propagate in the half-space $z > 0$.

The steps that were followed in the analysis are shown in Fig. 2. The analysis is written in terms of a slot admittance, which is a parameter that depends mostly on the dimensions of the slot and on the frequency, and only slightly on the method of electromagnetic inspection.

Internal Fields--If $b/a \ll 1$, the fields in the slot can be expressed in terms of transverse electric (TE) waveguide modes having no variation in the y direction. Since the tangential electric field must be zero at the bottom of the slot, suitable expressions for the interior electric (E) and magnetic (H) fields are:[3]

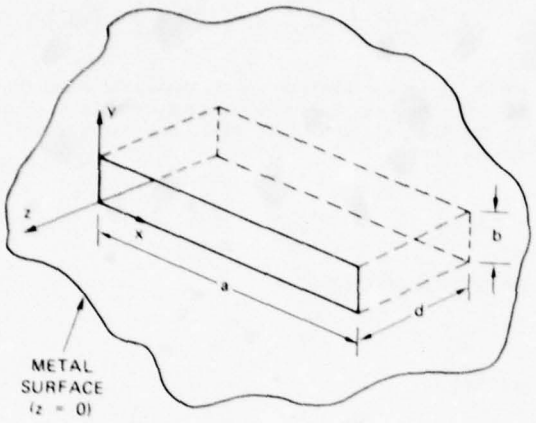

Fig. 1 Rectangular slot geometry

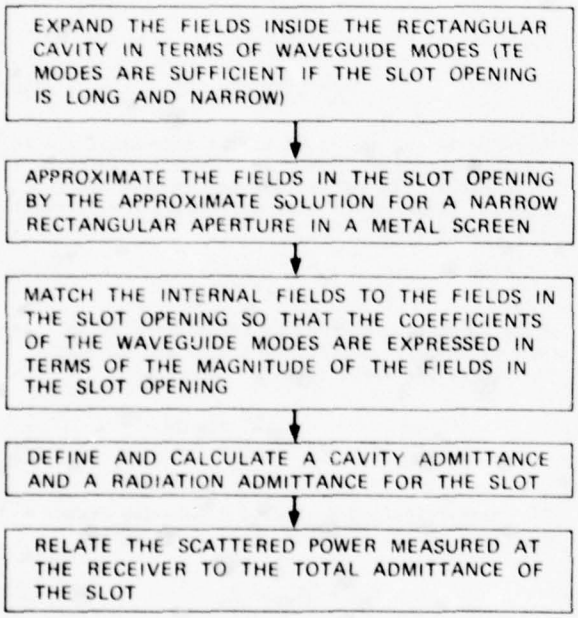

Fig. 2 Steps in the theoretical analysis of slot scattering

$$E_y(x,z,k) = \sum_{n=1}^{\infty} Q_n \sin\left(\frac{n\pi x}{a}\right) \sinh\left[\Gamma_n(z+d)\right] \tag{1}$$

$$H_x(x,z,k) = \sum_{n=1}^{\infty} -j\,\frac{\Gamma_n Q_n}{k\eta_0} \cdot \sin\left(\frac{n\pi x}{a}\right) \cosh\left[\Gamma_n(z+d)\right] \tag{2}$$

$$H_z(x,z,k) = \sum_{n=1}^{\infty} j\,\frac{Q_n}{k\eta_0} \cdot \frac{n\pi}{a} \cdot \cos\left(\frac{n\pi x}{a}\right) \sinh\left[\Gamma_n(z+d)\right] \tag{3}$$

where

$$\left(\Gamma_n a\right)^2 = (n\pi)^2 - (ka)^2 \tag{4}$$

and $k = 2\pi/\lambda$, $\eta_0 = 120\,\pi$ ohms. The quantity Q_n is an undetermined frequency-dependent amplitude coefficient.

Aperture Field--If $d/b > 1$, the distribution of electric field in the slot opening should be accurately approximated by the solution for the fields excited in a narrow aperture in a metallic screen. An approximate expression for such an aperture distribution is:[4]

$$E_y(x,z,k) = \frac{V_0}{b} \sin\left[k\left(\frac{a}{2} - \left|x - \frac{a}{2}\right|\right)\right] \tag{5}$$

where V_0 is an undetermined frequency-independent amplitude coefficient.

Amplitude Coefficients--By equating Equations (1) and (5), and by using the orthogonality properties of the trigonometric functions, one finds that for n odd,

$$Q_n = 4\,\frac{V_0}{b}\,(-1)^{\frac{n-1}{2}}\,\frac{ka\cos(ka/2)}{\left(\Gamma_n a\right)^2 \sinh\left(\Gamma_n d\right)}\,, \tag{6a}$$

and for n even,

$$Q_n = 0\,. \tag{6b}$$

Cavity Admittance--As is shown in Appendix A, a cavity admittance can be defined for the slot by the expression

$$Y_c = \frac{j\,\mathrm{Im}\int_0^a dx \int_0^b dy \left(\vec{E} \times \vec{H}^*\right)_{z=0-} \cdot \vec{a}_z}{|V|^2} \tag{7}$$

where the definition of voltage

$$V = -V_0\left(\frac{ka}{4}\right)\left(\frac{\sin\frac{ka}{4}}{\frac{ka}{4}}\right)^2 \tag{8}$$

is consistent with (5) and plane-wave excitation. Substituting (1) and (2) into (7) gives

$$|V|^2 Y_c = j\,\mathrm{Im}\left\{\frac{ab}{2jk\eta_0} \cdot \sum_{n=1}^{\infty} \Gamma_n^*\, Q_n Q_n^*\, \sinh\left(\Gamma_n d\right) \cosh\left(\Gamma_n^* d\right)\right\}\,. \tag{9}$$

Finally, substituting (6) and (8) into (9) and truncating the series at three terms gives

$$Y_c = -j \frac{1}{2} \frac{a}{b} \frac{1}{\eta_0} \frac{(ka)^3 \cos^2 (ka/2)}{\sin^4 (ka/4)} \sum_{n=1,3,5} \frac{1}{\left(\Gamma_n a\right)^3 \tanh \left(\Gamma_n d\right)} \quad . \tag{10}$$

This expression holds for the frequency range $0 < ka < 3\pi$. Note that for $ka > \pi$,

$$\left(\Gamma_1 a\right)^3 \tanh \left(\Gamma_1 d\right) = \left(\beta_1 a\right)^3 \tan \left(\beta_1 d\right) \tag{11}$$

where $\Gamma_1 = j\beta_1$.

5. Radiation Admittance--From Appendix A, the radiation admittance of the slot aperture can be written

$$\frac{1}{2}|V|^2 Y_r^* = \frac{1}{2} \int_0^a dx \int_0^b dy \left(\vec{E} \times \vec{H}^*\right)_{z=0+} \cdot \hat{a}_z \quad . \tag{12}$$

Assuming an aperture field of the form given in (5), Rhodes[5,6] has calculated this radiation admittance for the case $kb << 1$:

$$\mathrm{Re}(Y_r) = \frac{(ka)^2}{16\pi\eta_0 \sin^4 (ka/4)} \Big\{ \mathrm{Cin}\ (ka) + [\mathrm{Cin}\ (ka) - 1/2\ \mathrm{Cin}\ (2ka)] \cos ka - [\mathrm{Si}\ (ka) - 1/2\ \mathrm{Si}\ (2ka)] \sin ka \Big\} \tag{13a}$$

$$\mathrm{Im}(Y_r) = \frac{(ka)^2}{16\pi\eta_0 \sin^4 (ka/4)} \Big\{ \mathrm{Si}\ (ka) + [\mathrm{Si}\ (ka) - 1/2\ \mathrm{Si}\ (2ka)] \cos ka + [\mathrm{Cin}\ (ka) - 1/2\ \mathrm{Cin}\ (2ka) - \ell n \left(\frac{e^{3/2} a}{2b}\right)] \sin ka \Big\} \tag{13b}$$

where

$$\mathrm{Cin}\ (x) = \int_0^x \frac{1 - \cos u}{u} du \tag{14a}$$

and

$$\mathrm{Si}\ (x) = \int_0^x \frac{\sin u}{u} du \quad . \tag{14b}$$

Equation (13) differs slightly from that given by Rhodes because of the differing definitions of voltage [see Eq. (A-6a)].

Cross-Polarization Scattering Coefficient--Assume that the slot is excited by an illuminating mode designated by subscript V, and that it is desired to calculate the energy scattered into an orthogonal mode which is designated by subscript H. In Appendix B it is shown that the relevant scattering coefficient is given by the expression

$$\Gamma_{HV} = \frac{1}{4P_s} \int_0^a dx \int_0^b dy \left(\vec{E}_V \times \vec{H}_H\right) \cdot \left(-\hat{a}_z\right) \tag{15}$$

where P_s is the average power available from the source. Assuming plane-wave excitation and substituting (5) and (A-6) into (15), one obtains the result that

$$\Gamma_{HV} = - \frac{I_H V_V}{4P_s} \quad . \tag{16}$$

Since by definition,

$$V_V = I_V / Y_s \quad , \tag{17}$$

one has

$$\Gamma_{HV} = - \frac{I_H I_V}{4P_s Y_s} \quad . \tag{18}$$

For the particular case of plane-wave backscattering, the currents can be written explicitly as

$$I_H = 2H_0 a \cdot \sin \theta \tag{19a}$$

and

$$I_V = 2H_0 a \cdot \cos \theta \tag{19b}$$

where H_0 is the magnitude of the magnetic field in the incident plane wave at $z = 0$, and θ is the angle between $\vec{E}_V$ and the y axis. The incident magnetic field at the slot is related to the available power--i.e.,

$$H_0^2 = K_s P_s \tag{20}$$

where K_s must be determined by calibration, or perhaps by theory. Substituting (19) and (20) into (18) gives the final result

$$\Gamma_{HV} = - 1/2 \frac{K_s a^2 \sin 2\theta}{Y_s} \quad . \tag{21}$$

Cross-Polarized Scattered Power--The cross-polarized scattered power, P_{HV}, is given by

$$P_{HV} = |\Gamma_{HV}|^2 P_s \quad . \tag{22}$$

Substitution of (21) into (22) gives

$$P_{HV} = 1/4 \frac{K_s^2 a^4 \sin^2 2\theta}{|Y_s|^2} P_s \quad . \tag{23}$$

It is convenient to calculate the following normalized power:

$$\left(P_{HV}/P_s\right) \left(1/a^2 b^2 \eta_0^2 K_s^2 \sin^2 2\theta\right) = 1/4 \left(\frac{a}{b}\right)^2 \frac{1}{\eta_0^2 |Y_s|^2} \quad . \tag{24}$$

For the long-wavelength (Rayleigh) region ($ka \ll \pi$) $|Y_c| \gg |Y_r|$, so (24) becomes

$$\left(P_{HV}/P_s\right)\left(1/a^2b^2\eta_0^2K_s^2\sin^2 2\theta\right) \simeq \frac{\sin^8(ka/4)}{(ka/\pi)^6\cos^4(ka/2)}\tanh^2(\pi d/a) \quad . \tag{25}$$

Equation (24) is shown plotted in Fig. 3 as a function of normalized frequency, $0.35 \leq ka/\pi \leq 2.1$, for $a/b = 10$ and $0.1 \leq d/a \leq 1$. The resonant nature of the scattering is evident for $ka/\pi > 1$, particularly for the deeper slots. Resonance occurs when the net magnetic energy stored in the cavity balances the net stored electric energy outside the aperture. The difference in scattering cross section for slots of different depths is greatest in the resonance region. However, the cross section is a multivalued function of slot depth at a given frequency; consequently, a scattering measurement made at one frequency is ambiguous.

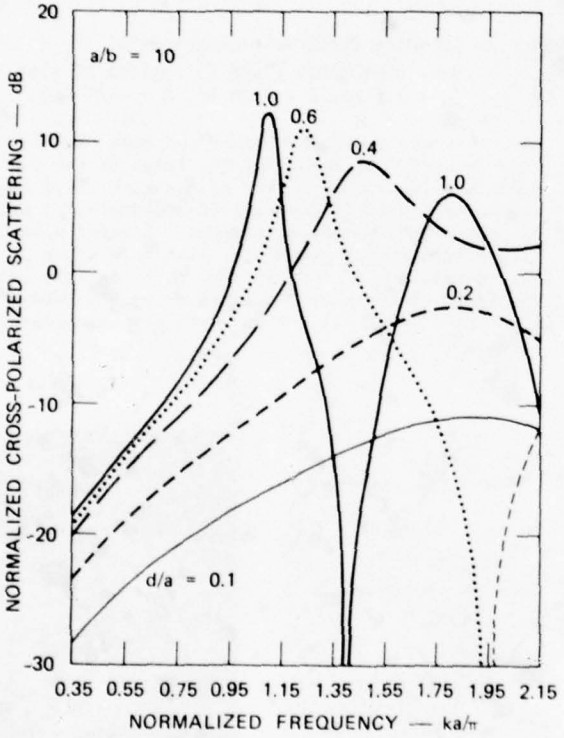

Fig. 3 Cross-polarized scattering from a rectangular slot versus frequency (Resonance region)

In the long-wavelength (Rayleigh) region, the scattering is much smaller than in the resonance region, but the scattering cross section is a monatonic function of slot depth. A plot of Eq. (25) which illustrates this behavior is shown in Fig. 4 for $0.01 \leq ka/\pi \leq 0.1$ and $0.1 \leq d/a \leq 1$. It can be seen from Fig. 4 that the scattering becomes insensitive to slot depth when the depth is about the same dimension as the slot length. This effect is a manifestation of the fact that the electromagnetic fields do not propagate inside the slot in this frequency region, and so they cannot fully penetrate a deep slot.

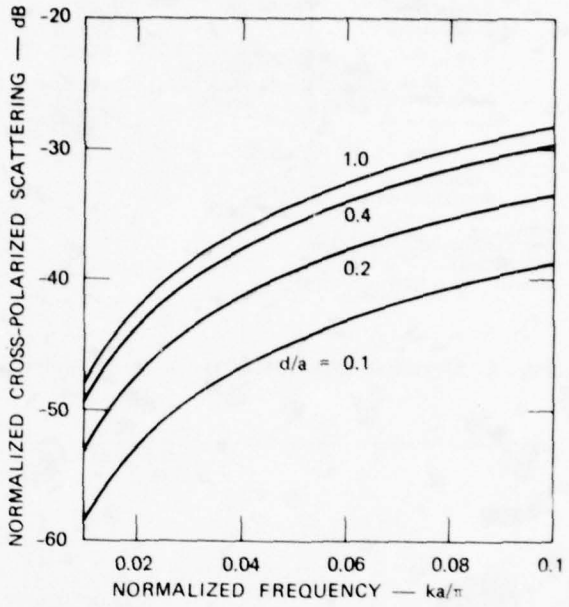

Fig. 4 Cross-polarized scattering from a rectangular slot versus frequency (Rayleigh region)

EXPERIMENT

Examination of the theory outlined in the previous section shows that if one knows the dimensions a and b of the slot cross section, and the calibration constant $\eta_0 K_s \sin 2\theta$, it should be possible to determine the slot depth, d, from a measurement of P_{HV}. This possibility was tested using the microwave-backscatter measurement system whose schematic diagram is shown in Fig. 5. This system uses an orthomode coupler to discriminate against copolarized backscatter, and a superheterodyne detection system. The IF attenuator (IF frequency = 400 MHz) permits precision measurements to be made of changes in backscattered power. The antenna used was a lens-focused horn with a beamwidth at its focal point of about 3.5 mm at the operating frequency of 100 GHz.

An aluminum plate with six slots of different sizes electrodischarge machined into its surface was prepared according to the layout shown in Fig. 6.* Slots 1, 2, and 3 have a cross section (a x b) of 0.100 in. x 0.010 in. (2.5 mm x 0.25 mm); slots 4, 5, and 6 have a cross section of 0.050 in. x 0.010 in. (1.25 mm x 0.25 mm). Thus,

* This test plate was prepared under the direction of Dr. O. Buck of the Rockwell International Science Center, Thousand Oaks, California.

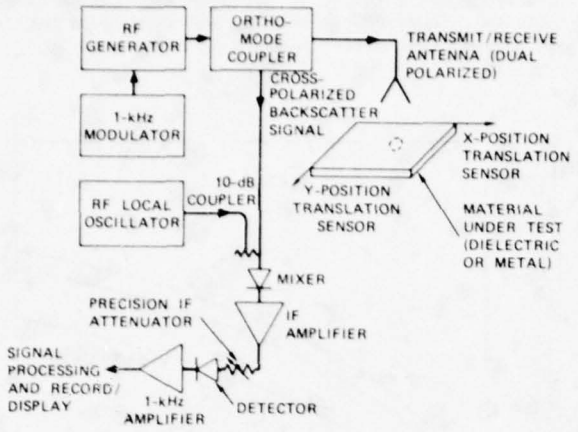

Fig. 5 Microwave-backscatter measurement system

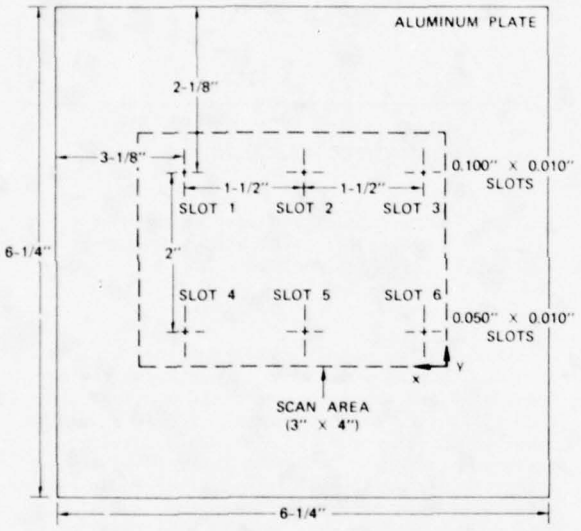

Fig. 6 Layout of slotted aluminum plate (Slots are aligned in the X direction)

a/b = 10 for the first set of slots, and a/b = 5 for the second set of slots. Also, at 100 GHz, $ka/\pi = 1.7$ for the first set, and $ka/\pi = 0.85$ for the second set. Finally, slots 1 and 4 were specified to be 0.010 in. (0.25 mm) deep, slots 2 and 5 0.020 in. (0.5 mm) deep, and slots 3 and 6 0.040 in. (1 mm) deep.

Actually, the electro-discharge machining process does not produce slots with a flat bottom, nor can the desired depth be achieved perfectly. To see the shapes of the slots and measure their depths, replicas of the slots were made by filling the slots with a rubbery compound (Dow-Corning RTV--Type E) and peeling it off the plate after the compound had set. Scanning-electron micrographs of the replica of slot no. 1 are shown in Fig. 7.

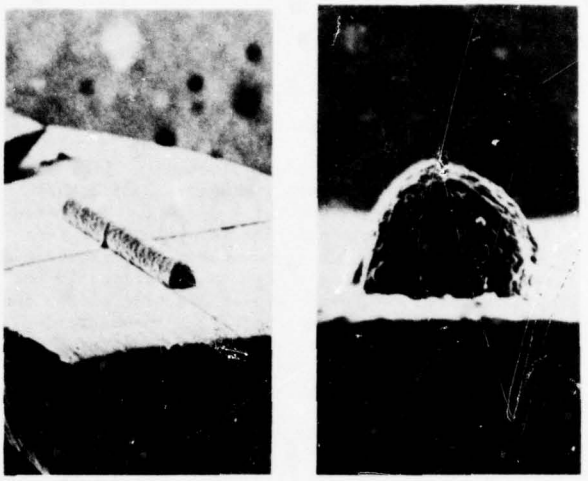

(a) 19X (b) 100X

Fig. 7 Scanning-electron micrographs of Dow-Corning RTV (Type E) replica of slot No. 1 (a = 2.5 mm, b = 0.25 mm, d - 0.25 mm)

The roundness of the bottom of the slot can be clearly seen. By measuring the image in the photograph showing the edge view of the slot [Fig. 7(b)], the actual depth of the slot (for example, to its deepest point) can be determined. Similar scanning-electron micrographs for slot no. 3 (the largest slot) are shown in Fig. 8. In this case, the depth of the slot was found to be 10% larger than specified. All of the slots were examined in this way.

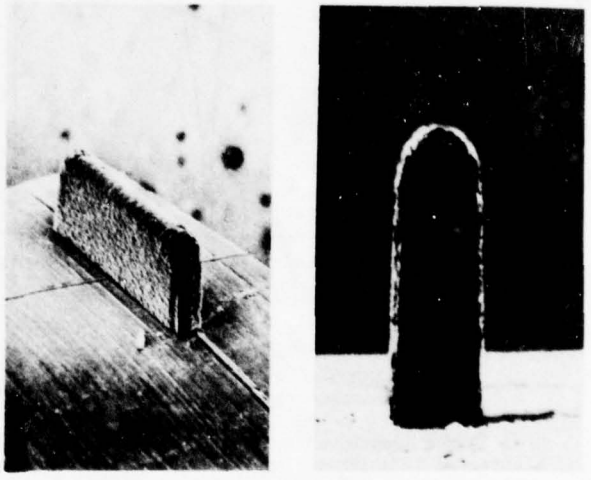

(a) 18X (b) 50X

Fig. 8 Scanning-eoectron micrographs of Dow-Corning RTV (Type E) replica of slot No. 3 (a = 2.5mm, b - 0.25 mm, d - 1.12 mm)

The measured cross-polarized power backscattered from the slots (the slots were oriented at 45° to the incident electric field) is shown as a function of beam position in Figs. 9 and 10 at its focal plane using an open-ended W-band waveguide sampling antenna, and this pattern is shown superimposed in Fig. 9 for comparison. The beam pattern appears about twice as large as actual

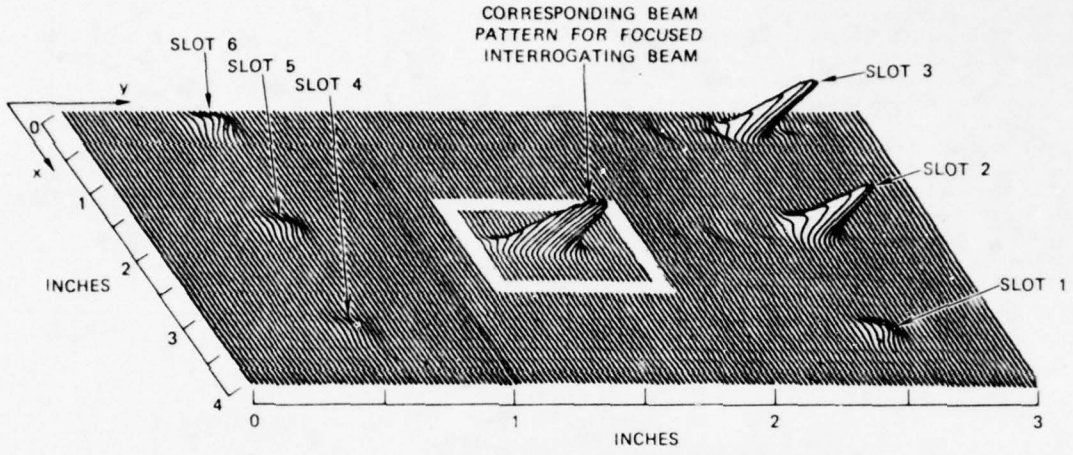

Fig. 9 Cross-polarized backscattered power from slotted aluminum plate versus beam position

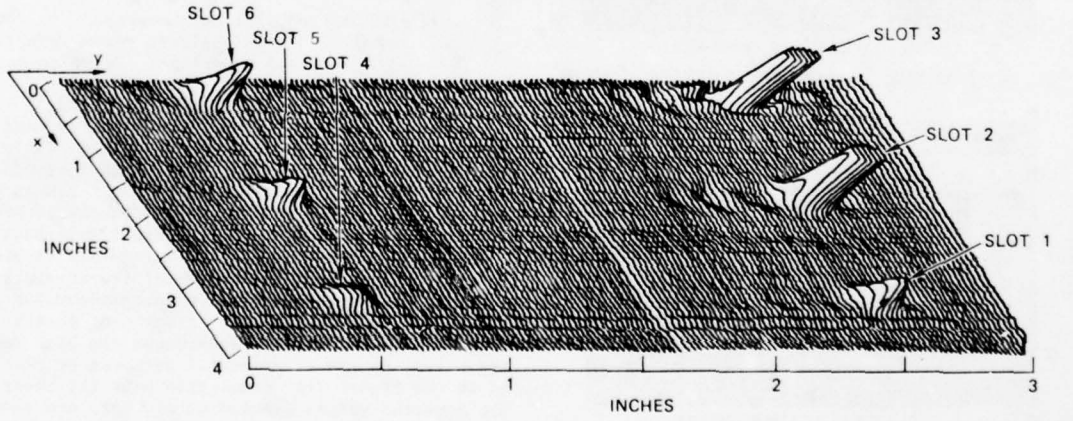

Fig. 10 Cross-polarized backscattered power from slotted aluminum plate versus beam position (Gain increased by a factor of 4 over that used on Fig. 9)

Figure 10 is the same as Fig. 9 except that the gain in Fig. 10 was increased by a factor of 4, so that the magnitude of the signal-to-clutter ratio would be more evident. Also, the beam pattern of the focused interrogating beam was measured size because it is produced by convolution with the relatively large sampling antenna. In any event, since the actual beamwidth is larger than the slot cross-sectional dimensions, the microwave C scan does not reproduce the detailed shape of the slot

cross section. Of course, this is the desired situation when one wants to deduce the slot depth from a single measurement of scattering cross section.

A quantitative measure of the scattering cross section for five of the six slots was obtained by determining the peak value of the backscattered power produced by these slots relative to that produced by the largest slot (slot 3). In other words, slot 3 was used as a reference scatterer or "standard." Photographs showing peak relative backscattered power versus beam position for all six slots are shown in Fig. 11. The relative values of the peak amplitudes are indicated in the figure. Figure 11(b) was obtained with the gain increased by 7 dB over that used to obtain Fig. 11(a). It can be seen in Fig. 11 (b) that the smallest slot (slot 4) produces a signal whose amplitude is on the order of that of the clutter signal. These data were taken without expending any effort to improve the signal-to-clutter ratio for the system.

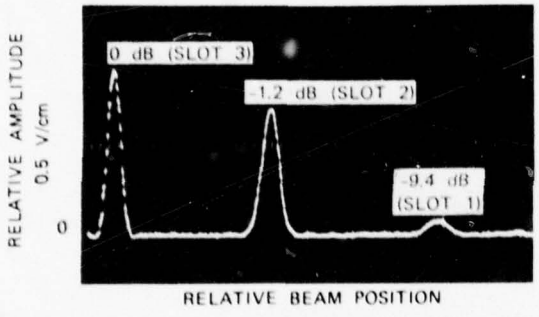

(a) SLOT NOS. 3, 2, 1 (IF ATTENUATION = 10 dB)

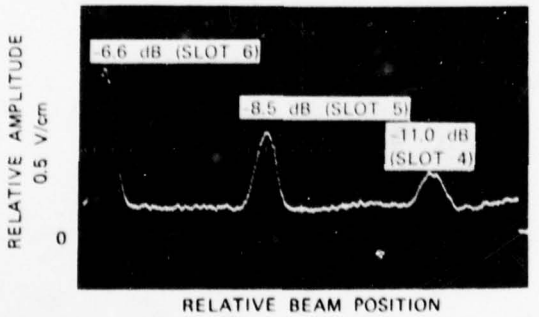

(b) SLOT NOS. 6, 5, 4 (IF ATTENUATION = 3 dB)

Fig. 11 Amplitude versus beam position showing peak values of backscattered power (Relative to Slot 3)

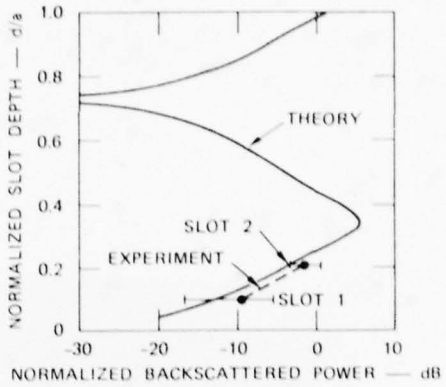

(a) ka/π = 1.7, a/b = 10

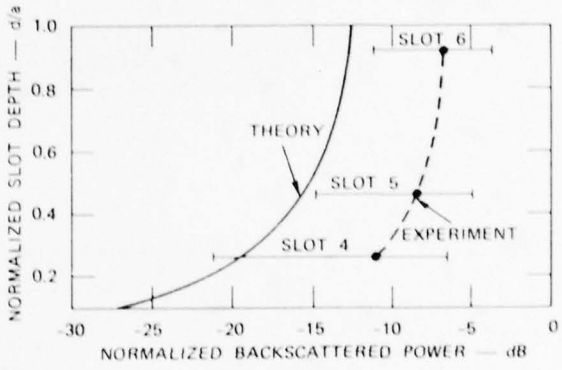

(b) ka/π = 0.85, a/b = 5

Fig. 12 Normalized slot depth versus normalized backscattered power--comparison of theory and experiment (Relative to Slot 3)

A comparison between theory and experiment is shown in Fig. 12 . Since the objective of the measurement is to determine slot depth (assuming a and b are known), the normalized slot depth is plotted as a function of normalized backscattered power (relative to slot 3). Figure 12(a) shows the above-resonance case where ka/π = 1.7 (slots 1 and 2). The multivalued nature of the theoretical curve precludes obtaining an unambiguous value for slot depth in this frequency times slot length range. However, in this experiment the slot depths are known, so the experimental data can be plotted, as in the figure, for comparison with the theory. The measured values (including clutter) are shown connected by a dashed line. The measured values of backscattered power are about 2 dB larger than the theoretical values, but the slope of data agrees well with theory.

In general, the clutter is composed of a combination of incoherent (noise) signals and coherent leakage signals. Sources of coherent leakage signals are located both inside and outside the measurement system. The worst case occurs when all of the clutter is coherent, since the clutter signal can then either add to or subtract from the

desired signal. The degree of coherence in the measured clutter is not known, but the corresponding uncertainty in the measured data that would occur if the clutter observed in this case [see Fig. 11(b)] were entirely coherent is indicated in Fig. 12 by the error bars drawn through the measured data points. It can be seen that the resulting uncertainty is quite large. On the other hand, if the measured clutter were composed entirely of noise, the true values of the measured backscattered power would only be slightly smaller than the observed values. It is clear from these results that coherent clutter should be minimized as much as possible.

The below-resonance case, where $ka/\pi = 0.85$ (slots 4, 5, and 6), is shown in Fig. 12(b). In this case, the theoretical curve is not multivalued, so there is a one-to-one relationship between scattered power and slot depth. Again, the measured data are shown connected by a dashed line, and the error bars show the uncertainty in the measurement that would exist if the observed clutter were coherent. The discrepancy between theory and experiment is larger in this case; the measured values of backscattered power are about 7 dB larger than the theoretical values. This discrepancy could be the result of inaccuracies in the theory caused by a failure to satisfy the approximation conditions (e.g., a/b is too small, the bottom of the slot is rounded, etc.), as well as being caused by measurement inaccuracies produced by the lower signal-to-clutter ratios associated with these smaller slots. It is interesting to note, however, that, again, the slope of the data agrees well with theory. In any event, the discrepancy in this case is large enough to prevent the determination of slot depth to reasonable accuracy using the measured data and theory described in this paper. The quantitative determination of slot depth from microwave backscatter measurements will require improvements in both theory and measurement technique.

IV SUMMARY

An approximate theory for the electromagnetic cross-polarized power backscattered from a rectangular slot has been developed. This theory, though approximate, reveals all of the essential features of the backscattering as a function of frequency and slot dimensions. For example, when the slot length is greater than one-half wavelength, resonances can occur, and this situation makes the determination of slot depth from measured backscattered power ambiguous. For smaller slot lengths, there is a one-to-one relation between slot depth and backscattered power, but the amplitude of the backscattered energy is smaller and slot depths that are greater than one slot length are not well resolved.

Experimental results obtained using electrodischarge machined slots in an aluminum plate were found to be in reasonable agreement with theory for the above-resonance case, with a slot length-to-width ratio of 10. Results obtained with smaller slots that had a smaller length-to-width ratio did not agree as well with the theory, except that the slope of the data did follow that of the theoretical curve. It was also found that signal-to-coherent-clutter power ratios of less than three can produce large uncertainties in the measurement of slot depth, particularly if the backscatter is small, as in the below-resonance case.

It can be concluded that the potential of obtaining a quantitative determination of crack depth from measurements of microwave backscatter in the below-resonance region does exist, but that further work is needed to improve the theory and the measurement technique. In particular, the theory should be extended to account for realistic crack geometries, probably by using finite-element techniques, and a measurement technique should be developed that minimizes the observed clutter level.

APPENDIX A

Slot Admittance--Consider an unfinitesimal volume, ΔV, whose cross-sectional dimensions a and b are the same as those of the slot, and that extends a depth, Δ, into the slot. Application of the Poynting energy theorem[3] to this volume gives

$$\frac{1}{2}\int_0^a\int_0^b \left(\hat{E}\times\hat{H}^*\right)_{z=0}\cdot\hat{a}_z\,dx\,dy + \frac{1}{2}\int_0^a\int_0^b \left(\hat{E}\times\hat{H}^*\right)_{z=-\Delta}\cdot\left(-\hat{a}_z\right)dx\,dy = -j\frac{\omega}{2}\iiint_{\Delta V}\left[\mu_0\hat{H}^*\cdot\hat{H} - \epsilon_0\hat{E}^*\cdot\hat{E}\right]dV - \frac{1}{2}\iiint_{\Delta V}\hat{J}^*\cdot\hat{E}\,dV \tag{A-1}$$

Here $\hat{a}_z$ is a unit vector pointing along the positive z axis, ω is the radian frequency, μ_0 and ϵ_0 are the permeability and permittivity of free space, respectively, and $\hat{J}$ is the current density driving the fields inside the volume. The physical meaning of Eq. (A-1) can be stated in words:

> The complex power radiated from the slot plus the complex power entering the slot equals the negative time rate of change of the difference between magnetic and electric energies stored in ΔV plus the complex power delivered to ΔV by the driving fields.*

The driving fields are those fields that exist in the absence of the slot. For simplicity, let the incident wave be plane and have an x component of magnetic field equal to H_{0x}. The magnetic field due to this wave at the unslotted metal surface is equal to $2H_{0x}$ because the wave is completely reflected. Hence the effective driving current is

$$\hat{J} = 2\hat{a}_z\times\hat{a}_x H_{0x}\,\delta\left(z+\frac{\Delta}{2}\right) = 2\hat{a}_y H_{0x}\,\delta\left(z+\frac{\Delta}{2}\right) \tag{A-2}$$

where $\delta(z)$ is the Dirac delta function. One may think of a current generator I driving the slot to produce a voltage V across the slot such that

*It is assumed that the conductivity of the metal walls is infinite.

$$\frac{1}{2}VI^* = \frac{1}{2}\iiint_{\Delta V} \vec{J}^* \cdot \vec{E}\, dV \qquad (A\text{-}3)$$

Substituting (A-2) and (5) into (A-3), one obtains

$$\frac{1}{2}VI^* = \frac{1}{2}\int_0^a dx \int_0^b dy \int_{-\Delta}^0 dz \qquad (A\text{-}4)$$
$$2H_{0x}^* \,\delta\left(z + \frac{\Delta}{2}\right) \frac{V_0}{b} \sin\left[k\left(\frac{a}{2} - \left|x - \frac{a}{2}\right|\right)\right]$$

or

$$\frac{1}{2}VI^* = \frac{1}{2}\left\{-V_0\left(\frac{ka}{4}\right)\left(\frac{\sin\frac{ka}{4}}{\frac{ka}{4}}\right)^2\right\}\left\{2H_{0x}^* a\right\} \qquad (A\text{-}5)$$

Hence, by definition,

$$V = -V_0\left(\frac{ka}{4}\right)\left(\frac{\sin\frac{ka}{4}}{\frac{ka}{4}}\right)^2 \qquad (A\text{-}6a)$$

and

$$I = 2H_{0x}a \qquad (A\text{-}6b)$$

The definition of slot admittance, Y_s, follows immediately in the usual way, viz.,

$$Y_s = I/V \qquad (A\text{-}7)$$

Now let $\Delta V \to 0$ so that the stored-energy term in (A-1) goes to zero. Using (A-3) and (A-7), (A-1) then becomes

$$\frac{1}{2}|V|^2 Y_s^* = \frac{1}{2}\int_0^a dx \int_0^b dy \left(\vec{E} \times \vec{H}^*\right)_{z=0-} \hat{a}_z \qquad (A\text{-}8)$$
$$+ \frac{1}{2}\int_0^a dx \int_0^b dy \left(\vec{E} \times \vec{H}^*\right)_{z=0-} \left(-\hat{a}_z\right)$$

or by definition

$$\frac{1}{2}|V|^2 Y_s^* = \frac{1}{2}|V|^2 Y_r^* + \frac{1}{2}|V|^2 Y_c^* \qquad (A\text{-}9)$$

Here Y_r is the radiation admittance of the aperture and Y_c is the cavity admittance. Y_r has been calculated for a narrow rectangular aperture by Rhodes.[5,6] Since the cavity is assumed lossless, the cavity admittance can be written as

$$Y_c = jB_c = \frac{j\,\mathrm{Im}\int_0^a dx \int_0^b dy \,(\vec{E} \times \vec{H}^*)_{z=0-} \hat{a}_z}{|V|^2} \qquad (A\text{-}10)$$

It is the computation of this cavity admittance with which this paper is concerned.

APPENDIX B

Cross-Polarization Scattering Coefficient*--Let $\vec{E}_V$, $\vec{H}_V$ and $\vec{E}_H$, $\vec{H}_H$ be two independent sets of solutions to Maxwell's equations for the interior of a closed surface S. In particular, the "V" fields exist in the presence of a crack in the test piece being inspected, and the "H" fields exist when no crack is present. The geometry for this situation is depicted in Fig. B-1 . In addition, the V and H fields are orthogonal within the transmit/receive waveguide (e.g., for linear polarization, they are cross polarized). Since S is assumed to be devoid of sources, the Lorentz reciprocity theorem[3] can be written as

$$\oint\!\!\oint_S \left(\vec{E}_H \times \vec{H}_V - \vec{E}_V \times \vec{H}_H\right) \cdot \hat{n}\, dS = 0 \qquad (B\text{-}1)$$

where $\hat{n}$ is a unit vector that points out of the volume enclosed by S. Now, the tangential electric field is zero on all metallic surfaces, including the crack-mouth surface, S_c, when no crack is present. Hence, (B-1) becomes

$$\iint_{S_\infty + S_w} \left(\vec{E}_H \times \vec{H}_V - \vec{E}_V \times \vec{H}_H\right) \cdot \hat{n}\, dS \qquad (B\text{-}2)$$
$$- \iint_{S_c} \left(\vec{E}_V \times \vec{H}_H\right) \cdot \hat{n}\, dS = 0$$

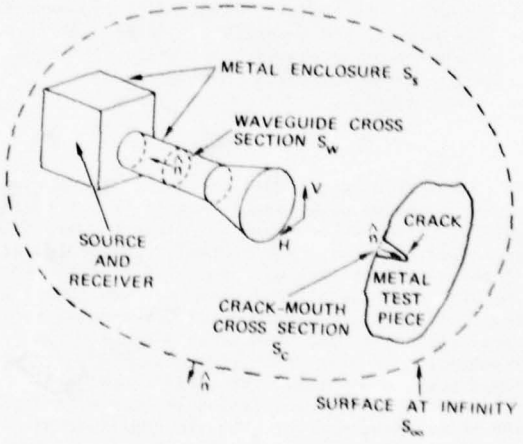

Fig. B-1 Geometry used in deriving cross-polarization scattering coefficient

First, consider the surface at infinity, S_∞. Here, only radiation fields exist. A general expression for the radiation fields due to an arbitrary source is[4]

*This derivation was provided by B. A. Auld of Stanford University.

$$\vec{E} = j\omega \hat{r} \times (\hat{r} \times \vec{A}) \tag{B-3a}$$

$$\vec{H} = -j \frac{\omega}{\eta_0} (\hat{r} \times \vec{A}) \tag{B-3b}$$

where $\vec{A}$ is a vector potential function and $\hat{r}$ is unit vector pointing from the origin of coordinates to the point where the fields are calculated. Using (B-3) it is easy to show that

$$\vec{E}_H \times \vec{H}_V = \vec{E}_V \times \vec{H}_H \tag{B-4}$$

on S_∞, and hence the integral over S_∞ is zero.

Now consider the surface, S_w, that cuts through the waveguide. The fields there can be written in terms of a wave traveling outward from the source and complex scattering (reflection) coefficients, Γ, that are a measure of the waves being scattered back to the source. The expressions for the fields on S_w are:

$$\vec{E}_H = \left(1 + \Gamma_{HH}\right) a_H \vec{e}_H^{+} \tag{B-5a}$$

$$\vec{H}_H = \left(1 - \Gamma_{HH}\right) a_H \vec{h}_H^{+} \tag{B-5b}$$

and

$$\vec{E}_V = \left(1 + \Gamma_{VV}\right) a_V \vec{e}_V^{+} + \Gamma_{HV} a_V \vec{e}_H^{+} \tag{B-6a}$$

$$\vec{H}_V = \left(1 - \Gamma_{VV}\right) a_V \vec{h}_V^{+} - \Gamma_{HV} a_V \vec{h}_H^{+} \tag{B-6b}$$

where a_H, a_V are the amplitudes of the waves emanating from the source. Without loss of generality, let $a_H = a_V = a$. Substituting (B-5) and (B-6) into the integral over S_w and using the orthogonality of the H and V modes gives

$$\iint_{S_w} \left(\vec{E}_H \times \vec{H}_V - \vec{E}_V \times \vec{H}_H\right) \cdot \hat{n}\, dS = \iint_{S_w} -2\Gamma_{HV} a^2 \left(\vec{e}_H^{+} \times \vec{h}_H^{+}\right) \cdot \hat{n}\, dS \tag{B-7}$$

Since the modes are assumed to be propagating in the waveguide, a, $\vec{e}_H^{+}$, and $\vec{h}_H^{+}$ can be chosen to be real and so

$$\iint_{S_w} -a^2 \left(\vec{e}_H^{+} \times \vec{h}_H^{+}\right) \cdot \hat{n}\, dS = 2P_s \quad , \tag{B-8}$$

where P_s is the average power available from the source. Substitution of (B-7) and (B-8) into (B-2) gives the final result for the cross-polarization scattering coefficient:

$$\Gamma_{HV} = \frac{1}{4P_s} \iint_{S_c} \left(\vec{E}_V \times \vec{H}_H\right) \cdot \hat{n}\, dS \tag{B-9}$$

ACKNOWLEDGEMENT

Technical discussions held with Dr. B. A. Auld and Mr. L. A. Robinson were a significant aid to the author in carrying out this work. The author is also grateful for the expert technical assistance provided by Messrs. P. C. Evans, R. E. Wanner, and J. P. Watjen.

This research was sponsored by the Center for Advanced NDE, operated by the Science Center, Rockwell International, for the Defence Advanced Research Projects and the Air Force Materials Laboratory under Contract F33615-74-C-5180.

REFERENCES

1. R. J. Hruby and L. Feinstein, "A Novel Nondestructive, Noncontacting Method of Measuring the Depth of Thin Slits and Cracks in Metals," The Review of Scientific Instruments, Vol. 41, pp. 679-683 (May 1970).

2. A Hussain and E. A. Ash, "Microwave Scanning Microscopy for Nondestructive Testing," Proceedings of the 5th European Microwave Conference, Hamburg, Germany, pp. 213-217 (September 1975).

3. R. E. Collin, Field Theory of Guided Waves, (McGraw-Hill Book Co., New York, N.Y., 1960).

4. R. W. P. King and C. W. Harrison, Jr., Antennas and Waves: A Modern Approach (The M.I.T. Press, Cambridge, Mass., 1969).

5. D. R. Rhodes, "On a Fundamental Principle in the Theory of Planar Antennas," Proc. IEEE, Vol. 52, pp. 1013-1021, September 1964.

6. D. R. Rhodes, "On the Stored Energy of Planar Apertures," IEEE Trans. Antennas and Propagation, Vol. AP-14, pp. 676-683, November 1966.

DISCUSSION

Jerry Tiemann (General Electric): I'm going to ask two or three questions. The first question is: What is the cause of the coherent clutter?

Alfred J. Bahr (Stanford Research Institute): The major cause in this particular system was leakage through the orthomode coupler and that is being worked on now. It is a matter of tuning that coupler to improve its isolation. There is a second cause that could be external, and that would be curvature of the specimen.

Jerry Tiemann: Okay, that brings me to the question as to whether the accuracy of alignment causes clutter. The other one is: Do you think it would be practical to apply this to the kind of engine disk contours that are found which are, in fact, multi-curved?

Alfred J. Bahr: The alignment is not too difficult using the focused horn. If you use a near field probe like an open ended wave guide, or any near field probe, it is more difficult. In the case of ceramics, which we have also looked at, it is a very big problem to align the receiver and the transmitter in the transmission measurement. In the back scatter measurement, the depth of field is several wave lengths and you can level your sample.

I don't have a good feel for the level of clutter caused by curvature yet. It's something you could calculate, but I haven't done it and so I'm not sure what limitations exist relative to real world geometries other than to say that probably the curvature would have to be small compared to the wave lengths. I don't have any better answer than that. That is an important question.

Harish Dalal (SKF Industries): Is the curvature that you mentioned the curvature of the sample?

Alfred J. Bahr: Yes.

Harish Dalal: The question I have relates to ceramics. Do you have any feel for the limit of the depth of flaw that you can detect using this technique?

Alfred J. Bahr: The depth of what, sir?

Harish Dalal: The depth of a crack. What is the minimum depth you might be able to detect?

Alfred J. Bahr: In ceramics, I don't know yet. We can detect voids in ceramics that are smaller than a wave length.

William Lord, Chairman(Colorado State University): Before we adjourn I would like to make one final comment on this afternoon's session. I think the speakers have shown that there are some exciting things happening in electromagnetic methods of non-destructive testing, both with regard to the development of new or improved techniques and in the modeling of field defect interactions.

I have had a long standing interest in the prediction of magnetic fields in ferromagnetic materials and over the years I've attended many of the ARPA/AFML conferences. I must say, I have been rather envious of the amount of progress that has been made in the ultrasonics area as part of this program. I've always felt that the research philosophy which was developed in this program was directly applicable to electromagnetic methods of nondestructive testing as well, including the more traditional leakage field and residual methods. Perhaps the time is ripe for someone to coordinate all of these isolated activities into one coherent program.

THE IMPORTANCE OF NONDESTRUCTIVE EVALUATION TO FUTURE ENERGY SYSTEMS

James S. Kane
Associate Director for Basic Energy Sciences
Office of Energy Research
U. S. Department of Energy
Washington, D. C. 20545

ABSTRACT

The Department of Energy conducts both applied and basic research on nondestructive evaluation. The importance of NDE is discussed with emphasis on future energy systems. Organization, needs, barriers and new developments are described.

The Nation is faced with an enormous task if it is to make the least painful transition from its current energy sources (chiefly petroleum and natural gas) to ones more abundant, and ultimately to those that are inexhaustible. This transition will require an unprecedentedly large and rapid shift to different, if not new, technologies.

In this transition, the role of nondestructive evaluation (NDE) is certainly clear to its practitioners, but unappreciated or ignored by almost everyone else. It will not be possible to rely on accumulated wisdom to predict the safety, reliability and lifetime of the new components that must be developed. Yet such knowledge can have a major effect on the cost of the new energy systems, as they are deployed industrially.

Within the Department of Energy, a variety of programs and projects are applying, and, in some cases, developing NDE techniques. I will discuss some of this work -- typical needs that have been identified, progress that is being made, barriers that have been encountered, and new developments, both in techniques and in quantitative understanding, that appear of special interest.

I will first describe the organizational framework in which the overall program is carried out.

The Department of Energy was formed on October 1, 1977. It operates with a budget of about $10 billion per year and has approximately 20,000 employees. It has consolidated under one cabinet level department the responsibilities and personnel from the former Energy Research and Development Administration, the Federal Energy Administration, and the Federal Power Commission as well as components previously under the Departments of Commerce, Defense and Interior.

Although the Department of Energy incorporates many programs and functions from other agencies, it is not an amalgamation of existing agencies with a new tier of leadership. Instead, many previous programs and functions have been reshaped to fit the national energy policy of the new department. The DOE organization and functions are represented in Fig. 1

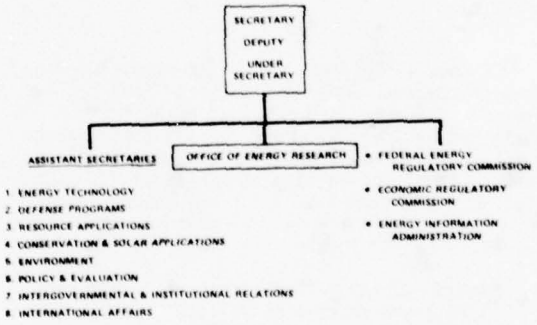

Fig. 1. Department of Energy

I especially wish to call to your attention the programs within Resource Applications, Conservation and Solar Applications, Energy Technology, Defense Programs and the Office of Energy Research. It is within these organizational units that most of the research and development programs are located. Except for the Defense Programs, a spectrum of research cuts across the Department, from the most basic in the Office of Energy Research, to technology development under Energy Technology to commercialization under Resource Applications, and under Conservation and Solar Applications. The structure of the Office of Energy Research is represented in Fig. 2

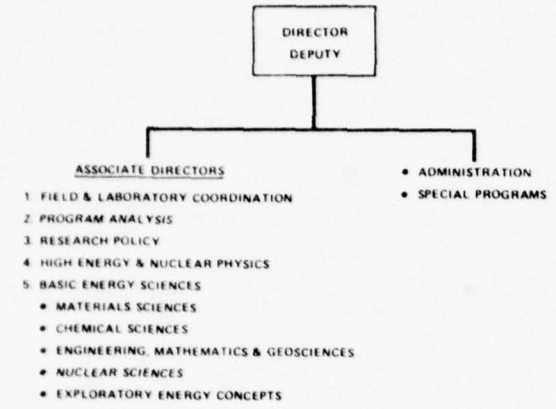

Fig. 2. Office of Energy Research

Of special interest to this community are our research programs under Basic Energy Sciences in Materials Sciences, and in Engineering, Mathematics and Geosciences where fundamental research on NDE occurs or will occur in the near future. These programs are located primarily at DOE laboratories. Additional programs are conducted elsewhere (universities, industry) based on submission of unsolicited proposals.

The DOE outlay for R&D programs in NDE for FY 1978 is approximately $5 million. Active NDE programs are being conducted under DOE sponsorship at a number of sites, primarily DOE laboratories and facilities. Essentially all the developmental effort is applications-oriented, with the principal thrust in most cases being the development of an NDE solution for specific components or problems. The broad scope of developmental activities includes all the more traditional methods of NDE (e.g., radiography, radiation attenuation, ultrasonics, eddy currents, acoustic emission, x-ray fluorescence and holography) and limited work in such areas as Mossbauer spectroscopy, positron annihilation, and neutron scattering. Interest is increasing in the use of computers for both signal processing and pattern recognition.

Some typical applied projects underway include:

Development and application of NDE techniques to flaw detection in ceramic turbine materials and components - under the Power Systems Division of the Fossil Energy Program.

- NDE in-situ techniques for the examination of thin coatings used to protect interior surfaces of components - under the Coal Conversion Division of the Fossil Energy Program.
- NDE techniques applied to the detection of incipient failure of drill pipes - under the Geothermal Energy Division.
- In-service inspection of coarse-grain austenitic stainless steel welds in reactor components, ultrasonic examination of primary and secondary piping welds in the Fast Flux Test Facility and in-service inspection of primary system reactor piping - under the Reactor Technology Division of the Nuclear Energy Program.
- Adaptation of acoustic emission, ultrasonics, eddy currents, x-radiography, radiation attenuation, neutron radiography, and holography to problems of film thickness measurements and weld integrity, and computer applications for data analysis and presentation; and signal analysis of NDE techniques - under the Defense Programs.

Although many organizations are working in the same general field, the complex nature of the methods and the varying application requirements has minimized (or virtually eliminated) redundancy. More information on programs underway can be obtained from the various divisions supporting this work. A recent compilation of projects was carried out under the auspices of an internal coordinating committee and is contained in the report, "Survey and Analysis of Selected Topics Within the Energy Research and Development Administration's Materials Research and Development Programs," DOE/ET-0006, January, 1978 available from NTIS.

The more fundamental NDE work within DOE, and that concerned with quantitative NDE in particular, occurs in the Office of Basic Energy Sciences. The major NDE interest here will be divided between the two Divisions - Engineering, Mathematics and Geosciences, and Materials Sciences. Research on detection systems and computer interfacing will be within the purview of our new program in Engineering Sciences that will commence on October 1, 1978. Work concerned with materials studies, especially quantitative predictive behavior and new techniques applied to the determination of remaining safe useful lifetime of materials in service, will fall within the scope of the Materials Sciences program.

Importance of NDE - The growing importance of NDE to future energy systems is based on sound and sophisticated awareness of factors such as economics, reliability, environmental effects and safety. Nondestructive evaluation takes on an especially important role in technology when the capital costs of an operating facility are large. For example, in the case of a forced shutdown of a 1000 MWe nuclear power unit, one day's outage costs approximately $0.6 million (estimate by EPRI, 1975), and 36% of the down time is due to forced outages. If only a small percentage of these forced outages could be prevented by proper

monitoring and repaired during normal down times, a tremenduous savings would result. The same general argument can be made for other capital intensive baseload energy sources. The growing awareness of the public in the areas of environment and safety further heightens the importance of NDE. In many cases, a technology could not survive the sociological consequences of a severe accident. Not only do facilities such as liquid natural gas storage tanks, nuclear plants and coal liquefaction plants have to be well designed and the materials carefully tested, but a monitoring system that nondestructively monitors significant flaw initiation and growth would help alleviate both perceived and actual fears. There are new systems also which must be monitored in addition to being carefully tested in view of the unknowns. Fusion reactors will be very large and expensive, and the technology would be set back years in the event of a disastrous surprise. Underground power transmission systems are under development that would carry ever increasing blocks of power, the ultimate being superconducting transmission lines. The dielectric breakdown behavior of insulators is still quite difficult to predict, but would be catastrophic for the transmission line if it occurred. Some methods for evaluating and monitoring these new systems must be developed before they can be confidently utilized.

Institutional Problems - In view of the increasing importance of NDE, one question that arises is: Are there satisfactory university programs set up to advance the science and to train future scientists in this area? At the present time, the NDE area is a multidisciplinary field drawing from materials science, mechanical engineering, electrical engineering, chemical engineering, physics and increasingly others such as mathematics and computer science. This makes the academic training process more difficult and time consuming, leaving much of it to on-the-job training. Some experiments should be tried to break down the departmental barriers in order to see if benefits could derive from a more coherent curriculum. Another institutional problem facing the NDE area is the problem of design philosophy that emphasizes initial design and construction of the facility rather than lifetime considerations. As our understanding of failure prevention increases and our ability to detect the onset of property deterioration increases, the systems designers should take advantage of this new understanding and build detection systems into the design. More cooperation between code formulating bodies, designers and the NDE community is needed to accomplish this.

Needs - For the field of energy technology, in addition to the more general needs such as trained personnel, there are many areas of need specific to particular energy systems. Safety and reliability are important criteria for fossil and nuclear electric baseload facilities. A more quantitative understanding between flaw detection and failure prediction is needed. This requires both a greater ability to detect flaws of a critical size and defects of a sub-critical size together with a greater understanding of their effect on properties. The ability to continuously monitor sub-critical defects in-situ, under service requirements of temperature, stress, radiation, etc., and to use such data to quantitatively predict the remaining safe lifetime of critical components prior to failure would provide a significant economic saving.

There continues to be a need to better evaluate welds in all applications, and to quantitatively relate NDE to the parameters of fracture mechanics. The area of radioactive waste disposal is currently receiving much attention. Monitoring of waste canisters for failure may assist in solving this crucial problem for the nuclear industry. Coal liquefaction and gasification plants will contain materials which have to operate in highly aggressive environments containing sulfur, hydrogen, carbon, oxygen and other elements. Monitoring of these systems for stress corrosion cracking, hydrogen attack and corrosion will be essential to prevent catastrophic shutdowns. With the push to higher temperatures in turbines and heat exchangers, there will be a need to monitor the effects of thermal excursions, thermal structural stability and a need to predict remaining life to fatigue failure. In the solar photovoltaic area, there is a need to monitor semiconductor junction behavior as a function of time. The heating and cooling cyclic behavior of solar collectors will have to be monitored for fatigue and property deterioration. Overriding all of these needs is the requirement for objective and accurate interpretation of the failure detecting signals, and for increasing the signal to noise ratio under realistic service conditions. Certainly more research is needed in the way of instrumentation and computerization to take the human interpretation out of the system. Of course this cannot be done without sufficient understanding of the role of defects and their influence on properties, especially a quantitative understanding.

Exciting New Areas - The entire field of NDE has come alive with new ideas in the past few years. Some of the energy-related areas, of course, do not require new ideas as much as they require the application of current knowledge to practical engineering systems. Significant progress has been made and should continue in the areas of instrument miniaturization for field applications, high frequency systems and circuit designs for optimum signal to noise ratios, computerization, theory of defect scattering of various probing signals, and the relationship between materials characterization and predictive behavior. However, I would like to close by mentioning a few new techniques (positrons, high intensity x-rays, neutrons) which may not be carried over directly into the NDE field, but will no doubt contribute to our understanding in a quantitative way.

Positrons injected into a material eventually annihilate together with an electron giving off a detectable gamma ray. Measurements such as the positron lifetime and Doppler line broadening give information on the structure of the material. Recent progress in instrumentation and theory has led to an ability to observe phenomena such as vacancy concentrations and dislocation pile-ups that are precursors to fatigue hardening. Positron annihilation has been shown to be sensitive

to the detection of hydrogen embrittlement in certain materials. Hydrogen-dislocation interactions and localized high concentrations of hydrogen are revealed through changes in the Doppler shape factor. A U.S. patent (#4064438) has recently been issued on the hydrogen embrittlement detection method.

With the advent of modern high energy electron storage rings, the possibility of very high flux sources of x-rays and vacuum ultraviolet radiation has opened new vistas in materials characterization. The radiation is emitted as high energy electrons are accelerated with a magnetic field. A number of facilities are now available, one not very far from here, at the Stanford synchrotron radiation project. The radiation emitted is inherently collimated, pulsed, plane polarized, has a continuous energy spectrum, and exceeds the intensity of other broadband sources by factors of 10^2 to 10^4. The Department of Energy has under construction a dedicated facility as an x-ray and ultraviolet radiation source at Brookhaven National Laboratory called the National Synchrotron Light Source. Synchrotron radiation has been used to produce x-ray pictures of thin samples with greatly improved resolution compared to the details in familiar radiographs. This x-ray lithography technique uses a thin plastic film (photo-resist) which is sensitive to x-rays to replace the usual x-ray photographic film. After exposure to radiation, the photo-resist is placed in a solvent where the parts receiving the most radiation are preferentially dissolved. The resultant "radiograph" can be studied with an electron microscope to reveal detail as fine as 10 nm (100Å). Topography is another technique where x-rays are used to image structure - in this case the x-rays are scattered rather than absorbed. The exciting feature of synchrotron radiation for topography is the marked reduction in exposure times made possible by the intense radiation. Experiments have been performed showing magnetic domain wall movements in materials, and the new and more intense synchrotron radiation sources being built open the possibility of x-ray motion pictures of dynamic events at the dislocation level.

The availability of high fluxes of cold neutrons (long wavelength) offers another possibility for examining and characterizing defects in materials. Cold neutrons can be used in either the absorption mode or the scattering mode. In the absorption mode, long wavelength neutrons can greatly improve contrast and resolution over normal radiographic methods. This improvement will be especially evident for hydrogenous materials (e.g., 1 mm of plexiglas contained within two 7 cm sections of steel). Small angle neutron scattering with cold neutrons is a new technique based on scattering of neutrons. It can be used to detect heterogeneities (10 - 1000Å) imbedded within a matrix of different neutron scattering power. The scattering technique has a much finer resolution than the radiography method. Although applications of the cold neutron methods are limited by the need to utilize the few nuclear reactor sources available, they offer the possibility of examining bulk specimens at resolutions never before attained.

Summary - The subject of nondestructive evaluation is one which will receive increasing attention in future energy systems because of the greatly increased public awareness of economic, reliability, safety and environmental issues. Some institutional problems such as the training of scientists and engineers and design philosophy need to be addressed for the proper utilization of NDE in these systems. Quantitative predictive NDE, the subject of this meeting, is, of course, the key to effective deployment of NDE.

OVERVIEW AND PURPOSE

Anthony G. Evans
Rockwell International Science Center
Thousand Oaks, California 91360

Our purpose in today's session is to discuss procedures for developing accept/reject criteria for NDE methods of inspection. Many of the methods we will describe this morning are not very familiar to members of the audience, so we have deliberately set the session at a fairly leisurely pace so you can assimilate these concepts as they are presented this morning. We would like the session to be relatively informal so we can ask questions and have a fairly extensive discussion period. Following the talks this morning, and after you have had a chance to assimilate some of the details, there will be a poster session immediately after lunch where we're really asking the question, "Are the measurements that are being made in the various labs and institutions in the country really the appropriate measurements to fit within the accept/reject frame work you will have heard described this morning?" Then, finally, after the posters are completed, there will be a general discussion whereby we will all assemble again to ask the question, "Are the right measurements being made; if not, what other measurements should be made?" and general questions of that nature.

Since it is partially a pictorial session this morning, I thought it might be worthwhile, before getting into some detailed talks, to very briefly acquaint you with some of the concepts involved in the development of accept/reject criteria.

There are at lease three components involved in the development of accept/reject decisions. There is the nondestructive measurement, which is the area that most of you are very familiar with. Secondly, one needs to understand the fracture condition; how does fracture occur from the defect that you have been measuring? There is also a need to obtain information about the typical populations of defects that occur within the materials. Once one has acquired information on these three aspects of the problem, then one is allowed to make an accept/reject decision. It turns out that, by necessity, we end up with a probablistic form of analysis. There are error functions associated with each of the above aspects, which require that the problem is probablistic in character. Further, one can develop probablistic accept/reject criteria from one of several data bases. Empirical data can be used which must include data on the three aspects that I described earlier. One can also use physical models for the measurements (such as the scattering from defects) and for the failure modes (such as the fracture mechanics of the defects). Optimally, one would like to combine physical models of each aspect of the problem with empirical data to achieve the best possible accept/reject decision making.

Let me describe, very quickly, before we get into the first talk, roughly the sort of thing that needs to be done in order to develop an accept/reject decision. The case in point is one which is of great interest to most of you, i.e., the case in which we have isolated non-interacting defects in the material. We will be inspecting that material in some fashion and trying to estimate its failure probability. It turns out that, firstly, one tries to estimate defect dimensions from the inspection process. Secondly, one tries to estimate from the defect dimensions what the fracture condition will be, that is, what is the time-to-failure for a particular stress. Thirdly, one needs to know (or have some knowledge of) the a priori distribution of defects in the component. This means that one needs to know the probability of a defect of a certain type occurring within the volume of the component that is being fabricated. These three pieces of information need to be appropriately combined to form the accept/reject decision base.

There is another further thought that must be mentioned here. One can apply dollars to the rejection probability and dollars to failure probability . When one starts to apply dollars in that fashion, one can get a total expected cost which includes the cost of the inspection and includes the cost of a failure. This curve will generally show a cost minimum. It is this minimum cost, of course, which specifies the inspection level that should be chosen for your inspection if dollars are ultimately the important parameter involved.

The different talks today will emphasize different aspects of the problem. Some will emphasize, almost exclusively, the use of empirical data. Others will emphasize, almost exclusively, the physical models and others will try to combine those two in the best fashion that is presently available.

THE IMPACT OF INSPECTION AND ANALYSIS UNCERTAINTY ON RELIABILITY PREDICTION AND LIFE EXTENSION STRATEGY

Charles A. Rau, Jr.
Failure Analysis Associates
Palo Alto, California 94304

ABSTRACT

Life extension of high cost components until measurable damage is detected can result in marked reductions in total cycle costs. The life extension strategy for turbine disks is based upon nondestructive inspection to detect defects, usage and stress analysis to define requirements, and fracture mechanics analysis and testing to evaluate the severity of any defects under future usage. Because there are uncertainties and inaccuracies in the inspection, analysis, testing and definition of past and future usage, the selection of the optimum life extension strategy requires quantitative evaluation of the costs and risks associated with each uncertainty during life extension. This paper summarizes recent developments in the basic methodologies necessary to quantify reliability. Specific examples are described which illustrate the concepts and payoff possible as well as the relative importance of inspection, analysis, and usage uncertainties on the optimum life extension strategy.

INTRODUCTION

Engineering components in high performance equipment may wear out due to fatigue or creep. Historically such components have been designed for replacement after a specified amount of service. The "specific design life" is that beyond which a significant number of failures are predicted to occur by analysis, lab testing and operating experience. Because however, there is significant variability in the loading conditions and the materials response, most nominally identical components could provide reliable service well beyond the "design life", but all components are retired because the precise amount of damage accumulation is not established for each. Figure 1 shows a typical variation in the actual life of nominally identical components. Because so much of the useful life of most components is not utilized, marked reductions in the total cycle costs would result by life extension of individual component until damage actually develops. To achieve such life extension without reducing equipment reliability requires reliable non-destructive inspection to detect defects or damage development, fracture mechanics analysis and testing to evaluate the severity of any defects present under continued operation, and a quantitative method to select the accept/reject conditions for life extension.

This paper will address four topics. First, it reviews briefly the basic concepts associated with probabilistic fracture mechanics (PFM), and retirement for cause (RFC); second, it discusses some recent developments in these methodologies; third, it describes two specific examples which quantify the impact of inspection and analysis uncertainties on the optimum RFC strategy; and fourth, it summarizes progress to date on an ARPA sponsored project to evaluate RFC for application to gas turbine disks.

BASIC CONCEPTS

Fracture Mechanics - The conventional approach to life prediction involves establishing an allowable design life at which all such components are removed from service. The fracture mechanics approach to life prediction differs from the conventional approach in that it acknowledges that defects are present or will develop and that failure will eventually occur by the gradual growth of cracks until they reach a critical size. The fracture mechanics design approach, therefore, establishes design allowables in terms of allowable defect sizes which cannot grow to a dangerous size between inspection intervals.

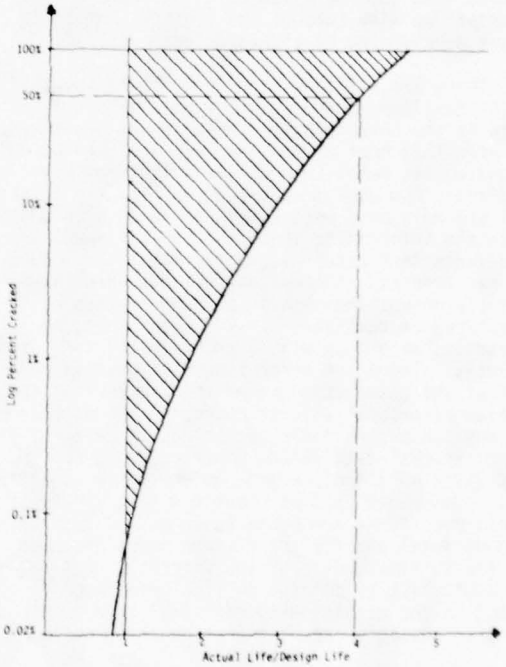

Fig. 1 Schematic representation of the distribution of actual failure lives compared to the nominal design life which is established to assure that less than one in 1,000 components develop a crack.

In order to effectively implement the fracture

mechanics approach, Fig. 2 shows the various types of input required. Analysis, materials, and inspection input are all required. As in the conventional design approach, the steady state, thermal, and vibratory stresses must be identified at the critical locations. The crack path through the structure must be calculated and specifically the crack driving force, that is the crack tip stress intensity factor, K, must be evaluated as a function of increasing crack size. Finally, the critical crack size at which unstable fracture occurs or the crack size in which arrest of a growing crack occurs must be calculated. These analytical efforts utilize as input certain materials properties. Specifically the threshold below which high frequency fatigue (HFF) does not occur, the mode of crack propagation, and the materials crack growth law, either for fatigue or creep conditions, must be determined as a function of crack tip stress intensity factor, K, operating temperature, frequency, and other loading conditions. The materials fracture toughness must also be determined and used to evaluate the critical crack sizes. Finally, the inspection input requires definition of the flaw size range of concern, the orientation and shape of flaws of concern and an estimation of the probability that flaws of various size exists prior to inspection of the component. These three types of inputs are combined to perform the lifetime prediction. For example, the number of cycles to grow a fatigue crack to failure (N_F) is calculated by taking the material crack growth law, rearranging and numerically integrating from the initial flaw size (A_i) to the final or critical crack size (A_f) over the appropriate distribution of K as the crack grows.

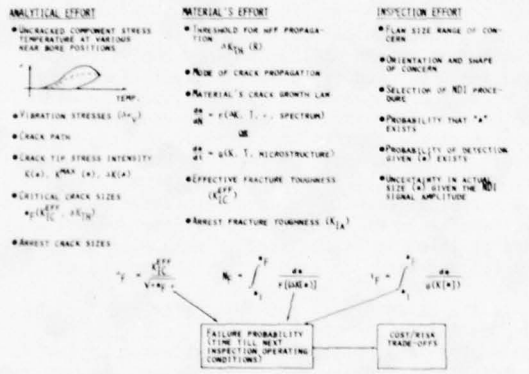

Fig. 2 Probabilistic fracture mechanics approach to lifetime prediction.

Probabilistic Fracture Mechanics - If each of the input parameters are assumed to be known exactly, we get an exact calculation of remaining life time. In practice, however, the input parameters are usually not known exactly; in fact, the uncertainties vary considerably from one input to another. The probabilistic fracture mechanics approach (1,2) accepts uncertainties in the various input parameters, quantifies them, and calculates a failure probability as a function of continued operating time or cycles, rather than a precise remaining lifetime. The engineering community has generally accepted the fact that various input parameters are uncertain and that the probabilistic approach is more realistic than the deterministic life prediction. However, most design engineers do not fully understand the quantitative requirements and do not have the needed tools to actually implement a probabilistic fracture mechanics approach. The combination of this lack of understanding as well as lack of quantitative data on the specific uncertainties involved has limited the full implementation of probabilistic fracture mechanics to a few instances.

Inspection Uncertainty - One of the key concepts which until recently limited the probabilistic analysis was a quantitative understanding of inspection uncertainty (3) and its impact on the reliability of the engineering component. More specifically, the inspector normally establishes an inspection level or sensitivity, shown as b on Fig. 3, and ideally the inspection should locate all imperfections of size greater than S and not indicate the presence of any imperfections smaller than size S. In Fig. 3, this is quantitatively stated as the probability of rejection for various actual flaw sizes (a) at inspection level S [P(R/a, S)]. For an ideal inspection, P(r/a,S) = 1 for crack sizes (a) bigger than S, and P(R/a, b) = 0 for crack sizes a < S. The typical eddy current inspection, like that used to inspect turbine disk bolt holes, is not perfect. As shown in Fig. 3, there is a finite probability of rejecting components with actual imperfections smaller than S, and a finite probability of not rejecting components with actual imperfections larger than S. Two other inspection methods are also shown on the same figure. That labeled A is an inspection method with the same sensitivity as the typical eddy current inspection, that is 50% of the time it rejects imperfections of size S; however, it has a reduced inspection uncertainty and more closely approaches the performance of the ideal inspection which has 0 inspection uncertainty. The dotted line indicates the performance of inspection method A when utilized at a higher sensitivity but with the same inspection uncertainty.

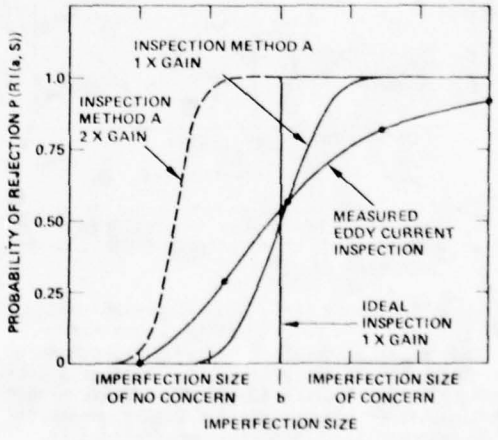

Fig. 3 Comparison of the inspection uncertainty, characterized by the probability of rejection as a function of flaw size, for ideal and real inspections.

Preinspection Material Quality - Qualification of the flaws which may get into service requires quantification of both the inspection uncertainty and the distribution of flaws in the material prior to the inspection (4). Deterministic fracture mechanics approaches have very conservatively assumed that the preinspection flaw frequency is larger for each crack size so that pn(a) = 1 and the probability of flaw occurrence in the inspected part was exactly equal to the probability of the inspection missing a flaw of size a, if it exists, which is one minus the probability of rejection, P(R/a, S), given that a flaw of size a exists. More realistically, when the inspection procedures of Fig. 3 are applied to a component which initially contains a distribution pn(a) of imperfections of various size (a), the distribution of imperfection sizes after inspection is modified as shown in Fig. 4. The ideal inspection would eliminate all imperfections of size greater than S, but with real inspections some larger imperfections will get into service and some components with smaller imperfection of no concern will be rejected and thereby increase the total costs. It is this probability distribution of imperfections after inspections, which is the product of the preinspection flaw distribution [pn(a)] and inspection reliability [1 - P(R/a, S)], that would be input as the probable initial flaw size (a_i) for a probabilistic fracture mechanics calculation of failure probability.

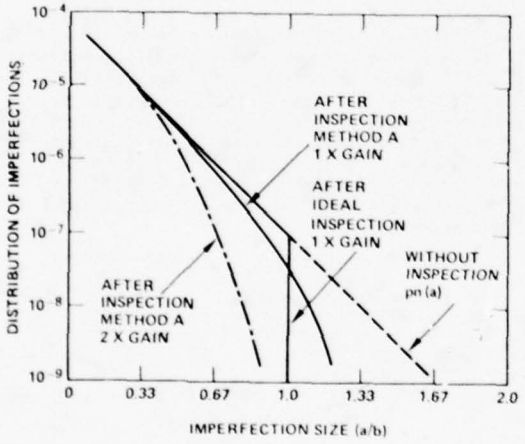

Fig. 4. The effect of various inspections on the distribution of imperfection sizes going into service.

Retirement for Cause (RFC) - A life extension strategy based upon retirement for cause rather than removal at a specified design life, can more completely utilize the available life of each component (5). The RFC procedures may utilize either deterministic or probabilistic fracture mechanics. In the deterministic case, the non-destructive inspection defines the maximum flaw size that could be missed and get into service; loading and stress analyses define the maximum cyclic and steady stresses in the areas of concern; and the deterministic fracture mechanics analysis calculated the maximum amount of crack progression from the largest initial flaw that might occur under continued operation at conservative (highest) cyclic and steady stresses. The RFC allowables are then established by selecting an appropriate safety factor based upon qualitative engineering judgment.

The probabilistic approach to RFC is similar, but instead of a specified maximum flaw size, a probability of occurrence of various flaw sizes is specified. Similarly instead of a maximum cyclic and steady stress, a probability distribution of various cyclic and steady stresses is input, and instead of a specific crack progression curve, the probabilistic fracture mechanics calculation yields a failure probability (reliability) as a function of time. Instead of a specific safety factor an appropriate accept/reject inspection size and inspection interval are selected to maintain a sufficiently low failure probability.

Successful implementation of the probabilistic fracture mechanics approach requires extensive measurements to obtain the statistical data and develop the appropriate probability distributions for the inspection, the mission loads, the local stress concentrations, and the materials crack propagation and fracture toughness properties. Large deficiencies in any one of these input parameters will require utilizing a conservative upper bound and thereby reduce the life extension and payoff which results from implementing the RFC program.

Combined Analysis - Life extension errors, which can reduce the effectiveness of RFC program, can be substantially negated with a modified RFC procedure which makes more direct use of past operating experience as reflected in the inspection information to establish the RFC strategy. This modified approach is a logical outgrowth of a statistical engineering method called Combined Analysis which has been developed by Failure Analysis Associates (5-8). Combined analysis (CA) utilizes the minimum amount of engineering modeling required to supplement the routine statistical analysis of actual in-service data on the frequency and severity of cracking, failures, and successes. Figure 5 shows typical results for a hypothetical but realistic population of turbine rotors. The conventional "design life" is established to assure an acceptably low failure rate. A significant percentage of rotors (≈ 10%) will be cracked but not failed while the balance will not even be cracked at the "design life". An RFC procedure based upon PFM would utilize a conservative calculation of the distribution of crack propagation lives, N_p, to establish allowables. The CA approach would utilize all available in-service data on N_p and the initiation lives, N_i, along with laboratory data or engineering models which relate N_i, N_p and N_f as shown in Fig. 5. As new service or test data reveal past errors in part usage (mission mix) or calculated stresses, the CA procedures continually and intrinsically account for them. Thus errors in the engineering model or materials data are not as critical in a CA/RFC life extension as with PFM/RFC because CA provides continual calibration with actual experience. The basic approach of incorporating a "fudge" factor in the design calculation to explain actual test and field experience is a common design approach. The CA approach simply provides a more formal and mathematically rigorous basis for incorporating actual performance data into the life prediction.

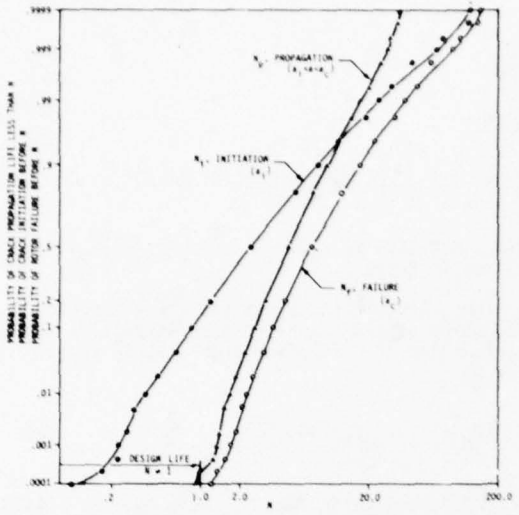

Fig. 5. Comparison of the variability of initiation lives, propagation lives, and total cycles to failure for a hypothetical but realistic population of turbine rotors.

An inspection-based CA/RFC procedure has been proposed which uses actual field data, such as the maximum apparent crack depth (a, measured non-destructively), to calibrate the calculated remaining life. As will be shown, life extension based upon the CA/RFC procedure is much more effective than purely analytical PFM/RFC because it is much less sensitive to analysis errors than PFM/RFC procedures which uses inspection only as a flaw screening device.

Reliability/Cost Optimization - Whether the RFC system is based upon deterministic fracture mechanics, probabilistic fracture mechanics, or combined analysis techniques, selection of the specific life extension strategy should be based upon optimization of the relative cost and reliability associated with various options. Specifically the effects of realistic inspection, analysis, or usage uncertainties must be quantified and incorporated in selection of the optimum life extension strategy.

The following two sections provide examples which illustrate the basis concepts.

TURBINE BLADE: SELECTION OF AN OPTIMUM INSPECTION REJECTION LEVEL

The following quality assurance problem (4) illustrates the use of inspection uncertainty, preinspection flaw frequency, probabilistic fracture mechanics, combined analysis and reliability/cost optimization concepts to select the optimum rejection level for inspections performed during manufacture of a population of gas turbine blades. Figure 6 summarizes the methodology applied in this example. The analysis inputs are: (1) the rejection probability as a function of inspection level (4) and imperfection size (a), (2) the flaw preinspection flaw frequency (FF) as a function of imperfection size, (3) the conditional probability of failure given an imperfection of size a, (4) the manufacturing cost per blade, (5) the inspection cost per blade, and (6) the average cost per failure including the many indirect costs. Four methods have been identified for determining the flaw frequency; and three methods for determining the conditional failure probability, one of which is probabilistic fracture mechanics. In this example, the actual failure history is used to predict the probability of failure given a flaw of size a rather than PFM analysis.

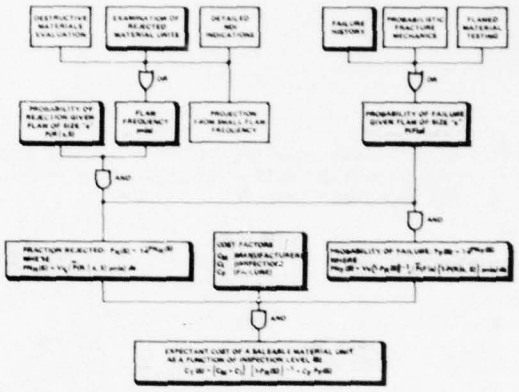

Fig. 6. Combined analysis and inspection procedure to determine the optimum inspection size, which minimizes the total product cost.

First, we consider the failure history. Assume that 100,000 blades have completed their design life, and 100 of the blades failure prematurely. The fraction failed is then $F_F = 10^{-3}$. The total cost of these 100 failures to the manufacturer, including estimated direct costs (e.g., customer relations), is estimated to be 10 million dollars. This given an average cost per failure C_F = $100,000.

The 100 failed blades are analyzed to determine the size of defect which initiated the failure, and the results are summarized in Table 1. A point estimate of the size distribution of defects which historically caused failure $P_{no}(F,a,S_o)$ is given in column three by dividing the number of initiating defects in each size interval by the interval size and the total volume of the material in the 10^5 blades, i.e., by dividing by 50 cm^3/blade x 10^5 blades / 10^{-1} cm = 5 x 10^5 cm^4.

The turbine blades before being admitted to service had to pass the historical inspection in which the inspection uncertainty was δ = .25 + 0.1 cm with the inspection size $S = S_o$ = 3/4 cm, and the rejection rate has been F_{RO} = 4.5%. A sample of 100 rejected blades were examined, and the imperfections in these blades which cause rejectable indications are summarized in Table 2. A point estimate of $pn_o((a,S_o)|R)$, the size distribution of imperfections which cause rejection, given that the blade has been rejected, is given in column three of Table 2. It is obtained by dividing the number of rejectable indications in each imperfection size interval by the volume of the 100 blades and the interval size, i.e., column two is divided by 100 blades x 50 cm^3/blade x 10^{-1} cm = 500 cm^4.

Table 1. Hypothetical problem: Number of failure initiating flaws of various sizes in 100 failed blades.

Flaw Size Interval in cm	Number of Flaws	$pn_o(F,a,S_o)$ in cm^{-4}	Flaw Size "a" in cm
0.00 - 0.10	0	0×10^{-6}	0.05
0.10 - 0.20	0	0×10^{-6}	0.15
0.20 - 0.30	0	0×10^{-6}	0.25
0.30 - 0.40	0	0×10^{-6}	0.35
0.40 - 0.50	1	2×10^{-6}	0.45
0.50 - 0.60	7	14×10^{-6}	0.55
0.60 - 0.70	25	50×10^{-6}	0.65
0.70 - 0.80	36	72×10^{-6}	0.75
0.80 - 0.90	22	44×10^{-6}	0.85
0.90 - 1.00	7	14×10^{-6}	0.95
1.00 - 1.10	2	4×10^{-6}	1.05
1.10 - 1.20	0	0×10^{-6}	1.15

Table 2. Hypothetical problem: Number of rejectable indications in each flaw size range in 100 rejected blades.

Flaw Size Interval in cm	Number of Rejectable Indications	$pn_o((a,S_o)\|R)$ in cm^{-4}	Flaw Size "a" in cm
0.00 - 1.10	16	32×10^{-3}	0.05
0.10 - 0.20	19	38×10^{-3}	0.15
0.20 - 0.30	19	38×10^{-3}	0.25
0.30 - 0.40	17	34×10^{-3}	0.35
0.40 - 0.50	13	26×10^{-3}	0.45
0.50 - 0.60	9	18×10^{-3}	0.55
0.60 - 0.70	5	10×10^{-3}	0.65
0.70 - 0.80	3	6×10^{-3}	0.75
0.80 - 0.90	1	2×10^{-3}	0.85
0.90 - 1.00	1	2×10^{-3}	0.95

Manufacturing and Inspection Costs - If the cost of manufacturing a blade is \$100 plus an additional \$10 to inspect the blade, the question is whether the total cost could be reduced by selecting a different inspection level (S). Using the data above as input, the dependence of the expectant cost per turbine blade upon inspection level (S) can be determined as indicated in Fig. 7. First the probable fraction of rejected blades is determined as a function of S. Assuming that the rejection probability for the historical inspection method has been determined to be

$$P_o(R|a,S) = (\delta_o(S)\sqrt{2\pi})^{-1} \int_{-\infty}^{a} \exp\left[-(x-S)^2/2\delta_o^2(S)\right] dx \quad (1)$$

with the historical inspection method uncertainty given by

$$\delta_o(S) = 0.2S + 0.1 \text{ cm} \quad (2)$$

the rejection probability for the specific inspection used on the 100,000 turbine blades (the historical inspection method with S = 0.75) is given by

$$P_o(R|(a,S_o)) = (\delta_o(S_o)\sqrt{2\pi})^{-1} \int_{-\infty}^{a} \exp\left[-(x-S_o)^2/2\delta_o^2(S_o)\right] dx \quad (3)$$

where S_o = 0.75 cm. The probable fraction of rejected blades if the historical inspection method is used is given by

$$F_{RO}(S) = 1-e^{-PN_{RO}(S)} \quad (4)$$

where

$$PN_{RO}(S) = V_u F_{RO}(S_o) \int_o^{\infty} \left[P_o(R|(a,S))\right]\left[P_o(R|(a,S_o)\right]^{-1} pn_o((a,S_o)|R)\, da \quad (5)$$

$F_{RO}(S_o)$ = 0.045, V_u = 50 cm^3, and $pn_o((a,S_o)|R)$ is given in Table 2.

The average cost to manufacture a turbine blade which passes the historical inspection method as a function of inspection level (S) is then given by

$$(C_M + C_I)(1-F_{RO}(S))^{-1} \quad (6)$$

and is illustrated in Fig. 7. Here $C_M + C_I$ = \$110.

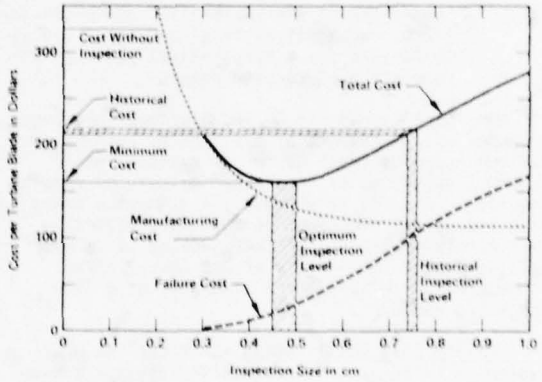

Fig. 7. Total cost per turbine blade as a function of rejection level when the average cost of a failure is \$100,000.

Failure Costs - Next the probable fraction of blades which would fail is given by

$$F_{FO}(S) = 1-e^{-PN_{FO}(S)} \quad (7)$$

where

$$PN_{FO}(S) = V_u \frac{1-F_{RO}(S_o)}{1-F_{RO}(S)} \int_o^{\infty} \frac{1-P_o(R|(a,S))}{1-P_o(R|(a,S_o))}\, pn_o(F,a,S_o)\, da \quad (8)$$

Here $pn_o(F,a,S_o)$ is given in Table 1, $F_{RO}(S)$ is calculated by Eq. 4, $P_o(R|(a,S_o))$ is given by Eq. 3, $P_o(R|(a,S))$ is given by Eq. 1, V_u = 50 cm^3, and $F_{RO}(S_o)$ = 0.045. The probable failure cost per blade in service as a function of inspection size is given by

$$C_F\, F_{FO}(S) \quad (9)$$

where C_F = \$100,000. This probable failure cost per blade is also shown in Fig. 7.

Inspection Level Optimization - The total expectant cost of a saleable turbine blade is the sum of average cost to manufacture a turbine blade which passes the inspection and the expectant cost due to the finite probability that the blade will fail. The total expectant cost per saleable blade is also illustrated in Fig. 7. The total expectant cost of a turbine blade if no inspection is conducted was calculated to be \$328. It is evident from Fig. 7 that the historical inspection level set by engineering judgment reduces the total cost of a saleable blade to \$215. However, this analysis shows that the total expectant cost of a blade can be further reduced from the present cost of \$215 per blade to \$159 per blade by reducing the inspection size from the historical level of S = 0.75 cm to S = 0.45 cm. Over the 10^5 blades, this represents a potential additional savings of approximately 6 million dollars by simply adjusting the rejection level for an existing inspection.

Now consider the optimum decision from the user rather than manufacturer's point of view. The user might experience an additional loss on the average of \$900,000, which results from the fact that a blade failure forces the turbine out of service for an extended period of time. Hence the average failure cost to the user might be \$1,000,000. Figure 8 illustrates the results of a similar optimization analysis where the new expectant costs of a saleable blade is very high (\$1,115 per blade) if the inspection size is left at the historical level. A change in inspection size from the historical level of 0.75 cm to the level of 0.35 cm will reduce the total expectant cost to the user of each blade to \$234.

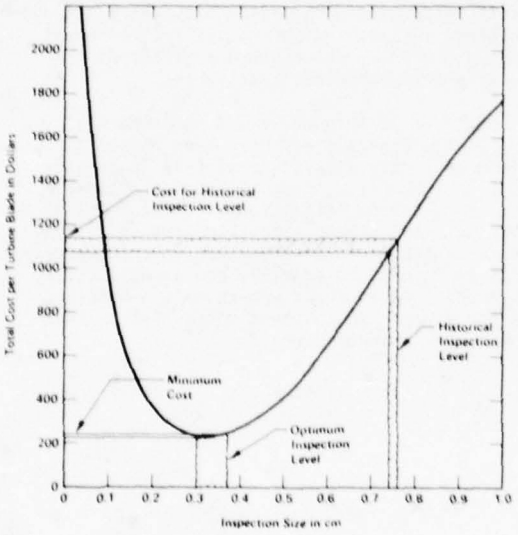

Fig. 8. Total cost per turbine blade as a function of inspection rejection level when the average cost of a failure is a million dollars.

Alternative inspection procedures with modified uncertainty have been (5) similarly evaluated to determine (1) the specific inspection level which produces the minimum cost, and (2) the magnitude of the minimum cost relative to the historical blade inspection utilized at the level which produces minimum cost. The quantitative comparisons clearly show the importance of selecting the optimum rejection level for the specific inspection and the importance of low inspection uncertainty, rather than high resolution alone, in minimizing the total cycle costs.

TURBINE DISK: IMPACT OF ANALYSIS AND INSPECTION UNCERTAINTY ON LIFE EXTENSION STRATEGY

FAA has developed analytical procedures (5-9) to evaluate the effectiveness of any proposed life extension procedure based upon retirement for cause (RFC), considering the in-service loading and analysis uncertainties as well as inspection uncertainty. This evaluation procedure, a probabilistic simulation model, has been applied to a population of 10,000 gas turbine disks to determine the impact of

a) Stress variations from disk to disk

b) Unknown precise age of past usage of the disks

c) Multiple (repeated) inspections rather than a single inspection

d) Reduced inspection intervals, and

e) Utilizing inspection results, through combined analysis (CA), rather than design calculations to establish RFC allowables.

The effect of analysis and inspection uncertainty was evaluted by considering the six hypothetical teams shown in Fig. 9. Each team consists of one analyst and one inspector of varying capabilities, and the total expectant cost savings possible through RFC procedures utilizing specific teams were computed for 1000 disks, averaged, and compared.

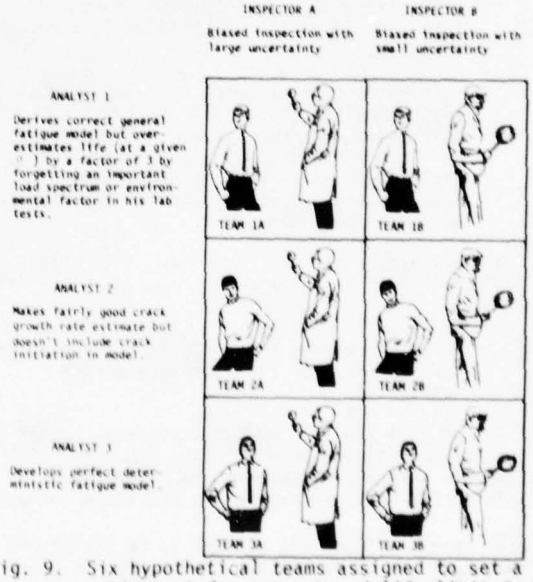

Fig. 9. Six hypothetical teams assigned to set a retirement-for-cause-based life limit for 10,000 inspected turbine disks.

Fatigue Life Simulation - The total fatigue life to brittle failure of a disk when a life-limiting rim can be expressed generally as

$$N_f = N_i + N_p$$

where

N_f = Life to failure of the shortest-lived of all the (up to 100 or more) rim slots of the rotor (in units of cycles, time, inspection intervals, or design lives)

N_i = Life to initiation of a crack of some small defined depth, a_i, (a_i = 0.001 inches in this report)

N_p = Life to propagate the crack from size a_i to critical size for brittle failure, a_c.

The specific equation used to simulate in-service fatigue life required for failure is given by

$$N_f = C_i/\sigma^6 + C_p \log (a_c/a_i)/\sigma^3. \quad (10)$$

The equation used to relate the crack depth a to the number of applied load cycles N is

$$N = C_i/\sigma^6 + C_p \log (a/a_i)/\sigma^3 \quad (11)$$

where

a = Crack depth (greater than a_i)

N = Number of vendor-specified design lives required to produce a crack of depth a

N_f = Dimensionless life expressed as the number of "worst-case" predicted retirement lives required for failure (i.e., a rotor with N_f = 7 would fail after seven times the predicted life)

σ = Effective alternative* nominal stress at the crack locus in ksi (treated as a random variable)

C_i, C_p = Parameters (treated as random variables) which simulate the variation of crack initiation and crack growth, respectively, at a given σ, as caused by geometric variables such as surface roughness and metallurgical variables such as local hardness or composition, and

$$a_c = (K_c/(2.5\sigma))^3 \quad (12)$$

with

K_c = Critical stress intensity factor expressed in ksi $(in.)^{1/2}$ (treated as a random variable).

The form of (10) and (11) and the numerical values of the parameters have been selected for simplicity and because they are representative of observed fatigue performance of certain gas and steam turbine rotor rims.

The exponent 3 in Eq. 12 accounts for the stress decrease below the crack surface (an exponent of 2 would be correct for certain crack geometries subject to uniform stress), and the factor 2.5 (with inherent units of $in.^{1/6}$** to make Eq. 3 dimensionally correct) is representative of the results of a stress intensity factor analysis of the rim crack geometry.

The cumulative probability distribution of C_i is assumed to be log-normal so that $\log C_i$ is a Gaussian or normally distributed variable. The selected parameters of this normal distribution are a mean or median of 10 and a standard deviation of 0.2. These assumptions about the probability distribution of $\log C_i$ can be compacted into the notation

$$\log C_i = \text{GAU}(10, 0.2) \quad (13)$$

or

$$C_i = 10^{\text{GAU}(10,\ 0.2)_{\text{ksi}^6}}** \quad (14)$$

The other assumed probability distributions are given by

$$C_p = 10^{\text{GAU}(5.0,\ 0.1)_{\text{ksi}^3}} \quad (15)$$

$$\sigma = \text{GAU}(40 \text{ ksi},\ 5 \text{ ksi}) \quad (16)$$

$$K_c = \text{GAU}(100 \text{ ksi } (\text{in})^{1/2},\ 15 \text{ ksi } (\text{in})^{1/2})*** \quad (17)$$

Figure 10 shows the probability distribution for inspectors A and B and Fig. 11 that for the operating stress (σ) given by (16). Considerable rotor-to-rotor stress variation has been assumed.**** This stress variation might result from aircraft mission differences which produce different in-service, thermomechanical transients.

Equations 10 through 17 and the numerical values of their parameters have been chosen to simulate many characteristics of real in-service fatigue performance. These include: a greater effect of stress on initiation life (exponent of 6) than on crack growth life (exponent of 3), greater scatter in initiation than in crack growth at a given σ (Eqs. 14 and 15), and a realistic, smaller increase in crack growth rate with crack depth for a crack in a stress concentration than for one under uniform stress.

*Steady stress effects are assumed to be negligible in this example. Refer to (4) for an RFC procedure that considers the relative contribution of steady and alternating sources.

*1 in. = .0254 m

**1 ksi = 6.894 x 10^6 Pa = 6.894 N/mm^2

***1 ksi $(in)^{1/2}$ = 34.745 $Nmm^{-3/2}$

****The coefficient of variation V_σ for the stress distribution is equal to 5/40 or 12.5%.

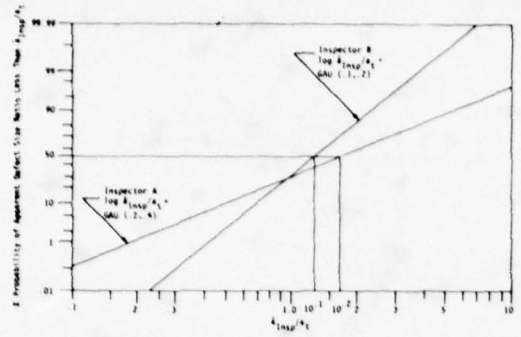

Fig. 10. Probability distribution of $\hat{a}_{Insp}/a_t$ for Inspectors A and B.

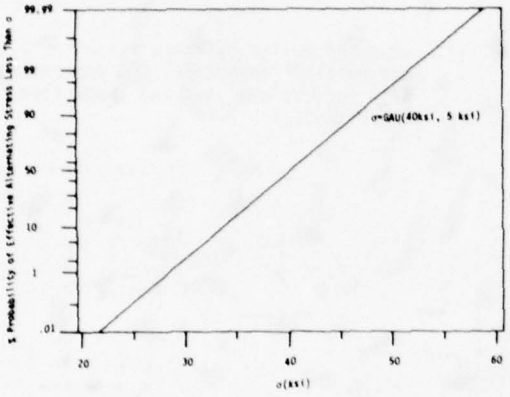

Fig. 11. Probability distribution of σ due to rotor-to-rotor variation.

Figure 5 presents the simulated life-to-failure N_f (also N_i and N_p) data for 10,000 rotors* obtained by applying the Monte Carlo simulation computer program in (2) to Eqs. 10 through 17. The results show that crack propagation, N_p, controls the early part of the N_f probability distribution and crack initiation the later part ($N > 20$). Furthermore, significant fatigue life scatter occurs and the first few failures occur between $N = 1$, the design life, and $N = 1.5$. This is intended to simulate a good initial life prediction or design analysis resulting in neither failure nor severe overdesign.

Actual Crack Depth at Inspection Time N_t - The actual crack size a_t at the actual inspection time N_t is solved from (11) as

$$\log a_t = (N_t - C_i/\sigma^6)(\sigma^3/C_p) + \log a_i \quad (18)$$

For further discussion, it is of interest to note that at the median values ($N_t = 1$, $C_i = 10^{10}$, and $C_p = 10^5$), a 7% to 8% change in σ will change a_t by a factor of approximately three. Thus, for each in-service rotor, an inspection error of a factor of three in the estimate of crack depth is equivalent to a 7% to 8% analysis error in the effective nominal alternating stress.

*These results, from an earlier 10,000 rotor simulation (1), also accurately represent the results of the present 1000 rotor simulation.

Apparent Crack Depth from Inspection N_t - The inspection uncertainty is simulated by calculating apparent crack depth from

$$\hat{a} = \text{maximum } (.001", \hat{a}_{Insp}) \quad (19)$$

where $\hat{a}_{Insp}$ is derived solely from the calibrated inspection signal given by

$$\log (\hat{a}_{Insp}/a) = GAU (b,u) \quad (20)$$

where b, taken to be either 0.1 or 0.2, reflects positive bias in the inspection (for example, $b = .1$ implies that typically the crack size will be overestimated by a factor of $10^{.1} = 1.26$). This bias could reflect conservative procedures or the fact that multiple rim slots create more change for a high, rather than low, estimate of the rotor's maximum value of a_t. Finally, u, taken to be either 0.2 or 0.4, is the "logarithmic standard deviation" of $\hat{a}_{Insp}/a_t$ and reflects inspection uncertainty in a similar manner as in (12). Eq. 20 is plotted in Fig. 10 for the two sets of parameters b and u, corresponding to inspectors A and B. Inspector A has available a relatively poor technique with large bias and uncertainty, while Inspector B has less bias and uncertainty.

Analysis Uncertainty - Three hypothetical analysts are considered. Analyst 1 uses the equation

$$\hat{N}_f = 3 \times 10^{10}/\hat{\sigma}^6 + 10^5 \log (\hat{a}_c/.001)/\hat{\sigma}^3 \quad (21)$$

to model the fatigue process. By comparing Eq. 21 to Eqs. 10,11, and 23, one can see that the form of Eq. 21 is correct, but that, on average, Eq. 21 will overpredict the median failure life by a factor of three. Such an error could be due, for example, to the use of inappropriate temperatures for laboratory fatigue tests.

Analyst 2 uses the equation

$$\hat{N}_f = .333 \times 10^{10}/\hat{\sigma}^6 + .333 \times 10^5 \log (\hat{a}_c/.001)/\hat{\sigma}^3 \quad (22)$$

to model the fatigue process. On the average, this analyst underpredicts life by a factor of three.

The third analyst develops a near-perfect deterministic model of the fatigue process that corresponds closely to the median life. Analyst 3's equation is

$$\hat{N}_f = 10^{10}/\hat{\sigma}^6 + 10^5 \log (\hat{a}_c/.001)/\hat{\sigma}^3 \quad (23)$$

It has been assumed that the analysts have included all relevant failure modes in their assessments. For example, the effect of a larger-than-anticipated vibratory stress could cause the effective critical crack depth to be limited by high frequency fatigue threshold rather than the material's fracture toughness. The turbine history, destructive metallographic examination of rim slots, and rotor-inspection data can be used to determine if vibratory stresses affect a_c and N_f significantly.

Cost Analysis - The RFC procedures described above have been programmed into a Monte Carlo simulation program which simulated 1000 individual rotors for each RFC procedure and team. The program does the following for each rotor: (1) generates "in-service" fatigue data, (2) performs a chosen RFC procedure on each rotor at the appropriate time and makes

random errors using the probability distribution input and other appropriate equations, and (3) checks for failure of the rotor. Costs are assigned to the various outcomes of the RFC procedure for the jth rotor. Each time the rotor is inspected, a negative dollar gain (cost) of

$$G_{ji} = -2000 \text{ dollars}$$

is assigned. Each time the life of the rotor is extended, a gain of

$$G_{je} = 20{,}000\ \hat{N}'_e \text{ dollars}$$

is assigned, where \$20,000 is the original cost of a rotor designed for one life unit and $\hat{N}'_e$ is the perceived amount of life extension until either the next inspection, retirement, or failure, whichever occurs. Should a failure occur before the rotor is retired, a negative gain (cost) of

$$G_{jf} = -1{,}500{,}000 \text{ dollars}$$

is assigned.

Clearly, the estimation of the expected cost of failure G_f is a complex, controversial subject (6,9,10,11) that touches on a variety of sensitive safety, economic, and political issues. However, G_f is finite, and the failure probability is greater than zero and to insist otherwise is unrealistic and impractical. If specification of G_f is undesirable, a maximum allowable failure probability can be specified instead of built into the RFC procedure constraints. This failure probability could be specified and justified by using several comparative criteria. For example, the failure probability may be acceptable if it is less than the in-service failure probabilities demonstrated during the design life of similar equipment accepted by society for general usage. For further discussion of the "how safe is safe enough" question, the reader is referred to the work of Starr (10) and Tetelman (11).

The total RFC cost savings for each rotor is obtained by summing

$$G_j = f_i G_{ji} + f_e G_{je} + f_f G_{jf}$$
(Repeated indices do not denote summation)

where f_i, f_e, f_f represent the number of incidents for each type of cost gain for the jth rotor.

The expected average dollar gain per rotor of the RFC procedure is then estimated by averaging all the simulations

$$\bar{G} = \sum_{j=1}^{1000} G_j/1000.$$

$\bar{G}$ is a measure of the RFC performance. The rms error of the $\bar{G}$ estimate (i.e., the sampling tolerance or standard deviation of $\bar{G}$) due to the use of the finite number of rotor simulations (1000) is estimated to be \$2000 near the optimum safety factor, where the simulated failure probability is of the order of .001. Thus, the curves reflect the simulated procedure with an accuracy of approximately ±2000 dollars.

RFC Evaluation Results - The average dollar gain (cost savings) G for each RFC procedure and analyst/inspector team was computed. Typical results are summarized by Figs. 12-14 and discussed below.

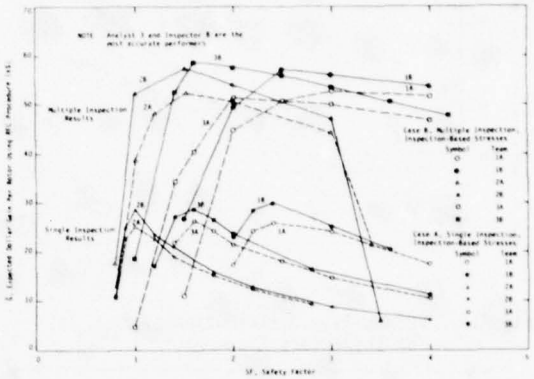

Fig. 12. Expected dollar gain per rotor for single and multiple inspection RFC procedures with various analysis and inspection uncertainties.

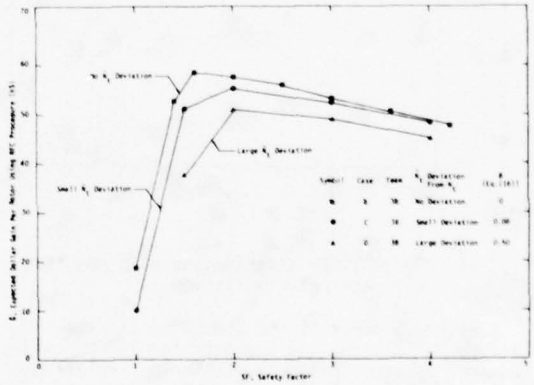

Fig. 13. Effect of uncertain past usage on expected dollar gain per rotor for multiple inspection RFC procedure.

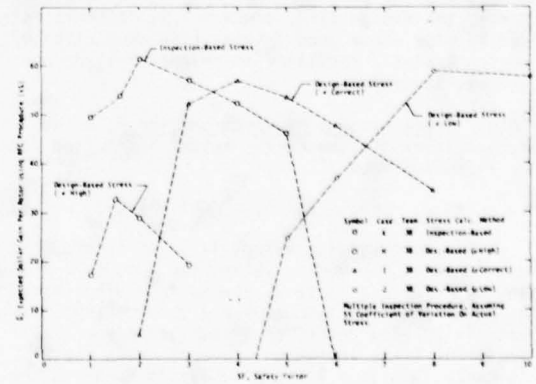

Fig. 14. Comparison of the expected cost savings per rotor with RFC procedures utilizing various stress input.

Single Inspection vs. Multiple Inspection - The $\bar{G}$ results for Cases A and B, single and multiple inspection-based-stress RFC procedures, respectively, are displayed in Fig. 12. Three conclusions are evident: (1) an optimum safety factor exists for each team within each case, (2) the teams with the better inspectors do consistently better than their less able counterparts although even the less accurate inspectors can still achieve substantial cost savings, and (3) provided that the safety factor is between 2 and 3, the multiple inspection RFC procedure is substantially better than the single inspection procedure.

The general shape of the $\bar{G}$ curve is due to the trade-off between premature failures and premature retirement. The optimum safety factor represents the best balance between these two competing effects and corresponds to simulated failure rates of the order of one failure in 1000 rotors. The sharp drop in the $\bar{G}$ curves on the low SF end corresponds to too many failures. The gradual drop in the $\bar{G}$ curves on the high SF end represents the cost of an increasing number of premature rotor retirements.

Figure 12 shows that the optimum safety factor is, unfortunately, a strong function of the analytical model. Since we assume that little or no knowledge of analysis error is available prior to formulation of the RFC procedure, there seems little chance to choose accurately an optimum safety factor. The situation would be significantly worse, however, if the minimum inspection interval was 1 rather than 1/2 times the design life as used. This computation showed an abrupt decrease in $\bar{G}$ at high SF values due to excessive premature retirements caused be a minimum inspection interval that is too large. The results showed that reduced inspection interval reduces the sensitivity to SF, as long as SF is chosen large enough to prevent failures. Furthermore, if an appropriately small minimum inspection interval is used, safety factors between 2.0 and 3.0 produce very substantial economic gains for all teams using the multiple inspection procedure.

It should be noted that none of the RFC procedures studied thus far have taken into account information received from either other rotors or earlier inspections of the same rotor. Thus, neither the analyst nor the inspector is allowed to learn from past experience. This simplification in the model is particularly unfair to the multiple inspection inspector who is made to ignore the results of previous inspections each time the rotor is reinspected.

Known vs. Estimated Component Age and Inspection Interval - It is quite likely that an analyst will not know exactly how many design lives have actually been used at the time of inspection. Figure 13 shows the relatively small effect of this uncertainty on the $\bar{G}$ results of the multiple inspection, CA/RFC procedure applied by Team 3B. The three usage uncertainties evaluated were:

1) Exact knowledge of N_t ($\beta = 0$)

2) A small deviation of N_t from $\hat{N}_t$ (factor of 1.2 ($\beta = 0.8$), i.e., 20% error or less, 68% of the time)

3) A large deviation of N_t from $\hat{N}_t$ (factor of 2 error or less ($\beta = 0.50$), 68% of the time)

Design-Based-Stress (PFM) vs. Inspection-Based Stress (CA)/RFC Procedures - The results of using a single best estimate design stress in Eq. 11 rather than a stress calculated from inspection information is shown in Fig. 14. The results in Fig. 14 are for a rotor population with realistic actual stress variations from rotor to rotor (a larger variation has been assumed throughout the rest of this study). The figure shows that the design-based procedure does reasonably well provided that the analyst chooses the correct stress value. Note, however, that if too high or too low a stress value is chosen, very poor $\bar{G}$ results are obtained, even with Team 3B, the best team. Thus, the inspection-based-stress RFC procedure is much more likely to produce substantial economic gains than the design-based procedure.

SUMMARY AND CONCLUSIONS

The results of this study have led to the following general conclusions:

1) It is evident that even with large inspection and analysis uncertainties, cost effective rotor life extension at extremely low failure probabilities can be effected using a Retirement-For-Cause (RFC) procedure which makes full use of in-service structural fatigue data.

2) Any proposed RFC procedure should be subjected to a parametric probabilistic evaluation using realistic simulated data to evaluate the procedure and to learn which areas of analysis, experiment, logistics, and inspection are most critical to the success of the RFC procedure.

3) Computer simulation of the fatigue crack initiation and growth process provides a viable means for evaluating the effect of both systematic and stochastic errors upon the payoff potential of an RFC procedure.

4) A more effective CA/RFC procedure would be based on probabilistic rather than deterministic life extension calculations and would make use of information obtained from other rotors and previous inspections of the same rotor.

A number of conclusions have been reached for the specific RFC example described. They are:

1) Life based safety factors of 2 to 3 will result in substantial economic gains with little chance of producing an unacceptably large number of failures if the CA/RFC procedure uses a stress value which is calculated from the inspection results, and if the minimum inspection interval is sufficiently small.

2) With regard to subcritical crack growth life, knowledge of the maximum crack depth to within a factor of three is equivalent to knowledge of the effective stress to within 8%.

3) Larger economic gain results from an RFC procedure which uses stress values calculated from inspection results rather than

conventionally calculated stress values.

4) Multiple inspection RFC procedures are at least twice as effective as single inspection procedures if a safety factor of 2 to 3 is used.

5) Uncertainty regarding the age at inspection has little effect on the overall results of the RFC procedure, per se, but may lead to early failures before the first scheduled RFC inspection.

6) Shortening the length of the minimum inspection interval in multiple inspection procedures can substantially reduce the overall cost due to premature retirements.

RECOMMENDATIONS AND ONGOING WORK

In addition to the results described in this paper, Failure Analysis Associates has also evaluated combined analysis/retirement for cause (CA/RFC) procedures for more difficult situations (5,8) where (1) the engineering model of the failure includes systematic and severe errors, like incorrect assessment of the failure mode, or (2) a key life controlling parameter is unavailable, e.g., the part is uninspectable. These studies have shown that cost effective life extension can be achieved using CA/RFC techniques even with serious analysis and inspection uncertainty. Furthermore, any proposed RFC procedure should be evaluated through parametric probabilistic simulation of the service population. These sensitivity studies should identify those analysis, inspection, logistics, and service data which are most critical to optimum payoff of the RFC procedure and the quality of the data required to assure sufficient payoff to implement.

Failure Asalysis Associates has initiated a three year ARPA-sponsored program with the Air Force (AFML) to develop a quantitative methodology and apply it to predict optimum RFC strategy for engine disk life extension. This program is now evaluating experimentally the inspection uncertainty of four disk bolt hold inspection systems using (1) conventional eddy current equipment, (2) conventional eddy current equipment with adaptive learning signal processing, (3) a higher resolution controlled reluctance eddy current (CREC) probe, and (4) a CREC probe with adaptive learning signal processing. The program will estimate the preinspection flaw sizes from the inspection results and calculate using both the probabilistic fracture mechanics and combined analysis approaches, the conditional failure probability for continued operation. A cost equation will be developed and used to assess the payoff of various RFC strategies. The methodology will be verified by a structural simulation testing of a number of bolt hold specimens subjected to the optimum RFC inspection and life extension procedure.

Additional work will be required to quantify the analysis, inspection and materials uncertainty information for the range of components and parts where RFC can produce cost savings.

ACKNOWLEDGEMENTS

The author would like to acknowledge his coworkers at Failure Analysis Associates, particularly Phil Besuner, Ken Sorenson, and Duane Johnson who performed much of the work described, and the Electric Power Research Institute and Advanced Research Projects Agency for their financial support of the work.

REFERENCES

1. Ray, Charles A., Jr., et al., "Failure Analysis and Failure Prevention in Electric Power Systems," Nuclear Engineering and Design 43 (1977), 1.

2. Besuner, P. M. and A. S. Tetelman, "Probabilistic Fracture Mechanics," IBID, p. 99.

3. Johnson, D. P., "Inspection Uncertainty: The Key Element in Nondestructive Inspection," Materials Evaluation, Vol. 39, No. 6.

4. Johnson, D. P., "Cost Risk Optimization of Nondestructive Inspection Level," Nuclear Engineering and Design 43 (1977), 207.

5. Besuner, P. M., K. G. Sorenson, and D. P. Johnson, "Retirement-for-Cause: A Workable Approach for Structural Life Extension and Response to In-Service Problems," Topical Report EPRI NP-855 (August 1978).

6. Besuner, P. M., A. S. Tetelman, G. R. Egan, C. A. Rau, "The Combined Use of Engineering and Reliability Analysis in Risk Assessment of Mechanical and Structural Systems," Proceedings of Risk-Benefit Methodology and Application Conference, Asilomar, CA, UCLA-ENG-7598, Ed. David Okrent (December 1975).

7. Besuner, P. M., K. G. Sorenson, and D. P. Johnson, "A Workable Approach for Extending the Life of Turbine Rotors," Presented at the ASME Gas Turbine Division Annual Meeting, Philadelphia, PA (March 1977). Published in the ASME Volume Fatigue Life Technologies, ed. by T. Cruse and J. Gallagher.

8. Sorenson, K.G., and P. M. Besuner, "A Workable Approach for Extending the Life of Expensive Life-Limited Components," Presented at the 1977 Energy Technology Conference, Houston, Texas (18-22 September 1977), Published in the ASME Vol. PVP-PB-023, Failure Data and Failure Analysis: In Power and Processing Industries, Ed. A. Gangadharan and S. Brown (September 1977).

9. Tetelman, A. S., and P. M. Besuner, "The Application of Risk Analysis to the Brittle Fracture and Fatigue Steel Structures," Presented at the Fourth International Conference on Fracture, Waterloo, Canada, (June 1977).

10. Starr, C. "Benefit-Cost Studies in Socio-Technical Systems," Colloquim on Benefit-Risk Relationships for Decision-Making, Washington, D. C., (April 1971).

11. Tetelman, A. S., "How Safe is Safe Enough?" Social Consequences of Engineering, Ed. L. S. Hager, Dun-Connelley Publishing Corporation (March 1977)

12. Graham, T. W. and A. S. Tetelman, "The Use of Crack Size Distribution and Crack Detection for Determining the Probability of Fatigue Failure," Materials Department, School of Engineering and Applied Science, UCLA, and Proceedings, AIAA Conference, Las Vegas, Nevada (April 1974).

ACCEPT/REJECT CRITERIA FOR STRUCTURAL CERAMICS:
PART 1: SOME EFFECTS OF CAVITIES ON THE FRACTURE OF CERAMICS
I. CYLINDRICAL HOLES

A. G. Evans
Rockwell International Science Center
Thousand Oaks, California 91360

D. R. Biswas and R. M. Fulrath
Materials and Molecular Research Division
Lawrence Berkeley Laboratory and Department of Materials Science
and Mineral Engineering, University of California,
Berkeley, California 94720

ABSTRACT

The problem of fracture from cylindrical cavities in brittle materials has been analyzed. The analysis is based on the conditions required to extend cracks that pre-exist at the cavity surface. It involves the combined use of fracture mechanics and statistics solutions for crack extension in the concentrated stress field around the cavity. The general pertinence of the approach is substantiated by experimental studies of fracture from cavities in polycrystalline alumina.

INTRODUCTION

The fracture of ceramic components frequently initiates at holes or voids,[1] and it is of considerable practical importance to comprehend the detailed influence of cavities on fracture initiation.

Fracture from cavities is most realistically treated by examining the extension of flaws at (or near) the cavity surface.[1,2] The flaws are considered to extend when the stress intensity, due to the combined stress field of the cavity and the flaw, attains the critical value for local crack extension. The flaw responsible for fracture in polycrystalline ceramics may either pre-exist or may develop due to subcritical extension of grain boundary cusps. In either case, a distribution of flaws should exist, prior to final fracture, in the vicinity of the cavity surface. The analysis of fracture from cavities is thus a statistical problem, involving the extension of crack arrays in localized stress fields. A preliminary attempt to address this problem[3] has used the unperturbed stress field at the cavity surface as the basis for the statistical analysis. This analysis only pertains, of course, when the cracks are small enough (vis-a-vis the cavity radius) that stress gradient effects across the crack and interaction effects[2] can be neglected.

Further progress in the characterization of fracture from cavities requires that the statistical approach be extended to include the entire range of crack sizes of practical concern (up to at least half the cavity radius)[1,4] and hence to incorporate the stress gradient and interaction effects on crack propagation. Three-dimensional stress intensity factor solutions for cracks emanating from the cavity surface# are needed for this purpose. These results can then be combined with statistical crack size distributions to obtain the appropriate fracture relationships. The present paper considers the problem of fracture from cylindrical cavities; while a companion paper examines the analagous problem of fracture from spherical cavities. These papers emphasize the basic approach for combining linear elastic fracture mechanics solutions with statistical results. For this purpose, the best available fracture mechanics and statistical analyses are invoked; recognizing that, in some instances, the solutions are still rather approximate. Evidently, improved solutions can be incorporated, as they emerge, using the same basic procedures.

To ascertain the general validity of the analytic results, it is required that cavities with well-defined surface crack distributions be prepared and tested. Preliminary results are obtained in this study by performing experiments on a hot pressed polycrystalline alumina containing cylindrical cavities.

STRESS INTENSITY FACTOR SOLUTIONS

Well-established stress intensity factor K solutions can be obtained directly from the literature for the two-dimensional problem of single (or double) radial cracks emanating from a cylindrical hole[5] (Fig. 1). However, there are few well-substantiated solutions for the more relevant three-dimensional problems, such as semi-elliptical cracks at the surface of cylindrical cavities. Approximate three-dimensional solutions are often obtained by linear superposition. Such solutions are particularly convenient to derive, and are the primary solutions used in the present studies. Hence, the methods of solution and the expected accuracy of the results are examined.

#A similar approach can be used to include volume cracks that do not terminate at the cavity surface. However, the analysis is complicated by subcritical crack/cavity linking effects, and the analysis is thus deferred to a subsequent publication.

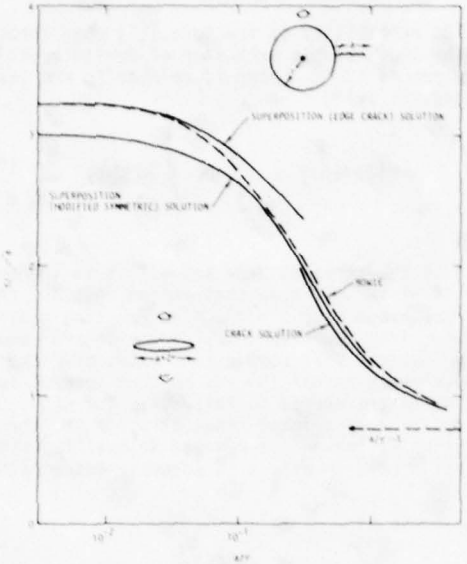

Fig. 1. Stress intensity factor solutions for a single radial crack emanating from a cylindrical hole.

The three primary superposition results are: for a two-dimensional symmetrically loaded crack of length 2a,[6,7]

$$K_I = \frac{1}{(\pi a)^{1/2}} \int_{-a}^{a} \sigma_\theta(z) \left(\frac{a+z}{a-z}\right)^{1/2} dz \qquad (1)$$

where z is the distance from the crack center and σ_θ is the tensile stress normal to the crack: for a two-dimensional edge crack of length a[8]

$$K_I = 2\left(\frac{a}{\pi}\right)^{1/2} \int_{0}^{a} \frac{[1 + F(z/a)]}{(a^2 - z^2)^{1/2}} \sigma_\theta(z) dz \qquad (2)$$

where, $F(z/a) = (1-z/a)[0.29-0.39(z/a)^2 + 0.77(z/a)^4 - 0.99(z/a)^6 + 0.59(z/a)^8]$: for a three-dimensional fully-contained crack[6,7,9]

$$K_I\big|_{\psi=0} = \qquad (3)$$

$$\frac{2}{(\pi a)^{3/2}} \int_{0}^{\pi} \int_{0}^{a} \frac{y[1-(y/a)^2]^{1/2}\,\sigma(y,\psi)}{[1-2(y/a)\cos\psi + (y/a)^2]} dy\, d\psi$$

where y is the radial distance from the crack center, and ψ is the angular coordinate with reference to the crack front location of interest (see Fig. 2).

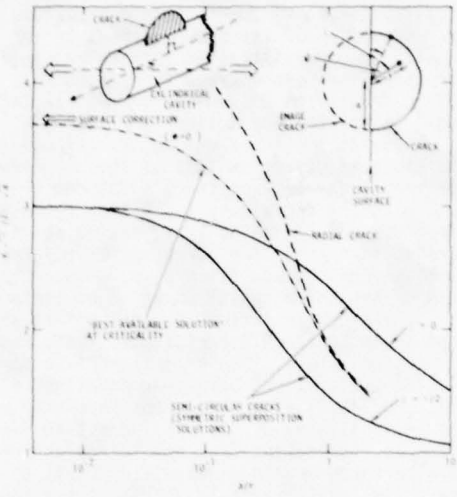

Fig. 2. Stress intensity factor solutions a semi-circular crack on the surface of a cylindrical cavity.

To examine the expected utility of the superposition method, a solution is derived for the radial crack configuration shown in Fig. 1. The tangential stress $\sigma_\theta(x)$ around a cylindrical cavity (radius r) normal to the applied stress σ_∞ is,[10]

$$\sigma_\theta = \sigma_\infty \left[1 + \frac{1}{2}\left(\frac{r}{r+x}\right)^2 + \frac{3}{2}\left(\frac{r}{r+x}\right)^4\right] \qquad (4)$$

where x is the distance from the cavity surface. Substituting Eqn. (4) into Eqns. (1) and (2) (and applying a single crack correction[7], $[(2r+a)/(2r+2a)]^{1/2}$ to convert the symmetric double crack solution to a single crack solution) yields the results plotted in Fig. 1. Also shown is the result for a crack of equivalent length (a+2r). It is apparent that the modified symmetric solution affords a very good approximation in the range $a/r \gtrsim 0.2$, as observed by Shah[7]; whereas the edge crack solution provides a superior correlation for smaller a/r. Carefully chosen superposition solutions thus appear to provide stress intensity factor approximations that should be satisfactory for present purposes.

The three-dimensional configuration of interest for the present statistical analysis is the semi-circular crack on the surface of a cylindrical cavity (Fig. 2). An approximate superposition solution for this problem considers a circular crack symmetrically loaded about the cavity surface, by the stress field of the cavity (Eqn. 4); i.e., it invokes an image crack within the cavity (Fig. 2). The solution is obtained by replacing x in Eqn. (4) with $y \sin[\phi+\psi]$ (ϕ is the angle defined in Fig. 2), substituting Eqn. (4) into Eqn. (3), and integrating. The results are plotted in Fig. 2 for crack front locations both coincident with the cavity surface

(ϕ=o) and remote from the cavity (ϕ=π/2). The stress intensity factors are in close agreement with those derived by Shah,[7] using a similar analysis. These solutions must be corrected for the presence of the cavity surface. The surface corrections for small a/r should be of the same order as those obtained for uniformly stressed surface cracks.[8] The correction for remote crack front locations (ϕ =π/2) is small, ~1.03; while for near surface locations# (ϕ ~o) the correction is relatively large, ~1.23, as indicated on Fig. 2. Allowing for possible surface corrections of this magnitude, a comparison of the surface crack solutions plotted in Fig. 2 with the radial crack solution (transposed from Fig. 1) indicates that, for relatively large cracks (a/r $\gtrsim$ 1), the stress intensity factor for a semi-circular crack (at ϕ=o) is substantially larger than that for a radial crack of equivalent length. Semi-circular surface cracks in this size range should thus extend subcritically, into radial cracks (or more likely, into an intermediate semi-elliptical configuration) before propagating to fracture. For small a/r, the stress intensity factors for semi-circular cracks are lower than for radial cracks, indicating that semi-circular cracks in this size range should propagate unstably to fracture. The "best available solution" for the stress intensity factor at criticality should thus exhibit the approximate form depicted in Fig. 2. A functional expression for this curve which is convenient for subsequent analysis (derived using a formulism proposed by Grandt)[11] is given by:

$$\frac{K_I \sqrt{\pi}}{2\sigma_\theta \sqrt{a}} = 1.07 + \frac{1.37}{0.52 + a/r} \qquad (5)$$

One other type of crack that is of interest for the cylindrical cavity problem is the corner crack (Fig. 3). Stress intensity factor solutions for this configuration[12] indicate that K will be augmented near the free surface intersection, by ~1.33. This correction will be applied when fracture is expected to initiate from corner cracks.

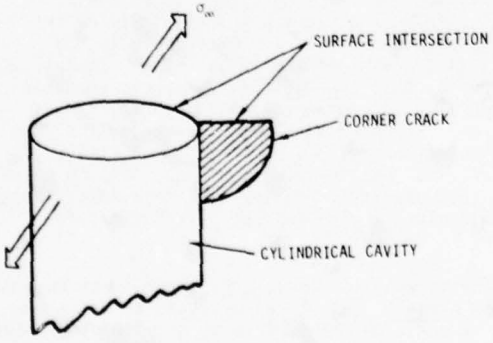

Fig. 3. A schematic of a corner crack.

#The singularity at the surface, ϕ=o, tends to zero[8]; but increases rapidly for ϕ > 0, to a maximum at ~0.05π .

FRACTURE STATISTICS

The probability of fracture Φ(S) when fracture occurs by the unstable extension of non-interacting surface cracks is, in general, related to the state of stress, S, by[13];

$$\ell n[1-\Phi(S)] = \int_A dA \int_o^S g(S)dS \qquad (6)$$

where A is the stressed area and g(S)dS is the number of flaws in unit area that extend unstably in the stress range S to S + dS. The function g(S) can be deduced from experimental strength data[3,4] and usually, several flaw populations exist over the entire strength range[4] (0 $\rightarrow \infty$); so that several functional forms are needed to fully-describe g(S). However, for a restricted range of strength, the mathematically convenient reduced Weibull function[5] is usually found to afford an adequate description;

$$\int_o^S g(S)dS = \left(\frac{S}{S_o}\right)^m \qquad (7)$$

where m is a shape parameter and S_o a scale parameter. This fracture probability relation can be used in conjunction with stress fields at cavity surfaces and K solutions to obtain expressions for cavity fracture. Some caution should be exercised, however, when the subcritical extension of surface cracks is involved (see Section 2), because this phenomenon can lead to instability conditions that violate the postulates used to derive Eqn. (6).

For a cylindrical cavity with a stress applied normal to the cylinder axis (Fig. 4) the stress at the cavity surface is biaxial[10] (except for the small plane stress condition near the ends). The tangential stress σ_θ is given by[10];

$$\sigma_\theta = \sigma_\infty[4\sin^2\theta - 1] \qquad (8)$$

where θ is the location on the cavity surface with respect to the applied stress axis. The longitudinal stress σ_z (Fig. 4) is equal to $\nu\sigma_\theta$.[10] Both stresses are thus tensile in the range, $5\pi/6 > \theta > \pi/6$.

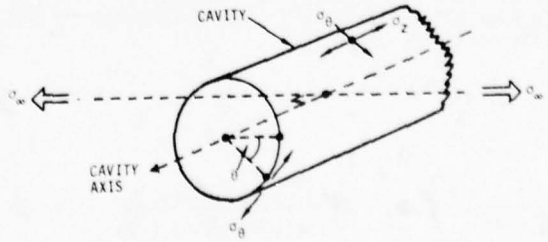

Fig. 4. A schematic indicating the configuration used for statistical analysis.

Fracture is considered to be restricted to the tensile region, because the crack extension stress under biaxial compression substantially exceeds that under biaxial tension.[6] In the tensile range, the pertinent strength distribution function is that which pertains to a principal stress ratio S_1/S_2 equal to ν. For the function given by Eqn. (7), it has been demonstrated[7] that probabilities of fracture in multiaxial tension can be related to those in uniaxial tension through a proportionality term $I(m, \nu, S_1/S_2)$; the fracture probability being greater in multiaxial tension than in uniaxial tension. This proportionality is contained in subsequent calculations of the fracture probability. The modified strength distribution is thus

$$\int_0^{S_1} g(S_1)dS_1 = I(m,\nu,S_1/S_2)\left(\frac{S_1}{S_0}\right)^m \qquad (9)$$

where S_1 is the maximum principal tensile stress. Hence, for very small cracks at the cavity surface ($a/r < 10^{-2}$) the fracture probability derived from Eqns. (6) to (9) by equating S_1 to σ_θ is,

$$-\ell n[1-\Phi(S_\infty)] = 4rt\left(\frac{S_\infty}{S_0}\right)^m I(m,\nu)\int_{\pi/6}^{\pi/2}(4\sin^2\theta-1)^m\,d\theta$$

$$\equiv 4rt\,A(m)(S_\infty/S_0)^m \qquad (10)$$

where S_∞ is the magnitude of the applied stress σ_θ at fracture and t is the length of the cylindrical cavity. For $S_1/S_2 = \nu = 0.2$, inserting the proportionality $I(m,\nu)$ derived from Ref. 7 into Eqn. (10) and integrating yields the A(m) plotted in Fig. 5.

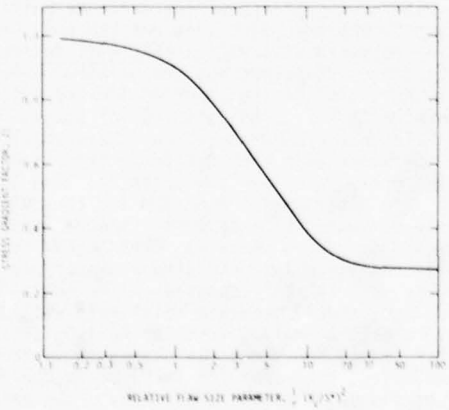

Fig. 5. The dimensionless fracture probability factor A(m) for fracture from a cylindrical cavity, plotted as a function of the shape parameter m of the flaw size distribution. Note that A(m) can be approximately expressed by $A(m) \sim 0.35\exp(1.06m)$.

For larger a/r, this result must be modified to account for stress gradient effects. The K solution that reflects the crack extension condition at instability (see Section 2) should be used for this purpose. For flaws normal to the applied stress, K_I in Eqn. (5) can be equated to the critical value K_c[#], to obtain the effective flaw strength S^* (i.e., the applied stress required to cause unstable crack extension), which can then be expressed in terms of the apparent strength S (that obtained by assuming uniform tension near the cavity surface, $S = \sqrt{\pi}\ K_c/7.38\sqrt{a}$) as (Appendix I);

$$\frac{S}{S^*} = 0.33 + 2B(0.11 - 0.056\alpha)^{\frac{1}{2}} \equiv Z(\alpha) \qquad (11)$$

where

$B = \cos(\beta/3)$, $\cosh(\beta/3)$ or $\sinh(\beta/3)$, $\cos\beta$, $\cosh\beta$, $\sinh\beta = (0.037 - 0.004\alpha)/(0.11 - 0.056\alpha)^{3/2}$

and

$$\alpha = \frac{1}{r}\left(\frac{K_c}{S^*}\right)^2$$

The choice of the cos, cosh or sinh relation for B depends on the magnitude of α, in the usual way. The stress gradient factor $Z(\alpha)$ given by Eqn. (11) is plotted in Fig. 6.

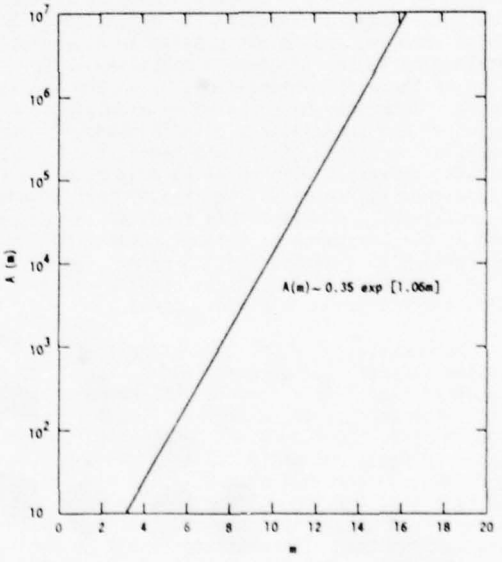

Fig. 6. The stress gradient correction term.

[#] Herein we assume that K_c is independent of crack length. This is not valid for cracks comparable in size to the microstructural dimensions.[1,2]

We now assume that a similar relation between S and S* pertains for all flaws in the tensile range (i.e., that the stress gradient is relatively insensitive to the flaw location and orientation). The fracture probability can then be obtained by substituting S from Eqn. (11) for S_∞ in Eqn. (10), to give;

$$-\ln\left[1-\Phi(\hat{S}_\infty)\right] = 4\pi t \left(\frac{\hat{S}_\infty}{S_0}\right)^m Z^m(\alpha) \qquad (12)$$

where $\hat{S}_\infty$ is the new value of the applied stress at fracture. Before proceeding, it is important to examine the implications of the assumption concerning the orientation independence of the stress gradient factor. An exact solution to the present problem would require that K_I, K_{II}, and K_{III} solutions be derived (for $5\pi/6 > \theta > \pi/6$) for all possible flaw locations and orientations at instability; and then to derive the equivalent S/S* functions. This is too extensive an exercise to attempt for present purposes. But it is instructive to develop a qualitative appreciation of the probable trends. For all flaw orientations within a specified element, $d\theta$ (Fig. 4), the two stresses σ_θ and σ_z are interrelated ($\sigma_z = \nu\sigma_\theta$). The stress gradient factor for given θ should, therefore, be orientation independent. The only substantive differences might occur at large a/r, where cracks with normals parallel to the cylinder axis (Fig. 4) tend to an annular shape at criticality, rather than the radial configuration analyzed in Section 2. However, these cracks are in an unfavorable orientation for extension in the present problem, and do not provide an appreciable contribution to the fracture probability. The effect of the axial orientation, θ, on the stress gradient factor may be surmized by examining the tangential and shear stress distributions.[10] The tangential stress gradient (and hence, the K_I gradient) decreases with rotation away from $\theta = \pi/2$, because the importance of the $(r+x)^{-4}$ term in Eqn. (4) diminishes. However, this tends to be counteracted by the emergence of a shear stress (or K_{II} component) with a strong $(r+x)^{-4}$ term. The orientation dependence of the stress gradient factor could, therefore, be relatively small.

The trends in the fracture probability with the relative strength $\hat{S}_\infty/S_0$, predicted by Eqn. (12) are plotted in Fig. 7 as a function of the relative cavity size (r/r_0), for a typical flaw size variability m of 4; the figure was constructed by letting $r_0 t$ and $K_c^2/r_0 S_0^2$ be unity. Also plotted on the figure are the fracture probabilities $\Phi(S_\infty)$ obtained from Eqn. (12) for the uniform tension case. It is apparent from Fig. 7 that the fracture probability deviates from the uniform stress result at low strengths (large a/r) and that the onset of the deviation S' occurs at higher strength levels (and fracture probabilities) as the absolute cavity size (r/r_0) decreases. In the deviant regime, the fracture probabilities are lower and initially exhibit a stronger dependence on the fracture stress than anticipated by the shape parameter of the flaw size distribution, i.e., the effective m values are larger. Thereafter, below S'', the fracture probabilities are identical to those obtained by considering the cavities as equivalent cracks.

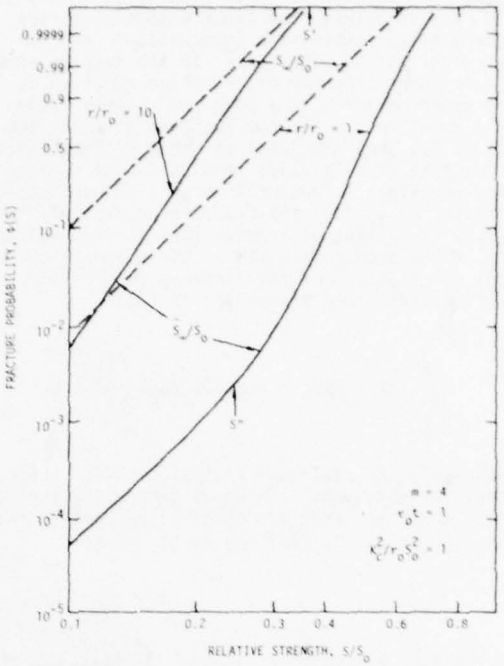

Fig. 7. The probability of fracture $\Phi(\hat{S}_\infty)$ from cylindrical cavities as a function of the relative strength ($\hat{S}_\infty/S_0$) plotted for three relative cavity radii, and for a shape parameter m of 4 ($r_0 t_0$ and $K_c^2/r_0 S_0^2$ are both unity); also plotted for comparison are the uniform stress results, $\Phi(S_\infty)$.

FRACTURE STUDIES

Concept

The applicability of the fracture relations derived in the preceding sections can only be adequately assessed if cavities with well-defined surface crack distributions are prepared and tested. Preliminary studies are reported for two types of cylindrical holes. The first set of samples contain holes prepared by drilling; these should contain surface cracks with a size distribution similar to that produced by surface grinding. The pertinent crack size distribution function for the hole might thus be estimated from separate strength tests on samples with ground surfaces. The second set of samples contain holes generated by incorporating W wires. The thermal expansion differential between W and Al_2O_3 should generate relatively well-defined radial cracks emanating from the W/Al_2O_3 interface. Further, since the W must be subsequently removed by oxidation, the expansion involved in the formation of the oxide causes additional crack extension, leaving a cylindrical cavity with relatively large radial cracks.

Experimental

The polycrystalline aluminum oxide material used for the fracture studies was prepared from Linde A aluminum oxide powder doped with 0.1 w/o magnesium oxide. The powders were milled in a

vibratory energy Sweco mill for 2 hr. using isopropyl and polyvinyl alcohols, and then dried for ~ 20 hrs. Consolidation was achieved by vacuum hot pressing at 1400°C for 1 hr. The resultant material was ~ 99% dense and had a grain size of ~ 2μm.

One set of samples was prepared by cutting rectangular (20 x 6.6 x 1.3 mm) beams from the hot-pressed disc, and rotary grinding the surfaces. Then, a through-thickness 0.7 mm radius hole was introduced into half of the samples (Fig. 8a) by diamond core drilling followed by reaming. The second set of samples was obtained by consolidating material containing a 127μm W wire. Rectangular beams were then cut such that the wire was in a through-width orientation (Fig. 8b). Finally, the W wire was removed by oxidizing in air for 2 hr. at 1150°C.

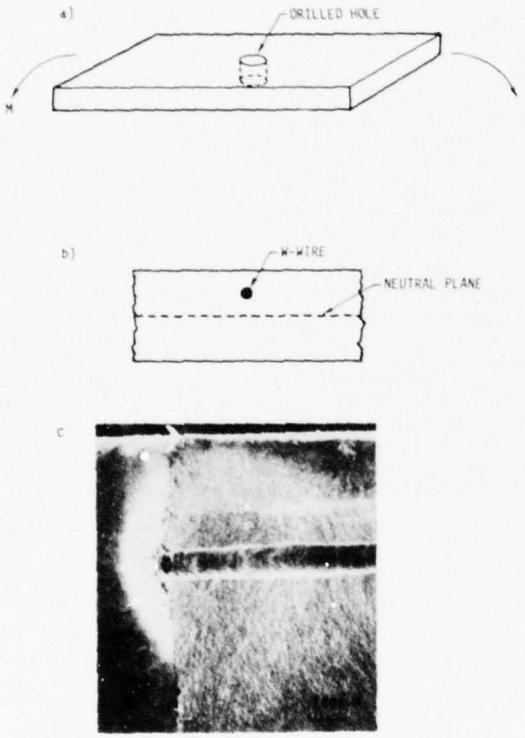

Fig. 8 (a) The drilled hole configuration.
(b) The hole configuration obtained using W wires.
(c) A fracture surface for a sample with a hole produced by a W wire; the initial length of the radial crack is indicated.

Strength tests were performed on each sample using a conventional four point flexure fixture with outer and inner spans of 19 and 6 mm, respectively. The tests were conducted in a dry nitrogen environment and at a rapid stress-rate (100 MPa s^{-1}), to minimize the influence of slow crack growth.[2] The fracture surface of each sample was examined in the optical or scanning electron microscope, in an attempt to identify the origin of fracture.

Results

The strength results obtained for the machined samples are plotted in Fig. 9. The results for the expansion induced cracks are summarized in Table I. As anticipated, the presence of the holes reduced the strength. Inspection of the samples containing the drilled holes indicated that the fracture always traversed the hole; but, fracture initiation could not always be unambiguously determined to occur from sites on the cavity surface. Examination of the fracture surfaces of the samples prepared with W wire indicated a clear demarkation of the profile of the radial crack that initiated failure (Fig. 8c).

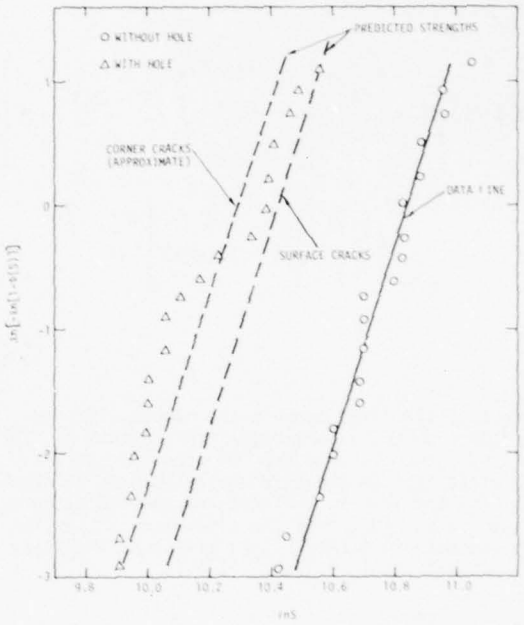

Fig. 9. A comparison of the fracture strengths of samples with and without drilled holes, showing the strengths of the latter predicted from the former.

TABLE I

STRENGTH RESULTS ON ALUMINA SAMPLES WITH AS-FABRICATED HOLES

Fracture Probability ($\phi = n/(N+1)$)	Fracture Strength (MPa)
0.14	183
0.29	190
0.43	204
0.57	230
0.71	251
0.86	254

The fracture toughness of the material was also determined, using the indentation technique.[8] For a load of 200N, the measured parameters were: indentation diameter, 100 μm; total crack length 250 μm. These values correspond to a toughness of 4.0 MPa √m.

Interpretation

(a) Drilled Cavities

For the samples without cavities, the fracture probability in four point flexure, for fracture occurring within the inner span, can be derived directly from Eqn. (6) as;

$$-\ell n\left[1-\Phi(\hat{S}_a)\right] = \left(\frac{\hat{S}_a}{S_o}\right)^m \left[\ell b + 2\ell \int_0^{d/2} \left(1 - \frac{2z}{d}\right)^m dz\right]$$

$$\equiv \left(\frac{\hat{S}_a}{S_o}\right)^m \ell \left[b + d/(m+1)\right] \qquad (13)$$

where ℓ is the inner span, b the sample width, d the sample depth, S_a the outer fiber stress at fracture and z the distance from the tensile surface (the first term in the parentheses relates to fracture from the tensile surface, and the second term allows for fracture from the side faces). For the samples containing the drilled cavities, the fracture probability (c.f. Eqn. (12)) is

$$-\ell n\left[1-\Phi(\hat{S}_H)\right] = \left(\frac{\hat{S}_H}{S_o}\right)^m$$

$$\left\{\left(\ell b - \pi r^2 + \frac{d\ell}{(m+1)}\right) + 4rA(m)Z^m(\alpha)\int_0^{d/2}\left(1 - \frac{2z}{d}\right)^m dz\right\}$$

$$\equiv \left(\frac{\hat{S}_H}{S_o}\right)^m \left\{\left(\ell b - \pi r^2 + \frac{d\ell}{(m+1)}\right) + \frac{2rdA(m)Z^m(\alpha)}{(m+1)}\right\} \qquad (14)$$

where $\hat{S}_H$ is the outer fiber stress at fracture, in the presence of the hole. The experimental results are interpreted in terms of Eqns. (13) and (14) by firstly obtaining the strength distribution parameters m and S_o, from a best fit of the data for the as-machined samples to Eqn. (13), as indicated by the data line on Fig. 9. Then, fracture probabilities in the presence of the hole can be derived for the same surface flaw population by inserting these distribution parameters and the pertinent A(m) and $Z(\alpha)$ values into Eqn. (14)(the α value pertinent to each strength level was evaluated by employing the measured polycrystalline K_c, of 4 MPa √m). The predicted strengths in the presence of the hole are plotted on Fig. 9. The predicted values conform relatively closely to the measured values at large probabilities ($\gtrsim 0.6$), but afford a substantial underestimate at lower probabilities. To assess the possibility that fracture from corner sites (see Fig. 3) might be the origin of the discrepancy at low probabilities, the corner crack correction factor (Section 2) is applied to z, and the fracture probabilities re-evaluated. The results are plotted in Fig. 9. A much closer correspondence with the data at low fracture probabilities is apparent; suggesting that the fractures in the low probability regime occur primarily from corner sites. However, the fractographic evidence is not sufficiently definitive for this suggestion to be fully substantiated.

As an indication of the influence of the distribution parameter m on the strength reduction effected by a cylindrical hole, the strength ratio $\hat{S}_a/\hat{S}_H$ at constant probability is derived for the specific specimen geometry used in the present tests, and for a strength level of ~200 MPa (this ratio is independent of the scale parameter S_o). The results for a surface crack and a corner crack are plotted in Fig. 10. Note that the strength ratio always exceeds the value expected from the stress concentration factor (0.33).

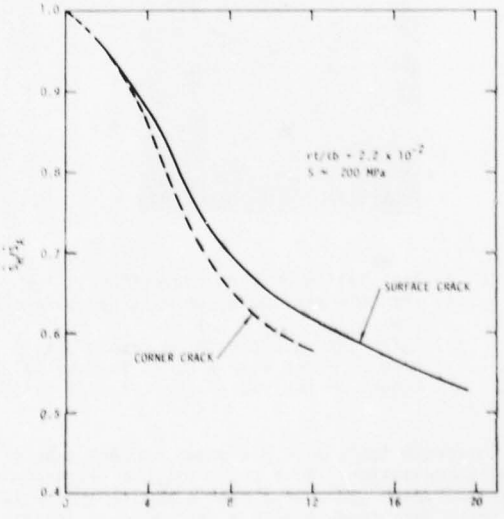

Fig. 10. The effect of the shape parameter, m, on the relative strengths of samples with and without drilled holes.

(b) Expansion Induced Cracks

The radial cracks generated by the fabrication of cavities from W wires appear to be ~2r in length (Fig. 8c). The stress intensity factor solutions (Fig. 1) would indicate that the cylindrical hole should exert a minor influence on the extension condition for radial cracks of this magnitude. However, several radial cracks of variable length emanate from each cavity (up to a maximum of 6). Also, the crack lengths are a significant fraction of the sample thickness. The quantitative interpretation of the measured fracture strength in the presence of these cracks is, therefore, a complex analytic problem. One sample, for which these complexities are minimized, has been chosen for analysis; this sample (strength 204 MPa) had five cracks, with the largest normal to the sample axis and the others at orientations >π/4. Fracture occurred from the crack normal to the sample axis (Fig. 8c). Initially, if the effects of the sample boundaries and the other radial cracks are neglected, the stress intensity factor at the crack front closest to the tensile surface is;

$$K_I = \sigma_o \left(\frac{2}{\pi a^*}\right)^{\frac{1}{2}} \int_0^{a^*} \frac{x^{\frac{1}{2}}}{(a^*-x)^{\frac{1}{2}}} \left[\frac{1-2(h+a^*-x)}{d}\right] dx$$

$$= \sigma_o \left(\frac{\pi a^*}{2}\right)^{\frac{1}{2}} \left[\frac{1-(2h+a^*/2)}{d}\right] \qquad (15)$$

where $a^*=2(a+r)$, σ_o is the outer fiber stress and h is the distance between surface and the crack front. An approximate (upper bound) correction for the influence of the boundary can be deduced from Isida's results[19] for a strip containing an eccentric crack. For the present problem - a ligament width h ~2a*/3 - the stress intensity factor at the upper crack front could be larger than that anticipated from Eqn. (15), by ~1.09. A maximum possible correction for the influence of the other radial cracks comes from Westman's solution[20] for the pressurized star crack; for 6 cracks, the correction is ~0.8.

Inserting the measured toughness (4 MPa $\sqrt{m}$), crack length (190 μm), hole radius (77 μm) and ligament depth (400 μm) into Eqn. (15), the fracture strength is predicted to be 207 MPa. The boundary correction decreases the predicted strength to a minimum of 190 MPa, while the crack interaction correction increases the strength to a maximum of 259 MPa. The latter cannot be reconciled with the measured strength (204 MPa), indicating that the crack interaction effect is of minor importance in this instance. Then, the relatively good correlation of the single crack solution with the measured strength tends to confirm that the pressure of the central hole had little influence on the crack extension condition.

IMPLICATIONS AND CONCLUSIONS

A method for predicting fracture probabilities, when fracture occurs from cavities, has been formulated by combining concepts from linear elastic fracture mechanics and from fracture statistics. The method has been applied to cylindrical cavities, using the best available fracture mechanics and statistics solutions. The same basic procedure can incorporate improved fracture mechanics solutions, as they emerge. The analysis demonstrates that fracture from cavities depends on the flaw population that exists at the cavity surface, the size of the flaws relative to the cavity radius and on the stress field around the cavity. The interpretation and prediction of fracture requires a detailed knowledge of each of these influences. Otherwise, the interpretation can only be subjective. This issue is addressed more extensively in the companion paper, in the context of fracture from spherical cavities.

Experimental results obtained on Al_2O_3 samples containing cylindrical cavities and relatively well-defined surface crack distributions indicated reasonable correspondence with the theory. The major uncertainties derive from inadequate stress intensity factor solutions for crack configurations of practical interest. This is an area for future study.

APPENDIX I

Defining S* as the flaw strength, or the applied stress needed to cause unstable crack extension, Eqn. (15) gives

$$\frac{K_c\sqrt{\pi}}{2S^*\sqrt{a}} = 1.07 + \frac{1.37}{0.52 + a/r} \qquad (A1)$$

Then, defining the apparent strength S as the strength of a flaw exposed to a uniform tension equal to that at the cavity surface;

$$S = \sqrt{\pi}\, K_c/7.38\sqrt{a} \qquad (A2)$$

Combining Eqns. (A1) and (A2) yields;

$$(S/S^*)^3 - (S/S^*)^2 + 0.12(S/S^*)\alpha - 0.032\alpha = 0 \qquad (A3)$$

where

$$\alpha = (1/r)(K_c/S^*)^2$$

Using the standard solution for a cubic equation then yields the relation for S/S* given by Eqn. (11).

ACKNOWLEDGEMENT

The authors are indebted to the Defense Advanced Research Project Agency for financial support, under Contract F33615-74-C-5180, and to Mr. J. Gysbers for his assistance in the numerical integration.

This research was sponsored by the Center for Advanced NDE, operated by the Science Center, Rockwell International, for the Defense Advanced Research Projects and the Air Force Materials Laboratory under Contract F33615-74-C-5180.

REFERENCES

1. See for example, R.W. Rice, Fracture Mechanics of Ceramics (Ed R.C. Bradt, D.P.H. Hasselman and F.F. Lange) Plenum, N.Y. 1974, p. 323.

2. A.G. Evans and T.G. Langdon, Prog. Mater. Sci. 21 (1976) p. 195.

3. O. Vardar, I. Finnie, D.R. Biswas and R.M. Fulrath, Int. J. Frac. 13 (1977) 215.

4. R.W. Davidge and G. Tappin, Proc. Brit. Ceram. Soc. 15 (1970) p. 47.

5. O.L. Bowie, Jnl. Maths and Physics 35,(1976) 60.

6. G.C. Sih, Handbook of Stress Intensity Factors (Lehigh Univ. Press) 1973.

7. R.C. Shah, "Mechanics of Crack Growth," ASTM STP 590 (1976) p. 429.

8. R.J. Hartranft and G.C. Sih, Mechanics of Fracture 1 (Ed. G.C. Sih) Noordhoff (1973) 179.

9. A.G. Evans and E.A. Charles, Acta Met 25 (1977) 919.

10. S. Timoshenko and J.N. Goodier, Theory of Elasticity (McGraw-Hill) 1951.

11. A.F. Grandt, Intl. Jnl. Frac. 11 (1975) 283.

12. A.S. Kobayashi and A.N. Enetanya, ASTM STP 590 (1976) 477.

13. J.R. Matthews, F.A. McClintock and W.A. Shack, Jnl. Amer. Ceram. Soc., 59 (1976) 304.

14. A.G. Evans and R.L. Jones, Jnl. Amer. Ceram. Soc., 61 (1978) 156.

15. W. Weibull, Jnl. Appl. Mech. 18 (1951) 193.

16. M. Adams and G. Sines, Jnl. Amer. Ceram. Soc. 59 (1976) 300.

17. A.G. Evans, Jnl. Amer. Ceram. Soc., May/June 1978, in press.

18. A.G. Evans and E.A. Charles, Jnl. Amer. Ceram. Soc. 59 (1976) 371.

19. M. Isida, "Methods of Analysis and Solutions of Crack Problems" (Ed. G.C. Sih) Noordhoff (1973) p. 56.

20. R.A. Westman, J. Maths. Phys. 43 (1964) 191.

ACCEPT/REJECT CRITERIA FOR STRUCTURAL CERAMICS:
PART 2: SOME EFFECTS OF CAVITIES ON THE FRACTURE OF CERAMICS
II. SPHERICAL CAVITIES

A.G. Evans
Rockwell International Science Center
Thousand Oaks, California 91360

D.R. Biswas and R.M. Fulrath
Materials and Molecular Research Division
Lawrence Berkeley Laboratory and Department of Materials Science
and Mineral Engineering, University of California
Berkeley, California 94720

ABSTRACT

Fracture probabilities associated with spherical cavities have been analyzed, by combining principles of fracture mechanics and fracture statistics. The analysis considers that fracture occurs from a distribution of cracks located at the cavity surfaces. It predicts effects of cavity size and cavity volume content (porosity) on strength, that depend sensitively on the flaw population vis-a-vis the cavity size distribution. The theory is shown to have limit solutions that coincide with several earlier models of fracture, derived for porous ceramics. The predicted effects of pore size on strength are compared with some available data.

INTRODUCTION

In a companion paper,[1] a general approach for predicting fracture from cavities, by combining linear elastic fracture mechanics solutions with statistics solutions, has been described: and applied to cylindrical cavities. The method is extended in this paper to include the analogous considerations pertinent to spherical cavities. Again, the emphasis is on the approach, recognizing that the available fracture mechanics and statistics solutions are inadequate in some instances. Improved solutions can be incorporated, using the same general approach, as they emerge.

Fracture mechanics solutions for cracks emanating from the surface of spherical cavities are examined in the first part of the paper. The best available solutions are then combined with statistical results - derived for the stress field around spherical voids - to obtain preliminary relations between the fracture probability, the cavity size and the surface flaw size distribution. Finally, the implications of the analysis for the effect on strength of individual voids and void arrays (porosity) are discussed.

STRESS INTENSITY FACTOR SOLUTIONS

The first problem of interest pertains to the equatorial annular crack emanating from a spherical cavity (Fig. 1). The tensile stress σ_z normal to the crack plane, for a remote stress σ_∞ is[2]

$$\sigma_z = \sigma_\infty \left[1 + \frac{(4-5\nu)}{2(7-5\nu)}\left(\frac{r}{x}\right)^3 + \frac{9}{2(7-5\nu)}\left(\frac{r}{x}\right)^5\right], (x \geq r)$$

$$\sigma_z = 0, \quad (x < r) \qquad (1)$$

where ν is Poisson's ratio and x is the distance from the center of the sphere (Fig. 1). An estimate of the stress intensity factor for the annular crack can be obtained[1] by imposing this stress onto the surface of a penny crack (Fig. 1).

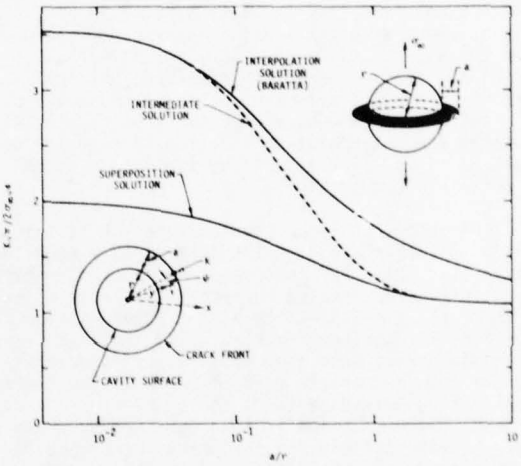

Fig. 1. Stress intensity factor solutions for an annular crack emanating from a spherical cavity.

The general linear superposition function used for three-dimensional problems of this type is,[1,3]

$$K_I\Big/_{\psi=0} = \frac{2}{(\pi a)^{3/2}} \int_0^{\pi} \int_0^{a} \sigma(y,\psi)\, y \frac{\left[1-(y/a)^2\right]^{\frac{1}{2}}}{\left[1-2(y/a)\cos\psi+(y/a)^2\right]} \, dy\, d\psi \qquad (2)$$

where y is the radial distance from the crack center, ψ is the angular location with respect to the crack front position of interest and a is the crack radius (see Figs. 1,2). The symmetry of the annular crack problem provides the following simplification; ψ=0 and x=y. Substituting Eqn. (1) into (2) then gives;

$$\frac{\sqrt{\pi}\,K_I}{2\sigma_\infty\sqrt{a}} = \int_{(r/a)}^{1} \frac{[2(7-5\nu)+(4-5\nu)(r/a)^3\chi^{-3}+9(r/a)^5\chi^{-5}]\chi\,d\chi}{2(7-5\nu)(1-\chi^2)^{1/2}} \qquad (3)$$

where $\chi=y/a$. Integration of Eqn. (3) for $\nu=0.2$ gives the result plotted in Fig. 1. Studies on radial cracks emanating from cylindrical cavities[1,3] have indicated that this type of solution is most pertinent for relatively large cracks ($a/r \gg 1$). For smaller cracks, the presence of the cavity surface allows an enhanced crack opening that tends to augment K_I (toward the edge crack solution, $\sqrt{\pi}K/2\sigma_\infty\sqrt{a}=3.52$). This small crack limit was recognized by Baratta[4] in his development of an interpolation solution for the annular crack problem. The interpolation solution for $\nu=0.2$ is plotted in Fig. 1. This solution predicts K values appreciably larger than the superposition solution, for all a/r. Additional studies are clearly needed; but for present purposes, it is assumed that the superposition solution is the more precise at large a/r ($\gg 1$) and that the interpolation solution is superior at small a/r ($< 10^{-1}$) - suggesting the intermediate solution plotted in Fig. 1.

The second configuration of interest is the partial circular crack on the surface of a spherical cavity (Fig. 2). For this case, consider the crack shown in Fig. 2, located such that the crack plane is normal to the applied tension. Superposition solutions for surface cracks usually invoke a symmetric image crack (and then apply a surface correction). However, in the present problem, the curvature of the surface perturbs the symmetry (Fig. 2). An approximate solution is thus obtained by assuming that the stress field for the crack/image combination is symmetric about the surface tangent 00' (Fig. 2). This solution should be most pertinent at small a/r, where the surface perturbation is small.

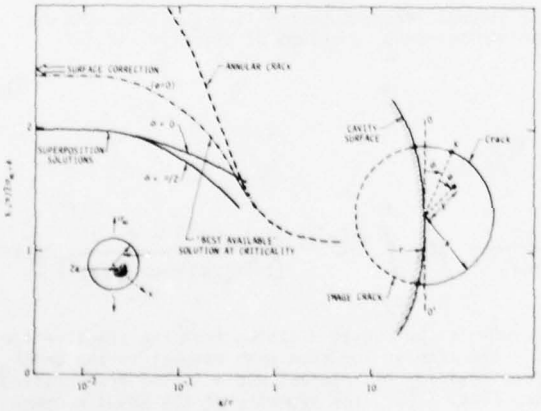

Fig. 2. Stress intensity factor solutions for an annular crack emanating from a spherical cavity.

The solution is obtained by noting that x and y are related by;

$$x = r + y\sin(\phi+\psi), \qquad (4)$$

where ϕ is the angle shown in Fig. 2; then, substituting Eqn. (1) into Eqn. (2) gives;

$$\frac{\sqrt{\pi}\,K_I}{2\sigma_\infty\sqrt{a}} = \int_0^1\int_0^\pi \chi(1-\chi^2)^{1/2} \qquad (5)$$

$$\frac{[2(7-5\nu)+(4-5\nu)(1+\chi\gamma\sin(\psi+\phi))^{-3}+9(1+\chi\gamma\sin(\psi+\phi))^{-5}]}{2[1-2\chi\cos\psi+\chi^2](7-5\nu)}\,d\chi\,d\psi$$

where $\gamma = r/a$. Integration of Eqn. (5) for $\phi = 0$ and $\pi/2$ yields the results plotted in Fig. 2, for $\nu = 0.2$. The stress intensity factor at $\phi = \pi/2$ is likely to be slightly enhanced by the presence of the surface,[1] by up to ~ 1.05 for small a/r; while K at $\phi = 0$ may be augmented by up to ~ 1.23. Allowing for possible corrections of this magnitude, a comparison of the partial circular crack results with the annular crack result indicates that K for the former is clearly the smaller at small a/r (< 0.5). Partial circular cracks in this size range should thus extend unstably in the presence of a critical applied stress. However, for larger a/r ($\gg 1$) the stress intensity factor for the annular crack may be smaller; suggesting the possible subcritical extension of a partial circular crack into an annular crack (analogous to the behavior proposed for cylindrical cavities)[1]. These considerations suggest that the resultant stress intensity factor at criticality might exhibit the form depicted in Fig. 2; which is used herein as the "best available" solution for surface cracks associated with spherical cavities. A convenient analytic expression for K deduced from Fig. 2 is;

$$\sqrt{\pi}\,K/2\,\sigma_\infty\sqrt{a} = 1 + 0.3[0.21 + a/r]^{-1} \qquad (6)$$

STATISTICAL ANALYSIS

Fracture probabilities for spherical cavities at small a/r have been evaluated[5] assuming a normal tensile stress criterion, and using Weibull's multiaxial stress method for flaws of a single population distributed throughout the volume of the body. A different analysis is presented in this paper, which uses a more fundamental statistical method for treating multiaxial states of stress[6,7], and applies the approach to a distribution of flaws at the cavity surface. For flaws located at the surface of a spherical cavity, the only stresses that exist are the tangential stresses,[8]

$$\sigma_\theta = \frac{3\sigma_\infty}{2(7-5\nu)}[4-5\nu+5\cos2\theta]$$

$$\sigma_\alpha = \frac{3\sigma_\infty}{2(7-5\nu)}[5\nu\cos2\theta-1] \qquad (7)$$

where θ is the angular coordinate with respect to the equatorial plane (Fig. 3).

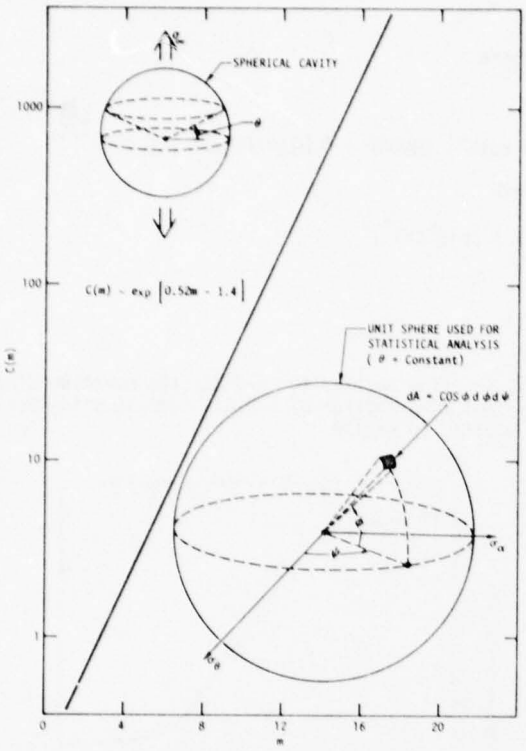

Fig. 3. The statistical parameter C(m) derived for a spherical cavity subjected to a uniaxial tension σ_∞. Also shown is the angular coordinate θ used to describe the stress variation, and the unit sphere used for statistical analysis.

The statistical problem is thus concerned with the analysis of biaxial fracture. Only the zone of tension is of interest.[1] For $\nu = 0.2$, σ_θ is tensile in the range $0.35\pi < \theta < -0.35$. The corresponding σ_α is compressive. The tension/compression quadrant thus pertains. The fracture criterion that has most successfully described multiaxial fracture[7] (as well as angular dependencies of fracture[9]) in ceramics is that based on the co-planar strain energy release rate#:

$$S_T^2 = \sigma_n^2 + \frac{4\tau_m^2}{(2-\nu)^2} \qquad (8)$$

where S_T is the flaw extension stress in equi-triaxial tension, σ_n is the tensile stress normal to the flaw and τ_m is the maximum in-plane shear stress. For flaws located in the surface element dA of a unit sphere (Fig. 3) that contains a complete sampling of flaws of all (random) orientations,[7] the stresses σ_n and σ_m are related to the stresses σ_θ and σ_α and the angles ϕ and ψ defined in Fig. 3 by;

$$\sigma_n^2 = \cos^4\phi\left[\sigma_\alpha^2\sin^4\psi + \sigma_\theta^2\cos^4\psi + 2\sigma_\alpha\sigma_\theta\cos^2\psi\sin^2\psi\right]$$

$$\tau_m^2 = \cos^2\phi\left[\sigma_\alpha^2\sin^2\psi(1-\cos^2\phi\sin^2\psi)\right. \qquad (9)$$

$$\left.+\sigma_\theta^2\cos^2\psi(1-\cos^2\phi\cos^2\psi) + 2\sigma_\theta\sigma_\alpha\cos^2\phi\cos^2\psi\sin^2\psi\right]$$

If the strength distribution in triaxial tension is now defined[7] by a Weibull-type function, with a scale parameter S_o^* and a shape parameter k,

$$g(S_T) = \left(\frac{S_T}{S_o^*}\right)^k, \qquad (10)$$

consideration of the eight equivalent areal elements, $dA = \cos\phi d\phi d\psi$ (Fig. 3), allows the biaxial strength distribution function to be derived, for given θ[7];

$$g(S_B)\Big|_\theta = \left(\frac{2}{\pi}\right)\int_0^{\psi^*(\theta)}\int_0^{\pi/2}\left(\frac{S_T}{S_o^*}\right)^k \cos\phi\, d\phi\, d\psi\, dS_T \qquad (11)$$

where $\psi^*(\theta)$ is the value of ψ at which σ_n first becomes negative, as deduced from Eqn. (9). Then substituting Eqn. (11) into the weakest link formulation,[1,6,7]

$$\Phi(S) = 1 - \exp\left[-\int_A dA\int_0^S g(S)\,dS\right] \qquad (12)$$

allows the probability of fracture from the cavity to be expressed as;

#This criterion has been used with good success for stress conditions wherein σ_n is tensile. It cannot be expected to apply when σ_n is compressive. In the present analysis, the fracture probability when σ_n is compressive is assumed to be zero. This will lead to underestimates of the failure probability, by an amount that depends on the initial opening of the flaw,[10] i.e., if the initial crack opening is small, as expected for the flaws of present interest, the underestimate will also be small.

$$-\ell n[1-\Phi(S_\infty^c)] =$$

$$8r^2 \int_0^{S_\infty} \left(\frac{S_\infty}{S_0}\right)^k dS_\infty \int_0^{0.35\pi} \int_0^{\psi^*(\theta)} \int_0^{\pi/2} \cos\phi\cos\theta$$

$$\left\{\frac{9\cos^2\phi}{4(7-5\nu)^2}\right. \left[\cos^2\phi\,(4-5\nu+5\cos2\theta)^2\cos^4\psi\right.$$

$$+ (5\nu\cos2\theta-1)^2\cos^2\phi\sin^4\psi$$

$$+ 2(4-5\nu+5\cos2\theta)(5\nu\cos2\theta-1)\cos^2\phi\cos^2\psi\sin^2\psi$$

$$+ (4/(2-\nu)^2)\,(5\nu\cos2\theta-1)^2\sin^2\psi(1-\cos^2\phi\sin^2\psi)$$

$$+ (4-5\nu+5\cos2\theta)^2\cos^2\phi(1-\cos^2\phi\cos^2\psi) + 2(4-5\nu$$

$$+ 5\cos2\theta)$$

$$\left.(5\nu\cos2\theta-1)\cos^2\phi\cos^2\psi\sin^2\psi\right] \left.\right\}^{(k+1)/2} d\psi d\phi d\theta \quad (13)$$

$$\equiv 8r^2 B(k,\nu)\; S_0^*(S_\infty^c/S_0^*)^{k+1}/(k+1)$$

where S_∞^c is the value of the applied stress σ_∞ at fracture, in the presence of the cavity. The equivalent fracture probability for uniaxial tension has been derived as;[7]

$$-\ell n[1-\Phi(S_\infty^u)] = A_g I_u(k,\nu)\; S_0^*\,(S_\infty^u/S_0^*)^{k+1}/(k+1) \quad (14)$$

where A_g is the gauge surface area, S_∞^u is the applied stress at fracture and $I_u(k,\nu)$ is a function that relates the uniaxial strength to the triaxial strength.[7] Expressing Eqn. (14) in a notation consistent with the more conventional Weibull formulism,[11]

$$-\ell n[1-\Phi(S_\infty^u)] = A_g(S_\infty^u/S_0)^m\,, \quad (15)$$

where the scale and shape functions are now S_0 and m, and substituting into Eqn. (13), the fracture probability for the cavity becomes;

$$-\ell n[1-\Phi(S_\infty^c)] = 8r^2\; C(m,\nu)(S_\infty^c/S_0)^m \quad (16)$$

where C(m) is plotted in Fig. 3, for $\nu = 0.2$. A useful analytic approximation is, $C(m) \sim \exp[0.52m-1.4]$. Comparison with the companion paper[1] indicates that, for the same area of cavity surface and the same flaw population, the probability of fracture from a spherical cavity is smaller than that from a cylindrical cavity.

Now, useing the same procedure described for the cylindrical cavity,[1] a stress gradient correction can be applied. The effective flaw strength S* derived from Eqn. (6) is;

$$\frac{S}{S^*} = 0.33 + 2(0.11 - 0.21\alpha)^{1/2}\cosh(\lambda/3) \equiv D(\alpha)$$

where

$$\lambda = \cosh^{-1}\,(0.037 + 0.021\alpha)/(0.11 - 0.21\alpha)^{3/2} \quad (17)$$

and

$$\alpha = (1/r)(K_c/S^*)^2$$

This solution applies for $\alpha<0.52$; the corresponding sinh solution applies of $\alpha>0.52$. The function $D(\alpha)$ is plotted in Fig. 4.

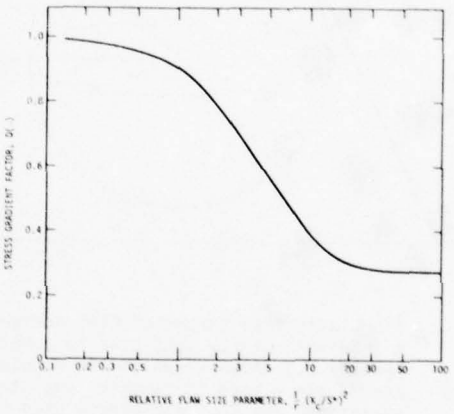

Fig. 4. The stress gradient factor $D(\alpha)$ for a spherical cavity.

Assuming that a similar relation pertains for all flaw locations and orientations in the tensile range,[1] the fracture probability becomes;

$$-\ell n[1-\Phi(\hat{S}_\infty)] = 8r^2\left(\frac{\hat{S}_\infty}{S_0}\right)^m C(m)\; D^m(\alpha) \quad (18)$$

where $\hat{S}_\infty$ is the new value of the applied stress at fracture. The fracture probabilities predicted by Eqn. (18) are plotted in Fig. 5, as a function of the normalized strength $(\hat{S}_\infty/S_0)$, for several relative void radii (r/r_0) and a typical m of 4; r_0 and $K_c^2/r_0S_0^2$ are chosen to be unity. The probabilities obtained from Eqn. (16) are also plotted for comparison. The same trends found for the cylindrical cavity are evident, but are accompanied by smaller reductions in the fracture probability.

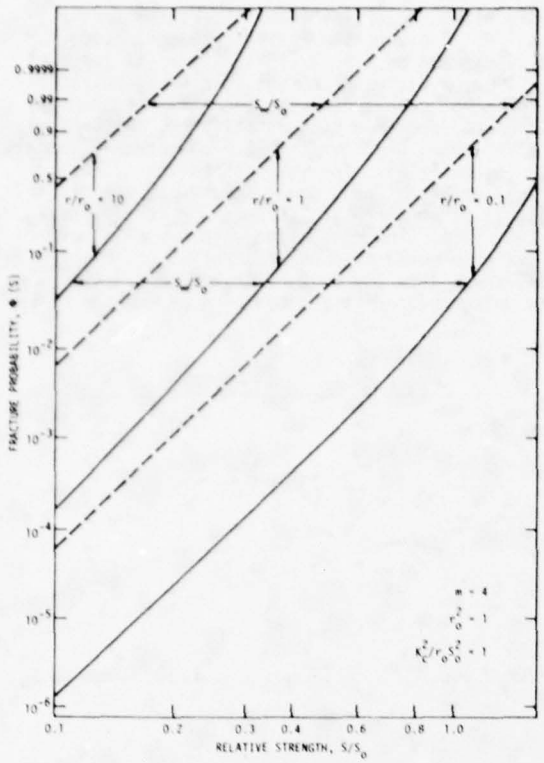

Fig. 5. Fracture probabilities for spherical cavities plotted as a function of the relative strength, for a value of the shape parameter m = 4.

EFFECTS OF POROSITY ON STRENGTH

Cavity Arrays

In porous ceramics, if the porosity is low enough that pore interaction effects cannot occur, the probability of fracture from flaws distributed at the pore surfaces can be determined, in the usual way[5,6,7] from the product of the survival probabilities of individual cavities. For a pore size distribution $\phi(r)dr$ (i.e., the fraction of pores in the size range r to r+dr) the probability of failure $\Phi_T(\hat{S}_\infty)$ from a volume V subjected to uniform tension, derived from Eqn. (18), is;

$$-\ell n[1-\Phi_T(\hat{S}_\infty)] = 4NV\left(\frac{\hat{S}_\infty}{S_o}\right)^m C(m)\int_{r_{min}}^{r_{max}} \phi(r) r^2 D^m(\alpha)\,dr \qquad (19)$$

where r_{max} and r_{min} are the radii of the largest and smallest pores, respectively; N is the number of pores in unit volume, which is related to the porosity, P, by;

$$P = \frac{4\pi}{3}\langle r^3\rangle N \qquad (20)$$

For pores of uniform size $\bar{r}$, Eqn. (19) becomes;

$$-\ell n[1-\Phi_T(\hat{S}_\infty)] = \frac{3PV}{\pi\bar{r}}\left(\frac{\hat{S}_\infty}{S_o}\right)^m C(m)D^m(\alpha) \qquad (21)$$

Hence, in the limit $a/r \to 0$, where D is independent of r, the fracture probability for a fixed flaw population is expected to slightly increase, (i.e., the strength to decrease) as the pore radius decreases. This condition arises because the relative cavity surface area increases as the cavity radius decreases, permitting a more extensive sampling of the flaw population. (It should be noted that this cavity size dependence does not exist when fracture initiates from volume distributed flaws[5]). However, the trend with cavity radius is counteracted by the decrease in D, associated with the concurrent increase in a/r. The resultant variation of strength with the relative cavity radius (r/r_o) at constant porosity (0.1) is plotted at constant probability in Fig. 6. These strengths scale with porosity through the sample proportionality, $p^{-1/m}$. (It is re-emphasized that the analysis is only valid when there is no significant pore interaction; the implications must, therefore, be restricted to low porosities.)

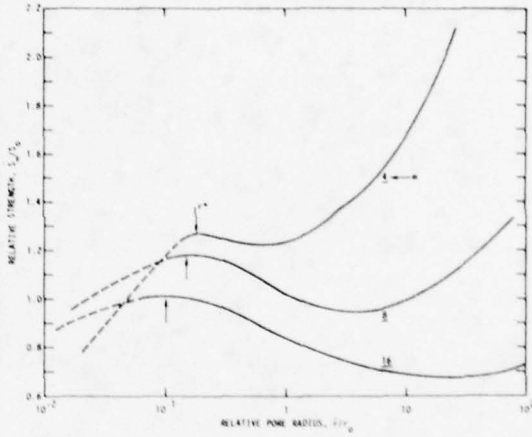

Fig. 6. Effects of relative pore radius $\bar{r}$ on the relative fracture strength at constant probability, plotted for three m values and a porosity of 0.1.

It is evident from the quite extensive regime of increasing strength (with decreasing void radius) that the influence of the stress gradient parameter D is dominant over a wide range of void radii. The inference of this result is that the strength for a fixed flaw population can be maximized either by collecting all of the porosity in a small number of large voids, or by producing voids of optimum size, r*. However, the former will not normally be a practicable solution. The latter should be feasible, but the possibility of other modes of fracture occurring at small void sizes may pre-empt the development of a strength maximum in many ceramic polycrystals. Also, for various microstructural reasons, the flaw population may change as the pore size changes, (e.g., an increase in the scale factor S_o as the pore size increases), leading to more substantial effects of pore size on strength than predicted by Fig. 6.

There are very few data in the literature concerning the effects of pore size on strength. The most comprehensive are data on borosilicate glass obtained by Bertolotti and Fulrath.[12] These data re-examined in the context of the present model, even though the uncertain influence of surface cracks (machining flaws) on the fracture data detracts from the utility of the correlation. For comparison with the model, the appropriate values of $D(\alpha)$ are first obtained for each void size, using a K_c of 0.7 MPa $\sqrt{m}$.[13] Then, the shape parameter m is estimated from the pore volume dependence of the strength at low porosity ($S \propto P^{-1/m}$) - and found to be in the range 10 to 20. The fracture strength, relative to the strength of the samples with the largest voids, can then be computed at constant failure probability, by direct insertion of these quantities into Eqn. (21). The results for m values of 10 to 20 are plotted in Fig. 7; also plotted on the figure are the data obtained from Bertolotti and Fulrath, at three levels of porosity. The predictions tend to slightly underestimate the measured pore size dependence. The uncertainty in the origin of failure for the test samples prevents definitive conclusions from the comparison. More precise experiments are needed to determine the principal deficiencies of the theory, in its present form.

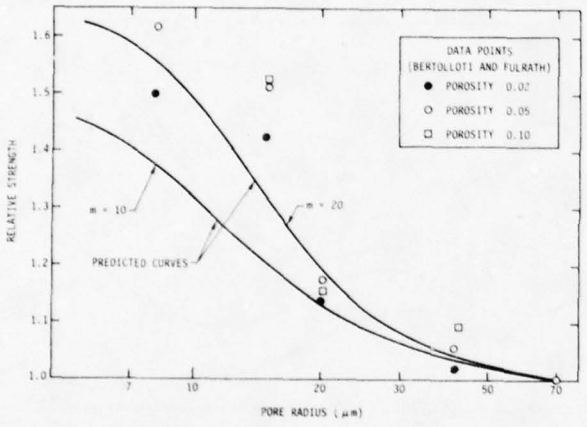

Fig. 7. A comparison of the predicted effects of pore radius on the strength (at constant porosity and constant probability) with data obtained for borosilicate glass.

Isolated Cavities

The effects of the size of an isolated cavity on strength can be deduced directly from Eqn. (18). These effects are plotted at constant probability in Fig. 8, to demonstrate that there are no simple relations between defect size and strength. However, a close examination of Eqn. (18) indicates important fracture trends, and illustrates the relation between the present analysis and earlier models of fracture from voids.[14,15] For large values of the shape parameter m, there is a high probability of a flaw at the large extreme of the population being located at the position of maximum tension on the cavity surface. Therefore, if α is small (small a/r), $D(\alpha) \to 1$, and Eqn. (16) applies. The strength will then be related to that of a sample without cavities (Eqn. 15) by the factor $C(m)^{-1/m}$. Applying the analytic approximation for $C(m)$ indicated on Fig. 3, this factor (at large m) is ~1.92, i.e., equal to the stress concentration factor. The connection with the stress concentration factor model is thus established. Alternately if α is large, $D(\alpha)$ tends to 0.5 and exactly cancels $C(m)$ in Eqn. (18). The strength is thus identical to that expected for a crack located at the cavity, i.e., it is equal to the strength in tension given by Eqn. (15). The connection with the cavity/crack equivalence model is thus apparent. For small values of m, there is a low probability of an extreme value flaw being located at the position of maximum tension.

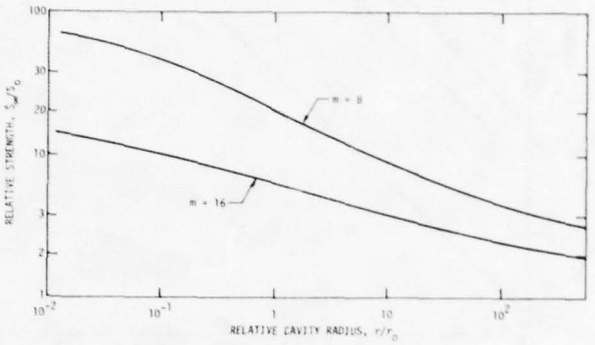

Fig. 8. Predicted effect of the relative cavity radius on the relative strength for a body containing a single cavity of the specified size. Results are presented for two values of the shape parameter m.

Hence, $C(m) \sim 1$ (see Fig. 3), and the influence of the cavity on strength is quite minimal. For small x, the effect of the cavity tends to reduce to a level similar to that expected from the increased surface area provided by the cavity. For larger α the effect is even smaller. The connection with models based on the void area is thus established. For intermediate values of m and the present model predicts strength effects that range continually between the limit solutions provided by the earlier models. It should thus exhibit the versatility needed to account for many of the trends observed experimentally. However, it is emphasized that certain important phenomena are not yet incorporated in the model (such as the linking of subsurface pores with surface cracks), and that the stress intensity factor solutions are approximate. Therefore, much additional analysis is still needed to develop the present model into a universal model of cavity fracture.

Finally, the prediction of failure from isolated cavities in dense ceramics can directly utilize Eqn. (18), when the cavities are nearly spherical in shape. The probability of service failure from cavities Φ_F, at a stress level σ_A, based on a nondestructive characterization of the cavity dimensions, if all cavities with an interpreted cavity radius r_0 are accepted, is;[16]

$$\Phi_F(\sigma_A, r_i^o) = \int_0^{\sigma_A} \int_0^{r_i^o} \int_0^{\infty} \phi(\hat{S}_\infty)\phi(r_i/r)\phi(r)dr\,dr_i\,dS_\infty \qquad (22)$$

where $\phi(\hat{S}_\infty)dS$ is the derivative of Eqn. (18); $\phi(r_i/r)dr_i$ is the probability that the nondestructively interpreted cavity radius r_i is in the range r_i to r_i+dr_i, given that its actual radius is r; $\phi(r)dr$ is the cavity radius distribution in the material. The concepts developed in this paper are thus an important constituent in any nondestructive failure prediction scheme for structural ceramics. The details are described in a separate publication.[16]

CONCLUDING REMARKS

Fracture from spherical cavities has been analyzed by considering that fracture occurs by the extension of a population of cracks located at the cavity surface. The analysis indicates trends in the fracture condition with cavity size and volume, that depend on the flaw size distribution relative to the cavity size. It has been shown that the present analysis provides limit solutions that are analagous to several earlier models of cavity fracture; thereby, providing the required connective link between the models. The analysis is only regarded as preliminary because the presently available stress intensity factor solutions are inadequate and because several important subcritical flaw linking phenomena have not yet been included in the analysis. Much additional study is needed to evolve a model of the above type that has universal utility for cavity fracture.

The analysis has been used to predict effects of pore volume (porosity) on strength that should be pertinent to small pore volumes (i.e., no pore interaction effects). The predictions have been compared with some available data for borosilicate glass. Although the correspondence was quite good, little value was gained from the correlation, because of the uncertain origins of fracture in the fracture tests. Precise studies are needed to correlate with the theory. The appropriate tests have recently been initiated.

ACKNOWLEDGMENT

This research was sponsored by the Center for Advanced NDE, operated by the Science Center, Rockwell International, for the Defense Advanced Research Projects and the Air Force Materials Laboratory under Contract F33615-74-C-5180.

REFERENCES

1. A.G. Evans, D.R. Biswas and R.M. Fulrath, submitted to Jnl. Amer. Ceram. Soc.
2. S. Timoshenko and J.N. Goodier, Theory of Elasticity (McGraw-Hill, N.Y.) 1951.
3. R.C. Shah, ASTM STP 590 (1976) 429.
4. F. Baratta, Jnl. Amer. Ceram. Soc., in press.
5. O. Vardar, I. Finnie, D.R. Biswas and R.M. Fulrath, Int. J. Frac. 13 (1977) 215.
6. S. Batdorf and J.G. Crose, Jnl. Appl. Mech. 41 (1974).
7. A.G. Evans, Jnl. Amer. Ceram. Soc., 61 May/June 1978.
8. J.N. Goodier, Trans ASME (Jnl. Apl. Mechs.) 55 (1933) 39.
9. J.J. Petrovic and M.G. Mendiratta, Jnl. Amer. Ceram. Soc. 60 (1977) 463.
10. M. Adams and G. Sines, Jnl. Amer. Ceram. Soc. 59 (1976) 300.
11. W. Weibull, Jnl. Appl. Mech. 18 (1951) 193.
12. R. Bertolotti and R.M. Fulrath, Jnl. Amer. Ceram. Soc., 50 (1967) 561.
13. S.M. Wiederhorn, Jnl. Amer. Ceram. Soc. 52 (1969) 99.
14. S.C. Carniglia, Jnl. Amer. Ceram. Soc. 56 (1973) 547.
15. R.W. Rice, Treatise on Materials Science and Technology 11 (1977) 199.
16. J.M. Richardson and A.G. Evans, to be published.

ACCEPT/REJECT CRITERIA FOR STRUCTURAL CERAMICS:

PART 3: PROBABILISTIC MODELS FOR INCLUSION INITIATED FRACTURE IN CERAMICS

A.G. Evans
University of California
Berkeley, California 94720

B.I. Davis and G. Meyer
Rockwell International Science Center
Thousand Oaks, California 91360

H.R. Baumgartner
Norton Co.
Worcester, Massachusetts

ABSTRACT

Fracture tests on hot-pressed silicon nitride containing several types of inclusions have been conducted. Fracture models pertinent to each inclusion type have been proposed and correlated with the data. The resultant fracture probability relations are one of the key inputs to accept/reject decisions for nondestructive failure prediction.

INTRODUCTION

Inclusions can be an important source of failure in structural ceramics. It is crucial for the structural utilization of these materials that the probability of fracture from typical inclusions be sufficiently characterized that effective nondestructive failure prediction schemes be devised. In this study, samples of silicon nitride containing typical inclusions are subjected to controlled fracture tests to determine both the fracture mechanism and the specific fracture stress at the inclusion. Fracture models pertinent to each inclusion type are then developed, and the fracture probability (derived from the test data) is related to the parameters of the model. The resultant probability functions constitute one of the three functions required to isolate the accept/reject criterion pertinent to nondestructive failure prediction.[1]

Preliminary studies of fracture from inclusions in ceramics[2,3] have indicated that the fracture process is likely to consist of the activation of small defects (voids, disbonds, grain boundary cracks), occurring within or near the inclusion, by the ambient local stress field associated with the thermal expansion mismatch and the applied stress. Usually, the influence of the inclusion on strength is expected to be less severe than that of a crack of equivalent dimensions.[2] The important exception is an inclusion with both a thermal expansion coefficient and a shear modulus lower than the host material (then, large radial cracks can develop that substantially reduce the strength). However, the incidence of such inclusions in structural ceramics such as silicon nitride is expected to be minimal, because these materials have a low intrinsic thermal expansion coefficient.

The inherent flaws that initiate inclusion fracture are likely to be statistically distributed in size and space. Therefore, the fracture stress should not be expected to relate uniquely to the inclusion dimensions; but rather, to exhibit a distribution of values for each inclusion size, as found for fracture from voids.[4,5] The determination of the fracture distribution functions is the primary objective of the present study.

EXPERIMENTAL

Technique

Samples containing the inclusion types that predominate in hot-pressed silicon nitride (Table I) were specially fabricated* in the form of 2.54 cm diameter discs, with the inclusions approximately located in the disc center. The samples were inspected using advanced ultrasonic techniques[6,7] to determine the precise location of the dominant inclusion. The samples were then machines until the defect was located ~ 200μm from one surface of the sample. This operation was conducted to ensure that the defect would be subjected to an appreciable tensile stress during subsequent flexure testing. Thereafter, each sample was annealed, in air at 1000°C for ~ 20 hr., to minimize the influence of surface cracks introduced during the grinding process. Finally, the samples were subjected to flexural, constant displacement-rate fracture tests, conducted at room temperature. Those samples with defects located at the disc center were tested in biaxial flexure.[8] Samples with defects displaced from the disc center were cut into beams (20 cm x 5 mm x 5 mm), such that the defect was located at the beam center, and then tested in three-point flexure. Acoustic emission was monitored on each sample throughout the test.

*The fabrication was conducted by the Norton Co., Worcester, Massachusetts.

TABLE I

Inclusion Type	Stress at Inclusion (MPa)	Inclusion Size z(μm)	x(μm)	V(m^3)
	401	50	265	-
	362	100	475	-
	375	75	425	-
	264	125	625	-
Silicon	243	250	875	-
	283	125	875	-
	272	250	675	-
	410	75	200	-
	432	75	275	-
	284	175	425	-
	357	100	100	-
	424	75	250	-
	434	50	100	-
	265	175	750	-
	252	125	625	-
	398			2.5×10^{-12}
	323			1.6×10^{-11}
	383			9.1×10^{-12}
	334			2.2×10^{-11}
	355			3.1×10^{-11}
	210			6.2×10^{-13}
Iron	217			7.0×10^{-11}
	404			6.2×10^{-13}
	258			7.0×10^{-11}
	296			6.1×10^{-11}
	333			3.3×10^{-4}
	283			6.5×10^{-11}
	173			2.9×10^{-10}
	281			1.1×10^{-19}
	206			3.2×10^{-10}
	190			1.8×10^{-10}
	550	75	175	
	590	125	150	
Tungsten	560	75	300	
Carbide	610	400	675	
	600	100	300	
	480	400	400	

Results

The results of the fracture tests were used to calculate the stress at the center plane of the defect, at the condition of fracture instability. These defect fracture stresses are summarized in Table I. The acoustic emission record did not generally indicate well-defined pre-fracture emission; except for the silicon inclusions, which exhibited consistent emission at about one-tenth of the final fracture load.

The dimensions of the fracture initiating defects on the fracture plane were measured on each sample, as summarized in Table I. Also, for samples in which defect removal could be effected, the defect volumes were measured. The detailed volume measurement technique is described in Appendix II. The results are summarized in Table I.

FRACTURE MODELS

General Considerations

It is instructive to provide a perspective of inclusion fracture by examining the stress fields associated with inclusions; and thereby, to identify the possible modes of fracture. (The fracture modes that occur for inclusions with a lower expansion coefficient than the matrix are excluded from consideration, as noted in the Introduction.)

The thermal expansion mismatch introduces hydrostatic tension within the inclusion. The magnitude of this stress, σ_α, is given by[9]

$$\sigma_\alpha = \frac{4G_M\Delta\alpha_\Delta T}{1+[2(1-2\nu_i)/(1+\nu_i)](G_m/G_i)} \equiv \beta^* \quad (1)$$

where Δ_α is the differential in thermal expansion coefficients, ΔT is the temperature differential, G is the shear modulus, ν is Poisson's ratio and the subscripts m and i refer to the matrix and inclusion, respectively. The equivalent stresses within the matrix are, for a spherical inclusion:

$$\sigma_{rr} = \beta^* (a/r)^3$$
$$\sigma_{\theta\theta} = \beta^* (a/r^3)/2 \quad (2)$$

The application of a stress σ_∞ also generates stresses in the inclusion. For a spherical inclusion and an applied pressure P_∞, the stress in the inclusion is given by[10]:

$$\frac{P_i}{P_\infty} = 1 + \left(\frac{2}{3}\right)\frac{[(K_i/K)-1](1-2\nu)}{(1-\nu)}\left[\frac{4G+3}{4G+3K_i}\right] \equiv \psi \quad (3)$$

where K is the bulk modulus.

The significance of these local stresses depends on the distribution of flaws within the inclusion, matrix and interface; as well as the intrinsic toughness of the inclusion and the matrix. When the toughness of the inclusion is appreciably larger than that of the matrix (as might pertain for WC inclusions in Si_3N_4), fracture will tend to initiate within the matrix, from flaws located either at the interface or within the matrix itself (Fig. 1). In this case, the location of fracture and the fracture probability depend primarily on the ratio of the inclusion and matrix elastic constants. Specifically, for inclusions with a smaller modulus than the matrix, the maximum local tensile stress occurs at the equatorial plane,[11] and fracture will initiate from flaws located in this vicinity, as indicated in Fig. 1(a). For inclusions with a higher modulus than the matrix, the maximum local tension (in the appropriate orientation for continued extension into the matrix, i.e., normal to σ_∞) occurs at the poles of the inclusion[11] (Fig. 1(b)). However, both the maximum tension and the extent of the tensile zone are appreciably smaller (for the same modulus mismatch) than the equivalent quantities for the low modulus inclusions. The

probability of fracture from the latter is thus anticipated to be relatively low.

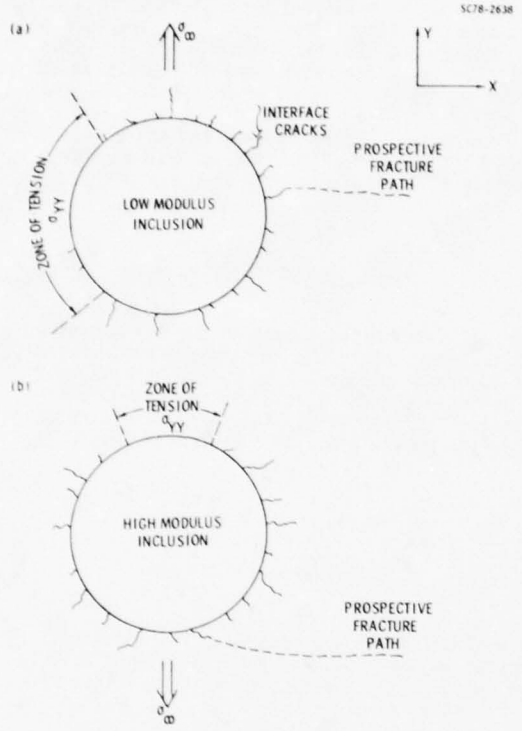

Fig. 1 Schematics indicating fracture initiated within the matrix from interface microcracks for (a) low modulus inclusions and (b) high modulus inclusions.

A more typical condition involves inclusions with a lower fracture toughness than the matrix. Then, inclusion fracture is likely. When the inclusion has a relatively high modulus (although not necessarily higher than that of the matrix), so that appreciable stresses develop within the inclusion, the fracture of the inclusion can be subcritical, i.e., an additional stress is required to initiate structural failure. Alternatively, if the inclusion has a low modulus (e.g., a porous inclusion, see Appendix I), the stress within the inclusion is low and inclusion fracture might then coincide with structural failure.

This multiplicity of fracture modes requires that each inclusion type be evaluated on an individual basis. The subsequent analysis comprises separate sections for each of the inclusion types listed in Table I.

Specific Fracture Models

Silicon Inclusions. The silicon inclusions are characterized by a lack of porosity, signifying that there is little thermal expansion mismatch at temperatures above ~1000°C (the temperature at which stress relaxation by mass transport becomes slow). This can be rationalized by noting that the large thermal contraction of the silicon between 1000 and 1800°C is counteracted by the unusual volume expansion that occurs during solidification. Between 1000° and 30°C the total contraction of the silicon is very similar to that of silicon nitride: indicating that the thermal mismatch stresses in the silicon inclusions should be small.

Dense silicon has elastic properties appreciably lower than those of silicon nitride (Youngs moduli of 110 and 320 GPa, respectively). These relative properties lead to a stress in the inclusion $\sigma_i \approx 0.64\ \sigma_\infty$ (see Eqn. 3). However, silicon has a very low fracture toughness (0.6 MPa$\sqrt{m}$) compared with the silicon nitride matrix (5 MPa$\sqrt{m}$); so that, despite the low stress level in the inclusion, the inclusion is liable to fracture before the matrix. This interpretation is consistent with the acoustic emission measurements (Section 2).

The subcritical fracture of the silicon inclusion introduces a crack with dimensions dictated by the dimensions of the inclusion. The cracked inclusion produces a complex stress intensification of the type[11]:

$$K_I = Z(a/c)F(G_i/G)\sigma_\infty a^\beta \qquad (4)$$

where Z is a function of the crack shape, F is a function of the relative elastic moduli and β is a constant ranging from 0.3 to 0.7. The present fracture model is developed on the premise that the modulus mismatch is small and that the crack inclusion can be treated as a crack in a homogeneous body. (This simplification is necessary at the present level of comprehension of the crack/inclusion problem, and will evidently introduce an error into the fracture characterization.) Then, introducing the macro-toughness of silicon nitride and the inclusion dimensions (on the fracture surface), a predicted fracture stress σ_p can be obtained from Eqn. (4).

$$\sigma_p = \frac{K_c}{Z(a/c)\sqrt{a}} \qquad (5)$$

The predicted stress for each sample is plotted in Fig. 2 as a function of the measured fracture stress. A reasonable correlation is apparent.

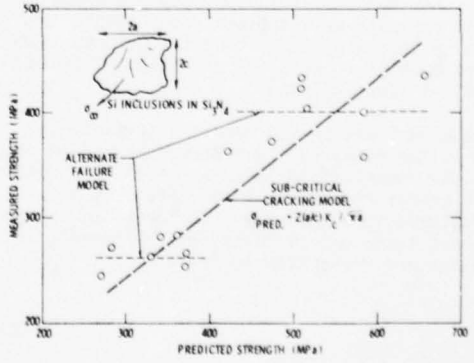

Fig. 2 A plot of the measured fracture strength of silicon nitride containing silicon inclusions as a function of the strength predicted by the subcritical cracking model.

A detailed statistical analysis has also been conducted to determine the level of correlation between the test data and the model. For this purpose, it has been supposed that the primary source of the variability in the measured strength is the variation in fracture toughness of the matrix circumventing the inclusion (which could be very difference from that of the remote matrix, because of an interaction zone). The inclusion/crack size is appreciably larger than the grain size; hence, the variability in toughness might be anticipated to conform to a normal distribution. The fracture data are thus analyzed to determine their conformance to the normal distribution.

The hypothetical model can be formally expressed as:

$$P_r[S \le \zeta | \sigma_p = x] = \frac{1}{v\sqrt{2\pi}} \int_{-\infty}^{\zeta} \exp\left[-\frac{1}{2}\left(\frac{y-(\alpha+\beta x)}{v}\right)^2\right] dy \qquad (6)$$

where v^2 is the variance of the strength S for any given σ_p and P_r is the conditional distribution of strengths S; note that the conditional expectation of S, given σ_p, is assumed to be a linear function of σ_p,

$$(S|\sigma_p = X) = \alpha + \beta x + \varepsilon \qquad (7)$$

where ε is a random variable having mean zero and variance v^2. Applying the usual null hypothesis tests to the available data is complicated by the fact that the fracture data comprise 15 observations of 12 random variables. Specifically, only the residual

$$e = (S|\sigma_p = x) - \hat{\alpha} - \hat{\beta} x \qquad (8)$$

can be observed, where $\hat{\alpha}$ and $\hat{\beta}$ are the maximum likelihood estimates of α and β. (An alternative hypothesis attributes the strength variability to variations in the shape of the crack at the criticality; this possibility is not examined in the present analysis.

The normality of the fracture data are thus analyzed using two approaches: (a) by disregarding the variance-convariance structure of the residuals and (b) by obtaining independent residual observations using an orthogonal transformation of the fracture data.

The first method of analysis assumes that these residuals are independent. The variation in the magnitude of the residuals with the magnitude of the observation can then be obtained directly, as plotted in Fig. 3. There does not appear to be a systematic trend in the residuals (as verified by values of α_1 (skewness) = 0.04 and α_2 (excess) = -0.93), indicating that the normality hypothesis may be reasonable. Also, if the residuals arranged in increasing order of magnitude are plotted (Fig. 5) against the expected value of the i'th order statistic, for a random variable having a standard normal distribution, the good linearity of the plot tends to support the contention that the residuals are observations of a random variable having a normal distribution. Separate analysis of the data at large and small σ_p, using a procedure proposed by Goldfeld and Quandt[12], indicates that the residuals exhibit a systematic increase with increasing magnitude of the observation. This does not invalidate the normality of the distribution, but suggests a variance that increases as σ_p increases; a result that can be tentatively rationalized, as discussed below. However, it should be noted that the data can also be shown to conform with similar confidence to a model in which the measured strength is independent of σ_p, but at two separate levels; one at $S \approx 263$ MPa for $\sigma_p < 400$ MPa, and the other at $S \approx 413$ MPa for $\sigma_p > 400$ MPa (Fig. 3). The data analysis does not, therefore, provide a unique confirmation of the proposed fracture model.

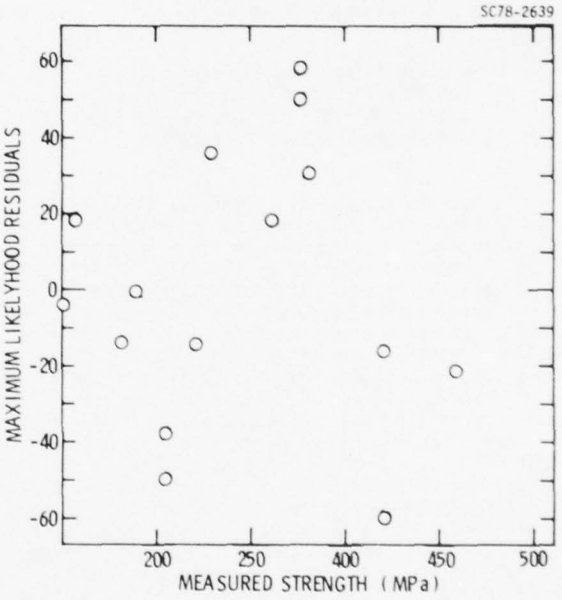

Fig. 3 A plot of the maximum likelihood residuals as a factor of the measured strength.

The second method of analysis uses a procedure proposed by Henry Theil.[13] It involves an orthogonal transformation through an identity matrix. Only 13 residuals can be obtained because 2 degrees of freedom (slope and intercept) are sacrificed in the estimation procedure. The residuals obtained in this fashion exhibit precisely the same trends as the maximum likelihood residuals, as exemplified in Fig. 4.

AD-A071 047 ROCKWELL INTERNATIONAL THOUSAND OAKS CALIF SCIENCE --ETC F/G 14/2
PROCEEDINGS OF THE ARPA/AFML REVIEW OF PROGRESS IN QUANTITATIVE--ETC(U)
JAN 79 D O THOMPSON F33615-74-C-5180
UNCLASSIFIED SC595.51AR AFML-TR-78-205 NL

3 OF 6
AD A071047

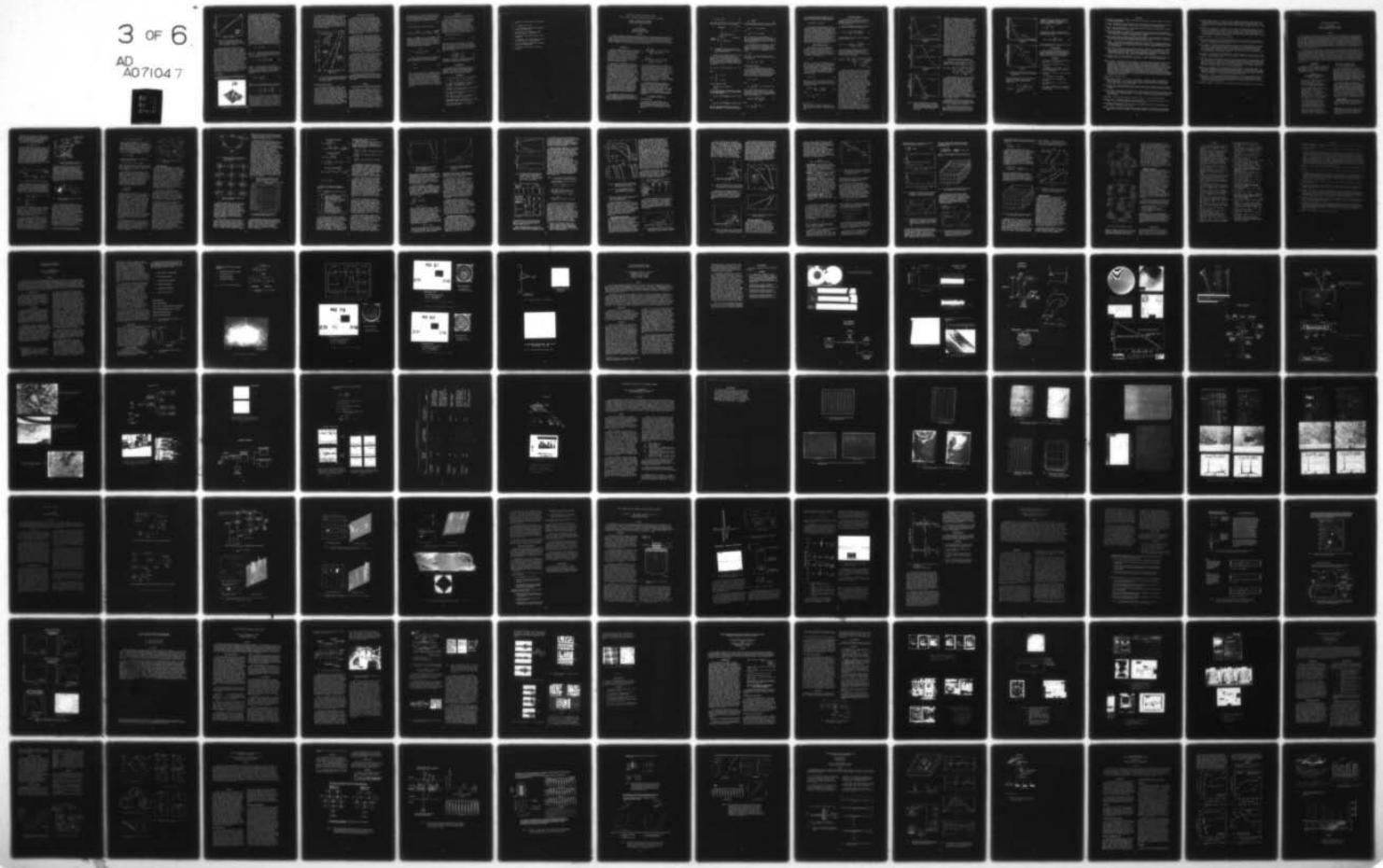

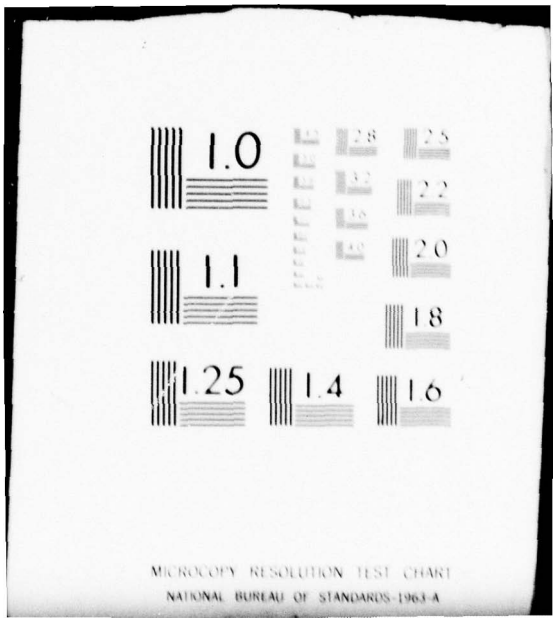
1.0
1.1
1.25
1.4
1.6
2.8
2.5
3.2
2.2
3.6
2.0
4.0
1.8
MICROCOPY RESOLUTION TEST CHART
NATIONAL BUREAU OF STANDARDS-1963-A

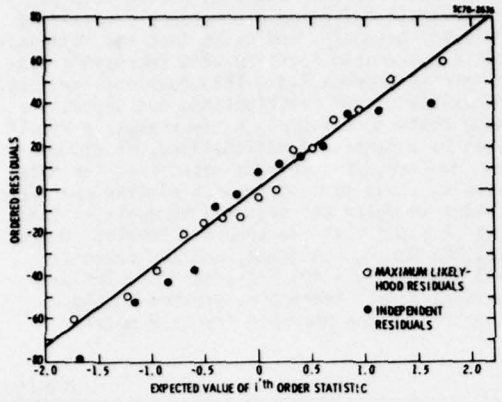

Fig. 4 A plot of the ordered residuals as a function of the estimate of the order statistics for both the maximum likelihood and the independent residuals.

It may be concluded, therefore, that the hypothesized fracture model, modified to allow for an increasing variance with increase in strength level, cannot be rejected by the data. However, this does not discount the possibility that the data might also be consistent with an alternate fracture model. If the assumed fracture model is indeed valid, the parameters of the model implied by the data are: α = 99.655 MPa, β = 0.541. The deviation of β from unity suggests, within the context of the model, that the local toughness of the matrix may be lower than the remote macro-toughness of the matrix (i.e., ~ 3 MPa$\sqrt{m}$ instead of 5 MPa$\sqrt{m}$). This effect can be justified on the basis of a matrix locally degraded by interaction with the inclusion. The relative extent of the degradation may also be supposed to increase as the inclusion size decreases, to account for the observed increase in variance with increase in the level of strength.

Iron Inclusion

Examination of the iron inclusions (Fig. 5) indicates that the inclusions contain several open cracks and/or porosity.

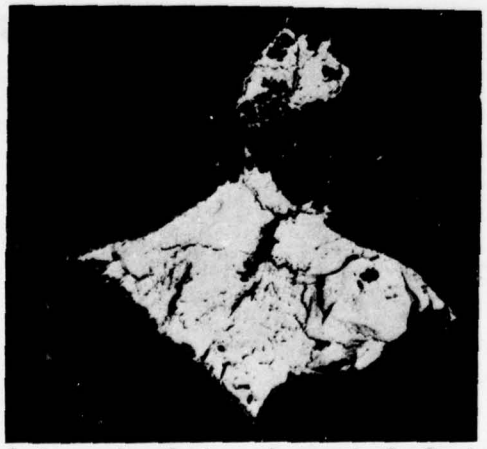

Fig. 5 A scanning electron micrograph of a fractured iron inclusion in hot-pressed silicon nitride.

The cracks and pores are presumably formed by diffusion within the inclusion (while at the elevated temperatures) to relieve the stresses introduced by thermal expansion mismatch (Appendix I). An unrelieved thermal expansion mismatch strain ϵ_α will, of course, still develop at temperatures below those capable of sustaining rapid mass transport. The presence of the open cracks reduces the effective bulk modulus of the inclusion. The stress within the inclusions, induced by the applied stress (Eqn. 3) and the thermal expansion mismath, should thus be appreciably lower than would be anticipated from the intrinsic modulus of the iron silicide material that comprises the inclusion. The proposed fracture model for these inclusions thus supposes that a critical fracture condition is attained when the stress within the inclusion reaches the level required to extend one of the internal cracks, i.e., that there is no subcritical inclusion fracture event. This hypothesis would be consistent with the lack of detectable acoustic emission prior to final fracture. The stress within the inclusion is a relatively uniform, hydrostatic tension p_i (or exactly uniform for an ellipsoidal inclusion) given by:

$$p_i = \psi \sigma_\infty + G_i^e \epsilon_\alpha \tag{9}$$

where G_i^e is the effective shear modulus of the inclusion. A weakest link model of inclusion fracture for a state of uniform tension would indicate a fracture probability,[14]

$$\Phi_i = 1 = \exp\left[-V_i \int_0^{P_i} g(S)dS\right] \tag{10}$$

where v_i is the volume of the inclusion and $g(S)dS$ is the distribution of flaw strengths that relates to the distribution of cracks within the inclusion (and the toughness of the inclusion). If we adopt the Weibull assumption, that $g(S)$ is given by:

$$\int_0^{P_i} g(S)dS = \left(\frac{P_i^c}{P_o}\right)^k \tag{11}$$

where p_o is a scale parameter and k a shape parameter, the inclusion fracture probability becomes:

$$\Phi_i = 1 - \exp\left[-V_i \left(\frac{\psi\sigma_\infty^c + G_i^e}{P_o}\right)\right]^k \tag{12}$$

where σ_∞^c is the applied stress at fracture. The available data are not well suited for comparison with the predictions of this model, because each datum is obtained for a different V_i. Hence, a fracture probability cannot be uniquely assigned to each strength result. However, as a very approximate assessment of the utility of this model, a fracture probability is obtained by assuming it to be given by the order statistic based on the level

of the measured strength, regardless of the inclusion volume. The results are plotted in Fig. 6, as $-\ln(1-\phi_i)$ vs. σ_∞^C. The curvature is presumed to signify an appreciable contribution from ϵ_α. The magnitude of $\epsilon_\alpha G_i^e$ is estimated to be, $100/\psi$ MPa (Fig. 6), and the corresponding value of k is ~ 11. Both values are reasonable. Additional experiments in which V_i is essentially invariant must be conducted, however, if a rigorous evaluation of the model is to be effected.

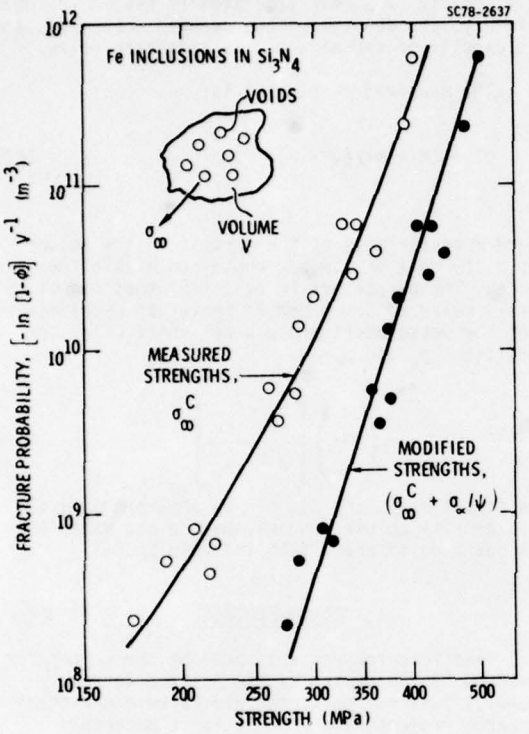

Fig. 6 A plot of the normalized failure probability as a function of the measured strength and the modified strength for iron inclusions in silicon nitride.

Tungsten Carbide Inclusions

The relatively minor effect of the Sl inclusions on the fracture strength of silicon nitride precludes the need for a detailed statistical analysis of strength. The innocuous nature of the tungsten carbide inclusion derives from a combination of relatively high toughness and modulus, as noted above. The analysis of fracture would involve considerations of the distribution of microcracks located with the matrix in the small zone of tension near the poles of the inclusion.[10] The mode of analysis would be essentially similar to that conducted for fracture from voids,[4,5] as modified by the different distribution of matrix stress and the presence of a high toughness inclusion.

IMPLICATIONS AND CONCLUSIONS

Good physical models of the probability of fracture from inclusions can greatly enhance the ability to predict failure from a nondestructive assessment of the inclusion type and size. Models pertinent to specific inclusion types have been presented, and correlations with fracture data have been attempted. The data are not inconsistent with the fracture models. However, to obtain good statistical confidence in the models, additional data are required, for well-controlled inclusion morphologies. Specifically, data sets are required for inclusions of given size, taken at several different size values.

The present results can be used directly in probablistic estimates of reliability, within the strength range that data have been obtained, even though the applicability of the models has not been substantiated with good statistical confidence. The confident substantiation of the present (or alternatives) models of fracture from inclusions would have the advantage of permitting the reliability predictions to be extended beyond the range of the data and, hopefully, to minimize the variance that must be applied to the fracture probability - thereby reducing the rejection probability associated with any given method of nondestructive analysis.

The strong influence of the inclusion type on the fracture strength is re-emphasized. Specifically, tungsten carbide inclusions can be regarded as almost innocuous, while silicon inclusions are extremely deleterious at low temperatures; iron inclusions and voids[5] are of intermediate severity. It is interesting to note that surface cracks in hot-pressed silicon nitride produces about the same strength degradation as silicon inclusions with the equivalent diameter. However, it should be noted that silicon develops appreciable toughness above ~ 1000°C, and melts at 1420°C. Silicon inclusions are thus likely to become less deleterious at elevated temperatures ($\gtrsim$ 900°C), tending to approach the behavior of voids of equivalent size.

Finally, the appreciable dependence of the fracture probability on the inclusion type clearly emphasizes the importance of defect type classification for effective nondestructive failure prediction schemes.

APPENDIX I

STRESSES PRODUCED BY THERMAL EXPANSION MISMATCH

The magnitude of the thermal expansion stress depends on the cooling temperature ΔT (Eqn. 1). An exact definition of this temperature differential presents several problems. The stress within the inclusion is purely hydrostatic (i.e., no shear stresses), and stress relaxation can only occur by mass transport processes. By contrast, the stress within the matrix has a zero hydrostatic component, $p(\sigma_{rr} + 2\sigma_{\theta\theta} = 0)$, but a very large shear component, $\sigma_{r\theta}(\equiv 3\beta^*/4)$; relaxation in the matrix can thus also occur by shear processes. The latter is similar to the elastic/plastic deformation of spherical cavity, for which the relative displacement of the cavity surface depends on the yield strength. However, there is no evidence that Si_3N_4 exhibits significant

shear plasticity. It is thus considered that the only appreciable relaxation occurs by mass transport. The chemical potential that acts as the driving force for atom migration is dictated within the inclusion primarily by the hydrostatic pressure

$$\mu_i = -p\Omega \tag{A1}$$

and within the matrix by the strain energy

$$\mu_m = G_m \frac{(\Delta\alpha\Delta T)^2}{[1+2(1-2\nu_i)/(1-\nu_i)(G_m/G_i)]^2}\left[\frac{3}{8(1-\nu_m)} + \frac{9}{16}\right]\left(\frac{R}{r}\right)^6 \tag{A2}$$

where Ω is the atomic volume. The incidence of atom transport will modify the chemical potential and the stress distribution. This will occur primarily by vacancy transport to the interface. However, if the stress within the inclusion is tensile, cavities may nucleate by vacancy condensation. Nucleation will occur when the stress exceeds[16]

$$p^2 = \frac{4\alpha_s^3}{kT\ell n(4\pi D_b \delta_b n_o / p\,\Omega^{4/3})} \tag{A3}$$

Once a cavity has nucleated, the stress at the cavity surface and the local chemical potential must be maintained at their equilibrium values

$$p = 2\alpha_s/r \tag{A4}$$

$$\mu = -\Omega\alpha_s/r$$

where r is the cavity radius. The chemical potential gradient now favors vacancy diffusion into the cavity, and cavity growth can be anticipated. Hence, if several cavities nucleate, the stresses within the inclusion remain at a moderate level, while mass transport is occurring. It should also be noted that the formation of cavities decreases the modulus G_i of the inclusion. This tends to minimize the stresses that develop on cooling below the temperature at which mass transport eventually ceases.

APPENDIX II

A POSTERIORI MEASUREMENTS OF INCLUSION VOLUME

Most of the naturally occurring inclusions in structural ceramics develop cracks during temperature excursions. Consequently, the inclusions are relatively friable after fracture, and can be readily separated from the matrix by suitable etchants. The remaining void space can then be filled with a low density wax and the density of the ceramic/wax system measured in a density column. This density is directly related to the inclusion volume v, the density of the ceramic host, p_c, and the density of the wax, p_w, as indicated below.

The measured density p' is:

$$p' = (M + m)/(v + v) \tag{A5}$$

where M is the mass of the ceramic, V its volume and m the maxx of the wax contained within the void space. The parameters in Eqn. (A5) that cannot be easily measured are m and V; these can be eliminated from the measurement process by substituting the densities p_w and p_c:

$$v = \left(\frac{M}{p_c}\right)\left[\frac{p_c - p'}{p' - p_w}\right] \tag{A6}$$

The densities p_c and p' can be obtained directly from density column studies, before and after the wax has been inserted into the void space.

ACKNOWLEDGMENT

This research was sponsored by the Center for Advanced NDE, operated by the Science Center, Rockwell International, for the Defense Advanced Research Projects and the Air Force Materials Laboratory under Contract F33615-74-C-5180.

REFERENCES

1. J.R. Richardson and A.G. Evans, to be published.
2. A.G. Evans, Jnl. Mater. Sci. 9 (1976) 1145.
3. F.F. Lange, Fracture Mechanics of Ceramics (Ed. R.C. Bradt, D.P.H. Hasselman, F.F. Lange) Plenum, N.Y. (1978) Vol. 4, p. 799.
4. O. Vardar, I. Finnie, D.R. Biswas and R.M. Fulrath Intl. Jnl. Frac. 13 (1977) 215.
5. A.G. Evans, D.R. Biswas and R.M. Fulrath, Jnl. Amer. Ceram. Soc., in press.
6. A.G. Evans, G.S. Kino, B.T. Khuri-Yakub and B.R. Tittmann, Materials Evaluation.
7. H.R. Baumgartner, R.H. Brockelman and P.M. Hansen, AMMRC Report, AMMRC TR 78-11 (June 1978).
8. J.B. Wachtman, W. Capps and J. Mandel, Jnl. Materials 7 (1972) 188.

9. J. Selsing, Jnl. Amer. Ceram. Soc. 44 (1961) 419.

10. J.D. Eshelby, Proc. Roy Soc.

11. G.C. Sih, Handbook of Stress Intensity Factors (Lehigh Univ. Press) 1973.

12. S.M. Goldfield and R.E.Quandt, Jnl. Amer. Statistical Assoc., 60, (1965) 539.

13. H. Theil, Jnl. Amer. Statistical Assoc., 60, (1965) 1067.

14. J.R. Matthews, F.A. McClintock and W.J. Shack, Jnl. Amer. Ceram. Soc., 59, (1976) 304.

15. J.J. Petrovic and M.G. Mendiratta, Jnl. Amer. Ceram. Soc. 59 (1976) 163.

16. A.G. Evans, J.R. Rice and J.P. Hirth, to be published.

ACCEPT/REJECT CRITERIA FOR STRUCTURAL CERAMICS:

PART 4: A COMPUTER SIMULATION OF NONDESTRUCTIVE RELIABILITY IN CERAMICS

G. Meyer, K. Fertig and J. Richardson
Rockwell International Science Center
Thousand Oaks, California 91360

and

A. G. Evans
Materials Department
University of California
Berkeley, California 94720

ABSTRACT

A computer simulation of nondestructure failure prediction in silicon nitride containing silicon inclusions has been developed. The preliminary application of the simulation examines the results of an inspection that uses a single transducer in the pitch/catch mode. The limitations of the inspection method, especially when applied to nonspherical inclusions, are exposed by the simulation. Also, the expected influences of the signal-to-noise ratio and the inclusion size distribution on the failure and rejection probabilities emerge from the analysis in quantitative form.

INTRODUCTION

Ceramic components are subject to failure from inclusions introduced during the fabrication stage of manufacture. The specific influence of various inclusion types on fracture have been studied for hot-pressed silicon nitride,[1] indicating that silicon inclusions are particularly deleterious. The present study will thus use results for silicon inclusions in silicon nitride to illustrate the analysis of structural reliability using nondestructive inspection methods.

Recent studies of nondestructive defect characterization in ceramics have indicated that ultrasonic methods have the greatest potential for obtaining the information concerning defect size and type required for failure prediction.[2] One candidate technique with considerable promise is the combined use of low frequency ($\lesssim$0.5 ka, where k is the wave number and a is the defect radius) and high frequency ($\gtrsim$5 ka) scattering information. The high frequency scattering can be analyzed to provide information about the defect type;[3] while the low frequency results (given the defect type) can be analyzed to yield an estimate of the defect volume.[4,5] In the present study it is assumed that the defect type can be unambiguously determined (this has yet to be unequivocally demonstrated). Estimates of the defect volume, given that the defect is a silicon inclusion, can then be made using long wave length results. The analysis of reliability will thus be the optimum that can be achieved using the concept of combined high/low frequency scattering information. Methods for obtaining this information are described elsewhere.[6]

The probabilistic analysis yielding the parameters needed to reach accept/reject decisions, based on long wavelength ultrasonic scattering results, indicates false accept ψ_A and false reject ψ_R probabilities given by;[7]

$$\psi_A = \frac{\int_{-\infty}^{Y^*} \int_0^{\infty} \phi(Y|x)\, \Phi(S < \sigma_\infty|x)\, \phi(x)\, dY dx}{\int_0^{\infty} \Phi(S < \sigma_\infty)\, \phi(x)\, dx}$$

$$\psi_R = \frac{\int_{Y^*}^{\infty} \int_0^{\infty} \phi(Y|x)\, \Phi(\sigma_\infty > S|x)\, \phi(x) dY dx}{\int_0^{\infty} \Phi(\sigma_\infty > S)\, \phi(x) dx} \qquad (1)$$

The probability $\Phi(S < \sigma_\infty|x)$ that the strength S will be less than the applied stress σ_∞, given the inclusion dimensions x, is derived from an analysis of data obtained for fracture from silicon inclusions in silicon nitride.[1] The probability $\phi(Y|x)dY$ that the long wavelength estimate Y of the inclusion dimensions x are in the range Y to Y + dY is obtained from the analysis of scattering by spheroidal inclusions in the long wavelength limit.[5] The probability $\phi(x)dx$ - the a priori inclusion size distribution - is assumed to conform to an extreme value distribution, typical of defect distributions in ceramics.[8]

The objective of the present study is to obtain false-accept/false-reject probabilities pertinent to long wavelength scattering from silicon inclusions in silicon nitride. The inspection is confined to the conventional, single transducer pitch/catch configuration. Subsequent studies will examine other transducer configurations, in an attempt to identify optimum transducer arrays for minimizing the false-reject probability.

THE FUNDAMENTAL PROBABILITIES

The Inclusion Size

The inclusions are considered to be spheroidal, typical of the silicon inclusions observed in hot-pressed silicon nitride.[1] The state $\underline{x}$ adopted in the present study is the size and orientation of silicon inclusions in silicon nitride

$$\underline{x} = (\theta, \phi, \ell_1, \ell_2) \qquad (2)$$

where θ and ϕ are defined in Fig. 1, and ℓ_1 and ℓ_2 are the two semiaxis lengths of the spheroid.

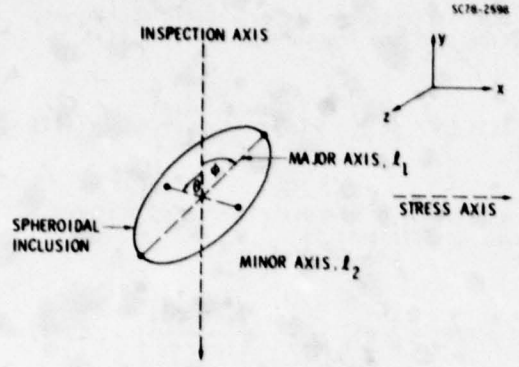

Fig. 1 A schematic indicating the orientation relationships for the spheroidal inclusions used in the simulation.

The angle ϕ is a uniform random variate on the interval $[0, 2\pi]$ and the direction cosine γ_z ($= \cos\theta$) is a Beta random variate with parameters ν_1 and ν_2. For the preliminary analysis $\nu_1 = \nu_2 = 1$, so that γ_z is a uniform random variate on the interval $[0,1]$. The lengths ℓ_1 and ℓ_2 of the semiaxis are assumed to be jointly distributed with density

$$P_{\ell_1, \ell_2}(x,y) = A\, f_{\ell_1}(x)\, f_{\ell_2}(y) L(\ell_2 - \ell_1) \qquad (3)$$

where

$$L(q) = \begin{cases} 0 & \text{if } q < 0 \\ 1 & \text{if } q \geq 0 \end{cases}$$

and A is chosen such that

$$\int_0^\infty \int_0^\infty P_{\ell_1, \ell_2}(x,y)\,dx\,dy = 1$$

The univariate densities are assumed to be extreme value and of the Weibull family, as often observed for the large extreme,[8]

$$f_{\ell_1}(x) = (x/b^*)^{k-1} \left(\frac{k}{b^*}\right) \exp\left(-x/b^*\right)^k \qquad (4a)$$

and

$$f_{\ell_2}(y) = (y/a^*)^{k-1} \left(\frac{k}{a^*}\right) \exp\left(-(y/a^*)^k\right) \qquad (4b)$$

where k is the shape parameter and a* and b* are the scale parameters. It can easily be shown that

$$A = 1 + \left(\frac{b^*}{a^*}\right)^k . \qquad (5)$$

To obtain Monte Carlo values for ℓ_1 and ℓ_2 a random variate was taken from each of the distributions

$$F_{\ell_1}(x) = 1 - \exp\left(-(x/b^*)^k\right)$$

and (6)

$$F_{\ell_2}(y) = 1 - \exp\left(-y/a^*\right)^k)$$

where k, a* and b* are input parameters. If $\ell_2 < \ell_1$, both random variates are discarded and two more are randomly selected. This is continued until two are selected such that $\ell_1 \leq \ell_2$ is far more likely than $\ell_2 < \ell_1$.

For the prediction of fracture it is required to obtain, from the state $\underline{x}$, the lengths of the semiaxes of the cross-sectional ellipse at the middle of the inclusion. If the stress is applied along the laboratory x-axis, the major axis a is simply

$$a = \ell_2;$$

while if $\xi = 1 - \gamma_x$ (γ_x is the direction cosine with respect to the x axis), the minor axis, b, can be obtained from

$$\frac{1}{b^2} = \frac{1}{\ell_2^2} + \left(\frac{1}{\ell_1^2} - \frac{1}{\ell_2^2}\right)\xi \qquad (7)$$

The Fracture Probability

The fracture model applied to the data for silicon inclusion initiated failure in silicon nitride has been derived[1] on the premise that the silicon inclusion fractures sub-critically to create a crack equal in size to the cross-sectional area of the inclusion. The predicted fracture stress σ_p can, for this model, be written as;

$$\sigma_p = Z(b/a) K_c b^{-1/2} \qquad (8)$$

where

$$Z(u) = \frac{1}{\sqrt{\pi}} \int_0^{\pi/2} \left(1 - (1 - u^2)\sin^2\theta\right)^{1/2} d\theta$$

and K_c is the fracture toughness of the silicon nitride matrix, assumed to be 5 MPa $\sqrt{m}$. Analysis of the fracture data indicated that σ_p was normally distributed, yielding a fracture probability at an applied stress σ_∞ given by;

$$\Phi(\sigma_\infty < S | \underline{x}) = B\left(\frac{\sigma_\infty - \alpha - \beta\sigma_p}{\sqrt{V(E_s)}}\right) \qquad (9)$$

where

$$B(x) = \frac{1}{\sqrt{2\pi}} \int_{-\infty}^{x} e^{-t^2/2}\, dt$$

E_s is a normal random variate describing the fracture strength S, with a variance $V(E_s)$ and a mean of zero; α and β are constants, given by;

$$\alpha = 99.66 \text{ MPa}, \quad \beta = 0.541 .$$

The location of the cross section of the inclusion at which inclusion fracture initiates has not yet been studied in detail. Presumably, the location will depend on the size distribution of pre-existing microcracks within the inclusion, or at the interface, and will exhibit some statistical variability. For the present analysis it is assumed that fracture occurs at the location with the maximum cross section exposed to the applied stress. This simplification eliminates one probability term from the final expression for the false-accept/reject probability; it also affords a lower limit for the fracture probability.

THE SCATTERING AMPLITUDE

The amplitude of a plane ultrasonic wave scattered in any direction by a spheroidal inclusion in the long wavelength limit can be calculated knowing the elastic properties of the inclusion and matrix as well as the axes and orientation of the spheroid.[4,5] This amplitude A is related to the frequency f by;

$$A = A_2 f^2 \tag{10}$$

where A_2 is a coefficient. The coefficient A_2 is used as a measure of the volume of the scatterer. The experimental determination of A_2 involves an error, associated both with background and extraneous reflections. It is assumed for the present calculation that the measured coefficient, Y (i.e., the slope of the amplitude in the f^2 scattering regime) is related to the absolute coefficient A_2 by;

$$(Y|\underline{x}) = A_2 + E_y \tag{11}$$

where E_y is a normal random variate with mean u = o and variance $V(E_y)$. The measured values† of the amplitude coefficient y thus have the conditional frequency distribution

$$h_{Y|\underline{x}}(y) = \frac{1}{\sqrt{V(E_y)}} \; H\left(\frac{y-A_2}{\sqrt{V(E_y)}}\right) \tag{12}$$

where,

$$H(y) = \frac{1}{\sqrt{2\pi}} \; e^{-y^2/2}$$

†Measured values of parameters are expressed in lower case, while the random variable from which the measurement is obtained is expressed in upper case.

THE FAILURE PROBABILITY

The intent of this section is to derive the probability of failure, given values for the measured ultrasonic scattering coefficient Y and the applied stress σ_∞.

If N is the number of Monte Carlo iterations, the estimate of the fracture probability is

$$\hat{\Phi}(S<\sigma_\infty) = \frac{1}{N} \sum_{i=1}^{N} B\left(\frac{\sigma_\infty - \alpha - \beta(\sigma_p)_i}{V(E_s)}\right), \tag{13}$$

and the estimate of the distribution of measured amplitude coefficients is

$$\hat{f}_y(y) \equiv F(Y) = \frac{1}{N} \sum_{i=1}^{N} \frac{1}{\sqrt{V(E_y)}} \; H\left(\frac{y-(A_2)_i}{\sqrt{V(E_y)}}\right). \tag{14}$$

Since the ultrasonic scattering and the fracture stress are stochastically independent in the present study, the estimate of the fracture probability for specific values of the ultrasonic amplitude coefficient becomes;

$$\hat{\Phi}(S<\sigma_\infty|Y) = \frac{\sum_{i=1}^{N} B\left(\frac{\sigma_\infty - \alpha - \beta(\sigma_p)_i}{\sqrt{V(E_s)}}\right) H\left(\frac{y-(A_2)_i}{\sqrt{V(E_y)}}\right)}{\sum_{i=1}^{N} \left(\frac{y-(A_2)_i}{\sqrt{V(E_y)}}\right)} \tag{15}$$

These three probabilities can be estimated by specifying values of the applied stress (σ_∞), the inclusion size parameters (a*, b* and k) and the measurement variance ($V(E_y)$), i.e., the signal-to-noise ratio. Preliminary results are obtained for a given applied stress of 250 MPa and three different values of the inclusion size and the measurement variance (Figs. 2(a), (b), (c)). Inspection of Fig. 2 indicates several important features. Firstly, note that the inclusion size distribution parameters have been chosen to enable the fracture probability without inspection $\Phi(S<\sigma_\infty)$ to be relatively invariant (ranging from 0.11 to 0.16). However, the location of the maximum density of scattering amplitudes F(Y) varies considerably. The trend toward a narrower distribution of Y from Fig. 2(a) to 2(c), reflects primarily the increase in the shape parameter k, with an additional superimposed influence of a decreasing signal-to-noise ratio. The most important results are the estimates of the variation in the fracture probability after ultrasonic inspection. This probability is just the probability of fracture at given values of the ultrasonic measurement amplitude Y, i.e., it is normalized by the distribution of Y values and contains no explicit dependence on this distribution. It would normally be anticipated that this probability should increase continuously as the measurement amplitude increases commencing, at small Y, below the fracture probability without

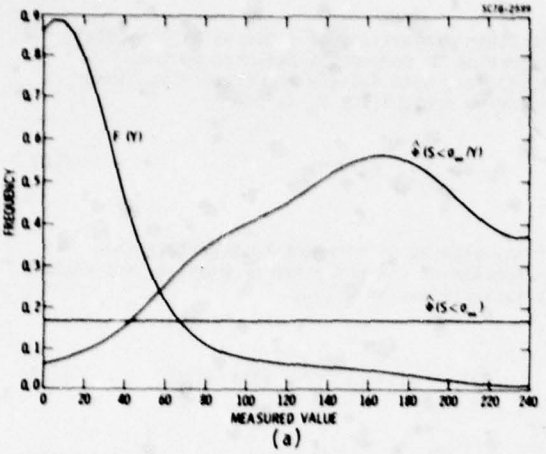

(a)

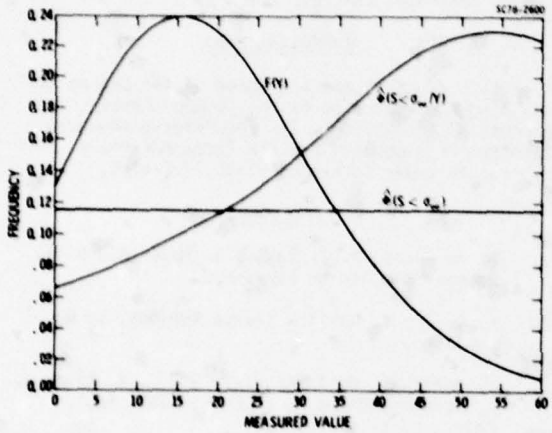

(b)

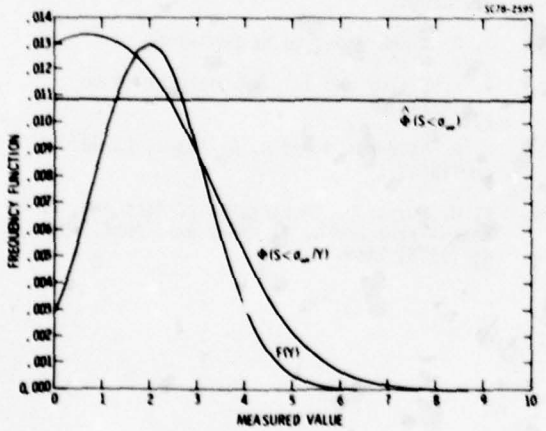

(c)

Fig. 2 Plots of the distribution of measured ultrasonic amplitudes F(V), the failure probability without inspection $\Phi(S<\sigma_{\infty})$ and the failure probability corresponding to a speific ultrasonic indication $\Phi(S<\sigma_{\infty}/Y)$.

inspection. This behavior, referred to as "normal behavior", is observed for the parameters chosen to compute the failure probabilities reproduced in Figs. 2a and b. However, the inverse trend is observed in Fig. 2(c), referred to as "abnormal behavior". The rationale for this phenomenon involves the following considerations. The large k chosen for this calculation implies a narrow distribution of inclusion sizes, as reflected in the narrow range of F(Y) values in Fig. 2(c). This effect, coupled with the relatively large aspect ratio of the inclusions ($a^*/b^* = 10$), leads to the realization that the large extreme of F(Y) values refers to inclusions with their long dimension (a) nearly normal to the inspection direction. Yet, since the stress is applied normal to the inspection orientation, the cross section subject to fracture (for inclusions in this orientation) is small, $\sim b$. It can thus be concluded that inclusions which yield large scattering amplitudes can exhibit low fracture probabilities. The inspection in this instance is thus providing misleading information about failure, and could be deleterious to failure prediction, in the absence of ancilliary information. This effect will be minimized, and probably eliminated, by collecting scattering information at other angles. The benefits to be derived from inspection procedures other than the pitch/catch method will be the subject of a subsequent study.

FALSE ACCEPT/FALSE REJECT PROBABILITIES

The estimates of the false-accept and false-reject probabilities are derived from Eqn. (1); for example, the false-accept probability is given by;

$$\hat{\Psi}_A\,(y|S<\sigma_{\infty}) = \frac{\sum_{i=1}^{N} B \left(\frac{\sigma_{\infty} - \alpha - \beta(\sigma_p)_i}{\sqrt{V(E_s)}}\right) H\left(\frac{y-(A_2)_i}{\sqrt{V(E_Y)}}\right)}{\sqrt{V(E_Y)}\ \sum_{i=1}^{N} B \left(\frac{\sigma_{\infty} - \alpha - \beta(\sigma_p)_i}{\sqrt{V(E_s)}}\right)} \qquad (16)$$

The false-accept and false-reject probabilities derived for the three cases discussed in the preceding section are plotted in Fig. 3. The separation of the peak densities of these two distributions affords a measure of the reduced false-reject rate that can be achieved by inspection. The separation is most apparent in Fig. 3(b): a case in which the signal-to-noise ratio is not excessive and the inclusion aspect ratio (and size distribution) does not lead to "abnormal" behavior of the fracture probability after inspection. The much reduced separation for the case shown in Fig. 3(a) is primarily a consequence of the relatively large signal-to-noise ratio in this simulation, while the separation in case(c) reflects the aspect ratio problem discussed in the preceding section.

Additional simulations will be conducted in subsequent studies to examine independent effects of the signal-to-noise ratio, the inclusion aspect ratio and the inclusion size distribution.

It should be noted that although the false-accept/reject relations afford a unique relative measure of the utility of different inspection methods, two other probabilities are of greater

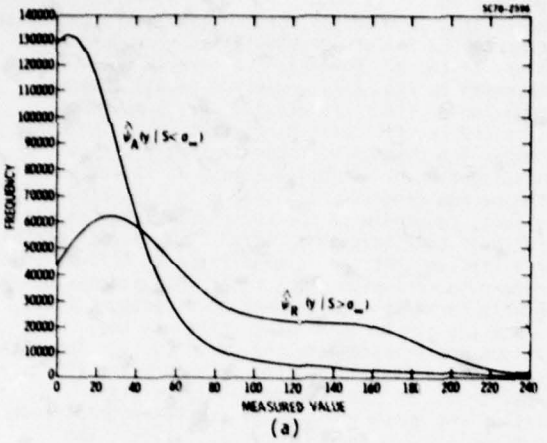

(a)

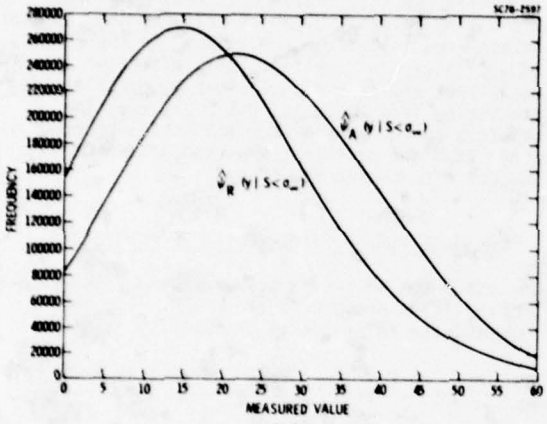

(b)

Fig. 3 Plots of the false-accept and false/reject probabilities as a function of the measure ment amplitude.

practical interest. The first is the probability of failure of components accepted by the inspection, i.e., the in-service failure probability P_F;

$$P_F(Y^*, \sigma_\infty) = \frac{\phi(S < \sigma_\infty) \int_{-\infty}^{Y^*} \psi_A(Y|S<\sigma_\infty)dY}{\int_{-\infty}^{Y^*} F(Y)dY} \qquad (17)$$

The other probability of interest is the total proportion of components rejected by the inspection, both falsely and correctly. This rejection probability P_R is simply

$$P_R = \int_{Y^*}^{\infty} F(Y)dY. \qquad (18)$$

It may also be of interest to ascertain that proportion of the rejection probability attributed to false-rejection $(P_R)_F$;

$$(P_R)_F = \phi(S<\sigma_\infty) \int_{Y^*}^{\infty} \psi_R(Y|S>\sigma_\infty)dY. \qquad (19)$$

Each of these probabilities can be derived from the curves presented in Figs. 2 and 3.

ACKNOWLEDGEMENT

This research was sponsored by the Center for Advanced NDE, operated by the Science Center, Rockwell International, for the Defense Advanced Research Projects and the Air Force Materials Laboratory under Contract F33615-74-C-5180.

REFERENCES

1. A. G. Evans, B. I. Davis, G. Meyer and H. R. Baumgardner, to be published.

2. A. G. Evans, Naval Research Reviews, to be published.

3. Y. Murakami, B. T. Khuri-Yakub, G. S. Kino, J. R. Richardson and A. G. Evans, Jnl. Appl. Phys., to be published.

4. W. Kohn and J. R. Rice, Jnl. Appl. Phys. to be published.

5. J. R. Richardson, to be published.

6. R. K. Elsley and J. R. Richardson to be published.

7. J. R. Richardson and A. G. Evans, to be published.

8. A. G. Evans, L. Ahlberg, B. R. Tittmann, B. T. Khuri-Yakub and G. S. Kino, Jnl. Appl. Phys., 49 (1978) 2669.

DISCUSSION

Robb Thomson, Chairman (NBS): We have a few minutes for discussion. Tony hasn't used all of his hour. Are there any questions?

Paul Höller (Saarbrucken): I was astonished by the limit of detection you mentioned for micro-focus X-ray. What was the diameter of focus you were using and what was the focusing system?

Anthony G. Evans (Science Center): I am in an odd position here because John Schuldies did the experiment. Did you hear that question, John?

John Schuldies (Airesearch): I think I did. The size of the focal spot in that system theoretically approaches 50 microns depending on the bias applied to the electron beam prior to hitting the target. It is a commercially available system manufactured by Magnaflux.

Anthony G. Evans: Maybe I can ask you a question, Professor Holler. Was the purpose of the question that you know of a system which might be capable of detecting surface inclusions of a smaller size, or was it the other way around; you were impressed how small it was?

Paul Höller: I think there are instruments which have fine focus which will give better resolution. I suppose you are aware of the work which has been done in Harwell. Their instrumentation is commercially available, so we have preliminary results which are going much below the 250 microns you were mentioning here.

Anthony G. Evans: Again, I don't know quite how to respond to that since I am not personally involved in the X-rays. My feeling is that the focal spot, the resolution, is not a problem here. The biggest problem is that the difference in the X-ray absorption by the defect is not sufficiently different from that of the matrix. When you have appreciable thicknesses of the component, you really can't see anything. Maybe there are some further things to be done.

Joseph Matakey (TRW): I have two questions. The first is: Can you scan complex geometry with a high frequency ultrasonic technique; and the second one is: What is the low frequency range?

Anthony G. Evans: The answer to the first question is an interesting one and we have got some thoughts on that which I can describe. The low frequency, in this case, was 15 megahertz. It was a focused system. Bob Addison did that work and he will describe that in one of the posters this afternoon. It turns out we probably need somewhat higher frequencies than that in order to get the smallest defects of importance--perhaps, 35 megahertz. As far as the complex shape is concerned, we have a number of concepts that we have been working on with the use of buffers, that is, a ceramic which has one flat surface and the other surface contoured to fit the geometry of the component. Most of these components have to be machined very accurately any way to make sure they will satisfy the service requirements. One can, therefore, make a buffer for much of the component with great accuracy (within a mil or less) and then one can scan over the flat surface of the buffer and get through to the ceramic.

Joseph Matakey: Have you tried it?

Anthony G. Evans: We tried it. I say "we." Neil Kuriakin, at Stanford, tried it in the case of a sperical ceramic ball. We had a matching buffer with the flat surface and it worked very well. Part of this program is, now, to expand those concepts to ceramic turbine parts to see how well it works there. The signs look fairly good.

Daniel Isaac (ITT): When you mentioned that the bulk area of the void is significant, did you mean that for all states of stress, or did you refer to that portion of the area that is subject to tensile stresses?

Anthony G. Evans: That comes out in the integration. When you work out the integral, you integrate over that fraction of the area under tension. Since that is a constant fraction of the total area of the void (regardless of shape) and because it is a constant fraction, you can take the total area outside the integral.

Daniel Isaac: But the fraction depends on the state of stress. It is not a constant fraction.

Anthony G. Evans: It depends on the state of stress, certainly. I refer to the uniaxial case. For a biaxial or triaxial stress condition, you're absolutely right.

George Rudder (Ames Laboratory): Have you tried using different polarizations at high frequencies to distinguish the different types of voids?

Anthony G. Evans: The people at Stanford have developed transducers for longitudinal and shear waves. In the program we have also developed inverse response functions for both longitudinal and shear waves.

Jerry Tiemann (General Electric): In one of your earlier slides you showed the fracture response as a function of the thickness of the void for silicon, tungsten carbide and other ionic types. One would have thought that they would have converged to the same level at zero thickness, but in fact, all the curves seem to approach different intercept values. Would you comment on the origin of that variance?

Anthony G. Evans: Let me see if I can find it so I can point out to everybody what you mean. You see I didn't take them to zero. The reason for that, of course, is that, if the defect thickness is really zero, the strength goes to the theoretical strength. So all of these curves should go to the theoretical strength at zero thickness. I referred to measurements that we actually made. The smallest defect we had in there was 50 microns. The actual results have to go up very, very rapidly to yield theoretical strengths at zero thickness.

Robb Thomson, Chairman: I think one more question, then.

Thomas De Lacy (Ford Aerospace): I am surprised that you continue to look at single discrete defects. Why aren't we looking at the effects of the interrelation of size distribution and maybe a range of inclusions or particulates within the material?

Anthony G. Evans: The reason that we have confined ourselves to so-called isolated defects, not interacting defects, is that our initial interest is in the case of a hot pressed silicon nitride for which all our fracture studies have indicated that (except in rare cases) fracture does indeed occur from individual, isolated inclusions or from surface cracks. There are no interaction effects between them. That's not the case, I know, in reaction bonded silicon nitride where, clearly, one has interaction effects before fracture.

Thomas De Lacy: But, you know, there are regression and oxidation mechanisms. There are lots of things that could be interrelated to the behavior of the ceramic in service; but your whole study is ceramic fracture. I guess that's the key.

Anthony G. Evans: There is a lot of work going on in the program in that vein in recognizing that oxidation does introduce a new population of surface cracks that weren't there at the onset of the inspection. What we find out, though, is that that population tends to level off after a certain while. There is a plateau in the strength as a function of oxidation time as it turns out. To design below that level, then, one is concerned with the cracks that existed prior to the oxidation which are deeper than the oxidation layer. That is our present prospective.

Thomas De Lacy: I understand, but the mechanism that might be working is the synergistic effect. Improved understanding of the oxidation mechanism that could change the chemical bond state is rather interesting. We looked at that some time ago at General Dynamics. I was associated with Mossbauer spectroscopy and there are lots of techniques that could be interrelated to this kind of work that could be very valuable. I am surprised we are not doing some of that.

Anthony G. Evans: I think your surprise will be moderated when you start looking at the dollars that will be mounted up even for the number of tests we have conducted. It is a lot of dollars. You are right, though. I think one should always have in the back of one's mind that these effects are occurring in service and they do modify the roughness of it as well as the flaw size. I think that is going to be further down the road.

Robb Thomson, Chairman: I think at this point we should terminate this part and go on to the next lecture.

POLYMER COMPOSITE RELIABILITY

D.H. Kaelble
Rockwell International Science Center
Thousand Oaks, California 91360

ABSTRACT

The structural performance, reliability and durability of polymer composites can now be correlated with three generic classes of internal defects. The first generic class of chemical structure defects (size 10-100Å) that control critical design properties such as glass transition T_g, moisture absorption, and dimensional changes can be controlled by chemical analysis of raw materials prior to manufacture. A second generic class of manufacturing defects (size greater than 1μm) include inclusions, voids and debonds which are related to manufacturing process control and recognized by ultrasonics, optical scanning and other techniques sensitive to interfacial imperfections. The interaction of these two classes of intrinsic defects with environmental and mechanical stresses produces a third class of macroscopic fatigue defects such as interconnected microcracks and macroscopic crack growth which can be detected by visual inspection and ultrasonic emission.

The recognition of intrinsic structural defects, and their contributions to polymer composite reliability, represents an important extension in the analytic modeling and reliability predictions for structural polymers, adhesively bonded metals and high strength fiber reinforced composites in which the physical chemistry parameters appear as primary control variables. This discussion introduces and discusses combined deterministic/statistical models for polymer composite reliability. The molecular process which determines the relation between environmental condition and macroscopic structural effect is detailed within such models and provides important criteria for chemical and manufacturing optimization of polymer composite reliability. Experimental data of aging effects on the statistical strength distributions of structure polymers, metal-to-metal joints and reinforced composites are examined and compared with model predictions.

INTRODUCTION

Concepts of structural design for reliability are old and well used. A classical expression of these concepts is well illustrated in the following excerpt of a poem by Oliver Wendell Holmes as described in Table 1.

TABLE 1
THE DEACON'S MASTERPIECE:
Or the Wonderful "One-Hoss-Shay."*
A Logical Story

Have you heard of the wonderful one-hoss-shay,
That was built in such a logical way
It ran a hundred years to a day,
And the, of a sudden - ah, but stay,
I'll tell you what happened without delay,

At age one hundred years to the day
There are traces of age in a one-hoss-shay
A general flavor of mild decay,
But nothing local, as one may say.
There couldn't be, - for the Deacon's art
Had made it so like in every part
That there wasn't a chance for one to start.
And yet, as a whole, it is past a doubt
In another hour it will be worn out!

This morning the parson takes a drive.
All at once the horse stood still,
Close by the meet'n'-house on the hill.
-First a shiver, and then a thrill,
Then something decidedly like a spill,-
And the parson was sitting upon a rock,

-What do you think the parson found,
When he got up and stared around?
The poor old chaise in a heap or mound,
You see, of course, if you're not a dunce,
How it went to pieces at once,-
All at once, and nothing first,-
Just as bubbles do when they burst.

The design of high performance, reliability, and durability into mobile structures such as spacecraft, airplanes, cars, or the one-horse-shay described above is a special branch of structural engineering in which weight minimization is an important design constraint. The rapidly evolving polymer composite technology represents new inputs which make exotic advanced structures such as the man-powered airplane "Gondor", and the Space Shuttle functional within their design constraints.

One specific objective of this discussion is to review current reliability concepts and identify new approaches, particularly relevant to polymer composite materials. A second objective is to indicate the important role that predictive models and computer aided design and manufacture (CAD/CAM) can play in achieving polymer composite reliability. A final objective is to illustrate the utility of determining the molecular processes which control macroscopic reliability and define environmental aging and nondestructive evaluation (NDE) directly in terms of the molecular process.

Current Concepts

Current concepts of engineering design to achieve structural reliability are detailed in an excellent review edited by Swedlow, Cruse, and Halpin[2]. Several of the important current

*exerpts from a poem by Oliver Wendell Holmes, in "The Autocrat of the Breakfast Table", pp. 252-256, The Riverside Press, Cambridge, Mass. (1895) relating to "Structural design for reliability."

definitions of reliability provide valuable insight into design concepts. A widely used and generally accepted definition of reliability is described by the so called "bathtub curve" of Fig. 1, and the following definition of reliability R by the following equation:

$$R = \exp - \int_0^t \lambda(t)\, dt \qquad (1)$$

where $\lambda(t)$ is defined as the failure rate at time t, or the "bathtub curve" and Eq.(1) define a break in period in which manufacturing defects are covered by warranty and repaired without charge. Following this break in period, the failure rate is minimized and dominated by circumstantial failure until a period where the wearout process characteristic of environmental aging begins to dominate. As pointed out by Heller[3], human existance is modeled by higher infant mortality (burn-in) followed by primarily accidental mortality during early maturity and terminating in wear out by aging as shown in Fig. 1.

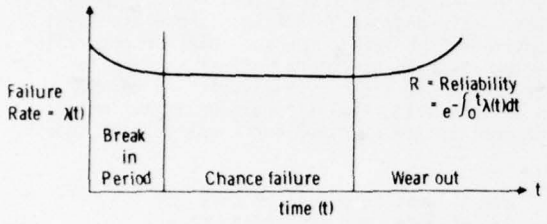

Fig. 1 Failure rate criteria for reliability.

With ceramic materials where time effects are nondominant and failure is primarily determined by stress initiated failure modes, the concept of structural reliability can be defined by applied and allowable stress distributions as shown by the curves of Fig. 2, and the following definition of reliability R as given in the following relation:

$$R = \int_{-\infty}^{\infty} \sigma(x) \int_{X}^{\infty} \sigma(X)\, dX\, dx \qquad (2)$$

where:

$$\int_{-\infty}^{\infty} \sigma(x)\, dx = 1.0$$

$$\int_{-\infty}^{\infty} \sigma(X)\, dX = 1.0$$

describe the areas beneath the stress distribution curves of Fig. 2. If the distribution of applied stresses (x) is less than the distribution of allowable stresses (X), the value R = 1.0, the greater the interpenetrations of these two distributions as shown by detail A of Fig. 2, the lower the structural reliability R.

In metal structures which exhibit ductility and slow crack growth under fatigue loading, a fracture mechanics approach to failure prediction is employed in the design of fracture resistant structures. The procedures to insure reliability outlined by Tiffany[5] and graphed in Fig. 3 include defect characterization (left view) combined with experimental studies of crack growth rates (right view) and the determination of critical crack size where rapid fracture occurs.

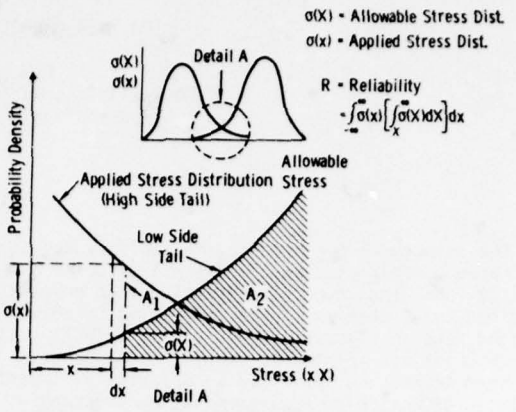

Fig. 2 Applied and allowable stress distribution analysis of reliability.

This design strategy for structure reliability assumes that pre-existing defects are either inherent in the material or produced during fabrication. Flaw detection by nondestructive inspection (NDI) becomes of primary importance in eliminating detectable flaws. Sacrificial proof testing may be applied to eliminate all flaws above a given size. The result of both NDI with rejection at flaw size B or proof testing with sacrificial failure at flaw size A is to establish the determined safe crack growth curves in the right view of Fig. 3.

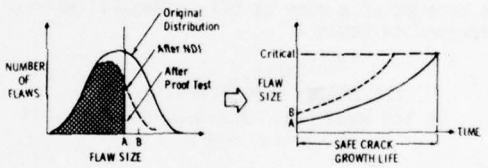

Fig. 3 Fracture mechanics criteria for structure reliability.

An intrinsic problem in designing large structures involves the extrapolation of strength and reliability data obtained from small coupon specimens to values appropriate to the large structure. In practice this problem is further complicated by the fact that manufacturing defects in the large structure may differ from those small coupon specimens manufactured separately. Materials which are not particularly sensitive to flaws, such as metals exhibit far less scatter in strength than brittle materials which are flaw sensitive. At the micro-mechanical response level the scatter in strength is due to the distribution of flaws. As discussed by Jerina and Halpin[6], the extreme value (or Weibull[7]) statistical distribution function has now been widely applied in materials science and engineering.

The Weibull distribution function defines reliability R by the following relation[6-8]:

$$R = 1-F = \exp\left[-V_i K_i N_i \left(\frac{\sigma}{\beta}\right)^m\right] \qquad (3)$$

where F is failure probability, V_i, K_i, N_i are respectively related to size, shape, and numeric complexity effects upon the mean strength β at reliability level $R = 1/e \approx 0.368$. The Weibull distribution shape factor m is determined from analysis of experimental data where the measured strengths σ are arranged serially, $j = 1,2,3.....N$ in increasing order of σ and the reliability is defined as follows:(7)

$$R = 1-F = \frac{j-0.50}{N} \qquad (4)$$

By taking logarithms of Eq.(3) we obtain the following linear relation:

$$\ln(-\ln R) = m(\ln\sigma - \ln\beta) + \ln V_i K_i N_i$$

where the ordinate becomes $\ln(-\ln R)$, the slope is m and the intercept at $\ln(-\ln R) = 0$ is a reference mean strength β_0 for the reference condition $V_i K_i V_i = V_o K_o V_o = 1.0$.

The several implications inherent in the Weibull criteria for structural reliability are graphically summarized in Fig. 4 and discussed in greater detail by Jerina and Halpin.(6) The left views of Fig. 4 trace the progressive effects of increasing size, shape with a hole stress concentration, and numeric complexity by N holes. In the upper right of Fig. 4, the predicted lowering of mean strength from β_0 for the reference coupon specimen to β_1, β_2 and β_3 is defined by the following relation:(6)

$$\frac{\beta_j}{\beta_i} = \left[\frac{V_i K_i N_i}{V_j K_j N_j}\right]^{1/m} \qquad (5)$$

which assumes that the Weibull slope m remains constant with varied V, K, and N. Both Eq.(5) and the lower right view of Fig. 4 point out the fundamental importance of the Weibull slope m in structural design. As shown in the lower right curves of Fig. 4, if the the Weibull slope factor m displays a high value m = 30, the increase in size or number complexity, such as $V_j/V_o = 100$ or $N_j/N_o = 100$, only slightly lowers the mean strength with $\beta_j/\beta_o = 0.86$. However, where the Weibull shape factor m is lowered to represent typical structural materials such as m = 4 for aluminum, the prediction is that with $V_j/V_o = 100$ or $N_j/N_o = 100$, a major lowering of mean strength with $\beta_j/\beta_o = 0.32$ results. Thus, where m represents a material property relating to the distribution of microflaws, the translation of this material property to large scale structural reliability R is well delineated in Weibull definitions.

This section has provided a brief review of statistical definitions of structural reliability which form the basis of current design practice in composite structures. The Weibull distribution provides an entry point for translating microscopic material responses, as defined by m and β_0 into predictions of large scale structural reliability.

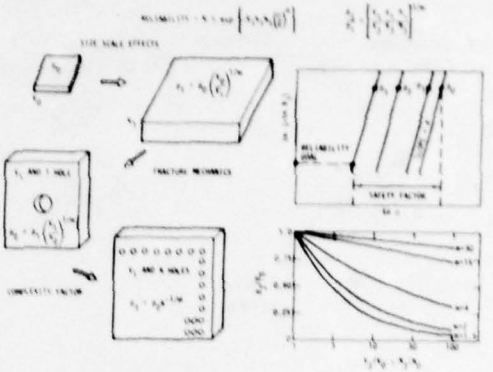

Fig. 4 Weibull criteria for structure reliability.

Dual Path Concept

The structural performance, reliability, and durability of polymer composites can now be correlated with three generic classes of defects. The first class of generic defects (size 1-200Å) that control critical design properties such as glass transition T_g, moisture absorption, and dimensional changes can be controlled by chemical analysis and selection of raw materials prior to manufacture.(9-12) A second generic class of manufacturing defects (size greater than 10μm) include inclusions, voids, and debonds which results from non-optimum process control in fabrication and manufacture. This second class of defects are detected by ultrasonics, optical scanning and other methods sensitive to interfacial imperfections as is well detailed by other papers at this conference.

The interaction of these two classes of intrinsic defects with environmental and mechanical stresses produces a third class of macroscopic fatigue defects such as networks of interconnected microcracks as well as singular macroscopic crack growth. These fatigue defects can be detected by ultrasonic emission, moisture diffusion analysis, and optical inspection.

Recognition that intrinsic chemical and manufacturing defects may, in large part, determine polymer composite reliability represents an important extension of analytical modeling in which physical chemistry parameters appear as primary control variables. A preferred dual path approach for correlating environmental (plus mechanical) aging with macroscopic strength is shown in Fig. 5. In addition to the statistical correlations for structure reliability discussed in the preceeding section, the dual path approach adds detailed spectroscopic analysis to define the molecular process of aging and strength change. As shown in Fig. 5, the preposition of process scale-up characterization to define and control manufacturing defects is inherent in the dual path approach. Utilization of the dual path approach usefully combines both deterministic and statistical models for polymer composite reliability. A highly evolved flow chart for polymer composite reliability analysis is shown by the block diagram of Fig. 6.(12)

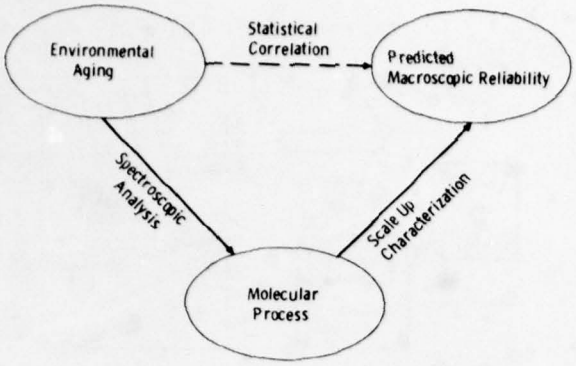

Fig. 5 Preferred dual path for correlating environmental aging with macroscopic strength.

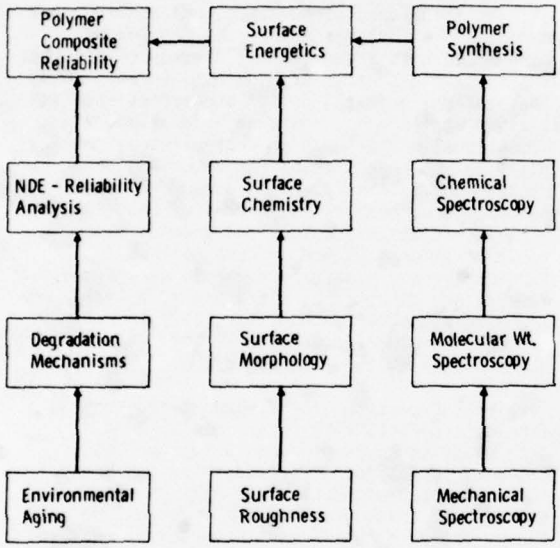

Fig. 6 Technical approach to polymer composite reliability.

The left column of Fig. 6 deals with studies of composite system response and develops the important statistical correlation between environmental aging and composite reliability. The central column of Fig. 6 defines special studies of interfacial bonding, which range from surface chemistry to macroscopic characterization of surface roughness. These studies are dominantly related to isolation and control of manufacturing defects introduced by improper surface treatment and process conditions for bonding and curing.

The right column of Fig. 6 defines essential studies in polymer properties which include chemical analysis, polymer synthesis, molecular weight characterization and mechanical spectrum analysis. In polymer studies, these four areas of study are presently closely interconnected. Failure of polymer cohesive response in composite applications is readily identified in molecular terms and corrective action involving polymer chemistry and chemical analysis becomes available to composite reliability studies.

The present problem with regard to full implementation of the technical approach shown in Fig. 6 is the failure of material scientists to convert their detailed physical data into parameters directly useful to the design engineer for large scale structures. This problem has been recognized and a semiformal approach for resolution has been proposed by Kelley and Williams[15] in the form of a morphological scheme termed the "Interaction Matrix". The interaction matrix, as shown in Table 2, lists mechanical property requirements as defined by the design engineer as column headings. A list of molecular properties as defined by the material scientist are listed in descending order as row headings. Within the box, defined by a design requirement and a molecular property, the degree of correlation is assigned on a numeric scale such as shown in Table 2. By summing these numbers across both the rows and columns as shown by the Σ values in Table 2, the position of both rows and columns can be rearranged to maximize the strong correlations within a matrix as shown in the upper left section of Fig. 2. This summing and rearrangement of the interaction matrix tends to focus communications and research toward the most fruitful sector of defined engineering need and molecular response.

Table 2. Interaction matrix between molecular property and mechanical requirement; 3=Strong interaction, 2=Medium, 1=Negligible, 0=Unknown, Σ=Sum of Interactions

	MECHANICAL REQUIREMENT					
Molecular Property	T_g	E_e	τ_o	n	E_g	Σ
Volume Fraction Plasticizer	3	3	3	1	1	11
Volume Fraction Filler	2	3	2	3	1	11
Degree of Crystallinity	1	3	3	3	1	11
Molecular Weight	3	3	1	1	1	9
Crosslink Density	1	3	1	2	1	8
Chain Stiffness	3	1	0	2	1	7
Monomeric Friction Coefficient	3	1	3	0	0	7
Heterogeniety Index	2	1	2	1	1	7
Entanglement Molecular Wt	1	3	1	1	1	7
Solubility Parameter	3	1	0	0	2	6
Σ	22	22	16	14	10	

* T_g = glass temp; Modules (E) vs time (t) = $E(t) = E_e + [E_g - E_e][1 + t/\tau_o)]^{-n}$ where E_e = elastomeric modulus, E_g = glass modulus, τ_o = glass to rubber relaxation time, n = exponent.

The development of quantitative and preferably deterministic relations between engineering design parameters and molecular response variables is, of course, the desired end point in the dual path approach. An illustrative reliability and durability model for the polymer subphase in composite response is detailed in the following set of six relations:

GLASS TRANSITION RESPONSE

$$T_{g\infty} = \frac{2}{R_o}\left[\frac{\Sigma U_c}{\Sigma h}\right] + C(t) \qquad (6)$$

$$T_g = T_{g\infty} + \left(\frac{\partial T_g}{\partial \sigma}\right)\sigma + \left(\frac{\partial T_g}{\partial C}\right) C_{H_2O} + \left(\frac{\partial T_g}{\partial M^{-1}}\right) M^{-1} \qquad (7)$$

RHEOLOGICAL RESPONSE

$$\log\,(1/a_T) = \frac{17.4(T-T_g)}{51.6 + T - T_g} \qquad (8)$$

$$M_i = \frac{M_o - M_\infty}{\left[1 + \frac{t}{a_t \tau_1}\right]^n} + M_\infty \exp -\left(\frac{t}{\tau_m a_T}\right) \qquad (9)$$

RELIABILITY-FAILURE RESPONSE

$$R_W = \exp -\left(\frac{\sigma}{\sigma_b}\right)^{m(\sigma)} \exp -\left(\frac{\epsilon}{\epsilon_b}\right)^{m(\epsilon)} \exp -\left(\frac{t}{t_b a_T}\right)^{m(t)} \qquad (10)$$

$$R_i = R_\infty + (1-R_\infty)\, R_W \qquad (11)$$

The details of symbols and parameter definitions for this model are summarized in Table 3.

Table 3. Nomenclature for polymer reliability relations

Symbol	Meaning
$T_{g\infty}$	Reference glass transition defined by monomer composition.
ΣU_c	Summation of molecular molar cohesion.
Σh	Summation of molecular degrees of freedom.
$C(t)$	Time scale correction factor $C(t) \simeq 250^oC$.
T_g	Nominal T_g as affected by mechanical (tensile) stress σ, moisture concentration C_{H_2O}, and U.V. radiation effects on polymer reciprocal molecular weight (M^{-1}, number average).
a_T	Time shift factor for rheological response.
T	Test temperature
M_i	Time dependent modulus.
M_b	Glass (solid) state modulus
M_∞	Rubbery state modulus
t, n	Test time and exponent.
τ_1	Relaxation time for glass to rubber transition.
τ_2	Terminal time for rubber to flow transition.
R_i	Reliability (= survival probability).
R_∞	Residual reliability at infinite time.
τ_o	Relaxation time for Weibull failure process.
σ_o	Stress (tensile) for Weibull failure process.
ϵ_o	Strain (tensile) for Weibull failure process.
$m(t)$, $m(\sigma)$, $m(\epsilon)$	Weibull distribution shape factors for time (t), stress (σ), and strain (ϵ) dominated failure.

This model starts by introducing chemical structure and measurement time contributions to define a reference $T_{g\infty}$ in Eq.(6). This relation was empirically developed by Hayes[17] and correlated with glass transition theory by Kaelble[18]. Monomer sequence distribution as discussed by Johnston[19] and semicrystallinity as discussed by Boyer[20] complicate use of Eq.(6) for some polymers. The important concept embodied in the relation is that functional group properties of the monomeric unit determine an important thermal transition relating to environmental durability.

In Eq.(7) the effects of mechanical stress, bulk moisture concentration C_{H_2O} and U.V. radiation effects on reciprocal polymer molecular weight M^{-1} are identified. Common values for the partial derivatives:

$$\left(\frac{\partial T_g}{\partial \sigma}\right) \simeq -0.1\ \frac{^oC\ cm^2}{Kg} \quad \text{(for polystyrene, ref.18)}$$

$$\left(\frac{\partial T_g}{\partial C_{H_2O}}\right) \simeq -6.0^oC/wt\%H_2O \quad \text{(for epoxy, ref.21)}$$

$$\left(\frac{\partial T_g}{\partial M^{-1}}\right) \simeq -0.06^oC/M^{-1} \quad \text{(general, ref.18,22)}.$$

The fundamental issue which is directly expressed by Eq.(7) is the direct description of local or macrosopic changes in nominal values of glass temperature T_g due to separate or combined effects of mechanical stress, moisture and U.V. exposure effects on M^{-1}. In general, one must assume effective local concentration effects in σ, C_{H_2O}, and M^{-1}. As examples, stress concentrations at crack tips, or high surface moisture concentrations will locally reduce T_g.

The familiar WLF equation[23] is presented as Eq.(8) is a nearly universal relation for calculating the time shift factor a_T at test temperature T which characterizes all rheology dominated response of the polymer interfacial subphase. Since T_g in this relation is previously defined by Eq.(7), all the comments presented above for spatially localized T_g states are, of course, transformed by Eq.(8) into spatially localized time response states in terms of a_T within both the bulk polymer and at the interface. It is particularly evident that a polymer composite at temperatures near its reference $T_{g\infty}$ will display a potentially wide distribution of a_T values with local variations in T_g.

The values of a_T generated from Eq.(8) appear as time t shift factors in both Eq.(9), which defines subphase modulus M_i and Eq.(10), which defines the Weibull type reliability R_i. A modified power law relation suggested by Kelley and Williams[15] for approximate fitting of viscoelastic data in polymeric materials over extremes of time response if presented in Eq.(8). An example calculation of M_i response over 30 decades of reduced time (t/a_T) for a typical amorphous polymer such as polystyrene is shown in the solid curve of Fig. 7.

In Eq.(10), which defines a reduced time function for reliability (equivalent to survival probability), the a_T parameter appears as a time reduction factor. The complexity in time scales of failure for uniform failure conditions is presented in physical terms by the Halpin and Polley[24] model for fracture. The Halpin-Polley model describes a statistical distribution of flaws as present in all polymeric materials and mathematically connects these defects to the well known Weibull frequency distribution[6-8] which assumes that failure is initiated at the weakest link. Gardon[25] has

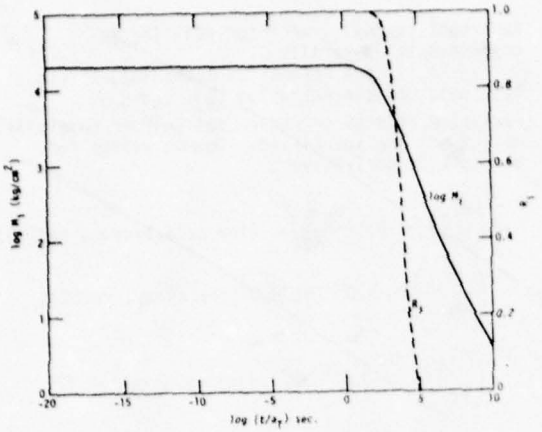

Fig. 7 Calculated function of M_j and R_j for $M_\infty = 20{,}000$ kg/cm^2, $M_\infty = 2.0$ kg/cm^2, $\tau = 100$s, $\tau_m = \infty$, $R_\infty = 0$, $\tau_0 = 10^4$s, $m = 1.0$.

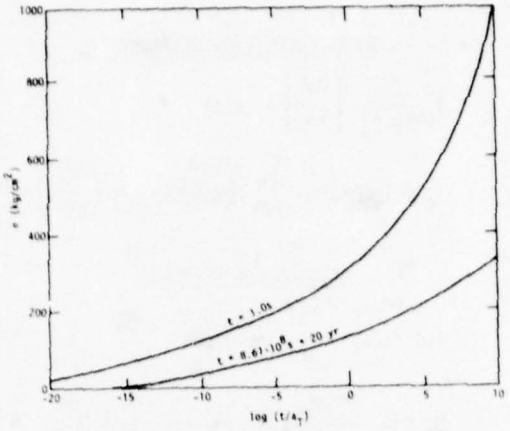

Fig. 8 Illustrative relations between tensile stress σ and time shift factor $\log (t/a_T)$.

shown that time fluctuations in steady state peel fracture appear to fit a Gaussian frequency distribution which is essentially identical to the distribution defined by Eq.(3) when the Weibull shape factor exponent takes the value $m = 3.67$. The dashed curve of Fig. 7 presents a plot of Eq.(10) with $m(t) = 1.0$ which is relatively low for typical polymer failure.

A simple calculation is introduced to demonstrate the fundamental propositions in terms of stress-strain behavior and failure response of a polymeric subphase. First, assume the M_j and R_j properties of this subphase are described by the curves in Fig. 7. Also assume the subphase is tested in tension somewhat below the subphase glass temperature with:

$$T - T_g = -30^oC$$

$$\left(\frac{\partial T_g}{\partial \sigma}\right) = -0.10^oC \ \frac{cm^2}{Kg}$$

and with

$$C_{H_2O} = M^{-1} = 0$$

By use of Eq.(7) and Eq.(8) the curves shown in Fig. 8 can be calculated to correlate stress magnitude σ with $\log t/a_T$. The curves in Fig. 8 illustrate the WLF prediction of stress effects on the time shift factor and show that tensile stresses readily supported by the cohesive or interfacial strength of a glassy polymer can change rheological response time of the material over many decades and, in fact, produce rubbery state response when $\sigma \geq 300$ Kg/cm^2 for the example shown. For a known stress-strain response for the material, such as defined by simple time dependent Hookian response:

$$\sigma(t) = \epsilon \cdot M_j(t)$$

It follows that stress-strain curves in tensile creep can be calculated. This calculation applies for the case of instant loading to constant stress σ, and maintaining this stress constant to a designated constant time t, which we set at $t = 1.0$ sec and $t = 8.61 \cdot 10^8$sec $= 20$yr. Isochronal creep stress vs strain curves can be constructed from the curves of Fig. 7 and Fig. 8.

The 20 year life of the polymer composite reflected by tensile creep curves for $t = 20$ yr $= 6.31 \cdot 10^8$ sec shown in lower Fig. 9 can be readily generated in the same fashion as the $t = 1$sec response curves shown in upper Fig. 9. In summary, the intent of this section and the above illustrative examples is to show that the right vertical arrows which connect chemical synthesis to mechanical spectroscopy in Fig. 6 are detailed by structure-property relations. In Eq.(8) the time shift factor a_T can be reset by changes in temperature T, stress σ, moisture concentration C_{H_2O}, and reciprocal polymer molecular weight M^{-1} to accelerate natural degradation processes which determine long term durability and reliability.

The data summary of Table 4 reports experimentally determined Weibull strength distributions of structural adhesives, fibrous reinforced composites, and adhesive bonded metal joints under different conditions of environmental aging. These strength distributions were obtained in conjunction with physical chemical characterizations which clarify the shift in the Weibull values of mean strength σ_c and distribution shape factor $m(\sigma)$ reported in Table 4 will, perhaps, provide practical insights into the proposed dual path concept sketched in Fig. 5.

Multiphase Structural Adhesives

Epoxy structural adhesives, toughened by a rubbery subphase, are now extensively used in aircraft structures[28]. Current adhesively bonded primary structures such as Air Force PABST (primary adhesive bonded structures technology) include carboxy terminated butadiene acrylonitrile (CTBN) rubber as a chemically combined constituent of the epoxy structural adhesive[29]. In CTBN modified epoxy adhesives, the rubbery subphase precipitates during curing of the adhesively bonded joint. This produces the multiphase morphology and microstructure that leads to a

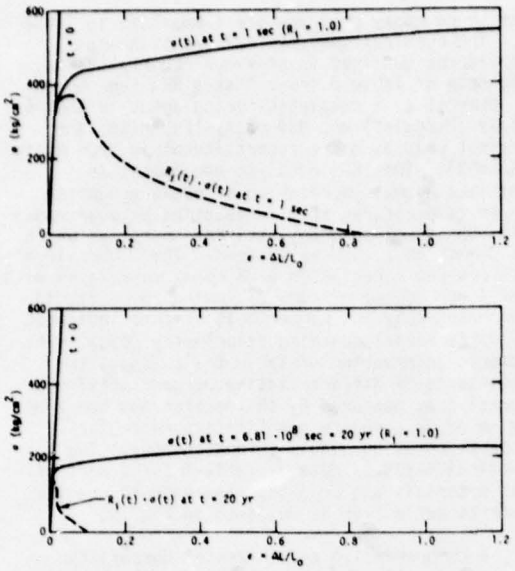

Fig. 9 Calculated tensile creep stress $\sigma(t)$ vs. strain $\epsilon(t)$ (solid curves) and reliability $R_1(t)$ reduced stress $R_1(t)$ $\sigma_1(t)$ vs. strain $\epsilon(t)$ (dashed curves) at t = 1 sec (upper view) and t = 20 yr (lower view).

Table 4. Weibull strength distributions

Composite Polymer		Test	$R = \exp -(\sigma_b/\sigma_0)^{m(\sigma)}$	
EPON 828/CTBN % CTBN	T(°C)	Tensile	σ_0 (Kg/cm²)	$m(\sigma)$
0	-150	N=15	812	7.64
17	-150	14	679	9.78
50	-150	14	1274	15.5
0	100	15	95.6	6.82
17	100	15	42.1	8.33
50	100	15	26.6	5.44
Uniaxial Graphite/Epoxy		**Interlaminar**		
Herc. AS/3501-5		Shear	σ_0(Kg/cm²)	$m(\sigma)$
23°C air + 232°C spike		N=18	1054	7.60
100°C water + 232°C spike		16	601	2.20
Metal-Adhesive Joint		**Single Lap**		
Al/2024T3-HT424 Epoxy SET(hr)	BET(hr)	Shear	σ_0(Kg/cm²)	$m(\sigma)$
0	0	N=12	232	14.5
0	165,449	12	184	15.4
0	808,1023	12	165	10.0
21	0	12	208	15.0
20	669,983	12	160	18.1
Ti-6Al-4V-HT424 Epoxy SET(hr)	BET(hr)		σ_0(Kg/cm²)	$m(\sigma)$
0	0	N=12	270	7.65
0	(670,1016)	12	182	6.22
21	0	12	272	7.65
21	(591,997)	12	202	6.35

SET = surface exposure time, BET = bond exposure time at 54°C and 195% relative humidity.

strongly enhanced fracture toughness[30-34], where (G_{IC} = 2.0 to 4.0 kJ/m² with 15% CTBN modifier, compared to 0.1 to 0.2 kJ/m² for unmodified epoxy resins[35].

Several detailed studies of the fracture properties of CTBN modified epoxy adhesives now show that their high fracture toughness is related to cavitation and crazing (stress-whitening) due to dilational strains in the triaxial stress field of the crack tip[34,35]. Since extensive microstructure degradation precedes final failure in CTBN toughened epoxy, an important question is whether the statistical distribution of cohesive strengths is adversely modified.

A special study was undertaken to clarify the multiphase morphology effects upon the statistical distributions of cohesive strengths using the materials summarized in Table 5. Microtensile test specimens (ASTM Method 1708-66) were die cut from the cured epoxy films while they were heated to rubbery state response at 120°C. Tensile tests were conducted at a strain rate $\dot{\epsilon}$ of 0.09 min^{-1}. Single specimen tests, at temperatures from -200°C to 200°C as shown in Fig. 10a, were conducted to determine the temperature dependence of nominal tensile strength σ_b. At -150°C and 100°C, which represent lower and upper service temperatures in structural applications, larger groups of specimens were tested to determine the statistical distribution of σ_b. Six groups of specimens, as summarized in upper Table 3, describe the bounds of strength variation indicated in Fig. 10a by the extreme high and low tensile strengths indicated by the bracketed error bars at -150°C and 100°C for each strength curve.

Table 5. Co-reactants for three-dimensional epoxy-nitrile rubber block copolymers.

1. Epoxy: DGEBA (Epon 828, Shell Chemical Company), 100 pbw (parts by weight), $M_n \approx 380$ gm/mole

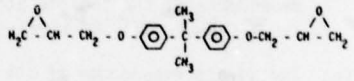

2. Catalyst: Piperidine - 5 pbw

3. Carboxy terminated nitrile rubber (HYCAR CTBN, B.F. Goodrich Chemical Company) - 0, 17, 29, 39, 50% by weight based on 100 pbw Epoxy + 5 pbw piperidine

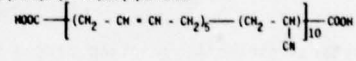

$M_n \approx 3300$ - 3500 gm/mole

4. Mix items (1), (2), (3), above, degas, and cure for 16 hours at 120°C under dry N_2.

In Fig. 10b, the strength data points are arranged serially j = 1, 2,...N in increasing order of σ_b, and the survival probability (≡ reliability) is defined by Eq.(4) where N is the number of observations and F is the failure probability. Six groups of data show the cumulative distribution of survival probability. The ratio of extreme strength values (Table 4) for pure epoxy is not dramatically modified by either extremes of test temperature or composition. The study thus supports the view that the statistical distribution of cohesive strengths is not strongly or adversely modified by addition of CTBN. Inspection of Fig. 10 provides the following conclusions in relation to fracture integrity:

(1) The effect of temperature change, from -150°C to 100°C, dominantly influences the cohesive strengths of CTBN toughened epoxy.
(2) Chemical composition changes, from 0-50% by weight CTBN epoxy modifier, is the second most dominant strength determinant.

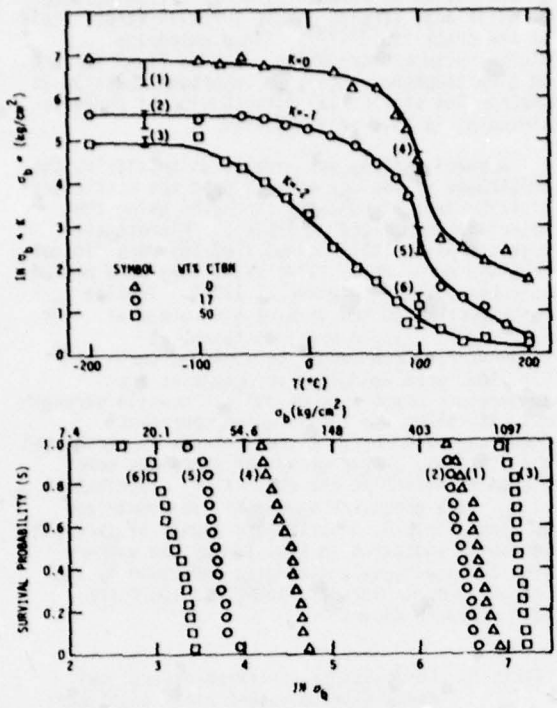

Fig. 10(a) The temperature and compositional dependence of the tensile strength for a rubber modified epoxy.

Fig. 10(b) The stress dependence of the survival probability for rubber modified epoxy at -150 and 100°C.

(3) Statistical strength variation, for a survival probability range from 0.05 to 0.95, is a minor strength determinant.

It thus appears that the 15-40 fold enhancement of fracture toughness by inclusion of approximately 15% CTBN in structural epoxy resins displays its principal adverse effect in shifting the entire distribution of high temperature tensile strengths to lower values, without change in shape. This adverse effect on high temperature strength is physically related to the lower crosslinking density for the three-dimensional network formed between CTBN and epoxy coreactants.

Fibrous Composite Reliability

Hydrothermal exposure (combined high moisture and temperature) of graphite reinforced epoxy matrix composites can produce irreversible reduction in shear strength and modifies the Weibull distribution of survival probabilities as shown in studies by Kaelble and Dynes[36]. Comparative chemical analysis of two catalytically cured graphite-epoxy composites and an aromatic amine cured epoxy matrix composite shows that curing mechanisms and epoxy network structure influence both thermal response and environmental durability. The results of chemical analysis of the three epoxy prepregs are summarized in Table 6. The chemical analysis follows standard procedures outlined in previous reports[10,12]. The data of Table 6 shows that a BF_3 type boron is present as a catalytic curing agent in 3501-5 epoxy (Hercules) and 934 epoxy (Fiberite) and present only as a trace constituent in 5208 epoxy (NARMCO). This BF_3 catalyst decomposes to initiate homopolymerization of epoxy groups at lower temperatures than co-reaction between epoxy and DDS (diaminodiphenyl-sulfone) curative which is common to all three systems. The higher level of free DDS curative in 5208 epoxy correlates with the lower degree of cure as indicated by liquid chromatography and higher heat of cure indicated by differential scanning calorimetry (DSC). The numeric information of Table 6 also shows the importance of differentiating between total DDS curative as measured by IR spectroscopy and free amine as measured by quantitative molecular separation using liquid chromatography. The chemical analysis data of Table 5 forms part of the materials and processes approach to chemical defects definition as outlined in Fig. 6.

A comprehensive environmental durability characterization has been carried out on the three composites described in Table 6. Some results of this study serve to highlight the direct importance of chemical analysis in composite reliability and durability predictions.

Table 6. Chemical characterization of grapnite-epoxy prepreg materials.

	This Study		Reference System
1. Epoxy Matrix	Hercules 3501-5	Fiberite 934	NARMCO 5208
2. Graphite Fiber	Hercules Type AS	U. Carbide T300	U. Carbide T300
3. % Total DDS Curative by IR Spectroscopy	29.2	27.8	22.1
4. % Free DDS Curative by Liquid Chromatography	18.1	14.5	17.8
5. Epoxide Equivalent	205	227	173
6. Wt.% BF_3 Type Boron	0.047	0.022	.0005
7. Relative Degree of Cure by Liquid Chromatography	22	27	6.9
8. Heat of Polymerization by DSC (cal/g polymer)	107	107	140

In the DSC thermograms of Fig. 11, the rate of chemical curing correlates with the amplitude of dH/dt, the heat release rate. The low temperature initiation of curing in 934 and 3501-5 epoxy correlates with the detected presence of the BF_3 catalyst as compared to uncatalyzed 5208 which requires much higher temperatures to complete the curing process.

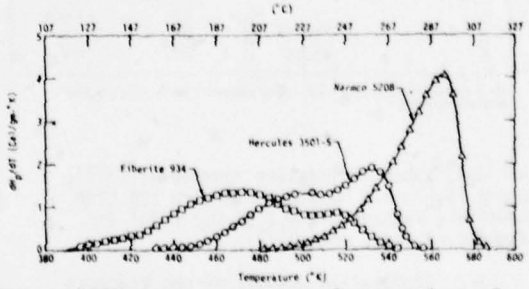

Fig. 11 DSC thermograms for curing reactions of commercial epoxy matrix materials extracted from prepreg. (DSC scan rate ϕ = 20°C/min)

The use of catalytically assisted curing clearly correlates with easier processability as shown in the lower temperature cure cycles shown in Fig. 11. The thermal scans of dynamic damping response in the fully cured uniaxial composites of these materials, as shown in Fig. 12, reveal that catalytic curing at lower temperatures produces a crosslinked network with substantially lower T_g. As shown in Fig. 12, the 934 epoxy displays onset of T_g response by an initial increase in tanδ at T = 200°C while cured 3501-5 epoxy shows initial rise in tanδ at 225°C and 5208 epoxy at T = 250°C for dry fully cured composite.

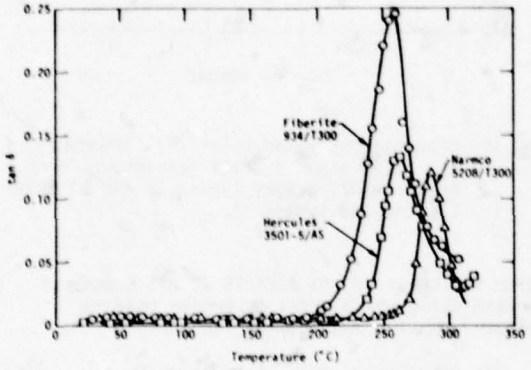

Fig. 12 Rheovibion thermal scans for flexural damping in cured uniaxial reinforced graphite-epoxy composite in the dry unaged condition.

The effects of prior moisture exposure to full saturation is shown in the damping curves of Fig. 13 to lower the T_g related initial increase in tanδ response to about T = 140°C for 934 epoxy and T = 160°C for 3501-5, while the 5208 resin maintains low tanδ response to above 200°C.

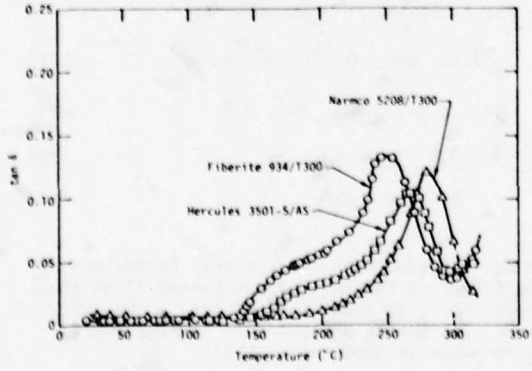

Fig. 13 Rheovibion thermal scans of flexural damping in cured uniaxial reinforced graphite-epoxy composite in the wet-aged condition.

The prediction offered by the dynamic damping response as measured by Rheovibron is that cured 3501-5 resin will display glass state response at 232°C in the dry state, and low strength rubbery response due to water plastization in the moisture saturated state at 232°C. The curves of Fig. 14 show the clearly separated interlaminar shear strength distributions for uniaxial 3501-5 epoxy matrix composite where dry and moisture exposed specimens were subjected to an equivalent 232°C thermal spike prior to strength measurement at 23°C. As predicted, the interaction of high moisture and high temperature produced internal damage which lowered both mean shear strength λ_o and also substantially lowered the Weibull distribution shape factor m.

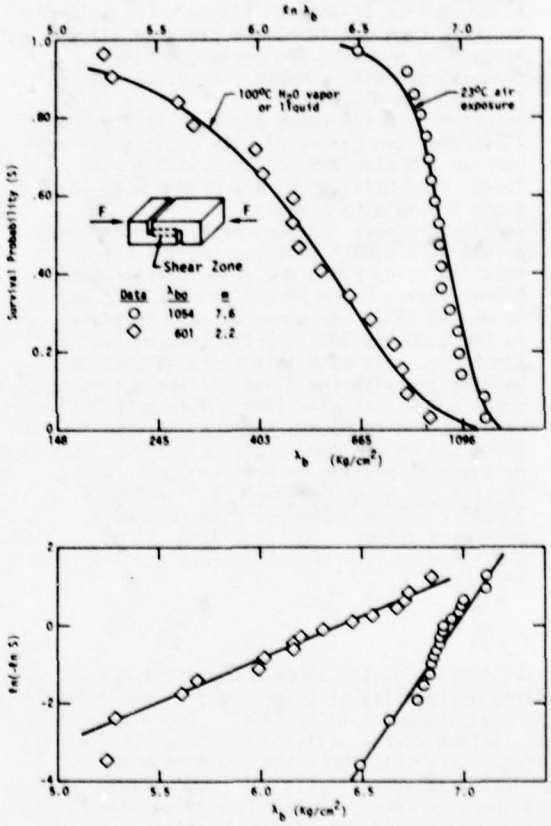

Fig. 14 Cumulative distribution function of survival probability.

Metal Joint Reliability

All metals, except gold, are chemically reactive with oxygen and moisture at room temperature and tend to form oxide or hydrated oxide surface layers[37]. In addition to oxidative chemical reaction, these high energy surface films are subject to further physical adsorption by water vapor and volatile organic contaminants. In structural metal to metal joints, the reliability of the bond may be directly related to the chemical stability of the

interfacial bond. Weibull statistical analysis has recently been applied to investigate the effects of both surface exposure time (SET) and bond exposure time (BET) on the distributions of single layer shear bonds of aluminum alloys[38]. Smith and Kaelble[39] have recently conducted a detailed study of combined SET and BET aging in normal (50% R.H., 23°C), and high moisture (95% R.H., 54°C). The experimental methods of the study by Smith and Kaelble are outlined in Table 7 with full details contained in the published report.

TABLE 7
Metal Joint Reliability Studies

1. Metal Adherends: Unclad 2024-T3 aluminum alloy surface treated by standard FPL sulfuric chromate etch and T8-6Al-4V titanium alloy treated by standard phosphate fluoride cleaning process. Coupon size 0.063" thick, 1" wide, and 4" long.
2. Adhesive: HT 424 epoxy-phenolic film adhesive (from American Cyanamid) with glass fiber carrier and standard weight 0.0135 ± .005 lb/sq. ft. Unfilled HT 424 primer with parts A and B used with adhesive.
3. Bonding Process: Treated metal coupons spray primed with 0.001" thickness HT 424 primer solution using clean dry argon carrier gas. Primer layers dried 30 min ambient 23°C and 60 min at 66°C. An adhesive film is placed in the 1.000"x0.500" overlap between two metal adherends. Six such joints are aligned in a bonding jig with the glass carrier acting to provide constant glue line thickness 0.008". Cure cycle with 60 min temperature rise to 171°C and 60 min cure cycle at 171° followed by cooling to room temperature.
4. Tensile Lap Shear Testing: 1.5" x 1.0" x 0.063" aluminum alignment shims bonded to eliminate offset. Tests at 23°C using 0.01"/min Instron crosshead rate and 4.5" jaw separation.

In this study the surface chemistry and related wettability of both adherends and adhesive were analyzed prior to bonding. The results of this surface energy analysis can be plotted on a surface energy map where the ordinant α and abscissa β as shown in Fig. 15 respectively refer to dispersion (monopolar) and polar components of surface energy and interfacial bonding mechanisms. The theory of interfacial adhesion experimentally verified in this analysis defines the thermodynamic work of adhesion W_a by the following relation:

$$W_a = W_{13} = 2(\alpha_1\ \alpha_3 + \beta_1\ \beta_3) \qquad (12)$$

where α_1, β_1 define the dispersion and polar surface properties of adhesive and α_3, β_3, those of the metal adherend.

As shown in Fig. 15, and further documented in detailed kinetic studies by Kaelble and Dynes[40], the α_3 and β_3 properties of aluminum alloy change dramatically with surface aging time after FPL etch. The α_1, β_1 surface properties of HT 424 adhesive are shown to lie

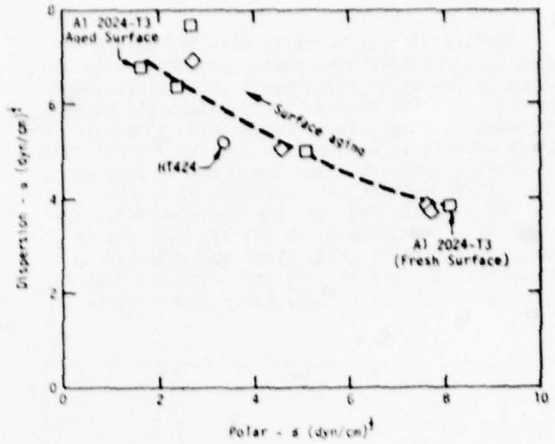

Fig. 15 Dispersion (α) and polar (β) components of the solid-vapor surface tension $\gamma_{SV} = \alpha_S + \beta_S$ for HT424 primer (phase 1) and Al 2024-T3 adherend (phase 3).

below the curve for Al 2024-T3 at all stages of surface aging which predicts proper bonding between adhesive and adherend in air.

The interfacial work of adhesion W_a as defined by Eq.(12) will decrease with surface aging time (SET) as shown by the upper curve of Fig. 16. As shown in the lower curves of Fig. 16, the lap shear bond strength varies with SET in a fashion that correlates closely with the predictions from work of adhesion calculations. A simple but now widely demonstrated correlation between surface energetics and fracture mechanics is available in the following relations for critical stress σ_c for Griffith type crack initiation under normal stress loading[41,42]:

$$\sigma_c = \left(\frac{2E}{C}\right)^{\frac{1}{2}} (R^2 - R_o^2)^{\frac{1}{2}} > 0 \qquad (13)$$

where E, and C are a characteristic modulus and crack length which are assumed constant and the surface energy parameters R and R_o are defined by the following relations[41,42]:

$$R_o = 0.25\ (\alpha_1 - \alpha_3)^2 + (\beta_1 - \beta_3)^2 \qquad (14)$$

$$R^2 = (\alpha_2 - H)^2 + (\beta_2 - K)^2 \qquad (15)$$

$$H = 0.5\ (\alpha_1 + \alpha_3) \qquad (16)$$

$$K = 0.5\ (\beta_1 + \beta_3) \qquad (17)$$

In Eq.(15) two new surface energy parameters α_2 and β_2 define the environment (phase 2) at the crack tip. The model for critical stress defined by Eq.(13) can be presented on surface energy coordinates as shown in Fig. 17.

As the adhesive joint changes from dry air immersion with $\alpha_2 = \beta_2 = 0$ to equilibrium response with water immersion with $\alpha_2 = 4.67(\text{dyn/cm})^{\frac{1}{2}}$ and $\beta_2 = 7.14(\text{dyn/cm})^{\frac{1}{2}}$, the

predicted decrease in critical stress σ_c of the HT 424 to Al 2024-T3 interface is:

$$\frac{\sigma_c\ (H_2O)}{\sigma_c\ (air)} = 0.644 \qquad (18)$$

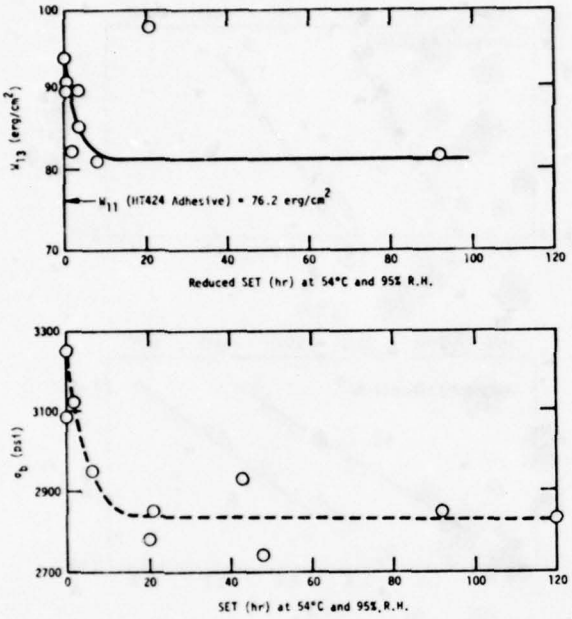

Fig. 16 Dependence of interfacial work of adhesion W_{13} (upper curve) and lap shear bond strength σ_b (lower curve) at varied SET.

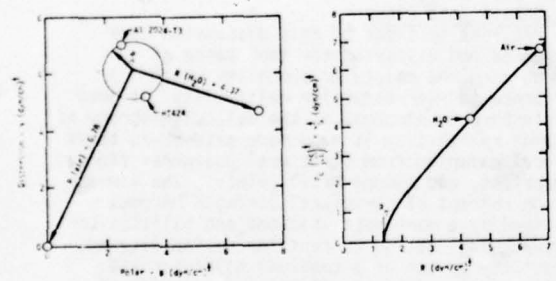

Fig. 17 Modified Griffith analysis of the effect of H_2O immersion in reducing critical failure stress σ_I for interfacial failure between HT424 and etched Al 2024-T3 ($\phi_I = 1 = \phi_c = 1.0$).

Extensive joint strength testing of this system was completed to determine the response surface of lap shear strength vs both SET and BET under high moisture (95% R.H., 54°C). These results are summarized on the response surface of Fig. 18 where each point represents the average of six tests. Comparing joint strengths for fully aged (20 hr SET, 1000 hr BET) and unaged (0 hr SET, 0 hr BET) provides (see Table 3) the following experimental ratio:

$$\frac{\sigma_b\ (\text{aged, wet})}{\sigma_b\ (\text{unaged, dry})} = \frac{2275\ \text{psi}}{3300\ \text{psi}} = 0.69 \qquad (19)$$

which is in close agreement with the prediction of Eq.(18).

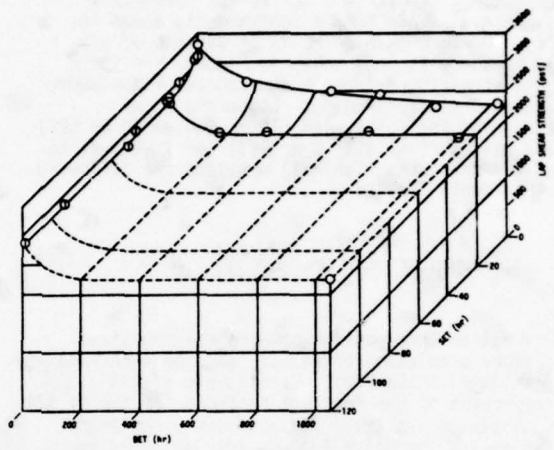

Fig. 18 SET and BET response surface for lap shear bond strength for Al 2024-T3-HT424.

An essentially parallel detailed study of surface aging showed a shift in α_3 and β_3 for phosphate-fluoride cleaned titanium alloy similar to that detailed in Fig. 15. Application of the modified Griffith analysis as shown in Fig. 19 provides the following predicted moisture degradation of bond strength at the HT 424 to Ti-6Al-4V interface:

$$\frac{\sigma_c\ (H_2O)}{\sigma_c\ (\text{dry air})} = 0.84 \qquad (20)$$

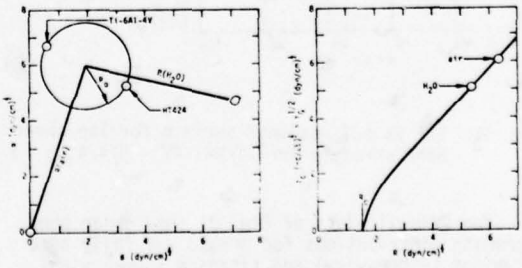

Fig. 19 Modified Griffith analysis of the effect of H_2O immersion in reducing critical failure stress σ_I for interfacial failure between HT424 and phosphate-fluoride treated Ti-6Al-4V, ($\phi_I = 1 - \phi_c = 1.0$).

An equivalent calculation for moisture degradation of the HT 424 cohesive bond produces the following prediction:

$$\frac{\sigma_c\ (H_2O)}{\sigma_c\ (\text{dry air})} = 0.63 \qquad (21)$$

Joint strength testing of the HT 424 to titanium alloy was carried out under conditions of separate and combined SET and BET in high moisture (95% R.H., 54°C). The SET vs BET response surface of shear bond strength σ_b is shown in Fig. 20 where each point is an average of six strength tests. As shown in Fig.20, the shear bond strength reaches an equilibrium value under extended moisture aging. Comparing joint strengths for fully aged (22 hr SET, 1000 hr BET) and unaged (0 hr SET, 0 hr BET) for Ti-6Al-4V to HT 424 bonds (see Table 4) provides the following experimental ratio:

$$\frac{\sigma_b\ (\text{aged, wet})}{\sigma_b\ (\text{unaged, dry})} = \frac{2873\ \text{psi}}{3840\ \text{psi}} = 0.75 \qquad (22)$$

which lies intermediate between the cohesive failure prediction of Eq.(21) and the interface prediction of Eq.(20). Microscopic visual inspection of the fracture surfaces for the HT 424 to titanium lap shear points shows predominant (above 50%) cohesive failure for lap shear bonds described in Fig. 20.

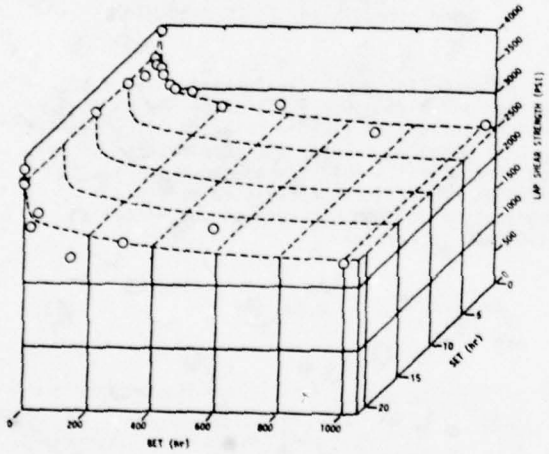

Fig. 20 SET vs BET response surface for lap shear bond strength for Ti-6Al-4V - HT424.

The Weibull plots of Fig. 21 show shear bond strength distributions for unaged and fully aged aluminum (upper view) and titanium (lower view) joints. The titanium bonds show lower Weibull m values in both unaged and aged states as evidenced in Fig. 21 and the data summary of Fig. 4. A design requirement of high reliability shear strength where R = 0.98 or ln(-lnR) = -4 is shown by Fig. 21 to predict higher performance for the aluminum alloy joints in both unaged and aged-wet states. Conversely, if mean strength with R = 0.37 and ln(-lnR) = 0 is applied as a design criteria, the curves show titanium alloy joints to display higher unaged and aged strengths.

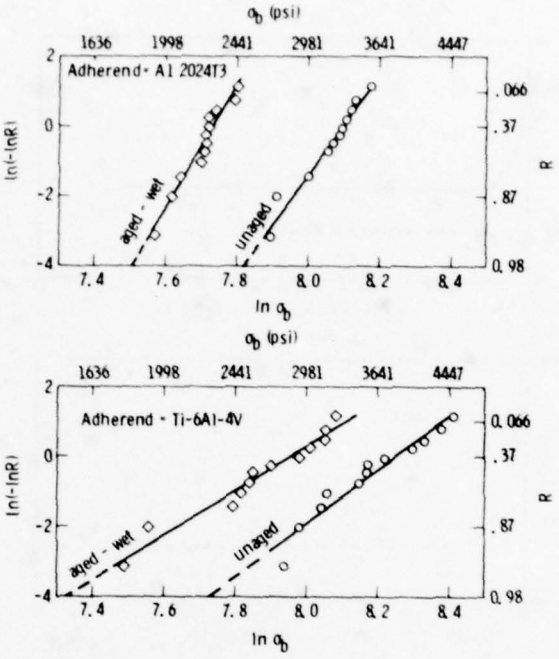

Fig. 21 Comparison of Weibull shear strength distributions for aluminum (upper view) and titanium (lower view) adherends.

Detail Test Plans

Previous sections of this discussion have presented and discussed the importance of recognizing the molecular processes which influence polymer composite reliability. A need for further development of the molecular theory of polymer reliability is also made evident in these several examples from structural polymers, fibrous composites, and bonded metal joints. The simple design concept of structural strength becomes replaced by a more sophisticated and holistic (or encompassing) design concept for reliability and durability by use of a combined molecular and mathematical modeling. If molecular theory of structure reliability were complete, the chemical analysis test plan outlined in Fig. 22 would provide sufficent design data to provide structural reliability predictions. Lacking a complete molecular theory requires that detailed experimental test programs for physical and mechanical analysis as outlined in Fig. 23 be employed in conjunction with chemical analysis, the detailed test programs outlined in Fig. 22 and Fig. 23 require advanced instrumentation and computer aided data processing.

Executing a complete chemical analysis of a polymer composite as outlined in Fig. 22 generally provides sufficient detailed information to replicate a commercial polymer adhesive or

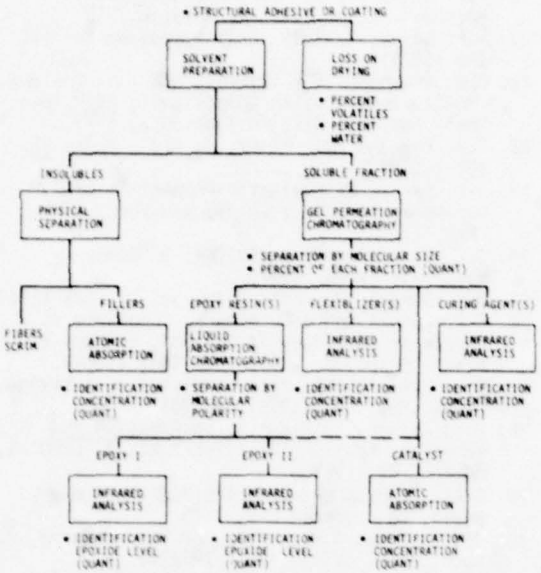

Fig. 22 Chemical analysis.

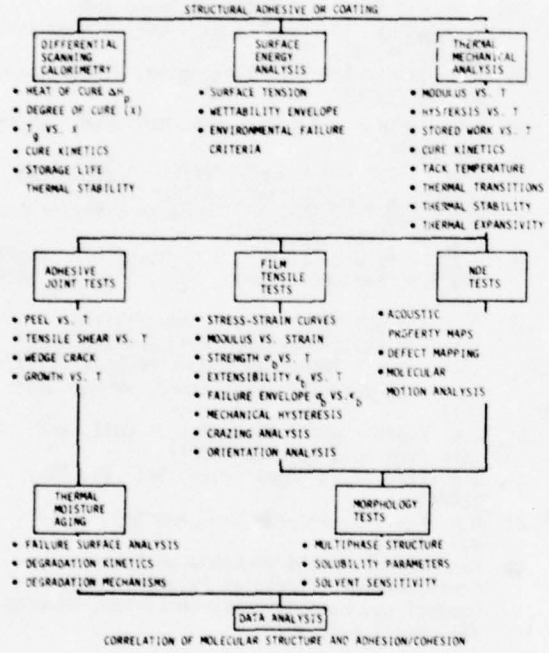

Fig. 23 Physical and mechanical analysis.

coating. In order to improve the reliability and durability of adhesives or coatings, essentially all aspects of the detailed physical and mechanical test program of Fig. 23 need to be employed. The upper rank experiments in Fig. 23 involving DSC, surface energetics, and thermal mechanical analysis (TMA) simulate manufacturing steps for surface treating, bonding, and curing polymer composites. The central tier of experiments in Fig. 23 incorporate NDE tests, adhesive joint tests in conjunction with study of polymer material response. The lower portions of Fig. 23 outline phases of study involving aging and failure mechanisms. The lower extremity of Fig. 23 describes a data analysis with correlation of molecular process and composite response. The detailed test plans outlined by Fig. 22 and Fig. 23 are presently utilized to determine and improve polymer reliability. The challenge to both theoretical and experimental analysis is, of course, to lower the cost and increase the reliability of currently functioning test programs as detailed in Fig. 22 and Fig. 23.

Summary and Conclusion

In summary, we may return to the mythical "one-hoss-shay" of Holmes poem (see Table 1) which presents the nearly perfect example of design for structural reliability and durability. An important point presented and hopefully well illustrated in this discussion is the importance of adding the analysis of molecular processes to present statistical theory of structure reliability. Implementation of the interaction matrix (see Table 2) establishes a direct avenue for communication between the specialist in engineering design and the materials scientist. The dual path approach (see Figs. 5 and 6) with combined deterministic/statistical testing and analysis is validated by extensive studies of which several are briefly reviewed in this discussion. A more general development and application of molecular theory of polymer reliability can lower the cost and increase the efficiency in present detailed test programs (see Figs. 22 and 23) for analyzing chemical, physical, and mechanical aspects of polymer composite durability.

A recent workshop on space environment effects on polymeric matrix composites in large scale space structures provides recommendations which also serve as conclusions to this discussion[43]:

1. Prior chemical analysis is necessary for materials identification.
2. Predictive modeling is mandatory.
3. All test designs should be based on the predictive model.

Implementation of the above recommendations promotes organization of present knowledge into an initial mechanistic model with molecular and macroscopic properties correlated. The model can be verified and refined as work progresses. The model elevates the engineering program to the level of conducting science and not simply data gathering.

ACKNOWLEDGEMENT

This research was sponsored by the Center for Advanced NDE, operated by the Science Center, Rockwell International, for the Defense Advanced Research Projects and the Air Force Materials Laboratory under Contract F33615-74-C-5180.

REFERENCES

1. Excerpts from a poem by Oliver Wendell Holmes, in "The Autocrat of the Breakfast Table", Riverside Press, Cambridge Mass. (1895), pp. 252-258.
2. Proceedings of the Colloquium on Structural Reliability (Editors: J.L. Swedlow, T.A. Cruse, and J.C. Halpin), Carnegie-Mellon University, Pittsburgh, October, 1972.
3. R.A. Heller, "Extreme Value Methods in Reliability Engineering", Ibid., pp. 104-
4. E.M. Lenoe and F.I. Barratta, "Recent Studies Toward the Development of Procedures Design of Brittle Materials, Ibid., pp. 433-462.
5. C.F. Tiffany, "The Design and Development of Fracture Resistant Structures", Ibid., pp. 210-216.
6. K.L. Jerima and J.C. Halpin, "Statistical Stress Concentration Effects in Composites", Ibid., pp. 308-322.
7. N.R. Mann, R.E. Shafer, and N.D. Singpurwalla, "Methods of Statistical Analysis of Reliability and Life Data", Wiley, New York (1974).
8. W. Weibull, J. Appl. Mech. 18, (1951), p. 293.
9. C.E. Browning, "The Effects of Moisture on the Properties of High Performance Structural Resins in Composites", Soc. of Plastics Industry, SPI Reinforced Plastics/Composites Division, 28th Ann. Conf. 1973: Section 15A, pp. 1-15.
10. J.F. Carpenter and T.T. Bartels, "Characterization and Control of Composite Prepregs and Adhesives", Proc. 7th Nat. SAMPE Conf., Vol.7, SAMPE, Azusa, CA (1975), pp. 43-52.
11. C.A. May, T.E. Helminiak, and H.A. Newey, "Chemical Characterization Plan for Advanced Composite Prepegs", Proc. 8th. Nat. SAMPE Conf., Vol. 8, SMPE, Azusa, CA (1976), pp. 274-294.
12. D.H. Kaelble and P.J. Dynes, "Preventive Nondestructive Evaluation (PNDE) of Graphite Epoxy Composites", AIAA paper No. 77-478, AIAA Conf. on Aircraft Composites, San Diego, CA, March, 1977.
13. D.H. Kaelble, P.J. Dynes, L.W. Crane, and L. Maus, "Composite Reliability", ASTM, STP 580, Amer. Soc. of Testing and Materials, 1975, pp. 247-262.
14. D.H. Kaelble, "Polymer Eng. and Science, 17 (1977), pp. 91-95.
15. F.N. Kelley and M.L. Williams, Rubber Chem. and Tech. 42, (1969), p. 1175.
16. D.H. Kaelble, Treatise on Adhesion and Adhesives, Vol. 4, (Editor, R.L. Patrick) Dekker, New York, 1975, pp. 194-208.
17. R.A. Hayes, J. Appl. Poly. Sci. 5, (1961), p. 318.
18. D.H. Kaelble, Physical Chemistry of Adhesion, Wiley-Interscience, New York (1971), Chapter 8, 12.
19. N.W. Johnston, J. Macromol. Sci. Rev. Macromol. Chem. C14 (2), 1976, p. 215.
20. R.F. Boyer, J. Poly. Sci: Symposium No. 50, 189 (1975).
21. C.E. Browning, G.E. Husman, and J.M. Whitney, "Moisture Effects in Composites", ASTM Spec. Tech. Pub. STP 617, Philadelphia, 1977.
22. T.G. Fox and P.J. Flory, J. Appl. Phys. 21, 581 (1950).
23. J.D. Ferry, Viscoelastic Properties of Polymers, 2nd. Ed., Wiley, New York, 1970, Chap. 11.
24. J.C. Halpin and H.W. Polley, J. Comp. Materials 1, 64 (1967).
25. J.L. Gardon, J. Appl. Poly. Sci. 7, 625 (1963).
26. R.F. Landel and R.F. Fedors, "Fracture Processes in Polymeric Solids", Editor: B. Rosen, Chap. 3B, Wiley, New York (1964).
27. D.H. Kaelble, Physical Chemistry of Adhesion, Wiley, New York (1971), p. 369.
28. J.C. Bolger, in Treatise on Adhesion and Adhesives (Editor, R.L. Patrick), 3, Chap. 1, Dekker, NY (1973).
29. PABST Roadmap Coordination Meeting, Long Beach, CA, October 8-9, 1976.
30. J.N. Sultan, R.C. Laible and F.J. McGarry, J. Appl. Poly. Sci. 6, 127 (1972).
31. N.J. Sultan and F.J. Mcgarry, J. Poly. Eng. and Sci. 13, 29 (1973).
32. E.H. Rowe, A.R. Siebert and R.S. Drake, Mod. Plastics 47, 110 (1970).
33. N.K. Kalfoglou and H.L. Williams, J. App. Poly. Sci. 17, 1377 (1973).
34. D.H. Kaelble, in Adhesion Science and Technology, 9A (Editor: L.H. Lee) Plenum Press, NY, 119 (1976).
35. W.D. Bascom and R.L. Cottington, J. Adhesion 7, 333 (1976).
36. D.H. Kaelble and P.J. Dynes, Mat. Eval. 35(4), 103 (1977).
37. J.C. Bolger and A.S. Michaels, in Interface Conversion for Polymer Coatings (Editor, P. Weiss and G.D. Cheever, American Elsevier Pub. Co., NY (1969) Chapter 1.
38. D.W. Levi, W.C. Tanner, R.C. Ross, R.F. Wegman and M.J. Bodnar, J. Appl. Poly. Sic. 20, 1475 (1976).
39. T. Smith and D.H. Kaelble, "Mechanisms of Adhesion Failure Between Polymers and Metal Substrates," Technical Report AFML-TR-74-73, Air Force Materials Laboratory, WPAFB, June 1974.
40. D.H. Kaelble and P.J. Dynes, J. Coll. and Interface Sci. 52, 562 (1975).
41. D.H. Kaelble, J. Appl. Poly. Sci. 18, 1869 (1974).
42. D.H. Kaelble, Polymer Eng. and Sci. 17 (7), 474 (1977).
43. Proceedings of the Workshop on Space Environmental Effects on Polymeric Matrix Composites, Langley Research Center, Hampton, VA., April 5-7, 1978.

George Martin (Consultant): Dave, have you considered the state of ionization of the air and related chemical degradation of surfaces?

David Kaelble (Science Center): Yes, of course. It appears in these models through the reciprocal molecular weight.

If you have radiation damage you are going to experience it in terms of a change in either by cross linking or scission within the polymeric phase. I don't expect that damage would be specific to the interface specifically unless you had a very high absorption cross-section for the interface itself. With orbiting space structures the radiation is from Van Allen type radiation environments. It is very difficult to model that particular situation in terms of the potential damage mechanisms in relation to the various types of energetic sources which range, of course, from photons to the high energy electron sources. The approach taken is simplify that whole argument by assuming that you are going to have surface protective mechanisms, that you will have thin foils which will essentially shield the surface from UV and, perhaps, the photon degradation and be left then with primarily the electron radiation damage effect.

George Martin: I was considering much lower levels of ionization; for instance, our Los Angeles smog here.

David Kaelble: Well, I'll tell you that, of course, is a subject of great concern and much study, even today.

Here again, protective mechanisms are obtained by molecular processes. In automobile tires, the tires are modified with a paraffin filler which actually comes out of solution and migrates to the surface to form a coherent film that replenishes itself throughout the life of the tire. Of course that is an old trick and it stablizes the system, that is, crack growth due to ozone or combined ozone and photolytic effects.

Robb Thomson (National Bureau of Standards): Questions? Please come to the micropnone. Remember to identify yourself.

Arthur Jonath (Lockheed Research): Dave, have you gone into studying the nature of the defect in the polymer in which the water condensation occurs, the origin of the defect, the actual molecular nature of the defect?

David Kaeble: Well, in epoxies, the only thing we have, of course, is the inference from molecular structure. One can do a sort of a cohesive energy density mapping of the molecular structure and you find that the regions or molecular sites which most closely correlate with the energy density properties of water will be the most highly interactive through physical solution. We haven't done spectroscopic studies. That is the simple answer, I guess, to that question.

Arthur Jonath: To add to that question, I guess what I am asking on a molecular level, are there sites that one could look at as being more polar in nature that would be more associated with defects, that would be more absorbent to the water?

David Kaelble: Yes, very definitely. I would say those beta hydroxyl sites on the amide crosslink and certainly ether oxygen sites on the nomopolymer crosslinks would be the sites that one would look at spectroscopically and expect to find the effect of water. That is, if you could use I.R. shifts or if you could use proton N.M.R., you might expect to see modification of degrees of freedom in that region.

Robb Thomson: Other questions? We will break for lunch then.

MICROFOCUS X-RAY AND IMAGE ENHANCEMENT OF CERAMICS

J. J. Schuldies
AiResearch Manufacturing Co.
Phoenix, Arizona

ABSTRACT

Microfocus X-ray and image enhancement techniques were applied to hot-pressed silicon nitride test specimens containing selected subsurface defects. These NDE techniques are being investigated to determine their defect characterization capabilities in various ceramic material systems. Illustrations are presented of defect detection limitations for microfocus X-ray which are primarily associated with low radiographic contrast between defect and parent material. Examples are also shown of defect detectability and geometric sharpness obtained in ceramic test specimens containing inclusions of high and low density with respect to the parent material.

INTRODUCTION

Microfocus X-ray and image enhancement techniques have shown potential to reduce the subjective interpretation of defects detected in ceramic materials.(1) The purpose of this study is to obtain a quantitative measure of the capability of these techniques for defect characterization in ceramic materials in terms of size, type, and location.

DISCUSSION

Radiography is widely recognized as a means of evaluating materials for subsurface defects. The applications and advantages of this technique are listed in Fig. 1. As is the case for most, if not all NDE methods, limitations are also known relative to defect detection and interpretation of radiographic film obtained using penetrating radiation. These important considerations are shown in Fig. 2.

Further indication of the importance of radiographic contrast between the indication of interest and the parent material is illustrated in Fig. 3. The difficulty in detecting low or comparable density defects in a material system, using visual interpretation means, is a function of the absolute contrast obtained on the radiographic film. Inclusions of high relative density, such as tungsten carbide (WC), produce a significant contrast enabling visual detection of inclusions in the tens of microns size range.

The use of microfocus radiography (Magnaflux Corporation), as compared to conventional radiography, is being evaluated to take advantage of the benefits derived from a smaller X-ray source. Control of the focal spot size, shape, and intensity distribution at the X-ray emitter (or target) suppresses radiation outside of the primary beam, which is essential in achieving a high resolution X-ray image. Other advantages, such as geometric enlargements, may be obtained while suppressing the effects of parallax obtained in the X-ray image. These advantages are listed in Fig. 4. A comparison of the theoretical focal spot shape and intensity distribution obtained on the X-ray target for conventional and microfocus X-ray systems is presented in Fig. 5. The variation in X-ray beam intensity is shown in Fig. 6, as indicated by the pattern and degree of film blackening (film density measured in H and D standard units) obtained using a 100-kV microfocus X-ray unit and GAF-100 film. As shown, an elliptical area having minor and major axis dimensions of approximately 1.25 and 2.5 inches should be used for evaluation when film density variations must be kept to a minimum.

Image enhancement through the computerization of X-ray film gray-scale data is also being evaluated to determine the degree of improvement obtained in defect characterization. The basic system components (Spatial Data Systems Model 820) are illustrated in Fig. 7.

Several radiographic and image enhancement examples are presented in Figs. 8 through 10 (photographically reduced approximately 18 percent). Two hot-pressed silicon-nitride specimens (NC-132), nominally 0.25 inches (6.4 mm) thick, and a hot-pressed silicon-nitride (NC-132) radiographic step-block standard are shown in the radiographs. The microfocus X-rays were obtained using specific exposure parameters. These parameters were varied about an optimum, which was

(1) Schuldies, J. J. and W. H. Spaulding, "Radiography and Image Enhancement of Ceramics," Proceedings of the 1977 ARPA/NAVSEA Ceramic Gas Turbine Demonstration Engine Program Review, March 1978.

determined by visually examining the radiographic film for geometric sharpness and contrast of the known defects. Enhanced outputs, using an algorithm that combines high-pass filtering and contrast expansion, are also shown in Figs. 8 through 10 for test specimen number 316. The arrows indicate both the WC inclusion placed in the specimen and a naturally occuring low-density defect. The arrows in the radiographs also indicate detection of a linear, low-density defect in specimen number 231 and a 0.020 inch (.500 microns) diameter hole 0.005 inch (125 microns) deep in the step-block standard.

An additional technique that employs thresholding or gray-scale level slicing is shown in Fig. 11. A selected gray-scale level divides the radiographic data into two colors, black or white, depending on the distribution of film density data. The enhancement photo reveals three WC particles in test specimen number 325 instead of a single 100 micron WC inclusion. The size of the large particle, measured on this output, is in good agreement with this size objective. A color coded output of this inclusion at greater magnification is shown in Fig. 12. While only two color levels are used, the system is capable of electronically classifying gray-scale data into thirty color levels. Figs. 11 and 12 were photographically reduced approximately 18 percent.

The color coded output, in Fig. 12, also shows an electronic scan line that runs through the largest of the three inclusions in specimen number 325. The degree of film contrast or density variance associated with the scan line is electronically displayed below the inclusions. As shown, this trace deviates in the region associated with the inclusion indicating a significant change in film density.

CONCLUSIONS

The detection of a single high density defect (i.e., 50 micron WC) has been demonstrated using microfocus X-ray. The use of image enhancement was also shown to improve the visualization of details associated with fabrication type low-density flaws. Image enhancement outputs indicated the importance of establishing exact radiographic procedures to obtain constant film densities prior to further reconstruction using computer algorithms. Although the efforts conducted to date indicate the utility of radiography to detect high-density inclusions, further advances in technology are required to detect low-density defects of comparable size.

ACKNOWLEDGEMENTS

The author is grateful to W. H. Spaulding and D. E. Watson, AiResearch Quality Assurance Department, for the radiographic and image enhancement work reported herein.

This research was sponsored by the Center for Advanced NDE, operated by the Science Center, Rockwell International, for the Defense Advanced Research Projects and the Air Force Materials Laboratory under Contract F33615-74-C-5180.

- WIDE VARIETY OF MATERIALS
- INCLUSION DETECTION
- LINEAR DEFECT DETECTION
- COMPLEX GEOMETRIES
- EQUIPMENT AVAILABILITY

Fig. 1. Radiographic applications

IMAGE CONTRAST

PARALLAX DISTORTION

DEFECT TYPE - PARENT MATERIAL RELATIONSHIP

DEFECT ORIENTATION AND EXACT LOCATION

RESOLUTION AND SENSITIVITY

SUBJECTIVE INTERPRETATION

Fig. 2. Typical radiographic limitations for s defect detection

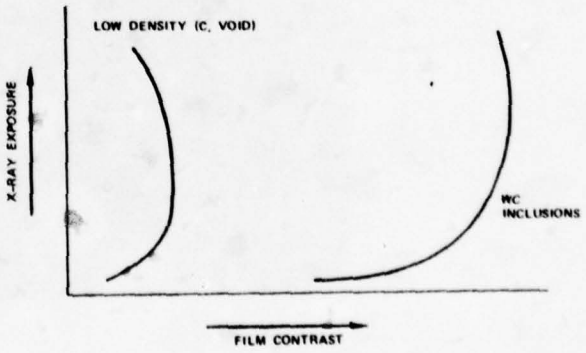

Fig. 3. Inclusion/parent material contrast relationship

CONTROL OF FOCAL SPOT SIZE, SHAPE, AND INTENSITY DISTRIBUTION

- REDUCED OFF-FOCUS (SECONDARY) RADIATION
- REDUCED PARALLAX EFFECTS
- IMPROVED EDGE RETENTION
- RADIOGRAPHIC ENLARGEMENTS

Fig. 4. Microfocus radiography advantages

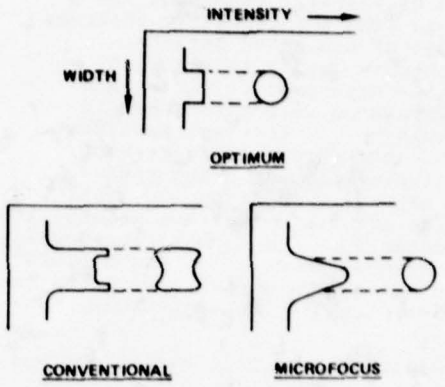

Fig. 5. Radiographic focal spot intensity distribution

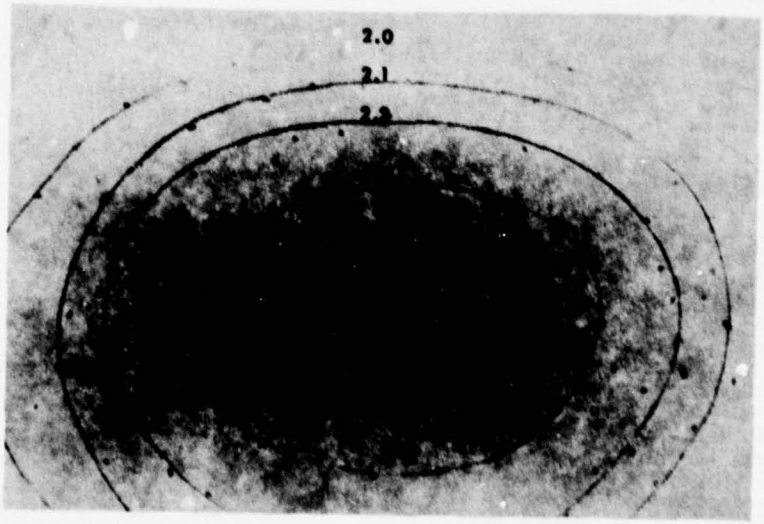

Fig. 6. Microfocus x-ray beam profile

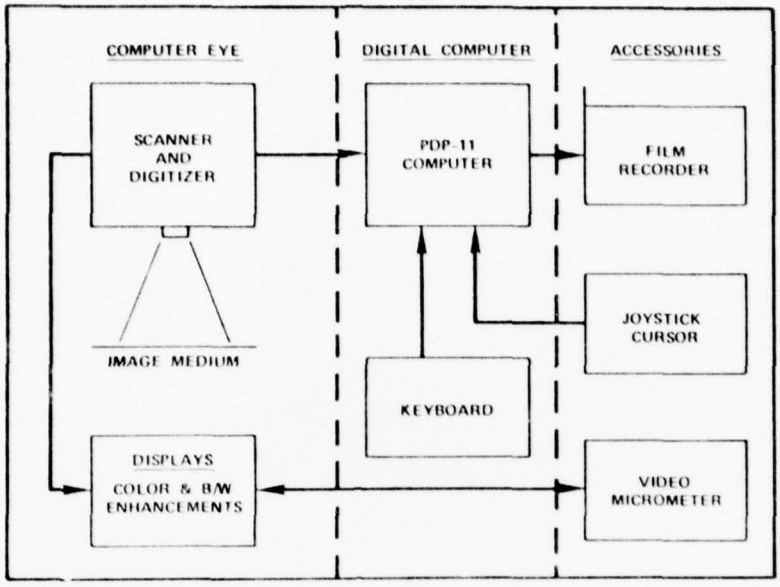

Fig. 7. Block diagram of computerized image enhancement system

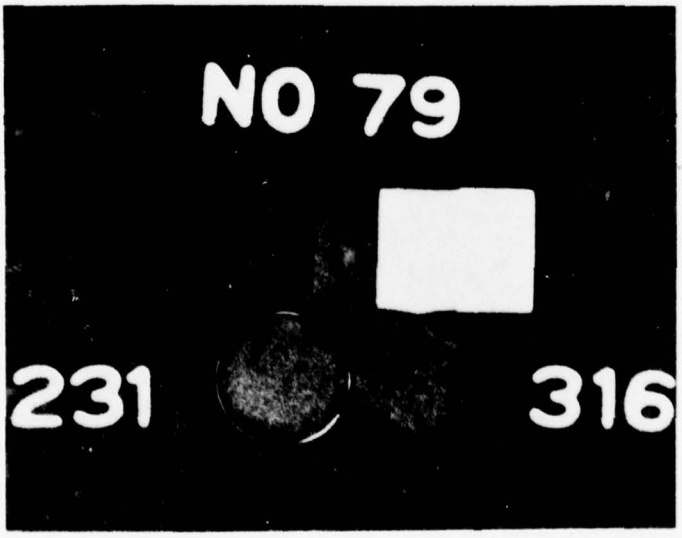

MICROFOCUS X-RAY

HOT-PRESSED SILICON NITRIDE
NO. 231 - 200 MICRON SiC
NO. 316 - 50 MICRON WC

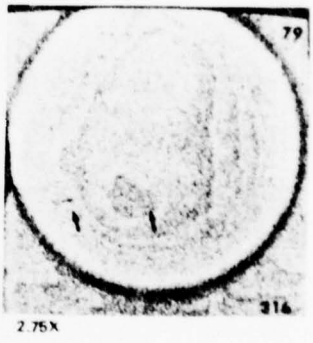

IMAGE ENHANCEMENT

FILTER/CONTRAST
EXPANSION ALGORITHM

Fig. 8. Radiographic and image enhancement - Examples

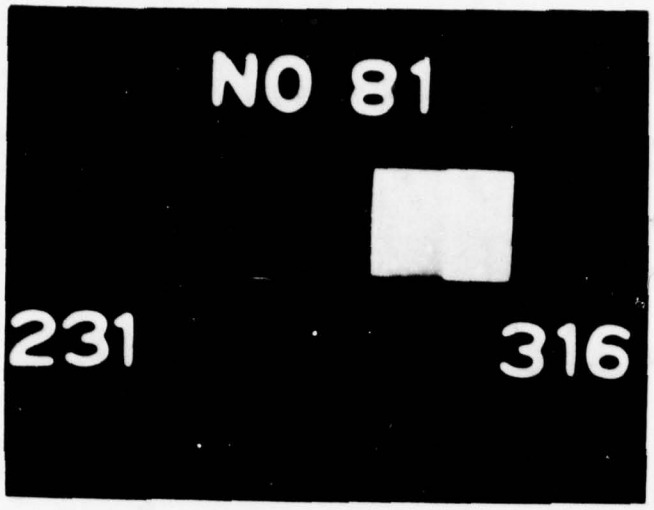

IMAGE ENHANCEMENT

FILTER/CONTRAST
EXPANSION ALGORITHM

MICROFOCUS X-RAY

HOT-PRESSED SILICON NITRIDE
NO. 231 - 200 MICRON SiC
NO. 316 - 50 MICRON WC

Fig. 9. Radiographic and image enhancement - examples

Fig. 9. Radiographic and image enhancement - examples

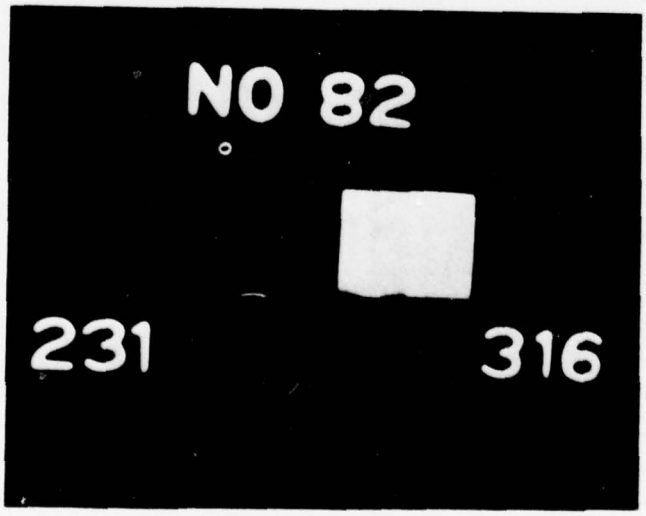

IMAGE ENHANCEMENT

FILTER/CONTRAST
EXPANSION ALGORITHM

MICROFOCUS X-RAY

HOT-PRESSED SILICON NITRIDE
NO. 231 - 200 MICRON SiC
NO. 316 - 50 MICRON WC

Fig. 10. Radiographic and image enhancement - examples

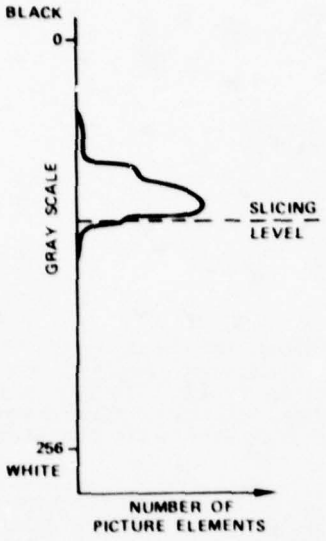

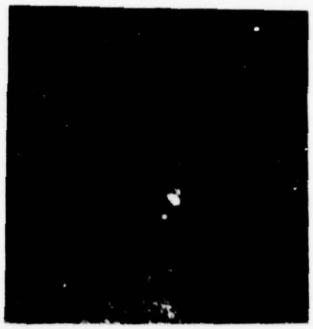

HOT-PRESSED SILICON NITRIDE
SPEC NO. 325
100 MICRON - WC
32X

Fig. 11. Image enhancement - thresholding

HOT-PRESSED SILICON NITRIDE - SPEC. NO. 325
100 MICRON - WC (≈70X)

Fig. 12. Color coding of radiographic data

PRELIMINARY EVALUATION OF NDE TECHNIQUES FOR STRUCTURAL CERAMICS

D. S. Kupperman, A. Sather, N. P. Lapinski,
C. Sciammarella**, and D. Yuhast†
Materials Science Division
Argonne National Laboratory
Argonne, Illinois 60439

ABSTRACT

A preliminary evaluation of several nondestructive testing methods for flaw detection in high-temperature structural ceramic components is being carried out. The ceramics components being investigated include silicon carbide heat-exchanger tubes and silicon nitride rotors. The nondestructive evaluation techniques under consideration include dye-enhanced radiography, holographic interferometry, infrared scanning, acoustic microscopy, acoustic-emission monitoring, acoustic-impact testing, and conventional ultrasonic testing.

The capability of each technique to detect critical-size flaws will be discussed. Preliminary results to date have shown that (a) dye-enhanced radiographic techniques are capable of detecting tight cracks missed with conventional x-ray methods, (b) acoustic microscopy techniques may be useful in detecting and establishing the size of subsurface defects in reaction-bonded silicon nitride, (c) holographic interferometry techniques should be valuable in locating surface cracks in silicon nitride/silicon carbide components, and (d) the results from various silicon carbide tubes suggests that infrared scanning techniques may reveal changes in heat-flow patterns which are related to variations in physical properties. The results for the other techniques mentioned will be discussed. Future efforts in this program will be directed toward in-depth investigations of the most useful nondestructive techniques.

INTRODUCTION

The objective of this investigation is to establish the feasibility and sensitivity of various NDE techniques for examination of high temperature ceramic components. The techniques under consideration which are discussed here include dye-enhanced radiography, holographic interferometry, acoustic microscopy, acoustic emission, acoustic impact testing and infrared scanning.

DISCUSSION

The first figure shows two silicon nitride rotor blade rings (supplied by Ford Motor Co. for this study) and three silicon carbide heat exchanger tube samples representative of those investigated. The next figure shows schematically the procedure for dye-enhanced radiography where surface flaws filled with an x-ray absorbing dye may be revealed even though missed with conventional radiographic techniques. The third figure shows the mass absorption coefficient ratio for silver nitrate to silicon nitride indicating an absorption edge at 25 KeV. Conventional x-ray machines have a broad spectrum up to a maximum energy value. The optimum setting for a silver nitrate dye appears to be around 50 KeV maximum. Figure 4 shows (for the purpose of illustration) the results using a cracked plastic rod. Figure 6 shows a cross section of a silicon carbide tube (1 mm thick wall) indicating two cracks. The larger crack was detected by both conventional and dye-enhanced radiography; the smaller only by dye-enhanced radiography. Dye-enhanced radiography appears to be useful for detection of tight cracks in ceramic rotors and silicon carbide tubes (particularly for inner wall cracks not accessible with dye-penetrant techniques). Figure 7 shows the schematic arrangement for holographic interferometry. Thermal or mechanical stressing causes visible distortions in holographic interferogram fringe patterns when flaws are present. Figure 8 shows loading modes for ceramic rotor blades. Figure 9 shows the expected fringe distortion for a crack at a blade root. Figure 10 shows examples of interferograms for various samples with mechanical loading. An example of how sensitivities may be enhanced by fringe multiplication techniques is included. Interferograms can be analyzed in a manner shown in Figs. 11 and 12. Surface cracks with characteristic lengths of 750 μm can be detected on the blade root. With special magnification techniques, the resolution may be as small as 100 μ.

Figure 13 describes the equipment arrangement for acoustic microscopy (employing Sonoscan Inc. acoustic microscope). Figures 14 and 15 describe the detection scheme and sample arrangement for ceramic rotor blades (removed from the blade ring). Figure 16 shows a flaw detected in a ceramic rotor blade through acoustic microscopy. This flaw (~500 x 300 μm) was missed in 3 of 4 radiographs but the presence revealed by the acoustic micrograph was virtually confirmed by metallographic sectioning of the blade (Fig. 17). The acoustic micrographs shown represent an area on the blade 2 x 3 mm. The electronically introduced interference lines are ~80 μm apart. Acoustic micrographs of SiC heat exchanger tubing show similar

**Illinois Institute of Technology, Chicago, Illinois
†Sonoscan Incorporated, Bensenville, Illinois

background structures. Figure 18 shows an acoustic micrograph and visual image of a slice of a ceramic heat exchanger tube (Carborundum αSiC). Surface flaws have been seen both acoustically and optically. Subsurface flaws have also been suggested by acoustic micrographs.

The equipment arrangements and an example for acoustic emission studies are shown in Figures 19-22. The equipment and some data for acoustic impact testing are shown in Figs. 23-26. Figure 27 summarizes the studies for silicon nitride rotors. Figure 28 shows a schematic arrangement for infrared scanning of SiC heat exchanger tubing. The tubes are heated in a water bath and transient patterns observed. Tubes 1, 6 and 7 (counting left to right) are Norton NC430; tubes 2,3,4,5 are Carborundum SiC tubes. Tube 4 is severely cracked. The Norton tubes show better axial heat conduction than the Carborundum tubes. The thermogram is originally in color. In this black and white copy the darker areas are associated with higher temperatures. The cracked tube, as expected shows the worst thermal transport characteristics. A maximum temperature gradient of about 2°C is indicated. Infrared imaging appears to be capable of visually displaying differences in heat transport properties due to variations in physical properties in ceramic tubes and the presence of gross flaws.

Details of the various aspects of this study as well as discussions of conventional ultrasonic testing and fracture mechanics analysis applied to silicon carbide tubing are discussed in references 1-4.

ACKNOWLEDGMENT

This work is supported by the U.S. Department of Energy.

REFERENCES

1. D. S. Kupperman, C. Sciammarella, N. P. Lapinski, A. Sather, D. Yuhas, L. Kessler and N. F. Fiore, "Preliminary Evaluation of Several Nondestructive Evaluation Techniques for Silicon Nitride Gas-Turbine Rotors," Argonne National Laboratory Report ANL-77-89, January, 1978.

2. "Nondestructive Evaluation Techniques for High-Temperature Ceramic Components," Quarterly Report ANL/MSD-78-2, February, 1978.

3. "Nondestructive Evaluation Techniques for High-Temperature Ceramic Components," Quarterly Report ANL/MSD-78-5, March, 1978.

4. Nondestructive Evaluation Techniques for High-Temperature Ceramic Components," Quarterly Report ANL/MSD-78-7, June, 1978.

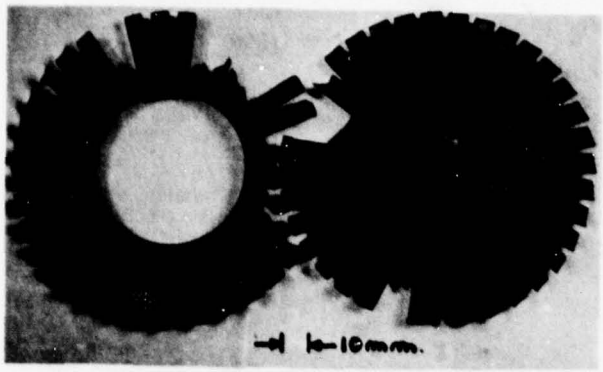

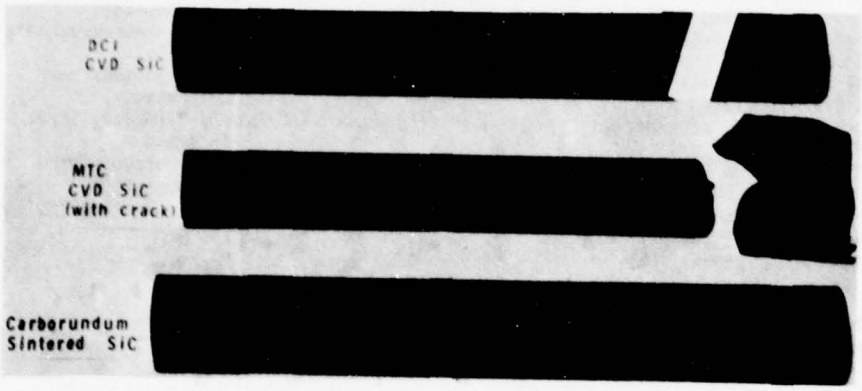

Fig. 1

Silicon Nitride Gas Turbine Rotors and
Silicon Carbide Heat Exchanger Tubing

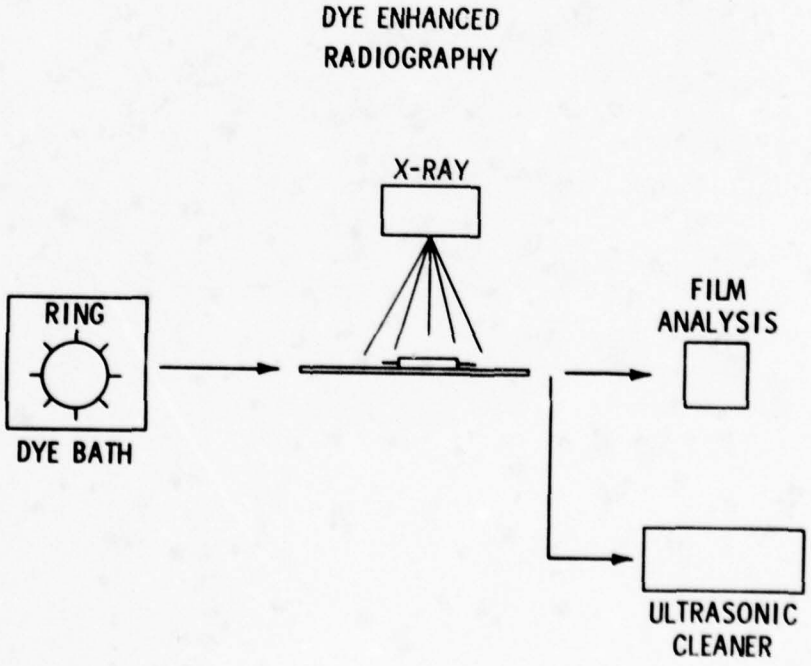

Fig. 2

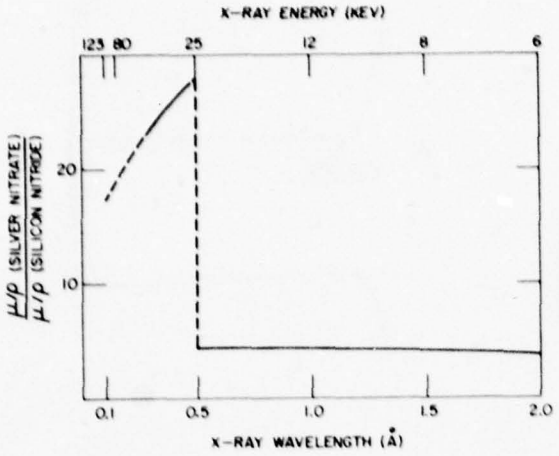

Fig. 3

RADIOGRAPHS OF CRACKED PLEXIGLASS ROD

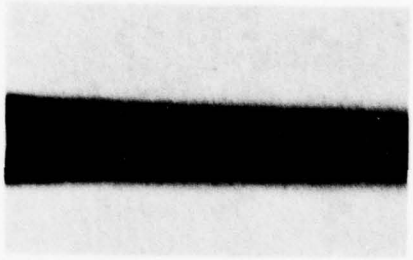

WITHOUT DYE

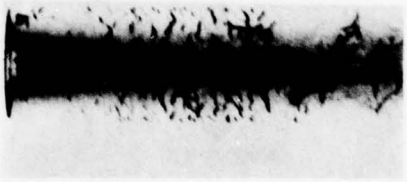

WITH DYE

Fig. 4

Anomaly Revealed in Blade-root Region of SN ROTOR. Mag. 20X.

Fig. 5

Detected by Dye-enhanced and Conventional Radiography

Detected by Dye-enhanced Radiography Only

Cross Section of Ceramic Heat Exchanger Tube, Showing Two Cracks

Fig. 6

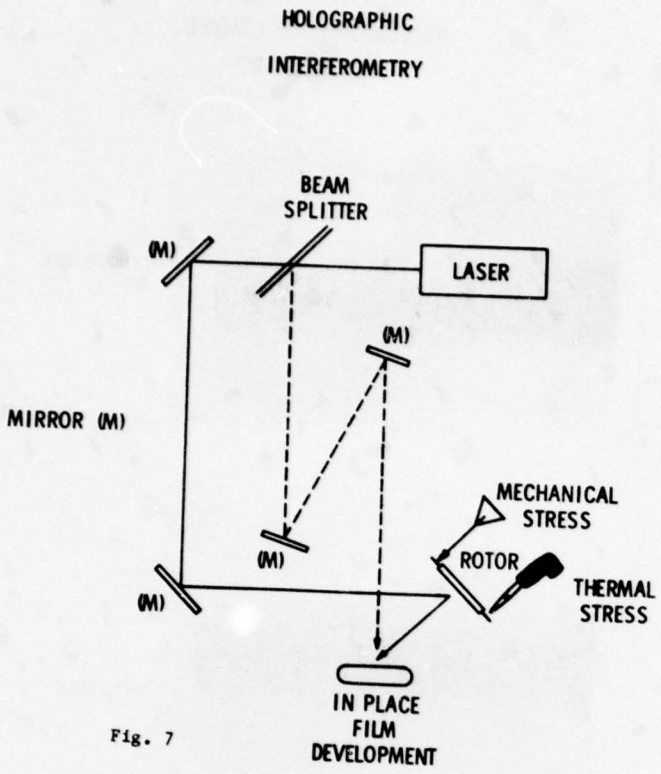

Fig. 7

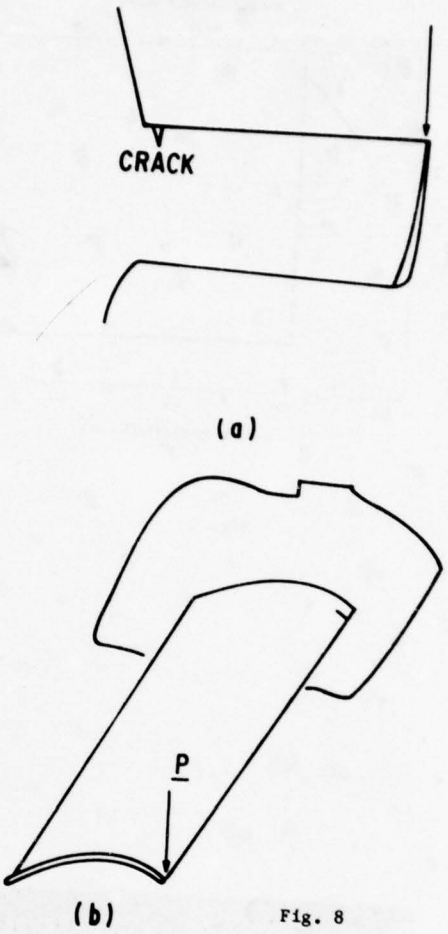

Fig. 8

Modes of Loading of a Turbine Blade

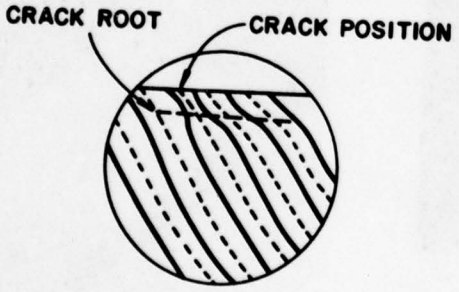

Fig. 9

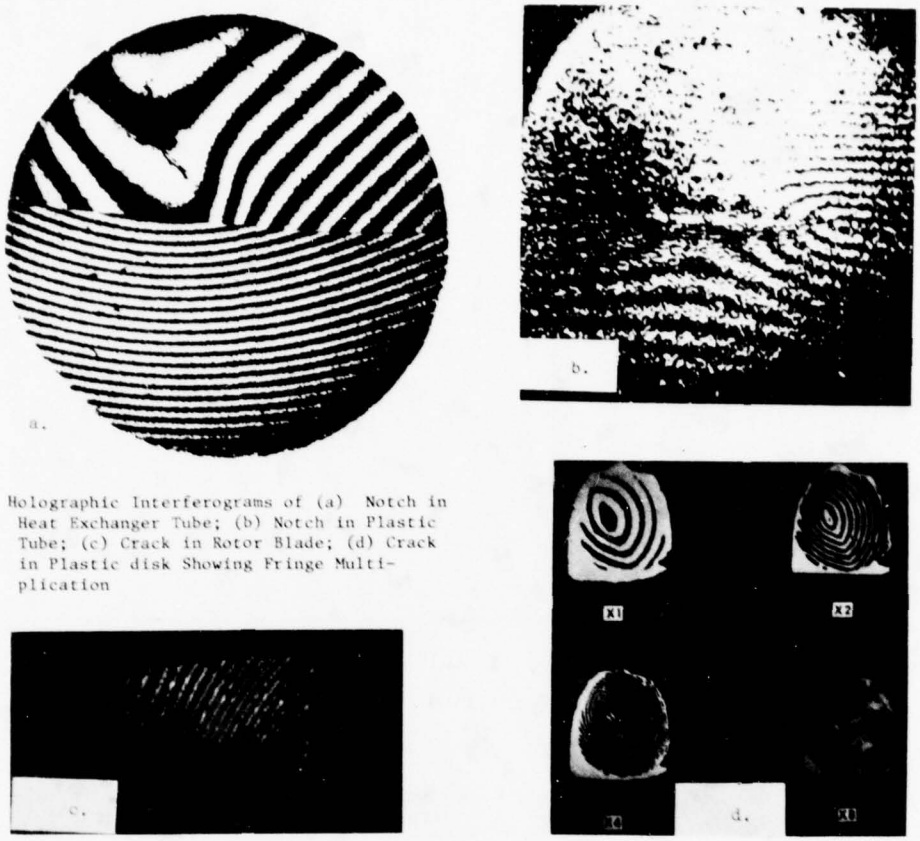

Holographic Interferograms of (a) Notch in Heat Exchanger Tube; (b) Notch in Plastic Tube; (c) Crack in Rotor Blade; (d) Crack in Plastic disk Showing Fringe Multiplication

Fig. 10

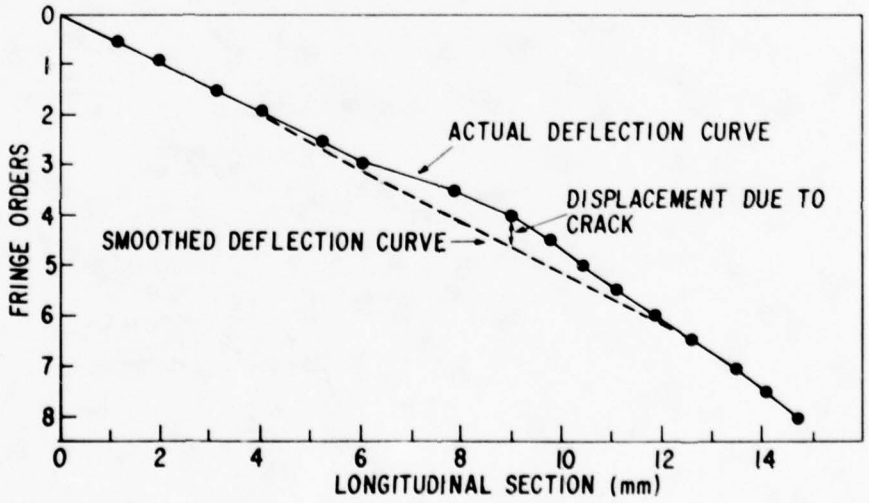

Fig. 11

Plot of Fringe Orders vs Position. By this plot, one obtains the contribution of the displacement field due to the crack from the overall field.

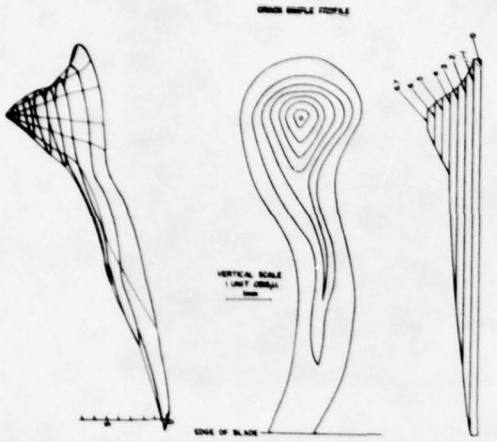

Profile of Dimple Produced by Presence of Crack on Blade

Fig. 12

ACOUSTIC MICROSCOPY

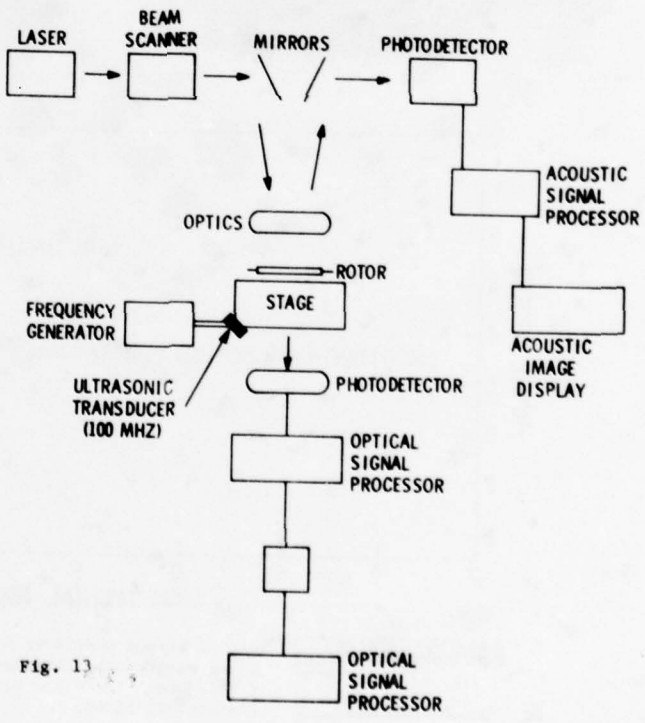

Fig. 13

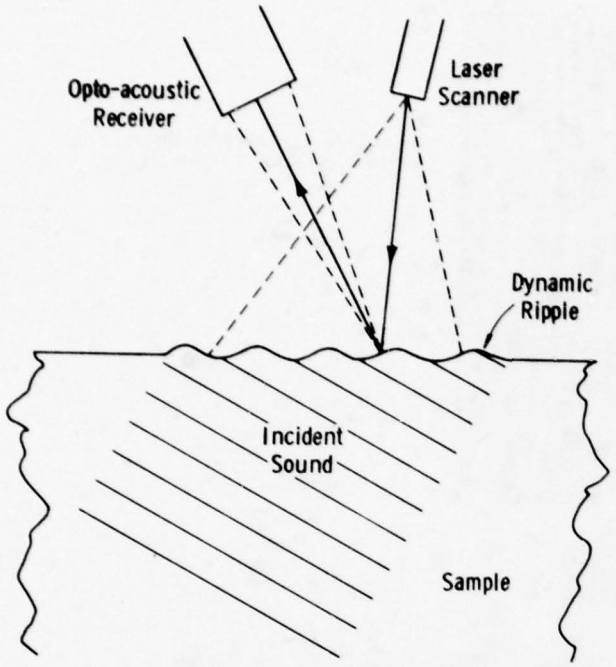

Schematic Diagram Illustrating Detection Scheme Used by Scanning Laser Acoustic Microscope

Fig. 14

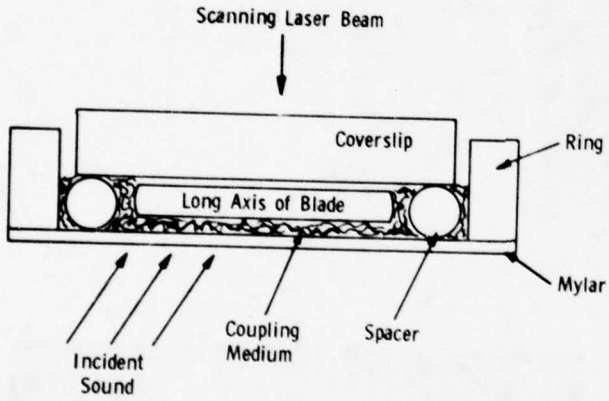

Schematic Diagram of Sample Configuration

Fig. 15

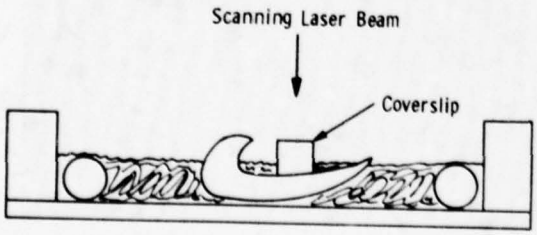

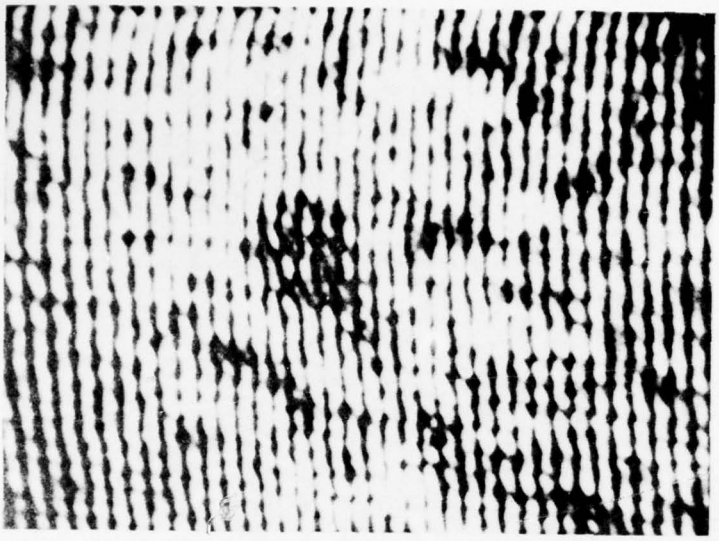

Defect Cluster (circled) Observed in Flatter Portions of Blade 28

Fig. 16

Cross Section of Blade at Location of Pore Indicated by Radiography and in General Region of Defect Indicated by Acoustic Microscopy

Fig. 17

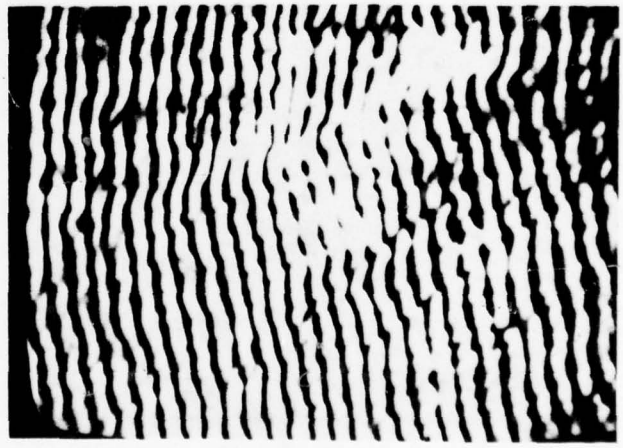

Acoustic Micrograph of Section of Silicon Carbide Heat Exchanger Tubing

Fig. 18

ACOUSTIC EMISSION

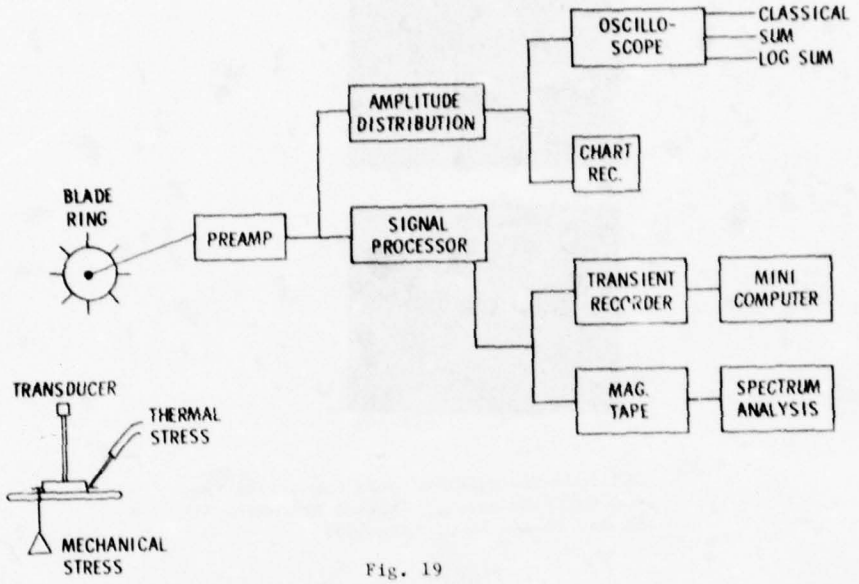

Fig. 19

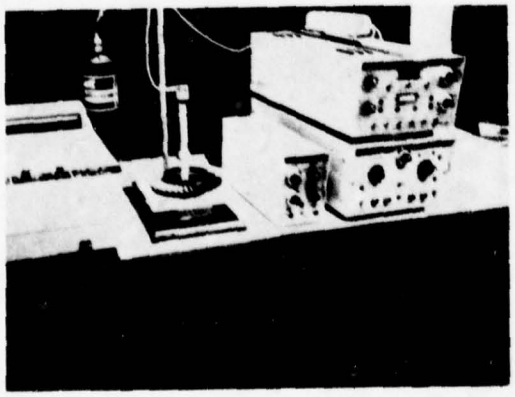

Photograph of SN Rotor, SN Stand, Amplitude-distribution Analyzer, and Signal Processor for Acoustic-emission (AE) Experiments

Fig. 20

BLADE RING 1957

Blades 16 and 20 of Blade Ring 1957

Fig. 21

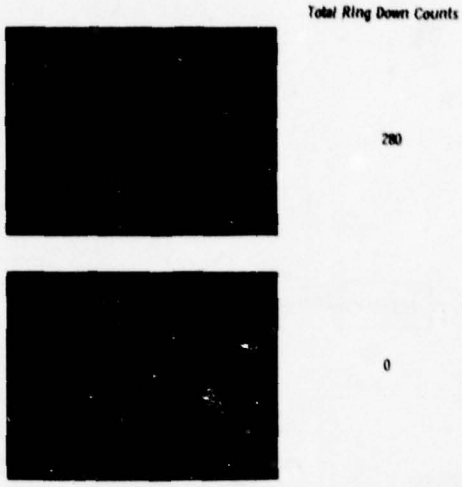

Amplitude-distribution-data Cumulative Log and Total Counts for Thermal Stressing of Blades 16 and 20 of Ring 1957.

Fig. 22

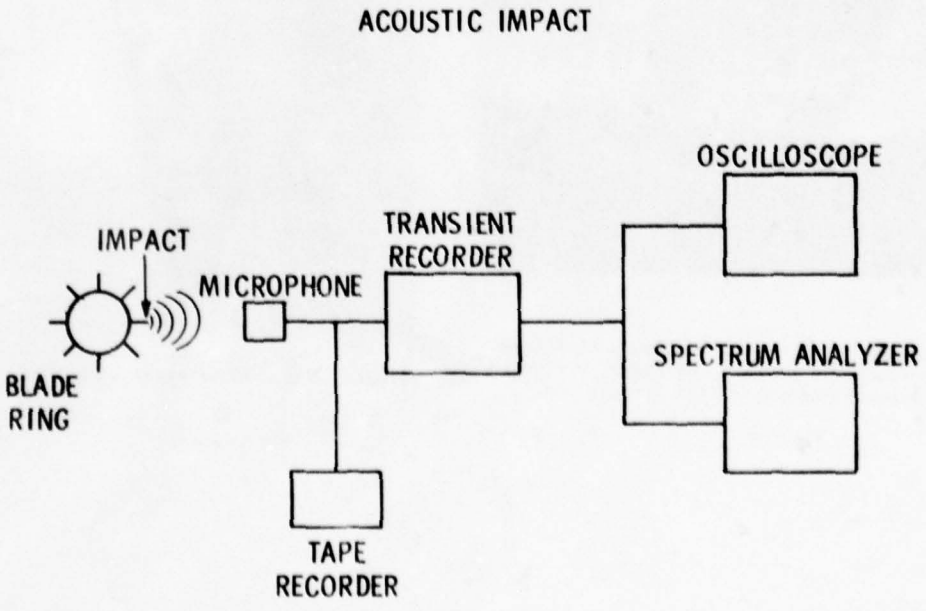

Fig. 23

RESONANCE FREQUENCY FOR ROTOR BLADE IN CANTILEVER MODE OF VIBRATION

$$f = \frac{A}{2\pi} \sqrt{\frac{E b^2}{12 \rho \ell^4}}$$

$E = 300 \times 10^{10}$ DYNES/CM^2 (MODULUS OF ELASTICITY)

$\rho = 2.7$ G/CM^3 (DENSITY)

$b = 0.2$ CM (AVERAGE THICKNESS OF BLADE TAPER)

$\ell = 2.5$ CM (BLADE LENGTH)

$A = 11.7$ (GEOMETRIC FACTOR FOR FUNDAMENTAL MODE WITH TAPERED 3b TO b)

$f_{CALC} = 9.1$ KHz

$f_{MEASURED} = 8$ KHz

Fig. 24

ACOUSTIC IMPACT TESTING

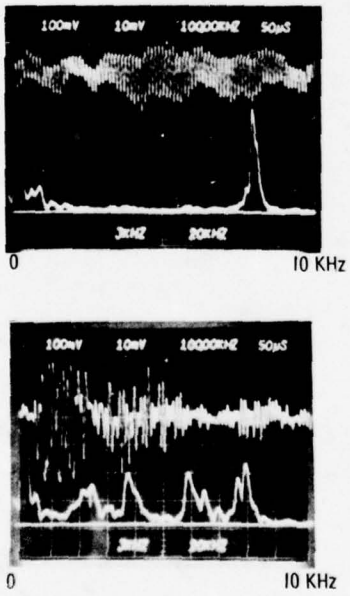

Frequency Spectra of Blades 16 and 20 of Blade Ring 1957, Indicating Variation in Blade Quality. Blade 16 has a tight radial crack from the blade tip to about midway between the blade tip and blade root.

Fig. 25

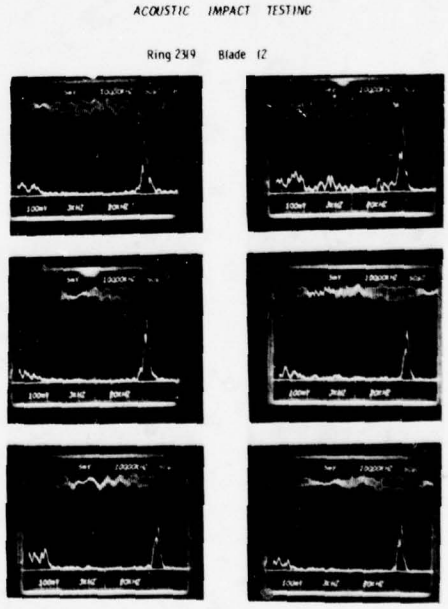

Six Consecutive Impacts (Using pencil-lead technique) and Resulting Frequency Spectrum from Blade 12 of Blade Ring 2319.

Fig. 26

NDE TECHNIQUES FOR SILICON NITRIDE ROTORS

METHOD	ADAPTABILITY TO ROTOR GEOMETRY	FLAW DETECTION		LEVEL OF DIFFICULTY TO DETECT CRITICALLY SIZED FLAWS	COMMENTS
		SURFACE	SUBSURFACE		
1) DYE ENHANCED RADIOGRAPHY	EXCELLENT	X		MODERATELY LOW	CAN REVEAL FLAWS NOT VISIBLE BY ORDINARY X-RAY OPTICAL OR DYE PENETRANT METHODS. VERY PROMISING
2) ACOUSTIC MICROSCOPY	FAIR	X	X	LOW	OVERALL QUALITY OF COMPONENT AS WELL AS SPECIFIC DEFECTS CAN BE OBSERVED. LIMITED TO 3 MM THICK SPECIMEN IN RB, 6 MM THICK SPECIMEN IN HP.
3) HOLOGRAPHIC INTERFEROMETRY	GOOD	X	?	MODERATE	PROBABLY ADAPTABLE TO AUTOMATIC SCANNING
4) ACOUSTIC EMISSION	FAIR	X	X	HIGH	DATA INTERPRETATION VERY DIFFICULT, RELIES ON FLAW POPULATION CHANGE DURING TEST TO RELEASE ACOUSTIC ENERGY FOR FLAW INDICATION
5) ACOUSTIC IMPACT TESTING	GOOD	X	X	HIGH	INDICATE OVERALL COMPONENT QUALITY
6) INTERNAL FRICTION	POOR	X	X	HIGH	PARTICULARLY DIFFICULT TO ADAPT TO ROTOR INSPECTION

Fig. 27

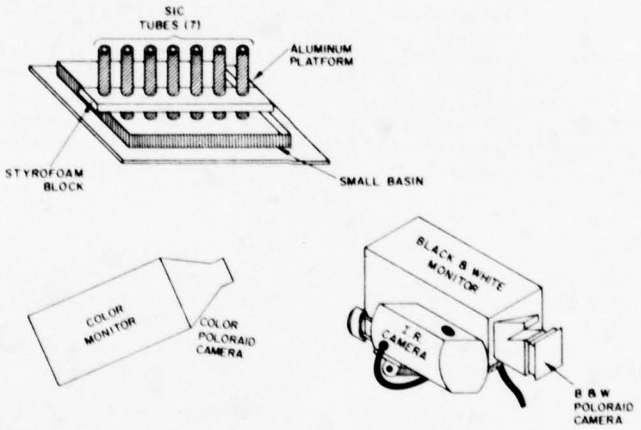

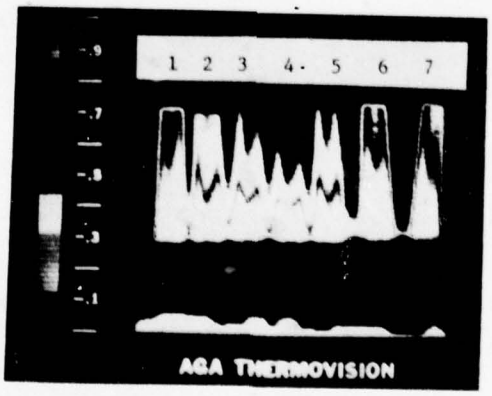

Fig. 28

Thermogram of Heat Exchanger Tubing

Tubes 1, 6, 7 are Norton Co.

Tubes 2, 3, 4, 5 are Carborundum

Tube 4 is cracked

NONDESTRUCTIVE INSPECTION OF HIGH PERFORMANCE CERAMICS

R. H. Brockelman
Army Materials and Mechanics Research Center
Watertown, Massachusetts 02172

ABSTRACT

Two ceramic materials, a hot-pressed silicon nitride and a siliconized silicon carbide, were manufactured with seeded particulates to evaluate the effectiveness of existing nondestructive test practices at AMMRC for defect detection in ceramics and to evaluate the effect of inclusions upon material strength. The types of seeded defects were of greater and lower density relative to the matrix materials and ranged in size from approximately 0.1 mm to 0.6 mm. The nondestructive methods used in the investigation were ultrasonics, radiography, eddy current and penetrant. Bend bar specimens were cut from the seeded regions of the billets and tested at 25°C, 1093°C and 1371°C. Fracture origins were examined by optical and electron microscopy and by microprobe to correlate the nature of the fracture initiating defects with the nondestructively detected defects. This permitted a ranking of defect detection sensitivity and defect effect upon strength.

SUMMARY

Two billets approximately 15 centimeters square of each matrix material were prepared with seeded inclusion particles from standard production powder mixes. The inclusion defects selected for incorporation into the hot pressed silicon nitride (HPSN) were graphite (C), iron (Fe), silicon (S) and tungsten carbide (WC) particles. The same types of particles, with the exception of tungsten carbide, were seeded into the silicon carbide (SiC) billets.

Maps of the seeded inclusion locations and corresponding ultrasonic pulse-echo C-scan recordings of the billets following surface machining are shown in Figs. 1-4. The nominal sizes of fine, medium, and course correspond to mean particle diameters of approximately 125, 250, and 635 microns. The ultrasonic test reveals the presence of many defects in the billets that are not listed on the seed location maps. Fig. 5 shows C-scan recordings of the variation in ultrasonic energy loss through the surface machined SiC billets. White areas represent a 3db or 2 times loss of energy compared to dark areas. Point by point ultrasonic velocity measurements in the billets showed an average longitudinal wave velocity for the HPSN billets of 1.12 cm/μsec with a variation of less than 1 percent between measurements. The SiC billets had variations up to 3 percent with an average of 1.21 cm/μsec.

Figure 6 presents variations in eddy current response of a SiC billet. The numerical values are only relative showing variation in resistivity with a single billet. Each billet was examined by liquid penetrant for surface cracks, porosity and edge laminations. A map of liquid penetrant indications in a SiC billet is shown in Fig. 7. The HPSN billets were free of indications. Positive prints of radiographs of the billets are shown in Fig. 9. All sizes of the tungsten carbide and iron contaminants in the HPSN billets are visible. The fine and medium size silicon and graphite particles were not visible in the HPSN billets. Only the large graphite particles and a surface scab are visible in the radiograph of the SiC billet.

Figures 10 and 11 contain examples of individual C-scans of rough-cut bend bars sectioned from the billets and the subsequent microscope analyses of defects contained within the corresponding bend bars. The latter includes photomicrographs of the fracture initiating defect and a photograph of the display of the energy dispersive microprobe. The photomicrographs are oriented such that the thickness direction of the bend bar corresponds to the vertical direction of the page. The C-scans were made from both the front and back sides of the bars. In addition to the two dimensional displays of the defect positions (in plane of paper), the depth (in direction perpendicular to plane of paper) of the defects are tabulated, as determined by the method of detection. Depths are measured relative to the back surface of the bar. The following abbreviations are used in the C-scans:

- F - Front surface view
- B - Back surface view
- DN - Defect number
- USD - Depth of defect as determined by ultrasonics distance measured from back surface (B) in inches.
- XRD - Depth of defect as determined by radiography distance measured from back surface (B) in inches.
- H - Defect density higher than that of matrix.
- L - Defect density lower than that of matrix.

In the listing of the defects below a C-scan figure, an arrow indicates the defect which was sought as the fracture origin (target defect). Multiple defects were present upon occasion at the same depth within the sample.

Results of bend bar testing and a ranking of defect detection sensitivity and defect effect upon strength can be found in the following Reference:

H. R. Baumgartner, R. H. Brockelman, P. M. Hanson, Development of Nondestructive Testing Techniques for High Performance Ceramics. AMMRC TR 78-11 (Army Materials and Mechanics Research Center, Jan. 1978).

ACKNOWLEDGMENT

This project was a joint effort with the Nondestructive Testing Industrial Applications Branch, at the Army Materials and Mechanics Research Center, and Norton Company, Worcester, Massachusetts, and has been accomplished as part of the U. S. Army Materials Testing Technology Program. The nondestructive evaluation of the ceramic materials was performed at AMMRC under the direction of Mr. C. H. Hastings. The Project Manager at Norton was H. R. Baumgartner.

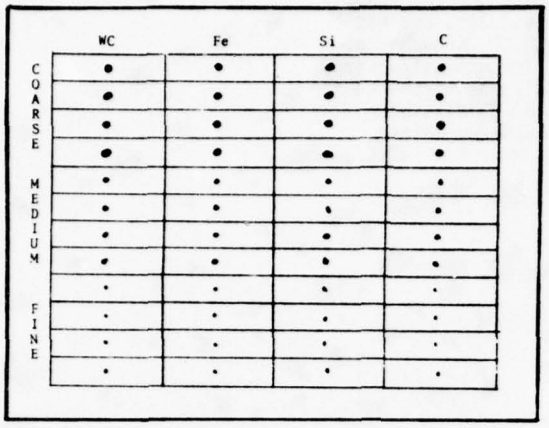

Fig. 1. Defect seeding plan for hot-pressed silicon nitride billets.

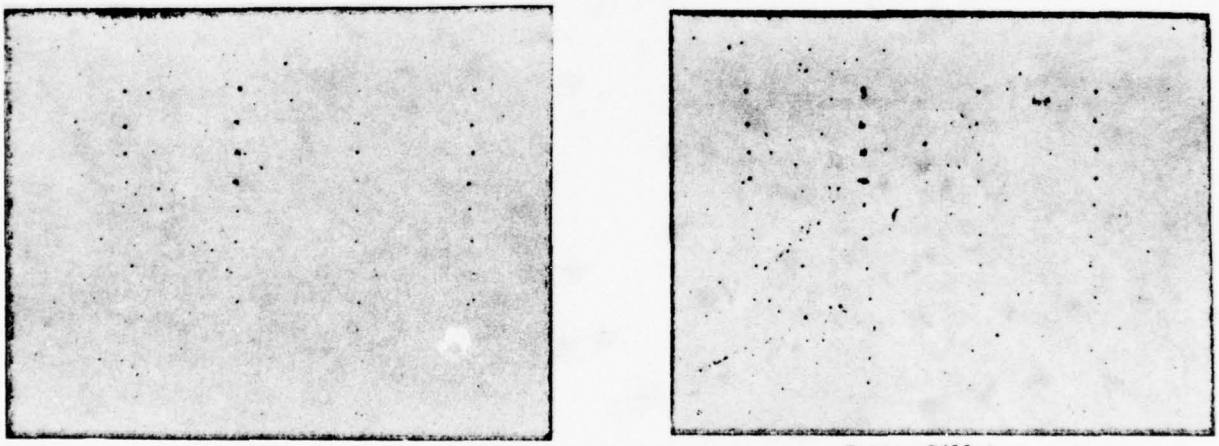

Top Billet

Bottom Billet

Fig. 2. Ultrasonic C-scan recordings at 25 MHz of defects in hot-pressed silicon nitride billets.

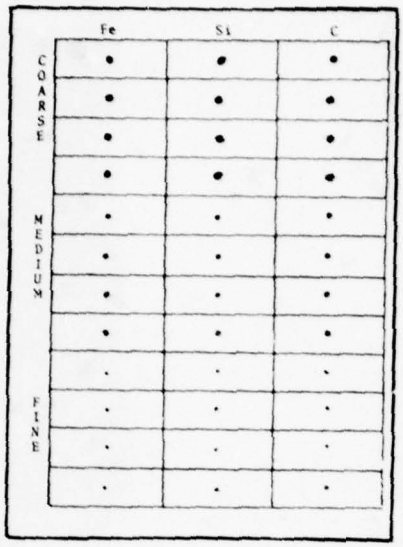

Fig. 3. Defect seeding plan for silicon carbide billet.

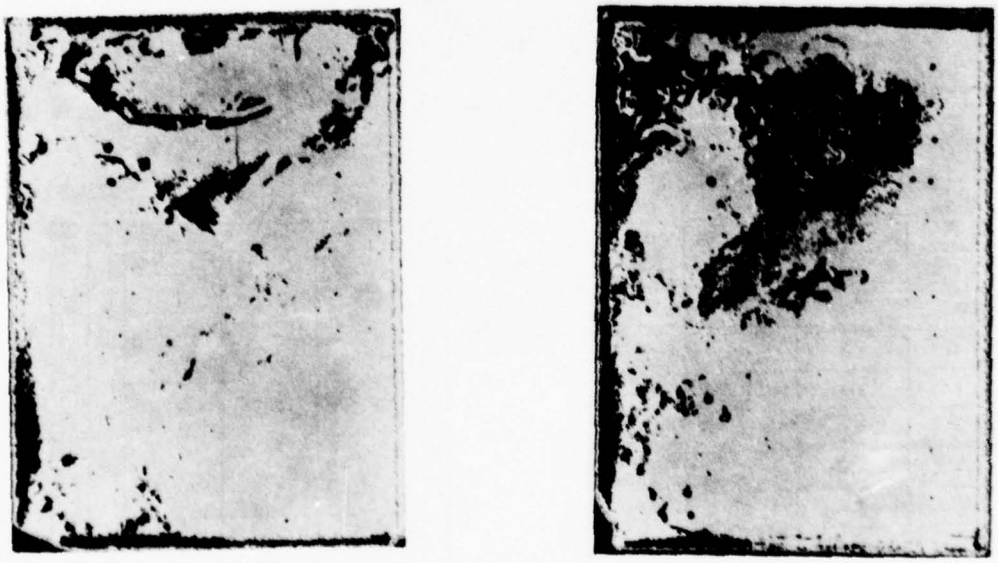

No. 1 Billet

No. 2 Billet

Fig. 4. Ultrasonic C-scan recordings at 25 MHz of defects in siliconized silicon carbide billet.

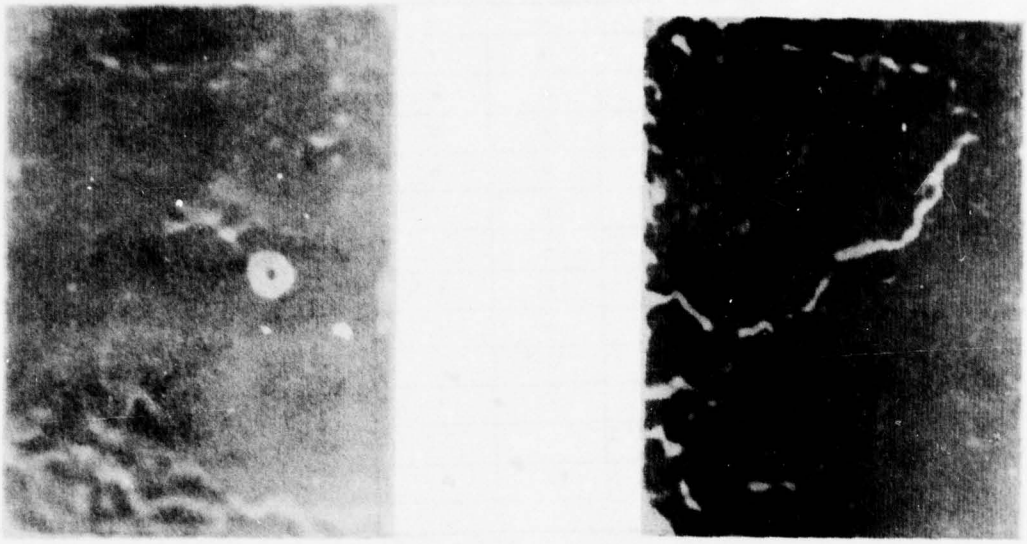

No. 1 Billet

No. 2 Billet

Fig. 5. Ultrasonic C-scan recordings at 15 MHz of attenuation changes in silicon carbide billets.

	Fe	Si	C
C	2.8	5.0	7.0
	3.0	6.0	7.6
	3.5	2.8	8.5
	2.3	2.9	8.4
	1.4	9.5	7.0
M	2.0	7.5	6.4
	2.8	6.2	6.2
	5.0	6.0	5.6
	6.2	5.4	5.4
F	4.9	4.9	4.6
	5.0	5.6	4.0
	5.1	2.4	2.0

Fig. 6. Variations in eddy current response of silicon carbide No. 2 billet.

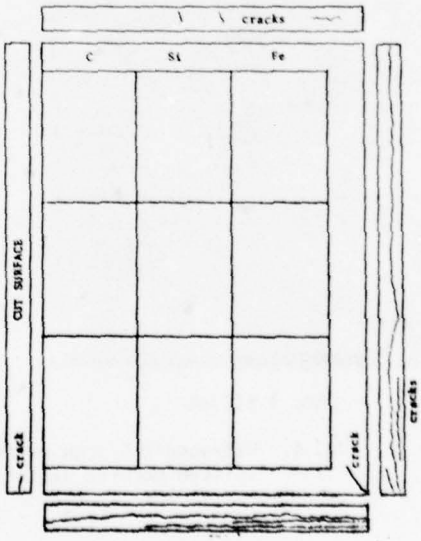

Fig. 7. Map of liquid penetrant indications of silicon carbide No. 2 billet, turned over.

Fig. 8. Black light photograph of fluorescent penetrant indications of silicon carbide.

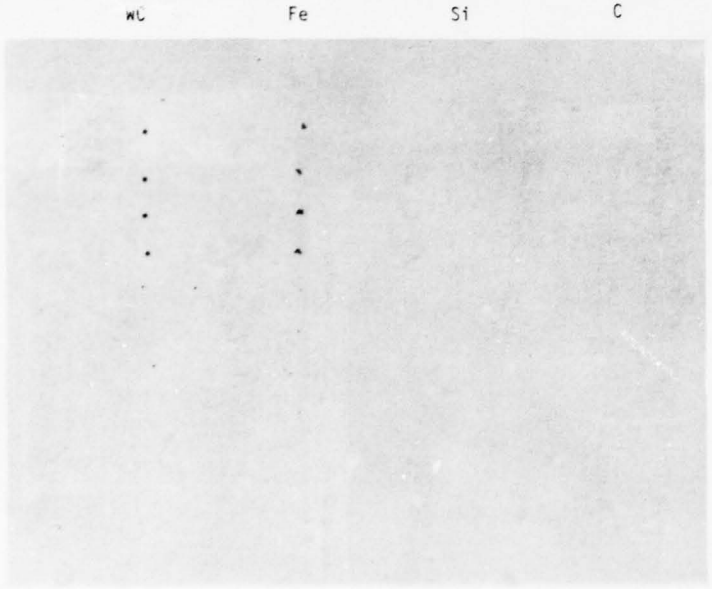

HPSN Top Billet

SiC No. 1 Billet

Fig. 9. Positive prints of radiographs of billets.

HPSN Bottom billet, medium size tungsten carbide inclusion, defect number (DN) 4.

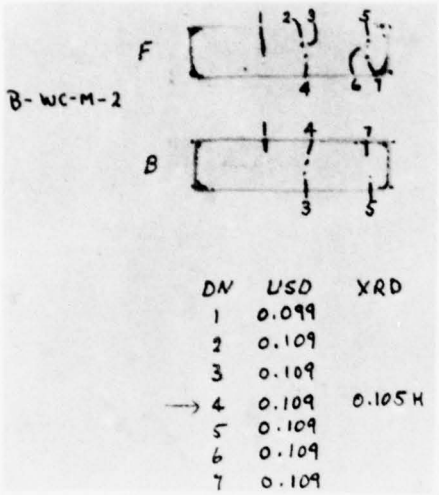

DN	USD	XRD
1	0.099	
2	0.109	
3	0.109	
→ 4	0.109	0.105 H
5	0.109	
6	0.109	
7	0.109	

HPSN Bottom billet, fine size iron inclusion, defect number (DN) 3, test temperature 1093°C.

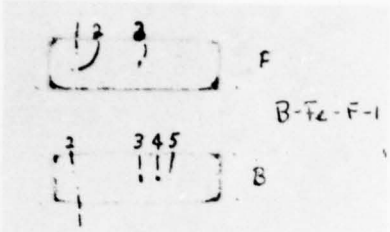

DN	USD	XRD
1	0.109	
2	0.109	
→ 3	0.109	0.105 H
4	0.118	
5	0.109	

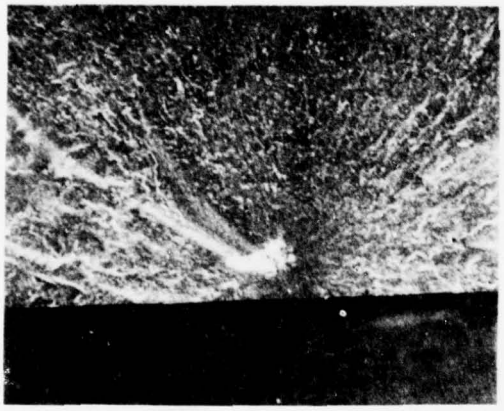

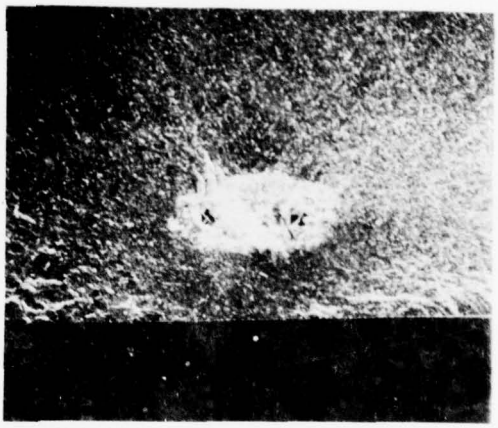

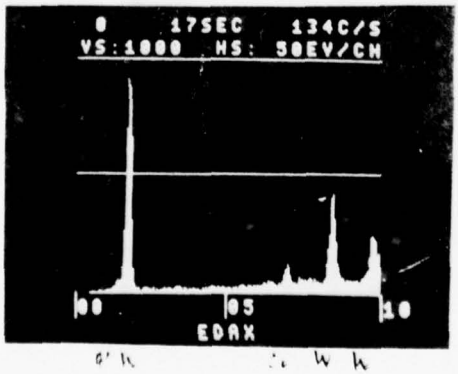

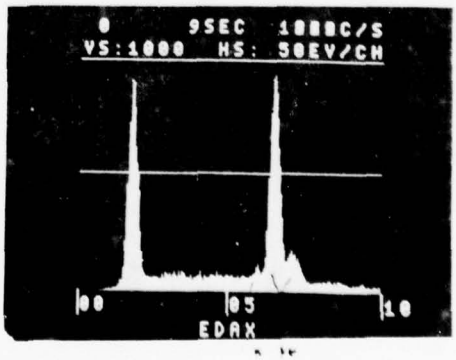

Fig. 10. C-scan (above), scanning electron microscope view of inclusion at fracture origin, 50X, (middle) and photograph of electron microprobe display (below) of hot-pressed silicon nitride bend bars.

SiC No. 1 Billet, coarse size iron inclusion, defect number (DN) 1.

SiC No. 2 Billet, medium size carbon inclusion, defect number (DN) 1, test temperature 1371°C.

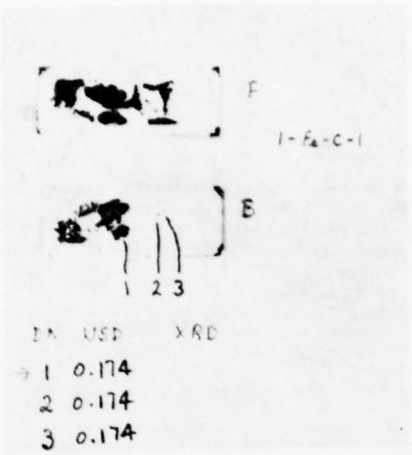

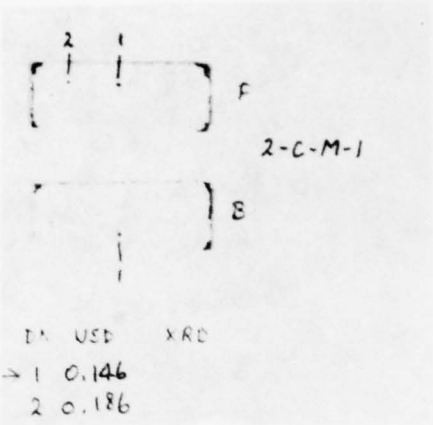

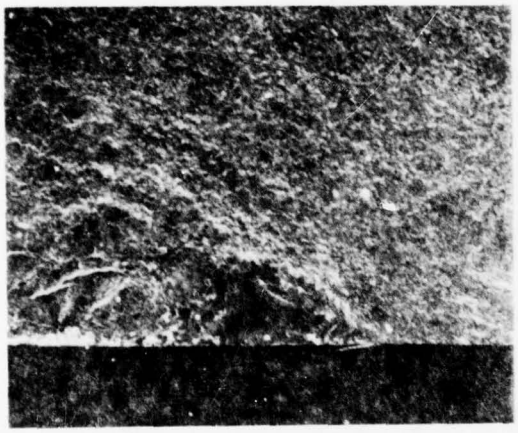

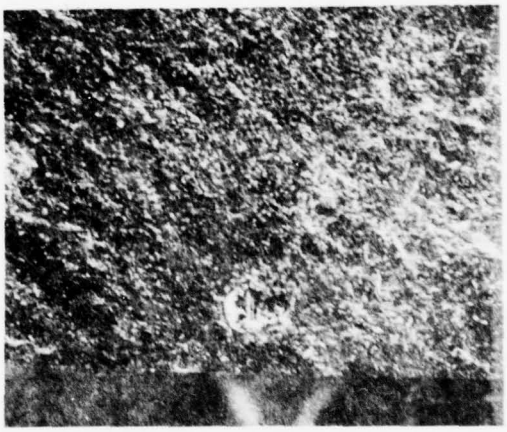

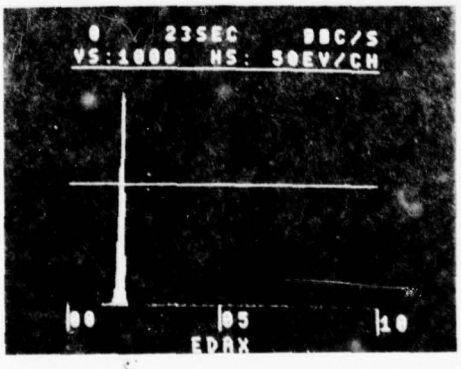

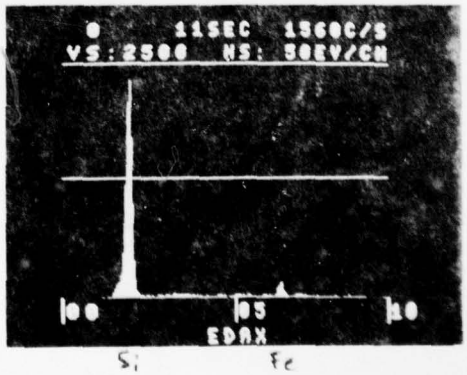

Fig. 11. C-scan (above), scanning electron microscope view of inclusion at fracture origin, 50X, (middle) and photograph of electron microprobe display (below) of silicon carbide bend bars.

MICROWAVE NDE OF CERAMICS

A. J. Bahr
SRI International
Menlo Park, California 94025

ABSTRACT

The objective of this work is to evaluate the potential of microwave techniques for detecting, classifying, and determining the dimensions of inclusions and surface cracks in structural ceramics such as Si_3N_4. Experimental results that show the feasibility of detecting various types of inclusions and voids in Si_3N_4 have been obtained, and these results are reviewed. In addition, the question of the quantitative capability of microwave NDE for this application is discussed.

INTRODUCTION

In recent years, the technology for generating and controlling electromagnetic energy at frequencies of 100 GHz and above has improved considerably, and such components are now readily available. In view of this fact, we have undertaken a program to assess the applicability of this technology to the NDE of ceramic materials and components.

We have found that Si_3N_4 is nearly transparent at these high frequencies, which permits the interior of components made from this material to be inspected using microwave energy. The dielectric constant of hot-pressed Si_3N_4 is about 7.5, so the wavelength in this material at 100 GHz is about 1 mm. This electromagnetic wavelength is comparable to the acoustic wavelength of 10 MHz ultrasound in this material. Thus, microwave C-scan images can have resolutions roughly comparable to those produced by commercial ultrasonic equipment, but do not require the use of a water bath or other coupling medium in order to achieve rapid scanning. In addition, electromagnetic and ultrasonic scattering will differ for a given flaw, and thus microwave NDE may provide better flaw discrimination in some cases.

EXPERIMENTAL RESULTS

Three typical experimental arrangements that are useful in microwave NDE are shown in Figure 1. All of these schemes make use of cross-polarized scattering in order to suppress the specular scattering from the surface(s) of the part being examined. Fig. 1(a) shows a transmission scheme that is suitable for inspecting low-loss dielectric materials. As indicated, video detection can be used, but, of course, this results in limited sensitivity. Figs. 1(b) and 1(c) show backscatter schemes that eliminate the requirement for precise alignment of the transmit and receive antennas, and which permit the inspection of both dielectric materials and metallic surfaces. The orthomode coupler is used to select the cross-polarized component in the backscattered wave. Super-heterodyne or homodyne detection provides a significant increase in sensitivity, with homodyne detection providing the most information about the scatterer (flaw).

Three different plates of Norton hot-pressed NC 132 containing seeded inclusions and voids were examined using the cross-polarized transmission technique. Fig. 2 shows a microwave C-scan of a portion of a plate containing 0.020" and 0.005" inclusions of WC, Fe, Si, and C. Fig. 2(a) shows the area covered by the scan and the intended flaw locations. Fig. 2(b) shows the portions of the scan area that produce a scattered signal greater than an arbitrarily selected threshold value. Finally, Fig. 2(c) shows the amplitude of the scattered signal as a function of position within the scan area.

Several features of this C-scan are noteworthy. First, all 0.020" flaws are detected. Iron provides the strongest signal, and is the only 0.005" flaw that is clearly detected in this figure (the other small flaws become more apparent if the frequency is changed). Second, X-rays show that diffusion of the iron inclusion during hot pressing produces an irregularly shaped scatterer that causes the spatial extent for this flaw to appear overly large in the microwave C-scan. Finally, it appears that a crack-like flaw is present between the 0.020-inch diameter iron and silicon inclusions. Apparently, X-ray, ultrasonic, and dye-penetrant examination by AMMRC did not reveal the presence of such a flaw. If this flaw is indeed found to be real, it would indicate the superior sensitivity of the microwave technique for detecting this type of flaw.

Fig. 3 shows a similar microwave C-scan, but for a Si_3N_4 plate containing different types and densities of inclusions. All of the 0.005" inclusions are detected in this scan, but, of course, the closer spacing between inclusions may enhance this detection.

In Fig. 4 we see another scan of the same plate as in Figure 3, but of only the area containing the 0.001" through 0.010"-diameter silicon inclusions. The sensitivity of our technique for the detection of unreacted silicon appears to be good, and may be better for this purpose than other techniques. This feature could be important in process-control application.

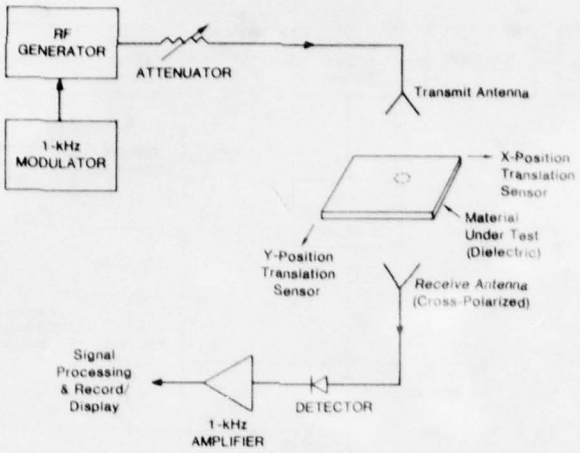

(a) CROSS-POLARIZED TRANSMISSION WITH VIDEO DETECTION (INCOHERENT)

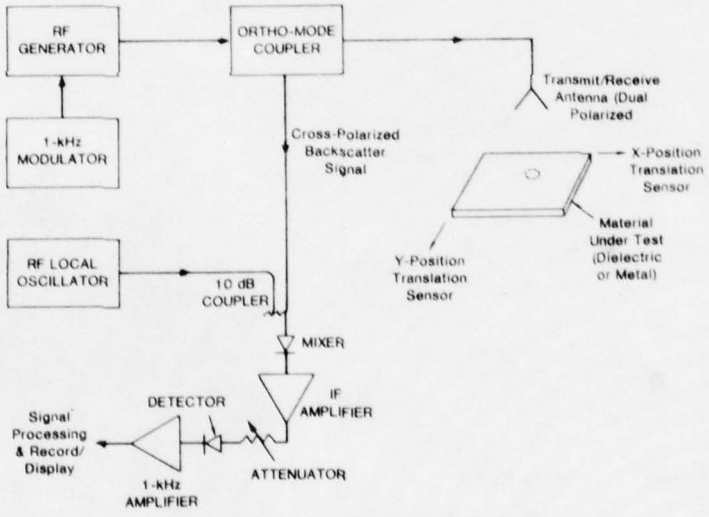

(b) CROSS-POLARIZED BACKSCATTER WITH SUPER-HETERODYNE DETECTION (INCOHERENT)

Fig. 1 Typical microwave NDE schemes

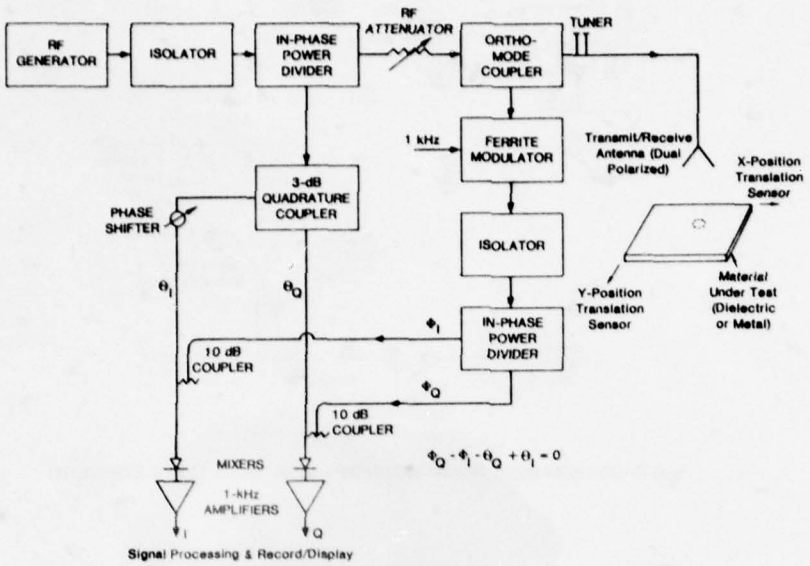

(c) CROSS-POLARIZED BACKSCATTER WITH HOMODYNE DETECTION (COHERENT)

Fig. 1 (Continued)

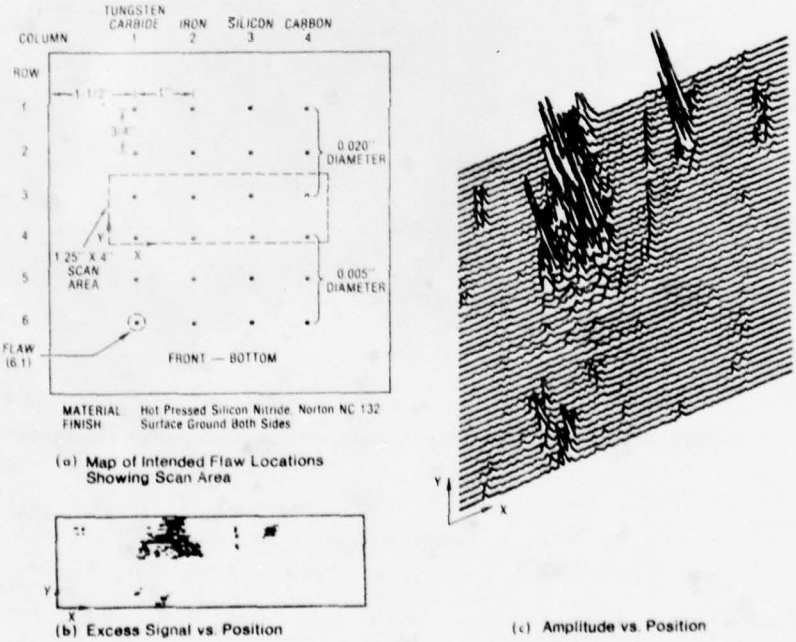

(a) Map of Intended Flaw Locations Showing Scan Area

(b) Excess Signal vs. Position

(c) Amplitude vs. Position

Fig. 2 Microwave cross-polarized-transmission C-scan of four types of inclusions in Si_3N_4 (frequency = 94 GHz)

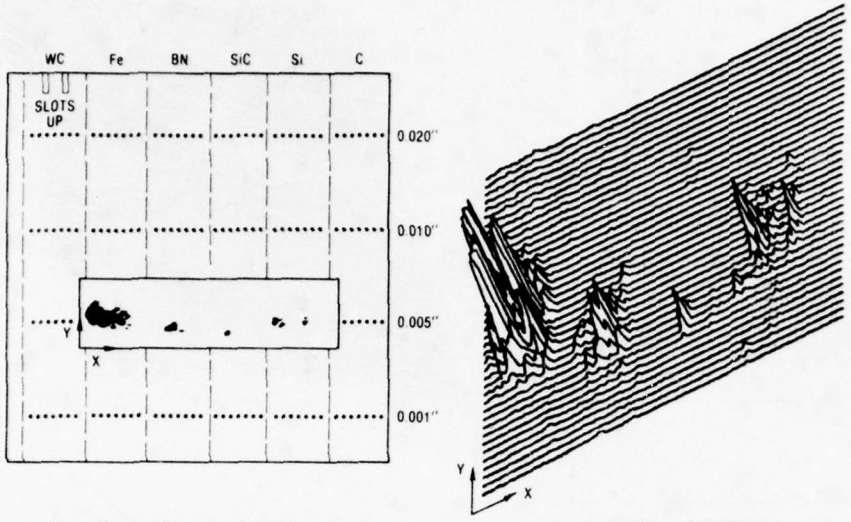

(a) Excess Signal vs. Position (b) Amplitude vs. Position

Fig. 3 Microwave cross-polarized-transmission C-scan of four types of inclusions in Si_3N_4 (frequency = 91 GHz)

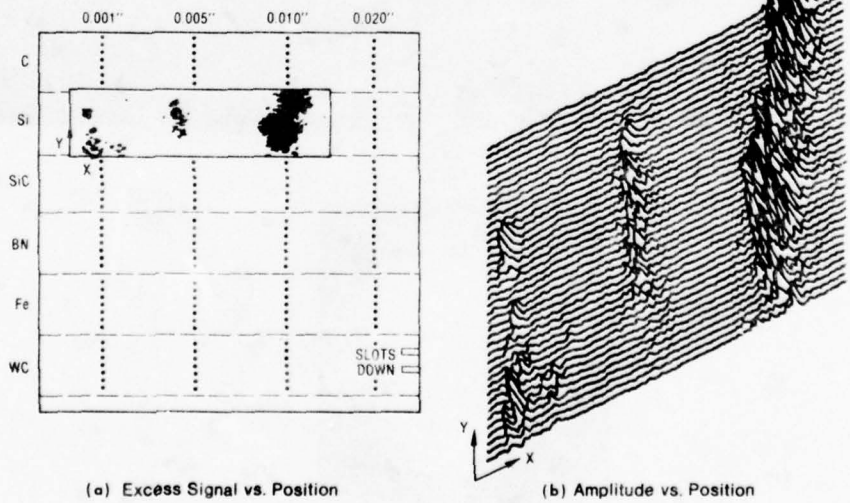

(a) Excess Signal vs. Position (b) Amplitude vs. Position

Fig. 4 Microwave cross-polarized-transmission C-scan of silicon inclusions in Si_3N_4 (frequency = 98 GHz)

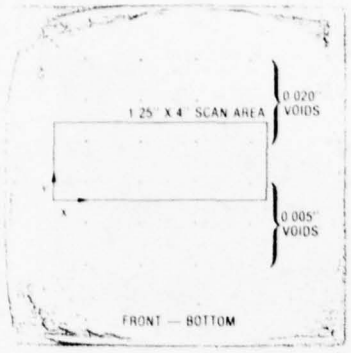

(a) Ultrasonic C-Scan (Focussed 25 MHz) Map Showing Void Locations and Scan Area

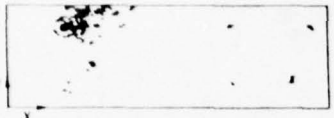

(b) Excess Signal vs. Position

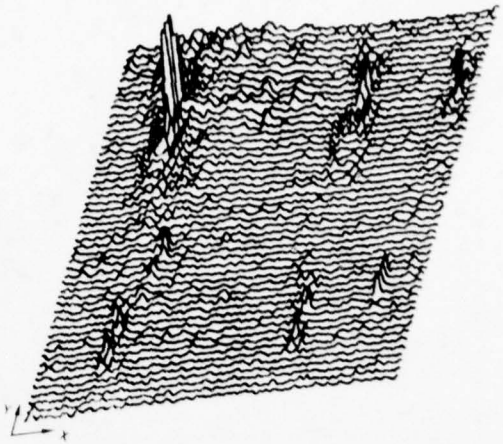

(c) Amplitude vs. Position

Fig. 5 Microwave cross-polarized-transmission C-scan showing voids in Si_3N_4 (Frequency = 94 GHz)

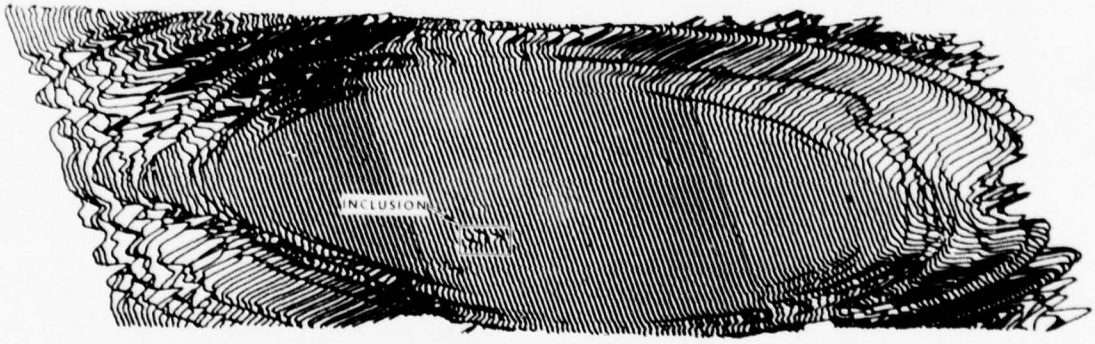

(a) Amplitude vs. position

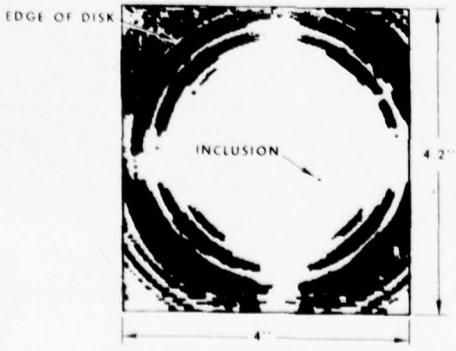

(b) Excess signal vs. position

Fig. 6 Microwave cross-polarized-transmission C-scan of 4" -Diameter hot-pressed Si_3N_4 disk (frequency = 94.4 GHz)

The data shown in Fig. 5 demonstrates our ability to detect small voids in Si_3N_4, as well as inclusions. The voids were formed in the interior of a 0.250"-thick plate by first drilling small holes in a 0.125"-thick plate, and then diffusion bonding this plate to a second 0.125"-thick plate. The voids that were not detected by microwaves were also weakly imaged in an X-ray, indicating that these particular holes probably were filled with some kind of material.

A hot-pressed Si_3N_4 billet in the form of a surface-ground disk was also examined using microwaves. The results are shown in Fig. 6. X-rays showed the presence of an unintended high-density inclusion in the disk, and this flaw is detected in the microwave C-scan. This experiment also shows the effect of diffraction near a sharp edge. The cross-polarized scattering from an edge is quite strong, and can be detected at a significant distance from the edge.

We conclude from these results that microwave techniques can be used to detect typical flaws that occur in ceramic materials like Si_3N_4, provided that the flaws are not located near a sharp edge.

QUANTITATIVE MICROWAVE NDE

Measurements aimed at assessing the quantitative potential of microwave NDE for ceramics using a homodyne backscatter system are planned for the near future. However, it is possible to make some general statements about the quantitative capability of microwave NDE without having specific experimental results.

In general, there are two basic approaches to the utilization of scattering data. One approach is to measure the scattered power in one direction and at one frequency, i.e., the scattering cross section, and to attempt to gain information about the flaw from this single number. The other approach can be called imaging, where the scattered power (or amplitude and phase of the scattered field) is measured over a range of directions and/or frequencies.

The measured value of scattered power in one direction depends on:

- The dimensions of the scatterer.
- The constitutive properties (dielectric constant, conductivity, etc.) of the scatterer.
- The characteristics of the transmitter and receiver, as determined at a given distance from the scatterer.

Therefore, quantitative NDE using cross section measurements requires either:

- Statistical calibration using characterized flaws in a fixed size and shape of test piece, or
- An accurate scattering theory for the flaws of interest.
- Determination of the transmitter/receiver characteristics by theory or calibration.
- Negligible (or predictable) scattering from the boundaries of the test piece.
- a priori information on all but one of the independent dimensional and constitutive parameters of the flaw.

It would appear that statistical calibration is the more feasible approach in this case.

In the case of imaging, it is sufficient to discuss two types: A-scan and C-scan. A-scan imaging involves the use of a short pulse (or many coherent frequencies) to measure the length and profile of the scatterer along the direction of propagation. Under some conditions the type of flaw may also be deducible from this measurement.

Quantitative A-scan imaging of typical internal flaws in ceramics is not feasible using microwaves. For example, even with a carrier frequency of 100 GHz, the best achievable resolution is still only on the order of 10 mm.

In C-scan imaging the transverse dimensions of the scatterer are measured by scanning the test piece (or the transmit/receive beam) perpendicular to the direction of propagation. With a microwave system it is possible to obtain a focused beam whose width is about one wavelength. For example, this width would be about 3 mm at 100 GHz.

Thus, a CW microwave C-scan imaging system can give a quantitative indication of the transverse dimension of flaws that are larger than about 3 mm and that are located several mm from the test-piece boundaries in the transverse plane. It should be noted again, however, that flaws much smaller in size can be detected by such a microwave system.

ACKNOWLEDGMENT

This research was sponsored by the Army Materials and Mechanics Research Center under Contract DAAG46-76-C-0048 and by the Center for Advanced NDE operated by the Rockwell International Science Center under Contract F33615-74-C-5180.

DEFECT CHARACTERIZATION IN CERAMICS USING HIGH FREQUENCY ULTRASONICS

G. S. Kino, B. T. Khuri-Yakub, Y. Murakami, and K. H. Yu
Stanford University
Stanford, California 94305

ABSTRACT

A high frequency A-scan system (150-450 MHz longitudinal, 150-300 MHz shear) has been used to characterize defects in ceramics. An Indium bonding technology has been developed to make broadband, and efficient transducers. Defect characterization is done by comparing the time domain backscattered signals from defects to theory. A Wiener filter is used in order to correct the response of the transducer and the propagating medium, and thus give the impulse response of real defects. A good agreement between theory and experiment is obtained for inclusions such as voids, WC, and SiC in Si_3N_4.

INTRODUCTION

Ceramic materials such as Si_3N_4 and SiC are becoming increasingly important structural materials because of their high strength, and high temperature capabilities. However, because ceramic materials are brittle, it is important to detect small inclusions in the size range of 10 - 100 μm. For this purpose we design our A-scan system to operate in the frequency range of 150 - 500 MHz with longitudinal wave transducers and in the range of 150 - 300 MHz with shear wave transducers.

In this work we describe pulse echo techniques and backscatter measurements as a function of frequency conducted on flaws in ceramics (Si_3N_4). We are concerned with comparing the reflected echo signals to theoretical calculations of scattering from flaws as a function of frequency. Alternatively, we are interested in the backscattered signal as a function of time due to an incident narrow acoustic base band pulse, which at least in theory has the form of a δ function.

We describe, in this paper how we have used Wiener filtering techniques to correct for the transducer response variation as a function of frequency and obtain after processing very narrow pulses. We correct not only for defects in the transducer characteristic itself, but also for distortion of the signals by the contacting system employed and by the attenuation in the sample varying with frequency. By this means we can use the corrected pulse to probe a flaw and the output signal obtained shows the true time domain response from the flaw, which can then be compared to theory. Experimental results obtained with real defects such as WC in Si_3N_4, and vacancies in Si_3N_4 are presented and used to predict the type and size of the defects.

The transducers used in our work were originally made by rf sputtering an 8 μm thick zinc oxide (ZnO) film on a sapphire (Al_2O_3) buffer rod.[1] The transducers thus obtained are longitudinal wave transducers resonant at a center frequency of 300 MHz. In order to achieve more efficient, and broadband transducers, we developed an Indium (In) bonding technology.[2] With In bonding, we can use single crystal piezoelectric materials such as Lithium Niobate ($LiNbO_3$), and we can make either longitudinal or shear wave transducers. A schematic diagram of an In bonded transducer is shown in Fig. 1. The Titanium (Ti) and Gold (Au) layers are first evaporated on the surfaces to be bonded. The samples are then placed in a vacuum station where In is evaporated, and the surfaces pressed against each other with a pressure of 500 kg/cm^2, without breaking the vacuum. The In and Au form an alloy which makes a very strong cold bond. The piezoelectric material is then polished to the desired thickness for operation in the frequency range of interest. The impulse of an In bonded, $LiNbO_3$ on Silicon Nitride (Si_3N_4) shear wave transducer is shown in Fig. 2. The untuned two-way insertion loss of the transducer of Fig. 2 is shown in Fig. 3. A loss of 4 dB is due to diffraction, and propagation loss in the Si_3N_4 buffer rod.

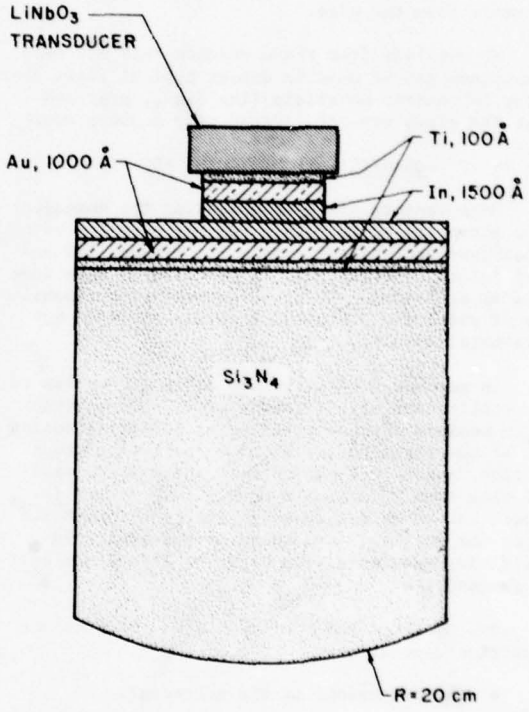

Fig. 1. Schematic diagram of Indium bonded transducer.

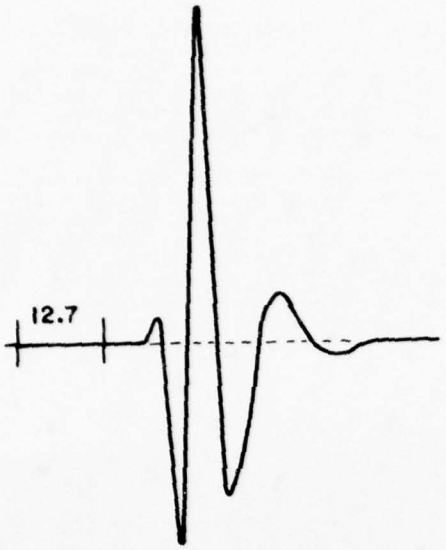

THEORETICAL IMPULSE RESPONSE

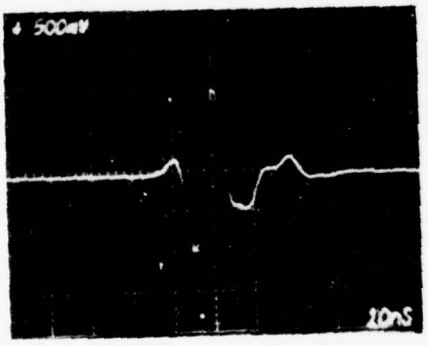

Fig. 2. Impulse response of $LiNbO_3/Si_3N_4$ shear wave Indium bonded transducer.

A schematic diagram of the A-scan system used in our study is shown in Fig. 4. The bottom end of the buffer rod is polished with a radius of curvature of 20 cm. Contact to the ceramic under study is made by pushing the curved end of the buffer rod against the ceramic without using a contacting layer such as gold.[3] The transducer is excited with a 30 V, 2 nsec electric pulse in order to obtain broad bandwidth operation.

The received signal at the transducer is passed into a sampling oscilloscope which yields an output which is a slowed down version of the pulse, a Biomation analog-to-digital converter is used to sample the slowed down pulse and digitize it for insertion into a PDP 11-10 minicomputer. The computer is used to take fast Fourier transforms and correct the received signal.

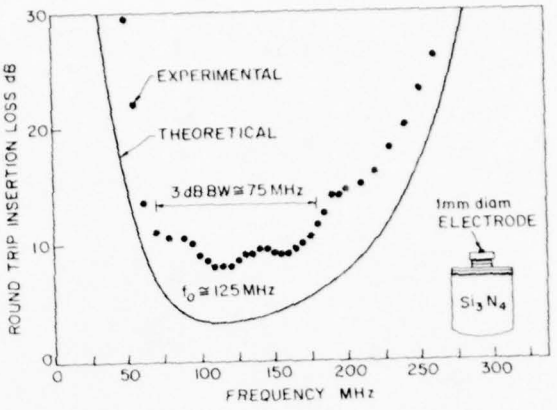

Fig. 3. Two-way insertion loss of a delay line with the transducer of Figs. 1 and 2.

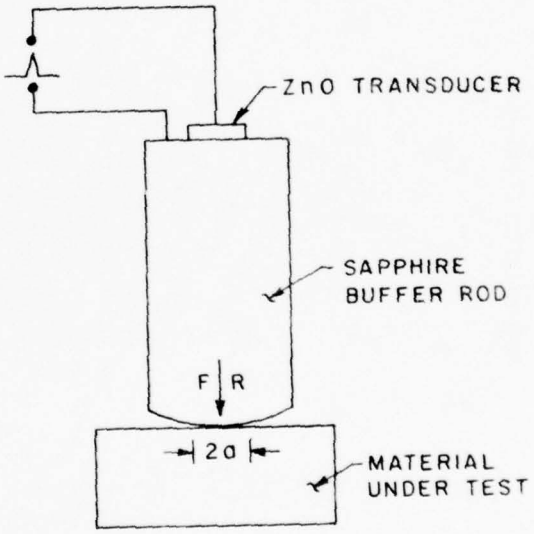

R = 20 cm
2a = .1 cm
F = 172 N ≅ 39 Lbs.

Fig. 4. Schematic of A-scan system.

The frequency response $X(\omega)$ of the transducer pulse is calculated by carrying out a 512 point Fast Fourier Transformation (FFT). Time and frequency responses to our transducer are shown in Figs. 5(a) and 5(b), respectively. Ideally we would like to correct the transducer response by constructing an inverse filter with a response $1/X(\omega)$. However, at frequencies where $X(\omega) \to 0$

the filter would not be realizable. Instead we have designed a Wiener filter with a response

$$W(\omega) = \frac{X^*(\omega)}{X(\omega)\,X^*(\omega) + N^2} \qquad (1)$$

where N^2 is the noise level in the system. In the computation we set N^2 at an arbitrary but constant level, for simplicity.

From the formula (1), it is apparent that the total bandwidth above the arbitrary noise level of the transducer is being used instead of the 3 dB bandwidth; thus we can utilize the 10 dB or even 20 dB bandwidth of the transducer, and considerably improve the depth resolution by this technique. It will be noted that if $X(\omega)X^*(\omega) \gg N^2$, $W(\omega) \to 1/X(\omega)$, i.e., the system behaves like an inverse filter.

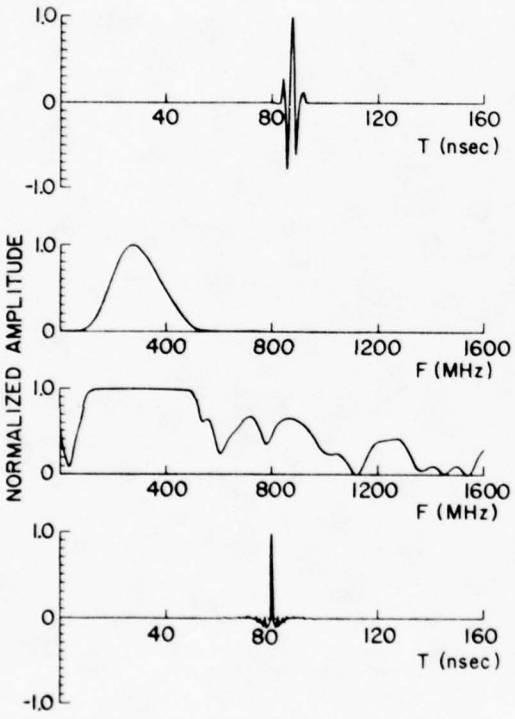

Fig. 5. Design of Wiener filter:
(a) Impulse response of $ZnO/A\ell_2O_3$ transducer.
(b) Frequency response of $ZnO/A\ell_2O_3$ transducer.
(c) Frequency response of $ZnO/A\ell_2O_3$ transducer after passing through the Wiener filter.
(d) Impulse response of $ZnO/A\ell_2O_3$ transducer after passing through the Wiener filter.

The output signal of the transducer pulse passed through this filter is calculated by multiplication in the frequency domain followed by the Inverse Fourier Transformation. As shown in Figs. 5(c) and 5(d) this output signal is uniform over a wide frequency range and is very close to a δ-function. Thus, we can effectively eliminate the defects in the transducer response, increase its effective bandwidth, and improve the impulse response and depth resolution by using a Wiener filter.

The picture in Fig. 6 shows the reflected pulse from an unknown defect in a silicon nitride ceramic. The adaptive filter technique was applied to the reflected signal in order to evaluate this defect. The output signal passed through the filter is shown in Fig. 7(a); its time domain response is compared with the theoretical response of a WC inclusion in Si_3N_4 shown in Fig. 7(b).

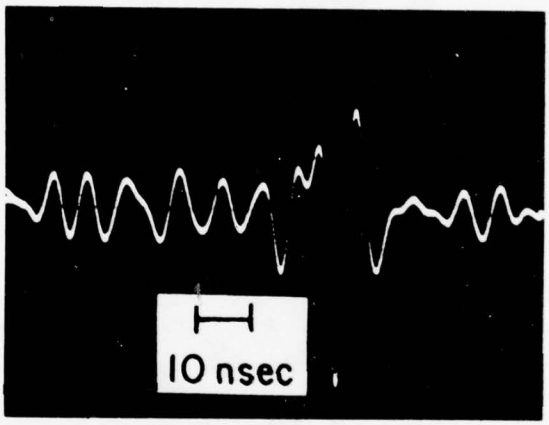

Fig. 6. Backscattered signal from an unknown inclusion in Si_3N_4.

Comparing Figs. 7(a) and (b), we conclude that the scattering from the unknown inclusion shown in Fig. 6 is equivalent to a WC sphere with a diameter of 90 μm. This result was obtained by measuring the delay between the front and back surface echoes in the time domain.

The normalized amplitude of the front surface echo from a spherical surface can be shown to have the following dependence[4]:

$$S_{11} \propto \frac{a\Gamma}{Z^2}$$

where a is the radius of the sphere, Γ is the reflection coefficient due to impedance mismatch, and Z is the distance from the transducer to the defect. By comparing the amplitude of the front surface echo to that of a hemispherical void drilled in the back of a piece of ceramic, we can make another estimate of the size of bulk defects. In the case of the defect shown in Fig. 6, we calculate a diameter of 100 μm. This result is in agreement with the size estimate from the time domain analysis.

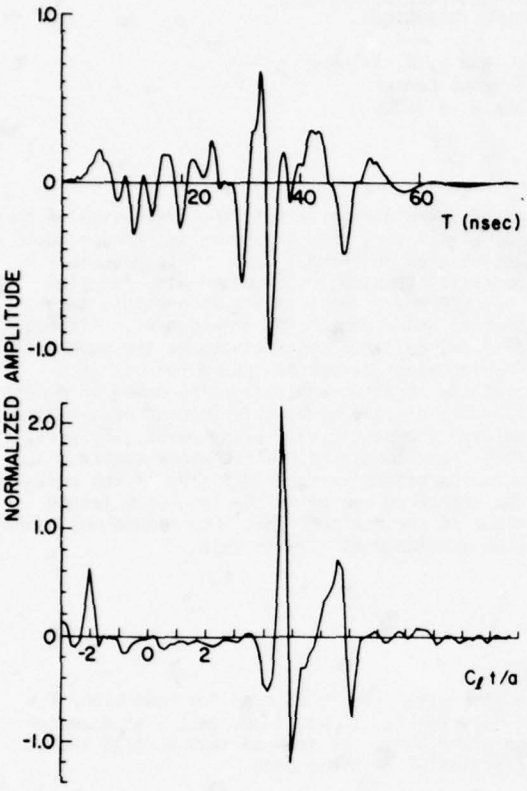

Fig. 7. Comparison of impulse responses in the time domain.
(a) Defect in Fig. 6.
(b) Theoretical WC inclusion.

The silicon nitride sample has been lapped down to the defect. The defect was found out at exactly the same location where we predicted, and its size was measured to be 160 μm diameter compared to our estimated 90 - 100 μm diameter. However the material within the defect has been analyzed by using X-ray spectroscopy, and turned out to be a two-phase mixture of Tungsten DiSilicide (WSi_2) and Silicon Carbide (SiC). Interestingly enough in our experimental time domain results shown in Fig. 7(a) there are extra peaks in the response between the two main pulses expected in the theory; this appears to be associated with the two-phase nature of the inclusion.

We note that our experimental measurement only gave a reasonable estimate of the size of the inclusion. But there was some error because the material of the inclusion had a higher velocity than expected for Tungsten Carbide. Thus we see that basically the technique determines the transit time of waves through the sample and the impedance mismatch at the sample. But other techniques such as low frequency angular scattering imaging measurements may be needed to supply one extra piece of information, the size or the density of the defect to allow all its parameters to be evaluated accurately.

A major advantage of the present technique over X-ray methods is that it very easily determines if the inclusion is in contact with the surrounding medium. Other samples of Tungsten Carbide in Silicon Nitride showed up in microfocus X-ray measurements, but behaved like vacancies acoustically. When they were lapped down, the Tungsten Carbide was found to be supported from the surrounding medium only by a small fillet.

Finally, this high frequency technique appears to yield information on the uniformity of the inclusion. In one case where a two-phase material was present, scattered signals from within the inclusion were clearly observed.

ACKNOWLEDGEMENTS

The work reported in this paper was supported by the Advanced Research Projects Agency through the U.S. Air Force under subcontract from Rockwell International under Contract RI74-20773.

REFERENCES

1. B. T. Khuri-Yakub and G. S. Kino, "Acoustic Pulse Echo Measurements at 200 MHz," Appl. Phys. Letters 30, 2 (15 January 1977).

2. C. Lardat, Thomson CSF, Cagnes-Sur-Mer, Private Communication.

3. S. Burns, J. Tien, B. T. Khuri-Yakub, and G. S. Kino, "Acoustic Coupling into an Elastic Solid by Hertz Contact Stresses," in press.

4. G. S. Kino, "The Application of Reciprocity Theory to Scattering of Acoustic Waves by Flaws," J. Appl. Phys. 49(6) (June 1978).

INSPECTION OF CERAMICS INCORPORATING SIZE ESTIMATION METHODS USING CONVENTIONAL ULTRASONICS

G. A. Alers, R. C. Addison, Jr. and L. A. Ahlberg
Rockwell International Science Center
Thousand Oaks, California 91360

ABSTRACT

One of the principal characteristics of the inspection of ceramic materials is the small size of the critical defects involved. In order to meet this challenge, either very high frequency techniques must be developed or conventional (low frequency) techniques must be used in special ways. This paper addresses the latter approach by investigating the use of commercial transducers combined with focusing techniques in a water bath at frequencies in the range of 5 to 20 MHz as well as signal analysis techniques using plane waves in the 30 to 40 MHz range using special order commercial transducers. Although the high velocity of sound in the ceramics used (silicon nitride) put some restrictions on the numerical aperture which could be obtained with acoustic lenses, a focused beam ultrasonic system for use in a water bath was designed and used to produce maps which showed the location and reflecting power of defects in flat ceramic specimens. Subsequent analysis of the reflectors discovered by this focused beam system was carried out by a hand-held ultrasonic probe which irradiated the sample with plane waves. By performing Fourier analysis of the echo signals from the "defects" and comparing the frequency spectrum observed with calculated spectra, it was possible to estimate the effective spherical size of the scattering objects. Analysis of the frequency dependence of the scattered energy in the long wave length limit also provides a measure of an effective spherical volume of the scatterer but this method was found to require additional signal processing methods which will be developed at a later date.

BACKGROUND

As described on Poster 1, the basic problem with inspection of ceramic materials arises from the fact that the critical defects are small (of the order of 100 microns). Thus the ultrasonic reflections are expected to be small and near the noise level not only because of the defect's geometric size but also because the wave length of the sound wave (of the order of 500 microns at 20 MHz) is larger than the defect. Furthermore, the estimation of the size and fracture mechanics parameters of the defect from analysis of the long wave length limit of the reflected energy requires accurate, quantitative data analysis that is a demanding process even with large signals. To overcome these drawbacks, two approaches are available. One is to increase the amount of ultrasonic scattering by increasing the ultrasonic frequency in order to make the wave length equal to or less than the defect dimensions. The other is to enhance the low frequency scattering by focusing more incident energy onto the defect. The former approach is described elsewhere[1] while the objective of this paper is to investigate the latter approach and to demonstrate the capabilities listed on the bottom of Poster 1.

Poster 2 describes the considerations necessary for implementing a focused ultrasonic beam technique for inspection of a ceramic plate. The demanding circumstance here is the unusually high ultrasonic velocity in the silicon nitride ceramic material which causes the outermost rays from the focusing transducer to be refracted strongly to a focus that is closer to the front surface than the focal point for the more centrally located sound rays. In order to minimize this effect (which is equivalent to spherical aberration in optics), the diameter or aperture of the transducer should be kept small or a liquid with a higher sound velocity than water should be used for immersion. For our experiments, it was found that a ½" diameter transducer had to be stopped down to 5/16 inches since a water bath was used.

Poster 3 describes a second and very important consideration that appears when low frequency ultrasonic waves are used either for convenience or for obtaining scattering data in the long wave length limit.[2] Under these conditions, the tail of the echo from the top surface of the sample may well still be present at the time of arrival of the defect echo so the two signals appear superimposed on one another and quantitative measurements of the defect echo are rendered very inaccurate. To circumvent this problem and to develop an accurate measure of the defect echo alone, the waveform characterizing the tail of the front surface echo and any other background noise was measured by moving the transducer to a defect free region and the computer was programmed to subtract this background signal from the defect plus background waveform. An example of the waveforms observed, and the results of the subtraction process are shown on the right side of Poster 3.

Once a "defect free" or background waveform had been established and stored in the computer, it could be used to subtract from all waveforms taken at different locations on the sample. Our computer was programmed to deduce and record the peak-to-peak amplitude of any signal found in a time interval chosen to encompass the region in which the sound was focused along with the X-Y coordinates of that region. From this data, a map such as the one shown in Poster 4 was made by printing X symbols with a density proportional to the signal amplitude at each coordinate location.

Following the establishment of the locations and relative scattering powers of the defects, the

ultrasonic inspection system shown in block diagram form on Poster 5 was used to irradiate the defect with high frequency, broad band, plane waves and to digitally analyze the reflected echoes. By using a sapphire buffer rod between the transducer and the sample, more energy could be delivered to the defect and far field approximations could be justified. Note that the transducer used in this system permits scattering versus frequency data to be obtained over a band of frequencies extending from below 10 MHz to above 40 MHz.

Some results of this analysis applied to echoes reflected from voids intentionally placed in silicon nitride samples are shown on Poster 6 where both theoretical and experimental curves of frequency versus reflected intensity are displayed. For voids, theoretical calculations[3] show that the first maximum in reflectivity occurs at ka = 1.05 which corresponds to a frequency of 7.5 MHz for a 500 micron void and 15 MHz for a 250 μ void. The experimental data obtained on voids presumed to be of these dimensions are shown at the bottom of Poster 6. The sample containing the 500 micron void was sectioned and the void shown in the photomicrograph was uncovered at the expected location. Its actual diameter was measured to be 580 $\pm$ 10 microns in reasonable agreement with the expectations based on the scattering data. The conclusions reached by this study were that a commercial transducer could be fitted with a lens for operation in a conventional water bath so that a moderately high resolution map of the interior defects in silicon nitride could be generated. Because the defect echoes were small and not well separated in time from the front surface echo, special signal processing methods had to be incorporated into an on-line computer in order to make these maps. Once the defect locations were determined, the approximate size of the defect could be successfully inferred from the frequency dependence of the reflectivity measured with a specially designed, plane wave transducer equipped with a buffer rod.

ACKNOWLEDGMENT

This research was sponsored by the Center for Advanced NDE operated by the Science Center, Rockwell International, for the Advanced Research Projects Agency and the Air Force Materials Laborabory under contract F33615-74-C-5180.

REFERENCES

1. G. S. Kino, B. T. Khuri-Yakub, Y. Murakami, and K. H. Yae, "Bulk Defect Characterization in Ceramics," Review of Progress in Quantitative NDE, La Jolla, 1978.
2. J. R. Rice, "Long Wavelength Defect Evaluation." Ibid.
3. J. M. Richardson, "Direct and Inverse Problems Pertaining to the Scattering of Elastic Waves in the Rayleigh (Long Wave) Regime." Ibid.

THE INSPECTION OF CERAMIC MATERIALS AT FREQUENCIES BETWEEN 10 AND 50 MHz PRESENTS SEVERAL PROBLEMS TO BE OVERCOME:

- THE CRITICAL DEFECTS ARE SMALL SO SIGNAL-TO-NOISE RATIOS ARE SMALL.
- LOW SIGNAL-TO-NOISE RATIO SIGNALS REQUIRE SPECIAL DATA PROCESSING TECHNIQUES.
- DEFECT SIZE ESTIMATION BY LONG WAVELENGTH SCATTERING REQUIRES SUBTRACTION OF LOW FREQUENCY COMPONENTS OF EARLIER REFLECTIONS IN THE SAMPLE.
- LACK OF WELL CHARACTERIZED REFERENCE SCATTERING CENTERS IN CERAMICS HINDERS ESTABLISHMENT OF DATA PROCESSING ROUTINES.

THESE PROBLEMS WERE ATTACKED IN THIS TASK BY THE FOLLOWING TECHNIQUES:

1. USE FOCUSSED TRANSDUCERS TO IMPROVE SIGNAL TO NOISE RATIOS AND TO LOCALIZE SCATTERNG CENTERS.
2. USE COMPUTER CONTROLLED SCANNING OF SAMPLES IN A WATER BATH TO PRODUCE MAPS SHOWING DEFECT LOCATIONS.
3. USE DIGITAL SUBTRACTION OF BACKGROUND NOISE TO BETTER DEFINE DEFECT REFLECTION SIGNAL.
4. USE DIGITAL FOURIER ANALYSIS OF SIGNALS TO ESTABLISH THE FREQUENCY DEPENDENCE OF THE SCATTERED ENERGY.
5. USE THE FIRST MAXIMUM IN THE FREQUENCY DEPENDENCE OF THE SCATTERED ENERGY TO ESTIMATE THE DEFECT SIZE.

Poster 1 The problem and approach used for the detection, location and characterization of small defects in ceramic plates.

WE WANT TO FOCUS THE ACOUSTIC BEAM TO LOCALIZE THE DEFECT AND *DISTINGUISH* BETWEEN MULTIPLE DEFECTS

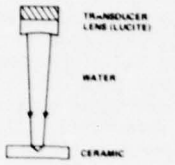

THE CERAMIC SAMPLE IS PLACED IN A WATER BATH AND THE ACOUSTIC BEAM IS FOCUSED WITH A LUCITE LENS. THE FOCAL LENGTH OF THE LENS IN WATER IS 38.1 MM (1.5 IN.)

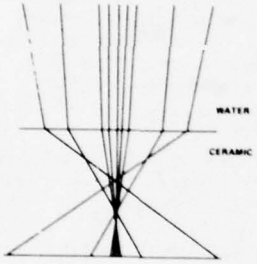

THE PARAXIAL RAYS OF THE FOCUSED BEAM FOCUS AT A SINGLE POINT. FOR LARGER CONVERGENCE ANGLES, THE RAYS FOCUS AT POINTS CLOSER TO THE LENS. THE ERROR, SPHERICAL OBSERVATION, IS LIMITED BY RESTRICTING THE APERTURE OF THE LENS.

RESOLUTION CONSIDERATIONS

THE RESOLUTION OBTAINED INCREASES AS THE CONVERGENCE ANGLE INCREASES. THE MAXIMUM CONVERGENCE ANGLE IS LIMITED BY SPHERICAL ABERRATION AND DEPENDS ON THE RELATIVE ACOUSTIC VELOCITIES IN THE WATER AND THE CERAMIC. FOR A GIVEN CONVERGENCE ANGLE, THE SPHERICAL ABERRATION CAN BE REDUCED BY DECREASING THE RATIO BETWEEN THE CERAMIC VELOCITY AND THE SURROUNDING LIQUID. A HIGH VELOCITY LIQUID SUCH AS LIQUID GALLIUM WILL PERMIT A LARGER CONVERGENCE ANGLE TO BE USED WHILE MAINTAINING NEGLIGIBLE SPHERICAL ABERRATION.

THE OTHER METHOD FOR INCREASING THE RESOLUTION IS TO INCREASE THE FREQUENCY. THE ULTIMATE LIMITS THAT CAN BE ACHIEVED IN THIS DIRECTION HAVE NOT BEEN FULLY EVALUATED.

Poster 2 Description of the problems faced when designing a lens for use on silicon nitride samples immersed in water.

PROBLEM:

THE RINGING FROM THE FRONT SURFACE ECHO BECOMES MIXED IN WITH THE SIGNAL FROM THE DEFECT AND CAUSES ERRORS IN THE APPARENT PEAK TO PEAK AMPLITUDE OF THE DEFECT SIGNAL.

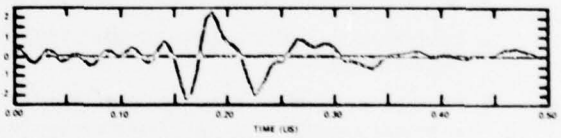

DEFECT SIGNAL + COHERENT NOISE

SOLUTION:

OBTAIN A REFERENCE WAVEFORM FROM A REGION OF THE PART THAT IS FREE OF DEFECTS AND DIGITALLY "SUBTRACT" THIS WAVEFORM FROM THE WAVEFORM CONTAINING THE DEFECT SIGNAL. RESULTS OF USING THIS TECHNIQUE ARE SHOWN BELOW.

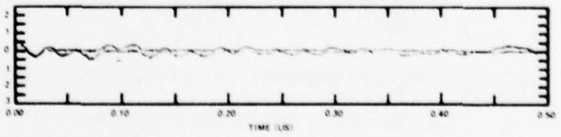

COHERENT NOISE

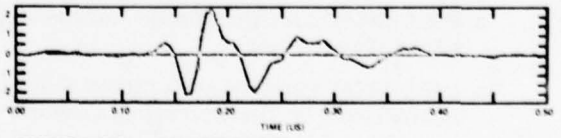

DEFECT SIGNAL – COHERENT NOISE

Poster 3 Graphic demonstration of the value of correcting the signal waveform for the background "noise" introduced by the front surface and other sources of ultrasonic reflections.

THE FOCUSED TRANSDUCER IS SCANNED OVER THE SAMPLE IN A RASTER PATTERN. THE PEAK TO PEAK AMPLITUDE OF THE DEFECT SIGNAL IS EXTRACTED FROM THE WAVEFORM BY USING WAVEFORM SUBTRACTION AND TIME GATING. THE RESULT IS PLOTTED USING A HALF TONE TECHNIQUE TO OBTAIN A COARSE GRAY SCALE. ONE OF THE MAPS OBTAINED IS SHOWN BELOW.

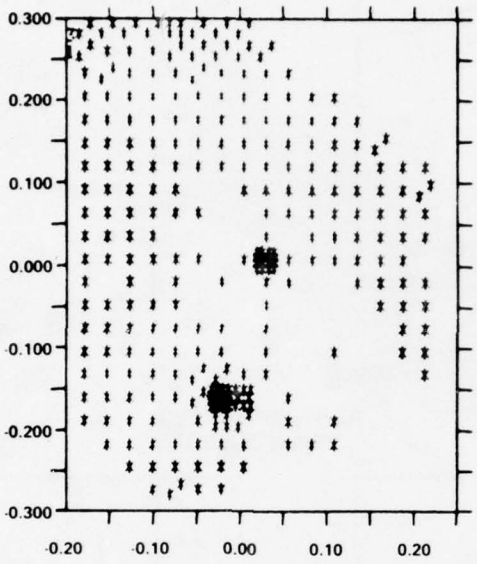

Poster 4 Computer generated map displaying the location of two "defects" within a silicon nitride sample.

TRANSDUCER CHARACTERISTICS

DIGITIZATION OF HIGH FREQUENCY WAVEFORMS IS ACCOMPLISHED BY COMPUTER CONTROL OF THE EXTERNAL SWEEP ON THE SAMPLING OSCILLOSCOPE.

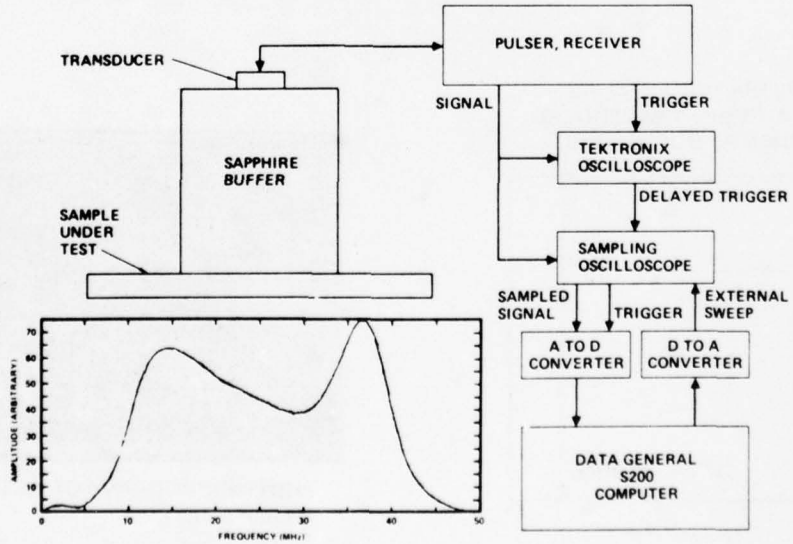

Poster 5 Block diagram of the system used to digitize RF ultrasonic signals for the computer and the frequency response of the transducer used for the measurements.

500μ DIA VOID IN Si_3N_4

SAPPHIRE BUFFER
TRANSDUCER

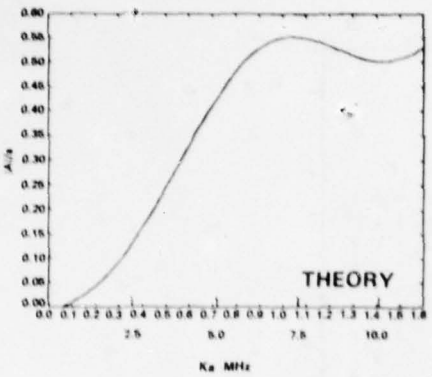

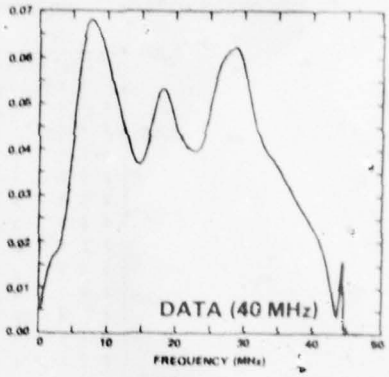

250μ DIA VOID IN Si_3N_4

SAPPHIRE BUFFER
TRANSDUCER

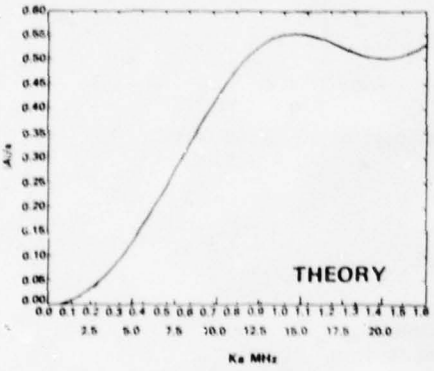

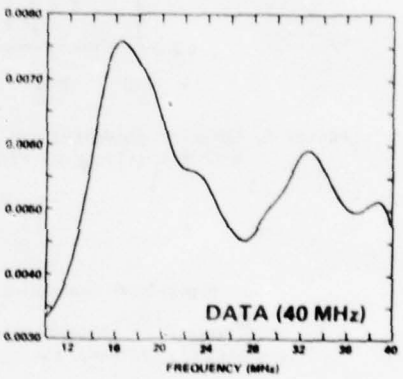

500μ DIA VOID IN Si_3N_4
USING A 10 MHz TRANSDUCER
AND AN Al. BUFFER ROD

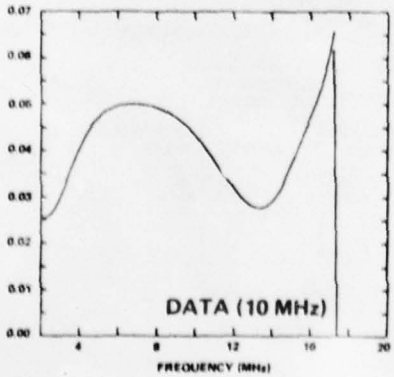

PHOTOMICROGRAPH OF ACTUAL
500 μm VOID

Poster 6 Comparison of experimental and theoretical reflection amplitude versus frequency curves for two voids in silicon nitride samples.

FLAW DETECTION AND CHARACTERIZATION IN CERAMICS WITH THE SCANNING LASER ACOUSTIC MICROSCOPE (SLAM)*

D. E. Yuhas and L. W. Kessler
Sonoscan, Inc.
Bensenville, Illinois 60106

ABSTRACT

The high resolving power coupled with the real time capability of the SLAM make it a useful technique for characterization of materials including ceramics. The elastic structure of ceramics is often dependent upon the details of the fabricationprocess, e.g., sintering, hot pressing, amount of binder, etc. Accordingly, acoustic micrographs and acoustic interferograms which reveal characteristic sonic transmission patterns and sonic velocity variations, respectively, can be used to nondestructively evaluate ceramics to ensure material uniformity. In addition, the ability to nondestructively detect flaws and inclusions is important in fracture toughness studies and in the evaluation of finished components.

This presentation will survey a series of acoustic micrographs obtained at 100 MHz. Micrographs illustrating the characteristic acoustic signatures of a variety of hot pressed and reaction sintered components will be presented. In addition to this characterizationdata, micrographs showing specific defects in silicon mitride and silicon carbide will be presented. The "library" of flaws includes implanted inclusions and induced surface flaws, as well as buried inclusions and surface flaws which occur as the result of the normal processing cycle. Work was done on fabricated test samples as well as molded parts, e.g., turbine blades. The ultrasonic detectability of defects is dependent upon many factors including acoustic frequency, acoustic energy mode, elastic properties of the flaw, and the background structure of the material under investigation. Because of the large acoustic impedance difference between some flaws and the host material, defects an order of magnitude smaller than the 25 micron resolution element at 100 MHz are easily detected. For example, the presence of micron-sized pores in reaction sintered turbine blades is readily discernable although individual pores are not resolved. The importance of SLAM real time capability, the influcence of acoustic background structure, and the use of different acoustic energy modes, e.g., bulk waves vs. surface waves on defect detectability and characterization will be discussed.

*This research was sponsored in part by the Center for Advanced NDE operated by the Science Center, Rockwell International, for the Advanced Research Projects Agency and the Air Force Materials Laboratory under contract F33615-74-C-5180, and in part by the Argonne National Laboratory.

ACOUSTIC MICROSCOPY FOR MATERIALS CHARACTERIZATION

A. Atalar, V. Jipson and C. F. Quate
Stanford University
Stanford, California 94305

ABSTRACT

An acoustic microscope with mechanical scanning and piezoelectric film transducers for the input and output has been developed for the microscopic examination of materials.[1] In the reflection mode it is possible to work with an acoustic wavelength of 0.5 micrometers and a resolution that compares to that of the optical microscope. The elastic images of material surfaces as recorded with this instrument display interesting features which provide information which complements the optical microscope. In particular we find that different phases show up with good contrast and in alloy material the texture of the grains can be recorded since the grain orientation influences the acoustic reflectivity.

THE SCANNING PRINCIPLE

With conventional microscopes it is common to view the entire field of view with one setting of the controls. The image appears either on the retina of the observer, on photographic film or on a fluorescent screen. With acoustic radiation there is no available method for recording the entire field of view in this manner. Other means must be found. We want to use piezoelectric films for they are efficient, highly sensitive and they operate over the entire range of interest. With this choice one could in principle build up an array of detectors to form an acoustic retina. In such an array careful attention must be given to both the phase and amplitude of the signal from each element. The degree of complexity in this system was such that we found that we were working on arrays whereas it was the microscope that held our interest. A single detector and a mechanically scanned object is the alternative. In an imaging system based on scanning the beam is tightly focused and the image field is constructed point by point as the object is moved in a raster pattern through the focus of the beam.

At first we turned to this system as an expedient but as we gained experience we found that a scanned system has advantages not found in conventional systems.

In electron microscopy the scanning principle is widely used in both SEM and STEM. They have found it advantageous to use single detectors where the response can be optimized to highlight selected parameters in the scattered radiation.

The primary drawback for the mechanical system required for acoustic scanning is the speed. It is slow. Several seconds are required to build up a single frame as compared to television rates of 30 frames/second. This will be overcome in time for we have built mechanical systems that operate at ten frames a second but the work to be reported here will be limited to the systems which use slow scans.

The advantages inherent to scanning systems with focusing were not obvious in the beginning. It is now becoming evident that scanning systems which record a single point at a time exhibit properties that are different from those that display the entire field of view. In the scanned system there is no problem with coherent radiation. Since the energy at the focus is confined to a diameter that is less than one wavelength in dimension there are no interference fringes of the type that are common with optical microscopes that use coherent laser radiation. These fringes arise from the scattered radiation from two points on the object that are separated by many wavelengths.

We have been operating a reflection microscope[2,3,4] for some time now at a frequency of 1100 MHz (λ = 1.4 μm). We have also carried out some preliminary work at 3000 MHz (λ = 0.5 μm). With this instrument we have learned that it has some interesting and perhaps unique properties when used to study the microscope features of materials and integrated circuits.

THE INSTRUMENT

The transmission instrument which has been developed at Stanford[5] consists of two confocal lenses, one to focus the acoustic radiation down to the smallest possible diameter, the "waist", the other to collimate the radiation transmitted through, or scattered by, the object which is placed in the focal plane and which is mechanically moved television-like in two orthogonal directions, in the focal plane. Figure 1 is a sketch of the geometry of the microscope which is almost as simple in reality as in the sketch. Water fills the space between the lenses and the object, held in place by capillary attraction.

The lenses are simple spherical surfaces ground into sapphire blocks. They are almost aberration-free because (1) they are small (typically 100 micron radius of curvature) and (2) the effective refractive index between water and sapphire is 7.45. The large change in velocity reduces spherical aberration to a negligible quantity.

The "field of view" for such a lens is small but this can be tolerated with a mechanically scanned microscope since good imaging quality is only required on the axis. The resolution of these lenses has been measured; it corresponds closely to the "Rayleigh-criterion" of a single lens, which states that the distance d between two object points which can be resolved is given by $d = (0.66\lambda / N.A.)$ where λ is the wavelength in the medium and N.A. is the numerical aperture (the sine of the half-angle of convergence). In our imaging system we use two lenses as shown in Fig. 1 and the spatial

frequency response of this combination is almost twice that of a single lens.

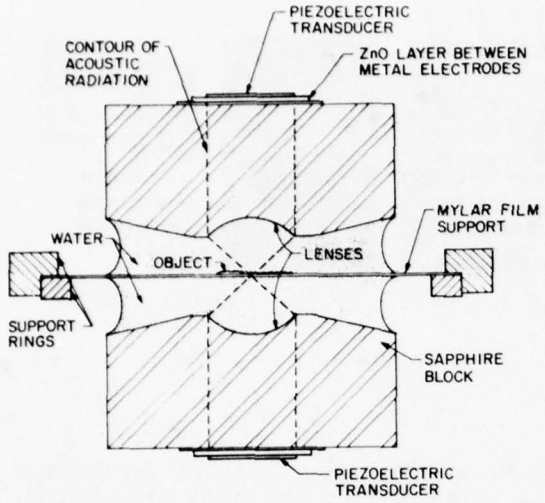

Fig. 1 --Sketch of microscope geometry.

In operation, a fraction of a watt of microwave power is converted into a plane acoustic wave in the sapphire block by one of the transducers. The spherical lens converts this into a spherically converging wave in the water. After it is modified or scattered by the object which is mechanically moved across the waist of the acoustic beam it is collimated, or made plane, by the second lens so that the radiation impinges everywhere in phase on the second transducer. The electrical signal from this transducer is amplified, rectified and used to modulate the display which may be a cathode-ray tube scanned in synchronism with the motion of the object. The magnification is simply the ratio of the deflection of the cathode-ray tube spot to the displacement of the object. Figure 2 shows the microscope with its mechanical scanning system.

So far the mechanical scanning we have used is sinusoidal at a frequency near 60 Hz in one, say, the x-direction and uniform motion in the y-direction, so that it takes several seconds to obtain a complete picture, recorded with a camera attached to the cathode-ray tube screen. The scan amplitude and hence the field of view is but a fraction of a millimeter; if a larger object is to be examined the picture has to be pieced together from adjoining pictures in the form of a mosaic.

The usual picture shows detail by way of an intensity modulation; the more radiation reaches the detedtor the brighter the image. It is an inherent feature of any scanning type of microscope that the contrast in the picture is under the control of the operator of the instrument. If the signal-to-noise ratio is adequate, a variation in the radiation transmitted through, or reflected by, the object of, say 1%, can easily be amplified to appear as a 100% modulation in the final picture. In the acoustic microscope, at microwave frequencies, we find that the contrast exhibited by most objects is large enough so that contrast amplification is not needed and it is possible to record a signal which is directly proportional to the amplitude of the radiation received by the second lens. Thus the instrument can be made quantitative in a very simple and direct manner.

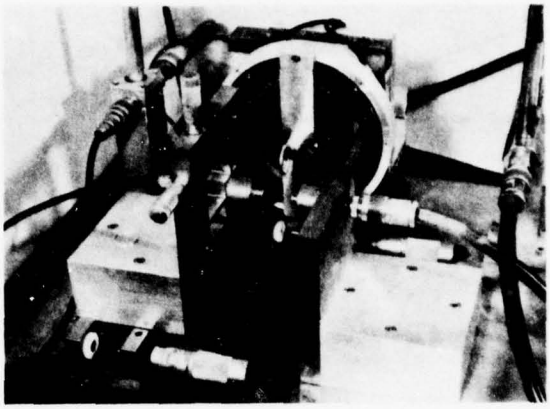

Fig. 2--Photograph of the acoustic microscope's mechanical components.

Much of our work has been done with a reflection mode. The essential parts of this form of the acoustic imaging system is shown in Fig. 3. The transducer which is piezoelectric generates the acoustic wave. It serves to convert the rf voltage across the piezoelectric film into a plane acoustic wave propagating normal to the surface. The acoustic lens is merely a spherical cavity on the opposing side of the crystal. It serves to focus the plane wave into a narrow waist at the focal point. A liquid, such as water, fills the gap between the object and the lens in order to provide a path for sound propagation. The reflected sound wave returns through the lens to the transducer which is now acting to convert the acoustic signal into the electrical signal. It is important to note that the transducer is sensitive to the phase of the returning wave and that the rf voltage at the output is obtained by integrating the acoustic field over the area of the transducer. A microwave circulator separates the reflected and incident signals. Normally the object is near the focus point and it is mechanically scanned in a raster pattern normal to the axis of the beam. The amplitude of the returning signal is used to control the intensity of a synchronously scanned electron beam in a CRT. In this way the image is displayed on the CRT and it is recorded by photographing the face.

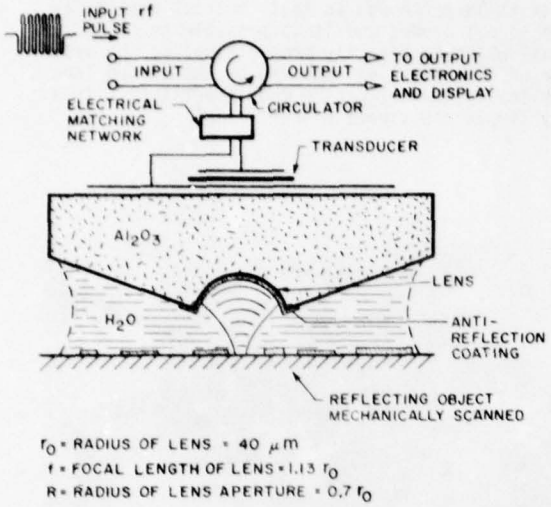

Fig. 3 -The configuration of the scanning acoustic microscope as used in the reflection mode.

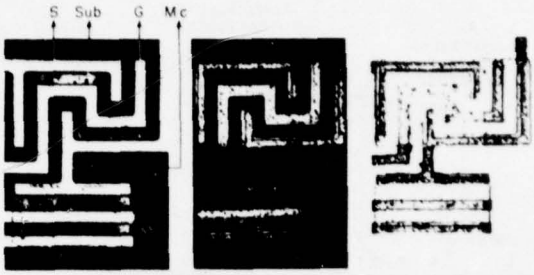

Fig. 5 -Optical (a) and Acoustic (b), (c) images of H-MOS transistors on an SOS chip. Acoustic images are recorded at different Z positions. Source (S), gate (G), metal connection (MC) and substrate (Sub) regions are indicated.

ACOUSTIC MICROGRAPHS FOR INTEGRATED CIRCUITS AND MATERIALS

The product of any investigation with a microscope is the final image and in this section we will include acoustic micrographs as selected to illustrate the present state of acoustic imaging at microwave frequencies.

In the first micrograph of Fig. 4 we show the cross section and optical image of an integrated circuit fabricated with silicon-sapphire. The acoustic images of this structure are shown in Fig. 5. There we see the change in contrast as we change the spacing between the lens and the sample.

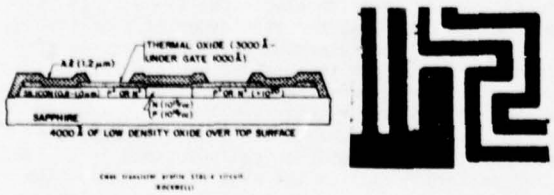

Fig. 4 -The cross section and optical image of the SOS device of Fig. 5.

This feature of altering the lens-sample spacing is further illustrated in Fig. 6. There we display the magnitude of the reflected signals as a function of the lens-sample spacing. In this case there is no transverse scanning as is common for imaging. We see that the maximum return occurs when the sample is at the focal point of the acoustic beam and it diminishes on either side of this point. The important point is that the shape of this curve is dependent on the elastic properties of the reflecting surface. We have carried out the analysis which tells us that this curve is a sensitive function of the shear wave velocity in material under examination. Still more on this topic can be seen in the micrographs of Fig. 7. There we show the response for pure silicon, for silicon with a 1 μm layer of aluminum and for silicon with 2 μm of silicon. The shape of the curve varies because of the acoustic energy that is confined to the aluminum layers. It suggests that one can exploit this effect to monitor changes in the thickness of metallization layers such as this.

Another application of this idea is shown in Fig. 8. At the top we have an optical image of an SOS circuit — the dark region is the sapphire substrate, the grey regions are silicon and the bright stripes are aluminum (7 μm in width). On top of the silicon layer and beneath the aluminum there is a 300 Å layer of oxide. This allows the aluminum to "crossover" the silicon without interference. At these points where they want the voltage on the aluminum stripe to control the silicon current (or gate) the oxide thickness is reduced from 3000 Å to 1000 Å. The two squares in the acoustic image indicate the regions where the oxide is reduced. In Fig. 9 we show the optical and acoustic images of a silicon IC circuit. The greater contrast in

the acoustic image results from the variations in the layering. In some ways this contrast improves the quality of the image in that it allows the viewer to more easily see the composition of the layering.

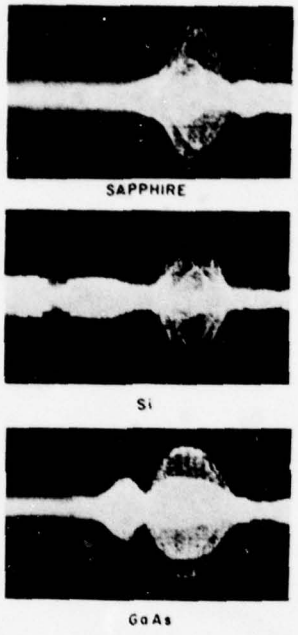

f = 750 MHz
3.75 μm/div
ENVELOPE OF THE CURVES SHOW REFLECTION AMPLITUDE

Fig. 6 --The V(Z) curves for single crystals.

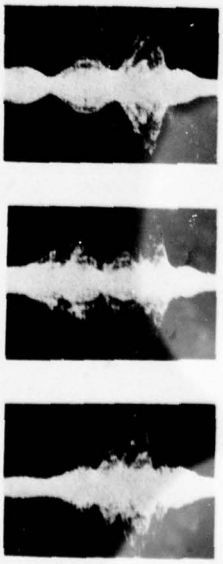

Fig. 7 -The V(Z) curves for silicon with layering.

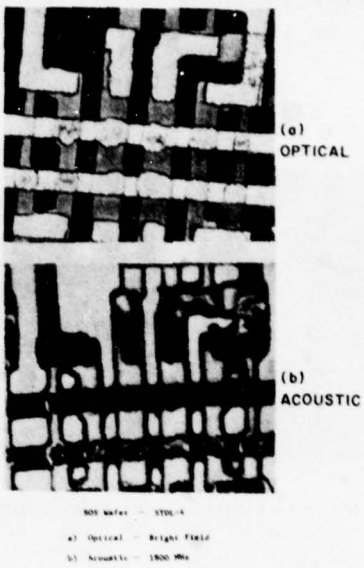

Fig. 8 -Optical and acoustic comparison of SOS silicon devices.

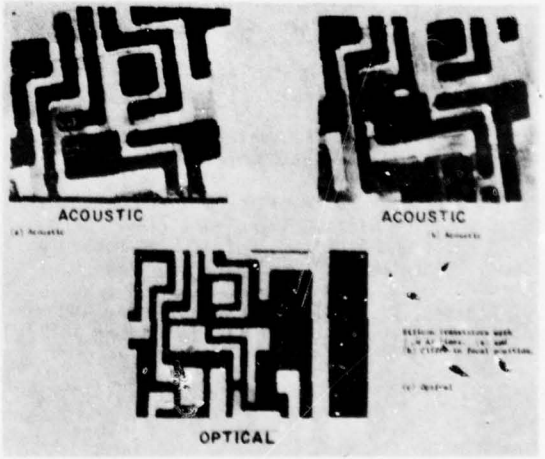

Fig. 9

And finally in Fig. 10 we compare the optical and acoustic image for the polished surface of an alloy of Cobalt-Titanium. The hillocks in the optical image represents surface contours. The dark region in the acoustic image represent regions where the phase of the material has changed. There are four possible phases in the Co-Ti alloy and each

of these phases have a different reflection coefficient for acoustic waves since the elastic constants vary from phase to phase. This shows up in the acoustic micrograph as four different shades of grey.

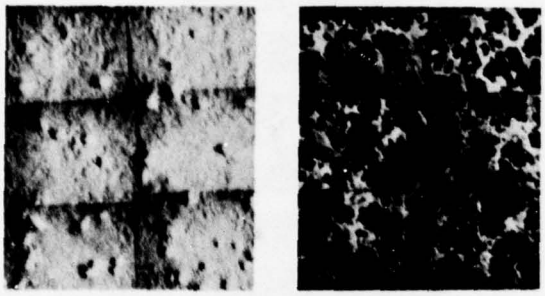

Co-Ti ALLOY SHOWING 4 PHASES. OVERALL COMPOSITION, 59% Co 41% Ti

Fig. 10

ACKNOWLEDGEMENTS

This work was supported in part by the NBS/ARPA Program on Semiconductor Electronics (Contract #5-35899) and in part by the Air Force Office of Scientific Research (Grant #AFOSR-77-3455).

REFERENCES

1. V. Jipson and C. F. Quate, Appl. Phys. Letters 15 June 1978 (in press).

2. R. A. Lemons and C. F. Quate, Appl. Phys. Letters 25, 251 (1 September 1974).

3. R. G. Wilson, R. D. Weglein, and D. M. Bonnell, Semiconductor Silicon/1977, vol. 77-2, (H.R. Huff and E. Sirtl, eds.), Electrochemical Soc., Princeton, N.J., p.431.

4. A. Atalar, C.F. Quate, and H.K. Wickramasinghe, Appl. Phys. Letters 31, 791 (15 December 1977).

IMAGING AND CHARACTERIZATION OF THICK PRODUCTION-LINE MICROELECTRONIC COMPONENTS USING TRANSMISSION ACOUSTIC MICROSCOPY

Chen S. Tsai, Jung K. Wang, and Chin C. Lee
Center for the Joining of Materials
and
Department of Electrical Engineering
Carnegie-Mellon University
Pittsburgh, PA. 15213

ABSTRACT

The interfacial regions of four types of production-line microelectronic components (die-bonded transistor headers, high power silicon transistors, chip-resistors, and multilayer chip-capacitors) have been examined using a transmission scanning acoustic microscope operating at 150 MHz and a combination of modes. Flaws, voids, and defects in these components have been detected. Some characterization of these defects has also been obtained.

INTRODUCTION

The characteristics of material joints, bonds, and composites are greatly influenced by the elastic faults such as stress distribution, microstructures, defects, and voids which occur in their interfacial regions. It is thus desirable to detect, identify, and ultimately characterize these faults using acoustic techniques. We had earlier employed a transmission-type scanning acoustic microscope [1](See Fig. 1), operating at 150 MHz, to image tne interfacial regions of a number of specially made joints of large thickness. [2,3] Also, by using a combination of the amplitude and the phase modes of operation with this microscope, we were able to map the acoustic velocity and the attenuation coefficient distributions in the bond layer of a thick adhesive joint. [4] Mapping of these acoustic parameters is important because the strength of an adhesive bond has been shown to be closely related to them. [5] Detection of defects and flaws in such thick specimens was facilitated through operation of the microscope in a combination of confocal and nonconfocal modes [4] at a relatively low acoustic frequency, namely, 150 MHz. In a nonconfocal mode of operation, the separation between the transmitter lens and the receiver lens is set slightly larger or smaller than the sum of the two focal lengths. Using this mode of operation it is possible to obtain large depth of focus and, thus, image thick specimens at a slight reduction in spatial resolution. The series of acoustic images shown in Fig. 2 for a test specimen serve to illustrate this capability. The test specimen was a copper plate of 0.5mm thick with the characters CJM and the pattern of various shapes etched on one face, and the characters NSF and straight bars on the other.

In this paper, we report further progress which has been made using this acoustic microscope. Emphasis of the present work is placed on the imaging and the characterization of the interfacial regions of thick production-line microelectronic components.

CAPABILITIES OF THE SCANNING ACOUSTIC MICROSCOPE

The modes of operation and key parameters of the scanning acoustic mirocsope (SAM) employed in this study are listed as follows:

Modes of Operation: Transmission Mode { Amplitude, Phase, Confocal, Nonconfocal }

Acoustic Lenses: f/4 (in water), focal length in water = 4 mm

Spatial Resolution: 30 μm in water at 150 MHz (confocal)

Field of View for the Sample: 3 X 4 mm

Magnification of Acoustic Images: 35

Total Electrical Throughput Loss (Without specimen): 55 DB

Dynamic Range: 30 to 50 DB at 1 mw (0dbm) input electric power, depending on the sample that has been examined.

IMAGING AND CHARACTERIZATION OF DISCRETE MICROELECTRONIC COMPONENTS

Four types of thick production-line microelectronic components have been examined using one or a combination of the modes of operation listed in Section II.

Die-Bonded Transistor Headers

The voids in the bond region of a die-bonded transistor header (See Fig. 3(a)) is known to result in "hot spots" and thus early failure of the power transistor. The spatial resolution and contrast obtainable with the existing instrument based on x-ray radiography are less than desirable. The three-dimensional locations of small voids (not detectable by the x-ray method) have been determined using the SAM (See Fig. 3(b)). Fig. 3(c) shows that one of type B headers has a very poor bond while the other has practically no bond at all.

High Power Silicon Transistors

"Alloy spikes" at the silicon-alloy interface are known to cause undesirable effect in drastically lowering the breakdown voltage of high power transistors (See Fig. 4(a)). Their location and size (See Fig. 4(b)) have been determined nondestructively from the data obtained using both the amplitude- and the phase- mode of operation of the SAM (See

Fig. 4(d)). Estimated sizes of the particular alloy spike detected are h = 15 μm and b = 100 μm.[6]

Thick-Film Circuits And Thin-Film Chip Resistors

In thick film circuits, the particle distribution in the film will affect the component value, and the defects in the film may reduce their reliability. The acoustic micrograph shown in Fig. 5(c) of a thick-film resistor (Fig. 5(a)) suggests a nonuniform distribution of the resistive particles and some defects in the resistor layer. Fig. 6(b) shows the acoustic micrograph of a thin-film chip resistor (Fig. 6(a)) in which the defects of the multi-layer structure (alumina substrate-NiCr-SiO-Coating) are clearly seen.

Multilayer Chip Capacitors

A variety of multilayer chip capacitors including those made of $BaTiO_3$ and ceramics have been examined. Defects such as voids and debonds which occur at the interfaces and inclusions which occur in the dielectric have been detected by recording a series of acoustic micrographs as the specimen was translated along the lens axis. For example, the acoustic micrographs shown in Fig. 7 (c) reveal clearly the defects in different cross-sectional planes of a $BaTiO_3$ chip capacitor (Fig. 7(a)) furnished by American Technical Ceramics. A typical amplitude profile of the transmitted acoustic energy (Fig. 7(d)) indicates that the acoustic wave suffers an attenuation of about 15 db when it impinges upon a defect located at P. This type of defect may result from some kind of inclusion. The optical image for an appropriate cross-section is shown in Fig. 7(b). Note that the sizes of the dark spots in the optical image are comparable to that of the acoustic micrograph. We have also observed that the acoustic attenuation associated with the voids or the debonds are greater than 35 db. Finally, it should be noted that the scanning laser acoustic microscope (SLAM) [7] had also been employed to examine the ceramic chip-capacitors. [8]

CONCLUSION

We have demonstrated that a scanning acoustic microscope, operating at transmission mode and 150 MHz, is capable of nondestructively detecting defects deep inside thick production-line multilayer microelectronic components. We have also succeeded in identifying and characterizing some of the defects such as voids, alloy spikes, debonds, and inclusions.

ACKNOWLEDGMENT

This work was supported by Material Research Laboratory Section of NSF Grant No. DMR72-03297-A03.

REFERENCES

1. R. A. Lemons and C. F. Quate, "Acoustic Microscope-Scanning Version, "Appl. Phys. Lett., 24, 163 (February 1974).
2. C. S. Tsai, S. K. Wang, and C. C. Lee, "Visualization of Solid Material Joints Using a Transmission-Type Scanning Acoustic Microscope," Appl. Phys. Lett., 31, 317 (September 1977).
3. C. S. Tsai, S. K. Wang, and C. C. Lee, "Acoustic Imaging of Joined Surfaces," Presented at 1977 ARPA/AFML Meeting on Review of Progress in Quantitative NDE, June 14-17, 1977, Cornell University, Ithaca, New York.
4. S. K. Wang, C. C. Lee, and C. S. Tsai, "Nondestructive Visualization and characterization of Material Joints Using a Scanning Acoustic Microscope," 1977 Ultrasonics Symposium Proceedings, pp. 171-175, IEEE Cat. No. 77CH1264-1SU.
5. G. A. Alers, P. L. Flynn, and M. J. Buckley, "Ultrasonic Techniques for Measuring the Strength of Adhesive Bonds," Material Evaluation, Vol. 35, No. 4, 77 (April 1977).
6. C. C. Lee, J. K. Wang, S. K. Wang, P. Hower, and C. S. Tsai, "Detection and Characterization of Alloy Spikes in Power Transistors Using Transmission Acoustic Microscopy," Presented at the First Internatlional Symposium on Ultrasonic Materials Characterization, National Bureau of Standards, Maryland, June 7-9, 1978.
7. L.W. Kessler and D. E. Yuhas, "Structural Perspective," Industrial Research, 20, 52 (January 1978).
8. G. J. Ewell and G. R. Love, "Acoustic Microscopy Applied to Hybrid Microelectronics," Presented at the First International Symposium on Ultrasonic Materials Characterization, National Bureau of Standards, Maryland, July 7-9, 1978.

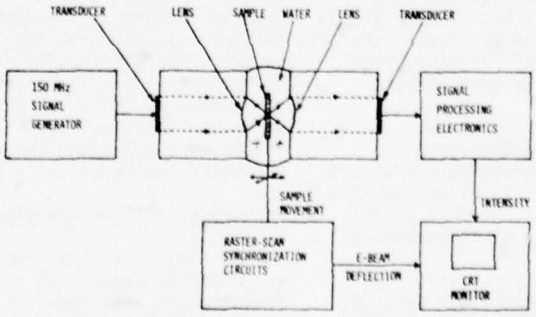

Fig. 1 Block diagram of a transmission scanning acoustic microscope.

(a) (b) (c) (d) (e) (f)

Fig. 2 Acoustic images of a test specimen obtained at different adjustment of focus: (a) - (e) short depth of focus centered at different planes, (f) long depth of focus.

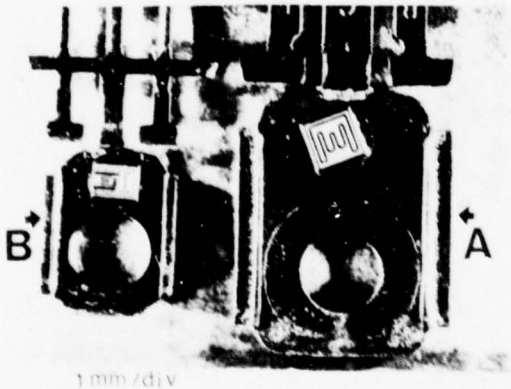

(a)

(I) (c) (II)

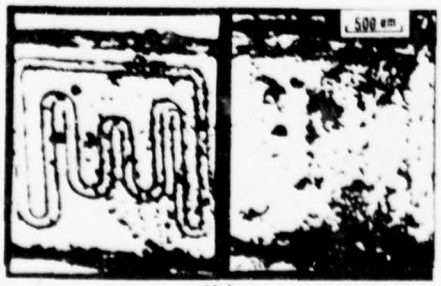

(I) (b) (II)

Fig. 3(a) Top view of die-bonded headers obtained by optical microscope
(b) Acoustic images of die-bonded header (A type: thickness = 42 mils)
(I) Long depth of focus centered at bond region
(II) Short depth of focus focused at bond region
(c) Acoustic images of two other die-bonded headers (B type: thickness = 30 mils)
(I) Very poor bonding
(II) No bonding at all

(a)

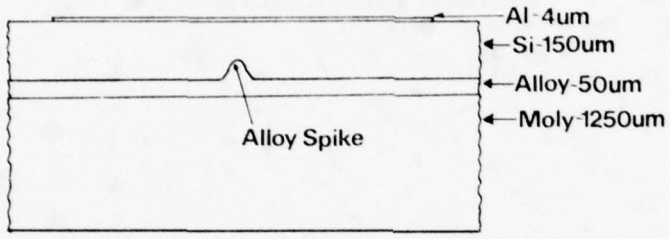

(b)

(c)

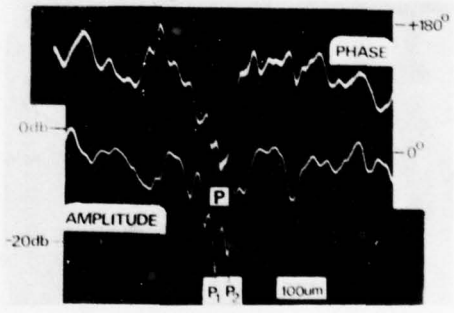

(d)

Fig. 4(a) Top view of the production-line power transistor under study (thickness: 58 mils)
(b) Cross-sectional sketch of the power transistor
(c) Acoustic amplitude images of a portion of the power transistor obtained with acoustic beam focused at the silicon alloy interface
(d) Acoustic phase variation (upper curve) and acoustic amplitude variaition (lower curve) along line C-D of Fig. 4(c)

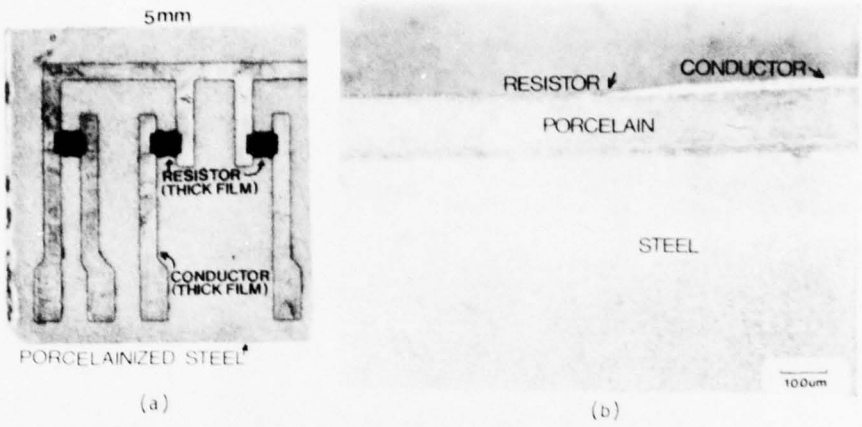

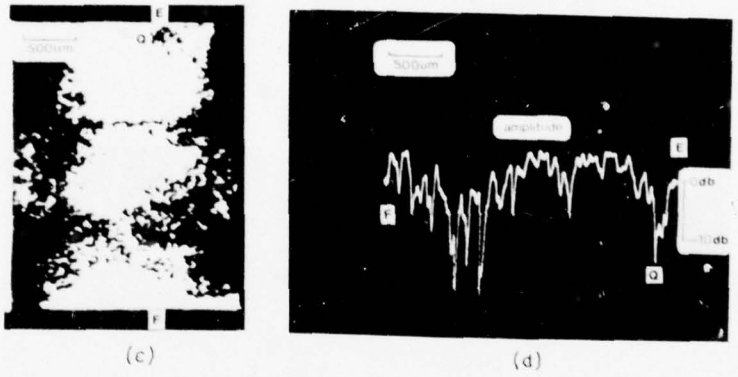

Fig. 5(a) Top view of the thick-film circuit (thickness: 44 mils)
(b) Crossectional view obtained by optical microscope
(c) Acoustic amplitude variation along line EQF

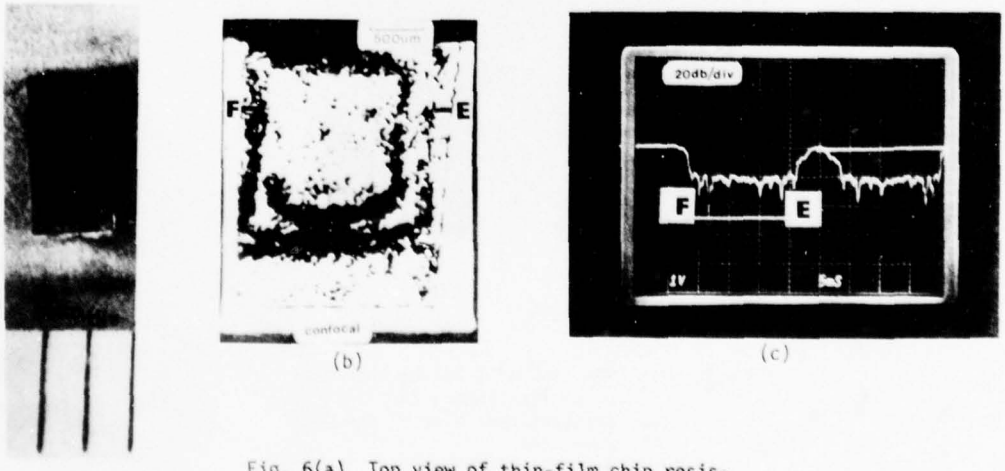

Fig. 6(a) Top view of thin-film chip resistor (thickness: 19 mils)
(b) Acoustic Micrograph
(c) Acoustic amplitude variation along line EF

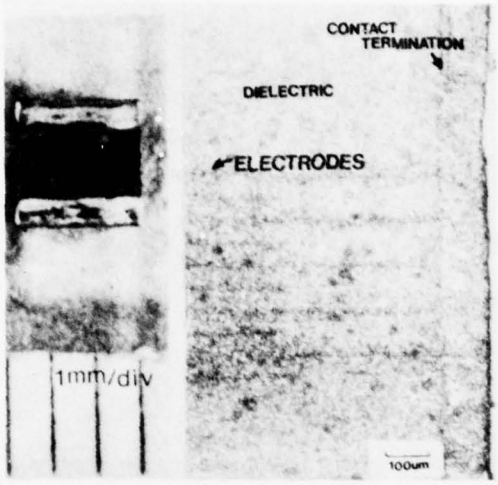

(a) (b)

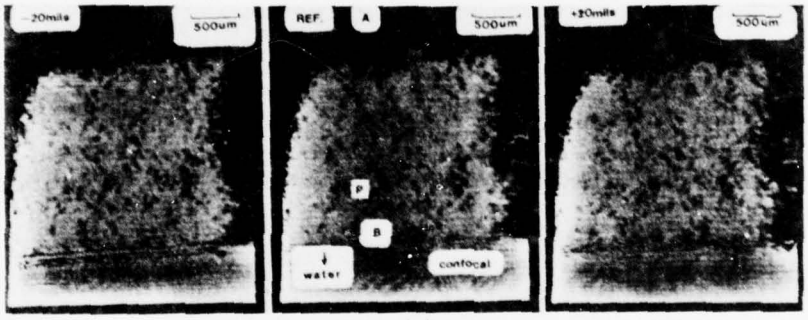

(c)

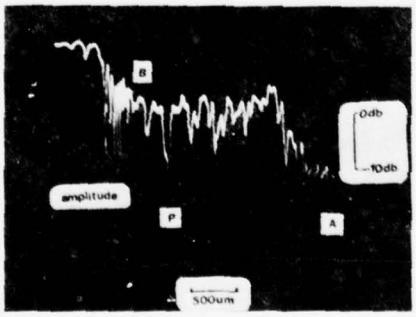

(d)

Fig. 7(a) Top view of a $BaTiO_3$ chip-capacitor (thickness: 74 mils)
(b) Crossectional view of the chip capacitor
(c) Acoustic micrographs
(d) Acoustic amplitude variation along line AB

ULTRASONIC EVALUATION OF ADHESIVE BOND STRENGTH USING SPECTROSCOPIC TECHNIQUES

F. H. Chang, R. A. Kline and J. R. Bell
General Dynamics
Fort Worth Division
Fort Worth, Texas 76101

ABSTRACT

In this program statistical analysis of ultrasonically determined parameters was used to identify the features of acoustic wave propagation in adhesively bonded structures which could be used to determine adhesive bond strength. The parameters associated with the interaction of ultrasonic waves with the adhesive-aluminum interfaces and adhesive interlayer which were investigated included bondline transit time, amplitude ratios of reflections from the various interfaces, frequency dependent attenuation and spectral resonance characteristics. Aluminum specimens with both etched and as-received surface preparation were studied. The capabilities of the Fokker bondtester for adhesive strength determination were also assessed. Adaptive learning techniques were used to statistically examine correlation between the observed acoustic properties and shear strength for 394 specimens.

INTRODUCTION

Adhesively bonded structures offer many attractive features in the design of modern aircraft. However, the utilization of these materials has been slowed by the inability to nondestructively evaluate adhesive bond strength. Much of the problem in ultrasonic NDT methods stems from the difficulty in distinguishing changes in acoustic wave propagation in poorly bonded regions, where the adhesive and adherend are in intimate contact but interfacial strength is low, and well bonded regions with high interfacial strength. A NDT methodology which is sensitive to adhesive bond strength must be developed.

In this program spectroscopic techniques were used to study a variety of sonic wave propagation features in adhesively bonded structures. In addition to quantifying the spectral response of the specimens, other acoustic parameters characterizing bondline properties were also determined including travel time through the adhesive and the relative amplitudes of the reflected waves from the various interfaces present. Subsequent to ultrasonic investigation, the specimens were mechanically tested to failure. The measurements were then analyzed to assess the potential of the ultrasonic parameters investigated for adhesive bond strength determination.

EXPERIMENTAL PROCEDURE

For ultrasonic testing adhesively bonded strips (Fig. 1a) were immersed in water and examined with a 10 MHz transducer operated in the pulse-echo mode. In this investigation the use or omission of proper surface treatment, (MEK degreasing, FPL etching) of the aluminum (2024-T81) prior to bonding with Reliabond 398 adhesive, was used to simulate bond strength extremes. Ultrasonic readings were taken at 0.5 inch intervals along the length of the specimen with digitization of the rf waveform and calculation of its Fourier transform for each position. The data processing system is illustrated in Fig 2. After this portion of the investigation was completed, the strips were machined in a single lap shear configuration (Fig. 1b) and tested to failure.

DATA PROCESSING

Acoustic wave propagation in these laminated structures is shown in Fig. 3. From the digitized RF waveform and its Fourier transform, a number of parameters characterizing specimen response could be determined (Fig. 4):

1. t - The time required for sound waves to traverse the adhesive.
2. AR_1 - The ratio of amplitudes for the reflected waves A_1 and A_2.
3. AR_2 - Similar to AR_1 except for A_1 and A_3.
4. b_2 - The maximum amplitude observed in the Fourier transform of the RF signal.
5. F_2 - The frequency at which the maximum amplitude (b_2) was observed.
6. B/2* - The half bandwidth associated with the anti-resonance of A_1 and A_2.
7. f_o - The frequency associated with the anti-response of A_1 and A_2.
8. Q* - $F_o/2B$
9. D - The anti-resonance depth.

* Denotes parameter where spectral asymmetry required measurement on both the low and high frequency sides of the anti-resonance frequency.

ULTRASONIC ATTENTUATION/FOKKER BOND TESTER

In addition to the amplitude ratio calculated from the digitized rf waveform, the frequency dependence of the reflected waves A_1 and A_2 could also be determined from the Fourier transforms of the two signals. $\text{Log}_e\ (AR_1)^{-1}$, indicative of the ultrasonic attenuation, is shown as a function of frequency in Fig. 5a for specimens with treated and untreated surfaces and of identical bondline thickness. Other than the general amplitude reduction (also shown in AR_1 calculated from the digitized signal) no dramatic difference in specimen response was observed for the two surface preparations. The bonded laminates were also studied with the Fokker bondtester, a spectroscopic device with the ability to detect gross changes in the resonance characteristics of a piezoelectric probe. No spectral change could be discerned for the two sample prepara-

tions. It was, however, possible to locate artificial defects (Kapton film) located in the bond using the instrument (Fig. 5b, identical settings for the two regions).

SAMPLE DISTRIBUTION

The distribution of shear strengths observed in these specimens is shown in Fig. 6a. As expected, there was a significant difference in the load bearing capability for the two surface treatments. Figures 6b, 6c, and 6d, illustrate the variety in the observed distribution of the ultrasonically determined parameters (and combination of parameters) ranging from virtually no separation in the distributions as in the case of F_2 (Fig. 6b) through intermediate separation capability, e.g., Q_2/Q_1 (Fig. 6c) with the largest difference observed for $f_o \log_e (AR_2)^{-1}$, an amplitude ratio with a thickness compensation factor. In general the parameters associated with frequency (Q_1, Q_2, B_1, B_2, F_2) showed little ability to distinguish between the two surface treatments. Improved resolution capability was observed for the measurements related to signal amplitude (AR_1, AR_2 $f_o \log_e (AR_1)^{-1}$, $f_o \log_e (AR_2)^{-1}$, D).

ADAPTIVE LEARNING

Bond strength classification was also examined using an adaptive learning network. For this approach, the behavior of a given parameter is modeled as a multinomial function of other measured quantities with the multinomial coefficients adjusted via an interative scheme to best fit the actual data. Figures 7a-d illustrate the results obtained for the four parameters (discussed above) as a function of f_o, essentially bondline thickness. Ideally, the separation between etched and as-received values should be sufficiently large to accommodate natural fluctuations in the measured quantities and uniform throughout the range of thickness to be encountered. Adaptive learning and sample distribution results are in good qualitative agreement. In no case was it possible to unambiguously discriminate between the two sample treatments using a single measured or calculated parameter. Further statistical studies are now in progress to examine possible improvements in resolution capability with multiple parametric combinations.

CONCLUSIONS

1. The Fokker bondtester was not found to have sufficient sensitivity to adhesive strength variations to adequately serve in the nondestructive evaluation technique investigation conducted in this program.
2. Parameters primarily associated with frequency dependent information (e.g., Q factor, bandwidth) are relatively poor classifiers of bond strength.
3. Parameters associated with signal amplitude (amplitude ratio, resonance depth) showed relatively good resolution capability between strong and weak bonds.
4. No single parameter could unambiguously distinguish well bonded specimens from poorly bonded specimens.
5. Multiple parameter classification offers the possibility of improved bond strength evaluation.

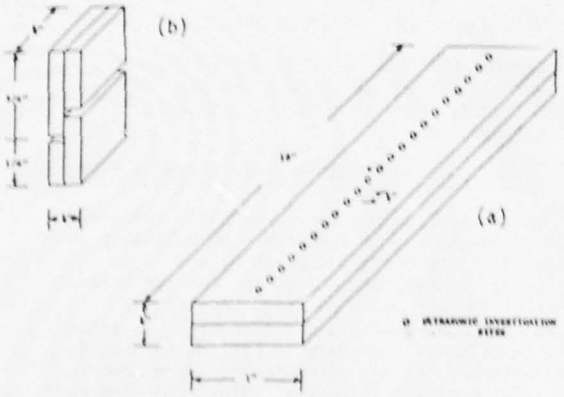

Fig. 1 a) Test geometry for shear strength determination; b) test geometry for ultrasonic investigation.

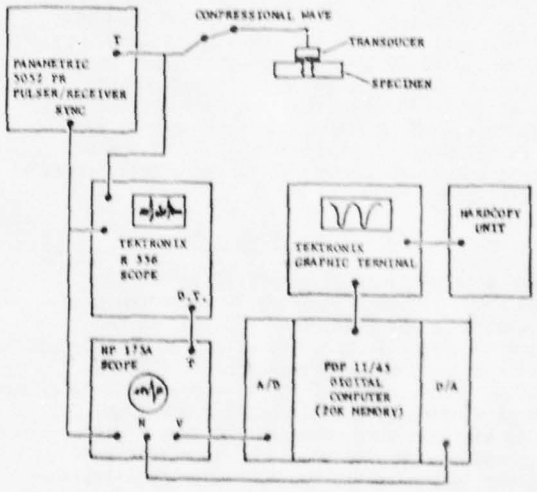

Fig. 2 Data acquisition system.

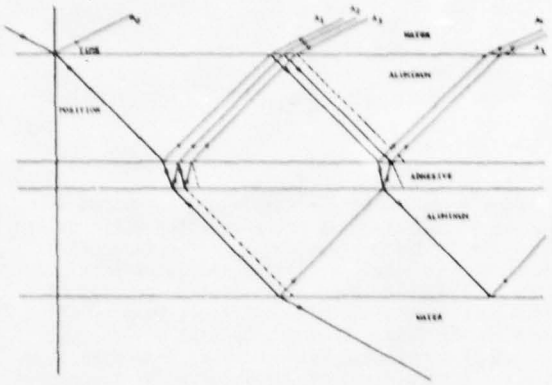

Fig. 3 Wave propagation diagram.

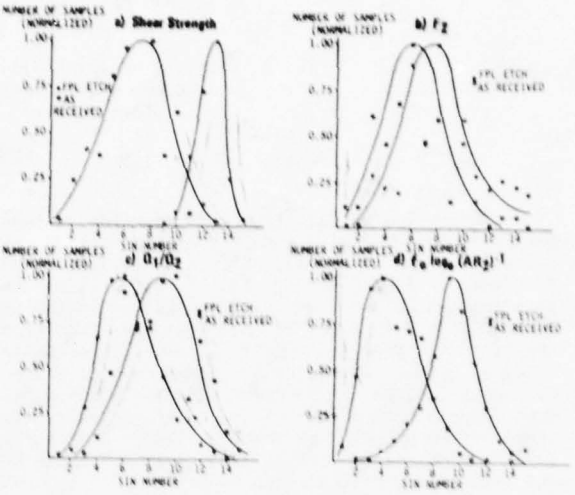

Fig. 6 Sample distribution.

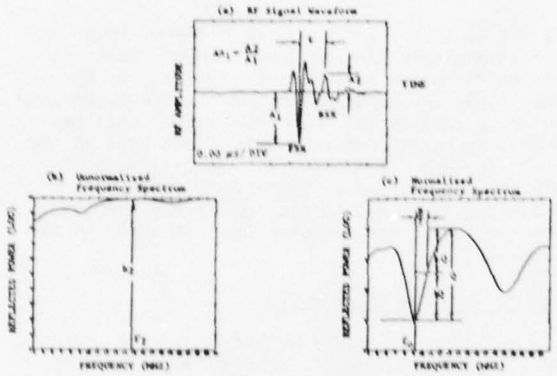

Fig. 4 Ultrasonic parameter identification.

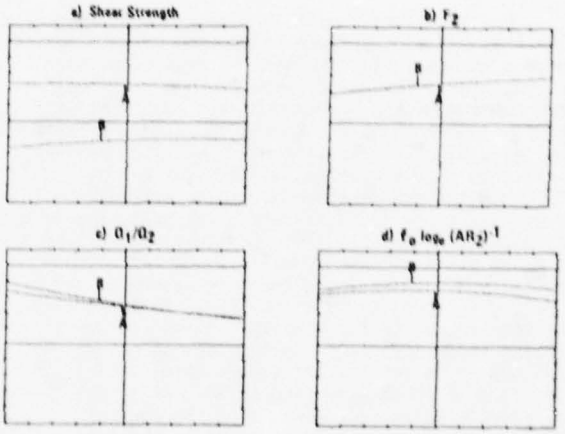

Fig. 7 Adaptive learning results - Curve A - FPL etch, Curve B - As received.

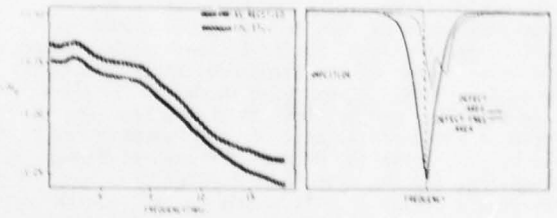

Fig. 5 a) Frequency dependence of AR_1; b) Fokker bondtester.

ULTRASONIC MEASUREMENT OF INTERFACIAL PROPERTIES IN COMPLETED ADHESIVE BONDS

G. A. Alers, R. K. Elsley, J. M. Richardson and K. Fertig
Rockwell International Science Center
Thousand Oaks, California 91360

ABSTRACT

The problem of detecting weak adhesion in completed adhesive bonds can be considered a problem in measuring the effective acoustic impedance of a thin layer at the adherend to adhesive interface. By calculating the ultrasonic reflection coefficient of the entire sandwich structure as a function of frequency including an interfacial layer, it can be shown that quite obvious changes in the reflection spectrum can be produced by minor changes in the properties of the thin layer. The inverse problem of deducing the properties of the thin layer from experimental measurements is more difficult because of the sensitivity of the results to small experimental errors in the data. However, special procedures based on estimation theory are being developed for use on actual ultrasonic data obtained from specimens with both optimum and degraded adhesive bonds. Once the elastic properties of the interfacial layer have been deduced from ultrasonic or other nondestructive measurements, they can be used to infer the physical state of the material at the interface. Models that relate the physical state of polymers to their failure probability such as that being developed by D. H. Kaelble can then be used to predict the strength and reliability of the adhesive bond.

APPROACH

Posters 1 and 2 describe the general strategy and the specific approach being used here to obtain a nondestructive method for predicting the strength of a completed adhesive bond. Although the optimum method of developing a quantitative NDE tool depends upon a knowledge of the mechanism of failure and utilization of an NDE tool appropriate to that mechanism, the present approach combines two new developments in an attempt to produce a semi-empirical technique for making a strength prediction. These two developments are the use of an on-line computer to perform a detailed analysis of the ultrasonic waveforms and a newly developed molecular theory of polymer reliability[1] to relate the computer output to a general mathematical model that describes mechanical failure in polymers. The experimental data is in the form of broad band (short time duration) ultrasonic pulses reflected from the various planar interfaces within the adhesive bond as shown in the Theoretical Time Domain Response graph. When this entire train or echoes is Fourier transformed, the Frequency Domain graph is obtained which shows many sharp minima in the reflectivity at frequencies corresponding to standing wave modes of vibration in each of the individual layers of the bond.

Mathematical Basis

Since a rigorous mathematical description of the reflection of ultrasonic waves by a layered medium exists,[2] it is easy to model a weak adhesive-to-metal joint by a thin layer of unknown material at the interface. In the parametric approach shown on Poster 3, the acoustic impedance of the layer was varied and the changes in the frequency domain presentation were noted to determine empirically what features in the spectrum were most likely to be good candidates for correlating with bond strength. In the inversion approach, shown on Poster 4, the techniques of estimation theory were used to deduce the properties of the adhesive layer as well as the unknown interfacial layer from the time domain echo train reflected by the adhesive layer alone. It has been found very valuable to use two transducers in order to provide the inversion process with two waveforms taken from each side of the bond at the same location. The results of an inversion of some theoretical wave form data in which the interface layer had an average impedance equal to one quarter of the adhesive layer is shown in the table.

Comparison with Experiment

In order to determine how well the ultrasonic measurements can predict adhesive bond strength, it was necessary to construct a series of specimens with weak adhesion between one aluminum plate and the adhesive. Poster 5 shows Probability of Failure type graphs for the two modes of failure available to adhesive bonds (peel failure and shear failure) for five different surface preparations. Those specimens which showed the least variation in bond line thickness and the greatest strength difference were the compression shear specimens prepared with an FPL etch and with no surface preparation. Poster 6 (upper right) shows how measurements of the resonances at and near the bond line resonance were used to define the bond line thickness and how this thickness was used to define a predicted location of the Dumbbell resonance. The deviation between the predicted resonance, F_D, and the measured resonance, F_M, provides a parameter that should correlate with the condition of the interfacial layer and hence the strength of the bond. In the lower left hand part of Poster 6, a cumulative distribution graph displaying the percentage of specimens which exhibited a value for the $(F_M - F_D)$ parameter that was less than the value plotted on the abscissa is shown for the two types of surface preparations. Obviously, the $(F_M - F_D)$ parameter (after correction for the bond line thickness) appears to correlate with bond strength but the distribution in values of strength and $(F_M - F_D)$

parameters for the specimens tested overlap one another.

CONCLUSIONS

1. Parametric studies of the effect of a thin interface layer at the metal to adhesive joint show that certain resonant frequencies and relative depths of minima in the reflectivity can be used to infer the interface properties.
2. The inverse problem of deducing the impedance of an interfacial layer from the time domain reflectivity of the total adhesive layer can be used for characterizing the interface in weak bonds.
3. Special procedures must be employed to correct the ultrasonic measurements for the local thickness of the bond line.
4. An experimental correlation between measurements of bond strength and the resonant frequency of the Dumbbell mode was observed on a set of specimens for which a bond line thickness correction could be made.

ACKNOWLEDGMENT

This research was sponsored by the Center for Advanced NDE operated by the Science Center, Rockwell International, for the Advanced Research Projects Agency and the Air Force Materials Laboratory under contract F33615-74-C-5180.

REFERENCES

1. D. H. Kaelble, "Polymer Composite Reliability", Proceedings of the 1978 Review of Progress in Quantitative NDE, La Jolla, 1978.
2. L. M. Brekhovshikh, "Waves in Layered Media," Vol. 6, Applied Mathematics and Mechanics Monographs, Academic Press, New York, 1960.

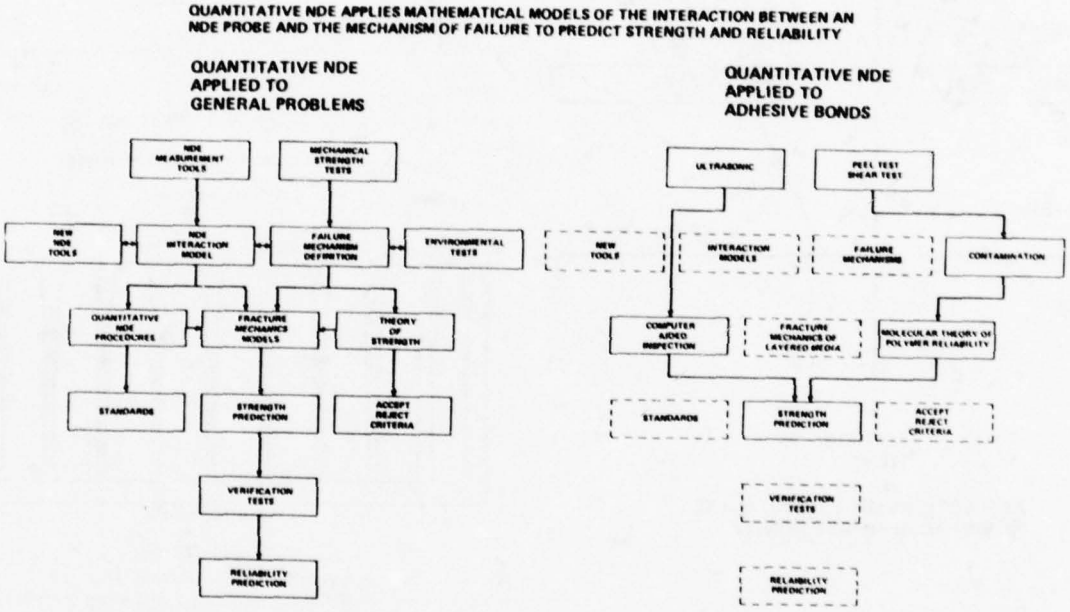

Poster 1 Block diagram comparing the approach used for general problems in quantitative NDE with the specific approach used here on adhesive bonds where new computer methods and molecular theories of polymer reliability have recently become available.

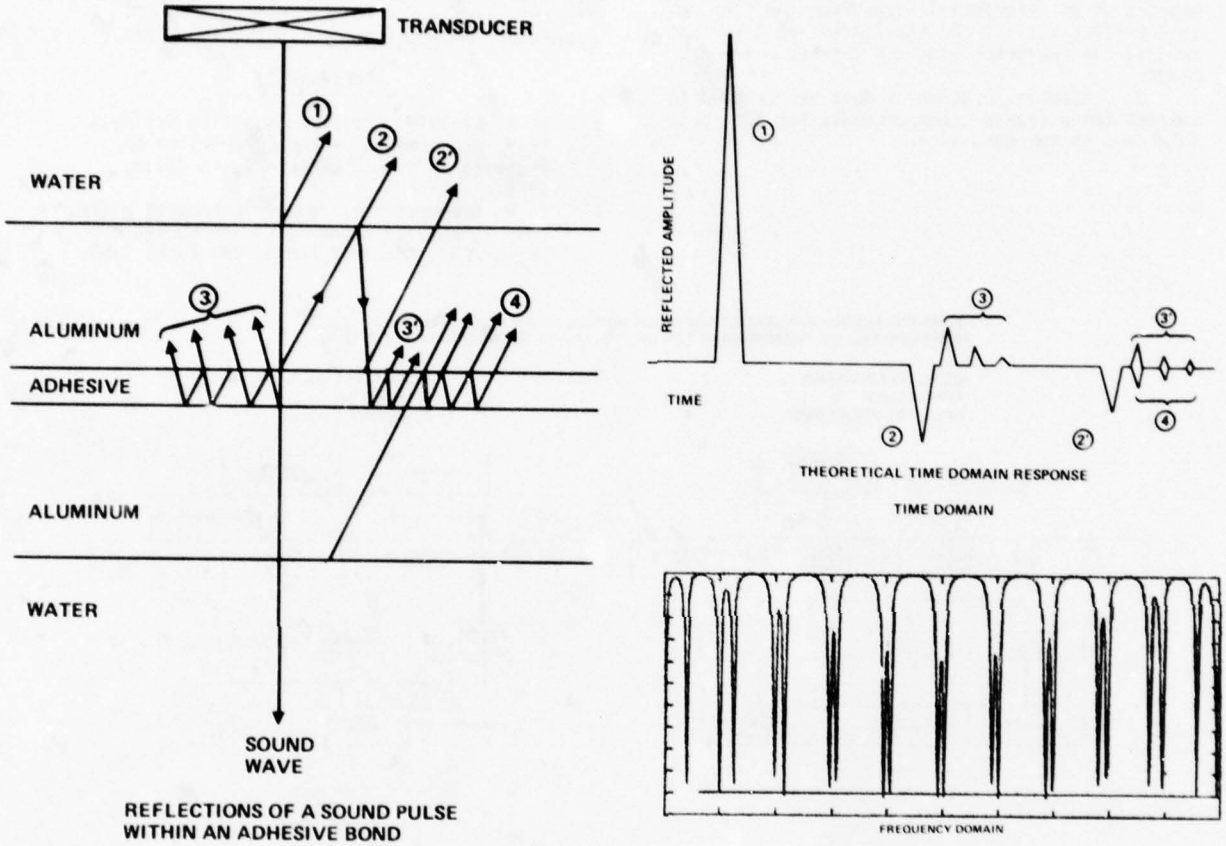

Poster 2 The general experimental arrangement and origin of the ultrasonic echos is shown on the left while the diagrams on the right show the time and frequency domain representations of these signals.

HOW DOES A THIN LAYER AT THE METAL-TO- ADHESIVE INTERFACE MODIFY THE FREQUENCY DEPENDENCE OF THE ULTRASONIC REFLECTIVITY?

EFFECT OF CHANGES IN METAL-ADHESIVE INTERFACE ON FREQUENCY DEPENDENCE OF *ULTRASONIC REFLECTIVITY.*

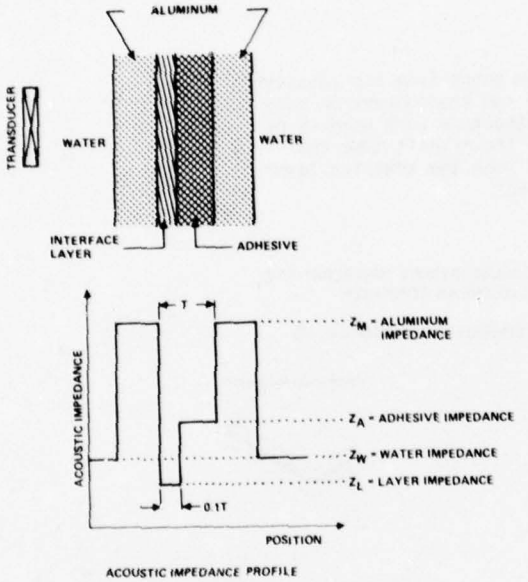

ACOUSTIC IMPEDANCE PROFILE

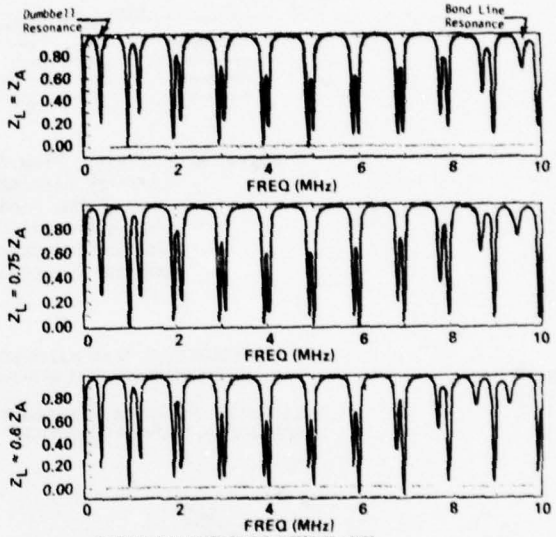

FEATURES INFLUENCED BY THE INTERFACE LAYER

1. Bond line resonance and dumbbell resonance positions are sensitive to both interface impedance and bond line thickness.
2. Bond line resonance frequency can be used to define the bond line thickness and the result used to correct the other features for bond line thickness variations.
3. Dumbbell mode resonance can be corrected for bond line thickness and should be correlated with interface impedance and bond strength.
4. Resonances midway between dumbbell and bond line resonances have a minimal sensitivity to bond line thickness.
5. Midway resonance depths and separations are obviously sensitive to interface impedance and hence should correlate with bond strength.

THE PRESENCE OF AN INTERFACIAL LAYER WHOSE IMPEDANCE IS EQUIVALENT TO A LAYER OF THICKNESS 10% OF THE ADHESIVE THICKNESS WITH AN IMPEDANCE 60% LOWER THAN THE ADHESIVE IMPEDANCE MAKES A CLEAR QUALITATIVE DIFFERENCE IN THE REFLECTIVITY SPECTRUM.

Poster 3 Diagram of a model adhesive bond between two aluminum plates in which one interface is weak and described by a thin layer with an impedance lower than that of the bulk adhesive.

ESTIMATION THEORY CAN BE USED TO DEDUCE THE ACOUSTIC IMPEDANCE OF AN INTERFACIAL LAYER

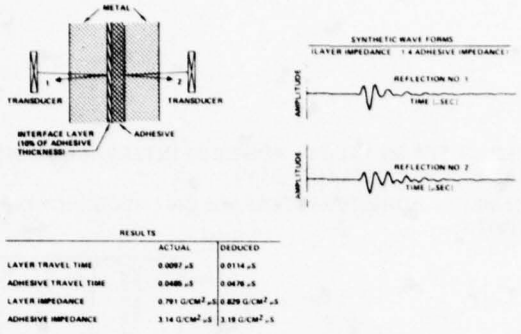

Poster 4 Synthetic time domain echos from the adhesive layer as detected by two transducers on each side of the bonded structure were used to estimate the values of the transit time and acoustic impedance of both the adhesive layer and the interface layer.

- **THE STRENGTH OF AN ADHESIVE BOND IS MEASURED BY TWO SEPARATE AND DISTINCT MODES: PEEL STRENGTH AND SHEAR STRENGTH**
- **EACH MODE RESPONDS DIFFERENTLY TO CHANGES IN THE METAL TO ADHESIVE INTERFACE CONDITION**

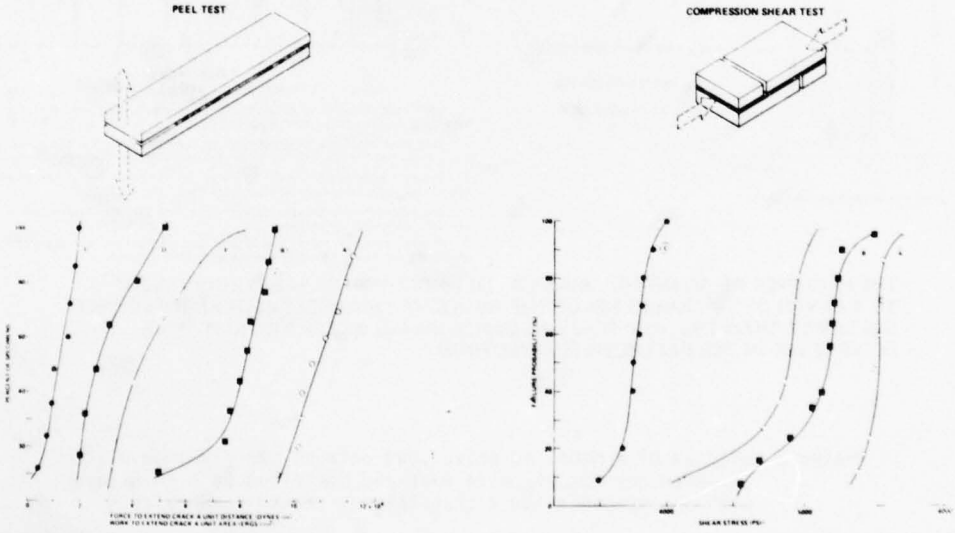

MODIFICATIONS OF THE METAL INTERFACE USED TO PRODUCE SPECIMENS WITH DIFFERENT ADHESIVE BOND STRENGTHS:

A. **PHOSHORIC ACID ANODIZE**
B. **FPL ETCH**
C. **NO SURFACE PREPARATION**
D. **ANODIZE AND MECHANICALLY RUB**
E. **FPL ETCH AND CONTAMINATE**

Poster 5 Cumulative distribution functions for both peel and shear strengths that were observed on specimens with one aluminum plate surface prepared in a manner indicated by the letter designations. (The opposite aluminum plate surface was prepared by an optimum FPL etch.)

ULTRASONIC MEASUREMENTS CAN DISTINGUISH BETWEEN SPECIMENS WITH DIFFERENT INTERFACIAL STRENGTHS

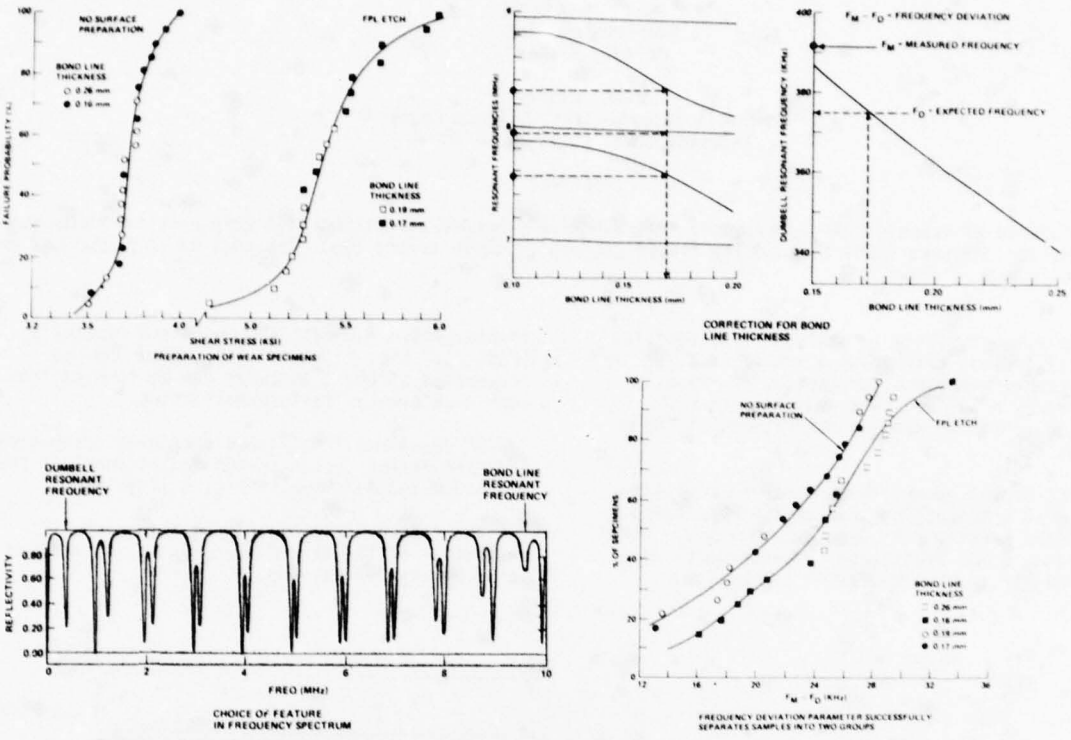

Poster 6 Detailed analysis of specimens showing the maximum degradation of shear strength due to the aluminum surface preparation. The method of using the bond line resonance to define the bond line thickness and then using that thickness to define the expected dumbbell resonance frequency is outlined in the upper right. The ability of the parameter (F_M-F_D) to segregate the specimens into the weak and strong groups is shown in the lower right.

CHARACTERIZATION OF DEFECTS IN ADHESIVE BONDS BY ADAPTIVE LEARNING NETWORKS

A. N. Mucciardi
Adaptronics, Inc.
Mclean, Virginia

R. K. Elsley
Rockwell International Science Center
Thousand Oaks, California 91360

ABSTRACT

Broadband ultrasonic pulses reflected from adhesively bonded structures have been used to train adaptive learning networks (ALN) to identify flawed regions of these structures. The goal is to identify four different types of flaws.

The steps involved in making a flaw decision (Fig. 1) include extracting a set of features from the measured waveforms, processing of these features by a set of ALN's and then using a decision scheme to combine the results of the various ALN's.

Four sample geometries containing built-in flaws were studied (Fig. 2). Normal incidence pulse echo measurements were made using a broadband 15 MHz transducer. Measurements were performed in a water bath with conventional transducers. The data was processed digitally (Fig. 3). Fig. 4 (right side) shows how the properties of the transducer can be removed from each waveform by "self-normalization."

RF waveforms from flawed specimens often show dramatic effects, such as the "quiet zone" in the disbonded sample shown in Fig. 4 (left side).

The current results (Fig 5) show good separation of the flawed specimens from unflawed and slightly flawed ones.

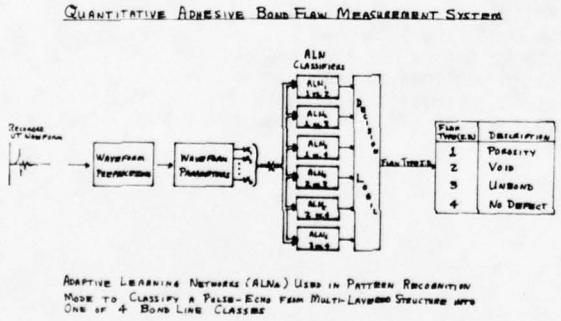

Adaptive Learning Networks (ALNs) Used in Pattern Recognition Mode to Classify a Pulse-Echo from Multi-Layered Structure into One of 4 Bond Line Classes

Fig. 1 Steps in the signal processing include feature extraction, ALN's and decision making.

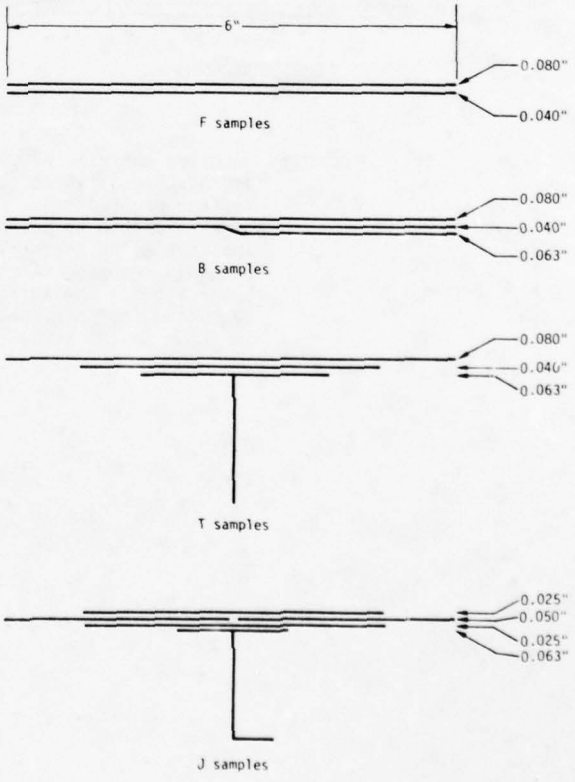

Fig. 2 Four sample geometries containing built-in flaws were studied.

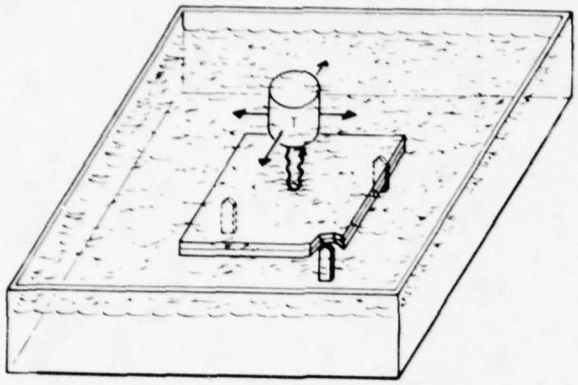

(a)

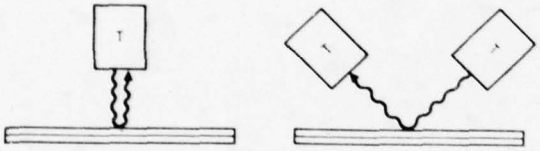

(b) (c)

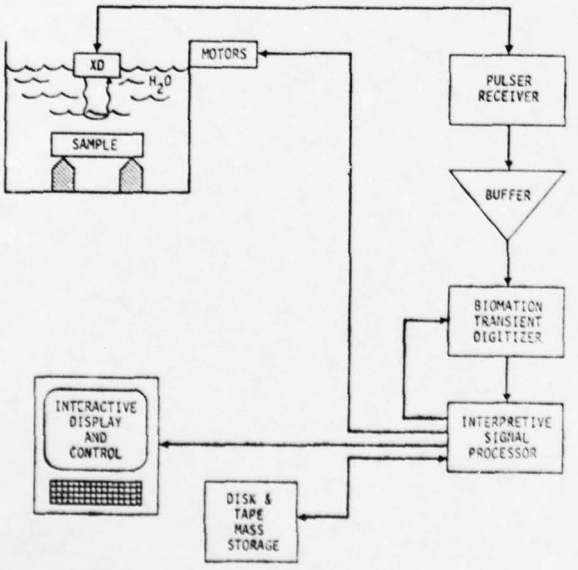

Fig. 3 Measurements were performed in a water bath with conventional transducers. The data was processed digitally.

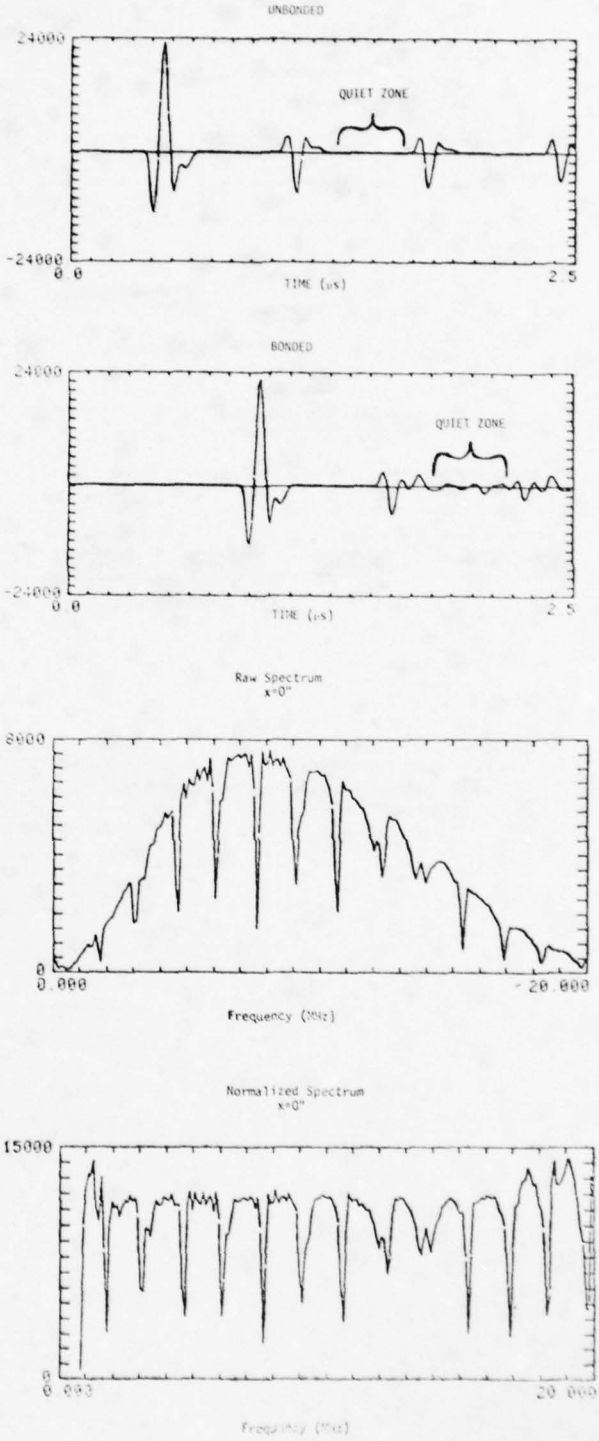

Fig. 4 RF waveforms from flawed specimens often show dramatic effects; the properties of the transducer can be removed from each waveform by "self-normalization".

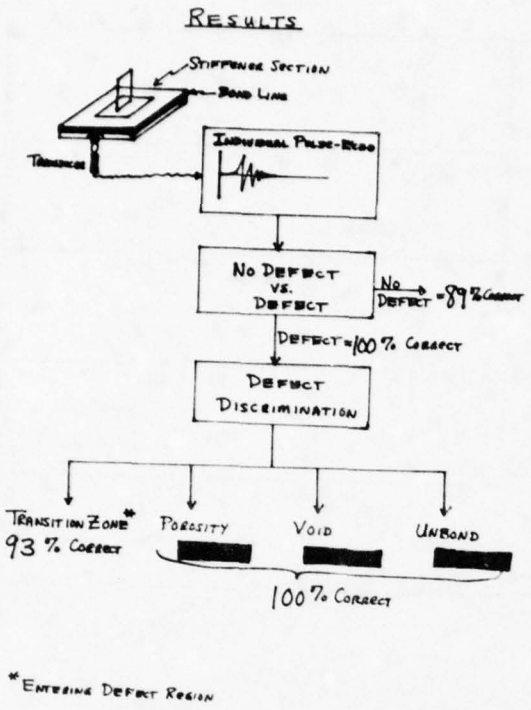

Fig. 5 Current results show good separation of the flawed specimens from unflawed and slightly flawed ones.

SURFACE CONTAMINATION: NDE MAPPING AND EFFECTS ON BOND STRENGTH

Tennyson Smith
Rockwell International Science Center
Thousand Oaks, California 91360

ABSTRACT

Al 7075-T6 samples have been surface treated by the phospheric acid anodize (PAA) and by the standard FPL etch for comparison. These samples were then deliberately contaminated, bonded and given lap shear or wedge endurance tests to discover the effect of the contamination. The results indicate that the PAA surface is very forgiving of certain types of contamination but not others. The FPL etch surface is sensitive to even a monolayer of contamination. Our NDI surface contamination automatic mapping facility can detect contamination well below the level that significantly degrades the adhesive joints.

INTRODUCTION

It has been established in a previous report[1] that our surface tools, ellipsometry, surface potential difference (SPD), and water contact angle (θ_{H_2O}) can be used to detect contamination on PAA surfaces. The ellipsometer was found to be especially useful because it could detect all forms of contamination, process errors and handling damage. An automatic computer operated mapping facility was used to demonstrate that contamination can be located and a warning given if a panel was improper prior to adhesive layup.

The purpose of the present research is to establish the levels of contamination that significantly degrade adhesive joints between Al 7075-T6 and FM 73 adhesive, and demonstrate our ability to detect and map contamination below these levels.

Procedure

Panels of Al 7075-T6 were anodized, contaminated to various levels in a controlled manner, then mapped for contamination. This panel was then bonded to an uncontaminated panel and cut up for lap shear or wedge tests. Correlations were then made between the contamination maps and the bond strength or crack growth, as a function of contamination level.

Comparison of PAA with FPL etch

Figure 1 is a plot of water contact angle vs stearic acid contamination thickness on FPL etched and PAA samples. A monolayer or so of stearic acid increases θ_{H_2O} to >100° for the FPL etched samples. The contact angle on PAA surfaces increases, but not as rapidly as for the FPL etch. Figure 2 shows that low levels of stearic contamination on FPL etch samples decreases the lap shear bond strength drastically, whereas the PAA surface maintains high lap shear values (4600 to 6500 psi) even up to 3000Å contamination.

Effect of Contamination Type

Figures 3 and 4 are water contact angle and lap shear bond strength vs contamination thickness for lubricating oil and silicone grease on PAA surfaces. The PAA surface can accommodate much more oil than silicone grease for the same increase in θ_{H_2O}. Figure 4 indicates that a small amount (~200Å) of oil or silicone grease actually increases the lap shear bond strength. Beyond 200Å the laboratory oil has little effect on the bond strength whereas the silicone grease drastically decreases the bond strength.

Mechanisms

Explanations for the behavior of the PAA and FPL surfaces toward contamination can be obtained from the models in Figs. 5 and 6. Figure 5 shows a schematic representation of the cross section of a FPL etched aluminum surface. This model was derived from SEM, TEM and ellipsometric measurements.[2] The FPL etched surface is highly pitted. The pits are of the order of 10 μm across and have smaller pits within. The smaller pits have still smaller pits of the order of 500-1000Å and ~400Å deep. The oxide film is only ~100-200Å thick. Contamination films, a few monolayers thick, form a continuous weak boundary layer on the FPL etched surface and thus yields large water contact angles and weak adhesive joints. Figure 6 represents the phosphoric acid anodized surface. The anodic film is 3000-5000Å and is made of a large density of individual columns of aiuminum hydroxide with a large porous region between columns. Ellipsometry indicates the films are about 20% porous. Contaminants are absorbed into these pores and actually increase the shear strength by filling the voids. The adhesive also penetrates the pores and creates a strong mechanical link to the substrate.

Experiments have shown that stearic acid and lubricating oil can dissolve into the FM 73 epoxy adhesive, so that large amounts of contamination can be accommodated without degrading the adhesive joint. On the other hand, silicone grease does not absorb into the FM 73 adhesive and therefore thick layers exceed the capacity of the anodic layer and strongly degrade the joint strength. These mechanisms are consistent with the water contact angle results and with the degradation of the tensile strength by cotton glove crushing during handling. It is our hypothesis that the individual hydroxide columns in the PAA anodic film are single crystals with large tensile strength perpendicular to the substrate. Cotton glove smudge crushes these crystals and destroys their tensile strength. This explains why the cotton glove smudge fails the wedge endurance tests (film under tension in humid atmosphere) but not the lap shear test.

NDI Mapping

Figure 7 shows a computer contamination map of the ends of six Al 7075-T6 PAA anodized samples

after controlled contamination with silicone grease. Sample 6 was not contaminated, the map is blank because the ellipsometer signal was suppressed for this control sample. The density of dots on other samples is proportional to the deviation of the ellipsometric signal outside the acceptance band of the control (No. 6). The contamination increases from samples 1 to 5. The control sample had a lap shear strength of about 5300 psi as indicated by the bar graph above the map. Samples 1 and 2 also had bond strengths equal to that of the control even though contamination was detected. The bond strength of samples 3, 4 and 5 decreases as the contamination increases. These results indicate that we have met our goal of detection of contaminaton below the level that causes bond degradation.

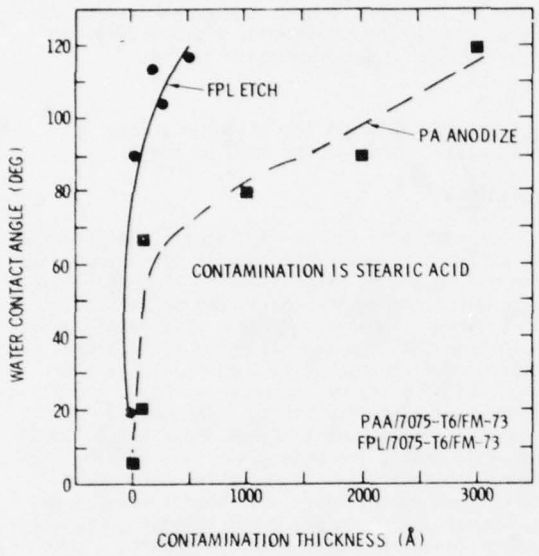

Fig. 1 Plot of contact angle vs contamination thickness.

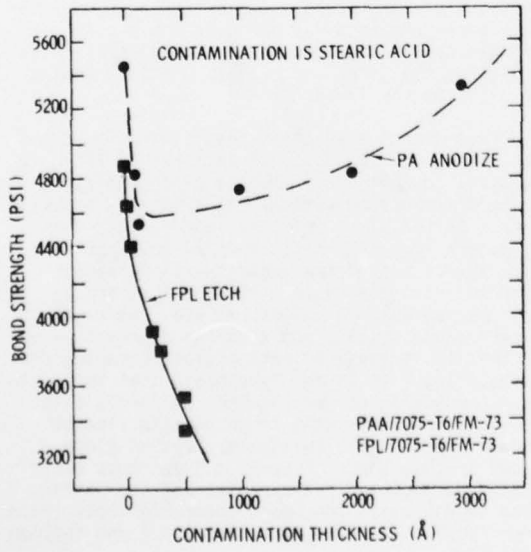

Fig. 2 Plot of bond strength vs contamination thickness.

REFERENCES

1. T. Smith, AFML-TR-74-73, June 1974, Part II, Oct. 1975.
2. T. Smith, AFML-TR-77-42, April 1977.

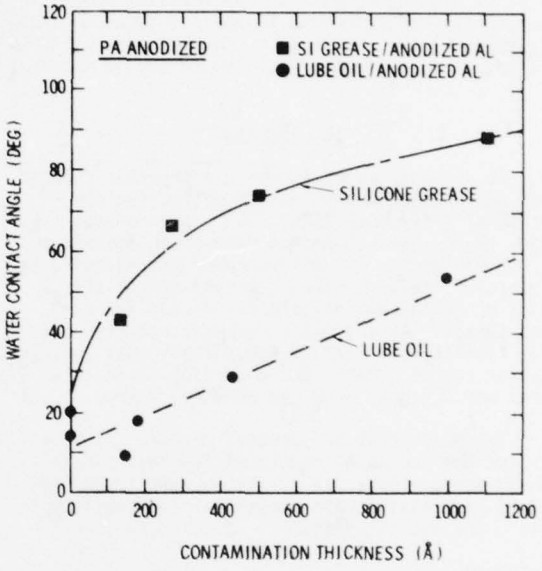

Fig. 3 Plot of contact angle vs contamination thickness.

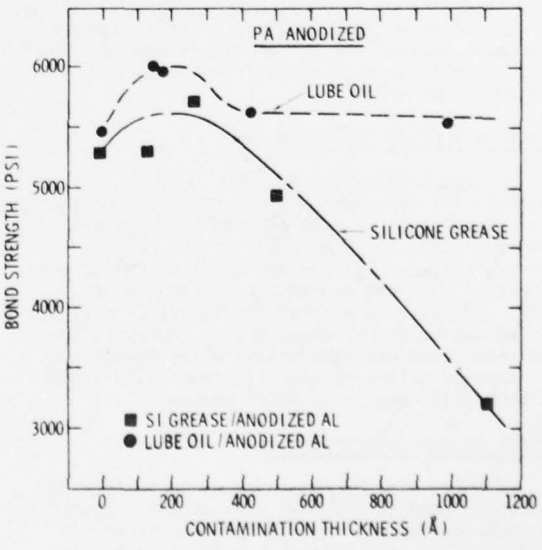

Fig. 4 Plot of bond strength vs contamination thickness.

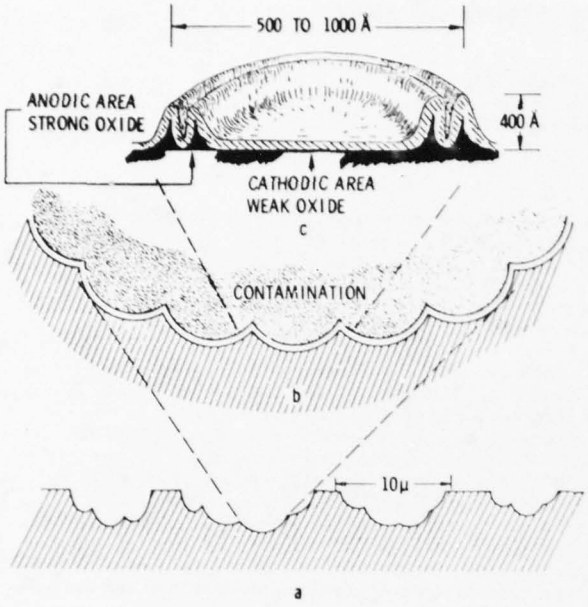

Fig. 5 Schematic representation of FPL etched aluminum with contamination, three magnifications.

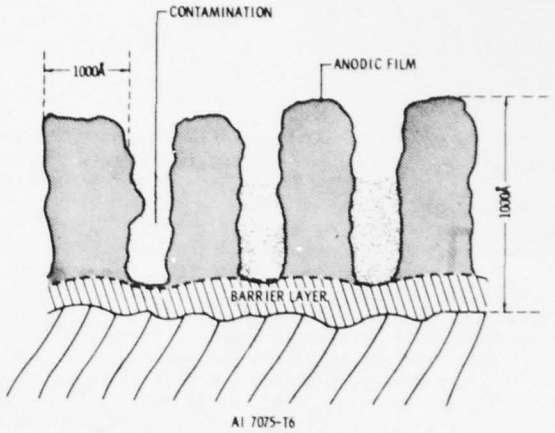

Fig. 6 Schematic representation of phosphoric anodized Al 7075-T6.

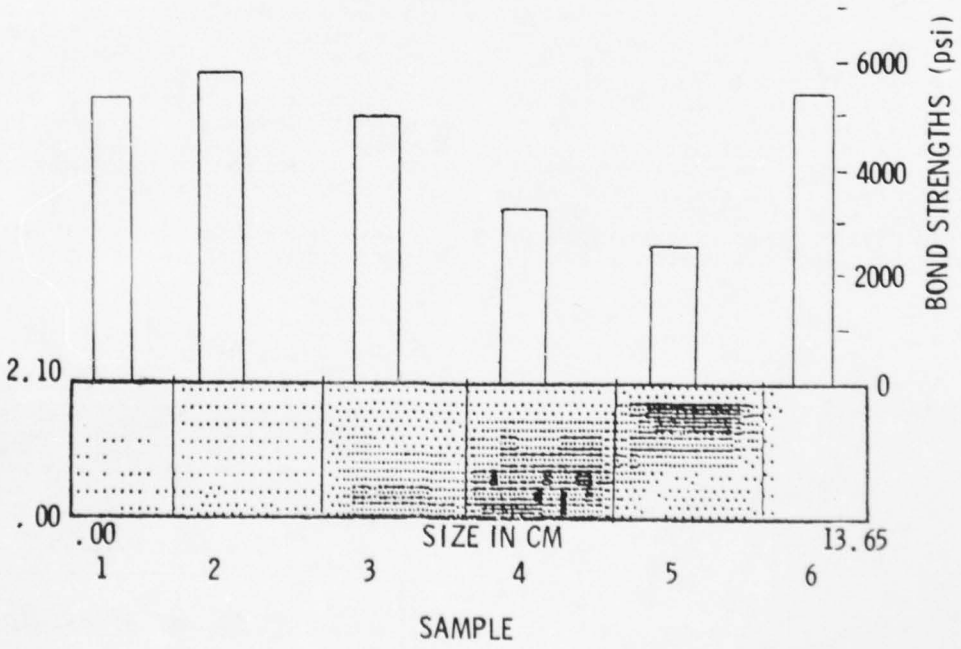

Fig. 7 Computer contamination plot for silicone grease on phosphoric acid anodized Al 7075-T6. Bars indicate relative lap shear bond strengths.

AD-A071 047 ROCKWELL INTERNATIONAL THOUSAND OAKS CALIF SCIENCE --ETC F/G 14/2
PROCEEDINGS OF THE ARPA/AFML REVIEW OF PROGRESS IN QUANTITATIVE--ETC(U)
JAN 79 D O THOMPSON F33615-74-C-5180
UNCLASSIFIED SC595.51AR AFML-TR-78-205 NL

4 OF 6
AD
A071047

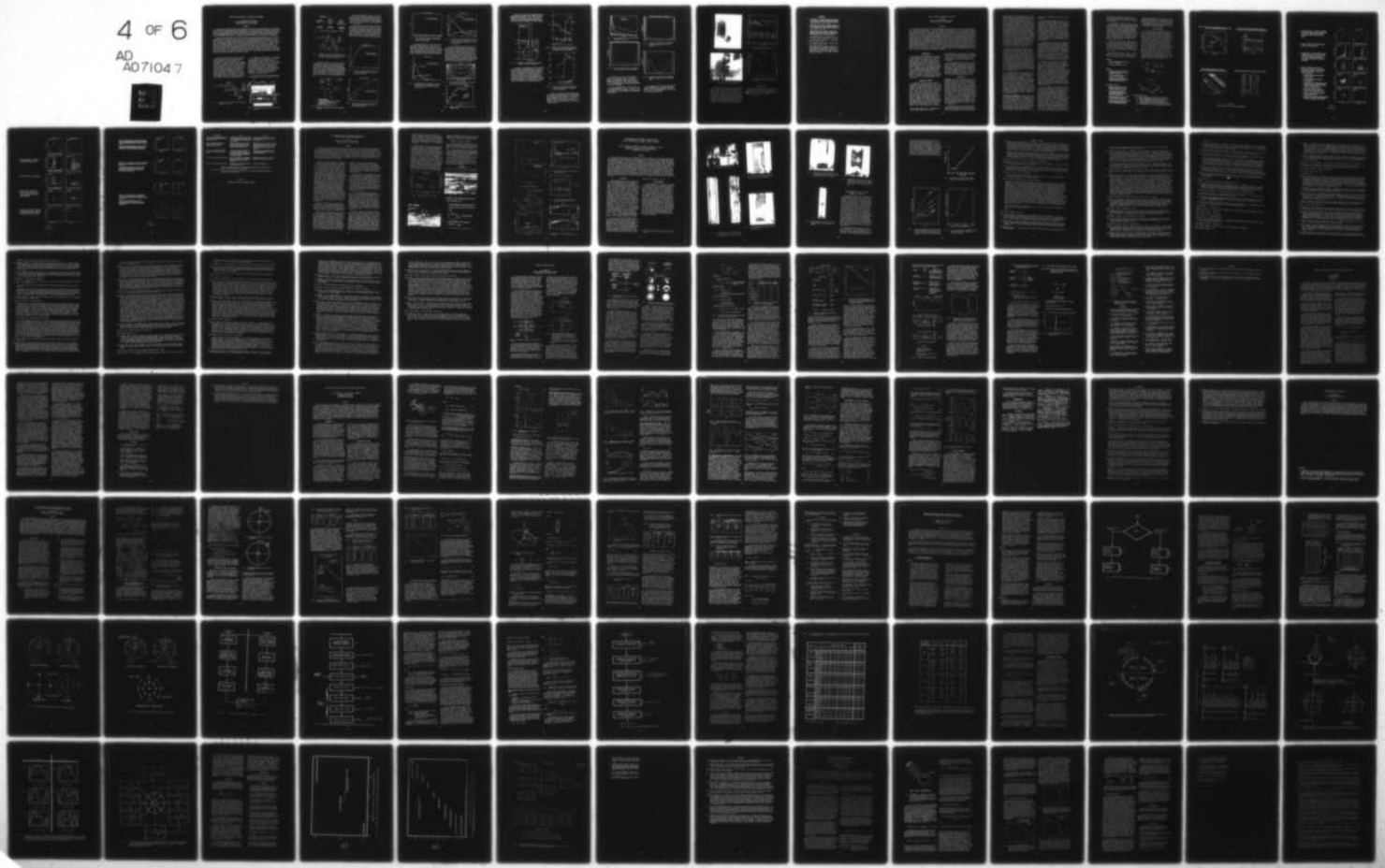

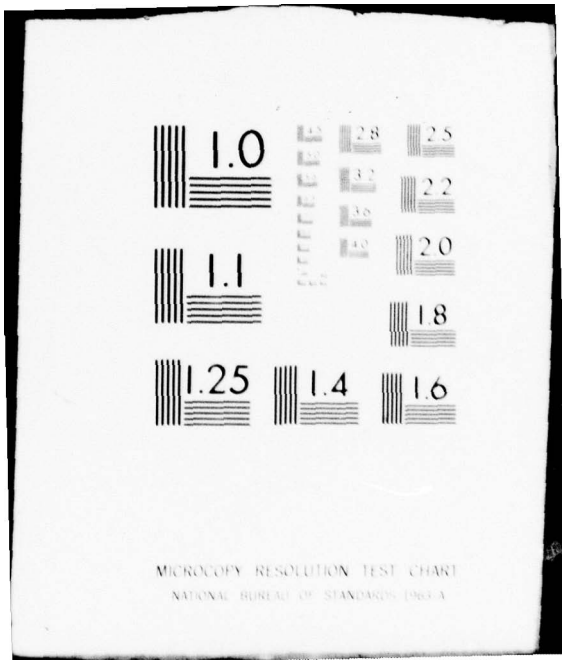
1.0
1.1
1.25
1.4
1.6
2.8
3.2
3.6
4.0
2.5
2.2
2.0
1.8
MICROCOPY RESOLUTION TEST CHART
NATIONAL BUREAU OF STANDARDS 1963-A

MOISTURE DIFFUSION ANALYSIS FOR COMPOSITE MICRODAMAGE

C. L. Leung and D. H. Kaelble
Rockwell International Science Center
Thousand Oaks, California 91360

ABSTRACT

The absorption of moisture into fibrous polymeric meterials has been recognized as one of the major mechanisms in the strength degradation of such materials as reported by several workshops (1-3) and publications (4-7). The objective of the work reported here is to use nondestructive evaluation (NDE) techniques to determine the moisture content (profile) within a composite by measuring the moisture diffusion rate and then subjecting the data to a statistical estimation analysis. This reveals the location of structural degradation and provides a sensitive inspection method for the serviceability of composites.

Hydrothermal aging effects on cured graphite-epoxy composites were determined using: (1) acoustic attenuation, α_L, (2) ultrasonic velocity, c_L, and (3) thickness measurements of the composites. Results showed that while ultrasonic acoustic properties, sample thickness and moisture diffusion profiles are highly sensitive to structural degradation, ultrasonic inspection becomes insensitive in areas of extensive internal damage, probably due to high acoustic attenuation which results in loss of signals. Moisture diffusion analysis (MDA), in this case, becomes highly sensitive as a quantitative detection tool. Presently, analytical methods are developed to quantify the depth profile of moisture penetration in graphite-epoxy composites. Measurement of effusion kinetics over a range of time intervals followed by application of statistical estimation theory enables the depth concentration of moisture at initial time t=0 to be calculated. For a particular model in which the sample is assumed to be exposed to periodically changing environments, the model predicts large fluctuations in moisture concentration near the surfaces while the interior concentration is relatively constant.

Moisture evolution from the composite samples are measured by the DuPont Moisture Evolution Analyzer (Model 902H) as shown below. The simplified block diagram shows the general theory of operation. The sample to be analyzed is weighed and placed in the oven. Moisture in the sample is vaporized, transported by the dry carrier gas to the electrolytic cell which is coated with a thin film of phosphorus pentoxide, and is absorbed by the P_2O_5. Electrolysis changes the water into oxygen and hydrogen, regenerating the P_2O_5. The current required (0.132μA per molecule of H_2O) to regenerate the P_2O_5 is integrated and displayed as total moisture content in micrograms. A strip-chart recorder can also be attached to measure the rate of moisture release as a function of time.

The sample cell provided with the instrument is not suitable for large specimens. Therefore, external sample cells have been devised to accommodate bar specimens (sleeve type cell) and plate specimens (face plate cells). To facilitate data collection and analysis, the Analyzer has been interphased with a mini-computer via a analog-to-digital converter. Thus temperature, moisture evolution rate and moisture content can be recorded automatically, then either stored or displayed. In conjunction with the external sample cells, the unit can be portable and suitable for field inspections.

The moisture Evolution Analyzer measuresthe moisture release rate, J_m, as a function of time.

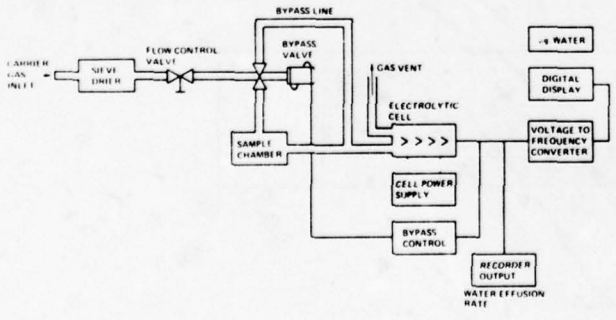

Fig. 1. Schematic block diagram of DuPont moisture evaluation analyzer.

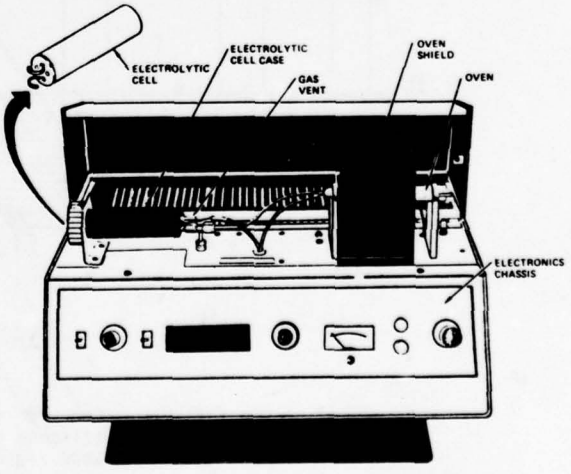

Fig. 2. Front view of Du Pont moisture evaluation analyzer.

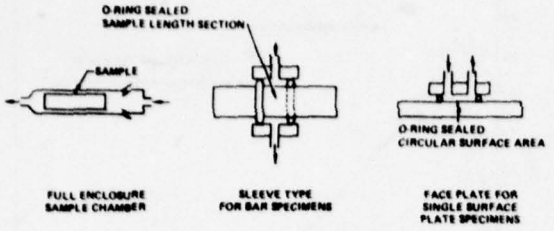

Fig. 3. Cross-section of sampling cell design.

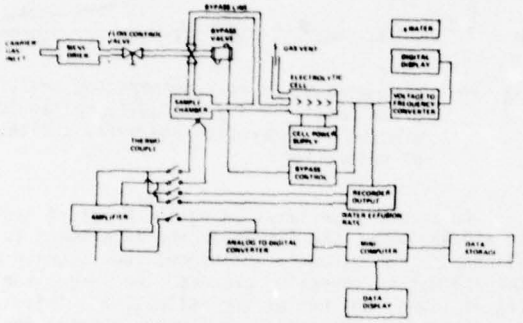

Fig. 4. Schematic block diagram of DuPont moisture evaluation analyzer modified for computerized data acquisition and analysis.

The moisture Evolution Analyzer measures the moisture release rate, J_m, as a function of time. The Analytical problem is then to calculate the initial time, t=0, moisture concentration profile from the time history of effusion rate measurements, applying statistical estimation theory to this analysis. The process is represented schematically in the following diagram. The values of $C^0(x)$, when plotted as a function of x, gives the moisture profile of the material with the corresponding set of J_m's.

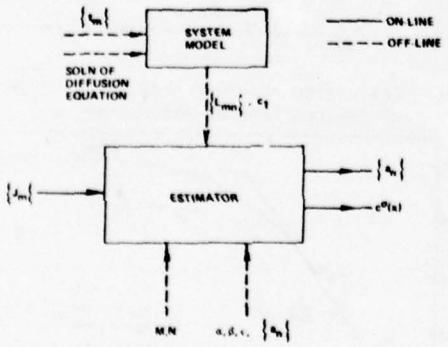

M = NUMBER OF MEASUREMENTS
N = NUMBER OF ESTIMATIONS
c_1 = CONCENTRATION OF WATER IN THE COMPOSITE CORRESPONDING TO THE CHEMICAL POTENTIAL μ_1
α = A PRIORI BIAS AGAINST LARGE AMPLITUDE $c^0(x)$
β = A PRIORI SMOOTHNESS WHICH IS APPLIED TO $c^0{}_x$ IN THE RANGE ϵ_x (1-ϵ)x
ϵ = NUMERIC RANGE FACTOR $0 < \epsilon < 0.5$
$\{s_n\}$ = OBSERVATIONALLY CONDITIONED AVERAGE FOR s_n

Fig. 5. Schematic representation of the estimation process.

The three accompanying graphs illustrate the accuracy of the estimator. Starting with a fully saturated material of known dimensions and diffusion coefficients, according to Fickian diffusion would have moisture distribution profiles represented by the solid lines, after 20, 100 and 2000 minutes of desorption.

After each time interval, a set of moisture release rates, J_m, can be obtained from Fick's Law. The inversion of each set of J_m through the Estimator would give the moisture profile of the material responsible for that set of moisture release rate. These estimated solutions are denoted by the dotted lines in the graphs. It can be ssen that the estimated profile agrees very well with the Fickian direct solution, thus verifying the Estimator model.

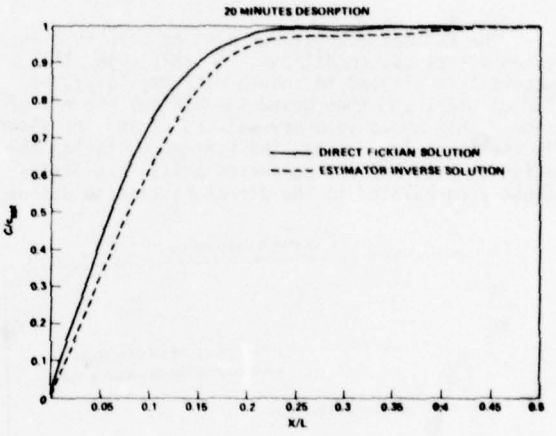

Fig. 6. Estimated moisture concentration profile for a saturated composite, after 20 minutes of desorption.

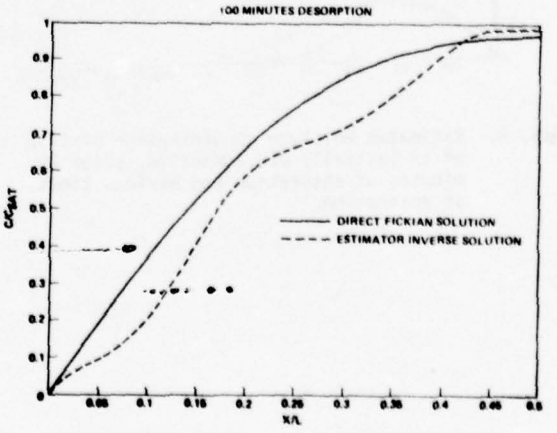

Fig. 7. Estimated moisture concentration profile for a saturated composite, after 100 minutes of desorption.

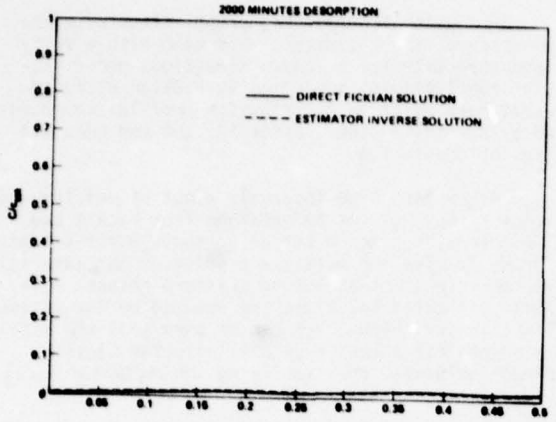

Fig. 8. Estimated moisture concentration profile for a saturated composite, after 2000 minutes of desorption.

The Estimator model can also be used in simulated actual use conditions. In this case, the material is allowed to absorb moisture for 20 or 100 minutes, and then dried for various amounts of time. This would be a dry-wet-dry cycle. As shown in the following graphs, the Estimator, taking the effusion rate values, generates moisture profiles closely correlated to the direct Fickian solutions.

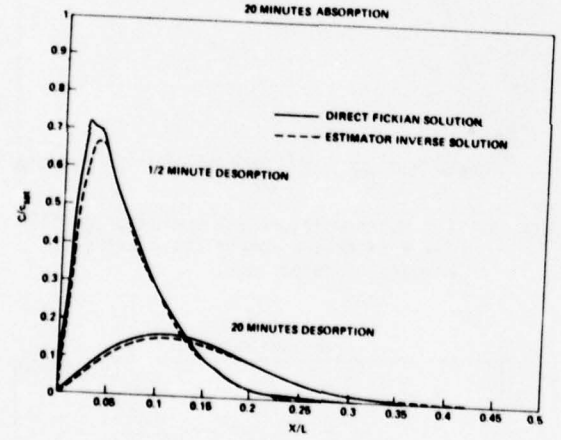

Fig. 9. Estimated moisture concentration profile of an initially dry composite, after 20 minutes of absorption and various times of desorption.

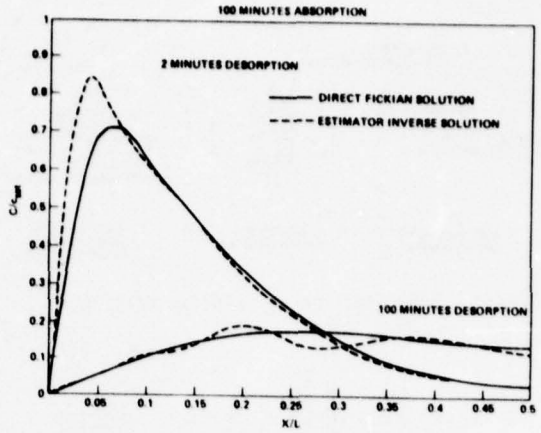

Fig. 10. Estimated moisture concentration profiles of an initially dry composite, after 100 minutes of absorption and various times of desorption.

In a real experiment using the Moisture Evolution Analyzer, the time span the experiment is allowed to run strongly influences the accuracy of the estimating inversion process. The larger the set of times, the better the estimation. This is illustrated by the following figures showing the moisture content as a function of exposure time. Taking the reduced time, $t^* = Dt/L^2$, for a typical 0.5 cm thick composite, to completely dry off the saturated material would require about 5000 minutes. A smaller set of times would give a low moisture profile at the sample core by the Estimator.

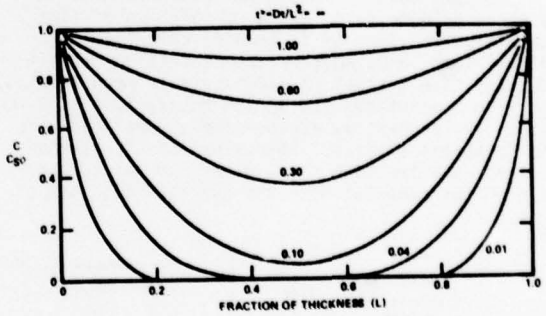

Fig. 11. Calculated moisture profile as a function of reduced time of absorption.

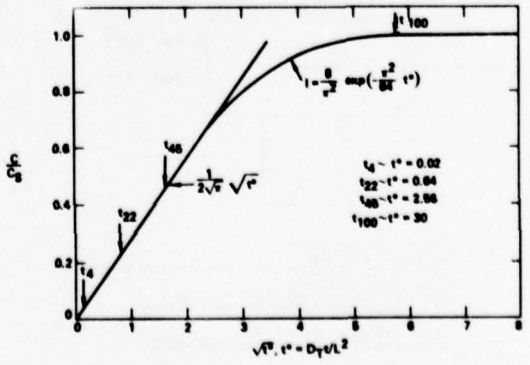

Fig. 12. Degree of moisture saturation at various reduced times.

The first figure shows the arrangement for variable moisture exposure of the composite (Fiberite 934/T300) aged for about a year. Four zones are obtained on the sample bar: exposure to ambient condition, sealed from ambient environment, exposure to water vapor and exposure to water immersion.

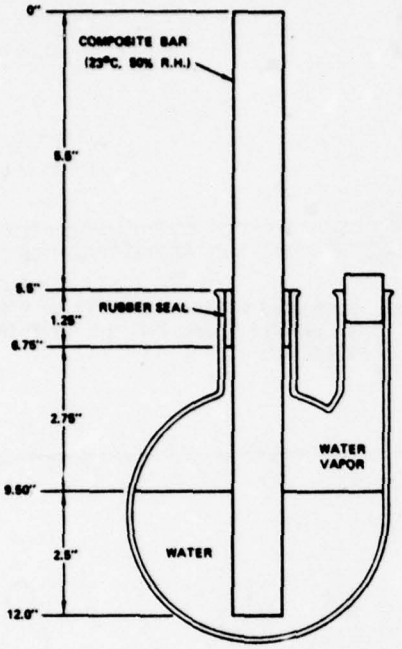

Fig. 13. Schematic of variable moisture exposure of composite (Fiberite 934/T300)

The extent of microdegradation of the composite bar due to moisture exposure along the length is characterized by ultrasonics (acoustic attenuation and ultrasonic velocity) through the thickness of the bar. Deformation in the physical dimension (width and thickness) can also be detected. It is seen that in areas of high moisture penetration, thus causing high levels of microdegradation, ultrasonics (attenuation, and velocity) are excellent detection techniques. The damaged zones also show signs of swelling because of water penetration.

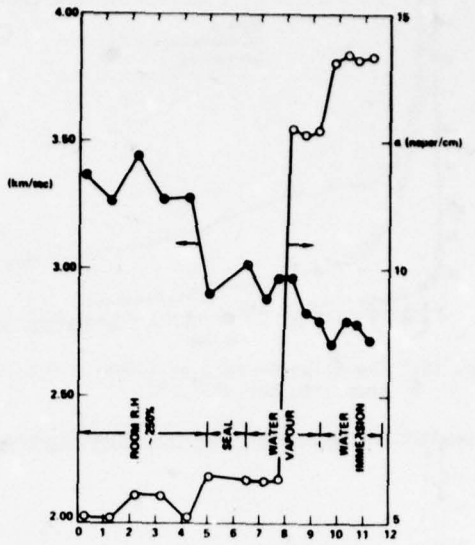

Fig. 14. Effects of varied moisture exposure on the ultrasonic velocity and attenuation of composite (Fiberite 934/T300)

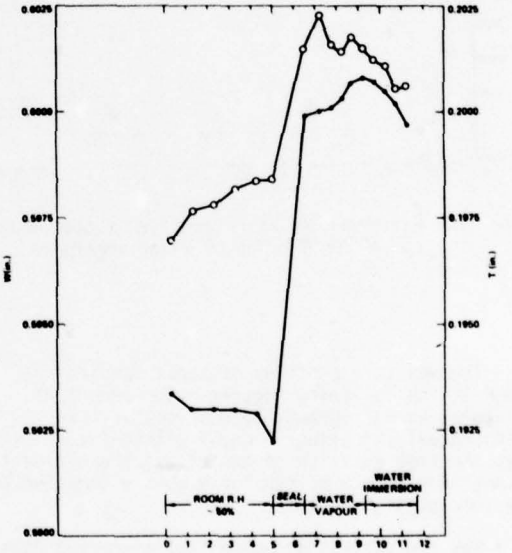

Fig. 15. Effects of varied moisture exposure on the width and thickness of composite (Fiberite 934/T300)

Sections of the composite bar exposed to ambient and water immersion conditions can be examined by the Moisture Evolution Analyzer and the moisture profile generated by the Estimator. A separate sample, immersed in water for only 6 hours, is also examined. The rates of moisture evolution, as a function of time for these samples are illustrated in the following.

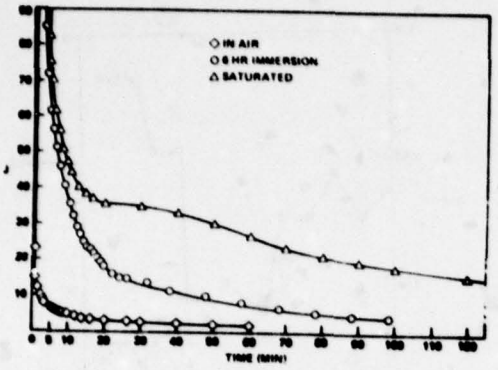

Fig. 16. The effusion rate of Fiberite 934/T300 composite bar at 7.5°C.

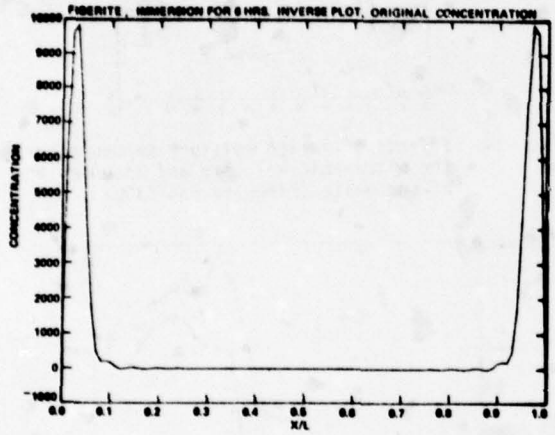

Fig. 17. Estimated moisture profile of composite bar after 6 hours of water immersion.

The moisture profiles of these samples are given in the following figures. The amount of moisture, in micrograms, agrees very well with weighing determinations. One limiting factor is that the time duration of the effusion experiment is not long enough to provide a good estimation for the core of the samples.

For the saturated sample, there are two dips in the moisture profile, at x/L = 0.1 and 0.9. The J vs time curve for this sample also shows a hump. These anomalies are due to defects in the composite, as shown below.

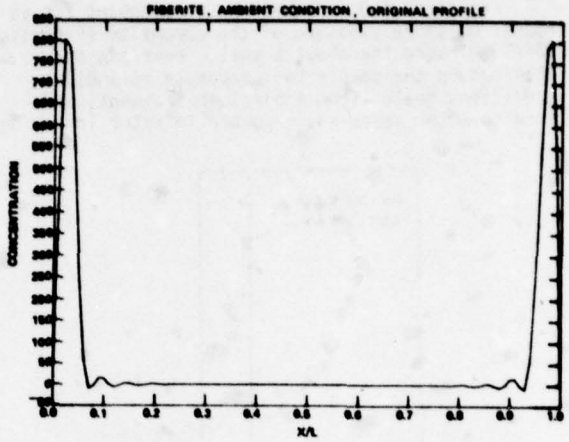

Fig. 18. Estimated moisture profile of exposed section of composite bar Fiberite 934/T300.

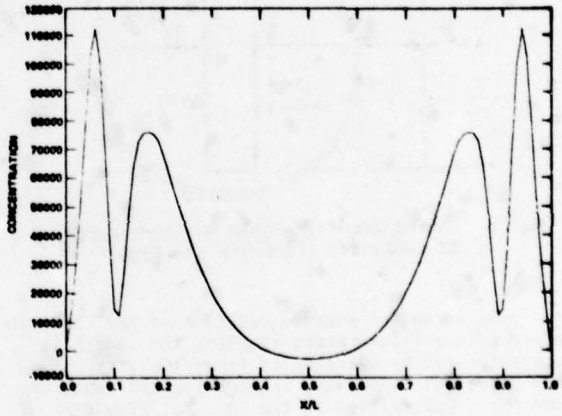

Fig. 19. Estimated moisture profile of immersed section of composite bar Fiberite 934/T300.

An enlarged view of the cross-section of the Fiberite 934/T300 used in this experiment show layers of voids in the interlaminar orientation due to faulty layer-up manufacture. This is shown by the following photographs.

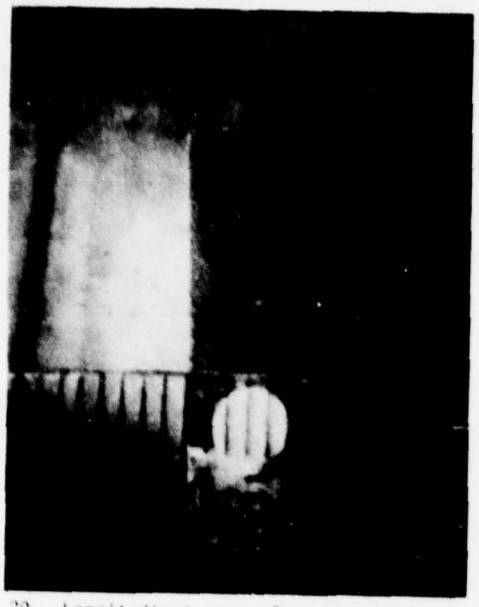

Fig. 20. Longitudinal view of composite bar showing air voids.

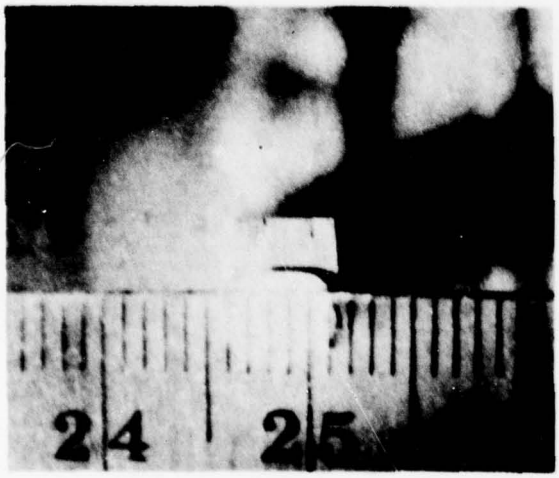

Fig. 21. Cross-sectional view of composite bar showing two layers of delamination.

Ultrasonic mapping techniques clearly show the layer of voids in the plane of the sample. Moisture evolution rates for the transfibrous orientation shows a lower moisture concentration because the moisture is being effused at a faster initial rate along the planes of the voids, depleting the interior moisture content of the sample more rapidly than in the transverse orientation, enabling the Estimator to lower the total amount of moisture in the sample. Also, the time duration of the effusion experiment is much longer (about 1000 minutes), enabling a better estimation at the sample core.

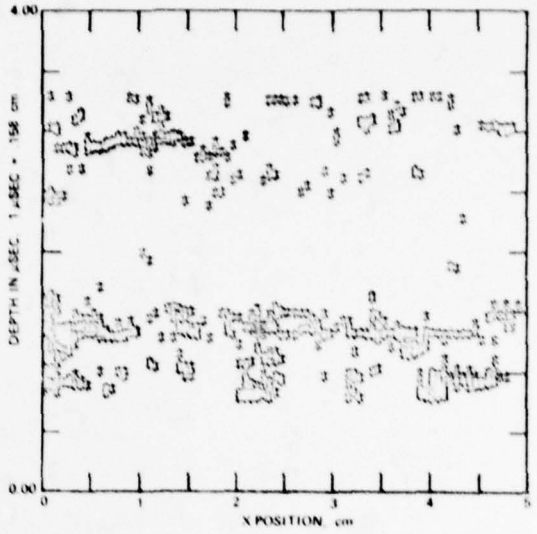

Fig. 22. Ultrasonic mapping profile of composite bar showing regions of voids.

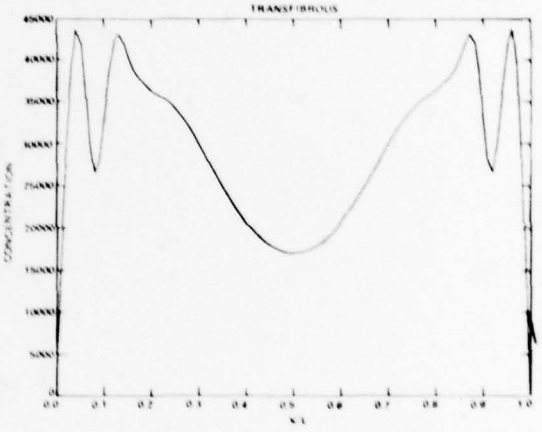

Fig. 23. Estimated moisture profile of composite bar Fiberite 934/T300 in transfibrous orientation.

ACKNOWLEDGMENT

This research was sponsored by the Center for Advanced NDE, operated by the Science Center, Rockwell International, for the Defense Advanced Research Projects and the Air Force Materials Laboratory under Contract F33615-74-C-5180.

REFERENCES

1. Proceedings of Critical Review of Techniques for Characterization of Polymeric Materials, Army Materials and Mechanics Research Center, Watertown, Mass., July 6-8, 1976.
2. Proceedings of Meeting on Chemical Composition Specifications for Composite Matrix Resins, Air Force Materials Lab., Wright-Patterson AFB, Ohio, October 27-28, 1976.
3. Proceedings of Workshop on the Role of the Polymer Substrate, Interface in Structural Adhesion, Sponsored by AFOSR and AFML, University of Dayton, Ohio, Sept. 9-10, 1976.
4. E. L. McKague, Jr., J. E. Halkios and J. D. Reynolds, J. Composite Materials, 9, 2 (1975).
5. C. H. Shen and G. S. Springer, J. Composite Materials, 10, 2 (1976).
6. D. H. Kaelble and P. J. Dynes, Materials Evaluation, April, 103 (1977).
7. D. H. Kaelble and P. J. Dynes, "Methods for Detecting Moisture Degradation" Interdisciplinary Program for Quantitative Flaw Detection, Special Report for Third Year Effort, July 1, 1976-June 30, 1977, Contract Number F33615-74-C-5180, pp. 319-363.

ACOUSTIC EMISSION IN COMPOSITES USING MPA

L. J. Graham
Rockwell International Science Center
Thousand Oaks, California 91360

ABSTRACT

The purpose of this study is to try to determine the current mechanical state of a composite specimen (or structure) and predict its remaining lifetime from the characteristics of the acoustic emission (AE) signals it emits under load. In previous studies of the characteristics of AE generated in graphite-epoxy composites, empirical observations were made relating the frequency content and the amplitude distributions of the AE signals to singular points on the loading curve of a specimen and to the composite's moisture content. Up to now, these relationships have been difficult to study systematically because of limitations in efficiently handling the large amount of data contained in the emission signals. With the Acoustic Emission Multi-Parameter Analyzer (AEMPA) (developed under a Science Center IR&D program), pertinent information is abstracted from each emission signal as it occurs during a test and is stored in compact digital form for subsequent data processing. Multi-parameter correlation and pattern recognition techniques among the 23 abstracted parameters are then used to identify distinct types of AE events, and various observations used to identify the microscopic mechanisms of flaw growth in the material which generate these different types. For those geometries and load conditions which product failure by a well-defined series of mechanistic steps (e.g., matrix crazing, fiber-matrix interface debonding, fiber fracture, interlaminar fracture), it may be possible to predict specimen failure by determining the relative amounts of the various mechanisms occurring at a given time in the life of the specimen from the AE signals. Progress along these lines using MPA is described.

INTRODUCTION

For several years broadband signature analysis of acoustic emissions from a variety of materials has been attempted, with some success, at the Science Center. This was done by recording the analog AE signals on a modified videocorder and then manually making time and frequency domain measurements on hundreds to thousands of the individual waveforms to try to extract features which could be related to specific AE generation mechanisms. To make this work easier and more quantitative, an Acoustic Emission Multi-Parameter Analyzer* was designed and constructed which makes a selected set of these measurements on each AE waveform as it occurs. These measured values are stored in the form of 32 bytes of digital data per event on a floppy disk for later computer processing. The first use of the AEMPA system is described here.

EXPERIMENTAL APPROACH

The objectives and experimental approach for this project are outlined on the first poster. As stated there, the ultimate objective is to be able to predict the remaining lifetime of a structural component from the signature of the AE generated during a proof load of that structure at any point in its service life. The success of the approach taken is predicated upon two essential conditions. The first is that the growth of the critical flaw proceeds by well-defined, sequential mechanistic steps. Substantial progress is being made in predicting this sequence for particular materials, geometries and loading conditions by the stress analysts. The second condition is that AE signatures for each of the critical mechanisms are unique and can be identified, which is the subject of the present study. Then, signature analysis can tell what mechanism, or statistical mix of mechanisms, are operating under the proof load and, therefore, at what point in the sequence of steps in its growth process the critical flaw is at that time. Knowing the expected future loading history, the remaining lifetime can then be estimated.

Four-point bend specimens with various orientations and geometries, as indicated in the first poster, were used to enhance specific fracture mechanisms. For the same purpose specimens were tested before exposure to moisture and after various degrees of hydrothermal aging. Identification of the mechanisms which occur in each case, although not complete at present, is being made from visual observations and loading curves obtained during the tests and SEM observations.

*A more complete description of the AEMPA system can be found elsewhere in this report.

TEST RESULTS

Background. Prior work showed two characteristics of the AE signals which could be related to the processes which were occurring during fracture of a composite specimen. The shape of the AE amplitude distributions, shown in Poster 2, indicates that more than one process occurs simultaneously and each produces its own distribution of AE amplitudes. Further, the process which produces the lower amplitude emissions is enhanced when the specimen is exposed to moisture, and this shows up as a change in the initial slope of the amplitude distribution curve. Since the ultimate strength of the material is decreased by exposure to moisture, the initial slope of the amplitude distribution should be a measure of that decrease. The fracture loads for two sets of specimens of different orientations and various amounts of moisture content plotted against the initial slope of the AE amplitude distribution in Poster 2 show this relationship.

The second distinctive characteristic noted was that the frequency spectra of individual AE events were different and the different types occurred at definite points in the loading history.

This suggested that the different spectral types were due to different mechanisms which occurred in the fracture process as the load increased. Examples of two different spectra are shown on Poster 2. Another comparison made in this figure is the appearance of the frequency spectral data when obtained by two methods. The AE signals from graphite-epoxy specimens were recorded on a modified videotape recorder and then during post-test analysis the two emission signals were analyzed by playing them back through a standard swept frequency spectrum analyzer (Hewlett Packard Model 141S/8553B/8552A) and an X-Y recording made of the spectrum, and through the AEMPA system. The same was done for a region of the electronic background noise immediately preceding each of the two emission bursts in order to establish the relative amplitude levels obtained by the two methods. Comparison of the discrete and continuous spectral data shows that the two spectral types are easily recognizable by either method. In fact a two point spectral analysis, say at 56 kHz and 560 kHz, would have been sufficient to separate the two types of emissions in this case.

The two characteristics of the AE signals shown in these figures, the amplitude distributions and the frequency spectral types, thus appear related to the mechanical state of the composite and might be used to define that state in a proof-test of a structure. Before that can be done, more quantitative relationships must be established between the particular mechanistic processes and the AE they produce. It should also be recognized that a particular process will produce AE having a statistical range of characteristics (e.g., amplitude) and that at any given time several different processes may be operative. Therefore, it must be demonstrated that the means for obtaining quantitative data on the AE characteristics is available and, further, that having these data the statistical mix of the various processes can be extracted from it.

In the past AE data acquisition systems commonly have measured one or two parameters of the emission signals and could display distributions of those parameters (e.g., number distribution with time, amplitude distribution). With the AEMPA system several measurements are made on each AE event as it occurs and 23 numbers are obtained which describe that event in terms of amplitude, timing, wave shape and frequency content. A description of these 23 parameters is shown on Poster 2. Each event also retains its individual identity which provides the possibility for extensive post-test statistical analyses on one or more parameters simultaneously and on the entire set or on sub-sets of the emission signals. Some results of such analyses for the composite specimens are shown in the following.

AE Signatures in Composites. Posters 3 and 4 show some results toward developing AE signatures for the various processes which occur during fracture of the composite specimens. Four specimen conditions are illustrated, all for the four-point bend specimen type of Poster 1 having the triangular reduced section. The conditions are that the graphite fibers (at the apex of the triangular section) are loaded in tension or compression and the specimens had never been exposed to moisture or are hydrothermally treated (in 95°C water) to attain a saturation water uptake. These four conditions result in emphasizing different fracture processes.

Each specimen was loaded through the elastic region into a region where fiber or matrix fracture or both occurred, further loaded until gross damage occurred from delamination (in tension) or fiber buckling (in compression), after which the specimens were unloaded. These various regions show up on the load curves and AE event rate curves as has often been seen in the past. Both of these parameters are difficult to interpret when only a small portion of the loading history of a specimen is available for analysis (such as in a proof-test situation). Their interpretation requires a comparison with values at earlier times in the specimen life to establish trends in the load bearing capacity or in the magnitude of the emission rate.

The time histories of the AE event amplitudes and frequency spectral types provide a fundamentally different type of information regarding the fracture processes which are occurring. These parameters contain information about the particular process which caused each event, presumably, and their interpretation requires no knowledge of what happened at some earlier time in the specimen history. If this is true then all that is required for interpretation is to obtain a large enough sample of AE events during a short time interval in the specimen life to define the statistical nature of the processes, and their quantitative mix if more than one process is operating.

Illustrative of this idea are the frequency spectral type plots at the bottom of Posters 3 and 4. Here a very simple measure of the spectral type is taken as the ratio of the peak amplitude of the AE in the 56 kHz filter band to that at 560 kHz. With reference to the spectra on Poster 2, a value of this ratio much greater than one indicates a low frequency type emission, about equal to one a broadband emission, and much less than one a high frequency type. For the compression specimens this ratio is about one for most of the emissions with a tendency for more high frequency events as the test progresses and more fibers fracture by buckling. The trends for the tensile specimens are quite different with the sudden occurrence of high frequency emissions coinciding with the onset of tensile fiber fracture, and then low frequency emissions occurring when delamination starts.

If the occurrence of these different spectral types truly correspond to occurrences of the different fracture processes, as is suggested by these data, then a sample of AE events at any time in the specimen history should define the processes going on independent of the past history. An example of this is shown at the bottom of Poster 5 where the four frames show number distributions of the "spectral type" parameter for four successive time periods for the wet tensile specimen data of Poster 4. Here it is seen how the distribution of AE events of different spectral types changes with time during the test. A quantitative decomposition of these distributions is suggested as being possible by the appearance of common peaks of differing amplitudes at -11, -4, and +5 dB. It should be pointed out here that the spectral type parameter used in these analyses is a very crude one and makes use of only two of the

eight pieces of spectral data which are available. Other definitions of spectral type using all eight pieces of data are expected to be even more informative.

The two figures at the top of Poster 5 show the big difference in the amplitude distributions of the AE events for tensile and compressive specimen failure. The nearly straight line (power law) distribution for the compression specimen suggests that a single mechanism predominates in the AE generation while the shape of the distribution for the tensile specimen suggests that more than one mechanism was operating. As with the spectral type distributions, a quantitative decomposition of the amplitude distributions may be possible to give the relative amounts of each mechanism which occurred.

The plots of spectral type vs amplitude shown in Poster 5 are less informative than the others but do show that the lower frequency events tend to higher amplitude. This type event shows clearly in the scatter diagram for the compression specimen illustrated which was the only specimen of this type in which delamination is believed to have occurred.

The AE signatures shown in Posters 3, 4 and 5 represent the results of only a preliminary attempt with the Multi-Parameter Analysis capabilities that are now possible. In the fracture of graphite-epoxy composites, where several different mechanisms generally occur simultaneously, there appears to be a wealth of information contained in the AE signals which can be used to determine the current mechanical state of the specimen. Means for more effectively extracting that information from the data are under development.

LIFE PREDICTION

As stated earlier the ultimate objective of this study is to use AE signatures obtained from a proof-test to establish the current mechanical state of the structure and hence its expected remaining lifetime under a specified load history. The steps required for doing this are well defined and are outlined in Poster 6. For simple load conditions and geometries such as the laboratory bend specimens of this study, these procedures could now be followed to predict the remaining life of a specimen which had previously been loaded an unknown amount. This example, however, is a trivial case which does not present the complexities likely to be encountered in a structural component. The steps are the same though for a more complicated structure, with a key element being a description of the most critical flaw which is activated by the proof load. This description now seems possible at some points in the flaw growth history through the AE signature, and further refinements in the signature analysis are expected to improve that description.

PURPOSES:

- DETERMINE THE CURRENT MECHANICAL STATE OF A COMPOSITE.
- PREDICT ITS REMAINING LIFETIME.

APPROACH:

- IDENTIFY CHARACTERISTIC ACOUSTIC EMISSION SIGNATURES USING MULTI-PARAMETER ANALYSIS.
- RELATE AE SIGNATURES TO SPECIFIC FLAW GROWTH MECHANISMS.
- COMBINE THIS INFORMATION WITH FRACTURE MECHANICS ANALYSIS TO PREDICT REMAINING LIFETIME.

EXPERIMENTAL METHOD:

- UNIDIRECTIONAL GRAPHITE EPOXY COMPOSITE (AS/3501-5) TESTED DRY AND HYDROTHERMALLY AGED.
- FOUR-POINT BEND SPECIMENS WITH VARIOUS ORIENTATIONS AND GEOMETRIES TO ENHANCE SPECIFIC FRACTURE MECHANISMS.
- USE MULTI-PARAMETER ANALYZER AND MINICOMPUTER TO COLLECT AND ANALYSE ACOUSTIC EMISSION DATA.
- OBTAIN LOAD CURVES, VISUAL OBSERVATIONS AND SEM PHOTOGRAPHS TO IDENTIFY FRACTURE MECHANISMS.

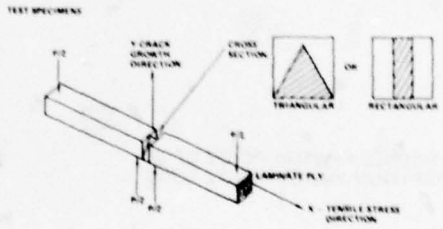

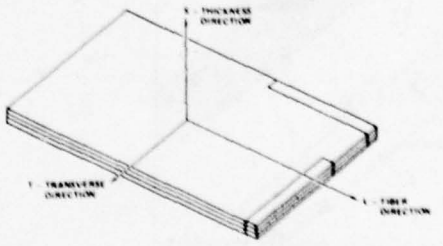

SPECIMEN DESIGNATIONS, XY:

LS – FIBERS IN TENSION, CRACK GROWTH THRU THICKNESS
LS – FIBERS IN COMPRESSION, CRACK GROWTH THRU THICKNESS
LT – FIBERS IN TENSION, CRACK GROWTH TRANSVERSE
LT – FIBERS IN COMPRESSION, CRACK GROWTH TRANSVERSE
TS – TENSION NORMAL TO FIBERS, CRACK GROWTH THRU THICKNESS
TL – TENSION NORMAL TO FIBERS, CRACK GROWTH ALONG FIBERS

Poster 1

EFFECT OF WATER IN THE COMPOSITE ON THE INITIAL SLOPE OF THE AE AMPLITUDE DISTRIBUTION

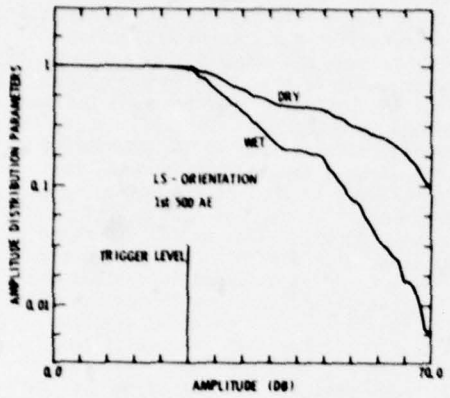

DISTINCTIVE TYPES OF AE FREQUENCY SPECTRA OBTAINED BY ANALOG SPECTRUM ANALYZER AND AEMPA

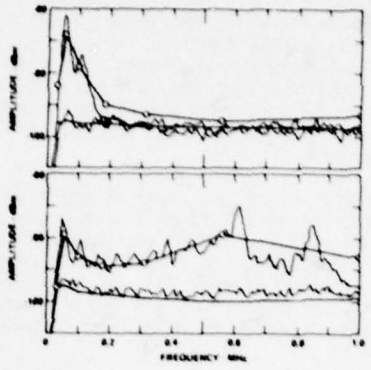

RELATIONSHIP BETWEEN INITIAL SLOPE OF AMPLITUDE DISTRIBUTION AND ULTIMATE LOAD

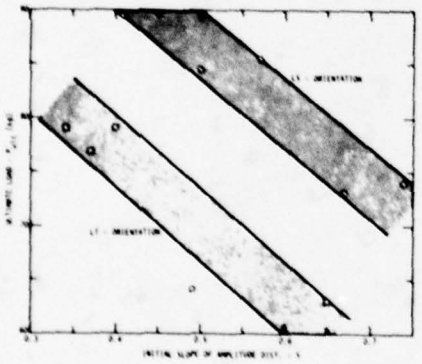

PARAMETERS MEASURED FOR EACH AE EVENT BY AEMPA

Measurement	Units	T.M.U.*	Range
1. Run Number	Hexadecimal		0 to FF
2. Event Number	BCD Counts		0 to 9999
3. Event Time	BCD Seconds		0 to 9999.999
4. Analog Volts	BCD Volts		0 to 10.00
5. Peak Amplitude	BCD dB	1 dB	0 to 99
6. Energy Counts	BCD 2000X Increment		0 to 1,999,999
7. Ring Down Count	BCD dB	1 count	0 to 110
8. Event Duration	BCD dB	1 us	0 to 110
9. Event Rise Time	BCD dB	1 us	0 to 110
10. Filter Amplifier Position	1 bit flag		0 or 1
11. 30.8 kHz Peak	BCD dB	10dB*	0 to 79
12. 96.2 kHz Peak	BCD dB	10dB*	0 to 79
13. 180 kHz Peak	BCD dB	10dB*	0 to 79
14. 177.8 kHz Peak	BCD dB	10dB*	0 to 79
15. 316 kHz Peak	BCD dB	10dB*	0 to 79
16. 562 kHz Peak	BCD dB	10dB*	0 to 79
17. 1 MHz Peak	BCD dB	10dB*	0 to 79
18. 1.778 MHz Peak	BCD dB	10dB*	0 to 79
19. Acquisition Delay Time	BCD us		0 to 655,350
20. Load Gate Delay Time	BCD us		0 to 65,535
21. Filter Amplifier Gain	BCD dB	40dB	0 to 79
22. Channel 1 Discriminator Gain	BCD dB	50 mV	0 to 99
23. Channel 2 Discriminator Gain	BCD dB	50 mV	0 to 99
2nd Channel Time Out	Decimal us		10 to 65,530
Load Start	Decimal us		0 to 32,760
Load Count	Decimal ms		0 to 32,760
Rate Delay	Decimal us		0.1 to 6.5

*Varies with filter amplifier gain.

Poster 2

Characteristic acoustic emission parameters.

- AE EVENT RATE – QUITE VARIABLE WITH TIME AND FROM SPECIMEN TO SPECIMEN. INDICATES DAMAGE RATE.

- LOAD – WHEN DRY, COMPRESSIVE STRENGTH IS GREATER.

- AMPLITUDE – LARGER AMPLITUDE EMISSIONS DUE TO TENSILE FRACTURE OF FIBERS AND INTERPLY DELAMINATION WHEN TESTED IN TENSION.

- RATIO OF AMPLITUDE IN TWO FREQUENCY BANDS – THIS DEFINITION OF FREQUENCY SPECTRAL TYPE SUGGESTS:
  1. FIBER FRACTURE IS HIGHER FREQUENCY.
  2. DELAMINATION IS LOWER FREQUENCY.
  3. FIBER-MATRIX DEBONDING AND MATRIX FRACTURE ARE INTERMEDIATE FREQUENCY.
  4. DELAMINATION TENDS TO CREATE LARGER AMPLITUDE.
  5. MATRIX FRACTURE TENDS TO LOWER AMPLITUDE.
  6. FIBER FRACTURE IN COMPRESSION TENDS TO LOWER AMPLITUDE.

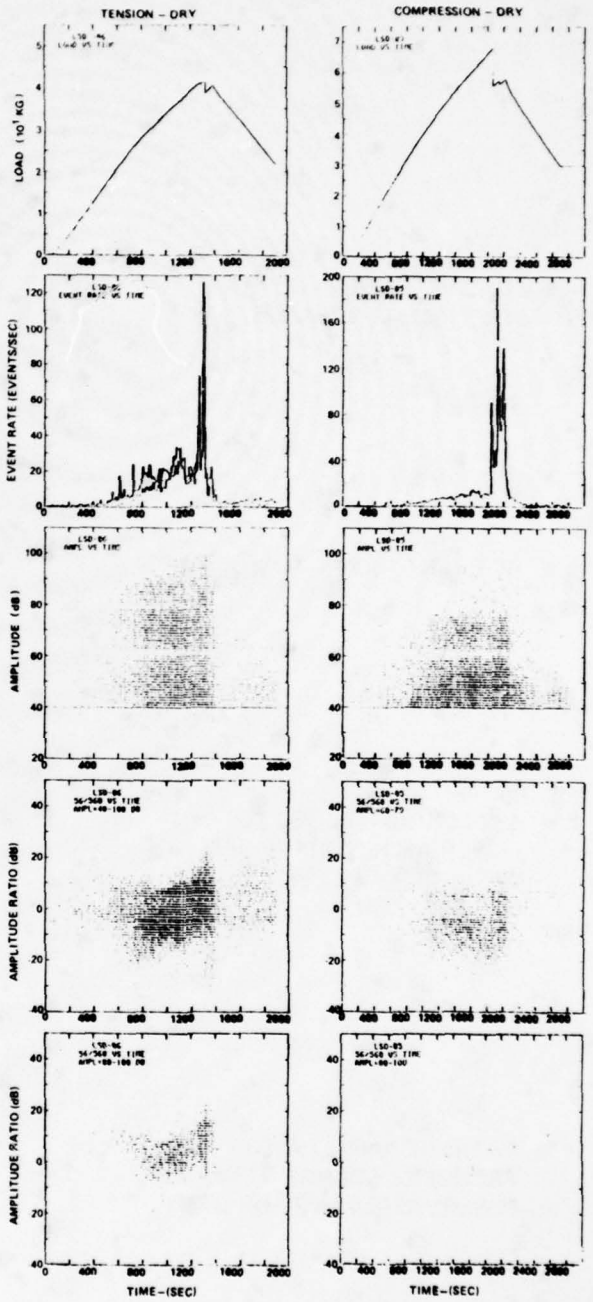

Poster 3

AE signatures

- LOAD WHEN WET – TENSILE STRENGTH IS GREATER.
- AE EVENT RATE – VARIABLE.
- AMPLITUDE – TENDS TO LOWER AMPLITUDES WHEN WET AND WHEN TESTED IN COMPRESSION.
- RATIO OF AMPLITUDE IN TWO FREQUENCY BANDS – SIMILAR OBSERVATIONS WET OR DRY

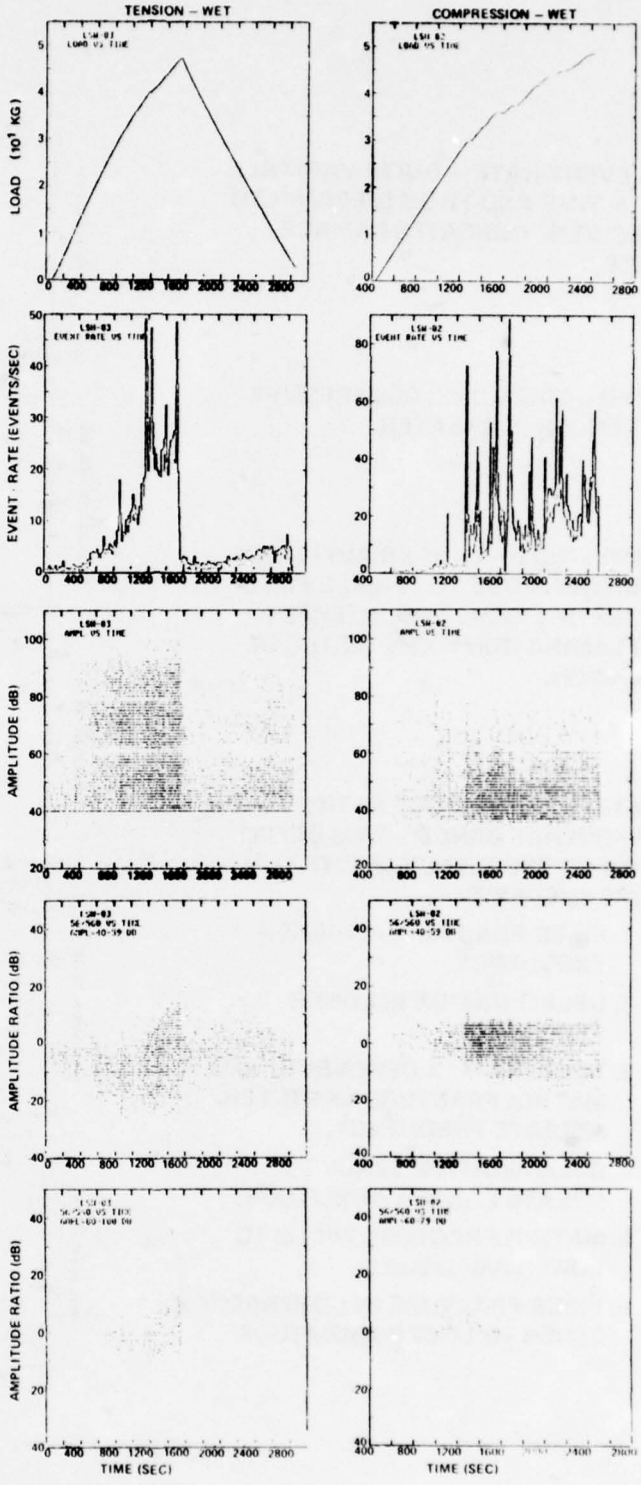

Poster 4

AE signatures

*AMPLITUDE DISTRIBUTION – A MARKED DIFFERENCE DUE TO THE MECHANISMS WHICH OCCUR IN TENSION AND IN COMPRESSION IS SEEN IN THE AMPLITUDES OF THE AE.

QUANTITATIVE DECOMPOSITION OF THESE DISTRIBUTIONS MAY BE POSSIBLE TO GIVE THE RELATIVE AMOUNTS OF EACH MECHANISM WHICH OCCURRED.

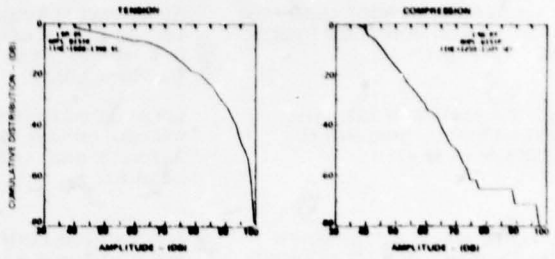

*SPECTRAL TYPE VS AMPLITUDE – THERE IS A TENDENCY FOR THE LOWER FREQUENCY EVENTS TO BE HIGHER AMPLITUDE.

THE COMPRESSION TEST RESULTS ARE ATYPICAL BECAUSE OF LOW FREQUENCY, HIGH AMPLITUDE EVENTS WHICH SUGGEST THAT DELAMINATION OCCURRED IN THIS SPECIMEN.

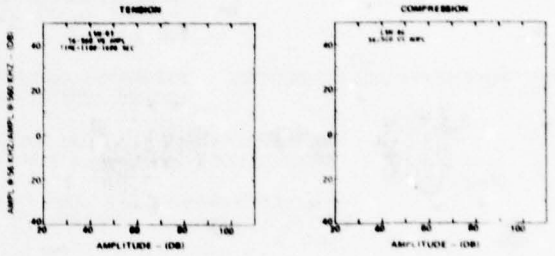

*SPECTRAL TYPE DISTRIBUTION – DISTRIBUTIONS CENTERED AT SPECTRAL AMPLITUDE RATIOS OF -11, -4 AND +5 DB CHANGE IN RELATIVE NUMBER OF EVENTS WITH TIME.

QUANTITATIVE DECOMPOSITION OF THESE DISTRIBUTIONS MAY BE POSSIBLE TO GIVE THE RELATIVE AMOUNTS OF EACH MECHANISM WHICH OCCURRED.

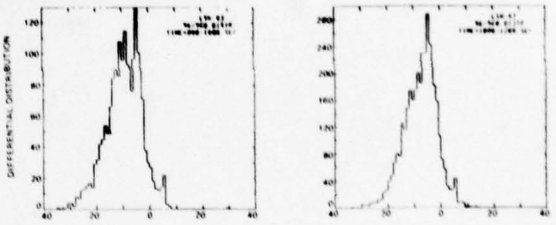

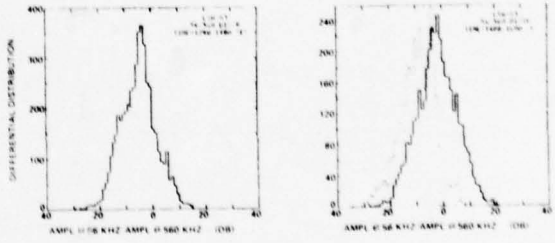

Poster 5

AE signatures

PROCEDURE	STEPS	RESULTS
APPLY A REALISTIC PROOF LOAD TO A COMPONENT AND MONITOR ACOUSTIC EMISSION ACTIVITY.	DETERMINE SERVICE LOAD SPECTRUM. LOCATE ACTIVE REGIONS IF MORE THAN ONE. MINIMIZE FURTHER DAMAGE DUE TO PROOF LOAD.	PREVIOUS MAXIMUM SERVICE LOAD OR EXTENT OF PREVIOUS DAMAGE THROUGH KAISER EFFECT.
COLLECT A SAMPLE OF ACOUSTIC EMISSION EVENTS USING MULTI-PARAMETER ANALYZER.	LOCALIZE DATA SET TO ONE ACTIVE REGION. OBTAIN SAMPLE FOR EACH ACTIVE REGION. ACCOUNT FOR GEOMETRICAL EFFECTS IN SIGNAL.	RELATIVE AMOUNT OF VARIOUS FRACTURE MECHANISMS WHICH OCCURRED THROUGH AMPLITUDE AND SPECTRAL TYPE DISTRIBUTIONS. LOAD LEVEL AT WHICH THEY OCCURRED.
CALCULATE STRESS DISTRIBUTION FOR EACH ACTIVE REGION AT PROOF LOAD.	ACCOUNT FOR COMPLEX STRUCTURE. ACCOUNT FOR PLY ORIENTATION. DETERMINE THROUGH THICKNESS DISTRIBUTION OF TENSILE, COMPRESSIVE AND SHEAR STRESSES.	MAGNITUDE AND THROUGH THICKNESS LOCATION OF MOST PROBABLE CRITICAL STRESS COMPONENT.
APPLY FRACTURE MECHANICS ANALYSIS.	ACCOUNT FOR MATERIALS PROPERTIES. ACCOUNT FOR PLY LAY-UP AND INTERACTIONS. DETERMINE FRACTURE CRITERION.	SEQUENCE OF MECHANISTIC STEPS IN THE GROWTH OF A FLAW TO CRITICALITY.
PREDICT FUTURE SERVICE CONDITIONS.	ESTIMATE LOAD SPECTRUM. ESTIMATE ENVIRONMENTAL EFFECTS.	FUTURE FLAW GROWTH RATE.

CONCLUSIONS:

- *PRESENT MAXIMUM FLAW SIZE AND TYPE AT EACH ACTIVE LOCATION AS A FUNCTION OF ITS ASSUMED LOCATION THROUGH THE THICKNESS.
- *PREDICTED SERVICE LIFE BASED ON PRESENT FLAW DESCRIPTION, SEQUENCE OF MECHANISTIC STEPS, AND FUTURE GROWTH RATE.

Poster 6

Life prediction using AE signature analysis.

INITIATION AND DISPLAY OF DELAMINATION FAILURE DURING FATIGUE OF GRAPHITE FIBER-EPOXY COMPOSITES

W. L. Morris
Rockwell International Science Center
Thousand Oaks, California 91360

ABSTRACT

Laminar microdiscontinuities which lead to the delamination of two unidirectional layup graphite fiber-epoxy composite materials during fatigue have been characterized, and discontinuity geometry and type related to the fatigue lifetime of specimens in which they occur. Two types of discontinuities were commonly observed: voids and organic inclusions consisting of regions of excess hardener. A stress intensity range based analysis applied to discontinuities found on the fatigue fracture place demonstrates that the several orders of magnitude scatter in fatigue life found for a series of test specimens is a result of a variation in the type and size of discontinuities present from specimen to specimen. A non-destructive acoustic pulse echo system used to study the progress of crack propagation from the discontinuities during fatigue is also described.

Scatter in the values of mechanical properties of graphite fiber-epoxy composites is substantially larger than that typically found for metallic structural materials. This has required the use of large safety factors in the design of structural components using such composite materials. A purpose of the present study was to determine the cause for scatter in the lifetimes of two graphite fiber-epoxy materials subjected to fatigue loading. The failure mode of particular interest was delamination, that is disbonding between layup plies. Delamination is the principal failure mode of fiber-epoxy composites loaded in shear, and is often a weak link in the failure sequence of such materials loaded in both tension and compression. The study was done using beam specimens loaded in 3-point bending, for an R = minimum load/maximum load = 0 loading condition. The materials characterized were 3501-5 epoxy/AS graphite and 934 epoxy/T300 graphite, a low and medium curing temperature material, respectively. Unidirectional fiber orientation 50 ply thick construction was used, providing a 0.63 cm thick specimen. Specimens where load in fatigue normal to the layup plane, with the fibers positioned parallel to the specimen axis as shown in Fig. 1. The specimens failed due to subcritical crack growth along a plane between plies, followed by a final tensile failure of the outer fibers due to loss in specimen stiffness with the delamination.

Fatigue lifetime data for the materials are shown in Fig. 1, in comparison to the peak shear stress experienced at the neutral plane of the specimen, resulting from the 3-point loading condition. The several orders of magnitude scatter in fatigue lifetime is typical of such materials.

Specimens were examined optically, after failure, to characterize areas on the delamination plane which might have acted as initiation sites for crack propagation. Principally, two types of microdiscontinuities were observed: voids and organic inclusions. The voids were apparently formed as the result of displaced fibers in the prepreg tape used to manufacture the composite panels. The organic inclusions were regions of excess hardener and were easily visible owing to their bright yellow color. General observations were that, typically, there was only one discontinuity of any appreciable size on the fracture surface, and for specimens with longer fatigue lifetimes the discontinuities tended to be smaller. To quantify the relationship between discontinuity size and fatigue life a mode two stress intensity range, ΔK_2, was associated with each discontinuity of any appreciable size on the fracture surface of a specimen, and the largest value of ΔK_2 found was compared with the specimen fatigue life.

The analysis entailed approximating the shape of each discontinuity as an ellipse, on the basis of the location of the preponderance of the area of the discontinuity. Major (2a) and minor (2b) axes of the ellipse were assigned by ignoring small appendages such as illustrated for the void in Fig. 2. A stress intensity solution by Kassir and Sih[1] was then used to determine ΔK_2 for the discontinuity. The cyclic shear stress at the site of the discontinuity, needed to complete the calculation, was determined from the cyclic applied load and the distance of the discontinuity from the neutral plane.

Results of such an analysis are shown in Fig. 3. For the 3501-5 epoxy/AS graphite, for instance, one finds that the lifetime data fall into two groups, one describing the effect of inclusions, the other of voids. The scatter in lifetime is substantially reduced by the analysis, demonstrating that it is a variation in type, size and location of the planar microdiscontinuities from specimen to specimen that is principally responsible for the lifetime scatter. The better fatigue properties of the 934 epoxy/T300 graphite is attributed to a smaller average size of discontinuity in the material tested, as also illustrated in Fig. 3.

The longer lifetime of specimens containing inclusions, as compared to voids having the same ΔK_2, is attributed to a longer interval of crack initiation at the inclusion sites. This was confirmed by a subsequent investigation in which the growth of cracks from the discontinuities was mapped, at increments in the fatigue life, using a computer controlled acoustic pulse-echo facility. The technique used is illustrated schematically in Fig. 4. A specimen was emersed in a water bath and an acoustic C-scan made using a 15 MHz broadband focussed transducer, with a point-to-point resolution of better than 0.05 cm. The X, Y position of the transducer over the specimen was computer controlled and echo samples were taken for a

square grid on the specimen at intervals of 0.025 cm. Because of the high acoustic attenuation and the acoustic echoes from each laminate, even in the absence of defects, it was necessary to make the acoustic amplitude for which a discontinuity was "recognized" a function of depth in the specimen. This procedure is also illustrated in Fig. 4.

Figures 5 and 6 show the results of such mapping for a specimen of 934 epoxy/T300 graphite. The display in Fig. 5 is of defect location as a function of depth normal to the layup plane in a sample, and shows that the principle discontinuities responsible for crack initiation in that particular specimen lay in poorly manufactured plies at either side of the center of the specimen. Figure 6 is a map of a limited area in depth taken normal to the layup plane. The discontinuity shown before fatigue was in this case a void, and subsequent crack growth from the defect after 1000 fatigue cycles is also illustrated. Test specimens were mapped, transferred to a loading apparatus for fatigue and then returned to the mapping facility. The procedure was continued until a specimen failed, at which time the acoustic map was compared to the actual discontinuities present. Using this technique, it was demonstrated that crack propagation from the voids began almost immediately, but there was a substantial time required for crack initiation at the void sites.

In summary, the major findings are:

1. Microdiscontinuities inadvertently introduced during manufacture of graphite fiber-epoxy materials are a major source of scatter in lifetime of the materials subjected to fatigue loading.
2. The principal discontinuities observed in a 3501-5 epoxy/As graphite and a 934 epoxy/T300 graphite are voids resulting from displaced fibers in the prepreg tape, and organic inclusions consisting of regions of excess hardener.
3. The type, size and location of such discontinuities are the principal factors which determine fatigue life of the materials.
4. Discontinuities as small as 0.05 cm in diameter can effect composite fatigue life, and can be detected in specimens 0.63 cm thick using acoustic pulse-echo techniques.

REFERENCES

1. Kassir and Sih, J. Appl. Mech. 33, 601 (1966).

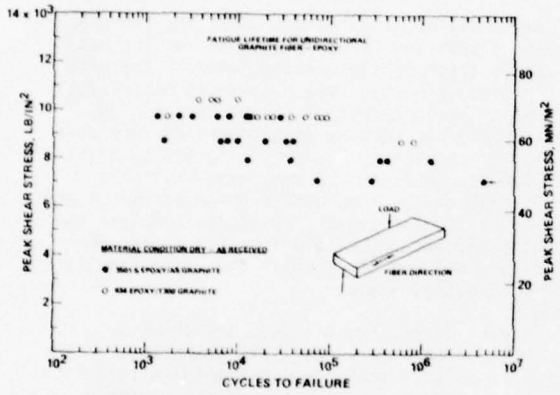

Fig. 1 Composite fatigue lifetime data.

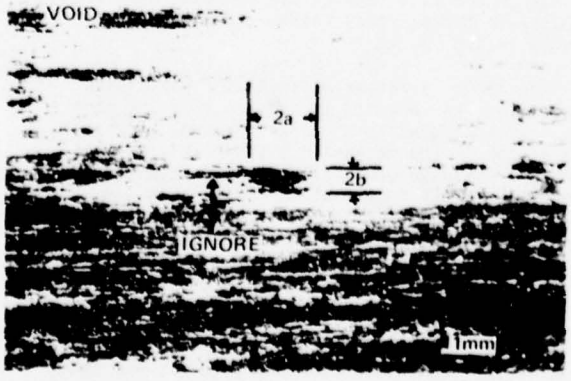

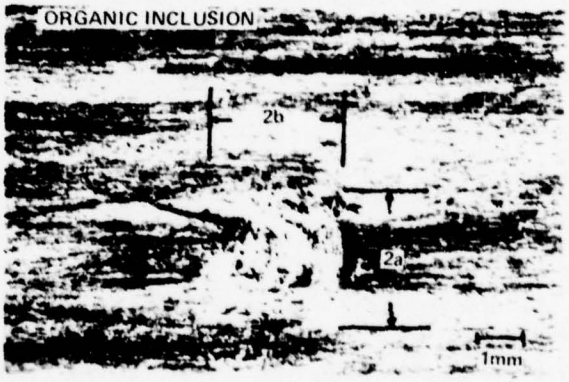

- MODEL FOR DESCRIBING EFFECT ON FATIGUE LIFE

I APPROXIMATE DISCONTINUITY AS AN ELLIPSE TO CALCULATE ΔK_2

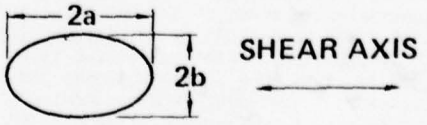

II DETERMINE PEAK SHEAR STRESS – τ_{MAX}

Fig. 2 Laminar discontinuity characteristics.

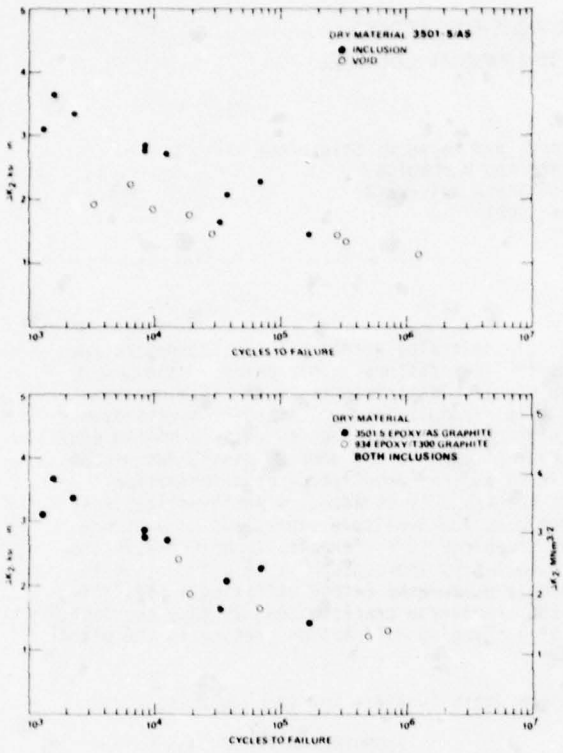

Fig. 3 Results of analysis.

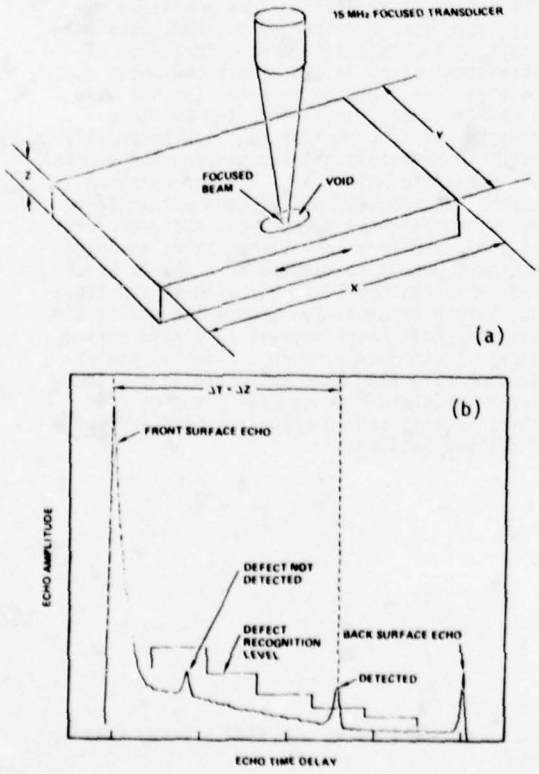

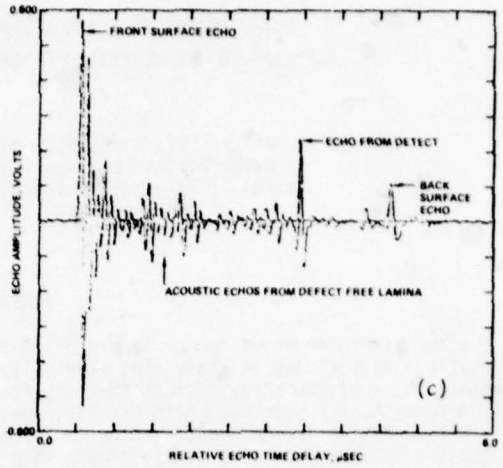

Fig. 4 Experiment technique for observing discontinuities; a,b,c.

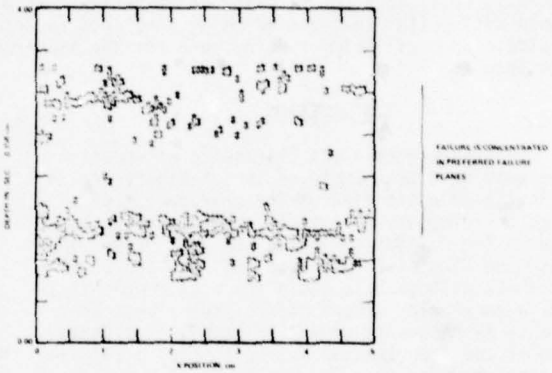

Fig. 5 Location of fatigue damaged areas in composite structure.

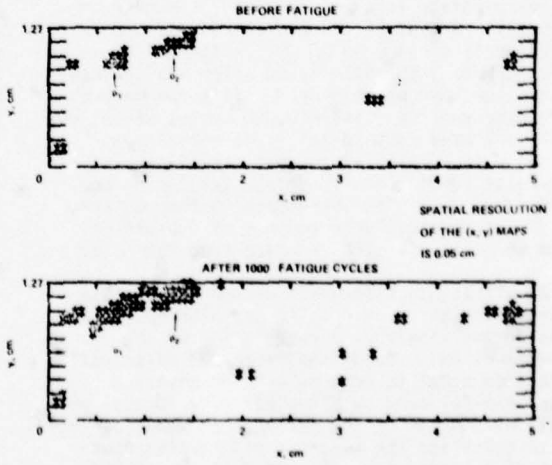

Fig. 6 Crack initiation and propagation during fatigue.

VIBROTHERMOGRAPHY AND ULTRASONIC PULSE-ECHO METHODS APPLIED TO THE DETECTION OF DAMAGE IN COMPOSITE LAMINATES

Edmund G. Henneke, II, Kenneth L. Reifsnider, and Wayne W. Stinchcomb
Department of Engineering Science and Mechanics
Virginia Polytechnic Institute and State University
Blacksburg, Virginia 24061

ABSTRACT

It has recently been shown in our laboratories that quasi-isotropic, graphite-epoxy, composite laminates develop a typical damage state that eventually leads to final failure. This damage state cannot be represented by a single through crack that propagates in a self-similar manner in the fashion ordained by fracture mechanics. To the contrary, the damage state is a complex one which begins by transverse cracking in the weakest lamina, continues by an increase in transverse crack density until a stable equilibrium spacing is achieved, proceeds by growth into the adjacent laminae and ends by final, catastrophic failure. In certain stacking sequences, the damage state is further complicated by delamination. Several NDE methods are being developed in our laboratories specifically to identify and quantitatively describe this damage state. The vibrothermography technique uses low amplitude vibrations as a steady state energy source in the composite laminate. The mechanical energy is preferentially absorbed in the region of damage and converted to heat, which can then be detected by thermography. This technique is especially applicable to detecting delamination. An ultrasonic pulse-echo method utilizing a straightforward diffraction analysis is being developed to detect the transverse cracks which, as they approach and attain an equilibrium spacing, present the appearance of a changing diffraction grating to the ultrasonic beam.

DISCUSSION

Vibrothermography and ultrasonic attenuation techniques have been employed in our laboratory to aid in the understanding of the development of a characteristic damage state in graphite-epoxy laminates. The following figures and photographs indicate the kind of information that one can obtain from these methods. To begin the poster demonstration, a very brief description of the vibrothermography technique is given. Figure 1 is a photograph of the experimental set-up showing a composite panel mounted in a low amplitude shaker. The thermographic camera and television monitor are also shown. Figure 2 a) and b) are photographs taken from edge replicas and show the characteristic damage state, discussed later, of uniform spacing of transverse cracks in the 90° plies and the edge delamination in a $[0, \pm 45, 90]_s$ laminate, respectively. A typical thermograph of an edge delamination is shown in Fig. 3. Figure 4 is a thermograph of a specimen taken after static loading to a low load while Fig. 5 is a thermograph of the same specimen after 10,000 cycles of fatigue at the same maximum load level. A boron-epoxy specimen with a circular cut-out was loaded in three-point bending until surface fracturing occurred, Fig. 6 . The corresponding thermograph, Fig. 7 , indicates large amounts of subsurface damage as well in regions removed from the hole.

An ultrasonic pulse-echo method was used to measure attenuation changes in graphite-epoxy laminates during loading. A description of the observations and a suggested crack and delamination diffraction model to account for the observed changes are followed by a typical experimental observation, Fig. 8 . The diffraction model can be used to calculate the expected attenuation downstream of a transducer. Figure 9 is the result for various depths of edge delaminations. Finally, the predicted attenuation as a function of delamination depth is given in Fig. 10 .

VIBROTHERMOGRAPHY

Vibrothermography is a nondestructive inspection technique that uses time-resolved thermographic detection of infrared radiation to detect regions of damage in materials. Low amplitude mechanical vibrations are used as a steady state energy input to the material. The interaction of the vibrational stress field with the damaged regions causes local heating to occur (at the site of the damage) which can be detected by videothermography. This technique has been especially successful in delineating delaminations and similar flaws in composite materials. The accompanying photographs are thermographs of heat patterns developed in graphite-epoxy specimens that were previously subjected to a load-time history as noted. The specimens were then mounted in a shaker which vibrated at approximately 18 kHz with an amplitude that was barely perceptible. Hence the shaker did not cause any additional damage; it simply served as a steady state energy source. Several analytical studies have also been performed in our laboratory to calculate surface heat patterns from subsurface sources and to calculate heat evolved during fatigue loadings.

* Work sponsored by AFML and NASA-Langley Research Center.

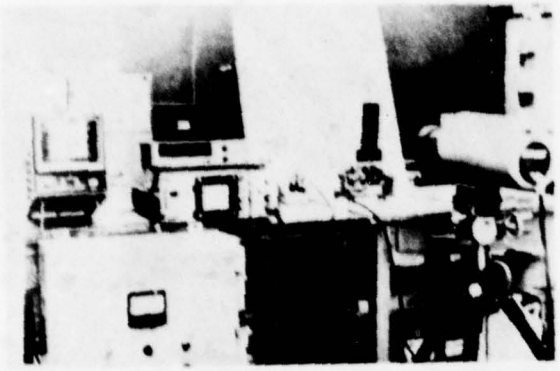

Fig. 1. The vibrothermography test set-up

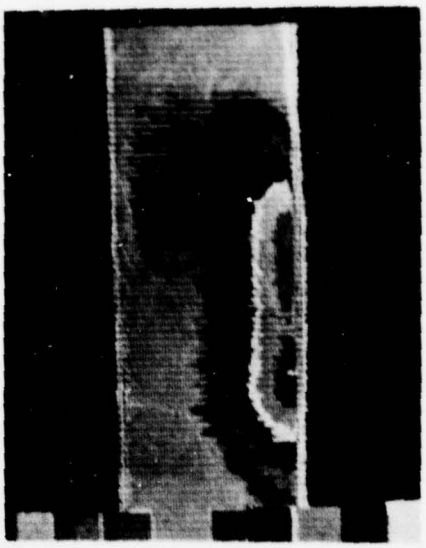

Fig. 3. Thermograph made by shaking a graphite-epoxy specimen with an edge delamination. The hot area is the delamination.

Fig. 2A

Fig. 2B

Fig. 2. A) Transverse cracks in 90° plies, and B) Edge delamination in 90° plies for a graphie-epoxy, $[0, \pm 45, 90]_S$ laminate

Fig. 4. Thermograph of graphite-epoxy specimen after loading statically to 2/3 of ultimate load

Fig. 5. Thermograph of same specimen as in Fig. 4 after 10,000 cycles of fatigue loading to a maximum load 2/3 of ultimate.

Fig. 7. Thermograph of specimen shown in Fig. 6 showing sub-surface damage in regions removed from the hole as well as the surface damage across the specimen at the hole.

Fig. 6. Surface damage on a $[0, \pm45, 0]_s$ boron epoxy specimen loaded in three point bending.

DIFFRACTION MODEL FOR THE DETECTION OF DAMAGE IN COMPOSITES

Recent work performed in our laboratory has shown that quasi-isotropic graphite-epoxy laminates of the type $[0,\pm45, 90]_S$ (Type I) or $[0, 90,\pm45]_S$ (Type II) develop a characteristic damage state. For both types of laminates, transverse cracking occurs first in the 90° plies at a load level of approximately 1/3 of the ultimate load. As the load increases, additional transverse cracks appear in the 90° plies until, at approximately 2/3 of the ultimate load, an equilibrium spacing of transverse cracks has been achieved. With additional load, the cracks in the 90° layers begin to grow into the adjacent 45° layers. These transverse cracks will appear to be a diffraction grating to an ultrasonic wave which is transmitted in a direction perpendicular to the laminate. As shown in the accompanying figures, the attenuation of the ultrasonic wave increases gradually with the load, and hence the number of transverse cracks, until the equilibrium number of cracks has occurred. After this point, the attenuation increases rapidly with load as the cracks begin to open wider and to grow into the adjacent layers.

An elementary diffraction model, following the earlier work of Truell and Papadakis, has been used to calculate the expected attenuation of a longitudinal stress wave caused by the diffraction of the wave. It was assumed that each transverse

crack serves as a rectangular screen across the aperture represented by the transducer. Each screen has a width w corresponding to the crack opening which is probably physically represented by the projection of the crack onto a plane parallel to the laminate. The number of such screens across the diameter of the transducer corresponds to the number of observed transverse cracks at each load. The calculated attenuation correlates quite well with the experimental observations, showing an increase of attenuation with the number of cracks and with the apparent crack opening.

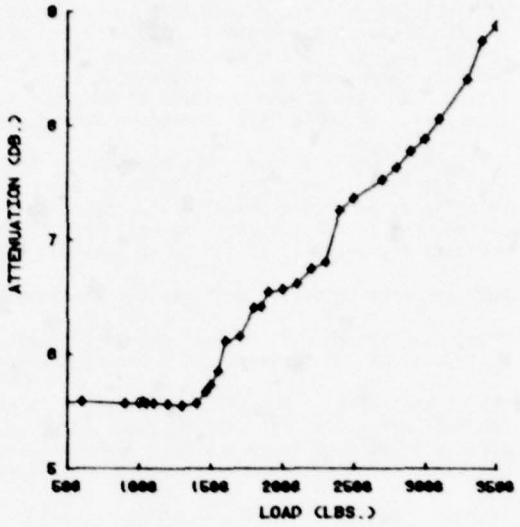

Fig. 8. Attenuation versus load for a graphite-epoxy specimen loaded quasistatically

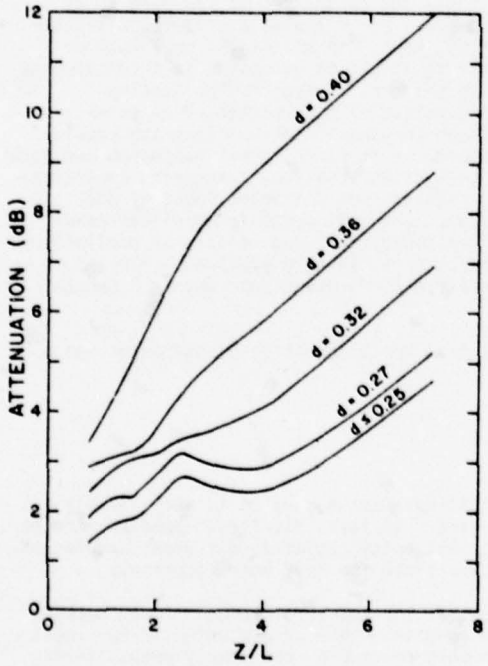

Fig. 9. Predicted attenuation due to diffraction effects downstream of a transducer in the presence of delaminations having various depths d into the field of the transducer

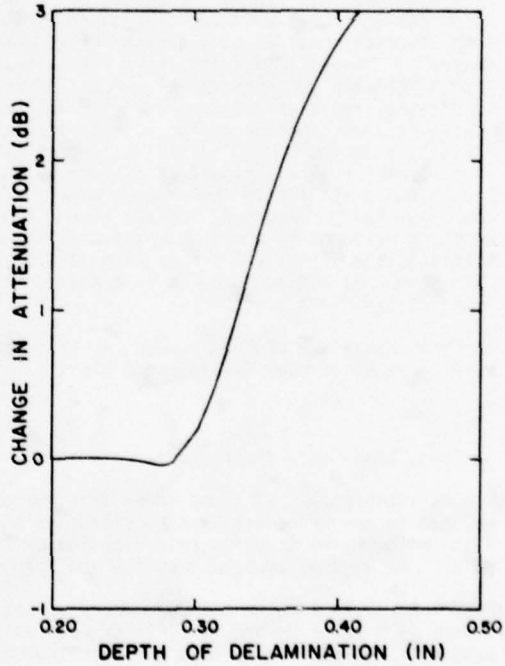

Fig. 10. Predicted attenuation as measured by the pulse-echo method as a function of delamination depth

SUMMARY DISCUSSION

Robb Thomson, Chairman (National Bureau of Standards): What I thought we would do this afternoon is to pull together, to the extent that we can, what we have heard earlier in the day in the plenary talks and the poster presentations that we have just observed. The plenary talks addressed methodology for reliability and two general categories of materials: ceramics and polymers. In the poster sessions there were quite a variety of topics covered, mostly having to do with specific instrumentation addressed to the question of NDT--not so much on the methodology side, but more at the NDE interface. We would like to explore the convergence of these two elements.

To begin, I would suggest that methodology be considered as the first category of concern (together with materials), and that attention be drawn primarily to the gaps in the methodology that we have relative to particular materials categories, even though primary attention in materials has been placed upon ceramics today. We will include, of course, metals and composites in our discussion. Now does anybody want to add to or subtract from these categories before we go ahead?

Otto Buck (Science Center): What are the elements of the methodology?

Robb Thomson, Chairman: I include under methodology three general subcategories. They are defects and distributions, measurements, and stress history.

Robert L. Crane (AFML): My only suggestion is in the area of ceramics and metals. You might wish to consider materials with limited ductility, i.e., not a classic brittle solid like ceramics and not a material as ductile as a metal. A material with limited ductility or a ductility which is very much a function of temperature would be of interest.

Robb Thomson, Chairman: Good. Anything else?

Since we apparently agree on our format, let's begin the discussion. Dr. Rogorsky of Drexel University has requested three minutes for comment.

Alexander Rogorsky (Drexel University): Thank you very much.

Gentlemen, I have listened to the speakers in the morning session with great interest. Actually, the problem of reliability and the determination of accept/reject criteria are most important elements of NDE. I would like, briefly, to present one idea which has been recently started at Drexel University. In many cases of ultrasonic inspections, the parameters of the part to be inspected and the associated testing conditions are unstable. For example, ultrasonic attentuation, surface considitions, quality of acoustical coupling, etc., can affect the amplitude of ultrasonic signal. To avoid these variables, ultrasonic signal can be presented as a function of random variable characteristics related to the defect, to the part tested, to the testing conditions, and signal distributions. Another approach consists of measurement of an experimental reference histogram for ultrasonic signals and their combination with scattering considerations and probabilistic distributions of other parameters. This experimental histogram can take into account real distributions of such variable parameters as attenuation, scattering condition, etc. The first step is to measure reference ultrasonic signals from different spots of the component being inspected, and the second step is to predict the most probable amplitude level which corresponds to the sensitivity of inspection. This second step uses results of preliminary statistical analysis. A simple algorithm using this approach can then be prepared. Results to date show that the accuracy of flat bottom hole size determinations using this approach can be improved by 3 to 4 times.

The main advantage of this procedure, we think, results from the elimination of standards and a consideration of real testing conditions.

Thank you.

Robb Thomson, Chairman: Thank you.

Gordon Kino (Stanford): It seems to me that the procedure that was just suggested is very closely related to the procedure that Mucciardi of Adaptronics uses. In fact, his first examples were on flat bottom holes in which he calibrated on a series of flat bottom holes in different samples of metal. He used an adaptive routine and then came back and sized the hole very accurately.

Alexander Rogorsky: I think this procedure is not repetitious of the Mucciardi method simply because I used it 8 years before for another problem of testing adhesion. Now we are using it for steel castings. We didn't use adaptive learning networks for this procedure, but simply probabilistic approaches.

Robb Thomson, Chairman: I'd like to suggest that we come to grips with a couple of general questions on the methodology.

Let us assume for now, anyway, that reliability can be achieved by putting the three elements referred to earlier together in the right combination.

John Brinkman (Science Center): I am bothered by a couple of things. First of all, requiring an a priori knowledge of a defect distribution tells me that somebody is assuming we are going to use sampling techniques as opposed to a hundred percent inspection. I believe that many industries are moving more and more toward the requirement of a one hundred percent on-production-line inspection. I know that the Army has committed itself to do this for the inspection of the metal parts for its large caliber projectiles. I believe I know that much of the automobile industry would like to do the same thing with respect to the inspection of many of the discrete parts that go into automotive production. If you assume that, then another question arises. That question is, what is the reliability, not of measuring the defect properly, but of detecting it first of all?

If we can solve that one, and I would like some comments on that, then it seems to me that if we do a hundred percent inspection and observe a hundred percent of all defects which are at or near critical size, we don't have to say we need to know the distribution of defects beforehand. We are going to measure it. Why shouldn't we strive for that goal?

Robb Thomson, Chairman: Are there any others? I suggest that we let several questions come up and then we will try to pull things together. Are there any further questions that you want to put up like that?

Fred Morris (Science Center): There is another related problem. There are classes of materials and loading conditions for which the parameters that control failure are not treatable with conventional fracture mechanics. I have in mind a material failure which is principally governed by crack initiation processes. I do not mean to say that cracking is not appropriately a part of what is commonly considered as initiation, but only that the laws that govern the growth of those cracks are not presently amenable to description by conventional fracture mechanics. This includes situations where the crack overloads are very large or where microcrack coalescence is an important aspect of failure. For a given alloy and loading conditions one is faced with the prospect that 95 percent of the fatigue life is in the initiation stage. Therefore, the window for failure detection is only five percent of the fatigue life, in terms of our present day NDE techniques. Thus, the core of the scatter in line time and reliability prediction has to ultimately look at initiation, either dealing with microcrack development in certain circumstances or more complex precursors to the microcrack formation. As Don Thompson, for instance, has pointed out, there are techniques for looking at this regime of the failure that are currently being looked at only cursorily, that have some promise in regard to looking at these types of situations and I hope we could talk about some of those in a little detail as well.

Robb Thomson, Chairman: Any further questions or concerns to put on the table?

M. Srinivasan (Corborundum): One of the things that concerns me in the methodology aspect relates to the problems we have in identifying and classifying defects. The actual parts are quite complex, and I wonder how much the design community appreciates the NDE people's problem. The philosophy of design could make the NDE people's life a little bit easier and yield a better product. If the designers can appreciate the problem of the NDE people, they can design the parts which will be amenable to an easier inspection. That would be a very welcome thing to the NDE community.

Robb Thomson, Chairman: Anything else? Yes?

Shirley McDonald (Lockheed): I think more attention needs to be placed upon the refinement of NDE instrumentation to be sure that we are really using it right. Not all people use a given instrument in a given way. The instrument may not even be optimized for some applications.

Robb Thomson, Chairman: Any further questions or concerns?

Cecil Teller (Southwest Research Institute): I am concerned that the importance of initial residual stresses might be overlooked in the probabilistic approach to fracture mechanics. I'd like to hear some comments or thoughts on this.

Robb Thomson, Chairman: Very good. Anything else?

Robert L. Crane (AFML): There is an area which you might consider as a problem area. That is related to the rejuvenation of alloys. Dipping or hot pressing an alloy may be used to close up a crack. The structure so treated will have to be requalified. The same thing is true for composites and bonded structures. The structure has to be requalified after the repair procedure.

Robb Thomson, Chairman: I have one specific comment in regard to methodology. If you are going to develop a fully probabilistic approach as was shown thir morning, I don't understand the use or omission of safety factors. It seems to me that if you are doing a full scale treatment of reliability problems, I don't understand where a safety factor comes in.

Yes, Don?

Don Thompson (Science Center): I would like to understand how various materials with various material properties can be placed in the context of an unified methodological approach. More specifically, can ways be found to account for ductility differences, as was suggested earlier, and other features such as time dependent stress-strain characteristics?

Robb Thomson, Chairman: We now have a number of comments to address. Why don't we let Tony Evans take a crack at what we have got on the floor so far. Maybe that will generate some more.

Anthony G. Evans (Science Center): Well, I think it appropriate, perhaps, that I address the question that John Brinkman raised first and then the others as I remember them.

I think you are under a misapprehension, John. I think it is fairly straightforward as to what these probability expressions really mean. Everything that was described this morning did apply to full inspection, hundred percent inspection. It wasn't sampling. The reason that we need the a priori distribution comes when you realize that, upon making a measurement, you only have an interpreted defect size and you are trying to estimate what the actual defect size is from the errors associated with the width of that band. To do that you need the a priori distribution.

John Brinkman: No. What you need then is to characterize the particular instrument or technique you are using as to the manner in which its errors are distributed over the spectrum of sizes (or whatever other parameter it is that you are measuring). But that doesn't mean that you need the a priori knowledge of the actual defect size distribution. That is a lot less demanding a requirement.

Anthony G. Evans: Maybe John Richardson can help me on this. Let's consider just the probability of estimating the actual size from a measured size. You need the a priori distribution as well as other information.

John Brinkman: No.

Anthony G. Evans: We are obviously not communicating too well.

John Brinkman: What you have said we need is sufficient. But it is more than sufficient. It is not necessary. All that is necessary is a knowledge of what is measured and what is the probability of distribution of defects that will give that measurement. That's right. That is a far less demanding requirement. If you have those two you have all the information you need.

John Richardson (Science Center): John, to get that you need the a priori distribution.

John Brinkman: No, you don't. This is what you use calibration standards for. You can get the latter set of functions from a series of calibration blocks.

John Richardson: No. Characterizing the instrument is not going to give you the defect size distribution, given the measurements, completely. You have to have more elements than that. That is a part of it. That is not all of it.

John Brinkman: If I have characterized my instrument so that I know how it errs, how frequently it errs, and in which direction and how far it errs, I have everything I need.

John Richardson: It is part of it.

Anthony G. Evans: It is clearly part of further debate. It would be better settled privately, I guess.

Robb Thomson, Chairman: I think so.

John Brinkman: May I ask a question?

Anthony G. Evans: I see about 6 hands up.

Charles Rau (Failure Analysis Associates): Is anybody else bothered by the same point? Because if they are, I think we should pursue it.

Robb Thomson, Chairman: I think we are.

Harris Marcus (University of Texas): Could I extend the question a step further?

Robb Thomson, Chairman: Yes.

Harris Marcus: The thing that bothered me about most of the discussion this morning is that you are looking for flaw sizes that will eventually become critical and that are detectable with some degree of reliability. Yet, the treatments go back to initiation as part of the statistical analysis. I don't know of any way to use NDT to characterize initiation state. So what you are doing is running the distribution out beyond the detection limit of any of the devices that are being discussed here; yet, NDT is being used as a baseline for this whole statistical analysis that you are talking about. I am confused by this and suggest that attention be given to measurement techniques for the microcrack regime.

Charles Rau: Different question, but we will address that one. I think it is important to get straight. It is key that we understand the need for both characterization of the inspection equipment, that is, its capability to detect a defect given that the defect of a certain size is there, and the a priori distribution.

John Brinkman: And the probability it has detected it wrong, quantitatively, by a given amount.

Charles Rau: Well, the key thing is, what does the instrument do given the fact that there is a flaw there of various sizes, what is the probability that instrument will detect that flaw.

John Brinkman: Not detect, but detect and measure.

Charles Rau: Detect and size, okay?

John Brinkman: Okay.

Charles Rau: That is only half the question though. If you want to know what distribution of defects really gets into service, you also have to know what preinspection defect distribution you started with which you then operated upon with you inspection tool, and the rejection that took place. Multiplication of those two functions gives you what gets into service. You do have to have the preinspection flaw distribution as well as the capabilities of you instrument. That is the point we are arguing. There are two distributions that you must have. This, in fact, is a key point which many inspection people over the years have failed to recognize. That is one of the reasons why we have had difficulties in getting to a quantitative NDE.

John Brinkman: There is a philosophical problem. The philosophical problem is that if we have to have an a priori knowledge before we can measure any distribution, we can never get there to begin with because we never have it. We have to measure one first.

Anthony G. Evans: No, we are talking about accumulating a knowledge of what a typical a priori distribution is, and then on a specific component, we are looking for whether that distribution is liable to cause failure. You need to characterize a batch -- a typical batch of material or a class of material in terms of typical a priori distributions. You can do that on sectioning a component or even inspecting components and inverting.

Robb Thomson, Chairman: I think there is a confusion between making the initial standardizing measurement and the measurement that the inspector has made. I think maybe that is the confusion.

Anthony G. Evans: That's where it lies.

Don Thompson: Tony, would you amplify upon the problem of obtaining the a priori distribution? These distributions must be obtained by a measurement of some kind, either destructive or non-destructive.

Anthony G. Evans: There are a couple of ways. Charlie mentioned one this morning and I mentioned another. The way we have done it is destructive. You take big billets of material and section through them metallographically. You can characterize the flaw size and the size distribution. We know from statistics that it is liable to fit an extreme value distribution and that helps us enormously because that gives us only three choices of distribution to fit it to. Then we can extrapolate it out to larger defect sizes to get into the range we need to for our prediction.

Don Thompson: How do you carry this procedure across to that product that comes off the line in which specific materials and especially specific procedures are used?

Anthony G. Evans: You have to take samples out of that product and characterize the a priori distribution on samples taken at random out of that product, probably on a continuing basis to make sure that the distribution isn't changing with time as the manufacturing process might change. So that's a rather laborious task and something that has to be done. You might have some other thoughts, Charlie.

Charles Rau: Here, in fact, is where the alternative technique of having identified what your instrumentation capabilities are may be used. You can then use just the nondestructive inspection results

themselves to back out what the preinspection flaw distribution is.

John Brinkman: Thank you. I'm sorry you weren't here when I asked my question, but that was my point. I made the point that many manufacturers are pushing toward a hundred percent on-line inspection. If you accept the fact that that is a goal, why shouldn't we make it our goal. Then we can address the fact that we then have to worry about detection probability as well as characterization capability. If you are going to measure the size distribution, why do you have to have it in an a priori manner?

Charles Rau: Somewhere along the line you must have an independent measure of what you are dealing with, or else you have to have some statistical way of massaging your data iteratively and tying it back into the actual failure rates. Somehow you must get an independent measure of what you have, otherwise you just go round and round in circles.

John Brinkman: You calibrate your instruments.

Charles Rau: No, somewhere you must also have a back-in to what the preinspection material distribution was. You have to have it.

Let me try to address a couple of the other quick questions that were brought up, if it is appropriate now.

With regard to the safety factor, Robb, we are not talking about a safety factor in the conventional safety factor sense in which you take the maximum stress and divide it by the stress base safety factor. This is a life base safety factor which means you calculate a probable life. You say it is going to last 1020 hours. Now what fraction of that do you actually use as an inspection interval? That's the safety factor I'm talking about. It's not the conventional safety factor.

Robb Thomson, Chairman: It seems to me that you should be able to calculate the best time for inspection without addressing a safety factor.

Charles Rau: You can. It is just semantics.

With regard to Don's question about the integration of a wide range of different materials into a single methodology, I don't really think that is a problem with the methodology. What will happen, of course, if you go to vastly different materials, you will find that various parameters in your total formulation will be dominant in one set of alloys or materials and others will be dominant in different materials. Obviously, in dealing with ceramics you are dealing with the inspection process as dominant. In certain metals it may be fatigue initiation that is important and the prior flaw distributions are relatively innocuous. The methodology doesn't change -- just the sensitivity to the specific parameters. If you get big scatter on certain parameters, they will be dominant in the total reliability of the product. I think the basic parameters are the same no matter what engineering system you are dealing with.

Let me answer Harris' question about the initiation.

If you use the conventional probabilistic fracture mechanics leading to a retirement for cause, that is strictly a propagation based analysis. In fact, initiation doesn't really enter into the process at all. Initiation enters into it when you start to utilize the combined analysis approach in which you are trying to make use of the success and failure data which you measure with your NDE in the parts which have already experienced some service. There, of course, you have to subtract out the initiation; otherwise you get a distribution of crack sizes at one lifetime in your whole fleet and if you sit there and assume that was all propagation, you'd be markedly in error because many of those sat there for 90 percent of that time before they initiated. So that has to be in the model. You can, if you like, take advantage of the total observation to make predictions about propagation on the sample you are going to operate on. That doesn't come across all that clearly; it is only when you go to taking advantage of the field data that you have to incorporate the initiation. If you are strictly going with probabilistic fracture mechanics you are not taking advantage of field data. You are right; it's all propagation.

Harris Marcus: How do you get the NDE to give you any information on that? That's the only question I really asked.

Charles Rau: Well, even when you operate with the combined analysis, you are still using the NDE to tell you what the current flaw size is, but you are using the initiation to back out from the total observation what the stresses must have been to get to the point where your population is now. Rephrased, you are using the NDE in more than one way. The NDE is in there in the same way with regard to the crack progression whether or not you get the stresses by a straight-forward design calculation or whether you are trying to infer what the actual stresses were from the observations made with nondestructive inspection. If you do the latter, then you have initiation tied up in your

statistics. If you do just the straight design approach, inspect it and make a decision, then you restrict the propagation basis.

Fred Morris: I don't think we should leave it, though, that our only recourse at this point is to use field data to deal with the initiation stage of the failure process. That is because there is now on-going research from which it may be possible to relate statistical microcrack growth and coalescence to propagation. Essentially, what we are talking about is extending out statistical models down into the initiation region using fracture mechanics where possible. There are non-destructive techniques for looking at microcracks that are only 10 or 15 microns long that are in the development stage. Again, I hope we don't leave initiation as a poor stepchild because there are things that can be done to treat that problem beyond a very mechanistic way of looking at differences between predicted and measured fatigue lives.

Anthony G. Evans: I might say something about that. I think we have confined ourselves mostly to propagation controlled phenomena because the defects are usually large unless they are distinguishable separately using ultrasonic measurement. That's a regime in which most people in the audience certainly are interested. But you are quite right, of course. One has to extend one's nondestructive method into a region in which individual defects are no longer discernable and you have to measure some other property of the material which can then be related to initiation times. As you well know, ultrasonic attenuation and a host of other measurements have that potential and they need to be explored. We certainly shouldn't ignore it.

Fred Morris: It is part of it because we're picking the problems that current technology can deal with. It's just that initiation problems aren't being tackled as yet.

Charles Rau: I didn't mean to imply that that's the only way to go. I would like to make another point which I didn't have time to really make in my presentation this morning. I don't look at using the field data as a last resort because we can't do it any other way. In fact, quite the converse is true. I look at the field data as being the more appropriate way to go if and when it's available, because that's the horse's mouth. It includes everything, if you like, within it. Let me give you an example. I went through an example this morning where I had a fatigue model which included both initiation and propagation. It contained the sixth power of stress dependence on initiation. Let's turn it around for propagation. We had a fourth power of dependence on the cyclic stress range and, say, a first power on the mean stress. We also ran that same analysis, assuming that the analyst was stupid and he confused fatigue with creep. Instead of having a fourth power in delta sigma and a first power in stress, he had it the other way around, a fourth power in mean stress and a first power in delta sigma. This yields a completely irrelevant engineering model, and via a conventional probabilistic fracture mechanics,you get all the wrong answers and make all the wrong decisions. But with the combined analysis approach of using the field data to calibrate your system, we found we still got, believe it or not, a very substantial cost benefit from the retirement for cause approach, approaching a 30 percent cost savings. It was, of course, an 80 percent cost savings if you had had the right model. The point is, however, it wasn't zero and the reason, of course, is that by using the field data to pin your point even if you employ a bad engineering model, you can't be too far off. On the other hand, start from scratch with your lab data and you've missed out on the mechanism or something, you are extrapolating over much longer distances and have, therefore, a much higher chance for large errors.

Robb Thomson, Chairman: We have spent quite a long time with this first category. I think it was appropriate, but let me just ask the two people on their feet for a brief summary of where you feel the major road blocks are for the ultimate application of this approach to reliability for use in materials. Could you do that? Could each of you do that in a cuple of minutes?

Anthony G. Evans: Give us a chance to think about it.

Robb Thomson, Chairman: Yes.

Jerry Tiemann (General Electric): While you're thinking, maybe I could ask about what seems to me to be a road block -- I call it the chicken and the egg problem. Tony, this morning, you wanted to use the low frequency data to determine the defect volume. However it's the defect volume times the acoustic impedance mismatch that's actually determined at the low frequencies. On the other hand, the high frequency data can give you the acoustic impedance only if you know what the volume is. So there you have the problem of the chicken and the egg.

Anthony G. Evans: Well, that I can answer. I think it turns out that in the high frequency method I described, you don't need to know the volume. You just need the details of the impulse response time.

Jerry Tiemann: The amplitude of that depends on how much of it is there.

Anthony G. Evans: It is the sequence of the respective peaks and the impulse response function that is

important, not the absolute amplitude. It is irrelevant in determining what the impedance of that defect is. You've got to know the sequencing of them.

Jerry Tiemann: Only if they are spheres. You don't know that when you come upon an arbitrary defect.

Anthony G. Evans: I showed some data, and I said we still have to prove some of these features for real shaped defects. It turned out, however, that the two or three we looked at so far, even though the shapes are quite irregular and by no means shperical, they still exhibit the same features you calculate for the sphere.

Jerry Tiemann: But only at a risk of increased uncertainty as to what the acoustical impedance is.

Anthony G. Evans: Sure, right.

Jerry Tiemann: So therefore you then don't know the acoustic impedance unless you know the shape.

Anthony G. Evans: It's not quite as black and white as you make out in the sense that one has a limited set of possibilities one knows can exist in the material. If there is an infinite set of possible defects in there, then I think the question you raise is a very serious problem. You know from a low of experience in working with materials, however, that there's a limited set of possibilities -- say six types of defects -- that you are liable to expect from the fabrication. When you have that limited set of possibilities, it appears, even though the defects are irregular in shape, the impulse response function retains enough of that shape, if you calculate for the sphere, that you can distinguish those six possibilities without even knowing its shape. Believe it or not, that's the way it seems to be working out. Then, of course, when you do have that in answer to the first part of the question, you do know the impedance. Then the volume comes out from a low frequency measurement.

Robb Thomson, Chairman: Charlie, since you didn't have to answer that question do you want to start with this other? Let's make it short. I would like to go on to the other topics up there.

Charles Rau: I have three things I jotted down. There is probably more, but three things which I think are limiting. First of all, overall, I don't think there are any insurmountable roadblocks. I think that we have the technology now and I am very excited about the combined analysis approach because it's gotten over some of what I felt were the major roadblocks with the conventional approach. However, there are two problems associated in applying it. One of the problems is that we really don't have the preinspection flaw distributions for most of the cases. In most cases I think, quite frankly, we still don't have the probability of detection, given the fact that a flaw of a given size A is there. We now appreciate that we need it under realistic field conditions. The last thing is just with the unknowns which crop up in the prediction of failure probability knowing that a crack of a given size "A" exists. These are related to such things as the loading, the guy doing something to it that he never should have done, something ridiculous tied in along with three or four other design problems. I still see a difficulty in quantifying those sorts of things from a limited amount of data.

Robb Thomson, Chairman: Thank you.

Anthony G. Evans: To some extent my concerns are the same. Certainly, I am concerned about the a priori distribution and we all agree that is a concern to get that with sufficient accuracy at low probabilities. Perhaps an overriding problem is to get all the accept/reject decisions very material specific, not just because of the a priori distribution but, perhaps, also because of the inspection and that means that it takes a lot of money to get the information you need for each particular system. Someone must recognize, I suppose, that if he wants to use inspection methods it is going to cost a lot of money at the outset to get the information that one needs at the statistical levels of confidence that are required. That is a concern that people will recognize. They must make the money available for that purpose.

Robb Thomson, Chairman: Okay. Thank you very much.

I suggest then that now we switch completely. Let's skip ceramics and metals unless there is an objection to that. It is 4:20 and I think we have at least had some implicit discussion of ceramics and metals in the discussion we have had so far. I suggest we jump down to bonds and to polymer materials. Unless there is an objection in particular, I would like to start that discussion by asking Dave Kaelble if he can relate the terms we have been hearing for the reliability description for ceramics and metals to the polymeric material. As I understood you this morning, I had difficulties bringing these two approaches together. I had difficulties understanding what were the primary parameters that we had to come to grips with in the polymeric situation. Maybe that would be a good place to start.

Dave Kaelble (Science Center): I believe the polymeric materials generically require somewhat more detailed descriptions in terms of major mechanism of failure. I think in running through the

statements for a mathematical criteria of Weible failure distributions, a generalized Weible distribution function is required which has in it a two parameter model for stress dominated failure. In other words, it says that failure in the range of very short time or low temperature will be a brittle criterion similar to that for ceramic failure. But in the condition where you go into ductile response, very often you have a strain limitation. Accessibility becomes a critical parameter as a failure criterion. One has then the state of strain over the mean strain characteristic of the Weible failure process. As we go further, then, there is a third condition. If one, in fact, has moved out in time under conditions of decreasing stress, one has a constant strain state. Including stress relaxation effects, one has failure by a time dominated flow process. The third criteria operates. These three effects are essentially independent of each other.

Robb Thomson, Chairman: I would like to focus on the question of overall reliability in terms that we have had it presented, i.e., defect distributions, measurements, and stress history.

Don Thompson: I'm not sure I know quite how to ask the question either, but let me ask Charlie (Rau) what happens if you put time dependent failure phenomena into the reliability formulas which you have developed.

Charles Rau: You get more complicated reliability formulas, but they work.

Don Thompson: Could you pinpoint in your methodology, Charlie, where that happens?

Charles Rau: It is in the engineering model. I suppose that if the defects extend without load, it would also tie into the preinspection defect distribution which may change with time. I haven't thought about it in detail however.

Dave Kaelble: I think I agree with Charlie. Most of these complexities I brought up this morning will be detailed in the engineering model. To relate the particular physical responses and degradations of the systems, of course, is a material science problem which I think needs to be worked in a sort of new interface between material science and design engineering.

Anthony G. Evans: I think I lost something, but I think in Dave's presentation he didn't specifically talk about individual defects and their detection non-destructively. In many cases, adhesive bonds and composites don't fail that way. They fail either due to a loss of load or compliance, or a linking of smaller defects related to Fred Morris' comment. We are therefore talking about completely different formulas and a completely different methodology in which we are not interested particularly in the a priori defect distribution. However, I think the generation of the reliability accept/reject model is relatively straight forward, but it is different than the ones Charlie and I described. I think if you worked it out, one stage says this is the way the thing breaks.

Dave Kaelble: I might just go one more step toward composite system response involving polymers. This step is a very simple system response model that contains the types of statements which were previously detailed for a single subphase. If one says that one has a system of phases, one can describe them in the conventional statement for reliability of a system response of several phases. You can also describe the system moduli in terms of the modulus for a series combinatior. The product of these become the reliability modulus. The same thing can be done in parallel and combined to produce a hybridized series parallel model. Now this has been developed without the reliability argument by Halpin as a composit analog model. It is very useful in early phases, i.e., before you come to a discrete laminate theory. One can do a lot of design optimization within the scope of such a model. That's the kind of picture I have, that if one were working toward a discrete design for composites, let's say fiber reinforced composites, one would use that kind of a model as a prelude to an exact finite element model with discrete mechanisms for probabilistic failure built within it.

Steven Wallace (Union Carbide): I do experimental work in measuring adhesive bonds. One of the things that bothers me is that there are no standards. It would appear that, with many organizations being interested in this field, that the Air Force Materials Lab would want to have standards. It appears that, if you don't have these standards, that it is every man on his own. I don't know how many other people feel this is a problem, but standards have always been a real problem with us in bond work.

Robert L. Crane: NASA did some work in the area of standards. No one was particularly interested. A principal problem was that the materials change. For example if I want to buy aluminum 7075, I can call Alcoa or call any place I want and they are going to give me 7075 within a very narrow range or composition, within a very narrow range of mechanical properties. But if I want to buy an adhesive, any adhesive, I can't guarantee that what I have today is what I am going to have next week. One organization who has done more work in this area than anybody else has been McDonald-Douglas, St. Louis on the F-15 program. It was many many years before they could standardize the adhesive for the bonding of the boron epoxy composites for the vertical-horizontal stabilizer to

the metal substructure. They got into lots of legal problems when they began to take apart the epoxies and characterize exactly what they were. The supplier was very cautious because it was all protected by proprietary rights. They don't patent it, and it is all trade secrets. It changes dramatically from day to day and that's the reason why the standards didn't make any sense. Things change so rapidly that I couldn't depend upon my standard.

Dave Kaelble: The bond is a composite. You have the independent responses of polymeric subphases. One finds it if you examine it. It is being done now, lot-to-lot variations in polymeric material inputs. There is an area of large variability in that alone.

Robb Thomson, Chairman: Any further discussion of failure modes in composites?

Fred Morris: A typical failure mode of a graphite fiber epoxy component in fatigue is to have crazing of the epoxy followed by a delamination, a cracking which proceeds from laminar defects in the layup planes subsequently followed by failure of the matrix in the piles that don't have fibers in the direction of the stress. Now, if you likened the crazing to an initiation process in metals, I think it is fair to say we know very little about how that proceeds and couples into crack development from the defects. It should be pointed out that these defects are often gross compared to what we are looking at in metals. It's not uncommon to see defects of the size of a centimeter across or more. In many cases the time to initiation can be practically zero and we are strictly in a propagation based failure situation where the main challenge is to be able to find the defects amid background clutter that is always present from the non-uniformities of the composite material. Much has yet to be learned about the coupling between the crazing aspects of the initiation process, the subsequent development of a crack at a defect site and a plane of delamination, and the composite material parameters as affected by the moisture content of the material.

Robb Thomson, Chairman: May I ask you a question? Does this mean that you feel at this stage the most crucial thing is the understanding of the physical processes of failure modes or is it in some other aspects, for example, development of instrumentation for the detection of defects?

Fred Morris: I think we know very little about failure modes in composite as compared to what we know about metallic failures. I think we are easily 5 years behind in understanding the details of failure modes. Of course, I have been lobbying heavily for looking more closely at the initiation failure mode aspects in metals. That hasn't been touched in composites. Propagation requirements in composites also need further work.

Robb Thomson, Chairman: Any other opinions on this point?

David S. Dean (P.E.R.M.E.): I would like to back up what has been said. We have recently been testing carbon fiber rocket motor cases and it is extremely difficult to find anybody who can tell you exactly what is required of the testing equipment. We have subjected these to a whole series of tests: ultrasonic, x-ray and acoustic emission tests and to date, I don't think we are very near to being able to predict which cases are really going to fail in service and which are not.

OVERVIEW OF QUANTITATIVE NDE

R. B. Thompson
Rockwell International Science Center
Thousand Oaks, California 91360

This paper presents an overview of the ARPA/AFML Program for Quantitative Ultrasonic Flaw Characterization which will serve as a framework to interrelate the papers which follow. Work supported by the ARPA/AFML program will be primarily discussed. However, it should be noted that other work has also played an important role in the development of this body of knowledge and will be cited in a more comprehensive review paper to be published elsewhere.

Figure 1 summarizes the basic NDE Decision Process, as has been presented in previous papers by Rau[1] and Evans[2]. Therein are indicated the three types of information which are needed to estimate the expected lifetime, or probability of failure, of a part. (It is assumed that the part design and service conditions are known and fixed parameters.) First, the naturally occurring flaw distribution should be known. This is then conditioned by the results of non-destructive measurements to produce a sharpened, more accurate estimate of the flaw sizes likely to be present. Finally, failure models must be used to predict the range of lifetimes which are consistent with the estimated flaw distribution. This information must then be combined with economic data to define the Accept/Reject criteria which minimizes the total costs of the system. The role of Quantitative NDE is to provide the most accurate data possible regarding the flaw size "a". This sharpens the functions P(a/m), P(n), and $ shown in Fig. 1, and thereby reduces system costs.

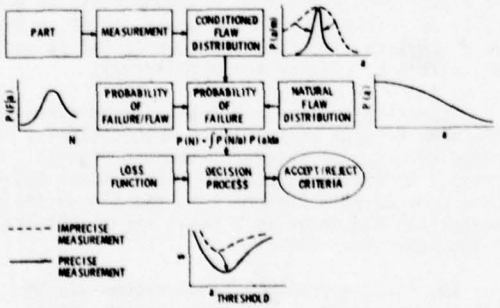

Fig. 1. Quantitative analysis of NDE decision process

This paper reviews ultrasonic techniques which have been developed for application to interior flaws and which are described in the papers immediately following. Similar work directed towards the ultrasonic and electromagnetic characterization of surface flaws is described elsewhere in these Proceedings.

One of the reasons why it is difficult to develop measurement techniques which sharpen the distribution P(a/m) is illustrated in Fig. 2. A pulse-echo ultrasonic measurement is shown for two cases. The upper sketch shows a planar flaw oriented parallel to the surface which will produce a large backscattered signal. For the in-plane loading shown, this flaw will have a size "a" of essentially zero. The lower sketch shows a similar flaw rotated 90° which produces a much weaker ultrasonic reflection. For the in-plane loading, this flaw will be much more likely to fail as "a" is equal to the full flaw radius. If the amplitude of the ultrasonic echo is used as the indicator, one finds that it is inversely related to flaw severity. It is thus necessary to derive more information from the ultrasonic signal so that the flaw severity can be more precisely determined.

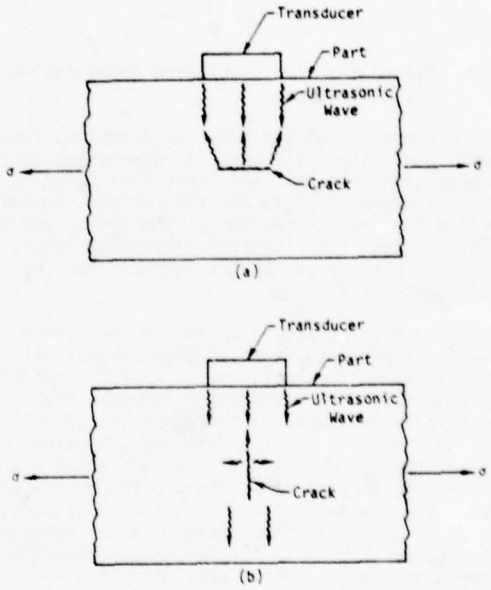

Fig. 2. Inverse relationship between ultrasonic pulse-echo data and flaw severity.
(a) Flaw parallel to surface produces large signal but is not a severe structural defect.
(b) Flaw normal to surface produces weak signal but can be a serious structural defect.

Figure 3 illustrates the methodology used to develop techniques which can deduce this information from the ultrasonic signals. It is first necessary to establish an understanding of the interaction of the ultrasonic energy with the flaw. This is done in a classical manner by comparing theory and experiment. Once sufficiently accurate models are available, they can be used as the basis for solution of the inverse problem. This addresses the problem of the greatest practical importance: How does one identify the properties

of an unknown flaw from measurements of the scattered ultrasonic fields? The solutions of the inverse problem take the form of predictors which convert experimental data into numerical flaw parameters to be used in fracture mechanics models. The final step is the verification of these results on controlled samples. When this has been completed, the techniques are available for more extensive verification evaluation on a statistically significant set of samples.

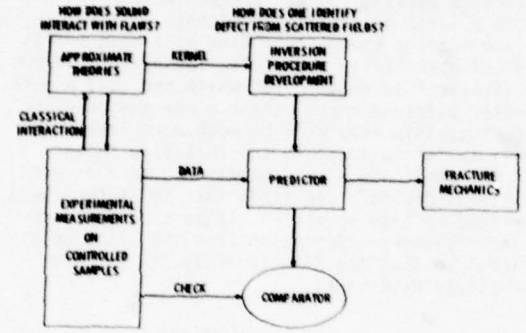

Fig. 3. Methodology for developing quantitative NDE techniques.

The remainder of the paper will amplify these concepts and discuss the specific approaches that have been adopted within the individual building blocks. Turning first to the theoretical studies, there are two basic objectives. The theory not only provides insight into the flaw-ultrasound interaction, but also serves as the "kernel" for the invasion procedure.

Figure 4 illustrates the former use. Here orthographic projections of angular contours of equal scattering intensity are shown for a spherical flaw and an oblate spheroid (pancake) flaw. These calculations were performed by the Cornell group, led by Prof. J. Krumhansl and are based upon the Born approximation.[3] The different shadings indicate varying strengths of ultrasonic scattering. For the case of an incident longitudinal wave, it is seen that the sphere produces symmetric scattering patterns with longitudinal scattering strongest near the backscattered direction and mode converted transverse wave scattering strongest at angles approaching 90°. For the case of the oblate spheroid whose normal is inclined at 45° with respect to the direction of incidence, the results are similar to those which would be expected on the basis of specular reflection. The longitudinal wave is most strongly scattered near, though not exactly at, the specularly predicted downward direction. The mode scattered signal is also greatest in this direction.

The fact that these are approximate results should be reemphasized. An important part of the program philosophy has been to pursue approximate techniques, which can be applied to fairly general flaw shapes, rather than to seek exact solutions which are tractable for a much smaller set of flaws. It is recognized, however, that the latter are quite important for both the detailed information which they contain and for calibrating the approximations.

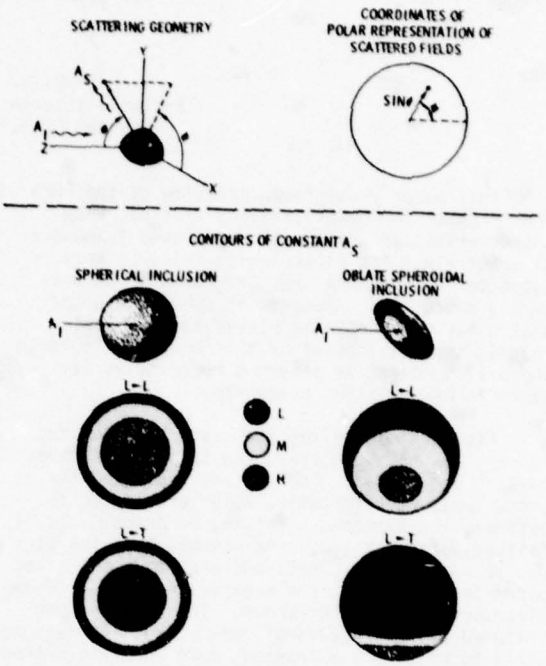

Fig. 4. Contours of equal scattering intensity for spherical and oblate spheroidal cavities.

Figure 5 illustrates the second role of the theory which is to serve as the basis for solutions of the inverse scattering problem. This is an adaptation of an analysis previously developed by Gubernatis.[4] It is noted that the ultrasonic scattering is a function of both the ratio of flaw size to wavelength and of the strength of the perturbation in elastic constants, or density, of the flaw. This functional dependence may be generally described by a double power series in the two parameters (the tensor nature of "c" is suppressed in this discussion for simplicity).

Approximations have been developed during the ARPA/AFML Program which may be mathematically described by a sum of selected elements of this series. As will be discussed later, these solutions provide both insight into the flaw-ultrasound interaction and serve as a basis for simplification of the inversion process.

The first approximation developed was the Born approximation.[3] The basic assumption is that the change in properties is small, so that the resulting expression is equivalent to including only those terms of the double series which are linear in $\Delta c/c$. Inspection of the closed form expressions for this sum show that it can be directly related to the spatial Fourier transform of the object shape function. Within this regime, the obvious strategy for inversion is to gather enough data to be able to evaluate the inverse Fourier transform.

Though of broad utility, the Born approximation breaks down for strongly scattering flaws. As a remedy, the Quasi-Static approximation was developed[5], which is correct at long wavelengths

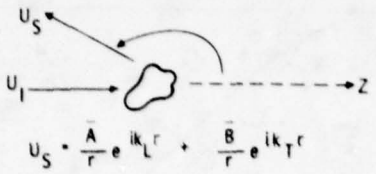

$$U_S = \frac{\bar{A}}{r} e^{ik_L r} + \frac{\bar{B}}{r} e^{ik_T r}$$

IN GENERAL:

$$|A| = \sum_{m=2,\, n=1}^{\infty} a_{m,n} (ka)^m \left(\frac{\Delta c}{c}\right)^n$$

$a_{m,n}$ is function of { ANGLE OF INCIDENCE, ANGLE OF SCATTERING, SHAPE }

BORN APPROXIMATION:

$$|A| = \frac{\Delta c}{c} \underbrace{\sum_{m=2}^{\infty} a_{m,1} (ka)^m}$$

SPATIAL FOURIER TRANSFORM OF OBJECT SHAPE

QUASI-STATIC APPROXIMATION:

$$|A| = (ka)^2 \underbrace{\sum_{n=1}^{\infty} a_{2,n} \left(\frac{\Delta c}{c}\right)^n}$$

LONG WAVE COEFFICIENT A_2

EXTENDED QUASI-STATIC APPROXIMATION:

$$|A| = \frac{\Delta c}{c} \sum_{m=2}^{\infty} a_{m,1} (ka)^m + (ka)^2 \sum_{n=2}^{\infty} a_{2,n} \left(\frac{\Delta c}{c}\right)^n$$

+ KEY ADDITIONAL HIGHER ORDER TERMS

Fig. 5. Relationships between approximation models for elastic wave scattering.

for all flaws. In the power series representation, this amounts to a sum of all terms quadratic in the (ka) variable. (The linear terms vanish identically.) The sum of the coefficients is the long wavelength coefficient, A_2, which will subsequently be shown to contain much important flaw information which can be used, in some cases, to directly determine the stress intensity factor from ultrasonic measurement.

The final approximation illustrated in Fig. 5 is the extended quasi-static approximation.[5] This is an ad hoc combination of the former two which is rigorously correct in both the long wavelength limit for all perturbations and in the weak scattering limit for all frequencies. In addition to the specific terms associated with the two previously discussed models, the quasi-static approximation contains selected higher order terms from the double power series which quantitatively appear to improve its accuracy. The inversion work of Rose[6] is based on this model as will be discussed in a subsequent paper.

Figure 6 reemphasizes the relationship of the approximate scattering models to the inversion procedures being developed in this program. In addition to the three models just discussed, work has been done in the area of the distorted wave Born approximation[7], aimed at irregularly shaped flaws, geometrical diffraction theory[8], applicable to crack-like flaws at short wavelengths, and scattering matrix[9,10] calculations. The latter is somewhat unique in that it provides essentially exact results for a variety of cases. As indicated by the solid (broken) checks, those models have been (are in the process of being) used as the basis of inversion techniques to be discussed in greater detail at the end of this paper. In addition, all have provided important insights such as new techniques for distinguishing signatures of crack-like and volumetric flaws.[11]

THEORY	INVERSE FOURIER TRANSFORM	LONG WAVELENGTH	ALR	IMPORTANT INSIGHTS
BORN	√		√	√
QUASI-STATIC		√		√
EXTENDED QUASI-STATIC	√		√	√
DISTORTED WAVE BORN				√
GEOMETRICAL DIFFRACTION THEORY			√	√
SCATTERING MATRIX			√	√

Fig. 6. Summary of theoretical approaches and their uses in inverting data.

The theoretical developments were supported, and often guided by experiments on controlled samples. These were fabricated using the diffusion bonding procedure developed by Paton[12] and illustrated in Fig. 7. This has enabled us to place cavities, or inclusion, at the center of an otherwise homogeneous piece of material. The sample initially is made of two halves with mating flaw sections. After bonding, grain growth across the boundary essentially returns the material to a homogeneous condition with only the flaw remaining.

Initial work was focused on ellipsoidal shaped cavities, selected because of the ease with which they could be theoretically modeled coupled with the fact that they approach, as a limiting case, a crack. More recently, this crack limit has been actively explored by constructing thinner and thinner discs by a variety of techniques. Very promising results have recently been obtained by placing ythia powder at a diffusion bonded interface. It has long been known that this contamination would inhibit bonding. It was not clear, however, whether the deformation occurring during bonding would place the treated region in compression and thereby cause it to behave as a ythia inclusion rather than a crack. Fortunately, ultrasonic measurements indicate that the flaw does, in fact, act like a crack, and this looks like a very useful way to model this important class of flaws.

Experimental measurements by Adler[13], Tittmann[14] and Elsley[14,15] have been performed on these controlled samples with a variety of objectives. First, the data have been used as a guide for the theoretical development and a check of the accuracy of the resulting approximations. This has been particularly important since exact theoretical solutions have only been available for "calibration" of approximate models in a few special cases. A further role of experiment has been to provide test

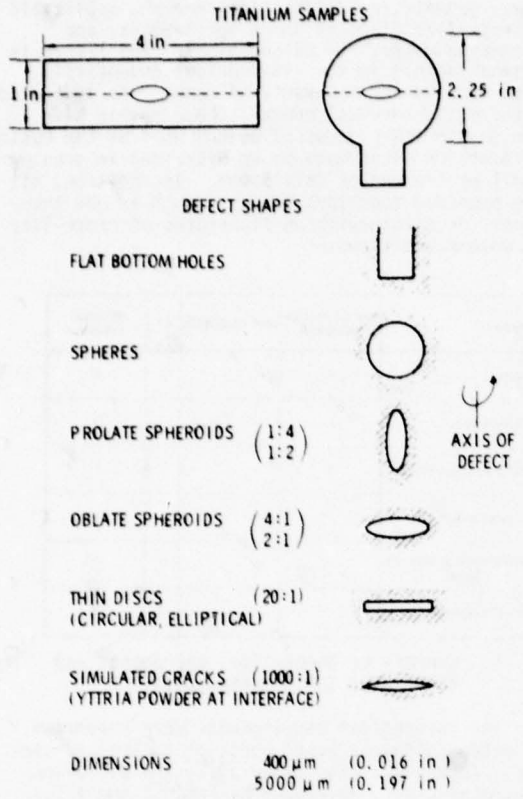

Fig. 7. Summary of defect shapes produced by diffusion bonding.

data to be used as input to evaluate the inversion procedures. Finally, the experience gained in developing precise measurement techniques for these purposes will lead to improved measurement procedures for field use.

Figure 8 illustrates the use of experiment to check and guide the theory. Here the angular dependence of the backscattered signal from a 400 x 800 μm oblate spheroidal cavity is plotted as a function of angle.[19] The theory is the Born approximation, averaged over the frequency content of the pulse. This both simulates the pulse response from the monochromatic theory, and also suppresses some of the detailed frequency response known to be inaccurate in this model. The agreement is quite good, which is somewhat surprising in view of the large change in properties presented by the cavity which place it outside the expected range of convergence of the Born approximation. Such agreements have demonstrated the utility of relatively simple models and have allowed an early consideration of the inverse problem.

The inversion techniques under consideration are summarized in Fig. 9. These have been classified in terms of their domain of application as measured in ka values. As a reference, the sketch at the bottom superimposes these regions on a plot of the frequency variation of the signal backscattered from a sphere. At high frequencies, $ka > 6.3$, an image will resolve the gross structure of the flaw since the diffraction limited spot

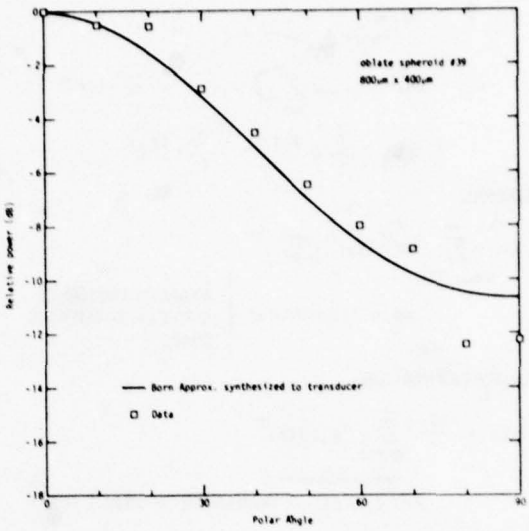

Fig. 8. Comparison of pulse-echo data as a function of polar angle with predictions of Born approximation (taking into account transducer bandwidth).

size is less than the flaw's radius. Under such conditions, the high information content and ease of interpretation make this the preferred mode of data processing and presentation. When the flaw size and/or material attenuation make is impossible to reach this high frequency limit, it is necessary to make use of specific knowledge of the flaw-ultrasound interaction. For $ka \lesssim 3$, it is still possible to reconstruct the flaw shape by incorporating a physical model into the data processing to increase resolution. At longer wavelengths, there is not sufficient information to fully reconstruct a flaw. However, adaptive learning networks have proven successful in the difficult regime of $ka \sim 1$ in which the flaw-ultrasound interaction is quite rich in structure, as shown in the sketch at the bottom.

Even at long wavelengths, $ka < 0.5$, it has been possible to measure a number of quite important flaw parameters, including in certain cases the stress intensity factor. The results go against intuition, and appear to have considerable potential for practical application.

Figure 10 summarizes the two approaches to imaging under consideration. Kino[16] is developing a synthetic aperture system in which a single transducer is scanned over the surface of the part. At each location, pulse-echo data is stored and subsequently combined to form the image. This recombination is accomplished by the superposition of the waveforms with appropriate time delays. Lakin[17] is considering a slightly different approach. His system uses a tone burst rather than impulsive excitation and images are constructed by a phased superposition of the signals received at a transducer array in a fashion equivalent to holography. Both techniques have the advantageous features that a) the image of any plane can be reconstructed once the data has been collected and b) modern advances in integrated

circuitry are being incorporated to make practical advanced signal processing procedures.

TYPE	REGIME	ADVANTAGES
IMAGING	ka>6.3 (λ<a)	HIGH INFORMATION CONTENT EASILY INTERPRETED DISPLAY RESOLVES MULTIPLE FLAWS
MODEL BASED RECONSTRUCTION	ka>3	PHYSICAL PRINCIPLES USED TO IMPROVE RESOLUTION AND TREAT MODE CONVERSION
MODEL BASED ADAPTIVE LEARNING NETWORKS	0.4<ka<3	MULTIPLE SCATTERING TAKEN INTO ACCOUNT GAIN MORE INFORMATION IN DIFFICULT REGIME
LONG WAVELENGTH SCATTERING	ka<0.5	FRACTURE RELATED PARAMETERS DEDUCED FROM A FEW MEASUREMENTS MAY BE USEFUL IN AUTOMATION

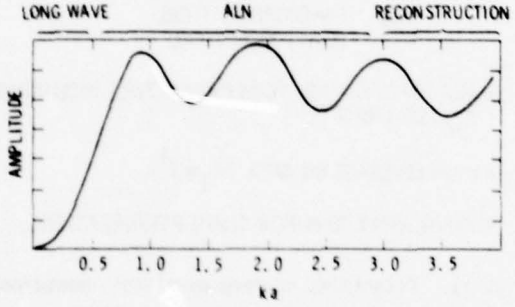

Fig. 9. Summary of inversion techniques.

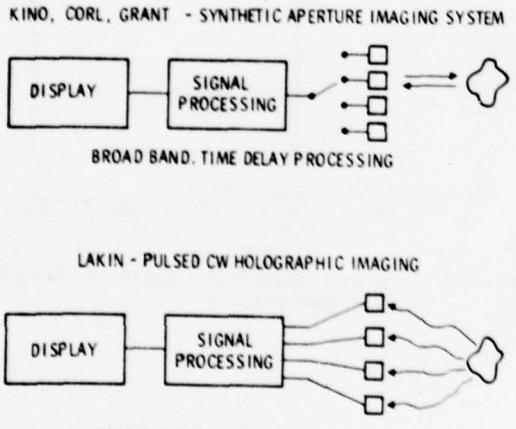

Fig. 10. Summary of imaging techniques.

Bleistein and Cohen[18] and Rose[6] have developed model based reconstruction algorithms based on a careful analysis of a forward scattering model. In each case, they consider the processing of backscattered data. Bleistein and Cohen base their results on a physical optics model and do their processing in the time domain. Rose bases his work on the extended quasi-static model and does his processing in the transform domain. In each case a reconstruction of the flaw shape results with somewhat improved resolution over that of a simple image.

Figure 11 shows an example of the reconstruction of a spherical cavity using the procedure of Rose. The dashed line indicates the actual result and the solid lines shown the output of the algorithm. For this measurement, ka ~ 5, and it can be seen that the sharpness of the edge was equivalent to a considerable better resolution.

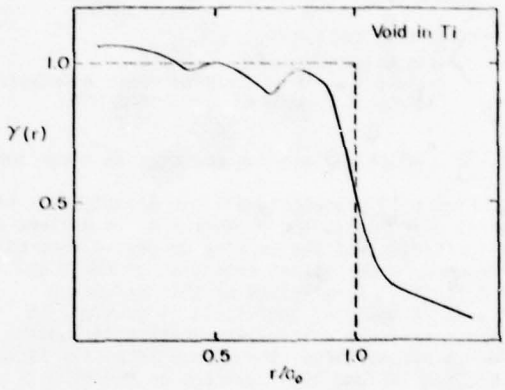

Fig. 11. Comparison of calculated and exact characteristic function for a spherical cavity based on Born inversion.

When ka ~ 1, the flaw-ultrasound interaction is quite complex, and analytical solution of the inverse problem has not yet been possible. Here, adaptive learning procedures have proven fruitful, as illustrated in Fig. 12. Whalen and Mucciardi[19] have used theoretical waveforms as a basis for training their networks and have then tested the result on experimental data. This approach has the advantage that expensive sets of samples with a wide variety of flaws are replaced by theoretical expressions in the training process. Early results based on the Born approximation were quite encouraging and the results obtained with other improved models are presented in this volume.[19]

One of the newest, and most exciting inversion procedures is the long wavelength technique developed during the last year. This has been the result of the efforts of many contributors. The early theoretical work was performed at the ARPA Materials Research Council by J. Rice, B. Budianski and W. Kohn. This is summarized by Rice[20] in this volume. Richardson[21] and Khuri-Yakub and Kino[22] further discuss the theory and present experimental verifications for the cases of bulk and surface flaws respectively.

WHALEN AND MUCCIARDI. INVERSION OF PHYSICALLY RECORDED UT WAVEFORMS USING ALN RECORDED NETWORKS TRAINED ON THEORETICAL DATA.

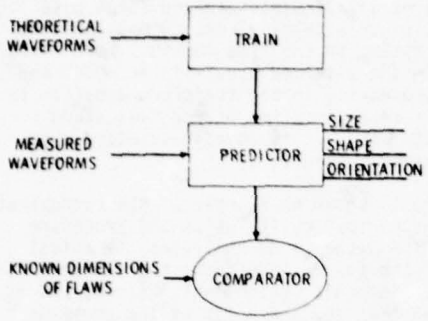

- EXCELLENT RESULTS IN THE DIFFICULT $0.5 \leq ka \leq 3$ REGIME
- HIERARCHY OF MODELS IN USE

  BORN TRAINING COMPLETED.
  EXTENDED QUASI-STATIC SCATTERING MATRIX IN PROGRESS.
  GEOMETRICAL DIFFRACTION THEORY TO BEGIN SOON.

Fig. 12. Adaptive learning approach to inversion.

Figure 13 presents the basic principles. At a particular angle, the parameter A is defined as the coefficient of the leading quadratic term of a frequency power series expansion of the scattered fields. From values of this parameter measured at a set of angles, it is possible to estimate fracture critical parameters including, in certain conditions, the stress intensity factor. Advantages include high leverage on the experimental data and insensitivity to minor shape perturbations.

Figure 14 presents the results of the use of this technique to measure the size of an ellipsoidal cavity in a diffusion bonded titanium sample.[21] Not only is the 400 μm value accurately determined, but the standard deviation of the estimate is extremely small due to the previously cited high leverage on the data.

As the research advances in these areas, the need for practical demonstrations under practical constraints presents itself. This is being addressed by Addison[23] in the Test Bed Program, which is coupled to the Quantitative Flaw Definition Program as shown in Fig. 15. This will lead to the demonstration of the utility of the techniques in sizing flaws and prediction lifetimes for a number of practical geometries and conditions. Other applications to the inspection of ceramic components are also developing rapidly.[24,25]

Finally, the same conceptual framework is being applied to the problem of quantitative characterization of surface flaws using both electromagnetic and ultrasonic techniques. Results are presented in Session IV, Eddy Current Techniques, and Session XIII, Surface Measurements, of the Proceedings.

RICE - LONG WAVELENGTH DEFECT CHARACTERIZATION SCHEMES

RICHARDSON - DIRECT & INVERSE PROBLEMS PERTAINING TO THE SCATTERING OF ELASTIC WAVES IN THE RAYLEIGH (LONG WAVE) REGIME.

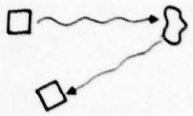

$$S(\omega,\theta) = A_2\omega^2 + A_3\omega^4 + \ldots$$

⇩

FRACTURE CRITICAL FLAW PARAMETERS

- MEASURES FEW KEY FLAW PARAMETERS INCLUDING K_{IC} FOR CRACKS.
- HIGH LEVERAGE ON DATA ($A_2 \propto a^3$).
- INSENSITIVE TO MINOR SHAPE PERTURBATIONS.

Fig. 13. Principles of long wavelength measurements.

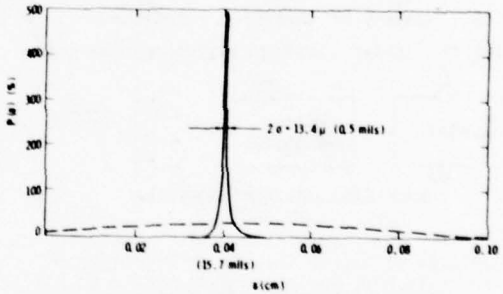

Fig. 14. Long wavelength measurement of size of oblate spheroid.

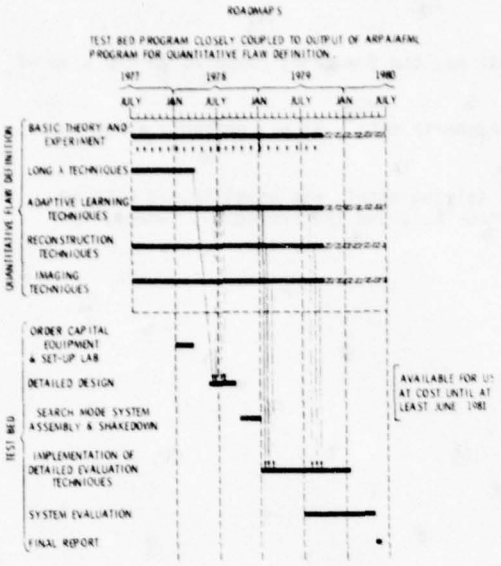

Fig. 15. Roadmap of Test Bed Program showing coupling to Program for Quantitative Flaw Definition.

REFERENCES

1. C. Rau, "The Impact of Inspection and Analysis Uncertainty on Reliability Prediction and Life Extension Strategies," these proceedings.

2. A. Evans, "Accept/Reject Criteria for Structural Ceramics," these proceedings.

3. J. A. Krumhansl, "Retrospective Comments on the Elastic Wave Scattering Problem," these proceedings.

4. J. E. Gubernatis, informal presentation at the 1976 ARPA Materials Research Council Summer Session, La Jolla, California.

5. J. E. Gubernatis, "Long Wave Scattering of Elastic Waves from Volumetric and Crack-like Defects of Simple Shapes," Proceedings of the ARPA/AFML Review of Progress in Quantitative NDE, AFML-TR-78-55, p. 21 (1978)

6. J. Rose, "Experimental and Theoretical Evaluation of Born Inversion Procedure," these proceedings.

7. K. Newman and E. Domany,"Calculation of Scattering by the Distorted Wave Born Approximation," these proceedings.

8. J. D. Achenbach, A. K. Gauteson, and H. McMaken, "Application of Geometrical Diffraction Theory to GNDE Analysis," these proceedings.

9. V. V. Varadan and V. K. Varadan, "Scattering of Elastic Waves by Oblate Spheroids and Cracks," these proceedings.

10. W. M. Visscher, "A New Method for Calculating Elastic Wave Scattering from a Defect in an Isotropic Homogeneous Medium," these proceedings.

11. J. E. Gubernatis, E. Domany, "Crack Identification and Characterization in the Rayleigh Limit," these proceedings.

12. N. Paton, "Ultrasonic Samples Using Diffusion Bonding Techniques," Proceedings of the ARPA/AFML Review of Quantitative NDE, AFML-TR-75-212, p. 89 (1976)

13. L. Adler and K. Lewis, "Frequency Dependence of Ultrasonic Wave Scattering from Cracks," these proceedings.

14. B. R. Tittmann and R. K. Elsley, "Experimental Measurement and Interpretation of Ultrasonic Scattering by Flaws," Proceedings of the ARPA/AFML Review of Progress in Quantitative NDE," AFML-TR-78-55, p. 26 (1978)

15. R. K. Elsley, "Low Frequency Scattering Measurements," these proceedings.

16. G. S. Kino, P. M. Grant, and P. D. Carl, "Digital Synthetic Aperture Acoustic Imaging for NDE," these proceedings.

17. K. Lakin, "Acoustic Imaging and Image Processing by Wavefront Reconstruction Techniques," these proceedings.

18. J. K. Cohen, N. Bleistein, and R. K. Elsley, "An Inversion Technique for Reconstruction of Shape Voids," these proceedings.

19. M. F. Whalen and A. N. Mucciardi, "Inversion of Physically Recorded U. T. Waveforms Using ALN Recorded Networks Trained on Theoretical Data," these proceedings.

20. J. R. Rice,"Long Wavelength Defect Evaluation", these proceedings.

21. J. M. Richardson, "Direct and Inverse Problems Pertaining to the Scattering of Elastic Waves in the Rayleigh (Long Wave) Regime," these proceedings.

22. G. S. Kino, B. T. Khuri-Yakub, J. C. Shyne, M. T. Resch, and V. Domarkas, "Surface Crack Characterization; Geometry of Stress Intensity Factor Measurements," these proceedings.

23. R. B. Thompson and R. C. Addison, "Test Bed for Quantitative NDE," these proceedings.

24. G. S. Kino, B. T. Khuri-Yakub, and Y. Murakami, "Bulk Defect Characterization in Ceramics," these proceedings.

25. G. A. Alers, R. C. Addison, Jr., and L. A. Ahlberg, "Inspection of Ceramics Incorporating Size Estimation Methods Using Conventional Ultrasonics," these proceedings.

DISCUSSION

George Wiley (unidentified): In the Born approximation, what was the frequency compared to the size of the defect?

Bruce Thompson (Science Center): I believe that it was 5 megahertz data. KA was probably about somewhere between 1 and 3.

Bernard Tittmann (Science Center): The defect, that we are talking about, was an ellipsoid with an aspect ratio of 2 to 1 ellipsoid, 800 by 400μm major-minus axis and the frequency, indeed, was 5 megahertz.

RETROSPECTIVE COMMENTS ON THE ELASTIC WAVE SCATTERING PROBLEM

J. A. Krumhansl
Cornell University *
Washington, D. C.

ABSTRACT

Developments over the past several years have led to renewed study of theoretical methods for treating scattering of ultrasound by defects in elastic solids. Characteristically, many theories of scattering, until a few years ago, dealt with scalar waves and simple obstacles. Within that context two distinct regimes were apparent -- the long wave length, and the short wave or imaging regime. The treatment of vector fields in elastic solids is considered the more cumbersome, but we now have made progress -- still for idealized configurations. Specifically, the talk will deal with hypotheses on the types of problems which face us in the next generation of situations.

As the abstract indicates, the remarks to be given in this talk are retrospective rather than constituting a report of a particular current piece of research. Perhaps the history and the flow of emphasis may be of use in giving us some idea of what has been accomplished and what might be looked for in the next phase of this very interesting area.

Before going further, however, I have to acknowledge my colleagues. Gubernatis, Domany, Rose, Teitel and several other students at Cornell have contributed significantly to this work. Stimulating interactions with Kohn, Budiansky, Rice, and Kino, among others at the Materials Research Council, have also been extremely useful.

In 1973 at the first workshop meeting for this group, the point was made that much of the experimental work that was being done was interpreted using acoustic wave results. Examples of scattering which had been studied were given which showed that, in fact, these scalar wave interpretations gave exactly wrong results for some important directions of scattering. This experience really set the stage for what I am reviewing here.

The Cornell group began its effort by attempting to place these results in context with some of the other approaches that have been carried out in the past. Clearly, elastic wave scattering has been one of the most venerable problems in mathematical physics. A partial inventory of some useful techniques include: partial wave expansions, the collection of groups of these partial waves to form a T-matrix (i.e., transition matrix, using quantum mechanical terminology), integral equation techniques, reciprocity methods, variational methods, and geometric diffraction methods. There are two regimes that must be considered in choosing a method: the short wave regime, which is the imaging regime, and the long wave length regime, in which the differences between the acoustic and the elastic cases are most pronounced. The question is "which method should you use in which regime?"

Our feelings are quite definite as regards the purposes at hand. We are concerned with applied physics and engineering applications. There is another closely related enterprise, namely mathematical physics and applied mathematics. In engineering, a useful theoretical framework should be one in which physical intuition or engineering data can be entered as conveniently as possible. On the other hand, it may well be that the method is approximate and the limits of that approximation have to be known. For that reason it is important that one have, as a resource from mathematical physics, some exact solution to the problem.

For that reason, we examined this set of possible methods and chose to concentrate, at least in the initial phase, on the integral equation method. The partial wave expansion, including work by Ying and Truel[1], and the matrix work by Pao and Varadan[2], all furnish an important reference for the theoretician and, eventually, for the experimentalist. However, the point about the integral equation methods and, more recently, the reciprocity methods, to which I will just refer briefly because Kino[3] and Auld[4] will develop these in detail, is that engineering data or physical intuition can be entered relatively easily.

Given that motivation as a background, we now write down the key equation and indicate the strategy which has been formulated, particularly by Gubernatis[5], in going about solving it at two levels of approximation. At the frequency ω the scattering process is described by the integral equation

$$U_i(\vec{r}) = U_i^o(\vec{r}) + \delta\rho\omega^2 \int_R d\vec{r}' G_{im}(\vec{r},\vec{r}') U_m(\vec{r}') + \delta C_{jklm} \int_R d\vec{r}' G_{ij,k}(\vec{r},\vec{r}') U_{l,m}(\vec{r}') \qquad (1)$$

where G_{ij} is the Green's function (response function) satisfying

$$C_{ijkl} G_{km,jl} + \rho\omega^2 G_{im} + \delta_{im}\delta(\vec{r}-\vec{r}') = 0 \qquad (2)$$

In the above expressions, $U_i(\vec{r})$ is the total displacement field and $U_i^o(\vec{r})$ is the so-called incident displacement field, which would equal the above total field if no scatterer were present. In the scatterer domain R we assume that the property deviations are uniform, i.e., the density deviation $\delta\rho$ and the elastic tensor deviation δC_{ijkl} are independent of $\vec{r}$ in R. The host material is of course characterized by the unperturbed density ρ and elastic tensor C_{ijkl}. Where convenient we have used indicial notation in which the subscripts i, j, k ..., represent the Cartesian directions and in which repeated indices imply summation. A comma preceding a subscript implies differentiation with respect to the coordinate corresponding to the subscript (e.g., $U_{l,m} = \delta U_l/\delta x_m$). In order to

*Presently at the National Science Foundation.

evaluate that integral one has to specify the displacement, which is unknown. This is where the approximations begin. In contrast to the partial wave method, it is possible to enter into the integrals of (1) the best guess for the displacement field U_m and strain $U_{l,m}$ in the vicinity of the flaw. This turns out to be very important from the point of view of the most recent developments as regards cracks and fracture parameters.

The systemization of the perturbation scheme is illustrated by the first Born approximation. If one assumes that the fields in the integrand are equal to the incident fields, then the scattering is found to be linear in $\delta\rho$ and δC_{ijkl}. This is the simplest case of the full systemization of the perturbation scheme. One can regard the eventual solution by perturbation expansions of equation (1) as a procedure in which, for example, one can order the terms according to powers of $\delta\rho\omega^3$ or, in another way, in terms of powers of δC_{ijkl}. If one thinks of the derivative in the second integrand (eq. 1) as being a wave number, then the terms containing C_{ijkl} could be viewed as a gradient expansion in first order strain, second order strain and so on. There are many ways in which one could conceive of developing these terms as part of an approximate solution. The Born approximation is that one in which only first order terms in $\delta\rho$ and δC_{ijkl} are included.

There is something else to note about this equation. The long wave length limit does not necessarily make the Born approximation a good one -- a very important point. The term proportional to $\delta\rho$ vanishes at low or small ω in the exact case, as predicted by the Born approximation. However, the term proportional to δC_{ijkl} must give the solution to the static elastic problem, i.e., for $\omega = 0$. This can be understood by imagining an applied, asymptotically uniform stress. If the flaw happens to be ellipsoidal in shape, one uses the Eshelby[6] solution with a uniform internal strain. This exact solution must be the sum of all of the zero frequency terms in the expansion with respect to δC_{ijkl}. This is not the case for the Born approximation.

This leads to a second approximation, in which the incident displacement and the strain fields appropriate to the exact solution around the flaw in the static limit are used to evaluate the integral. This gives a result, the quasi-static approximation, which is rigorously valid at low frequency.

This formulation provides a nice basis for going up higher and higher in the order of approximation. That, basically, is the motivation for why we felt that this approach is an engineering approach as contrasted with a sole emphasis on exact results. It is therefore complementary to the exact results which can be obtained by the partial wave expansion techniques which will be discussed elsewhere at this symposium.

An observation was made by Gubernatis[5] in 1975 that the scattering can be, in general, represented in terms of a so-called f-vector, which again involves the basic parameters. The exact results in the long wave length limit were then developed by Kohn and Rice[7] to systematize the interpretation of scattering in this regime. A very important point was the observation that there is richness in the elastic wave scattering which simply does not exist in the acoustic wave scattering and that this richness has to do with the structure of the term involving δC_{ijkl}. Using an orderly procedure involving the manipulation of tensor quantities, Kohn and Rice were able to specify a systematic technique for inverting data appropriate for this low frequency, long wavelength regime. In addition, other work has been stimulated from the long wave length scattering point of view. Richardson[8] has developed a probabilistic inversion technique for this regime in which an exact low frequency theory is used in the modeling of the scattering measurements.

The appropriate philosophy is that there is not a single best way. For ka << 1, the Born approximation[9] has compared well with some exact solutions. The quasi-static scattering model which uses the Eshelby solution, is an improvement. This has enabled one to write down the recipe which has later developed into an experimental flow diagram for looking for the major properties of flaws. More remarkably, Budiansky and Rice[10], also in the long wave length limit, are able to relate the scattering by a crack directly to the critical fracture parameters.

Not much has been yet said about the short wave length limit. Here the integrals in the integral equation (1) are evaluated asymptotically. It could be evaluated by the standard method of constant phase, which leads to a series of approximations, the simplest of which is the Fraunhofer approximation. Keller's technique[11] for treating this problem for other applications made use of certain canonical exact solutions -- for example, the Kirchhoff solution for an edge. These were used to correct the simple Fraunhofer picture by patching in these singular edge fields at non-analytical edge points. In the same sense, the treatment of the elastodynamics problem requires some exact solutions and this is the approach that Achenbach[12] and his group have developed in detail in the last few years. In order to guide this approximate technique, i.e., geometric diffraction theory, one must again have available some exact solutions. Future interest will then focus on joining these two regimes, the long wave length regime and the short wave end of the elastodynamics regime.

As one proceeds further, the earlier methods perhaps seem primitive and indirect. In particular, it is clear that the reciprocity techniques which Kino[3] and Auld[4] have now added to the subject are operationally even more oriented toward engineering because they take the essence of the scattering matrix right out through the transducer to the electrical terminals. Indeed, this combines the dynamics, or the response, if you wish, of the circuitry with reciprocity relations for the elastic fields. This was again redeveloped on the basis of earlier results obtained for electromagnetic fields. Again, it is possible to go through a hierarchy of expansions. As before these can be guessed at using the incident field, static deformations, and so on. The whole machinery of entering in the engineering data or physical intuition applied to the reciprocity technique, with the added feature that the results can be used in the Fresnel as well as the Fraunhofer regime.

This, in a sense, is the history of where we have been. The program still has much richness in the matter of relating theory to more sophisticated interpretations of experiments on single defects. However, the next step certainly has to be that of treating systems with many defects. This case may not be so difficult in one sense. If the spacing between defects is very much greater than the wave length, that is the transit time between defects is very much greater than the transient time across the defect, it is clear that then one can use simply time windowing and reduce the problem to that of, essentially, a single defect. That is an obvious thing to say but it is not necessarily obvious from the point of view of the mathematical physicist. What it means is that one operates in the high frequency limit as regards the interdefect scattering even though one may be operating in the low frequency limit with respect to the intradefect scattering.

However, there is another regime when the spacing between the defects is much less than the wave length. In that case one has to do an entirely different problem and that problem probably can get some guidance from the techniques which have been used to deal with the propagation of Schroedinger waves in disordered alloys (so called random alloys), in which case it is possible, I believe, to consider effective bulk elastic quantities because the defect is smaller than the wave length. This places one in the long wave length regime where one might take the Rice-Kohn results and do a further averaging to develop a correction to the propagation constant -- an average propagation constant of the system.

ACKNOWLEDGEMENT

This research was sponsored by the Center for Advanced NDE operated by the Science Center, Rockwell International, for the Advanced Research Projects Agency and the Air Force Materials Laboratory under contract F33615-74-C-5180.

REFERENCES

1. C. F. Ying and Rohn Truell, J. Appl. Phys. 27, 1086-1097 (1956).

2. See, for example, V. V. Varadan and V. K. Varadan "Scattering of Elastic Waves by Oblate Spheroids and Cracks", paper in these proceedings.

3. G. S. Kino "The Application of Reciprocity Theory to Scattering of Acoustic Waves by Flaws." Stanford University Report, (1976).

4. B. Auld "Characterization of Surface Wave Scattering by Surface Breaking Cracks", paper in these proceedings.

5. J. E. Gubernatis, E. Domany and J. A. Krumhansl, "Formal Aspects of the Theory of Scattering of Ultrasound by Flaws in Elastic Materials," J. Appl. Phys., Vol. 48, p. 2804 (1977).

6. J. D. Eshelby, "The Determination of the Elastic Field of an Ellipsoidal Inclusion and Related Problems," Proc. Roy. Soc., Vol. A241, pp. 376-396, (1957).

7. W. Kohn and J. R. Rice, "Scattering of Long Wavelength Elastic Waves from Localized Defects in Solids", submitted to J. Appl. Phys. See also, J. E. Gubernatis "Crack Identification and Characterization in the Rayleigh Limit', paper in these proceedings.

8. J. M. Richardson, "The Inverse Problem in Elastic Scattering at Long Wavelengths", 1978 Ultrasonics Symposium Proceedings, Catalog No. 78CH1344-ISU. See also, J. M. Richardson, "Direct and Inverse Problems Pertaining to the Scattering of Elastic Waves in the Rayleigh (Long Wavelength) Regime", paper in these proceedings.

9. See, for example, J. E. Gubernatis, J. A. Krumhansl, and M. Huberman, "The Born Approximation in the Theory of Scattering of Elastic Waves by Flaws", J. Appl. Phys. 48, 2812 (1977).

10. B. Budiansky and J. R. Rice, "On the Estimation of a Crack Fracture Parameter by Long Wavelength Scattering," Trans. ASME, J. Appl. Mech., Vol. 45, pp. 453-454,(1978).

11. J. B. Keller, "Geometrical Theory of Diffraction," J. Opt. Soc. Am., 52, 116-130 (1962)

12. See, for example, J. D. Achenbach, A. K. Gautesen, and H. McMaken "Application of Geometrical Diffraction Theory to QNDE Analysis", paper in these proceedings.

DISCUSSION

Chen Tsai (Carnegie-Mellon University): Being a layman in this field, I would like to ask Professor Krumhansl and Bruce Thompson, as well, a question. You have developed and studied various analytical techniques for calculating scattering from defects or voids and I would imagine that these kinds of techniques can be also applied to anisotropic media in principle. My question is whether these kinds of theories have been used in specific applications involving anisotropy.

James Krumhansl (National Science Foundation): I can give you a partial answer. In the past, there have been calculations for the static case. I think one can see now how the static information can be plugged into the long wave lengtn scattering problem. The answer to your question, therefore, is "Yes, the intregal equation technique can be used in the long wave length limit for the static case. The Greens function is to be developed in Fourier representation and simply has to be calculated in integral form for an anisotropic system. Jim Gubernatis and I have done this to try to calculate the elastic limit. Now one has to solve the Greens function by brute force, but I believe one can do it."

APPLICATION OF GEOMETRICAL DIFFRACTION THEORY TO QNDE ANALYSIS

J. D. Achenbach, A. K. Gautesen and H. McMaken
Technological Institute
Northwestern University
Evanston, Illinois 60201

ABSTRACT

The direct problem of the diffraction of time-harmonic waves by cracks in elastic solids is analyzed for high-frequencies, when the wavelengths are of the same order of magnitude as a characteristic length dimension, a, of the crack. It is shown that good approximations at high frequencies can be obtained on the basis of elastodynamic ray theory. An elastodynamic version of geometrical diffraction theory is briefly reviewed. We also present a hybrid theory, wherein the crack opening displacement is computed on the basis of geometrical diffraction theory, and the scattered field is subsequently obtained by the use of a representation theorem. This hybrid approach avoids the difficulties at shadow boundaries and caustic surfaces that plague a direct application of geometrical diffraction theory. Explicit results are computed for slits and penny-shaped cracks, and these results are compared with numerical results obtained on the basis of exact integral equation formulations. The relatively simple structure of the expressions for the scattered fields displays some characteristic features, whose possible role in the inverse problem is discussed.

INTRODUCTION

Experimental apparatus for quantitative flaw definition by the ultrasonic pulse method generally includes instrumentation to gate-out and spectrum analyze the various components of the signal diffracted by a flaw. After the scattering data have been corrected for transducer transfer functions and other characteristics of the system, amplitudes and phase functions are obtained, as functions of the frequency and the scattering angle. Such processed experimental data can then be compared with theoretical results.

For short pulses the frequency spectrum is centered in the high frequency (short wavelength) range. In this paper we present analytical results for diffraction of high frequency time harmonic waves. We consider frequencies corresponding to wavelengths that are of the same order of magnitude as the dominant cross-sectional dimension of the flaw. When the probing wavelength is that short, there are many interference processes, whose characteristic forms can provide the basis for an inversion procedure. A study of the direct problem is a necessary preliminary to the solution of the inverse problem, to generate understanding of the structure of the high-frequency diffracted field.

In this report we present analytical results that have been obtained by an approximate method which is based on elastodynamic ray theory.

Elastodynamic ray theory was presented in some detail by Karal and Keller[1]. The reflection of ray-carried signals at a boundary is well understood. The application of ray theory to diffraction by smooth obstacles has also been investigated in some detail, see e.g., Resende[2]. Reference 2 also appears to be the first one to deal with diffraction by a crack edge, at least in a two-dimensional geometry. A three-dimensional ray theory for diffraction by cracks has recently been discussed in some detail by Achenbach, Gautesen and McMaken[3-6]. The work presented in 3 is an extension to elastodynamics of geometrical diffraction theory, which was introduced by Keller[7] for acoustic and electromagnetic diffraction problems. Geometrical diffraction theory has been extensively applied in electromagnetic scattering, see e.g. 8 and 9. The elastodynamic version of geometrical diffraction theory provides relatively simple results, and it can be applied to cracks of complicated shape. The theory is applicable if $\omega a/c_L$ is sufficiently larger than unity, where ω is the circular frequency, a is a characteristic dimension of the crack, and c_L is the velocity of longitudinal waves.

HIGH FREQUENCY THEORY

At high frequencies the diffraction of elastic waves by cracks can be analyzed conveniently on the basis of elastodynamic ray theory. For time-harmonic wave motion, ray theory provides a method to trace the amplitude of a disturbance as it propagates along a ray. In a homogeneous, isotropic, linearly elastic solid the rays are straight lines, which are normal to the wavefronts. An unbounded solid can support rays of longitudinal and transverse wave motion. In this paper these rays are denoted as L-rays and T-rays, respectively. The free surface of a solid can, in addition, support rays of surface-wave motion, which are denoted as R-rays.

In analogy with geometrical optics, the simplest theory for diffraction of elastic waves by cracks may be called geometrical elastodynamics (GE). In GE a crack acts as a screen, which creates a shadow zone of no motion, and zones of reflected waves. The shadow zone is bounded by all rays passing through the source point and the edge of the crack. The geometrical reflections of these rays bound the zone(s) of reflected rays. The displacement field according to GE, is of the same order of magnitude as the incident field. The GE-field is, however, physically unrealistic, because of discontinuities at the boundaries of the shadow zone and the zone(s) of reflected waves.

The geometrical theory of diffraction (GTD) provides a first correction to GE. This correction is valid for $\omega a/c_L \gg 1$, and at points where $S/a > 1$. Here ω is the circular frequency, a is a length dimension of the crack, c_L is the velocity of longitudinal waves, and S is the distance from a crack edge. The correction provided by GTD is of order $(\omega a/c_L)^{-1/2}$.

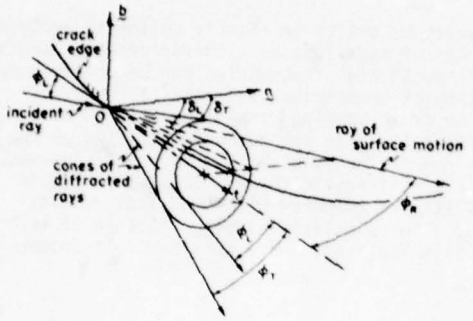

Fig. 1. Diffracted surface-wave ray and cones of diffracted body-wave rays.

Basic to GTD is the result that the incidence of a body-wave ray on the edge of a crack gives rise to two cones of diffracted body-wave rays and two R-rays (one on each crack face), see Fig. 1. The surfaces of the inner and outer cones of body-wave rays consist of L-rays and T-rays, respectively. When an R-ray intersects the edge of a crack, a ray of reflected surface wave motion is generated, as well as cones of diffracted body-wave rays.

With GE and GTD the total displacement field is still not valid at the boundaries of the shadow zone and the zone(s) of reflected waves. In a further refinement which is called uniform asymptotic theory (UAT), the fields at these boundaries are corrected. For some details on UAT we refer to Ref. 5.

For incident waves with curved wavefronts and for curved diffracting edges, the cones of diffracted rays have envelopes, at which the rays coalesce and the fields become singular. The envelopes are called caustics, and GDT breaks down at caustics.

Summary of GDT Results. Geometrical diffraction theory is based on the use of canonical solutions, which are asymptotic results for diffraction of a plane wave by a semi-infinite crack. In geometrical diffraction theory these canonical solutions are appropriately adjusted to account for curvature of incident wavefronts and curvature of crack edges, and for finite dimensions of the crack. For an incident longitudinal wave, the pertinent canonical solutions have been obtained by Achenbach et al, see Refs. 3 and 4.

Within the context of the GTD theory of Refs. 3 and 4, the diffracted field at a point of observation Q is comprised of contributions corresponding to "primary" diffracted body-wave rays, which are directly generated by incident body-wave rays, and contributions corresponding to "secondary" diffracted body-wave rays. The latter are generated by rays travelling via the crack faces. Thus, the diffracted displacement field at Q can be represented by

$$\underline{u}^d = \sum \underline{u}^{\alpha}_{\beta} + \sum \underline{u}^{\alpha}_{\beta\gamma} \qquad (1)$$

where

$\underline{u}^{\alpha}_{\beta}$ = primary diffracted field (2)

$\underline{u}^{\alpha}_{\beta\gamma}$ = secondary diffracted field (3)

In (2) the symbol α defines the incident ray, i.e., $\alpha = L$ or $\alpha = T$, while β defines the diffracted ray, $\beta = L$ or $\beta = T$. In (3) the symbol β defines the crack-face ray, i.e., $\beta = RS$ (surface-symmetric), $\beta = RA$ (surface-antisymmetric) or $\beta = TH$ (horizontally polarized transverse). The symbol γ defines the body-wave rays generated by diffraction of a crack-face ray; thus $\gamma = L$ or $\gamma = T$. The summations in Eq. 1 are carried out over all rays of a particular type passing through Q.

Primary diffracted body-wave rays. For an incident ray of longitudinal motion, the displacement fields on the diffracted body-wave rays are

$$\underline{u}^L_{\beta} = e^{i\omega S_{\beta}/c_{\beta}} \left[S_{\beta}(1+S_{\beta}/\rho^L_{\beta})\right]^{-1/2} D^L_{\beta}(\theta;\phi_L,\theta_L)\ \underline{i}^L_{\beta} U^L \qquad (4)$$

Here U^L defines the incident wave at the point of diffraction. In Eq. (4) the superscript β defines the nature of the wave motion on the diffracted rays. Thus we have $\beta = L$ or $\beta = T$. The distances S_{β} are along the diffracted rays from the point of diffraction O, to the point of observation. Also

$\underline{i}^L_{\beta}$ = unit vector,

which relates the displacement directions of the diffracted fields to those of the incident fields, and

$D^L_{\beta}(\theta;\phi_L,\theta_L)$ = diffraction coefficient.

For $\theta_L = \pi/2$ and $\phi_L = \pi/2$ the diffraction coefficents have been plotted in Fig. 2. Furthermore,

ρ^L_{β} = distance from O to caustic.

For an incident longitudinal wave we have

$$\rho^L_{\beta} = -\, a \sin^2\phi_{\beta} \left[a(d\phi_{\beta}/ds)\sin\phi_{\beta} + \cos\delta_{\beta}\right]^{-1} \qquad (5)$$

where a is the radius of curvature of the edge at the point of diffraction, s is the distance measured along the edge, and δ_{β} are the angles between the relevant diffracted rays and the normal to the crack edge, see Fig. 1. The angles ϕ_L and ϕ_T are

related by

$$c_L \cos\phi_T = c_T \cos\phi_L \qquad (6)$$

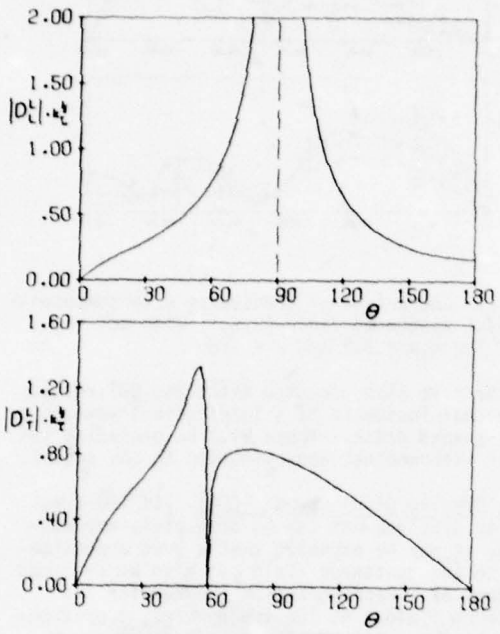

Fig. 2. Absolute values of diffraction coefficients:

$D_L^L(\theta) = D_L^L(\theta;\pi/2,\pi/2)$ and $D_T^L(\theta) = D_T^L(\theta;\pi/2,\pi/2)$

for Poisson's ratio $\nu = 1/3$.

Diffracted surface wave rays. Both symmetric and antisymmetric surface wave motions are generated on the faces of the crack. The appearance of surface wave rays in diffraction problems has been discussed in considerable detail in Ref. 4.

Reflection of surface wave rays. A surface wave ray which intersects the edge of a crack, gives rise to a ray of reflected surface waves, and to two cones of diffracted body rays. For a surface wave incident on the edge of a semi-infinite crack these reflection and diffraction processes have been studied by Freund[10]. In the spirit of geometrical diffraction theory, we can immediately introduce the appropriate corrections for curvature of the incident wavefront and for curvature of the edge of the crack.

A surface wave ray is reflected such that the angle between the reflected ray and the tangent to the edge is just the same as the angle of incidence between the incident ray and the tangent to the edge. Moreover, rays of symmetric (antisymmetric) surface waves are reflected as rays of symmetric (antisymmetric) surface waves. Expressions for the reflection coefficients can be found in Ref. 4.

Body-wave rays generated by diffraction of surface-wave rays. These rays and the associated fields have also been studied in Ref. 4, where expressions for the diffraction coefficients have also been presented.

Comparison of GDT with Numerical Results. Since GDT is an asymptotic theory, it is not possible to precisely determine a lower limit of validity for $\omega a/c_L$. Thus, information on the range of validity of the theory must come by comparison with exact solutions. This has been done in Ref. 5 for diffraction of a normally incident longitudinal wave by a slit. Exact results for this problem have been computed in Ref. 5 by numerically solving a governing singular integral equation which has been derived by Mall[11].

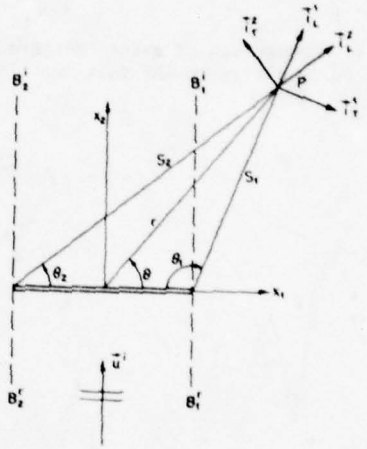

Fig. 3. Geometry for normal incidence of a longitudinal wave on a crack of width 2a.

The crack shown in Fig. 3 can be either a two-dimensional slit or a penny-shaped crack. For the slit, Figs. 4 and 5 show the exact and approximate scattered displacements at $\theta = 45^\circ$ versus the dimensionless wavenumber ($k_T a = \omega a/c_T$) for two values of r/a. The solid lines represent GDT solutions which include secondary diffractions. Good agreement is achieved for $k_T a > 1.5$, especially for r/a = 10. Since one must assume at the outset that results produced by an asymptotic theory of the kind presented in this paper are valid only for $k_T a >> 1$, it is quite remarkable that acceptable agreement is already achieved for values of $k_T a$ as low as 1.5, especially for higher values of r/a.

For $k_T a = 5.2$ the contributions from the longitudinal and transverse waves to the displacement components of the scattered field have been plotted separately in Figs. 6 and 7, versus θ. The corrections from the uniform asymptotic theory work very well; the curves are smooth and they show satisfactory agreement with the exact results, even though $D_T^L(\theta)$ is unbounded at the shadow boundary. There are some discrepancies in the contributions from the transverse waves at values of θ which appear to correspond to the boundary of the head-wave region.

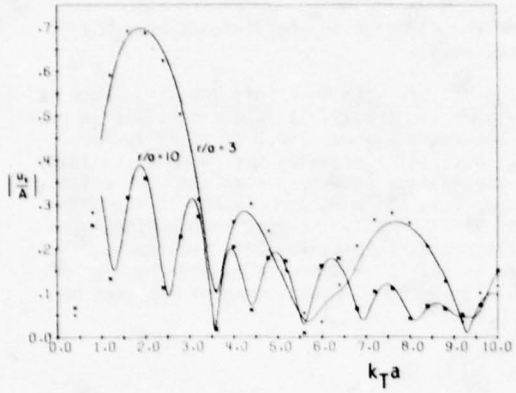

Fig. 4. Comparison of exact scattered u_1-field (+,x) for a slit with GDT solutions; $\theta = 45^o$, $\nu = 1/3$.

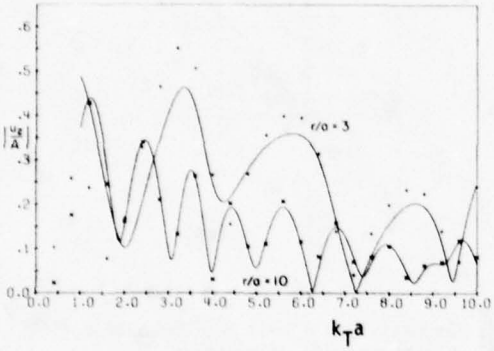

Fig. 5. Comparison of exact scattered u_2-field (+,x) with GDT solutions; $\theta = 45^o$, $\nu = 1/3$.

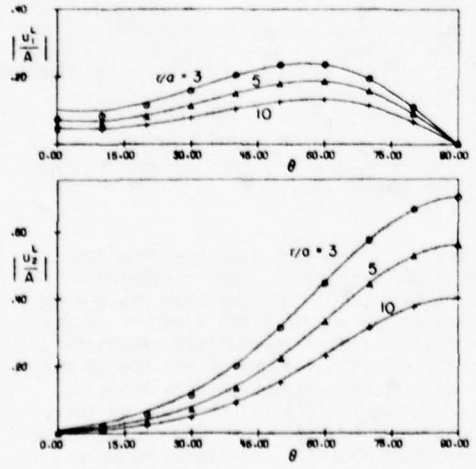

Fig. 6. Comparisons of longitudinal wave components of exact scattered field (0,Δ,+) with GDT solutions for $k_T a = 5.2$ and $\nu = 1/3$.

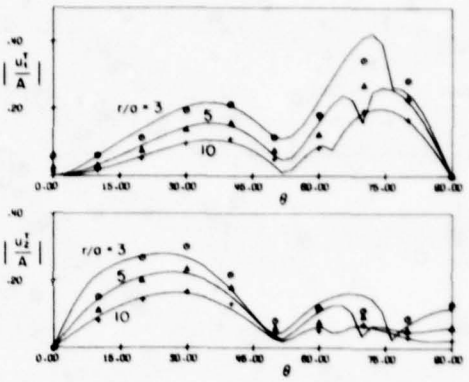

Fig. 7. Comparison of transverse wave components of exact scattered field (0,Δ,+) with GDT solutions for $k_T a = 5.2$ and $\nu = 1/3$.

We have also computed exact and GDT results for normal incidence of a longitudinal wave on a penny-shaped crack. These will be presented together with another approximation in the sequel.

Crack Opening Displacement (COD). If the crack opening displacement can be adequately approximated, it may be expected that a good approximation to the scattered field can also be obtained by means of a representation theorem for the scattered field. At low frequencies, approximations to the crack opening displacement can be obtained on the basis of quasi-static calculations. At high frequencies Δu_i can be computed on the basis of GDT.

Within the context of the geometrical diffraction theory discussed in this section, the principal contribution to the crack opening displacement comes from the geometrical elastodynamic part of the solution, i.e. from the direct reflection from the crack faces. For normal incidence we have

$$\Delta u_2 = -2\,A \tag{7}$$

The body waves associated with the primary diffractions do not generate displacements on the crack faces, except for transverse motions which are polarized in the crack faces. The latter are, however, of order $O(\omega a/c_L)^{-1/2}$ as compared to (7). Important contributions to the crack opening displacements are, however, generated by the surface wave motions.

For the case of normal incidence of a longitudinal wave on a slit, the absolute value and the phase of the crack opening displacement have been computed for various values of $k_L a$, where

$$k_L a = \omega a/c_L \tag{8}$$

At low frequencies (small $k_L a$) the phase is approximately ¶/2, and the absolute value has an elliptical shape. As $k_L a$ increases, waveforms develop, which are generated by surface motions of the crack faces. The exact crack opening displacements at high frequencies have been compared with the GDT results. For the slit the comparison is

shown in Fig. 8. Results for normal incidence on a penny-shaped crack are shown in Fig. 9. The displacements according to GDT at the center of the penny-shaped crack, which is a caustic point, have been corrected as discussed in Ref. 4. It is noted that both for the slit and the penny-shaped crack reasonably good agreement was obtained.

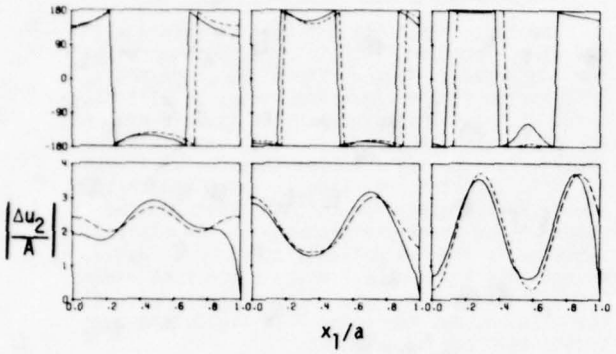

Fig. 8. Phase and $|\Delta u_2/A|$ versus x_1/a for $k_L a$ = 3, 4 and 5, for a slit, ν = 1/3, - - -GDT, —— exact.

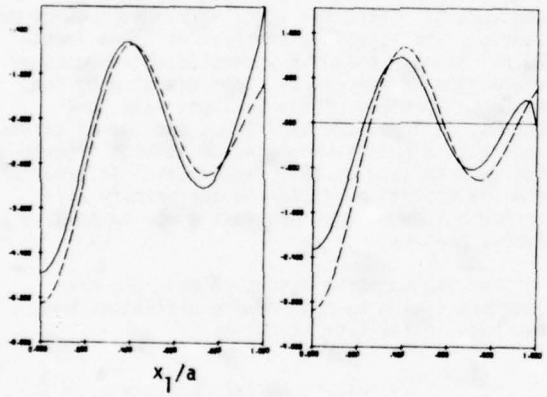

Fig. 9. Re $(\Delta u_2/A)$ and Im $(\Delta u_2/A)$ for a penny-shaped crack for $k_L a$ = 4.4, $\nu \cong 1/3$; - - - GDT, —— exact.

COD - Representation Theorem Approach. The results of geometrical diffraction theory are not valid at shadow-boundaries. Moreover, for curved wavefronts and for curved diffracting edges, the cones of diffracted rays have envelopes, at which the rays coalesce and the fields become singular. The envelopes are called caustics. The results of the geometrical theory of diffraction are also not valid near caustics. Even though it is possible to extend the theory to shadow boundaries and caustics, it becomes rather cumbersome. In an alternative approach, the crack opening displacements, which can be computed by GDT as shown earlier, can be used as an input in a representation integral of the scattered field. The scattered displacement fields computed in this manner will be valid at shadow boundaries and at the boundaries of the zones of reflected waves, and there will not be caustic surfaces. Even if Δu_i computed from GDT should show singularities due to caustics, these singularities will be integrable and the scattered field will be well behaved everywhere.

Let Σ be the area of a flat crack in an unbounded domain. By using the elastodynamic reciprocity relation and the appropriate radiation condition, the displacement components at points not on the crack faces can be expressed by

$$u_k(\underline{x}) = \frac{1}{4\pi r} \int_{\Sigma} \tau^G_{ij;k} \, \Delta u_i \, n_j \, dA \qquad (9)$$

where Δu_i is the displacement discontinuity across Σ, and

$\tau^G_{ij;k}$ = tensor of rank three

representing the stress components for the basic singular elastodynamic solution. For details on Eq.(9) we refer to Ref. 6.

For the slit results that have been obtained by means of Eq.(9) have been plotted in Fig. 10. In this figure we have also plotted direct GDT results and exact results. The crack opening displacement (COD) plus representation theorem approach is quite good for the displacements from the longitudinal waves, but it requires further improvement for the displacements corresponding to the transverse waves

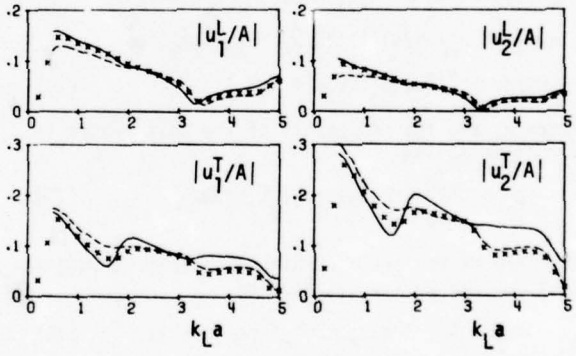

Fig. 10. Contributions to the displacement components from longitudinal and transverse waves, for normal incidence of a longitudinal wave on a slit, for θ = 30°; - - - GDT, —— COD + Rep. Thm, x exact results, υ=1/3.

Analogous results for normal incidence of a longitudinal wave on a penny-shaped crack are shown in Fig. 11. In this figure we have plotted a further simplification which is obtained when Eq.(9) is replaced by its far-field approximation.

Error analysis. It is perhaps surprising that the relatively small errors in the crack opening displacements shown for $k_L a$ = 3, 4, and 5 in Figs.8,9 should still give rise to rather substantial deviations in the diffracted fields, as shown by Figs.10 and 11. The reason is that errors of certain wavelengths in the crack opening displace-

ment are amplified by the representation integral.

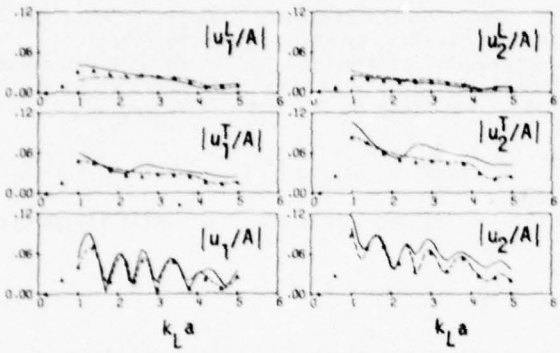

Fig. 11. Contributions to the displacement components from longitudinal and transverse waves, for normal incidence of a longitudinal wave on a penny-shaped crack, for $\theta = 30^o$; - - - GDT, ——— COD + Rep. Thm, Δ exact results, υ=1/4.

Let us consider the specific example of the two-dimensional case of normal incidence of a plane longitudinal wave of amplitude A upon a slit with edges at $x_1 = \pm a$, $x_2 = 0$. The far field approximation yields

$$u_k(\underline{x}) \sim i\,\hat{x}_k\left[1-2(\hat{x}_1 c_T/c_L)^2\right] J_L^L\,(8\pi r/k_L)^{-1/2}\,\exp\left[i(k_L r + \pi/4)\right] + 2i\,\hat{x}_2\,(\delta_{2k}-\hat{x}_2\hat{x}_k)\,J_T^L\,(8\pi r/k_T)^{-1/2}\exp\left[i(k_T r + \pi/4)\right] \quad (10)$$

where $\hat{x}_i$ are the components of the unit vector in direction $\underline{x}$, and

$$J_\beta^L = -\int_{-a}^{a} \Delta u_2 \exp(-ik_\beta \hat{x}_1 X)\,dX \quad (11)$$

The form of the crack opening displacement suggests that Δu_2 can be approximated by

$$\Delta u_2 \sim A\,(-2 + U_R \cos k_R X + \varepsilon \cos kX) \quad (12)$$

Here -2 represents the COD due to geometrical elastodynamics, $U_R \cos k_R X$ represent the crack face motion predicted by GDT, and ε and k represent the approximate error from the GE+GDT approximation. Substitution of (12) into (11) yields

$$J_\beta^L = -A\,a\{-4\,H_\beta(0) + U_R[H_\beta(k_R) + H_\beta(-k_R)] + \varepsilon[H_\beta(k) + H_\beta(-k)]\} \quad (13)$$

where

$$H_\beta(k) = [(k-k_\beta \hat{x}_1)a]^{-1} \sin[(k-k_\beta \hat{x}_1)a] \quad (14)$$

We note that $H_\beta(k)$ takes on its maximum value of unity at $k = k_\beta \hat{x}_1$, i.e. for a specific combination of frequency and angle of observation.

Equation (13) also provides insight on the influence of the surface wave terms on the diffracted field. Near $x_1 = 0$ (i.e., $\theta = \pi/2, 3\pi/2$) the contribution from the GE term dominates the contribution from the surface waves in both the longitudinal and transverse fields, while near $x_1 = 1 (\theta = 0, \pi)$ the contribution from the surface waves dominates the transverse field, since k_T/k_R (where $k_R = \omega a/c_R$) is generally slightly less than unity.

SOME COMMENTS ON THE INVERSE PROBLEM

So far, this paper has been concerned with the direct problem, that is, the computation of the scattered field when the size, shape and orientation of the crack are known. We will conclude with a few comments on the inverse problem for plane waves incident on slits and penny-shaped cracks, for the special case that the diffracted field is symmetric relative to the plane through the x_1 and x_2 axes. For both the slit and the penny-shaped crack the geometry in the plane of symmetry is then essentially as shown in Fig. 3, except that the incident wave is under an angle, say θ_o, with the x_1 axis. For a given point of observation, say the point P in Fig. 3, the unknowns then are θ_o, a and θ.

In experiments the nature of diffracted signals is largely determined by their arrival times. Since the first arriving signal is longitudinal, it is often possible to gate out the purely longitudinal diffracted signals from subsequent signals. The frequency spectrum of these longitudinal signals contains a considerable amount of information on the crack. Upon division by the frequency spectrum of the incident wave, one obtains, in fact, the amplitudes and phases corresponding to single harmonic waves at high frequencies. Comparison of this experimental information with the analytical fields on the primary diffracted body wave rays provides a way to solve the inverse problem.

For the geometry discussed here the displacement fields on the primary diffracted body wave rays follow from Eq. (4) as

$$\underline{u}_L^L = e^{i\omega S_L/c_L}\left[S_L(1+S_L/\rho_L^L)\right]^{-1/2} D_L^L(\theta;\pi/2,\theta_L)\,\underline{i}_L^L U^L \quad (15)$$

It is convenient to define a dimensionless diffraction coefficient as

$$\bar{D}_L(\theta;\theta_L) = k_L^{1/2}\, e^{-i\pi/4}\, D_L^L(\theta;\pi/2,\theta_L) \quad (16)$$

The angles of incidence at the two points of diffraction are $\theta_1 = \theta_o$ and $\theta_1 = \pi - \theta_o$, respectively. If the point of observation is sufficiently far from the crack, we have, see Fig. 3

$$S_{L1} \sim r - a\cos\theta \quad (17)$$

$$S_{L2} \sim r + a\cos\theta \quad (18)$$

$$\theta_2 \sim \pi - \theta_1 \sim \theta \quad (19)$$

$$(\underline{i}_L^L)_1 \sim (\underline{i}_L^L)_2 \sim \underline{i}_r \quad (20)$$

$$(U_L^L)_1 \sim U_o^L \exp(ik_L a\cos\theta_o) \quad (21)$$

$$(U_L^L)_2 \sim U_o^L \exp(-ik_L a \cos\theta_o) \qquad (22)$$

where U^L defines the incident wave at the center of the crack. Adding the primary diffracted longitudinal fields from the points 1 and 2, we obtain

$$(u^d)_L \sim U_o^L (k_L r)^{-1/2} (1+r/\rho_L)^{-1/2} e^{i\pi/4} e^{ik_L r} F \qquad (23)$$

where

$$F = \bar{D}_L(\pi-\theta;\pi-\theta_o) e^{-ik_L a(\cos\theta-\cos\theta_o)} + \bar{D}_L(\theta;\theta_o)\, e^{ik_L a(\cos\theta-\cos\theta_o)} \qquad (24)$$

Of particular interest is the absolute magnitude of F :

$$|F| = \{[\bar{D}_L(\pi-\theta;\pi-\theta_o)]^2 + [\bar{D}_L(\theta;\theta_o)]^2 + 2\,\bar{D}_L(\pi-\theta;\pi-\theta_o)\bar{D}_L^L(\theta;\theta_o)\cos[2k_L a(\cos\theta-\cos\theta_o)]\}^{1/2} \qquad (25)$$

This result implies that the amplitude of the primary diffracted field is modulated with respect to k_L, with period

$$P = \pi / a\,|\cos\theta - \cos\theta_o| \qquad (26)$$

An analogous expression can be derived for the primary diffracted transverse field. From the practical point of view this latter expression is of less importance, because measurements of the transverse field usually are polluted by other signals.

Figure 12 shows the amplitude envelopes of the radial displacements corresponding to the primary longitudinal rays at three positions $\theta = 30^o$, 45^o and 60^o for the case of normal incidence of a longitudinal wave on a penny-shaped crack. The three curves show the characteristic behavior discussed in the previous paragraph, and it is easily checked that the increment $\Delta k_L a$ between peaks indeed equals $\pi/\cos\theta$ (note that $\theta_o = 90^o$).

Experimental results also show the modulation displayed in Fig.12, see e.g. Ref.12. The unknowns in Eq.(26) are a, θ and θ_o. Suppose we have four points of observation Q_o, Q_1, Q_2 and Q_3, on a straight line in the plane shown in Fig.3, distances ℓ_1, ℓ_2, and ℓ_3 apart. The angles θ corresponding to Q_1, Q_2 and Q_3 are θ_1, θ_2 and θ_3, respectively. The arrival times of the first longitudinal diffracted signals are denoted by t_o, t_1, t_2 and t_3, respectively. It then easily follows that

$$\gamma_1 = \theta_2 - \theta_1 = \cos^{-1}[c_L(t_2-t_1)/\ell_2] - \cos^{-1}[c_L(t_1-t_o)/\ell_1]$$

$$\gamma_2 = \theta_3 - \theta_2 = \cos^{-1}[c_L(t_3-t_2)/\ell_3] - \cos^{-1}[c_L(t_2-t_1)/\ell_2]$$

If P_1, P_2 and P_3 have been measured at Q_1, Q_2 and Q_3, we then have five equations for the five unknowns a, θ_o, θ_1, θ_2 and θ_3, which can easily be solved.

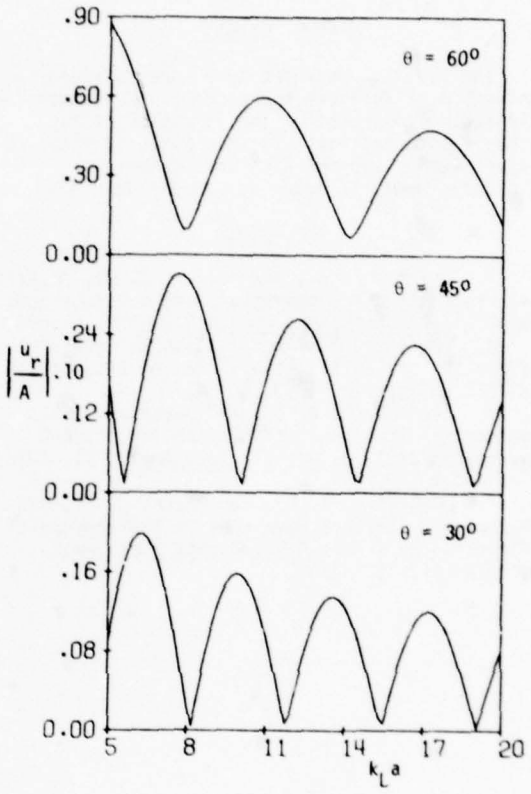

Fig. 12. Amplitude envelopes versus $k_L a$ for r/a = 10 and ν = 1/4.

CONCLUDING COMMENTS

For normal incidence of longitudinal waves on slits and penny-shaped cracks it has been shown in this paper by comparison with exact numerical results that geometrical diffraction theory (corrected at shadow boundaries and caustics) provides surprisingly good results at relatively small values of the frequency (say $k_L a > 1.5$) and relatively close to the crack (say $r/a > 5$). For more complicated geometries (elliptical cracks) the corrections at shadow boundaries and caustics become, however, more cumbersome. We have, therefore, also explored an alternative approach in which the crack opening displacement, which can be computed by GDT with relative ease, is used as an input in an exact or approximate representation integral for the scattered field. The scattered displacement fields computed in this manner are valid at shadow boundaries and they do not have caustic surfaces. The crack opening displacement computed by GDT may have singular points or curves, but the singularities are integrable. Comparison of the results obtained by this hybrid approach with exact results shows good agreement for the longitudinal wave

contributions, but some improvements are desirable for the transverse wave contributions.

The simple structure of the high frequency longitudinal wave results suggests a simple approach to the inverse problem, which has been briefly discussed.

ACKNOWLEDGEMENT

The results presented here were obtained in the course of research sponsored by the Center for Advanced NDE operated by the Science Center, Rockwell International, for the Advanced Research Project Agency and the Air Force Materials Laboratory under Contract No. F33615-74-C-5180.

REFERENCES

1. Karal, F. C., and Keller, J. B., "Elastic Wave Propagation in Homogeneous and Inhomogeneous Media," J. Acoust. Soc. Amer., 31, 1959, p. 694.

2. Resende, E., "Propagation Reflection and Diffraction of Elastic Waves," Ph.D. Dissertation, New York University, 1963.

3. Achenbach, J. D., and Gautesen, A.K., "Geometrical Theory of Diffraction for Three-D Elastodynamics," J. Acoust. Soc. Amer., 61, 1976, pp. 413-421.

4. Gautesen, A. K., Achenbach, J. D., and McMaken, H., "Surface Wave Rays in Elastodynamic Diffraction by Cracks," J. Acoust. Soc. Amer., 63, 1978, pp. 1824-1831.

5. Achenbach, J. D., Gautesen, A. K., and McMaken, H., "Application of Elastodynamic Ray Theory to Diffraction by Cracks," Modern Problems in Elastic Wave Propagation, Wiley-Interscience, New York, 1978.

6. Achenbach, J. D., Gautesen, A. K., and McMaken, H., "Diffraction of Elastic Waves by Cracks - Analytical Results," in Elastic Waves and Non-Destructive Testing of Materials, American Society of Mechanical Engineers,in press, 1978.

7. Keller, J. B., "A Geometrical Theory of Diffraction," Calculus of Variations and Its Applications, McGraw-Hill, 1958.

8. Keller, J. B., "Diffraction by an Aperture," J. Appl. Phys., 28, 1957, pp. 426-444.

9. Kouyoumjian, R. G., "The Geometrical Theory of Diffraction and its Application," Numerical and Asymptotic Techniques in Electromagnetics, Springer-Verlag, New York, 1975.

10. Freund, L. B., "The Oblique Reflection of a Rayleigh Wave from a Crack Tip," Int. J. Solids Structures 7, 1971, p. 1199.

11. Mal, A. K., "Interaction of Elastic Waves with a Griffith Crack," Int. J. Eng. Sc. 8, 1970, p. 769.

12. Adler, L., "Identification of Flaws from Scattered Ultrasonic Fields as Measured at a Planar Surface," Interdisciplinary Program for Quantitative Flaw Definition, Rockwell International, September 1977. pp. 122-158.

DISCUSSION

Tom Kincaid (General Electric): I have to lead up to my question with a little preamble. I tried to use this theory for cracks on steam turbines. When I did that I said, "Well, it is going to be easy because those 2 corners are going to radiate. I am going to end up getting a nice zero in the spectrum which will tell me the length of the crack," and we spent several months working on the theory and then we took a look at some cracks. The first thing I noticed was that a crack is not as flat as you assumed here. A crack is ragged in the middle with the main reflections coming off those ragged surfaces that are oriented in the direction of observation. I think that we will have to consider we are going to have such real cracks. I would like to get some comments from you on how we are going to handle the real problem.

J. D. Achenbach (Northwestern University): Yes, you are absolutely correct, this is a problem. Naturally, the solution depends upon the direction of observation. If you observe from behind the crack, you can deal with the crack in the above fashion. The problem you are talking about is in interpreting the back reflections from rough surfaces

Tom Kincaid: That is correct. In general, one receives a very complicated spectrum. Only in a very few cases does this spectrum have any similarity with the one you are talking about. You are saying that by observing from behind the crack all those ragged surfaces are basically invisible. That does not really avoid the problem: Frequently you cannot inspect the part so as to avoid the problem. I am trying to make an appeal to this group to understand that we need solutions that are not critically dependent on the crack geometry. These solutions should not depend on the fact that the crack is a smooth mirror with corners. To be useful, research will have to take these facts into consideration. The raggedness of the fracture surface is a statistical problem, in part, that we have to solve to be able to perform the inversion.

J. D. Achenbach: I agree with you, that is the problem. We should get some idea on the relative magnitudes of the characteristic dimensions of the roughness.

Tom Kincaid: Using micrographs you can get a good idea about the roughness.

J. D. Achenbach: I think the incident wavelength will have to be of the same order of magnitude as the crack, but it certainly has to be much larger than the crack's roughness. Certainly, if the roughness is of the same magnitude as the acoustic wavelength, you get the kind of problem you are alluding to.

Gordon Kino (Stanford University): Perhaps I could try and bridge this gap a little. We have been using an imaging system to look at cracks. In fact, we showed some pictures last year. What you see with an imaging system, illuminating an elox crack, is a smooth crack with sharp fronts, as Dr. Achenbach pointed out.

Using a real crack with real roughness you see scattered acoustic energy from everywhere, as Mr. Kincaid points out. I would suggest that as the theoretical techniques keep on developing and as we will learn to do the inverse process properly (which in one way is by imaging, the other way is essentially by mathematical techniques), we will not only see its front but we will see some information from all along the fracture surface. We will still get the length which is what we want to know, basically. I think you have to allow the theoriticians time because what they have got to do is the simplest problem first and then work up to the complicated ones.

Bernard Tittmann (Science Center): I would like to make a comment. Tomorrow morning I will show data on a real crack in ceramics and I will use a diffraction theory, similar to that by Young, to analyze the radiation pattern from a crack and I will show that this theory works. This pattern is as clean as that of an elox notch, but it does yield crack length information, as Gordon Kino has pointed out. I agree with Dr. Kino. I think we can achieve the solution to the problem.

Vernon Newhouse (Purdue University): I would like to plead with the theorists to stop casting their results in the time domain which, of course, is just a question of Fourier transforming the spectral results. It is, naturally, a lot more convenient to measure arrival times than to start analyzing a frequency spectrum and, furthermore, it may simplify the mathematics. If you are looking at a crack and measure arrival time of the first array and the last array at several different points, you probably will get information in a simpler way than you can from spectral results even when the crack is distorted.

J. D. Achenbach: I agree. From my point of view the time domain is just as good as the frequency domain. In fact, in some of our work we are trying to combine time domain and frequency domain considerations. Not being an experimentalist, I thought that even though there are definite peaks in the time domain it was still quite easy to make slight errors in the interpretation. On the other hand, if you take a frequency spectrum, where you integrate, you don't run into danger of making a significant error. Otherwise, I will go along with you.

W. Sachse (Cornell University): One comment, time domain is the approach that we are using in studying scattering of cracks experimentally.

John Zurbrick (General Electric): We grow cracks that we ask our inspectors to find for us. There is something that I have observed over the last couple of years in this program that is quite interesting to note and I think it tends to bridge some of the gaps that we are discussing. We have done a lot of acoustical microscope work, we have done a lot of imaging of flaws in real time and the time domain and we have done adaptive learning network experiments. The point is this. We are looking heavily at the surface convolutions of a crack and the indications that are or are not coming from the center. The center of the crack isn't really what causes the part to fail. It really is the plastic zone around the crack which has a shape that is very close to an oblate spheroid. I like the approach of looking at hollow oblate spheroids, but let's keep in mind that a fatigue crack, together with this plastic zone around it, reflects, defracts, mode converts, etc. I would encourage this kind of an approach. We are not just looking at a hole. We are looking for the degraded material around the crack tip. Actually, you can see certain similarities to an oblate spheroid because the crack grew from the middle to its present tip.

J. D. Achenbach: I don't think that the method I described would be suitable to describe this situation.

Earl Duback (General Dynamics): My background is in sonar and acoustics and I worked on problems similar to the one you are describing, a multi path situation. If you are able to obtain a cross correlation function and your signal is frequency-wise not broad enough, you can separate out the various acoustic paths. If you are looking at the amplitude information versus frequency, and if you look at the phase, you will find ripples in the phase. By zeroing out the signals in the correlation function from the various paths, you obtain nice linear phase information that will show you the energy coming along the different paths.

J. D. Achenbach: I am aware of what has been achieved along those lines in your field, and we would like to take similar approaches.

LONG WAVELENGTH DEFECT EVALUATION

J. R. Rice
Brown University
Providence, Rhode Island 02912

ABSTRACT

This is a summary of work with B. Budiansky[1] and W. Kohn[2] on the interpretation of long wavelength scattered fields from defects. The maximum information content of the long-wavelength fields is shown to consist of 22 parameters, one of which is the excess mass δM, and 21 of which are determined by the excess elastic moduli tensor δC and quasi-static response properties of the defect region[2]. It is shown that these parameters can, in principle, be determined by longitudinal to longitudinal wave scattering experiments only, and that they can provide evidence, necessarily incomplete, on the type, shape, orientation, and size of the defect. Particularly, when the defect is in the form of a planar crack, it is shown that the crack orientation can be determined[1,2] and that an approximate estimate can be made of the maximum stress intensity factor that would be induced by tensile stresses acting normal to the defect plane[1].

References

1. B. Budiansky and J. R. Rice, "On the estimation of a crack fracture parameter by long-wavelength scattering," in Preliminary Reports, Memoranda and Technical Notes of the Materials Research Council Summer Conference, July 1977, Univ. of Michigan Dept. Materials and Met. Engr., ed. M. J. Sinnott, pp. 1-9. (To appear in Trans. ASME, J. Appl. Mech.)

2. W. Kohn and J. R. Rice, "Scattering of long wavelength elastic waves from localized defects in solids," in Preliminary Reports . . . (ibid.), pp. 390-416. (Submitted to J. Appl. Phys.)

DIRECT AND INVERSE PROBLEMS PERTAINING TO THE SCATTERING OF ELASTIC WAVES IN THE RAYLEIGH (LONG WAVELENGTH) REGIME

J. M. Richardson
Rockwell International Science Center
Thousand Oaks, California 91360

ABSTRACT

It is well known that in the scattering of elastic waves from localized inhomogeneities the scattering amplitude A is proportional to the square of the frequency ω in the Rayleigh (long wavelength) regime, i.e., $A = A_2\omega^2 + \ldots$ This talk deals with the problem of (1) extracting A_2 from experimental scattering data, (2) calculating A_2 for an assumed scatterer and (3) deducing the properties of the scatterer from a set of values of A_2 measured for various transducer configurations. A review of experimental and theoretical results for A_2 will be presented for the case of spheroidal voids and the remaining discrepancies between the two kinds of results will be discussed. The inverse problem (i.e., deducing the scatterer properties from the scattering measurements) will be discussed in detail. The probabilistic inverse problem, which provides the appropriate framework for the interpretation of real data, will be covered at greater length. In the case in which it is assumed that the scatterer is an ellipsoid void, whose size, shape and orientation are unknown a priori, a number of computational results involving best estimates and associated measures of significance will be given. Analogous results will be derived for parameters related to fracture mechanics.

INTRODUCTION

A number of techniques have recently emerged for the determination of fracture related parameters of defects from measured ultrasonic fields. One of the newest of these, and perhaps the most unexpected, is the observation that considerable information can be derived from ultrasonic scattering measurements in which the wavelength is large with respect to the flaw size. From the familiar concept of resolution of an image, one would expect to obtain little useful information under such conditions. However, the elastic nature of the ultrasound-flaw interaction leads directly to results that are quite in contrast to this overly simple point of view. For example, the long wavelength scattering of elastic waves depends upon 22 parameters representing properties of a general scatterer. This is very different from the situations in the scalar wave scattering case.

Here, we summarize recent progress on the demonstration of the feasibility and usefulness of low frequency scattering of elastic waves in the context of nondestructive evaluation. Here we attempt a partial "vertical integration" to show, at least theoretically, that the results of such measurement can be interpreted in terms of the central concepts of fracture mechanics. This gives an indication that the remaining steps in an overall NDE decision process could be taken without significant difficulties.

Before considering the detailed results, it is important to ask: What advantages would such an approach have relative to other approaches for defect characterization? The following points can be made in its favor:

(1) The theory of the scattering of elastic waves at low frequencies is well established for the case of ellipsoidal inclusions and voids. Thus, the inverse scattering problem for this class of scatterers is quite tractable. At higher frequencies, this is not the case.

(2) Low frequency measurements are sensitive only to the overall shape and size of the defect and not to small textural details. This is also the information of importance in fracture.

(3) Low frequency scattering measurements are particularly sensitive to cracks compared with other scatterers (e.g., inclusions of the same volume or even the same area). In particular, the scattering measurements are significantly more sensitive to a large crack than to a number of small cracks with the same total area.

(4) The elastic processes involved in low frequency scattering are intimately related to those involved in the early stages of the fracture process (at least in most metals) as has been pointed out by Budiansky and Rice.[1] A further advantage is that the relevant stress intensity factor is proportional to the 1/6 power of the scattering amplitude, yielding thereby a substantial reduction of variance in the estimation process, a fact emphasized by Kino.[2]

(5) Another advantage is the fact that long wavelength scattering is insensitive to the position of the scatterer and thus precise location of the scatterer is unimportant.

Of course, there are also disadvantages. Some of these are:

(1) Relatively complex post-experiment data processing is involved in deducing the low frequency scattering characteristics. However, the main problems appear to be satisfactorily solved.[3]

(2) A significant problem, not yet confronted, is the isolation of each dominant scatterer from competing scatterers in taking the low frequency limit.

It is useful to direct the reader's attention, at least temporarily, to the overall NDE decision process of which the present topic is a part. In Fig. 1 we illustrate a typical NDE decision process in the case of a metal in which a possible failure process involves conventional

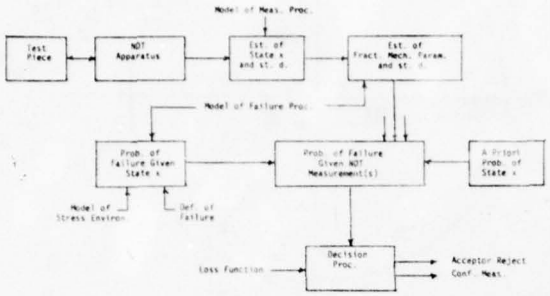

Fig. 1 Block Diagram of NDE Decision Process.

fracture mechanics. A similar decision structure has been discussed by Evans[4] at this meeting. Starting at the upper left we show the NDT apparatus (involving long wavelength longitudinal-to-longitudinal scattering in the present discussion) in bilateral interaction with the test piece. The results of measurement are fed into another box whose function is to provide a good estimate of the state x of a particular scatterer. The state is a set of parameters that provides a sufficiently good characterization for the purpose at hand. This box also provides estimates of the standard deviations (a posteriori) of the components of x. Although it is not shown, this estimation process also involves the a priori probability of the state. The final stage of the decision process on the first row of the block diagram is involved in producing corresponding estimates of a relevant fracture mechanics parameter and its standard deviation (a posteriori).

The next row of the block diagram involves calculation of the probability of failure for a given state x and the final collation of probabilistic inputs (relating to failure, NDT measurement and a priori probability) to yield the probability function that is needed for the final accept/reject decision. As shown in the figure, the central box has several inputs from above. This is meant to indicate that estimates based upon scattering data from several defects are used.

The subsequent discussion deals only with the first row of boxes in the figure.

THEORY OF SCATTERING OF ELASTIC WAVES AT LOW FREQUENCIES

The longitudinal-to-longitudinal scattering of elastic waves from an arbitrary scatterer is described by the scalar scattering amplitude $A = A(\hat{e}^s, \hat{e}^i, \omega)$ where $\hat{e}^s$ is the scattered (observer) direction e^i is the incident direction, and ω is the frequency (expressed in radians per unit time). This scattering amplitude can be expanded in a power series in ω in the following form:

$$A = A_2\omega^2 + iA_3\omega^3 + A_4\omega^4 + iA_5\omega^5 + \ldots \quad (1)$$

where the $A_n = A_n(\hat{e}^s, \hat{e}^i)$. The vanishing of A_0 and A_1 is a general property of localized scatterers. If the scatterer has inversion symmetry about the origin, then A_3 also vanishes,[5] but this question need not concern us here. The absolute value of A can also be expanded in powers of ω but here only even powers will enter, namely

$$|A| = a_2\omega^2 + a_4\omega^4 + \ldots \quad (2)$$

where, of course, $a_2 = |A_2|$. In Fig. 2 these relationships are illustrated for the case of longitudinal-to-longitudinal backscatter from a spherical B_4C inclusion in a SiC matrix.[6]

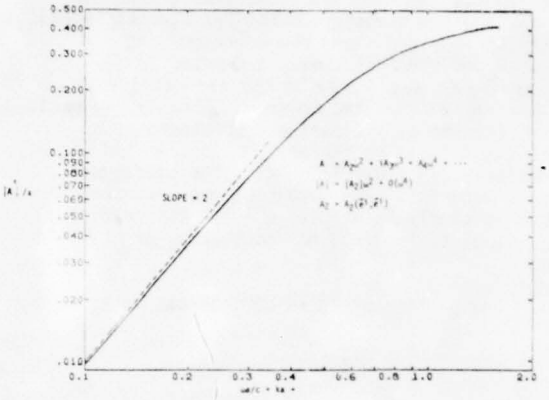

Fig. 2 Magnitude of scattering amplitude vs ka - ℓ → ℓ backscatter from spherical B_4C inclusion in SiC matrix.

In the experiments only the absolute magnitude $|A_2|$ is yielded. Since it is known theoretically that $A_2 > 0$ for spheroidal voids, the absence of the sign of A_2 in the experimental output is of no consequence. However, this may be a serious lack in the case of more general scatterers.

In Fig. 3 we illustrate the logical equations involved in obtaining experimental values of A_2,

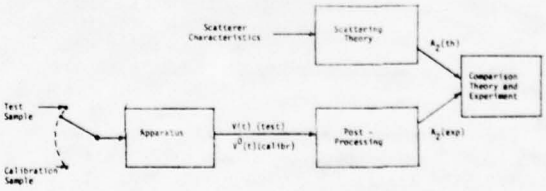

Fig. 3 Experimental determination of A_2 and comparison with theory.

the computation of the corresponding theoretical values and the comparison of the two. The problems entailed in the extraction of A_2 from experimental data are discussed by Elsley.[3] The remainder of the present section is devoted to the discussion of the computation of the theoretical values of A_2. The comparison of theory and experiment is taken up in the next section.

We will not give a detailed discussion here of the theoretical treatment[7-9] of the low frequency scattering of elastic waves from general spheroidal inclusions. It will suffice here to present a description of the input and output of the computer program LOWSCATEL. Actually, the input is presently given in a form suitable for general ellipsoidal inclusions of isotropic material even though the internal algorithm has not yet been extended beyond the spheroidal case. In setting up a framework for the description of the input, we use a Cartesian coordinate system (x,y,z) with the associated unit vectors $\hat{e}_x$, $\hat{e}_y$ and $\hat{e}_z$. The principal axes of the ellipsoid are defined by the mutually perpendicular vectors $\hat{u}$, $\hat{v}$, and $\hat{w}$ and the corresponding semi-axis lengths are directed by a, b, and c. The material properties of the host material are the density and the two Lame constants denoted by ρ, λ and μ and the corresponding properties of the inclusion are denoted by $\rho + \delta\rho$, $\lambda + \delta\lambda$ and $\mu + \delta\mu$. In the case of a void we set $\delta\rho = -\rho$, $\delta\lambda = -\lambda$ and $\delta\mu = -\mu$. Finally, we must include the set of incident and scattered wave directions defined by the unit vectors $\hat{e}^i$ and $\hat{e}^s$, respectively, in order to specify the configurations of interest. The output of the computer program is simply $A_2 = A_2(\hat{e}^s, \hat{e}^i)$ for the case of longitudinal-to-longitudinal scattering of elastic waves.

In the particular cases of interest here, we took

$\hat{u} = \hat{e}_x$, $\hat{v} = \hat{e}_y$, $\hat{w} = \hat{e}_z$

$a = b = 0.04$ cm and $c = 0.02$ cm

$\rho = 4.42$ gm cm^{-3}, $c_l = 0.634$ cm μsec^{-1}

$c_t = 0.303$ cm μsec^{-1}

The λ and μ for the host material (titanium) were determined from the above values of the host material longitudinal and transverse propagation velocities, c_l and c_t, respectively. The selected sets of incident and scattered directions will be indicated in the next section.

COMPARISON OF THEORY AND EXPERIMENT

We turn now to a comparison of the theoretical and experimental results. Both pitch-catch and pulse-echo types of scattering measurements are considered. In Figs. 4 and 5 the geometries and associated notation pertaining to these types are presented.

Figure 4 shows the geometrical setup in which the incident beam propagates in the negative z-direction (the z-axis is chosen as the axis of symmetry of the spheroid). All of the scattering (i.e., observer) directions chosen in the experiments are co-planar with each other and with the incident direction (i.e., there is a single scattering plane common to all experiments). The scattered direction is defined by the polar angle θ as shown. Clearly, in the case of a spherical void, all incident directions are equivalent.

In Fig. 5 the geometry of the pulse-echo type of measurement is shown. Here the common angular position of the "points" of entry and exit of the incident and scattered waves, respectively, is

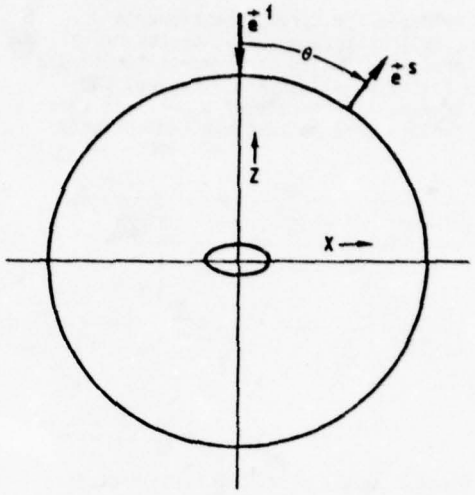

Fig. 4 Experimental geometry for pitch-catch measurements

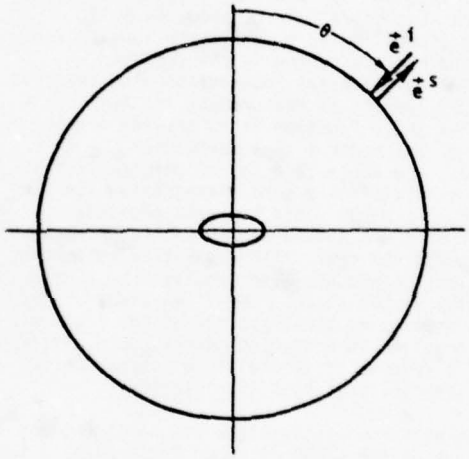

Fig. 5 Experimental geometry for pulse-echo measurements.

defined by the polar angle θ. As in the previous case the measurements are confined to a single scattering plane.

We first discuss the pitch-catch measurements obtained by Tittmann and Morris. The absolute value of deconvolved experimental results (appropriately desensitized) were extrapolated from a range of frequencies for which they were valid, to low frequencies to obtain a quantity that is proportional to $|A_2|$. The proportionality factor enters because of the calibration experiments used to normalize the data for variation in the transducer efficiency have slightly different diffraction properties than the scattering measurement. Assuming that the proportionality factor is the same for all experiments, we can obtain this factor by comparison of a set of control experiments with theory. For the latter, scattering from a spherical void of 400 μm diameter was chosen. The results are presented in Table I for the configurations of Fig. 4 corresponding to

Table 1. Scattering from a spherical void determination of experimental factor β.

($a = b = c = 0.02$ cm, $\vec{e}^{\,i} = -\vec{e}_z$, $\vec{e}^{\,s} = \vec{e}_x \sin\theta + \vec{e}_z \cos\theta$)

θ(deg)	Theory		Experiment	
	A_2 (cm μsec^2)	$\beta^{-1}A_2$	β	A_2 (cm μsec^2)
35	0.225×10^{-4}	7.1×10^{-4}	3.17×10^{-2}	0.215×10^{-4}
45	0.208	6.8	3.06	0.206
55	0.189	6.2	3.05	0.188
65	0.171	5.7	3.00	0.172
75	0.154	5.4	2.85	0.163
		Av	3.03×10^{-2}	

θ = 35°, 45°, 55°, 65°, and 75°. The results are denoted by $\beta^{-1}A_2$ where β is the experimental proportionality factor. Actually, as stated before, the absolute value $\beta^{-1}|A_2|$ is measured, however, since A_2 is known to be positive, the absolute value symbol $|\cdot|$ will be dropped. The experimental values of $\beta^{-1}A_2$ given in the third column of Table I are divided into the theoretical values of A_2 given in the second column to yield the values of β given in the fourth column. The average value of these last results turned out to be 3.03×10^{-2}, a value used for converting all experimental results into meaningful values of A_2 expressed in the units: cm μsec^2. The comparison of the experimental and theoretical values of A_2, given in the second and fifth columns of Table I are shown graphically in Fig. 6. The agreement of the sample-average values is, of course, tautological. However, the agreement of trends, which is not tautological, can be seen to be quite satisfactory.

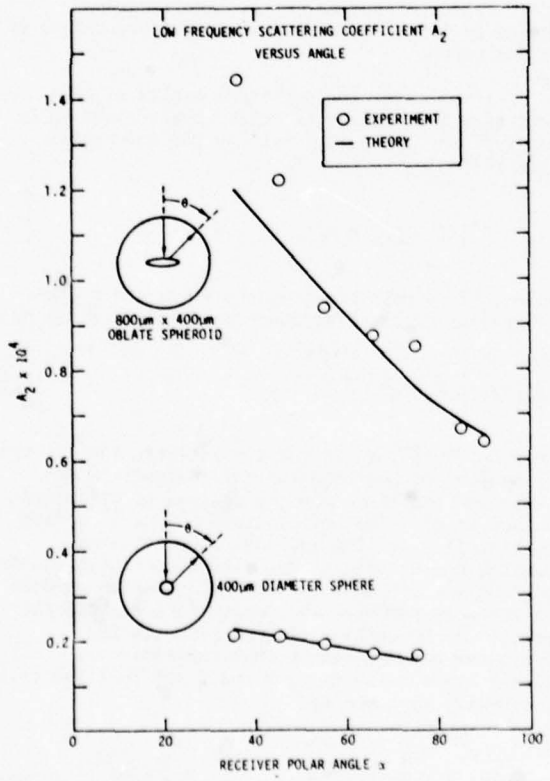

Fig. 6 Scattering in configuration of Fig. 4 for spherical void and spheroidal void.

It is worthy of note that the experimental proportionality factor β can be determined theoretically with the result:

$$\beta = \frac{R}{8\pi^2}$$

in which R is the radius of the sphere in Fig. 4 and where a factor of $(2\pi)^2$ in the denominator comes from the conversion of frequency in cycles per unit time to radians per unit time. Since R = 1.1 in = 1.79 cm, we obtain β = 0.035 cm which compares surprisingly well with the experimental value 0.0303.

In Table II we give the experimental results $\beta^{-1}A_2$ and the corrected results A_2 for the configurations of Fig. 1 with θ = 35°, 45°, 55°, 65°, 75°, 85°, and 90° for an oblate spheroidal void. It is assumed that the same value of β applies. The comparison with the theoretical values of A_2 is very good if the points for θ = 35° and 45° are omitted. The rather significant deviations at the latter values of θ are believed to involve a substantial systematic component which is presumably due to the spurious propagation effects discussed by Elsley.[3] The comparison is also shown graphically in Fig. 6.

Table 2. Scattering from a spheroidal void (configurations of Fig. 4(a))

($a = b = 0.04$ cm, $c = 0.02$ cm, $\vec{e}^{\,i} = -\vec{e}_z$, $\vec{e}^{\,s} = \vec{e}_x \sin\theta + \vec{e}_z \cos\theta$)

θ(deg)	Theory	Experiment	
	A_2 (cm μsec^2)	$\beta^{-1}A_2$	A_2 (cm μsec^2)
0	1.402×10^{-4}	---	---
35	1.197	47.8×10^{-4}	1.45×10^{-4}
45	1.085	40.3	1.22
55	0.968	31.0	0.94
65	0.856	28.8	0.87
75	0.759	28.1	0.85
85	0.685	22.0	0.67
90	0.658	21.2	0.64

We turn now to a discussion of the pulse-echo measurements obtained by Elsley and Nadler.[11] Their results are compared with theory in Table III and Fig. 7. The comparison is surprisingly good with a relative error of only 3.9%. It must be emphasized that we have used the old value of the experimental factor β, namely 0.0303. An adjustment of this value could bring down the relative error to 2.8%. It is clear that these measurements are less vulnerable to the kinds of systematic error involved in the earlier pitch-catch measurements.

Table 3. Scattering from a spheroidal void pulse-echo case

($a = b = 0.04$ cm, $c = 0.02$ cm, $\hat{e}^i = \hat{e}^s = \hat{e}_x \sin\theta - \hat{e}_z \cos\theta$)

	Theory	Experiment	
θ(deg)	A_2 (cm μsec^2)	$\beta^{-1}A_2$ (dB)	A_2 (cm μsec^2)
0	1.402×10^{-4}	-46.7	1.4×10^{-4}
15	1.374	-47.5	1.3
30	1.296	-47.65	1.25
45	1.189	-48.7	1.11
60	1.080	-49	1.08
75	0.999	-50	0.96
90	0.969	-50	0.96

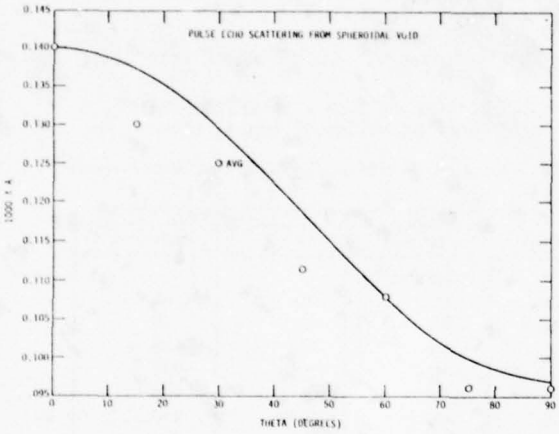

Fig. 7 Pulse-echo measurements of scattering from spheroidal void.

INVERSE SCATTERING AND FRACTURE MECHANICS

In the present section we discuss the inversion procedure employed in deducing the geometrical parameters of the spheroidal void from the scattering data. We also include a short discussion of the calculation of the normalized stress intensity factor k_I. For the purpose of inversion we assume, of course, that we do not know, a priori, the geometrical parameters--only that we know that the scatterer is a spheroidal void of some kind. The material properties of the host material are assumed known and have the values listed in Section II. The total inversion procedure is represented by the block diagram shown in Fig. 8.

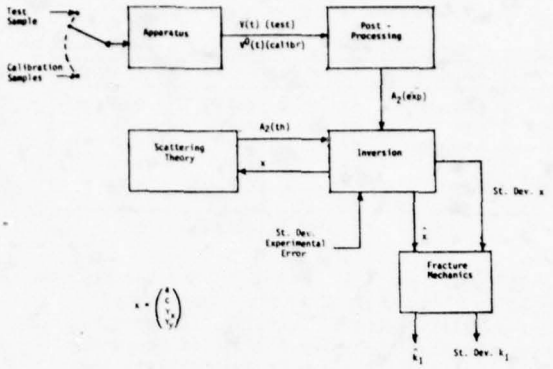

Fig. 8 The inverse scattering procedure.

We will pursue a probabilistic approach in which we start with a statistical ensemble of scatterer properties and measurement errors and then remove the members inconsistent with the scattering data obtained from the measurements. The best estimates of the geometrical properties of the spheroidal void are then the average or most probable values of these properties in the resultant reduced ensemble. The a posteriori variances of these properties (i.e., the variances in the reduced ensemble) are used as a measure of significance or, equivalently, the "leverage" exerted by the scattering data on the properties of the scatterer.

Let us model the possible results of the scattering measurement (assumed in all cases to be longitudinal-to-longitudinal) by the stochastic expression:

$$y_n = f_n(x) + \nu_n, \quad n = 1, \ldots, N \tag{1}$$

where y_n is a possible measured value and ν_n the measurement error. The function $f_n(x)$ is given by

$$f_n(x) = |A_2(\hat{e}_n^s, \hat{e}_n^i; x)| \tag{2}$$

where $A_2(\hat{e}^s, \hat{e}^i; x)$ is the coefficient of ω^2 in the ω-expansion of the longitudinal-to-longitudinal scattering amplitude $A(\hat{e}^s, \hat{e}^i, \omega; x)$ as discussed in Section II. The unit vectors $\hat{e}^i$ and $\hat{e}^s$ define the directions of the incident and scattered longitudinal elastic waves. The subscript n added to these vectors denotes the configuration used in the nth measurement. The vector x represents the geometrical properties of the void. In the spheroidal case we assume that the semi-axis lengths are denoted by a, a and c and that the axis of symmetry is given by

$$\hat{w} = \hat{e}_x \gamma_x + \hat{e}_y \gamma_y + \hat{e}_x (1 - \gamma_x^2 - \gamma_y^2)^{1/2} \tag{3}$$

where $\vec{e}_x$, $\vec{e}_y$ and $\vec{e}_z$ are the unit vectors in the x, y and z directions and where γ_x and γ_y are the direction cosines associated with the x and y directions as shown in Fig. 9. Thus the vector x is given by

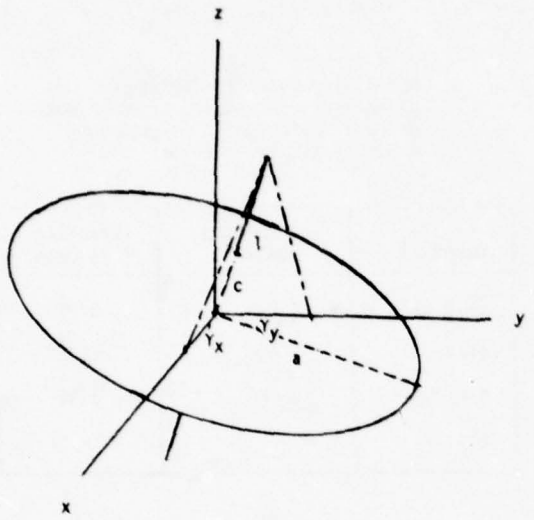

Fig. 9 Characterization of spheroidal geometry.

$$x = \begin{pmatrix} x_1 \\ x_2 \\ x_3 \\ x_4 \end{pmatrix} = \begin{matrix} a \\ c \\ \gamma_x \\ \gamma_y \end{matrix} \qquad (4)$$

It is to be stressed that the Cartesian coordinates (x,y,z) are defined in the laboratory frame of reference and have no necessary relation to the axis of symmetry of the spheroid. It is hoped that the state vector x and the Cartesian coordinate x will not be confused.

The definition of the stochastic model is completed by the specification of the a priori statistical properties of the state vector x and the ν_n and is characterized by the probability density (p.d.) P(x). The measurement errors ν_n are assumed to the Gaussian* random variables with properties

$$E\ \nu_n = 0 \qquad (5)$$

$$E\ \nu_n\ \nu_{n'} = \sigma_\nu^2\ \delta_{nn'}$$

where E is the averaging (or expectation) operator in the a priori sense.

Whatever is chosen for the criterion of performance of the estimation process, we must calculate the observationally conditioned p.d. of x given by

$$P(x|y) = P(y|x)P(x)/P(y) \qquad (7)$$

where

$$y = \begin{pmatrix} y_1 \\ \cdot \\ \cdot \\ \cdot \\ y_N \end{pmatrix} \qquad (8)$$

and where

$$P(y) = \int dx\ P(y|x)P(x) \qquad (9)$$

From the previous assumptions we obtain

$$\log P(y|x) = -\frac{1}{2\sigma_\nu^2}\,\psi + \text{const.}\ , \qquad (10)$$

where

$$\psi = \sum_{n=1}^{N} \left(y_n - f_n(x)\right)^2 \qquad (11)$$

is the sum of squares of the deviations of the y_n from the functions $f_n(x)$.

Let us consider the mean square criterion of optimality

$$\epsilon = E(\hat{x}-x)^T\ W(\hat{x}-x) \qquad (12)$$

where $\hat{x} = \hat{x}(y)$ is the estimator of x and where W is a symmetric positive-definite matrix of weighting factors. The minimum of ϵ with respect to the functional form of $\hat{x}(y)$ is given by a posteriori average

$$\hat{x}(y) = E(x|y)$$
$$= \int dx\ x\ P(x|y) \qquad (13)$$

where P(x|y) is given by (7). We will use the a posteriori covariance matrix defined by

$$\text{Cov}(x|y) = E(x\ x^T|y) - E(x|y)E(x^T|y) \qquad (14)$$

as the measure of confidence or significance. This tells us how much the a priori p.d. P(x) is "narrowed down" by the experimental factor P(y|x] in (7). In other words, how much "leverage" the experimental data has on the scatterer parameters defined by x. The measuring of a posteriori variances (or equivalently a posteriori standard

*The assumption of Gaussianity is inconsistent with the assumption that y_n and the f_n are positive. However, this is unimportant if $f_n/\sigma_n \gg 1$.

duration) is illustrated in Fig. 10 with a scalar state a.

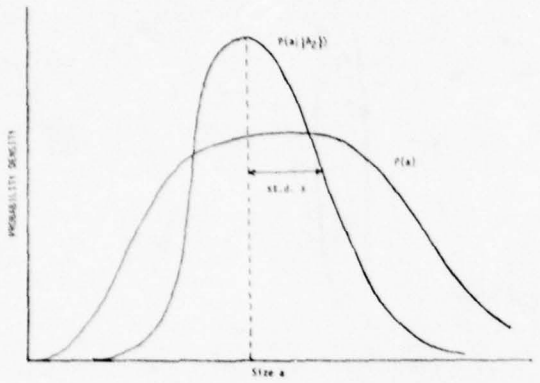

Fig. 10 Variance reduction by conditioning on measurements.

In the explicit computations we made several approximations. The first was approximating the a posteriori average by the a posteriori mode, i.e.,

$$\hat{x} = E(x|y) \simeq x_{max} \qquad (15)$$

where x_{max} is the value of x for which $P(x|y)$ is a maximum. Alternatively, we could have used a different optimality criterion, in terms of which the mode is exact. The second approximation is the computation of the a posteriori covariance by expanding ψ, defined by (11), in a power series about the point x_{max} and ignoring terms higher than quadratic.

The first set of estimates were made with pitch-catch data as inputs. We considered both noiseless theoretical data and actual experimental data as summarized in Table II.

In Table IV we present estimates of a, c, γ_x, and γ_y based upon the above experimental data. For the same of verification, we also present estimates

Table 4. Estimates based on pitch-catch measurements

Parameter	Exact	Estimates	
		Experimental Data	Theoretical Test Data
a(cm)	.04	.043	.03999
c(cm)	.02	.016	.02001
γ_x	0	14×10^{-6}	-8×10^{-9}
γ_y	0	0	0

based upon theoretical noiseless test data. The estimates based on actual experimental data compare surprisingly well with the exact values, even in spite of the effects of systematic error.

In Table V are given the a posteriori standard deviations of the scatterer parameters (i.e., the square roots of the diagonal elements of Cov(x|y) defined by (14)), appropriately

Table 5. Normalized standard deviations (a posteriori) (A summary of estimates based on pitch-catch measurements. R.M.S. Measurement error* = 10^{-5}

Quantity	Experimental Data	Theortical Test Data
$(s.d.a)/\hat{a}$	0.071	0.21
$(s.d.c)/\hat{c}$	0.62	1.28
s.d. γ_x	0.28	0.54
s.d. γ_y	-	-

*Relative r.m.s. error = 10%

normalized. In the case of the semi-axis lengths a and c we divide their respective standard deviations by their best estimates. In the case of the dimensionless direction cosines γ_x and γ_y such normalization seems to be unnecessary. In these computations, the r.m.s. experimental error is assumed to have the value $\sigma_v = 10^{-5}$ (corresponding to an approximate relative r.m.s. relative error of 10%). Since the experimental data, synthetic or actual, is confined to a single scattering plane (assumed to be the xz-plane in our coordinate system), the standard deviations of γ_y (the cosine of the angle between y-axis and the symmetry axis of the spheroid) is omitted because the approximation involved in its computations is not valid.

It may appear inconsistent to present a posteriori standard deviations based on noiseless theoretical test data. It must be pointed out that the standard deviations of x are actually based upon the model (1) with the associated assumptions (5) and (6) giving the statistical nature of the experimental errors. The variance of the experimental errors is determined from an independent comparison of experiment with theory and not from the input data used in the estimation procedure.

We turn next to a consideration of estimates based upon pulse-echo data. Here we use the actual experimental data and noiseless theoretical test data summarized in Table III of the last section. In Table VI we present estimates of the scatterer parameters a, c, γ_x and γ_y for both kinds of input data. The agreement between the estimates based on actual experimental data and the exact parameter values is unbelievably good and must be regarded as partially accidental. But it is perhaps also due to the fact that it appears, as we will discuss later, that the pulse-echo data has considerably

Table 6. Estimates based on pulse-echo measurements.

Parameters	Exact	Estimates	
		Experimental Data	Theoretical
a	0.0400	0.03947	0.04000
c	0.0200	0.01999	0.02000
γ_x	0	-1.24×10^{-5}	2.3×10^{-6}
γ_y	0	0	0

better "leverage" on the scatterer parameters than does the pitch-catch data.

In Table VII we give the normalized standard deviations (a posteriori) of the scatterer parameters in the present case of pulse-echo

Table 7. Normalized standard deviations (a posteriori) based on pulse-echo measurements

Quantity	*R.M.S. Meas. Error=0.46x10^{-5}		**R.M.S. Meas. Error = 1x10^{-5}	
	Experimental Data	Theoretical Test Data	Experimental Data	Theoretical Test Data
(s.d.a)/a	0.0168	0.0156	0.0364	0.0340
(s.d.c)/c	0.0608	0.0608	0.1320	0.1320
s.d. γ_x	0.1120	0.1057	0.2434	0.2295
s.d. γ_y	-	-	-	-

* Relative r.m.s. error = 4.6%

** Relative r.m.s. error = 10%

measurements. In the second and third columns are listed the values of these quantities based on actual experimental and on noiseless theoretical test data, respectively. In these computations, we assume that the r.m.s. experimental error has the value $\sigma_\nu = 0.46 \times 10^{-5}$, a result based upon the deviations between experimental and theoretical results discussed in the last section. It is to be noted the relative standard deviation of the long semi-axis length a is only about 1.6%. The corresponding quantity for the short semi-axis length c is, as usual, many times larger. The standard deviation of γ_x is about 10% which is still satisfactory for our purposes. The values of the standard deviation of γ_y have been omitted for the same reasons as before.

It is of fundamental interest to reconsider the normalized standard deviations, both in the present pulse-echo case and in the previous pitch-catch case, as measures of experimental "leverage" on the scatterer parameters. For the purpose of comparison, we have recomputed the normalized standard deviations in the pulse-echo with the same value of σ_ν as was used in the pitch-catch case, namely $\sigma_\nu = 1 \times 10^{-5}$. The results are tabulated in the fourth and fifth columns. Comparing the results for noiseless theoretical test data in both cases, the reader will note that the relative standard deviation of a is about 1/6 as large in the pulse-echo case as in the pitch-catch case, the relative standard deviation of c is about 1/9 as large and, finally, the standard deviation of γ_x is about 1/2 as large. Thus, the experimental leverage is markedly better in the pulse-echo case than in the pitch-case, particularly for the parameter c. The number of data points is nearly the same in both cases.

It is of critical importance to consider the significance of the present results in the context of failure prediction or, almost equivalently, the making of an accept-vs-reject decision. Clearly, as discussed in Section I, there exists a more complex theoretical structure connecting our present results with the concerns of the final user of an NDE system. In any case, a significant first step in this direction is the estimation of certain quantities of significance in fracture mechanics. One such quantity is the stress intensity factor k_I measuring the tendency of a crack in, for example, a metal to propagate under the application of a mode I stress (i.e., a uniaxial stress oriented perpendicular to the plane of the crack).

To be sure, the spheroidal void, considered in the previous discussion, is hardly sufficiently degenerate to be regarded as a crack. However, based upon the discussion of Tetelman and McEvily,[12] it appears that the concept can be meaningfully extended to the case of not-so-degenerate spheroidal voids. In any case the definition

$$k_I = K_I/\sigma = (\pi a)^{1/2}, \qquad (16)$$

where σ is the applied stress, will suffice for our present purposes.

In Table VIII we give both the best estimate $\hat{k}_I$ and the relative standard deviation $s.d.k_I/\hat{k}_I$ for both pitch-catch and pulse-echo input data. In our view, the significance of these estimates (as

Table 8. Estimate of k_I and relative st. dev. ($K_I/\sigma \equiv k_I (\pi a)^{1/2}$)

Using Pitch-Catch Data:

Quantity	Experimental Data (a)	Experimental Data (b)	Experimental Data (c)	Theoretical Test Data	
				1 scatt. plane	2 scatt. plane
$\hat{k}_I$	0.341	0.359	0.368	0.354	0.354
$(s.d.k_I)/\hat{k}_I$	0.246	0.078	.036	0.105	0.060

Using Pulse-Echo Data:

Quanity	Experimental Data	Experimental Test Data
$\hat{k}_I$	0.352	0.354
$(s.d.k_I)/\hat{k}_I$	0.008	0.008

measured by the relative standard deviation) is more than adequate for NDE purposes, particularly in the pulse-echo case.

V. DISCUSSION

Our accomplishments can be briefly summarized as follows:

(1) Successful determination of A_2 ($A = A_2\omega^2 + \ldots$) from scattering measurements.

(2) Comparison of experiment with exact theory with highly satisfactory results.

(3) Solution of inverse scattering problem (under spheroidal void assumption).

(4) Development of software for all modules involved in deducing fracture mechanics parameters from low frequency scattering measurements.

Even though these results have been obtained under simplifying constraints, they strongly suggest that this approach has promise for NDE.

The principal advantages of the present approach are listed below:

(1) Exact scattering theory is available for ellipsoidal voids.

(2) Low frequency scattering measurements are sensitive mainly to features that are important in fracture.

(3) Low frequency scattering measurements are relatively insensitive to attenuation and spurious scattering in host medium.

(4) In the inversion program the parameter a (the long dimension of the spheroidal void) is estimated with good "leverage" and the fracture mechanics parameter k_I is estimated with even better "leverage."

(5) Good potential for the implementation of high speed automation.

Clearly, there remain a host of problems for future consideration. A few of these are:

(1) Further improvement of the post-experiment data processing in the pitch-catch case.

(2) Isolation of a particular scatterer from competing scatterers in taking the low frequency limit.

(3) Extension of the analysis to include general ellipsoidal inclusions (voids are a special case).

(4) Extension to the more general case of scatterers not having ellipsoidal geometry.

(5) Transfer of algorithms to minicomputers suitable for field equipment.

(6) Formulation of the theoretical structure extending from the outputs of the inverse scattering algorithms to the final accept-vs-reject decision.

REFERENCES

1. B. Budiansky and J. R. Rice, "On the Estimation of a Crack Fracture Parameter by Long-Wavelength Scattering," Informal Report, Aug. (1977).

2. G. S. Kino, "Measurement of a Crack Stress Intensity Factor," informal report, Sept. (1977).

3. R. K. Elsley, "Low Frequency Scattering Measurements," paper in the present proceedings.

4. A. G. Evans, "Accept/Reject Criteria for Structural Ceramics," paper in the present proceedings.

5. J. M. Richardson, "Scattering of Elastic Waves at Low Frequencies," to be published.

6. J. M. Richardson, "The Longitudinal-to-Longitudinal Backscattering of Elastic Waves from a Spherical Void and from Various Inclusions in Silicon Nitride," Informal Report Feb. 15, 1978.

7. J. E. Gubernatis, J. A. Krumhansl and R. G. Thomson, "Interpretation of Elastic Wave Scattering Theory for Analysis and Design of Flow Characterization Experiments: I. Long Wavelength Limit." Los Alamos Scientific Laboratory Report, LA-UR-76-2546, 1976.

8. W. Kohn and J. R. Rice, "Scattering of Long Wavelength Elastic Waves From Localized Defects in Solids," to be published.

9. J. M. Richardson, "Scattering of Elastic Waves in the Rayleigh Limit. I. The Direct Problem," to be published.

10. B. R. Tittmann and W. L. Morris, Private communication.

11. R. K. Elsley and H. Nadler, private communication.

12. A. S. Tetelman and A. J. McElvily, Jr., Fracture of Structural Materials," John Wiley, New York (1967) pp. 48-50.

INVERSION OF PHYSICALLY RECORDED ULTRASONIC WAVEFORMS USING ADAPTIVE LEARNING NETWORK MODELS TRAINED ON THEORETICAL DATA

M. F. Whalen and A. N. Mucciardi
Adaptronics, Inc.
McLean, Virginia 22102

ABSTRACT

The objective of this work has been to demonstrate the feasibility of estimating automatically the size and orientation of subsurface defects in metals. The approach has been to (1) obtain computer-generated spectra from various elastic scattering theories, (2) use these spectra to train empirical nonlinear Adaptive Learning Network (ALN) models, and (3) evaluate the theoretically trained ALN's on eight physically recorded defect specimens via a blind test. The results demonstrate that very good defect characterization is possible and that a fully automatic and general purpose NDE system can be implemented. An average orientation error of 10.2 degrees has been achieved and the defect average volume error is 17.5 percent.

The ALN models were synthesized using theoretically generated spectral scattering data from the Born Approximation (BORN), the Extended Quasi-Static Approximation (EQSA), and the Scattering Matrix Method (SMM) digital computer programs. The type of defects simulated were oblate spheroidal voids in a Titanium alloy.

The ultimate significance of this work is to further support the mounting evidence that theoretical computer models can be used as ultrasonic calibration data in place of building physical specimens. The capability of (1) simulating many difficult-to-produce defect/geometrical reflector scenarios in various metal matrices and, (2) using the ALN methodology to develop automatic detection, characterization and sizing methods using the simulated ultrasonic echoes will yield tremendous economic benefits.

SUMMARY OF RESULTS, CONCLUSIONS, & RECOMMENDATIONS

Results:

1. The lowest average percentage errors made in estimates of the defect size parameters "A" and "B" were 20.0 and 5.9 percent, respectively. For the orientation parameters "α" and "β", the errors were 6.7 and 5.1 percent, respectively. The error in estimating the defect volume computed from the individual estimates of "A" and "B", was 17.5 percent. Furthermore, the three-dimensional average orientation error over the eight experiments was only 10.2 degrees. These results demonstrate the feasibility of producing an automatic flaw characterization algorithm via ALN means.

2. It was found that the long wavelength A_2 coefficient provides significant information relative to the size and orientation of spheroidal defects. For pitch-multiple-catch (PMC) data, A_2 was successfully used in conjunction with other spectral features to estimate the shorter defect radius (A) and the defect's polar angle (α). Also, a favorable comparison existed between experimental and theoretically generated PMC data. This favorable comparison could not be observed for pulse-echo (PE) data since the PE experimental data had been optimized to give maximum spectral bandwidth rather than reliable information in the low frequency (long-wavelength) regime. However, for the theoretical data, a correlation of 0.97 was found to exist between the defect's larger radius (B) and the average value of A_2 computed from the inner ring (θ=30°) PE transducers; also, a correlation of 0.96 existed between the defect's polar angle (α) and the ratio of inner to outer ring average value of A_2. These results clearly demonstrate the value of A_2 as a parameter for size and orientation estimates.

3. A completely automatic and general ALN processing algorithm has been developed for defect flaw characterization which also includes a fully automatic means of computing the long wavelength A_2 coefficient. The algorithm employs deconvolution of the transducer characteristic so that the solution of problems can be achieved using any commercially available 5 MHz search unit.

4. Use of the transducer arrangement in the pulse-echo (PE) mode yielded better results than the pitch-multiple-catch (PMC) mode, at least when using ALN models trained on the BORN approximation data. This statement is supported by the fact that the average orientation error improved by 7.3 degrees when changing from a PMC to a PE transducer arrangement. Also, the total number of waveforms needed for PE array processing was a factor of 3 less than that of PMC.

5. A qualitative comparison of the PE scattering data generated by each of three theories (BORN, EQSA, and SMM) and experimental data was performed. The BORN and EQSA spectral

shapes were found to be identical for oblate spheroidal void scatterers. The only observed difference between BORN and EQSA data was that EQSA's spatial distribution of the total power feature (in the range of $0.4<ka<3.5$) was more closely matched to the experimental data. The spectral bandwidth (i.e., the second spectral moment) for these two theories was also in good agreement with that observed from experiment. Spectral data produced by the SMM theory possessed greater detail than that of the BORN and EQSA theories. In this respect, SMM spectra provided a closer match to experimental spectra. The SMM data was the closest of three theories to faithfully mimic the center frequency (first spectral moment) spatial distribution.

6. From a quantitative viewpoint, the three theories yielded almost identical orientation estimates, with an average error of approximately 12 degrees (over a possible 180 degrees). However, the average error in computing the defect's size varied among the three theories. For BORN, EQSA, and SMM, the average size errors were 32, 26, and 54 microns, respectively.

Conclusions

1. Use of theoretically generated data combined with ALN technology to accurately and automatically characterize spheroidal-shaped flaws via ultrasonic inspection has been favorably established.

2. The EQSA theory, compared to the BORN theory, provides a closer approximation to experimental scattering data. This is supported by the facts that (1) the EQSA-trained size models were more accurate than BORN when evaluated on experimental data; and, (2) the EQSA total power spatial distributions were in excellent agreement with the experimentally observed distributions. The EQSA program (written by J. Gubernatis) is also very efficient in generating large data bases. It is therefore recommended that other groups interested in inversion techniques consider the EQSA theory in place of the BORN theory. The SMM theory provides the closest match to experiments than the other theories investigated. However, it is believed more analysis is needed to make best use of the "more detailed" spectral information.

3. The orientation estimates for BORN PE models are superior to the BORN PMC models probably because the BORN approximation is most accurate in the backscatter position. A qualitative observation to support this fact was that the radiation pattern (or polar plot) of the scattered energy was "sharper" (i.e., more peaked) for the PE mode than in the PMC mode and matched experimental results more closely.

Recommendations

1. Improvements in estimating defect size and orientation can be achieved by (1) increasing the number of experiments in the training set from, say, 240 to about 1000; (2) increasing the number of elements in the transmit/receive array; and (3) possibly, changing the transducer array to a more equispaced configuration.

2. The present study was concerned with evaluating three scattering theories on a common basis. In doing so, the SMM theory was considerably under-utilized because the phase information, not found in the BORN or EQSA program, was discarded from analysis for the sake of maintaining a common basis for comparison. The additional information provided by the phase spectrum should be very useful in characterizing flaws. Therefore, it is recommended that the SMM phase information be incorporated in all future work.

3. J. Rose's transformation from frequency to R-space should be incorporated into the ALN procedure to test its utility for yielding further improvements in defect characterization.

4. In the development of further flaw characterization systems, a "combined theory" data base might be considered, where the best features of each theory would be used for ALN model synthesis. In this manner, a larger and more representative feature set could possibly be postulated.

5. The present study is concerned with L→L mode scattering only; however, L→S mode scattering should also be considered in future work since the ripple period in the scattered shear wave spectrum is more observable than in the scattered longitudinal spectrum.

6. In order to realize a quantitative NDE flaw characterization system, the ability to discriminate between crack-like defects and ellipsoidal-shaped defects is necessary. A completely automatic ALN-based NDE system will need to characterize both two- and three-dimensional flaws. The present work has addressed three-dimensional defects. A similar effort should now be performed to characterize the size and orientation of two-dimensional flaws. Also, an ability to discriminate between two- and three-dimensional flaws will be needed as illustrated in Fig. 1. It is recommended that the coming year's work focus on implementing the system shown in Fig. 1.

INTRODUCTION

The determination of the characteristics of subsurface defects in materials by non-invasive techniques is an important and challenging task in the non-destructive evaluation (NDE) of materials.

The description of the scattering wave equations for defects of known geometries and material properties -- the "forward" problem -- has been a topic of several investigations. Krumhansl, Domany and Gubernatis were responsible for applying the BORN approximation to estimate the scattered power spectrum from spheroidal-shaped defects. [1]. Gubernatis later used a more powerful technique, known as the extended quasi-static approximation, to estimate scattered fields from spheroids

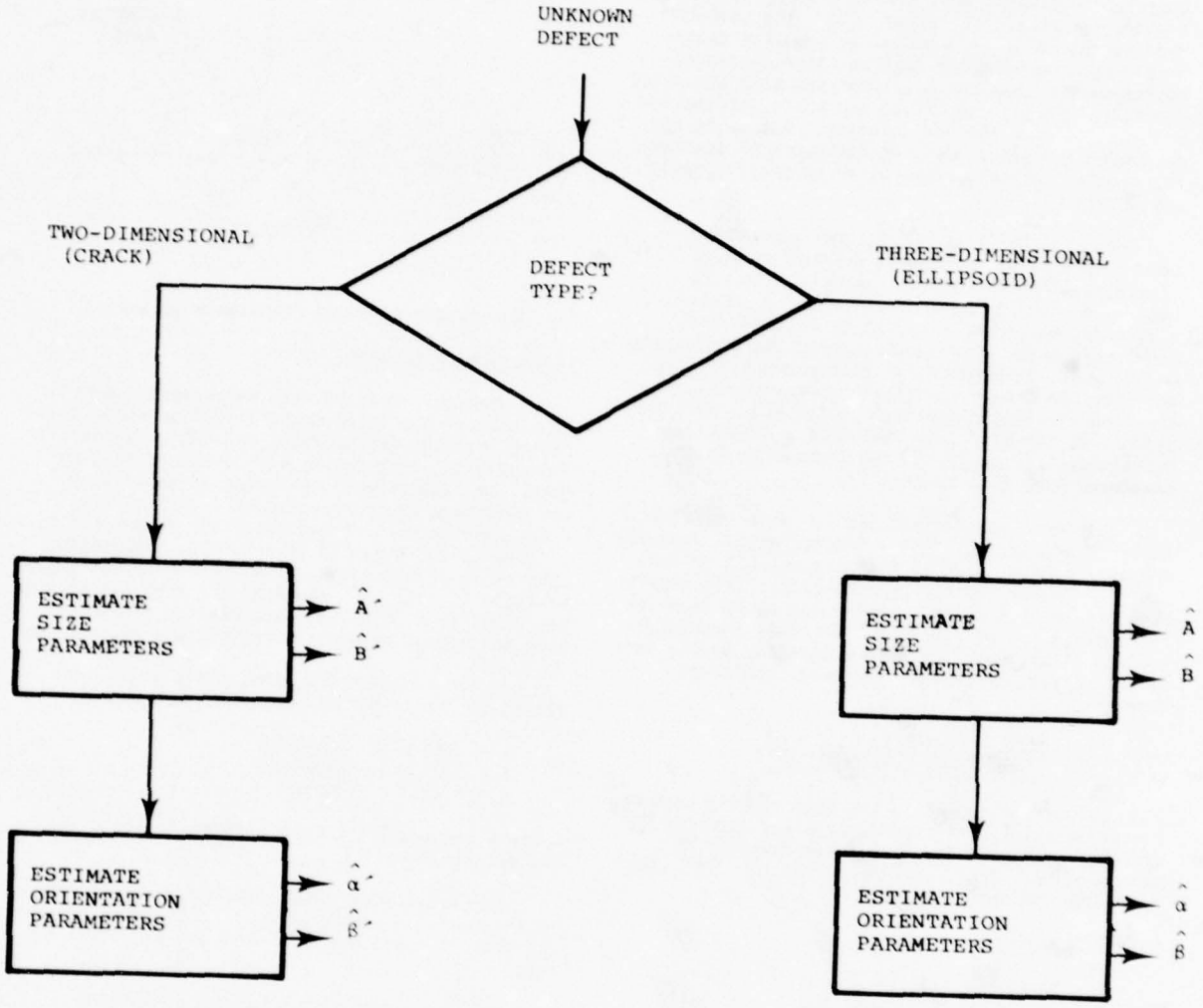

Fig. 1. Decision logic for characterizing both two and three-dimensional defects.

[2]. Rapid convergence is an advantage of both of these methods. Varadan and Poa introduced a matrix approach to elastic wave scattering applicable to arbitrarily shaped scatterers [3]. The computer implementation of this technique requires considerably more computation than the aforementioned approximation, but the solutions are more accurate. Additionally, both amplitude and phase information are yielded from the SMM solution. Achenbach has developed and programmed the equations of scattering from elliptical cracks based on elastodynamic ray theory [4].

From the NDE standpoint, the interest has been in the solution of the "inverse" problem; namely, how can the defect characteristics be described knowing the theoretical, or observed, scattering waveform. Studies by Tittmann and Cohen have shown some success using the BORN approximation [5]. Richardson has been successful with an inversion procedure utilizing measurements in the long wavelength Rayleigh regime [6]. Rose has shown that the effective radius of a defect can be estimated by applying sine transforms to the scattered amplitude spectra [7].

Mucciardi, Whalen and Shankar were the first to apply a systematic and automatic signal processing approach -- Adaptive Learning Network methodology -- to the inverse problem [12]. This report presents results of this continuing study in which characteristics of spheroidal defects, imbedded in a Ti-64 alloy, were measured accurately by analysis of the ultrasonic energy scattered from these defects.

DEFECT GEOMETRY, DATA BASE, AND ARRAY CONFIGURATION

The defect geometry, theoretical data base characteristics, the transducer array geometry, and the experimental data set are described in this section. The present work has been confined to oblate spheroidal voids.

Defect Geometry

A spheroid is a three-dimensional surface formed by rotating an ellipse about one of its axes. When the rotation is about the minor axis, the result is an oblate spheroid. The spheroid's size and orientation can be specified uniquely by four parameters (labelled A, B, α, and β) as illustrated in Fig. 2. The following definitions apply:

- A - minor radius (along one dimension)
- B - major radius (along two dimensions)
- α - polar orientation: angle between positive Z-axis and the symmetry axis
- β - azimuthal orientation: angle between positive X-axis and projection of the symmetry axis on the X-Y plane

Throughout the remainder of the report, the defect's geometry will be represented by these four parameters. Also, the ALN models are synthesized to directly estimate these four parameters. The spheroid's volume is defined as $(4\pi/3)AB^2$.

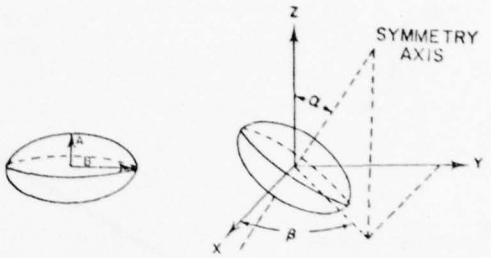

Fig. 2. Oblate spheroid coordinate geometry.

Theoretical Data Base

Identical training data bases were generated from each of the three computerized spheroid scattering theories (BORN, EQSA, and SMM). A total of 240 synthetic experiments were produced in each case. An "experiment" consisted of generating the scattered power spectrum of a differential cross-section at 17 fixed positions in space for a given defect size and orientation. Six sizes, each at 40 orientations, were represented as shown in Table 1. The ka[1/] range of the theoretical data was 0.297 to 4.361. So, information in both the long and medium wavelength regimes was represented.

In the computer programs, the elastic constants of the Ti-64 host material were set to:

λ = .965 x 10 dynes/cm
μ = .406 x 10 dynes/cm
ρ = 4.42 gm/cm^3

where λ and μ are the Lamé parameters and ρ is the material density.

The longitudinal and shear wave velocities in the medium are determined from these values. The elastic constants of a void are all equal to zero.

Only L+L mode scattering was considered. (The shear wave spectrum should be considered in future work since the period of the spectrum is about one-half that of the longitudinal spectrum. This is an important consideration in physical band-limited systems since the ripple period contains information relative to the physical characteristics of the defect.

Transducer Array Geometry

Both pitch-multiple-catch (PMC) and pulse-echo (PE) transmitter/receiver arrays were used to measure the scattered spectrum. Theoretical PMC data were generated only for the BORN program due to cost considerations. PE data were generated from each of the three scattering theories. The 17 transducer positions were fixed to cover a 120-degree solid angle aperture on the surface of

1/ "ka" is the product of the wave number ($\frac{2\pi}{\lambda}$, λ = wavelength) and the defect radius. If ka < 1, the wavelength is larger than the defect radius.

Table 1. Spheroidal defect sizes and orientations represented by the theoretically-generated power spectra. Scattering data at 40 orientations were produced for each defect size.

SIZE NUMBER	DEFECT SIZE		ka RANGE	
	A (MICRONS)	B (MICRONS)	MIN.	MAX.
1	50	300	0.297	2.616
2	150	300	0.297	2.616
3	100	400	0.396	3.488
4	200	400	0.396	3.488
5	100	500	0.496	4.361
6	300	500	0.496	4.361

6 SIZES

ORIENTATION NUMBER	DEFECT ORIENTATION	
	a (DEGREES)	β (DEGREES)
1	1	65
2	10	
3	20	
4	30	
5	40	
6	50	
7	60	
8	70	
9	80	
10	89	65
11	1	150
↓	↓	↓
20	89	150
21	1	235
↓	↓	↓
30	89	235
31	1	320
↓	↓	↓
40	89	320

40 ORIENTATIONS

a spherical "part". Hence, 33 percent of the total surface area was covered.

The transducer arrangements for the PMC mode are shown in Fig. 3.

The transducer configuration consisted of two circular arrays of eight elements each, and a top center (a north pole) transducer. The "inner ring" array covered a 60-degree solid angle surface, and the "outer ring" a 120-degree solid angle surface. The "north pole" transducer plus four transducers in the outer ring were used to transmit a longitudinal wave. Both inner and outer rings were used as receivers for the north pole transmitter, but only the inner ring receivers were used when transmission was initiated at any of the four outer ring transmitters. Hence, no PE information was used in the PMC mode. A total of 48 waveforms per experiment was generated in this manner.

The theoretical spectral bandwidth was chosen, for each waveform, to lie between 1.0 and 8.8 MHz in incremental steps of .39 MHz. Hence, each waveform contained 21 points. Only the received longitudinal waves considered in this study (to conform to the available experimental data which were only recorded in the L→L mode).

In the pulse-echo mode, each of the 17 transducers were used in the backscatterer mode only. Therefore, only 17 waveforms were processed in each experiment, compared to the 48 in the PMC mode. The PE array configuration is shown in Fig. 4.

Experimental Data Base

The eight physical defect specimens were fabricated by the Rockwell Science Center; the construction process and the data collection can be found in Reference [5]. The size and orientation parameters of the defects are listed in Table 2.

Table 2. Size and orientation parameters of the eight physically recorded spheroidal defect specimens

EXPERIMENT NUMBER	DEFECT SIZE		DEFECT ORIENTATION	
	A (MICRONS)	B (MICRONS)	α (DEGREES)	β (DEGREES)
1	200	400	0	0
2	200	400	30	225
3	100	400	80	160
4	100	400	0	0
5	200	400	80	160
6	100	400	30	180
7	200	400	30	180
8	100	400	30	225

WAVEFORM PROCESSING: DECONVOLUTION & FEATURE EXTRACTION

Overview

The general processing strategy of the spheroidal flaw characterization algorithm is diagrammed in Fig. 5. A set of "primary" and "secondary" features were computed from the extensive set of "experiments" generated from each of the scattering theory programs. The primary features were selected to measure global characteristics of the scattered spectra; the secondary features were spatial combinations of the primary features. The secondary features were used as inputs to train four ALN models to estimate the defect's size and orientation parameters, respectively. These models were evaluated subsequently via a blind test on physically recorded defect specimens processed in a manner compatible with the theoretical data, as shown in Fig. 5.

Primary Spectral Features

The primary feature computation was identical for both PMC and PE experiments. Fig. 6 shows the basic steps for computing primary features from the ultrasonic experimental data. Each scattered experimental UT waveform was digitized at 100 MHz and a block of 250 samples was the time window of interest. The time domain waveforms (x(t))

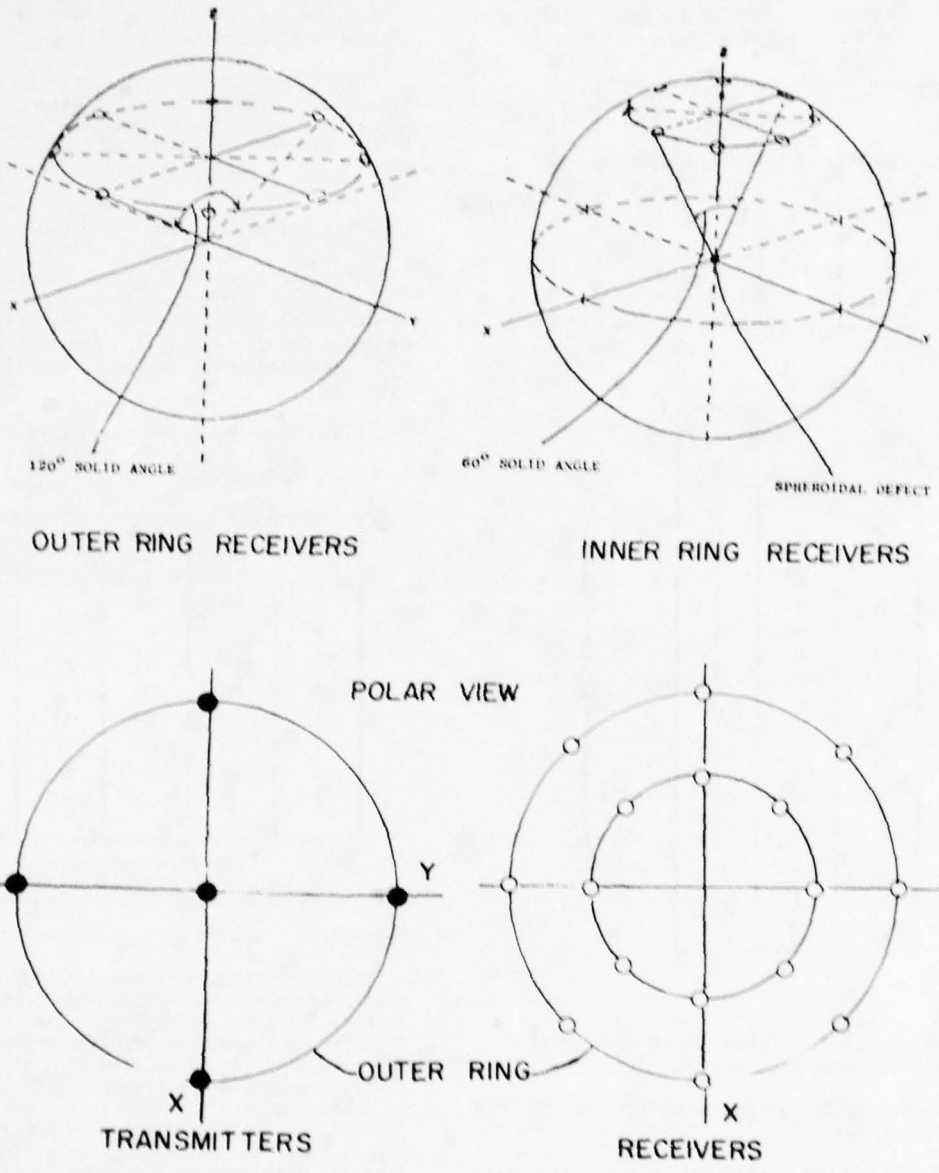

Fig. 3. Pitch-catch transmitter and receiver positional configuration

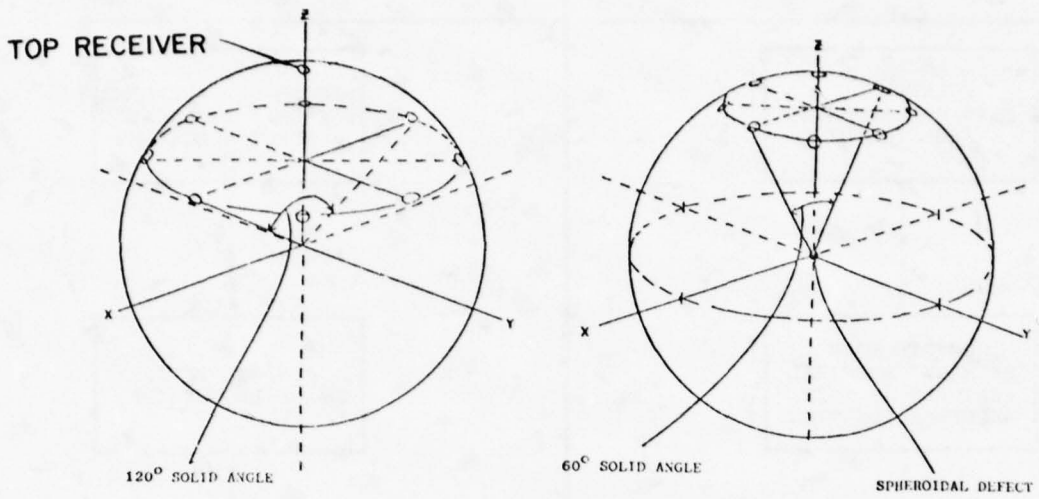

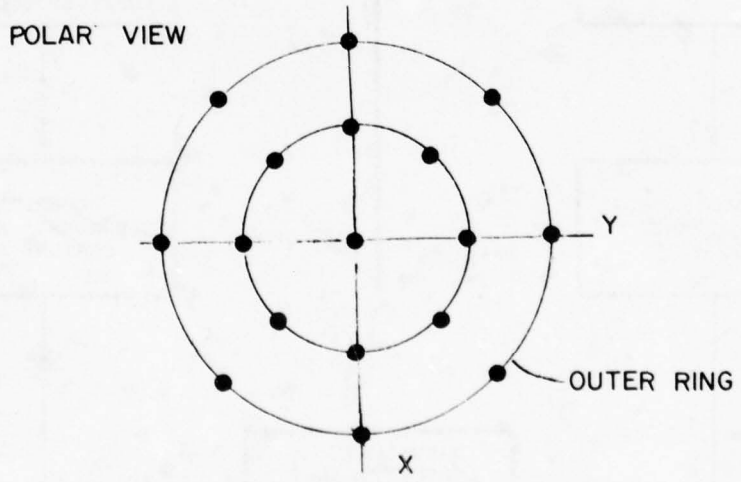

Fig. 4. Pulse-echo transmitter and receiver positional configuration

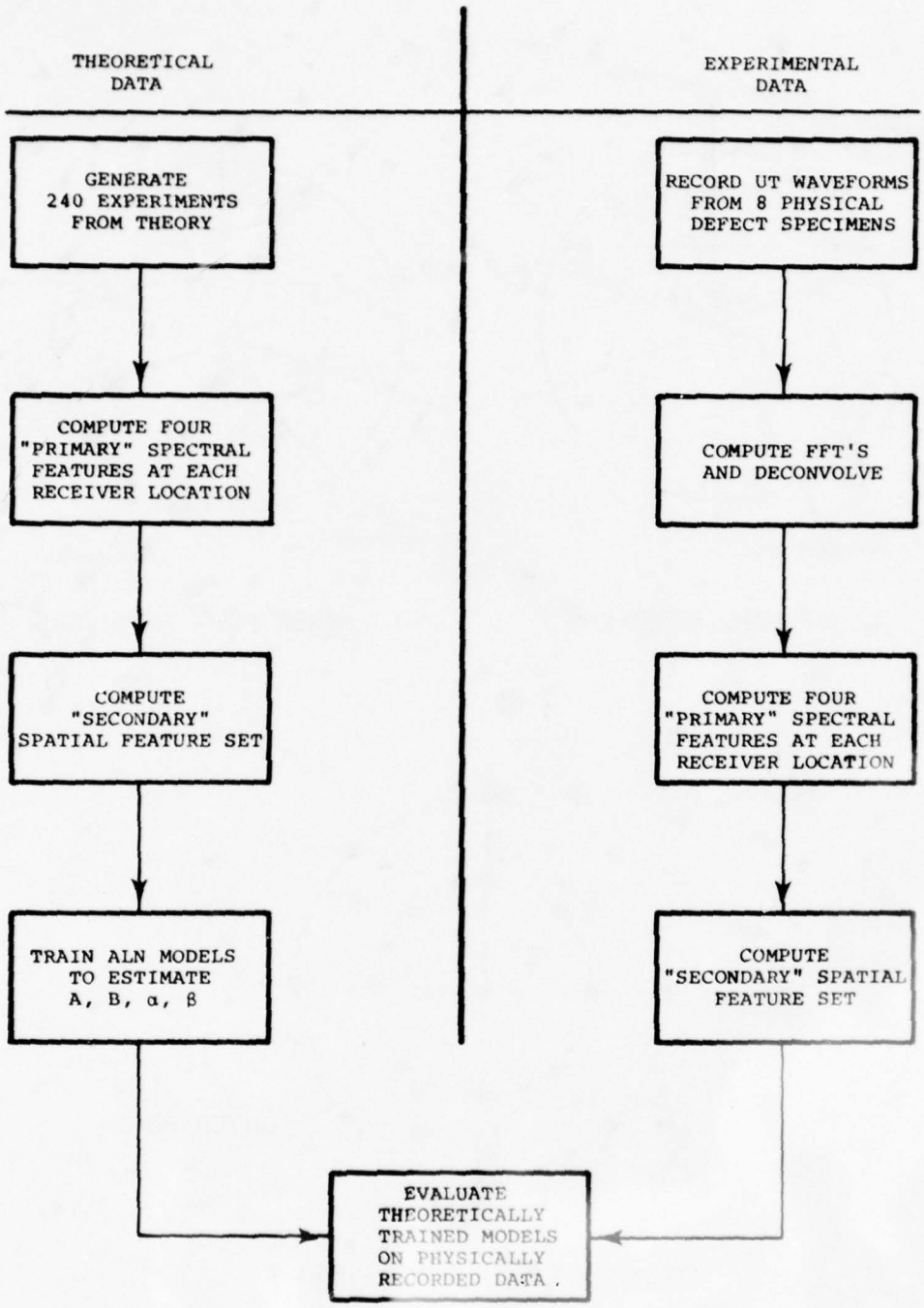

Fig. 5. Processing strategy for spheroidal flaw characterization algorithm

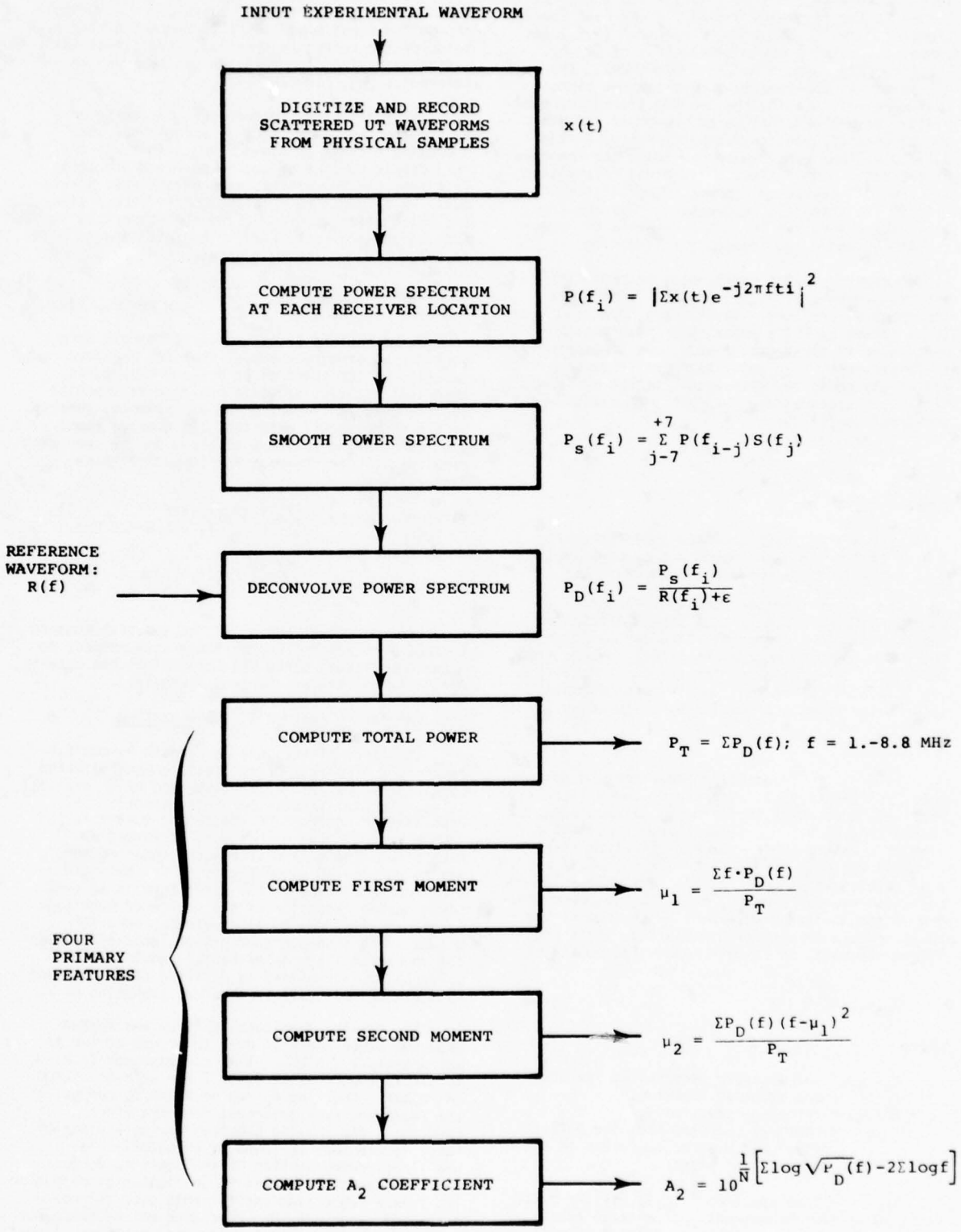

Fig. 6. Flow chart showing primary feature computation for both PMC and PE experimental data

were padded with zeros to 1024 samples and transformed to the frequency domain via the Fast Fourier Transform. A 512-point power spectrum ($P(f)$) was computed, having a maximum frequency of 50 MHz. The frequency resolution was 0.09766 MHz. The last 412 points in the spectra were discarded since they were well outside the 1-8 MHz transducer bandwidth. Visual examination of the power spectra showed considerable low frequency energy in the 0.1- to 0.9-MHz band, which was below the response of the transducer. (This artifactual information was probably caused by the recording instrumentation.) The spectral components in this low frequency band were set to zero as a means of removing the unwanted low frequency information.

Another somewhat undesirable characteristic was the presence of jagged ripples "riding" on the spectral envelope. These could have been side lobes caused by FFT processing or information pertaining to the defect itself. To de-emphasize their presence, a 15-point symmetric smoothing filter was convolved with each spectrum to low-pass-filter the spectral ripples. This operation was performed as follows:

$$P(f_i) = \sum_{j=-7}^{+7} P(f_{i+j})\, S(f_j) \; ; \; i = 1,93 \qquad (1)$$

where

$P_S(f_i)$ = the i-th smoothed spectral point,
$P(f_i)$ = the i-th unsmoothed spectral point,
$S(f_i)$ = the symmetric smoothing filter.

The filter function $S(f)$ was Spencer's smoothing formula. A list of the coefficients and the transform characteristics can be found in Reference [8]. An equivalent effect to smoothing could also be obtained by implementing a multiplication window on the time domain echo responses such as the Hamming or Kaizer-Bessel windows.

Deconvolution

In order to desensitize the algorithm to the specific effects of the transducer and pulser/receiver, a deconvolution process was employed. In addition to being desirable from the point of view of creating a more general algorithm, deconvolution was necessary to accurately compute the long wavelength A_2 coefficient. The deconvolution operation was performed by dividing the power spectra of the scattered waveforms by the sum of the power spectra of a reference waveform and a stabilizing constant, as represented by the equation:

$$P_D(f_i) = \frac{P_S(f_i)}{R(f_i) + \epsilon} \qquad (2)$$

where

$P_D(f_i)$ = the discrete deconvolved spectrum,
$P_S(f_i)$ = the smoothed spectrum,
$R(f_i)$ = reference spectrum,
ϵ = constant computed from the noise level and desired bandwidth of the deconvolved signal.

The reference spectrum, $R(f_i)$, was the power spectrum of the through-wall pitch-catch echo response in a Ti sample when no defect was present. The quantity, ϵ, in (2) is added to each value of $R(f_i)$ to inhibit deconvolution instability at the tail ends of the transducer bandwidth. A suitable choice for ϵ was found to be 10 percent of the peak value of the reference spectrum. Additional information regarding deconvolution can be found in References [9], [10] and [11].

The total power feature, P_T, was computed by summing the power spectral values over the approximate range of 1.0-8.8 MHz. This was the full usable portion of the deconvolved spectrum. This spectral feature has been established previously as informative relative to the defect size and orientation when comparing BORN-generated data to physical data [12]. The total power feature was computed as follows:

$$\text{total power: } T_p = \sum_{f_i = 1.0\text{-}8.8\ \text{MHz}} P_D(f_i); \qquad (3)$$

The first and second spectral moments were included as primary spectral features in order to: (1) monitor spectral shifts and changes in bandwidth relative to different receiver spatial locations and different sized and oriented defects in the experimental data and, (2) compare these spectral changes to those observed in the theoretical data. The formulas for computing these features are:

$$\text{first moment: } \mu_1 = \left(\frac{1}{T_p}\right) \sum_{f_i = 1.0\text{-}8.8\ \text{MHz}} P_D(f_i) f_i; \qquad (4)$$

$$\text{second moment: } \mu_2 = \left(\frac{1}{T_p}\right) \sum_{f_i = 1.0\text{-}8.8\ \text{MHz}} P_D(f_i)(f_i - \mu_1)^2; \qquad (5)$$

One convenient aspect of the spectral moments is that they are self-normalizing with respect to signal amplitude, hence the theoretical and experimental values can be compared directly.

Long Wavelength Feature (A_2) Computation

Inclusion of the long wavelength A_2 coefficient as a primary spectral feature was motivated by Richardson's favorable comparison of theoretical to experimental results for this parameter [6]. Considerable analysis of scattering theory in the long wavelength regime has been performed by Rice [13]. The goal of the work presented here was to develop an automatic means for determining A_2, the coefficient of the first term in an even power series expansion of the scattered magnitude spectrum. In order to eliminate the need for establishing a constant of proportionality between the theoretical and experimental results, each spectrum was normalized by dividing each component by the total power feature before computing A_2.

The log-log magnitude spectrum was formed from the power spectrum over the range of 1.0 to approximately 2.5 MHz. This corresponded to ka values in the range of 0.4-1.2 for defects of 400 μM radius. Now, log A_2 can be found by computing the log-power axis intercept from the linear portion of the log-log spectrum having a slope of two. A_2 can then be found by exponentiation. The slope-of-two portion of the power curve was not known and, hence, had to be located by computing 120 linear regression coefficients over the above-mentioned range and then determine which contiguous group of points in the log-log spectrum came closest to having a slope of two. The intercept was then

formed by the extrapolation formula:

$$\text{intercept: } \text{Log } A_2 = \frac{1}{N}\sum_{j=1}^{N} Y_i - \frac{2}{N}\sum_{j=1}^{N} X_i \qquad (6)$$

where, X and Y are the logarithmic spectral values f_1 and $P_D(f_i)$ over the best fitting slope-of-two range. A flow chart showing computation of A_2 is shown in Fig. 7.

The primary features were computed from the theoretical data bases in the same manner as mentioned above, with the exception of the steps involving power spectral computation, spectral smoothing, and deconvolution.

Computation of the primary features represented a considerable reduction in the amount of data associated with each experiment. Instead of storing a scattered waveform at each receiver location, only four representative values need be saved.

Secondary Spectral Features

The "secondary" features were statistical quantities computed mainly from the circular receiver arrays. Their purpose was to quantify the spatial distribution of the primary features. The number and type of features varied slightly between the PMC and PE experiments due to the greater number of receivers for PMN. Also, the total power of the BORN PMC data was normalized around each receiver ring instead of a single constant for all total power in the experiment. It had been noted that in last year's effort [12], the power distribution in the polar direction was significantly greater from the BORN program than that observed in the experimental data.

Secondary Spectral Features: Pitch-Multiple-Catch Mode

Four general types of PMC secondary features were computed:

1. Statistical: sample means and standard deviations;
2. Circular: circular mean and circular variance;
3. Ratios of primary features;
4. Eigenvalues of correlation matrix.

The statistical features were averages and standard deviations of the primary features around the inner and outer receiver arrays. The mean values for the total power primary features were not included since they were normalized as mentioned above.

The circular mean was an angular feature which located the first moment of the scattered power around a circular receiver array. This feature was thought to be useful in determining β, the azimuthal defect orientation angle. Calculation of the CM was as follows:

$$CM = \tan^{-1}(S/C) + Y$$

where:

$$S = \sum_{\phi=0}^{315^\circ} P(\phi,\theta)\sin\phi$$

$$C = \sum_{\phi=0}^{315^\circ} P(\phi,\theta)\cos\phi$$

and

$Y = 0$ if $S > 0$, $C > 0$

$= \pi$ if $C < 0$

$= 2\pi$ if $S < 0$, $C > 0$

$P(\phi,\theta)$ = one of the primary features at receiver position (ϕ,θ)

S and C were also used as secondary features. In the above computation, θ remained fixed at either 30 degrees (inner ring) or 60 degrees (outer ring); therefore, eight terms were summed in computing either S or C.

The circular variance feature is defined between zero and unity and was a measure of the power dispersion about the circular mean of a given circular array:

$$CVAR = 1 - \sum_{\phi=0}^{315^\circ} P(\phi,\theta)\cos(\phi - CM)$$

For each of the four outer ring (θ=60 degrees) transmitters, a ratio feature RI was computer, defined as follows:

$$RI(\phi) = \frac{[P(\phi-45),\ 30) + P(\phi-90,\ 30) + P(\phi-135,\ 30)]}{[P(\phi+45),\ 30) + P(\phi+90,\ 30) + P(\phi+135,\ 30)]}$$

A four-by-four correlation matrix was computed by correlating the primary features distributions at the inner ring receivers for each pair of the four outer ring transmitters. For instance, the correlation coefficient, $\rho_{i,j}$, for transmitters i and j can be computed as follows:

$$\rho_{i,j} = \frac{\sum_{\phi=0}^{315^\circ} [P_i(\phi,30) - \bar{P}(30)]\,[P_j(\phi,30) - \bar{P}(30)]}{\sigma_{P_i}\sigma_{P_j}}$$

where,

$i = 1,2,3,4;\ \ j = 1,2,3,4$

The eigenvalues of the $\rho_{i,j}$ matrix were used as features.

As mentioned above, the standard deviations (σ) around the 8-element arrays were computed. For each of four outer transmitters, one such σ was computed. The mean and standard deviation of these four σ's were also used as features.

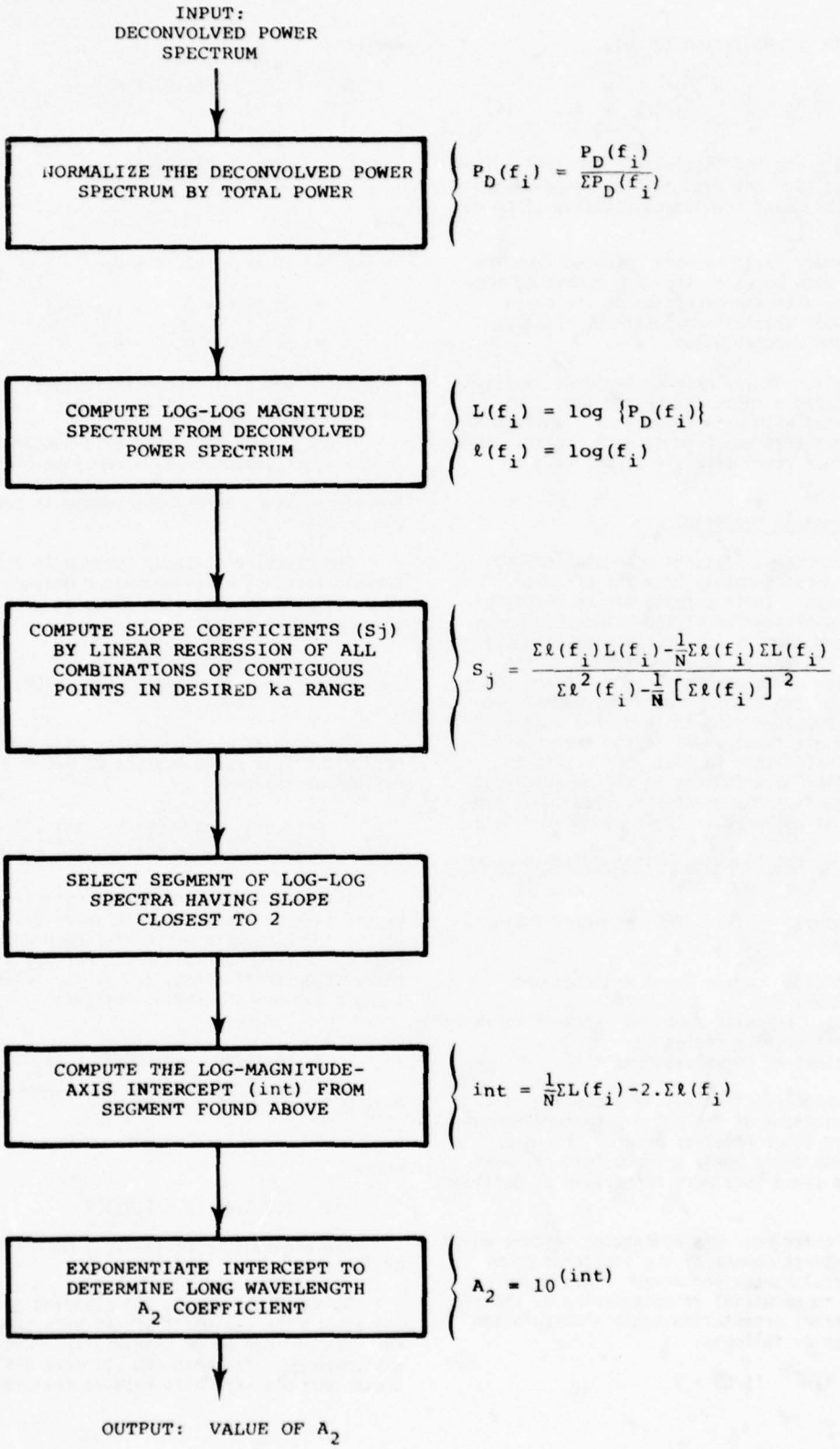

Fig. 7. Flow chart to compute long wavelength A_2 coefficient

Secondary Spectral Features: Pulse-Echo Mode

The PE total power at each receiver was normalized by the sum of the total power of all 17 receivers. In this manner, the three-dimensional relative scattered power distribution was not destroyed. There were five types of features computed from the PE primary features:

1. Statistical;
2. Circular;
3. Ratios;
4. Eigenvalues;
5. β-plane features.

The statistical features were the sample mean and variance of the primary features computed from the inner and outer receiver rings. The circular means and variance were also computed around these rings, in the same manner described above. The ratio features were the mean inner ring primary features divided by the mean outer ring primary features.

The eigenvalue features for the PE data were different from those described above in the following way. A spatial covariance matrix was computed, weighted by the values of the primary features. For instance, using the total power (P_i) as the weighting coefficient, the spatial covariance matrix was computed as:

$$\bar{C} = \begin{bmatrix} \sum_{i}^{17} P_i X_i^2 & \sum P_i X_i Y_i & \sum P_i X_i Z_i \\ \sum P_i X_i Y_i & \sum P_i Y_i^2 & \sum P_i Y_i Z_i \\ \sum P_i X_i Z_i & \sum P_i Y_i Z_i & \sum P_i Z_i^2 \end{bmatrix}$$

The three eigenvalues of this matrix yield information about the spatial distribution of total power (P_i), which, in turn, yields information about the defect's orientation and size. An explanation of the meaning of these eigenvalues can be found in Reference [14].

Another type of secondary feature was computed from five receivers in the β-plane. An estimate for the defect azimuthal angle "β" was computed from the circular mean of the inner and outer rings. If the estimated value of β -- denoted as $\hat{\beta}$ -- fell along an increment of 45 degrees, five receivers were found at 30-degree increments in that plane. If $\hat{\beta}$ fell at an arbitrary position, the values at these missing receiver positions were estimated by interpolation. From these five receivers, the mean, standard deviation, first and second moments, and ratio of three inner to four outer values were taken. There were 52 secondary PE features computed.

RESULTS

The most significant aspect of this work was to establish that the theoretically trained ALN models yielded accurate size and orientation estimates when evaluated on eight physically recorded spheroid samples via a blind test. These numerical estimates are presented below. It was also interesting to note that the ALN modeling procedure recognized different spectral feature sets for each of the different theories, which suggests that even better performance might be obtained by synthesizing models on a combined theory feature set. This is recommended for future work. It should be noted that the evaluation was "blind" in the sense that no portion of the physical data was used to influence the ALN model synthesis procedure.

Qualitative comparisons of the theoretical and experimental data are presented below in the form of radiation patterns (polar plots) of the primary features. Also, a comparison of the scattered spectra for the three theories is shown. The BORN and EQSA shpectra were identical in their overall shape (i.e., smooth and sinusoidal in nature), while the SMM-generated spectra possessed greater spectral detail. The SMM spectral most closely matched the experimental data.

The numerical estimates for the physical defect parameters A, B, α, and β for each of the eight experiments are presented in Table 3. Also listed are the estimated volume (V), computed from the ALN outputs for A and B; and the "orientation error", computed from the ALN estimates for α and β. Four methods were used in estimating each parameter as shown. The average absolute error (AAE) and the percentage average absolute error (%AAE) were computed on all estimates over the eight experiments and appear in the right-hand columns[2/]. The "true" experimental values for A, B, α, β, and V are shown in the top row of each group.

Estimates for the size parameters "A" and "B" were comparable for each of the four methods. The lowest percentage average absolute errors for these parameters were 20.0 percent for "A", yielded by the EQSA PE model, and 5.9 percent for "B", yielded by the BORN PE model. Note, however, that the average absolute errors are about the same for these two models (about 25 microns). Also, note that each of the three theories yielded approximately the same results.

Figure 8 is a pictorial display of the size estimates presented in Table 3. Here, ellipses are drawn whose major and minor axes are the model estimates for A and B for each of the four methods. The true estimates are shown at the top of the figure.

Estimates for the polar orientation "α" were definitely superior in the PE models compared to those produced by the BORN PMC model. Improvements of approximately 12 percent were observed for the former methods. The probable reason for increased performance was due to reliable generation of theoretical "backscatter" data. The BORN program's ability to generate pitch-catch data is suboptimal. Pitch-catch data from the theories other than BORN were not pursued because of cost considerations in generating the computer data.

2/%AAE for A and B was computed by dividing the absolute difference between true and estimated values by the true value, then averaging over eight experiments. The %AAE and α and β was computed by dividing the AAE for these values by their respective ranges, 90 and 180.

Table 3. Size and orientation estimates for the eight experimental spheroidal defect samples determined from the theoretically-trained ALN models.

PARAMETER TYPE	METHOD	EXPERIMENT NUMBER								ERROR	
		1	2	3	4	5	6	7	8	AAE	%AAE
MINOR AXIS A (MICRONS)	TRUE 'A'	200	200	100	100	200	100	200	100	--	--
	BORN PMC	207	250	88	73	433	106	226	96	45.6	25.9
	BORN PE	198	189	178	101	191	201	195	175	35.3	33.6
	EQSA PE	209	174	129	149	194	135	157	95	25.3	20.0
	SMM PE	186	147	259	121	175	145	147	64	50.7	41.7
MAJOR AXIS B (MICRONS)	TRUE 'B'	400	400	400	400	400	400	400	400	--	--
	BORN PMC	442	412	424	419	426	421	481	394	28.9	7.2
	BORN PE	474	417	365	428	385	397	399	417	23.8	5.9
	EQSA PE	383	364	379	361	434	371	379	389	26.0	6.5
	SMM PE	278	342	285	458	395	410	354	444	57.3	14.3
POLAR ANGLE α (DEGREES)	TRUE 'α'	0	30	80	0	80	30	30	30	--	--
	BORN PMC	10	13	80	23	38	31	6	2	18.1	20.1
	BORN PE	14	18	76	8	63	34	41	38	9.8	10.3
	EQSA PE	4	28	80	11	67	42	53	36	8.9	9.9
	SMM PE	7	14	80	-5.9	83	24	40	29	6.0	6.7
AZIMUTHAL ANGLE β (DEGREES)	TRUE 'β'	--	225	160	--	160	180	180	225	--	--
	BORN PMC	--	225	166	--	209	180	180	225	9.2	5.1
	BORN PE	--	207	158	--	189	200	199	217	16.0	8.9
	EQSA PE	--	198	160	--	183	195	192	209	15.5	8.6
	SMM PE	--	223	169	--	183	188	188	232	9.5	5.3
VOLUME[1] V (MICRONS^3 x 10^6)	TRUE 'V'	134	134	67	67	134	67	134	67	--	--
	BORN PMC	169	179	66	54	329	79	219	62	48.9	39.4
	BORN PE	186	138	99	77	119	133	130	127	30.4	38.3
	EQSA PE	128	97	78	81	153	78	94	60	18.1	17.5
	SMM PE	60	72	88	119	114	102	77	53	41.9	42.6
ORIENTATION ERROR[2] 'OE' (DEGREES)	BORN PMC	10.0	17.0	5.9	23.0	57.7	1.5	23.9	28.0	20.9	11.6
	BORN PE	14.0	14.0	4.5	8.0	32.2	11.4	15.5	8.9	13.6	7.5
	EQSA PE	4.0	13.1	0.0	11.0	25.6	14.9	24.2	10.4	12.9	7.2
	SMM PE	7.0	16.0	8.9	4.9	22.9	7.0	11.0	3.6	10.2	5.6

[1] $V = AB^2(4\pi/3) \times 10^{-6}$

[2] $OE = \cos^{-1}[x\hat{x} + y\hat{y} + z\hat{z}]$

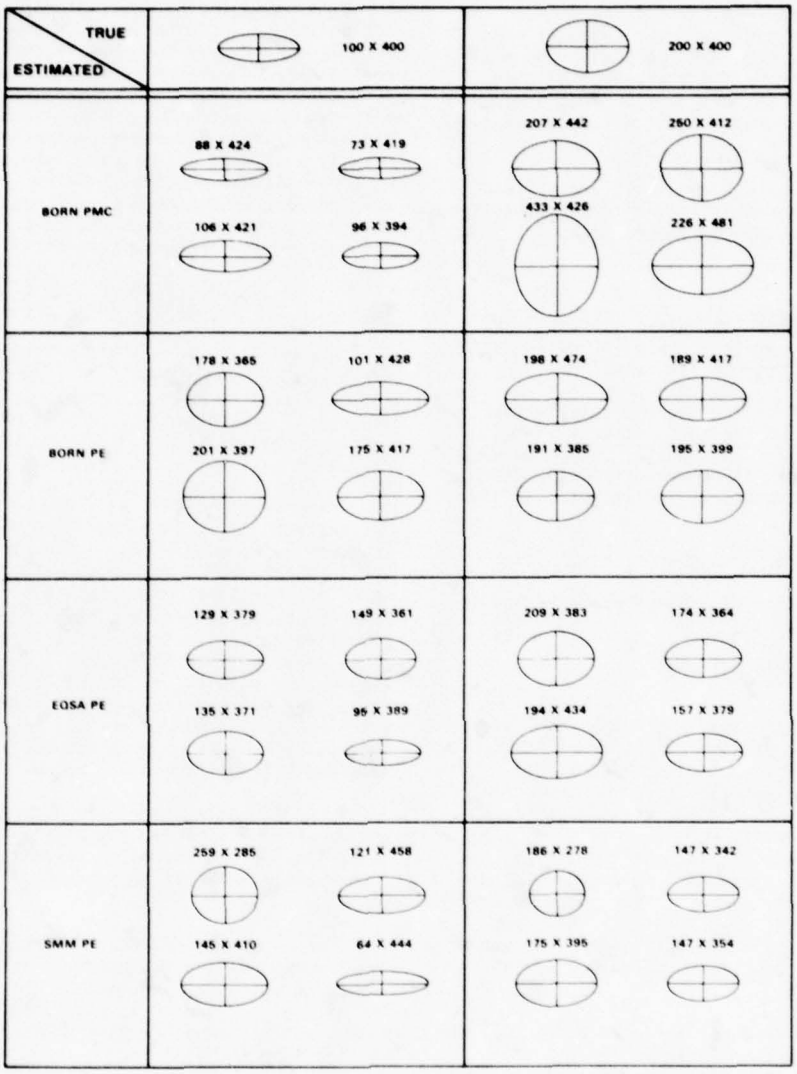

Fig. 8. True versus estimated sizes for eight experimentally recorded oblate spheroid defects.

Four methods were used to trains ALN's: 1) BORN pitch-multiple catch; 2) BORN pulse echo; 3) Extended Quasi-Static Approximation (EQSA) pulse echo; and 4) the Scattering Matrix Method (SMM) pulse echo. The "true" sizes were 100 x 400 microns and 200 x 400 microns, each at four orientations.

The smallest observed average absolute error for the orientation estimates were 6.0 degrees for the polar angle "α", yielded by the SMM PE model, and 9.2 degrees for the azimuthal angle "β", yielded by the BORN PMC model. Both values are excellent error estimates for the defect orientation considering the sparse spatial separation of the transducers: 30 degrees in the polar direction and 45 degrees in the azimuthal direction. One way that the orientation accuracy could be improved is by increasing the number of array elements.

Estimates of the spheroid's volume ($\hat{V}$) were computed from the individual A and B estimates for each of the four methods by the formula:

$$\hat{V} = (4\pi/3)\hat{A}\hat{B}^2$$

The results are listed in Table 3. The EQSA PE models provided the best estimates of volume with a 17.5 percent average absolute error.

Another way of presenting the orientation error is by measuring the absolute angle between the true symmetry axis (S) and the estimated symmetry axis ($\hat{S}$). This is computed from the definition of the inner product of the two orientation vectors:

$$S\cdot\hat{S} = |S||\hat{S}|\cos\psi = S_x\hat{S}_x+S_y\hat{S}_y+S_z\hat{S}_z$$

If the magnitudes of S and $\hat{S}$ are arbitrarily set to unity:

$$\psi = \cos^{-1}(S_x\hat{S}_x+S_y\hat{S}_y+S_z\hat{S}_z)$$

where the X, Y, and Z components of S and $\hat{S}$ are computed from the true and estimated orientation angles, α and β. Table 3 shows the smallest average absolute orientation error to be 10.2 degrees for the SMM PE models. A way of viewing the orientation error is shown in Fig. 9. Each axis represents zero orientation error for each of the four methods. The smaller arrows on the outside of the circle represent the computed errors for each of the eight experiments. (The error will never be negative, by definition.) Note that each of the three theories produced comparable results in the PE mode.

A list of the features selected by each of the four methods is given in Table 4. From left to right, the columns in each group refer to the primary feature type, the receiver group from which the secondary feature was computed, a description of the secondary feature, and the ALN models which selected that feature as being important. Note that the selected BORN PMC feature set was considerably larger than those selected by the other methods. This was due to the more extensive candidate features list accommodating the larger number of PMC receivers.

The ALN model based on EQSA PE selected a total power feature almost exclusively, whereas the other methods utilize more of the spectral features.

Radiation plots of the four primary features for a 200 μM by 400 μM oblate spheroid defect with orientation α = 80 degrees and β = 160 degrees are shown in Fig. 10. In each plot, the magnitude of the primary feature at each inner ring receiver was plotted as a function of the azimuthal receiver angle φ. Both theoretical and experimental data are superimposed on each plot. Notice the similarity between all three theories and experiments for the total power feature. Also, it can be seen how dissimilar the A_2 coefficients are when comparing theory and experiment. As mentioned previously, one reason for this is that the PE experimental data were recorded with the pulser set to provide the broadest band response. This yielded very few data points in the ka < 0.5 region; hence, the values of A_2 for the experimental data were greatly distorted. (But, as discussed above, the A_2 parameter was found to be very informative with respect to the theoretical data. Therefore, one of the recommendations is to rerecord data with better low frequency content.)

COMPARISON OF THEORETICAL AND EXPERIMENTAL SPECTRA

A comparison of the theoretical (SMM) and experimental power spectra is shown in Fig. 11. The data used in generating these plots were the pulse-echo data described in Section 3 of this report. Each plot was normalized by its peak value; hence, the largest value in each plot is unity. The left-hand plots -- Fig. 11 (a,b, and c) -- are from the 100 μM by 400 μM defect at polar orientations of 30, 60, and 90 degrees, respectively. The right-hand plots -- Fig. 11 (c,d, and e) -- are from the 200 μM by 400 μM defect at the same three orientations. Note that Fig. 11 (a and b) have favorable comparisons over the entire frequency range of 1.0 to 8.8 MHz. Fig. 11 (d) compares quite well up to 7.0 MHz. The remaining figures are slightly stretched in the mid-frequency range, but the general shapes of the theoretical and experimental curves are the same. Also, note that all six plots compare favorably in the long wavelength (low frequency) regime.

Unfortunately, there was much variation in the experimental data. Low signal-to-noise ratio caused the defect's impulse response to be unrecognizable in about 30 precent of the experimental data.

The major reasons for differences between the theoretical and experimental data are: (1) limited transducer bandwidth at the low and high frequencies; (2) error in experimental measurements; and (3) possible divergence in the theory at high frequencies.

The plots in Fig. 11 show that marginal information relative to the shorter defect size parameter "A" is contributed by the spectral moment primary features. Note that there is very little shift in the major peaks between the 100 μM by 400 μM plots and the 200 μM by 400 μM plots. However, it does appear that plots having the larger "A" dimension also have a greater "ripple" in their spectra. This ripple could be quantified by performing a cepstrum transformation on the defect's time domain impulse response. Another method of quantifying this ripple is by application of J. Rose's sine transformation inversion technique [7]. Both approaches will be investigated in next year's work.

The variance in the experimental data is demonstrated in Fig. 12. The outer ring (θ=60°) time domain defect impulse responses for experiment

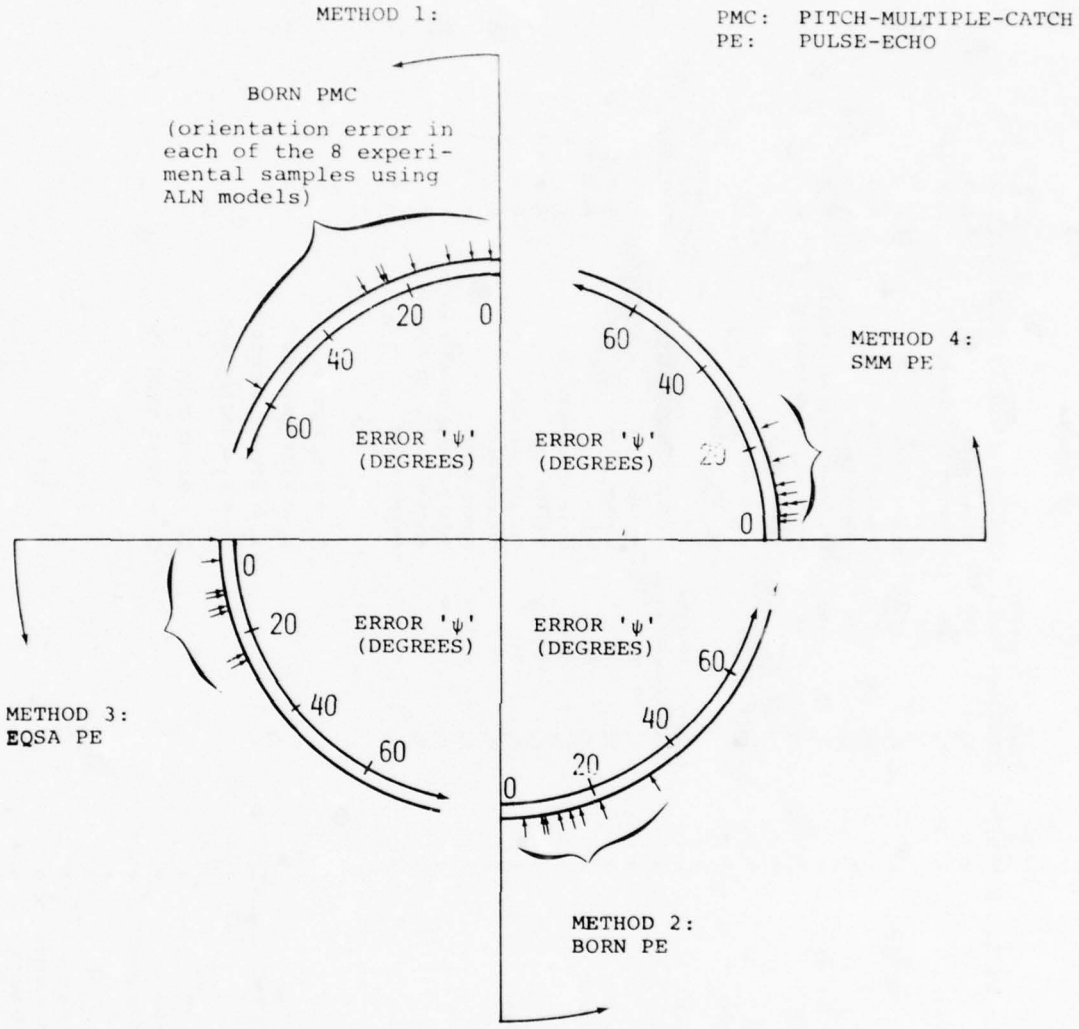

Fig. 9. Scatter plot illustrating the error between the true and estimated defect orientation. (Perfect estimation would result in no scatter about the 0° point.)

Table 4. Important features selected by the ALN models to estimate A, B, α, β.

a) BORN PMC

Primary Feature	Receiver Group	Secondary Feature Description	Useful For Estimating
P_T	OR	Circular variance	B, α
P_T	OR	S-part of circular mean	B, α
P_T	OR	Circular mean	β
P_T	IR	Average of S.D.'s for ORT's	A
P_T	IR	RI ratio for T = 0	α
P_T	IR	RI ratio for T = 90	α
μ_1	IR	Second eigenvalue of P-matrix	A
μ_1	IR	S.D. of S.D.'s for ORT's	B, α
μ_1	IR	Circular Variance	B, α
μ_1	OR	Circular Variance	B
μ_1	OR	C-part of circular mean	B, α
μ_1	OR	Circular mean	α
μ_1	IR	C-part of circular mean	α
μ_1	IR	RI ratio for T = 0	α
μ_1	IR	RI ratio for T = 90	α
μ_1	IR	RI ratio for T = 270	α
μ_2	IR	S.D. of S.D.'s for ORT's	A
μ_2	OR	Circular Variance	B, β
μ_2	OR	Circular mean	B, α
μ_2	OR	S-part of circular mean	B
μ_2	IR	RI ratio for T = 90	α
A_2	OR	Circular variance	A
A_2	Ik	RI ratio for T = 90	α
A_2	IR	RI ratio for T = 180	α
A_2	IR	RI ratio for T = 270	α

b) BORN PE

Primary Feature	Receiver Group	Secondary Feature Description	Useful For Estimating
P_T	IR	Average value	A, B, α
P_T	IR	S-part of circular mean	A, B
P_T	OR	S.D.	B, α, β
P_T	OR	Circular mean	β
μ_1	OR	C-part of circular mean	A, α
μ_2	IR	Average value	A, B
μ_2	All	Third eigenvalue of C-matrix	A, B
μ_2	OR	S-part of circular mean	α

c) EQSA PE

Primary Feature	Receiver Group	Secondary Feature Type	Useful For Estimating
P_T	IR	Average value	A, B
P_T	OR	Average value	A, B, α
P_T	OR	S.D.	A, B, α
P_T	IR/OR	Ratio of averages	α
P_T	β-plane	Average value	A, B, α,β
P_T	OR	Circular variance	B, α
P_T	OR	Circular mean	β
P_T	β-plane	Second moment	A
P_T	β-plane	Ratio of inner to outer power	A
P_T	All	first eigenvalue of C-matrix	α
μ_2	OR	Average Value	A, B, α,β

d) SMM PE

Primary Feature	Receiver Group	Secondary Feature Description	Useful For Estimating
P_T	OR	Average value	α, β
P_T	OR	S.D.	A, α
P_T	IR	Circular variance	α
P_T	OR	C-part of circular mean	B
P_T	β-plane	Ratio of inner to outer power	α
P_T	β-plane	First moment	α
P_T	OR	Circular mean	β
P_T	All	First eigenvalue of C-matrix	A
P_T	All	Second eigenvalue of C-matrix	A
P_T	All	Third eigenvalue of C-matrix	α, β
μ_1	OR	Average value	B
μ_1	All	First eigenvalue of C-matrix	A
μ_1	All	Second eigenvalue of C-matrix	B
μ_1	All	Third eigenvalue of C-matrix	A, B
μ_2	OR	Average value	B

P_T = Total power
μ_1 = First moment
μ_2 = Second moment
A_2 = A_2 coefficient
IR = Inner ring
OR = Outer ring

λ = wavelength) and the defect radius. If
ka < 1, the wavelength is larger than the defect
radius.

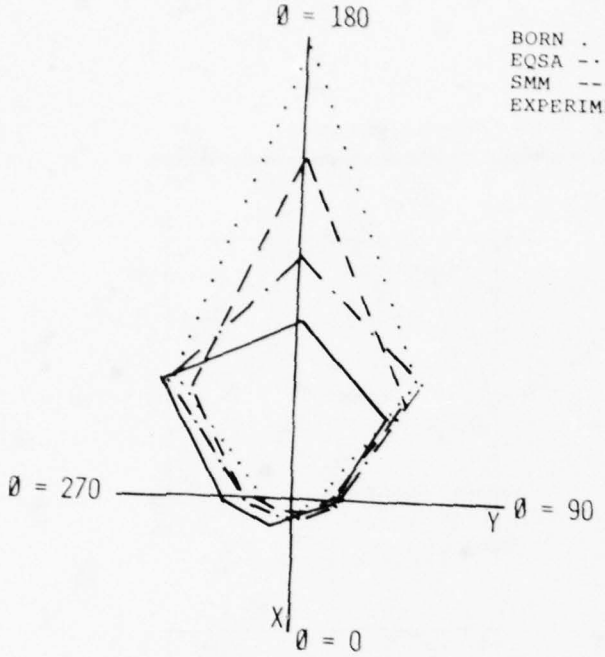

a) TOTAL POWER (P_T)

BORN . . . .
EQSA - - - -
SMM - - - - -
EXPERIMENTAL ———

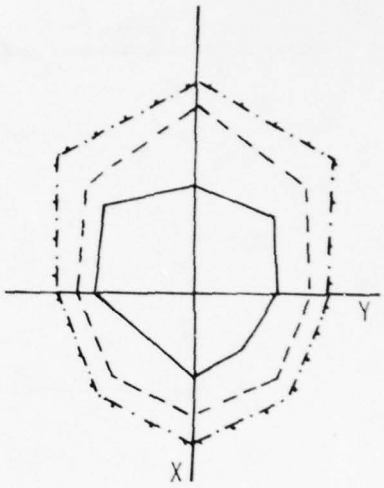

b) FIRST MOMENT (μ_1)

DEFECT SIZE: 100 X 400 μM OBLATE SPHEROID
DEFECT ORIENTATION: $\alpha = 30^0$; $\beta = 180^0$
TRANSDUCERS: 8 IN INNER RING (θ=30), PULSE-ECHO MODE
FREQUENCY RANGE: 1.0-8.8 MHz.

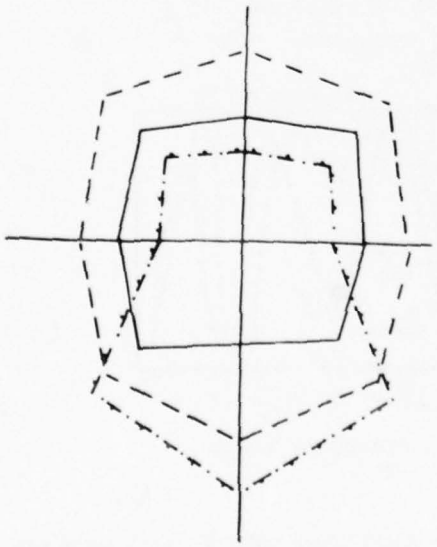

c) SECOND MOMENT (μ_2)

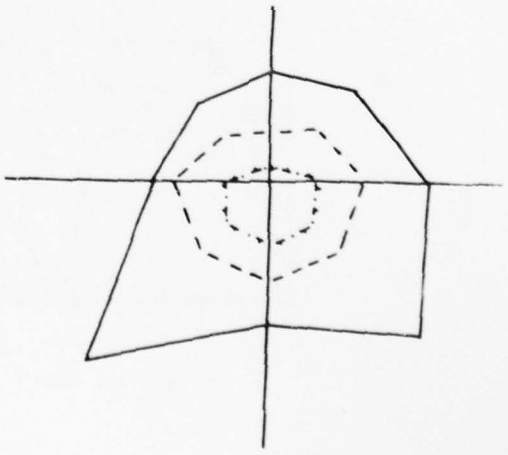

d) LONG WAVELENGTH COEFFICIENT (A_2)

Fig. 10 Polar plots of the four primary spectral features versus azimuthal transducer position for a spheroidal void in titanium, comparing experimental data to theoretically-generated data (BORN, EQSA, SMM)

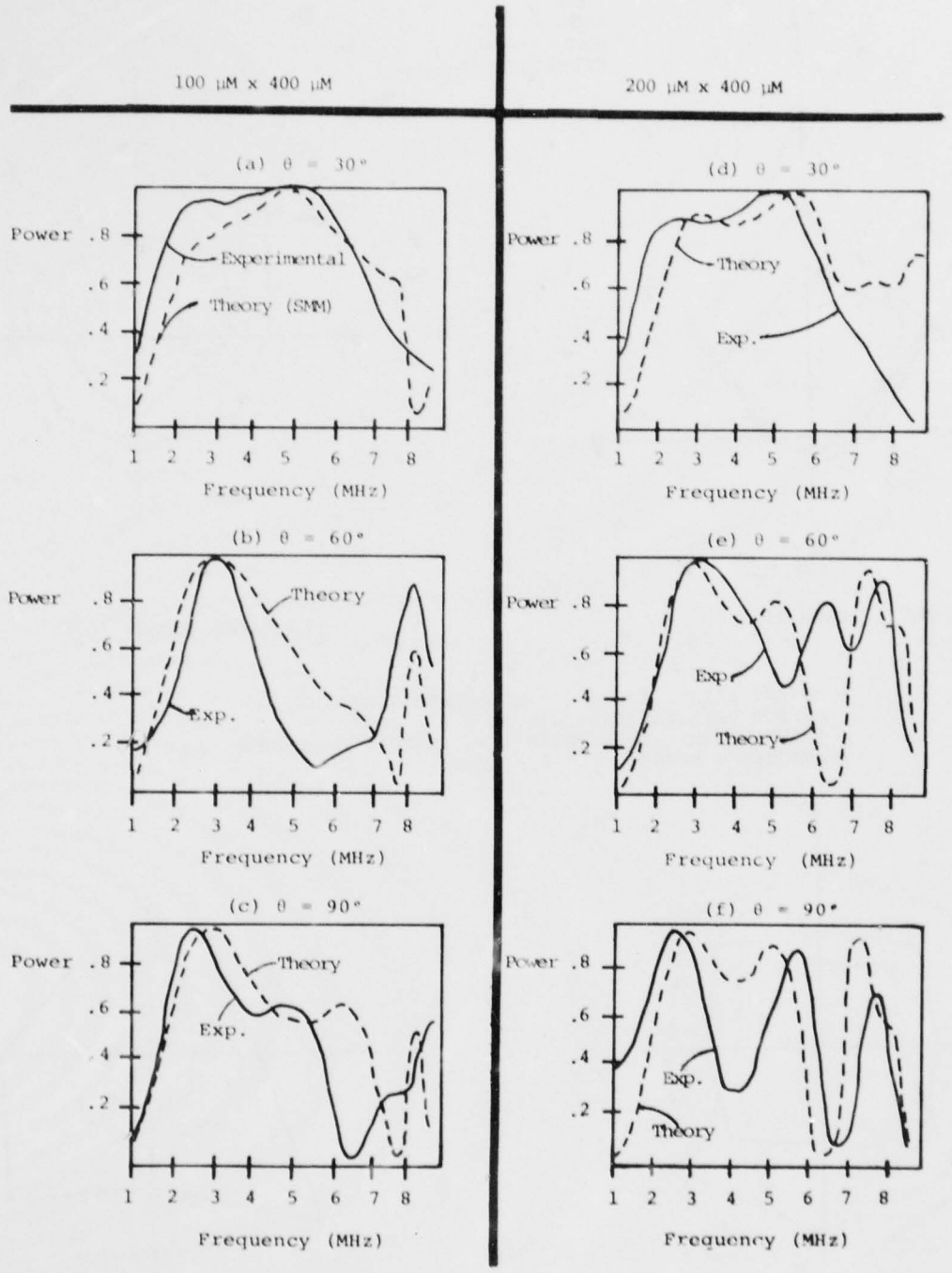

Fig. 11. Comparison of the theoretical (SMM) and experimentally obtained power spectra. Each curve was normalized by its peak value. The left three plots are for a 100 μM by 400 μM oblate spheroid at pulse-echo transducer orientations of 30, 60, and 90 degrees. The right three plots are for 200 μM by 400 μM oblate spheroid at the same PE transducer orientations.

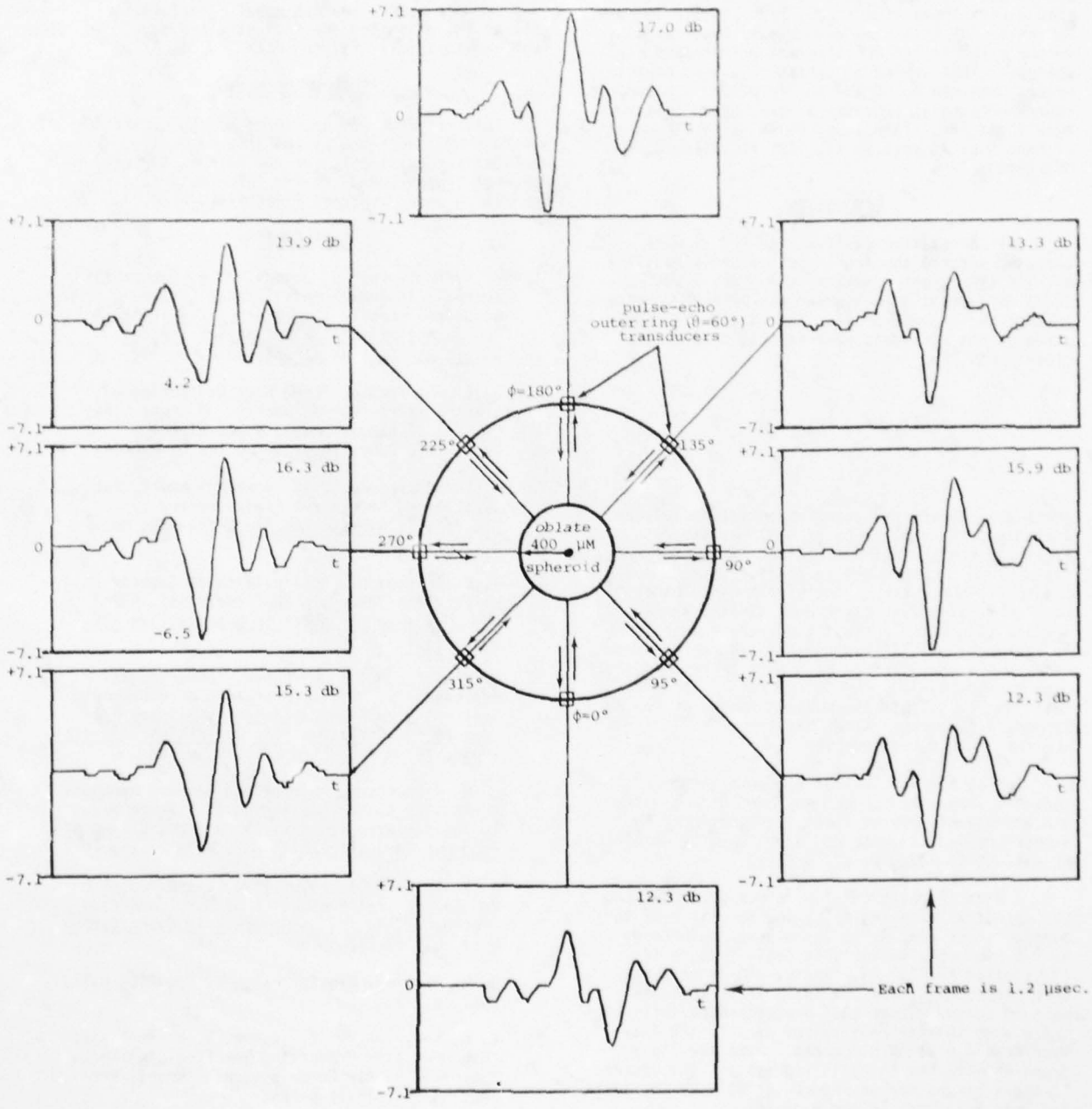

Fig. 12. Experimental pulse-echo responses from A 200 by 400 micron oblate spheroid showing the variance in the data. All experimental waveforms should by identical. The defect axis of symmetry is normal to the page. The transducers are located on the outer ring (θ=60°). (db values are derived from mean peak-to-peak levels)

number 1 of Table 2 are shown. This PE experiment was a 200 μM by 400 μM defect having an orientation at $\alpha = 0°$ and $\beta = 0°$. All outer ring transducers therefore have the same polar orientation with respect to the defect's symmetry axis. Hence, all waveforms should be identical. Note, however, that differences in peak amplitude vary up to 4.7 decibels. Also, the waveforms taken at $\phi = 0$, 45, and 90 degrees appear to have quite different shapes than those at $\phi = 225$, 270, and 315 degrees. Variations of this kind undoubtedly contributed to the error in the ALN size and orientation evaluations. This source of variation in the experimental data can be termed an "irreducible error" source because it provides a lower bound to the modeling error. This lower bound is not known at present but, as seen in Fig. 12, it is certainly non-zero.

DISCUSSION

The correlation coefficients ($\rho_{i,j}$) were computed between the secondary features involving A_2, and the defect geometry parameters A, B, α, and β as a means of measuring the defect geometry information content of A_2. The $\rho_{i,j}$'s were computed on the EQSA data over the 240 theoretical experiments, as:

$$\rho_{i,j} = \frac{\sum_{k=1}^{240} (x_{ik} - \bar{x}_i)(x_{jk} - \bar{x}_j)}{\sigma_i \sigma_j}$$

where the σ's are the standard deviations of the variables. A correlation of 0.97 was found to exist between the defect's larger radius (B) and the average of the eight A_2 coefficients computed around the outer ring. The significance of this high correlation is better demonstrated in Fig. 13 where B is plotted against the average outer ring A_2 feature. All 240 experiments are represented here. Only three values of B were present in the data base, 200, 300, and 400 microns. The heavy solid lines indicate the maximum spread of the A_2 secondary features. Note that the trend is linear and the lines do not overlap.

The conclusion is that a good estimate of the defect's larger radius can be found directly from the average of several spatial estimates of A_2. A more precise estimate could be found by combining A_2 with other features via ALN's.

A high correlation of 0.96 was found between the defect's polar angle (α) and the ratio of the average inner ring A_2 to the average outer ring A_2. A plot of α versus this ratio feature is illustrated in Fig. 14. Again, 240 experiments were represented, and the solid lines indicate a maximum spread rather than a standard deviation. There were 10 different values of α in the data base from 1.0 to 89.0 degrees. Note the linear trend in α as the A_2 ratio increases. The spread of these ranges may be reduced greatly by considering only receivers in the β-plane.

One of the resultant ALN's is shown in Fig. 15. This model was trained with BORN-generated pulse-echo data to estimate the defect's polar angle (α). Each "element" in the network consists of a six-term quadratic multinomial of two input variables (with the exception of element "f" which has only four terms). The input features at the left of Fig. 15 are the "secondary" spatial features computed from the scattered ultrasonic waveforms. The outputs of the leftmost elements provide inputs to subsequent elements. The rightmost element output renders an estimate for α. Nesting, or "layering", of polynomials as shown allows for many hundreds of nonlinear terms to be represented in a compact form. The ALN model structure, as well as the weighting coefficients, are developed from the empirical training data.

ACKNOWLEDGEMENT

This research was sponsored by the Center for Advanced NDE, operated by the Science Center, Rockwell International, for the Defense Advanced Research Projects and the Air Force Materials Laboratory under Contract F33615-74-C-5180.

REFERENCES

1. J. A. Krumhansl, E. Domany, J. E. Gubernatis, Rockwell International (Science Center) technical report, Interdisciplinary Program for Quantitative Flaw Definition Special Report Second Year Effort, 1975, p. 102.

2. J. E. Gubernatis, "Long Wave Scattering of Elastic Waves from Volumetic and Crack-Like Defects of Simple Shapes", Los Alamos Scientific Laboratory, Supported by USERDA.

3. V. Varatharajulu (V. V. Varadan) and Y. Pao, "Scattering Matrix for Elastic Waves .I. Theory", J. Acoust. Soc. Am., Vol. 60, No. 3, Sept. 1976.

4. J. D. Achenbach, "Applications of Geometrical Diffraction Theory to QNDE Analysis", ARPA/AFML Review of Progress in Quantitative NDE, July 17-21, 1978

5. B. R. Tittmann, E. R. Cohen, "Experimental Measurements and Interpretation of Ultrasonic Scattering by Flaws", Interdisciplinary Program for Quantitative Flaw Definition. Special Report Third Year Effort, 1976, p. 82.

6. J. M. Richardson, "Direct and Inverse Problems Pertaining to the Scattering of Elastic Waves in the Rayleigh (Long Wave) Regime", Review of Progress in Quantitative NDE, July 17-21, 1978.

7. J. Rose, Cornell University, "Experimental and Theoretical Evaluation of Born Inversion Procedure", Review of Progress in Quantitative NDE, July 17-21, 1978.

8. R. W. Hamming, Digital Filters, Prentice-Hall, 1977, p. 45.

9. E. S. Fergeson, R. E. Twyman, V. L. Newhouse, "Deconvolution Processing for Flaw Signatures", Supported by Air Force Systems Command, Project No. F33615-75-C-5252.

10. T. J. Ulrych, T. N. Bishop, "Maximum Entropy Spectral Analysis and Autoregressive Decomposition", Review of Geophysics and Space Physics, Vol. 13, No. 1, Feb. 1975, p. 183.

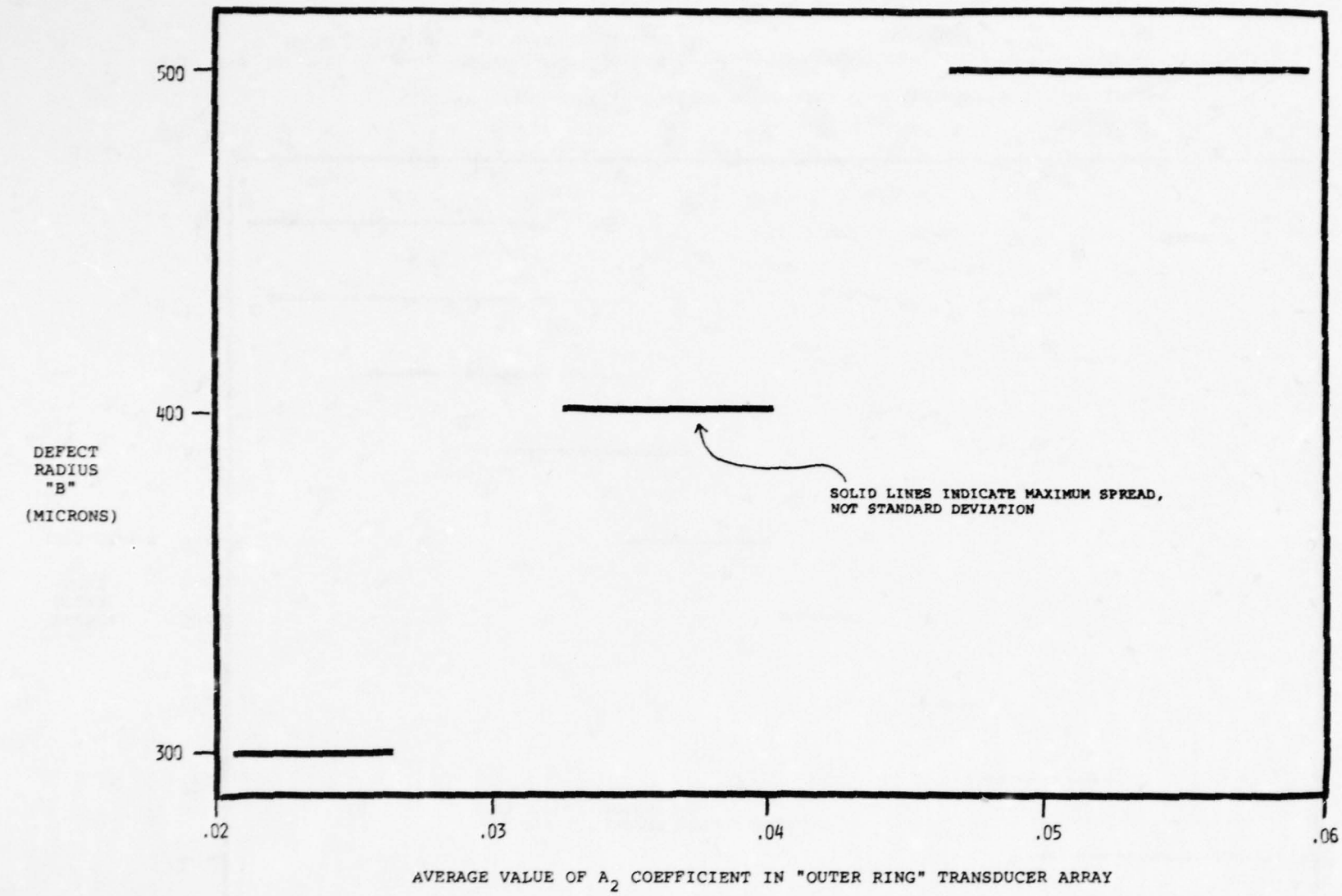

Fig. 13. Plot of defect radius "B" versus the average A_2 coefficient over 240 BORN pulse-echo experiments

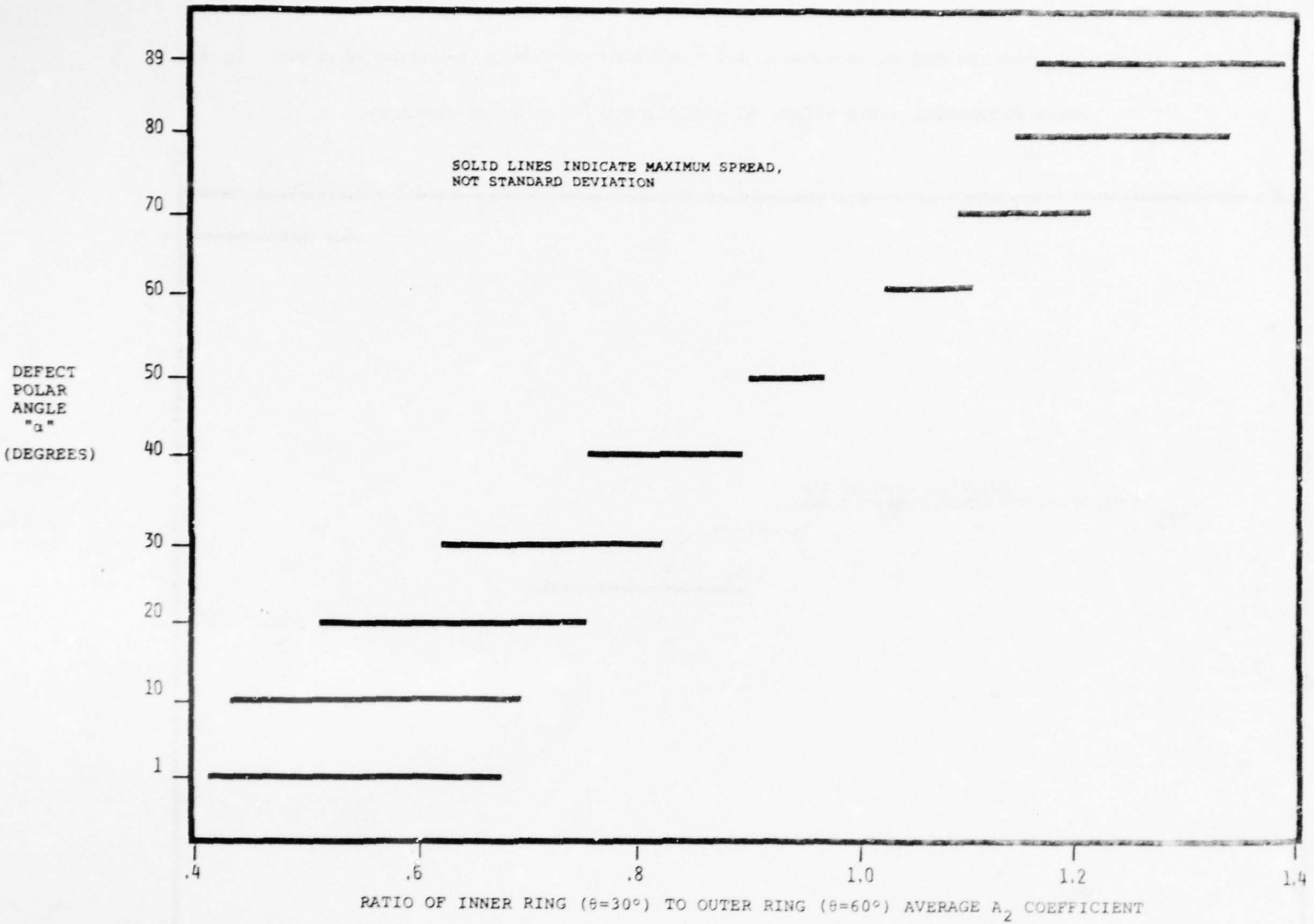

Fig. 14. Plot of defect polar angle "α" versus ratio of average A_2 coefficient from inner ring (θ=60°). 240 BORN pulse-echo experiments represented.

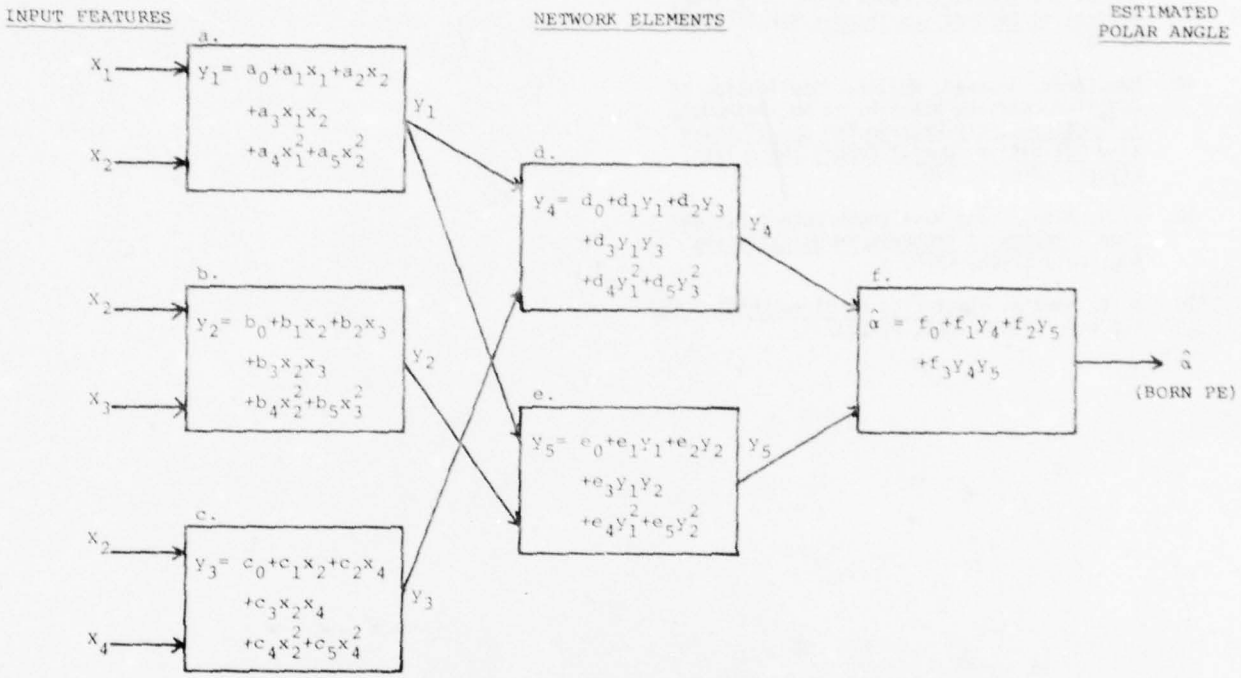

	ALN WEIGHTING COEFFICIENTS					
Element	0	1	2	3	4	5
a_i	.126E3	-.283E4	.375E3	.450E4	.168E5	-.230E4
b_i	.116E2	.992E3	-.577E2	.215E3	-.317E4	-.266E4
c_i	.112E2	.981E3	-.545E2	.734E3	-.329E4	-.399E3
d_i	-.178E2	.166E1	.800E0	.105E0	-.555E-1	-.656E-1
e_i	-.205E2	.103E1	.150E1	.793E-1	-.381E-1	-.581E-1
f_i	.136E0	.435E0	.482E0	.130E-2		

FEATURE DESCRIPTION

X_1: Average inner ring total powers

X_2: Standard deviation of outer ring total power

X_3: C-part of circular mean, outer ring first moment

X_4: S-part of circular mean, outer ring, second moment

Fig. 15. Adaptive Learning Network (ALN) structure for estimating the defect polar angle (α). The ALN's were synthesized using BORN-generated pulse-echo data.

11. R. W. Clayton, T. J. Ulrych, "A Restoration Method for Impulsive Functions", IEEE Transactions on Information Theory, March 1977, p. 267.

12. Mucciardi, Shankar, Whalen, "Application of Adaptive Learning Networks to NDE Methods", Interdisciplinary Program for Quantitative Flaw Definition Special Report Third Year Effort, 1976, p. 176.

13. J. R. Rice, "Long Wavelength Defect Evaluation", Review of Progress in Quantitative NDE, July 17-21, 1978.

14. K. V. Mardia, Statistics of Directional Data, Academic Press, 1972, p. 223.

DISCUSSION

Don Thompson (Science Center): Was there anything evident in the treatment, Mike, that would indicate a systematic preference for the pulse-echo rather than pitch-catch technique?

M. F. Whalen (Adaptronics): The tracking of the polar angle seemed to be much better for the pulse-echo than it did for the pitch-catch. The thing that I can think of offhand is that the Born approximation is most accurate in the back scattered direction.

Walter Kohn (Materials Research Council): Could you explain the rationale behind the polynomial expression that you use in your scheme?

M. F. Whalen: It is basically an empirical modeling process in which we take all pair-wise combinations of the candidate features and obtain a best fit to the dependent variable that we are trying to model. In the process only the best candidates will survive. We do this first by considering all the possible candidates; the ones that have survived the first layer will be used as candidates to go into the second layer: this is extended out to as many layers as are needed until we get a sufficient fit. But there are certain means taken to avoid overfitting.

Anthony N. Mucciardi (Adaptronics): I could further answer the question. It is a multi dimensional phase shift, if you think about it that way. Consequently, any function could be represented as a power curve. Consequently, whatever underlying unknown transfer function there may be between defect size and parameters of the wave form, can be adaptively learned. The idea is to attempt to find if the underlying function can be represented by a polynomial. You have the ability to synthesize. The reason for the choice of the two term element has to do with computational efficiency.

Bernard Budiansky (Harvard University): In view of that explanation, why learn on theoretical models rather than the actual experimental data? Why insert a Born approximation into it?

Anthony N. Mucciardi: It is cheaper. If you have to learn on physical data, which is what we normally do, you spend many tens of thousands of dollars developing samples, even then you can't simulate all geometries and peculiarities. If you have a model that can, at least roughly, mimic a very expensive set of samples, you can generate your sample set in the computer. To me, the value of the thing is truly powerful because in principle, you may be able to simulate very strange geometries and put defects into very peculiar places by computer to generate a theoretical set of data. With any kind of luck, you will obtain a pretty good approximation of something which may be terribly expensive or impossible to build.

Paul Holler (Saarbrucken University): I would agree that having a forward series which fits is a very good basis for applying this empirical method to make the inversion, but I have two questions. Did you apply the minimization of the mean square or did you also apply a stockaster variation of the coefficients you get? The second question is, could you say in physical terms which variables survived in the particular cases? It is striking that with beta you only have two variables survived, in other cases up to twelve were required.

M. F. Whalen: Each of the elements represents a least squares fit. The reason that we had only two variables that remained in the case of the beta term was simply that that was all that was needed to best solve that problem. The beta term was the easiest variable. We had two variables that did the best job and the process figured out that was all that was needed. The solutions for the size parameters were dependent on much more information. If you remember, the direction of beta can be best found by looking simply at the direction where the maximum power is directed. Nothing else is needed.

A TECHNIQUE FOR DETERMINING FLAW CHARACTERISTICS FROM ULTRASONIC SCATTERING AMPLITUDES

J. H. Rose* and J. A. Krumhansl+
Laboratory of Atomic and Solid State Physics
and
The Material Science Center
Cornell University
Ithaca, New York 14853

ABSTRACT

We report an approximate technique for determining the characteristics of flaws in elastic media from a knowledge of their ultrasonic scattering amplitudes. The technique is rigorously valid in the weak scattering limit. Good results have been obtained for strongly scattering flaws. In particular, we tested the technique for a 2-1 oblate spheroidal void in Ti, and for various strongly scattering spherical defects. For these tests the technique yields good results for the volume of the flaws. In the case of the oblate spheroid, satisfactory results were obtained for the calculated ratio of major to minor axis, indicating that the technique is sensitive to the shape of the flaw.

INTRODUCTION

We present an inversion algorithm for determining the size, shape and orientation of flaws in elastic media from ultrasonic scattering amplitudes. The algorithm is based on the extended quasi-static approximation of J.E. Gubernatis[1], and is rigorously valid in the weak scattering limit. We have tested the algorithm for some strongly scattering flaws, and obtained good results as we report below.

The extended quasi-static approximation leads to two pieces of independent information which can be used to determine the characteristics of the flaw. The first piece of information is the dependence of the long wavelength scattering amplitude on the orientation of the flaw. The second piece of information is the spectral distribution of the reflected ultrasound as a function of orientation. In this paper we have concentrated on what we can learn from the spectral distribution of the ultrasound and we have "divided out" the long wavelength information. However, the two kinds of information are complementary, and using both of them together one may be able to learn something about the material composition of the flaw, as well as its size, shape and orientation. This possibility is discussed in the final section, and a technique is proposed which may make it possible to determine the density of the material in the flaw.

A major thrust of the current Non-Destructive Testing program is to use adaptive learning techniques to determine flaw characteristics in an empirical way.[2] Approximate inversion techniques such as that proposed in this paper could be used to preprocess the scattering amplitudes before its introduction to the adaptive learning network. Since the inversion algorithm will produce functions which look at least roughly like the actual flaw, such preprocessing may greatly enhance the adaptive learning approach.

The structure of this paper is as follows. We start with this introduction; then provide a general description of the theory. The third section is a discussion of a simplified form of theory which is available for all ellipsoidally shaped flaws. The fourth section contains empirical tests of the inversion algorithm for strongly scattering flaws. In particular, we have tested the procedure both for a 2-1 oblate spheroidal defect in Ti and for spherical cavities and inclusions in various materials. Our tests up to the present date indicate that the volume of the flaw is given rather accurately by our technique. We conclude the paper by giving a general discussion of the technique and indicate some of the work we intend to pursue in the future.

General Theory

The theory presented in this section is designed to provide information on flaw characteristics in the scattering regime. In this case the wavelength of the ultrasound is approximately equal to or longer than the size of the object. This regime is quite important for NDT applications where the size of the critical flaws may be quite small and as a result imaging techniques may be unavailable. The algorithm which we will propose is a procedure for approximately determining the Fourier transform of the characteristic function, $\gamma(\vec{r})$, of the flaw. Here $\gamma(\vec{r}) = 1$, $\vec{r}$ inside the flaw, and $\gamma(\vec{r}) = 0$ for $\vec{r}$ outside the flaw. The procedure to be described is rigorously valid in the weak scattering limit, where the material parameters of the flaw are only slightly different from those of the host material.

A pulse echo type experiment is assumed as shown in Fig. 1. Here a longitudinally polarized plane wave is incident on the flaw, and the directly backscattered longitudinal scattering amplitudes are determined. The longitudinal to longitudinal pulse echo scattering amplitudes can be written for an arbitrarily shaped flaw as

$$A_{L \to L}(\vec{k}) = a(\vec{k},\{\mu\})\, S(2\vec{k})\, k^2 \qquad (2.1)$$

Here $S(2\vec{k})$ (called the shape factor) is the Fourier transform of the characteristic function of the flaw. The wavevector of the incident wave is denoted by $\vec{k}$ and $a(\vec{k},\{\mu\})$ is a function to be calculated to yield the correct scattering amplitudes $A_{L \to L}$ for an arbitrary $\vec{k}$. Here $\{\mu\}$ denotes the material parameters of the flaw and the host material.

*Current address: Dept. of Physics, Univ. of Michigan, Ann Arbor, Mich.
+Current address: National Science Foundation Washington, D.C.

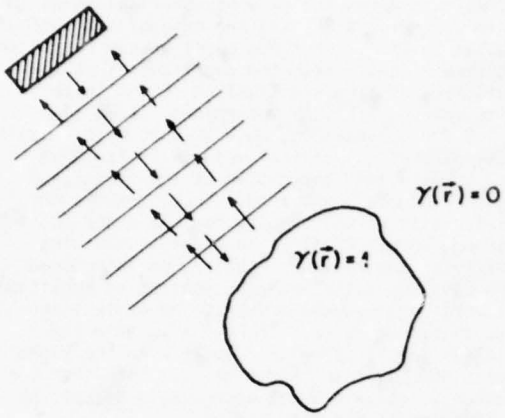

Fig. 1 The geometry of a typical L→L, pulse-echo experiment. The matrix material has one set of material parameters, ρ_1, μ_1, λ_1 ; while the flaw is considered to consist of a second homogeneous material with parameters ρ_2, μ_2, λ_2 .

The virtue of writing the scattering amplitudes in the form of Eqn. 2.1 is that several approximate theories yield very simple forms for the factor $a(\hat{k},\{\mu\})$. In particular, we will use the form of $a(\hat{k},\{\mu\})$ which can be derived from the extended quasi-static approximation. In that approximation one takes account of the long wavelength elastic deformation of the flaw correctly, and hence obtains the angular features of the scattering correctly in this limit. For the extended quasi-static approximation $a(\hat{k},\{\mu\})$ is independent of $|\vec{k}|$ and depends only on $\hat{k}$ and $\{\mu\}$ We denote this approximate form of $a(\hat{k},\{\mu\})$ as $a_{QSA}(\hat{k},\{\mu\})$. Using this approximation we rewrite Eqn. 2.1 as

$$S(2\vec{k}) \approx A_{L\to L}(\vec{k}) \,/\, (k^2\, a_{QSA}(\hat{k},\{\mu\})) \quad . \tag{2.2}$$

Experimentally, a_{QSA} can be obtained for an arbitrarily shaped object by measurements of the long wavelength scattering amplitudes. In that limit $S(2\vec{k})$ goes to a constant, a_{QSA} can be determined from the angularly dependent coefficients of A

$$a_{QSA}(\hat{k},\{\mu\}) = \lim_{k\to 0} A_{L\to L}(\vec{k}) \,/k^2 \quad . \tag{2.3}$$

Once a_{QSA} is obtained, we can determine $S(2\vec{k})$ from Eqn. 2.2 via an experimental measurement of the backscattered amplitudes. Taking the Fourier transform of $S(2\vec{k})$ then allows us to determine the characteristic function of the flaw, and hence its size, shape and orientation. The major approximation in using a_{QSA} is that we assume that it depends only on $\hat{k}$ and not on $|\vec{k}|$. The characteristic function is given explicitly in terms of the shape function as

$$\gamma(\vec{r}) = \text{const.} \int d^3\vec{k}\; e^{2i\vec{k}\cdot\vec{r}} A_{L\to L}/(k^2 a_{QSA}(\hat{k},\{\mu\})) \tag{2.4}$$

Simplified Theory for Ellipsoidally Shaped Flaws

In the last section we described an approximate procedure for determining the size, shape, and orientation of an arbitrary three dimensional flaw. In order to use this inversion technique, one requires pulse-echo measurements from all incident directions $\hat{k}$. The characteristic function is then obtained (Eqn. 2.4) as an inverse Fourier transform which involves integrating over both $|\vec{k}|$ and $\hat{k}$. For the class of ellipsoidally shaped flaws, one can obtain all relevant information about the flaw by inverting each pulse-echo record independently as discussed below. This avoids the angular integration over $\hat{k}$ in the inverse Fourier transform, and significantly simplifies the application of the algorithm.

In order to illustrate how this simplification comes about, let us consider the weak scattering limit. Then the theory of the last section is rigorously valid and Eqn. 2.2 becomes

$$S(2\vec{k}) = \text{const.}\; A_{L\to L}(\vec{k}) \,/\, k^2 \tag{3.1}$$

We have used the fact that $a(\hat{k},\{\mu\})$ is a constant in the weak scattering limit as a function of $\hat{k}$. For an ellipsoid we know that $S(2\vec{k})$ is given by the following equations

$$S(2\vec{k}) = \frac{\sin(2\,k\,r_e) - 2\,k\,r_e\cos(2\,k\,r_e)}{(2\,k\,r_e)^3} \quad . \tag{3.2}$$

and

$$r_e = (a_x^2\cos^2\theta\sin^2\phi + a_y^2\cos^2\theta\cos^2\phi + a_z^2\sin^2\theta)^{\frac{1}{2}} \tag{3.3}$$

Here the axes of the ellipsoid are $a=(a_x,a_y,a_z)$, and θ and ϕ define the direction of $\hat{k}$ in spherical coordinates. The angular dependence of the shape factor comes in strictly through the function which we have called $r_e(\theta,\phi)$. In a pulse-echo measurement, the incident direction $\hat{k}$ is kept fixed, and r_e is a constant for that set of data. We note for a fixed incident direction, Eqn. 3.2 has the same form as a Fourier transform of a sphere with an effective radius r_e. For each incident direction $\hat{k}$, we obtain r_e in the following way. First we obtain $S(2|\vec{k}|)$ from Eqn. 3.1. Then we extend $S(2|\vec{k}|)$ to be spherically symmetric in $\vec{k}$-space. Thus we obtain the three-dimensional Fourier transform of a sphere of radius $r_e(\theta,\phi)$. This Fourier transform is then inverted to yield

the effective radius for that direction. The resulting, calculated, effective radius will vary according to Eqn. 3.3. An important consequence of Eqn. 3.3 is that pulse-echo measurements along the axis of an ellipsoid yield the axis length directly. For example, a measurement along the a_x axis yields an effective radius equal to a_x. Hence one can obtain the length of the ellipsoid axes directly from three measurements if one knows the orientation of the ellipsoid.

So far we have been discussing the weak scattering limit for the sake of illustration. The appropriate extension to the strong scattering case is straightforward. Eqn. 2.2 is

$$S(2k) \approx \text{const. } A_{L\to L}(\hat{k})/(k^2\, a_{QSA}(\hat{k},\{\mu\})) \qquad (3.4)$$

For a given incident direction $a(\hat{k},\{\mu\})$ is just a constant since it doesn't depend on $|\vec{k}|$ in the quasi-static approximation. With this approximation we recover Eqn. 3.1 and can proceed in an approximate way with the entire procedure which was given above. Of course, for a strongly scattering flaw, our analysis is only approximate and must be checked empirically. In the next section we provide some empirical tests of the strong scattering limits.

Results: Test of Inversion Procedure

Here we report our tests of the proposed inversion algorithm. These results are given in two parts. First we report tests for spherical voids. Then we report preliminary results for the case of a 2-1 oblate spheroidal cavity in Ti. The most direct test of our inversion procedure is shown in Fig. 2. Here we show the results of inverting experimentally obtained ultrasonic scattering amplitudes for a spherical void in Ti.[3] For this case the band width of the data was $.5<kR<4$, where we use R to denote the radius of the sphere. As can be seen, the inversion algorithm does a good job of determining the flaw radius (even in this experimentally realistic case with a rather restricted bandwidth).

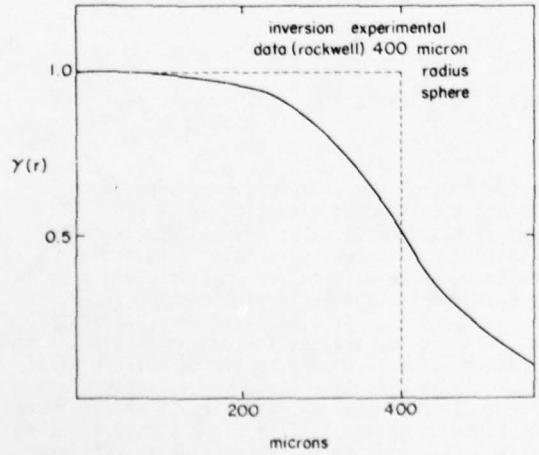

Fig. 2 Calculated characteristic function for a 400μ void. This result was obtained by inverting experimental ultrasonic scattering amplitudes with a bandwidth of $.5<kR<4$, with R the radius of the sphere.

In order to further test our inversion procedure, we considered the case of spherical voids in stainless steel and Ti, and the case of an aluminum inclusion in Ti.[4] For these cases we can obtain the exact theoretical scattering amplitudes from the calculations of Ying and Truell.[5] Using these results for $A_{L\to L}(\hat{k})$, we determined $S(2\vec{k})$ from Eqn. 2.2 for a bandwidth, $0 < kR < 10$. The result for the case of a spherical void in Ti is shown in Fig. 3. Quite good definition of the radius and hence the volume is obtained. These results are characteristic of the results for the other cases mentioned above. Finally, in order to test the stability of the routine to noise, we introduced random Gaussian noise into the scattering amplitudes. The inversion procedure proved to be quite insensitive to random noise. In Fig. 4 we show the result for the Ti spherical cavity when the signal contains 50% Gaussian random noise. Note that the inclusion of noise did not appreciably effect the determination of the flaw radius.

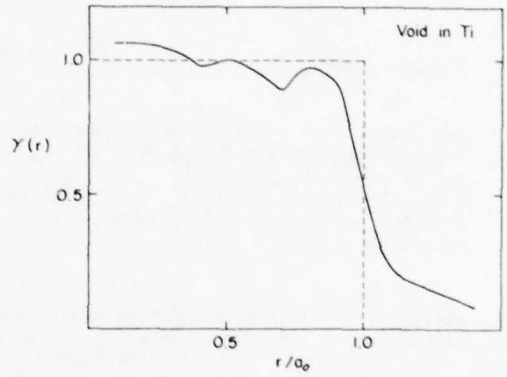

Fig. 3 Calculated characteristic function for a spherical void of radius a_0 in Titanium. The result was obtained by inverting theoretical scattering amplitudes. The bandwidth used above was $0 < k\, a_0 < 10$.

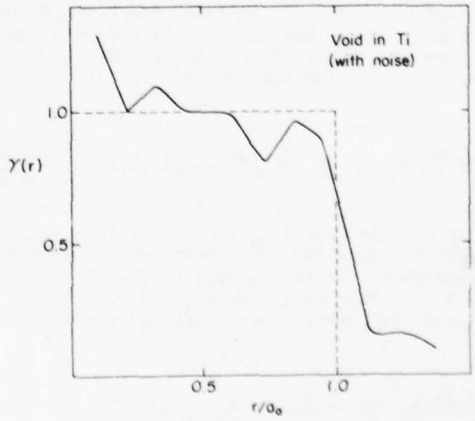

Fig. 4 The relatively weak effects of noise on the inversion procedure is illustrated. Here we show the same calculation as in Fig. 3 for a void in Ti but have included a random component in the signal (the random component is on the average 50% of the exact signal). Note that the determination of the radius of the sphere is hardly effected by the inclusion of this extremely large random error.

We, also, report preliminary results for inverting the scattering amplitudes from a 2-1 oblate spheroid using the simplified theory of section II. Here the scattering amplitudes used in the inversion procedure were theoretical results provided by W. Visscher who used a series expansion technique capable of providing numerically exact results.[6] Our preliminary analysis consisted of considering only two different pulse-echo measurements. The first calculation was for a beam incident along the symmetry axis ($\theta = 0°$). The second calculation was for a beam incident in the plane of the spheroid ($\theta = 90°$).

The results obtained for the length of the axes are:

	calculated	exact
major axis	850	800
minor axis	360	400

The calculated ratio of axes was .42 while the exact result is .50. Finally, we note that the computed volume is equal to the exact volume of the spheroid within our calculational accuracy.

Discussion and Conclusions

We have proposed a method for determining the size, shape and orientation of flaws in elastic media. This inversion procedure is rigorous in the weak scattering limit. For strongly scattering flaws the validity of the inversion procedure was uncertain. Hence, we performed empirical tests for strongly scattering flaws. We have concentrated on voids since they are strong scatterers and are important in various fracture processes. For spherical voids in Ti, we obtained strikingly good results in determining the flaw radius and volume. For these tests we used both experimentally measured and theoretically generated scattering amplitudes in different examples. We have also reported preliminary results for a 2-1 oblate spheroidal void in Ti. Here our preliminary calculations indicated excellent agreement for the flaw volume, and satisfactory agreement for the relative length of the axes. We have not yet been able to test the procedure for its sensitivity to the orientation of the flaw. If future tests over a wider range of flaw shapes continue to give good determinations of the flaw volume, this will have important consequences for determining the material parameters of the flaw as will be discussed below. Currently, work is in progress with several groups to obtain experimentally and theoretically generated scattering amplitudes for a wide range of axially symmetric flaws: prolate and oblate spheroids and pill boxes (both voids and inclusions will be considered).[7] These efforts should result in an extensive empirical test of the inversion algorithm and give a good idea of its range of validity.

We have concentrated in this paper on determining the characteristic function of a flaw from a determination of the shape factor. As discussed in another talk in these proceedings, there is additional information about the shape of the flaw in the long wavelength factor $a_{QSA}(\hat{k},\hat{u})$.[8] Together with the inversion algorithm which we have proposed in this paper, it appears likely that not only the size, shape, and orientation of simple volume flaws may be obtained, but also we may be able to determine the material composition of the flaw. An example of one way the two techniques may be used together to determine the density of the material in the flaw region is discussed below.

Kohn and Rice[9] have shown that the long wavelength scattering amplitudes can be used to determine the mass defect, ΔM, of the flaw. ΔM is the difference in mass of the flaw and the mass it would have if there were host material in the flaw region. Together with an accurate knowledge of the flaw volume, V, one may infer the density of the flaw material

$$\rho_{flaw} = \rho_{host} + \frac{\Delta M}{V} \tag{5.1}$$

If sufficient accuracy can be obtained in the inversion algorithm which determines V and in the determination of ΔM, then one should be able to infer the material composition of the flaw. It should be stressed that such a determination depends on an absolute measurement of the scattered power.

In conclusion, we note that the general formalism (Eqn. 2.1 to 2.4) applies in principle to not only volume type flaws but also to crack like defects.[10] Again, the correspondence should be exact for weakly scattering flaws. We have not had the necessary data to test the algorithm yet for the strongly scattering case. However, this work is in progress, and we hope to provide an empirical determination of this technique for the case of cracks in the near future.

ACKNOWLEDGMENTS

We would like to thank Drs. Vasu and Vijay Varadan, Bill Visscher, Dick Elsley, and Bernie Tittmann very gratefully for their various aids.

This research was sponsored by the Center for Advanced NDE, operated by the Science Center, Rockwell International, for the Defense Advanced Research Projects and the Air Force Materials Laboratory under Contract F33615-74-C-5180.

REFERENCES

1. J.E. Gubernatis, Proc. ARPA-AFML Review of Quantitative NDE, Cornell University (AFML Report), 1977; and Los Alamos Scientific Laboratories Report LA-UR-771339.

2. M.F. Whalen and A.N. Mucciardi, Proc. ARPA-AFML Review of Quantitative NDE, University of Calif., San Diego (AFML Report), 1978.

3. These experimental scattering amplitudes were provided by R. Elsley of the Rockwell International Science Center.

4. J.H. Rose and J.A. Krumhansl, Material Science Center Report #2846, Cornell Univ., (1977) unpublished. A copy of this report can be obtained by writing to the first author.

5. C.F. Ying and R. Truell, J. Appl. Phys. 27, 1086 (1956).

6. W. Visscher kindly made available his calculations for the L→L scattering amplitudes for a 2-1 oblate spheroid prior to publication. Similar results were also kindly provided by V.V. Varadan.

7. The persons involved are: 1) B. Tittmann and R. Elsley at the Rockwell International Science Center and V.V. Varadan and V.J. Varadan at Ohio State University.

8. J.M. Richardson, Proc. ARPA-AFML Review of Quantitative NDE, UCSD (AFML Report), 1978.

9. W. Kohn and J.R. Rice (submitted to J. Appl. Phys.).

10. E. Domany, J.A. Krumhansl and S. Teitel, J. Appl. Phys. 49, 2599 (1978).

DISCUSSION

Norman Bleistein (Denver Applied Analytics): Are your data far field data?

Jim Rose (Cornell): I don't really know the answer to that question. Certainly the theoretical data are far field. I don't really know about the experimental data.

Norman Bleistein: That is very important though, because if you are in a far field regime, there is another justification for ending up with your Fourier Transform results.

Jim Rose: I have not worked in the high frequency regime in establishing a justification for this procedure. What I have done is to justify the low frequency regime and to extend it to higher frequencies.

Gordon Kino (Stanford University): Is the high frequency regime any different from just using straight pulse-echo and getting the reflection which should be proportional to the radius of curvature?

Jim Rose: Of course, if you are in the very high frequency regime, you are absolutely correct. If you come down, as Achenbach has indicated, it is probably not too bad a procedure if you put in these corrections to get down to KA = 1. The kind of flaws I am interested in are flaws where you have a band width of KA of about 5.

James Krumhansl (National Science Foundation): What you say about the imaging part is absolutely true.

Gordon Kino: I am not saying imaging; I am just saying straight pulse-echo.

David Lee, Chairman (Applied Mechanical Research Laboratory): I have a question for the speaker. Is there something a little bit inconsistent in the fact that your model is accurate for wave lengths that are long compared to the scatterer and yet, the Fourier Transform has in it sharp information about gamma which results from higher frequencies?

Jim Rose: Right. I think the way to answer this is that the Born approximation is not good in the frequency domain. However, it gets the first peak and first valley rightly. It is off quantitatively in a differential sense, but it has got a peak and a valley where a peak and a valley ought to be and it has got *another* peak up where the second peak ought to be. Again, they are off in frequency. I see this as an integrated, average way to find the position of the first peak. You know that you can essentially take the position of the first peak from the sphere and guess the radius darn well. If you just look at the position of the first peak itself, that is a differential quantity. Here I have got an integral average. That's how I would understand it. The kernel is multiplied by an interference pattern and that is the same as averaging.

David Lee, Chairman: Forgive me, but one more question on this. Of course, the numerical inversion model like Fourier Transforms is one of the archtypical field force problems; one suspects that your insensitivity to noise arises because of whatever you did had the effect of a low pass filter.

Jim Rose: Absolutely. That's the beautiful thing about the Born approximation for elastic waves. In the long wave length limit, you get information on the size of the object. That is where you get your best information; the opposedness, I think, comes out because you have got a limited band width of higher frequencies and I have got long wave lengths.

Phillip Hodgetts (Los Angeles Div., Rockwell): Did I hear you say that you injected random noise in the experiment to duplicate noise in titanium?

Jim Rose: No, I took Gaussian random noise into my theoretical data that I had generated and, not knowing anything more about it, I simply added a random amount to each number, 50 percent.

Phillip Hodgetts: The reason I am asking is that down in the real world where I work, where we look at titanium with our present crude methods, what we call noise is really a misnomer because it is absolutely repeatable and it comes up all the time.

Jim Rose: I think the point again is that my information is really in the position of the first peak in some averaged way. Now, you can move things around differentially by putting in small cracks and influence the low frequency behavior, but their main influence is at high frequency where K is of the size of a little flaw. I am getting the information out basically at lower frequencies. So I think I just average out there.

Phillip Cook (University of Houston): There is literature in radar which says that if you will send towards the void a ramp-shaped pulse and detect that ramp-shaped pulse in the time domain, then you can get information which is related to the area of the void. I think it all carries over very closely to this theory. It is all based on the long wave length approximation, and is based upon the face that the surface is radiating.

AD-A071 047 ROCKWELL INTERNATIONAL THOUSAND OAKS CALIF SCIENCE --ETC F/G 14/2
PROCEEDINGS OF THE ARPA/AFML REVIEW OF PROGRESS IN QUANTITATIVE--ETC(U)
JAN 79 D O THOMPSON F33615-74-C-5180
UNCLASSIFIED SC595.51AR AFML-TR-78-205 NL

5 OF 6
AD A071047

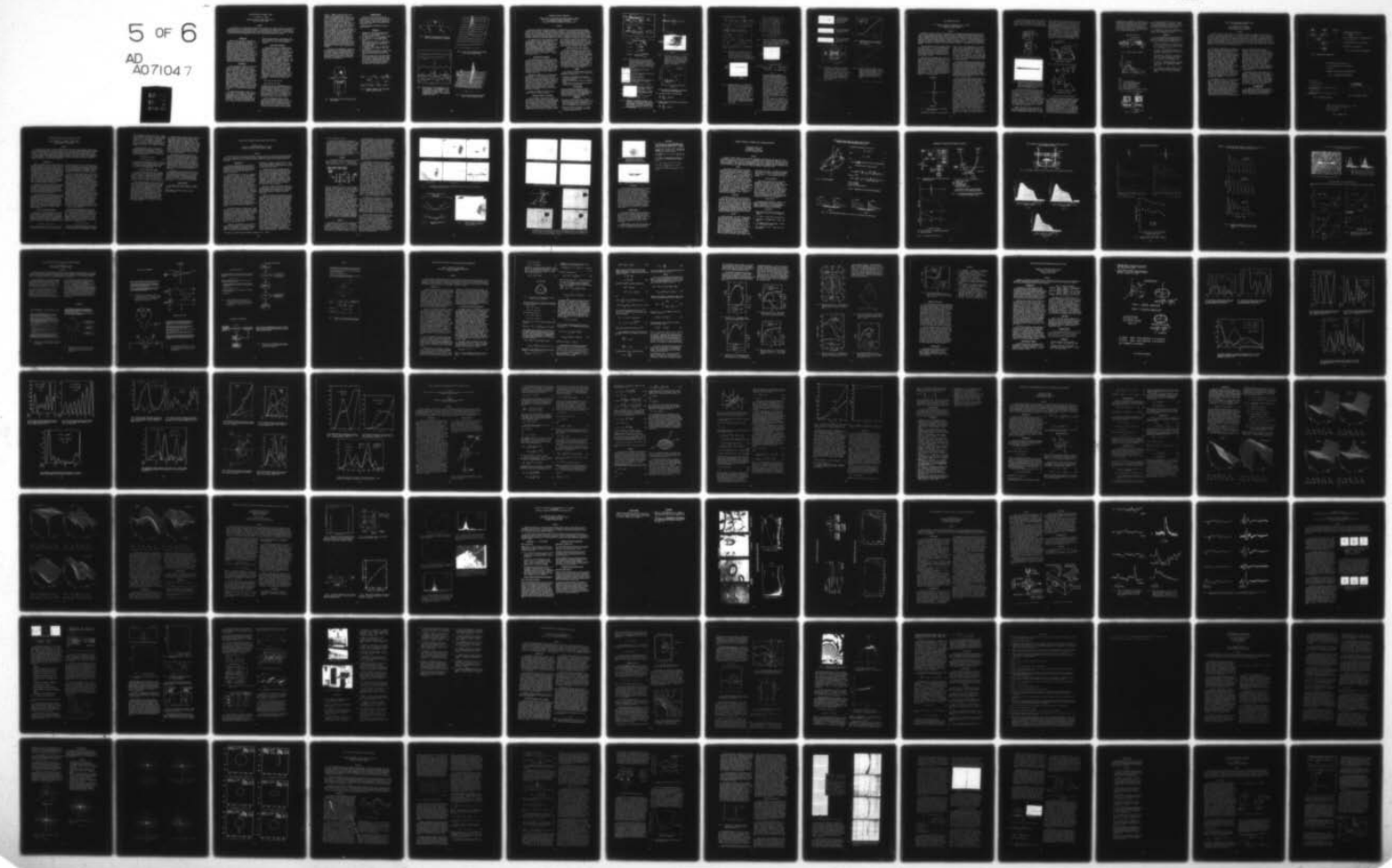

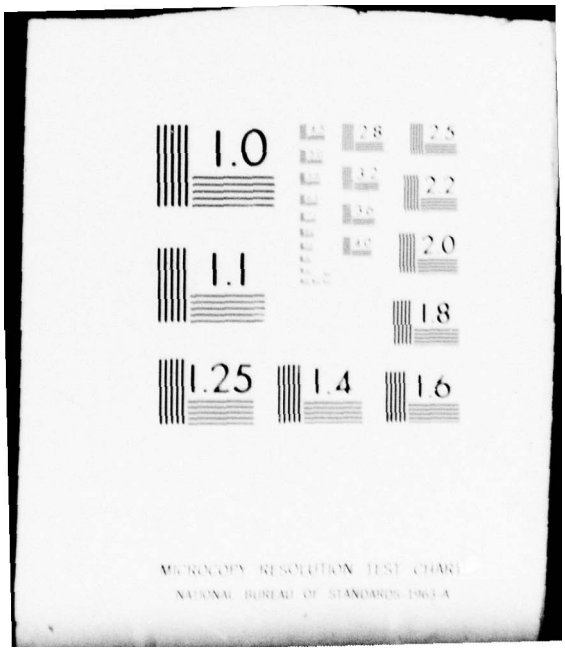
1.0
1.1
1.25
1.4
1.6
2.8
3.2
3.6
4.0
2.5
2.2
2.0
1.8
MICROCOPY RESOLUTION TEST CHART
NATIONAL BUREAU OF STANDARDS 1963-A

LASER PHOTOACOUSTIC TECHNIQUE FOR NDE

Y.H. Wong and R.L. Thomas

Department of Physics, Wayne State University
Detroit, Michigan 48202

ABSTRACT

The technique of laser photoacoustic spectroscopy is applied to the studies of surface and sub-surface structures of solids in a nondestructive fashion. In the present case, special attention is focused on reaction-bonded Si_3N_4 ceramics, which are used for the manufacturing of turbine blades. Good correlation is obtained between the observed photoacoustic signal and surface microstructures. In addition, the photoacoustic signal reveals inhomogeneities that are not visually detected under a microscope.

INTRODUCTION

Recently, there has been considerable interest in a "new" spectroscopic technique called photoacoustic (or optoacoustic) spectroscopy.[1,2] Although the photoacoustic effect was discovered by A.G. Bell in 1880,[3] and although it has been used for many years to perform optical studies on gases,[4] it was not until 1973 that this effect was developed[5] into a spectroscopic tool for the optical investigation of solid materials. In the last four years, photoacoustic spectroscopy has been found to be a very useful technique for research and analysis, not only in Physics and Chemistry, but also in Biology and Medicine.[6] It is especially well suited for investigating amorphous and powder systems in which the Rayleigh scattering makes transmission and reflectance studies difficult.

EXPERIMENTAL

In this technique, a sample is placed inside a specially designed cell (resonant or non-resonant acoustically)[1] containing a suitable gas and a sensitive microphone. A non-resonant PAS cell used in the present study is shown in Fig. 1. The sample is then illuminated with chopped radiation as shown in Fig. 2. Light absorbed by the sample is converted, in part, into heat by non-radiative de-excitation processes[1] within the sample. The resulting periodic heat flow from the sample to the surrounding gas creates pressure fluctuations in the cell, which are detected by the microphone as a signal which is phase coherent at the chopping frequency. The signal is subsequently analyzed by a lock-in amplifier and displayed on the x-y recorder, either as a function of the wavelength of the incident radiation, or as a function of the scanning position.

The resulting photoacoustic signal is directly related[7] to the amount of light absorbed by the sample. This is especially the case for highly opaque and low fluorescence systems. Furthermore, since only the absorbed light is converted to sound, scattered light presents no difficulties. A quantitative treatment[7] shows that, in addition, both the magnitude and the phase of the photoacoustic signal depend on the thermal properties of the sample and those of the gas in the cell, as well as on the chopping frequency.

RESULTS AND DISCUSSIONS

In the present report, we demonstrate that the technique can be applied to study the microstructures of solid surfaces, i.e. for non-destructive evaluation (NDE) of surface flaws and sub-surface inhomogeneities. The geometric considerations for flaw detection at or near the surface are shown in Fig. 3. As the laser beam illuminates the sample, a well-defined effective volume, $V_{eff} = a x d_{eff}$ is heated because of absorption of the electromagnetic radiation. The area A depends on the focusing of the laser light and can be as small as $\sim 10^{-12} m^2$. A characteristic optical penetration depth d_{op} = (absorption coefficient)$^{-1}$ exists, which depends on the wavelength of the incident light. In addition, the chopping frequency dictates an effective thermal diffusion length $d_{th} = \sqrt{\frac{\kappa}{\rho C \omega}}$ for the heat to couple to the gas environment. Here, κ is the thermal conductivity, C is the specific heat, ρ is the specific gravity of the sample, and ω is $2\pi x$ (chopping frequency). It is a combination of these two effects which limits the depth of the material evaluated. Therefore, we define an effective absorbing depth d_{eff} given by

$$d_{eff} = d_{th}, \text{ for } d_{th} < d_{op} \text{ and}$$

$$d_{eff} = d_{op}, \text{ for } d_{th} > d_{op}.$$

The presence of flaws or inhomogeneities in the illuminated region will change the effective volume (optically and thermally). If the flaw is a different material (foreign inclusion) than the host, the absorption coefficient will also differ. If a crack or a void is present, the effective volume will differ. The combination of these effects will give rise to a change in the magnitude and phase of the acoustic signal.

We have investigated a number of silicon nitride ceramic samples[8] with chopping frequencies ranging from 50 to 2000 Hz. Some of the samples have surface cracks approximately 50μm x 100μm, which are visible under the microscope. Others show no obvious surface cracks. In Fig. 4, typical traces are shown of the photoacoustic

signal (F = 800Hz) as one scans across such surfaces. The surface profile is very reproducible for repeated scans along the same line, as illustrated by traces (a,b) and (d,e). Also, as one improves the focus, the resolution improves accordingly, and more detailed microstructure is revealed as illustrated in traces d and e in Fig. 4. For these traces, the diameter of the minimum focal point is ~30μm. The difference between samples with and without cracks is also evident in Fig. 4. This is further illustrated in Fig. 5 and 6, where an x-y scan is presented. We find a reasonably good correlation between the photoacoustic signal with features which are observed under the microscope. Furthermore, the photoacoustic signal shows features not detected visually with a microscope. These sub-surface features may be related to the presence of nitrogen deficient clusters or to precipitated impurities such as silicides.[9] Spectroscopic experiments utilizing a tunable dye laser should provide information for more precise identification, both of the chemical composition and the depth of these inhomogeneities. Such studies are presently in progress.

In conclusion, the photoacoustic technique has the capability of characterizing surface and sub-surface structures in condensed matter, as illustrated in these preliminary studies on the technically important silicon nitride ceramics. We believe that the technique also shows excellent promise for nondestructive evaluation applications to other materials.

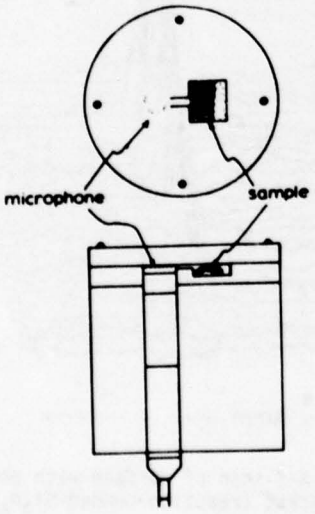

Fig. 1 Non-resonant PAS cell with Si_3N_4 turbine blade sample.

ACKNOWLEDGEMENTS

The authors would like to express their thanks to Dr. J. Fisher and D. Cassidy for providing the silicon nitride turbine blades, and to Drs. R. Terhune, P. Selzer, and T. Kushida for their helpful discussions on the design of the photoacoustic cell.

Research supported by AFOSR under Grant No. AFOSR-77-3374.

REFERENCES

1. "Optoacoustic Spectroscopy and Detection," edited by Y.H. Pao (Academic Press, N.Y. 1977) and references therein.
2. A. Rosencwaig, Rev. Sci. Ins. 48, 1122 (1977).
3. A.G. Bell, Am. J. Sci. 20, 305 (1880).
4. M.F. Delaney, Sci. Prog. London 47, 459 (1959).
5. See A. Rosencwaig's article in "Optoacoustic Spectroscopy and Detection," edited by Y.H. Pao (Academic Press, N.Y. 1977) for historical development.
6. A. Rosencwaig, Anal. Chem. 47, 592A (1975).
7. A. Rosencwaig and S. Gersho, J. App. Phys. 47, 64 (1976).
8. The samples are small pieces of turbine blade made of reaction-bonded Si_3N_4 and appropriately sliced to the size of 1cm x 1cm x 1mm.
9. It was noted that on the cross-section after cutting the turbine blade into small pieces and ultrasonic cleaning, there exists spots of the size of D ~100μm beneath the surface. This, we think, may be due to nitrogen deficient clustering of the silicon atoms in the formation of the ceramic material.

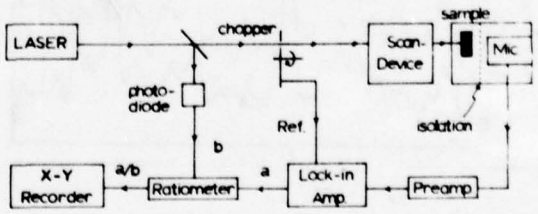

Fig. 2 Schematic diagram of the laser photoacoustic scanning system.

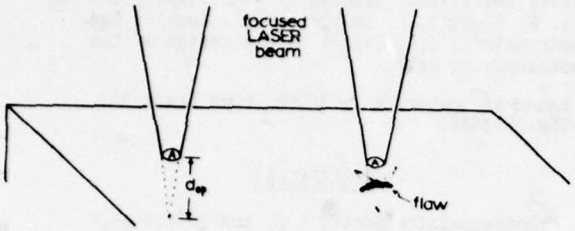

Fig. 3 Geometric consideration of flaw detection with the photoacoustic technique.

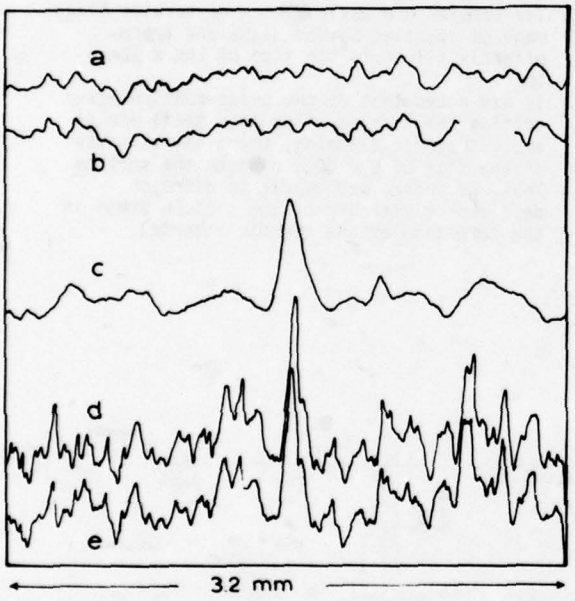

Fig. 4 Typical traces of the photoacoustic signal (F=800 Hz). (a,b) Repeated scan on surface with no obvious crack; (c) scan on surface with obvious cracks; (d,e) repeated scan on surface (c) with better focused laser beam.

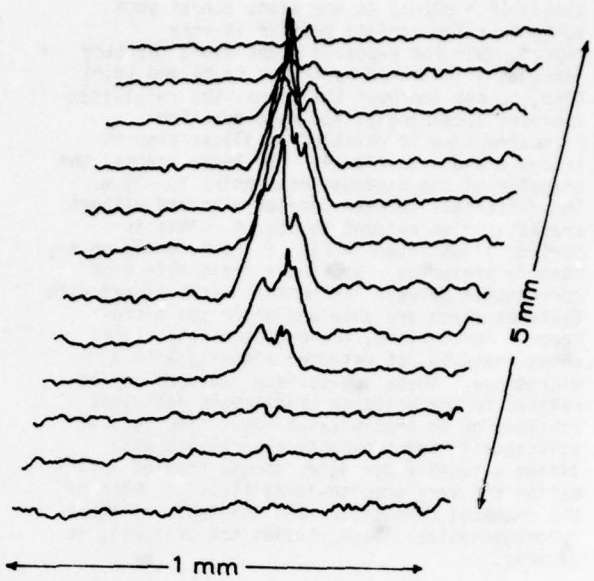

Fig. 5 An X-Y scan of surface with obvious cracks; (hot pressed Si_3N_4).

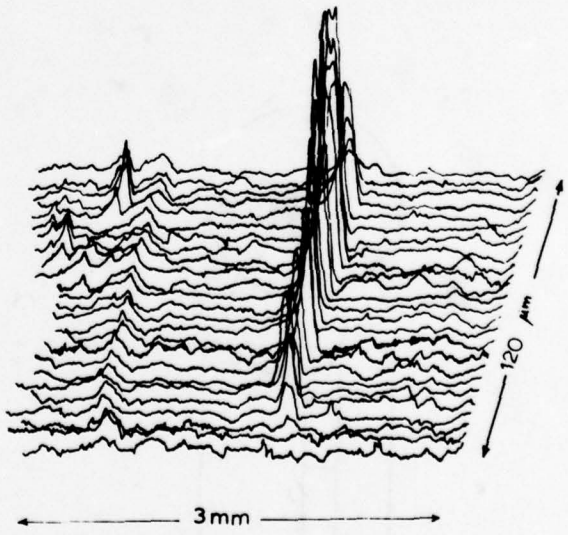

Fig. 6 An X-Y scan of surface with obvious cracks; (reaction-bonded Si_3N_4).

INTEGRATED ULTRASONIC TRANSDUCER

Richard M. White, Sze-Hon Kwan, Kent Chuang, Richard S. Muller
Department of Electrical Engineering and Computer Science
and Electronics Research Laboratory
University of California, Berkeley, California 94720

ABSTRACT

The typical transducer considered consists of a piezoelectric film, and associated electrodes, connected to one gate of a dual-gate field-effect transistor in the silicon wafer on which the piezoelectric film is situated. An individual transducer responds to various modes of excitation (flexural, surface, bulk) at frequencies which may range from far below one Hertz to hundreds of megahertz. The second gate of the field-effect transistor can be used for electrical amplitude control or for mixing purposes. Connection of a number of these small transducers together to form arrays permits realizing ultrasonic receiving devices having variable directivity, and progammable surface-wave signal processors.

The transducer structures considered are shown in cross section in Fig. 1 (the vertical scale is exaggerated) with schematic symbols for easy representation. In the PI-DMOS transducer a single-gate field-effect transistor has a piezoelectric ZnO film deposited in the gate region on top of a thermally-grown SiO_2 layer. In the lower structure a commercial dual-gate double-diffused MOS transistor has one gate connected to a deposited piezoelectric ZnO film. Figure 2 shows the four modes of excitation of this transducer. Some waveforms appear in Fig. 3.

THE INDIVIDUAL TRANSDUCER

Upon comparing the two transducer structures, one notes that the PI-DMOST structure offers both piezoelectric and pyroelectric response down to zero frequency owing to isolation of the ZnO film by high-quality thermally-grown SiO_2. Fabrication of the second transducer structure is safer as no sputtering in the gate region is required. The second structure offers additional design freedom in the shaping of the piezoelectric region (hence control of directivity) and in its area for control of transducer sensitivity.

Response of PI-DMOST and the dual-gate sensor to application of static strain in a cantilever fixture (Fig. 4). At top, voltage across load resistance decreased as source-drain current dropped when strain was applied and remained at constant value for duration of test, 17.8 hours, after which it returned to original value. Lower scope trace shows that no dc response is observed with the second structure in which the ZnO film is not isolated by thermally-grown SiO_2. It appears possible to provide such isolation with the dual-gate sensor if desired.

In Figs. 5-7 temperature sensitivity and dimensional design criteria are given.

ELECTRICAL CONTROL OF TRANSDUCER

In the PI-DMOST a voltage may be applied externally to the gate, and in the dual-gate transducer (second structure) one may utilize the second gate to control the response to a signal applied via the piezoelectric film connected to the first gate. The amplitude of response can be adjusted with a control voltage V_{G2}. Sampling of a low frequency output can be achieved by means of sampling pulses of short duration. Mixing in the dual-gate transistor is achieved by application of a local oscillator signal at the second gate. In signal-processing arrays based on use of a number of these transducers, separate pieoelectric films could drive first and second gates to provide nonlinear coupling of different input signals.

TRANSVERSAL FILTER SIGNAL PROCESSOR

Dual-gate transducers can be connected in an array to form a transversal filter structure as shown in Fig. 11. Although dependence of transducer amplitude upon second gate bias is nonlinear over part of its range (Fig. 12), by differencing two such transistor outputs a highly linear dependence of amplitude or tap weight upon bias is obtained, simplifying setting of tap weights (Fig. 13). An array processor operating near 27 MHz is being fabricated at present. Arrays of these transducers with second-gate control of weighting also appear attractive for use as ultrasonic receiving (and perhaps also transmitting) devices for scanning in defect characterization.

SUMMARY

The integrated transducers based on use of a piezoelectric film and field-effect transistor are versatile devices offering

-- response to various modes of excitation
-- wide frequency response from dc if desired to hundreds of megahertz
-- useful electronic control within the transducer itself
-- possibility of interconnection into arrays for signal processing and detection.

ACKNOWLEDGMENT

Research sponsored by the National Science Foundation Grant ENG76-21818 and the Center for Advanced NDE operated by the Science Center, Rockwell International, for the Advanced Research Projects Agency and the Air Force Materials Laboratory Contract F33615-74-C-5180.

REFERENCES

"Detection of Acoustic Waves with a PI-DMOST Transducer," K. W. Yeh, R. S. Muller, S. H. Kwan, Proc. 8th Conference (1976 International) on Solid State Devices, Tokyo, 1976, Jap. J. Appl. Phys. 16, Supplement, 16-1, 527-521 (1977).

"Integrated Ultrasonic Transducer," S. H. Kwan, R. M. White, R. S. Muller, Proc. 1977 IEEE Ultrasonics Symposium, 843-846.

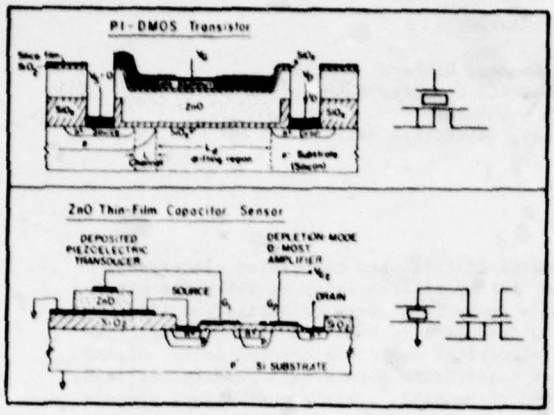

Fig. 1

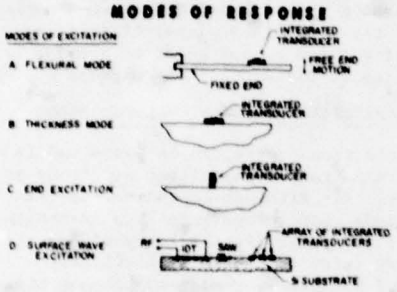

Fig. 2 Modes of excitation of the transducer. All four types of response have been observed experimentally, at frequencies ranging (for the PI-MOST structure) from less than one Hz in the flexural mode to about 90 MHz with surface acoustic wave excitation.

RF source to PZT-5. Vertical scale=1v/div

PI-DMOST output with bias turned off Vert. scale=50mv/div

RF source to PTZ-5, Vertical scale=1v/div

PI-DMOST output with bias turned off -Response delay =21μs. Vertical scale=50mv/div

Horizontal scale = 5 μs/div Freq = 6.25 M Hz

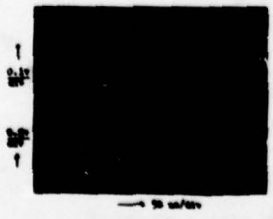

Top trace: output from interdigital transducer delay time = 4.2 μs

Bottom trace: response from D-MOST delay time = 5 μs

V_{DS} = 11v V_{G2} = -Pv · ·

I_{Do} = 9.4 mA

Fig. 3. Response of a PI-DMOST transducer (first structure) to bulk waves at 5 MHz and the ZnO dual-gate device (second structure) to SAW at 90 MHz. In latter, an output from an IDT on the same silicon wafer is shown for comparison.

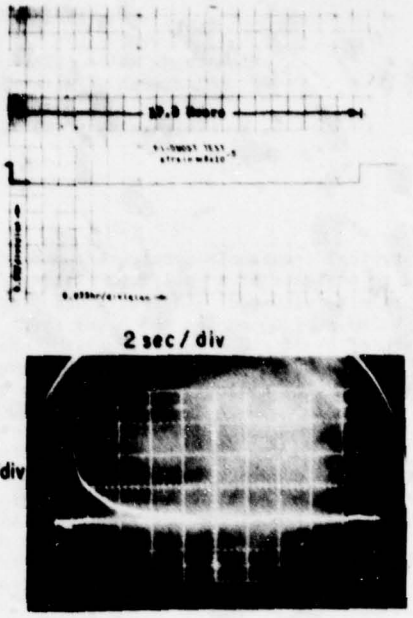

Fig. 4

Fig. 5 Temperature sensitivity of PI-DMOST. Owing chiefly to pyroelectric effect, threshold voltage changed each time temperature was altered and remained constant during the approximately 20 minutes of each step during which temperature was stable.

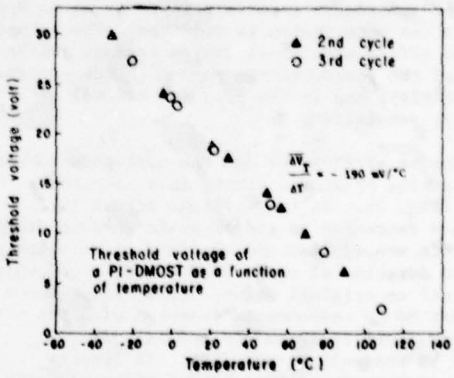

Calculated Temperature Dependence of Threshold Voltage for PI-DMOS Transducer

(1) Pyroelectric effect in the ZnO layer

$$\frac{\Delta V_T}{\Delta T} = \frac{Q_{PI}}{C_{ZnO}} \approx -160 \text{ mV/°C}$$

(2) Thermal mismatching between the ZnO layer and the substrate

$$\frac{\Delta V_T}{T} = \frac{Q_{P2}}{C_{ZnO}} \approx -30 \text{ mV/°C}$$

(3) Contribution from the Si substrate

$$\frac{\Delta V_T}{T} = -\frac{1}{T}\left(\frac{E_g}{2} - |\phi_{fp}|\right)\left\{1 - \frac{1}{C_o}\frac{Q_B}{2\phi_{fp}}\right\} \approx -10\ \text{mV/°C}$$

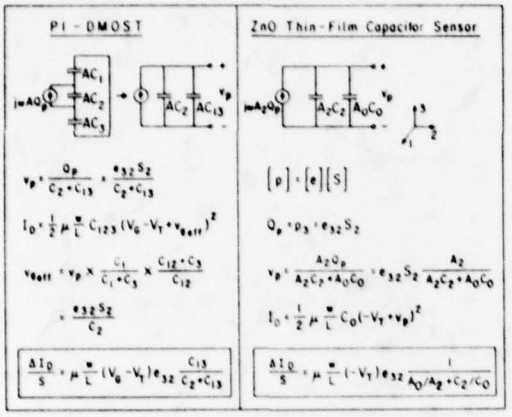

Fig. 6 Equivalent circuit models for the two transducer structures showing dependences upon area and capacitance per unit area ratios for ZnO (denoted 2), upper and lower oxides in PI-DMOST (1 and 3), and gate oxide in dual-gate DMOST (0).

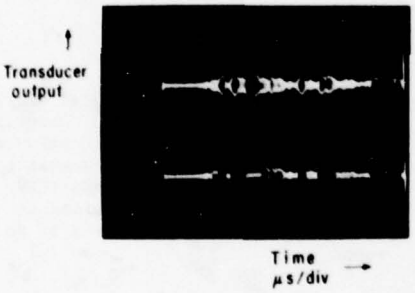

Fig. 8 Amplitude Control. Top trace of Fig. 8 shows output of dual-gate sensor in response to acoustic bulk longitudinal wave excitation at approximately 5 MHz with constant dc bias on second gate and signal applied to first gate. Lower trace shows effect of reduced gain near center of trace resulting from an 8 microsecond negative pulse superimposed on the dc second-gate bias. Such amplitude control could be used to deaden receiving transducer during "main bang" of nearby transmitting transducer or to select a portion of the output for display.

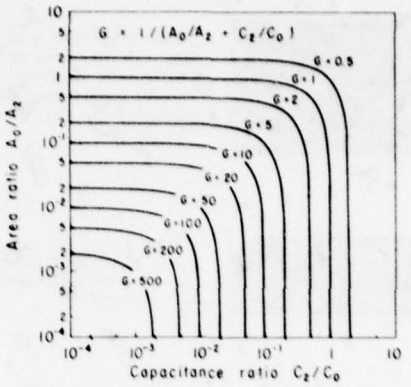

Fig. 7 Gain factor appearing in expression for sensitivity of second structure as function of area and specific capacity ratios. Typical transducer design would have gain factor ranging from 10 to 100.

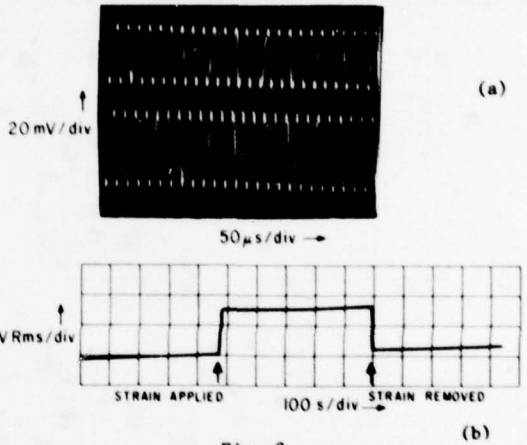

Fig. 9

Frequency Translation (Mixing).

(A) Frequency shifting with PI-DMOST. In Fig. 9 50 kHz CW voltage was superimposed on the gate electrode of the first transducer structure during low-frequency strain measurements. Transducer output is at 50 kHz permitting use of lock-in detection and plotting on a chart recorder. Upper trace in photo shows output of transducer in non-strained state; lower trace shows output when strain is applied (roughly 8×10^{-5} strain magnitude). Portion of chart recording (Fig. 9b) shows corresponding output of lock-in amplifier (shift in baseline is believed due to drift of ions in gate oxide under influence of dc gate bias).

(B) Mixing in dual-gate transducer (Fig. 10). With signal on first gate the application of a local oscillator signal at second gate can produce mixing in the integrated transducer itself and output at an intermediate frequency. Maximum sum or difference output is observed when dc second-gate bias is adjusted for maximum rate of change of transconductance with second-gate bias voltage.

OUTPUT DISPLAYED DIRECTLY (NO LOCAL OSCILLATOR ON SECOND GATE) IN RESPONSE TO 5.5 MHz COMPRESSIONAL WAVE EXCITATION. 1=S/DIV. HORIZONTAL SCALE.

MIXING IN DUAL-GATE TRANSDUCER. LOCAL OSCILLATOR 25.8 MHz. OUTPUT OF 30 MHz IF AMPLIFIER WITH DETECTOR.

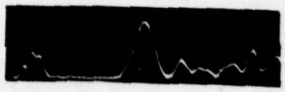

MIXING IN DUAL-GATE TRANSDUCER. LOCAL OSCILLATOR 35.2 MHz. OUTPUT OF 30 MHz IF AMPLIFIER WITH DETECTOR.

Fig. 10

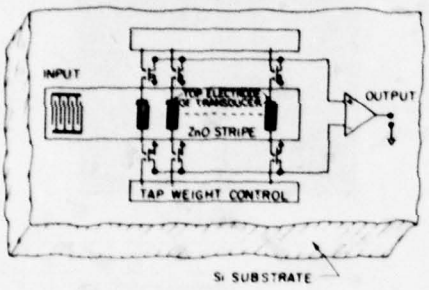

Fig. 11 Arrangement of transducers in differencing circuit to form SAW transversal filter processor. Outputs of the individual taps, the ZnO stripes with their electrodes, are amplified by controlled amounts by dual-gate transistors whose gains are set by the tap-weight block. Entire device could be integrated on a single silicon wafer. Bias circuitry is not shown.

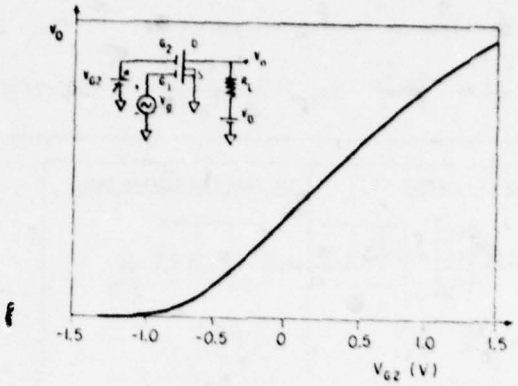

Fig. 12 Dependence of gain of a single dual-gate transistor upon control gate bias voltage V_{G2}.

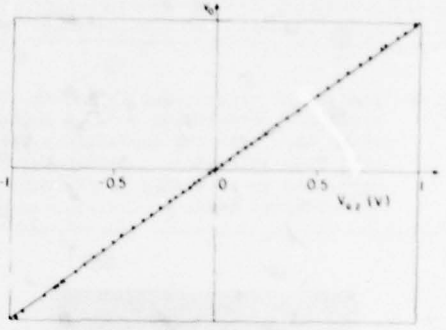

Fig. 13 Results of test of a simulated single tap in differencing scheme. Control biases of equal and opposite value were applied to two dual-gate transistors connected to differential amplifier. Analysis of result shows output is linear to within ±1 db over a 51 db range.

PVF_2 TRANSDUCERS FOR NDE

W. H. Chen, H. J. Shaw, D. G. Weinstein, and L. T. Zitelli
Ginzton Laboratory, Stanford University
Stanford, California 94305

ABSTRACT

We report on recent calculations and experiments on the broadband properties and impulse characteristics of PVF_2 transducers and arrays. Experimental wedge transducers show bandwidths of approximately 100% in the excitation of surface acoustic waves at 7 MHz on nonpiezoelectric silicon nitride ceramic substrates. Computer calculations predict similar bandwidths for interdigital transducer arrays on PVF_2 films for surface acoustic wave excitation on similar substrates. Insertion loss versus frequency measurements on bulk longitudinal wave transducers in water at frequencies in the 1 to 30 MHz range show good agreement with theory. A computer program for multilayer piezoelectric films predicts included angles of acceptance exceeding 60^0, and control of acceptance angle profiles, in face plates using multilayer PVF_2 films.

PVF_2 bulk wave transducers are made by bonding 25 μ PVF_2 film ($\approx$ 1/2" $\times$ 1/2") onto brass backing rods with V-6 epoxy. The PVF_2 film is obtained from Kureha Corporation in stretched, poled and electroded form. We etch off the aluminum electrodes, which erode quickly when placed in water, and put down a thin layer of chrome followed by a layer of gold ($\simeq$ 1000 Å).

These bulk wave transducers have a very flat frequency spectrum up to 20 MHz when radiating into water.[1] This is expected, since the acoustic impedance and velocity of longitudinal waves in PVF_2 (3.83×10^5 gm/cm^{2}sec and 2.15×10^5 cm/sec, respectively) match relatively well to the impedance and velocity of water (1.48×10^5 gm/cm^{2}sec and 1.48×10^5 cm/sec). As the impedance mismatch at the brass/PVF_2 interface is large, little energy is radiated into the brass. These characteristics of PVF_2 result in a clean, nearly bipolar impulse response (Fig. 1). PVF_2 transducers have shown a 60 dB two-way insertion loss at their resonance frequency (λ = 4 $\times$ film thickness).

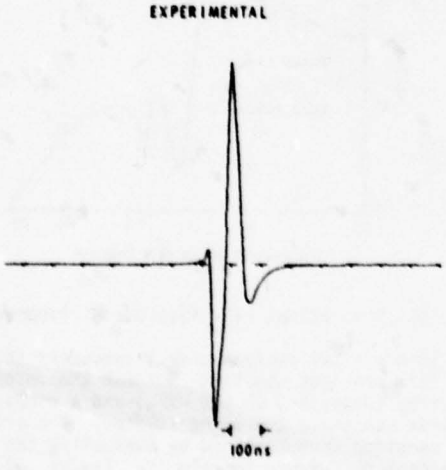

Fig. 1. Impulse response of a broadband PVF_2 transducer.

Although the piezoelectric coupling coefficients of PVF_2 are low compared to PZT, the power output of a PVF_2 transducer remains linear with higher applied voltage than PZT. We have carried out power measurements at higher frequencies (13.56 MHz). The power output of a PVF_2 transducer remained linear up to 750 volts ($3^2 \times 10^5$ v/cm), the limit of the signal generator. It is expected that the power-voltage relation will remain linear above 3×10^5 volt/cm. Calculations have shown that PVF_2 can produce approximately 5 times the power/volume that PZT can produce.[2]

Multilayer transducers also have been investigated. By folding and bonding an electroded film, PVF_2 transducers can be operated with high applied RF electric fields without requiring high voltage. This provides a multilayer transducer in which the voltages of the individual layers are in parallel while their acoustic fields are in series. This also provides a way of obtaining lower resonant frequencies with a given film thickness. Multilayer transducers have been constructed and used to observe the movement of the mitral valve of the human heart (see Figs. 2 and 3).

We are currently examining the possibility of a PVF_2 face plate which could receive acoustic radiation at angles other than normal incidence. For a face plate used as a receiver, broadband frequency response leads to broad angular response.[3] Therefore a PVF_2 face plate should have a very broad angular response. Just as a wide aperture optical lens has better resolution than a narrow aperture lens, a broad angular response transducer will lead to better resolution than a transducer with a relatively narrow angular response. Thus, a PVF_2 face plate promises good resolution. Photolithography would be used to produce periodic electrode patterns on the PVF_2 surface which could then be electronically scanned to achieve imaging. At present, theoretical studies on the angular response of brass backed PVF_2 face plates are underway using a computer program developed by Auld and Roberts.[3] Figure 4 shows the voltage response as a function of angle of a PVF_2 brass backed film. The three curves show the effect of the value of the piezoelectric coupling coefficient e_{zx} transducer response. (Shear wave effects have been suppressed in order to simplify understanding of the result.) As e_{zx} and e_{zz} have opposite signs, it is seen that e_{zx} detracts from the uniform character of the voltage response from 0^0 to 30^0.

Calculations have also been made which involve both shear and longitudinal waves. These show a large shear wave resonance near a 55° angle of incidence. The tail of these resonances contributes to the uniform character of the response from 0° to 30°.

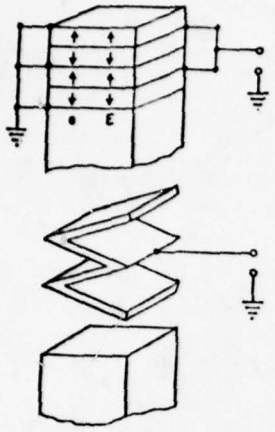

Fig. 2. Multilayer transducer structure.

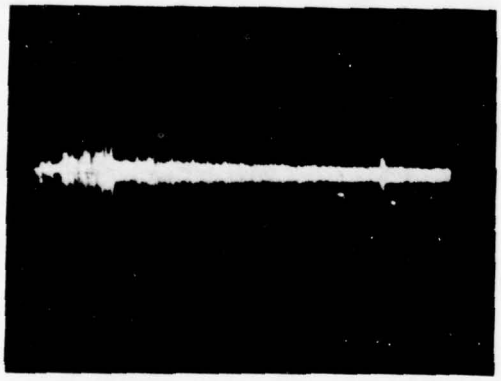

Fig. 3. Photo shows an echo from a mitral valve leaflet. The right-hand pulse is the mitral valve echo; the near-in signals are echoes from inhomogeneities in the brass used as the transducer backing.

We have devised a scheme that involves stacking three layers of PVF_2 in such a way that the resulting e_{zx} and e_{zz} of the stacked films have the same sign. By rotating a film 90° about an axis perpendicular to the plane of the film we can interchange e_{zx} and e_{zy}, which differ by a factor ≈ 5. By inverting a film we change the sign of e_{zx} and e_{zz}. Using these changes, we theoretically construct a three-layer stack with the properties shown on Fig. 5. This figure also shows the voltage response of such a stack. The theoretical response of such a stack is more favorable (out to 45°) than a single film.

Wedge transducers have been constructed for the excitation of surface acoustic waves on high velocity nonpiezoelectric substrates. These could be used to perform NDE on surface flaws. In this case, a PVF_2 transducer irradiates the substrate at an angle such as to phase match with a surface acoustic wave propagating on the substrate. The experimental wedge transducers have a resilent RTV wedge between the PVF_2 transducer and the surface wave substrate allowing experimental variation of the wedge angle by distorting the RTV, this being a critical parameter.[4] (See Fig. 6). As PVF_2 can be used at frequencies near 20 MHz, the wavelength of such a surface wave will be small, and resolution will be good. Using 30 μ PVF_2 films, a bandwidth of approximately 100% has been observed at 7 MHz in initial measurements using two identical wedge transducers on a silicon nitride substrate.

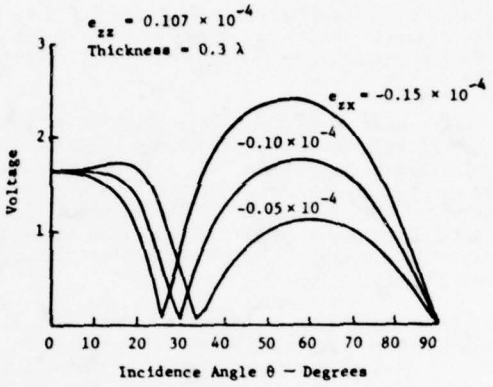

Fig. 4. Theoretical PVF_2 face plate response.

	e_{zx}	e_{zz}	Thickness λ
Layer 1 --	-1.0	+1.07	0.07
Layer 2 --	0.2	-1.07	0.07
Layer 3 --	0.2	-1.07	0.07

$Q_e = 5$

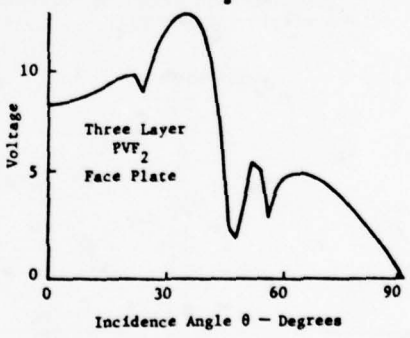

Fig. 5. Theoretical PVF_2 face plate response.

Interdigital surface wave transducers in which PVF_2 film provides coupling between the interdigital array (deposited on the PVF_2) and a nonpiezoelectric substrate are being studied. The effective coupling is determined by evaluating the fractional difference in velocity ($\Delta v/v$) of a surface wave propagating in the film substrate combination under two conditions: (1) no electrodes are present at the surface which is to contain the interdigital array, and (2) a uniform conductor is placed at that surface. The surface wave velocities have been calculated using a computer program

developed by Kino and Wagers,[5] are shown in Fig. 7. Focusing on the curve label 10-00, we see that this curve rises to a reasonably high value (0.8%) and is also fairly broad. This implies that an IDT with the 10-00 structure would be capable of a broad frequency response. The resulting transducer will be flexible and mechanicaliy conformable for use on curved surfaces (see Fig. 8).

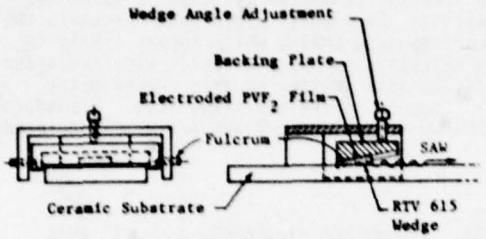

Fig. 6. Wedge transducer schematic.

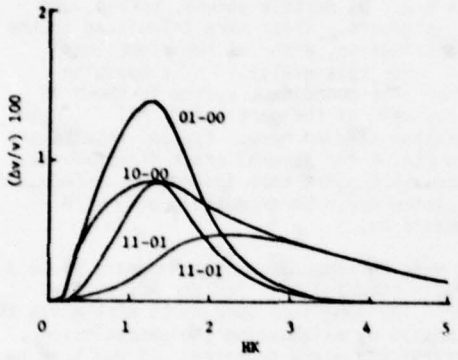

Cases

01-00 - IDT on top of PVF_2
short at sub-PVF_2 interface
10-00 - IDT at PVF_2 sub-interface
short on top of PVF_2
11-01 - IDT at sub-PVF_2 interface
11-10 - IDT on top of PVF_2
(H = film thickness, K = propagation constant)

Fig. 7. Δv/v versus film thickness.

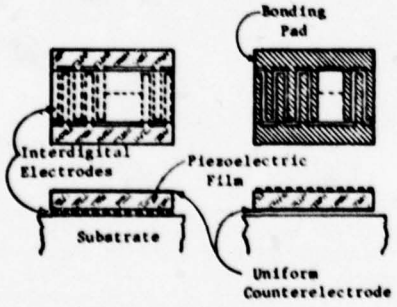

Fig. 8. IDT schematic.

The PVF_2 program at Stanford also includes a material synthesis group. C. Frank and S. Bowker of the Chemical Engineering Department are studying the chemistry and synthesis of PVF_2, aimed at improving the piezoelectric properties of PVF_2.

R. Reigelson, R. Route, and R. DeMattei are involved in melt press production of PVF_2 films at the Stanford Center for Materials Research.

References

*The work reported in this paper was supported by the Office of Naval Research under Contract N00014-77-C-0582 and the Air Force Office of Scientific Research under Grant No. AFOSR-77-3386.

1. L. Bui, H. J. Shaw, and L. T. Zitelli, "Experimental Broadband Ultrasonic Transducers using PVF_2 Piezoelectric Film," Electronics Letters 12, 16, 393 (August 5, 1976).

2. John Linvill, "PVF_2-Models Measurements, Device Ideas," Stanford Electronics Laboratories Report No. 4834-3, 71 (1978).

3. B. A. Auld, M. E. Drake, and C. G. Roberts, "Monolithic Acoustic Imaging Transducer Structures with High Spatial Resolution," Appl. Phys. Letters 25, 9, 478 (November 1974).

4. J. Fraser, B. T. Khuri-Yakub, and G. S. Kino, "The Design of Efficient Broadband Wedge Transducers," Appl. Phys. Letters 32, 11, 698 (1 June 1978).

5. G. S. Kino and R. S. Wagers, "Theory of Interdigital Couplers on Non-Piezoelectric Substrates," J. Appl. Phys. 44, 4, 1480 (April 1973).

CALCULATION OF THE RESPONSE OF ANGLE BEAM EMATs TO FLAWS IN THE FAR FIELD

W. J. Pardee and R. B. Thompson
Rockwell International Science Center
Thousand Oaks, California 91360

ABSTRACT

In the design of a system for NDE, it is necessary to quantify the relationship of flaw size and orientation to transducer signal levels. This is particularly true for automated systems, in which the transducer coordinates cannot be adjusted by an operator to maximize the signal. This paper presents the result of a model calculation for the case of angle beam inspection using EMATs, which appear likely to find extensive use in such systems. Included in the model are calculations of the elastic wave radiation pattern in three dimensions for plates, calculations of the elastic wave scattering from cracks using existent approximate models, and calculation of the electrical response to the scattered wave. Transducer apodization is used to reduce spurious side lobe signals and "blind areas" where flaws are weakly detected. Emphasis is placed on the case of SH wave generation.

One of the most important assets of EMATs for NDE is the possibility of producing an ultrasonic beam of relatively well controlled polarization, intensity, and angular distribution. The mathematical ingredients of a systematic approach to the design of EMATs for an optimized automated NDE system are shown in the flow chart of Fig. 1. The inputs are of three distinct sorts, EMAT parameters, material properties, and the types of flaws which are sought. The design algorithm contains separate modules which calculate the surface tractions resulting from the EMAT parameters, and a medium transfer function depending only on the material properties. These are combined to produce the displacements and stresses in the far field region of the transducer. A third major program module calculates the signal produced by a reflection of these fields from the flaw. This permits such important system characteristics as the variation of signal with flaw orientation to be evaluated and transducer parameters to be optimized to minimize this variation.

The calculation of the surface tractions for a particular EMAT, that of Fig. 5, is described in Fig. 2. These are straightforward, albeit lengthy, expressions from ordinary electromagnetic theory. They result in expressions which are in closed form as a function of x and y (Cartesian coordinates in the plane of the surface), and are numerically Fourier transformed using an FFT algorithm after apodizing with a Kaiser-Bessel window. Because the EMAT studied here (Fig. 5) directly produces tractions only parallel to the surface, the normal (z) component of the displacement was neglected in the medium response (Fig. 3). Though not rigorously correct, this approximation is plausible for moderate distances. The form of the resulting far field expression is shown in Fig. 3. Figure 4 describes the model used for scattering. A result due to Auld exhibits the change in signal as an integral over the crack of certain stress, strain, and velocity products. These were calculated in the Born approximation, with the two dimensional numerical integrals evaluated by a Gaussian algorithm. The coordinate system is shown in Fig. 5, as well as the particular EMAT configuration studied here. Typical results are shown in Fig. 6 for several crack orientations. These results suggest that inspection performance of the system would be acceptable only with orthogonal scans.

The modular computer program appears to be a potentially powerful tool for the NDE system designer. The immediate need is to strengthen the medium module by eliminating the approximate treatment of the plate geometry. It may then be necessary to modify the scattering theory module to utilize a theory more powerful than the Born approximation. One expects that large computers may eventually play a role in QNDE comparable to that they have come to enjoy in optics.

ACKNOWLEDGEMENT

This research was sponsored by the Center for Advanced NDE operated by the Science Center, Rockwell International, for the Advanced Research Projects Agency and the Air Force Materials Laboratory under Contract F33615-74-C-5180.

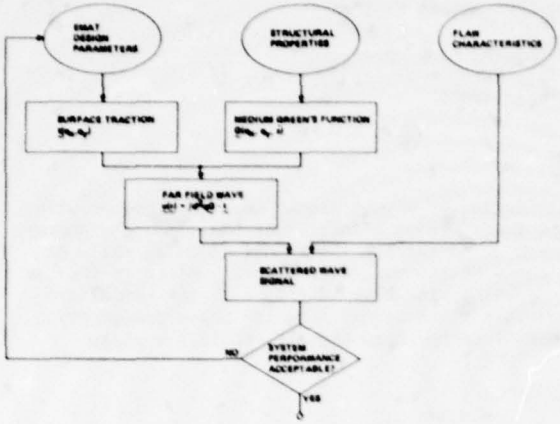

Fig. 1 Optimized NDE system design.

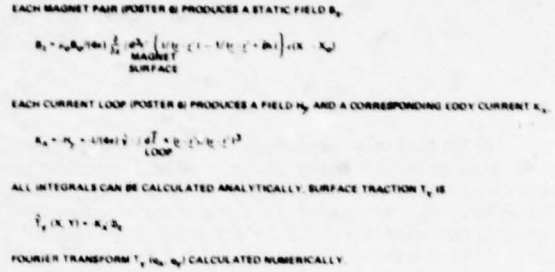

Fig. 2 The (SH) source (or detector).

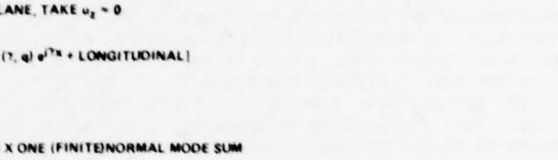

Fig. 3 The medium (SH approximation).

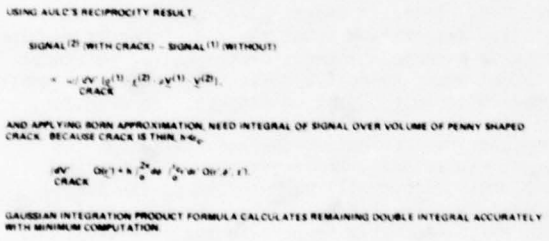

Fig. 4 The defect scattering.

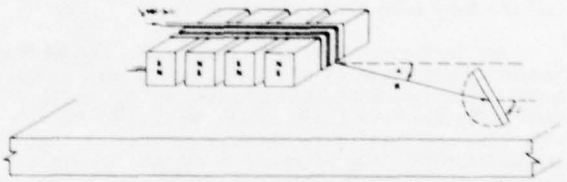

Fig. 5 Configuration of EMAT.

PENNY SHAPED CRACK 0.005" THICK, 1 MM RADIUS ON BOTTOM SURFACE OF 3/8" THICK PLATE, SH TRANSDUCER AT 1.8 MHz

RELATIVE SIGNAL WITH CRACK CENTERED ON DIRECTION OF TRANSMISSION, R = 4 CM

ANGLE	0°	45°	90°
SIGNAL	0.00	0.00	1.00

Fig. 6 Sample results.

BEAM INTENSITY PROFILING USING CORRELATION SYSTEMS

E. S. Furgason, G. F. Johnson, and B. B. Lee
School of Electrical Engineering, Purdue University
West Lafayette, Indiana 47907

ABSTRACT

Techniques are described in which the intensity distribution of an ultrasound beam is measured with high resolution by means of the radiation reflected from a target whose effective backscattering diameter is smaller than one wavelength. Correlation receivers are used to improve the signal-to-noise ratio of the echo. As the target is scanned across the beam, the phase of the reference signal applied to the correlation receiver must be adjusted to compensate for changes in the time of flight of the ultrasound echo. The broadband beam intensity mapping technique employs a noise signal in which phase compensation is adjusted manually. The other technique, which is used with narrow band signals, applies a phase quadrature technique to achieve phase compensation.

INTRODUCTION

When it is necessary to accurately predict the acoustic beam pattern of a transducer or array, one may either resort to mathematical models or attempt direct measurement of the intensity distribution. Although the mathematical models of highly idealized transducers that exist in the literature come close to predicting the far field intensity patterns for both narrowband and broadband signals, they cannot represent the details of the beam patterns for real, non-ideal transducers. This is especially true for both the near field and the beginning of the far field, the regions in which most transducers are used. This shortcoming is apparent in our measurements of single frequency intensity distributions near the beginning of the far field zone.

Commercially available equipment for ultrasonic beam measurement typically lacks sufficient resolution and sensitivity to adequately characterize the beam. In addition, these systems have difficulty dealing with the two cases in which we have the greatest interest, the single frequency signal and the very wide band random signal.

Two techniques have been developed in which the intensity distribution of an ultrasound beam is measured with high resolution by means of the radiation reflected from a hemispherical target whose effective backscattering diameter is smaller than one wavelength. One of these techniques provides high resolution beam plots for narrow band beam signals. The second is used to examine broad band beam patterns. Correlation receivers are used in both techniques to enhance the signal-to-noise ratio of the echo.

SYSTEM FOR NARROW BAND SIGNALS

Beam plots for single frequencies are obtained from a system based on a modification of a directional ultrasonic Doppler flow meter. The system transmits a pulse modulated burst of RF with center frequency described by $\cos(\omega_0 t)$. The echo expected from a point reflector, due to this transmitted signal, will contain a frequency component described by

$$A(x,y;z)\cos\{\omega_0 t+\Phi(x,y;z)\} \qquad (1)$$

In this expression $A(x,y;z)$ is proportional to the intensity distribution of the ultrasound field in the plane normal to the axis (z-direction) of the acoustic beam and $\Phi(x,y;z)$ is a phase factor dependent on the distance, in wavelengths, between the transducer and the point of measurement. The objective of the measurement is to accurately extract the amplitude function $A(x,y;z)$ from expression 1.

The most straightforward approach to this determination is to simply measure the envelope of the echo signal as a function of target position. This method suffers from two serious drawbacks. Since it is necessary to pulse the transmitted signal to control multiple reflections, the transmitted signal is not a single frequency but an entire spectrum whose bandwidth is inversely proportional to the transmitted pulse length. As a result, the envelope of the echo signal actually contains contributions from many frequency components, making interpretation of the measurement difficult. In addition, direct measurement of the echo envelope provides no signal-to-noise ratio enhancement. This is an extremely important shortcoming, especially when detailed information about the side lobes is required. Accurate beam measurements also require the use of a target whose effective reflecting surface is small compared to an acoustic wavelength. In practice, this is accomplished by using a target which has a hemispherical reflecting surface. Although the target may actually be larger than an acoustical wavelength, sound will be returned to the transducer from only that portion of the spherical surface which is nearly tangent to the beam axis. As a result, little of the transmitted acoustic energy is returned to the transducer.

The system we have constructed overcomes the limitations of the envelope detection system by using a degenerate heterodyne, or homodyne receiver. If the received echo is mixed with a reference signal, it is possible to filter the mixer output to obtain only the information contained in a single frequency component of the received echo. If the reference signal is derived from the same master oscillator as the transmitted signal, the resulting signal, after filtering, will be

$$A(x,y;z)\cos\{\Phi(x,y;z)\} \qquad (2)$$

The use of a homodyne system allows selection of a single received frequency component, even though the transmitted signal is pulse modulated. Further-

more, this type of system provides signal-to-noise ratio enhancement proportional to the band compression of the receiver, the ratio of the output bandwidth to the received bandwidth. This type of system, however, still retains the phase term $\phi(x,y;z)$. To remove the phase term, we take advantage of the quadrature signals available in the single-sideband receiver of the directional Doppler system.

The two quadrature signals, $\cos(\omega_0 t)$ and $\sin(\omega_0 t)$, derived from the master oscillator are each mixed with the received echo. If the output of these multipliers is passed through a sufficiently narrow band low-pass filter, the only signals which survive are:

$$A(x,y;z)\cos\{\phi(x,y;z)\}$$

$$A(x,y;z)\sin\{\phi(x,y;z)\} \qquad (3)$$

By taking the vector magnitude of these two signals, the desired intensity function $A(x,y;z)$ is extracted. Thus we can obtain accurate measurements of the single frequency beam profile with significant signal-to-noise ratio enhancement.

SYSTEM FOR BROAD BAND SIGNALS

To obtain maximum resolution, most flaw detection systems take full advantage of the available transducer bandwidth. Broadband signals are also used in the high sensitivity random signal flaw detection that we have developed. Thus there is a significant need to accurately characterize the broadband intensity patterns of acoustic transducers.

The beam plotting system used to measure broadband sound intensity patterns is based on a modification of the random signal flaw detection system. In the flaw detection system, broadband ultrasonic random signals are gransmitted into the sample. echoes reflected from inhomogeneities are picked up by the transducer and amplified as in a conventional pulse-echo system. The received signal is then correlated with a time delayed copy of the transmitted acoustic signal which has been stored in a delay line. The amplified echo signal, together with the reference signal emerging from the delay line, enter a correlator which consists of a multiplier followed by an integrator in the form of a low-pass filter.

The system will produce a non-zero output only when the delay imposed on the reference signal approximately equals the time of flight of the transmitted signal to the target and back. The output of the system is a maximum when the time of flight and the delay are identical. If the length of the time delay of the reference signal is slowly changed, the system scans along a line in the test object, producing an output on each occasion that the varying delay time nearly equals the time of flight. The output of the correlator is actually the cross-correlation function of the echo signal and the reference signal.

Since the auto-correlation function is for the entire transmitted signal, every frequency component of the transmitted signal contributes to the peak of the function. Therefore, if the peak of the auto-correlation function is tracked as a function of the target position as the target is moved through the ultrasonic beam, the output will represent the beam pattern due to the transmitted broadband signal. Since this system uses a correlation receiver and provides band compression the output will have a greatly enhanced signal-to-noise ratio.

Beam profiles of the near field and far field have been made using both systems and the same 1/4 inch diameter wideband transducer. The far field intensity patterns were found to match computer simulations very well. The measured narrow band profile for the far field also showed additional details due to the non-ideality of the transducer under test.

ACKNOWLEDGEMENT

The authors would like to thank V. L. Newhouse for several useful discussions relating to this project.

*Work supported by ARPA under AFML contract #F33615-75-R-5252.

VISUALIZATION OF TRANSDUCER-PRODUCED SOUND FIELDS IN SOLIDS

Wolfgang Sachse*
Department of Theoretical and Applied Mechanics
Cornell University, Ithaca, New York - 14853

ABSTRACT

Broadband ultrasonic pulses and monochromatic ultrasonic waves are visualized in various transparent solids using a photoelastic visualization technique. Application is made to the characterization of the sound field radiated by various ultrasonic transducers operating under various excitation and coupling conditions.

INTRODUCTION

This poster paper describes several results obtained from the photoelastic visualization of piezoelectric transducer-produced sound fields in transparent elastic solids. Publication of these results will be in the 1978 IEEE Ultrasonics Symposium Proceedings.

The characterization of ultrasonic transducers can be made in two steps.[1] In one, the transduction process is characterized such that when a transducer is used as a source of ultrasound, the relationship between the electrical excitation and the acoustical output is established. A similar relationship is established for a transducer operating as a receiver. In the second step, the radiation field of the transducer is determined. While it should be possible to compute the radiated field of a transducer for which the excitation traction force and velocity are known, it has only been done in a few, limited situations. These are principally cases in which the transducer is modeled as a piston radiator, operating either in a continuous or pulsed mode with specified velocity boundary conditions between the transducer and the test medium. While this model may accurately represent the case of a transducer radiating into a liquid, it is unlikely to do so for a transducer coupled to a solid test medium. The latter is usually formulated as a traction boundary value problem and, as pointed out in a forthcoming review article,[2] aspects of this problem remain to be solved.

As reviewed in detail by Sachse and Hsu[2], the sound field of a transducer radiating into a liquid can be easily measured with microprobing transducers, spherical reflectors and optical methods, including interferometric and schlieren techniques. Most often measured are the transducer's beam or directivity patterns, its sound field amplitudes and intensities. The latter, when measured over a planar region of the sound field, can be used to reconstruct the transducer's sound field at any point in its near- or far-field.

In contrast, measurements of the sound field of a transducer coupled to a solid can only be made by indirect means. With particular specimen geometries, capacitive or electomagnetic transducers can be used to map out portions of a piezoelectric transducer's radiation field. Most often, however, optical techniques are used. These include interferometric, optical probing, schlieren and photoelastic techniques.

The implications of the foregoing are that since the sound field of a transducer radiating into a liquid can be computed, a comparison can be made between the computed and the measured sound fields and any disagreement between them can be used to indicate an anomalous behavior in the operation of the transducer. In contrast, since the analysis of a transducer coupled to a solid is incomplete, assessment of the performance of the transducer cannot be made reliably. This underscores the usefulness of field visualization measurements for these situations.

Our choice of using a photoelastic technique was based on its simplicity, its use of non-critical specimen geometries and materials (as long as they are transparent) and its potential for allowing absolute determination of various sound field quantities.

Interest in photoelastic techniques for visualizing ultrasonic fields in solids has recently redeveloped. The first application of the technique appears to have been made by Hiedeman and Hoesch[3] to visualize the stress field near a quartz transducer radiating into a glass block. The basis of the technique is that the light birefringence induced by transverse and longitudinal ultrasonic waves can be related to the refraction ellipsoid of the solid. Consequently, linearly polarized light emerges elliptically polarized when it passes through a region where an ultrasonic wave is propagating. Thus, such waves can be made visible with ordinary photoelastic techniques. The sound fields associated with longitudinal and shear waves can be studied simultaneously or separately. For optimal visualization of longitudinal waves, the polarization of the incident light should be 45° to the sound propagation direction. For shear waves, the direction of light polarization and sound propagation should be parallel. Shear waves whose particle displacements are parallel to the axis of the polariscope cannot be visualized. Application of the technique has been made to the visualization of the sound fields produced by various transducers and their interaction with various specimen geometries. Review of this past

* Visiting at: National Bureau of Standards, Washington, D.C. - 20234.

work is in References 2 and 4.

While there is nothing new regarding the application of the technique in this report, there are important differences with past work. In this report, a comparison between broadband, narrowband and continuous-wave excitation of a transducer coupled to a solid is explored, the temporal and field development of the radiated wave field is studied and transducer size and frequency effects are described. As in some of the recent publications, the intereaction of sound fields with artificially-produced, isolated scattering obstacles is also visualized.

TECHNIQUE

The apparatus used in our visualization experiments is equivalent to that used by Wyatt[5] and Hall[6] and is shown in Fig. 1 . It differs from theirs principally in cost. The items associated

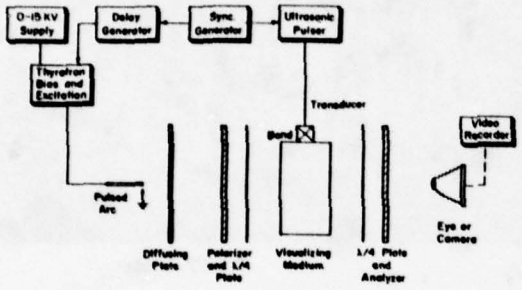

Fig. 1

with the visualization system, including its delay generator and light source, total less than $500. Secondly, while a commercially available narrowband flaw detector has been used in some of the measurements, other ultrasonic sources were also used. One was a high amplitude (-1500 volt, 40 nsec) broadband pulser which was constructed with a thyratron-based circuit. For the continuous-wave excitation, an amplitude-modulated function generator was used to obtain long r.f. bursts which were amplified with a 20 watt r.f. power amplifier. Tuned and broadband piezoelectric transducers of various sizes and frequency characteristics were coupled to blocks of glass or fused silica. The specimens were generally much larger than those used by previous investigators to allow the visualization of the long-duration r.f. bursts without interference of side-wall reflections. Critical in the visualization is a jitter-free light source which can be delay-triggered in synchronization with the ultrasonic pulse. The arc used for this purpose was a thyratron-based device reproduced from Wyatt[7]. The repetition rate of the experiments ranged from 20 to 200 Hz, allowing 1 sec exposures on ASA 200 film.

RESULTS

The propagation of a broadband ultrasonic pulse in fused silica resulting from a 12.7 mm diameter transducer is shown in Figs. 2(a) -(f) . The illuminating arc was triggered at various times relative to the excitation pulse as shown. It is clear that even initially the transducer generates not only plane waves, but also spherical waves in the solid. The secondary pulses include waves propagating with the bulk longitudinal and shear wave speeds and they appear to originate from the edge of the transducer. In the sound field of a transducer radiating into a liquid there is the obvious absence of the shear wavefront. The other pictures show that a pulse, after one reflection from a planar surface has a wavefront which appears to be spherical and there is some spreading of the pulse evident (Fig. 2(e)). After a second reflection (Fig. 2(f)), there is additional spreading and the sound field has become quite complex as a result of the reflection and mode conversion of the secondary pulses comprising the sound field. A schematic drawing of the visualized sound field prior to the occurrence of any reflections from the boundaries of the specimen is shown in Fig. 3.

Visualization of the entire sound field of a transducer appears to be most easily obtained by using long-duration r.f. bursts to excite the transducer. Figure 4 shows the sound field of broadband transducer, 6.35 mm in diameter, under a 2 MHz long-duration burst excitation. The transducer's near-to-far-field transition region can be identified. The sound field of a 6.35 mm diameter broadband transducer with long-duration r.f. burst excitation of 500 kHz and 4 MHz center frequency is shown, respectively in Figs. 5(a) and (b) . Clearly evident is the spherical nature of the sound field at the higher frequency. The effect of transducer size is shown in Figs. 6(a) and (b) in which the excitation was an identical 1 MHz r.f. burst, but (a) and (b) are respectively the sound field of a 6.35 mm and a 25.4 mm diameter transducer. Finally, Fig. 7 shows a comparison of the sound fields produced by 24° angle beam transducers under broadband, narrowband and long-duration r.f. burst excitation. Both the longitudinal and the shear wave sound fields are visible. The expected wave propagation directions are shown in (a), while (b) and (c) show the sound field generated by a broadband and a narrowband transducer under shock excitation. In (d) the narrowband transducer is excited with a 3.2 MHz, 12 μsec long r.f. burst.

The photoelastic visualization technique was used to investigate the effectiveness of the transducer coupling to the test medium. One example of the results observed is shown in Fig. 8 . In this case, a small air bubble was trapped in the coupling layer. In the resulting field, the planar wavefront in the central region of the sound field was too low in amplitude to visible photoelastically even though the two sets of spherical waves emanating from the edge of the transducer are still present. Such phenomena are clearly distinct from the sound fields present when transducers are radiating into liquids.

The use of known scattering obstacles in a test block for which the scattered sound field can be computed so as to be useful for the calibration of ultrasonic transducers is often suggested as the basis of an acceptable calibration technique. The visualization of the sound field scattered by a 1 mm diameter cylindrical side-drilled hole in glass is shown in Fig. 9 . Other scattering obstacles, such as crack-like slots, have also been studied. In each case, the complexities of the scattered sound field resulting from mode conversion and diffraction effects are apparent and thus must be accounted for when considering any obstacle as the basis of a transducer calibration block.

(a) 3.5 μsec (b) 5.5 μsec (c) 9.5 μsec

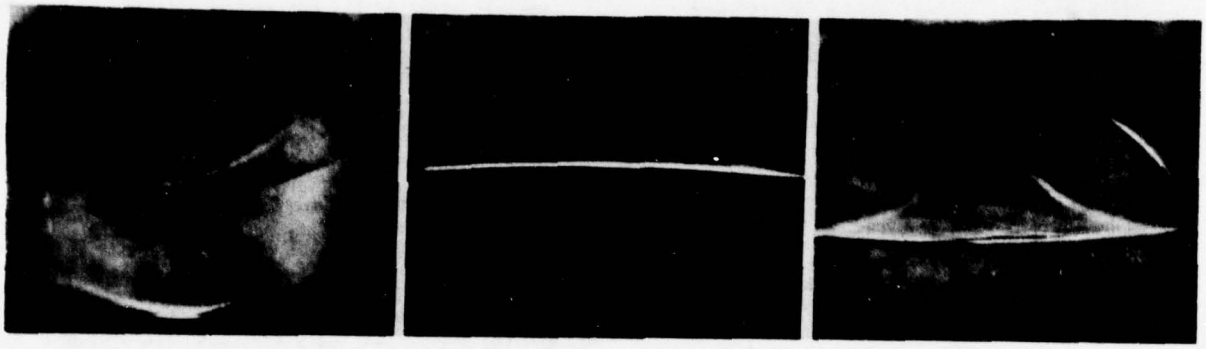

(d) 11.5 μsec (e) 43.5 μsec (f) 52.9 μsec

Fig. 2 - Photoelastic visualization of a broadband ultrasonic pulse at various locations in a large fused silica block.

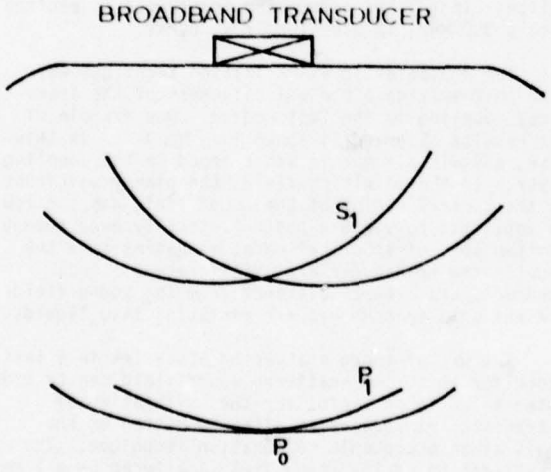

Fig. 3 Wavefronts appearing in Figure 2(c)

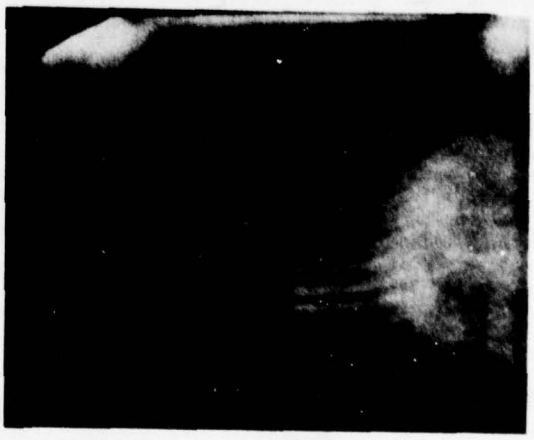

Fig. 4 Acoustic field in fused silica of a 6.35 mm dia. transducer excited at 2 MHz.

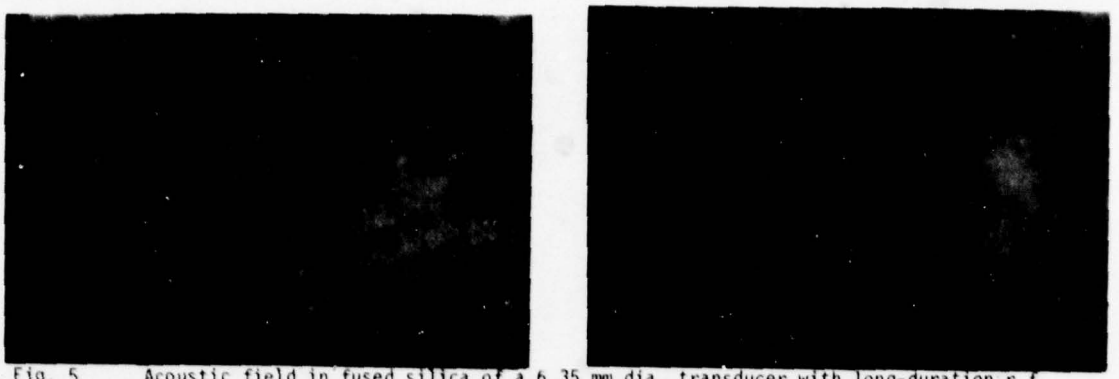

Fig. 5 Acoustic field in fused silica of a 6.35 mm dia. transducer with long-duration r.f. burst excitation. (a) 500 kHz; (b) 4 MHz.

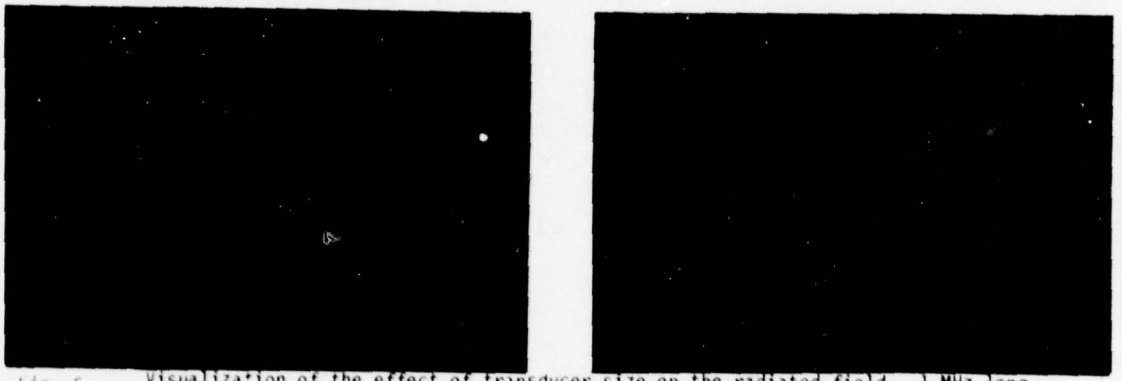

Fig. 6 Visualization of the effect of transducer size on the radiated field. 1 MHz long-duration burst excitation. (a) 6.35 mm dia.; (b) 25.4 mm dia.

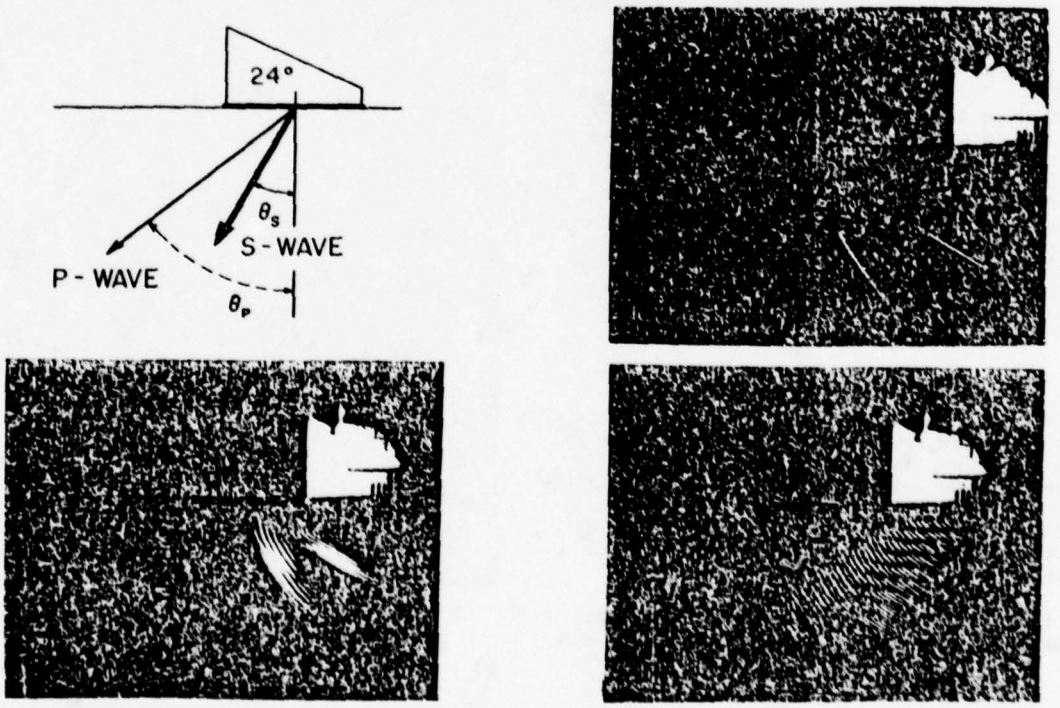

Fig. 7 Sound field of a 24° angle beam transducer coupled to a glass block. (a) Expected shear and longitudinal wave propagation directions; (b) Broadband pulse; (c) Narrowband pulse and (d) 3.2 MHz, 12 μsec long burst. (b) and (c) different transducers, same source; (c) and (d) same transducer, different sources.

Fig. 8 Sound field of a transducer operating through a bad bond. (Air bubbles in coupling layer)

Fig. 9 Scattering by a 1 mm side-drilled hole.

CONCLUSIONS

The effectiveness of the photoelastic technique to visualize various transducer-produced sound fields in transparent solids has been shown. The technique, which is simple to use, has been applied to observe features of transducer sound fields in solids which differ from those of a transducer radiating into a liquid. While only qualitative results have been shown here, it is possible to quantify the technique. Recent advances in signal processing may play a role in the analysis of photoelastically obtained transducer field patterns. By digitizing the field either directly from the polariscope or from films, the image of the field can be processed to yield the absolute principal stress differences associated with a transducer's sound field.

ACKNOWLEDGMENTS

This work was performed while the author was a guest of the NDE Program at the National Bureau of Standards during his sabbatic leave from Cornell University. The author acknowledges the hospitality shown him by Mr. H. Berger and others in the program. In that regard, the sabbatic support of the College of Engineering at Cornell is also appreciated.

Special thanks go to B. Chick for assistance in designing the high-amplitude, broadband pulser and to S. Parks for designing the delay circuitry.

REFERENCES

1. W. Sachse and N. N. Hsu, Proceedings of the First International Symposium on Ultrasonic Materials Characterization (1978). To appear.
2. W. Sachse and N. N. Hsu, in Vol. 14, Physical Acoustics, W. P. Mason and R. N. Thurston, Eds. Academic Press, New York (1978).
3. E. Hiedemann and K. H. Hoesch, Z. Physik, 104, 197 (1937).
4. D. M. Marsh, in Research Tech. in NDT, Vol. 2, R. S. Sharpe, Ed., Academic Press, London (1973).
5. R. C. Wyatt, Brit. J. NDT, 17, 133 (1975).
6. K. G. Hall, Ultrasonics, 15, 57 (1977).
7. R. C. Wyatt, J. Phys. E: Sci. Instr., 7, 437 (1974).

FREQUENCY DEPENDENCE OF ULTRASONIC WAVE SCATTERING FROM CRACKS

Laszlo Adler and Kent Lewis
Department of Physics
The University of Tennessee
Knoxville, Tennessee 37916

ABSTRACT

Studies of spectral analysis of the scattered longitudinal and shear waves from crack-like flaws in solids were carried out in the region of $ka \geq 1$. Experimental data are analyzed and compared to two new theories developed recently for elastic wave diffraction from cracks. These theories relate the amplitude spectra of scattered L and S waves to crack parameters such as size, orientation, surface roughness, etc. On the development of the interpretation obtained from phase spectral information the scattered phase from spherical cavities was calculated from exact theory and compared to experimental data.

THEORY

The scattering (diffraction) of ultrasonic waves from circular cracks in metals was analyzed based on two approximate diffraction theories.
(1) Developed by Adler et al.:[1] This theory works for normal incidence. It is based on modifying Keller's geometrical theory of diffraction[2] for the elastic wave problem (modified Keller). The diffraction coefficients for the diffracted shear and longitudinal waves are calculated by using the solutions of Maue[3] for the diffraction of waves by semi-infinite plane. For a circular crack with radius a (Fig. 1) the diffracted L field at a point is given by equations (Fig. 2). Similar expressions may be obtained for the scattered shear waves. Fig. 3 and Fig. 4 are calculated L and S diffracted field amplitude as a function of frequency.
(2) Developed by Achenbach et al.:[4] The so-called elastic dynamic theory (described in detail by Achenbach in this report).

EXPERIMENT

The normally incident L wave diffracted by a circular crack of 2500μ radius is analyzed by both an analog and digital spectrum analyzer system (Fig. 5). The various incident and scattered waves are illustrated by a "time mapping" scheme (Fig. 6). Capability of the signal processing system is shown on Fig. 7 by the transfer function. Correction of the data has to be made because the spectra through the liquid-solid interface changes with angle. This is demonstrated by rotating the sample and recording the transmitted spectra for different angles of orientation (Figs. 8, 9, 10, 11).

RESULTS

Typical scattered L and S data from the 2500μ crack are shown on Figs. 12 and 13. In addition to the RF, the amplitude and phase spectra are shown. The amount of L and S wave produced at various angles at the cavity is shown on Fig. 14. Fig. 12 is corrected by the transmission spectra given by Fig. 11 and compared to both theories (Fig. 15) favorably. The shear data clearly differs from the theoretical prediction given on Fig. 4. The surface ray contribution—predicted by Achenbach's theory—may explain the origin of such irregularities. The radiograph on Fig. 16 gives the side view of a circular crack inside the titanium. The diffusion process introduces a small bending on the top surface of the crack. No significant difference was observed in the spectra by turning the sample around (Fig. 17). This confirms the prediction of the ray theory, i.e., rays originating at sharp corners.

PHASE SPECTROSCOPY

Since digital spectrum analysis gives phase information, the possibility of using phase spectroscopy (in addition to amplitude spectroscopy) to characterize defects is also studied. Calculations for scattered L waves from spherical cavities in titanium based on exact theory of Ying and Truell[5] shows that the scattered phase spectra is size dependent. There is also angular dependence. See Figs. 18, 19, 20. Experimental results compare reasonably well with theory—shown on Fig. 21—to assume that phase spectroscopy coupled with amplitude spectroscopy can be developed to be a powerful tool of flaw characterization.

ACKNOWLEDGEMENT

This research was sponsored by the Center for Advanced NDE operated by the Science Center, Rockwell International, for the Advanced Research Projects Agency and the Air Force Materials Laboratory under Contract F33615-74-C-5180.

REFERENCES

1. Kent Lewis, Peter Szilas, Dale Fitting, and Laszlo Adler, J. Acoust. Soc. of Am., 63, 574 (1978).

2. J. B. Keller, J. Appl. Phys., 28, 426 (1957).

3. A. W. Maue, Z. Für Angew. Math. U. Mech., 33, 1 (1953).

4. J. D. Achenbach and A. K. Gautesen, J. Acoust. Soc. of Am., 61, 413 (1977).

5. C. F. Ying and R. Truell, J. Appl. Phys., 27, 1086 (1956).

Diffraction of Elastic Waves by Circular Cracks in Metals.
Modified Keller Theory Developed by Adler et al.

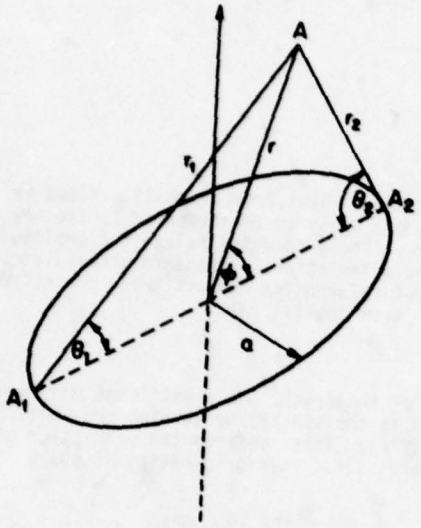

Fig. 1. Circular aperture

The amplitude of the diffracted L wave is given as

$$u_D(P) = f(r)g_L(\phi) \tag{1}$$

where

$$f(r) = -A\frac{e^{ikr}}{r} \tag{2}$$

and

$$g_L(\phi) = \frac{k^2}{\sqrt{\pi}}\frac{\cos\phi}{\left(\frac{a\sin\phi}{a}\right)^{1/2}}\left([\cos(ka\sin\phi)][P(-ka\sin\phi)] + P(ka\sin\phi)\sin(ka\sin\phi)\right]$$

$$- i[P(-ka\sin\phi)\sin(ka\sin\phi) + P(ka\sin\phi)\cos(ka\sin\phi)]\Big) \tag{3}$$

where

$$P(\lambda) = \frac{1}{2\pi}\left(\frac{K-\lambda}{\lambda}\right)^{1/2}\cdot\frac{F_2(\lambda)}{F_2(0)}\cdot\frac{\left(\frac{K^2}{2}-\lambda^2\right)\left(\frac{K^2}{2}\right)}{\left(\frac{K^2}{2}-\lambda^2\right)^2+\lambda^2\sqrt{(k^2-\lambda^2)(K^2-\lambda^2)}} \tag{4}$$

where $F_2(\lambda) = e^{f_2(\lambda)}$

$$f_2(\lambda) = \ln\frac{\lambda_R-\lambda}{K-\lambda}+\frac{1}{\pi}\int_k^K \arctan\left(\frac{\left(\frac{K^2}{2}-z^2\right)^2}{z^2\sqrt{(z^2-k^2)(K^2-z^2)}}\right)\cdot\frac{dz}{z-\lambda} \tag{5}$$

k is the L wave number
K is the S wave number
$\lambda_R = \frac{\omega}{C_R}$ C_R is the Rayleigh velocity.

Fig. 2. Expressions for the diffracted amplitude

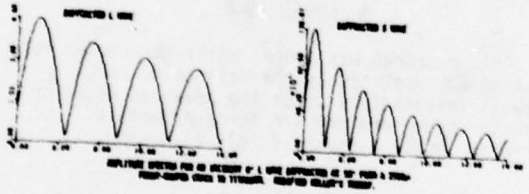

Fig. 3

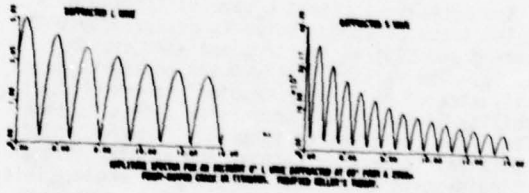

Fig. 4

Fig. 3 & 4. Calculated amplitude spectra for diffracted longitudinal and shear waves

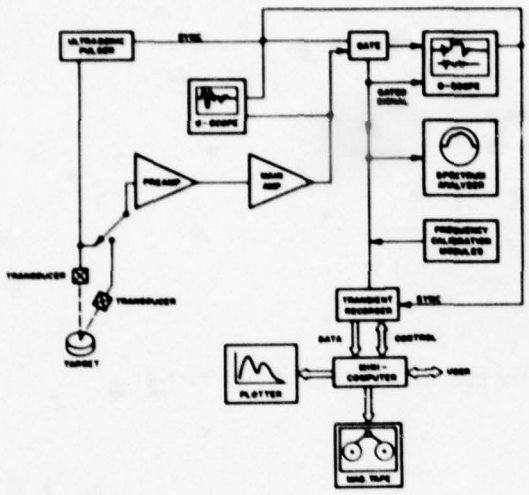

Fig. 5. Experimental system for analog and digital spectrum analysis

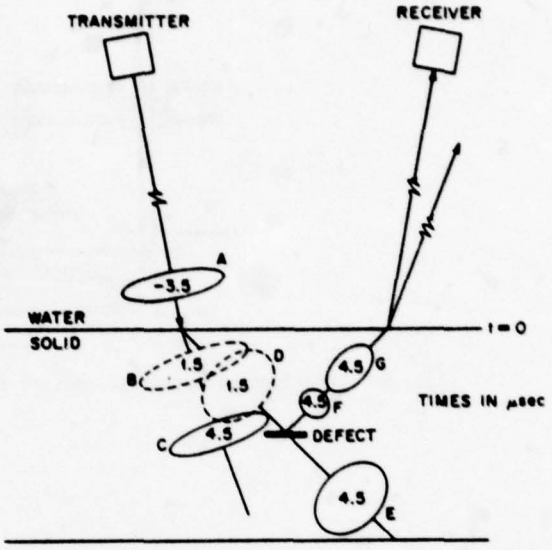

A INCIDENT WAVE IN WATER
B & C SHEAR WAVES
D & E LONGITUDINAL WAVE
F SCATTERED SHEAR
G SCATTERED LONGITUDINAL

Time Mapping" of Shear and Longitudinal Waves before and after Interaction with Defect.

Fig. 6. Experimental technique and "time mapping" of incident and scattered pulses

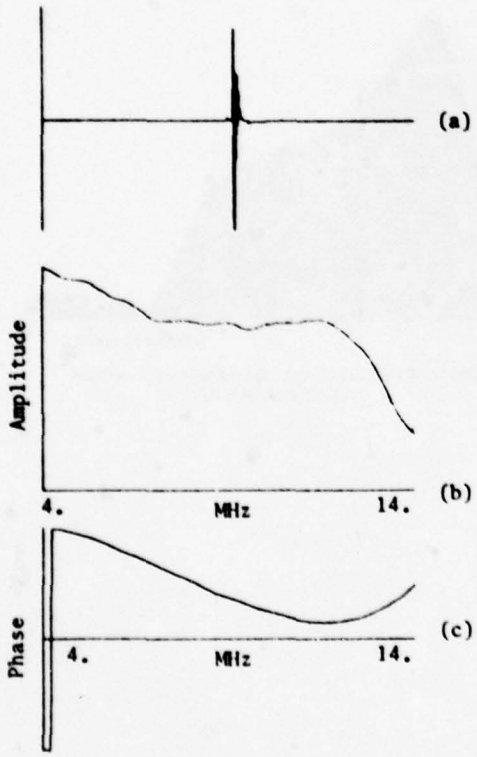

Transducer Output

(a) R.F. waveform; (b) amplitude spectrum; (c) phase spectrum.

Fig. 7. Transducer transfer function

The Distribution of the Transmission Spectra Through Liquid-Solid Interface Changes with Angle

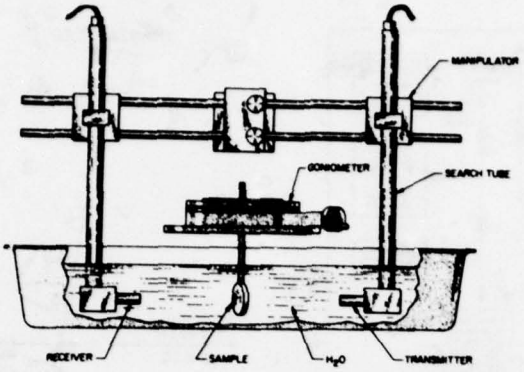

Fig. 8. Experimental system to measure transmitted spectra through titanium sample

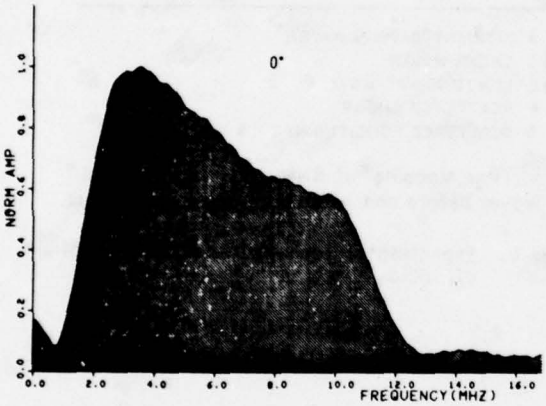

TRANSMISSION SPECTRUM OF AN L WAVE THROUGH A 2.5 cm-THICK TITANIUM DISK IN WATER

Fig. 9

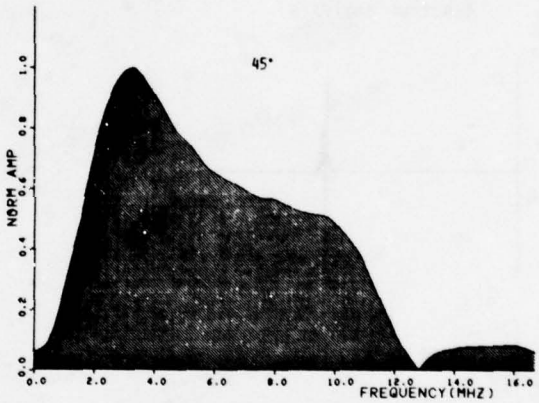

TRANSMISSION SPECTRUM OF AN L WAVE THROUGH A 2.5 cm-THICK TITANIUM DISK IN WATER

Fig. 10

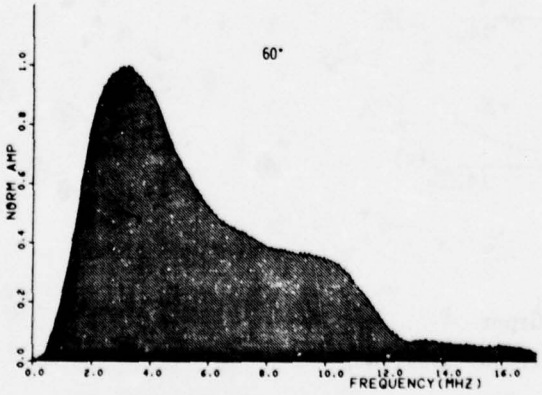

TRANSMISSION SPECTRUM OF AN L WAVE THROUGH A 2.5 cm-THICK TITANIUM DISK IN WATER

Fig. 11

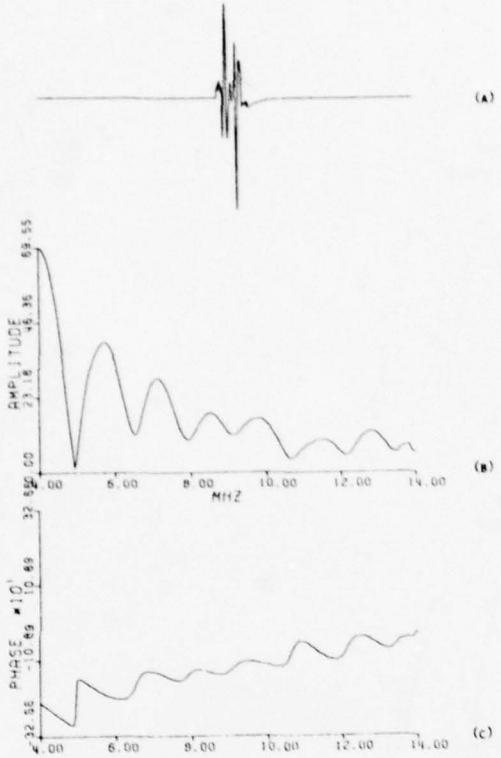

SCATTERED LONGITUDINAL WAVE FROM A 2500μ RADIUS CRACK IN TITANIUM. SCATTERING ANGLE IS 60°. (A) R.F. WAVEFORM; (B) AMPLITUDE SPECTRUM; (C) PHASE SPECTRUM.

Fig. 12. Longitudinal wave

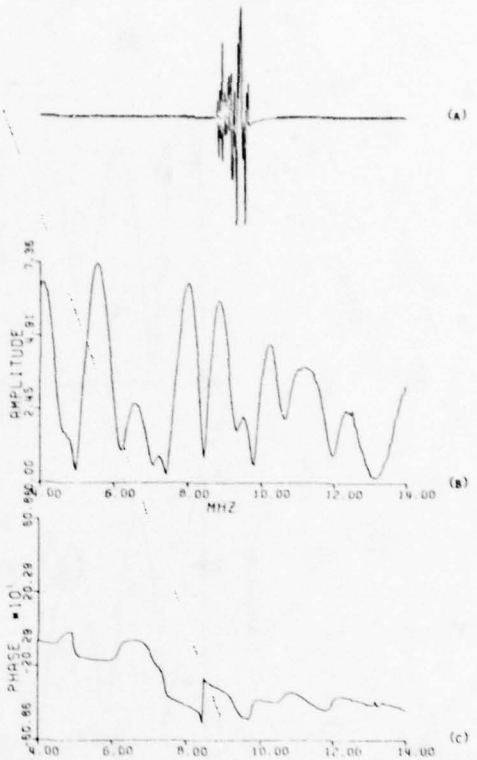

SCATTERED SHEAR WAVE FROM A 2500μ RADIUS CRACK IN TITANIUM. SCATTERING ANGLE IS 60°. (A) R.F. WAVEFORM; (B) AMPLITUDE SPECTRUM; (C) PHASE SPECTRUM.

Fig. 13. Shear wave

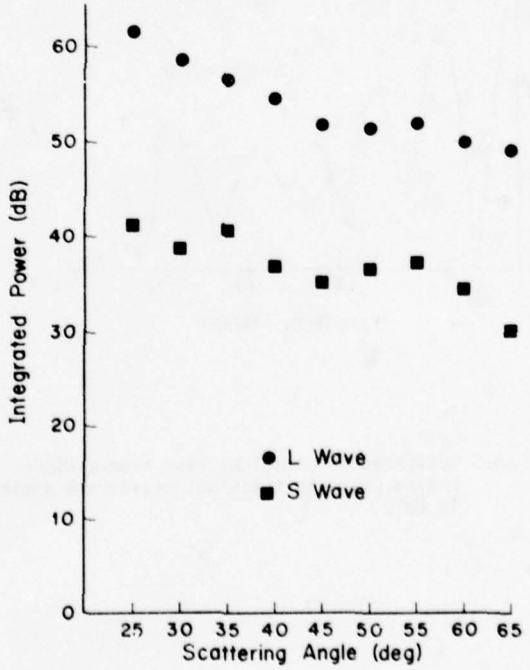

Fig. 14. Incident L wave scattered from a penny shaped crack of 2500μ radius in titanium

Comparison of Experimental Data to Modified Keller Theory (by Adler et al.)
and to Elastodynamic Theory (by Achenbach et al.)

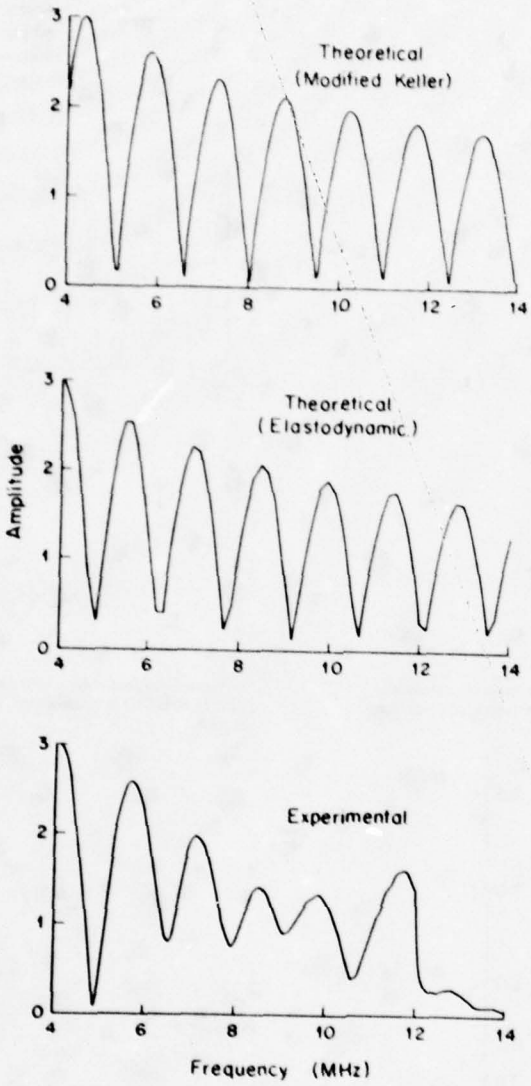

Fig. 15. Scattered longitudinal wave from a 2500μ radius crack in titanium, scattering angle is 60°.

Slight Curvature on the Crack Will Not Affect Significantly the Diffracted Amplitude Spectra

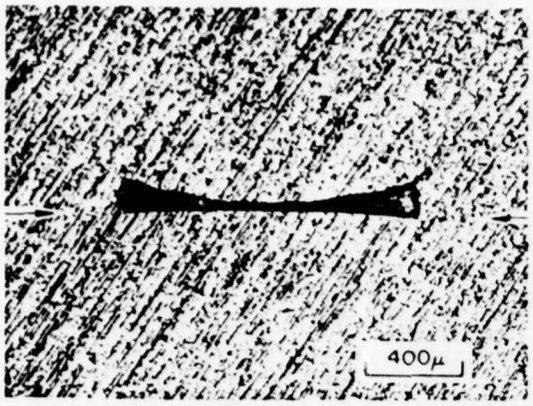

Fig. 16. Side view radiography of the defect

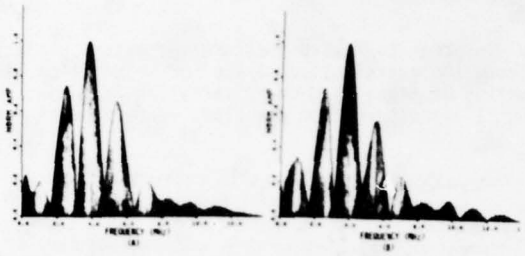

Fig. 17. Amplitude spectra for an incident 0° L wave diffracted to a 60° L wave from a 2500μ penny-shaped crack in titanium alloy. (A) top side; (B) bottom side

Phase Spectroscopy for Flaw Characterization

Exact Theory of Elastic Wave Scattering by Spherical Cavity in Titanium Relates Phase Spectra to Cavity Size.

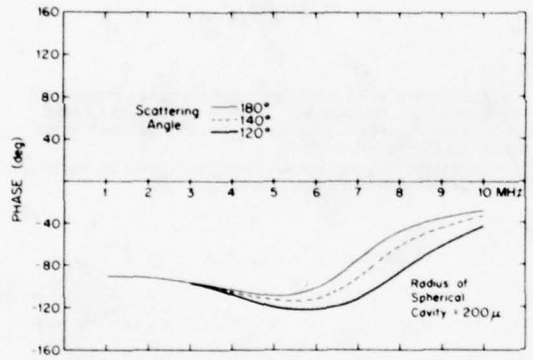

Fig. 18

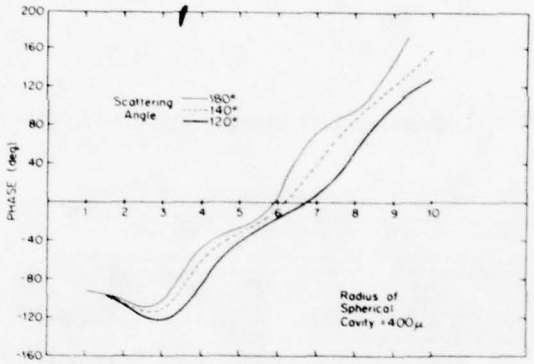

Fig. 19

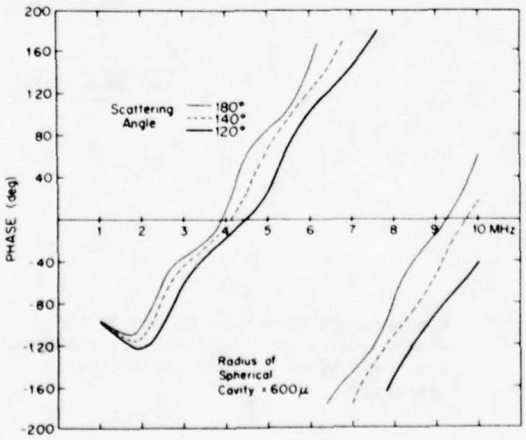

Fig. 20

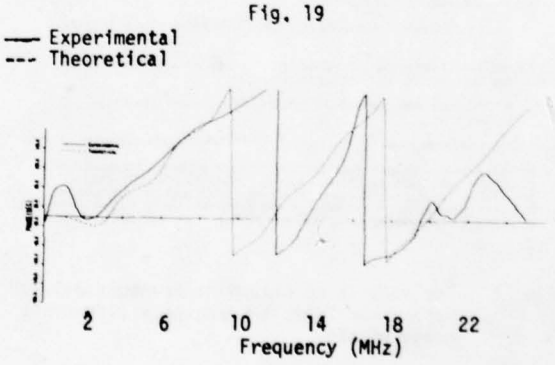

Fig. 21. Phase behavior for a 180° scattered L wave from a 400μ radius spherical cavity in titanium

FLAW CHARACTERIZATION BY LOW FREQUENCY SCATTERING MEASUREMENTS

R. K. Elsley
Rockwell International Science Center
Thousand Oaks, California 91360

ABSTRACT

In order to make a fracture mechanical prediction of the remaining lifetime of a part, it is necessary to know the overall size, shape and orientation of the flaws in the part. This paper describes the determination of these flaw characteristics from measurements of the scattering of low frequency (long wavelength) ultrasound from the flaw. Experimental results are excellent.

The goal of this work is to determine fracture related parameters from low frequency ultrasonic measurements. Figure 1 outlines this goal. The measurements (Fig. 2) were made on manufactured ellipsoidal flaws in Ti-6Al-4V; scattered waveforms were recorded and digitally processed.

A pulse of low frequency (long wavelength) ultrasound is physically long and therefore provides poor resolution of nearby scatterers (Fig. 3). To achieve good resolutions, a short broadband pulse of high frequency (5 MHz) ultrasound was used. Low frequency data was obtained from the low frequency components of this pulse. Low frequency sound diffracts in all directions from a transducer, producing unwanted sound paths in pitch-catch measurements (Fig. 4). To overcome this, a waveform recorded in a flaw free region can be substracted (Fig. 5). After frequency analysis and removal of the properties of the transducer, the lowest order coefficient A_2 (proportional to frequency squared) of the frequency spectrum is determined. The set of A_2 coefficients from a number of directions are combined with theory to estimate flaw parameters (Fig. 6). Figure 7 shows the results. The estimated flaw parameters agree very well with the true values.

DIRECT MEASUREMENT OF STRESS INTENSITY FACTORS

ACHIEVING A FRACTURE MECHANICS BASED STRUCTURAL DESIGN PROGRAM REQUIRES THAT FLAWS BE DETECTED AND SIZED WITH THE GREATEST POSSIBLE RELIABILITY. AS THE ACCURACY OF THIS FLAW SIZING INCREASES, SYSTEM COSTS ARE REDUCED BY PREVENTING THROWAWAY OF GOOD PARTS.

AN IMPORTANT STEP TOWARD THIS GOAL IS THE DIRECT MEASUREMENT OF THE STRESS INTENSITY FACTOR OF A FLAW. THIS PAPER DESCRIBES THE MEASUREMENT OF FLAW SIZE, SHAPE, ORIENTATION AND THEREBY, STRESS INTENSITY FACTOR USING THE TECHNIQUE OF LOW FREQUENCY SCATTERING. IN THEORETICAL PAPERS, RICHARDSON HAS PRESENTED THE TECHNIQUE FOR DETERMINING FLAW PARAMETERS AND RICE HAS DESCRIBED FOR ELLIPTICAL CRACKS, THE SUBSEQUENT DETERMINATION OF THE MAXIMUM STRESS INTENSITY FACTOR.

THE ADVANTAGES OF USING LOW FREQUENCY (LONG WAVELENGTH) ULTRASOUND FOR THESE MEASUREMENTS ARE

1. AN EXACT THEORY IS AVAILABLE TO RELATE FLAW PROPERTIES TO SCATTERED FIELDS
2. THE MEASUREMENTS ARE SENSITIVE ONLY TO THE OVERALL PROPERTIES OF THE FLAW, NOT TO SMALL TEXTURAL DETAILS
3. ATTENUATION AND GRAIN SCATTERING ARE USUALLY SMALLER AT LOW FREQUENCIES
4. ONLY ONE NUMBER NEEDS TO BE MEASURED FROM EACH ULTRASOUND WAVEFORM

THE CHIEF DISADVANTAGES OF THIS TECHNIQUE ARE THE LARGE VOLUME OCCUPIED BY A LONG WAVELENGTH PULSE, THE SMALL AMPLITUDE OF LOW FREQUENCY SCATTERING, AND THE DIFFRACTION OF LOW FREQUENCY SOUND OUT OF A WELL COLLIMATED BEAM. THIS PAPER PRESENTS THE EXPERIMENTAL TECHNIQUES DEVELOPED TO OVERCOME THESE PROBLEMS IN THE FIRST DEMONSTRATION OF THIS APPROACH.

Fig. 1 The goal is to determine fracture related parameters from low frequency ultrasonic measurements.

MEASUREMENTS

MEASUREMENTS WERE PERFORMED USING A CONVENTIONAL TRANSDUCER AND ULTRASONIC PULSER. THE FLAWS ARE SMALL VOIDS IN THE FORM OF ELLIPSOIDS OF REVOLUTION, BUILT IN THE CENTER OF SPHERES OF Ti-6Al-4V.

THE R.F. WAVEFORMS (PULSE-ECHO OR PITCH-CATCH) ARE DIGITIZED AND THEN PROCESSED IN A MINICOMPUTER

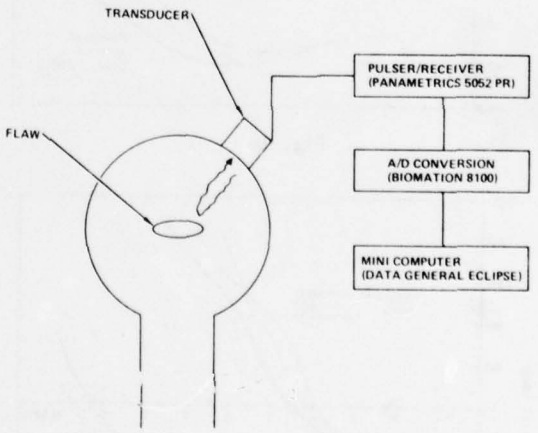

Fig. 2 Measurements were made on manufactured ellipsoidal flaws in Ti-6Al-4V; scattered waveforms were recorded and digitally processed.

WHAT TYPE OF TRANSDUCER

IN ADDITION TO THE ECHO FROM THE FLAW, THERE ARE USUALLY ECHOS FROM NEARBY SURFACES AND PERHAPS OTHER FLAWS, AS SHOWN ABOVE RIGHT.

IF THE LOW FREQUENCY ULTRASOUND IS GENERATED BY A LOW FREQUENCY (LONG WAVELENGTH) TRANSDUCER, THEN THE PULSE OF ULTRASOUND WILL BE SO LONG THAT OTHER, LARGER, ECHOS WILL OVERLAP THE FLAW ECHO AND MAKE IT UNDETECTABLE. THIS IS SHOWN AT RIGHT.

HOWEVER, A HIGH FREQUENCY BROADBAND PULSE (LOWER RIGHT) IS SHORTER, WHILE STILL CONTAINING SOME LOW FREQUENCY ENERGY. THEREFORE, IN ORDER TO MAKE LOW FREQUENCY MEASUREMENTS IN THE 0.5 – 1.0 MHz, WE HAVE USED A 5 MHz BROADBAND TRANSDUCER.

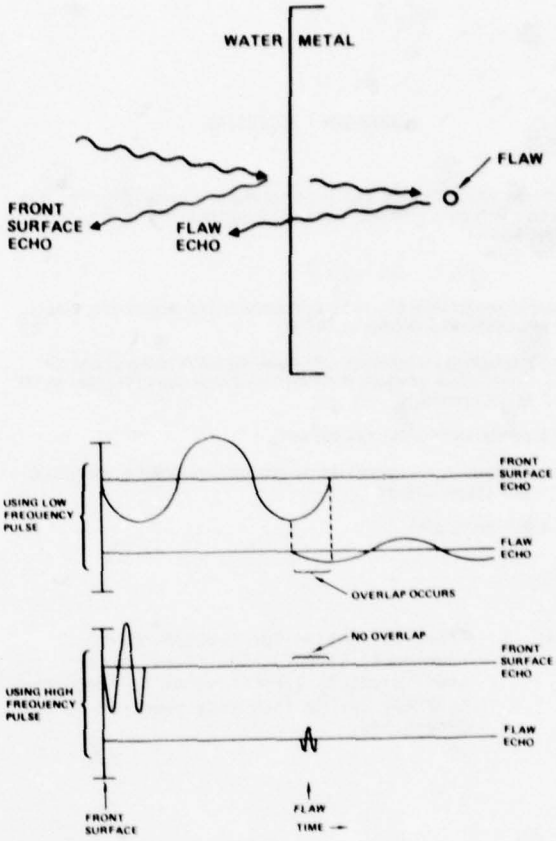

Fig. 3 To achieve good resolutions, a short broadband pulse of high frequency (5 MHz) ultrasound was used. Low frequency data was obtained from the low frequency components of this pulse.

UNWANTED SOUND PATHS

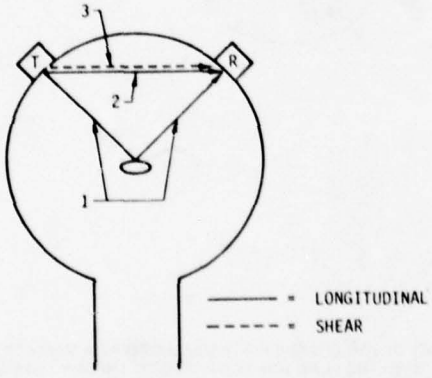

(a)

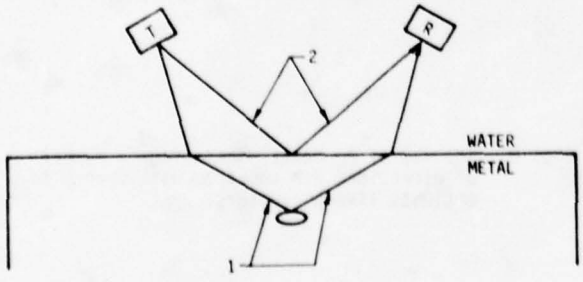

(b)

LOW FREQUENCY ULTRASOUND SPREADS OUT IN A BROAD BEAM FROM A TRANSDUCER RATHER THAN FORMING A NARROW BEAM AS IT DOES AT HIGHER FREQUENCIES. FOR PITCH-CATCH MEASUREMENTS, UNWANTED "DIRECT BEAM" PATHS CAN EXIST BETWEEN TRANSMITTER AND RECEIVER.

FOR THE "TRAILER HITCH" GEOMETRY USED IN THESE EXPERIMENTS (FIGURE a), BOTH LONGITUDINAL (2) AND SHEAR (3) DIRECT BEAMS CAN ARRIVE SHORTLY BEFORE OR DURING THE FLAW SIGNAL.

FOR THE FLAT SURFACE GEOMETRY (FIGURE b), THERE IS A CORRESPONDING FRONT SURFACE DIRECT BEAM (2).

FOR PULSE ECHO MEASUREMENTS, THE PROBLEM IS SIMILAR, WITH THE DIRECT BEAM REPLACED BY THE MAIN BANG (a) OR FRONT SURFACE (b) ECHOS.

A SOLUTION TO THIS PROBLEM IS TO SUBTRACT FROM THE FLAW WAVEFORM A WAVEFORM FROM A FLAW FREE REGION OF THE SAME GEOMETRY. BECAUSE WE ARE INTERESTED IN LOW FREQUENCIES, SMALL POSITIONING ERRORS AND GEOMETRY DISSIMILARITIES BETWEEN THE TWO WAVEFORMS ARE NOT A PROBLEM.

Fig. 4 Low frequency sound diffracts in all directions from a transducer, producing unwanted sound paths in pitch-catch measurements.

WAVEFORM PROCESSING

AT LOW FREQUENCIES, THE SCATTERING IN A GIVEN DIRECTION IS DESCRIBED BY 1 NUMBER, THE COEFFICIENT $A^{(2)}$ OF FREQUENCY SQUARED:

$$S(f) = A^{(2)} f^2$$

WAVEFORMS FROM SEVERAL DIRECTIONS ARE RECORDED. EACH IS PROCESSED AS SHOWN AT RIGHT:

1. (OPTIONAL) SUBTRACT A FLAW-FREE WAVEFORM IN ORDER TO REMOVE REMNANTS OF EARLIER SIGNALS AND UNWANTED SOUND PATHS.
2. FREQUENCY ANALYZE (BY FFT)
3. REMOVE THE PROPERTIES OF THE TRANSDUCER BY DIVIDING OUT ITS SPECTRUM
4. ESTIMATE $A^{(2)}$

PROCESSING EACH WAVEFORM

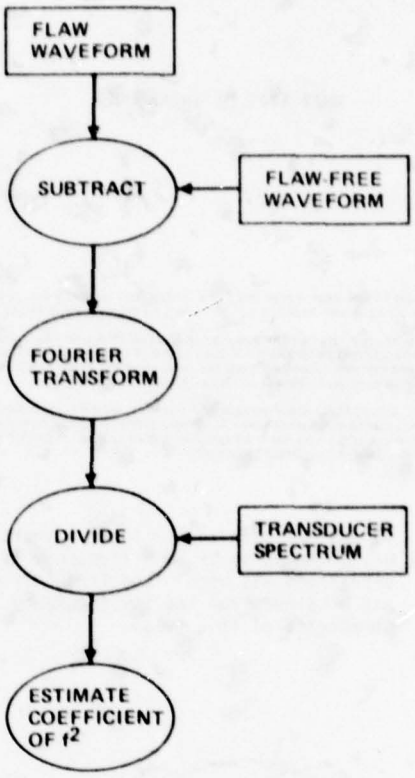

Fig. 5 After correcting for background and transducer effects, the lowest order coefficient A_2 (proportional to frequency squared) of the frequency spectrum is determined.

DETERMINING FLAW PARAMETERS

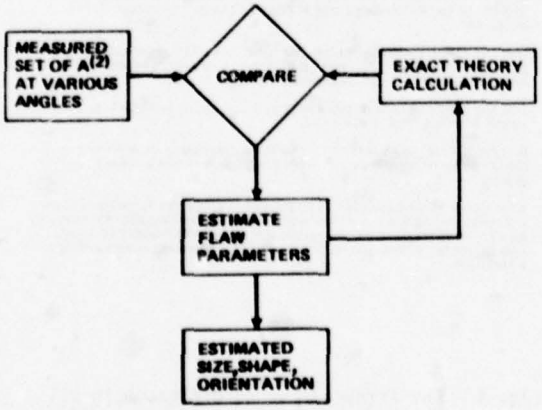

A SET OF $A^{(2)}$ COEFFICIENTS MEASURED AT A VARIETY OF ANGLES AROUND THE FLAW ARE COMPARED TO THEORY CALCULATIONS IN ORDER TO ITERATIVELY ARRIVE AT BEST ESTIMATES OF THE FLAW SIZE, SHAPE AND ORIENTATION.

Fig. 6 The set of A_2 coefficients from a number of directions are combined with theory to estimate flaw parameters.

RESULTS

ESTIMATED VALUES OF THE SIZE AND ORIENTATION OF AN ELLIPSOIDAL VOID OF MAJOR DIAMETER 0.08 CM (0.032 IN.) ARE SHOWN AT RIGHT.

a, b, c ARE THE SEMI AXES OF THE ELLIPSOID; γ_X IS A DIRECTION COSINE MEASURING THE ORIENTATION.

THE RESULTS ARE REMARKABLY GOOD.

FROM THESE FLOW PARAMETERS, THE STRESS INTENSITY FACTOR k_I CAN BE CALCULATED. AGAIN, AGREEMENT IS VERY GOOD.

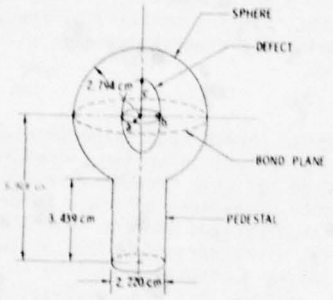

QUANTITY	TRUE VALUE	ESTIMATE	STANDARD DEVIATION ESTIMATE
SIZE:			
a, b	0.04 CM	0.03947	0.0168
c	0.02 CM	0.01999	0.0608
ORIENTATION:			
γ_X	0	1.24×10^{-5}	0.1120
STRESS INTENSITY:			
k_I	0.354	0.352	0.008

Fig. 7 Results: The estimated flaw parameters agree very well with the true values.

CALCULATION OF SCATTERING BY THE DISTORTED WAVE BORN APPROXIMATION

Kathie E. Newman and Eytan Domany
Department of Physics, University of Washington
Seattle, Wa 98195

ABSTRACT

An approximate scattering theory that utilizes the exact solutions for spherical defects is being developed. A defect of arbitrary shape can be represented by a sphere S and a remainder volume δv. By treating δv as a perturbation, one obtains an approximate solution that contains non-trivial frequency dependence and phase information. The approach is expected to be useful for studying defects with small but significant deviations (such as sharp edges) from spherical shape.

INTRODUCTION

The basic problem of defect characterization by ultrasonic techniques has received considerable attention in recent years. Two different but complimentary aspects of the problem have been approached. These are known as the direct and inverse problems. The direct problem is that of calculating the scattering of elastic waves from a known defect. The inverse problem is that of characterizing an unknown defect from a set of measured scattered waves. Obviously, these two are closely related. Solutions of either provide clues as to what measurements to perform and which features of the scattered power would be the most useful for defect characterization.

Due to the considerable mathematical complexity inherent in solving for elastic wave scattering, exact solutions are available for only a small number of scatterer geometries. This has led to the development of approximate solutions such as the Born Approximation[1] (BA) and the Quasi Static Approximation[2] (QSA). The BA is useful for obtaining information on the angular distribution of frequency averaged power.[3] However, it is known[3] to yield quite unreliable frequency dependence for the scattered power. The QSA is exact in the long wavelength limit; recently suggested inversion procedures based on the frequency dependence (extrapolated to low frequencies) show great promise[4,5]. The QSA is unfortunately limited to ellipsoidal scatterers, for which exact solutions based on T-matrix expansion methods also exist[6]. Neither the BA nor the QSA are capable of calculating phase information.

In the investigation reported here we aim at filling various gaps in the existing approximate solutions. We hope to obtain an approximation scheme that will provide non trivial phase information and more reliable frequency dependence over a wider range of frequencies. At the same time we aim at obtaining information about non elliptical defects.

The motivation is quite obvious. Past experience indicates that the frequency dependence is very useful in defect characterization[3,7,8]. Frequency dependence is also a much more flexible experimental tool than the study of angular distribution, since a wide range of frequencies can be studied in a single (broad band) experiment. We believe that an efficient inversion procedure will have to build from reliable frequency information. Reliable frequency dependence of phase information[8] should be also incorporated into an inversion procedure. Finally, since present models of inversion rely on representing a general defect by an effective ellipsoid, we feel that a generalization of the direct problem to non-ellipsoidal shapes is important. We hope to investigate the effects of sharp edges and surface roughness, topics that may be most relevant in the NDE context.

THE DISTORTED WAVE BORN APPROXIMATION

The DWBA is based on a perturbative solution of the scattering equation, much in the same way as the Born Approximation. However, while in the BA the unperturbed problem (or zeroth order solution) is the incident wave[1] (propagating in a homogeneous medium with no defect), the DWBA uses the solutions of the scattering problem for a spherical defect[10] as the unperturbed zeroth order approximation. Thus, while the BA is exact only in the limit of vanishing difference between the properties of medium and defect, the DWBA has an additional "small parameter", i.e. a measure of the deviation of the defect from spherical. As shown below, in order to calculate the scattered wave within the DWBA, one needs the Green's function, g^S, of an infinite medium with a spherical defect. When g^S is approximated by the infinite medium Green's function g^0, we obtain an approximation expected to be of intermediate quality between BA and DWBA. In this paper we present results based on the intermediate approximation. Work aimed at evaluating g^S is in progress; when g^S is obtained, we hope to use it in the existing integration routines, thus obtaining the DWBA.

To present a precise statement of the ideas discussed above, consider the differential equation for the propagation of elastic waves in a medium, characterized by the (position dependent) elastic constants C_{ijkl} and density ρ, given by

$$C_{ijkl}u_{k,jl} + \rho\omega^2 u_i = 0 \qquad (1)$$

where u_i is the displacement field and ω the frequency. Consider the geometry depicted in Fig. 1, i.e.,

$$C(\underline{r}) = C^0 + \theta_R(\underline{r})\delta C$$

$$\rho(\underline{r}) = \rho^0 + \theta_R(\underline{r})\delta\rho \qquad (2)$$

where $\theta(r) = 1$ if $\underline{r} \in R$, and zero otherwise. The defect R is separated into two regions: a spherical one (S) and a remainder $\bar{R}$, such that $R = S + \bar{R}$. Then one can define $\theta_S(\underline{r})$ and $\theta_{\bar{R}}(\underline{r})$ in a similar way, so that (see Fig. 1)

$$\theta_R(\underline{r}) = \theta_S(R) + \theta_{\bar{R}}(\underline{r}) . \qquad (3)$$

$$R = S + \bar{R}$$

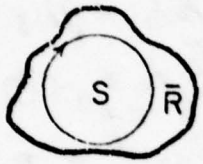

Fig. 1 The defect R is represented as a sphere S and A "remainder" volume $\bar{R}$.

We can now consider as our unperturbed problem the case where only the spherical defect S is present. To do this, define

$$C^S(\underline{r}) = C^0 + \theta_S(\underline{r})\,\delta C$$

$$\rho^S(\underline{r}) = \rho^0 + \theta_S(\underline{r})\,\delta\rho , \qquad (4)$$

and we can obviously write

$$C(\underline{r}) = C^S(\underline{r}) + \theta_{\bar{R}}(\underline{r})\,\delta C$$

$$\rho(\underline{r}) = \rho^S(\underline{r}) + \theta_{\bar{R}}(\underline{r})\,\delta\rho . \qquad (5)$$

Using now (5) in (1), the scattering equation takes the form

$$C^S_{ijkl}u_{k,jl} + \rho\omega^2 u_i = -\theta_{\bar{R}}\left[\delta C_{ijkl}u_{k,jl} + \omega^2\delta\rho u_i\right] \qquad (6)$$

If the right hand side vanishes, the solutions of this equation are the scattered waves by a spherical defect, obtained previously by various investigators[10]. These solutions have been programmed and are readily evaluated numerically. Proceeding in a similar fashion as Gubernatis et al.[9], we obtain the integral equation

$$u_i(\underline{r}) = u^S_i(\underline{r}) + \delta\rho\omega^2 \int_{\bar{R}} d\underline{r}'\, g^S_{im}(\underline{r},\underline{r}')u_m(\underline{r}')$$

$$- \delta C_{jklm}\int d\underline{r}'\, g^S_{ij,k'}(\underline{r},\underline{r}')u_{l,m'}(\underline{r}') , \qquad (7)$$

where $u^S_i(\underline{r})$ is the solution of the scattering problem with a spherical defect only, i.e.,

$$C^S_{ijkl}u_{k,jl} + \rho^S\omega^2 u_i = 0 , \qquad (8)$$

and $g^S_{im}(\underline{r},\underline{r}')$ is the Green's function in the presence of a spherical defect, i.e.,

$$C^S_{ijkl}g^S_{km,jl}(\underline{r},\underline{r}') + \rho^S\omega^2 g_{im}(\underline{r},\underline{r}') = -\delta_{im}\delta(\underline{r}-\underline{r}') . \qquad (9)$$

Note that in equation (7)

$$g^S_{im,j'}(\underline{r},\underline{r}') = \frac{\partial}{\partial r'_j}\, g^S_{im}(\underline{r},\underline{r}') \qquad (10)$$

and that since C^S_{ijkl} and ρ^S are not translationally invariant, $g^S_{ij}(\underline{r},\underline{r}')$ is not a function of $\underline{r}-\underline{r}'$ only. The DWBA consists of replacing $u_i(\underline{r}')$ in the integrands on the right hand side of equation (7) by $u^S_i(\underline{r}')$:

$$u^{DWB}_i(\underline{r}) = u^S_i(\underline{r}) + \delta\rho\omega^2 \int_{\bar{R}} d\underline{r}'\, g^S_{im}(\underline{r},\underline{r}')u^S_i(\underline{r}')$$

$$- \delta C_{jklm}\int_{\bar{R}} d\underline{r}'\, g^S_{ij,k'}(\underline{r},\underline{r}')u^S_{l,m'}(\underline{r}') \qquad (11)$$

To evaluate u^{DWB}_i, we need the functions u^S and g^S, and perform the integration over the region $\bar{R}$ numerically. The relative corrections to the Born approximation are of order $R\delta C$; to the DWBA of order $\delta C\bar{R}/S$. This means that we introduced a geometrical "small parameter", namely the deviation of the defect from spherical. We also hope to determine the "optimal sphere" to be used for treatment of various defects. Since the function g^S has not been calculated previously, we start by setting up an intermediate approximation, replacing g^S in equation (11) by the infinite medium Green's function g^0. Since g^S satisfies an equation of the form (schematic)

$$g^S = g^0 + \int_S \delta C\, g^0 g^S$$

the error caused by replacing g^S by g^0 in (11) is of order $R\delta C \cdot S\delta C$. This intermediate approximation is given by

$$u^I_i = u^S_i + \delta\rho\omega^2 \int_{\bar{R}} d\underline{r}'\, g^0_{im}(\underline{r}-\underline{r}')u^S_i(\underline{r}')$$

$$+ \delta C_{jklm}\int_{\bar{R}} d\underline{r}'\, g^0_{ij,k'}(\underline{r}-\underline{r}')u^S_{l,m'}(\underline{r}') \qquad (12)$$

(where we used $g^0_{im,j'} = -g^0_{im,j}$).

To calculate the scattered power and phase, the observation point $\underline{r}$ is taken to infinity. Asymptotic forms for $u^I_i(\underline{r})$ are found for the spherical solution $u^S_i(\underline{r})$ (outside the integral only) and, in a manner similar to Gubernatis et al.[9]) for the Green's function. In the limit $r \to \infty$, the scattered wave can be written

$$u_i^{scatt} \sim \frac{e^{i\alpha r}}{r} A_i + \frac{e^{i\beta r}}{r} B_i \qquad (13)$$

where α,β are the longitudinal and shear wave numbers respectively. A_i and B_i can be broken into a piece from the integral and a piece from the spherical solution,

$$A_i = A_i^S + A_i^{int}$$

$$B_i = B_i^S + B_i^{int} \qquad (14)$$

where A_i^{int} and B_i^{int} are given in general by

$$A_i^{int} = \hat{r}_i \hat{r}_j f_j(\underline{\alpha})$$

$$B_i^{int} = (\delta_{ij} - \hat{r}_i \hat{r}_j) f_j(\underline{\beta}) \qquad (15)$$

and

$$f_i(\underline{k}) = \frac{k^2}{4\pi\rho\omega^2} \left(\delta\rho\omega^2 \int_{\overline{R}} dV' u_i^S(\underline{r}') \exp(-i\underline{k}\cdot\underline{r}') \right.$$

$$\left. + ik\hat{r}_j \, \delta C_{ijkl} \int_{\overline{R}} dV' u_{k,l'}(\underline{r}') \exp(-i\underline{k}\cdot\underline{r}') \right). \qquad (16)$$

For an incident longitudinal plane wave $\hat{z}\, e^{i\alpha z}$, A_i^S and B_i^S are calculated from the solution to the spherical problem[10]

$$A_i^S = -ia \sum_m (2m+1) A_m^* P_m(\cos\theta)$$

$$B_i^S = ia \sum_m (2m+1) B_m^* \frac{dP_m(\cos\theta)}{d\theta} \qquad (17)$$

where A_m, B_m are defined by Johnson-Truell[10]

The longitudinal and shear differential cross sections are defined in the same way as Gubernatis et al.[9]

$$\frac{dP_\ell(\omega)}{d\Omega} = |A_i|^2 ,$$

$$\frac{dP_t(\omega)}{d\Omega} = |B_i|^2 . \qquad (18)$$

The phase angles δ_ℓ and δ_t are defined from

$$\tan\delta_\ell = \frac{\mathrm{Im}A_i}{\mathrm{Re}A_i} ,$$

$$\tan\delta_t = \frac{\mathrm{Im}B_i}{\mathrm{Re}B_i} . \qquad (19)$$

The results summarized in the following section are based on equations (18) and (19).

RESULTS

Prior to using the method we performed various checks. First we checked the accuracy of our numerical integration procedure.[11] To do this, we made use of the integral equation for an elastic wave u_i^o scattered off a sphere of radius a ;

$$u_i(\underline{r}) = u_i^o(\underline{r}) - \delta\rho\omega^2 \int_S dV' g_{im}^o(\underline{r},\underline{r}') u_m^q(\underline{r}')$$

$$- \delta C_{jklm} \int_S dV' g_{ij,k'}^o(\underline{r},\underline{r}') u_{l,m'}^q(\underline{r}') \qquad (20)$$

We employ the notation of Johnson and Truell, where the total displacement wave solution is given by

$$u_i(\underline{r}) = \begin{cases} u_i^q(\underline{r}) & r < a \\ u_j^o(\underline{r}) + u_i^S(\underline{r}) & r > a \end{cases} \qquad (21)$$

In the limit $r \to \infty$, the asymptotic form of the integral is given by

$$-\left(A_i^{int} \frac{e^{i\alpha r}}{r} + B_i^{int} \frac{e^{i\beta r}}{r} \right) \qquad (22)$$

and the asymptotic form of $u_i^S(\underline{r})$ for incident longitudinal plane wave by

$$A_i^S \frac{e^{i\alpha r}}{r} + B_i^S \frac{e^{i\beta r}}{r} \qquad (23)$$

We thus can numerically compare A_i^S and $-A_i^{int}$ and B_i^S and $-B_i^{int}$. Note that this comparison checks both numerical integration and the calculation of the expansion coefficients for the spherical function because the A_i^S, B_i^S use the expansion outside the sphere and the A_i^{int}, B_i^{int} use the inside expansion. We were able to reduce our numerical error to $\sim$ 1% by choice of a sufficiently fine grid.

As a check on the approximation method itself we evaluated the scattering by a large spherical defect, using a small sphere as the unperturbed problem. We considered two cases with incident longitudinal wave for both.

1. Al Flaw in Ti, with a ratio of 2 between the radii of the two spheres. For example, this amounts to calculating the scattering by a spherical defect of radius 400μ, using the solution of

the scattering by a defect of 200μ as our zeroth order approximation, and treating the volume difference between the two spheres as a perturbation. Note that the volume of the perturbation defect is seven times the unperturbed defect volume!

Thus the results presented below serve as a quite strong test on treatment of large volume deviations by our technique. The results for scattered power and phase as functions of ka, for the backscattered longitudinal wave are presented in Fig. 2, and for the mode converted shear wave (at 90°) on Fig. 3.

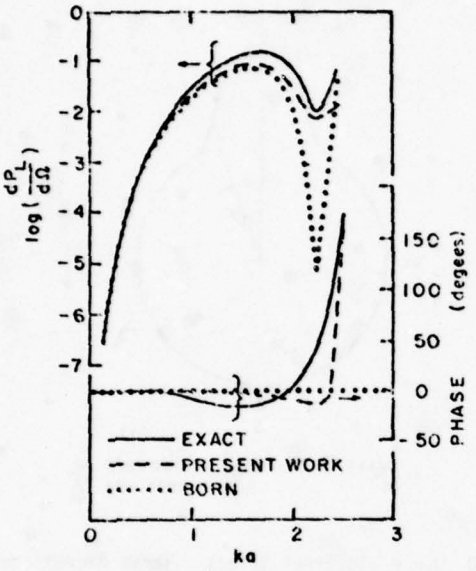

Fig. 2 Al sphere in Ti: Longitudinal backscattered wave, power and phase versus ka for a ratio of radii of 2.

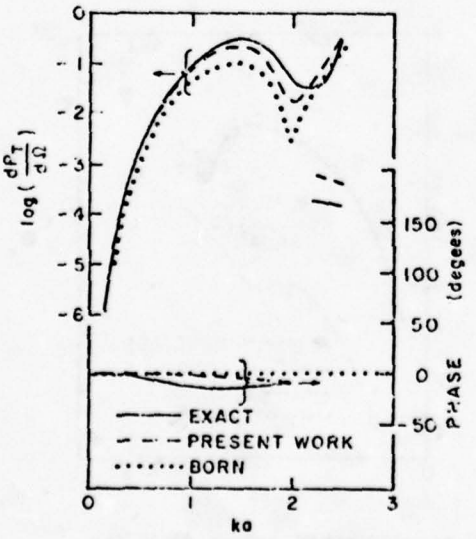

Fig. 3 Al sphere in Ti: Mode converted shear wave scattered at $\theta = 90^0$, power and phase versus ka for a ratio of radii of 2.

2. Spherical Cavity in Ti - Since the cavity constituted a much stronger defect than an aluminum inclusion, we chose to investigate a situation where radii of the actual defect and the one used as zeroth order approximation are closer, namely a ratio of 4/3. Still, this corresponds (see Fig. 1) to $\bar{R}/S = 1.37$, i.e. we still deal with a rather large perturbation. The results for backscattered longitudinal and the mode converted shear wave at 90° are shown in Figs. 4 and 5, as plotted versus ka, and on Fig. 6 and 7, for ka = 2, plotted vs the scattering angle.

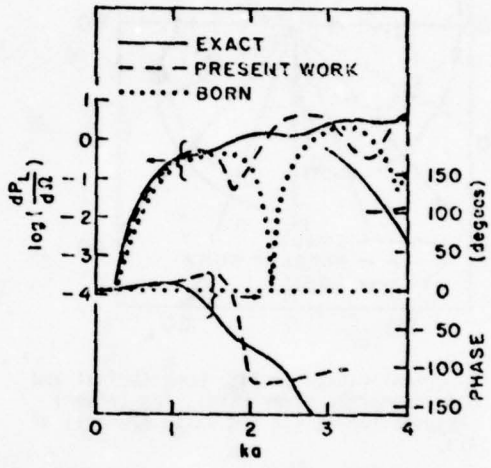

Fig. 4 Spherical cavity in Ti: Longitudinal backscattered wave, power and phase versus ka for a ratio of radii of 4/3.

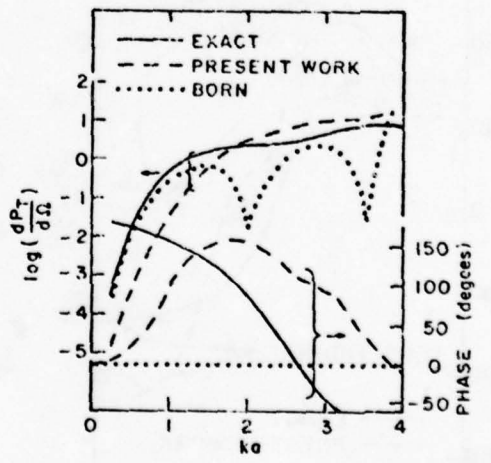

Fig. 5 Spherical cavity in Ti: Mode converted shear wave scattered at $\theta = 90^0$, power and phase versus ka for a ratio of radii of 4/3.

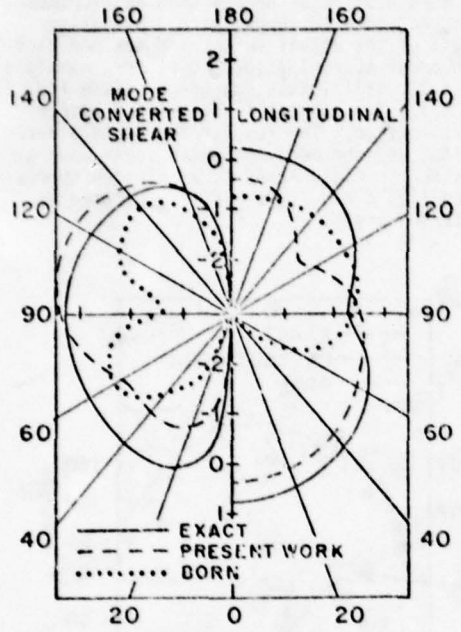

Fig. 6 Spherical cavity in Ti: Longitudinal and mode converted shear waves, log (power) versus θ for ka = 2 and ratio or radii of 4/3.

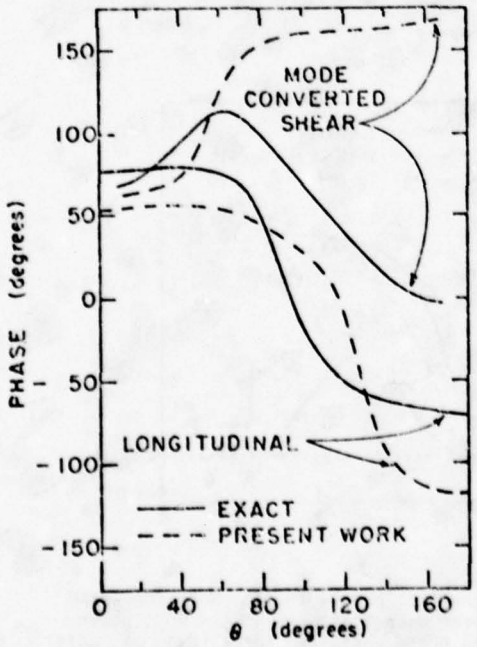

Fig. 7 Spherical cavity in Ti: Longitudinal and mode converted shear waves, phase versus θ for ka = 2 and ratio or radii of 4/3.

3. Non-ellipsoidal defects - To demonstrate the applicability of our method for non ellipsoidal defects, we considered backscattering by an Al inclusion in Ti, of the shape shown in Fig. 8. Three directions of incidence (of longitudinal waves) were studied, as also indicated on Fig. 8. The results for scattered longitudinal and shear power and phase are shown in comparison with that of a perfect sphere in Figs. 9-10. (No shear shown for sphere for backscattered.)

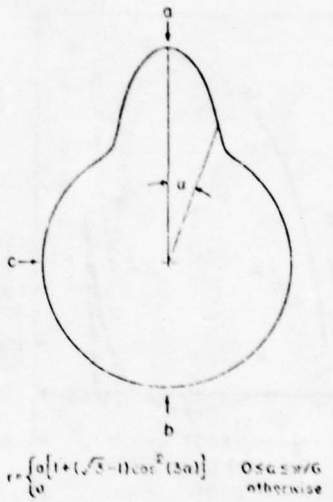

Fig. 8 Non-ellipsoidal defect: Three directions of incidence of the longitudinal wave. Defect is rotationally symmetric about the α = 0 axis.

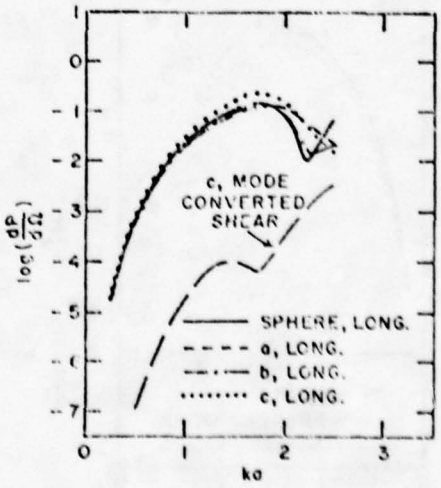

Fig. 9 Non-ellipsoidal defect, Al in Ti: Longitudinal and mode converted shear waves for three directions of incidence, log (power) versus ka.

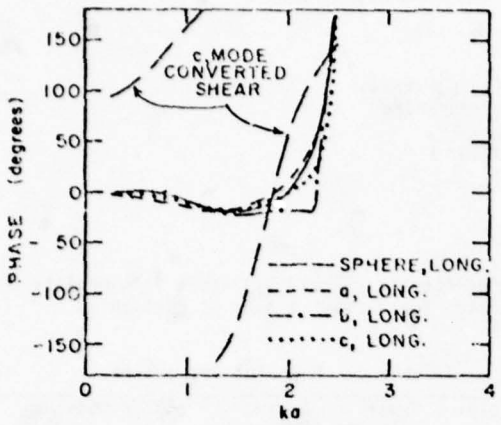

Fig. 10 Non-ellipsoidal defect, Al in Ti: Longitudinal and mode converted shear waves for three directions of incidence, phase versus ka.

SUMMARY AND DISCUSSION

We have developed an approximation method that can be used to study defects that are perturbations away from a spherical volume. We have found that this present theory constitutes a quite significant improvement over the Born Approximation. This is so in spite of the fact that we treat cases of large volume perturbations. The theory is not as good for the case of the cavity. This is reasonable because the other small parameters in the approximation (quantities like $\delta\rho/\rho$)are not small, but 1. This provides strong motivation to calculate the spherical Green's function and calculate with the DWBA. The DWBA is an expansion in both volume perturbations $\delta V/V$ and parameters like $\delta\rho/\rho$. To a given order in $\delta V/V$, all orders in $\delta\rho/\rho$ are included within DWBA. Thus reasonable results for cavities can be expected for small $\delta V/V$ for DWBA.

With this new approximation, investigation of non-ellipsoidal defects is now more feasible. Any shape that is a positive (larger volume) perturbation away from a sphere can be investigated. With the inclusion of the complete spherical Green's function into the calculation, negative perturbations from a sphere for inclusions will also be able to be handled. We intend to investigate a select class of interesting defects and continue in parallel with the development and inclusion of the spherical Green's function into the calculation. We hope to also learn about possible applications of phase information in classifying defects.

ACKNOWLEDGMENT

This research was sponsored by the Center for Advanced NDE, operated by the Science Center, Rockwell International, for the Defense Advanced Research Projects and the Air Force Materials Laboratory under Contract F33615-74-C-5180.

REFERENCES

1. J. E. Gubernatis, E. Domany, J. A. Krumhansl and M. Huberman, J. Appl. Phys. 48, 2812(1977).
2. J. E. Gubernatis, to be published.
3. E. Domany, Interdisciplinary Program for Quantitative Flaw Definition, Special Report Third Year Effort, p. 70 (1977).
4. J. Richardson, these Proceedings.
5. B. Budiansky and J. R. Rice, preprint.
6. V. Varadan and V. Varadan, these proceedings.
7. A. Mucciandi, these proceedings and references therein.
8. B. R. Tittman, R. K. Elsley, H. Nadler and E. R. Cohen, Special Report Third Year Effort p. 82 (1977); L. Adler, ibid. p. 122.
9. J. E. Gubernatis, E. Domany and J. A. Krumhansl, J. Appl. Phys. 48, 2804(1977).
10. C. F. Ying and R. Truell, J. Appl. Phys. 27, 1086(1956); G. Johnson and R. Truell, J. Appl. Phys. 36, 3466(1965); N. G. Einspruch, E. J. Witterholt and R. Truell, J. Appl. Phys. 31, 806(1960). See also Ref. 1, Appendix A,B.
11. We thank B. Yanoff for programming assistance.

T-MATRIX CALCULATIONS FOR SPHEROIDAL AND CRACK LIKE FLAWS

Vasundara V. Varadan and Vijay K. Varadan
Department of Engineering Mechanics
The Ohio State University
Columbus, Ohio 43210

ABSTRACT

Numerical calculations are presented for the scattering of elastic (P- and S-) waves from prolate and oblate spheroids and two-dimensional, rough, crack-like flaws for various angles of incidence, observation and frequencies using the T-matrix approach.

INTRODUCTION

Previously the T-matrix[1] method has been successfully used for two dimensional elastic scatterers[2,3] for arbitrary scattering geometry and for spheroidal elastic scatterers[4] when a P-wave is incident along the symmetry axis of the spheroid. We have now obtained numerical results for the scattering of P- and S- waves incident at arbitrary angles on prolate and oblate spheroidal cavities and inclusions for a wide range of frequencies.

Some preliminary numerical results have also been obtained for infinitely long cylinders of elliptic cross section when the aspect ratio is very small ~0.07. This will correspond to a two dimensional elliptic crack. For incident SH-waves we have shown that systematic expansions of the T-matrix in powers of ka, a non-dimensional wave number, agree with the exact far field results using matched asymptotic expansions or Mathieu functions for both cavities and inclusions, if the limit of zero aspect ratio is taken in the analytic expressions of the T-matrix. We have also checked the numerical results for aspect ratio ~0.07 against the exact crack results with excellent agreement. We are now incorporating the limiting procedure into the numerical scheme which should make the calculations much more efficient. We will also extend this approach to penny shaped cracks in the near future.

All of these calculations have been made for the purpose of flaw detection in real materials. But real flaws are rarely smooth although most theoretical calculations are based on smooth boundaries. In order to make the scatterer more realistic we have presented some results for the scattering of SH-waves from an elliptic cylinder whose boundary is perturbed by a periodic function. There is considerable difference in the scattering signatures of a rough and smooth surface.

DESCRIPTION OF FIGURES

For spheroidal cavities and inclusions, the host material is taken to be Ti6%Al-4%V and the inclusions are of Tungsten Carbide (WC). The two dimensional results are for Aluminum. A table of material properties follows.

Table I: Material Properties

Material	P-wave velocity	S-wave velocity	Shear modulus
Ti6%Al-4%V	6340 m/s	3030 m/s	4.06×10^{10} N/m^2
WC	6660 m/s	3980 m/s	2.19×10^{11} N/m^2
Aluminum	6420 m/s	3040 m/s	2.5×10^{10} N/m^2

The figures are self descriptive and the scattering geometry for each one of them is clearly indicated. For spheroids, the z-axis is taken as the axis of revolution. For elliptic cylinders, the z-axis coincides with the cylinder axis. 'α' is the angle of incidence measured with respect to the positive z-axis for 3-D geometries and the azimuthal angle is set equal to zero with no loss of generality. The direction of observation is specified by the angles θ, ϕ. For 2-D geometries, the polar angle of incidence, $-\alpha$, and observation, θ, are measured with respect to the positive x-axis which coincides with the major axis of the ellipse.

CONCLUSIONS

These results are yet to be compared with experiments. The data presented here is also being used as a data base for the inversion procedure developed by J. Rose and the adaptive training procedure developed by A. Mucciardi and M. Whalen. The outcome of their calculations should be interesting to see.

ACKNOWLEDGEMENTS:

This research was sponsored by the Center for Advanced NDE, operated by the Science Center, Rockwell International, for the Defence Advanced Research Projects and the Air Force Materials Laboratory under Contract F33615-74-C-5180.

REFERENCES

1. 'Scattering Matrix for Elastic Waves. I. Theory', J. Acoust. Soc. Am. 60, 556 (1976).

2. 'Scattering Matrix for Elastic Waves. II. Application to Elliptic Cylinders', J. Acoust. Soc. Am. 63, 1014 (1978).

3. 'Spectral Analysis of Scattered Elastic Waves', ARPA/AFML Review on Progress in Quantitative NDE, Ithaca, New York (1977).

4. 'Matrix Theory for Elastic Wave Scattering from Spheroids', Sixth Canadian Congress of Applied Mechanics, Vancouver, B.C. (1977).

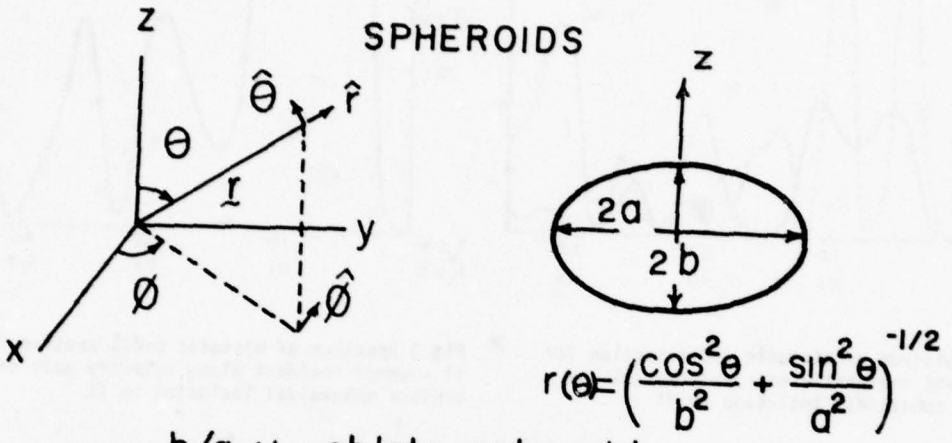

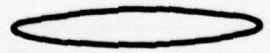

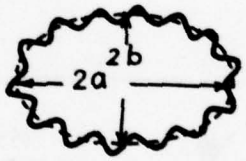

S1-wave shear wave polarized in $\hat{\theta}$ direction
S2-wave shear wave polarized in $\hat{\phi}$ direction
s/a - roughness parameter

Fig.1 Notation and geometry

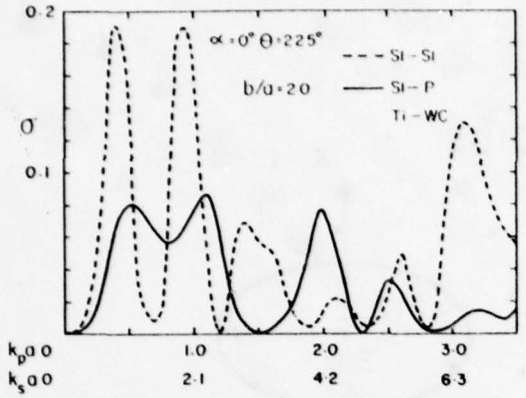

Fig.2 Spectrum of bistatic cross section for Sl - waves incident along symmetry axis of prolate spheroidal inclusion in Ti.

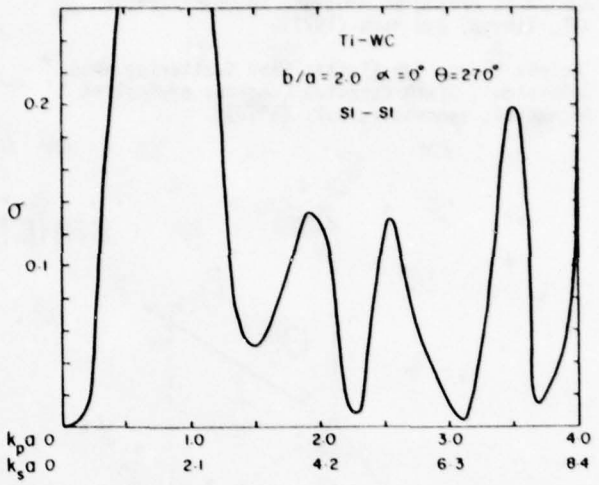

Fig.3 Spectrum of bistatic cross section for Sl - waves incident along symmetry axis of prolate spheroidal inclusion in Ti.

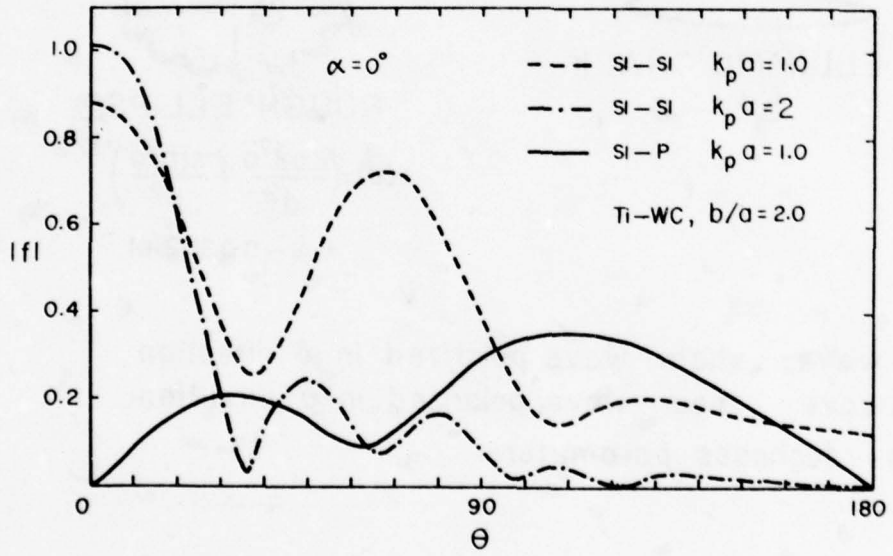

Fig.4 Angular variation of scattered field amplitude for Sl - waves incident at different frequencies along symmetry axis of prolate spheroidal inclusion in Ti.

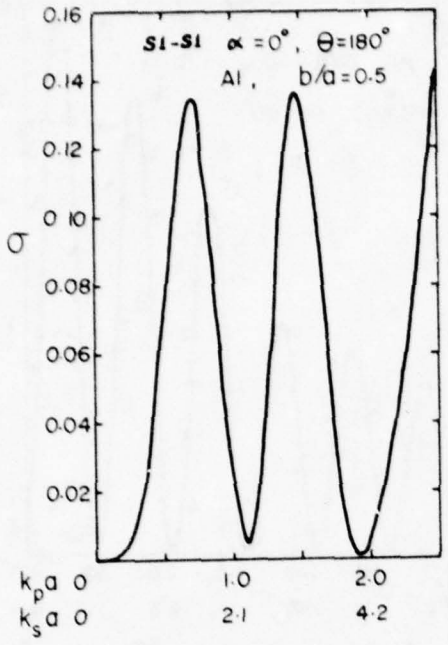

Fig.5 Spectrum of back scattering cross section for P - waves incident along symmetry axis of oblate spheroidal cavity in Al.

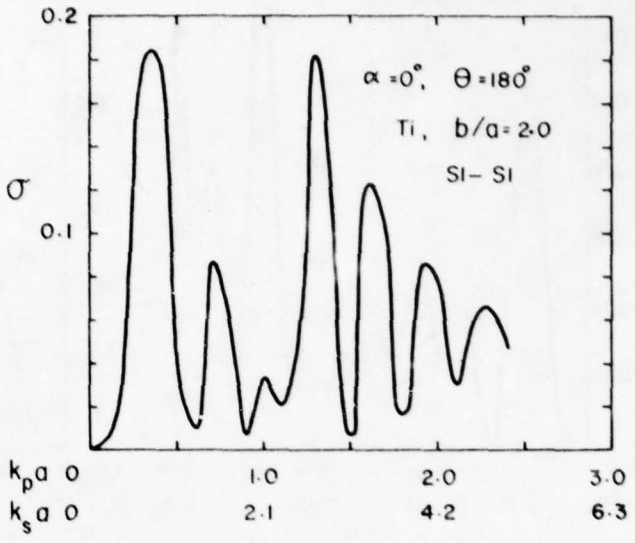

Fig.6 Spectrum of back scattering cross section for Sl - waves incident along symmetry axis of prolate spheroidal cavity in Ti.

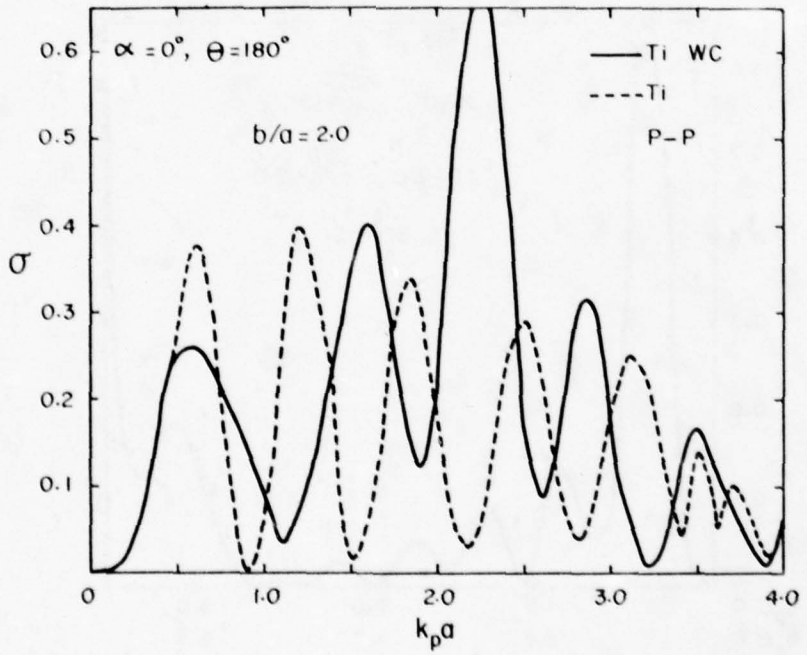

Fig.7 Spectrum of back scattering cross section for P - waves incident along symmetry axis of prolate spheroidal cavity and inclusion in Ti.

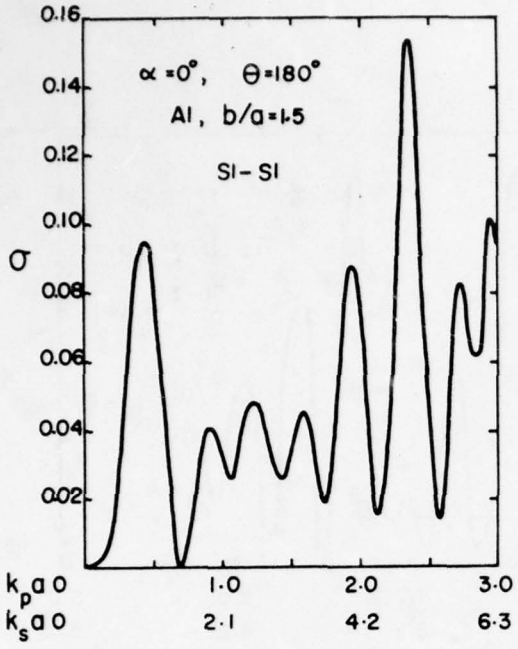

Fig.8 Spectrum of back scattering cross section for Sl - waves incident along symmetry axis of prolate spheroidal cavity in Al.

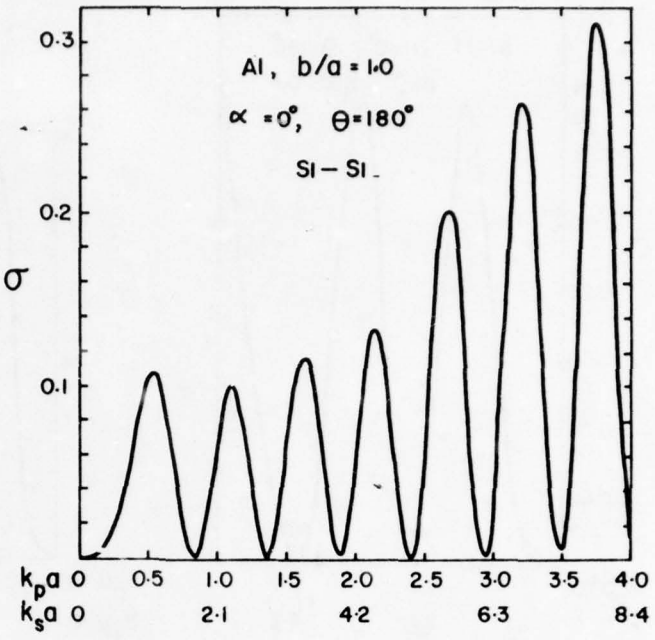

Fig.9 Spectrum of back scattering cross section for Sl - waves incident along symmetry axis of spherical cavity in Al.

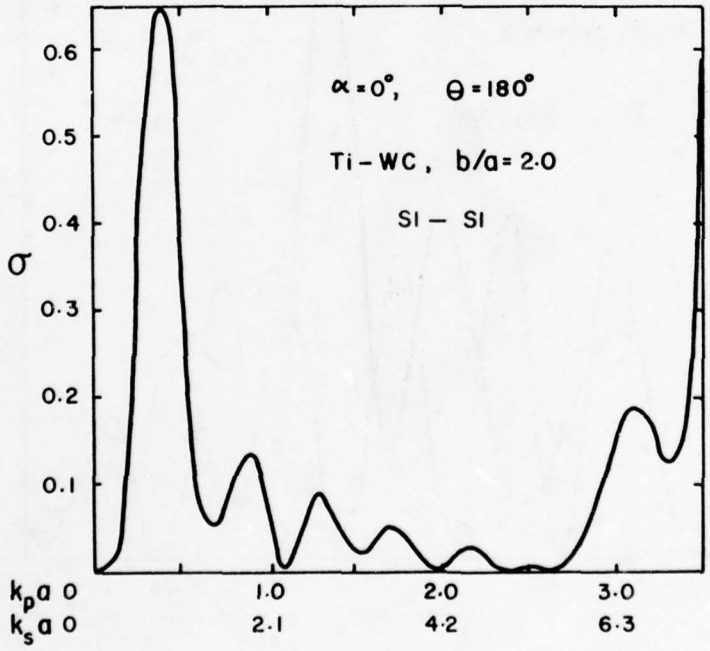

Fig.10 Spectrum of back scattering cross section for Sl - waves incident along symmetry axis of prolate spheroidal inclusion in Ti.

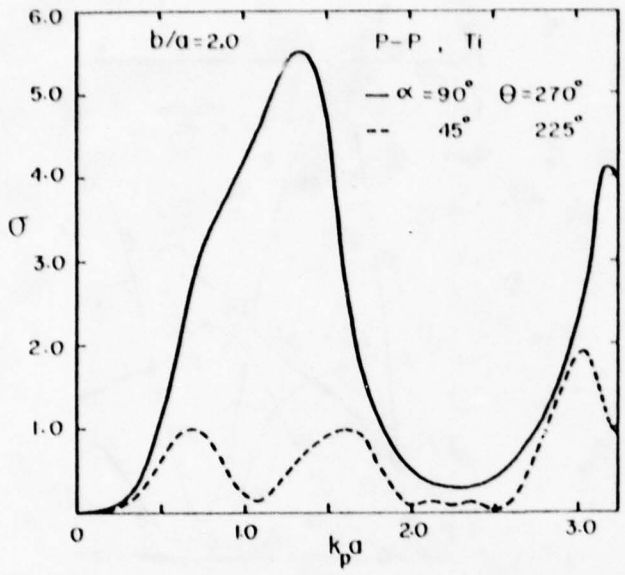

Fig.11 Spectrum of back scattering cross section for P - waves incident at 45 and 90 degrees with respect to symmetry axis of prolate spheroidal cavity in Ti.

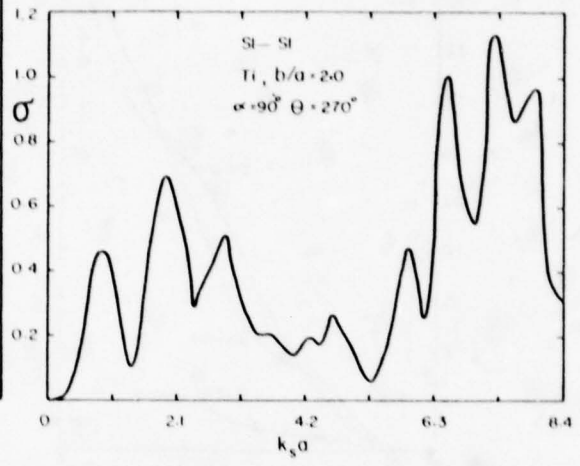

Fig.12 Spectrum of back scattering cross section for SI - waves incident at 90 degrees with respect to symmetry axis of prolate spheroidal cavity in Ti.

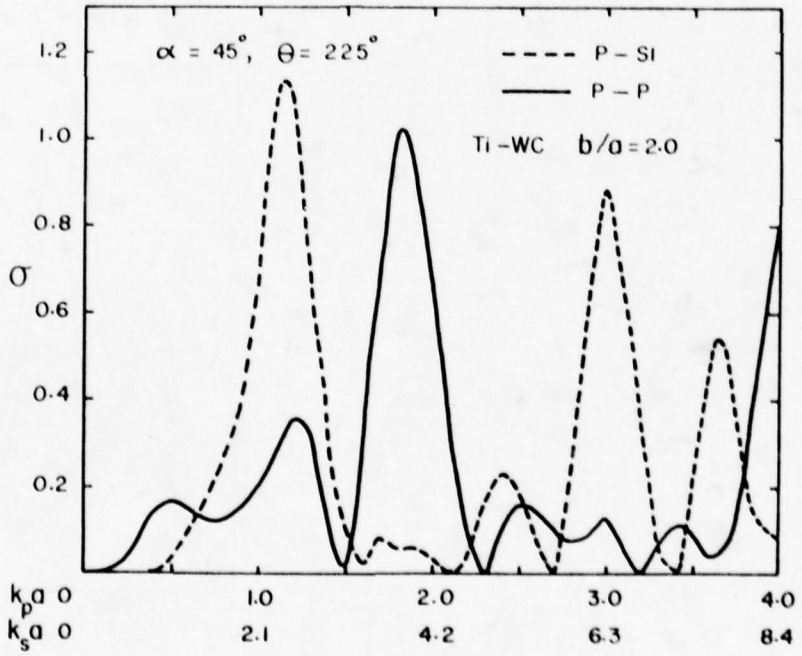

Fig.13 Spectrum of back scattering cross section for P - waves incident at 45 degrees with respect to the symmetry axis of prolate spheroidal inclusion in Ti.

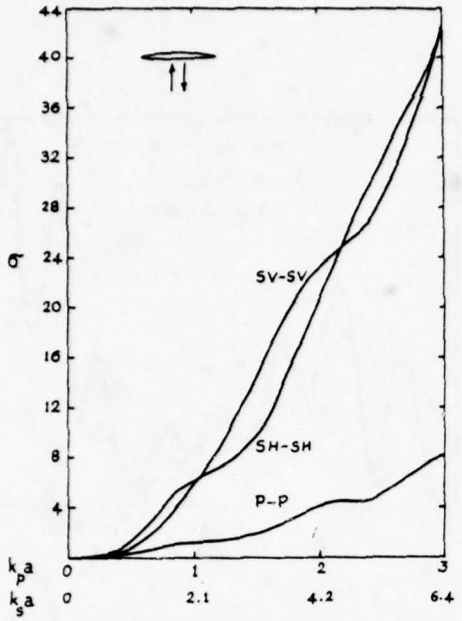

Fig.14 Spectrum of back scattering cross section for P -, SV -, and SH - waves incident normal to an elliptic crack in Al.

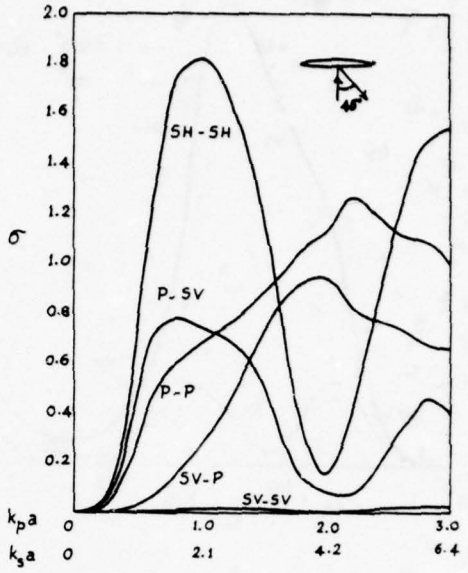

Fig.15 Spectrum of bistatic cross section for P -, SV -, and SH - waves incident normal to an elliptic crack in Al.

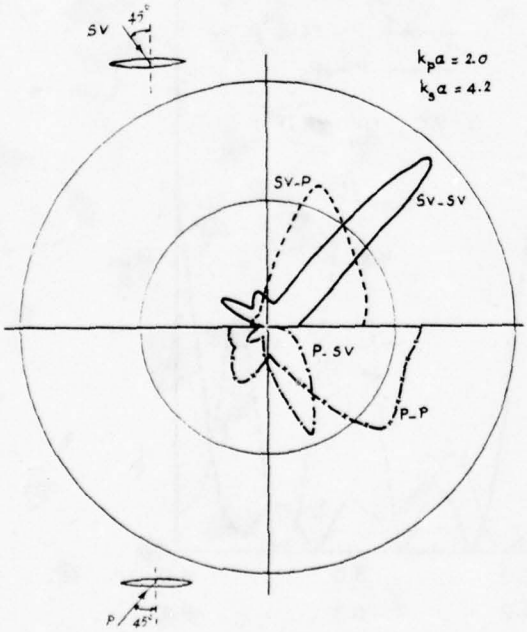

Fig.16 Polar plot of scattered field amplitudes for P -, and SV - waves incident at 45 degrees to an elliptic crack in Al.

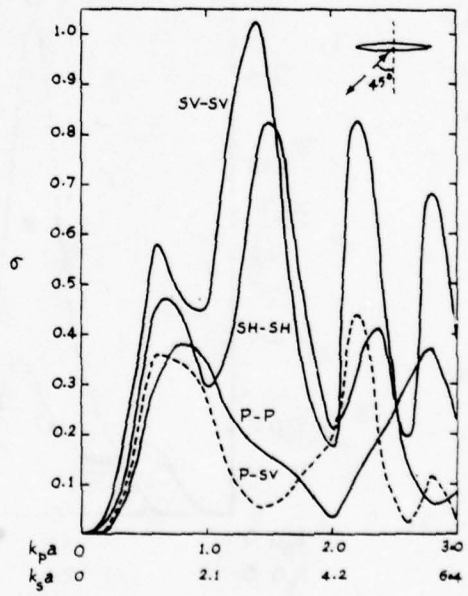

Fig.17 Spectrum of back scattering cross section for P -, SV -, and SH - waves incident at 45 degrees to an elliptic crack in Al.

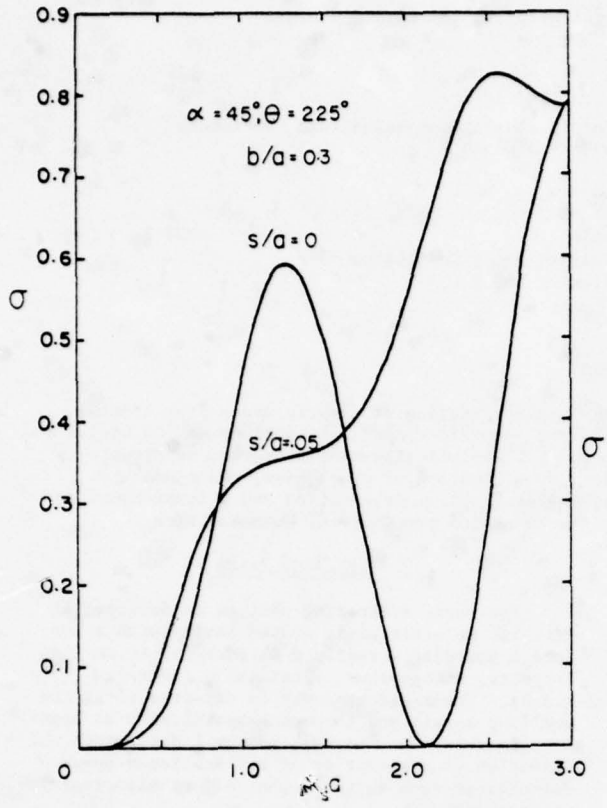

Fig.18 Spectrum of back scattering cross section for SH - waves incident at 45 degrees to the major axis of a rough and smooth ellipse in Al.

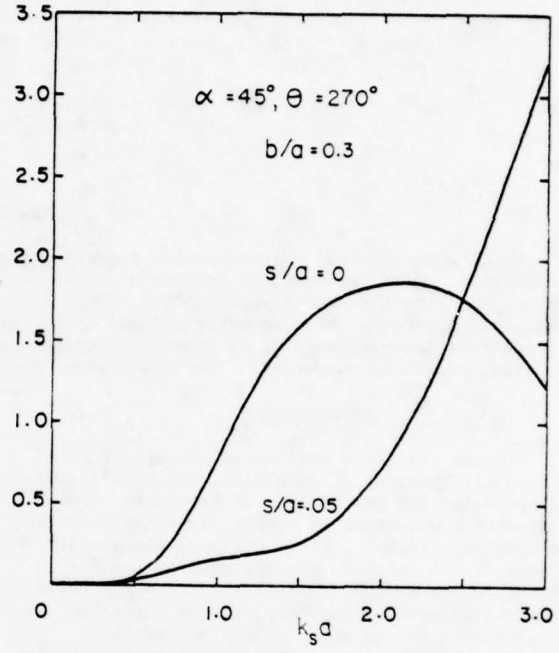

Fig.19 Spectrum of bistatic cross section for SH - waves incident at 45 degrees to the major axis of a rough and smooth ellipse in Al.

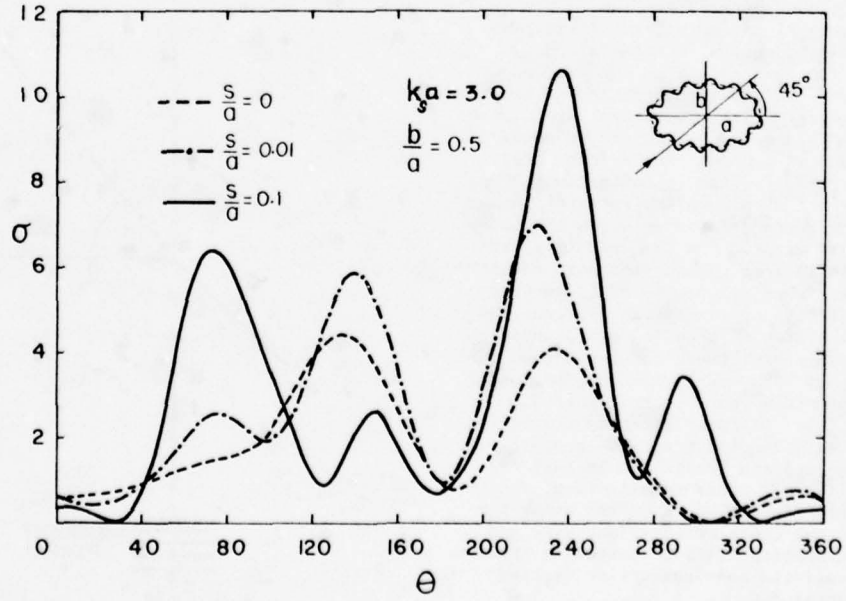

Fig.20 Angular variation of scattered field amplitude for SH - waves incident at 45 degrees to the major axis of a rough ellipse.

CRACK IDENTIFICATION AND CHARACTERIZATION IN THE RAYLEIGH LIMIT

J. E. Gubernatis
Theoretical Division, University of California, Los Alamos Scientific Laboratory
Los Alamos, New Mexico 87545

and

E. Domany
Department of Physics, University of Washington
Seattle, Washington 98195

ABSTRACT

We discuss apparent characteristic features of Rayleigh scattering of elastic waves from cracks. Interpreting these features, we propose a procedure that in some experimental situations may be useful to distinguish generally-shaped cracks from volume defects. For elliptically-shaped cracks, we propose additional procedures that in principle allow the unique specification of crack size, shape and orientation; however, we suggest that in practice only the crack plane orientation and a lower bound on the crack length is measurable. We also comment upon the inversion procedure of Kohn and Rice.

INTRODUCTION

Cracks can cause significant changes in the mechanical behavior of materials, the most dramatic change being the possibility of fracture. Non-destructive detection of cracks, especially cracks critical to fracture, often utilizes ultrasonic techniques in which an elastic wave propagates through the material and is scattered by the crack. From features of the scattering, the detection and characterization of the crack is attempted. Clearly, in these important experiments the dominant physical process to be understood is the scattering of the elastic wave by a single crack. In this respect, a simple model problem is that of an elliptical or circular "soft" crack embedded in an infinite, homogeneous isotropic medium.

Recently, several investigators[1-5] independently considered theoretical studies of this problem for the limiting case when the wavelength of the elastic wave is considerably larger than the crack. In this quasi-static (Rayleigh) limit, the exact form of the scattered fields can be obtained.

In this paper we continue the spirit, but extend the analysis, of these investigations. Our approach is to start with a volume integral formulation of the scattering[8,9] for which several useful approximations exist.[9-12] The approximation used here is identical to the quasi-static result derived by Datta.[3] Our purpose is to illustrate in the context of this approximation apparent characteristic features of elastic wave scattering from cracks, to interpret these results and to discuss experimental procedures that may be useful for their detection and characterization.

More explicitly, we first identify scattering signatures which distinguish cracks of general shape from volume defects (voids and inclusions). Then, we specialize our study to elliptical cracks and propose scattering signatures which allow the determination of the crack orientation, size and shape. Also the applicability of measuring these signatures in realistic non-destructive testing situations is assessed.

BASIC EQUATIONS

The basic scattering picture is depicted in Fig. 1. An arbitrarily shaped cavity with a surface S bounding a region R is embedded in an infinite, homogeneous, elastically isotropic medium. The incident power is directed along the positive z-axis and is monochromatic with an angular frequency ω. The unit vector $\hat{r}$ determines the direction of observation of the scattered power relative to some suitably chosen Cartesian coordinate system.

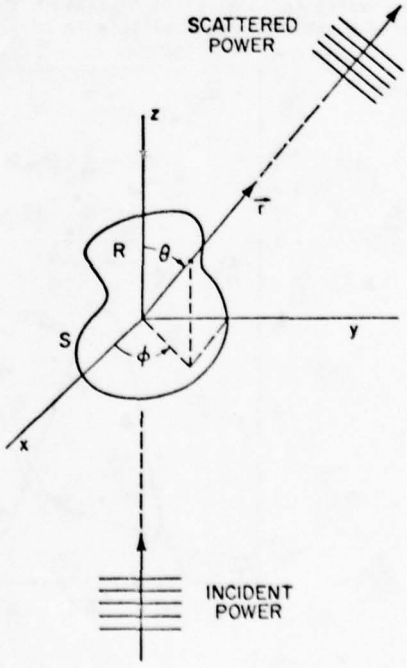

Fig. 1. A typical scattering geometry. For purposes of illustration the incident power is along the positive z-axis.

The scattering effectiveness of this cavity is measured by the differential cross-section which is essentially the time average of the fraction of incident power scattered into a particular direction. For incident power associated with a displacement field [omitting $\exp(-i\omega t)$]

$$u_i^0 = a_i e^{i\underline{\alpha}^0 \cdot \underline{r}} + b_i e^{i\underline{\beta}^0 \cdot \underline{r}} \tag{1}$$

where α and β are the wavenumbers of the longitudinal and transverse made with a_i and b_i, the corresponding vector polarization amplitudes, and $\underline{\alpha}^0 = \alpha\hat{\underline{a}}$ and $\underline{\beta}^0 = \beta\hat{\underline{a}}$, the incident wavevectors. The differential cross-section is found[8] to be given by

$$\frac{dP(\omega)}{d\Omega} = \frac{\alpha(\lambda+2\mu)|A_i|^2 + \beta\mu|B_i|^2}{\alpha(\lambda+2\mu)|a_i|^2 + \beta\mu|b_i|^2} \tag{2}$$

with λ and μ the Lamé parameters of the medium hosting the cavity, $d\Omega$ a differential element of solid angle, and A_i and B_i the vector amplitudes of the displacement field associated with the scattered (far-field) power:

$$u_i^0 \sim A_i \frac{e^{i\alpha r}}{r} + B_i \frac{e^{i\beta r}}{r} \tag{3}$$

The scattered amplitudes are related to a quantity called the f-vector[8]

$$A_i = \hat{r}_i \hat{r}_j f_j(\underline{\alpha}) \tag{4a}$$

and

$$B_i = (\delta_{ij} - \hat{r}_i \hat{r}_j) f_j(\underline{\beta}) \tag{4b}$$

where summation over repeated indices is implied (as throughout the rest of the paper), $\hat{\underline{r}}$ is the unit vector in the scattered (observation) direction, and $\underline{\alpha} = \alpha\hat{\underline{r}}$ and $\underline{\beta} = \beta\hat{\underline{r}}$. For a void the explicit form of the f-vector is

$$f_i(\underline{k}) = \frac{-k^2}{4\pi\rho\omega^2}\left[\rho\omega^2 \int_R dV u_i e^{-i\underline{k}\cdot\underline{r}} + ikC_{ijk\ell}\hat{r}_j \int_R dV \varepsilon_{k\ell} e^{-i\underline{k}\cdot\underline{r}}\right] \tag{5}$$

where $C_{ijk\ell} = \lambda\delta_{ij}\delta_{k\ell} + \mu(\delta_{i\ell}\delta_{jk} + \delta_{ik}\delta_{j\ell})$.

One of our objectives is to apply Eq. (5) to the long wave scattering from a crack. To indicate the nature of our approximation, we write

$$f_i(\underline{k}) \equiv f_i\left[u_i e^{-i\underline{k}\cdot\underline{r}};\ \varepsilon_{k\ell} e^{-i\underline{k}\cdot\underline{r}}\right] \tag{6}$$

to symbolize that in (5) there are two independent integrations, one with $u_i \exp(-i\underline{k}\cdot\underline{r})$ in the integrand and the other with $\varepsilon_{k\ell}\exp(-i\underline{k}\cdot\underline{r})$; that is,

$$f_i[x_i;\ y_k] = \frac{k^2}{4\pi\rho\omega^2}\left[\rho\omega^2 \int_R dV x_i + ikC_{ijk\ell}\hat{r}_j \int_R dV y_{k\ell}\right] \tag{7}$$

A specific choice of these fields will produce the exact $f_i(\underline{k})$. Our approximation is based on substituting known fields for x_i and $y_{k\ell}$, and as choices for these fields, we consider first a static problem of a cavity embedded in a medium that has a uniform stress σ_{ij}^0 as $R \to \infty$. The resulting strain field can be written as

$$\varepsilon_{ij}^\sigma = e_{ij}^0 + \int_R dV G_{ijk\ell}^{(0)} C_{k\ell mn} \varepsilon_{mn}^\sigma \tag{8}$$

where e_{ij}^0 is the strain field associated with σ_{ij}^0 in the defect-free medium, $G_{ijk\ell}^{(0)}$ is the static Green's function[13,14] and ε_{ij}^σ is a fictitious field defined in the cavity. For ellipsoidal cavities ε_{ij}^σ was calculated by Eshelby.[7] It is exactly this static field used in approximate solution. Returning now to the scattering problem, we note that for an incident wave of the form

$$u_i^0 = u_i^\sigma e^{i\underline{k}^0\cdot\underline{r}} \tag{9}$$

the associated strain field is

$$\varepsilon_{ij}^0 = e_{ij}^0 e^{i\underline{k}^0\cdot\underline{r}}$$

where

$$e_{ij}^0 = i\left(u_i^\sigma k_j^0 + u_j^\sigma k_i^0\right)/2 \quad . \tag{10}$$

With e_{ij}^0 as a static, uniform strain, the tensor ε_{ij}^σ (associated with the corresponding static problem) is defined. When f_i^{QS} is used in Eq. (4), the approximation

$$f_i^{QS} = f_i\left[u_i^\sigma\ ;\ \varepsilon_{k\ell}^\sigma\right] \tag{11}$$

can be shown[3,11,12] to produce the scattered amplitudes exactly to the leading order in ω (which is ω^2). Equation (10) is called the quasi-static approximation[11]; it gives the Rayleigh limit to the scattering.

For ellipsoidal cavities, the ε_{ij}^σ needed in Eqs. (8) and (11) is given by Eshelby; furthermore, ε_{ij}^σ is itself a uniform (constant) strain. For an ellipsoid, Eq. (5) becomes

$$f_i^{QS}(\underline{k}) = \frac{-Vk^2}{4\pi\rho\omega^2}\left[\rho\omega^2 u_i^\sigma + ikC_{ijk\ell}\hat{r}_j \varepsilon_{k\ell}^\sigma\right] \tag{12}$$

where V is the volume of the cavity. ε_{ij}^σ is related to e_{ij}^0 by

$$\varepsilon_{ij}^\sigma = [(I-S)^{-1}]_{ijk\ell}\, e_{k\ell}^0 \equiv \Gamma_{ijk\ell}\, e_{k\ell}^0$$

where I is the identity fourth rank tensor and the fourth rank tensor S is calculated by Eshelby.[7]

To obtain results for an elliptical crack, we first consider an ellipsoid with principal axes $a > b > c$, and then take the following limits:

$$\lim_{c\to 0} V = 0$$

$$\lim_{c\to 0} V\Gamma_{ijk\ell} \equiv \gamma_{ijk\ell}$$

More explicitly, if a and b are along the x- and y- directions, we find

$$\gamma_{3311} = \gamma_{3322} = \frac{4\pi a^3}{3} \frac{2\nu(1-\nu)\kappa_1^2}{E(\kappa)(1-2\nu)} \tag{13a}$$

$$\gamma_{3333} = \frac{1-\nu}{\nu} \gamma_{3311} \tag{13b}$$

$$\gamma_{2323} = \frac{2\pi a^3 \kappa_1^2}{3} \left[\frac{E(\kappa)}{1-\nu} - \frac{\nu\kappa_1^2[F(\kappa)-E(\kappa)]}{\kappa^2(1-\nu)} \right]^{-1} \tag{13c}$$

$$\gamma_{1313} = \frac{2\pi a^3 \kappa_1^2}{3} \left[E(\kappa) + \frac{\nu\kappa_1^2[F(\kappa)-E(\kappa)]}{\kappa^2(1-\nu)} \right]^{-1} \tag{13d}$$

where ν is Poisson's ratio [$\nu=\lambda/2(\lambda+\mu)$] and $F(\kappa)$ and $E(\kappa)$ are complete elliptic integrals of the first and second kind with $\kappa = (1-b^2/a^2)^{\frac{1}{2}}$ and $\kappa_1^2 = 1 - \kappa^2$. The corresponding expressions for a circular crack of radius a are

$$\gamma_{3311} = \gamma_{3322} = \frac{16a^3}{3} \frac{\nu(1-\nu)}{1-2\nu} \tag{14a}$$

$$\gamma_{3333} = \frac{(1-\nu)}{\nu} \lambda_{3311} \tag{14b}$$

$$\gamma_{2323} = \gamma_{1313} = \frac{8a^3}{3} \frac{(1-\nu)}{(2-\nu)} \quad . \tag{14c}$$

For both elliptical and circular cracks $\gamma_{ijk\ell} = \gamma_{jik\ell} = \gamma_{ij\ell k}$. Terms that cannot be obtained from (13) by these interchanges of indices are zero. We note that $\gamma_{ijk\ell}$, and hence the scattered fields, are proportional to $4\pi a^3/3$, the volume of the smallest sphere that can encircle the crack independent of b. We note that

$$\gamma_{3311}/\gamma_{1313} + \gamma_{3311}/\gamma_{2323} = 2(2-\nu)/(1-2\nu) \tag{15}$$

and hence that only two of the $\gamma_{ijk\ell}$ are independent.

RESULTS

In this section we address the problem of flaw characterization in two stages. First, several features are found that distinguish cracks from volume defects, including one valid for arbitrarily-shaped (not necessarily planar) cracks. Second, for the special case of elliptical cracks, we discuss procedures for determining crack orientation, size and shape. The applicability of these procedures to realistic non-destructive testing situations is also assessed.

Crack Identification - In the quasi-static limit the f-vector for scattering from a cavity has form[1]

$$f_i = VPu_i^o + Q_{ij}\hat{r}_j \tag{16}$$

where

$$P = -k^2/4\pi \tag{17a}$$

and

$$Q_{ij} = \frac{-ik^3}{4\pi\rho\omega^2} C_{ijk\ell} \int_R d\underline{r}\, \epsilon_{k\ell}^o(\underline{r}) \tag{17b}$$

Alternately, Q_{ij} can be obtained using the surface integral formulation of the problem. With a crack regarded as the limiting case of the volume $V \to 0$,

$$f_i = Q_{ij}^* \hat{r}_j$$

with

$$Q_{ij}^* = \lim_{V\to 0} Q_{ij}$$

But as seen from (17b) the tensor Q_{ij}, and hence Q_{ij}^*, depends only on the incident field and not on the scattered direction $\underline{\hat{r}}$. Thus, from (4a) the magnitude of the longitudinal field is

$$A_i\hat{r}_i = f_i\hat{r}_i = Q_{ij}^*\hat{r}_i\hat{r}_j$$

which is invariant under the replacement of $\underline{\hat{r}}$ by $-\underline{\hat{r}}$. Physically, for any incident direction this means the scattering in all diametrically opposite directions is identical (Fig. 2). This general result is valid only for cracks since the first term in (16) is nonzero for all cavities (and more generally for all inclusions). Consequently, if the measured scattered fields are equal at all diametrically opposite points, the defect must be a crack. A similar analysis can be made for the amplitude of the transverse scattered fields with the identical conclusion.

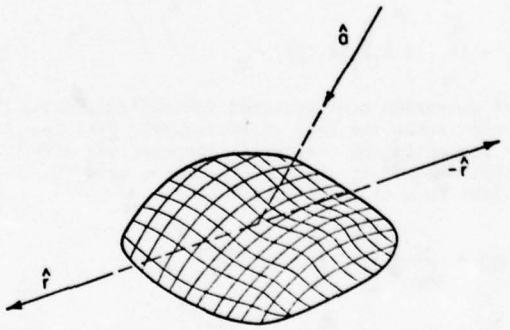

Fig. 2. An invariance property of Rayleigh scattering from cracks. For an incident direction $\underline{\hat{a}}$ the scattering in the direction $\underline{\hat{r}}$ is equal to the scattering in the direction $-\underline{\hat{r}}$.

Considering the special case of elliptical cracks, we can find other scattering signatures of cracks. Below we give for an incident longitudinal plane wave the Rayleigh limit scattered amplitudes and explicitly illustrate these signatures. In our equations, $\gamma^{(0)} = \gamma_{3311}$, $\gamma^{(1)} = \gamma_{1313}$ and $\gamma^{(2)} = \gamma_{2323}$; the incident direction $\underline{\hat{a}}$ is characterized by the angles θ_0 and ϕ_0; and the scattered direction $\underline{\hat{r}}$, by θ and ϕ. All angles are defined in a coordinate system fixed by the principal axes of the crack and by $\underline{\hat{n}}$, and the semi-major axis a and semi-minor axis b are in the x- and y- directions while $\underline{\hat{n}}$ is in the z-direction (Fig. 3).

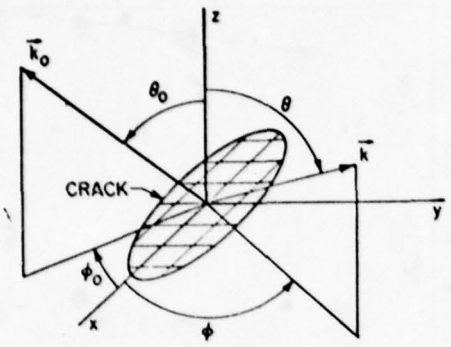

Fig. 3. The coordinate system defining the incident angles θ_0 and ϕ_0 and the scattered angles θ and ϕ relative to the crack orientation.

For a longitudinal wave incident in an arbitrary direction,

$$\hat{u}^0 = \cos\phi_0 \sin\theta_0 \hat{x} + \sin\phi_0 \sin\theta_0 \hat{y} + \cos\theta_0 \hat{z}$$

and

$$\alpha^0 = \hat{u}^0,$$

the scattered longitudinal (L) and transverse (T) displacement fields are

$$A_i = \hat{r}_i \frac{\alpha^2}{4\pi} \frac{\nu}{1-\nu} \Big\{ \gamma^{(0)} \left[1 + \frac{(1-2\nu)}{\nu} \cos^2\theta\right] \times \left[1 + \frac{(1-2\nu)}{\nu} \cos^2\theta_0\right] + \frac{(1-2\nu)}{2\nu} \left[\gamma^{(1)} \cos\phi \cos\phi_0 + \gamma^{(2)} \sin\phi \sin\phi_0\right] \sin 2\theta \sin 2\theta_0 \Big\} \quad (18a)$$

$$B_i = \frac{\alpha\beta}{4\pi} \Big(\theta_i \Big\{ -\gamma^{(0)} \left[1 + \frac{(1-2\nu)}{\nu} \cos^2\theta_0\right] \sin 2\theta + \sin 2\theta_0 \cos 2\theta \left[\gamma^{(1)} \cos\phi \cos\phi_0 + \gamma^{(2)} \sin\phi \sin\phi_0\right] \Big\} - \phi_i \sin 2\theta_0 \cos\theta \left[\gamma^{(1)} \sin\phi \cos\phi_0 - \gamma^{(2)} \cos\phi \sin\phi_0\right] \Big) \quad (18b)$$

where $\hat{\theta}$ and $\hat{\phi}$ are unit vectors in the θ and ϕ directions. By inspecting these equations, we found 3 additional crack identifiers: One, if both the incident and scattered directions are anywhere in the crack plane ($\theta = \theta_0 = 90°$), then the magnitudes of the scattered fields, and hence the cross-sections, are constants:

$$A = \alpha^2 \nu \gamma^{(0)}/4\pi(1-\nu) \quad (19a)$$

$$B = 0 \quad (19b)$$

Thus, the plane of the crack is a "plane of constant scattering". Furthermore, the existence of such a plane is a special property of elliptical cracks and is useful not only to distinguish these from volume defects, but also to determine the crack plane orientation, $\hat{n}$. (See below.)

Two, for normal incidence and for incidence along the crack edge ($\theta_0 = 0°$ and 90°), the angular distribution of scattered L waves (and similarly for scattered T waves) is identical and also independent of ϕ_0 and ϕ, that is,

$$A \propto 1 + \frac{(1-2\nu)}{\nu} \cos^2\theta \quad (20a)$$

$$B \propto |\sin 2\theta| \quad (20b)$$

Three, as seen from (20), the scattering for normal incidence is twofold symmetric about $\theta = 90°$ (i.e. the crack plane). This feature is also absent in the scattering from volume defects. [From (4) and (12) it can be demonstrated that the ρ contribution gives rise to an additional $\cos\theta$ dependence for L waves and a $\sin\theta$ dependence for T waves.]

Thus, to leading order in ω, the scattered power has a higher symmetry than the scatterer; furthermore, there are simple, measurable, qualitative features of the scattering that not only distinguish an elliptical crack from volume defects, but also determine the crack plane orientation.

Crack Characterization - Maintaining our specialization to elliptical cracks, we now discuss features that characterize the crack. This characterization consists of the determination of the orientation, size and shape.

Our first task is to determine the orientation of the crack plane. For elliptical cracks this task can be accomplished concurrently with the task of differentiating cracks from ellipsoidal defects. For example, the plane of constant scattering is coincident with the crack plane.

The more difficult task is to determine the orientation within this plane of the crack major axis. Knowing the crack plane allows us to specify θ and θ_0 in (16). To complete the specification of the crack orientation one must utilize the ϕ-dependence of the scattering. By inspecting (18) one sees that the relative magnitude of the ϕ-dependent terms is maximized when $\theta = \theta_0 = 45°$. In that case, for a pulse-echo experiment ($\phi = \phi_0$), the scattered longitudinal amplitude is, for example,

$$A_i \hat{r}_i = p + q \cos^2\phi \quad (21a)$$

where

$$p = \frac{\alpha^2}{16\pi(1-\nu)} \left[2\nu\gamma^{(0)} + (1-2\nu)\gamma^{(2)}\right] \quad (21b)$$

$$q = \frac{\alpha^2}{16\pi(1-\nu)} (1-2\nu) \left[\gamma^{(1)} - \gamma^{(2)}\right] \quad (21c)$$

Since $p, q > 0$, the maxima of the backscattered power (at $\phi = 0°$ or 180°) locate the direction of the major axis. However the ϕ dependence is proportional to $\gamma^{(1)} - \gamma^{(2)}$, which (Fig. 4) may be too small to measure for all b/a ratios. Consequently, the orientation of the major axis may be hard to determine experimentally. Physically, in the Rayleigh limit, scattering by an elliptical crack is similar to scattering by a circular crack.

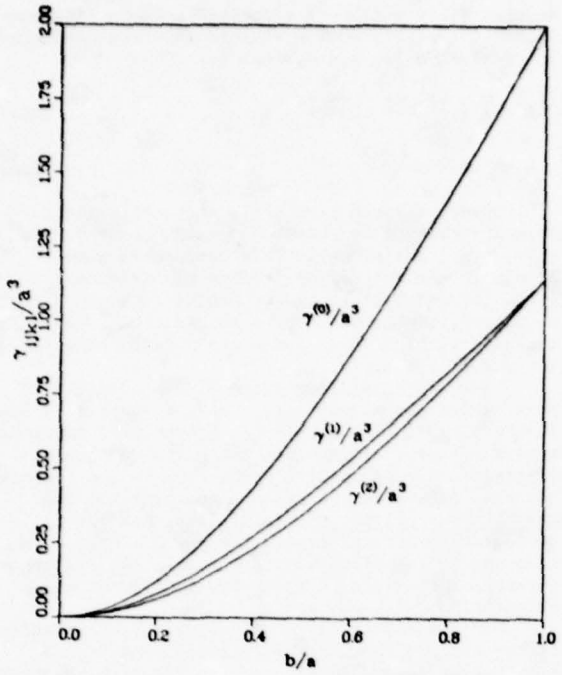

Fig. 4. Curves of $\gamma^{(0)}$, $\gamma^{(1)}$ and $\gamma^{(2)}$ as a function of b/a. The $\gamma^{(0)}$, $\gamma^{(1)}$ and $\gamma^{(2)}$ have units of volume with the unit of length the same as a and b. $\nu = \frac{1}{4}$.

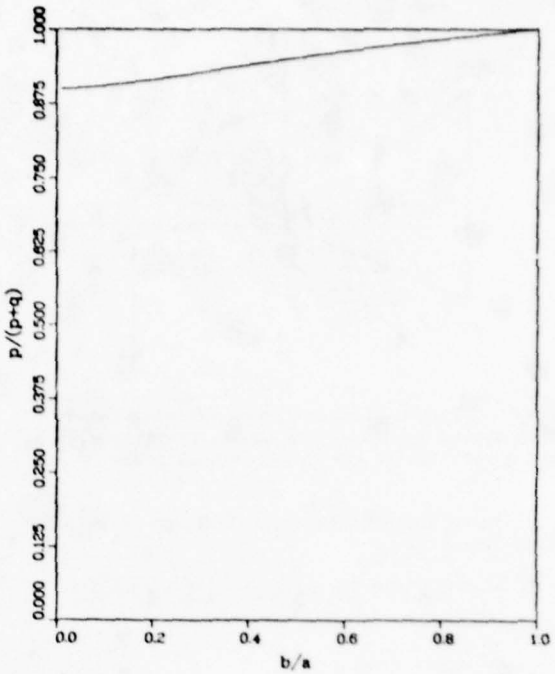

Fig. 5. A measure of the sensitivity of the scattering from an elliptical crack to its shape, b/a. $\nu = \frac{1}{4}$.

This discussion bears directly on the last task of characterizing the crack, the determination of a and b/a. In principle, knowledge of any two of $\{\gamma^{(0)}, \gamma^{(1)}, \gamma^{(2)}\}$ is sufficient to uniquely determine a and b/a. However, Figs. 4 and 5 reveal that $\gamma^{(1)} - \gamma^{(2)}$ and p/(p+q), the ratio of the minimum to maximum value of (21a), depend very weakly on b/a; as such, experimental determination of b/a may be difficult. For example, from Fig. 5, the value of b/a would be determined by exact measurement of p/(p+q). Then, with Fig. 4, knowledge of $\gamma^{(0)}$ determines a. However, from Fig. 5 one sees that the variation from b/a = 0 (needle-shaped crack) to b/a = 1 (circular crack) results at best in a 10% change in p/(p+q). Thus, it seems that the Rayleigh limit cannot be used effectively to determine b/a (or the orientation of the crack major axis). One can, though, estimate the crack length, a, provided some assumption concerning the range of b/a values is taken. If $x_0 < b/a < 1$ and a specific value $\gamma^{(0)}$ is obtained from measurement then

$$\left[\gamma^{(0)}/\gamma^{(0)}(1)\right]^{1/3} < a < \left[\gamma^{(0)}/\gamma^{(0)}(x_0)\right]^{1/3} \qquad (22)$$

where $\gamma^{(0)}(x) = \gamma^{(0)}(b/a)$.

A similar analysis with the same conclusions can be made for incident shear waves. We discuss this elsewhere.[15]

CONCLUSIONS

In contrast to long wavelength scattering of acoustic or quantum mechanical waves, which are isotropic with little information about the scatterer, the scattering of elastic waves, in addition to an isotropic component, possesses dipolar and quadrapolar components with important information about the scatterer.[1] We examined the angular content for the scattering from cracks and, after examining this content, identified features that may be useful in crack characterization experiments.

With great generality, we found that for any angle of incidence the Rayleigh scattering from any crack, in contrast to the scattering from volume defects, is identical in all diametrically opposite directions. This feature identifies the defect as a crack, but does not characterize the crack as to its size, shape and orientation. Additional identifying features, as well as a characterizing procedure, were specified for an elliptical crack. In this case, we found that it is in principle possible to characterize the crack uniquely. In practice, because of certain shape insensitive parameters, we believe the crack may appear circular, and possibly the best one can do is to measure the crack plane orientation and bounds for the crack length a.

Our analysis, demonstrating the complete and unique characterization of an elliptical crack, should be contrasted to the results predicted by the scattering inversion procedure suggested by Kohn and Rice.[4] They claim that the eigenvectors of a matrix $\underline{D}$, which for cracks equals

$$D_{mn} = -\frac{1}{3} C_{iik\ell} \gamma_{k\ell mn} ,$$

defines what may be called the principal axes of a

defect, i.e. the defect orientation. From (16) D_{mn} is easily specified in the principal axis system of an elliptical crack and equals

$$\underline{D} = K\gamma^{(0)} \begin{pmatrix} 1 & 0 & 0 \\ 0 & 1 & 0 \\ 0 & 0 & (1-\nu)/\nu \end{pmatrix}$$

with the bulk modulus $K = \lambda + \frac{2}{3}\mu$. However, since the eigenvalues are doubly degenerate, the complete specification of the orientation, according to the claim of Kohn and Rice, would be precluded. Consequently, their inversion procedure is incomplete.

ACKNOWLEDGEMENTS

This research was sponsored by the center for Advanced NDE, operated by the Science Center, Rockwell International, for the Defense Advanced Research Projects and the Air Force Materials Laboratory under Contract F33615-74-C-5180; also supported by the U.S. Department of Energy.

REFERENCES

1. Gubernatis, J. E., J. A. Krumhansl and R. M. Thomson, "Interpretation of Elastic Wave Scattering Theory for Analysis and Design of Flaw Characterization Experiments: The Long Wavelength Limit", Los Alamos Scientific Laboratory Report LA-UR-76-2546, submitted to J. Appl. Phys.
2. Domany, E., J. A. Krumhansl and S. Teitel, "Quasistatic Approximation to the Scattering of Elastic Waves by a Circular Crack", J. Appl. Phys. 49 (1977): 2599.
3. Datta, S. K., "Diffraction of Plane Elastic Waves by Ellipsoidal Inclusions", J. Acoust. Soc. Am. 61 (1977): 1432.
4. Kohn, W., and J. R. Rice, "Scattering of Long Wavelength Elastic Waves from Localized Defects in Solids", submitted to J. Appl. Phys.
5. Budiansky, B. and J. R. Rice, "On the Estimation of a Crack Fracture Parameter by Long Wavelength Scattering", unpublished.
6. Kraut, E. A., "Review of Theories of Scattering of Elastic Waves by Cracks", IEEE Tran. Sonics Ultrason. 23 (1976): 162.
7. Eshelby, J. D., "The Determination of the Elastic Field of an Ellipsoidal Inclusion and Related Problems", Proc. Roy. Soc. London 271 (1957): 376.
8. Gubernatis, J. E., E. Domany and J. A. Krumhansl, "Formal Aspects of the Theory of the Scattering of Ultrasound by Flaws in Materials", J. Appl. Phys. 48 (1977): 2804.
9. Gubernatis, J. E., E. Domany, J. A. Krumhansl and M. Huberman, "Theory of the Scattering of Ultrasound by Flaws", in 1975 Ultrasonics Symposium Proceedings, ed. by J. de Klerk. New York, IEEE, 1975, p. 107.
10. Gubernatis, J. E., E. Domany, M. Huberman, and J. A. Krumhansl, "The Fundamental Theory of Elastic Wave Scattering by Defects in Elastic Materials: Integral Equation Methods for Application to Ultrasonic Flaw Detection", Materials Science Center Report 2654, Cornell University, 1975.
11. Gubernatis, J. E., "Long Wave Approximations for the Scattering of Elastic Waves from Flaws", Los Alamos Scientific Laboratory Report LA-UR-77-2900, submitted to J. Appl. Phys.
12. Gubernatis, J. E., "The Scattering of Long Wavelength Elastic Waves from Ellipsoidal Voids and Inclusions", unpublished.
13. Gubernatis, J. E., E. Domany and J. A. Krumhansl, "The Elasticity of Polycrystals and Rocks", J. Geo. Res. 80 (1975): 4851.
14. Gubernatis, J. E. and J.A.Krumhansl, "Macroscopic Engineering Properties of Polycrystalline Materials: Elastic Properties", J. Appl. Phys. 46 (1975): 1875.
15. Gubernatis, J. E. and E. Domany, "Rayleigh Scattering of Elastic Waves from Cracks", Los Alamos Technical Report, LA-UR-78-1604, submitted to J. of Appl. Phys.

OPTIMIZATION OF SCATTERING MATRIX FOR ELASTIC WAVES FROM VOIDS AND OBSTACLES†

William M. Visscher
Theoretical Division
Los Alamos Scientific Laboratory
Los Alamos, NM 87545

ABSTRACT

It is shown that a family of scattering matrices for elastic and acoustic waves may be directly deduced from the boundary conditions at the surface of the defect, which in the present work is constrained to be a void or rigid immovable obstacle in a homogeneous isotropic medium, although the method can be readily generalized. From this family of matrices (which includes those derived and used by Waterman, and Pao and Varatharajulu) an optimum one may be chosen, and a criterion is given for doing so. This optimum T-matrix is numerically calculated for a variety of axially symmetric voids and obstacles and results are given for direct and mode-converted differential and total cross-sections.

INTRODUCTION

The scattering of elastic waves by flaws in a homogeneous and isotropic elastic medium is one of the simplest and most basic problems whose solution is of vital interest in nondestructive testing. Although it is simple on a relative scale, it can still be mathematically and computationally very involved, which is the principle reason numerical results have been sparse up to now, except for scattering from flaws with shapes of very high symmetry. The present work is an attempt to add a weapon to the arsenal which can be used to attack this problem.

In this report we shall present the principle of the method, its relation to other methods, and a sample of results which have been obtained. Details will be given elsewhere.

PRELIMINARIES

We will illustrate the procedure using equations for scalar waves, because the formalism is simpler. The development is parallel, but the equations are more complicated, for elastic waves.

The Helmholtz equation is

$$(\nabla^2 + k^2)\psi = 0 \quad , \tag{1}$$

and we wish to find a solution

$$\psi = \psi_{in} + \sum_s a_s \psi_s \tag{2}$$

which is a scattering wavefunction: i.e., the sum of an incident plane wave ψ_{in} and outgoing partial waves ψ_s. ψ_{in} and ψ_s are solutions of (1); we need only to find the amplitudes a_s for which ψ satisfies the boundary conditions imposed by the presence of the defect, which we take to be either a void or an immovable obstacle in an otherwise homogeneous, isotropic, infinite medium.

Specifically we take the eigenfunction ψ_s to be

$$\psi_s = \psi_{\ell m} = h_\ell^{(1)}(kr)Y_\ell^m(\theta,\varphi) \tag{3}$$

where $h_\ell^{(1)} = j_\ell + iy_\ell$, and

$$\psi_{in} = e^{i\vec{k}_o\cdot\vec{r}} = \sum_s d_s \tilde{\psi}_s = 4\pi \sum_{\ell,m} i^\ell Y_\ell^{m*}(\theta_o,\varphi_o) j_\ell(kr) Y_\ell^m(\theta,\varphi) \tag{4}$$

with

$$\tilde{\psi}_s = \tilde{\psi}_{\ell m} = j_\ell(kr)Y_\ell^m(\theta,\varphi) \quad , \tag{5}$$

i.e., the part of ψ_s that is regular at the origin, which is always inside the defect.

BOUNDARY CONDITIONS

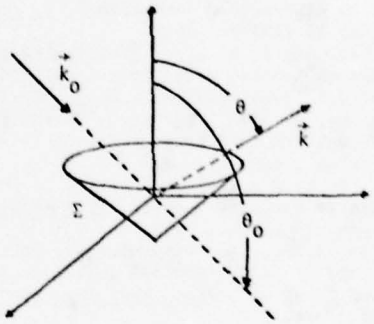

Figure 1 shows the geometry we assume; a defect with surface Σ of so far arbitrary shape, an incoming plane wave with wavevector $\vec{k}_o$ at spherical polar angles θ_o, φ_o, and a direction of observation θ, φ.

The wavefunction ψ may be taken to be a velocity potential, in which case it is proportional to the pressure in an irrotational compressible fluid. The boundary conditions are then clearly

$$\psi = 0 \quad \text{on } \Sigma \quad : \text{ void} \tag{6a}$$

$$\hat{n}\cdot\vec{\nabla}\psi = 0 \quad \text{on } \Sigma \quad : \text{ obstacle} \tag{6b}$$

(where $\hat{n}$ is a unit outward normal on Σ) for the two types of defects we are considering. If we combine (2), (4), and (6) we get

†Work supported by the U.S. Department of Energy.

$$\sum_s (d_s \tilde{\varphi}_s + a_s \varphi_s) = 0 \quad \text{on } \Sigma\text{: void} \tag{7a}$$

$$\sum_s (d_s \hat{n}\cdot\vec{\nabla}\tilde{\varphi}_s + a_s \hat{n}\cdot\vec{\nabla}\varphi_s) = 0 \quad \text{on } \Sigma\text{: obstacle} \ . \tag{7b}$$

MATRIX EQUATIONS

Suppose now we introduce a set of functions $\{f_j\}$ which is complete on Σ, but otherwise arbitrary, multiply (7a), (7b) by one of them, and integrate over the surface Σ. Then

$$\sum_s [d_s (f_j, \tilde{\varphi}) + a_s (f_j, \varphi_s)] = 0 \quad : \text{ void} \tag{8a}$$

$$\sum_s [d_s (f_j, \hat{n}\cdot\vec{\nabla}\tilde{\varphi}_s) + a_s (f_j, \hat{n}\cdot\vec{\nabla}\varphi_s)] = 0 \quad : \text{ obstacle} \tag{8b}$$

are, because $\{f_j\}$ is complete, equivalent to (7a), (7b). We have introduced the following notation for the surface integral.

$$(u,v) = \int_\Sigma d\sigma \, u^* v \ . \tag{9}$$

Equations (8a), (8b) are of the form

$$\tilde{Q}d + Qa = 0 \ , \tag{10}$$

which may in principle be solved for

$$a = -Q^{-1}\tilde{Q}d \equiv Td \ , \tag{11}$$

defining the T-matrix, which linearly transforms the incident wave amplitudes d_s into the outgoing wave amplitude a_s. If $\{f_j\}$ is complete, T is symmetric. Then (11) is identical to the relation between T and Q given in ref. (1); namely $T = -(Q^{-1}\tilde{Q})^T$.

CONSTRAINTS ON $\{f_j\}$

In a computer calculation all of the sets $\{f_j\}$, $\{\varphi_s\}$, $\{\tilde{\varphi}_s\}$ are finite, and although (11) gives the exact answer for complete (infinite) sets (T is a matrix of infinite rank), one must in practice always truncate the basis sets and matrices.

Then, if one keeps the same number of basis functions in all sets

$$j,s = 1,2\cdots N$$

we will be calculating $T^{(N)}$ which is an NXN approximation to the $\infty \times \infty$ T matrix, and the goodness of the approximation will be dependent on the truncated set $\{f_j\}_N$ we choose. Our choice of $\{f_j\}_N$ will affect

(1) the rate of convergence of $a_s^{(N)}$ to the exact a_s as N increases,

(2) the conditioning of the $Q^{(N)}$-matrix, and

(3) the convenience, speed, and accuracy of the numerical evaluation of the Q-matrix elements.

(2) above means that, for example, if a poor choice of $\{f_j\}_N$ is made, then some of the equations (8) may be nearly linearly dependent on the others, causing numerical instabilities and/or inaccuracies in the inversion of $Q^{(N)}$.

The choice of $\{f_j\}_N$ which was made by Waterman[1], and which corresponds to that used in the elastic wave case by him[2] and by Varatharajulu and Pao[3], is, for the case of the obstacle, $f_j = \tilde{\varphi}_j$, giving

$$Q_{js} = (\tilde{\varphi}_j, \hat{n}\cdot\vec{\nabla}\varphi_s) \ , \tag{12}$$

$$\tilde{Q}_{js} = (\tilde{\varphi}_j, \hat{n}\cdot\vec{\nabla}\tilde{\varphi}_s) \ .$$

They made this choice of f because it was natural and convenient in their development of the formalism, which was very different from ours. We will choose f differently.

OPTIMIZATION

In order to motivate a unique specification of $\{f_j\}_N$, we ask what can be learned by considering the surface integrals

$$I = (\varphi,\varphi) \quad : \text{ void} \tag{13a}$$

$$I = (\hat{n}\cdot\vec{\nabla}\varphi, \hat{n}\cdot\vec{\nabla}\varphi) \quad : \text{ obstacle} \ . \tag{13b}$$

These vanish if and only if φ satisfies the boundary conditions exactly, which is possible for most surfaces Σ only if $N \to \infty$. For finite N, $I > 0$, and we require that the N coefficients a_s in (2) be chosen so that I is a minimum, which implies

$$\frac{\delta I}{\delta a_s^*} = 0 \quad s = 1,\cdots N \ . \tag{14}$$

Specifically, for the void,

$$\frac{\partial I}{\partial a_s^*} = \frac{\partial}{\partial a_s^*} \int_\Sigma d\sigma \left| \hat{n}\cdot\vec{\nabla}\varphi_{in} + \sum_{s'=1}^{N} a_{s'} \hat{n}\cdot\vec{\nabla}\varphi_{s'} \right|^2 = 0 \ , \tag{15}$$

which is (10) with

$$Q_{js} = (\hat{n}\cdot\vec{\nabla}\varphi_j^*, \hat{n}\cdot\vec{\nabla}\varphi_s) \tag{16a}$$

$$\tilde{Q}_{js} = (\hat{n}\cdot\vec{\nabla}\varphi_j^*, \hat{n}\cdot\vec{\nabla}\tilde{\varphi}_s) \ . \tag{16b}$$

These are to be compared with (12). Corresponding differences appear between the Q-matrices our criterion prescribes and those which are used in refs. (2) and (3) for elastic wave scattering.

It is intuitively reasonable, because of our optimization criterion that the solution we obtain should maximize fidelity to the boundary conditions on Σ, that the results of our calculation should converge better for displacements and stresses in the near zone (surface stress concentration, etc.). But it is not a priori obvious that our results for cross sections, which depend on far fields only, should be optimum. This can only be determined by comparing detailed calculations.

APPLICATION

We will not present the formal expressions for displacements, stresses, and matrix elements here, that being reserved for later publication. We will just show some results for direct and mode-converted scattering from spheres, prolate and oblate spheroids, pillboxes and cones. There is a good reason that the above set of shapes are all axially symmetric, as follows.

If $s = p,\ell,m$ where $p = 1$ (longitudinal polarization), 2,3 (transverse polarization), $\ell = 0,1, \cdots \ell_{max}$, and $m = -\ell, \cdots +\ell$, then it can easily be shown that, if Σ is axially symmetric,

$$Q_{p\ell m,p'\ell'm'} = \delta_{mm'} Q_{p\ell m,p'\ell'm} \quad , \qquad (17)$$

for all boundary conditions and also for $\bar{Q}$ and T. This is the basis for a gross simplification and acceleration of the calculation, because T can be computed for each azimuthal eigenvalue m separately. For axially symmetric flaws, as will be seen from the figures, we can get good results for quite large ka; it being sufficient to take ℓ_{max} of the order of 1 or 2 × ka to obtain visual convergence (i.e., the computer-generated plots for successively larger ℓ_{max} are indistinguishable to the eye). The largest matrix (17) which must be inverted has rank 3 (ℓ_{max} + 1), which is trivial for $\ell_{max} = 14$, the largest we have needed.

But if Σ has no symmetries, (17) has no $\delta_{mm'}$ factor, the rank of Q is $3(1 + 3 + 5 + \cdots + 2\ell_{max} + 1)^2 = 3(\ell_{max} + 1)^2$ and the situation is quite different. Only relatively long wavelengths could be considered.

The figures which follow will be self-explanatory, with the following guide to notation.

Differential cross-sections are plotted as functions of (θ,φ), the spherical polar angles in the coordinate system of the flaw, whose axis of symmetry is along the Z axis. The incoming wave is longitudinally polarized with wavevector k. A zero cross-section is plotted at -100 db.

θ_o = angle of incoming wavevector ($\varphi_o = 0$)

σ_ℓ = 10 $\log_{10}$ (longitudinal cross-section/πa^2)

$\sigma_{t_1}, \sigma_{t_2}, \sigma_t$ = partial and total mode-converted contributions.

λ, μ = Lamé elastic parameters.

a = largest radius of flaw.

Type = (0,1) = (void, rigid obstacle)

AR = (height/diameter) of defect

H = { height of pillbox/a if H > 0; 0 if defect is a sphere or spheroid; − height of cone/a if H < 0 }

ℓ_{max} = cutoff in ℓ; varies from 2 to 14 in plots

n_{leg} = number of points in numerical integration of surface integrals; performed by Gauss-Legendre quadrature.

The time consumed by a CDC 6600 for a given flaw in computing 25 × 25 values of σ_L and σ_T for each of 5 incident angles θ_o is approximately $\ell_{max} \cdot n_{leg}/5$ sec.

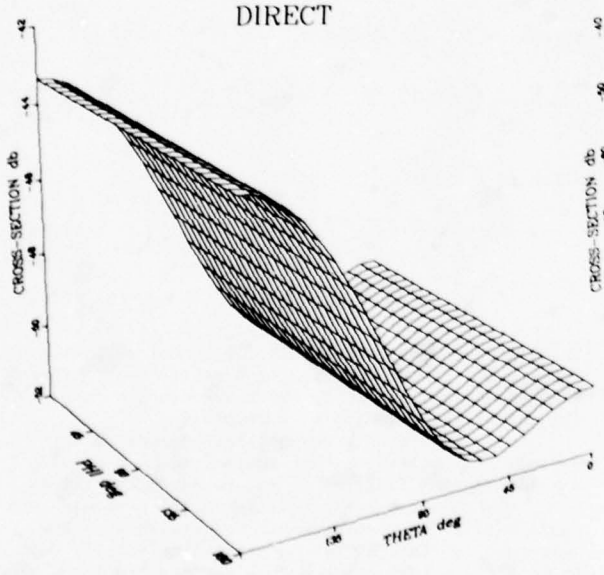

θ_o	σ_l	σ_{tl}	σ_{t2}	σ_t
0 000	-37 062	-100 000	-34 021	-34 021

λ	μ	ka	Type	H	AR	$l_{max} n_{leg}$
2 000	1 000	100	0 0	000	1 000	2 12

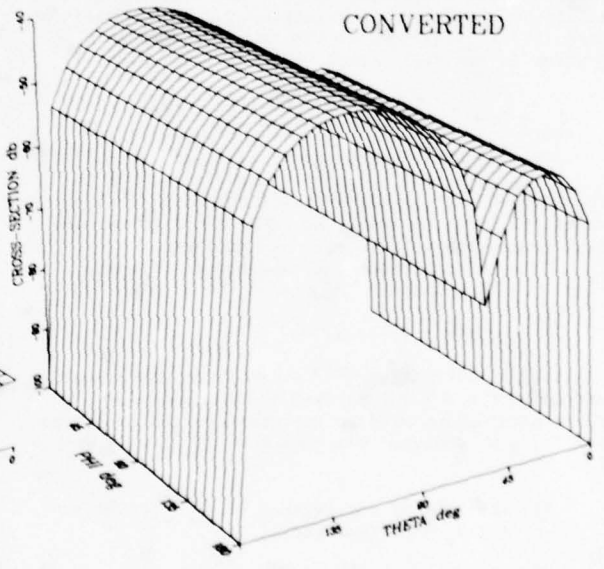

θ_o	σ_l	σ_{tl}	σ_{t2}	σ_t
0 000	-37 062	-100 000	-34 021	-34 021

λ	μ	ka	Type	H	AR	$l_{max} n_{leg}$
2 000	1 000	100	0 0	000	1 000	2 12

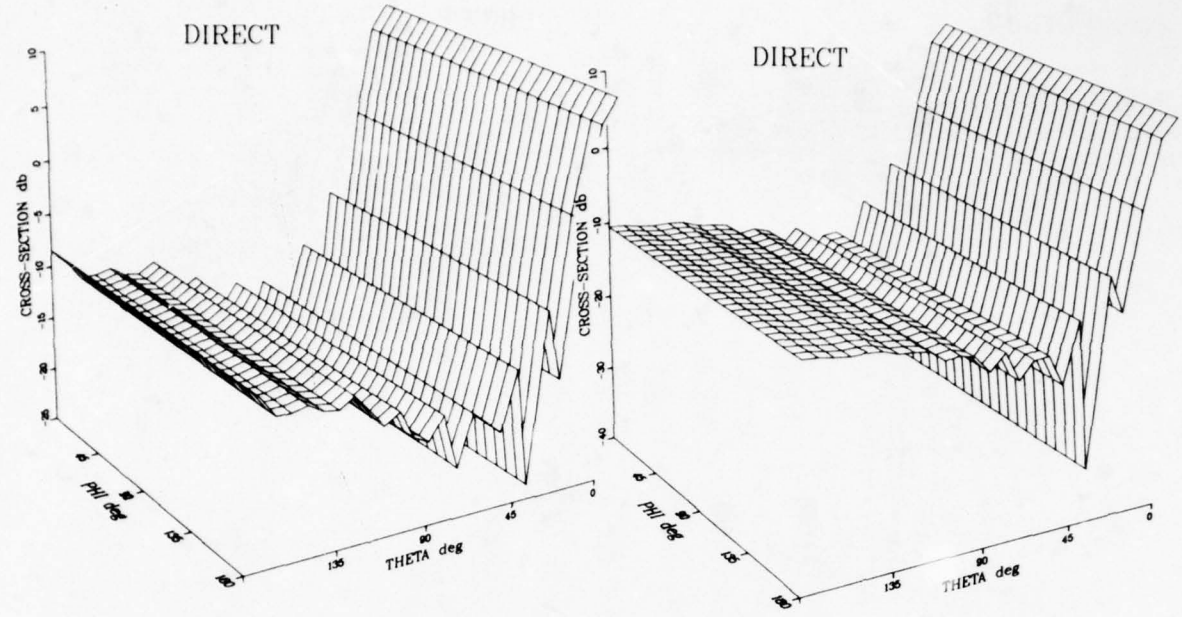

θ_o	σ_l	σ_{t1}	σ_{t2}	σ_t
0.000	1.595-100	.000	-1.097	-1.097

λ	μ	ka	Type	H	AR	l_{max}	n_{leg}
2.000	1.00010	.000	0 0	.000	1.000	10	30

θ_o	σ_l	σ_{t1}	σ_{t2}	σ_t
0.000	1.632-100	.000	-.707	-.707

λ	μ	ka	Type	H	AR	l_{max}	n_{leg}
2.000	1.00010	.000	0 0	.000	1.000	12	30

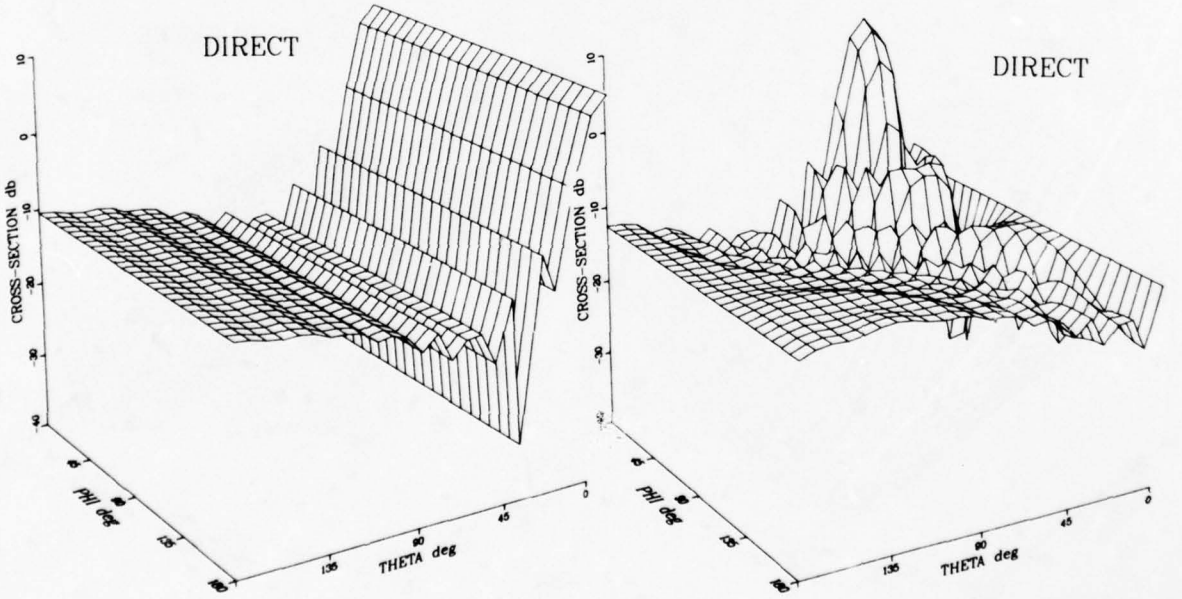

θ_o	σ_l	σ_{t1}	σ_{t2}	σ_t
0.000	1.633-100	.000	-.706	-.706

λ	μ	ka	Type	H	AR	l_{max}	n_{leg}
2.000	1.00010	.000	0 0	.000	1.000	14	30

θ_o	σ_l	σ_{t1}	σ_{t2}	σ_t
45.000	1.633-100	.000	-.706	-.706

λ	μ	ka	Type	H	AR	l_{max}	n_{leg}
2.000	1.00010	.000	0 0	.000	1.000	14	30

CONVERTED

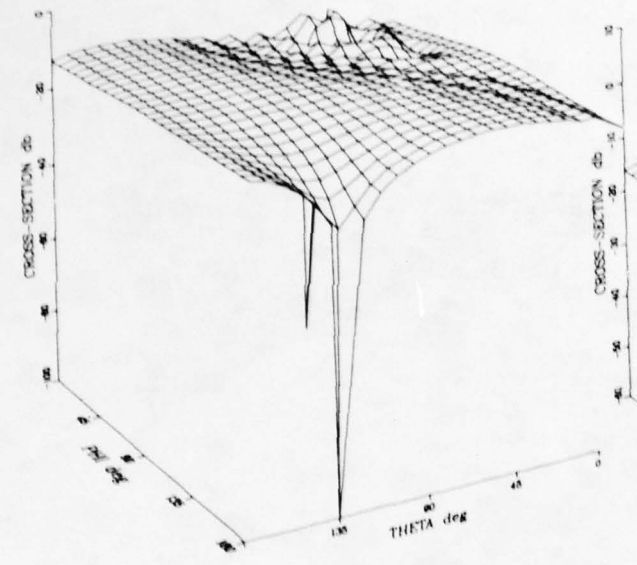

θ_o	σ_i	σ_{t1}	σ_{t2}	σ_t
45.000	1.633	-100.000	-.706	-.706

λ	μ	ka	Type	H	AR	$l_{max} n_{leg}$
2.000	1.00010.000		0 0	.000	1.000	14 30

DIRECT

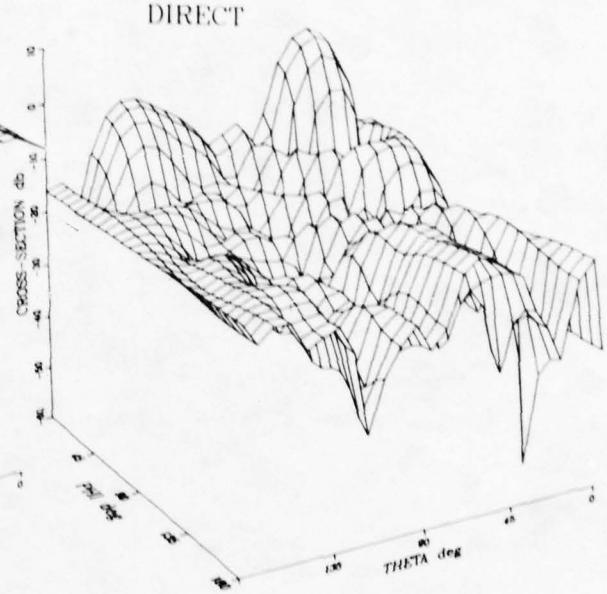

θ_o	σ_i	σ_{t1}	σ_{t2}	σ_t
45.000	.223	-5.213	-2.156	-.412

λ	μ	ka	Type	H	AR	$l_{max} n_{leg}$
2.000	1.00010.000		0 1	.000	.500	14 30

DIRECT

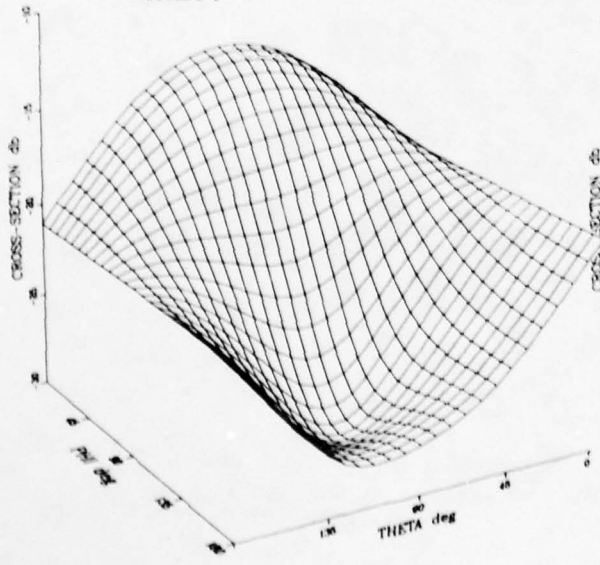

θ_o	σ_i	σ_{t1}	σ_{t2}	σ_t
45.000	-8.143	-13.496	-9.570	-8.093

λ	μ	ka	Type	H	AR	$l_{max} n_{leg}$
2.000	1.000	5.000	0 0	.000	.141	10 24

CONVERTED

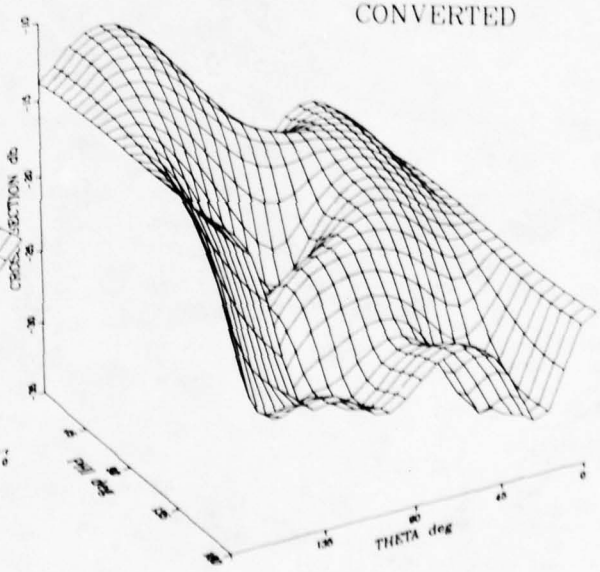

θ_o	σ_i	σ_{t1}	σ_{t2}	σ_t
45.000	-8.143	-13.496	-9.570	-8.093

λ	μ	ka	Type	H	AR	$l_{max} n_{leg}$
2.000	1.000	5.000	0 0	.000	.141	10 24

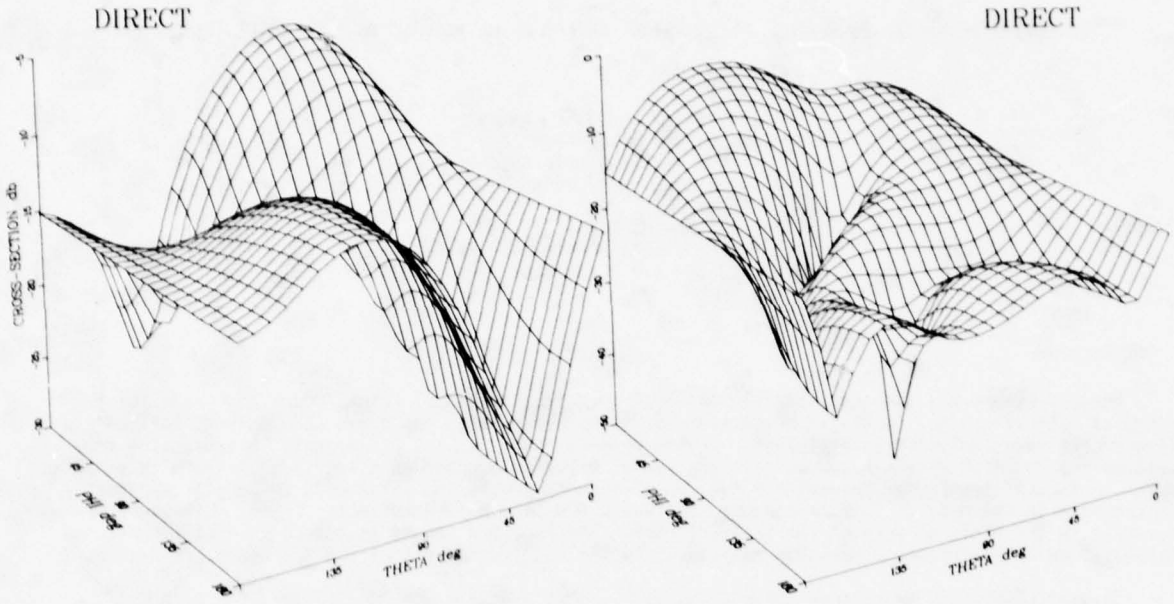

θ_o	σ_l	σ_{tl}	σ_{t2}	σ_t
45.000	-1.562	-7.446	-8.785	-5.054

λ	μ	ka	Type	H	AR	$l_{max} n_{leg}$
2.000	1.000	5.000	0-1	1.000	.500	12 30

θ_o	σ_l	σ_{tl}	σ_{t2}	σ_t
135.000	-1.974	-7.750	-6.570	-4.110

λ	μ	ka	Type	H	AR	$l_{max} n_{leg}$
2.000	1.000	5.000	0-1	1.000	.500	12 30

Some indication of the rate of convergence of the calculation with increase of the truncation parameter ℓ_{max} can be obtained by studying the results for the scattering from a sphere for ℓ_{max} = 10, 12, and 14 of an incident wave with ka = 10. The differences between cross-sections for ℓ_{max} = 12 and ℓ_{max} = 14 are typically about .1 db or less (too small to see on the graphs), which is about 2%. In contrast, the cross-section for ℓ_{max} = 10 and ℓ_{max} = 12 are sometimes as much as 2 db. Although we have not studied the rate of convergence in any systematic, quantitative way, these trends are not inconsistent with the results of Johnson and Truell[4] on scattering from spherical elastic inclusions. To obtain .6% accuracy for scattering with ka = 10 from an elastic inclusion, they find it necessary to go to ℓ_{max} from 10 to 16, depending on the materials involved. Admittedly, the sphere is a poor test of the method, because the matrices are then diagonal in ℓ as well as m; consequently any expansion in ℓ,m eigenfunctions should give the same answers.

A better test is afforded by some less symmetric defect. It would be interesting to compare, for an unsymmetric shape like a cone, the rates of convergence of our method, the method used by Varadan and Pao, and the one proposed by Waterman,[5] in which he would force the T-matrix to be symmetric at each stage of truncation N.

GENERALIZATION

Many directions for further development suggest themselves. Relatively easy is the extension to elastic inclusion with axial symmetry. The calculations for this case are no more difficult than for the void and obstacle, but the rank of the matrices one must manipulate is doubled, because now the wavefunctions inside the inclusion must also be determined. Little more difficulty is involved in calculating scattering from some surface defects. Here Σ becomes the infinite plane plus a surface flaw whose axis of symmetry is perpendicular to the plane. Surface integrals over the plane can be performed analytically, and φ_{im} will become, in one instance, an incident plane longitudinal wave plus reflected longitudinal and transverse waves.

Outside of the scattering domain the principle of maximization of fidelity to boundary conditions can be used to solve for near-zone fields; e.g., stress concentrations and ultrasonic lens design.

ACKNOWLEDGMENT

Thanks are due Dr. James Gubernatis, who introduced me to the subject of elastic waves, and who still serves as an able consultant and patient guide to the venerable and copious literature.

REFERENCES

1. P. C. Waterman J. Acoust. Soc. Am. 45, 1417 (1969).

2. P. C. Waterman J. Acoust. Soc. Am. 60, 567 (1976).

3. Vasundara Varatharajulu and Yih-Hsing Pao J. Acoust. Soc. Am. 60, 556 (1976); Vasundara V. Varadan J. Acoust. Soc. Am. 63, 1014 (1978).

4. Gregert Johnson and Rohn Truell Jour. Appl. Phys. 36, 3466 (1965).

5. P. C. Waterman Phys. Rev. D3, 825 (1971).

DETECTION OF RADIAL BOLT-HOLE CRACKS USING SAMPLED CW ULTRASONIC DOPPLER-SHIFT TECHNIQUES*

N. K. Batra and J. M. Raney**
Systems Research Laboratories, Inc.
2800 Indian Ripple Road
Dayton, Ohio 45440

R. M. Panos†
Air Force Materials Laboratory/LLP
Wright-Patterson Air Force Base, Ohio 45433

ABSTRACT

Recently there has been considerable interest in detecting radial cracks under fasteners in the wings of C-5A aircraft. Generally, detection is accomplished using the pulse-echo method, reflections from cracks being detected in real time. In the present study, cracks are detected by observing the Doppler-shifted frequency. A sample having a radial crack is mounted on a rotating platform in a water bath. A focused transducer transmits a tone burst such that only the shear mode propagates tangential to the hole in the metal. This transducer receives a Doppler-shifted reflected signal whenever a moving crack is in the field of view of the incident beam. The received signal is heterodyned, filtered, and displayed on a low-frequency spectrum analyzer. Merits and limitations of the technique are discussed.

Several ultrasonic techniques[1] have been used to detect and measure the size of cracks--scattered wave amplitude methods, bulk-wave timing methods, and spectroscopic analysis. This paper deals with the use of a Doppler-shift technique to detect and measure the size of radial bolt-hole cracks. The Doppler effect refers to the change in frequency of an ultrasonic wave reflected from a crack that is moving relative to the incident ultrasonic beam. The technique is outlined schematically in Fig. 1 which shows the ultrasonic beam intersecting a flaw as the sample is rotated. It should be noted that (1) the spectral width of the reflected wave is due to the radial distribution of velocity along the crack, and (2) the crack is only in a position to reflect the incident wave for a short time during the rotation of the sample (Fig. 2). The Doppler shift f_D due to the rotating crack is given by

$$f_D = \frac{4\pi r}{T_c} f_o \sin i \qquad (1)$$

and the total broadening of the Doppler peak by

$$\Delta f = \frac{a}{r} f_D + \frac{2\pi^2}{T \cos^{-1} \frac{r}{r+a}} \qquad (2)$$

where r is the radius of the hole, a is the crack size, T is the period of rotation, f_o is the frequency of the ultrasonic beam, and i is the angle of incidence. The first term in Eq. (2) is due to the aforementioned velocity distribution, and the second term is an instrumental broadening due to the short reflection time.

The experimental setup is shown schematically in Fig. 3. A focused transducer transmits a 35-μsec-long tone burst of 11.65 MHz at a repetition rate of 10 kHz. The transducer is placed such that only shear waves are transmitted tangential to the bolt hole in the sample. The received signal is heterodyned with the incident and then fed to a low-pass filter, the output of which--the Doppler shift--is displayed on a spectrum analyzer.

In the present study, Doppler-shift data were taken on various Al 6061-T6 disks containing different size EDM notches or real cracks. Figure 4 shows a typical plot of amplitude vs frequency. The Doppler shift has a sine dependence upon angle of incidence (Fig. 5) and is linearly dependent upon both reference frequency (Fig. 6) and the angular velocity of the notch (Fig. 7). The analysis of the broadening of the Doppler peak yielded values of 0.044 ± 0.006 in., 0.054 ± 0.011 in., and 0.078 ± 0.012 in. for 0.040-, 0.060-, and 0.080-in. EDM notches, respectively. From analysis of the data on the EDM notches of known radial depth, it seems that the radial sizes of these notches can be estimated to within 20%. Data taken on radial fatigue cracks at the bolt holes in rectangular plates are shown in Fig. 8. Analysis of the broadening of the Doppler peak for one of these samples yielded a radial-crack size of 0.117 ± 0.012 in. Examination of the sample under an optical microscope (Fig. 9) revealed the actual size of the crack to be 0.106 in.

There is a close agreement between the predicted and measured size of the cracks at the bolt holes. It has been demonstrated that Doppler-shift techniques are useful for detecting and sizing the radial cracks. The method is free from the uncertainties in the amplitudes of reflected waves from cracks. However, because of the small Doppler shift, the sampling time is large and the method is, at present, relatively slow. The adjustment of the direction of the incident beam is quite important for avoiding spurious peaks due to eccentricity.

REFERENCES

1. P. A. Doyle and C. M. Scala, "Crack Depth Measurement by Ultrasonics: A Review," Ultrasonics 16, 164 (1978), and references therein.

*Supported in part under AF Cont. F33615-77-C-5022.

**AiResearch Div., PO Box 5217, Phoenix, AZ 85010.

†Science Center, Rockwell International, Thousand Oaks, CA 91360.

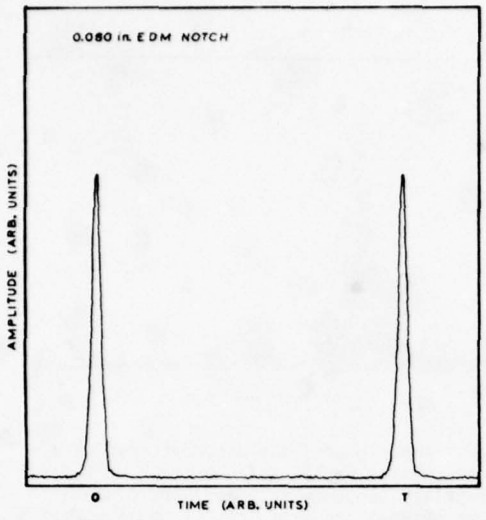

Fig. 1 Amplitude of the backscattered ultrasonic wave vs time. Crack is in view only for a fraction of the period of rotation of the disk. During this time the crack rotates 2ϕ radians.

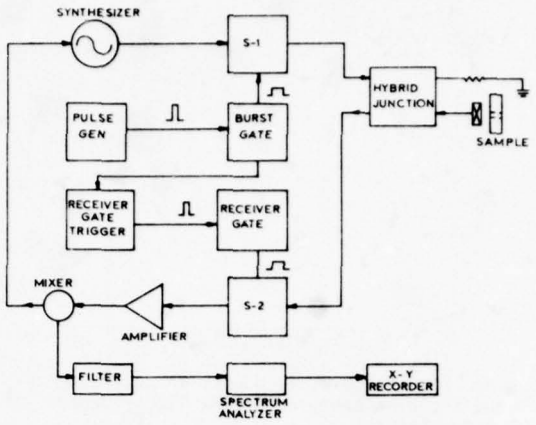

Fig. 3 Experimental setup for the Doppler-shift studies of radial cracks.

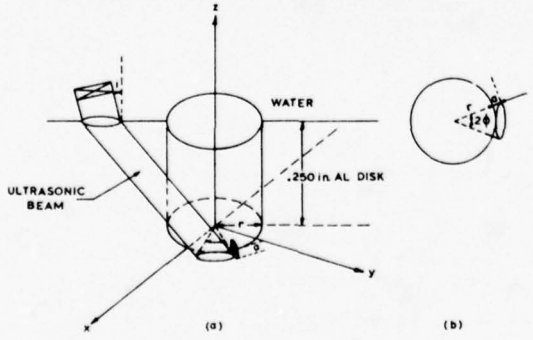

Fig. 2 (a) Detailed geometry of the ultrasonic beam and the rotating crack. (b) Top view of the disk and ultrasonic beam.

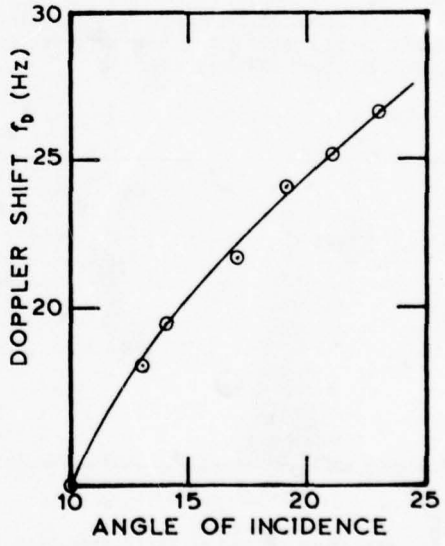

Fig. 4 Doppler-shift frequency f_D vs angle of incidence. Note the sine dependence of f_D upon the angle of incidence.

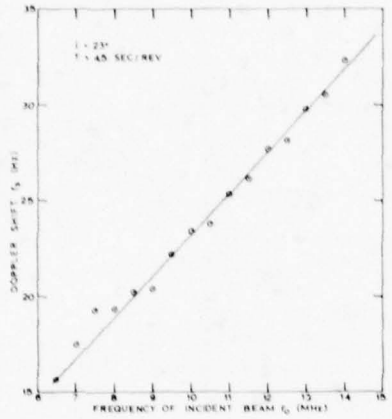

Fig. 5 Doppler-shift frequency f_D vs frequency f_0 of the incident beam. Note the linear dependence of f_D upon f_0.

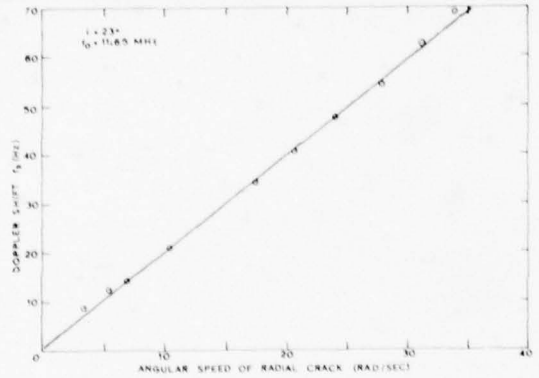

Fig. 6 Doppler-shift frequency f_D vs angular speed of the crack. Note the linear dependence of f_D upon angular speed of the crack.

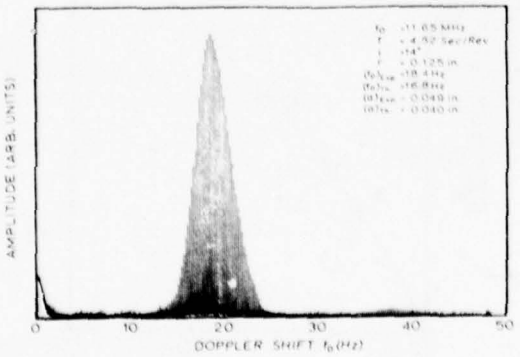

Fig. 7 Amplitude of the backscattered beam from the rotating radial EDM notch vs the Doppler-shift frequency f_D. The broadening of the Doppler peak is related to the radial size of the EDM notch. The spikes are due to the sampling. Only one spike appears per revolution.

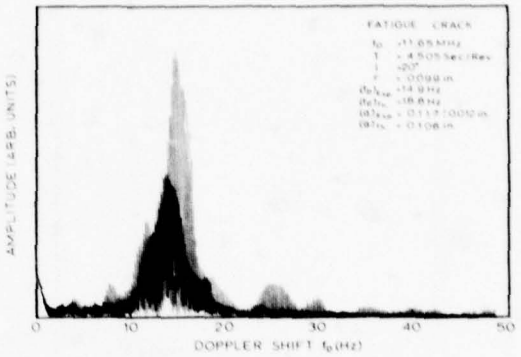

Fig. 8 Amplitude of the backscattered wave from the rotating radial fatigue crack vs the Doppler-shift frequency f_D. Note the close agreement between the experimental and theoretical crack sizes.

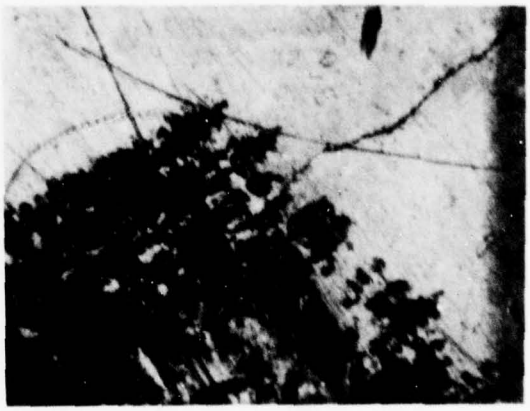

Fig. 9 Optical micrograph of the fatigue crack used to obtain the Doppler data in Fig. 8. The hole is the darkest area at the lower left-hand corner, with the fatigue crack running diagonally across the micrograph.

CAPABILITY OF DETERMINING FATIGUE MECHANISMS IN 7075 ALUMINUM BY COMBINING ULTRASONIC ATTENUATION AND ACOUSTIC EMISSION MONITORING

J. C. Duke, Jr., and R. E. Green, Jr.
Department of Mechanics and Materials Science
The Johns Hopkins University
Baltimore, Maryland 21218

ABSTRACT

Despite the prevalence of fatigue and fatigue related failures little is known about the actual mechanisms which cause fatigue. Two nondestructive investigation techniques which have been found to be extremely sensitive to the microscopic changes in the material during fatigue deformation are ultrasonic attenuation and acoustic emission monitoring.

The work reported here indicates the ability of both techniques to provide an early warning of fatigue failure in 7075 aluminum. Additionally, the results point out the sensitivity of the techniques to different mechanisms active during fatigue deformation. Through the complementary use of solitary and combined monitoring the potential of these techniques for revealing the actual mechanisms responsible for fatigue is shown.

METALLURGY . . . 7075 ALUMINUM

About the Material

Composition: 5.5% Zn, 2.5% Mg, 1.5% Cu, 0.3 Cr. Typically 7075 is found to contain three distinctively different types of particles in addition to the matrix material(1)

1) Fe, Si, and Cu rich primary inclusions ranging in size from 0.1 to 10μ in diameter, 1 to 5 percent by volume, appearing light in optical micrographs.

2) Cr, Mn, or Zr rich intermediate particles ranging from 0.5 to 5μ in diameter, which serve to control recrystallization and grain growth, 0.05 to 0.5 percent by volume, appearing dark in optical micrographs.

3) Precipitate particles ranging from 0.01 to 0.1 in diameter, a transition form of $MgZn_2$, strengthen the matrix and are only visible by transmission electron microscopy. Additionally, spherical dispersoids of $Al_{12}Mg_3Cr_2$ having a mean diameter of 0.05μ are also present, and like the $MgZn_2$ are finely dispersed.

ACOUSTIC EMISSION DURING TENSILE DEFORMATION

Sources of Acoustic Emission

Burst type emissions occurring prior to yield in the as received condition and throughout the deformation in the solution treated condition may be related to the breakaway of dislocations from pileups. The increase in acoustic emission, not associated with burst emission, occurring after yield in both materials results from the fracture of inclusions, decohesion of these inclusions and cracking of the aluminum matrix initiated by the fractures. Creation of dislocations, which trigger other dislocation sources, cause the large peak in emission at yield in the solution treated material. (2)

SPECIMEN AND TESTING CONFIGURATION

Experimental Consideration

All of the materials were subjected to reverse bending at 1725 cycles per minute. The peak to peak amplitude of the deflection was 0.9 cm.

Ultrasonic attenuation monitoring was performed continuously with the pulse being generated synchronously with the fatigue cycle at a fixed point in the cycle.

Acoustic emission monitoring was facilitated by a system designed by the Admiralty Materials Laboratory incorporating special electromagnetic shielding. The system afforded extremely sensitive monitoring at 70 dB gain because of lower signal to noise than conventional systems.

COMBINED MONITORING DURING FATIGUE

Test Result Implications

Combined results tend to indicate in the as received material that the breakaway of piled up dislocations during the early portion of the fatigue life does not provide dislocations which remain mobile and thereby increase the ultrasonic attenuation. However, fatigue damage culminating in failure activates mechanisms to which both techniques are sensitive.

In the solution treated material the breakaway of dislocations during the initial portion of the fatigue life does provide dislocations which remain mobile due to the greatly reduced number of pinning points. These mobile dislocations increase the ultrasonic attenuation, and perhaps contribute to the final failure. As with the as received material, at the onset of failure mechanisms are activated to which both techniques are sensitive.

ACKNOWLEDGMENTS

This work was supported in part by the Air Force Office of Scientific Research (AFSC), United States Air Force; a special note of appreciation is due to Mr. William J. Walker in this regard.

REFERENCES

1) Hahn, G. T. and Rosenfield, A. R., "Metallurgical Factors Affecting Fracture Toughness of Aluminum Alloys," Met. Trans. A, 6A, 653, 1975.

2) Duke, Jr., J. C., Nondestructive Investigation of the Mechanical Deformation of 7075 Aluminum, Ph.D. Thesis, The Johns Hopkins University, Baltimore, 1978.

METALLURGY ..... 7075 ALUMINUM

POLISHED
AS RECEIVED

FATIGUED
AS RECEIVED

SOLUTION TREATED

ACOUSTIC EMISSION DURING TENSILE DEFORMATION

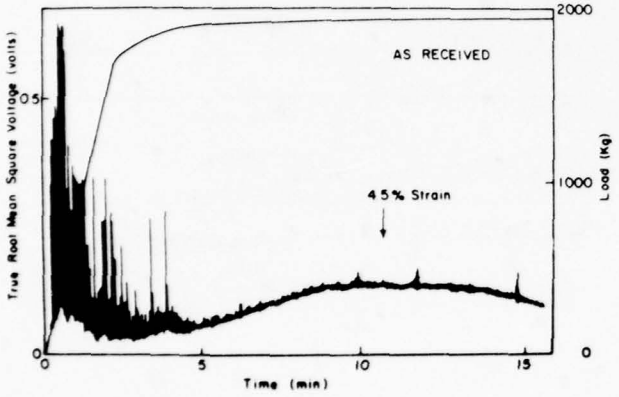

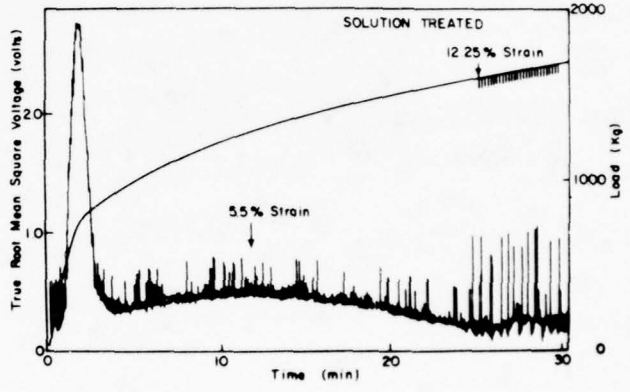

SPECIMEN AND TESTING CONFIGURATION

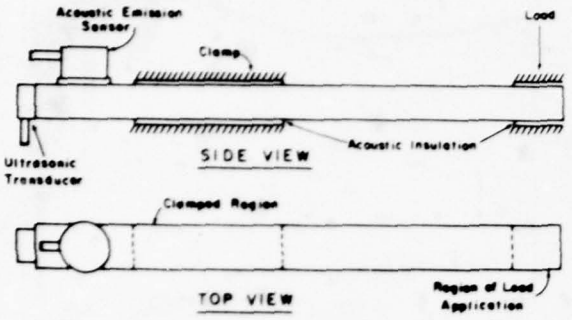

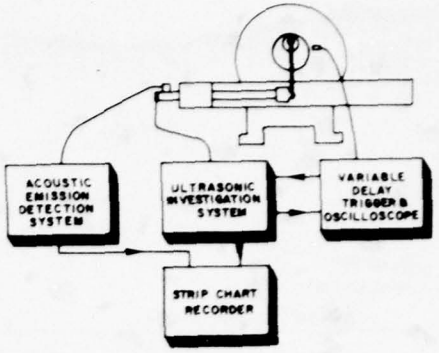

COMBINED MONITORING DURING FATIGUE

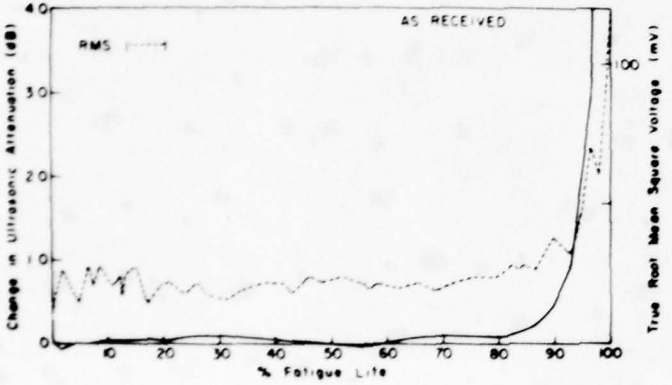

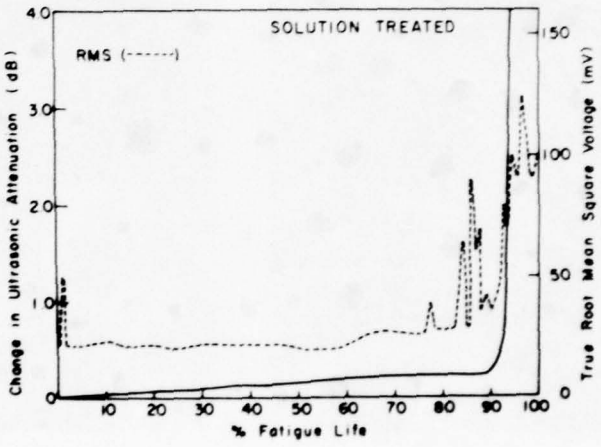

OPTICAL MEASUREMENT OF ACOUSTIC EMISSION AT HIGH AND LOW TEMPERATURES

C. Harvey Palmer
Department of Electrical Engineering
The Johns Hopkins University
Baltimore, Maryland 21218

ABSTRACT

Optical probing of acoustic displacement waveforms has a number of advantages over other methods. Among these advantages is the possibility of quantitative, local measurement of acoustic emission waveforms at high and low temperatures. This paper reports the results of some measurements on various materials as a function of temperature.

INTRODUCTION

It is often assumed that acoustic emission signatures are in some way characteristic of the emitting source (growing crack, twinning, slip, void formation, or the like). This hypothesis, reasonable as it is, has never been properly tested because the essential data do not exist.

To test the hypothesis, we need to know the characteristic signature of the various possible sources, including waveform, component wave types, and radiation pattern. We should know how this waveform changes with material, temperature, and specimen size and shape (because of resonances, reflections,and mode conversions). Further, we need to know how the waveform changes with propagation distance (and direction if the material is anisotropic). We can expect the waveform to change for several reasons:

(1) The component wave types -- dilatational, shear, and, perhaps, surface -- travel at different speeds.
(2) The spreading wave is attenuated geometrically, and the geometric factor is different for bulk and surface waves.
(3) Various loss mechanisms depend on frequency, temperature, and material.
(4) Both anisotropy and inhomogeniety will further distort the propagating wavefront.

Accurate measurement of the various waveforms to test the theory evidently requires a transducer whose sensitive area has a diameter much smaller than the shortest wavelength to be measured (for 5 MHz the Rayleigh wavelength is about 0.6 mm). The probe should be non-contact, have a broad frequency response, and be useful at both high and low temperatures. It must be amenable to absolute calibration. Optical methods satisfy these requirements, and they have the further advantage of being able to probe internally in transparent materials.

INSTRUMENTATION

The basic optical sensor, shown in Fig. 1, has been described elsewhere.[1,2] It is a modification of the Michelson interferometer in which the illumination is collimated laser light. Lenses are used to focus the light on the specimen, forming a sensitive area perhaps 0.01 mm diameter. The reference beam is focused on a piezoelectrically driven mirror (at the top of the diagram). Low frequency components of the photocurrent (0 - 1 kHz) are mostly caused by mechanical vibrations and atmospheric disturbances; they are amplified and used to drive the piezoelectric correction unit so as to maintain an optical phase difference of 90^0 between the two beams for optimum sensitivity. The high frequency signal components are amplified and displayed or recorded. The signal amplifier band pass is adjusted to 5 kHz to 5 MHz. Signals are ususally video taped unless the frequency response of the video tape (about 3 MHz) is too limited; then they must be recorded directly from the oscilloscope or from a digital transient recorder. Signals played back from the video tape can be filtered to remove any undesired frequencies.

Figure 2 shows the method of mounting indium ingots used in some of the twinning experiments. The specimen (3 x 3 x 40 mm) was held between two teflon blocks to minimize clamp noises. In turn these teflon blocks were supported in a bakelite mount which permitted suitable adjustment of the position of the specimen. Measurements could be made either at the end of the specimen or at the side very close to the region where twins were generated when the ingot was bent. Probing at the side was necessarily qualitative because the generation of twins distorted the polished surface. Measurements made at the end eliminated this difficulty, but at the expense of attenuating some of the high frequency components as a result of the extra 15 mm of propagation distance through the clamped region.

The specimen temperature could be measured approximately with the thermocouple wires as shown. The No. 30 gauge wire was fine enough to minimize heat transfer to or from the specimen while permitting temperature measurements. The specimen could be heated with a specially constructed tubular oven which slid over the exposed end, or cooled by pouring liquid nitrogen over it.

In another experiment the acoustic emission during the phase change in iron at about 900^0C was measured. An iron wire, about 10 cm long, was clamped between two specially designed binding posts which were mechanically insulated from the mount by teflon washers to reduce clamp noise. The wire was kept under slight tension so that it would not sag when heated by an electric current. Then about halfway along its length the wire was compressed between a flat glass plate and a steel cylinder so that it could act as a mirror.

RESULTS

Figure 3 shows the effect of temperature on the acoustic emission from the twinning of indium. The two upper waveforms, recorded at a temperature of about -190°C, show frequencies of the order of 200 kHz. The lower two waveforms, recorded at a temperature of about +100°C, show considerable attenuation of the higher frequencies. Above this temperature, few signals were seen.

If the AE signals were sensed at the side of the specimen, close to the AE emission sites, the observed rise time was much faster than when observed at the end, some 15 mm distant from the sites. Figure 4 shows some rise time measurements. At the top is the rapid rise, about 0.2 μsec, observed in the stress corrosion cracking of E4340 steel within a millimeter of the crack (recorded with a transient digitizer). The two lower waveforms show rise times of about 1 μsec in the indium at a temperature of -190°C, also within a millimeter of the twin generation.

Figure 5 shows some characteristic twin signals in indium sensed at the polished end of the specimen (left side of figure) and from a phase change in iron wire at about 900°C (right side). In both sets of waveforms the sweep speed was 20 μsec/div as indicated. The upper two waveforms of each set are almost indistinguishable, and the ones below are recognizably similar in general form. As we have seen above, the high frequency component content of the indium waveforms will be less than when observed at the side, but the signature is still recognizable. As reference 2 shows, the emission from twinning in different metals such as indium, tin, zinc, and cadmium is very similar, though there may be subtle differences.

Experiments have also been done on the duration of the acoustic emission bursts, but the results are not conclusive because it is difficult to sort out the primary characteristic signatures from reflected waves.

CONCLUSION

The experiments reported here are only preliminary, but they clearly demonstrate the power of optical probing methods. (A greatly improved instrument is now under construction.)

Provisionally, we conclude that the hypothesis under consideration, that acoustic emission signatures are characteristic of sources, is at least partially valid. There appears to be a distinctly different signature for twinning and for a phase change in iron. Differences in other kinds of signatures is not so evident, though there may be more subtle distinctions. The frequency spectrum may, perhaps, reveal some differences, but this is not certain. Frequency spectra of events measured far from the source do not seem to be repeatable from event to event.

ACKNOWLEDGEMENT

It is a pleasure to acknowledge the support of the U.S. Army Research Office, and Dr. George Mayer in particular. In addition, the author wishes to thank his colleagues Dr. Robert E. Green, Jr., Dr. Steven E. Fick, Dr. Richard O. Claus, Dr. Ronald A. Kline, and Professor Robert B. Pond, Sr.

REFERENCES

1. C.H.Palmer and R.E.Green, Jr., Appl. Opt. 16, 2333-2334, (1977).
2. C.H.Palmer and R.E.Green, Jr., Proc. of the ARPA/AFML Review of Progress in NDE, June 14-18, 1977.

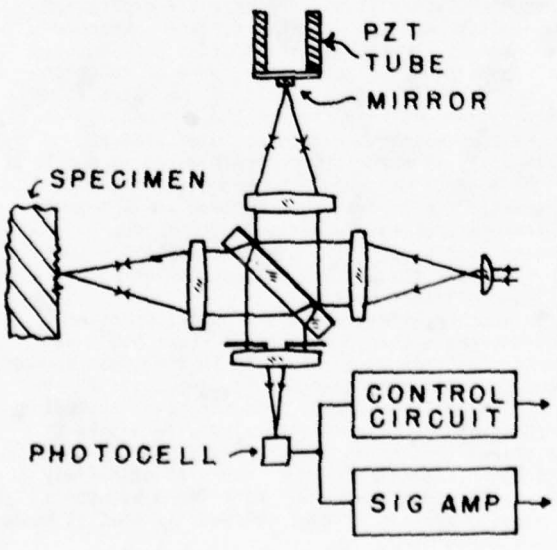

Fig. 1. Acoustic emission interferometer

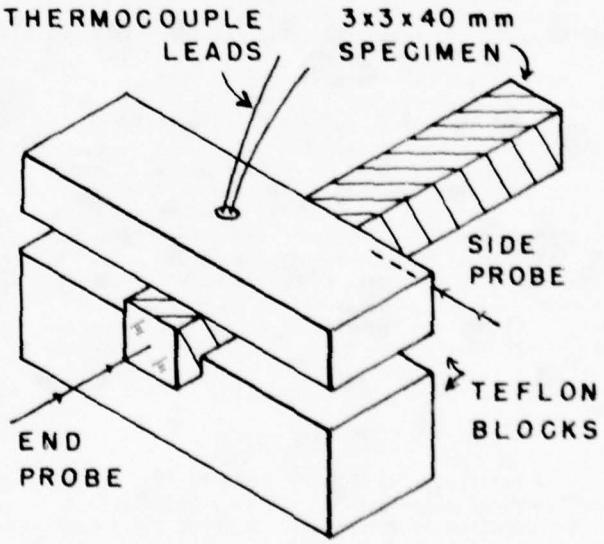

Fig. 2. Mounting for twinning specimens

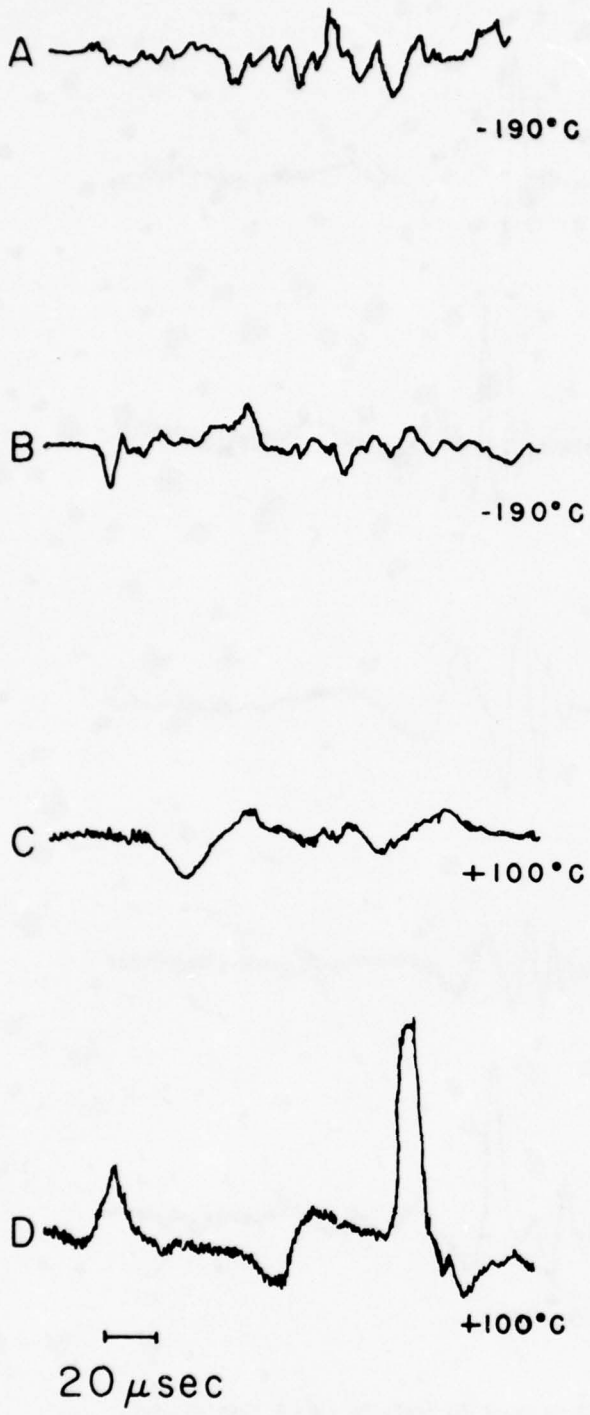

Fig. 3. Effect of temperature on twin signals in indium. Traces A and B: temperature -190°C, gain 500 mVolts/Div. Traces C and D: Temperature +100°C, Gain 200 m Volts/div.

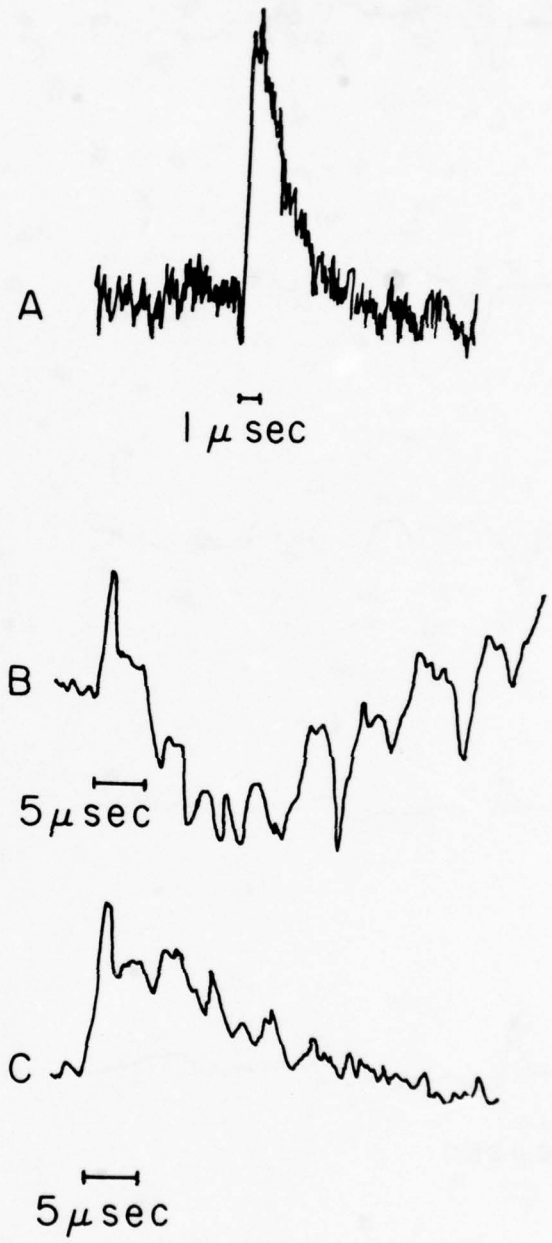

Fig. 4. Rise time measurements. Trace A: Stress corrosion cracking in E4340 steel (note sweep indication). Traces B and C: twinning in indium, temperature -190°C. All measurements within 1 mm of AE source.

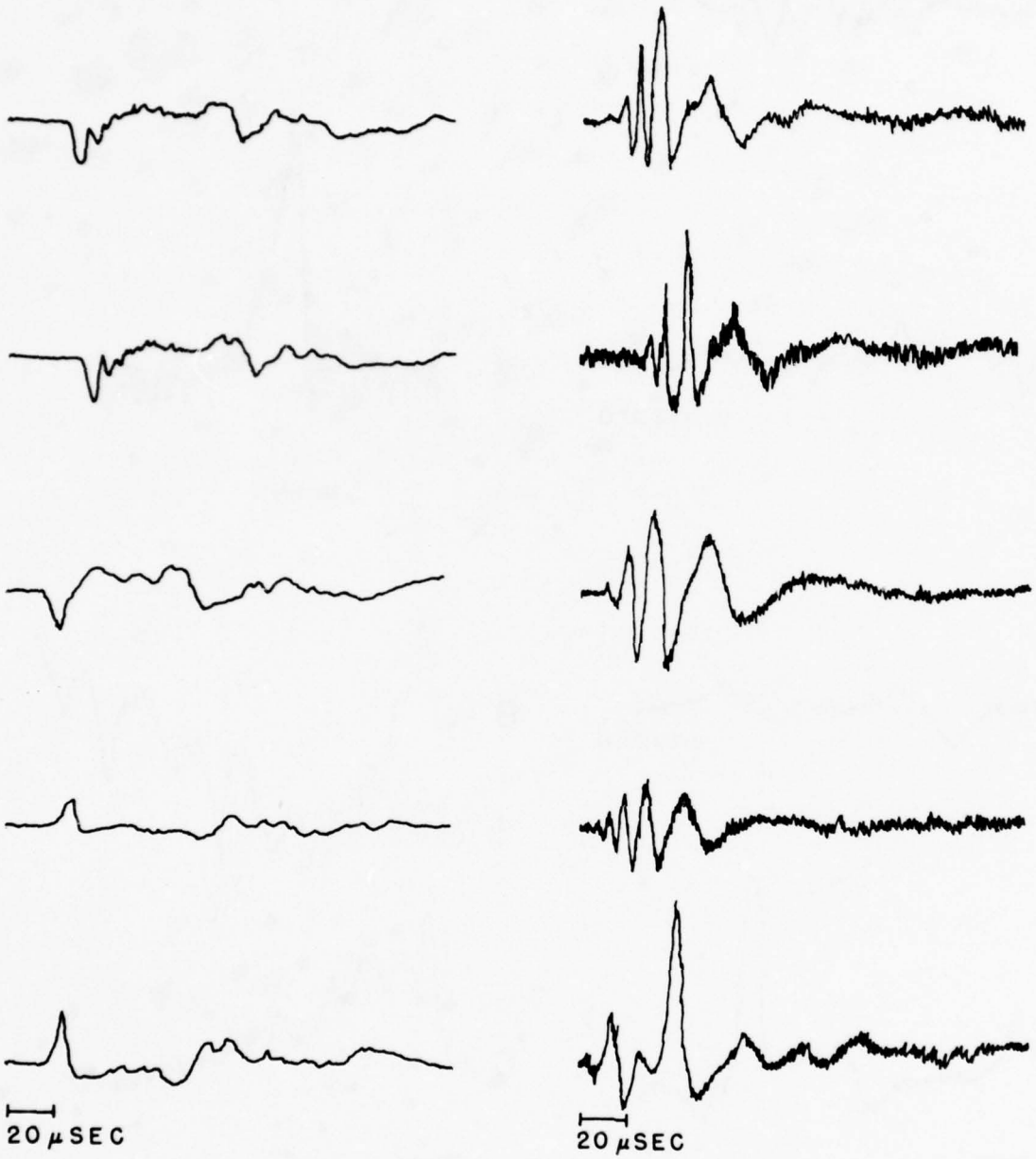

Fig. 5. Characteristic acoustic emission signals. Left: Indium twinning measured at the specimen end. Temperature 20°C. Right: Phase change in iron wire, temperature about 900°C.

ULTRASONIC TESTING -- RECONSTRUCTION OF REFLECTORS FROM TIME-DELAY AND AMPLITUDE-LOCUS CURVES

P. HÖLLER, O.A. BARBIAN, R. WERNEYER
Institut für zerstörungsfreie Prüfverfahren der Fraunhofer-Gesellschaft
Saarbrücken, Universitat

ABSTRACT

For ultrasonic testing (pulse-echo or tandem) the surface of a test piece is scanned by a probe or a probe array. Time-delay and amplitude for each pulse, locus of incidence, reflector inside the beam and wave path, are measured. Shape and position of reflectors are reconstructed from time-delay locus curves. In addition, isolated amplitude-locus curves derived from measurements are compared to calculations for several reflector modes. The best fitting model is selected. Diameter or width and inclination are determined.

Physics and science in general are the most important resources for progress in NDT. Real industrial problems are complicated. Normally, they cannot be solved just by applying physics, mathematics, computer science, etc. It is the aim of NDT research to solve industrial problems or to contribute to solutions. Therefore, beside applying science, decisions based on practical experience and engineering common sense are involved in any major innovation in NDT.

In ultrasonic testing the basic unsolved problem is RECONSTRUCTION OF REFLECTORS from measurements obtained by scanning a component to be tested with small probes or probe arrays. Amplitude, phase or time delay, and spectrum are measured or at least can be measured for each position of the probes where a pulse is emitted. What finally is obtained are cross sections through the radiation patterns reflected from defects or other obstacles. When amplitude, phase and spectrum are measured physically, it is possible to reconstruct reflectors. There are several ways to do it; e.g. holography (1-4), synthetic aperture (5), spectrum analysis (6-14), inversion of scattering patterns (15-19), etc. None of these possible procedures to reconstruct reflectors is well enough developed for full practical application but all basically are well understood.

In a practical case, a decision has to be made as to the methods of reconstruction. For such a decision not only testing procedures, data acquisition, mathematical models for reconstruction, but also disturbances which happen during the testing procedure have to be considered.

We present in this paper an ultrasonic testing system involving twofold reconstruction. The system primarily has been developed for in-service inspection in the nuclear industry, but it can be applied more generally. With regards to materials integrity and for safety demand, the primary circuit and therein the reactor pressure vessel are most important. This vessel is cladded with austenitic stainless steel. Most of the in-service inspection is done under water from the inside. The welded cladding as well as the water coupling gaps are sources for phase disturbances. As an example, Figs. 1 - 3 show holographic reconstructions of a pattern of flat circular reflectors (20).

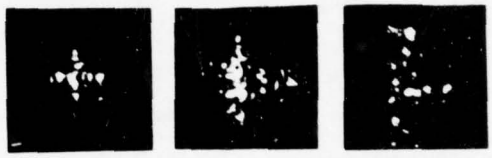

Fig. 1. Reconstructions of a flawpattern in an ungrounded plated test specimen.
Material: 22 NiMoCr 37
Cladding: 23 Cr/11 Ni
Surface roughness 65 µm

In the first Fig. the ultrasonic hologram was picked up through an austenitic cladding in an as weld condition; in the second the cladding was ground and in the third the specimen was not cladded at all. It is clearly shown that the cladding and especially the surface of the cladding causes serious disturbances of the hologram. Similar disturbances are to be expected for other phase-sensitive methods like synthetic aperture. For reasons previously mentioned and others there are limitations on the application of phase-sensitive reconstruction methods.

Fig. 2. Reconstructions of a flawpattern in a plated test specimen.
Ground surface: 2,5 µm

Fig. 3. Test specimen without cladding.
Flaw depth: 100 mm
us-frequency: 5 MHz

Typical linear dimensions for limits of detection demanded for big forgings are millimeters; that means kd ≈ 6 for frequencies in the 10 MHz range. When the size of an obstacle is smaller or equal to the wavelengths, imaging is not appropriate. In thick forgings, plates and components fabrication or operation induced defects may occur which are bigger or even much bigger than a wavelength. Imaging in this case is the most appropriate evaluation method to reconstruct defects. This situation demands the twofold approach based on scattering models for the smaller defects and imaging for the bigger ones. The key-terms of the system we have developed are given in Fig. 4 (19,21,22).

- sampling
- pulse echo, tandem, through-transmission,
- amplitude- and time-delay-locus-curves,
- elimination of stochastic and coherent background by time-delay-locus-curves,
- resolving reflectors by time-delay-locus-curves,
- reconstruction of borders of reflectors by time-delay-locus-curves,
- determination of the type of reflector by pattern recognition methods using diffraction theory,
- determination of the selected types.

Fig. 4. Steps of flaw reconstruction.

The major features of the system are described below.

By means of automatic testing procedures, data for each particular reflector are sampled from different positions of the probes. At least in the far-field of the incident beam reflectors normally are smaller than the beam diameter. Therefore, the reflector is covered by the beam for several positions of the probe.

The probe array used for pulse-echo and tandem testing and also through-transmission is shown in Fig.5. This array meets the demands of the German regulations for in-service inspection in the nuclear industry (23).

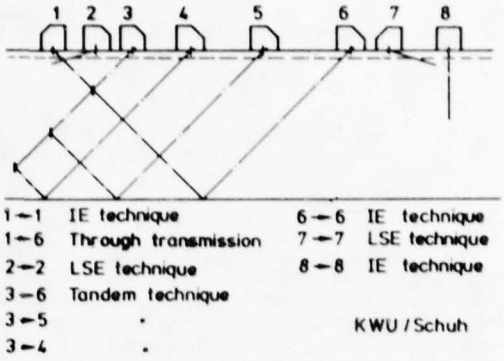

Fig. 5. Probe array for testing pressure vessels.

The first and the last probes are used for through-transmission and pulse-echo from two directions. The probes in between are transmitters for tandem measurements. The tandem technique covers cracking at the "weld-base metal" interface inside the wall.

For each pulse-echo or tandem shot amplitude and time-delay of each peak are measured. Amplitude and time-delay-locus-curves are obtained. Typical curves are shown in Fig.6 for vertical and oblique incidence. For each reflector several time-delay-locus-curves are obtained; Fig.7; two for direct access from the left and the right side, two more for access through bottom reflections and up to eight more curves due to the side lobe reflections. Normally wide beams are used. More than one reflector can be inside the beam for the same position of the probe, but the time-delay-locus-curve will be different for each reflector.

In reality, the time-delay-locus-curves are different from those shown in Fig.6. There may be fadings due to fluctuations or scattering at the back wall. Also stochastic and coherent noise may occur. An example is shown in Fig.8. There are welding and metallurgical defects in the plate. Besides these, there are side-drilled and flat bottomed holes. Noise may be caused by scattering due to segregations, or at the surfaces and outside the system.

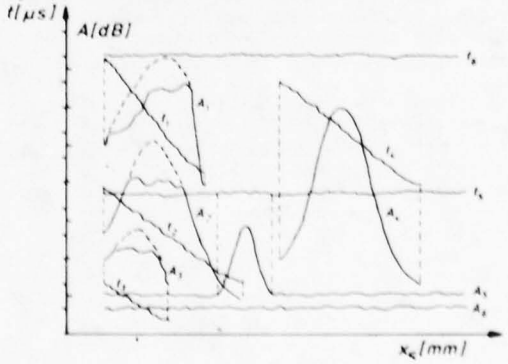

Fig. 6. Typical signal locus curves.

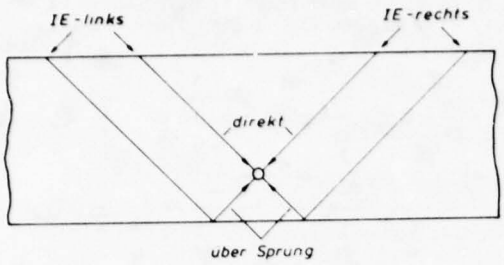

Fig. 7. Ways of ultrasound to one reflector.

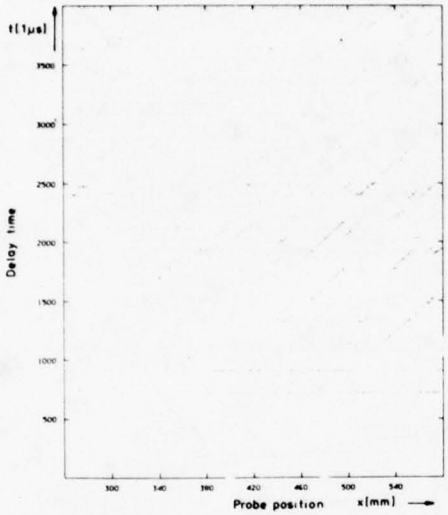

Fig. 8. Time delay locus curves testing values with noise.

Whatever the source of the noise, and independent of whether noise is stochastic or coherent, it does not give a time-delay-locus-curve with a regular shape. Therefore, by simple algorithms, signals belonging to the locus curves caused by reflectors can be selected. The result is shown in Fig. 9. Moreover, these curves have been smoothed and completed.

By means of the geometrical procedures indicated in Fig. 10, the borders of any particular reflectors can be reconstructed. Further details are given in (22).

For further evaluation using scattering mathematics (24,25), only those amplitude values are selected which belong to time-delay-locus-curves. The measured radiation pattern of the emitter, the reflector and the receiver. Moreover, the distance of the reflector from the emitter and receiver is involved. Before applying diffraction theory, the radiation pattern of the reflector has to be isolated. This can be done by known procedures as long as the probes are properly designed or the radiation pattern properly measured. The distance is known from time-delay measurements.

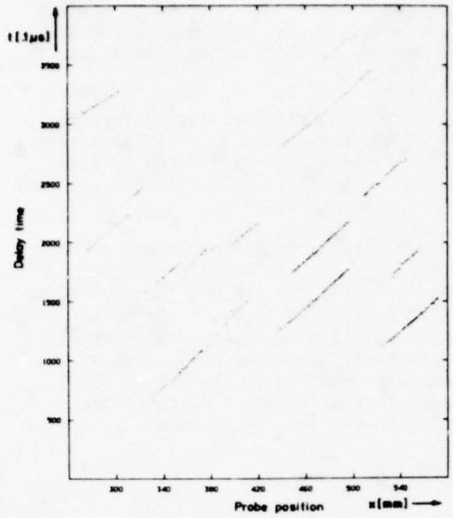

Fig. 9. Time delay locus curves testing values without noise

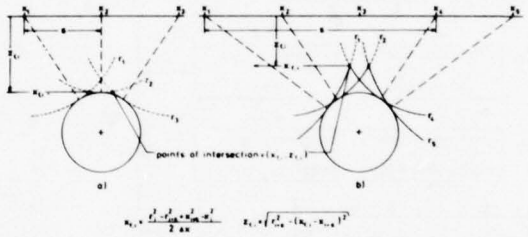

Fig. 10. Flaw border reconstruction through
a) points of intersection
b) circular sectors

Fig. 11 shows the result after isolation. The measured and the isolated amplitude-locus-curve are shown.

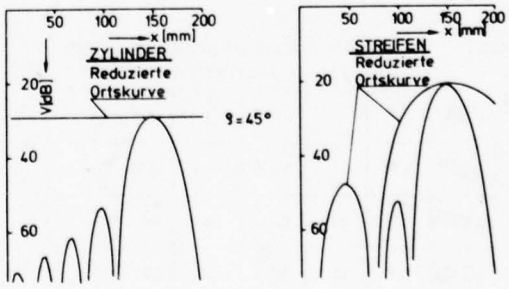

Fig. 11. Isolated amplitude-locus curves

In the case of an isotropic reflector - globe or cylinder - a horizontal line is obtained as an isolated directivity pattern.

If the reflector has a directivity itself, the isolated amplitude-locus curves are no longer linear. Therefore globular and flat reflectors can be distinguished by their directivity patterns.

The distance law allows a decision whether a globular reflector is more like a globe or a cylinder and whether a flat is more like a disc or a strip (26,27).

Finally, by inverting scattering formula the parameters of the selected models can be determined; diameters of the globe and the cylinder, inclination and diameter of the disc or width and inclination of the strip (19).

The block diagram of the whole procedure is shown in Fig. 12. Typical results are given in Fig. 13; in the first two columns the true diameters, widths and inclinations, in the next two the reconstructed values of measurements in water using the procedure described above, and in the last column data obtained by the DGS diagrams, i.e. equivalent diameters of a circular disc perpendicular to the axis of the beam.

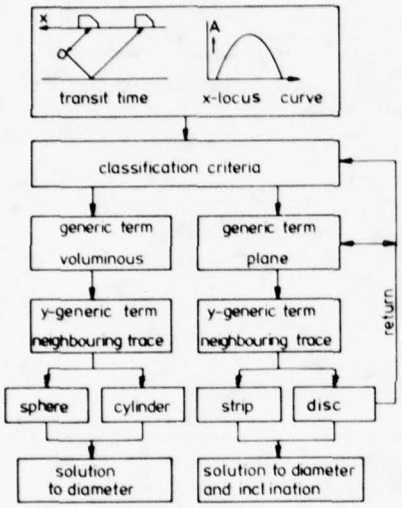

Fig. 12. Diagram of reconstruction with amplitude locus curves.

MODEL	MEASUREMENT		RECONSTRUCTION		DGS-METHOD	
	D_R [mm]	ϑ [°]	D_R [mm]	ϑ [°]	D_R [mm]	ϑ [°]
SPHERE	3 ⌀	-	3,25 ⌀	-	1,2 ⌀	-
CYLINDER	4 ⌀	-	3,9 ⌀	-	4,5 ⌀	-
STRIP	6	35	6,3	39	3,8	-
DISC	6 ⌀	40	5,1 ⌀	43	1,8	-

Fig. 13. Results of reconstruction.

In the last figures the border reconstruction is demonstrated by means of a test block with side-drilled and flat bottomed holes. Fig. 14 shows a two-dimensional reconstruction using locus-curves obtained from four directions. The reconstruction is not completely cleaned. Fig. 15 shows a three-dimensional reconstruction again not completely cleaned, and Fig. 16 the final result.

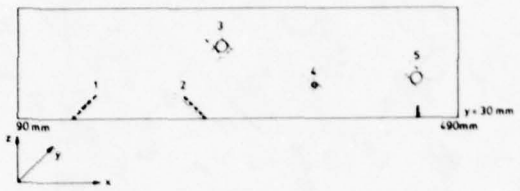

specimen 11

Fig. 14. Flaw border reconstruction 2D.

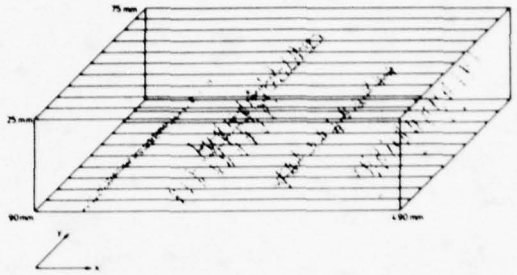

Fig. 15. Flaw border reconstruction 3D.

specimen 11

Fig. 16. Final result of flaw border reconstruction 3D.

At present, work is continuing on the task of completing hard-and software and on obtaining further approval for test blocks and components with real defects. The PISC blocks as well as others have been investigated.

We wish to use the last two figures to give an impression about the experimental devices. Fig. 17 shows a central mast manipulator which fits as well in our laboratory water tank and in an experimental pressure vessel (28). The ultrasonic equipment (29) for activating the probes measuring amplitude versus time-delay, searching peaks and measuring peak amplitude and related time-delay is shown in Fig. 18.

This work has been performed in scope of the reactor safety research program of the Federal Ministry of Research and Technology (30).

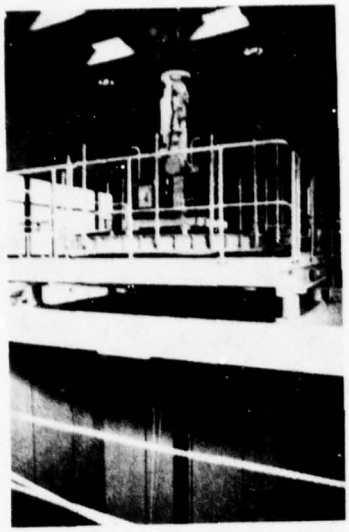

Fig. 17. Central mast manipulator

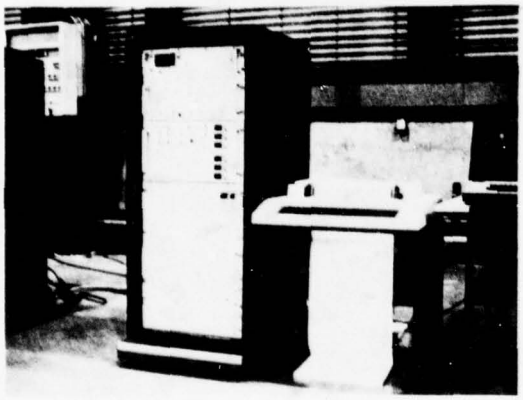

Fig. 18. Ultrasonic equipment.

BIBLIOGRAPHY

(1) B.P. HILDEBRAND, B.B. BRENDEN, "An Introduction to Acoustical Holography". New York, Plenum Press, 1972.

(2) A.E. HOLT, W.E. LAWRIE, "Acoustical Holography", Volume 7, pp 599-609. New York, Plenum Press, 1976.

(3) E.E. ALDRIDGE, A.B. CLARE, M.I.J. BEALE, D.A. SHEPHERD, "Ultrasonic Holography for the Inspection of Thick Steel Specimens". Research Agreement No.6210.GA/8/801 ECC-AERE-G 1002, 1976.

(4) J. KUTZNER, H. WÖSTENBERG, "Acoustic Line Holography as a Tool for Interpretation of Ultrasonic Indications". (in German) Materialprüfung, Vol.18, No.6, 1976, p. 189.

(5) J.R. FREDERICK, R.C. FAIRCHILD, B.H. ANDERSON, "Improved Ultrasonic Nondestructive Testing of Pressure Vessels". Annual Progress Report NUREG-0007-2, August 1, 1975 - July 31, 1976, University of Michigan, 1977.

(6) L. ADLER, K.V. COOK, and W.A. SIMPSON, "Ultrasonic Frequency Analysis". Research Techniques in Nondestructive Testing. Volume 3, Chapter 1. London, Academic Press 1977.

(7) O.R. GERICKE, "Determination of the Geometry of Hidden Defects by Ultrasonic Pulse Analysis Testing". Journal of the Acoustical Society of America, Vol. 35 (March 1963), p. 364.

(8) A. FREEDMAN, "The High Frequency Echo Structure of Some Simple Body Shapes". Acustica, Vol. 12, 1962, p. 61

(9) E.P. PAPADAKIS, "Ultrasonic Diffraction Loss and Phase Change for Broad Band Pulses". Journal of the Acoustical Society of America Vol. 52, 1972, p. 847.

(10) H. PROEGLER, "Determination of Criteria for the Distinction of Defects by Means of Ultrasonic Spectrometry" (in German). Neuere Verfahren zur Analyse von Ultraschallbefunden. Ed. by Deutsche Gesellschaft für Zerstörungsfreie Prüfung e.V., Berlin, 1977.

(11) M. KLEIN, R. WERNEYER, "Ultrasonic Spectroscopic Investigations for the Distinction between Cracks and Pores" (in German). Final Report, Research Agreement 6210/GA/1/101 ECC/VDEh, Institut für zerstörungsfreie Prüfverfahren, Saarbrücken, 1977, Report No. 770226-TW.

(12) Y. H. PAO, "Theory of Normal Modes and Ultrasonic Spectral Analysis of the Scattering of Waves in Solids". Journal of the Acoustical Society of America, Vol.59, No. 5, May 1976

(13) Y. H. PAO, W. SACHSE, "Interpretation of Time Records and Power Spectra of Scattered Ultrasound in Solids". Journal of the Acoustical Society of America, Vol. 56, No. 5, Nov. 1974

(14) E. NABEL, "Evaluation of Flaw Indications by Ultrasonic Pulse Amplitude and Phase Spectroscopy" (in German). Materialprüfung, Vol. 19 No. 2, 1977, pp. 58-64.

(15) J.E. GUBERNATIS, E. DOMANY, M. HUBERMAN, J.A. KRUMHANSL, "Theory of Scattering of Ultrasound by Flaws". 1975 Ultrasonics Symposium Proceedings, IEEE. p. 107.

(16) B.R.TITTMANN, "Ultrasonic Scattering Studies for Failure Prediction". 1976 Ultrasonics Symposium Proceedings, IEEE. pp. 74-79.

(17) A.N. MUCCIARDI, "Adaptive Nonlinear Signal Processing for Characterization of Ultrasonic NDE Waveforms. Task 1, Interference of Hole-Size". U.S.Air Force Materials Laboratory, Air Force Systems Command, Wright-Patterson AFB, OH, by Adaptronics Inc., McLean, VA, Jan. 1975.

(18) J.L. ROSE, "A 23 Flaw Sorting Study in Ultrasonics and Pattern Recognition". Materials Evaluation, Vol. 35, No. 7, 1977, pp. 87-92.

(19) R. WERNEYER, F. WALTE, M. KLEIN, "Mathematical Model for the Reconstruction of Defects When Using Ultrasonic Pulse-Echo and Tandem Methods, and Results of Model Experiments". (in German). Materialprüfung, Vol. 20, No. 2, 1978, pp. 68-72.

(20) V. SCHMITZ, M. WOSNITZA, "Experiences in Using Ultrasonic Holography in Laboratory and in the Filed with Optical and Numerical Reconstruction". 8th Int. Symp. Acoust. Imaging, May 29 - June 2, 1978, Miami, Florida, U.S.A.

(21) O.A. BARBIAN, U. KLOCKE, W. LOTZE, "Border Reconstruction of Defects by Means of Time-Delay-Locus-Curves - Results of Automatic Tests of Specimens With Natural and Artificial Defects -". European Conference on Nondestructive Testing, Mainz, 1978, Paper 13.

(22) P.HÖLLER, O.A. BARBIAN, "Non-Destructive Materials Testing by Ultrasonics and Reconstruction of Defects by Signal-Locus-Curves". (in German). Automatisierungstechnik im Wandel durch Mikroprozessoren, INTERKAMA-Kongreß 1977. Berlin, Heidelberg, New York, Sqringer-Verlag, 1977. pp. 59-71

(23) "Instructions for Water Pressure Reactors". Chapter 4.1, Reactor Coolant Pressure Components" (in German). RSK/4-02/1, 30 Apr. 1974.

(24) A. SCHOCH, "Sound Reflection, Sound Refraction, and Sound Diffraction" (in German). Ergebnisse der exakten Naturwissenschaften XXIII (1950), pp. 127-234.

(25) H. STENZEL, O. BROSZE, "Guide to the Calculation of Sound Processes" (in German). Berlin, Göttingen, Heidelberg, Sprinver-Verlag, 1958.

(26) V.G. SHCHERBINSKII, V.E. BELYI, "New Informatice Index for the Nature of Flaws in Ultrasonic Inspection". Defectoskopiya, Vol. 3, 1975, pp. 27-37.

(27) I.N. ERMOLOV, "The Reflection of Ultrasonic Waves from Targets of Simple Geometry". Non-Destructive Testing, Vol. 5, 1972, p. 87.

(28) H.J. MEYER, W. RATH, "Ultrasonic Apparatus for Repetitive Testing of Reactor Pressure Vessels". Fachtagung No.9, Nuclex 72, Basel.

(29) R. NEUMANN, "A New Hardware System for the Improved Data Recording in Ultrasonic Testing of Reactor Components". European Conference on Nondestructive Testing, Mainz 1978, Paper 86.

(30) H.G. SEIPEL, O. LUMMERTSHEIM, and O. RITTIG, "German Light-Water-Reactor Safety Research Program". Nuclear Safety, Vol. 18, No. 6, 1977.

ULTRASONIC MEASUREMENTS OF INHOMOGENEOUS STRESS FIELDS

G. Hermann, Division of Applied Mechanics
G. S. Kino, Ginzton Laboratory
Stanford University, Stanford, California 94305

ABSTRACT

An acoustic technique for measuring inhomogeneous stress fields in externally loaded solids is described. This method requires a measurement of transit time of a longitudinal acoustic wave through a stressed thin metal specimen using a small diameter water-coupled acoustic transducer. The transducer is mechanically scanned over the surface of the sample by a computer controlled system to take stress field contour plots. Samples investigated include an aluminum plate with a centrol hole, a double edge-notched panel and a single edge-notched panel. In addition to measuring stress fields, the nondestructive determination of stress intensity factors is also discussed.

INTRODUCTION

An ultrasonic technique has been developed for the measurement of acoustic wave velocity. By use of a mechanically scanned transducer the technique has been employed to measure stress variations across several different types of metal samples. Measurements are made through the thickness of planar metal samples by normally incident longitudinal waves. A mechanical scanning system is used to move a water coupled acoustic transducer from point to point on a stressed specimen and acoustic transit time variations with applied stress are measured at each point in the scanned area.

As a calibration, uniaxial tension specimens of aluminum and steel have been tested to determine the third order elastic constant governing the dependence of velocity on stress with results comparable to earlier measurements.[1-4] Acoustic behavior of aluminum and steel have been examined and inplane loaded panels containing edge notches and central holes have been scanned. These tests are conducted in a specially constructed hydraulically operated testing machine that permits specimen loading and transducer scanning in a water bath. The scanning and measurement systems are automatically controlled by a minicomputer. Data is stored, processed and plotted to produce contour maps of the non-uniform stress fields in the scanned areas.

The paper summarizes recent work carried out at Stanford University employing the ultrasonic techniques described above.

EXPERIMENTAL APPARATUS AND TECHNIQUES

Electronic and mechanical systems were developed for imaging non-uniform stress fields and studying acoustoelastic effects. An unfocused 3 mm diameter commercial longitudinal wave ultrasonic transducer was used in a reflection mode near a 12.5 MHz operating frequency. The metal samples employed were typically 10 mm thick. Immersion of the transducer and specimen in water provided an acoustic path and permitted easy scanning of the transducer. Two-dimensional motion and location of the transducer at measurement positions is accomplished by a perpendicular pair of digital stepping motor driven translatory slides. These slides, manufactured by Unislide Corp., have a 250 mm span and a positioning accuracy of 0.1 mm.

A loading machine with tensile and compressive load capability of 100,000 Newtons was developed for these experiments. The machine has provisions for precisely maintaining the relative position and alignment of transducer and specimen. A water-filled tank for immersion of the specimens and transducer is an integral part of the assembly. Loading is provided by a hydraulic cylinder supplied with oil at an accurately controlled pressure. A Lebow Resistance Bridge Load Cell monitors the applied force. Specimens are held in pinned grips which reduce alignment and bending errors.

Point by point acoustic measurements along straight lines at one millimeter spacings are taken over areas as large as 20 cm^2. These measurements are repeated for each value of applied load. Collection and analysis of this data is handled by a PDP-11T-10 minicomputer. By using interpolation on the computer, X - Y plots showing stress field contours of the scanned area can be generated for each load level. Artificially generated fringe contours, similar to photoelastic stress images can also be displayed on a TV screen.

The electronic system for making precision acoustic measurements was designed with the aim of carrying out all measurements under computer control. Thus techniques such as the usual pulse overlap methods were not appropriate. We employed, however, a modification of the pulse echo overlap technique. A longitudinal acoustic pulse from the transducer traverses the water path to be reflected by the front and back faces of the specimen is indicated by time delay in the return of the back echo after the front echo. Variations in transit time are measures of changing thickness and pulse velocity. Because the returning pulses travel the same water path, variations in temperature and water path length should not affect the transit time measurement. The time separation of the two transmitted pulses is adjusted to be equal to the transit time through the specimen and back so the front and back face echos overlap.

The total phase change between the front and back face echos is

$$\phi = 2\omega\, d/V \qquad (1)$$

where ω is the radian frequency of the rf carrier, d the sample thickness and V the acoustic velocity. Because the sample thickness and acoustic

velocity are dependent on stress, the phase of the emerging pulse is altered by changes in applied stress, as it is by a change in frequency. So by logarithmically differentiating Eq. (1) it will be seen that

$$\frac{\Delta\phi}{\phi} = \frac{\Delta\omega}{\omega} + \frac{\Delta d}{d} - \frac{\Delta V}{V} \qquad (2)$$

If zero phase change ($\Delta\phi = 0$) is maintained during the measurement by adjustment of frequency ω, then

$$\frac{\Delta\omega}{\omega} = \frac{\Delta V}{V} - \frac{\Delta d}{d} = \frac{\Delta V}{V} - \varepsilon_{11} \qquad (3)$$

The system for phase change measurements as well as other details are described in a forthcoming paper.[5] The system is capable of setting a null at 12.5 MHz to within 60 cycles, or 5 parts in 10^6.

EXPERIMENTAL RESULTS

Uniaxial Homogeneous Tension. The initial tests were performed on aluminum and steel uniaxial tension specimens and panels. For the plane state of stress of these specimens, the transverse strain is $\varepsilon_{11} = \Delta d/d$ and velocity change $\Delta V_1/V_{10}$ is proportional to the sum of the principal stresses. Thus it follows from Eq. (3) that the relative frequency change is proportional to the sum of the principal stresses or first stress invariant.

$$\frac{\Delta f}{f} = \frac{\Delta\omega}{\omega} = \frac{\Delta V}{V} - \varepsilon_{11} = B(\sigma_1 + \sigma_2) \qquad (4)$$

where B is the proportionality constant.

Uniaxial specimens machined from a rolled bar of 6061-T6 aluminum and a plate of pressure vessel steel* were used to determine B. All specimens were loaded parallel to the rolling direction. The aluminum specimen had a (12.0 x 12.5) mm x 75 mm long measurement section. Strain gages were applied in both longitudinal and transverse directions. For aluminum the value of B was found to be $B = 18 \times 10^{-6}\text{MPa}^{-1}$.

For steel the measured value of B is $2 \times 10^{-6}\text{MPa}^{-1}$ again consistent with previous work[2,4]. Because system accuracy is 5 parts in 10^6, the limit of stress resolution for aluminum and steel are respectively 0.28 MPa and 2.5 MPa.

Specimen with Central Circular Hole. A second set of measurements was then carried out on a specimen whose state of stress was inhomogeneous. For this purpose a 6061-T6 aluminum panel with a central hole was chosen because comparison could be made with the available theoretical solution for this plane stress problem.[6] The panel dimensions were 63 x 120 x 10 mm with a 19 mm central hole as illustrated in Fig. 1. One quadrant of the panel was scanned as shown with a 1 mm point spacing. A scan at zero load provided initial data for the determination of relative changes.

* - Supplied by Dr. K. Stahlkopf, EPRI, Palo Alto, CA

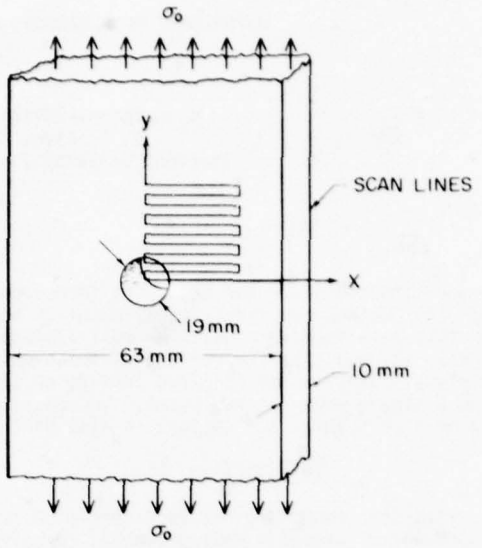

Fig. 1 Specimen geometry for 6061-T6 aluminum panel with central hole.

Experimentally and theoretically determined contours of the first stress invariant normalized with respect to the far field uniaxial stress are in Fig. 2 for a far field stress of 85 MPa. The theory for this finite panel predicts that the stress maximum at the edge of the hole is approximately 3.3 times the remote uniaxial stress and that the top of the hole is in a state of lateral compression. It will be seen from the figure that the experimental results are in good agreement with the theory throughout the panel. In particular, the contour separating

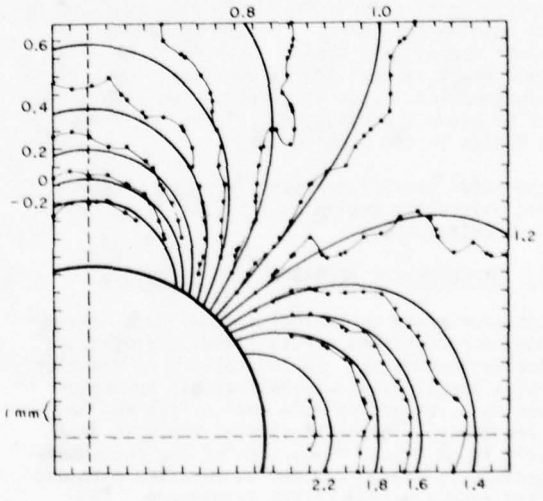

Fig. 2 Stress contour plots of results for 6061-T6 aluminum panel with central hole; normalized stress invariant —— Theory , • Acoustic experiment .

the compressive and tensile regions is well defined experimentally. The value of the acoustoelastic constant B used in Figure 1 is that value which was determined by the uniaxial test. The value of B which gives the best fit of the experimental data to theory differs from B (uniaxial) by less than 5%.

Double Edge-Notched Specimen. In another set of experiments a double edge-notched panel under remote tension was scanned and stress field contours prepared. The width and thickness of the specimen illustrated in Fig. 3 are 60 mm and 8 mm. Two collinear 20 mm deep notches with a 0.5 mm root radius were cut perpendicular to the panel edges. Stress field contours obtained for a load of 30,000 Newtons and 1 mm scan point spacing are shown in Fig. 4 with a numerical elastic solution for comparison. The results give a value of B within a few percent of that for the calibration sample.

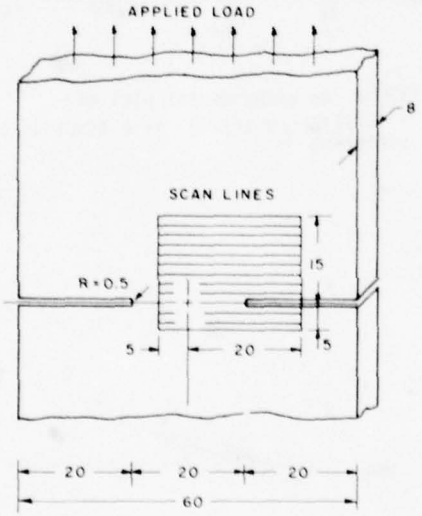

Fig. 3 Specimen geometry for double edge-notched 6061-T6 aluminum panel showing scanned area dimensions in millimeters.

Single Edge-Notched Specimen. Figure 5 shows the geometry of the single edge-notched specimen used in this study. The specimen is mechanically loaded by smooth pins through the shoulders. A crack has been machined into the specimen, but it is not fatigue-sharpened at the root. The specimen in this condition will sustain larger loads without yielding or fracturing. It was loaded to 5 x 10^4N and $\Delta f/f$ was measured at 1 mm intervals in a region 30 x 30 mm. The acoustic transducer recorded the information in the vicinity of the crack tip by moving in a vertical raster pattern.

Figure 6 is a photograph of a computer interpolation of $\Delta f/f$ in the crack tip region. The crack is on the upper left hand side of the photograph and was intentionally not centered in the 30 x 30 mesh. The acoustic fringe contours are reminiscent of photoelastic patterns at crack tips but for this case we observe the sum rather than the difference of the principal stresses. The singular

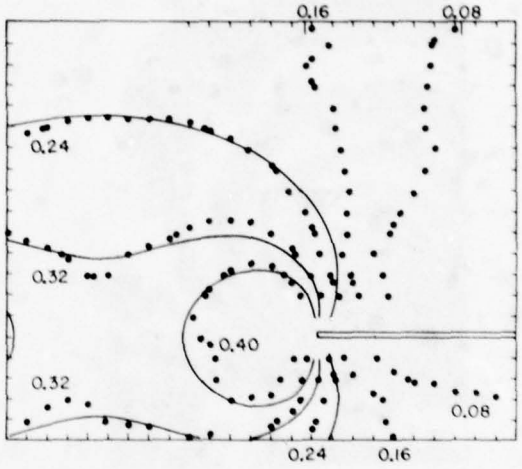

Fig. 4 Stress and frequency contour plots of results for 6061-T6 aluminum double edge-notched panel 30,000 Newton tensile load.

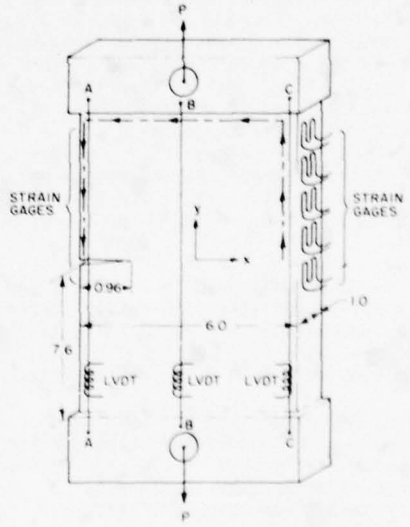

Fig. 5 Specimen geometry for single edge-notched 6061-T6 aluminum panel.

stress term, from the linear elastic crack tip stresses is known to be

$$\sigma_1 + \sigma_2 = \frac{K}{(2\pi r)^{\frac{1}{2}}} 2 \cos(\theta/2) \qquad (5)$$

where r is the distance from the tip of the crack to the field point and θ is the angle from the x axis to the field point. The crack tip was identified as approximately at $x = 9$ mm, $y = 9$ mm. The product $(\pi r/2)^{\frac{1}{2}} \Delta f/[fB \cos(\theta/2)]$, which represents

Fig. 6 Computer generated representation of $\sigma_1 + \sigma_2$ near the crack tip.

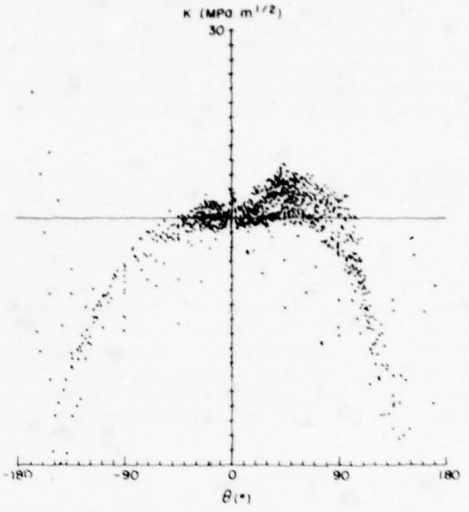

Fig. 7a An experimental plot of $(\pi r/2)^{\frac{1}{2}}\Delta f/[fB \cos(\theta/2)]$ as a function of θ for different r.

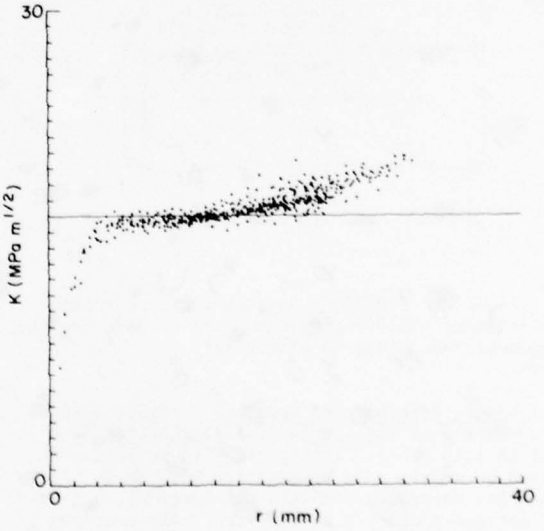

Fig. 7b An experimental plot of $(\pi r/2)^{\frac{1}{2}}\Delta f/[fB \cos(\theta/2)]$ as a function of r for different θ restricted to $\pm 45°$.

the stress intensity factor K, was calculated after positive frequency measurements, and plotted as a function of θ (Fig. 7a) and as a function of r (Fig. 7b). If the stress field were to contain only the singular term, and if the crack tip was positioned correctly, then the ordinates in Figs. 7a and 7b should be independent of θ and r, respectively. For large values of θ and for very small and large values of r, however, the singular stress term does not represent well the actual state of stress. It is for this reason that K depends on θ and r in Figs. 7a and 7b, respectively.

For the applied load of 5×10^4 N, the theoretically calculated stress intensity factor has the approximate value $K = 17$ MPa $m^{\frac{1}{2}}$, as shown by the horizontal line in Figs. 7a and 7b. This number correlates well with experimental data.

Direct Measurement of the J-Integral. Rice's path-independent J-integral has been directly determined experimentally in a single edge-notched specimen by measuring the contributions to J along a convenient path surrounding the crack tip. It is well known that the J-integral represents the crack extension force (or energy release rate) and is related to the stress intensity factor K,

The J-integral is defined as

$$J = \int_{\Gamma} \left(W dy - \bar{T} \cdot \frac{\partial \bar{u}}{\partial x} ds\right) \qquad (6)$$

Here Γ is a curve surrounding the crack tip, the integral being evaluated in the counter clockwise sense starting on the lower crack surface. $\bar{T}$ is a traction vector defined according to the outward normal along Γ. $\bar{u}$ is the displacement vector, W is the energy density, x and y are rectangular coordinates and ds is an element of arc length along Γ. The value of J in this study is to be evaluated by measuring W, $\bar{T}$ and $\partial\bar{u}/\partial x$ on an outer path of the test specimen.

The test specimen shown in Fig. 5 was instrumented with 10 strain gages on the outside edges of the sample. The gages are placed only on the upper half of the specimen from symmetry considerations. The displacement of the upper shoulder of

the specimen relative to the lower shoulder was measured using displacement gages, linear variable differential transformers (LVDT), between A-A , B-B and C-C .

The path used to evaluate J is shown by the dashed line on the upper half of the sample. On the vertical sides of the sample $\bar{T} = 0$ so the contribution to J is only from $\int W dy$. Across the top of the sample, $dy = 0$ and $ds = dx$ so only $-\int \bar{T} (\partial \bar{u}/\partial x)\, dx$ contributes to J . W is evaluated from the strain gages on the vertical sides of the specimen. $W = 1/2\, E\varepsilon^2$ with E - Young's modulus and ε the strain, for a traction-free plane stress boundary. It has been assumed that the material where the gages are placed is linearly elastic. If the entire specimen is linearly elastic, W is proportional to P^2 , where P is the load on the sample. The dimensions of the specimen were chosen such that the strain just below the shoulders would be approximately uniform. This is achieved by making the sample long with respect to the crack length. The uniform strain produces two effects: first, W on the cracked and uncracked side of the sample approach the same value and therefore the next contribution of $\int W dy$ to J in these regions is zero; secondly, a uniform stress state allows $\partial \bar{u}/\partial x$ to be evaluated using only several points across the specimen.

The strain gage outputs were linear with load. The contribution to J/EP^2 was found to be

$$\int_{\Gamma} \frac{W dy}{EP^2} = \int \frac{\varepsilon^2}{P^2}\, dy = 2.52 \times 10^{-18}\ \frac{m}{N^2} \qquad (7)$$

The evaluation of $-\int \bar{T} (\partial \bar{u}/\partial x)\, dx$ across the top of the specimen was experimentally found by recording $\bar{u}$ on three displacement gages across the specimen (see Fig. 5). It has been assumed that $T_y u_y$ only contribute to the integral on this boundary. If $\bar{T}$ is constant, then $\Delta \bar{u}$ across the sample only needs to be measured. If the upper boundary is rigid, such that the rotation $\partial \bar{u}/\partial x$ is constant, then $\int T dx = P/b$; P/b and the rotation would be used to evaluate the contribution to J . For the specimen geometry tested, a nearly constant stress with a nearly rigid rotation has been achieved. Note that $\bar{T}$ and $\partial \bar{u}/\partial x$ are both proportional to the load for a linearly elastic sample, thus J is proportional to P^2 , as is well known in linear elastic fracture mechanics. The contribution to J/EP^2 from the upper and lower boundary was found to be

$$1.96 \times 10^{-17}\ \frac{m}{N^2} \qquad (8)$$

The total contribution to J is found by adding (7) and (8)

$$J = 2.21 \times 10^{-17}\ P^2 E\ \frac{m}{N^2} \qquad (9)$$

The equivalent stress intensity value is $K = [JE/(1 - \nu^2)]^{\frac{1}{2}}$ for plane strain cracks. Thus, the experimental method permitted to measure K/E The value in (9) may be compared with the analytic handbook value [7], assuming our measured value of $E = 7.03 \times 10^{10} N/m^2$ is correct, which is

$$J = 2.15 \times 10^{-17} P^2 E\ \frac{m}{N^2} \qquad (5)$$

There is excellent agreement between the theoretical value and the value measured. Note that only about 10% of the value of J comes from the vertical part of the integral for the specimen of our geometry. The measurement of that contribution to J has been carried out also using acoustic techniques, but the accuracy was somewhat smaller than employing strain gages.

CONCLUSIONS

It has been shown that quantitative acoustoelastic measurement of stress field profiles can be made. The highly precise measurements can be made over large areas of relatively thin specimens.

Ongoing and planned work concerns the acoustic behavior of plastically yielded material, scanning measurements with shear waves, investigation of three-dimensional states of stress, study of curved specimens and improved techniques for measuring stress intensity factors at crack tips.

ACKNOWLEDGMENT

Numerous persons contributed to the work reported here. They include, in particular, D.M. Barnett, S.J. Burns, J.B. Hunter, G.C. Johnson, A.R. Selfridge and C.R. Steele. As already mentioned, a detailed account of this research will be presented in separate journal publications.

This work was supported by EPRI Contract No. RP-609-1 and NSF Contract No. DMK-76-00726 through the Center for Materials Research at Stanford Univ.

REFERENCES

1. Crecraft, D.I., "The Measurement of Applied and Residual Stresses in Metals Using Ultrasonic Waves", J. Sound Vib., 5 (1), 173-192 (1967).

2. Smith, R.T., Stern, R. and Stephens, R.W.B., "Third-Order Elastic Moduli of Polycrystalline Metals from Ultrasonic Velocity Measurements", J. Acoust. Soc. A., 40, 5, 1002-1008 (1966).

3. Hsu, N.N., "Acoustical Birefringence and the Use of Ultrasonic Waves for Experimental Stress Analysis", Exp. Mech., 14, 5, 169-176 (1974).

4. Egle, D.M. and Bray, D.E., "Measurements of Acoustoelastic and Third-Order Elastic Constant for Rail Steel", J. Acoust. Soc. A., 60, 3, 741-744 (1976).

5. Kino, G.S., J.B. Hunter, G.C. Johnson, A.R. Selfridge, D.M. Barnett, G. Herrmann and C.R. Steele, "Acoustoelastic Imaging of Stress Fields" to be published.

6. Howland, R.C.J., "On the Stresses in the Neighborhood of a Circular Hole in a Strip under Tension", Trans. Roy. Soc. (London), Ser. A., 229, 49-86 (1930).

7. Sih, G.C., Handbook of Stress-Intensity Factors, Vol. I, Lehigh University, Bethlehem, PA (1973).

DISCUSSION

W. Sachse (Cornell University): Did I understand you correctly to say that these measurements you showed us were longitudinal waves only?

G. Hermann (Stanford University): Yes.

W. Sachse: Well, I guess maybe that it is just a matter of semantics, but I think that carrying over the photoelastic ideas to these particular measurements and calling them acoustoelectric measurements is probably not quite right because, in the photoelastic technique, as I understand it, it is infringement induced. They are shear waves.

G. Hermann: I say acoustoelectric in the sense that we have the coupling between the stresses on the one hand and acoustics on the other hand. It doesn't have to be precisely the same type of wave.

W. Sachse: Except that I think the interference here is almost like electronic interference. You are interfering, as I understood your schematic diagram, the incident bursts (RF bursts), with bursts having traveled through a specimen.

G. Hermann: Yes.

W. Sachse: Thus, it is really a non-linear elastic effect.

G. Hermann: Yes.

W. Sachse: It is by infringement. There are two waves.

Gordon Kino (Stanford University): It is still a photoelastic effect between light and elastic waves. This is photoacoustic--not elastic.

Robert Green (Johns Hopkins): Not in the definition of photoelasticity as defined in the standards. Maybe the name photoelasticity is all right. But Sachse is right if you are going to be a purist and talk about photoelasticity.

G. Hermann: I think the German word for photoelasticity, which is phononoptic, is perhaps even better because there it relates stresses with optics. Here we relate acoustic with stresses.

W. Sachse: It is a semantics question. I have a more serious question. How wide is your transducer?

G. Hermann: Three millimeters.

W. Sachse: Is that the spacing between points?

G. Hermann: No. The spacing between points is one millimeter.

Gordon Kino: The actual beam is probably a little smaller, even though the actual diameter of the transducer is three millimeters. The effective beam is smaller and it gives some averaging, which helps.

J. Rice (Brown University): I am wondering why you used strain gauges? Wouldn't your wave speed cut the procedure?

G. Hermann: Yes. The time set for this particular sample for this particular measurement was not quite the ideal one, as I understand it, to make the measurements along the rims. The strain gauges gave us a little bit better data than the acoustic measurements.

J. Rice: So you can't get too close to the edge of the specimen with acoustic measurements?

G. Hermann: Yes, I think that is a problem.

P. Hildebrand, Chairman (Battelle-Northwest): I will entertain one more question.

Bernard Budiansky (Harvard): George, what happens to acoustoelasticity in the presence of plastics flow? Do you have an acoustoelasticity theory?

G. Hermann: That is a very interesting question and, as I say, we are pursuing the problem. It turns out that if you stress the sample into the plastic range and unload, then the acoustoelastic effect disappears even though there is permanent strain there. But we have no handle whatsoever on the mechanism which might cause this. We have been talking to people like Charley Elbaum, who is interested in vibrating dislocations and so on, but, of course, we need something more phenomonological and on a different level. We don't understand it. The biggest difficulty, you see, in making and extending these types of measurements into the plastic range is that you have no more the proportionality between the strain and the sum of the principal stresses. That is the difficulty which we have yet

to overcome. But, as I say, we have some encouraging results and I have just no time.

P. Hildebrand, Chairman: Thank you. I think we'd better go on.

NONDESTRUCTIVE DETECTION OF VOIDS BY A HIGH FREQUENCY INVERSION TECHNIQUE

Jack K. Cohen and Norman Bleistein
Denver Applied Analytics
2555 S. Ivanhoe
Denver, Colorado 80222

and

Richard K. Elsley
Rockwell International Science Center
Thousand Oaks, California 91360

ABSTRACT

A direct solution of the ultrasonic inverse scattering problem, known by the acronym POFFIS, which stands for Physical Optics Far Field Inverse Scattering, has been developed. This technique has been used to reconstruct the shape and size of both simulated and real void flaws in materials.

When a wave (e.g., acoustic, elastic, electromagnetic) propagates through a medium, the wave is deformed by irregularities in that medium. The deformation of the probing wave is characteristic of the irregularity. This is the basis of a method for nondestructive evaluation of solid materials. A known high frequency probing wave is introduced into the medium. The wave scattered by the irregularity is observed. The nature of the irregularity is to be inferred from the nature of the scattered wave.

The type of problem we have described here is called an inverse problem. The corresponding direct problem would be to find the scattered wave given the "incident wave" (probe) and the irregularities of the medium. Inverse problems are often attacked indirectly; i.e., one solves the direct problems for prescribed irregularities, seeking an irregularity for which the scattered wave most nearly approximates the data.

In contrast, we are engaged in research on direct solutions of the inverse problem. An inverse method for nondestructive detection of scatterers of high contrast, such as voids or strongly reflecting inclusions will be described here. This method is known by the acronym POFFIS, which stands for Physical Optics Far Field Inverse Scattering. In this method, the phase and range normalized far field scattering amplitude is shown to be directly proportional to the Fourier transform of the characteristic function of the scatterer. The characteristic function is equal to unity inside the region occupied by the scatterer and is zero outside. Thus, knowledge of this function provides a description of the scatterer. However, for bandlimited data, it is easier to reproduce a directional derivative of the characteristic function. These ideas were developed in a series of papers[1,2,3,4,5].

The specific application here is to describe flaws contained in a sphere. Observations of backscatter acoustic signals are made on the surface of the sphere. The following formula may be derived for the radial derivative of the characteristic function (see 2):

$$R\hat{x}\cdot\nabla\gamma(\underline{x}) = A\int_{\Omega} d\Omega\ \hat{x}\cdot\hat{x}_0\ \frac{\partial V}{\partial t}(\hat{x}_0,\ 2(x_0 - \underline{x}\cdot\hat{x}_0)/c). \qquad (1)$$

Here, R is the unknown reflection coefficient, γ is the unknown characteristic function, $(\hat{\ })$ denotes unit vector, A is a known constant which depends on the source configuration, V is the range normalized backscattered ("pulse-echo") impulse response in the direction $\hat{x}_0$ at a time $t = 2(x_0 - \underline{x}\cdot\hat{x}_0)/c$, x_0 is the radius of the observation sphere and the integration domain Ω is the unit sphere with variable $\hat{x}_0$. Thus implementation of the POFFIS result requires an integration over the directions of observation of the scattered data.

We now present the results obtained from a computer implementation of this method. The conuter program uses either simulated flaws or experimental data from real flaws and incorporates the following "real world" constraints: (1) bandlimiting: only a limited range of frequencies are present in an ultrasonic pulse, (2) aperture limiting: a flaw can usually be viewed from only a small range of angles due to the geometry of the part in which it is located.

Several types of graphical display of the results are presented. Consider a longitudinal "slice" through the flaw, as depicted in Fig. 1. In order to see the radial derivative function which results from the integration, its value can be displayed along a number of radii of the flaw. Two such radii are shown in Fig. 1. This type of display is used in Figs. 2-7. The estimated position of the surface of the flaw is at the peak of the radial derivative function along each radius. A simple display of the estimated shape and size of the flaw is obtained by plotting the locus of these peak positions in a variety of radial directions. This type of display is labeled "flaw" in Fig. 1, and is used in Figs. 8-13.

The first tests of the method involved the use of synthetic backscattered data from a spherical void of 400 microns radius. The value of the dimensionless parameter "ka" was about seven. Tests were run with ninety-eight observations and two hundred observations around the surface of the observation sphere. Output of the type in Fig. 1 is plotted for a slice at longitude 0^0 for several latitudes.

Figure 2 shows the result for ninety-eight observations. Figure 3 shows the result for two hundred observations. In each case, the maximum error in location of the boundary is less than 5%.

The above cited papers also develop a theory for dealing with data given over less than the full 4π steradians of the observation sphere Ω. For such aperture limited data, the function $\partial V/\partial t$ in the integrand above is taken to be zero outside the aperture of observation and the same integration formula is applied. The theory predicts that only a portion of the boundary will be produced, namely that section for which the normal to the boundary is in the aperture of the non-zero data.

This theory was tested on a series of synthetic examples. Figure 4 shows the output when the aperture is taken as a pair of opposite octants in the lower hemisphere. This requires fifty observations at 25% aperture. Here the longitudinal slice is taken symmetrically through the aperture. Figure 4 demonstrates the validity of this limited aperture theory.

Figure 5 depicts the output when the aperture consists of one octant - 25 observations or 12.5% aperture - in the lower hemisphere. Again the output slice cuts the aperture symmetrically.

Figure 6 shows the output from a 7.5% aperture. The longitudinal slice is taken through the center of the aperture and the appropriate quarter circle is detected.

Figure 7 tests the constraint that the dimensionless parameter of the theory used to predict the peak across the boundary really remain large. Here the bandlimited Fourier transform of the characteristic function of an ellipsoid is processed. The radial derivative still demonstrates a detectable peak, even though the so-called large parameter is as small as three. In the second quandrant the true boundary points on each ray are connected and the computed boundary on each ray are shown by dots. In the third quandrant the computed boundary points are connected to yield the approximate ellipse.

In order to explore the robustness of the POFFIS algorithm with respect to having only a limited amount of data available in the temporal domain (i.e., bandlimiting), a set of calculations was performed using a "simulated ultrasonic transducer." This transducer's output is a maximum at a center frequency f_0 and drops smoothly to zero by zero frequency and by 2 f_0. An appropriate measure of the "highness" of the frequencies being used is

$$ka = 2\pi f_0 \, a/v \qquad (2)$$

which is numerically equal to about 1/2 f_0 in MHz in this case. Because it is a high frequency technique, POFFIS would be expected to perform less well as f_0 is reduced.

Figure 8 shows the estimated flaw outline for a 450 μm sphere inspected by an 8 MHz transducer (ka = 4). The shape is well reconstructed and, as the statistics accompanying the figure show, the size is only slightly underestimated. As the transducer frequency is reduced, the shape is still well reconstructed, but the size underestimation becomes more serious. Figure 9 shows the case of ka = 1.5. Thus, POFFIS works relatively well even at frequencies as low as ka ~ 2.

Another important question is: how coarse can the spatial sampling of the scattered sound field be without leading to incorrect results. In other words, how few transducer positions are needed?

Figure 8 was obtained using 100 observations around the full 4π sterradian solid angle. As the number of observations is decreased, the size of the flaw remains unchanged but its outline begins to become slightly irregular. Eventually, the algorithm begins to make errors. Figure 10 shows the case of using only 8 observations spread over the entire angular range. At the north and south poles, substantial errors occurred.

The reason for these errors is that at a given frequency, the spatial sampling must be fine enough to adequately sample the rate at which the scattered sound field can vary with angle. A corollary is that if high frequencies are used, more observation positions are needed. Also, more observations are needed for irregularly shaped flaws. A rule of thumb for sphere-like flaws is that the angular separation θ between observations obey

$$\theta < \frac{2}{ka} \text{ radians}$$

This equation is an angular equivalent of the Nyquist sampling theorem.

In Figs. 4-7, it was shown that when the flaw is observed through a limited aperture, the part of the flaw facing the aperture is accurately reconstructed. In Fig. 11, the calculation of the surface of the flaw was automatically terminated when the amplitude of the radial derivative function dropped below a specified level. In practice, this level could be the noise level of the measurements. In this case, the calculation was allowed to continue beyond the edges of the aperture and the characteristic asymptotic behavior is seen. A more conservative use of the algorithm might involve also terminating the calculation at the edges of the aperture.

What pattern of transducer positions gives the best reconstruction? Because the reconstruction works only within the aperture of available observations, it follows that the reconstruction at a given point is determined primarily by the observations at nearby angles. Therefore, by observing the quality of reconstruction at various points on the angular sampling grid, one can judge what local arrangement of transducers does the best job. The following conclusions have been drawn. A grid which

approximates a square array (checkerboard) does better than one having a measurement point in the middle of a circle of other measurement points. This, in turn, does better than a grid consisting of the ring of points with no center point.

For a nonspherical flaw, the POFFIS technique reproduces the shape well. Figure 12 is the reconstruction of a simulated oblate spheroid of semi-axes 200 μm x 400 μm.

Finally, POFFIS has been applied to experimental data. Figure 13 is a reconstruction of a 400 μm radius spherical void built into a block of Ti-6Al-4V by the diffusion bonding process. The size and shape are well reproduced. The "roughness" of the shape is due primarily to the metallurgical noise of the titanium.

Note that all of the above reconstructions have been done with only the limited range of frequencies present in a commercial ultrasonic transducer. No attempt has been made to deconvolve the transducer out of the data. The results were seen to be fairly insensitive to the type of transducer. This means that there may be no need to remove the transducer properties.

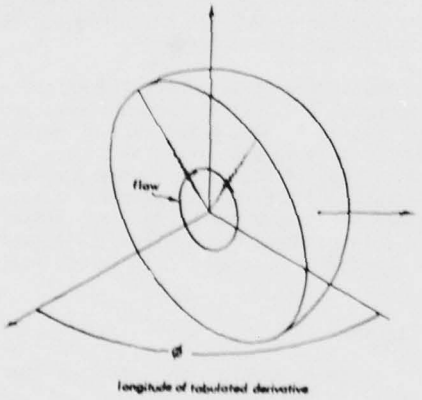

Fig. 1

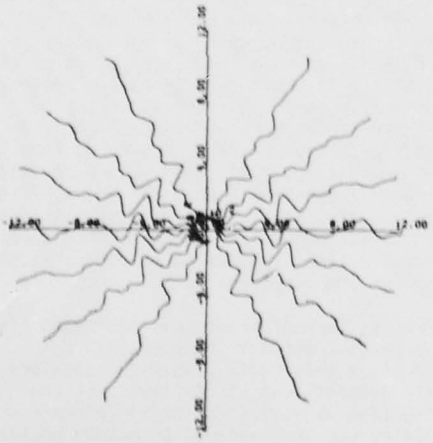

MODEL: 400 MICRON CIRCLE

LONGITUDE 0 DEGREES

MI=7

Fig. 2

ACKNOWLEDGEMENTS

This research was sponsored by the Center for Advanced Nondestructive Evaluation operated by the Science Center, Rockwell International, for the Defense Advanced Research Project Agency and the Air Force Materials Laboratory under Contract No. F33615-74-5180.

REFERENCES

1. Bojarski, N. N., Three Dimensional Electromagnetic Short Pulse Inverse Scattering, Syracuse University Research Corporation, Syracuse, New York, NTIS #AD-845 126 (1967).
2. Bleistein, N., Physical Optics Far Field Inverse Scattering in the Time Domain, J. Acoustical Soc. Amer., 60, 6, 1249-1255, (1976).
3. Mager, R. D., and Bleistein, N., An Approach to the Limited Aperture Problem of Physical Optics Far Field Inverse Scattering, IEEE Trans. Ant. and Prop., to appear.
4. Armstrong, J., An Analysis of the Aperture Limited Fourier Inversion of Characteristic Function, Thesis, (1978).
5. Bleistein, N., and Cohen, J. K., Application of a New Inverse Method to Nondestructive Evaluation, Denver Research Report, MS-R-7716 (1977), Interdisciplinary Program for Quantitative Flaw Definition, Rockwell International Science Center, report for period 07/01/76 - 06/30/77.

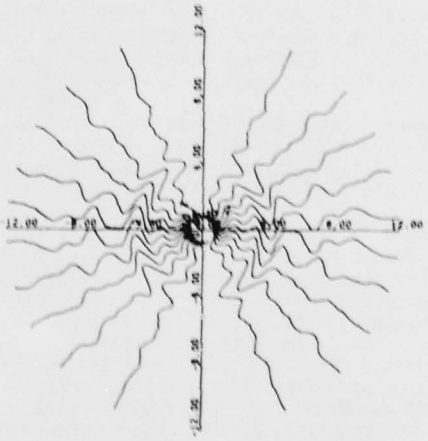

MODEL: 400 MICRON CIRCLE

LONGITUDE 0 DEGREES

MI=10

Fig. 3

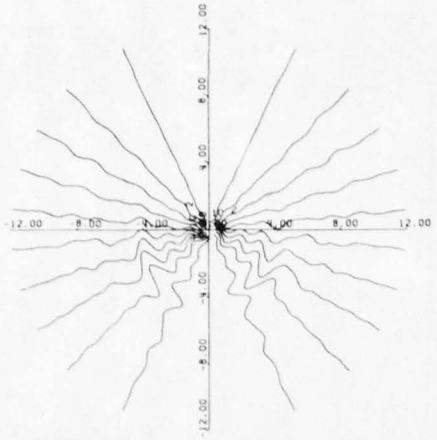

OPPOSITE OCTANTS IN LOWER HEMISPHERE

25 PERCENT APERTURE (50 OBSERVATIONS)

Fig. 4

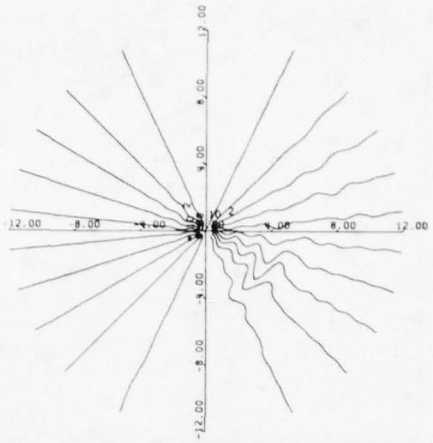

OCTANT IN LOWER HEMISPHERE

7.5 PERCENT APERTURE (15 OBSERVATIONS)

Fig. 6

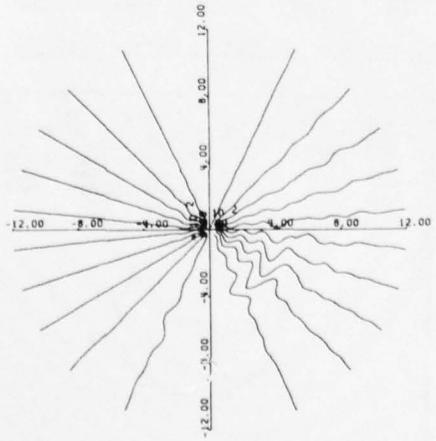

OCTANT IN LOWER HEMISPHERE

12.5 PERCENT APERTURE (25 OBSERVATIONS)

Fig. 5

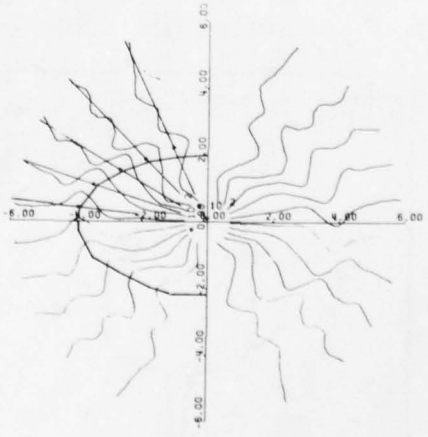

400 X 200 MICRON ELLIPSE

Fig. 7

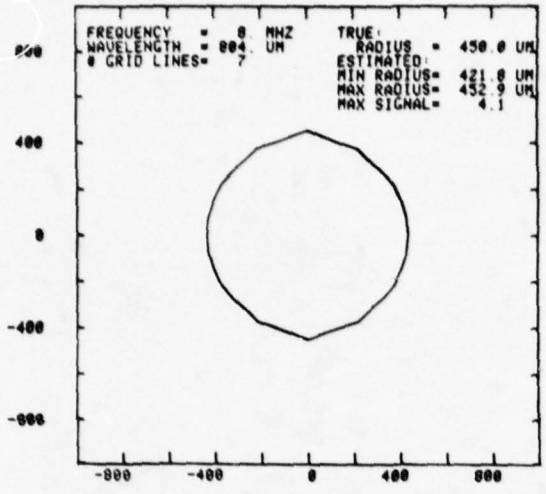

Fig. 8 450 μm sphere, 8 MHz transducer, ka = 4.

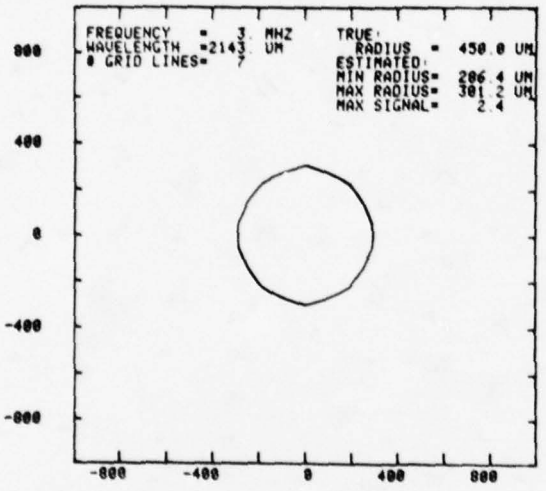

Fig. 9 450 μm sphere, 3 MHz transducer, ka = 1.5.

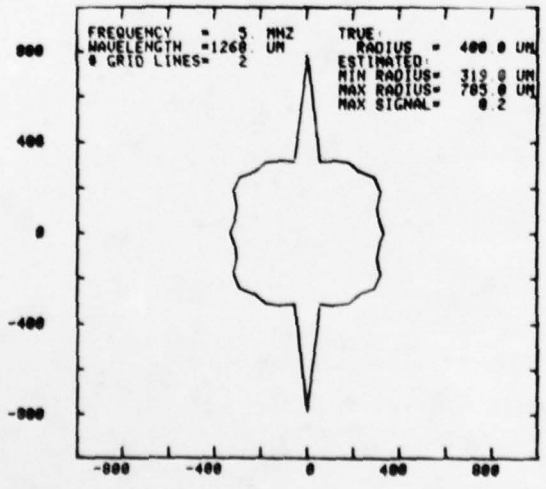

Fig. 10 Insufficiently fine angular sampling.

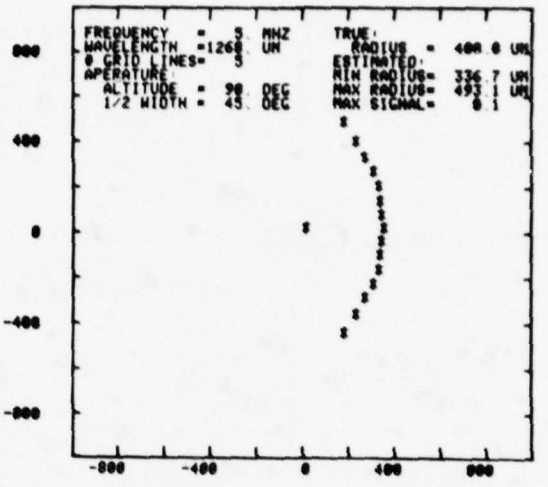

Fig. 11 Limited aperture of observations.

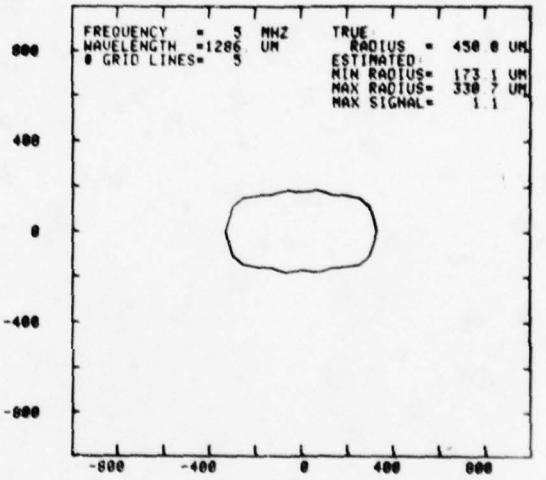

Fig. 12 200 μm x 400 μm oblate spheroid.

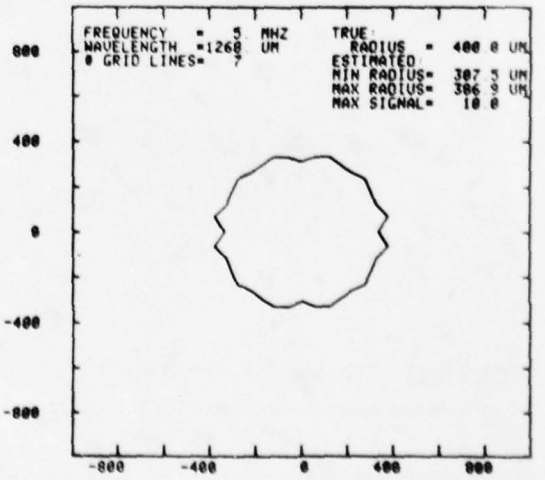

Fig. 13 400 μm radius spherical void.

DIGITAL SYNTHETIC APERTURE ACOUSTIC IMAGING FOR NDE

G. S. Kino, P. M. Grant, P. D. Corl, and C. S. DeSilets
Ginzton Laboratory, Stanford University,
Stanford, California 94305

ABSTRACT

Real time synthetic aperture or synthetic focus techniques for acoustic imaging have been investigated and a prototype digital imaging system has been developed. It operates by exciting, with an impulse, one element from a transducer array, digitizing the return echoes, and storing them in a Random Access Memory. When this process has been repeated for all the array elements, the focus information is loaded from a mini computer. The system then generates a series of swept-focus lines, which are arranged perpendicular to the array face. Our processor handles typical input data at rates sufficient to generate real time images.

As only one transducer at a time is excited it has been necessary to develop a high efficiency broadband transducer array with quarter wavelength matching layers. The array we have developed has an 11 dB return loss, a 2.7 – 4.3 MHz frequency range with a pulse response approximately 5 half cycles long. The digital processor operates at a 10 – 16 MHz sample rate with 8 bit quantization. Theoretical and experimental images will be presented for a system with a 96 line display employing 8 and 32 active transducer elements, which has a resolution of < 1 mm.

We will also discuss methods of reducing the sidelobe responses in these systems. We have carried out experiments and theory, and we can considerably reduce the sidelobe level with input gain compression from the current experimental value of -12 dB to beyond -20 dB in our prototype 8 transducer system. In addition, we are investigating inverse filtering techniques for shortening the effective pulse length to 1 rf cycle to further improve the image quality and range resolution.

INTRODUCTION

Description of Real Time Synthetic Focus Imaging Technique. This paper describes the design and initial operation of a new real-time synthetic focus or synthetic aperture digital acoustic imaging system.[1] The term synthetic aperture can be used to describe our system as the signal processing is equivalent to that used in synthetic aperture radar.[2] However as we employ a transducer array whose physical aperture is equal to the aperture we synthesize in our processor, the system has also been described as synthetic focus imaging.[2] It is functionally equivalent to a tomographic imaging system with filtered back-projection, operating in real-time. The basic principles of a very closely related system have already been demonstrated by Johnson, et al,[2] using relatively slow computer reconstruction techniques. We have obtained high speed operation by performing the synthetic focus processing in dedicated digital hardware which is capable of operating at up to 16 MHz data rates.

In this system, we transmit from one element at a time and receive the return signal on the same element. The received signal passes through an analog multiplexer, an amplifier and an Analog-to-Digital (A to D) converter before storage in the signal memory, Fig. 1 . This operation is repeated for successive array elements, with the analog multiplexer selecting the desired element. To implement this synthetic focus imaging system we must be able to store a complete set of signals, one from each transducer element. In order to do this, we use a video A-to-D converter and semiconductor Random Access Memories (RAM). To provide adequate sampling of amplitude and phase we must operate the A-to-D converter at a sampling rate typically 3 - 4 times the upper cutoff frequency of the transducer elements. Thus if the upper cutoff frequency of the transducer elements is 4.3 MHz, the system clock rate must be greater than 13 MHz. Once we have stored the signals from a sufficient number of elements, we can reconstruct an entire two-dimensional image by adding the information from the appropriate locations in the signal memories. Equal time delays to the point of interest, are inserted during the display process, Fig. 2 , to reconstruct points in the image plane.

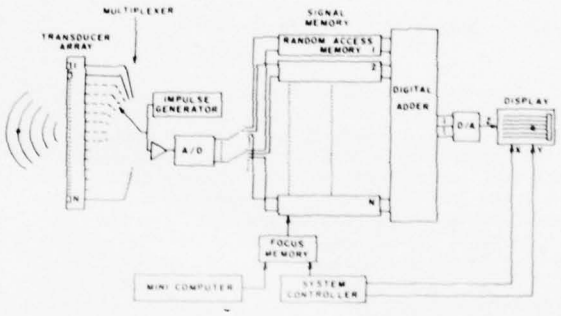

Fig. 1. Digital imaging system.

The reconstruction of a two-dimensional image from the set of signals stored in the digital memories is a formidable computational task and to accomplish this we have implemented the back-projection method which requires a set of geometric calculations to control the addressing of the signal memories. However, once the required addressing information has been computed, it can be stored in

table form in a high speed memory which we refer to as the focus memory, Fig. 1 . In a typical 32-element system, the focus memory will be about 1/4 the size of the signal memory. Alternatively, the focus memory can be implemented using a Programmable Read Only Memory (PROM) which is much denser than the RAM we are using for signal memory. However, the initial advantage of using a RAM rather than a PROM is that the scan format can be programmed at will from a computer or microprocessor. With this technique we can generate scan lines perpendicular to the array, perform a radial sector scan, or synthesize any other desired scan format. We can also vary the spacing between scan lines either by reprogramming the focus memory from a microprocessor, or by interpolation techniques. We have chosen to display our image as a raster scan with lines perpendicular to the array face.

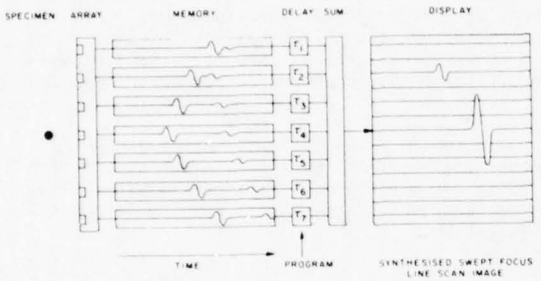

Fig. 2. Schematic of system operation.

One reason for this choice of scan format is the possibility of carrying out integration of the image on a scan converter, much as in a conventional mechanical B scan system. Suppose, for instance, 128 elements in total are employed and the image from 32 elements is read into a scan converter. Then by passing to the next 32 elements a new image is formed, and read into the scan converter. With the scan format employed, integration will take place on scan lines common to both images. Repeating this process with an array whose elements possess a wide angle of acceptance, produces an image which is equivalent to a very wide aperture system.

Comparison with Other Acoustic Imaging Systems

An important advantage of the synthetic focus approach is that it requires only a single front-end amplifier, regardless of the number of elements in the transducer array. This means that a great deal of effort can be put into the design of the front-end amplifier with little regard for its complexity, number of adjustments, expense, etc., all of which are important considerations in a system where an amplifier is required for each element of the array.

Another important advantage of the synthetic focus approach over other acoustic imaging systems is that the transverse resolution is twice as good as that of an equivalent system in which a parallel beam is transmitted and the system is focused on receive. This is due to the fact that the time and phase difference to a point, Z , from a transducer element is doubled, because the signal travels to the image point and back. Thus our system has a transverse resolution which is equivalent to that of a conventional imaging system operating at twice the frequency. The range resolution is essentially determined by the pulse length (bandwidth) as with other imaging techniques. The system therefore provides the same improvement in transverse resolution capability which has already been demonstrated in scanned holographic imaging.[3] But, in addition, as we are using time delay rather than phase delay techniques to reconstruct the image, we should also obtain excellent range resolution.

One problem with most electronically scanned acoustic imaging systems is that the display line and frame times are not usually compatible with a TV monitor. This is a disadvantage as the grey scale image quality of magnetically deflected cathode ray TV tubes, is superior to that of the electrostatic deflection tubes used in oscilloscopes.[1] Our present design can easily be made compatible with the line time of a TV display by controlling the speed at which the focused lines are read out. However, the number of lines currently employed, 96, is far less than in a TV display (525). So the image will not look continuous. One technique to eliminate this difficulty is to use only part of the screen. Another is to use interpolation routines for filling in.

Theory of Synthetic Focus Imaging. We have carried out an analysis of resolution and sidelobe levels in the system. We assume that the system is excited by a pulse of the form $F(t) \exp j\omega t$, and is focused on the point (x_0, z_0) . Then after suitable time delays have been introduced, the sum of the delayed signals returning to the transducers at $(x',0)$ is of the form

$$G(t) = \int_{x_n} F(t-2\Delta R/v) \exp j\omega(t-2\Delta R/v)\, A(x')dx' \qquad (1)$$

where v is the acoustic velocity in the medium, $A(x')dx'$ is the response of the transducer in the transmit-receive mode in the region between x' and $x'+dx'$,

$$\text{and} \quad \Delta R = \sqrt{z^2 + (x'-x)^2} - \sqrt{z_0^2 + (x'-x_0)^2} \qquad (2)$$

is the difference in range from $(x',0)$ to (x,z) and (x_0,z_0) .

By making the paraxial approximation that $(x' - x)^2 \ll z^2$, taking $x_0 = 0$, for simplicity we can write

$$\Delta R \approx \Delta z - x'\Delta x/z_0 \qquad (3)$$

where $\Delta z = z - z_0$, $\Delta x = x - x_0$. It follows that the range resolution, i.e., the result with $\Delta x = 0$ is determined by the function $F(t - 2\Delta z/v)$ for all transducers. So the range resolution is determined by the pulse shape and length.

On the other hand, the transverse definition of a line reflector and sidelobe levels $(\Delta z = 0)$

are determined by the integral

$$G(t) = \int F(t + 2x'\Delta x/z_o v) \exp j\omega(t + 2x'\Delta x/z_o v) \times A(x')dx' \quad (4)$$

We note that at $t = 0$, $\Delta x = 0$ the output is

$$G(0) = F(0)\int A(x')dx \quad (5)$$

So it is determined by the maximum amplitude of the pulse and the spatial integral of the transducer response.

More generally, it will be seen that at $t = 0$ the transverse response of the system as a function of Δx is the Fourier transform of the function $A(x')F(2x'\Delta x/z_o v)$. In the special case when the pulse is many rf cycles long we regard $F(t)$ as constant and for simplicity take the transducer to consist of N infinitesimally thin elements ℓ apart, excited uniformly. In this case $A(x')$ takes the form

$$A(x') = \sum_{0}^{N-1} \delta(x' - n\ell) \quad (6)$$

where $\delta(x)$ is a delta function.

After summary, Eq. (4), $|G(t)|$ takes the form

$$|G(t)| = \left|\frac{\sin(\pi\Delta x/d_s)}{\sin(\pi\Delta x/d_g)}\right| \quad (7)$$

where d_s, the 4 dB definition of the system, is given by[5] the relation

$$d_s = \lambda z_o/2D \quad (8)$$

and the grating lobe spacing d_g is

$$d_g = \lambda z_o/2\ell \quad (9)$$

with $D = N\ell$ the width of N elements of the array.

Now consider the situation when $F(t)$ is a short constant amplitude pulse extending from $-T/2 < t < T/2$. In this case for a given Δx the maximum value of x' at $t = 0$ is

$$x'_{max} = \pm z_o vT/4\Delta x \quad (10)$$

for the array element at x' to be excited. This implies that at the first grating lobe, where $\Delta x = d_g$, the number of elements excited is

$$M' = vT/\lambda = M \quad (11)$$

where M is the length of the pulse measured in cycles of the center frequency ω_o.

The implication is that the grating lobe amplitude is down by a factor M/N from the main lobe. So ideally an rf pulse only 1 rf cycle long should be employed to eliminate the grating lobe. Furthermore, for points further from the main lobe than d_g, the maximum value of the sidelobe amplitude is a factor $1/N$ down from the main lobe. More generally, if $\Delta x < d_s M$ and the pulse is M rf cycles long $|G(0)|$ is given by Eq. (7) with $t = 0$. But for $\Delta x >> Md_s$ the sidelobe level approaches $1/N$. In the intermediate range of Δx the sidelobe level can only be accurately predicted if the pulse shape is known accurately. An assumption of a square topped pulse is not adequate, because this would assume a bandwidth much wider than the center frequency, thus leading to inaccurate results in this intermediate range of Δx. The more general case, therefore, still needs further study.

We may summarize these results by saying that beyond the first zero of the main lobe, not all the elements contribute, but the behavior of the focusing system near the main lobe is like that of a conventional lens operating with signals of wavelength $\lambda/2$. For Δx large, however, only one element contributes at a time, and so the response falls off by a factor $1/N$ where N is the number of elements. Thus by using only a short rf pulse grating lobes should be eliminated. We would therefore expect that with a 32 element system, the far out sidelobe level would be approximately -30 dB, and that because of the absence of grating lobes, relatively sparse wide aperture arrays can be used to give improved resolution.

IMAGING SYSTEM DESIGN

Transducer Array. In order to achieve the desired transducer array characteristics, that is, array elements with high efficiency, short duration impulse response, and broad angular beamwidth, quarter-wave acoustic matching techniques[4] were used in conjunction with tall, narrow, piezoelectric ceramic elements.[5] Proper application of quarter-wave acoustic matching allows highly efficient transduction of acoustic energy into the low impedance load medium, typically water ($Z = 1.5 \times 10^6$ kg/m^2-sec), from the high acoustic impedance ceramic ($Z = 29.7 \times 10^6$) over octave frequency bandwidths. Short duration impulse response, which is essential for good range resolution, is obtained by designing the transducer to achieve as nearly as possible a Gaussian-shaped passband.[4] Elements with a height-to-width ratio on the order of two-to-one allow the excitation of a pure, piston-like extensional mode with a very high electromechanical coupling coefficient ($k^2 = 0.47$ for PZT-5A).[5] Broad angular beamwidth is achieved by using narrow elements and by reducing the element to element cross-coupling to a minimum.

With these characteristics in mind, a 180-element quarter-wave matched array was designed and built to operate with fully-slotted elements at a 3.8 MHz center frequency, Fig. 3. The array was fabricated by epoxying a 0.46 mm thick × 10 cm long × 1.25 cm wide slab of PZT-5A with 2000Å thick chrome nickel electrodes to a 1.30 mm × 10 cm × 1.16 cm piece of borosilicate glass, which formed the first matching layer. The extra width of PZT-5A was included in order to make electrical connection. This slab was then bonded to a backing of silicon carbide loaded epoxy ($Z = 9.4 \times 10^6$) formed into a long wedge shape (6.35 cm × 1.27 cm) with a lossy flexible epoxy coat around the edge. Electrical connection was made with 0.025 mm thick brass leads, 0.25 mm wide on 0.51 mm centers soldered to both edges of the ceramic. A 0.10 mm thick piece of Dow 332 epoxy was then cast onto the front of the glass to make the outer quarter-wave plate, Fig. 3. The electrical connections were brought down the sides of the backing by leads on printed circuit boards. The individual elements

were cut with a 0.15 mm diamond saw blade. With a 0.20 mm saw kerf the elements were 0.305 mm wide on 0.51 mm centers. These elements were 0.05 mm wider than expected, which had some deleterious effects on the response of the array. An additional 0.10 mm thick layer of epoxy was glued onto the face of the array so that the total thickness of the epoxy was 0.20 mm, since the slotted epoxy matching section mode-hopped to a higher order mode which affected the impedance matching property of the section.

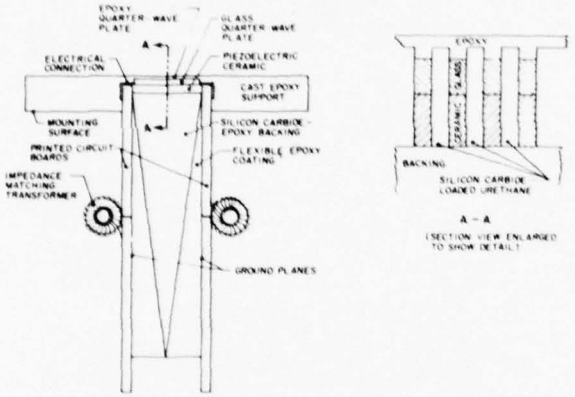

Fig. 3. Sections through transducer array.

The addition of the extra layer of epoxy smoothed out the frequency response of the elements as shown in Fig. 4 . The match between theory and experiment is not good, especially at the high frequency end where the theory does not predict the low radiation resistance seen in the experimental data. The complicated nature of the modes excited in the slotted epoxy matching section precludes a better prediction of the transducer characteristics. However, the smooth frequency response of the element does yield a short duration impulse response, and the insertion loss is low. In addition, before this layer was attached, a mixture of highly absorptive silicon carbide loaded polyurethane was vacuum impregnated into the grooves between the array elements. This measure served to damp out the lateral resonance of the transducer elements which resulted from their excess width. It also gave greater structural rigidity to the array.

The insertion loss of the transducer array elements was determined by first connecting 14 elements in parallel (to eliminate the diffraction loss in the following reflection mode experiment). This procedure gave an input impedance of 52 ohms at -45° measured at 3.5 MHz permitting matching to a 50 ohm generator. The transmitted signal was reflected off an air-water interface approximately 0.5 cm away, and the received signal measured with a high impedance probe. The total 14-element length was 0.7 cm making the path length in water well within the Rayleigh range (approximately 10 cm in this case).

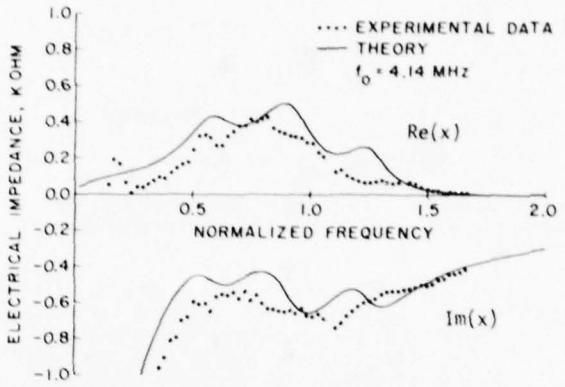

Fig. 4. Effect of adding epoxy face plate onto array.

The measured minimum round-trip insertion loss, Fig. 5 , is 11 dB at 3.85 MHz, and the 3 dB fractional bandwidth is 45% when an additional 2.2 dB was subtracted from the experimental data to account for the reflected signal which was incident upon the gaps between the elements. For comparison, the theoretical insertion loss of an element with the same parameters as in Fig. 4 is also shown in Fig. 5 . The theoretical case shows 6 dB round-trip insertion loss and an 82% 3 dB bandwidth. The extra 5 dB loss in the experimental data is difficult to explain but is consistent with practically every transducer we have made. The decrease in bandwidth is responsible for the extra 1-1/2 cycles in the experimental impulse response shown in Fig. 7 , over that expected of a 70 - 80% bandwidth transducer.

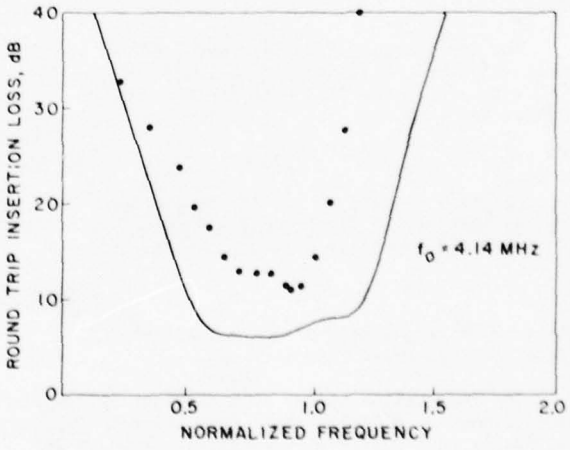

Fig. 5. Theoretical and experimental array two-way insertion loss.

Since each transducer element has a very high impedance, 750 ohms, it is necessary to transformer match into a 50 ohm cable. Transformers were wound with an 8:31 turns ratio on high permeability ferrite cores (Indiana General 7704) so that the impedance of an element was 50 ohm at 3.5 MHz. The transformers take 50 V impulses on the primary without saturation. The large number of turns was necessary to increase the parasitic parallel inductance and resistance in the transformer to large enough values so that they had minimal effects on the bandshape and insertion loss of the elements. This introduces a slight tuning effect which lowers the insertion loss by a small amount.

The impulse responses of 32 impedance matched elements were measured by reflecting a signal off a thin 0.18 mm diameter wire target. The excitation was a 0.17 μsec wide square pulse. A 3.5 MHz 5 half-cycle impulse response, consistent with the measured 45% bandwidth was observed for each of the connected 32 elements.[1]

The angular acceptance of a single impedance matched element was measured by rotating the array about the long axis of the element while insonified by plane waves from a transmitting transducer. The measured angular acceptance is shown in Fig. 6 compared to the theoretical response. The low acceptance angles which were measured over a range of frequencies are attributed to strong cross-coupling between the array elements, in the continuous epoxy layer on the face of the array. Future arrays are being built with face plates whose properties are similar to water to avoid this limitation. However, due to Snells Law,[6] our current array is more than adequate for imaging metal samples submerged in the water tank.

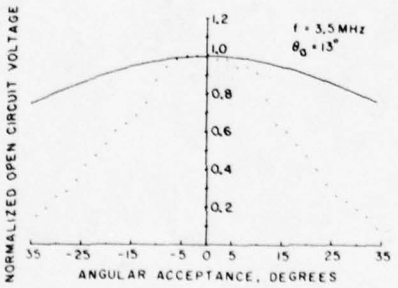

Fig. 6. Theoretical and experimental angular acceptance of a double quarter-wave matched transducer array.

Control Electronics. In our initial experiments, we have constructed an 8-element system, to verify the basic principles of operation, and to gain experience with the hardware design. With the transducer array described earlier, the system has a field of view in water which is 5 cm wide and 4-7 cm deep dependent on the system operating frequency. The initial range can be varied under software control. Using shear waves in metal, the field of view will be 5 cm wide and 8-14 cm deep.

The system hardware comprises 32 printed circuit boards, the associated power supplies and card racks. The signal memory associated with each transducer element consists of a RAM board incorporating eight Intel 2125-AL 1K × 1 static RAM's arranged to give 1024 8-bit bytes of serial storage. When used in conjunction with the Tektronix ADC-820T A-to-D converter, the system is capable of digitizing and storing signals at up to a 16 MHz rate. The eight channel system we have constructed uses eight equally spaced transducer elements from the center 32 elements of the array. The system is designed to display a 96 line raster scanned image with a line-to-line spacing which is 1/4 of the element-to-element spacing. Typically, we use every fourth element of the array which gives an interelement spacing of 2.0 mm, and a line-to-line spacing of 0.51 mm. For reasons of flexibility and simplicity, we chose to use the same RAM boards for the focus memory. For the 96 line display we have described, we require 128 lines of focus information. Fortunately, due to the symmetry about the center of the array, it is necessary to store only 64 lines of focus information. Since each line of focus information is 1024 × 1 bit, we can store the required amount of focus information on eight of the 1024 byte RAM boards. In operation, the system is designed to acquire the 8 signals in approximately 2.5 msec and display the complete image in approximately 7.5 msec which will allow a frame rate of approximately 100 Hz. For a larger system, using more transducer elements and displaying more lines, the frame rate would be correspondingly reduced; however, a 32-element system, displaying 400 lines at a 30 Hz frame rate is feasible using this technique.

IMAGING SYSTEM OPERATION

Figure 7 shows the signals as received on all 32 transducer elements from a single isolated 0.18 mm diameter wire target in a watertank. The top trace shows the input 170 ns 50 volt impulse while the other traces show the target reflection after 20 dB amplification and 92 μs delay. The difference in timing of the stored signals for the range Z = 70 mm is clearly seen. When focused on the scan line through the target all these delay differences are compensated by the focus information, giving a focused image of amplitude N times the individual signal amplitudes (N equals the number of active transducers). On other scan lines the information is not correctly timed and hence does not add coherently to form an image.

While we have been constructing the electronics for real time imaging we have been evaluating the expected performance of our system by taking real data from our transducer array and loading it into a mini computer, via a Biomation recorder. With this arrangement we can simulate the system operation by reconstructing the image field in the computer. This is a very slow process, typically requiring 1 hour per image frame, and the focused, raster-scanned image must be read onto a scan converter to be displayed on a TV monitor.

Figure 8 shows a set of images obtained using this computer reconstruction technique. The test object consisted of three 1 mm diameter wire targets located close to a 4 cm thick aluminum plate, in a water tank. The aluminum plate was placed approximately 7 cm from the transducer array, with the wires spaced from 3 to 9 mm in front of the plate. Figure 8(a) shows the image obtained using

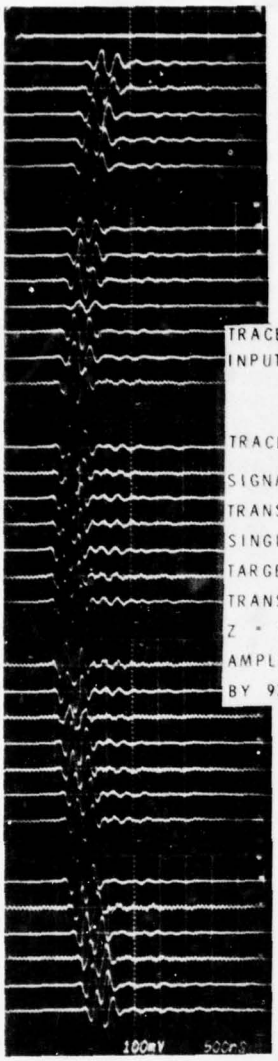

Fig. 7. Transducer responses to single target.

8 active transducer elements. All three wires, which have images of amplitude 20 dB lower than the front face echo, are visible, although one wire is nearly obscured by the sidelobes from the plate. Figure 8(b) shows the image obtained using 8 active transducer elements, with square-root gain compression at the input and corresponding expansion at the output. This nonlinear signal processing technique, which will be discussed more fully in the next section, yields a significant reduction in the sidelobe levels, as can be seen by comparing Figs. 8(a) and 8(b).

Figure 8(c) shows, for comparison, the image which would be obtained if all 32 transducers were used. This image has a measured sidelobe level of -20 dB compared to a theoretical -30 dB. It is most encouraging to achieve these low sidelobe levels at this early stage of system development, as our previous system[6] has taken considerable time

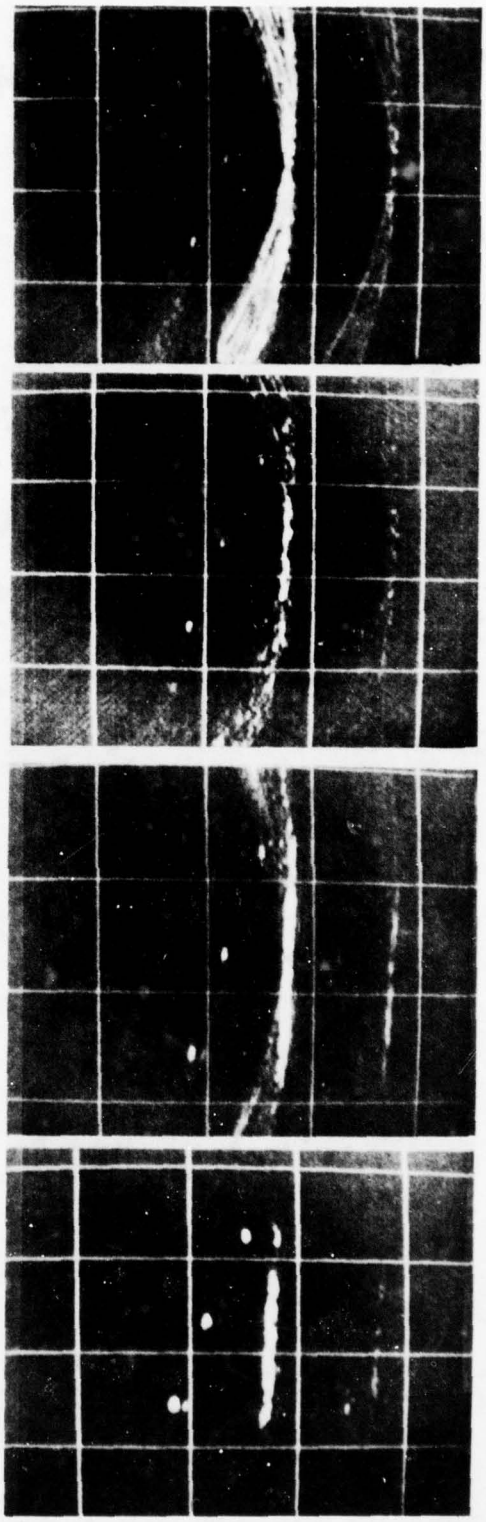

Fig. 8. Computer processed images. For system with 8 (A&B) and 32 (C&D) active elements with (B&D) and without (A&C) input gain compression.

and effort accurately matching the gain of the transmit and receive electronics between channels to reach this sidelobe level. Figure 8(d) again shows significant reduction of sidelobe levels when square root gain compression is used with the 32-element system. Here, the far out sidelobes are reduced to less than -32 dB making them almost undetectable on our display.

There are several significant points of image detail which are apparent in the images of Fig. 8 , which we have not previously been able to observe in our earlier chirp-focused system.[6] Both the front and rear face echoes from the metal plate are visible in Fig. 8(d) , and since the longitudinal wave velocity in aluminum is four times that of water, the image of the rear face appears 1 cm behind the image of the front face. In addition, since the metal plate acts as a specular reflector, its image is only seen over a length approximately equal to the aperture of the array, 1.6 cm. The wire targets are visible both as true images in their correct spatial positions, and as mirror images about the front face of the aluminum plate which acts as a reflector. There is also a subsidiary image of each of the wires which is due to the converted surface wave which travels around the circumference of the wire[7] and arrives at the array somewhat delayed from the main return. These subsidiary images may be useful in the interpretation of an acoustic image for determining the size and nature of a flaw.

The measured and theoretical sidelobe levels for the four cases are summarized in Table 1. Here a single wire target was imaged to obtain accurate measurement of system sidelobe levels. The theoretical values in Table 1 were calculated for an array with uniform wide fractional beamwidth, and no sampling loss in the digital system. Table 1 also neglects the grating lobe, which is introduced by the current array having an impulse response duration of 5 half cycles, Fig. 7 , instead of the ideal 2 half cycles. We will discuss later in Section 4.2 an inverse filtering technique for overcoming this problem.

TABLE 1. System Sidelobe Levels

	Sidelobe Level (dB)	
	Measured	Theoretical
8 element	-13	-18
8 element with gain compression	-22	-36
32 element	-20	-30
32 element with gain compression	< -32	-60

In addition to these computer focused images, preliminary measurements of real time images have been made on our hardware system. This system, which does not currently incorporate gain compression employs 8 active transducer elements connected via an electronic multiplexer to the signal processing hardware. The image of three 1.25 mm diameter wire targets close to a metal plate located at a range of 7 cm is shown in Fig. 9. Here the grey scale quality of the oscilloscope display is clearly inferior to the earlier TV displays. The 4 dB resolution[1] has been measured as ~ 0.9 mm and the sidelobe levels were -12 dB. The grating lobes which occur are not visible in Fig. 9. When imaging a single wire target, the grating lobes occur 13 scan lines on either side of the focused image[1] with relative amplitude -8 dB compared to the theoretical value of 2.5/N (-10 dB).

Fig. 9. Real time image processing with 8 channel system.

We are greatly encouraged by the excellent results from the computer processed images and confidently believe that we can repeat the 8-element gain compressed results in real time hardware within the next few months. We are also proceeding to design a second system with 32 channels which we believe will yield images which will be considerably superior to those obtained using our earlier chirp focused system.[6] When this system is completed we will extend these tests to shear, Rayleigh, and Lamb wave imaging in metal samples.

FURTHER SYSTEM DEVELOPMENTS

Sidelobe Response. One problem with all imaging systems is that associated with sidelobes, since the sidelobe level controls the dynamic range. One approach[8] to overcome this problem is to compress the dynamic range of the signals at the system inputs and expand again at the output after summing the signals prior to display. Because the synthetic focus system requires only a single front-end amplifier, it is ideally suited to the implementation of such a compression technique, since we need not worry about matching the characteristics of a large number of compression circuits. We have the choice of implementing the compression with either analog circuits or a digital table look up.

To show the improvement obtainable using a compression technique, consider the case where we take the square root of the amplitude of the signal, but leave the sign or phase of the signal unchanged. Suppose the ratio of a main lobe to sidelobe is M. Then if one point on the object of amplitude a excites the main lobe and another point of amplitude b excites the sidelobe the ratio of their outputs will be Ma/b . Now suppose we take the square root of the output of each transducer before summing. The main lobe to sidelobe ratio will still be M but the ratio of the two outputs will be $M\sqrt{a/b}$. If we now square the summed output the ratio of the two signals will be M^2a/b and the original linear relation of the signals is restored,

but the effective sidelobe levels have changed from M to M^2. This gives a consequent decrease in sidelobe level by a factor of 2 in dB, which is of major importance for detecting a small target in close proximity to a large reflector. Figure 8 has clearly shown the significance of this input compression. However, this improvement is only obtained at the expense of degradation in the SNR. Thus we intend to investigate, with a digital table look up approach, the operation of our prototype system with square root and other weaker nonlinearities.

Resolution Improvement. We have been performing additional analysis of the system to optimize its performance. We have concluded that the conflicting requirements of a short transmitted pulse, for good range resolution, with ideally a CW transmission for optimum transverse resolution can best be satisfied with a transducer impulse response comprising a single cycle sinusoid at its resonant frequency. We have already shown in Figs. 7 and 10 that our array currently falls short of this requirement, resulting in the introduction of the grating lobe.

One promising method of achieving the required waveform appears to be an inverse filter[9,10] implemented with a weighted tapped delay line. Computer simulations, Fig. 10, using real transducer data gathered from wire target reflections have shown that after inverse filtering we can achieve the desired single cycle sinusoid response with -12 to -18 dB spurious levels. The tap weights were calculated with a Least Mean Squares (LMS)[10] adaptive filter algorithm, which gave convergence after ~100 iterations.

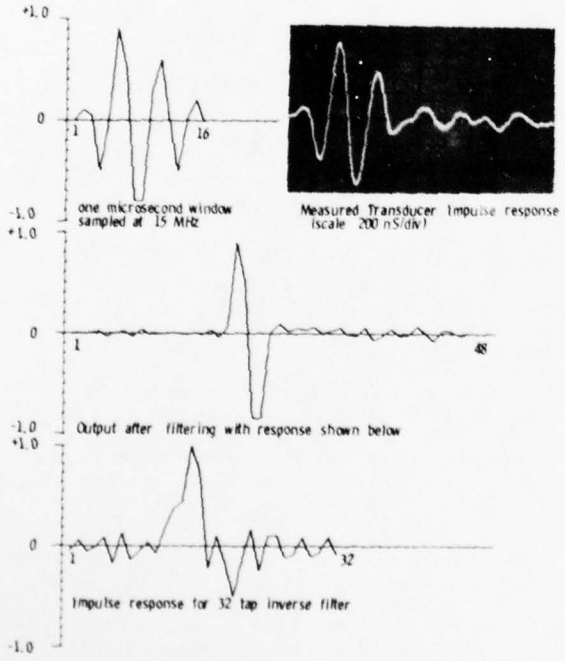

Fig. 10. Inverse filter simulation for digital imaging system.

We intend to implement the inverse filter at the output of our processor as this will require the tap weights to be set only once to optimize to the composite impulse response of the transducer array. This impulse response will have to be loaded into the computer and the calculated tap weights read out and stored within the filter. We are currently fabricating the transversal filter with a hybrid digital analog approach, Fig. 11. It comprises a 16 stage × 8 bit digital shift register with 16 multiplying D to A converters and a summing amplifier, and will occupy an additional four printed circuit cards.

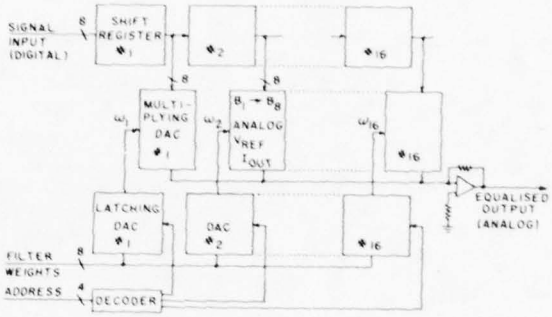

Fig. 11. Digital implementation of inverse filter.

CONCLUSIONS

A new design approach for acoustic imaging has been described and initial practical results on a prototype real time system have been presented. We have also shown that nonlinear (gain compressed) processing can offer most significant improvements in image quality. The consequent reduction in sidelobe levels is of major importance because acceptable sidelobe levels (-30 dB) may ultimately be achievable with a system comprising only 8 or 16 active elements. In addition inverse filtering permits us to shorten the impulse response to obtain improved range resolution. Inverse filtering also eliminates the grating lobes, enabling us to employ a sparse array with a wide aperture to obtain good transverse resolution. Thus it now becomes practical to consider a two-dimensional sparse array of transducer elements to obtain good definition in all three dimensions. As the sidelobe level in this case should be on the order of 1/N, three-dimensional imaging with good definition in all three directions does appear to be possible using this approach.

Another advantage of the time delay focusing approach is that we can use a very wide transducer aperture for improved transverse resolution with a scan converter for obtaining the electronic equivalent of mechanically scanned B-scan system, but with focusing. The additional electronics required for this approach involves only a larger multiplexer and the use of a scan converter. Thus we confidently predict that digital synthetic focus processing will become increasingly attractive as systems are developed further.

ACKNOWLEDGEMENTS

This work was sponsored by the Center for Advanced NDE operated by the Science Center, Rockwell International for the Advanced Research Projects Agency and the Air Force Materials Laboratory under contract F33615-74-C-5180.

REFERENCES

1. P. D. Corl, G. S. Kino, C. S. DeSilets, and P. M. Grant, "A Digital Synthetic Focus Acoustic Imaging System," to be published in Vol. 8, Acoustical Imaging and Holography, A. F. Metherell (ed.), Plenum Press, New York.

2. S. A. Johnson, J. F. Greenleaf, F. A. Duck, A. Chu, W. R. Samayou, and B. K. Gilbert, "Digital Computer Simulation Study of a Real-Time Collection, Post Processing Synthetic Focusing Ultrasound Cardiac Camera," Acoustical Holography, Vol. 6, Plenum Press (1975), p. 193.

3. H. Dale Collins, "Acoustical Interferometry Using Electronically Simulated Variable Reference and Multiple Path Techniques," Acoustical Holography, Vol. 6, Plenum Press (1975), p. 597.

4. C. S. DeSilets, J. D. Fraser, and G. S. Kino, "Design of Efficient, Broadband Transducers," IEEE Trans. Sonics and Ultrasonics, SU-25, No. 3 (May 1978), pp. 115-125.

5. C. S. DeSilets, J. Fraser, and G. S. Kino, "Transducer Arrays Suitable for Acoustic Imaging," 1975 IEEE Ultrasonics Symposium Proceedings, pp. 148-152.

6. G. S. Kino, "New Techniques for Acoustic Nondestructive Testing," ARPA-AFML Interdisciplinary Program for Quantitative Flaw Detection Contract F33615-74-C-5180 3rd Year Report, pp. 159-175, September 1977.

7. Y. H. Pao and W. Sachse, "Interpretation of the Records and Power Spectra of Scattered Ultrasonic Pulses in Solids," J. Acoust. Soc. Am., 56, No. 5 (Nov. 1974), pp. 1478-1486.

8. F. L. Thurstone and O. T. Von Ramm, "A New Imaging Technique Employing Two-Dimensional Beam Steering," Acoustical Holography, Vol. 5, Plenum Press (1973).

9. R. M. White, "Signal Processing Research in Connection with Ultrasonics in Nondestructive Testing," ARPA-AFML Interdisciplinary Program for Quantitative Flaw Detection Contract F33615-74-C-5180 3rd Year Report, pp. 43-58, September 1977.

10. B. Widrow, et al., "Stationary and Nonstationary Learning Characteristics of the LMS Adaptive Filter," Proc. IEEE, Vol. 64, No. 8 (August 1976), pp. 1151-1162.

ACOUSTIC IMAGING AND IMAGE PROCESSING BY WAVEFRONT RECONSTRUCTION TECHNIQUES

K. Lakin
University of Southern California
Los Angeles, California 90007

ABSTRACT

Acoustic imaging may be accomplished by a process involving the measurement of the amplitude and phase of the wavefront at a remote region and then the reconstruction, using mathematical techniques, of the fields at or near the scattering region. Since the system is coherent, both amplitude and phase images may be obtained. The current system under study employs pulsed CW tone bursts in order to reduce stray echo problems, with quadrature phase detection followed by a digital hardware processor for implementing the reconstruction algorithm. Finally, the image is processed for display and analysis.

INTRODUCTION

The objective of this task is to study acoustic image processing and to implement a pulsed CW imaging system as an extension of the work done previously on the amplitude and phase contrast imaging of transducer near and far field radiation patterns. In that work the precision of the imaging process using CW excitation suggested that the method might well be applied to the problem of defect imaging if the same degree of accuracy could be achieved when the system was used in the pulsed mode. The pulsed mode of operation should be a requirement if real flaws in solids were to be imaged instead of simple objects in water. In the CW system, the overall accuracy was obtained because of the large dynamic range of the network analyzer and its narrow-band, high-resolution phase detection capability. In addition, by using a synthetic array approach, i.e., scanning a 64 x 64 grid using a single transducer, all elements of the array were assured to be identical in response. However, the system was not convenient in terms of data throughput and image processing speed. In addition, the CW mode of operation allows multiple reflections to obscure the desired data, a severe problem in defect imaging where the scattering from front surfaces (such as water-solid) is much stronger than scattered signals coming from the defect located within the solid.

In order to clarify the overall project, we will first discuss the theoretical basis of this particular imaging approach, then describe the previous implementation and its results, next the proposed system will be described, and then the procedure for implementation and progress to date.

Theoretical Approach

The basis of the imaging system, Fig. 1, starts from Huygens theory describing the superposition of a radiation field from many point sources of the source or scattered field[1]

$$UM(u,v) = \frac{2\pi}{jk}\int\int_{-\infty}^{\infty} U(x,y)\,\frac{e^{ikr}}{r}\,dxdy \qquad (1)$$

where UM(u,v) is the measured field in the u,v plane located a distance R from an assumed scattering plane, K is the wavenumber, U(x,y) the source or scattered field, and r is the distance between a scattering element and field position,

$$r = R\left[1 + \frac{1}{R^2}\left((x-u)^2 + (y-v)^2\right)\right]^{\frac{1}{2}}. \qquad (2)$$

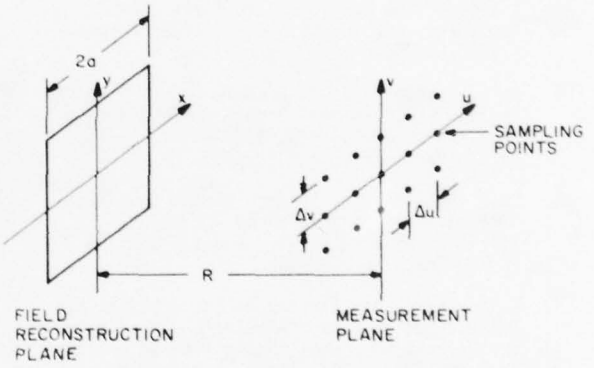

Fig. 1. Reconstruction coordinate system

Using the small angle approximation, we essentially restrict the transverse dimensions of the scattering region and measurement plane such that they are much less than R the distance between planes. In practice, this para-axial approximation restricts the maximum angle between r and R to approximately 30 degrees. However, for the usual cases of water-solid interfaces, this represents a more than adequate angle of incidence due to longitudinal wave cutoff conditions.

Using the para-axial ray approximation, the distance r is approximated by

$$r \approx R + \frac{1}{2R}\left[(x-u)^2 + (y-v)^2\right] \qquad (3)$$

and (1) becomes

$$U(u,v) = 2\pi\frac{e^{ikR}}{ikR}\int\int U(x,y)\exp i\left(\frac{k}{2R}\right)\left[(x-u)^2 + (y-v)^2\right] dxdy \qquad (4)$$

The quadratic phase factor may now be expanded and a normalized relationship is obtained

$$\bar{U}M(u',v') = C\iint \bar{U}(x',y') \exp -ik'(u'x'+v'y') \, dx'dy' \quad (5)$$

where

$$\bar{U}M(u',v') = U(u',v')\exp -ik'(u'^2+v'^2)/2 \quad (6)$$

$$U(x',y') = \bar{U}(x',y')\exp -ik'(x'^2+y'^2)/2 \quad (7)$$

$$C = 2\pi a^2 \frac{e^{ikR}}{ikR} \quad (8a)$$

$$x' = x/a \quad (8b)$$

$$y' = y/a \quad (8c)$$

$$u' = u/a \quad (8d)$$

$$v' = v/a \quad (8e)$$

$$k' = \frac{ka^2}{R} = 2\pi(a/\lambda)^2/(R/\lambda) \quad (8f)$$

$$\text{or } k' = \frac{\pi a}{\Delta s} \quad (8g)$$

where $\Delta s = \frac{R\lambda}{2a}$ maximum sampling internal allowed without considerable information loss. At the widest angle of operation, R/a would have a minimum value of $\sqrt{3}$ and the maximum allowed sampling interval would be $\Delta s = (\sqrt{3}/2)\lambda$.

The image processing starts by processing the measured data by first multiplying UM(u',v') by a weighting function which accounts for the fact that the measuring plane actually contains less than the entire energy of the scattered fields. Clearly, small defects or sharp edges of defects such as crack tips scatter widely, and a truncation of the fields due to finite spatial sampling causes a smoothing in the image. The weighting function is used to eliminate the Gibb's ringing created by this artificial truncation. Other image processing will be detailed later.

The smoothed data may now be normalized by effectively removing the parabolic phase, as in (6), which now places the data in the format of a two-dimensional Fourier transform, (5). By taking the inverse transform of (5) we obtain

$$\bar{U}(x',y') = C'\iint UM(u',v')\exp +ik'(u'x',v'y') \cdot du'dv' \quad (9)$$

which is the normalized image field. If phase information is desired, then the parabolic phase unnormalization is carried out, (7). Note that the plane of reconstruction is determined by the parabolic phase normalization and that many images may be formed from one set of measured data.

The concept of superposition implies other useful image processing techniques. For example, since the fields UM(u,v) are made up of a sum of scatter contributions, known scatter fields may be subtracted from the total measured field to yield the field due to a small defect alone. An "aperture stop" may be effectively implemented by numerically weighting the measuring data in an appropriate manner. For example, the central fields could be zeroed or allowed to drive the receiver non-linear in order to gain more dynamic range for the edge fields which define small objects.

Since the imaging technique has its roots in conventional optics, many processing techniques employed there may be usefully employed with the added advantage of having phase and amplitude as variables and not just intensity.

The imaging process may now be summarized: 1) measure the amplitude and phase UM in the measurement plane, 2) weight the fields and correct for known measurement errors such as array non-uniformities, 3) choose a reconstruction plane and phase normalize the measured fields, 4) do a two-dimensional Fourier transform to obtain the normalized scattered fields, and 5) phase unnormalize to obtain the complete fields. This data is now ready for display and possible enhancement.

CW Imaging System

The imaging system shown in Fig. 2 was employed in the study of transducer fields reported in last year's final report. The system is briefly described here in order to set the stage for the system currently under study. The system in Fig. 2 used, almost entirely, "off-the-shelf" laboratory components. The major components include 1) the Tektronix 4051 Graphics System which is basically a desk top calculator with limited graphic capability, 2) a numerically controlled x,y stage to position the transducer in the measurement plane, 3) a network analyzer to measure the magnitude and phase of the transducer signal, 4) digital voltmeters to perform the A/D conversion of the network analyzer results, 5) frequency synthesizer for stable frequency control, and finally 6) an IEEE 488 instrumentation bus to tie all components together under control of the Tektronix 4051.

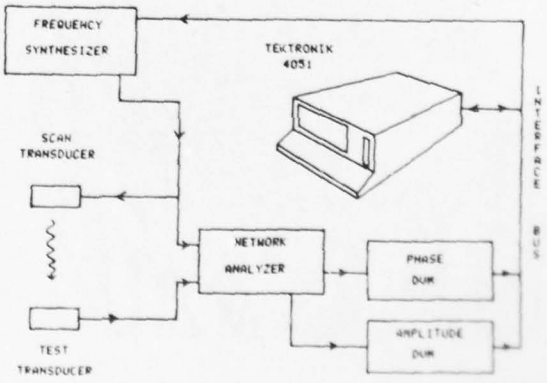

Fig. 2. CW imaging system.

AD-A071 047 ROCKWELL INTERNATIONAL THOUSAND OAKS CALIF SCIENCE --ETC F/G 14/2
PROCEEDINGS OF THE ARPA/AFML REVIEW OF PROGRESS IN QUANTITATIVE--ETC(U)
JAN 79 D O THOMPSON F33615-74-C-5180
UNCLASSIFIED SC595.51AR AFML-TR-78-205 NL

6 OF 6
AD A071047

END
DATE FILMED
8-79
DDC

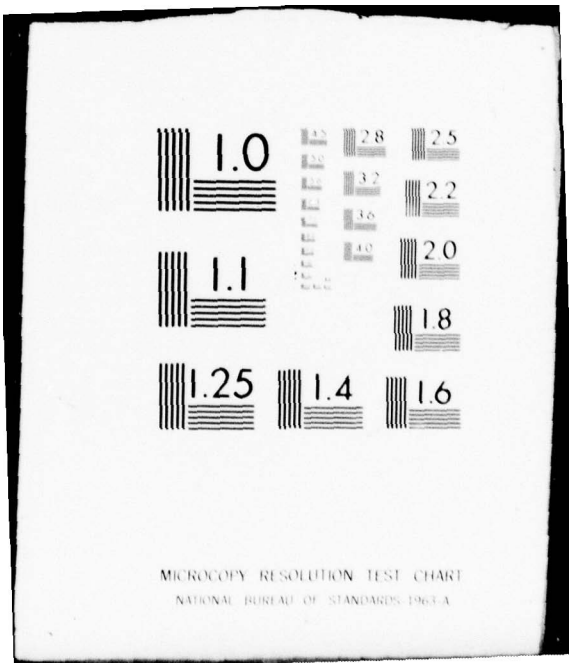
1.0
1.1
1.25
1.4
1.6
2.8
2.5
3.2
2.2
3.6
2.0
4.0
1.8
MICROCOPY RESOLUTION TEST CHART
NATIONAL BUREAU OF STANDARDS-1963-A

The resultant data was stored on magnetic tape one scan row at a time because of limited memory, and then sent over a 2400 baud RS232C line to a PDP-10 computer. Here the necessary image processing was performed and the image data sent to USC's Image Processing Institute for display, or to a perspective plot subroutine and then back to the 4051 for display and recording. Representative results of the system are shown in Figs. 3a, 3b, and 3c as perspective amplitude and phase plots and as grey scale amplitude respectively.

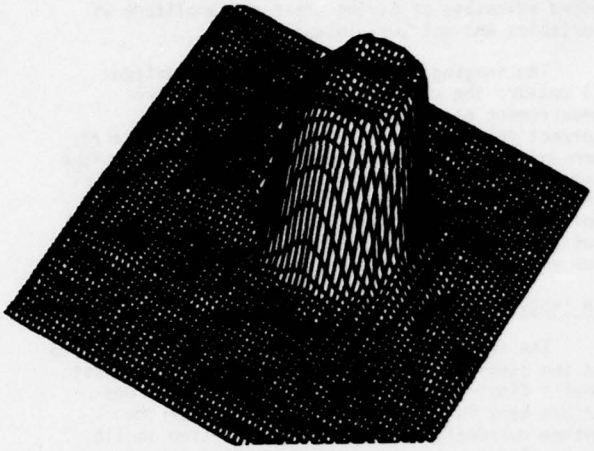

(a)

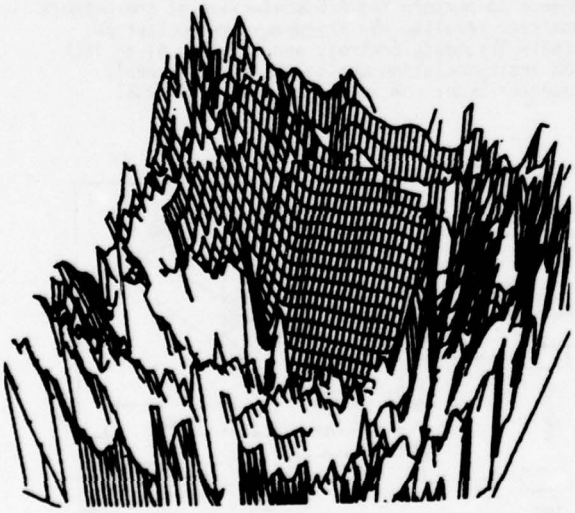

(b)

Fig. 3. Reconstructed transducer near field
(a) amplitude
(b) phase
(c) grey scale of amplitude

Whereas the imaging results are very favorable, the system through-put was agonizingly slow for any real imaging system or an imaging study requiring many image formations. The data acquisition time alone was 3-4 hours, due to limitations in the phase measurement caused by mechanical vibrations induced by the stepping motors on the x,y table. In addition, the DVM's were limited in through-put to one reading per second. Data transfer times to the PDP-10 were upward of one hour, due to the inability of the system to accept sustained data bursts. However, once having demonstrated the basic imaging process, we can now define what a more practical system might consist of.

Pulsed CW Imaging System

The natural evaluation of the previous imaging system is the system currently under study which duplicates some of the previous one in functional detail. Clearly, the system must work in the pulsed CW or tone burst mode of operation in order to avoid interference from standing waves caused by extraneous reflections. This requires a tone burst transmitter-receiver combination which must accurately measure the magnitude and phase of the radiation field over a dynamic range of 70 dB (12 bits). The system should have a local array processor to handle the image processing in real time once the data has been taken. An ultrasonic array would considerably speed up the data acquisition process, either in the form of a one-dimensional array mechanically scanned or a two-dimensional array electronically scanned. In the latter case, data could be gathered at a rate of 10-100μs per element or 40-400 ms for a 4096 element array assuming a fast 12 bit A/D converter.

The display system need not change from that type used before except that it should be close to the array processor for rapid data transfer.

In order to efficiently implement this study, we have defined a number of subtasks which are ordered in the approximate flow of image data. The description of the various subtasks and their implementation are described below.

IMPLEMENTATION

Pulsed CW Measuring System

The pulsed measuring system consists of an analog region and A/D converters to provide 2's complement data for reduction and display. The analog portion of the system is a super-heterodyne receiver consisting of a front end mixer followed by a high gain 30 MHz IF amplifier having 4 MHz bandwidth, over 100 dB gain and -120 dBm sensitivity. The first mixer takes the nominally 5 MHz signal from the transducer (or array element) and mixes with a 25 MHz carrier to give the 30 MHz IF signal. The output of the IF amplifier is either a 30 MHz pulse or an envelope of the pulse. In our system, the 30 MHz pulse is sent to two double balanced mixers with proper phase shift and mixed with quadrature shifted 30 MHz reference signals. The output of the detectors is then the real and imaginary components of the pulse signals. These base band pulses are then sent to gated sample and hold modules and then to fast 12 bit A/D converters and then to memory via the IEEE 488 interface bus. Because the analog portion of the system uses the super-heterodyne principle, the input signals may be pulses as well as tone bursts. The generation of the transmit signal also uses the heterodyne principle in order to maintain phase coherence between pulses. The analog and digital positions of the receiver have been completed and are now being calibrated.

Array Design

An array to be used for a holographic imaging system has somewhat different requirements than those used for focused imaging. The holographic transducer array may be constructed with elements more widely spaced than those used for focused beams, the elements are sampled in sequence rather than simultaneously, and the requirements for cross talk in the array are probably somewhat more severe than in focused beam arrays. The more widely spaced array elements make the array construction somewhat more tractable and the sequential access should make the electronics less costly since 2N electronic elements are required for an array of size NxN, rather than N squared similar circuits. Several array designs have been considered with an emphasis placed upon the compatibility of acoustical design and electronic scanning. In general, the array of interest is of size 64x64 with an element spacing of 8 wavelengths, and an operating frequency of 5 MHz. Since the holographic system uses coherent tone burst for measurement, the transducer elements need not be as heavily damped as those used for focused beam A scan. It is hoped that the easing of the damping requirement alone will make the array construction more practical and the elements more uniform and reliable.

Some effort has been directed toward a study of potential array configurations that could be usefully employed in this imaging system. Currently we are looking at arrays that might be used for transmitting only, since the sequential accessing of such elements seems more appropriate to conventional digital circuits. Both array element construction and multiplexing methods are being considered. It is clear that an in-depth study of new array concepts and actual array construction are not within the financial constraints of the current program. However, the initial study has turned up some preliminary useful results.

Acoustic Image Processing

In order to form an image from the acoustic signals, the data must first be cast into a format that allows the inversion to be done with Fourier transform methods. Initially, the data must be windowed to prevent image ringing due to the truncation of the transform and then the parabolic phase factor must be subtracted from the total phase. The formalism may also be recast into the form of a double convolution as shown in (10) for the continuum and in (11) for the discrete case.

$$U(x',y')=\int\int UM(u',v')F(y'-v')F(x'-u')dv'du' \tag{10}$$

$$U_{IJ} = \sum_{KL}\sum UM_{KL}\, F_{JL}\, F_{IK} \tag{11}$$

$$\text{where } F(z) = \exp(-ik'z^2) \tag{12}$$

Clearly, with the parabolic phase factored in, the problem is one of convolving the circular functions with the field data. For the case of a 64x64 data set, 4096 complex multiplications are required for each of the 64 rows and the process is repeated for each of the 64 columns for a total of over 500,000 complex multiplications. Accordingly, we are planning to use hardware multipliers to do the complex arithmetic and directly cycle the data to the multipliers transparent to the microprocessor. In this manner, we can achieve a good compromise between hardware cost and computational time, since memory is relatively inexpensive and the hardware multipliers are less than $200 each, and multiply in less than 150 ns. Thus by using two multiplications per memory cycle, we can obtain the product of two 12 bit numbers in 300 ns and the two-dimensional convolution in less than 200 ms, which should allow for a near real time display of the transform and a feature for zoom focusing of the image by the operator. In the case of imaging through a water-solid interface, as many as 4096 transforms would be required in the worst case to find the interface fields, but this would take less than 14 seconds. Once having the interface fields, the image within the solid would be obtained in the usual manner in less than 200 ms.

By implementing the FFT in hardware, we could achieve a time compression by a factor of 10, but with somewhat more circuit complexity, since the parabolic phase normalization could not be done with the FFT processor. Implementing the two-dimensional convolution by a succession of FFT operations is more time consuming than doing the FFT directly. Our current effort is to brute force the Fourier transform because of circuit simplicity and the need to do the parabolic phase normalization. In the future we intend to implement the FFT array processor and the phase normalization as separate pieces of hardware. The brute force Fourier transform processor is about 50% completed in hardware construction.

Image Display

For our initial work, the mode of display will be the 8 bit grey scale using black and white with the operator having the option of zoom focus and level slicing (contour plots). Eventually, it will be useful to present the data in the form of perspective plots, as was done in the transducer studies, although this requires a lot of code and processing time if hidden lines are to be blanked out. In the meantime, perspective plots have been generated on the Tektronix 4051 Graphics System directly using recently purchased graphic firmware packages and using software written at USC during the third quarter of the project.

ACKNOWLEDGMENT

This research was sponsored by the Center for Advanced NDE, operated by the Science Center, Rockwell International, for the Defense Advanced Research Projects and the Air Force Materials Laboratory under Contract F33615-74-C-5180.

REFERENCE

1. K.M. Lakin and A. Fedotowsky, "Characterization of NDE Transducers and Scattering Surfaces Using Phase and Amplitude Measurements of Ultrasonic Field Patterns", IEEE Trans. SU-23, No. 5, September 1976.

THE USE OF NOISE SIGNALS FOR MULTI-MODE BEAM SHAPING

E.S. Furgason, V.L. Newhouse and B.B. Lee
School of Electrical Engineering, Purdue University
West Lafayette, Indiana 47907

ABSTRACT

Noise as a transmitted signal has been used in radar, ultrasonic Doppler flow measurement, and ultrasonic flaw detection. In each of these applications, the unique properties of noise have mainly influenced the design and operation of the signal processing portions of the system in which it was used. Our present work shows that the use of noise as a transmitted signal may also benefit the properties of phased array transducers used in imaging systems.

Some imaging systems excite the transducer array sequentially in several modes. The echoes resulting from each of the transmitted modes are stored separately and then processed together to yield an effective beam pattern which cannot be realized by any elementary mode of the array. Although phased arrays are frequently used to simultaneously receive in a number of modes, it has not, up to now, been possible for an array to transmit more than one mode at a time.

A technique is described which allows several modes to be transmitted simultaneously from a transducer array. This is achieved by exciting each mode with its own independent random signal. The echoes corresponding to each transmitted signal can then be unambiguously identified by correlation with the desired reference signal. This technique generally leads to simplified system design and permits operation in real time.

Preliminary results for a small random signal phased array system will be described.

INTRODUCTION

Noise as a transmitted signal has been used in radar (1) as well as in ultrasound Doppler systems applied to flow measurement (2) and in ultrasound correlation systems applied to flaw detection. (3) In all these applications the unique properties of noise have mainly influenced the design and operation of the signal processing portions of the systems in which it was used. We have recently shown that the use of noise as a transmitted signal can also benefit the properties of phased or delayed arrays. (4) The term "phased or delayed array" as used here refers to the arrays of antenna elements or electro-acoustic transducers which are used in transmission or reception to sweep and shape beams of electromagnetic or sound radiation.

The reader will recall that phased arrays are used to transmit and receive beams in different configurations or modes and that each of these modes is produced by a unique way of amplifying and delaying or phasing the signals supplied to or received from the various array elements. Although phased arrays are frequently used to simultaneously receive in a number of modes, it has not, up to now, been possible for an array to transmit more than one mode at a time. This limitation is due to the fact that with present techniques, if more than one mode is transmitted simultaneously, it will not be possible to distinguish the echoes of these various transmitted modes from one another. We have shown that a phased array can transmit and receive in many modes simultaneously provided that a separate incoherent noise signal is used for each mode and than an equivalent number of correlation receivers is used to pick out the echoes corresponding to each transmited beam configuration. (4)

The ability of phased arrays to transmit (as) well as receive) many modes simultaneously should lead to significant performance improvements in wide angle scanning, in which the use of noise signals should enable several sectors to be scanned simultaneously. A second application is to methods of side lobe suppression and beam shaping in which different modes are transmitted sequentially with their echoes being stored and processed. (5) In this application the use of noise signals will permit the different modes to be transmitted simultaneously allowing echoes to be processed without intermediate A/D conversion and storage

A third application is to dynamic focusing in which the focus during reception is shifted in synchronism with the signal. Here the use of noise will allow the focus to be shifted during transmission as well as reception thus squaring the array directivity with respect to current systems. Finally the use of simultaneous noise signals will allow an array to scan with one pattern for imaging while simultaneously keeping another beam fixed in space for Doppler measurements.

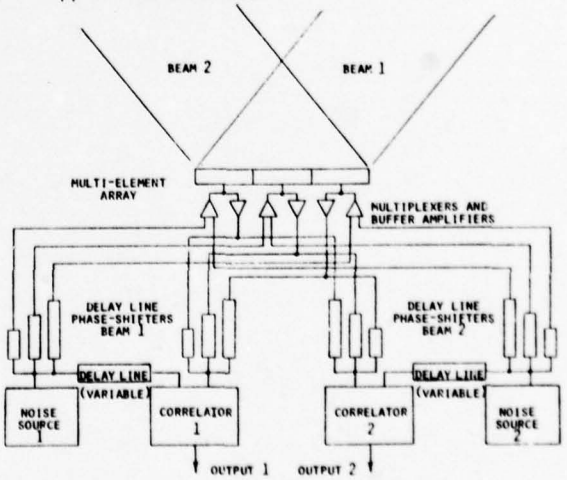

Fig. 1. An ultrasonic random signal phased array.

Our noise array principle can be understood in more detail by reference to the figure. Noise source 1 drives the various elements of the array through a set of delay line shifters and transmits a signal in the direction of beam 1. Similarly noise source 2 transmits a signal along beam 2. The echoes received by the array are distributed to correlators 1 and 2 through two additional sets of phase shifters. Both correlators receive echoes due to both noise sources. Each correlator also receives a delayed version of the transmitted signal of its associated noise source. The variable delay through which it received this reference signal is adjusted depending on the range at which the system is to operate. Even though each correlator receives echoes from the transmitted signals of both noise sources, only that echo which corresponds to the reference signal it receives will produce an output from the correlator. Thus two independent outputs are produced by the system illustrated.

In many applications a single set of delay line phase shifters will be used for transmission and reception of each signal instead of two sets as shown in the figure. Furthermore any number of independent modes can be transmitted by providing a noise source and correlator for each mode. Of course if n independent noise signals are transmitted then each correlator will have a deteriorated signal-to-noise ratio which in the worst case will be of order 1/n. Since we have shown that the resolution of noise correlation systems is independent of the length of the transmitted signal, (3) this degraded signal-to-noise ratio can be improved by lengthening the transmitted pulses. The attractiveness of multi-mode noise operation for a specific application will depend on the degree to which the signal-to-noise ratio can be kept high without sacrifice of operating time.

In this presentation a double noise source, triple transducer system used for beam shaping will be described.

ACKNOWLEDGMENT

This work supported by ARPA under AFML contract #F33615-75-R-5252.

REFERENCES

(1) McGillem, C. D., Cooper, G. R. and Waltman, W. B., "An Experimental Random Signal Radar," Proc. Nat. Electr. Conf. 23, Oct. 1967.

(2) Bendick, P. J. and Newhouse, V. L., "An Ultrasonic Random Signal Flow Measurement System," Journal of the Acoustical Society of America, Vol. 56, No. 3, pp. 860, 865, Sept. 1974.

(3) Furgason, E. S., Newhouse, V. L., Bilgutay, N. M. and Cooper, G. R., "Applicationof Random Signal Correlation Techniques to Ultrasonic Flaw Detection," Ultrasonics, Vol. 13, No. 1, pp. 11-17, Jan. 1975.

(4) Furgason, E. S., Newhouse, V. L. and Lee, B. B., "The Use of Noise Signals for Multi-Mode Operation of Phased Arrays," Proc. of NBS Conf. on Ultrasonic Imaging and Tissue Characterization, June 1978.

(5) Burckhardt, C. B., Grandhcamp, P. A. and Hoffman, H., "Focusing Ultrasound Over a Large Depth with an Annular Transducer - An Alternative Method," IEEE Trans. on Sonics and Ultrasonics, Vol. SU-22, No. 1, pp. 11-17, Jan. 1975.

DISCUSSION

N. Batra (System Research Lab): I have a question regarding your delay lines. Were the water delay lines that you used the best?

E. S. Furgason (Purdue University): Are you referring to the delay line in this system?

N. Batra: Yes

E.S. Furgason: Yes, we did use a water delay line. Just for convenience, there is nothing magical about a water delay line. It could just as easily be an electronic delay line.

PANEL DISCUSSION

INTERNATIONAL NDE EFFORT: FUTURE DIRECTIONS

Michael J. Buckley, Moderator
Defense Advanced Research Projects Agency
Arlington, Virginia

Panel Members:

Paul Höller, Institut fur Zerstörungsfreie Prüfverfahren, Saarbrücken, West Germany
Gerard Quentin, University of Paris VII, France
Peter Doyle, Aeronautical Research Laboratories, Melbourne, Victoria, Australia
Stewart McBride, Royal Military College of Canada, Kingston, Ontario, Canada
D. Stanley Dean, P.E.R.M.E., Aylesburg, Westcott, England

M. J. Buckley, Chairman (ARPA): Good Morning. My name is Mike Buckley. This morning we are fortunate to have several visitors here from overseas. We wanted to give them the opportunity to give us a summary of what is going on in their country or their institutions and, if they want to make some comment as to how it compares to what is going on here.

Prof. Paul Höller (University of Saarbrücken): Good morning, Gentlemen. I will try to use these ten minutes to make some more general comments on what we are doing in our country and mention the impressions that I received here.

The first point we should ask is why do we have reasonable support for NDE research in any country these days. I think it is worthwhile to make the point that the reason for that is that NDE already has a number of very important applications in many branches of industry. The other point is that we must all try to promote interactions with the people who represent the industrial applications of NDE. I got the impression during the meeting that this interaction between those who are applying NDE and those who are doing research is no stronger than in our country. Another point is that we regard NDE as a technology. It is not yet a science. We need science to improve NDE, but NDE itself is a technology to be applied in industry. That means the goals and the objectives of research primarily have to be determined by those who should later on apply what is the result of research. The main point the scientists have to contribute is to show and demonstrate the potential of scientific methods to contribute to solutions to very important problems.

In our country, the most important problem which people in applied NDE are discussing is the reliability. They fear they are not well enough informed about the capabilities of the present NDE art. They want to know what the capabilities are with regard to real materials defects. And we all, I suppose, as well as you in your country and we in ours during the last years, have been really shocked several times. I would like to ask the question as to whether or not we react properly to those shocks. That means, those who are developing new methods need to know of the true, very difficult problems which occur in practical work. This aspect means that the testing systems and the testing procedures must be appropriate to the environmental conditions encountered in practice.

Another point, which is not shocking but striking, is the experience that in different countries there are exactly the same problems. Physics and the techniques to approach these problems are the same. Nevertheless, the solutions which the experts reached in the past and the research and development programs they have at present are very different. In the sphere of my experience, the most pronounced case is that of pressure vessels. If you look at the recommendations and specifications, they are different in this country and in Europe. The in-service inspection systems used and the philosophy which is behind them is different here than in our country and other European countries. The projects going on to develop the future systems for that application are again different. There is an international exchange of results and ideas in the form of round robins, however. I think that is a very good thing to make the exchange of knowledge and results more substantial. I don't know whether similar things are going on in the aircraft industry.

With regard to basic research, I admire the efforts you are making here. I must say very frankly that we have nothing similar, not with regard to the developing theoretical basis for future NDE systems. On the other hand, perhaps we are doing more work in getting the basis for theoretical engineering. We are calculating and designing systems of probes for particular applications and we are doing much research to improve that. But with regard to the scattering theory and diffraction theory, much less is going on in our country than I have heard this time and upon other occasions here.

Another very particular point not understandable for me is the fact that all engineers and mainly American engineers say the most important area of any component is the surface. Because by stress distribution the surface cracks are very much more dangerous than the interior, and also the surface is rough. There is much more attack for instance by corrosion. There is a probability of starting

cracks at the surface for many reasons. It is much, much greater than the probability of initiating cracks inside the wall. But if you look into the literature and the research programs, I would say the ratio of money and time and brains spent for developing surface methods and quantified methods for surface inspection to the amount spent for interior inspection, it is exactly vice versa. The efforts expended don't seem according to the demands. Maybe this is not so important for thin section components, but for thicker components I think it is a very important fact.

The NDE effort in Germany is organized in three parts. The first one is the actual NDE research, both basic and applied. The second part is devoted to development and the third one to the application. In some cases we may be able to go immediately from research into the application. This is certainly not the normal path which would be to go from research through development to the application. As I understand the present ARPA project, it takes the normal path and is devoted to research and development. We in Germany concentrate more on the overlapping area between development and application. There is some research going on but it is more of an applied nature than in the U.S.

G. Quentin (University of Paris): The NDE effort in France is not as well supported as in the United States and Germany. Nevertheless, there is a lot of work being done in France and I shall give a short summary of this work.

One of the groups in France working in NDE is the Atomic Energy Commission. Much of their work is devoted to usage of focused transducers. They have implemented focused transducers for detecting badly oriented defects in nuclear reactors.

Another group of people is trying to produce artificial defects by diffusion bonding of steel (similar to the work going on at Rockwell). In steel they have produced some one hundred of different kinds of defects. This group uses these diffusion bonded specimens for the characterization of defect by multidirectional analysis under ultrasonic spectroscopy. They also work on the Barkhausen effect, which yields very good results about the state of the material just close to the surface. They have made studies on the decarburization of steel and also the influence of superficial stresses on Barkhausen noise.

In my laboratory the main objective is to determine the scattering of ultrasonic waves by rough surfaces. We determine the signature of the surface with randomly rough surfaces and natural nonrandom rough surfaces (some results of this work have been presented this morning).

The characterization of surface defects by Raleigh waves is an example of Franco-American collaboration. The work has been initiated with the assistance of Bernie Tittmann in our lab. Dr. Tittmann will present a paper on this subject. We have also used the Schlieren method to characterize the ultrasonic field generated by very short pulses which is a Franco-English collaboration with the City University of London. We have also studied detection of edge waves.

I am sure I have not given you a complete list of all the laboratories working in France. Let me just add that there is also some interesting work going on at one of the medical centers. They have obtained some good results with pseudo random binary coded, fast modulated ultrasonic, high resolution echograms.

Peter Doyle (Aeronautical Research Lab): First, I would like to say how much I have enjoyed coming to this conference. It is obviously something we lack in Australia, having a large number of people interested in this field. There is only a relatively small effort, not surprisingly, in NDE in Australia and for that reason I will probably speak rather more briefly than the other speakers. But some work I would like to mention: first of all, in acoustic emission, there is work going on at the Atomic Energy Commission and also at Aeronautical Research Labs (ARL) relating the acoustic emission signals to the microstructural properties of materials, particularly in zirconium. Also in acoustic emission there is some work beginning at ARL on the early detection of corrosion, and particularly paying attention to separating corrosion signals from noise coming from other sources. Actually it is a very important problem in aircraft in Australia because a lot of them are stationed in the tropics in the north and corrosion, and particularly stress corrosion cracking, is very important. Another aspect of acoustic emission work is monitoring the growth of actual fatigue cracks in trainer aircraft, jet aircraft, which are in service.

Next, in ultrasonics, there is some work concerned with the development of computer controlled testing of rails. On the theoretical side of ultrasonics, there is some work commencing at ARL which will deal with the geometrical theory of diffraction, and hopefully this will complement, rather than repeat, the work that is going on within the Rockwell program.

Next, there is some work on eddy currents which is concerned with coil design. This work is done at the University of New South Wales for the testing of wire rope. Again, at ARL they are concerned particularly with the effects of surface coatings on the reliability of the magnetic rubber replica technique. ARL is using this technique to monitor fatigue crack growth in aircraft which are in service.

Stewart McBride (Royal Military College of Canada): Well, again as in Australia, the problems that we face in Canada are a little bit different from the United States in that the country really doesn't have a substantial aircraft industry and so we are relying very heavily on having the vehicles and

the components, etc., supplied from outside. As a result of this, probably there is in the statistical sense, very little work being done. We just don't have any massive fleets of aircraft and therefore we cannot develop any statistics. Rather we would be hoping to use American statistics to do some evaluation on what is an extremely small fleet. With this in mind, it is most unlikely that there will be a massive effort going on in defect characterization as has been done here. However, at Drawn Military College in a way we are having a good look at the problem of transferability of the information from the laboratory to the field, and this includes aspects that haven't been discussed here at the conference. For instance, one of the aspects of the program that I am involved in is a post-graduate program in essentially nondestructive evaluation where we take in military officers subjecting them to a Master's Degree program which involves quantitative ultrasonics and acoustic emission, studies in holography, a modest background in microprocessing, stress waves in solids and so on. We are hoping that we will essentially be putting these people into positions as they apply to field units. We are hoping that these officers will be able to make some contribution to this transition from NDT in the laboratory to field applications. We take into consideration that in Canada we are really talking about the evaluation of American equipment rather than trying to really develop new things on our own.

From the technical point of view, the tendency in Canada is to say "Keep up with the state-of-the-art in NDE and the transition to wherever it will be in a couple of years in NDE." But at the same time, the trick has to be to be able to detect the defects in service. Furthermore, the more complex the methods become, the farther and farther we are almost bound to go away from a hundred percent inspection of the vehicle. That is why we are going toward continuous in-service monitoring and the particular technique we are using at the present time--and we seem to be using it successfully, at least in the cases we are working on--is acoustic emission. I would envisage that there will be a shift towards a fairly serious look at in-service engine health monitoring.

Now, in the acoustic emission effort, which is the one that I am most actively involved in, it has taken three directions. One is, by our standards, a fairly massive attempt in the laboratory. We've taken essentially the material that we have the biggest problems with, 7075 aluminum, spend a lot of time on fatigue crack propagation in this material, and try to essentially use acoustic emission in a way that it was really a criticality detector. In other words, not really thinking about actual flaw size, but trying to concentrate on the size of the next jump that the crack is going to make. With that in mind, the work has been directed toward trying to relate the acoustic emission signal to the amplitude of the acoustic emission signal, in particular to the new area of the fracture surface that was generated by the most recent crack advance. What this means is that we are really talking about looking at unstable crack propagation in vehicles, trying to wed together the continuously periodic maintenance procedure with the possibility that something unusual happens during the life of the component. So, obviously, laboratory work is much cheaper than doing it on the real thing. Having done that, we felt that there had to be an effort going simultaneously with this one where we would be looking at the problem of transferring the acoustic emission data from the laboratory into the field. Therefore, we are fairly successful now in that we can take the acoustic emission data and transfer it from one geometry to another.

The third effort with respect to the acoustic emissions program is to try to start putting together a library of in-flight noises in aircraft. In other words, rather than have the services faced with another feasibility study every time they ask us if we can tackle a problem, we are anticipating this request and putting together a book of in-flight noises in the acoustic emission range.

Finally, we have tackled the logistical problem, which is always the most difficult one, of course: the logistical problem of having data collected in-flight and transferred to a data analysis center which we have at the military college.

So far we have been successful in this effort. I understand that there have been some failures in use of acoustic emission in-flight. We, in Canada, have not run into any problems. We have got a good handle on the size of the acoustic emission signals, how they are related to fairly gross features on the fracture surface. We have demonstrated this and successfully done feasibility studies in one aircraft. A crack and the crack growth has been detected in flight. The data are in good agreement with expectations on newly cracked fracture surfaces and the acoustic emission data. Another airplane that I had a look at is the CF104 and, indeed, there is no reason to suspect that acoustic emission monitoring cannot take place on wing-fitting type components.

David Dean (P.E.R.M.E.): I propose to limit my contribution today to ultrasonic techniques. Looking at the U.S. effort here, I was amazed at the quantity and quality of it and it was very difficult, in fact, for me to find any area where we are doing something different. But, nevertheless, I hope today to try to concentrate on these areas where perhaps there is some difference between what we in England are doing and what is happening in the U.S.

We, also, have a number of people who are using mini and microcomputers. These are used for acquisition and processing of data, control of scanners, plotters, etc. In fact, I can list the NDT Center at Harwell, the Royal Aircraft Establishment at Farnborough, and my own group at Perme Westcote who are all building and using equipment based on these devices. And, of course, with modern high speed digitizers it is possible to store complete information about wave forms up to tens of megahertz these days.

To turn to imaging systems, here we began work ourselves on trying to image defects in rocket motors and rocket motor propellants. This is an area which I don't think has been attacked very much, if at all, in the U.S. We began using techniques which are being pursued still by Allbridge at Harwell for the examination of metals, and I think his work is also used for human NDT, working at fairly high frequencies. On the other hand, we have been working with ultrasonic frequencies of about a hundred hilohertz to one megahertz. You cannot go any higher, unfortunately, because the attenuation is so high in rocket propellant. Over the last few years we have developed an acoustic holographic technique working at 500 kilohertz. We can image defects in 15-inch cubes of dummy propellant and obtain a resolution of about two wave lengths. Now, we want to develop a system to work in real time. At the moment, it is a fairly straight forward scanning system with a single transducer. We have also developed, in conjunction with another UK firm, a 124 element matrix of three millimeter square transducers. These are switched by a light beam that enables us to select any element of the matrix. This matrix, we hope, should be able to sense holograms. Plessey in the U.K. has developed for us a rapid hologram recorder. Using photochromic film, it can produce typically a 200 by 200 raster in less than a second and, as far as resolution goes, one can get down to about a thousand by thousand raster in an 8 mm square. Naturally, scanning in the field is often not at all easy to accomplish. We will now try to use a manually operated device which senses the position of the transducer with sufficiently high resolution to form polygrams from the hand scan data. And again, of course, one can put this on the photogramic film for later projection.

Ashby and Turner at Bristol University are imaging in glass rather similar to the technique we saw in the poster session. They are using glass which is acoustically matched to steel and produces images in the glass of defects in the steel.

We are just starting work with Lethbridge University to look at the ultrasonic equivalent of the X-ray tomographic technique whereby one scans the specimen in a number of directions and from, say, the attenuation or the phase change, time delay through the material, etc., any changes in the material.

Now, moving away from imaging devices to the area where defects are comparable to the wave length. We had a particular problem with trying to find very small defects in fairly large areas of material. We set up a water bath system in which we used a lens and put a detector at the focal point of the lens. We look at the defects using the diffracted energy from the defect. Of course, the lens will carry out the Fourier transform provided one puts the detector at the focal point in the Fourier plane. We used a piezoelectric detector with annular rings and detected the energy falling on the annular rings away from the center of the beam.

Now, there is a variety of techniques available in the U.K. for assessing the depth of surface breaking cracks. One of them, due to Hunt, relies on reflection from the crack tip. Silk and Liddington, for example, at the NDT Center, produced a variety of techniques which rely upon travel times of ultrasonic waves around surface cracks. One needs a very good understanding, of course, of the travel paths and the possible mode conversions in order to make these techniques work, but I have no doubt that these will be developed further in the coming years.

This practical work is backed by theoretical work at City University. Bond uses a Ricker pulse to evaluate the effect of surface cracks on Rayleigh waves. He uses a finite difference technique in order to calculate deflections in the material and displays this on a grid which is distorted by the pulse. Of course, you have a series of these grids at different time scans. It is extremely easy to understand these phenomena and one can see progress. This work is going to be extended to other types of models. There is similar work going on by Temple at the NDT Center, Harwell.

DISCUSSION

M. J. Buckley, Moderator (ARPA): Well, we have some time now for questions. First, I would like to make one comment. I think people get somewhat of a misconception, perhaps, of what the NDE activity in this country consists of by this one meeting. I don't know what percentage of research in NDE is represented by this meeting, but it is probably about 5 percent and certainly it is the most basic part of any of the research which I am aware of, at least as a large entity. Most of the resources that are spent by the government are in far more applied areas of solving specific problems and I think you see that sort of a trend is coming about here. But this program was trying to create a different level of technology and so we are slowly trying to move that towards a reduction to practice and that's the reason for the test beds. But just basically, most of the work is much more applied in this country and we have never quite figured out how to put the researchers and the applied research side and everything else together and keep any large percentage of the audience in the room at the same time.

Ellis L. Foster (Battelle Columbus Lab): I would like to ask the speakers to maybe comment on any directions in the evaluation of composites that might be going on in their country.

David S. Dean (P.E.R.M.E.): We do have problems, trying to examine carbon fiber optics. We have used a variety of techniques. As I said before, ultrasonics, X-ray, acoustic emission. In short, you can see areas where the winding is not exactly how you would like it to be and so on. But it is extremely difficult to know what these are going to do in practice and I just cannot find anybody yet who can tell me. About the only technique we have found which looks like it may be helpful is acoustic emission. You get a massive acoustic emission signal in mutilated materials.

Philip Hodgetts (Rockwell, LAD): I would like to ask Mr. McBride if he has had any problems with type 2 errors (erroneous signals) with your in-flight monitoring? It is our goal to put expensive equipment on airplanes to keep them flying and sometimes we worry about grounding an airplane because we have got a false indication.

Stewart McBride (Royal Military College of Canada): Our emphasis has been trying to make the matter as quantitative as we possibly can and we have only done it in one material. But at this point we are saying we have indeed made it quantitative in that material in terms of the change in size of the crack. We are not really using it as a method of just finding the noises. In fact, at the present time the effort has been fairly primitive. We have just started using microprocessor methods to look at the data. But we have literally set a threshold, collected a lot of structural noises plus a very small number of acoustic emission signals. Six, I think it is today, in 6 months out of thousands of noise signals. We have literally scanned all the spectra of all the signals. We have the characteristic difference between the spectra of the acoustic emission and the noises and we know what the size of a particular signal means in terms of the change in the fracture area. We are not at the present time really concerned or worried about type 2 errors. We think we have solved it in the one case we have tackled.

The other thing I should point out on the in-flight monitor is that we got one side pay-off, which might be a very important one. We were able to pin down exactly where in the flight pattern unstable crack growth is taking place in a particular component. And this has turned out to be of great interest to the people who are doing the laboratory testing of the simulated structures.

Unidentified Speaker: The question is what type of an area of in-flight monitoring did you monitor? Was it a localized area or was it a fairly large area?

Stewart McBride: The entire effort at the present time is directed toward a single wing fitting. In other words, we are specifically picking components that are not really fail-safe components. If they go, the aircraft goes, essentially. It is an isolated wing fitting that we are looking at.

W. Sachse (Cornell University): I wonder if I could hear some comments about approaches that have been taken on calibration blocks, development of test blocks, and things like that which can be used to calibrate and standardize ultrasonic measurements.

Paul Höller (Saarbrücken): With regard to just physically calibrating instrumentation, I think there is nothing extraordinary to say besides perhaps a point that we are relying more in the ultrasonic field on flat reflectors instead of globulars.

With regard to simulating defects, we try to make artificial defects which are similar to real defects. Eddy current work is done with very narrow actual cracks. We are also trying to make corrosion defects and other types of real defects and trying to maintain a collection of specimens which have failed, in the sense of NDE.

Tom Cooper (AFML): I would like to direct a question to Doctor McBride. Several years ago under the auspices of T.T.C.P., which is the U.S.-Canada-England-Australia-New Zealand cooperative effort, we were trying to develop a noise source, a standard for use of acoustic emission, I think based on the helium jet test that you worked on. Can you tell us what the status of that is? Has that been accepted now as a calibration standard for acoustic emission?

Stewart McBride: I suppose I have accepted it. The general status of it is that there has been an internal test within T.T.C.P. program. I don't think, really, the test has been sufficiently wide enough however. We seem to have at least convinced ourselves that we are able to use a helium gas jet to get some indication of the acoustic response.

In terms of acceptance, I suppose the answer would be a guarded yes. It seems to be becoming a little bit more accepted. It has a serious disadvantage, however, in that it only gives you amplitude versus spectrum and no phase and no rise time information. But from the particular approach that I have been using it is giving me the information that I feel I need at this time.

Peter Doyle (Aeronautical Research Lab): I would like just to add, too, the acoustic emission people from Alpha prefer the helium jet to any other technique they use.

SCATTERING OF ULTRASOUND (INCLUDING RAYLEIGH WAVES) BY SURFACE ROUGHNESS AND BY SINGLE SURFACE FLAWS. A REVIEW OF THE WORK DONE AT PARIS 7 UNIVERSITY

G. Quentin, M. de Billy, F. Cohen-Tenoudji, A. Jungman
Groupe de Physique des Solides de l'Ecole Normale Supérieure,
Université Paris VII, Paris, France

B.R. Tittmann
Groupe de Physique des Solides de l'Ecole Normale Supérieure,
Université Paris VII, Paris, France
and
Science Center, Rockwell International, Thousand Oaks, California 91360, USA

ABSTRACT

Since some years our team has worked on the characterization of rough surfaces from a study of the angular and frequency dependence of the backscattered intensity of ultrasonic waves. We shall discuss, in view of our experimental results, the different components of the signature of the surface profile which can be evaluated by these means:

-r.m.s. roughness h with a precision of the order of 1 μm in the range 6-100 μm,
-influence of the autocorrelation distance L,
-when present, surface periodicities with a precision which can be better than 1%.

In the case of quasiperiodic surfaces, we shall present a comparison between the spectra theoretically predicted in the low-frequency approximation for various samples, and the ultrasonic spectra actually observed.

Since 1977, we have also used Rayleigh waves to study surface properties and surface cracks in ceramics and metals and we shall give an introduction to the results obtained at the present time. This topic will be developed by B.R. Tittmann in a following paper.

INTRODUCTION

The scattering of ultrasonic waves by rough surfaces has been studied quite extensively at frequencies below 1 MHz because of its great importance in underwater acoustics. In the field of NDE where the ultrasonic frequencies are one or two orders of magnitude higher, this problem has received much less attention. In certain circumstances of practical interest, the control of surface roughness may be very useful, among them we can quote:

- roughness of the paint on super tankers is one of the main limitations to their velocity,
- roughness of the internal surfaces of vessels submitted to intensive corrosion (chemical and nuclear industries),
- influence of the surface roughness on the propagation and entrance of ultrasound waves and of the roughness of crack faces on the possibility of obtaining the "signature" of these flaws.

We shall describe in the first main section the two experimental approaches used in our laboratory and then present the results obtained on surfaces with random and periodic roughness. The next two sections will be devoted to the problem of natural surfaces where both periodic and random components are present in the profile and to an outline of the work done this year on the characterization of surface flaws by Rayleigh waves.

EXPERIMENTAL PROCEDURES

In our experiments on the scattering of ultrasound by rough surfaces, we always use water as a coupling medium between the transducer and the surface under test. The transducer acts as transmitter and receiver and the target is placed in the far field of the probe. Two different experimental set-ups are used:

- the first one is derived from a classical narrow-band pulse-echo apparatus which has been fully automated and records the variation of the back-scattered ultrasonic energy versus the angle of incidence,
- the second one uses wide-band ultrasonic pulses and signal processing of the received echo including frequency analysis.

Narrow-Band Apparatus

This equipment has been described elsewhere.[1] The ultrasonic pulses have a duration of 1.5 μs and center frequencies of 2, 5, 15 or 25 MHz; the pulse repetition frequency is 1 KHz. The rotation of the sample is achieved by means of a stepping-motor and each step of the motor corresponds to a variation $\Delta\theta=0.9°$ of the angle of incidence θ, which can be varied from -27° to +27° with respect to normal incidence ($\theta=0$). For each value of θ in this range, the normalized value $I_\theta=I(\theta)/I(0)$ of the back-scattered echo is recorded.

Wide-Band Experiments. Ultrasonic Spectroscopy -

The ultrasonic pulse emitted has quite a large bandwidth (2 to 9 MHz within 3 dB). The spectrum of the echo received from a perfect reflector is given in Fig. 1. The received signal is amplified and gated in order to select the portion of the signal to be processed (Fig. 2). This time-domain signal can then either be fed to a conventional spectrum analyzer or be sampled, converted to digital, and then processed by the calculator (Fourier spectrum via the F.F.T. algorithm, autocorrelation, ...). The 2000 channels analyzer is used for randomly rough surfaces to calculate the mean value of the spectrum for various parts of the target at the same incidence. It is also used in a rather

peculiar way when we extract the periodicity of natural samples by the method of "contracted spectra" (see § IV).

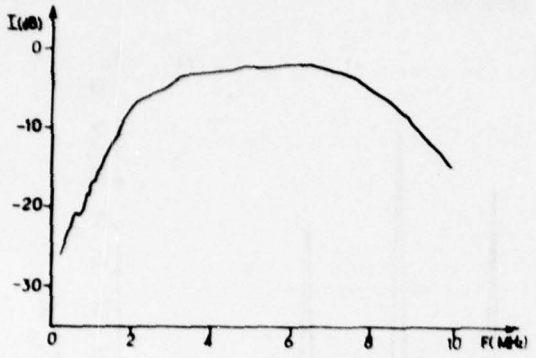

Fig. 1 Ultrasonic spectrum of the signal reflected by a perfect reflector at normal incidence.

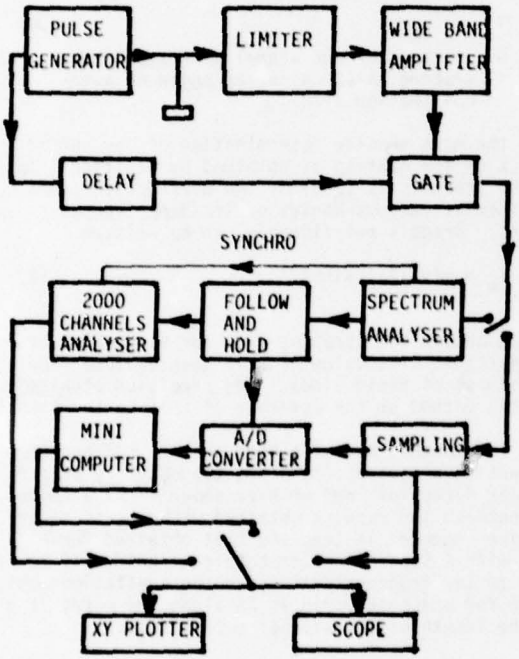

Fig. 2 Block diagram of the electronic equipment (wide-band).

RANDOMLY ROUGH SURFACES

The main component of the signature of such scatterers is the r.m.s. roughness h of the profile. We had shown previously that the angular variations of the backscattered ultrasonic power are correlated to the value of this parameter and independent of the specific nature of the surface (monocrystal, metal, paint, tissue). We have recorded in the memory of the calculator the results obtained for surfaces with a known value of h. Examples are given in Figs. 3 and 4 for roughnesses ranging from 5 to 93 μm studied at 5 MHz.

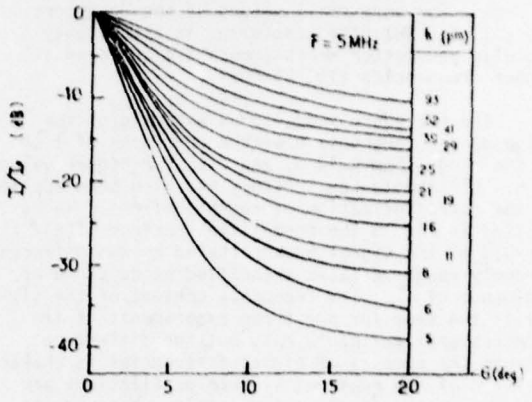

Fig. 3 Plot of the variations of the normalized backscattered ultrasonic intensity I_θ versus the angle of incidence for various value of the r.m.s. roughness h.

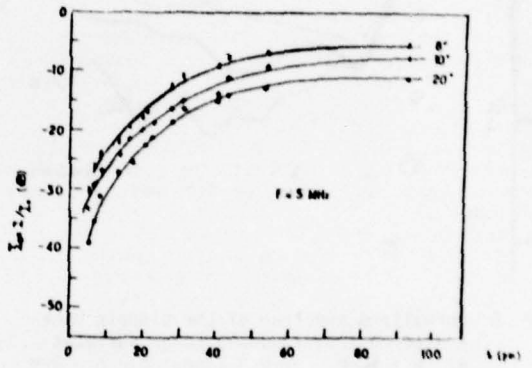

Fig. 4 Plot of the variations of the normalized intensity I_θ versus the r.m.s. value of the roughness h.

When we want to obtain an ultrasonic estimate of the roughness of a given surface, we put the sample in the apparatus and the calculator controls the whole experiment, records the backscattering diagram for angles of incidence varying from -27° to +27°, and calculates the mean value $\bar{I}_\theta$ for n sets of experiments corresponding to the same angle of incidence θ but on different parts of the sample, or corresponding to rotation of the surface in its own plane. Then the calculator uses the least square method to obtain an analytical form of the function $\bar{I}_\theta = f(\theta)$, makes a comparison with the reference values (Figs. 3 and 4) and displays the ultrasonic estimate of h and its absolute error Δh.

We see in Fig. 4 that for roughness greater than 40 μm at 5 MHz, the curve $I_\theta(h)$ tends to saturate, leading to a bad estimate of h along this procedure. For samples exhibiting quite a large roughness, we use a smaller ultrasonic frequency (2 MHz). For very small values of the roughness (<5 μm) at 5 MHz, the scattering is almost only specular and better measurements are achieved at higher frequencies (15, 25 MHz).

The procedure leads to an estimate of the value of the roughness h with a precision of 1 μm in the range (5μm<h<40μm) and 2 μm for higher values of h. Ultrasonic spectroscopy has also been applied to the characterization of rough surfaces. We have plotted in Fig. 5 the normalized spectrum [$I(\theta)/I(\theta=0)$] of the signal backscattered by two different randomly rough surfaces insonified at an angle of incidence of 4°. The frequency content of the signal is the same for the three experiments at frequencies smaller than 3 MHz, but the difference between the spectra of higher frequencies is characteristic of the roughness. Some oscillations are observed in the spectrum for sample c because its profile has a noticeable periodic component.

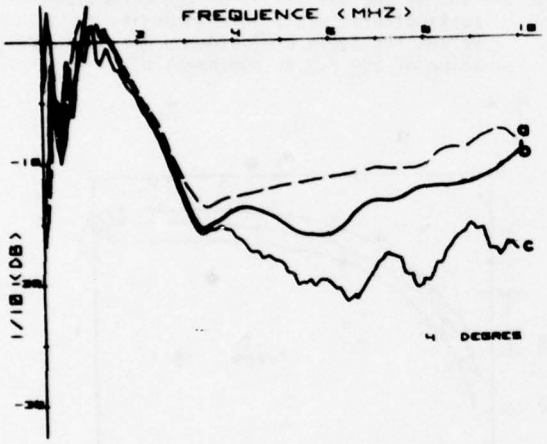

Fig. 5 Normalized spectrum of the signals backscattered from randomly rough surfaces: a) h = 18μm, b) h = 13μm, c) h = 8μm

Experiments are beginning on the scattering by back surfaces of random roughness where the ultrasonic beam enters a metallic slab by a smooth surface.

PERIODICALLY ROUGH SURFACES

For periodically rough surfaces, ultrasonic spectroscopy has proved to be a very powerful means of profile characterization.

Like in optics, the spectrum of the signal scattered by a diffraction grating exhibits diffraction lines corresponding to the different orders n of diffraction. Their frequencies f_m are given by Bragg's formula

$$2\Lambda \sin\theta = m\lambda = m(v_S/f_m) , \qquad (1)$$

where Λ= grating spacing constant, λ = wave length, θ = angle of incidence (autocollimation), and v_S = velocity of sound.

Figure 6 represents the spectrum of the signal diffracted by a grating (Λ=400μm) for an angle of autocollimation of 70°. This spectrum has not been corrected by the spectrum of the incident pulse. Four sharp diffraction lines corresponding to the fundamental and three first harmonics (m=1,2,3,4) are observed.

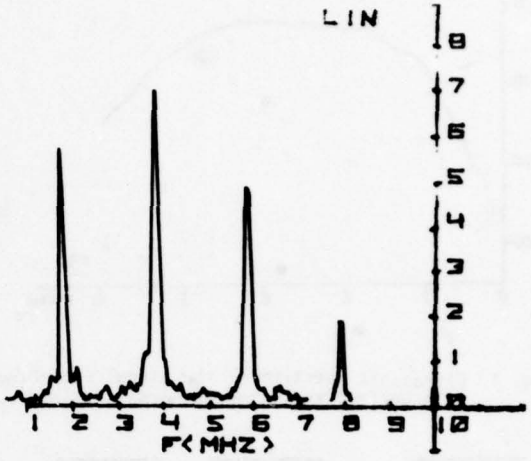

Fig. 6 Spectrum of the signal diffracted by a grating (Λ=400μm) at an angle of autocollimation θ=70°.

The most precise determination of the periodicity Λ of the grating is obtained by plotting (Fig. 7) the frequencies $f_m(\theta)$ of the diffraction lines obtained at various angles of incidence versus $1/\sin\theta$. Bragg's relationship can be written

$$f_m = m(v_S/2\Lambda)(\sin\theta)^{-1} \qquad (2)$$

and we obtain one straight line for each order of diffraction. The value of Λ is then deduced from the slopes of these lines. The precision attained by this method on the estimate of Λ is better than 1%.

This method has also been applied to samples presenting a periodicity along two mutually perpendicular directions and we have shown[1,2] by a comparison between the results obtained with a true square lattice engraved in lead and that obtained for a grid with a square mesh that this technique is sensitive to the true periodicity in the crystallographic sense for which the grid is 2a along the wires if a is the length of the side of each square.

We have also explained[2] how the periodicity can be deduced from the angular scattering diagram obtained in narrow-band experiments with a precision of the same order.

We had observed previously that for gratings exhibiting defects in periodicity, "Rowland ghosts" are present in the ultrasonic spectra. These secondary diffraction lines correspond to sub-gratings with periodicities 2Λ, 3Λ, 4Λ, 5Λ. As many as 17 such ghosts have been observed for a poor periodic grating where the grooves were equally spaced, but had different depths. All these "Rowland ghosts" can be plotted on the graph $f_m(1/\sin\theta)$ and are disposed along straight lines corresponding to the

order of diffractions m=n/p where n and p are integers (diffraction by the sub-grating pΛ). We could roughly correlate these properties of the ultrasonic spectra with the periodicity defects of the autocorrelation function of the profile.

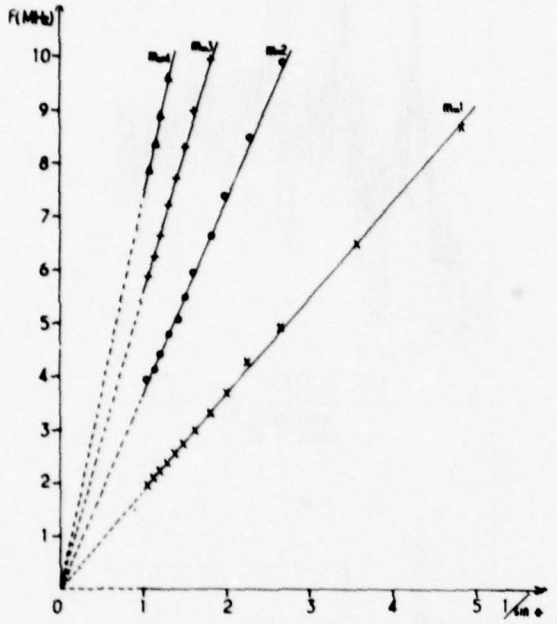

Fig. 7 Plot of the frequencies f_m of the diffraction lines of order m versus (1/sinθ) for a diffraction grating with a spacing constant Λ = 400μm.

In 1976-77[3] we have successfully applied the Kirchkoff method in the low frequency approximation to deduce from the known profile ξ(x) of a given grating the ultrasonic power spectrum diffracted at a given frequency f and angle of autocollimation θ.

For a grating with a spectral periodicity Λ (along an axis x of the surface), the amplitude of the diffracted wave A(f,θ) for an incident plane wave is given by

$$A(f,\theta)=G_1(\theta)\int_{-L}^{+L}\exp\{2ik[x\sin\theta-\xi(x)\cos\theta]\}dx \qquad (3)$$

where 2L is the length of the grating and k the magnitude of the wave vector of the ultrasonic waves. Many theoretical approaches leading to this same formula[4,5,6] differ only by the angular dependence factor $G_1(\theta)$.

In the low frequency approximation

$$2k\,\xi(x)\cos\theta \ll 1 , \qquad (4)$$

$$A(f,\theta) = fG_2(\theta)\int_{-L}^{+L}\exp\left[\frac{4i\pi fx\sin\theta}{v_S}\right]\xi(x)\,dx \qquad (5)$$

and the amplitude of the m^{th} diffraction line for a perfect grating is proportional to the m^{th} coefficient of the development of the profile ξ(x) in Fourier series.

In order to test the validity of this very simple theoretical approach, we have built 8 diffraction gratings exhibitng different profiles (peak-to-valley heights: 4μm<R<23μm), but having the same periodicity (Λ=400μm). The profile of each grating has been measured with a sampling distance of 40 m and the values obtained are used in the subsequent theoretical calculations of the Fast Fourier Transform of the profile.

Figure 8 is a theory versus experiment comparison for the values of the intensities of the two first diffraction lines (m=1,2) and two different angles of autocollimation (θ=62°,70°). The values indicated in dB are normalized versus the value obtained for the roughest of our 8 samples. The correlation r^2 is equal to 0.95 and the slope of the regression line is very close to 1 (1.03).

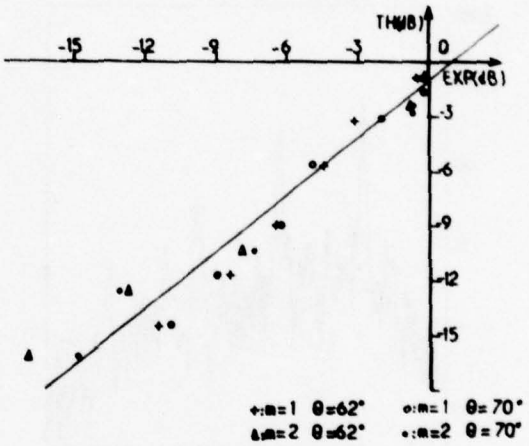

Fig. 8 Experimental values of the ratio $I_{mi}(\theta)/I_{nj}(\theta)$ versus the theoretical ones $I_{mi}(\theta)$ = Intensity of the line of order m for sample i.

In Fig. 9, we present a comparison between the ultrasonic spectra and the spectra computed from the F.F.T. of the profile and corrected for the spectrum of the incident ultrasonic pulse. The comparison is only valid for frequencies smaller than 5 MHz, which corresponds to the limit of validity of the low-frequency approximation that we use.

Figure 9-1 corresponds to the roughest sample (R=23μm) and Fig. 9-2 to a smoother one (R=8.4μm). A rather good agreement exists between the experimental results and the theoretical expectations, especially for the diffraction lines. The background between the peaks is not very well predicted and this "noise" is generally greater in the theoretical result than in the experimental one. Two explanations can be given for these discrepancies: 1) the non-uniformity of the insonification of the grating and the shape of our electronic gate which can give rise to a smoothing of the spectrum between the lines (like the Hanning window in F.F.T. computations); 2) the lack of a statistical treatment of different profiles

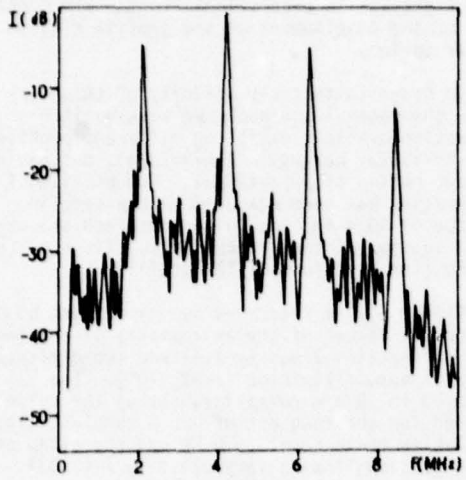

Fig. 9-1(a)

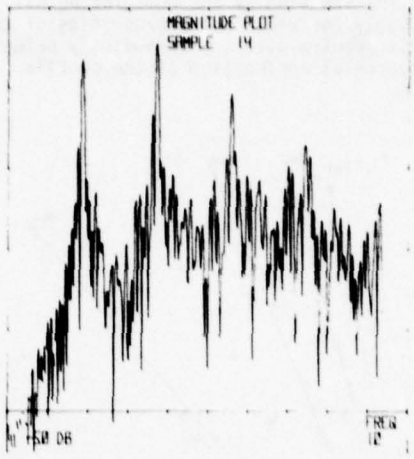

Fig. 9-1(b)

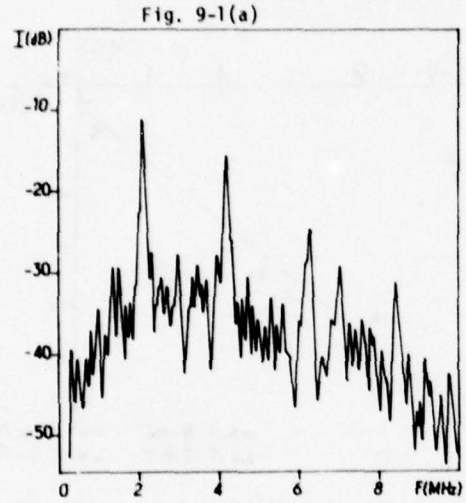

Fig. 9-2(a)

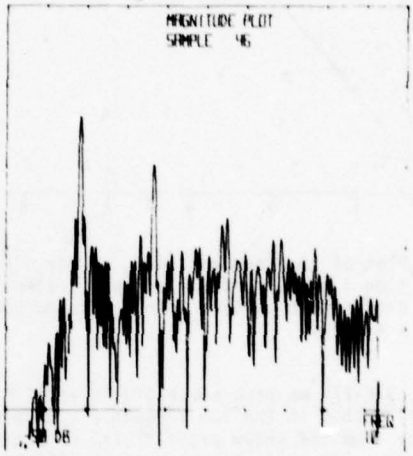

Fig. 9-2(b)

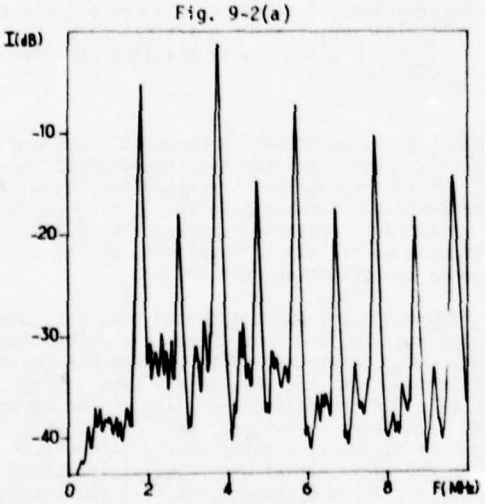

Fig. 9-3(a)

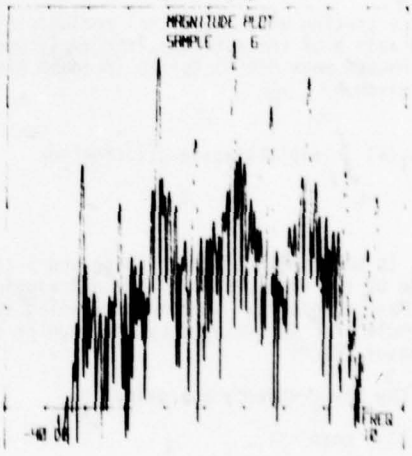

Fig. 9-3(b)

Fig. 9 Comparison between a) ultrasonic spectrum; b) spectrum computed from the F.F.T. of the profile (corrected)

SCATTERING OF RAYLEIGH WAVES BY SURFACE FLAWS

During the stay of B.R. Tittmann in our laboratory, we began a set of experiments in this field, and I want only to introduce the paper that he will give in this same session. We have studied penny-shape surface flaws in ceramics and metals. The radius of the flaws where less or equal to 100μm in ceramics and of the order of one millimeter in metals and three different techniques have been used for the generation of surface waves: SAW delay line in contact with the surface for high frequency experiments (100 MHz), wedge transducers for low frequency narrow-band experiments (2 to 10 MHz), water bath coupling for wide band experiments at low frequencies (2 to 9 MHz). The first parameter that we have been able to measure ultrasonically is the radius of the cracks with a 10% accuracy.[7]

CONCLUSION

We have shown that with good accuracy, ultrasonic backscattering experiments can lead to an estimate of the first statistical parameter characteristic of randomly rough surfaces: the r.m.s. roughness h. At the present time, we are not able to deduce from our experiments the values of the autocorrelation distance L of the profile; the influence of this parameter on the backscattering is much less than that of the roughness. For periodically rough surfaces, it is quite easy to measure ultrasonically the periodicity with a precision better than 1%, both using narrow-band or wide-band pulses (ultrasonic spectroscopy). We have also been able to predict theoretically quite correctly the spectra of the echoes diffracted from gratings in the low frequency range. Nevertheless, the inverse problem remains unsolved and we continue its study. For "natural" surface, we have shown that the method of summation of "contracted spectra" is very powerful to detect hidden periodicities.

Besides rough surfaces, we also are studying the scattering of ultrasound by surface cracks and by cylindrical targets, but I also want to emphasize the good results that we have obtained for the characterization of living tissues.[8] For this purpose we use an extension of the techniques developed in this paper. A review of our results in that field will be presented at the 1978 Ultrasonics Symposium.

REFERENCES

1. M. de Billy, F. Cohen-Tenoudji, A. Jungman, G. Quentin, "The Possibility of Assigning a Signature to Rough Surfaces Using Ultrasonic Backscattering Diagrams", IEEE Trans. on Sonics and Ultrasonics, SU-23 no. 5, 356-363, 1976.

2. G. Quentin, M. de Billy, F. Cohen-Tenoudji, J. Doucet, and A. Jungman, "Experimental Results on the Scattering of Ultrasound by Randomly and Periodically Rough Surfaces in the Frequency Range 2 to 25 MHz", 1975 Ultrasonics Symp. Proc., 102, 106, IEEE Press, 1975.

3. A. Jungman, F. Cohen-Tenoudji, G. Quentin, "Diffraction Experiments in Ultrasonics Spectroscopy; Preliminary Results on the Characterization of Periodic or Quasi-periodic Surfaces", Ultrasonics International 77 Conf. Proc., 385-396, IPC Science, 1977.

4. C. Eckart, "The Scattering of Sound from the Sea Surface", J. Acoust. Soc. Am. 25, 566-570, 1953.

5. D.M. Johnson, "Model for Predicting the Reflection of Ultrasonic Pulses from a Body of Known Shape", J. Acoust. Soc. Am. 59, 1319-1323, 1976.

6. L.R. Brownlee, "Reflection from a Sinusoidal Surface", J. Acoust. Soc. Am. 56, 361-368, 1974.

7. B.R. Tittmann, F. Cohen-Tenoudji, M. de Billy, A. Jungman, G. Quentin, "A Simple Approach to Estimate the Size of Small Surface Cracks with the Use of Acoustic Surface Waves", to be published in Appl. Phys. Letters (July 1978).

8. M. de Billy, G. Quentin, A. Jungman, F. Cohen-Tenoudji, "An Extension of Two Methods used in N.D.E. to the Field of Tissue Characterization". 3rd International Symp. on Ultrasonic Imaging and Tissue Characterization, NBS, Gaithersburg, 1978.

sampled along parallel lines perpendicular to the direction of periodicity (the theoretical calculation uses only one profile and small local inhomogeneities are present in the samples). Fig. 9-3 corresponds to a grating with inhomogeneities related to a sub-grating with a periodicity 2Λ and the 'Rowland ghosts" observed are predicted by the theoretical calculation.

NATURAL ROUGH SURFACES

The profile of a natural surface has both a periodic and a random component. The signature of such a scatterer must contain information about these two components. We have proposed a method ("contracted spectra") leading to an ultrasonic estimate of the periodicities of the profile, even when its main part is random. This method is based upon Bragg's formula which can be written

$$f_m \sin\theta = mv_S/2\Lambda \qquad (6)$$

One can deduce that if, instead of recording the spectrum I(f), we record the "contracted spectrum" I(f sinθ), in the second one the diffraction line of a given order m occurs for all values of the angle θ at the same abscissa $f_m \sin\theta$. The procedure uses the 2000 channels analyzer (Fig. 2). For each angle of incidence θ_i, the sweep time of this apparatus is adjusted in order that only the (2000 $\sin\theta_i$) first channels of the analyzer are filled during the time T of readout of the whole spectrum (0,10 MHz) from the spectrum analyzer. For each rough sample a set of n experiments (N ≈ 20) is performed using different values θ_i ranging from 14° to 70°, and the analyzer carries out the summation of these "contracted spectra" I(f $\sin\theta_i$) and finally displays the corresponding curve

$$\sum_{i=1}^{n} I(f \sin\theta_i)$$

This is illustrated in Fig. 10 where you can compare the very messy spectrum observed with a rough surface where the main component of the profile is random and the rather nice result of the summation of 22 "contracted spectra" exhibiting three diffraction lines. From the values of $f_m \sin\theta$ we deduce for this sample a spatial periodicity $\Lambda_{exp}=(395\pm7)\mu m$. Actually, this sample has been made by first engraving in lead a grating with a spacing constant $\Lambda=(400\pm2)\mu m$ and then roughening the surface until the grooves become unnoticeable, even on a microphotograph (Fig. 10a).

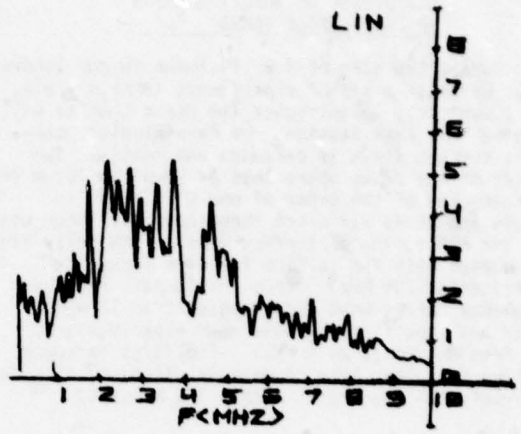

(a)

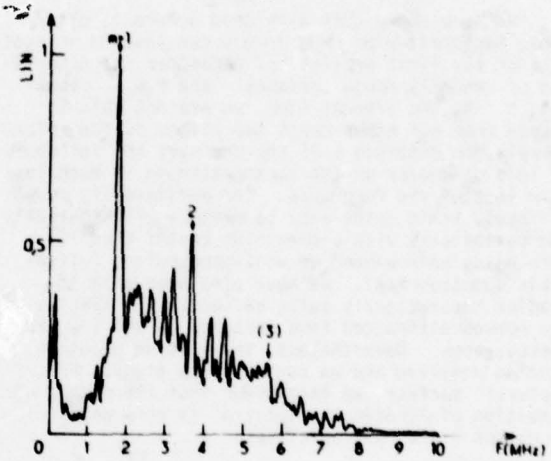

(b)

(c)

Fig. 10 - Sample 34. Comparison between the spectrum displayed on the frequency analyzer (a), and the content of the 2000 channels when 22 experiments have been performed using the procedure described in the text, (b); a microphotograph of the surface of the sample is given in (c).

DISCUSSION

G. Hermann (Stanford University): I was wondering if there are any practical situations where periodic surface roughness exists?

G. Quentin (University of Paris VII): Yes. In a practical situation materials which have been machined always have a periodic roughness if they are not polished. Usually in industry you don't polish the sample. It is only physicists which polish samples. Another point that I did not mention concerns roughness and random roughness. Random roughness seems to appear even on a polished surface.

G. Hermann: Under the periodic structure on the periodic surface properties, you have made measurements on periodic gratings which you have manufactured yourself in the lab?

G. Quentin: Yes, but some work has been on metal surfaces machined in the usual fashion.

REVIEW OF CRACK DEPTH MEASUREMENT BY ULTRASONICS

P.A. Doyle and C.M. Scala
Aeronautical Research Laboratories
Box 4331,GPO Melbourne, Australia

ABSTRACT

Research concerning bulk and surface wave methods for the measurement of the depth of surface-breaking cracks will be reviewed. This review will examine techniques for measuring crack depths which are based on the scattered pulse amplitude, time-of-flight methods, and ultrasonic spectroscopic analysis. Measurement of the transit time of bulk waves appears most likely to provide simple and reliable depth measurement in the near future. Promising directions for future research will be discussed.

INTRODUCTION

Ultrasonic methods are widely used in the detection of both internal and surface defects in structural materials. Because of increasing design complexity, e.g., the application of fracture mechanics concepts to aircraft design,[1] there is a special motivation to develop quantitative, rather than simply qualitative, techniques for non-destructive evaluation (NDE).

This paper reviews recent ultrasonic research directed towards the measurement of the depth of surface-breaking cracks which have already been located by ultrasonic or other NDE methods. Both bulk (P or S) and surface (R) wave techniques are included. The first general approach considered is the relationship between crack depth and the strength of the signal scattered by a crack from an ultrasonic beam. Next, depth measurement based on the transit times for waves following various paths around the crack is reviewed. Finally, the potential of ultrasonic spectroscopic analysis to measure small cracks and indicate crack morphology is discussed. When it helps clarify the state of the art for surface flaws, brief consideration is given throughout the paper to related work dealing with the ultrasonic examination of internal flaws. The potential of ultrasonic and acousto-optical imaging techniques is not discussed in this review.

SCATTERED AMPLITUDE METHODS

The Pulse-Echo Technique

The most common use of an ultrasonic probe is in the simple pulse-echo technique which detects the return signal scattered by a flaw situated beyond the 'dead zone' of the transducer.[2] The strength of the signal gives some indication of the size of the flaw, but quantitative estimation of size requires careful interpretation. One approach to this analysis is to compare the signal with that scattered by a known standard defect. Hitt[3] introduced flat-bottomed holes in test blocks made from the same material as the specimen under test as reference standards for scattering by internal defects. While flat-bottomed hole standards are still used, Hislop[4] argued that the so-called AVG (distance-signal voltage-defect size) diagram of Krautkrämer,[5] which quantifies the flatreflector system without actually needing sets of test blocks, provides a simpler standard for internal flaw measurements.

For the surface cracks of primary interest in this paper, reference standards often consist of spark eroded slots or saw cuts produced in a position geometrically similar to that for the crack to be measured. However, many difficulties are associated with the use of artificial reference defects.[6] Even after transducer coupling variations are avoided, the return signal is influenced by crack shape, crack surface roughness, and mode conversion upon reflection. The signal also varies with the frequency mode and bandwidth of the probe. Further, much of the ultrasonic intensity can be transmitted across an unloaded fatigue crack, causing the return pulse to depend on the state of stress in the region of the crack.[7] For an assembled structure, this state of stress is determined by material type, crack growth history, the amount of stress relaxation, and induced stresses.[8] Finally, ignoring interference effects, which depend on crack size and orientation, can cause under-estimation of crack depth. These effects prevent the intensity of the reflected pulse from always increasing monotonically with crack depth, as is assumed in simple theory.[9,10]

Corbly et al[7] overcame some of the above difficulties by using a known fatigue crack, in the same material and geometrical configuration as the unknown crack, as a reference standard for the pulse-echo technique. They employed S-wave reflection to find the depths of fatigue cracks as small as 0.5 mm to ± 0.2 mm. While this accuracy is excellent, the unknown cracks were prepared by the same constant amplitude loading cycle as the standard crack. Further work is needed to establish if and when the varying loading history of cracks encountered in practice significantly alters their reflectivity, thereby influencing the reliability of this technique.

Depth Measurement from First Principles

In parallel with the development of empirical methods which rely on reference standards, a more fundamental approach to crack depth measurement is being sought through more detailed consideration of the scattering processes involved. The complexity of the interaction of a beam with a surface flaw has been graphically illustrated by Baborovsky et al,[11] who used Schlieren visualization to demonstrate the interaction of an S-wave pulse with a slit. They describe fourteen possible main P and S scattered pulses produced by various combinations of mode conversion and diffraction from a single incident pulse. Not all of these scattered pulses are strong for any one crack orientation and incident pulse direction, although a strong return will occur for almost any of them at suitable incident angles. Figure 1 sketches as an example the field produced by a 2 MHz shear wave pulse incident at 35° on a slit two wavelengths deep in steel. It is possible for the back-scattered pulse to disappear altogether

at suitable angles and depths, which emphasizes the caution needed in applying the pulse-echo technique.

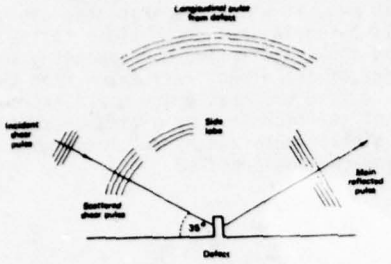

Fig. 1 Sketch of a cross-section through the field produced by a 2 MHz shear wave pulse incident at 35° on a slit two wavelengths deep in steel.[12]

The more fundamental and general approach to depth measurement would be to solve rigorously for the interation between the beam and the flaw, then determine depth by comparing theory and experiment at suitable scattering angles. A major obstacle to development along these lines is the difficulty of obtaining exact solutions for the scattering of elastic waves; even for scatterers in infinite media, solutions exist for only a few simple geometrical shapes.[13] This difficulty has led to a search for suitable approximate solutions. For the case of internal spheroidal and cylindrical defects, calculations based on the first Born approximation[14,15] have been compared with experiments by Tittmann[16] who found good agreement for back-scattering from small obstacles. Tittmann[16] and Adler and Lewis[17] used Keller's geometrical theory to approximate the scattering from disc-shaped flaws (which resemble internal cracks), and found good agreement with experiments for the larger scatterers for which Keller's theory is valid.

For surface cracks, multiple scattering due to the proximity of the surface to the obstacle is a further serious complication. Bennett[18] expressed the total field for a set of scatterers due to all multiple scattering in terms of the field reflected by each scatterer in isolation. He calculated as an example the field in the neighborhood of a cylinder adjacent to a plane free surface, which required numerical approximation by steepest descent of some integrals. Extending this work to the case of a crack at a surface would be valuable, though the formulation is complicated. A useful, but less rigorous, approach was adopted by Baborovsky et al[19], who numerically treated each point on the illuminated crack face as a Huygen's source radiating in all directions (Fig. 2). The calculated field at an exit point includes up to eighteen contributions from waves undergoing one to three scattering events, having due regard to mode conversion. Empirical corrections are included for head waves, surface waves and waves generated at the crack tip. These authors found broad agreement between computed scattered fields and Schlieren photographs of the type sketched in Fig. 1. They made a preliminary study of the pulse-echo technique by concentrating on the back-scattered part of the field, and found encouraging agreement between calculated and measured curves of intensity versus defect depth. The value of further work along these lines may depend on the validity of the approximations inherent in the numerical calculations for the near field of the scatterer.

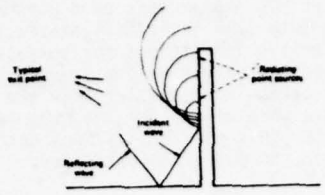

Fig. 2 Illustrating the model of Baborovsky et al[19]; for clarity only radiated waves of one mode caused by direct illumination are shown.

The approach to crack depth measurement from first principles, as discussed here, is providing the necessary understanding of the interaction between ultrasound and defect, which in itself is sufficient motivation for its continued pursuit. It may be that, for the next few years at least, simpler and more reliable crack depth measurement will be based on other approaches, particularly the timing methods discussed below.

Other Amplitude Methods

A number of other methods using scattered amplitude to measure crack depth have been proposed. Böttcher et al[20] arranged two angle probes on opposite sides of a slit in mild steel (Fig. 3); a signal dependent on slit depth reaches the receiver due to scattering by those grain boundaries beyond the slit edge. Silk and Lidington[21] pointed out that diffraction by the edge also contributes to the signal. Crack depth could be measured by comparing the signal received from an unknown defect with those from known slits, provided the calibration could be reliably established. However, there are significant differences between measurements by the two groups of authors, and further work would be needed to improve the calibration. Silk and Lidington indicate a number of disadvantages of this method; these include commonly occurring random errors caused by scattering from inclusions in the steel and by probe coupling variations. Also, the technique is limited to cracks at least 3-4 mm deep, due to the physical size of transducers and probe beam width and to the need to eliminate interfering surface waves. They found that a more accurate and reliable depth measurement can be made with this probe configuration by using a timing technique, as discussed below.

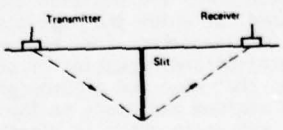

Fig. 3 The two-probe configuration used by Böttcher et al.[20]

During a study by photoelastic visualization of the interaction of surface waves with slits, Reinhardt and Dally[22] noted that the variation of transmission and reflection coefficients with crack depth might provide a basis for the measurement of small cracks less than half a wave-length deep. The transmission of surface waves past a crack in a fatigue test specimen has in fact been used[23] to monitor crack growth from an initial precrack 1.2mm deep. The reflection coefficient for surface waves, which varies more markedly than the transmission coefficient for cracks much smaller than the wavelength, may prove more useful for the measurement of very small cracks; this possibility does not yet seem to have been thoroughly investigated.

Finally, we consider a rather different technique proposed recently by Silk.[24] When a surface wave is directed towards a crack, part of the energy travels down the crack face and is radiated over a wide range of angles as S-waves from the tip (Fig. 4). An S-wave detector of known angle β should give maximum response at two positions, one at each side of the crack tip. Once these two positions are located (for one surface of the specimen), the crack depth can be readily found geometrically. This technique has the advantage of requiring neither a reference standard nor a detailed study of the scattering process. Silk measured fatigue crack depth greater than 8 mm to an accuracy of 13% with this method, though it is unsuitable for application to small cracks.

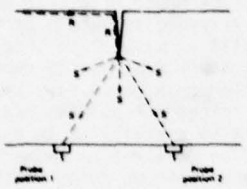

Fig. 4 Depth Measurement be detecting S-waves produced by mode conversion of R waves at the tip using an S-wave detector of known angle β.

TIMING METHODS

Bulk Wave Timing Methods

Di Giacomo et al[25] directed an S-wave towards a crack at an angle by reflection from the back face of a plate (Fig. 5), then shifted the probe away from the crack face until the position shown in Fig. 5a was reached, at which the back-scattered pulse was about to disappear. They measured the time lag between generation and reception of the reflected pulse, as well as that when the transducer was moved back through the maximum amplitude to the point where the signal was again about to disappear (Fig. 5b). The crack depth was found from these two measurements by eliminating the effective beam divergence from the calculation. The technique gave the depth of tight fatigue cracks in plate specimens within a standard error of 2-3 mm for cracks up to about 30 mm deep.

Di Giacomo et al described an alternative method having similar accuracy which is suitable for deep cracks ($\geq$ 10 mm), in which they replaced one of the measurements by moving the probe close to the crack, and measured the transit time corresponding to disappearance of the direct reflection from the crack tip. A focussed beam probe could improve both variations of the technique by giving greater sensitivity for tight cracks and by resolving more abrupt changes in crack edge profile.

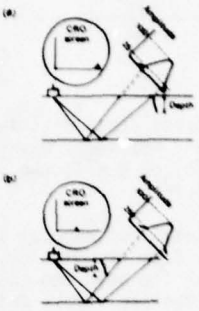

Fig. 5 The technique developed by Di Giacomo et al.[25] (a) and (b) show the two positions at which readings were taken.

Although these authors did not discuss the possibility, their methods could be readily modified to provide depth measurement for cracks opening onto inaccessible surfaces. While use was made of signal amplitude to eliminate the finite beam width, the self-normalization implicit in the technique led Di Giacomo et al to find values for depth almost independent of the absolute magnitude of the scattered pulse. Thus this technique provides a bridge between those methods described above which depend on signal amplitude, and those which are solely variations on the time-of-flight approach.

Silk and Lidington[21] used the configuration of Fig. 3 to determine the depth of artificial slits by measuring the time delay between the transmission of a short longitudinal pulse, and its reception after scattering by the crack edge. With a knowledge of probe separation and wave speed in the specimen, elementary geometry relates crack depth to this time. A shallow angle of 20° for beam entry was required to achieve a scattered pulse height significantly above noise level; this geometry causes a loss in the accuracy of depth measurement proportional to sin 20°. However, given this sufficiently strong diffracted P-wave, the required pulse was easily identified, since it preceded any other pulses arriving at the receiver, such as mode converted S-waves or possibly surface waves. Slots 10-40 mm deep were measured to an accuracy of ± 0.5 mm. Silk and Lidington[26] later used this technique, making meaningful time measurements as short as 20 ns, to measure the depth of artificial slite 1-30 mm deep to within ± 0.25 mm. For slits of varying depth, they measured the profile of the edge. A very shallow beam entry angle of 10° was necessary for the smaller slits, in order to maximize the diffracted

pulse by causing the centre of the beam to impinge more nearly on the edge of the crack.

Recently, actual fatigue crack depths in steel have been measured[27] to ± 0.2 mm using 2.5 MHz longitudinal probes, though in all cases reported the cracks were at least 6 mm deep. Since the measured depth is a weighted average over the beam spread along the crack edge, less accuracy is obtainable near sharp changes in depth along the crack profile. The principal limitation on accuracy is the change in pulse shape, which complicates identification of corresponding points in the transmitted and received waveforms. Tests carried out under compressive load demonstrated the continued accuracy of this technique even for tight cracks, whose ability to transmit ultrasound is a serious problem for both amplitude techniques and for the surface wave methods discussed below. This P-wave technique has been developed at Harwell to the point where visual estimation of transit time has been replaced by an electronic measurement system. Hence, an automatic accurate crack depth meter could become available in the near future. In addition, different probe arrangements suitable for a wide variety of specimen geometries are being investigated.[28]

One particularly simple method is to mount a single probe on the face opposite the crack, and to use time measurement to determine distance from the crack tip to the opposite face of the specimen. This approach was used by both Hunt[29] and Winters[30] to measure the depth of fatigue cracks opening on the inside of large gun barrels. The observed weak signals were attributed to reflections by facets near the crack tip; some cracks tending to be normal to the surface were missed by this method.[29] The technique was reliable only for cracks deeper than 2-4 mm. Both authors reported a systematic depth indication 0-1 mm below the true values. Silk and Lidington[28] also found considerable variations in the success of this technique when applied to fatigue cracks. They discussed in an oversimplified way the relative contributions to the signal from diffraction, refraction and scattering by micro-defects near the crack tip. A more detailed theoretical study of these mechanisms including the effect of mode conversion is needed to establish when this single probe timing method is reliable. This study would be doubly valuable if carried out in conjunction with photo-elastic or Schlieren visualization experiments.

The use of the slower S-waves rather than P-waves increases the accuracy in converting from time delay to crack depth by a factor of about two. This advantage is not easily realized in practice with conventional S-wave probes, due to difficulty in identifying the relevant S-wave echoes among interfering signals.[27,28] However, using a specially constructed short pulse S-wave probe arranged as in Fig. 6, Lloyd[31] measured the depth of artificial slits 0.75-4.5 mm deep to ± 0.25 mm. His method is based on the theory of Freedman[32], which shows that the return signal consists predominantly of pulses scattered from discontinuities, in this case the base and the tip of the slit. Further work directed towards exploiting the lower speed of S-waves for other probe configurations could prove profitable, particularly if more attention is paid to probe design to reduce spurious signals.

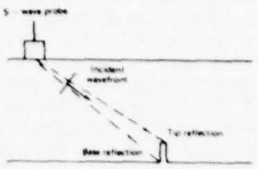

Fig. 6 The S-wave method of Lloyd;[31] the base reflection is coincident with the specular reflection.

Surface Wave Timing Methods

Several authors have recently investigated the use of surface waves for crack depth measurement. Because they follow the crack profile, surface waves measure the length L along the crack face to its tip, rather than the more useful crack depth of the tip below the specimen surface (Fig. 7a); however, as we shall see later, more complicated experiments can eliminate this restriction. Also, the greater ability of these waves to penetrate small gaps often requires tight cracks, or cracks with solid or liquid filled gaps, to be opened by suitable loading of the specimen if depth measurement is to be achieved.

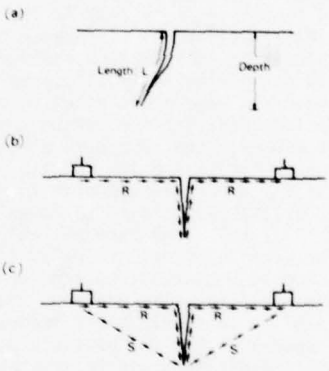

Fig. 7 Crack length measurement using surface waves.
a) Distinction between crack depth and the crack length L.
b) Crack length measured by the surface wave propagating around the crack.
c) The three main pulses expected at the receiver. Note that P, S and both reflected and transmitted R-waves are in general all produced at each discontinuity.

When a surface wave reaches a discontinuity such as a crack opening or tip, part of the energy will be radiated as P or S waves into the body of the specimen and part will be reflected back as a surface wave, leaving the remainder to bend around the corner and continue as a surface wave. Cook[33] found the crack length L by measuring the time taken for the surface wave to pass around the crack between two transducers (Fig. 7b). This method was later

found to be accurate for most fatigue cracks having L above 2 mm, provided the transmitted signal could be unequivocally identified.[34] Unfortunately, attenuation of the surface wave caused by the crack morphology and the roughness of the surface finish prevented this method being accurate in some cases, and perhaps more importantly, it was not possible to know beforehand which cracks would be unsuitable. Hall[35] further clarified this technique by using photoelastic visualization of the interaction between a surface wave and notches in glass specimens. He demonstrated that three main pulses are expected at the receiver - the R-wave transmitted around the crack, a mode converted S-wave propagating from the tip over a range of directions including that towards the receiver, as well as a diffracted S-wave caused by an unwanted bulk wave produced at the transmitter (Fig. 7c). This insight facilitated the measurement of 9 mm deep fatigue cracks in steel using specially designed 4.2 MHz Rayleigh wave probes. Notches down to about 1 mm were indicated by broadening of the received pulse, though quantitative depth measurement by simple timing only becomes possible when the three main signals are resolved.

Hudgell et al[34] introduced an alternative method suitable for parallel-sided specimens (Fig. 8), which uses only a single probe. This method is less accurate than that originated by Cook[33], but more reliable because it more consistently provides an identifiable signal. Total transit time is measured for that part of the surface wave which is converted to an S-wave at the tip, reflected from the opposite face of the flat specimen, then reconverted to a surface wave due to glancing incidence at the tip, and finally travels back to the probe. Because of the relatively small difference between R and S wave velocities, this method required measurement to ± 10 ns by time interval averaging to estimate fatigue crack edge profiles only to within about 1 mm. An inherently more accurate single probe technique measures the time between R-wave reflections from the crack opening and tip. Lidington and Silk[36] used this approach to measure the depth of an artificial slit up to 30 mm deep to an accuracy of ± 0.2 mm. They were not able to deal with slits below about 4 mm, since for smaller depths the tip reflection was not resolved from the moderately short pulse from the slit opening. For a fatigue crack profile in steel, their accuracy in measuring L dropped to ± 0.8 mm, possibly due to a large inclusion concentration giving greater background intensity in the signal. Some spuriously high and low readings were found for this real crack, probably caused by changes in the crack angle and by regions of cracking parallel to the plate surface.

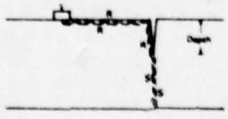

Fig. 8 Crack length measurement using the difference between speeds for R and S waves.

Silk[24] proposed several methods aimed at finding depth rather than length for a real crack. The most interesting of these first measures the times of flight between two transducers for the surface wave propagating around the crack, and for the mode converted S-wave originating at the tip (Fig. 9). Next, the roles of transmitting and receiving probes are reversed, and the measurements repeated. With these four readings, the time delay involving surface waves can be eliminated altogether, leaving the algebraic equivalent of the bulk S-wave timing method of Lloyd.[31] Silk used this method to find the depth rather than L for conveniently deep (22-30 mm) fatigue cracks to ± 0.5 mm.

Fig. 9 Elimination of R-wave transit times to find crack depth.[24]

The surface wave techniques described here have generally not been able to measure such small fatigue cracks as have the more successful of the bulk wave methods considered above, nor have they usually been so accurate, reliable, or versatile. Nevertheless, the approach is at a comparatively early stage of development, and as Silk[24] pointed out, may not yet have reached its full potential, particularly if viewed in the light of the more sophisticated treatment of the received pulses discussed in the following section.

ULTRASONIC SPECTROSCOPIC ANALYSIS

The transit time techniques considered so far rely on one or more pulses being identified at the receiver without any need for processing the total signal. One approach to extending these methods to smaller cracks and to mapping the morphology of the crack face is to pursue further analysis of the signal, either in the time domain or in the frequency domain, that is, to adapt the development of ultrasonic spectroscopy[37,38] to signals from surface flaws. Work in this field has to date been mainly directed towards the study of internal defects. We shall briefly discuss this work, as it will help guide the development of the spectroscopic study of surface defects.

Because of the difficulty in developing the theoretical analysis, Gericke[37] and Wüstenberg and Mundry[39] suggested empirically forming an atlas of signatures for reflections from different types of internal flaws, to which one could refer to interpret the spectral traces obtained from unknown defects. However, ultrasonic spectroscopy has developed along rather more manageable lines through experimental and theoretical studies of the spectral traces from simply shaped objects. This work includes a method for the determination of the size of arbitrarily oriented flaws of two-dimensional (crack-like) geometry[40,41] and studies of cylindrical inclusions[42-44] and of spheroidal cavities[17] in elastic solids.

The same general approach described above for internal defects was adopted for surface flaws by Morgan.[45] He applied spectroscopic analysis techniques to the study of surface wave reflections from a slot milled in aluminum. The reflections from this slot using a broad-band (0.5-10 MHz) interdigital transducer were as in Fig. 10a. Each corner in the slot, whose shape is shown in Fig. 10b, acts as a scattering center. He introduced two methods - the time reconstitution method and the cepstral method - which allow later signals to be resolved from each other, provided the signal from the first scatterer can be separated. The time reconstitution method requires that both amplitude and phase of the reflected signal be retained for analysis. For this method, Morgan wrote the impulse response function for the surface crack in terms of reflection and transmission coefficients for a set of scatterers, which in this case were the corners in the slot. He assumed no change in pulse shape upon reflection, thereby neglecting dispersion. Fig. 10c shows the experimentally reconstituted time signal for the artificial slot and illustrates the correlations with the five scattering centres. The cepstral method, which does not require the phase of the reflected signal, gave results almost identical to Fig. 10c for the artificial slot. For this alternative method, analogue spectrum analyzers are applicable, instead of the digital processing requires to obtain phase information for the time reconstitution approach.

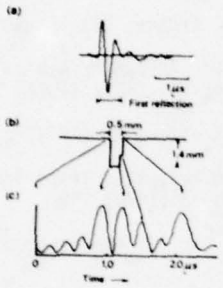

Fig. 10 The spectroscopic analysis carried out for surface waves by Morgan.[45]
a) The original reflected signal.
b) The geometry of the slot.
c) The experimentally reconstituted time signal.

In defining his original impulse response function, Morgan did not consider the effect of internal cycles between scatterers in the series. To improve the correlation between signal and slit morphology, these contributions to the signal should be evaluated and compared with the errors inherent in the computational procedures. The future development of his methods also depends on their extension to the morphologies of real surface cracks.

The energy carried by a surface wave is spread over a finite depth below the surface, governed by the wavelength. Therefore, the time taken to pass around a crack whose depth is of the order of the wavelength is frequency dependent. Silk[24] suggested developing a technique for crack depth measurement based on this dependence which, while being less accurate than conventional transit time measurements, would be largely independent of the angle of the crack. We believe that a study of this frequency dependence may prove most valuable in the analysis of broadened pulses received in the interrogation of shallow cracks, such as have been reported by Hall.[35] In any case, a more rigorous treatment of the frequency dependence than has been given to date is required.

DISCUSSION

From the techniques considered in this review, bulk wave transit time measurements appear to hold the main hope for the near future to provide simple and reliable quantitative crack depth measurement. Surface wave timing methods are also promising, though they are perhaps at a slightly earlier stage of development. Further fundamental scattering studies such as those described will be valuable in providing the necessary general understanding of the basic processes involved, particularly if applied to the scattering in the region of the crack tip.

Not only greater accuracy and reliability of depth measurement are desirable, but also the ability to measure smaller cracks; for example, cracks 0.5mm deep are often critical in high strength steels in aircraft components. Research in ultrasonic spectroscopic analysis, possibly along the lines suggested, should contribute to the study of small cracks. For some specimen geometries, another approach which may be developed to provide quantitative measurement is the use of guided ultrasonic waves. These waves have been used to detect cracks down to 0.05 mm in thin tubes.[46]

The ultrasonic probes used are another area for development. Greater accuracy and sensitivity in measuring the depth of the profile of small cracks may be possible by the use of focused probes,[47] and particularly by the use of single pulse generation.[48-51] Again, improved probe design may allow exploitation of the inherent advantage of shear waves over pressure waves for timing techniques. Finally, we should mention that only single cracks have been studied to date; multi-branched cracks and close clusters of cracks are subjects for future study.

ACKNOWLEDGMENT

This research was sponsored by the Center for Advanced NDE, operated by the Science Center, Rockwell International, for the Defense Advanced Research Projects and the Air Force Materials Laboratory under Contract F33615-74-C-5180.

REFERENCES

1. R.B. Thompson, A.G. Evans, IEEE Trans. Sonics and Ultrasonics SU-23 (1976) 292.

2. J. Krautkrämer, H. Krautkrämer, Ultrasonic Testing of Materials, Springer-Verlag (1969).

3. W.C. Hitt, Proc. ASTM Symposium (1952) 53.

4. J.D. Hislop, Non-destructive Testing 2 (1969)183.

5. J. Krautkrämer, Brit. J. Appl. Phys. 10(1959)240.

6. J.R. Birchak, C.G. Gardner, Mat. Evaluation 34 (1976) 275.

7. D.M. Corbly, P.F. Packman, H.S. Pearson, Mat. Evaluation 30 (1970) 103.

8. B.G.W. Yee, J.C. Couchman, J.W. Hagemayer, F.H. Chang, Non-destructive Testing 7 (1974) 245.

9. R. Werneyer, U. Schlengermann, Material-prüfung 13 (1971) 213.

10. B.H. Lidington, D.H. Saunderson, M.G. Silk, Non-destructive Testing 8 (1975) 185.

11. V.M. Baborovsky, D.M Marsh, E.A. Slater, Non-destructive Testing 6 (1973) 200.

12. V.M. Baborovsky, D.M.Marsh, T.I. Research Labs Report 307 (1971).

13. E.A. Kraut, IEEE Trans. Sonics and Ultrasonics SU-23 (1976) 162.

14. J.F. Gubernatis, E. Domany, M. Huberman, J.A. Krumhansl, Ultrasonics Symposium Proceedings, IEEE New York (1975) 107.

15. J.E. Gubernatis, E. Domany, J.A. Krumhansl, M. Huberman, J. Appl. Phys. 48 (1977) 2812.

16. B.R. Tittmann, Interdisciplinary Program for Quantitative Flaw Definition Special Report, 2nd Year Effort, Rockwell (1976) 123.

17. L. Adler, D.K. Lewis, IEEE Trans. Sonics and Ultrasonics SU-23 (1976) 351.

18. S.B. Bennett, J. Appl. Mech. 39 (1972) 1019.

19. V.M. Baborovsky, E.A. Slater, D.M. Marsh, Ultrasonics Inter. 1975 Conf. Proc. (1975) 46.

20. B. Böttcher, E. Schulz, H. Wüstenberg, Proc. 7th Inter. Conf. on Non-destructive Testing, Warsaw (1973).

21. M.G. Silk, B.H. Lidington, Non-destructive Testing 8 (1975) 146.

22. H.W. Reinhardt, J.W. Dally, Materials Evaluation 30 (1970) 213.

23. C.L. Ho, H.L. Marcus, O. Buck, Experimental Mechanics 14 (1974) 42.

24. M.G. Silk, NDT International 9 (1976) 290.

25. Di Giacomo, J.R. Crisci, S. Goldspiel, Materials Evaluation 30 (1970) 189.

26. M.G. Silk, B.H. Lidington, Brit. J. Non-destructive Testing 17 (1975) 33.

27. B.H. Lidington, M.G. Silk, P. Montgomery, G. Hammond, Brit. J. Non-destructive Testing 18 (1976) 165.

28. M.G. Silk, B.H. Lidington, NDT International 10 (1977) 129.

29. C.A. Hunt, RARDE Technical Report 20/75 (1975).

30. D.C. Winters, 1975 Ultrasonics Symp. Proc., IEEE Cat #75, CHO 994-4SU (1975) 572.

31. E.A. Lloyd, Birt. J. Non-destructive Testing 17 (1975) 172.

32. A. Freedman, Acustica 12 (1962) 10.

33. D. Cook, Proc. Brit. Acoustical Soc. Spring Meeting, Loughborough (1972) 72U19.

34. R.J. Hudgell, L.L. Morgan, R.F. Lumb, Brit. J. Non-destructive Testing 16 (1974) 144.

35. K.G. Hall, Non-destructive Testing 9 (1976) 121.

36. B.H. Lidington, M.G. Silk, Brit. J. Non-destructive Testing 17 (1975) 165.

37. O.R. Gericke, Ultrasonic Spectroscopy, Ch. 2 in Research Techniques in Non-destructive Testing. Ed. R.S. Sharpe Academic Press, London and N.Y. (1970).

38. A. Brown, Ultrasonics 11 (1973) 202.

39. H. Wüstenberg, E. Mundry, Brit. J. Non-destructive Testing 15 (1973) 36.

40. L. Adler, H.L. Whaley, J. Acoust. Soc. Am. 51 (1972) 881.

41. L. Adler, K.V. Cook, H.L. Whaley, R.W. McClung, Materials Evaluation 35 (1977) 44.

42. W. Sachse, J. Acoust. Soc. Am. 56 (1974) 891.

43. F. Bifulco, W. Sachse, Ultrasonics 13 (1975) 113.

44. W. Sachse, Proc. ARPA/AFML Review of Quantitative NDE. AFML-TR-75-212 (1976) 147.

45. L.L. Morgan, Acustica 30 (1974) 222.

46. W. Mohr, P. Höller, IEEE Trans Sonics and Ultrasonics SU-23 (1976) 369.

47. J.T. McElroy, Int. J. Non-destructive Testing 3 (1971) 27.

48. N.D. Dixon, T.J. Davis, Battelle Northwest Labs. Report BNWL-1256, VC-37, Instruments (1971).

49. M.V. Korolev, Sov. J. Non-destructive Testing 12 (1976) 296.

50. R-I.Y. Kazhis, A.I. Lukoshevichyus, S.I. Sayouskas, Sov. J. Non-destructive Testing 9 (1973) 628.

51. J.P. Weight, A.J. Hayman, J. Acoust. Soc. Am. 63 (1978) 396.

DISCUSSION

John Brinkman, Chairman (Rockwell International Science Center): Let me ask a question. On your last chart you showed an experimentally reconstituted signal.

Peter Doyle: (Aeornautical Research Lab): Yes.

John Brinkman, Chairman: Can you comment on the reconstitution?

Peter Doyle: Yes. What we did was simply to write the impulse response function in terms of the reflection and transmission coefficients and then, provided that you can identify the reflection in the first corner, you can go to the answer.

John Brinkman, Chairman: Okay.

CHARACTERIZATION OF SURFACE WAVE SCATTERING BY SURFACE BREAKING CRACKS

S. Ayter and B. A. Auld
Edward L. Ginzton Laboratory
Stanford University, Stanford, California 94305

ABSTRACT

Various analytical methods based on the real reciprocity relation are applied to the problem of Rayleigh wave scattering by a surface crack. In one formulation, the reflection coefficient observed at the transducer terminals is expressed in terms of an integral over the crack surface of the product of the perturbed and unperturbed fields. This integral is then converted to a volume integral and the Born Approximation is applied. In the other formulation a "Kirchoff" type approach is used such that the effect of the crack is expressed as an equivalent body force distribution. That force distribution is then approximated and normal mode techniques are used to find the scattered field amplitude. The two methods are compared with each other and with the results obtained from geometrical diffraction theory. An experimental procedure is also proposed for the inverse problem.

INTRODUCTION

New experimental results have been obtained on the surface scattering of Rayleigh waves in the medium and short wavelength regimes during the past year, especially by Khuri-Yakub and co-workers at Stanford, by Tittman at Rockwell, and Quentin and co-workers at the University of Paris. The theoretical calculations we present here apply in the same regime and show agreement as far as the angular scattering from the surface crack is concerned. In the frequency response, the theory does not predict the resonances observed experimentally, but agrees well with the general behavior of the scattering.

We basically used two approaches to the problem. In the first one we used Auld's reciprocity relation[1] in volume integral form and applied the Born Approximation. In the second one, we replaced the crack by approximately equivalent body sources and found the scattered field using normal mode theory. We called this approach a "Kirchoff" method due to the fact that we calculate the scattering from a set of secondary sources that do not satisfy the boundary conditions everywhere.

Born Approximation — Consider the general scattering geometry shown in Fig. 1. Starting from the piezoelectric reciprocity relation in a source free medium

$$\nabla \cdot \left\{ \underline{V}_1 \cdot \underline{T}_2' - \underline{V}_2' \cdot \underline{T}_1 + E_1 \times H_2' - E_2' \times H_1 \right\} = 0 \qquad (1)$$

It can be shown that[1]

$$\delta\Gamma_{21} = \frac{1}{4P} \int_{S_F} \left\{ \underline{V}_1 \cdot \underline{T}_2' - \underline{V}_2' \cdot \underline{T}_1 \right\} \cdot \hat{n} \, dS \qquad (2)$$

where the field quantities with subscript 1 are those excited by incident power P at terminal 1 in the absence of the crack and those with subscript 2 are excited with an incident power P at terminal 2 in the presence of the crack. Here, $\delta\Gamma_{21}$ is the change in the transmission coefficient from terminal 1 to terminal 2 due to the presence of the crack. We use primes with subscript 2 to emphasize the presence of the crack.

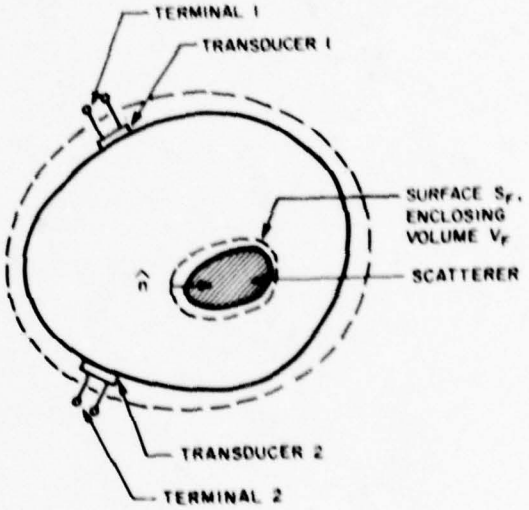

Fig. 1. General scattering geometry

Take the acoustic field equations

$$\nabla \cdot \underline{T}_2' = -\omega \rho_2 \underline{V}_2' \qquad (3)$$

$$\nabla_s \underline{V}_2' = -\omega \underline{s}_2 : \underline{T}_2' \qquad (4)$$

$$\nabla \cdot \underline{T}_1 = -\omega \rho_1 \underline{V}_1 \qquad (5)$$

$$\nabla_s \underline{V}_1 = -\omega \underline{s}_1 : \underline{T}_1 \qquad (6)$$

Multiplying (3), (4), (5), (6) by

$$-\underline{V}_1, \underline{T}_1, \underline{V}_2', -\underline{T}_2'$$

respectively, adding them up, using the tensor identity

$$\nabla \cdot (\underline{V} \cdot \underline{T}) = \underline{V} \cdot \nabla \cdot \underline{T} + \underline{T} : \nabla_s \underline{V}$$

and the constitutive relations

$$\underline{\underline{T}}_2 = \underline{\underline{c}}_2 : \underline{\underline{S}}_2 \quad , \quad \underline{\underline{T}}_1 = \underline{\underline{c}}_1 : \underline{\underline{S}}_1$$

one gets

$$\nabla \cdot (\underline{V}_2' \cdot \underline{\underline{T}}_1 - \underline{V}_1 \cdot \underline{\underline{T}}_2')$$

$$= i\omega(\rho_1 - \rho_2)\underline{V}_2 \cdot \underline{V}_1 + i\, \underline{\underline{S}}_2 : (\underline{\underline{c}}_1 - \underline{\underline{c}}_2) : \underline{\underline{S}}_1 \qquad (7)$$

Taking the volume integral of both sides, applying the divergence theorem and comparing with Eq. (2), we obtain finally

$$\delta\Gamma_{21} = \frac{i\omega}{4P}\int_{V_F}\left\{(\rho_1 - \rho_2)\underline{V}_2' \cdot \underline{V}_1 + \underline{\underline{S}}_2' : (\underline{\underline{c}}_1 - \underline{\underline{c}}_2) : \underline{\underline{S}}_1\right\} dV \qquad (8)$$

For an air filled crack, this result reduces to

$$\delta\Gamma_{21} = \frac{i\omega}{4P}\int_{V_F}\left\{\rho\, \underline{V}_2' \cdot \underline{V}_1 + \underline{\underline{S}}_2' : \underline{\underline{c}} : \underline{\underline{S}}_1\right\} dV \qquad (9)$$

where ρ is the density and $\underline{\underline{c}}$ is the stiffness matrix of the surrounding medium.

Now we make the key assumption that $\underline{V}_2'$ and $\underline{\underline{S}}_2'$ are the fields excited with an incident power P at terminal 2 in the absence of the crack (Born Approximation). In other words, we assume that the disturbance of the fields in the void region is negligible. Therefore, from here on, we will drop the primes in the field quantities with subscript 2 to indicate that they are unperturbed fields; i.e.,

$$\delta\Gamma_{21} = \frac{i\omega}{P}\int_{V_F}(\rho\, \underline{V}_2 \cdot \underline{V}_1 + \underline{\underline{S}}_2 : \underline{\underline{c}} : \underline{\underline{S}}_1)\, dV \qquad (10)$$

This is a very drastic assumption, but has been found to produce useful results for volume voids and cracks.[2] Throughout the calculations, we will assume that

i) The crack is in the far field of the transducer, therefore, for constant power input and constant efficiency of the transducer with frequency, the fields vary proportionally to ω. There is an $\omega^{1/2}$ factor coming from the transducer itself[3] and another $\omega^{1/2}$ factor due to diffraction.

ii) The crack is small enough that, in the vicinity of the crack, the plane wave approximation to the fields is possible in the frequency range of interest.

We have investigated two types of geometries. The first one is the single transducer system Fig. 2) where only one transducer moved around a circular path, is used for both transmission and reception. In Eq. (10) this can be simulated by changing the subscript 2 to 1 everywhere. The other is the double transducer system (Figure 3) where the receiving transducer stays fixed in the direction normal to the crack and the transmitting transducer is moved around a circular path. By angular scattering, we mean the variation of transmission (or reflection) coefficient (normalized with respect to the value for $\theta = 0$) with the angle θ defined in Figs. 2 and 3. By frequency response, we mean the variation of the (arbitrarily normalized) reflection coefficient for normal incidence ($\theta = 0$) with frequency. The arbitrary normalization is due to the fact that we cannot evaluate P in Eq. (10) without the knowledge of the transducer used in an actual experiment.

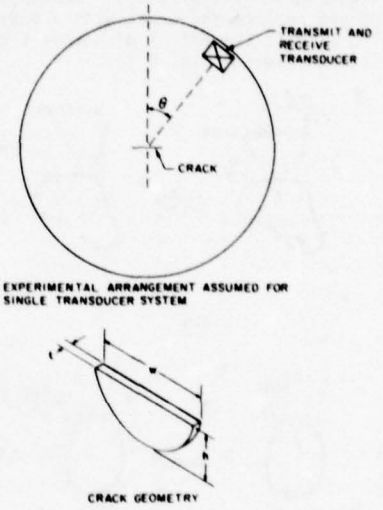

Fig. 2. Single transducer system and crack geometry

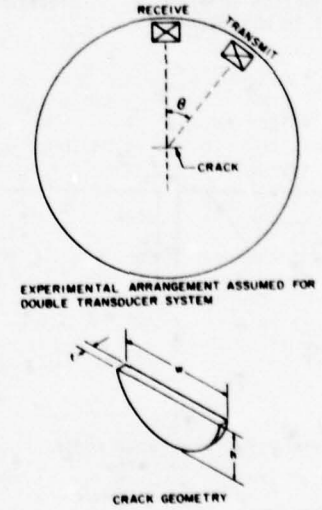

Fig. 3. Double transducer system and crack geometry

Throughout the analysis, we assume that the crack is elliptic in cross section and uniform in thickness.

"Kirchoff" Approach – Consider an electromagnetic problem in which a set of sources are radiating in the presence of a conductive obstacle (Fig. 4a). Using the induction theorem,[4] one can replace the incident field by equivalent surface currents in the presence of the obstacle. The problem is still as

hard as the original problem, but for some geometries, one can use image theory to simplify the problem. Using the same idea we can say that the effect of the incident ultrasonic field on a void can be represented by a body force layer with the void present (Fig. 4b). In what we call "Kirchoff" approach, we neglect the effect of "images" to be considered and replace the crack with a body force layer which cancels the effect of normal traction of the incident field (Fig. 5).

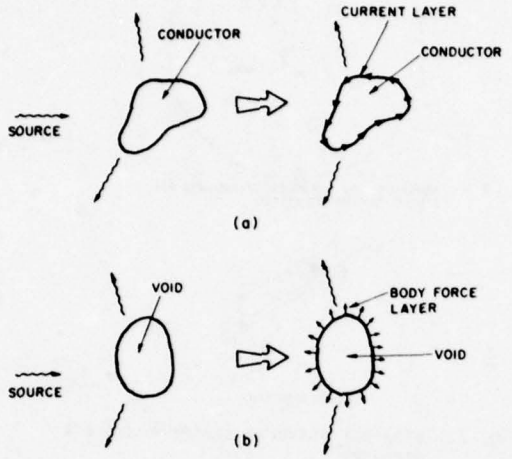

Fig. 4. Induction theorem (a) in electromagnetics, (b) in ultrasonics.

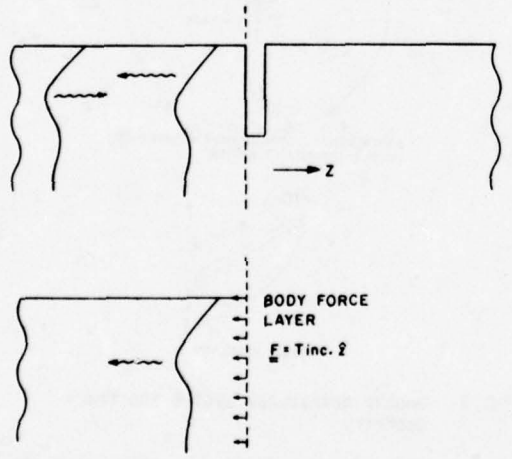

Fig. 5. "Kirchoff" approach to the scattering problem.

For the general geometry shown in Fig. 6 , defining the Rayleigh wave field modes, as

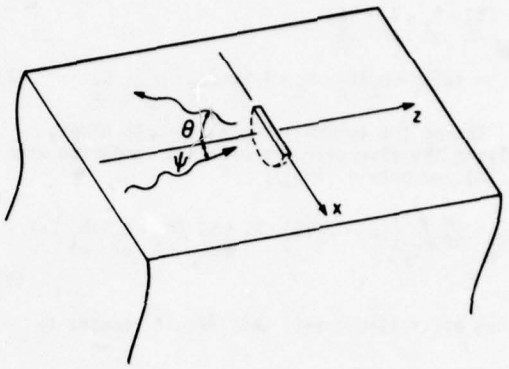

Fig. 6. Coordinate system used in defining Rayleigh wave modes.

$$\underline{V}_{\mu} = \underline{V}_{\mu}(x,y)e^{-i\mu z} \qquad (11)$$

$$\underline{\underline{T}}_{\mu} = \underline{\underline{T}}_{\mu}(x,y)e^{-i\mu z} \qquad (12)$$

where

$$\mu = \beta \cos \psi \qquad (13)$$

and using mode expansion techniques,[3] it can be shown that

$$a(\theta) \propto \frac{1}{\lambda} \int_{S_F} (V \cdot F)\, dxdy \qquad (14)$$

where

- F is the body force distribution over the crack surface in Figure 5,
- V is the modal field propagating in the θ direction,
- θ is the angle between the propagation vector of the scattered wave component and normal vector to the crack,
- $a(\theta)$ is the amplitude of the scattered field in the θ direction.

Numerical Methods — The integrals in Eqs. (10) and (14) were first converted to a single integral along the depth of the crack. That integral was then evaluated using 16 point Gauss' Integration Formula.[5] The calculations were carried out and plotted using an HP 9820 calculator. The results were also checked for accuracy with those calculated using the IBM 370 computer in double precision mode.

Comparison of Methods – For deep cracks ($h > \lambda$) where the width is in the order of several wavelengths, one can form a model based on geometrical and optical diffraction theory[6,7] and can deduce that the backscatter pattern for a single transducer system goes as sinx/x where

$$x = 2\pi \frac{W}{\lambda} \sin\theta$$

and the transmission pattern for double transducer goes as sinx/x where

$$x = \pi \frac{W}{\lambda} \sin\theta \quad .$$

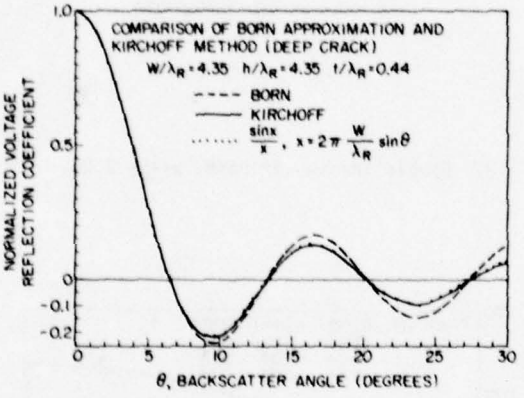

Fig. 7. Comparison of Born, Kirchoff and the Geometrical Diffraction methods for a deep crack.

In Fig. 7 we compare our results for Born, Kirchoff, and the Geometrical Diffraction methods. The crack is fairly deep and single transducer geometry is used. All three methods agree reasonably well. From the position of the nulls, one can determine the width of a deep crack. In Fig. 8 the same comparison is made for a shallow crack. We observe that the nulls of the patterns shift for a shallow crack. Note that the amplitude level for Kirchoff approximation is almost the same as that for sinx/x but the amplitude for Born is always greater. Experimentally, the reflection coefficient amplitude is very much larger than sinx/x . For this reason we consider that the Born Approximation gives more realistic results than Kirchoff.

In Figs. 9 and 10 we show the shift of null for another crack with two different thicknesses. As is easily seen, the thickness change does not cause a null shift. In Fig. 11 we plot the effect of thickness change more explicitly. The only effect is the increase in relative amplitudes.

For the double transducer system, we observe the same behavior except that the position of the first null occurs at the position of the second null for the single transducer system. In Fig. 12 we show the null shift for the double transducer case.

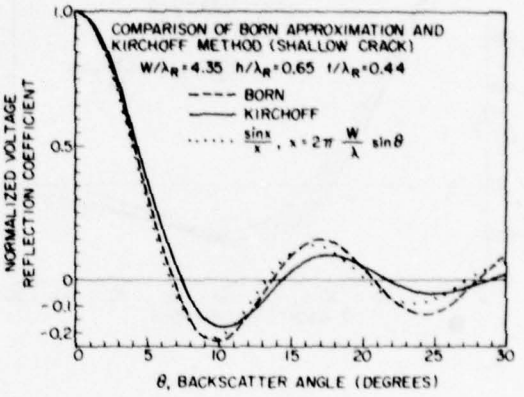

Fig. 8. Comparison of Born and Kirchoff methods for a shallow crack.

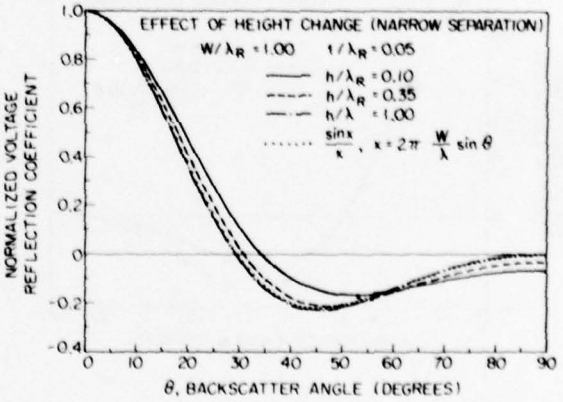

Fig. 9. Effect of height change for a thin crack.

In Figs. 13 and 14 we show the frequency response (both curves normalized with the same value estimated from experimental results) at normal incidence for some EDM notches[8] tested by Khuri-Yakub and co-workers[9] at Stanford. Although we do not obtain the resonances observed experimentally, the theoretical calculations predict reasonably well the background variation of scattering with frequency.

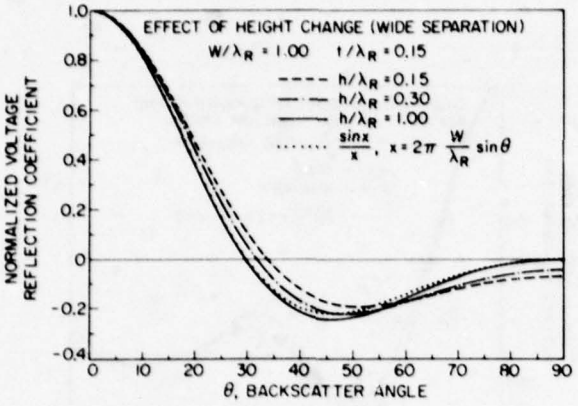

Fig. 10. Effect of height change for a thick crack (Born Approximation).

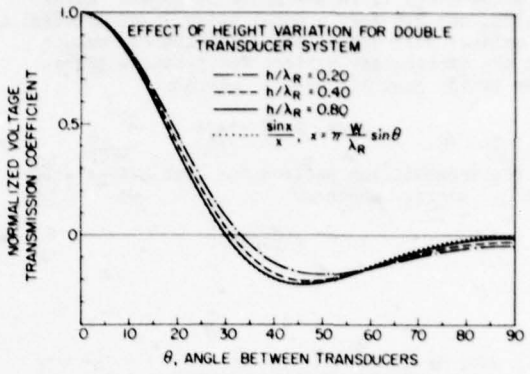

Fig. 12. Double transducer case, $w/\lambda_R = 2.00$.

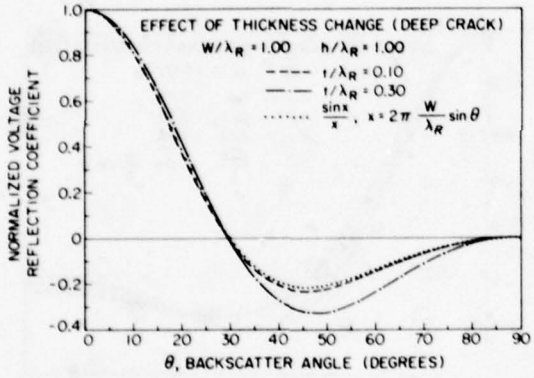

Fig. 11. Effect of thickness change (Born Approximation).

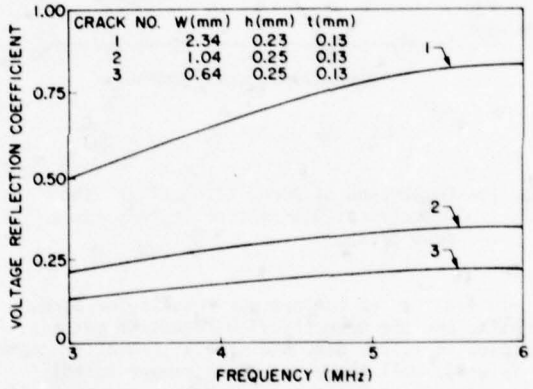

Fig. 13. Frequency response of cracks 1, 2, 3.[8,9]

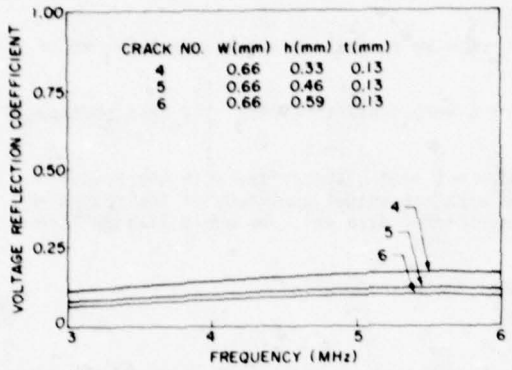

Fig. 14. Frequency response of cracks 4, 5, 6.[6,9]

Inverse Problem – The shift of the nulls with crack depth change suggests the following procedure for predicting the depth. Since at high frequencies the nulls are the same as those for sinx/x pattern, the first aim is to find a "high" frequency, f_h, where the crack is effectively deep. This can be achieved by measuring the position of a specified null (say the m-th null) at different frequencies and observing its convergence towards that of the sinx/x pattern. Once that high frequency is found, one can determine the width of the crack using the formula

$$\frac{w}{V_R} = \frac{m}{2 \sin \theta \cdot f_h} \qquad (15)$$

where V_R is the Rayleigh wave velocity.

Then at a low frequency, f_L, one can compare the position of the null with the one obtained from

$$\sin \theta = \frac{m}{2(w/V_R) f_L} \qquad (16)$$

and if a shift is observed, one can determine the height using a look-up table. If no shift is observed at the lowest frequency where a null is observed, the conclusion is that the depth is greater than $\sim 3/4\ \lambda$ at that frequency. The accuracy of the method depends on the choice of the frequency f_h. If it is chosen greater than necessary, the nulls occur with very close spacing in θ and the error in determining the width increases.

Conclusion – In this paper, we investigated the Rayleigh wave scattering from surface cracks using two approximate methods. Although we put emphasis on the Born Approximation in this paper, we are not sure which method gives better results on the shift of nulls with effective depth change. Owing to the fact that we did not have enough experimental data, we still are unable to favor one method over another.

The deficiency of the methods is that they do not predict the resonances observed experimentally in frequency response. We are now trying to obtain a variational expression for the form factor of the scattering pattern to be able to see the resonances in frequency response.

ACKNOWLEDGMENT

This research was sponsored by the Center for Advanced NDE, operated by the Science Center, Rockwell International, for the Defence Advanced Research Projects and the Air Force Materials Laboratory under Contract F33615-74-C-5180.

REFERENCES

1. B. A. Auld, "General Electrochemical Reciprocity Relations Applied to the Calculation of Plastic Wave Scattering Coefficients," submitted for publication in Wave Motion.

2. J. E. Gubernatis, E. Domany, J. A. Krumhansl, and M. Huberman, "The Born Approximation in the Theory of the Scattering of Elastic Waves by Flaws," J. Appl. Phys. 48, No. 7 (1977).

3. B. A. Auld, Acoustic Fields and Waves in Solids, (Wiley-Interscience, 1973), Vol. II.

4. R. F. Harrington, Time Harmonic Electromagnetic Fields (McGraw-Hill, 1961).

5. M. Abramowitz and I. E. Stegun, Handbook of Mathematical Functions (Dover, 1972).

6. F. C. Karal and J. B. Keller, "Elastic Wave Propagation in Homogeneous and Inhomogeneous Media," J. Acoust. Soc. Am. 31, 694 (1959).

7. B. R. Tittmann, F. Cohen-Ténoudji, M. de Billy, A. Jungman, and G. Quentin, " A Simple Approach to Estimate the Size of Small Surface Cracks with the Use of Acoustic Surface Waves," accepted for publication in Appl. Phys. Letters.

8. Steel sample courtesy of C. Fortunko of Rockwell International Science Center.

9. B. T. Khuri-Yakub, G. S. Kino, J. C. Shyne, M. T. Resch, and V. Domarkas, "Surface Crack Characterization: Geometry and Stress Intensity Factor Measurements," Paper submitted to the ARPA/AFML Conference, La Jolla, 1978.

DISCUSSION

Walter Kohn (University of California, San Diego): Could you please clarify one point for me? On the one hand you explain that you are referring to earlier remarks to the effect that, for the crack, the born approximation doesn't really give anything. On the other hand, you then show the results. Could you clarify this situation?

B.A. Auld (Stanford University): What I'm saying, Walter, when we're talking about born here, we're talking about EDM slots. They have a finite effect.

Walter Kohn: However, you seem to get good results even for a very small thickness. Is that because you just show relative values?

B.A. Auld: Yes. We are looking at the variation and we have not made a comparison with the actual amplitude of the return. We haven't made a comparison with the actual amplitude of the return because, in fact, I don't know that we have enough experimental data yet. We would like to look at that.

Walter Kohn: So, only when the thing becomes very thin, then the method fails.

B. A. Auld: Something terrible happens, yes, I'm sure.

Gordon Kino (Stanford University): I think there is a form of the born approximation which can be used for cracks which is fair. With an infinitesimally thin crack, you might turn to a surface integral rather than a volume integral and assume that the displacement on the surface is the unperturbed displacement. I believe you get results out of it that are okay.

B. A. Auld: Yes, I agree with you.

Gordon Kino: It comes down, in fact, to exactly what you have said. You then turn it back into a volume integral. Further, I would like to ask about variational principles. I think there have already been variational principles derived in this field by the reciprocity theorem which would work on this.

B. A. Auld: Yes, that is true and we do want to look at that. In fact, I think you did.

SURFACE CRACK CHARACTERIZATION: GEOMETRY AND STRESS INTENSITY FACTOR MEASUREMENTS

B. T. Khuri-Yakub, G. S. Kino, J. C. Shyne, M. T. Resch, and V. Domarkas
Stanford University
Stanford, California 94305

ABSTRACT

The reflection coefficient of a Rayleigh wave at a surface crack is measured in both the long wavelength and the short wavelength limits. From the long wavelength measurement, the maximum value of the stress intensity factor is evaluated. Using glass samples, we have formed surface cracks, measured their reflection coefficient, and predicted failure stress with an error of less than 5% from the measured fracture stress. In short wavelength limit, the reflection coefficient is measured versus frequency. Length and depth resonances of the crack are observed and used to estimate the crack geometry with an accuracy of 10-20% for EDM notches in steel.

INTRODUCTION

It is important to characterize surface cracks, so as to be able to determine their size, and effect on the breaking stress of a structure. In this work, we describe two different techniques for characterizing surface cracks. The reflection coefficient of a Rayleigh wave at the crack is measured versus frequency in both the long wavelength and the short wavelength limits. From the long wavelength measurement, the maximum value of the stress intensity factor is calculated, and the fracture stress due to the presence of the surface crack is estimated. For larger cracks, the short wavelength measurement of the reflection coefficient versus frequency is employed. Length and depth resonances are detected by measuring maxima and minima in the reflection coefficient and used to estimate the length and depth of the crack. The fracture stress is then estimated from the knowledge of the exact dimensions of the crack. It is important to note both the long wavelength and short wavelength measurements are done at one angle of incidence only.

STRESS INTENSITY FACTOR MEASUREMENT OF SURFACE CRACKS

In order to understand the principles of the measurement, consider first a sample with a flat elliptical shaped crack present in the interior. When a far field stress is applied with a component σ_{zz} normal to the face of the crack, the local stress σ in the plane of the crack will be of the form

$$\sigma = \frac{K_I(s)}{\sqrt{2\pi r}} = \frac{k_I(s)\sigma_{zz}}{\sqrt{2\pi r}} \qquad (1)$$

where r is the distance along the normal from the crack edge and $K_I(s)$ is known as the stress intensity factor at a distance s along the crack edge. The crack will grow, and hence a brittle sample will break at the point where the maximum value of $K_I(s)$ exceeds the fracture toughness K_{Ic} of the material.

It was shown by Budiansky and Rice[1] that by carrying out three measurements of the reflection coefficient of an acoustic wave with a wavelength much larger than the dimensions of the crack, the maximum value of the normalized stress intensity factor (SIF), $k_I(s)$ defined in Eq. (1) could be determined. They showed that the measured normalized maximum SIF should vary by less than 10% for an elliptic crack where the ratio of major to minor axis varies from 20 to 1 for cracks of the same area.

Our aim has been to check this theory experimentally. For this purpose we decided to work with surface cracks of a roughly semi-elliptical shape, for they are easier to produce. We assumed that the same type of theory would hold for surface cracks as for cracks in the bulk. We decided to carry out the experiments with a brittle material, glass, so that the critical maximum SIF could be checked by a simple fracture test. Finally, we modified the theory to make it appropriate for use with acoustic surface waves, and to simplify the experimental measurement technique as much as possible. This was done by supposing that the crack location and alignment could be found by a high frequency measurement or in our case by locating it by eye. Then, we showed a single measurement of the reflection coefficient of a surface acoustic wave incident normal to the surface of the crack is needed to evaluate the maximum value of the normalized SIF.

The reflection coefficients of a surface acoustic wave is given by the relation[2]

$$S_{11} = \frac{i\omega}{4} \int_{S_{crack}} \sigma_{zz}\, \Delta u_z\, dS \qquad (2)$$

for the crack configuration in Fig. 1, where S_c is the crack area, σ_{zz} is the stress at the crack, before introduction of the crack, associated with an incident surface wave of unit power, and Δu_z is the displacement of crack surface. The parameters Δu_z and σ_{zz} are proportional to the equivalent quantities for an applied static stress when the depth of the crack is much smaller than a wavelength. It has been shown by Budiansky and Rice that for elliptic cracks, the displacement jump integral is also given by the relation[1,2]

$$\int \Delta u_z\, dS = \frac{1-\nu^2}{3E^2}\, \sigma_{zz}\, \frac{\pi^3}{8}\, k_{Imax}^2 \qquad (3)$$

where E is Young's modulus. By using the scattering theory, it can then be shown that the following expression for k_{Imax} of a surface crack can be obtained in terms of the reflection coefficient

of a surface wave,

$$k_{Imax} = \left[\frac{3}{2\pi^5} \frac{V_E^2}{V_s^2} \frac{\lambda_R^3 Z}{\omega f_z} \frac{|S_{11}|}{\left[1 - (V_s/V_\ell)^2\right]^2} \right]^{1/6} \qquad (4)$$

where λ_R is the Rayleigh wavelength, V_S, V_E, and V_ℓ the shear, extensional, and longitudinal wave velocities, respectively, Z the distance of the transducer from the crack, and f_z a normalized quantity ~ 0.5 tabulated by Auld for Rayleigh waves.[3,4] We note that k_{Imax} is proportional to $|S_{11}|^{1/6}$. This is because k_I is proportional to the square root of the crack size while S_{11} is proportional to the cube of the crack size. Hence a large experimental error in measuring $|S_{11}|$ results in a much smaller error in k_{Imax}.

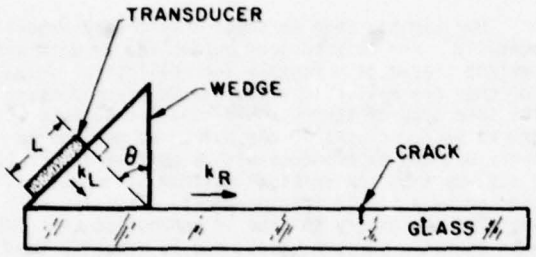

Fig. 1. Schematic diagram of surface crack and test set up.

Pyrex discs 3 mm thick by 7.6 cm in diameter in the annealed condition were prepared for fracture toughness testing by introducing small, semi-elliptical surface cracks in the center of each disc. These pre-cracks were made in a controlled way by applying a bending moment of approximately 2 Newton-meters to the disc, and on the side in tension, pressing a Knoop microhardness indentor quickly into the specimen with a force of 50-100 grams. This technique produces roughly half penny shaped cracks with radii between 100 and 500 micrometers (μm) depending on the combinations of bending moment and force on the Knoop indentor. Such small cracks were required to limit the crack size to less than the acoustic wavelength ~ 9 mm. Additionally, these half penny shaped cracks may be coaxed to an extended semi-elliptical shape by applying additional bending moment to the disc after the initial crack is started.

The strength of each disc in biaxial flexure was determined by the method of Wachtman, et al.[5,6] This involves supporting the specimen on three equally spaced balls concentric with the load, which are applied to the center of the specimen by a flat small diameter, flat end piston.

The discs were loaded to fracture at a loading rate of approximately 60 MPa per second using an MTS System 810 servohydraulic testing machine operated in stroke control mode. The loading rate was chosen to minimize possible slow crack growth effects.[7] To further insure against environmental influences (humidity), the specimens were pumped down in a vacuum for 1 hour prior to strength testing, and subjected to a stream of dry nitrogen gas for 3 minutes prior to and during the flexure test.

Once the specimens were fractured, the geometry of the precracks was studied by examining the fracture surface with a metallograph using reflected light and at a magnification of 50 – 100 X. The aspect ratio (a/c) of the semi-elliptical surface precracks could then be easily measured using an eyepiece with a properly graduated reticle.

The stress intensity factor for the precrack is evaluated by the method of Shaw and Kobayashi.[8] This analysis was chosen because it not only takes into account the proximity of the back surface to the precrack, but also allows for the presence of linearly varying stress field along the glass width. The expression for the maximum stress intensity is

$$K_I = \frac{M_B \sigma_B \sqrt{\pi a}}{E(k)} \qquad (5)$$

where $E(k)$ is an elliptic integral of the second kind, M_B is a magnification factor which takes into account the aspect ratio and the proximity of the crack depth to the neutral axis, σ_B is the maximum bending stress at the surface of the specimen, and a is the length of the semi-minor axis (depth) of the precrack.

The ten samples tested gave a normally distributed set of fracture toughness measurement, and the mean value of fracture toughness, K_{IC}, at a confidence level of 90% is: 0.76 ± 0.04 MPa $m^{\frac{1}{2}}$. This compares very well to Wiederhorn's experimental results of 0.75 ± 0.010 MPa $m^{\frac{1}{2}}$ for 6 pyrex specimens and 0.778 ± 0.011 MPa $m^{\frac{1}{2}}$ for 8 specimens.[9]

The experimental set-up for measuring the acoustic surface wave reflection coefficient $|S_{11}|$ is shown schematically in Fig. 1. A wide band, high efficiency wedge transducer[10] is used to excite and detect the surface acoustic waves. The transducer has a center frequency of 3.4 MHz, a bandwidth of 50% and a one-way insertion loss of 9.2 dB. Calibration of the transducers was carried out by measuring the transmission between a pair of transducers, as described in reference 10. All measurements were taken in the far field of the transducer ($Z > w^2/\lambda_R$).

A set of acoustic measurements were taken with the front of the wedge a distance $Z = 2.3$ cm from the crack and with the acoustic surface wave normal to the crack surface. The measurements were taken in the bending jig, using a bending moment of approximately 2 Newtons-meters to ensure the crack was open.

A series of reflection measurements on 10 different cracks was made, and k_{Imax} calculated from Eq. (4).

In Fig. 2 the acoustic prediction of σ_C is plotted against the mechanically measured value of σ_C for 10 specimens. A least squares fit of this data indicates a linear relationship between theoretical and experimental measurements with a slope of 0.85. We see that for larger, more irregular cracks, where the assumption of the theory that the diameter of the crack is less than 1/4 wavelength is not well satisfied, the error between theory and experiment increases. It is interesting to note that the effect of the ellipticity of some of the small surface precracks appears not to affect the accuracy of the acoustic prediction of k_{Imax} to any appreciable degree. This confirms the prediction of Budiansky and Rice[1] that effect, if any, should be less than 10%.

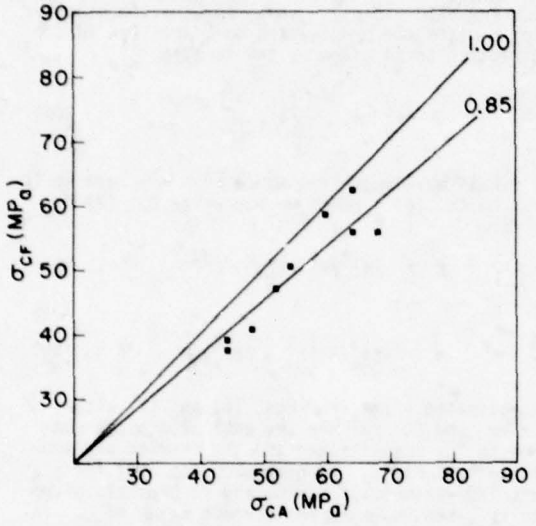

Fig. 2. Actual fracture stress versus predicted fracture stress.

LENGTH AND DEPTH MEASUREMENT OF SURFACE CRACKS

Several acoustic techniques for the purpose of determining crack size have been reported in the literature. For instance, Tittman et. al.[11] have measured the length of a crack accurately, by determining the scattering of a Rayleigh wave as a function of angle. As this function has a $\sin\theta$ dependence the length of the crack can be estimated from the distance between the nulls. The problems with this technique are that it assumes that space is available to carry out the angular scattering measurement, and gives no information about the depth of the crack. In another example, Lidington, et al.[12] discuss several techniques for determining the depth of a crack several wavelengths deep, but do not determine its length.

In our work, we measure the reflection of the crack versus frequency at normal incidence only. When a surface acoustic wave excites a crack, of the type shown in Fig. 3, its edges act as sources that excite surface waves which propagate along the crack surface. We postulate that when the crack is a multiple of a half wavelength long (the x direction) it acts as a resonator and tends to absorb energy, whereas when it is $(2n+1)\lambda/4$ long, where λ is the wavelength, it exhibits very little displacement of its top edge and so there is a maximum in the back scattered reflected signal. Similarly, when the depth (y direction) of the crack is a multiple of a half wavelength long the top surface displacement of the crack tend to be very small, as it is at its tip, and so there is again a maximum in the reflection coefficient of a wave incident on the crack. Thus, even though it is difficult to calculate end effects, we might expect that we could estimate the crack length a and depth b from the formula

$$a = V_x/2\Delta f_x \tag{6}$$

$$b = V_y/2f_y \tag{7}$$

where V_x, V_y are the surface wave velocities in the x and y directions on the crack surface and Δf_x is the frequency separation between the reflection maxima, while f_y is the frequency for a reflection maximum when the depth is one half wavelength.

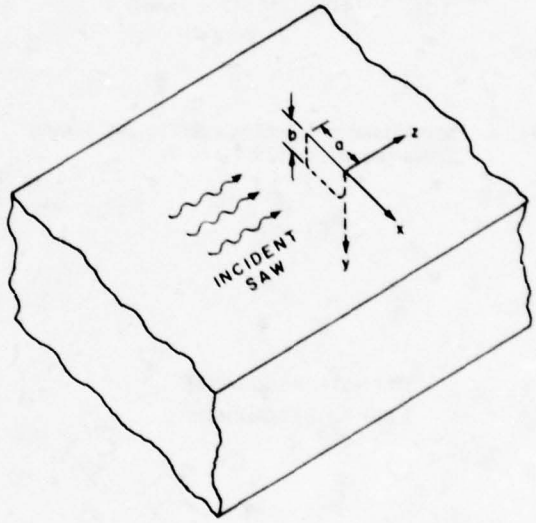

Fig. 3. Schematic diagram of crack configuration.

We carried out our experiments on 6 EDM notches of known length and depth in a steel sample.[13] We use a highly efficient wide bandwidth wedge transducer to excite the SAWs. The transducer had a center frequency of 5 MHz and a 3 dB fractional bandwidth of 50%.[10] The reflection coefficients of the notches versus frequency are shown in Figs. 4 and 5. The length resonances and a half wavelength depth resonances can be clearly seen. We use this data to estimate the lengths and depths of the notches. It will be noted that the depth resonances are typically stronger than the length resonances because the excitation of the depth resonance is uniform over the length of the crack. The results obtained are very similar in nature to those for volume wave backscattering from a penny shaped crack.[14]

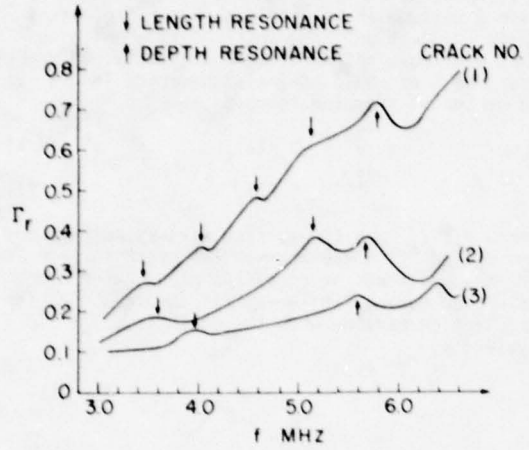

Fig. 4. Normalized reflection coefficient versus frequency of cracks 1, 2. 3.

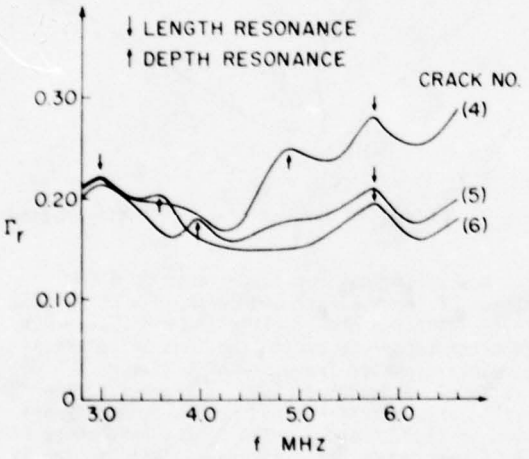

Fig. 5. Normalized reflection coefficient versus frequency of cracks 4, 5, 6.

In making the estimates of length, it is important to use a reasonable approximation for the effective surface wave velocities along the crack surface in the x and y directions. As far as propagation in the x direction is concerned, we can regard the Rayleigh wave that is excited in the x direction as being a wave propagated along the corner region bounded by the crack surface and substrate surface. It has been shown by Lagasse et al.[15] that such guided modes propagate at a velocity just slightly less than the Rayleigh velocity; so we have taken $V_x = V_R$ to calculate the length resonances and used a measured value of $V_R = 3.02\ 10^5$ cm/sec. On the other hand for the depth resonances, we regard the wave as propagating in a surface waveguide of width a, for the edges of the crack are held rigidly. Thus, for the lowest order mode, we take the propagation constant k_y in the y direction to be given by the formula

$$k_y^2 = \frac{4\pi^2 f_y^2}{V_R^2} - \frac{\pi^2}{a^2} \tag{8}$$

for a half wavelength resonance $k_y b = \pi$ and as is given by Eq. (6). Hence we may write Eq. (7) in the form

$$b = (4f_y^2/V_R^2 - 1/a^2)^{-1/2} \tag{9a}$$

or

$$b = (V_R/2)\left[f_y^2 - (\Delta f_x^2)\right]^{-1/2} \tag{9b}$$

The estimated sizes from Eqs. (6) and (7) with $V_y = V_R$ and Eq. (9) are the estimated sizes compared to the actual sizes and the results are summarized in Table I. We have used Eq. (9b) for a corrected estimate of depth, and in brackets given results based on using the correct value of a in Eq. (9a). It will be seen that because the length resonance estimate is somewhat in error, the use of the correct value of a can give considerably better estimates of the depth of the crack. The maximum error will be seen to be of the order of 18% and the results are often considerably better than this.

It is worthwhile to note that such resonances should be obtained where the angle of incidence is not normal to the crack as the same phenomena takes place. Hence only one angle of incidence on a crack need be available for an accurate crack size estimation. Furthermore as the basic technique is one by which resonances are determined, we might expect to be able to generalize it to determine resonances of odd shaped cracks, and estimate their major dimensions. Working with B. A. Auld we are developing a theory to predict the nature of the scattering which we hope will provide further insgiht into the phenomenon.

ACKNOWLEDGEMENTS

This work was supported partly by NSF contract No. DMK-76-00726 through the Center of Materials Research at Stanford University, and partly by the Office of Naval Research under Contract N00014-78-C-0283.

TABLE I. Estimate of Length and Depth

Crack #	Actual Length a (mm)	Frequency Shift Δf_x MHz	Estimated Length a - Eq.(6)	Error	Actual Depth b (mm)	Frequency f_y for Maximum Reflection	Estimated Depth Eq. (7) $v_x = v_R$	Corrected Estimate Depth Eq. (9)	Error in Estimated Depth %
1	2.34	0.56	2.69	+15	0.228	5.8	0.26	0.261 (0.261)	+14 (+14)
2	1.04	1.54	0.98	- 6	0.254	5.7	0.265	0.275 (0.274)	+8.3 (+8.3)
3	0.64	2.44	0.619	-3.3	0.254	5.6	0.269	0.296 (0.30)	+16.5 (+17)
4	0.66	2.8	0.53	-18	0.33	4.9	0.308	0.378 (0.348)	14.7 (5.8)
5	0.66	2.8	0.53	-18	0.347	4.0	0.378	0.529 (0.668)	15.7 (+1)
6	0.66	2.8	0.53	-18	0.587	3.6	0.419	0.668 (0.54)	+11 (+2)

REFERENCES

1. B. Budiansky and J. K. Rice, "On the Estimation of a Crack Fracture Parameter by Long Wavelength Scattering," Preprint of a Report for ARPA Materials Research Council, July 1977.

2. G. S. Kino, "The Application of Reciprocity Theory to Scattering of Acoustic Waves by Flaws," accepted for publication in J. Appl. Phys.

3. B. A. Auld, "General Electrochemical Reciprocity Relations Applied to the Calculation of Plastic Wave Scattering Coefficients," submitted for publication in Wave Motion.

4. B. A. Auld, Acoustic Fields and Waves in Solids, (Wiley-Interscience, 1973), Vols. I and II.

5. J. B. Wachtman, Jr., W. Capps, and J. Mandel, "Biaxial Flexure Tests of Ceramic Substrates," J. of Materials, 7, 188-194 (1972).

6. A. F. Kirstein and R. M. Wooley, J. of Research, National Bureau of Standards, JNBAA, 71C, 1-10 (1967).

7. A. G. Evans and H. Johnson, "The Fracture Stress and Its Dependence on Slow Crack Growth," J. Materials Science 10, 214-222 (1975).

8. R. C. Shah and A. S. Kobayashi, "On the Surface Flaw Problem, The Surface Crack: Phys. Problems and Computational Solids," Presented at Winter National Meeting of ASME, New York November 26-30 (1972).

9. S. M. Wiederhorn, "Fracture Surface Energy of Glass," J. Am. Ceramic Soc. 52(2) 99-105 (1969).

10. J. D. Fraser, B. T. Khuri-Yakub, and G. S. Kino, "The Design of Efficient Broadband Wedge Transducers," Appl. Phys. Letters 32(11) (1 June 1978).

11. B. R. Tittman, F. Cohen, M. Tenoudji, A. deBilly, A. Jungman, and G. Quentin. Accepted for publication in Appl. Phys. Letters.

12. B. H. Lidington, D. H. Saunderson, and M. G. Silk, Nondestructive Testing, August 1975.

13. Steel sample courtesy of C. Fortunko of Rockwell International Science Center.

14. J. D. Achenbach, A. K. Gautesen, and H. McMaken, Rockwell International Science Center Report #SC595.32SA.

15. P. E. Lagasse, I. M. Mason, and E. A. Ash, IEEE Trans. M.T.T., MTT-21, 225-236 (April 1973).

DISCUSSION

M. Srinivasan (Carborundum): *You discussed the results on glass. Do you expect imaging in ceramics to be more difficult?* It can be very difficult with ceramics.

B. T. Khuri-Yakub (Stanford): We believe that this work could be directed to ceramics and we are in the process of setting up experiments to try these with Tony Evans.

SURFACE WAVE SCATTERING FROM ELLIPTICAL CRACKS FOR FAILURE PREDICTION

B. R. Tittmann*, O. Buck and L. Ahlberg
Rockwell International Science Center
Thousand Oaks, California 91360 USA

M. De Billy, F. Cohen-Tenoudji, A. Jungman, and G. Quentin
Groupe de Physique des Solide de L'Ecole Normale Superieure**
Universite Paris VII, Tour 23, 2 Place Jussieu
75221 Paris Cedex 05, France

ABSTRACT

The scattered radiation patterns of surface cracks irradiated by acoustic surface waves are interpreted to provide estimates of crack length and aspect ratio, geometric crack parameters needed to enable failure prediction. The technique is demonstrated for circular and elliptical cracks as small as 100 μm in depth with an accuracy of about 10%. The key features are the positions and spacing of peaks and nulls in angular and frequency dependence of scattered surface intensity. A simple model based on optical diffraction theory is demonstrated on cracks in commercial hot-pressed silicon nitride studies at 100MHz and on spark eroded slots in commercial aluminum studies at 2-10 MHz. The results are used to calculate the stress intensity factors and to describe the direction of crack propagation for a variety of real and simulated cracks. Implications of the technique with respect to crack closure and effects of stress and time are also discussed.

INTRODUCTION

Surface cracks are playing an ever increasingly important role in the fracture of structural materials and are now being given concentrated attention from the point of view of characterization towards more effective failure prediction. In a recent paper Doyle and Scala[1] presented a review of both bulk and surface wave ultrasonic methods of the measurement of the depth of (part-through) cracks. They give a rather extensive survey of the literature and considered the research which relates to techniques for measuring crack depth by studying the scattered pulse amplitude, by using time-of-flight methods, or by carrying out ultrasonic spectroscopic analysis. On the basis of the techniques developed up to the time of their survey, they suggested that measurements of the transit time of bulk waves appears most likely to provide simple and reliable depth measurements in the near future.

On the other hand, since this review was written there have been several reports on new techniques and approaches using surface waves which show considerable promise. Khuri-Yakub and Kino[2] have developed a new technique for exciting high-frequency (100 MHz range) surface and shear acoustic waves on non-piezoelectric materials. Fraser, Khuri-Yakub and Kino[3] have produced a design for an efficient broad-band wedge transducer. Resch et al.[4] have carried out measurements with a surface wave probe and predicted fracture stresses in good agreement with those measured. The calculations of the fracture stress were based in part on theoretical developments by Kino.[5] Domarkas et al.[6] have observed structure in the frequency dependence of the acoustic surface reflection coefficient associated with a rectangular slot which they have interpreted in terms of resonances across the length and depth of the slot. Ayter, Auld and Tan[7] have developed two theoretical approaches based on real reciprocity relations for the scattering of Rayleigh surface waves by part-through cracks. In a short letter we[8] have reported experimental data and a simple model on the estimation of the size of small surface cracks.

In this paper we present the details of our work both for crack length and crack depth determination and cast these results into the context of the fracture mechanics of part-through cracks to delineate the stress intensity range (for a given stress application) and determine the remaining fatigue life of structural materials. The considerations include, specifically, the differences between cracks in ductile and brittle materials, the degree of crack closure, the crack orientation, and the specimen geometry. These factors are shown to play an important role in selecting those types of scattering measurements most directly useful for failure prediction.

CRACK PARAMETERS FOR FAILURE PREDICTION

Since failure prediction is the ultimate objective of the quantitative NDE (nondestructive evaluation) studies reported here, our approach has been to delineate the important fracture mechanics parameters and ask what ultrasonic measurements must be made, and how they must be interpreted to obtain these parameters as directly and accurately as is needed for failure prediction.

Table I presents values for parameters which are important in defining the approach to the study of cracks in technologically important materials. It lists some key alloys and ceramics ordered according to their ductility (percent elongation) and shows the importance of considering both the case of fatigue cycling to failure and brittle fracture. In columns three and four of Table I, respectively, are listed approximate values of

*Part of the work by B. R. Tittmann was carried out during his stay at Universite Paris VII as "professor accocie".
**Laboratoire associe au C.N.R.S.

TABLE I

ORDER OF MAGNITUDE ESTIMATES OF CRITICAL FLAW SIZES IN METAL AND CERAMIC SYSTEMS, ORDERED ACCORDING TO DUCTILITY

Material	% Elong.	Crit. Flaw Size (mm)	f_c
2024-T351 aluminum	20	25.0	20 kHz
18Ni-4Co-20C steel	19	18.0	25 kHz
6Al-1Mo-1V @ titanium	17	14.5	35 kHz
2014-T651 aluminum	13	4.5	100 kHz
6Al-4V titanium	13	2.5	200 kHz
A540 steel	13	1.5	300 kHz
D6AC steel	10-13	1.0	500 kHz
Hot pressed Si-Nitride	~0	0.05	30 MHz
Sintered Si-Nitride	~0	0.02	80 MHz
Silica Glass	~0	0.003	150 MHz
Soda Lime Glass	~0	0.001	500 MHz

$\sigma_{max} = 0.5\,\sigma_{yield}$

critical flaw sizes a_c for these materials based on an assumed stress of one-tenth of the yield stress and the critical ultrasonic frequencies f_c corresponding to the criterion $ka_c = 1$, where $k_c = 2\pi f_c/v$ is the ultrasonic wave vector (v is the ultrasonic wave velocity). Very qualitatively speaking the regime of frequencies below f_c is called the Rayleigh regime and long- wavelength techniques such as already described by Resch et al.[4] are appropriate. Considering the low values of f_c shown for some of the more ductile alloys, such factors as specimen size and Rayleigh wave generation techniques are seen to be important limitations on the general usefulness of the Rayleigh regime.

Driven by these considerations this paper attempts to address the short wavelength regime, i.e., $ka_c \geq 1$, emphasizing cracks in ductile materials but demonstrating the applicability of the ultrasonic techniques to cracks in ceramics, where the critical crack sizes are small and therefore the wavelength must be very short. To demonstrate the somewhat specialized nature of the approach that must be taken for ductile materials, Fig. 1 displays a typical example of part-through

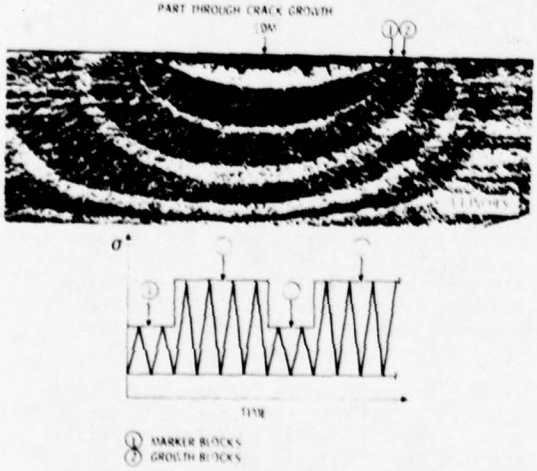

Fig. 1. Photo of crack surface for metal plate fatigue-cycled to failure.

growth of an EDM notched sample[9] where the progress of crack propagation during cyclic fatigue is depicted in terms of marker and growth blocks (light and dark shaded regions), respectively, which correspond to growth under low and high applied stress. Since the crack growth takes place over a relatively long time it is important to speak in terms of a stress intensity range and a remaining life in terms of the number of cycles for failure. After Irwin[10] the stress intensity range (in mode I) ΔK_I is

$$\Delta K_I = C\Delta\sigma\sqrt{a/Q} \qquad (1)$$

where $C = 1.95$

$$Q = \Phi^2 - 0.212\left(\frac{\sigma_{max}}{\sigma_{yield}}\right)^2$$

$$\Phi = \int_0^{\pi/2} [\sin^2\psi + (a/c)^2\cos^2\psi]^{1/2}\, d\psi$$

and where $\Delta\sigma$ is the stress range, a is the crack depth, 2c is the crack length, σ_{yield} is the yield stress, σ_{max} is the maximum applied stress and ψ is the angle in the crack plane with respect to the crack length. The symbols are identified in Fig. 2a. For a given applied stress the stress intensity range ΔK_I may be calculated from a knowledge of the metallurgy of the part (i.e., σ_{yield}), the crack depth a and the depth-to-length ratio.

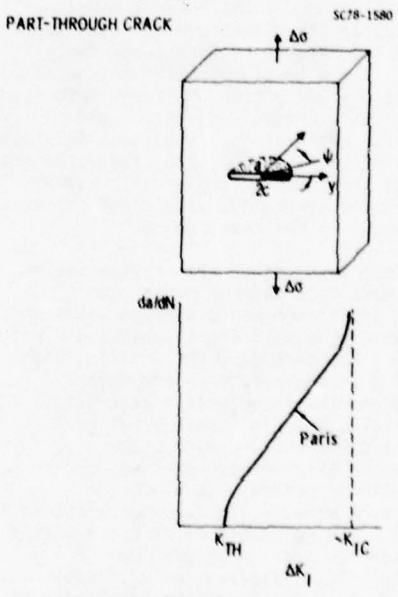

Fig. 2. (a) Geometry of part-through crack (b) Schematic graph of functional dependence of crack growth rate on stress intensity range ΔK_I.

Assuming the crack is in the Paris regime of validity, the crack-depth-increase-per-unit fatigue cycle da/dN is[11]

$$da/dN = A(\Delta K_I)^m \qquad (2)$$

where A and m are material constants. The remaining life or number of cycles to failure is then

$$\Delta N = \frac{2}{(m-2)A(CQ^{1/2}\Delta\sigma)^m}\left\{\frac{1}{a^{(m-2)/2}} - \left(\frac{CQ^{-1/2}\sigma_{max}}{K_{1c}}\right)^{m-2}\right\} \qquad (3)$$

Failure is imminent, i.e., N = 0, when

$$a_c = \left(\frac{K_{1C}}{CQ^{-1/2}\sigma_{max}}\right)^2 \qquad (4)$$

A typical curve of da/dN as a function of ΔK_I is shown schematically in Fig. 2b. Equation (4) was used to estimate the critical flaw sizes of Table I.

In summary, aside from the metallurgical properties of the material, the important fracture mechanics parameters which NDE must give are the crack depth and length.

EXPERIMENTAL APPROACH

The approach used in these measurements embraces both the techniques of Rayleigh generation/detection and spectroscopic analysis. These techniques are in general not new, since surface waves have been used for quite some time as a basis of measurement of crack depth. For example, Reinhardt and Dally[12] noted that the variation of the surface wave transmission and reflection coefficients with crack depth might provide results for cracks less than half a wavelength deep. Buck, Frandsen, and Marcus[13] have used surface waves to monitor crack growth and crack closure. Silk[14] has made crack depth measurements by detecting S-waves produced by mode conversion of R-waves at the crack tip. Cook[15], Hudgell, Morgan and Lumb,[16] Hall[17] and Lidington and Silk[18] have used surface timing methods for crack depth measurement. Ultrasonic spectroscopy originally applied primarily to bulk defects as discussed by Gericke[19] and Brown[20] has also now been applied to surface flaws with Rayleigh waves. Morgan[21] used the time reconstitution method and crystal method to not only detect the crack, but also map its morphology.

Our approach combines several of these methods in a new way by studying the scattered radiation pattern of surface waves from cracks in the time and frequency domain. In some of the experiments, commercial broad-band longitudinal wave transducers were used with water wedges to provide both the transmitter and receiver. The actual transducer configuration consisted of a small metal box which was filled with water and into which was mounted a Parametrics M-series transducer whose inclination angle to the specimen surface was adjusted to the Rayleigh angle. The metal box was glued to the specimen surface with had low viscosity quick drying cement and in order to minimize the attenuation of the surface waves as they cross beneath the edge of the box, the edge was tapered into a knife-edge.

In other experiments at high frequencies (100 MHz) an interdigital transducer deposited on a $LiNbO_3$ delay line was used[2] on plates of commercial hot-pressed silicon nitride (NC 132) into which cracks were placed by the indentation technique which has been shown to give semi-circular crack shapes.[22] In the narrow band experiments at 2.2 MHz wedge transducers were used on plates of commercial rolled Al into which semi-circular slots had been cut by the spark erosion technique. In other broad-band experiments the transducers were again commercial broadband transducers (2-9 MHz at 3 dB) inclined to the sample surface with both transducer and specimen immersed in water at the critical Rayleigh angle. The samples were plates of Duraluminum into which slots had been cut by indentation with a flat, semi-circular tip of a hard tool. In each of the experiments the angular dependence data were obtained by either rotating the sample or the transducer about an axis through the center of the crack. The precision of determining the angle is estimated at ± 0.5 degrees.

Figure 3 shows a photograph of the apparatus of one of the experiments and depicts the goniometer that was used with circular plates and the water-wedge transducers (in the form of boxes) discussed above. Also shown are the associated electronics such as a Parametrics Pulser-Receiver and a Tektronics sampling scope which was used to digitize the rf signals received and provide an interface with a Data General S/200 Eclipse computer. This minicomputer was used to obtain the Fourier transform of the signal, which was typically divided by the transducer transfer functions and to so calculate, and display the normalized magnitude of the resulting Fourier transform. The transducer transfer function was obtained in a separate experiment in which the surface waves were back-scattered from an ideal scatterer, typically, a sharp edge of quasi-infinite extent.

RESULTS

Theoretical Model

A rigorous treatment of the scattering of acoustic surface waves from semi-circular surface cracks at arbitrary wavelength-to-crack radius ratio is not presently available. However, approximate theories[23,24] in the long and short wavelength limits are currently being given much attention and preliminary comparisons between theory and experiment show high promise.

In particular Auld et al[7] have formulated two theoretical approaches based on real reciprocity relations; one of them utilizes the volume integral form of the reciprocity relation, which gives the scattering coefficient as an integral o product of unperturbed and perturbed fields and Bor 's approximation is applied to evaluate the perturbed fields. The other approach utilizes the ultrasonic analog of the induction theorem in electromagnetics, in which the crack is represented

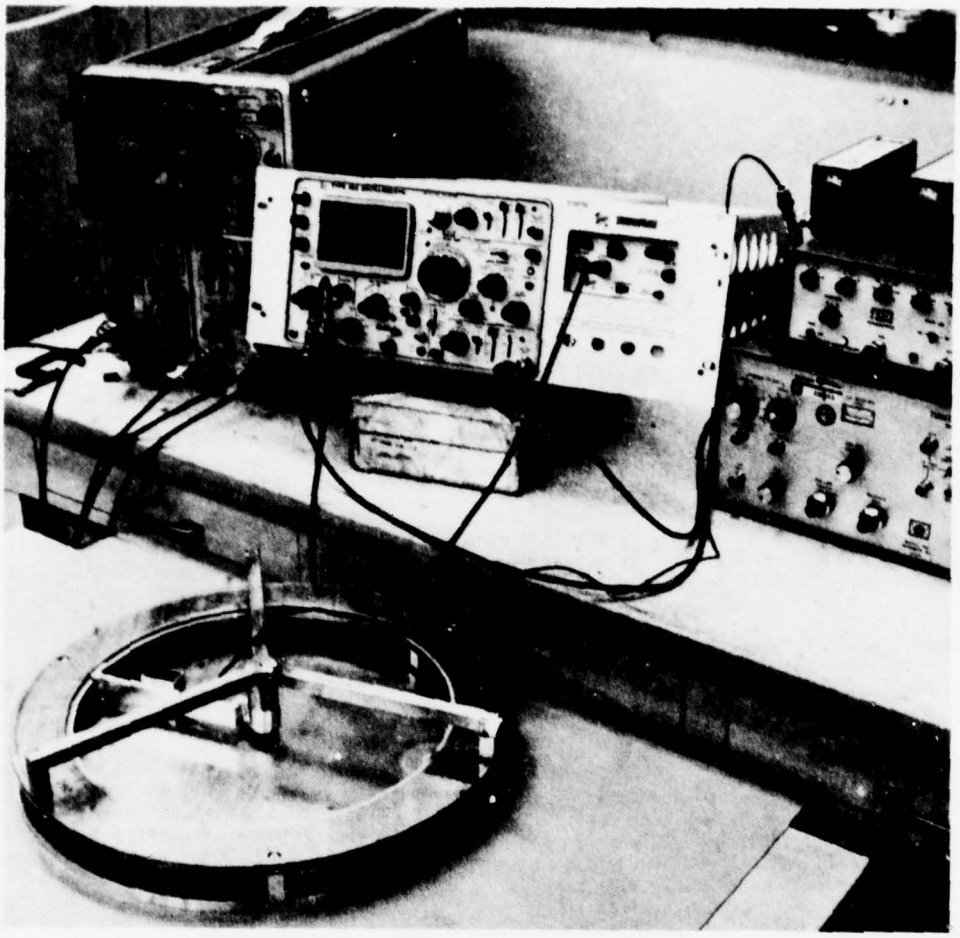

Fig. 3 Photo of apparatus, sample holder, and transducer goniometer.

by a surface distribution of equivalent body forces. This force distribution is then approximated and normal mode techniques are used to find the scattered amplitude. These theoretical approaches apply in the same regime as is of interest here and show agreement with the experimental results for angular scattering reported on here. However, in the frequency response the theory does not predict the resonances observed experimentally, although showing agreement with the background radiation.

We have formulated a model which we have found useful in analyzing both the angular and frequency dependencies of the Rayleigh wave scattering by a surface crack. This model is based on geometrical and optical diffraction theory and is applicable when the crack is long and deep compared to the Rayleigh wavelength. The interaction may be viewed as being concentrated near the surface, since the fields of the wave propagating on the free surface diminish rapidly or decay as they reach deeper into the material and are unable to probe the region near the crack tip. In this context the back-scattered radiation pattern is the Fourier transform of the complex amplitude distribution across an irradiated aperture. In general, using the mathematical expression of the Huygens-Fresnel principle,[24], we can write the field amplitude at point (u_o, v_o) as

$$U(u,v) = \iint_{\infty}^{\infty} h(u,v;\, x,y)\, U(x,y)\,dx\,dy \qquad (5)$$

where $h(u,v;x,y) = (1/i\lambda)\frac{1}{r}\exp(ikr)\cos(\overline{n},\overline{r})$ and

where $U(x,y)$ is the complex amplitude distribution across the aperture and is identically zero outside the aperture. k is the wave number and r is the distance between points (x,y) and (u,v). $\cos(\overline{n},\overline{r})$ is the obliquity factor and is approximately equal to one in this case where the distance to the detector is much greater than the maximum linear dimensions of the aperture and only a finite region about the aperture normal is used. The distance r is given by $r^2 = R^2 + (u-x)^2 + (v-y)^2$. If the Fraunhofer approximation $R \gg \frac{1}{2}k(x^2 + y^2)$ is adopted, the quadratic phase factor is approximately unity of the entire aperture and the observed field distribution can be found directly from a Fourier transform of the aperture distribution itself. Thus

$$U(u,v) = C \iint_{-\infty}^{\infty} U(x,y) \exp[-(ik/R)(ux+vy)]dxdy \qquad (6)$$

where $C = (1/i\lambda R) \exp(ikR) \exp[(ik/2R)(x^2 + y^2)]$

For a rectangular aperture with apertures ℓ_x and ℓ_y normally illuminated by a unit-amplitude, monochromatic wave

$$U(u,v) = C\, \ell_x \ell_y \operatorname{sinc}(\ell_x f_x) \operatorname{sinc}(\ell_y f_y)$$

where $f_x = u/\lambda R$, $f_y = v/\lambda R$ are the frequencies at which the Fourier transform is evaluated. The intensity (square of absolute value of U) is

$$I(u,v) = \frac{\ell_x^2 \ell_y^2}{\lambda^2 R^2} \operatorname{sinc}^2 \frac{\ell_x u}{\lambda R} \operatorname{sinc}^2 \frac{\ell_y v}{\lambda R} . \qquad (7)$$

In the context in which the interaction between the surface waves and the crack is viewed, the result is specialized to a very narrow aperture of length 2a, such that the intensity is approximately given by

$$I(\alpha,\theta,\omega) = I(0,0,\omega)(\sin^2\psi)/\psi^2 \qquad (8)$$

$$\psi = (a\omega/V_R)(\sin\alpha + \sin\theta)$$

where ψ takes into account oblique incidence of the radiation from the transmitter with an angle α to the aperture normal. In a backscattering experiment (typically encountered in a commercial application) $\alpha = \theta$ where θ is the angle of the receiver with respect to the crack normal. V_R is the Rayleigh wave velocity, ω is the frequency in radians and $I(0,0,\omega)$ is the intensity at $\alpha = 0$, $\theta = 0$ at a given frequency.

Angular Dependence

The results are summarized in Figs. 4, 5 and 6 where data and calculations are presented for the three types of experimental conditions. All three figures are similar in that they show structure typical of diffraction patterns, normalized at $\theta = 0$, i.e., the direction normal to the crack plane. The theoretical curves (solid line) are compared with the experimental data (dashed line) with a fit at $\theta = 0$. Considering the experimental errors in angle determination especially of the crack plane normal, reasonable agreement is observed between theory and experiment, especially in the positions of the nulls and peaks.

Considering the simplicity of the model the comparison with the experiment in the intensities is interesting. The experimental intensity curves generally fall above the theoretical curves, especially for the cracks in the ceramic samples. A tentative explanation is based on previous work on scattering from rough surfaces[25] which demonstrated that this behavior represents a diffuse back-scattering as from rough surfaces rather than the ideal scattering from a perfect planar reflector. This suggests the presence of roughness inside the crack, that is the crack face is not smooth but rough, and it is obvious that the crack made by the indentation technique is much rougher than that made by spark erosion technique. A following step in the experiments is to use the results to interpret the degree of roughness of the crack face from the deviation of intensities from the ideal diffraction intensities. An additional source of deviation at large angles off broadside may perhaps be attributable to the inadequacies of the model. Auld et al[7] have shown that for angles $\theta >> 10$ in backscatter experiments the Born approximation begins to yield higher amplitudes for the higher order sidelobes.

Frequency Dependence

Equations (5) and (6) show that the frequency dependence of the radiation pattern at fixed angle may also be used to derive information on the crack radius. This is demonstrated in Fig. 7 which shows the frequency dependence of back-scattered power from the spectral analysis of a broad-band pulse for a semi-circular slot of radius a = 800 μm indented into a plate of aluminum. As predicted, the graph shows the same type of diffraction pattern as those in the angular dependence studies. While this graph was obtained for $\theta = 18$, similar graphs may be generated quite readily for other angles. Such data may then be stored in the computer which can then be called upon to present the data with either angle or frequency as independent variable to show the complete equivalence of $\sin\theta$ or frequency as parameter. Figure 6 is actually a graph of the angular dependence as reconstructed at one frequency from a compilation of frequency dependence graphs obtained at various angles.

Inversion

The fields U(x,y) and V(u,v) in Eq. (6) are related by a two-dimensional Fourier transform. The inverse transform may be used to give the source distribution U(x,y) from the measured or otherwise known remote field distribution,

$$U(x,y) = C \iint_{-\infty}^{\infty} U(u,v) \exp[-(ik/R)(ux + vy)]\, dxdy \qquad (9)$$

Carrying out a procedure to evaluate (9) from known or measured field distributions constitutes the inverse scattering problem. The specific implementation of Eq. (9) is dependent of the nature of the field distribution and data format.

At this point the specific objectives of Section II come into play and the inversion is specialized to merely obtaining the fracture mechanics parameters, i.e., crack length and depth. Since the crack depth determination is accomplished by another procedure as discussed in section (5), the inversion procedure here need only provide a determination of the crack length. The Fraunhofer radiation pattern described in Eq.(8) is ideally suited to accomplish such a calculation by virtue of the nulls in the sinc function. The crack radius a is obtained by calculations based on the observed positions of the nulls in the angular

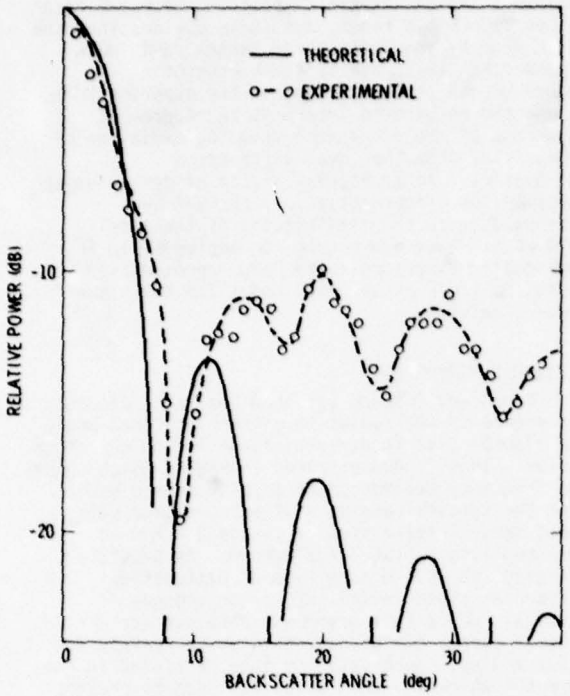

Fig. 4. Plot of relative power as a function of the back-scatter angle in acoustic surface wave experiments. The data, averaged over several runs, are for a sample of silicon nitride with a crack of radius 100 μm illuminated by wave of λ = 55 μm in a narrow band experiment at 100 MHz. The crack was produced by the indentation technique.

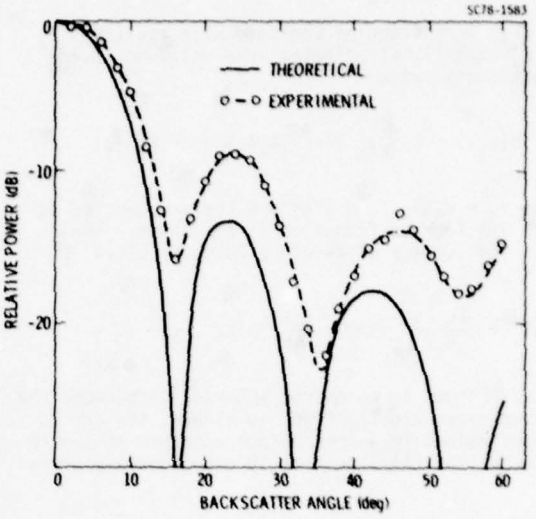

Fig. 5. Angular dependence of power of 2.2 MHz surface waves (λ = 1293 μm) back-scattered from a semi-circular slot of radius 1190 μm) cut into commercial rolled aluminum by spark erosion technique.

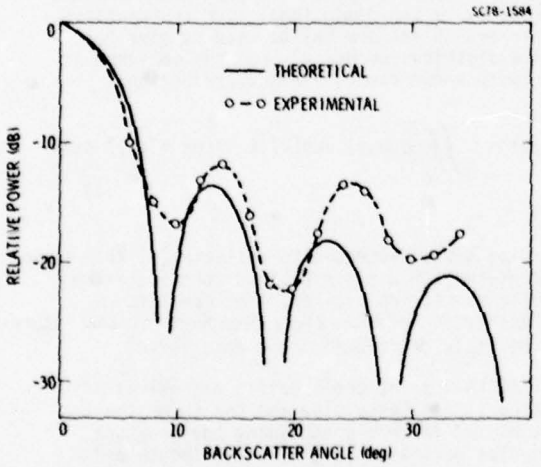

Fig. 6. Reconstruction of angular dependence of back-scattered power from spectral analysis of broadband pulses. The points were deduced at one frequency, i.e., 5 MHz (λ = 585 μm) from a series of spectra obtained for a variety of angles. The results are for a semicircular slot (radius a = 900 μm) indented into a plate of aluminum.

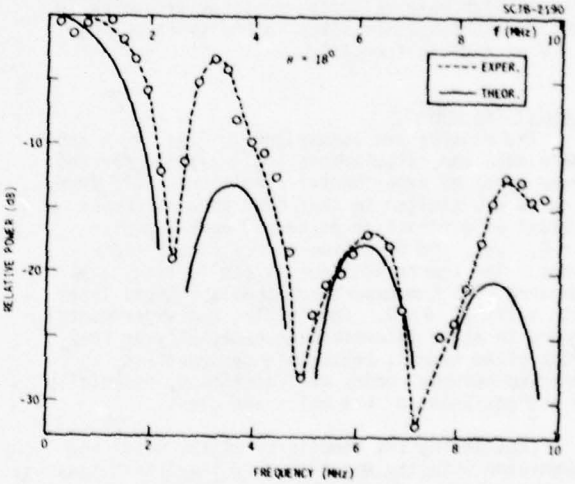

Fig. 7. Frequency dependence at fixed angle (θ = 18°) of back-scattered power from spectral analysis of broadband pulses for semicircular slot (radius a = 900 μm) indented into a plate of aluminum

(α,θ) or frequency (ω) dependence of the radiation pattern, for example: from the positions of the n^{th} null from broadside

$$a = \frac{n V_R}{\omega} / (\sin\alpha + \sin\theta). \qquad (10)$$

Since each of the nulls, by virtue of its position, can be used to predict the length of the crack with the aid of the model, a statistical distribution of estimates may be obtained, and this is demonstrated in Table II. The comparisons between the crack (slot) radii estimates and the "actual" values obtained by micrographical examination show agreement within about 10 percent. The crack lengths estimated from the data are at most equal to real crack lengths because of the shape of the crack under the surface which provides a diminishing "effective" crack length with depth.

TABLE II

COMPARISON OF ESTIMATED AND "ACTUAL" CRACK RADIUS "a"

Experimental conditions	Diffraction order	Angular positions of nulls (deg) Observed	Theoretical	Estimate of "a" (μm)	Mean estimate of "a" (μm)	"Actual" size of "a" (μm)* [1 mil = 25.4 μm]
100 MHz silicon nitride with indentation crack	n = 1	9	8	87		
	n = 2	17	16	92	93 ± 4	100 ± 3
	n = 3	25	24	96		
	n = 4	34	33	97		
2.2 MHz commercial rolled aluminum with spark erosion slot	n = 1	16	16	1170		
	n = 2	35	33	1130	1160 ± 20	1190 ± 20
	n = 3	55	54	1180		
5.0 MHz Duraluminum with indentation slot	n = 1	10	9	966		
	n = 2	19	18	897	880 ± 16	900 ± 25
	n = 3	30	28	877		

* determined by micrographical examination of crack outline on sample surface.

Crack Depth Determination

For semi-circular cracks, the treatment given above is sufficient to provide a good estimate for the crack dimension. However, whenever elliptical-shaped cracks are encountered, the crack depth or, at least, the crack depth-to-length ratio must also be obtained for use in, for example, fracture mechanical life predictions.

The crack depth is readily derived from measurements of the same type as described above. Figure 8 shows a graph of the scattered amplitude as a function of the frequency for a slot of length 0.254 cm and depth 0.039 mm spark erosion cut into a plate of commercial aluminum. In contrast to the previous experiments which were pulse-echo, the results discussed here are for a fixed transmitter oriented normal to the slot face and a receiver whose angular position is allowed to vary. The principal feature of the graph is a peak at 3.45 MHz which remains stationary in frequency as the receiver angle is increased, in contrast to the other peaks which form a background that changes rapidly with angle (see for example the curve marked $\theta = 30^0$). The stationary peaks correspond to surface waves traveling along the slot face down to the slot tip and back up again to surface of the plate. The depth b is given by

$$b = V_R/2f_b \qquad (7)$$

The peak arises because of interference between the waves scattered from the crack tip and those scattered by the edge where the slot breaks the surface of the plate. The accuracy of the crack depth estimation by this technique is given in Table III for two different crack depths.

SC78-2191

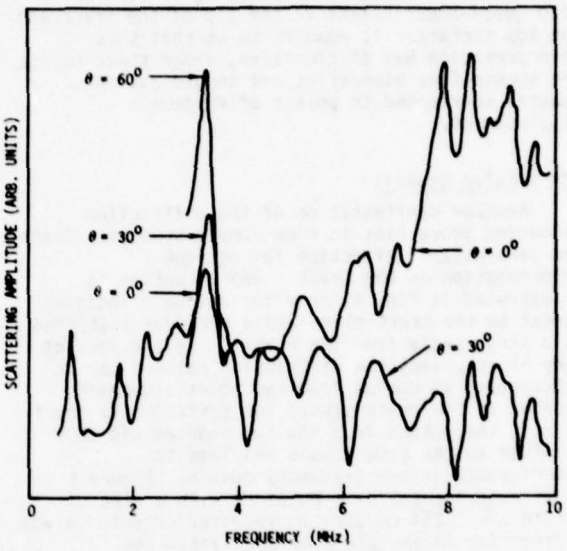

Fig. 8. Frequency dependence of scattering amplitude (pitch-catch) for an elliptically shaped slot (length 0.254 cm, depth 0.038 cm) in a plate of commercial aluminum.

TABLE III

CRACK DEPTH ESTIMATION

Transd Angle (deg)	Observ. Res (MHz)	Estim. Depth (mm)	Mean Estim. Depth (mm)	"True" Depth (mm)	Percent Error (%)
0	3.45	.412			
30	3.47	.409			
60	3.40	.418			
90	3.40	.418			
120	3.42	.415	0.408	0.38	3%
150	3.50	.406			
180	3.45	.412			
210	3.50	.406			
240	3.90	.364			
270	3.40	.418			
0	1.34	.107			
20	1.34	.107			
30	1.33	.106			
45	1.32	.099	0.104	0.102	2%
60	1.60	.089			
75	1.35	.105			
90	1.22	.116			

Domarkas et al[6] have recently reported observing peaks in the frequency dependence of the Rayleigh wave reflection coefficient obtained normal to rectangular slots. They have interpreted these peaks in terms of resonances within the slot, i.e., when the depth of the crack is a multiple of a half-wavelength long the top surface displacement tends to be very small, as it is at its tip and so there is again a maximum in the reflection coefficient of a wave incident on the crack. One may infer from this interpretation that the resonances are essentially standing surface waves with quasi-nodal points at the tip of the crack and the top surface. It appears to us that this interpretation has difficulties, since these points are stress-free boundaries and should not in general correspond to points of minimum displacement.

Short Pulse Studies

Another manifestation of the diffraction discussed above lies in time domain studies. These are particularly effective for oblique interrogation of the crack. The situation is illustrated in Fig. 4 for a surface wave incident normal to the crack plane and a receiver scattered at a large angle from the normal. In the case of very short pulses the diffraction pattern can be interpreted as coming from two point sources located at the crack tips. for sufficiently short pulses, the pulses from the two sources can be resolved in the time domain and lead to interference in the frequency domain. Figure 5 shows experimental data obtained with a slot of length a = 0.254 cm and the receiver oriented along a direction in the plane of the slot. The separation of the pulses is in good agreement with a time-delay calculated on the basis of a Rayleigh wave traveling along the length of the slot. Good agreement is also observed between the observed and calculated pulse separation at angles other than 90° as is indicated in Table IV.

TABLE IV

TIME DOMAIN PULSE SEPARATION
FOR 0.254 cm x 0.254 cm SLOT

Receiver Angle θ (degs)	Observed $\Delta\tau$ (μsec)	Theor. $\Delta\tau$ (μsec)
0	0	0
30	.4	.45
60	.7	.77
90	.9	.89

The existence of two somewhat separated pulses in the time domain is equivalent to interference in the frequency domain and Fig. 10 shows the magnitude of the Fourier Transform of the time domain signal of Fig. 9. Also shown are the calculations corresponding to the model described earlier in good agreement with the experiment with respect to the positions of the nulls and peaks. This comparison is shown more quantitatively on Fig. 11 which plots the null frequencies f_m versus the null indices m for several receiver angles. The straight lines labeled "theory" are derived on the basis of

$$f_m = m V_R/2a \sin\theta .$$

where as before 2a is the slot length and V_R is Rayleigh wave velocity.

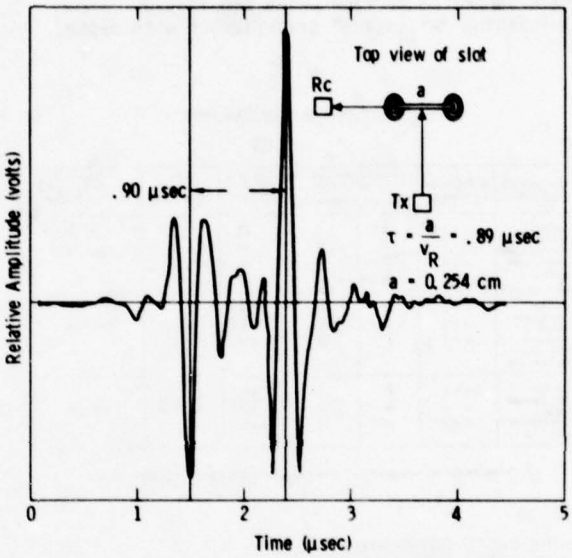

Fig. 9. Time-domain r.f wave form of signal scattered from slot (length 0.254 cm) irradiated at normal incidence.

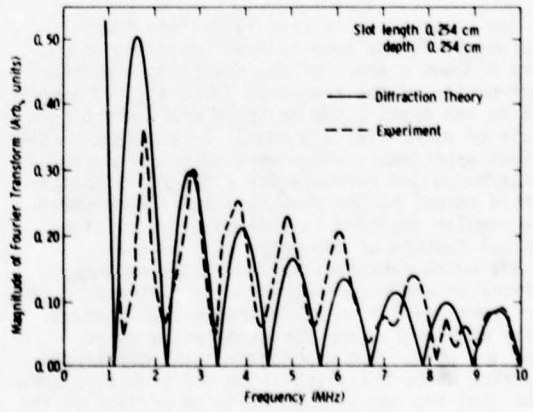

Fig. 10. Waveform of Fig. 9 in frequency domain.

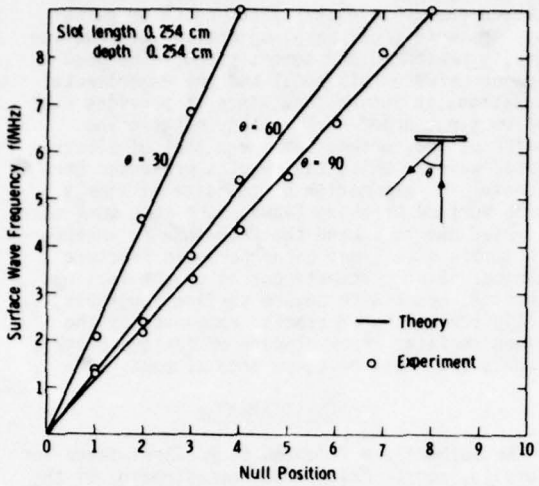

Fig. 11. Frequency domain location of nulls as a function null index for data such as shown in Fig. 10.

TABLE V

FLAW SIZE	TYPE/MATERIAL	k_I ($\sqrt{mm}$)	CRACK PROP
2.5mm, 0.4mm, ψ	EDM/ALUMINUM	1.11	$\psi = 90^0$
2.5mm, 1mm	EDM/ALUMINUM	1.26	$\psi = 90^0$
2.5mm, 2.5mm	EDM/ALUMINUM	1.41	$\psi = 0^0, 180^0$
0.4mm, 0.2mm	CRACK/SI-NITRIDE	0.40	$\psi = 0^0 \ldots 180^0$
2.5mm, 1.3mm	EDM/ALUMINUM	1.41	$\psi = 0^0 \ldots 180^0$
1.8mm, 0.9mm	CRACK/ALUMINUM	1.21	$\psi = 0^0 \ldots 180^0$

Fracture Mechanical Predictions

With the techniques described above we have examined six slot/crack configurations with various depths and lengths and have calculated the reduced stress intensity factors $K_I = K_I/\sigma_{max}$ (which describes, basically the geometry of the crack--see Eq. (1)) and qualitatively predicted the direction of crack growth based on an assumed applied stress parallel to the specimen surface and the slot/crack plane. This information is summarized in Table V. For example, the crack in silicon nitride having a length of 0.4 mm and a depth of 0.2 mm has a $K_I = 0.40\sqrt{mm}$ and is going to grow in the direction $\psi = 0, \psi = 180$ or in a direction along its length (see Fig. 2a). On the other hand, the spark eroded slot (in commercial aluminum) with dimensions 2.5 mm in length and 0.4 mm in depth has a $K_I = 1.11\sqrt{mm}$ and will grow deeper in a direction normal to the surface.

Crack Closure

Part-through crack growth in ductile materials is often associated with partial crack closure as the applied stress is changed dynamically such as during fatigue cycling or as a function of time during stress relaxation. The process is shown in more detail in Fig. 12 which displays schematically a crack in the absence and presence of applied stress. On unloading, a crack starts to close down on itself at a stress level σ_{cc}, the so called closure load. Unloading the specimen completely leaves the crack partially open, however, due to excessive compressive stresses along the closed fracture stress area. An NDE measurement capable of determining effective crack depth during partial crack closure would be important since it could determine quantities such as the crack closure stress, residual stress, and time dependent stress relaxation which are important parameters that modify Eqs. (1) and (2).[13]

PART-THROUGH CRACK GROWTH IN DUCTILE MATERIALS

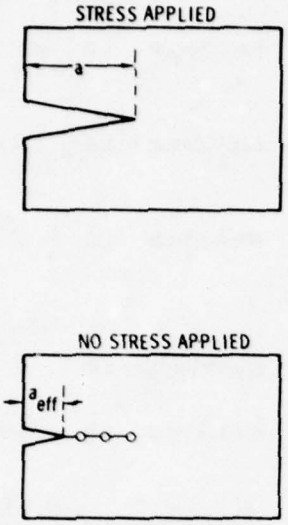

Fig. 12. Schematic of part-through crack in presence and absence of applied stress.

The crack depth measurements described above with the use of surface waves appears to represent a promising technique to shed light on this question. The position of the crack depth in the frequency domain would be observed as a function of the applied stress and interpreted in terms of the degree of partial crack closure. Under ideal conditions the peak amplitude might give information on the nature of the crack tip and distinguish between temporary mechanical crack closure and crack healing. Experiments along these lines are now in the planning stage and will be reported on in the near future.

CONCLUSION

This report presents results on a simple approach to describe the size of surface breaking flaws. The scattered radiation patterns of the flaws when irradiated by acoustic surface waves are interpreted to provide estimates of flaw length and depth with an accuracy of 10% or better. The key features are the positions and spacings of nulls or peaks in the angular and frequency dependence of scattered energy in either pitch-catch or pulse echo. A simple model based on optical diffraction theory is presented and demonstrated. The good agreement between this model and the experimental observations is interesting since it provides - at least to first order - an analogy between the behavior of the surface waves and that of electromagnetic waves. While the results presented here are useful for estimation of the size of simply shaped, surface breaking flaws, much more work must be carried out to extend the technique to include all possible situations encountered in fracture mechanics. Such circumstances as cracks inclined to surface, crack with severe surface roughness, nonelliptically-shaped cracks, roughness of the specimen surface, crack closure of fatigue cracks, to name a few, must be taken into account.

ACKNOWLEDGEMENT

The authors are indebted to P. Khuri-Yakub for the design, construction, and demonstration of the 100 MHz surface wave transducers (see Ref. 2) used in one of the three experiments, to A. E. Evans for the preparation and characterization of the half-penny shaped crack in the ceramic sample. The authors are also grateful to H. Nadler for the design of 100 MHz goniometer, to J. Doucet for the construction of the low frequency goniometers, and to C. Picard for the micrographical examination of the samples. The first part of this work was carried out in France at the "Groupe de Physique des Solides de l'Ecole Normal Superieure," during B. R. Tittmann's stay as "Professor Associe" at the University of Paris VIII, and was supported by the CNRS (Centre National de la Recherche Scientifique). This work was later complemented by work done at theScience Center and one of the author's (B.R.T.) research was sponsored by the Center for Advanced NDE operated by the Science Center, Rockwell International, for the Advanced Research Projects Agency and the Air Force Materials Laboratory under Contract F33615-74-C-5180.

REFERENCES

1. P.A. Doyle and C.M. Scala, Ultrasonics 16, 164 (1978).

2. B.T. Khuri-Yakub and G.S. Kino, Appl. Phys. Lett., 32, 513 (1978).

3. J.D. Fraser, B.T. Khuri-Yakub, and G.S. Kino, App. Phys. Lett., 32, 698 (1978).

4. M.T. Resh, B.T. Khuri-Yakub, G.S. Kino and J.C. Shyne, Proceedings of the First International Symposium of Ultrasonic Material Characterization at Gathersburg, Md., June 1978 (in press).

5. G.S. Kino, J. Appl. Phys. 49, 3190 (1978).

6. V. Domarkas, B.T. Khuri Yakub, G.S. Kino, Appl. Phys. Lett. 33, 557 (1978).

7. B.A. Auld, S. Ayter and M. Tan, 1978 Ultrasonics Symposium Proceedings, IEEE Cat. No. 78, Ch. 1344-1SU, in press.

8. B.R. Tittmann,F. Cohen-Tenoudji, M.De Billy, A. Jungman and G. Quentin, App. Lett. 33, 6 (1978), see also 1978 Ultrasonic Symposium Proceedings IEEE, Cat. No. 78, Ch. 1344-1SU, in press.

9. J.E. Collipriest, Jr., The Surface Crack (edited by J.L. Swedlow) The Am. Soc. of Mech. Eng., 43 (1972).

10. G.R. Irwin,J.Appl. Mechanics 29, 651 (1962).

11. P.C. Paris and F. Erdogan, J. Basic Eng. 85, 528 (1963).

12. H.W. Reinhardt and J.W. Dally, Mat. Eval. 30, 213 (1970).

13. O. Buck, J.D. Frandsen, and H.L. Marcus in Fatigue Crack Growth Under Spectrum Loads, ASTM STP 595, Am. Soc. Testing and Materials 101 (1976).

14. M.G. Silk, NDT Int. 9, 290 (1976).

15. D. Cook, Proc. Brit. Acoust. Soc. Spring Meeting, Loughborough, 72 U19 (1972).

16. R.L.Hudgell, L.L.Morgan, and R.F.Lumb, Brit. J. Nondestructive Testing 16, 144 (1974).

17. K.G. Hall, Nondestructive Testing 9, 121 (1976).

18. B.H. Lidington and M.G. Silk, Brit. J. Nondestructive Testing 17, 165 (1975).

19. O.R. Gericke, Ultrasonic Spectroscopy, Ch. 2 in Research Techniques in Non-destructive Testing, Ed. R.S. Sharpe, Academic Press, London and N.Y. (1970).

20. A. Brown, Ultrasonics 11, 202 (1973).

21. L.L. Morgan, Acoustica 30, 222 (1974).

22. J.J. Petrovic and M.G. Mendiratta, Jnl. Amer. Ceram. Soc., 59, 163 (1976).

23. Y.D. Achenbach, private communication.

24. Y. Goodman, Fourier Optics, McGraw-Hill Book Company New York, 1968.

25. M. DeBilly, F. Cohen-Tenoudji, A. Jungman and G. Quentin, IEEE Trans. on Sonics and Ultrasonics S.U. 23. 356-363 (1976).

DISCUSSION

Gordon Kino (Stanford University): Bernie, have you experienced any difficulties in observing tight cracks? We had some experience with glass, for instance. We had to take the precaution of putting a little bit of stress on it to make sure the crack was open to get the full area of the crack.

Bernie Tittmann (Rockwell International Science Center): Yes, if you noticed in one of the tables where I list the predicted crack radii and compare them to the true crack radii, you find that the experiments underestimate the answers. We associate that partly with the tightness at the crack edges, but also the fact that, after all, the surface waves impinging on an elliptically shaped crack sample, not just the top part, but also the flanks of the crack which are, in fact, narrower. I think we will address that problem with our fatigue specimens where, of course, we can control the crack opening at will.

Gordon Kino: Actually watch it change?

Bernie Tittmann: Yes.

Gordon Kino: That will be nice.

R. E. Green (Johns Hopkins): Are you going to measure the crack opening continuously with ultrasound while you are fatiguing it?

Bernie Tittmann: Yes.

SUMMARY COMMENTS

John Brinkman, Chairman (Rockwell International Science Center): There is one item scheduled yet on the program you will notice called Summary Comments. We would ask you, we will promise you, this won't be very long, but we do have two more people that would like to speak. I will tell you, first of all, that the second of these is Don Thompson. Don's remarks will be short.

The first one is Gary Laurentzen. Gary is with the Naval Ship R & D Center and is going to tell us briefly, about the tour to the Naval Development and Training Center, Fleet Maintenance Assistance Group-Pacific.

Cary Laurentzen: The Command that I am with is staffed by about 1700 to 2000 sailors, mostly of the senior rates. Although we don't pursue research, our purpose is to try to develop them as better sailors and provide them some training ashore.

With regard to your own interests, on the tour this afternoon we will back up a little bit and return you to earth, so to speak. In terms of what we have, we are using several nondestructive testing techniques. This was, I guess, a step from nothing in terms of what the Navy was using. We are beginning, however, to use a greater number of procedures. We have been a Command for about ten years or so. It was designed originally in Admiral Zumwalt's day to try to give the sailors a billet ashore because they are at sea all the time. Then we decided to train them in ship repair techniques. The Command is really someplace in between a floating repair ship and a shipyard because we don't have the real experienced personnel that a shipyard would have, but we do an awful lot of similar work.

We have a number of facilities at the Command. These include testing facilities as well as chemical and metallurgical laboratories. These facilities are central to other activities at the Command. For example, we do a considerable amount of pipeshop work. One of the areas where we use nondestructive testing is to determine what piping needs to be renewed. We use ultrasonic techniques to try to measure piping thickness sometimes before it is removed from the ship.

Another area is welding. I would say 50 to 60 percent of our nondestructive testing involves the inspection of welds. A lot of it is done in the shop, an immense amount of welding is also done aboard ship.

A third area of interest is the lagging shop. There has been much publicity recently on asbestos. We are trying to develop a means to identify the presence of asbestos in lagging. In the older ships, the lagging may contain asbestos which is used to insulate steam piping. If you have any ideas concerning identification of asbestos, I would surely like to have that. We also use NDT procedures in our foundry. We pour some of the more exotic alloys. We do have to radiograph some castings, and we will do some ultrasonics on them. We do not have any shear wave capabilities. This is sort of the next step for the Navy. An additional use for NDT procedurs is in oil analysis to detect engine wear. The Navy has quite a campaign now in attempting to use this technique for the diesel engines in which we perform spectroscopic examinations of oils after every hundred hours or so to detect the presence of wear metals and determine how soon we may need to overhaul an engine.

The corrosion and erosion of pumps in salt water environments is a major problem area in terms of ship maintenance. We are not doing too much in terms of NDE in this area. It is just a matter of finding an alloy that will hold up under this type of environment where we have so many problems.

This has been a short preview of what you will see on the tour. I hope it will be of interest to you. As I said, we are not a research Command, but we would certainly appreciate any comments from you as you observe our work that would improve our NDE activities. Thank you.

John Brinkman, Chairman: Thank you Gary. Before I can Don up here, I just want to say I know I speak for everyone here and everyone who has been here this week in wanting to express our gratitude to Don for everything that he has done to make this conference possible. I learned he does some things that I didn't know he did. As a matter of fact, I found myself with him on a couple of occasions and ended up doing carpentry work, janitorial work and a few other things. Really, Don personally looks after everything from a long time before this conference takes place until a long time afterward. I think that we should give Don a hand before asking him to come up here for his final remarks.

Don Thompson (Rockwell International Science Center): Thank you for the very kind remarks, John. I just have a few comments to make in the way of acknowledgments before we close. I wish to thank you all for coming to the meeting. I wish also to acknowledge the people at Scripps. We have had good cooperation from the people at the Scripps organization. We also had a number of overseas visitors whom we want to welcome. I would also like to acknowledge the many good works interactions that participants of this program have had with the ARPA Materials Research Council. Some of the MRC work, in parallel with work in this program, has really been of importance in bringing about key advances in this area In this context I especially want to acknowledge the contributions of MRC members W. Kohn, B. Budianski, J. Rice and R. Thomson. I would also like to thank Mrs. Diane Harris and Mrs. Nadine Brinkman for their excellent work in arranging and managing the many details associated with this meeting. If you feel inclined I think they are still outside the door and as you go out

you might like to give them a thanks.

Finally, I would like to thank both ARPA and AFML for their support in this work and for the privilege of being able to present it at a meeting like this. The proceedings of the meeting will be published as an Air Force Materials Lab report. Those of you who are registered at this meeting should receive a copy in the mail.

Many thanks to Mr. Jim Kelly and Mr. Gary Laurentzen of the Navy in preparing the tour this afternoon. I think it will be an interesting tour and I hope you will be able to participate in it. It is always a revelation, I think, for a research person to see the environment in which his product eventually must be used. It is enough to make one throw up his hands in despair at times, but it is a worthwhile experience in the sense that it often suggests different approaches to research if you know something of the final geometric and environmental constraints in which it has to be used.

With that, I think I have nothing more to say. I will repeat the announcements that Mike made this morning. The desire is to hold the meeting here at Scripps again next year. I certainly endorse that. The grounds, the surroundings, the climate, the people, have certainly all been cooperative. Again, thank you.

ATTENDEE LIST

REVIEW OF PROGRESS

IN

QUANTITATIVE NDE

SCRIPPS INSTITUTION OF OCEANOGRAPHY

JULY 17-21, 1978

Dr. J. D. Achenbach
Department of Civil Engineering
Northwestern University
The Technical Institute
Evanston, IL 60201
(312) 492-5527

Dr. Robert C. Addison, Jr.
Rockwell International Science Center
P. O. Box 1085
Thousand Oaks, CA 91360
(805) 498-4545

Dr. Laszlo Adler
Department of Physics
University of Tennessee
Knoxville, TN 37916
(615) 974-5330

Mr. Lloyd Alberg
Rockwell International Science Center
P. O. Box 1085
Thousand Oaks, CA 91360
(805) 498-4545

Dr. George A. Alers
Rockwell International Science Center
P. O. Box 1085
Thousand Oaks, CA 91360
(805) 498-4545

Dr. B. A. Auld
Edward L. Ginzton Laboratory
Stanford University
Stanford, CA 94305
(415) 497-0264

Dr. Sevig Ayter
Edward L. Ginzton Laboratory
Stanford University
Stanford, CA 94305
(415) 497-2300

Dr. Alfred J. Bahr
SRI International
Menlo Park, CA 94025
(415) 326-6200 X4631

Mr. N. K. Batra
Systems Research Laboratories, Inc.
2800 Indian Ripple Road
Dayton, OH 45440
(513) 426-6000

Mr. R. D. Beaver
Vetco Services, Inc.
1600 Brittmoore
Houston, TX 77043
(713) 461-6112

Mr. Jack Becker
Pratt Whitney Aircraft
West Palm Beach, FL 33402
(305) 844-7311 X2417

Dr. Robert A. Blake, Jr.
University of Delaware
Newark, DE 19711
(302) 738-2980

Dr. Norman Bleistein
Denver Applied Analytics
Denver, CO 80222
(303) 757-8097

Mr. Chris Bolkan
NORTEC
3001 George Washington Way
Richland, WA 99352
(509) 943-9141

Mr. John Bosko
Rockwell International
Rocketdyne Division
6633 Canoga Avenue
Canoga Park, CA 91304
(213) 884-2440

Mr. John A. Brinkman
Albuquerque Development Laboratory
Rockwell International
2340 Alamo, S.E., Suite 200
Albuquerque, NM 87106
(505) 842-0535

Mr. Robert H. Brockelman
Army Materials & Mechanics Research Center
Watertown, MA 02172
(617) 923-3333

Mr. J. W. Brophy
Babcock & Wilcox Company
Lynchburg, VA 24505
(804) 384-5111 X5142

Dr. Otto Buck
Rockwell International Science Center
P. O. Box 1085
Thousand Oaks, CA 91360
(805) 498-4545

Dr. Michael J. Buckley
DARPA/MSO
1400 Wilson Boulevard
Arlington, VA 22209
(202) 694-1664

Ray Buckrop, Commander
U. S. Army Armament Command
Attention: DRSAR-RDS
Rock Island, IL 61201
(309) 794-5342

Professor Bernard Budiansky
Division of Engineering & Applied Science
Harvard University
Cambridge, MA 02138
(617) 495-1000

Dr. Christian Burger
Iowa State University
Ames, IA 50011
(515) 294-5853

Dr. Harris M. Burte
Air Force Systems Command, AFML/LL
Wright-Patterson AFB, OH 45433
(513) 255-2738

Dr. David Carver
Lockheed Missiles & Space Company
Bldg. 102, ORG. 7574
Sunnyvale, CA 94088
(408) 742-9198

Dr. Henry Casso
National Institute for Professional
Development, Inc.
P. O. Drawer 3099
Albuquerque, NM 87110
(505) 883-0667

Dr. Richard Chance
Grumman Aerospace Corporation
Bethpage, NY 11714
(516) 575-3243

Dr. Francis H. Chang
Applied Research Laboratory
General Dynamics
Fort Worth, TX 76101
(817) 732-4811 X5375

Dr. M. V. K. Chari
Corporate Research & Development
General Electric Company
Bldg. 37, Room 355
Schenectady, NY 12301
(518) 385-2575

Dr. J. K. Cohen
Denver Applied Analytics
Denver, CO 80222
(303) 757-8097

Dr. Dorothy M. Comassar
General Electric Company
Cincinnati, OH 45215
(513) 243-4640

Mr. John T. Conroy
U. S. Army Aviation Systems Command, AMSAV-L
P. O. Box 209
St. Louis, MO 63166
(314) 268-2513

Dr. William D. Cook
University of Houston
Houston, TX 77004
(713) 749-1011

Mr. Thomas Cooper
Air Force Materials Laboratory, MXA
Wright-Patterson AFB, OH 45433
(513) 255-5428 or 3137

Lt. Col. Colin E. Copeland
National Defense Headquarters
Ottawa, Ontario, Canada
(613) 993-2147

Dr. Douglas Corl
Stanford University
Stanford, CA 94305
(415) 497-2300

Dr. James Corones
Iowa State University
Ames, IA 50011
(515) 294-9162

Dr. Robert L. Crane
Air Force Systems Command, AFML/LLP
Wright-Patterson AFB, OH 45433
(513) 255-5561

Dr. Ben Cross
Rockwell International
Atomics International, Rocky Flats Plant
P. O. Box 464
Golden, CO 80401
(303) 497-2352

Mr. Harish Dalal
SKF Industries
1100 First Avenue
King of Prussia, PA 19406
(215) 265-1900

Dr. Isaac Daniels
IIT Research Institute
10 West 35th Street
Chicago, IL 60616
(312) 567-3000

Professor Douglas A. Davids
Polytechnic Institute of New York
333 Jay Street
Brooklyn, NY 11201
(212) 643-8709

Mr. T. J. Davis
Battel e-Northwest Laboratories
P. O. Box 999
Richland WA 99852
(509) 946-2290

Dr. D. S. Dean
P.E.R.M.E., Ministry of Defense
Aylesburg, Westcott
Bucks, England
HP18 Onz.
(Aylesbury) 5989 X352

Professor W. E. Deeds
Department of Physics
University of Tennessee
Knoxville, TN 37916
(615) 974-5336

Mr. Richard C. Deitrich
Naval Air Engineering Center
Code 92724
Lakehurst, NJ 08733
(201) 323-7464

Dr. Thomas J. DeLacy
Senior Staff Scientist
Aeronutronics - Ford
3939 Fabian Way, MS G97
Palo Alto, CA 94303
(415) 494-7400 X4155

Mr. G. DeYoung
Electric Power Research Institute
P. O. Box 10412
Palo Alto, CA 94303
(415) 855-2416

Mr. Ronald DeSpain
Rockwell International
Rockeydyne Division
6633 Canoga Avenue
Canoga Park, CA 91304
(213) 884-2100

Dr. Eytan Domany
Department of Physics
University of Washington, Seattle
Seattle, WA 98195
(206) 543-7305

Mr. E. D. Dominik
The Timken Company
Canton, OH 44706
(216) 453-4511 X319

Dr. Peter A. Doyle
Aeronautical Research Laboratories
P. O. Box 4331
GPO Melbourne, Victoria 3001
Australia

Mr. Earl DuBack
General Dynamics
Electric Boat Division
Groton, CT 06340
(203) 446-5960 X6515

Dr. John C. Duke, Jr.
The Johns Hopkins University
Room 15, Medical Hall
Baltimore, MD 21218
(301) 338-7126

Mr. Robert Dukes
Admiralty Marine Technical Establishment
Holton Heath Poole
Dorset BH 166JU
England

Mr. John R. Edson
Boeing-Seattle, MS 42-34
P. O. Box 3707
Seattle, WA 98124
(206) 655-2121

Dr. Donald Eitzen
National Bureau of Standards
Washington, DC 20234
(301) 921-3646

Mr. Charles M. Elias
Systems Research Laboratories
2800 Indian Ripple Road
Dayton, OH 45440
(513) 255-4740

Mr. J. K. Elliott
Research & Development Center
General Electric Company
P. O. Box 8
Schenectady, NY 12301
(518) 385-8156

Dr. Richard K. Elsley
Rockwell International Science Center
P. O. Box 1085
Thousand Oaks, CA 91360
(805) 498-4545

Mr. Robert Erwin
Northrop Corporation
3901 W. Broadway
Hawthorne, CA 90250
(213) 970-2001

Dr. Anthony G. Evans
Department of Materials Science & Mineral Engineering
University of California
Hearst Mining Building
Berkeley, CA 94720
(415) 642-3821

Dr. Ching Feng
Endevco Corporation
3700 Rancho Viejo Road
San Juan Capistrano, CA 92675
(714) 493-8181 X344

Mr. D. M. Forney, Jr.
Air Force Materials Laboratory/LLP
Wright-Patterson AFB, OH 45433
(513) 255-5309

Dr. Christopher M. Fortunko
Rockwell International Science Center
P. O. Box 1085
Thousand Oaks, CA 91360
(805) 498-4545

Mr. Ellis L. Foster
Battelle Columbus Laboratories
505 King Avenue
Columbus, OH 43201
(614) 424-4120

Mr. Charles Frederick
NORTEC
3001 George Washington Way
Richland, WA 99352
(509) 943-9141

Dr. E. S. Furgason
School of Electrical Engineering
Purdue University
LaFayette, IN 47907
(317) 493-9201

Dr. Gerald C. Gardner
Electrical Engineering Department
University of Houston
Houston, TX 77004
(713) 749-1794

Mr. S. W. Gill
General Dynamics/Convair
P. O. Box 80847
San Diego, CA 92138
(714) 277-8900 X1964

Mr. V. S. Goel
U. S. Nuclear Research Commission
Washington, DC 20555
(301) 443-6929

Mr. James F. Goff
Naval Surface Weapons Center, White Oaks
Silver Springs, MD 20910
(202) 394-1484

Professor Uli Gonser
Universitat
Institute for Metalphysik
66 Saarbrücken, West Germany
(0681) 302. 3408

Mr. Lloyd J. Graham
Rockwell International Science Center
P. O. Box 1085
Thousand Oaks, CA 91360
(805) 498-4545

Dr. Peter M. Grant
Edward L. Ginzton Laboratory
Stanford University
Stanford, CA 94305
(805) 497-0118

Professor Robert E. Green, Jr.
Mechanical & Materials Department
The Johns Hopkins University
Charles & 34th Streets
Baltimore, MD 21218
(301) 338-7126

Dr. J. E. Gubernatis
Los Alamos Scientific Laboratory
T11, MS 457
P. O. Box 1663
Las Alamos, NM 87544
(505) 667-6727

Dr. Marvin A. Hamstad
Lawrence Livermore Laboratory
P. O. Box 808
Livermore, CA 94550
(415) 422-7038

Dr. Stephen D. Hart
Naval Research Laboratory, Code 8435
4555 Overlook Avenue
Washington, DC 20375
(202) 767-3613

Mr. Donald B. Heckman
Development Engineer
AMF Electronics Research Laboratory
3001 Centerville Road
Herndon, VA 22070
&703; 471-3014

Mr. Clinton Heiple
Rockwell International
Atomics International, Rocky Flats Plant
P. O. Box 464
Golden, CO 80401
(303) 497-2680

Dr. Edmund G. Henneke
Department of Science & Mechanics
Virginia Polytechnic Institute & State University
Blacksburg, VA 24061
(703) 951-5316

Dr. R. E. Herfert
Senior Technical Specialist, Material Research
Northrop Corporation
3901 W. Broadway
Hawthorne, CA 90250
(213) 970-4963

Dr. George Hermann
Department of Applied Mechanics, School of Engineering
Stanford University
Stanford, California 94305
(415) 497-4134

Mr. B. P. Hildebrand
Battelle Northwest Laboratories
P. O. Box 999
Richland, WA 99352
(509) 946-2102

Mr. Philip J. Hodgetts
Rockwell International
Los Angeles Division
5701 West Imperial Highway
Los Angeles, CA 90009
(213) 670-9151

Professor Paul Höller
Institut Fur Zerstorungsfreie Prufverfahren
Universitat, Gebaude 37
6600 Saarbrucken, West Germany
0681-3023800

Mr. Christopher E. Horton
Naval Ship Engineering Center
SEC 6107C6
Washington, DC 20362
(202) 692-0180

Dr. D. Ilic
Stanford Electronics Laboratories, ERL 264
Stanford University
Stanford, CA 94305
(415) 497-1232 or 1234

Dr. Hector C. Ingrao
Transportation Systems Center
Mail Code 733, Kendall Square
Cambridge, MA 02142
(617) 494-2310

Mr. George Jahn
Corporate Research Division
Varian Associates
611 Hansen Avenue
Palo Alto, CA 94340
(415) 493-4000

Mr. Warren Junker
Research & Development Center
Westinghouse Electric Corporation
Churchill Boro
Pittsburgh, PA 15235
(412) 256-7000

Mr. David L. Kaelble
Rockwell International Science Center
P. O. Box 1085
Thousand Oaks, CA 91360
(805) 498-4545

Mr. James S. Kane
Associate Director for Basic Energy Science
Department of Energy
Office of Energy Research
Washington, DC 20545
(301) 353-5565

Mr. James J. Kelly
David W. Taylor Naval Ship, Research &
Development Center
Code 2803
Annapolis, MD 21402
(301) 267-2637

Dr. Larry Kessler
Sonoscan, Inc.
752 Foster Avenue
Bensenville, IL 60106
(312) 766-8795

Mr. Pramod Khandelwal
Detroit Diesel, Division of General Motors
Dept. 5827, MS W-5
P. O. Box 894
Indianapolis, IN 46206
(317) 243-4536

Mr. John Khoury
Rockwell International
Automotive Operations
2135 West Maple Road
Troy, MI 48084
(313) 435-1000

Dr. B. T. Khuri-Yakub
Department of Electrical Engineering
W. W. Hansen Laboratory of Physics
Stanford University
Stanford, CA 94305
(415) 497-0718

Mr. T. G. Kincaid
General Electric Company
Bldg. 37, Room 523
Schenectady, NY 12345
(518) 385-4128

Mr. Gordon A. King
Rockwell International
Atomics International
8900 DeSoto Ave.
Canoga Park, CA 91304
(213) 341-1000

Professor Gordon S. Kino
Department of Electrical Engineering
W. W. Hansen Laboratory of Physics
Stanford University
Stanford, CA 94305
(415) 497-0205

Mr. T. D. Kinsella
General Dynamics
P. O. Box 748
Fort Worth, TX 76101
(817) 732-4811 X2005

Dr. Ronald A. Kline
General Dynamics
MS 5984
P. O. Box 748
Fort Worth, TX 76101
(817) 732-4811 X5131

Mr. Richard Klinman
Homer Laboratories
Bethlehem Steel Corporation
Bethlehem, PA 18016
(215) 694-3330

Professor Walter Kohn
Department of Physics
University of California
La Jolla, CA 92037
(714) 452-3267

Mr. William J. Kreins
Rockwell International
Los Angeles Division
815 Lapham Street
El Segundo, CA 90245
(213) 670-9151 X3391

Professor James Krumhansl
National Science Foundation
1800 G Street, NW
Washington, DC 20550
(202) 632-7342

Mr. David Kupperman
Materials Science Division, Bldg. 212
Argonne National Laboratory
Argonne, IL 60439
(312) 972-5108

Dr. Kenneth Lakin
Department of Electrical Engineering
University of Southern California
Los Angeles, CA 90007
(213) 741-6393

Mr. Stephen Lane
Adaptronics, Inc.
7700 Old Springhouse Road
McLean, VA 22101
(703) 893-5450

Mr. M. Lauriente
Research & Special Programs Administration
Department of Transportation
400 7th Street
Washington, DC 20590
(202) 426-9364

Mr. K. J. Law
K. J. Law Engineers, Inc.
23660 Research Drive
Farmington Hills, MI 48024
(313) 478-3150

Dr. David Lee
Applied Mechanics Research
AFIT/ENC, Bldg. 640
Wright-Patterson AFB, OH 45433
(513) 257-1110

Dr. Chuk L. Leung
Rockwell International Science Center
P. O. Box 1085
Thousand Oaks, CA 91360
(805) 498-4545 X224

Mr. Theodore Libers
IIT Research Institute
10 West 35th Street
Chicago, IL 60616
(312) 567-3000

Mr. Dean Lingenfelter
Lockheed Missiles & Space Company
MS 0184-34, B/154
P. O. Box 504
Sunnyvale, CA 94088
(408) 742-2197

Mr. Richard Lingle
Terra Tek
420 Wakara Way
Salt Lake City, UT 84108
(801) 582-2220

Dr. Gilbert London
Naval Air Development Center
Warminster, PA 18974
(215) 441-2808

Professor Stuart A. Long
Department of Electrical Engineering
University of Houston
Houston, TX 77004
(713) 749-2511

Dr. William Lord
Department of Electrical Engineering
Colorado State University
Fort Collins, CO 80573
(303) 491-1101

Mr. G. Lorentzen
U. S. Navy, Naval Development & Training Center
Fleet Maintenance Assistance Group - Pacific
Naval Station Box 106, Code 5200
San Diego, CA 92136
(714) 225-4011

Mr. Frank N. Lundberg
Rockwell International Science Center
P. O. Box 1085
Thousand Oaks, CA 91360
(805) 498-4545

Dr. Keith C. MacMillan
Lawrence Livermore Laboratories
University of California
Livermore, CA 94550
(415) 422-7929

Mr. Edward Maestas
P. O. Box 3111
Fairview, NM 87533

Mr. Murray W. Mahoney
Rockwell International Science Center
P. O. Box 1085
Thousand Oaks, CA 91360
(805) 498-4545

Dr. Florian Mansfeld
Rockwell International Science Center
P. O. Box 1085
Thousand Oaks, CA 91360
(805) 498-4545

Professor Harris Marcus
Mechanical Engineering Department, TAY-167
University of Texas at Austin
Austin, TX 78712
(512) 471-1504

Dr. George Martin, Consultant
1660 9th Street
Santa Monica, CA 95062
(213) 451-9271

Mr. James Martin
Rockwell International Science Center
P. O. Box 1085
Thousand Oaks, CA 91360
(805) 498-4545

Mr. Steve Matay
TRW, Inc.
MS TM-2966
23555 Euclid Avenue
Cleveland, OH 44117
(216) 383-2121

Dr. James R. Matthews
Defense Research Establishment Pacific
c/o Fleet Mail Office
Victoria, British Columbia, Canada
(604) 388-1919

Dr. Bruce Maxfield
Lawrence Livermore Laboratories
University of California, MS L415
Livermore, CA 94550
(415) 422-7969

Mr. William P. Maynard
Rohr Industries
Department 749, Zone 3E
"H" Street
Chula Vista, CA 92012
(714) 575-4111

Dr. Stewart McBride
Royal Military College of Canada
Kingston, Ontario, Canada K7L2W3
(613) 545-7418

Dr. Robert W. McClung
Metals & Ceramics Division
Oak Ridge National Laboratory
Oak Ridge, TN 37830
(615) 483-8611

Ms. Shirley L. McDonald
Lockheed Missiles & Space Company
ORG. 8123
P. O. Box 504
Sunnyvale, CA 94086
(408) 742-5368

Mr. Jerry T. McElroy
Southwest Research Institute
8500 Culebra Road
San Antonio, TX 78206
(512) 684-5111 X2053

Dr. B. J. McKinley
Lawrence Livermore Laboratories, L415
University of California
Livermore, CA 94550
(415) 422-7974

Mr. Andrew Messer
Rohr Industries
"H" Street
Chula Vista, CA 92012
(714) 575-4111

Mr. David T. Mih
Northrop Corporation
3901 W. Broadway Street
Hawthorne, CA 90250
(213) 970-6727

Mr. James Miller
Lockheed California Company, Plant A-1
P. O. Box 551
Burbank, CA 91520
(213) 847-4177

Dr. Jovan Moacanin
Jet Propulsion Laboratory
California Institute of Technology
4800 Oak Grove Drive
Pasadena, CA 91125
(213) 354-3176

Mr. John F. Moore
Rockwell International
Los Angeles Division
5701 W. Imperial Highway
Los Angeles, CA 90009
(213) 670-3191

Dr. Thomas J. Moran
Air Force Systems Command, AFML/LLP
Wright-Patterson AFB, OH 45433
(513) 255-4740

Dr. Winifred Morris
Rockwell International Science Center
P. O. Box 1085
Thousand Oaks, CA 91360
(805) 498-4545

Mr. Walter F. Morris, Jr.
Lord-Kinematics Corporation
1635 W. 12th Street
Erie, PA 16512
(814) 456-8511

Mr. J. Moyzis
Air Force Materials Laboratory/LLP
Wright-Patterson AFB, OH 45433
(513) 255-5428 or 3137

Dr. Anthony N. Mucciardi
Adaptronics, Inc.
Westgate Research Park
7700 Old Springhouse Road
McLean, VA 22101
(703) 893-5450

Dr. Yochikazu Murakami
Edward L. Gintzon Laboratory
Stanford University
Stanford, CA 94305
(415) 497-1981

Professor V. L. Newhouse
School of Electrical Engineering
Purdue University
LaFayette, IN 47907
(317) 493-9201

Ms. Kathie Newman
Physics Department, FM-15
University of Washington
Seattle, WA 98195
(206) 543-5074

Dr. Louis Odor
Rockwell International
Columbus Aircraft Division
4300 E. 5th Avenue
Columbus, OH 43216
(614) 239-2477

Dr. Jon Opsal
Lawrence Livermore Laboratories, MS L333
University of California
Livermore, CA 94550
(415) 422-1100

Dr. Harvey C. Palmer
Mechanical & Materials Department
The Johns Hopkins University
Charles & 34th Streets
Baltimore, MD 21218
(301) 338-7012

Dr. Rod Panos
Rockwell International Science Center
P. O. Box 1085
Thousand Oaks, CA 91360
(805) 498-4545

Mr. E. Papadosrankazis
Research & Development Department
General Electric Company
P. O. Box 8
Schenectady, NY 12301
(518) 385-8156

Dr. William J. Pardee
Rockwell International Science Center
P. O. Box 1085
Thousand Oaks, CA 91360
(805) 498-4545

Mr. John A. Patsey
U. S. Steel Research Center
125 Jamison Lane
Monroeville, PA 15146
(412) 372-1212 X2483

Dr. Neil Paton
Rockwell International Science Center
P. O. Box 1085
Thousand Oaks, CA 91360
(805) 498-4545

Mr. Thomas J. Pojeta
Aviation Research & Development Command
Department of the Army, DRDAV-QP
P. O. Box 209
St. Louis, MO 63166
(314) 268-2513

Mr. R. Polichar
Science Applications, Inc.
1200 Prospect
La Jolla, CA 92037
(714) 459-0211

Mr. G. J. Posakony
Battelle-Northwest
P. O. Box 999
Richland, WA 99352
(509) 946-2138

Dr. Calvin F. Quate
Department of Applied Physics
Stanford University
Stanford, CA 94305
(415) 497-0213

Dr. Gerard Quentin
Solid State Physics Group
University of Paris VII
75221 Paris Cedex 05
France
336-25-25 x46-89

Dr. S. Ramasamy
Department of Electrical Engineering
Colorado State University
Fort Collins, CO 80573
(303) 491-6018

Mr. C. Rau
Failure Analysis Associates
750 Welch Road, Suite 116
Palo Alto, CA 94304
(415) 321-6350

Dr. George Reiter
Ames Laboratory
Iowa State University
Ames, IA 50011
(515) 294-9162

Professor James R. Rice
Division of Engineering
Brown University
Providence, RI 02912
(401) 863-2868

Dr. John M. Richardson
Rockwell International Science Center
P. O. Box 1085
Thousand Oaks, CA 91360
(805) 498-4545

Mr. Mike Riley
Rockwell International
Space Division
12214 Lakewood Boulevard
Downey, CA 90241
(213) 922-2111 X5122

Mr. W. Ray Roberts
Quality Engineering
Aerojet Liquid Rocket Company
Hwy. 50 & Aerojet Road
Sacramento, CA 95813
(916) 355-2851

Commander Kenneth Robinson
Office of Naval Research
1030 East Green Street
Pasadena, CA 91106
(213) 795-5971

Dr. Alexander Rogorsky
Mechanical Engineering Department
Drexel University
32nd & Chestnut Streets
Philadelphia, PA 19104
(215) 895-2374

Dr. James H. Rose, Jr.
University of Michigan
Ann Arbor, MI
(313) 764-4476

Professor Joseph L. Rose
Department of Mechanical Engineering
Drexel University
Philadelphia, PA 19104
(215) 895-2295

Dr. Wolfgang Sachse
Department of Theoretical & Applied Mechanics
Cornell University
Ithaca, NY 14850
(607) 256-5065

Mr. J. J. Schuldies
Airesearch Corporation
D/93-393
P. O. Box 5217
Phoenix, AZ 85010
(602) 267-4213

Dr. William R. Scott
Naval Air Development Center, Code 30233
Warminster, PA 18974
(415) 441-3232

Mr. Marvin Segel
Adaptronics, Inc.
Westgate Research Park
7700 Old Springhouse Road
McLean, VA 22101
(703) 893-5450

Dr. Allen Selfridge
Department of Electrical Engineering
W. W. Hansen Laboratories of Physics
Stanford University
Stanford, CA 94305
(415) 497-2300

Mr. Patrick Serao
U. S. Army ARRADCOM
DRDAR-QAS, B62
Dover, NJ 07801
(201) 328-6534

Mr. Clinton L. Shank
Vought Corporation
P. O. Box 225907
Dallas, TX
(214) 266-5945

Dr. H. J. Shaw
Microwave Laboratory
Stanford University
Stanford, CA 94305
(415) 497-0203

Dr. William H. Sheldon
Aircraft Division
Northrop Aircraft Company
3901 W. Broadway
Hawthorne, CA 90250
(213) 970-3301

Mr. Larry Shepherd
Corporate Research & Development
General Electric Company
P. O. Box 8, Bldg. K1, Room 5C19
Schenectady, NY 12301
(518) 385-8078

Professor John C. Shyne
Materials Science & Engineering Department
Stanford University
Stanford, CA 94305
(415) 497-2535

Mr. Stan Silverstein
NAVSEA Systems Command
Code 6613-C33, National Center #2
Arlington, VA 20360
(202) 692-7949

Dr. John A. Simmons
National Bureau of Standards
B-120 Materials Bldg.
Washington, DC 20234
(301) 921-3355

Major Wilbur C. Simmons
Air Force Office of Scientific Research
Bldg. 410
Bolling AFB, DC 20332
(202) 767-4931

Dr. G. P. Singh
Mechanical Engineering Department
Drexel University
32nd & Chestnut Streets
Philadelphia, PA 19104
(215) 895-2374

Mr. James R. Skorpik
Battelle-Northwest
P. O. Box 999
Richland, WA 99352
(509) 946-2168

Dr. Kempton A. Smith
Corporate Research & Development
General Electric Company
1 River Road
Schenectady, NY 12345
(518) 385-8521

Dr. R. T. Smith
Director, NTIAC
Southwest Research Institute
8500 Culebra Road
San Antonio, TX 78206
(512) 684-5111

Dr. Tennyson Smith
Rockwell International Science Center
P. O. Box 1085
Thousand Oaks, CA 91360
(805) 498-4545

Dr. M. Srinivasan
Research & Development Division
The Carborundum Company
P. O. Box 1054
Niagara Falls, NY 14072
(716) 278-2570

Mr. Craig H. Stephan
Ford Motor Company
24500 Glendale Avenue
Detroit, MI 48239
(313) 592-2044

Mr. Ronald D. Strong
Los Alamos Scientific Laboratory
Group M-1, MS 912
Los Alamos, NM 87545
(505) 667-6262

Mr. T. W. Strouble
The Timken Company
1835 Dueber Avenue, S.W.
Canton, OH 44706
(216) 453-4511 X303

Mr. Wayne Stump
Rockwell International
Atomics International, Rocky Flats Plant
P. O. Box 464
Golden, CO 80401
(303) 497-2352

Mr. William R. Sturrock
Northrop Corporation
3109 W. Broadway
MS 3882/84
Hawthorne, CA 90250
(213) 970-6727

Dr. Thomas L. Szabo
RADC/EEA
Hanscom AFB, MD 01731
(617) 861-4663

Dr. Norman M. Tallan
Air Force Systems Command/LLP
Wright-Patterson AFB, OH 45433
(513) 255-2802

Dr. Stephen Teitel
LASSP Clark Hall
Cornell University
Ithaca, NY 14853
(607) 256-3963

Dr. Cecil Teller
Southwest Research Institute
P. O. Box 28510
San Antonio, TX 78284
(512) 684-5111 X2939

Dr. Graham Thomas
Drexel University
Philadelphia, PA 19104
(215) 895-2319

Dr. Donald O. Thompson
Rockwell International Science Center
P. O. Box 1085
Thousand Oaks, CA 91360
(805) 498-4545

Dr. R. B. Thompson
Rockwell International Science Center
P. O. Box 1085
Thousand Oaks, CA 91360
(805) 498-4545

Dr. Robb Thomson
Institute of Material Research, Room B354
National Bureau of Standards
Washington, DC 20234
(301) 921-3814

Mr. Daniel Tichenor
Sandia Laboratories - Livermore
Livermore, CA 94550
(415) 422-3007

Dr. Jerry Tiemann
General Electric Company
Schenectady, NY 12345
(518) 385-8667

Dr. Bernard Tittmann
Rockwell International Science Center
P. O. Box 1085
Thousand Oaks, CA 91360
(805) 498-4545

Dr. Chen S. Tsai
Department of Electrical Engineering
Carnegie-Mellon University
Pittsburgh, PA 15213
(412) 578-2461

Dr. M. "Buck" Van Wanderham
Florida Research & Development Center
Pratt & Whitney
P. O. Box 2691
West Palm Beach, FL 33402
(305) 844-7311 X3435

Dr. Vasundara Varadan
Mechanics Department, Boyd Laboratory
Ohio State University
155 W. Woodruff Avenue
Columbus, OH 43210
(614) 422-3531

Professor Vijay K. Varadan
Ohio State University
155 W. Woodruff Avenue
Columbus, OH 43210
(614) 422-6446

Dr. C. F. Vasile
Rockwell International Science Center
P. O. Box 1085
Thousand Oaks, CA 91360
(805) 498-4545

Mr. Rolf S. Vatne
ORGN. B-6620, MS 73-05
Boeing Airplane Company
P. O. Box 3707
Renton, WA 98055
(206) 237-7584

Dr. John R. M. Viertl
Research Center, Bldg. 37, Room 5030
General Electric Company
Schenectady, NY 12345
(518) 385-3980

Mr. William M. Visscher
Theoretical Division
Los Alamos Scientific Laboratory
P. O. Box 1663
Los Alamos, NM 87545
(505) 667-6100

Mr. Steven A. Wallace
Union Carbide Nuclear Division, Bldg. 9203
Oak Ridge Y-12 Plant
P. O. Box Y
Oak Ridge, TN 37830
(615) 483-8611 X3-5801

Mr. R. D. Weglein
Hughes Research Laboratories
3011 Malibu Canyon Road
Malibu, CA 90265
(213) 456-6411 X214

Dr. David Weinstein
W. W. Hansen Laboratory of Physics
Stanford University
Stanford, CA 94305
(415) 497-2300

Mr. Michael F. Whalen
Adaptronics, Inc.
Westgate Research Park
7700 Old Springhouse Road
McLean, VA 22101
(703) 893-5450

Professor R. M. White
Department of Electrical Engineering
Electronics Research Laboratory
University of California
Berkeley, CA 94720
(415) 642-0540

Mr. George A. Whiteside
Systems Research Laboratories
2800 Indian Ripple Road
Dayton, OH 45440
(513) 426-6000

Mr. A. Whiting
Southwest Research Institute
8500 Culebra Road
San Antonio, TX 78206
(512) 684-5111

Mr. F. T. Williams
NASA KSC
VE-MSP
Kennedy Space Center, FL 32899
(305) 867-2039

Dr. Y. H. Wong
Department of Physics
Wayne State University
Detroit, MI 48202
(313) 577-2720

Mr. Larry Youngblood
Rohr Marine, Inc.
P. O. Box 2300
Chula Vista, CA 92012
(714) 575-4111

Dr. Frank Yu
Department of Electrical Engineering
W. W. Hansen Laboratories of Physics
Stanford University
Stanford, CA 94305
(415) 497-2300

Dr. John R. Zurbrick
Aircraft Engine Division
General Electric Company
MS M87
Cincinnati, OH 45215
(513) 243-2154

Address Unknown

J. Camahort
A. D. Jonath
Wendall Lehr

*U.S.Government Printing Office: 1979 — 657-002/653